14th International Conference on Clouds and Precipitation

Proceedings — Volume 3

Bologna, Italy

19-23 July 2004

14th International Conference on Clouds and Precipitation
Bologna, Italy
18-23 July 2004

Conference Organization

International Commission on Clouds and Precipitation (ICCP)
(All members were on the Program Committee)

G.A. Isaac, President	Canada	Z. Levin, Vice President	Israel
D. O'C. Starr, Secretary	USA		
M. Barth	USA	A. Blyth.	UK
A. Bott	Germany	N. Chaumerliac	France
A. Chernikov	Russia	T. Choularton	UK
P.C.S. Devara	India	Yasushi Fujiyoshi	Japan
S. Fuzzi	Italy	W.W. Grabowski	USA
J. Hallett	USA	J. Jensen	USA
A. Korolev	Canada	D. Lamb	USA
H. Larsen	New Zealand	Jinli Liu	China
U. Lohmann	Canada	S. P. Malinowksi	Poland
M. Nicolini	Argentina	K.J. Noone	Sweden
G. Raga	Mexico	J. Stith	USA
D. Terblanche	South Africa		

Honorary Members: Sir John Mason, UK and H. Pruppacher, Germany
Past Presidents: P. Jonas, UK and P. Hobbs, USA

Local Arrangements Committee

Sandro Fuzzi, Chair
Vincenzo Levizzani, Deputy chair
Franco Prodi, ISAC Director
Maria Teresa Tibaldi, Secretary
Giuseppe Bortolotti, Francescopiero Calzolari, Elsa Cattani, Fabrizia Cavalli, Stefano Decesari, Lorenza Emblico, Maria Cristina Facchini, Carlo Franceschi, Elisabetta Masetti, Mihaela Mircea, Francesca Pollini, Sara Poluzzi, Fabrizio Roccato, Francesca Torricella, Giuliano Trivellone

The International Commission on Clouds and Precipitation

dedicates

the 14th International Conference on Clouds and Precipitation

to

Prof. Dr. Hans R. Pruppacher

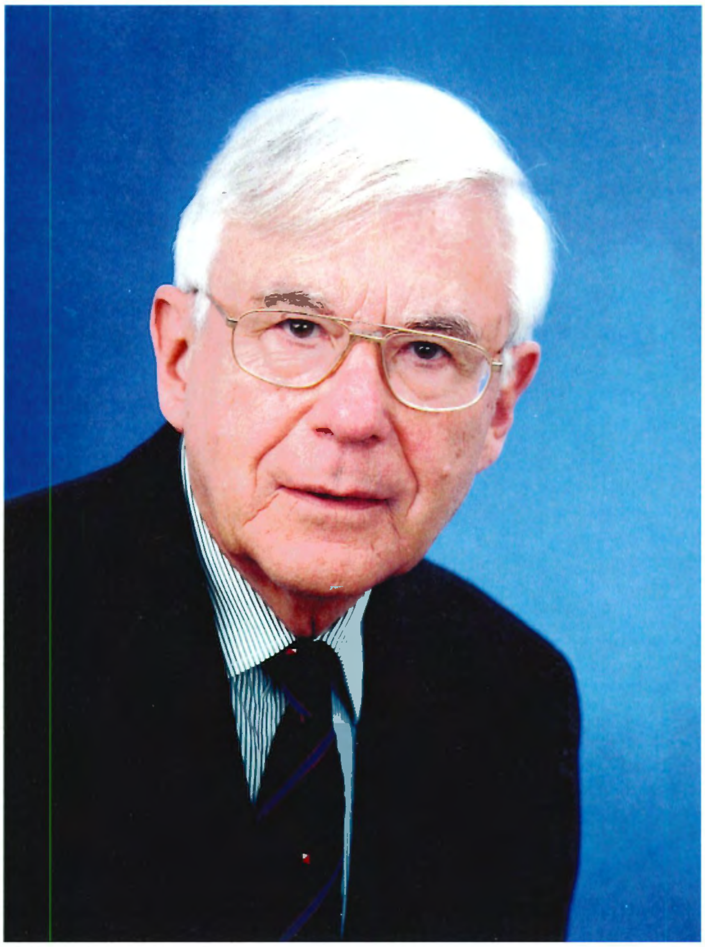

for his fundamental contribution to increase the level of understanding of clouds and precipitation and their physical and chemical mechanisms. Hans Pruppacher has dedicated a lifetime to explore the frontiers of cloud microphysics, steer interdisciplinary research, and teach a great number of students the fundamentals of science and life.

Thank you, Hans!

Paper	Table of Contents – Papers	Page

Paper	Table of Contents – Papers	Page

Paper	Table of Contents – Papers	Page

Paper	Table of Contents – Papers	Page

TOPIC 7: CLOUD ELECTRICITY

TOPIC 8: INSTRUMENTATION

Paper	Table of Contents – Papers	Page

TOPIC 12: CLOUD DYNAMICS AND STRUCTURE

Author Index

NUMERICAL MODELLING OF MOIST DECAYING TURBULENCE: CLOUD-CLEAR AIR MIXING AT RESOLUTION BETTER THAN 1CM.

Mirosław Andrejczuk[1], Wojciech W. Grabowski[2], Szymon P. Malinowski[1] and Piotr K. Smolarkiewicz[2]

[1]Warsaw University, Institute of Geophysics, Warsaw, Poland
[2]National Center for Atmospheric Research, Boulder, CO, USA

1. INTRODUCTION

Despite recent progress in cloud physics, the understanding of key issues such as spatial distribution of cloud particles, turbulent mixing of clouds with the environment, or interaction of turbulence and microphysics, is still far from being complete. These issues are important, beyond fundamental understanding, in applications such as radiative transfer through clouds, initiation of precipitation in warm (i.e., ice-free) clouds, and parameterization of small-scale and microscale processes in models resolving larger scales.

Cloud observations at very small scales (sub-meter) are scarce and incomplete. Thus strong assumptions about cloud turbulence are typically made in small-scale studies concerning interactions among cloud microphysics, thermodynamics, and dynamics. Usually, it is assumed that cloud turbulence is generated at larger scales (say, 100~m or more) and a well-developed inertial range of turbulent eddies exists down to the dissipation scale (see the reviews by Vaillancourt and Yau 2000 and Shaw 2003). At small scales, turbulent velocities are assumed to be homogeneous and isotropic, and they are described by statistical distributions that fit measurements (laboratory, wind tunnel, atmospheric boundary layer, etc.) or results from Direct Numerical Simulation (DNS). Also, it is typically assumed that temperature and moisture are merely passive scalars that do not influence small-scale dynamics through buoyancy effects (e.g., Pinsky and Khain 1997, and Shaw and Oncley 2001). In general, however, it is unclear how results based on such assumptions correspond to natural processes in clouds (Grabowski and Vaillancourt 1999). The present work is an attempt to answer these uncertainities by direct simulation of the interfacial microscale mixing (i.e., mixing occuring at sub-meter scales).

Authors study the impact of evaporative cooling and cloud droplets' sedimentation on the generation of the turbulent kinetic energy (TKE) and other properties of microscale turbulence. We discuss here results from a series of idealized numerical simulations of decaying moist turbulence in a sample volume 64cm*64cm*64cm. Evolution of turbulent, filamented cloud-clear air structure is simulated on the mesh of 64^3, 128^3 and 256^3 gridpoints. These simulations are straightforward continuation of work by Andrejczuk et. al. 2004. They obey simulations with higher spatial resolution in order to understand influence of incomplete representations of smallest scales of motion on the experiment.

Corresponding author address:
Szymon Malinowski, Warsaw University, Institute of Geophysics, ul. Pasteura 7, 02-093 Warsaw, Poland;
e-mail: malina@igf.fuw.edu.pl

2. SETUP OF THE NUMERICAL EXPERIMENT

Deatils of the setup are given in Andrejczuk et. al., 2004, here only a short decription will be given. Authors simulate in an idealized way selected aspects of the laboratory experiment described in Malinowski et. al., 1998 and Malinowski et. al., 2004. The initial setup is, however, not aimed at the most realistic repetition of the lab case which would be very costly in term of computation demands and questionable due to difficulties proper description of the outflow from the chamber. Numerical experiments are intended rather to investigate some physical features of mixing, as small-scale TKE generation by evaporative cooling at the edges of cloudy filaments and possible role of droplet sedimentation in LWC transport across the cloud-clear air interface. Similar approach is widely used in many DNS (Direct Numerical Simulations) of turbulence: they do not start from realistic initial and boundary conditions, simulations are, however, carefully planned to represent properly key features of the flows.

The model used in this simulations is nonhydrostatic anelastic model (encryption EULAG) described by Smolarkiewicz and Margolin (1997), with moist thermodynamics by Grabowski and Smolarkiewicz (1996). Dynamics and and thermodynamics of the model are prescribed in the following set of equations:

$$\frac{D\mathbf{v}}{Dt} = -\nabla\pi + \mathbf{k}B + \mu\Delta\mathbf{v}\ ;$$

$$\nabla\mathbf{v} = 0\ ;$$

$$\frac{D\theta}{Dt} = \frac{L\theta_e}{c_p T_e} C_d + \mu_\theta \Delta\theta\ ;$$

$$\frac{Dq_v}{Dt} = -C_d\ ;$$

where **v**-velocity vector, π-pressure perturbation with respect to a hydrostatically balanced environment profile normalized by the density, **k**-vertical unit vector, L, c_p - latent heat of condensation and specific heat at constant pressure, C_d - condensation rate; θ - potential temperature; q_v, q_c - water vapor and cloud water mixing ratios, μ μ_θ - viscosity and thermal diffusivity of the air. Index "e" denotes environmental undisturbed value and B is buoyancy defined as:

$$B = g\left(\frac{\theta - \theta_e}{\theta_0} - \varepsilon\,(q_v - q_{ve}) - q_c\right);$$

where $\varepsilon=R_v/R_d-1$, R_v/R_d - ratio of gas constants for water vapour and dry air, g- acceleration of gravity, θ_e- environmental temperature profile.

We use two alternative parameterizations of microphysical processes:

1) Bulk microphysics, where production/depletion of LWC depends in simple manner on condensation/evaporation:

$$\frac{Dq_c}{Dt} = C_d.$$

2) Detailed parameterization of microphysics, closely following Grabowski (1989), where we solve conservation equation for the number density function of cloud droplets $f(x,r,t)$ accounting for droplet sedimentation velocity. Here $f(x,r,t)dr$ is the concentration of droplets of radius between r and $r+dr$ at a given point x in space and at given time t evolving according the equation:

$$\frac{Df(\mathbf{x},r,t)}{Dt} = \frac{\partial\eta}{\partial t} - \frac{\partial}{\partial r}\left(f(\mathbf{x},r,t)\frac{dr}{dt}\right).$$

Here $D/Dt=\partial/\partial t$ + $(v-v_t(r_i))\nabla$, $v_t(r_i)$ is sedimentation velocity for the droplets of the radius r_i . dr/dt describes changes of the number density function due to diffusional growth of cloud droplets $dr/dt=AS/r$, $A=10^{-10}$ m^2/s, $S=q_v/q_{vs}$, is supersaturation, and $\partial\eta/\partial t$ is the nucleation rate. For the finite number of droplet size bins the condensation rate is given by:

$$C_d = \sum_i f_i \frac{dm_i}{dt}.$$

In the simulation presented here we use 16 classes of droplets (radius in range 0.78-24 μm). Sedimentation velocity is prescribed for each class according to Stokes law: $v_t(r)=Cr^2$, where C gives 1 cm/sec for 10 μm droplet.

Initial dynamical setup was adopted from typical DNS simulations with decaying turbulence, formulated after Herring and Kerr (1993) in Fourier space:

$$\begin{pmatrix} u \\ v \\ w \end{pmatrix}(k,0) = Ak^2 \exp\left(-\left(\frac{k}{k_0}\right)^2\right)(\cos(2\pi\psi) + i\sin(2\pi\psi)).$$

Here u,v,w are velocity components, k – wavenumber, k_0=4.7568, A – depends on initial TKE, ψ- is random. The value of constant A is the same as in the low TKE case of simulations of Andrejczuk et al., 2004 and corresponds to low levels of TKE dissipation observed in clouds. Identical as in Andrejczuk et al. 2004 is also the initial field of LWC, boundary conditions (cyclic in three dimensions). Potential temperature of the environmental air was set to 293K and relative humidity to 65%. Thermodynamical conditions should be representative to the top of the warm summer Cumulus cloud and resemble conditions in the cloud chamber.

3. RESULTS

Results presented here compare outputs from six numerical experiments: three with bulk parameterization of microphysics thermodynamics and three with the detailed one, each calculated on grid of 1cm, 0.5cm and 0.25cm spatial resolution. Increase of the resolution causes, that small-scale dynamics has a better representation in the model. On the other hand, at the maximum resolution, parameterization of microphyisics becomes questionable. In typical the volume corresponding to the gridbox size we may expect few tens of droplets.

In the following we present most important results in series of seven figures.

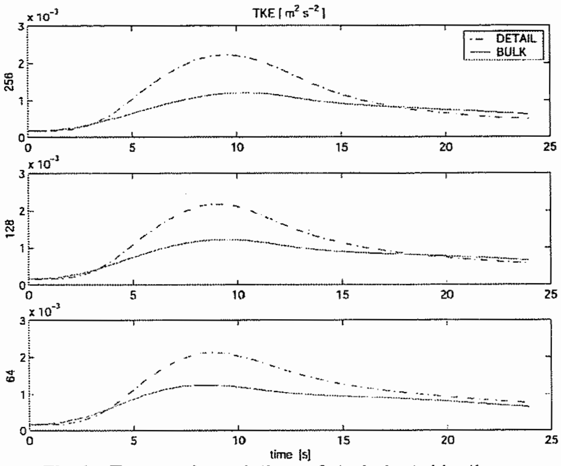

Fig.1. *Temporal evolution of turbulent kinetic energy (TKE) in the experiment with grid 256^3 (upper panel) 128^3 (middle panel) and 64^3 (lower panel). Continuous line presents results for bulk microphusics, while dash-dot line for detailed.*

Fig. 1 indicates the whole evolution of TKE, which is governed by production due to evaporative cooling of droplets (dominating till 9th second) and dissipation. Is almost identical in all three meshes.

In Fig. 2 temporal evolution of the volume averaged enstrophy ($E_n=0.5<\omega^2>$, where ω is vorticity) is presented. While shapes of the corresponding curves in all three panels are almost identical, the values are increasing with increase of the domain size. The reason can be better representation of cloud-clear air interface on a dense mesh.

Vorticity is generated by evaporative cooling and resulting density gradient at the cloud-clear interface. At 256^3 gridboxes, which allows for more convolutions than 64^3, the surface of the interface is much larger. There is experimental evidence, that such small-scale filaments exist, in the paper by Malinowski et al., 2004, image from the cloud chamber presents convoluted filaments of cloudy and clear air at scales of millimeters. The second reason for such behavior is also geometrical: gradients of density on finer mesh can be larger. Both effects lead to the better representation of the interface which results in stronger vorticity and larger enstrophy value.

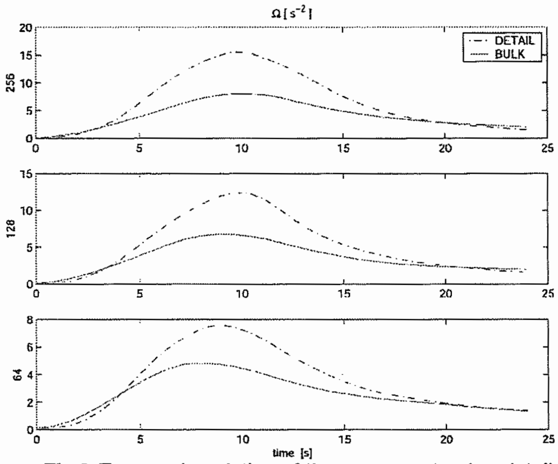

Fig.2 *Temporal evolution of the mean enstrophy, details as in Fig.1.*

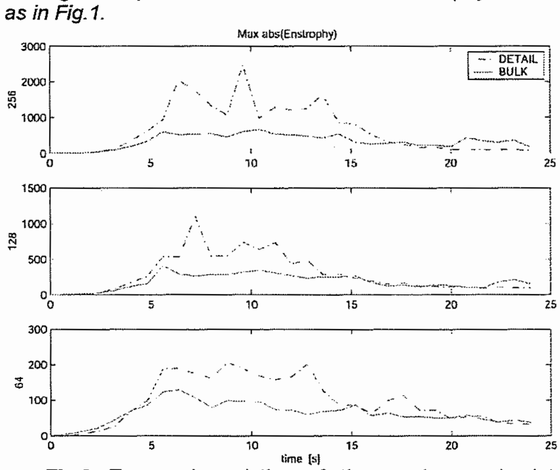

Fig.3 *Temporal evolution of the maximum absolute enstrophy, details as in Fig.1.*

This second reason seems dominating after analysis of Fig. 3, where evolution of maximum absolute enstrophy is presented. Again, enstrophy values increase with the increasing grid resolution, but taking the maximum value accounts accounts for the local properties (gradients), not the integral properties (surface of the interface) of the flow.

In Fig.4 a temporal evolution of the Taylor microscale Reynolds number is presented. It is defined by the equation:

$$R_\lambda = \frac{TKE}{\mu} * \left(\frac{10}{3E_n}\right)^{1/2}$$

Result is consistent with Figs.1 and 2: evolution is almost independent on the gridbox size in the investigated flows, slight differences in the value result from differences in mean enstrophy suppressed by the square root in the equation.

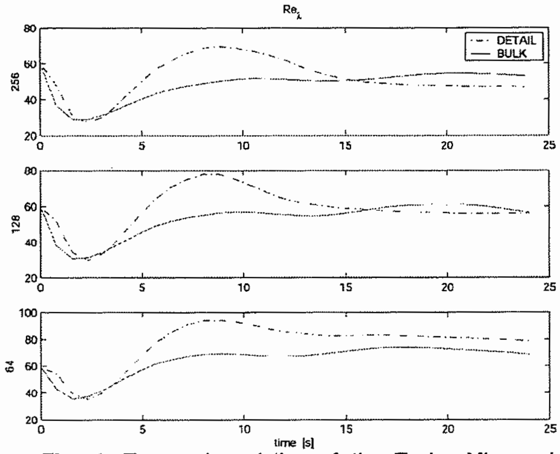

Fig. 4. Temporal evolution of the Taylor Microscale Reynolds number, details as in Fig.1.

It is interesting, how anisotropy of the flow, reported by Andrejczuk et al. is dependent in on the grid resolution. This can be answered by inspection of Figs. 5 and 6 presenting temporal evolution of the horizontal and vertical velocity derivative skewness. For i-th component of the flow, the velocity derivative skewness is defined by the equation:

$$S_i = \left\langle \left(\frac{\partial u_i}{\partial x_i}\right)^3 \right\rangle / \left\langle \left(\frac{\partial u_i}{\partial x_i}\right)^2 \right\rangle^{-3/2} .$$

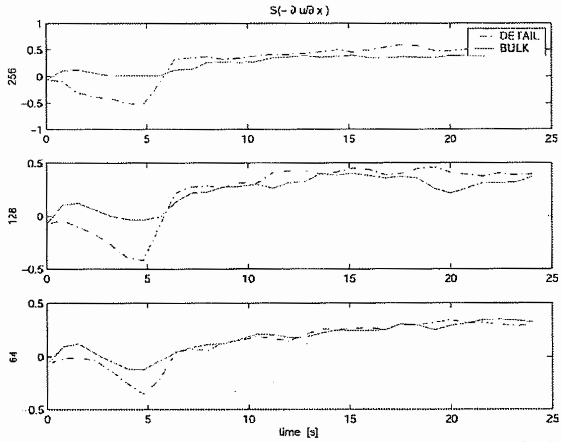

Fig.5 *Temporal evolution of the horizontal velocity derivative skewness, details as in Fig.1.*

It seems, that increase in grid resolution leads to slightly greater value of skewness, while does not influence the temporal evolution of this value.

Vertical velocity derivative skewness practically does not depend on the grid resolution. This is an interesting result, suggesting, that horizontal gradients are better represented in a dense grid, while for the vertical gradient representation is good enough already at 1cm resolution.

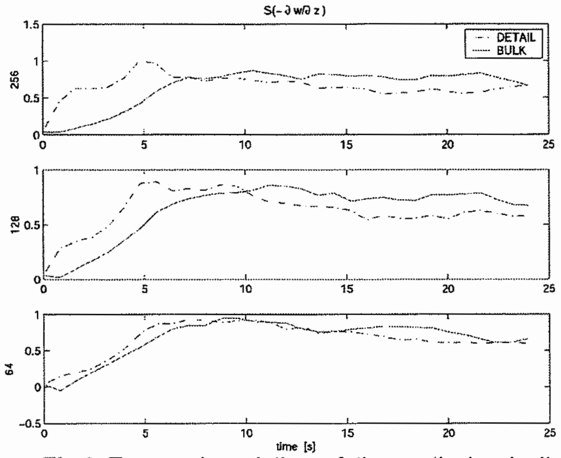

Fig.6 *Temporal evolution of the vertical velocity derivative skewness, details as in Fig.1.*

This, together with differences in evolution and values of horizontal and vertical velocity skewness (compare Figs 5 and 6) proves, that anisotropy in the cloud-clear air mixing is important.

Finally we present evolution of the mean volume diameter of droplets, which can be investigated in runs with the detailed microphysics only.

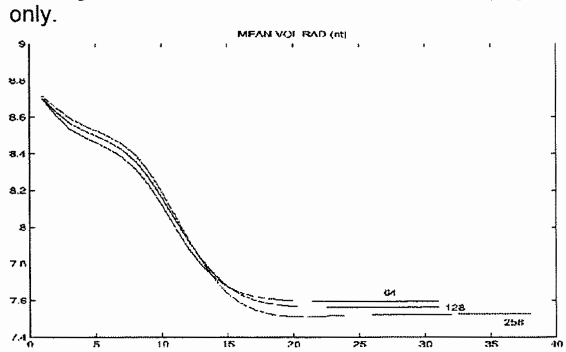

Fig.6 *Temporal evolution of the volume mean droplet radius.*

We see from the above plot, that in the first stage of simulations, when droplets evaporate cooling, due to which TKE and enstrophy are produced during mixing leads to initially slow and then faster reduction of the mean volume radius. Differences between grids are minor. Additional analysis of LWC and droplet spectra (not shown here), leads to the conclusion that modeled mixing is in between two extreme models of homogeneous and inhomogeneous mixing process.

4. CONCLUSIONS

In the analyzed scales kinetic energy of microscale motions comes not only from the classical downscale energy cascade, but it is also generated internally due to the evaporation of cloud droplets. In a case of low initial TKE in simulations, mixing and homogenization are dominated by the TKE generated as a result of evaporation of cloud water and its impact on the microscale buoyancy. Enstrophy production by microscale buoyancy is substantial, leading to high anisotropy of small-scale turbulence.

Differences between simulations with 1cm and 0.25cm resolution are minor, except for enstrophy production, which is substantially larger when smallest scales are fully resolved. This suggests importance of very small turbulent structures at the edge of filaments characterized by large shear.

Impact on cloud microphysics is also quantified. Cloud droplet spectra at the end of the simulations correspond to neither extremely inhomogeneous nor homogeneous mixing scenarios, the two possible limits where neither cloud droplet size nor the number of cloud droplets is allowed to change, respectively.

5. ACKNOWLEDGMENTS

This research was partially supported by European Commission V-th Framework program project EVK2-CT2002-80010-CESSAR. The National Center for Atmospheric Research is supported by the National Science Foundation

6. REFERENCES:

Andrejczuk M, W.W. Grabowski, S.P. Malinowski and P.K. Smolarkiewicz 2004. *J. Atmos. Sci.*, accepted for publication.

Grabowski, W. W., 1993: Cumulus entrainment, fine scale mixing and buoyancy reversal. Q. J. R. Meteorol. Soc., 119, 935-956

Grabowski, W. W., and P.K. Smolarkiewicz, 1996: Two-time-level semi-Lagrangian modeling of precipitating clouds. *Mon. Wea. Rev.*, 124, 487-497.

Grabowski, W. W. and P. A. Vaillancourt, 1999: Comments on "Preferential Concentration of cloud droplets by turbulence: Effects on the early evolution of cumulus cloud droplet spectra"., J.Atmos.Sci., 56, 1433-1436.

Herring J.R. and R.M. Kerr, 1993: Development of enstrophy and spectra in numerical turbulence. *Phys. Fluids A* 5 (11), 2792-2798.

Malinowski, S.P., I. Zawadzki and P. Banat, 1998: Laboratory observations of cloud clear air mixing in small scales. *J. Atmos. Oceanic Technol.*, **15**, 1060-1065.

Malinowski S.P., Piotr M. Korczyk and Tomasz A. Kowalewski, 2004: Mixing of cloud and clear air in centimeter scales observed in laboratory by means of particle image velocimetry. *In this volume.*

Pinski, M.B. and A.P. Khain, 1997: Turbulence effects on the collision kernel.I: Formation of velocity deviations of drops falling within a turbulent three-dimensional flow. *Q. J. R. Meteorlol. Soc.*, **123**, 1517-1542.

Shaw, R. A. and S. P. Oncley, 2001: Acceleration intermittency and enhanced collision kernels in turbulent clouds. Atmos. Res., 59-60, 77-87.

Shaw R. A. 2003. Particle-turbulence interactions in atmospheric clouds. *Annu. Rev. Fluid Mech.* 35, 183-227, 2003.

Smolarkiewicz, P.K., and L.G. Margolin, 1997: On forward -in-time differencing for fluids: An Eulerian / semi-Lagrangian nonhydrostatic model for stratified flows. *Atmos.-Ocean*, 35, 127-152.

Vaillancourt, P.A. and M. K. Yau, 2000: Review of particle-turbulence interactions and consequences for cloud physics. *Bull. Amer Meteorol. Soc.*, 81 (2): 285-298.

ADVANCES IN CLOUD ASSIMILATION AT ECMWF USING ARM RADAR DATA

Angela Benedetti[1] and Marta Janisková

European Centre for Medium–Range Weather Forecasts, Reading, RG2 9AX, UK

1. INTRODUCTION

One of the most challenging aspects of weather and climate prediction is the accurate treatment of clouds and precipitation. In recent years, models have been improved to obtain more accurate forecasts and analysis of cloud and rain fields. At the same time, there has been an increase in observational programs aimed at offering cloud measurements from active and passive instruments. Among those, the Atmospheric Radiation Measurement (ARM) program has created a high–quality, exhaustive data base of cloud observations that represents a great resource for model evaluation and improvement. The ARM data sets also offer an ideal platform to study the impact of assimilation of new observations from cloud radars or lidars in preparation for upcoming satellite missions such as CloudSat, CALIPSO, and EarthCARE.

In this study, cloud radar reflectivity profiles from the Multi–Mode Cloud Radar (MMCR) are used in a one–dimensional (1D–Var) method to improve model first guess of temperature and specific humidity. The model background fields (temperature, specific humidity and surface pressure) come from a twelve–hour ECMWF forecast while cloud fields are computed using a new statistical large–scale scheme (Tompkins and Janisková, 2004) and a convective scheme (Lopez and Moreau, 2004), both developed for assimilation purposes. Radar reflectivity profiles at 35 GHz are derived from the model cloud fields and temperature using precomputed look–up tables based on Mie calculations for the hydrometeor optical properties.

Results from the 1D–Var are verified against the radiosonde soundings routinely taken at the ARM sites. Indirect verification is also provided by comparison with total column water vapor observations. The lessons learned from the 1D–Var will serve as guidance toward 4D–Var assimilation of cloud–related observations .

[1] Corresponding author address: Angela Benedetti, European Centre for Medium–Range Weather Forecasts, Shinfield Park, Reading, RG2 9AX, UK;
E-mail: Angela.Benedetti@ecmwf.int

2. DESCRIPTION OF THE 1D–VAR SYSTEM

The goal of the 1D–Var retrieval is to find the optimal model state, $\mathbf{x}_a$, that simultaneously minimizes the distance to the observations, $\mathbf{y}_o$, and to a background model state, $\mathbf{x}_b$ (i.e., a previous short-range forecast). The model state $\mathbf{x}$ consists of the vertical profiles of temperature and specific humidity, which are the control variables. A quasi-Newton algorithm is employed to minimize the following cost function

$$\begin{aligned} J \; = \; & \frac{1}{2}(\mathbf{x}-\mathbf{x_b})^{\mathbf{T}}\mathbf{B}^{-1}(\mathbf{x}-\mathbf{x_b}) + \\ & \frac{1}{2}(H(\mathbf{x})-\mathbf{y_o})^{\mathbf{T}}\mathbf{R}^{-1}(\mathbf{H}(\mathbf{x})-\mathbf{y_o}) \end{aligned} \tag{1}$$

where $\mathbf{B}$ and $\mathbf{R}$ are respectively the background and observation error covariance matrices, and H is the observation operator which projects the model state into observation space. Here, $\mathbf{B}$ is the ECMWF operational background matrix. The operator H consists of two simplified parameterizations of moist atmospheric processes: a convection scheme (Lopez and Moreau, 2003) and a large–scale condensation scheme (Tompkins and Janisková, 2004) plus the radar forward model to convert model fields into reflectivities. In the next section we briefly describe the approach used to compute the equivalent radar reflectivity.

3. RADAR REFLECTIVITY MODEL

The radar backscattering cross-section derived from the radar return power can be related to the amount of solid precipitation (rain and snow) and the amount of cloud ice/water content that the radar signal encounters in its path. The forward modeling of this radar signal can be performed by assuming a size distribution of the scatterers and by computing their optical properties. Here it is assumed that all rain/snow/cloud ice and water particles are spherical. Their optical properties are computed using the Mie solution at the frequency of interest and as functions of temperature, and then integrated by assuming a Marshall–Palmer distribution for the precipitation–sized particles and a modified–gamma distribution for the cloud particles. The radar reflectivity factor is proportional to the integral of the backscattering cross–section over the size distribution. A variable commonly used to describe the radar return is the equivalent radar reflectivity, hereafter indicated with the symbol Z, which represents the radar reflectivity factor that an equivalent volume of spherical water droplets would be associated with. If the target particles are in a solid phase, it is necessary to convert the raw reflectivity factor into an equivalent reflectivity. This is done in the forward model assuming a fixed density for the snow (ρ=0.1 g cm^{-3}) and cloud ice (ρ=0.9 g cm^{-3}). In presence of intense precipitation, the radar signal is attenuated. By computing the total optical depth and the path–integrated attenuation, the attenuated profile of reflectivity can be computed. To speed up computational time, all reflectivity values are collected in a look–up table and organized according to the values of temperature and cloud liquid/ice water and precipitation contents. A bilinear interpolation is then applied to extract the reflectivity value corresponding to the given model temperature and hydrometeor contents. A special treatment of the melting layer is also included in the computation of the look–up table, although is only applied at exactly 0°C. The reflectivity values contained in the look–up table were verified against those derived from other forward models and those derived from simple Z–R/LWC relationship. Comparisons show that the current forward model is reliable within a few dBZs. Research to better quantify forward modeling errors is currently undergoing.

4. SGP ARM OBSERVATIONS

The assimilation experiments were carried out using reflectivity observations taken at the ARM Southern Great Plains site (36.6N–97.5W) during January 2001. The reflectivities are averaged over one hour interval (Morcrette, 2002). In a previous study by Janisková *et al.* (2002), an older version of the 1D–Var system described above was used to assimilate longwave and shortwave radiative fluxes together with total column water vapor (TCWV) and cloud liquid–water path (LWP) derived from the SGP Microwave Radiometer (MWR). Results from the assimilation of these measurements were evaluated by computing an equivalent radar reflectivity using Z–LWP/IWP relationships and by comparing the latter against the radar reflectivity measured by the SGP MMCR.

In this study, we investigate the use of MMCR reflectivities for direct assimilation using the forward radar model described in section 3. to compute the model–equivalent reflectivities. The other available observations such as TCWV are used , in turn, to evaluate the performance of the reflectivity 1D–Var. A comparison is also made between the retrieved temperature and humidity profiles and observations from the radiosoundings at Lamont (Oklahoma).

5. ASSIMILATION EXPERIMENTS

5.1 Background profiles

The background temperature and specific humidity profiles are taken from the 12–hour forecast from the ECMWF model with T511 spectral truncation (corresponding to approximately 40 km) and 60 vertical levels. The profiles represent mean values for the the nearest grid–points around the ARM–SGP site. These profiles of T and q, along with surface pressure, p_s, tendencies, and surface quantities are used in the moist physics routines to compute cloud properties (cloud cover, ice and liquid–water contents) and precipitation fluxes. The radar observation operator is then applied to the model fields to obtain the equivalent reflectivity.

5.2 Observation quality control and errors

Preliminary tests show that the model gives values of reflectivity which are consistently higher than the MMCR observations when rain is present. The nominal dynamic range of the MMCR is between -40 and 20 dBZ. However, the signal might be already saturated at reflectivities between 8 and 10 dBZ due to the gradually slower clipping in the receiver. After several discussions with some of the MMCR experts (E. Clothiaux, P. Kollias, K. Moran, private communication), it was decided to only use reflectivity observations between -40 and 8 dBZ and above 1 km elevation to minimize the clipping effect of the range correction. Plans for the future include the monitoring of heavy rainy situation using independent data sets such as rain gauge observations, and the black–listing of the observations in dubious, i.e. heavy–precipitating, conditions. In such occurrences, it could be sensible to apply a larger error to the observations. Currently, the error on observed reflectivities is fixed to 1dBZ (approximately 25%) at all levels.

5.3 Discussion of the results

Results of the assimilation for January 2001 are shown in Figs. 1–3. Panel 2 shows a comparison of the first guess and the 1D–Var retrieved radar reflectivity versus the MMCR observations. The 1D–Var analysis is closer to the observations for most of the profiles. Focusing on the first days of the month, it is possible to see that the 1D–Var showed skills in increasing the reflectivity at lower levels. A reduction in reflectivity consistent with the observations is shown by the analysis at upper levels around January 6–7. Less effective is the reduction around January 10, when the observations showed no clouds while the model first guess had large values of reflectivity. Good agreement between analysis and observations is shown on January 16–17 where the cloud patterns are well adjusted to the observations. Major adjustments from the 1D–Var are also evident toward the end of the month (January 27–28).

Figure 1 shows the profiles of relative humidity bias and standard deviation averaged over a month. The dashed line represents the background departures (radiosonde observations minus background) while the solid line represents the analysis departures (radiosonde observations minus analysis). The analysis produces relative humidity profile which is closer to the observations (lower bias) and has a smaller standard deviations at most levels. This positive impact is partially diluted by the fact that the statistics are computed for the whole month, whereas the 1D–Var is active only when the MMCR recorded the presence of clouds.

The comparison against observed TCWV (only available for non–rainy situations) is presented in Figure 3 as difference between the absolute value of first guess minus the observations, and the absolute value of the 1D–Var analysis minus the observations. When this difference is positive, the analysis is closer than the first guess to the observed values, i.e. the 1D–Var has correctly modified temperature and specific humidity to produce values of TCWV that better match the observations. The contrary is true when the difference is negative. The general trend in Figure 3 shows slightly more positive values than negative values indicating a generally good skill of the 1D–Var.

6. PRELIMINARY CONCLUSIONS

Generally the assimilation of the reflectivity observations produces a positive impact on the model fields. Direct comparison with the MMCR reflectivities showed that the 1D–Var minimization was mostly successful and the changes to the temperature and humidity profiles produced cloud fields that provided a better match to the observed reflectivity. Comparison with independent radiosonde measurements shows a reduction in bias and standard deviation. TCWV is also improved by the 1D–Var.

In those few situations where the model did not have clouds initially, for example at the beginning of the month, the 1D–Var still attempted to trigger clouds. In general, however, the 1D–Var system might have difficulties in initiating cloud formation. This is a known behavior of the 1D–Var in the context of the weakly non–linear approximation. If the initial state is not close to saturation and large increments are not allowed by the system design, then it is not possible to force a dramatic change in model state which would allow condensation and cloud formation. Cloud reduction appears to be more effective. This is somewhat intuitive given the nature of the supersaturation process. If the state is close to saturation, even small changes in temperature can induce a large response in condensation/evaporation. Given the amount of water vapor available, the change in cloud cover and liquid or ice–water contents will be noticeable. In general, increments are larger for specific humidity than for temperature. Even if in principle the sensitivity of the moist physics to temperature and specific humidity is comparable, the errors on the background temperature are assumed smaller and the system changes preferentially q rather than T.

Assimilation of radar reflectivities appears to be promising and will be further explored in the near future. We plan to assimilate radar profiles along with observations that constrain the radiative fields such as satellite–observed shortwave and longwave radiation at the top of the atmosphere. The sinergy of different cloud observations will be beneficial toward improving the performance of the cloud assimilation system and exploring 4D–Var assimilation of cloud–related measurements. Further improvements in the model will also allow to exploit the wealth of satellite observations that will become available in the near future.

ACKNOWLEDGMENTS

The useful advice and help of Jean–Jacques Morcrette are gratefully acknowledged. We thank Peter Bauer for help with the radar reflectivity model and Philippe Lopez for useful discussions on the radar 1D–Var. E. Clothiaux, P. Kollias and K. Moran are thanked for their input on the MMCR performance. The SGP observation were courtesy of the ARM Program which is sponsored by the US Department of Energy, Office of Science, Office of Biological and Environmental Research, Environmental Sciences Division. This research was performed under CloudSat NASA grant NAS5–99237 and ESA Contract 13151/98/NL/GD.

REFERENCES

Janisková M., Mahfouf J.–F., and J.–J. Morcrette, 2002: Preliminary studies on the variational assimilation of cloud–radiation observations, *Q.J.R.Meteorol. Soc.*, **128**, 2713–2736.

Morcrette, J.–J., 2002: Assessment of the ECMWF model cloudiness and surface radiation fields at the ARM SGP site, *Mon. Wea. Rev.*, **130**, 257–277.

Lopez, P. and E. Moreau, 2004: A convection scheme for data assimilation: Description and initial tests, ECMWF Technical Memorandum No. 411.

Tompkins, A. M. and M. Janisková, 2004: A cloud scheme for data assimilation: Description and initial tests, *Q.J.R.Meteorol. Soc.*, accepted for publication.

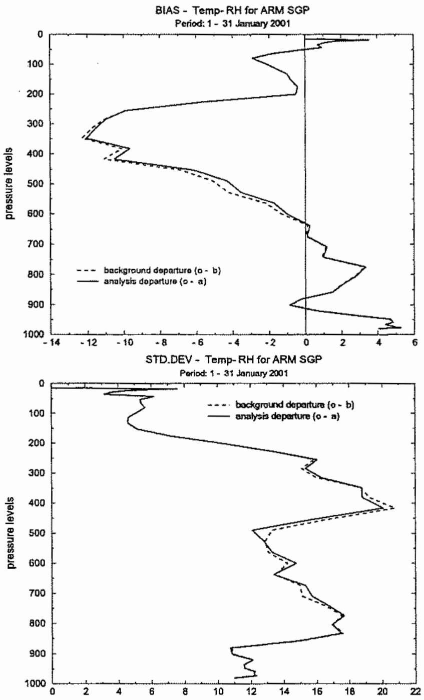

Figure 1: Bias and standard deviation with respect to radiosounding observations in relative humidity for background (dashed line) and 1D-Var retrieved profiles (solid line).

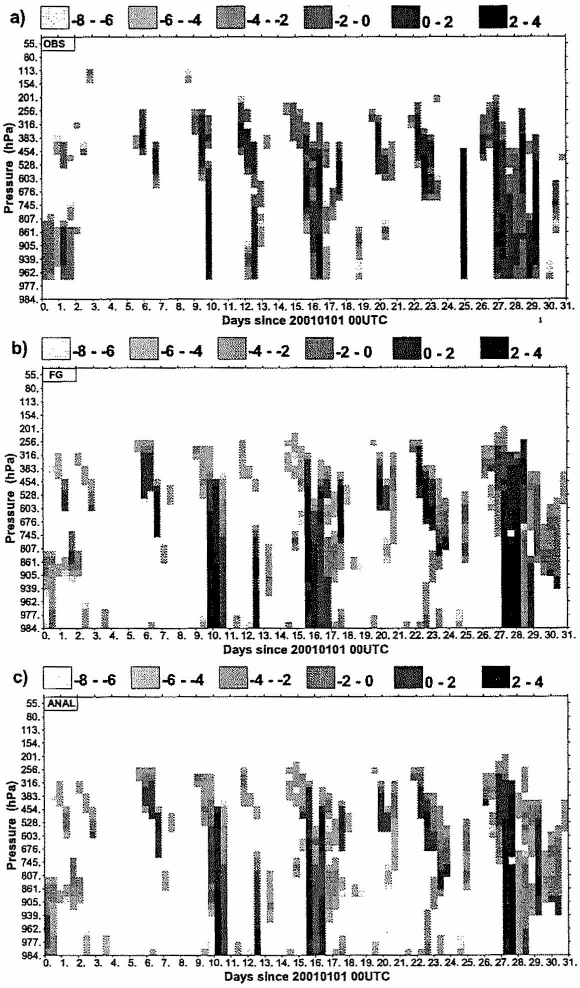

Figure 2: 35 GHz radar reflectivity in dBZ/10 for the month of January 2001: (a) SGP observations; (b) model first guess; (c) 1D–Var retrieval.

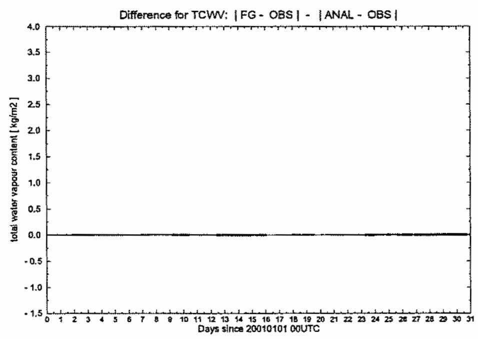

Figure 3: Time series of TCWV differences in $kg.m^{-2}$ (see text for explanations).

PAFOG - A NEW EFFICIENT FORECAST MODEL OF RADIATION FOG EVENTS

Andreas Bott
Meteorologisches Institut, Universität Bonn, Germany

1. INTRODUCTION

The occurrence of fog and low level stratus clouds plays an important role for the safety of ground and air transportation systems. For instance, in the autumn radiation fogs are very often observed over large areas of the northeastern United States, (Jiusto and Lala, 1980) thus disturbing the time–table of airports and the ordered traffic flow on the roads. The literature provides a wide range of numerical models of different complexity for the simulation of radiation fogs, (e. g. Fisher and Caplan, 1963 Forkel *et al.*, 1987 Bott *et al.*, 1990 Siebert *et al.*, 1992 von Glasow and Bott, 1999). In the model MIFOG of Bott *et al.* (1990) fog evolution is simulated by means of a two-dimensional spectral cloud microphysics model. In the past years MIFOG has been extended by including vegetation models for low (Siebert *et al.*, 1992) and tall vegetation (von Glasow and Bott, 1999). With these model versions it is possible to describe the interaction between the atmosphere and the earth's surface covered with different types of vegetation.

Since due to its complexity the coupled fog-vegetation model cannot be used for routine fog forecasts, the parameterized fog model PAFOG has been developed. The main difference between PAFOG and MIFOG is that now the original spectral cloud microphysics module has been replaced by a parameterization scheme. Input parameters of PAFOG are standard meteorological data, that is vertical profiles of temperature and specific humidity as well as the geostrophic wind. In addition to this, PAFOG needs the characteristic data of the vegetated surface, such as canopy height, shielding factor, leaf area index etc. In case of stratiform clouds, the large scale subsidence must also be provided. Besides the usual meteorological model output, PAFOG provides the time evolution of the visibility in different heights of the atmosphere. By running PAFOG on a normal PC, it is possible to obtain within several minutes for a given location a 36 hours forecast.

Corresponding author's address: A. Bott, Meteorologisches Institut, Auf dem Hügel 20, Universität Bonn, 53121 Bonn, Germany. Email: a.bott@uni-bonn.de

2. MODEL DESCRIPTION

A detailed model description of MIFOG is given in Bott *et al.* (1990) and in von Glasow and Bott (1999). Here only a short summary of the governing model equations will be presented. The dynamic part of PAFOG is a one-dimensional model of the atmospheric boundary-layer consisting of a set of prognostic equations for the horizontal wind field, the potential temperature and the specific humidity. Radiation calculations are performed by means of the δ-two stream approximation of Zdunkowski *et al.* (1982) while turbulent mixing is calculated with the 2.5 level model of Mellor and Yamada (1974).

In the microphysical part of PAFOG two prognostic equations are solved for the total droplet concentration N_c and the total specific cloud water content q_c. These equations include advection, turbulent mixing, sedimentation as well as condensation/evaporation processes. The droplet size distribution is described by a log-normal function of the form

$$dN_c = \frac{N_c}{\sqrt{2\pi}\sigma_c D}\exp\left[-\frac{1}{2\sigma_c}\ln^2\left(\frac{D}{D_{c,0}}\right)\right]dD \quad (1)$$

Here, D is the droplet diameter and σ_c is the standard deviation of the given droplet distribution. This quantity depends on the particular aerosol type (maritime, continental, urban) and is prescribed in the model. $D_{c,0}$ is the mean droplet diameter.

At a given supersaturation S the number of activated cloud droplets is calculated according to Twomey's relation

$$N_{act} = CS^k \tag{2}$$

The values of the constants k and C (cm^3) depend on the choice of the particular aerosol model (maritime: $k = 0.7$, $C = 100$, continental: $k = 0.9$, $C = 3500$, urban $k = 0.9$, $C = 10000$). The calculation of the supersaturation S follows the work of Sakakibara (1979), see also Chaumerliac *et al.* (1987).

The vegetation model is due to Siebert *et al.* (1992). It describes the interaction of land surface processes with the overlying atmosphere in terms of three balance equations for the energy and moisture transfer at the surface as well as the energy state of the vegetation layer. Within the soil, heat and moisture transport is treated as a coupled multi-layer system.

3. MODEL RESULTS

The performance of PAFOG has been tested by comparing the model results with routine observations which have been made by the German Weather Service (DWD) at the Lindenberg observatory in Germany during 1998 and 1999. Nine different weather periods comprising of altogether 45 days have been investigated. Weather period I (during 24.09.98–29.09.98) was characterized by the daily formation and dissipation of a typical radiation fog at the ground. During period III (20.11.98–20.11.98) low level stratiform clouds were observed. The periods VIII (10.02.99–12.02.99) and IX (29.03.99–05.04.99) yielded no fog or clouds while the remaining periods produced a mixture of cloud-free days and low level stratiform clouds.

The aim of the investigation was to show that in all different weather situations PAFOG produces acceptable results. In more than 90 % of all investigated days PAFOG agreed with the observations in terms of occurrence or non-occurrence of radiation fog or low level stratiform clouds. Table 1 compares for period I (radiation fog) the observed and modeled times of radiation fog. It is seen that the times of fog formation and dissipation agree quite well between observations and the model. The only exception occurs on 26.09.98 where, in contrast to the observations, the model predicts fog between 0–9 h.

Table 1: Observed and modeled times of radiation fog.

Date	Observation	PAFOG
24.09.98	5–10 h	5–10 h
25.09.98	4–11 h	6–11 h
26.09.98	–	0–9 h
27.09.98	4–9 h	5–9 h
28.09.98	0–10 h	4–9 h
29.09.98	no obs.	6–8 h

Figures 1 and 2 show the simulated time evolution of the liquid water content for the days 24.09.98 and 25.09.98. Figure 1 represents a relatively thin radiation fog event with maximum liquid water contents below 0.3 g m^{-3} and corresponding visibilities of more than 200 m (not shown). Figure 2 is an example for a dense radiation fog with maximum liquid water content of 0.5 g m^{-3} and visibilities below 100 m.

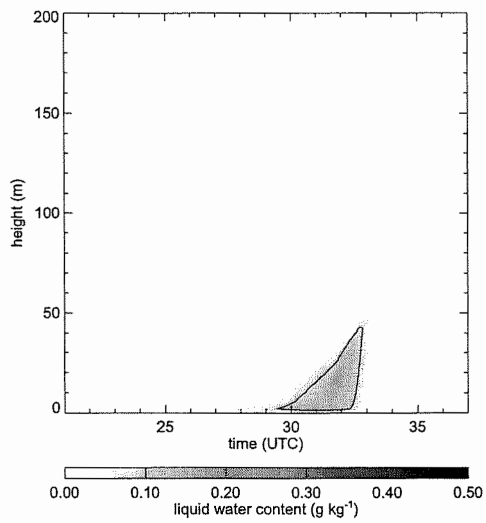

Fig. 1: Fog water content on 24.09.98 as function of time and height.

Figure 3 shows a typical result of a comparison between observed and simulated visibilities. Most

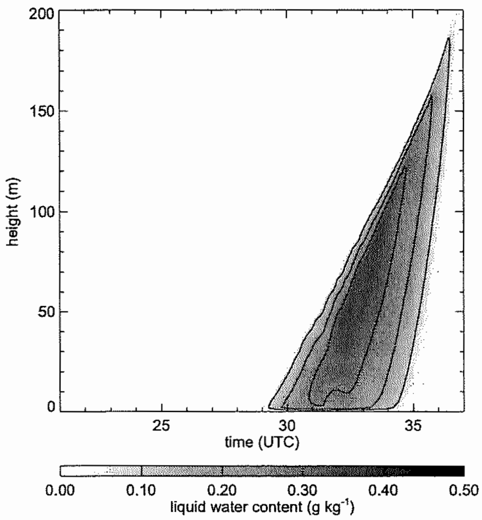

Fig. 2: Fog water content on 25.09.98 as function of time and height.

of the time PAFOG reproduces the evolution of the visibility in reasonable agreement with the observations. On 25.09.98 the simulated fog formation and the corresponding visibility decrease are somewhat delayed. However, the minimum values as well as the time of fog dissipation agree quite well.

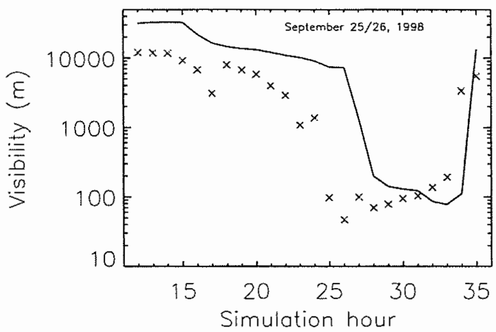

Fig. 3: Observed (crosses) and modeled (full curve) visibility in 2m height on 25.09.98 as function of time.

Sensitivity studies have been performed with PAFOG in which the vegetation parameters entering the model have been varied within reasonable limits. These studies showed that the times of fog formation and dissipation depend on several characteristics of the vegetation. For instance, increasing the shielding factor of the vegetation yields a denser fog since the evapotranspiration is increasing. Furthermore, the growing factor describing the growing activity of the vegetation during the year, has a strong impact by increasing the fog density and duration with increasing growing activity. On the other hand, the vegetation height seems to be less important.

In order to simulate low level stratiform clouds, a large scale vertical subsidence w_s has been included in PAFOG similar to the treatment of other one-dimensional stratus models, (e. g. Bott *et al.*, 1996; Duynkerke, 1989). The effect of this subsidence is that the clouds remain relatively stable at a given height within the atmosphere. Values of w_s have to be prescribed by the model.

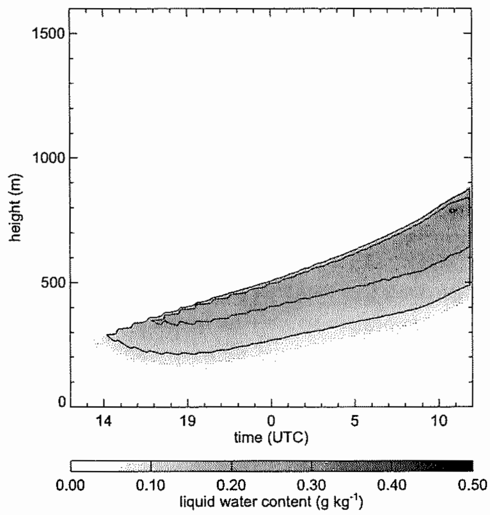

Fig. 4: Cloud water content on 21.11.98 as function of time and height. $w_s = 0$ cm s^{-1}.

Figures 4 and 5 show the results of a sensitivity study where w_s has been chosen to $w_s = 0$ cm s^{-1}(Figure 4) and $w_s = -0.6$ cm s^{-1}(Figure 5). It is seen that in the case of $w_s = -0.6$ cm s^{-1} the vertical growth of the cloud is clearly suppressed. Similar results were obtained in the other investigated cases. Thus, it is concluded that the large subsidence is an important factor controlling the time evolution of low level stratiform clouds.

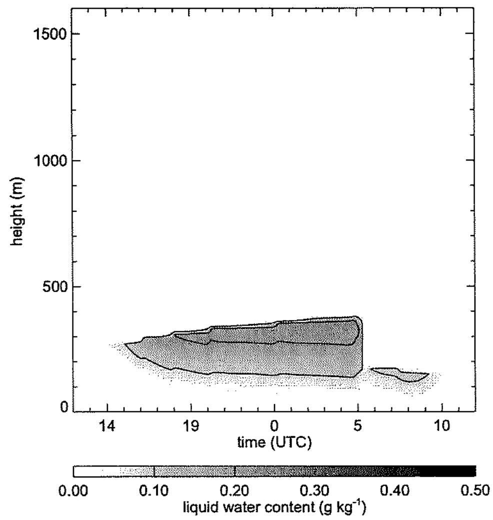

Fig. 5: Cloud water content on 21.11.98 as function of time and height. $w_s = -0.6$ cm s^{-1}.

4. CONCLUSIONS

PAFOG is a new forecast model for radiation fogs and low level stratiform clouds. The main purpose of the model is to produce a visibility forecast for airports or other neuralgic traffic locations. The model is designed to run on a normal PC. Input parameters are standard meteorological data and the characteristic vegetation data of a particular location. In case of low level stratiform clouds the value of the large scale subsidence is also needed.

The performance of PAFOG has been investigated by comparing model results with observations which have been made at the Lindenberg observatory in Germany on 45 cases with different weather conditions. In more than 90% of the investigated days the model reproduced the observations in terms of occurrence or non-occurrence of fog or low level stratus. Visibility was predicted in reasonable agreement with the observations. Sensitivity studies were performed showing that radiation fog is strongly influenced by vegetation. In case of low level stratus the large scale subsidence is an important factor controlling the time evolution of the clouds.

ACKNOWLEDGEMENTS

This research was funded by the German Weather Service (DWD), Offenbach, Germany.

REFERENCES

Bott, A., T. Trautmann,, and W. Zdunkowski, 1996: A numerical model of the cloud-topped planetary boundary-layer: Radiation, turbulence and spectral microphysics in marine stratus. *Q. J. R. Meteorol. Soc.*, **122**, 635–667.

Bott, A., U. Sievers, and W. Zdunkowski, 1990: A radiation fog model with a detailed treatment of the interaction between radiative transfer and fog microphysics. *J. Atmos. Sci.*, **47**, 2153–2166.

Chaumerliac, N., E. Richard, and J.-P. Pinty, 1987: Sulfur scavenging in a mesoscale model with quasi-spectral microphysics: Two-dimensional results for continental and maritime clouds. *J. Geophys. Res.*, **92**, 3114–3126.

Duynkerke, P. G., 1989: The diurnal variation of a marine stratocumulus layer: A model sensitivity study. *Mon. Weather Rev.*, **117**, 1710–1725.

Fisher, E. L., and P. Caplan, 1963: An experiment in numerical prediction of fog and stratus. *J. Atmos. Sci.*, **20**, 425–437.

Forkel, R., U. Sievers, and W. Zdunkowski, 1987: Fog modelling with a new treatment of the chemical equilibrium condition. *Beitr. Phys. Atmos.*, **60**, 340–360.

Jiusto, J. E., and G. G. Lala, 1980: Radiation fog formation and dissipation. A case study. *J. Rech. Atmos.*, **14**, 391–397.

Mellor, G. L., and T. Yamada, 1974: A hierarchy of turbulence closure models for planetary boundary layers. *J. Atmos. Sci.*, **31**, 1791–1806.

Sakakibara, H., 1979: A scheme for stable numerical computation of the condensation process with large time steps. *J. Meteorol. Soc. Jpn.*, **57**, 349–353.

Siebert, J., A. Bott, and W. Zdunkowski, 1992: Influence of a vegetation-soil model on the simulation of radiation fog. *Beitr. Phys. Atmos.*, **65**, 93–106.

von Glasow, R., and A. Bott, 1999: Interaction of radiation fog with tall vegetation. *Atmos. Environ.*, **33**, 1333-1346.

Zdunkowski, W. G., W.-G. Panhans, R. M. Welch, and G. J. Korb, 1982: A radiation scheme for circulation and climate models. *Beitr. Phys. Atmos.*, **55**, 215–238.

THE SENSITIVITY OF LARGE-EDDY SIMULATIONS OF STRATOCUMULUS TO THE PARAMETRIZATION OF DRIZZLE.

Philip R.A. Brown[1], Glen Richardson[1] and Robert Wood[2]

[1]Met Office, Fitzroy Road, Exeter, EX1 3PB, UK
[2]Department of Atmospheric Sciences, University of Washington, Seattle, U.S.A.

1. INTRODUCTION

Observations of stratocumulus show that the formation, precipitation and evaporation of drizzle has a large influence on its evolution (Nicholls and Leighton 1986), (Martin *et al.* 1995). Precipitation acts to reduce the liquid water path (LWP) of the cloud layer, its optical depth and hence the intensity of turbulence generated by longwave radiative cooling at cloudtop. Drizzle evaporation below cloud leads to cooling and stabilization of the temperature profile and may decouple the cloud layer from the surface fluxes of heat and moisture. It is important that the effects of drizzle should be accurately represented in large scale atmospheric models used for numerical weather prediction (NWP) or climate simulations.

Large Eddy Simulation (LES) models with fully-explicit representations of the cloud microphysics have been used to study the evolution of drizzling stratocumulus layers (Kogan *et al.* 1995), (Khairoutdinov and Kogan 1999). Such schemes remain computationally-intensive, however, and beyond the capability of operational NWP models as these approach resolutions of a few kilometres in the horizontal. Hence there is a continuing requirement for the use of bulk-water schemes with the prognostic variables of liquid water content (LWC) or drop concentration (N_C).

The Met Office LES incorporates such a bulk-water scheme to enable its use as a cloud-resolving model (CRM). The aim of this study is to demonstrate the performance of the LES model in simulating drizzling stratocumulus using different parametrizations of drizzle production. The model results are compared with in-situ aircraft observations of drizzle obtained using the Met Office C-130 research aircraft.

2. OBSERVATIONS

In-situ measurements of drizzling stratocumulus clouds were obtained during 12 flights made with the Met Office C-130 research aircraft. 11 of these were sampled during the daytime over sea areas around the British Isles with a nighttime case from the Atlantic Stratocumulus Transition Experiment (ASTEX) that took place in the vicinity of the Azores (NE Atlantic) in 1992. Each flight included horizontal legs within the cloud layer and slant profiles through it.

Measurements were obtained using a PMS Forward Scattering Spectrometer Probe, which counts and sizes droplets in the range of radius between 1 and 23 μm. Larger drops were measured using a PMS 2D-C Optical Array Probe (OAP), which measures particles in the nominal range of radius between 12.5 and 400 μm. In practice, optical and electronic response time effects limit its detection efficiency below 50-75 μm radius. Drizzle bulk properties were merged from the two instruments, integrating moments of the spectra above a threshold radius of 20 μm.

Table 1 shows the flight dates and overall properties of the cloud layer in each case, including cloud depth, LWP and mean cloud droplet concentration.

Date	Loctn	Depth [m]	LWP [gm^{-2}]	N_C [cm^{-3}]	P_b [mm d^{-1}]
6/12/90	SW	625	260	310	0.49
12/6/92	AZ	395	170	120	0.47
29/2/96	NW	370	100	90	0.24
3/12/98	NS	680	360	420	0.054
14/12/98	SW	1650	90	20	0.66
28/1/99	SW	1360	85	8	1.12
29/1/99	SW	325	80	60	0.095
8/7/99	NW	280	80	110	0.41
12/6/00	SW	315	80	95	0.28
14/6/00	SW	240	45	85	0.34
15/6/00	SW	300	70	65	0.44
28/6/00	NS	415	90	110	0.78

Table 1. Flight date, location (SW=SW Approaches, NW=NW of Ireland, AZ=Azores, NS=N.Sea), cloud thickness, liquid water path (LWP), mean cloud droplet concentration (N_C) and cloudbase precipitation rate (P_b).

3. LES MODEL

a) Formulation

The Met Office LES model is described by (Brown 1999) and its microphysics scheme by (Swann 1998), hereafter S98. All ice species are disabled, with only the processes of condensation, autoconversion, accretion and evaporation being allowed. Cloud liquid water is assumed non-precipitating and is now a prognostic variable rather than a diagnostic as in S98. The condensation rate is that required to remove sub- or supersaturation within one timestep.

Corresponding author's address: Philip R.A. Brown, Met Office, Fitzroy Road, Exeter, EX1 3PB, UK. E-mail: phil.brown@metoffice.com

Wood (2000) has examined the behaviour of different parametrizations of autoconversion in a 1-d column model. He finds that the scheme of (Khairoutdinov and Kogan 2000), hereafter KK, best reproduces relationships between drizzle parameters and cloud macroscopic parameters such as liquid water path (LWP) that have been derived from the aircraft observations. The KK autoconversion rate is obtained by statistically fitting data from an LES model with fully explicit liquid phase microphysics:

$$\left(\frac{dq_R}{dt}\right)_{aut} = 1350 N_C^{-1.79} q_C^{2.47} \quad (1)$$

where q_R and q_C are the mixing ratios of drizzle and cloud water, respectively, and N_C is the cloud droplet number concentration. This expression reflects the observed tendency for drizzle to occur more commonly in maritime clouds with lower cloud droplet concentrations.

S98 uses a single variable, the water content, to describe liquid precipitation. In the present study an additional variable, the drizzle number concentration may also be used. Its autoconversion source term is derived from (1) assuming that the initial drizzle drops have a radius, r_{crit}, of 25 μm, hence:

$$\left(\frac{dN_R}{dt}\right) = \left(\frac{dq_R}{dt}\right) / \left((4/3)\pi r_{crit}^2 \rho_w\right) \quad (2)$$

where ρ_w is the density of liquid water. No parametrization of the number source term due to drop breakup was included, it being assumed that drizzle drops will not grow large enough to reach the diameter of a few millimetres where it becomes effective. This assumption is justified *a posteriori.*

The drizzle size spectrum is a modified gamma distribution of the form

$$N(D) = N_0 D^{\alpha} \exp(-\lambda D) \quad (3)$$

where α is a spectral shape factor, with a value of 2.5 being assumed. In dual-moment simulations, N_0 is calculated from the model variables of drizzle water mass and number concentration. The standard single moment simulation uses a fixed N_0 of $1.15*10^{15}$ (in SI units) so as to give the same effective total drop number for a given water mass as the Marshall-Palmer spectrum, which has an exponential form with α=0 and $N_0=8*10^6$ m^{-4}.

The broad-band fluxes of solar and thermal infrared radiation are calculated using the scheme of (Edwards and Slingo 1996). Cloud droplets are assumed to have a fixed effective radius of 10 microns. Hence, there is no possibility of any feedback between radiative and microphysical processes. Drizzle drops are excluded from the radiation calculations.

Results from four different configurations of the microphysics code will be shown in this study:

2M : standard dual-moment simulation
1M : standard single-moment simulation
1M-HI-N : single-moment with N_0 increased by 10^5.
2M-LO-V : dual-moment with reduced drizzle drop fall velocity.

b) Case specification

Simulations are based on the first Lagrangian case tobserved during the Atlantic Stratocumulus Transition Experiment (ASTEX), which took place in the eastern Atlantic Ocean in June 1992 (Bretherton et al. 1999). We simulate only an initial 15-hour period during which the cloud top height remained almost constant.

Surface fluxes of heat and moisture are derived assuming a fixed sea-surface temperature (SST) and numerically solving the Monin-Obukhov similarity equations using values of temperature, water vapour and horizontal velocities at the first model grid level above the surface. SST is initially 290K, increasing linearly to 290.4K after 9 hours and 292.6K after 18 hours. The large-scale divergence remains constant at 5.10^{-6} (SI units).

The simulations use a 2-d domain of 64*64 grid points with a horizontal resolution of 50m. The vertical resolution was 25m below 1000m, increasing to 100m at the top of the model domain (3000m). In all cases, the model is initialized with horizontally uniform profiles of temperature and water vapour mixing ratio. Random temperature fluctuations of +/-0.1K were imposed on the grid scale below 1000m.

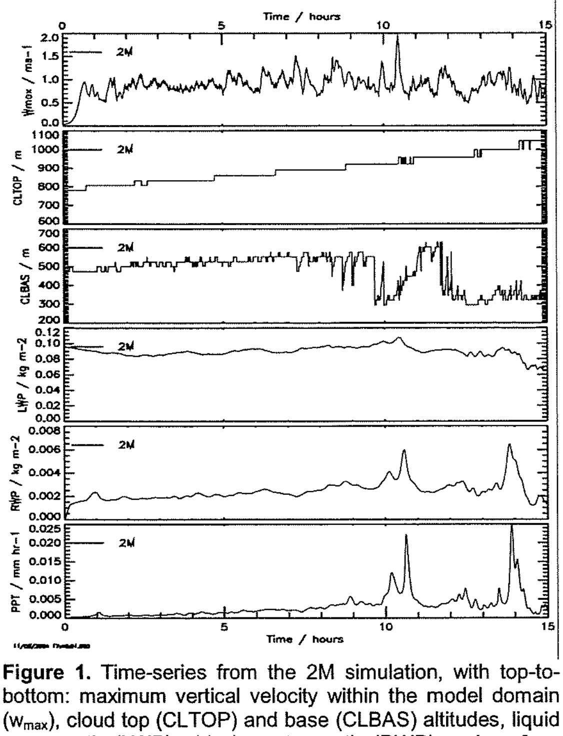

Figure 1. Time-series from the 2M simulation, with top-to-bottom: maximum vertical velocity within the model domain (w_{max}), cloud top (CLTOP) and base (CLBAS) altitudes, liquid water path (LWP), drizzle water path (RWP) and surface precipitation rate (PPT).

4. RESULTS

Fig 1 shows some time-series of a number of model output parameters to illustrate the general evolution of the simulations. Spin-up of the model vertical velocity field in response to the initial random temperature perturbations occurs during the first hour. Cloudbase, LWP and drizzle water path (RWP) all remain approximately constant between hours 1 to 9. Cloud top grows steadily throughout the simulation, rising from an initial 800m to 1050m at hour 15. This contrasts with observations which showed the cloud top approximately constant during this period. It is thought that this results from the relatively low horizontal resolution employed in this study which leads to excessive parametrized sub-grid scale turbulence at the inversion layer at cloud top. This is not considered to hinder usage of these simulations to examine the impact of and sensitivity to drizzle. After hour 9, the cloud base periodically lowers, and there are short-period fluctuations in RWP and the peak vertical velocity. These illustrate the occurrence of cumulus convection originating in the near-surface layer below a decoupled stratocumulus deck.

Fig. 2 shows a number of comparisons of bulk microphysical quantities between the model simulations and the aircraft observations. Fig. 2a) confirms that the model simulation lies within the middle of the observed range of cloud depth and LWP and that the model clouds have approximately the same degree of sub-adiabaticity in LWC as observed. Fig.2b) shows that the 1M simulation produces lower cloudbase precipitation rates that fall well on the low side of the range of observed values for a similar LWP.

Fig.2c) shows that the 1M, 2M and 1M-HI-N simulations both generate in-cloud drizzle water contents that are significantly outside the range of observed values for comparable cloud base precipitation rates. 1M produces precipitation rates that are towards the low end of observed values although it should be noted that this run also produces the largest surface precipitation rates. Fig.2d) shows that both the dual-moment simulations have drizzle number concentrations that lie within the envelope of observed values, although 2M is towards the low end of the observed range. These two runs both produce similar drizzle drop mean volume radii at around 30-70 μm, comparable with observations.

The impact of changes to the microphysics on the budgets of drizzle water is illustrated in Figure 3. In 1M, the balance is largely between autoconversion and precipitation within cloud, with a small contribution from accretion. Below cloud, the evaporation rate is small and almost constant with height. By contrast, in 2M-LO-V accretion is larger than autoconversion at all levels within cloud and there are significant sinks (near cloudbase) and sources (near cloudtop) of drizzle water due to the turbulent transport of drops.

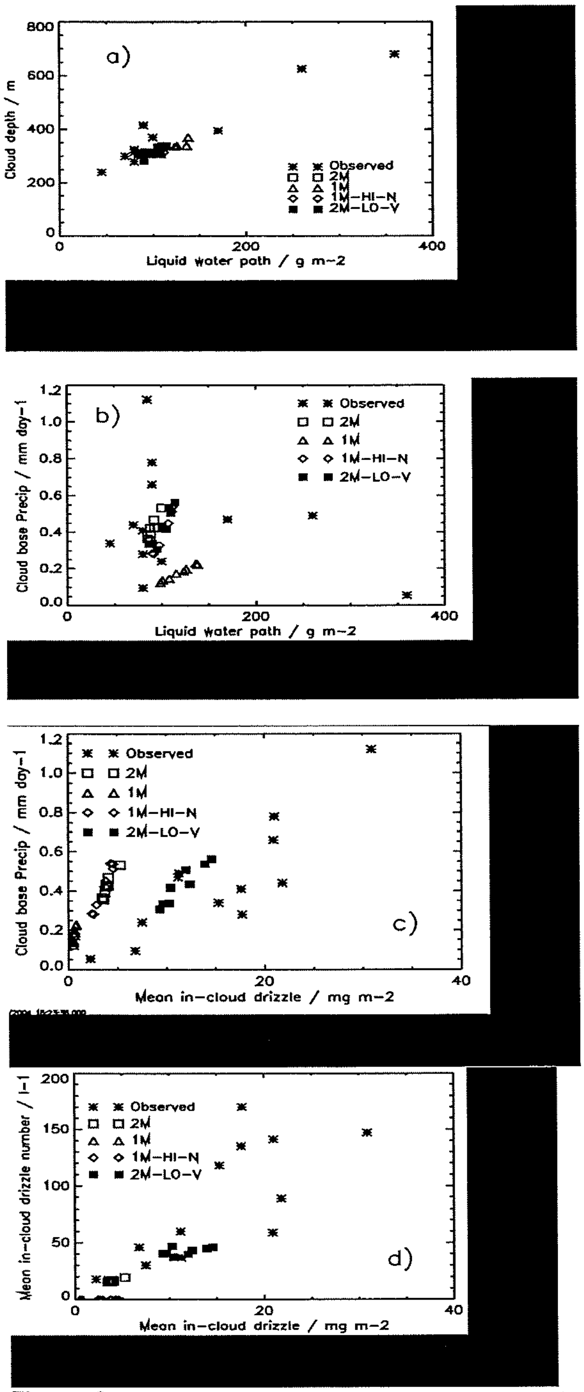

Figure 2. Mean bulk properties of modeled stratocumulus compared to aircraft observations. Model data points are taken from hours 3 to 9.priot to sub-cloud cumulus formation.

Evaporation of drizzle below cloud is of similar magnitude to the microphysical production terms within cloud but remains largely balanced by precipitation. Both 2M and 1M-HI-N generate profiles of drizzle budget terms that have similar form and magnitude to 2M-LO-V.

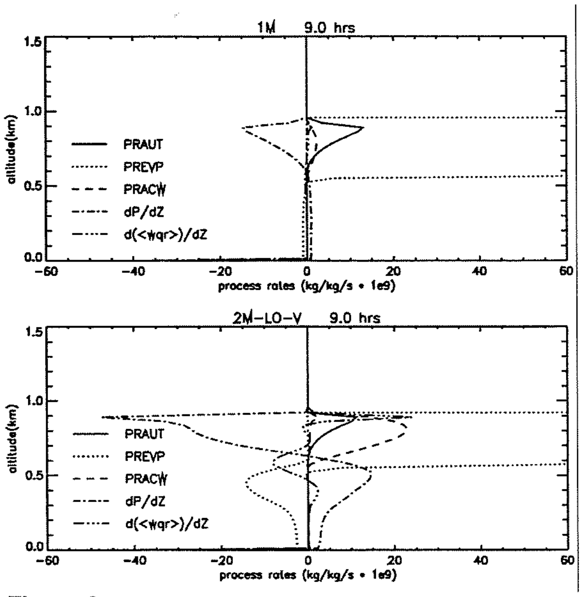

Figure 3. Vertical profiles of terms in the budget of drizzle water, showing autoconversion (PRAUT), accretion (PRACW), evaporation (PREVP), and the vertical gradients of precipitation (dP/dZ) and turbulent flux (d<wqr>/dZ).

5. DISCUSSION

2M generated drizzle mean volume radii (MVR) that were comparable with observation (30-70 μm). By contrast, values from 1M were higher (150-200 μm). Increasing N_0 by 10^5 in a single-moment simulation implies the drizzle water mass is distributed among a larger number of drops reducing the MVR. The effect is apparent in 1M-HI-N. Increased total drop surface area means that evaporation below cloud base is comparable with the two dual-moment runs. Accretion within cloud is greatly increased due to the drops' lower fallspeeds and longer in-cloud residence times. The absence of sub-cloud evaporation in 1M inhibits decoupling of the cloud layer.

In both 2M and 1M-HI-N, whilst cloudbase precipitation rates are within the range of observation, the in-cloud drizzle water contents are low. This suggests that the drop fallspeeds in these experiments are too large. In common with other models with bulk-water microphysics, the LES uses a power law representation of the form

$$V_{fall}(D) = aD^b$$

where a=362 and b=0.65. These approximate the fallspeed data of (Beard 1976) for sizes above about 0.3mm radius. This is appropriate for heavier rain.

2M-LO-V uses values a=59400 and b=1.59 which empirically fit the Beard data in the range 40-70 μm, which is more appropriate to the MVR that are generated. The lower drop fallspeeds in 2M-LO-V ensure that more drizzle water remains in cloud for a given cloud base precipitation rate. In addition, the magnitude of the turbulent flux of drizzle is larger so that its convergence at cloud top provides a drizzle source that exceeds the autoconversion and accretion terms.

6. CONCLUSIONS

- 1M with standard model parameter values for rain generates insufficient evaporation of drizzle with adverse impacts on boundary layer evolution.
- Increased N_0 in a single-moment simulation broadly simulates the features of a dual-moment run.
- The use of fallspeed appropriate to drizzle drop MVR (30-70μm) gives the best agreement between modelled and observed bulk drizzle properties.

These results suggest that a single-moment representation of drizzle with appropriate control of fallspeed parameters may be capable of performing adequately in a kilometer-resolution NWP model.

7. REFERENCES

Beard, K. 1976 Terminal velocity and shape of cloud and precipitation drops aloft. Journal of the Atmospheric Sciences, 33, 851-864

Bretherton, C.S., Krueger, S.K., Wyant, M.C., Bechtold, P., Van Meijgaard, E., Stevens, B., and Teixeira, J. 1999 A GCSS boundary-layer cloud model intercomparison study of the first ASTEX Lagrangian experiment. Boundary-Layer Meteorology, 93, 341-380

Brown, A.R. 1999 Large-eddy simulation and parametrization of the effects of shear on shallow cumulus convection 254. Boundary-Layer Meteorology, 91, 65-80

Edwards, J.M. and Slingo, A. 1996 Studies with a flexible new radiation code .1. Choosing a configuration for a large-scale model. Quarterly Journal of the Royal Meteorological Society, 122, 689-719

Khairoutdinov, M. and Kogan, Y. 2000 A new cloud physics parameterization in a large-eddy simulation model of marine stratocumulus. Monthly Weather Review, 128, 229-243

Khairoutdinov, M.F. and Kogan, Y.L. 1999 A large eddy simulation model with explicit microphysics: Validation against aircraft observations of a stratocumulus- topped boundary layer. Journal of the Atmospheric Sciences, 56, 2115-2131

Kogan, Y.L., Khairoutdinov, M.P., Lilly, D.K., Kogan, Z.N., and Liu, Q.F. 1995 Modeling of Stratocumulus Cloud Layers in A Large-Eddy Simulation-Model with Explicit Microphysics. Journal of the Atmospheric Sciences, 52, 2923-2940

Martin, G.M., Johnson, D.W., Rogers, D.P., Jonas, P.R., Minnis, P., and Hegg, D.A. 1995 Observations of the Interaction Between Cumulus Clouds and Warm Stratocumulus Clouds in the Marine Boundary-Layer During Astex. Journal of the Atmospheric Sciences, 52, 2902-2922

Nicholls, S. and Leighton, J. 1986 An Observational Study of the Structure of Stratiform Cloud Sheets .1. Structure. Quarterly Journal of the Royal Meteorological Society, 112, 431-460

Swann, H. 1998 Sensitivity to the representation of precipitating ice in CRM simulations of deep convection. Atmospheric Research, 48, 415-435

Wood, R. 2000, The validation of drizzle parametrizations using aircraft data. 13th ICCP, 14-18 August, Reno, USA

MODELLING STUDIES OF ICE CONCENTRATION IN FRONTAL CIRRUS CLOUDS

J.Cardwell, T.W.Choularton,
P.J.Connolly, M.W.Gallagher & K.N.Bower

UMIST Physics Dept,
Manchester, M60 1QD

1. INTRODUCTION

Cirrus clouds are widespread throughout the globe and their radiative properties are therefore important to the global warming debate. Their albedo will depend on the ice concentration and structure of the cloud. The ice concentrations from two cases of evolving frontal sub-tropical cirrus observed during the EMERALD-1 airborne experiment are compared with simulations using an explicit microphysical parcel model (200 aerosol bins and 200 ice bins). Given the uncertainty in dynamics and microphysics there is a very good agreement. At the temperature range simulated (<-40C) it is thought that homogeneous freezing of aerosol produces ice particles. The composition, distribution, growth and freezing properties of the aerosol are an area of great interest and debate. The growth and shape of the small ice produced are equally difficult to quantify and model.

The model has simple dynamics and can produce either a single parcel or multi-parcel simulation. A parcel of air is lifted adiabatically from below cloud base to cloud top by a constant updraft, during which time aerosol grows and freezes to produce ice particles, which then grow as well. The single parcel simulations agree with similar studies; the number of ice particles produced increases with the updraft (as found by spice et al, 1999) and the number of ice crystals produced is also very sensitive to the deposition constant chosen in the ice growth equation (Gierens 2003).

Simulations using multiple parcels to represent the cloud allow the examination of the cloud properties in the vertical. Each parcel represents a layer of cloud a meter in depth and ice particles are allowed to fall from parcel to parcel. These simulations show that ice nucleation will occur predominantly in the upper region of the cirrus cloud rather than near cloud base as suggested by single parcel models. However strong embedded convection will nucleate equally throughout the cloud depth provided there is significant ice nuclei availability.

Corresponding author's address: John Cardwell, Physics Dept. UMIST, PO Box 88, Manchester M60 1QD. UK; E-Mail: John@cardwell.it

2. THE EMERALD DATA SET

Ten cloud penetration flights are available from the EMERALD-1 database with a large variety of instrumentation conducted near Adelaide, South Australia in September 2001. From this, two clouds (Flights numbered 8 and 11) were selected for comparison with the modeling work. The Cloud Particle Imager (CPI) and an FSSP-100 data were combined to provide the ice concentrations observed. LIDAR images were used to estimate cloud base and cloud top and to view cloud structure.

3. THE MODEL

The Model is based on that of Cardwell et al. (2003). The microphysics was extended to include growth of aerosol (assumed to be $(NH_4)_2SO_2$) using the parameterization of Gerber (1991) and the freezing of the aerosol follows that of Spice et al. (1999). An array of 200 logarithmically spaced discrete size bins was used to approximate an initial lognormal dry aerosol spectrum, total concentration of *200 cm^{-3}*, with a mode radius *0.02 μm* and standard deviation of *2.3*. Unlike the subsequent 200 ice particle bins the aerosol bins were allowed to change size as they followed the actual growth of the particles so as to minimize numerical diffusion.

For model treatment, frontal cirrus may be considered as essentially a thin layer cloud continually undergoing uplift with a typical updraft velocity of around $0.01 ms^{-1}$. However in many of the EMERALD-1 cases turbulence and aircraft. LIDAR measurements revealed significant structure with embedded thermals of around $1 ms^{-1}$ or more. A range of vertical velocities was therefore used for sensitivity tests. For the single parcel model, the parcel was started below cloud (Temperature = -38°C and Relative Humidity = 60%, chosen to make cloud base the same height as observed) and forced to rise adiabatically until the observed cloud depth was achieved. The multi parcel model similarly lifts parcels in the same way, except that they represent only part of the cloud (a layer 1m in depth) with new parcels being created at below cloud when the previous parcel has been lifted by 1m. These parcels interact by sedimentation, ice particles fall into the parcel from the parcel above and fall out of the parcel into the parcel below due to their terminal velocity, consequently cloud base is lower in some cases. If a snap shot is taken as the first parcel reaches cloud top, this essentially represents a single thermal. However these clouds are long lived and cloud would already be present above the thermal so the model is allowed to continue until it reaches a dynamic equilibrium (when a parcel reaches cloud top it is removed and its contents lost). Sometimes the dynamic equilibrium is periodic and requires averaging.

4. RESULTS

First the single parcel simulations are presented and their sensitivity to different parameters are discussed. The multi parcel simulations are then described. Ice particle concentrations from the EMERALD-1 flight cases are shown on the relevant figures for comparison.

4.1 Single parcel simulations

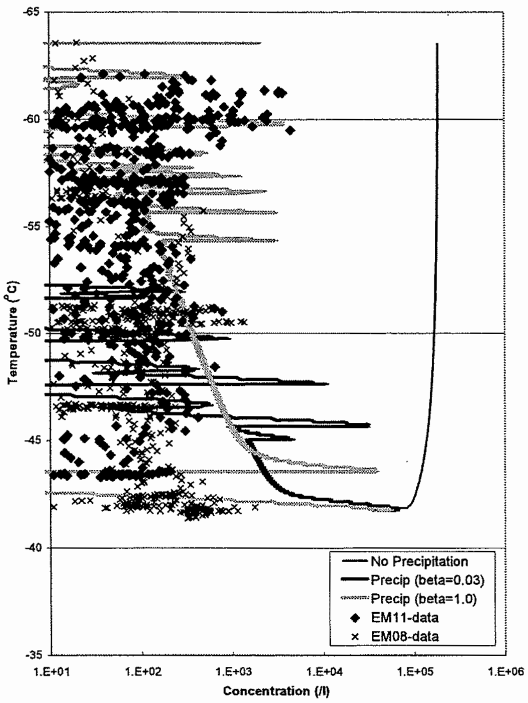

Figure 1 Ice Concentrations for 0.1ms^{-1} runs

Figure 1 shows ice concentration profiles for 3 different simulations using a 0.1 m s^{-1} updraft velocity. If no precipitation is allowed the concentration of ice formed by homogeneous increases rapidly near cloud base and begins to level off, for the rest of the vertical ascent a constant value is attained as ice growth competes for the available vapor preventing further nucleation. The single parcel simulations were carried out to compare directly with other authors' work, but this is taken further to investigate whether the inclusion of particle sedimentation is important. The two additional curves in *Fig. 1* represent sensitivity studies with precipitation activated and where it is assumed that the parcel has a depth of 10m. It can be seen in both cases that a considerable amount of ice has been lost from the parcel. The two curves differ from one another in that they use different deposition coefficients, $\beta = 1.0$, and $\beta = 0.03$ respectively. There is a significant difference between the concentration profiles produced in each case. Decreasing β slows the ice growth and therefore there is more vapor available at each stage for homogeneous nucleation.

4.2 Multi parcel simulations

In some of the single parcel simulations with precipitation it was found that the aerosol was rapidly depleted and with the subsequent lack of new ice formation the supersaturation could reach extremely high values. This also occurred in the some of the multi-parcel simulations, if the model was examined before equilibrium. However, this approach as discussed above is more akin to modeling a convective cirrus case. All the simulations presented here were allowed to continue to completion defined by a dynamic equilibrium being reached and this prevented such situations from happening. This equilibrium will sometimes be oscillatory and requires averaging over a model cycle.

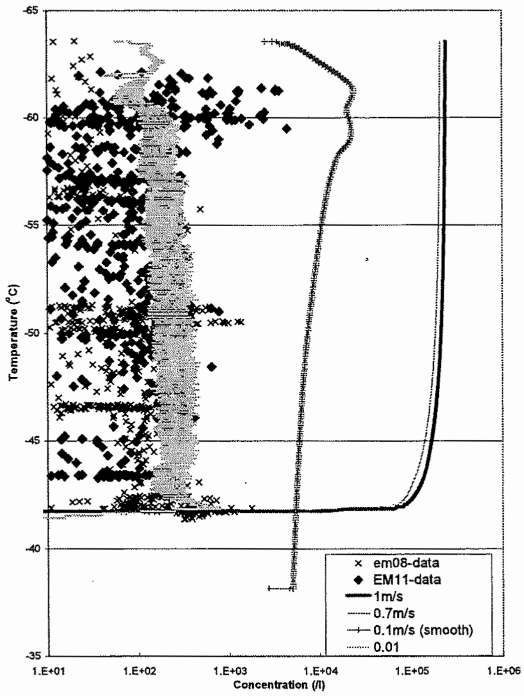

Figure 2 Ice Concentrations for multi parcel runs

Figure 2 shows ice concentration profiles produced by four multi-parcel simulations. The model runs with $1.0\ m\ s^{-1}$ and $0.7\ m\ s^{-1}$ updraught velocities produce very similar results. This is to be expected as other authors have found that ice concentration increases logarithmically with updraught velocity. To further confirm this, as *Fig.2* is plotted on logarithmic axis the distance between the two curves (*0.1 m* s^{-1} and *1.0 m* s^{-1})is roughly the same as for updraught velocities of (*0.01* and *0.1 m* s^{-1}).

The range of results that can be obtained by changing the updraft velocity is extremely large and this parameter must be well prescribed from observations to reduce model sensitivity and allow interpretation of contributions to ice crystal number and size by possible nucleation mechanisms. The agreement between the 0.01ms^{-1} and the data suggests that the idea that the cloud is produced by a continuous but small updraft is correct. The higher velocity simulations produced ice concentrations that were higher than observed in EMERALD-1, however, it is likely that sheer in the cloud where the thermals were seen on the LIDAR imaged, would prevent 100% collection of ice from above into each model parcel and therefore these predictions represent the maxim concentrations likely under no shear conditions.

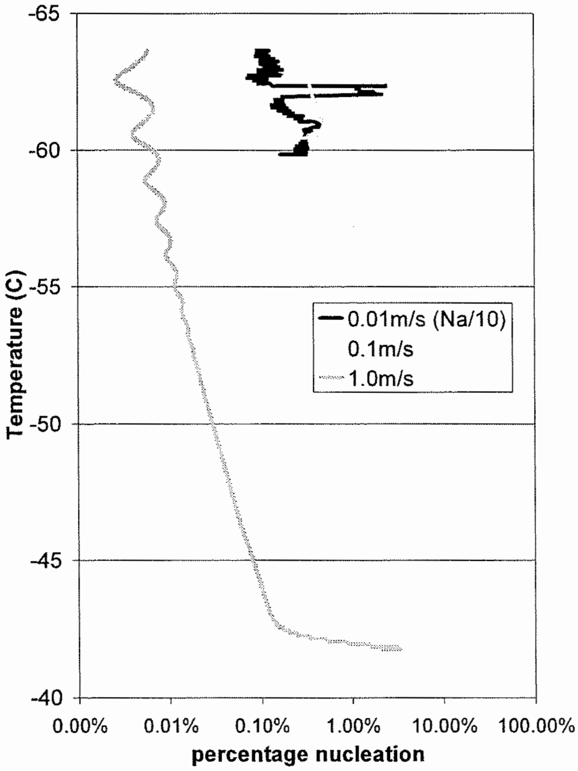

Figure 3: Percentage of total nucleation at each layer height

Figure 3 illustrates where significant nucleation is occurring within the cloud and it is clear that for some cases the ice is produced much more efficiently at higher levels, this is different from the suggestion of the single parcel models that most nucleation occurs near cloud base. This difference is important in understanding the microphysical structure and evolution of cirrus clouds. The 0.01ms^{-1} was run with 10 times less aerosol because otherwise virtually all nucleation took place in the 2 layers at the top of the cloud.

5. CONCLUSIONS

A single and multi-parcel model was used and shown to be capable of simulating aircraft observations of ice concentrations and particle sizes in cirrus from the EMERALD-1 database. However the model simulated ice concentrations are extremely sensitive and can easily vary by several orders of magnitude. These large uncertainties are primarily due to of lack of knowledge of the underlying mechanisms controlling the microphysics in cirrus, including the aerosol present and variations in dynamics. The type of sensitivity results we have presented here agree with other researchers assertions. It was found that maximum ice crystal concentrations were strongly dependent on the deposition coefficient, employed as was found by Gierens *et al.* (2003). Ice crystal concentrations were found to increase with the updraft velocity applied, again consistent with previous model studies.

Single parcel model simulations and multi-parcel models give approximately the same predicted ice concentrations and sizes. An important difference, however, is that the multi-parcel model predicts that the region where significant nucleation occurs can be significantly higher in the cloud. The advantage of this model over the single parcel model was discussed and it was shown that it can represent the cloud through many layers adequately when compared to observations, thus, although still effectively averaging the cloud properties in the horizontal plane, some of the structure in the vertical can be examined. Single parcel models will always show a large amount of nucleation at cloud base as there are so few sinks of water vapour prescribed that the supersaturation will be high allowing for large growth in aerosol sizes and subsequent freezing to proceed.

6. REFERENCES

Cardwell, J 2003 et al.: A modeling study of ice-spectrum modes in deep frontal clouds. Q.J.R Met. Soc, 129 1873-1890

Gerber, H., 1991: Supersaturation and droplet spectral evolution in fog. J. Atmos. Sci., 48, 2569-2588.

Gierens, K. M., 2003: The deposition coefficient and its role for cirrus. J.G.R. 108 D2 4069

Spice, A. et al., 1999: Primary ice nucleation in orographic cirrus clouds: A numerical simulation of the microphysics. Q.J.R Met. Soc. **125**, 1637-1667

AN ASSESSMENT OF THE MESO-NH CLOUD SCHEME USING SATELLITE OBSERVATIONS FROM THE VISIBLE TO THE MICROWAVES

J.-P. Chaboureau[1]*, P. Dubuisson[2], J. Pardo[3], C. Prigent[4], J.-P. Pinty[1], P. J. Mascart[1], E. Richard[1]

[1]Laboratoire d'Aérologie, Observatoire Midi-Pyrénées, Toulouse, France
[2]Ecosystèmes Littoraux et Côtiers, Université du Littoral, Wimereux, France
[3]Departamento de Astrofísica Molecular e Infrarroja, Instituto de Estructura de la Materia, Madrid, Spain
[4]Laboratoire d'Etude du Rayonnement et de la Matière en Astrophysique, Observatoire de Paris, Paris, France

1. INTRODUCTION

Clouds are among the most important regulators of the weather and climate of the earth's atmosphere. They are the product of complex interactions between large-scale circulations, moist convective transport, small-scale turbulent mixing, radiation and microphysical processes. Cloud resolving models are now able to resolve a large range of scales, using the gridnesting capabilites as well as to follow the evolution of several microphysical species (cloud droplets and crystals, rain drops, snow?akes and graupel) in the context of real meteorological ?ows. Thus a successful simulation of cloud systems in a mesoscale model outlines at ?rst a geographically and timely accurate prediction of the vertical motions in the atmosphere and then a correct representation of the condensed phase amounts. This makes the objective evaluation of simulated cloud ?elds against observational datasets, here satellite pictures, so dif?cult because of the well-known intricate links between small-scale dynamics and the microphysical state of the clouds.

On the other hand, satellite observation offers potential for direct validation of simulation at the spatial resolution of mesoscale models. First, observations in the window channels sense different characteristics of the cloud according to the wavelengths: the cloud optical depth in the visible, the cloud top in the infrared, and the hydrometeor column in the microwaves. Second, the model-to-satellite approach, in which satellite brightness temperature (BT) images are directly compared to synthetic BTs computed from predicted model ?elds, is helpful in validating mesoscale simulations but since these are suf?ciently realistic. In previous studies, Chaboureau et al. (2000, 2002) showed such an interest by comparing synthetic BTs from simulations performed with the Meso-NH mesocale model with the METEOSAT infrared and water-vapor channels. In particular, due to its high sensitivity to cloud cover, only information brought by the thermal infrared window allows to adjust parameters of the cloud scheme.

Direct comparison between synthetic and observed BTs has also been conducted in the microwave range by Wiedner et al. (2004) using the Tropical Rainfall Measuring Mission (TRMM) Microwave Instrument (TMI) observations. The encouraging comparisons done on two convective cases give a strong con?dence in the hydrometeor columns simulated by the model. Preliminary work done in the visible range on a banded structure (gravity wave case) over the Alps con?rms such a con?dence for the cloud optical depth. The experiences from all these studies based on different meteorological situations are now gathered on the evaluation of a single simulation using satellite observation from the visible to the microwaves. The present study bene?ts from TRMM that carries both TMI and the Visible Infrared Scanner (VIRS). Section 2 presents brie?y the Meso-NH model and the cloud parameterization, the radiative transfer models and the TRMM observations used here. Section 3 shows results obtained from a convective line located in the South Atlantic Convergence Zone (SACZ) off the Brazilian coast, on February 7, 2001, already studied in the microwave by Wiedner et al. (2004). Section 4 concludes the paper.

2. MODELS AND OBSERVATIONS

2.1 The Meso-NH Atmospheric Model

Meso-NH is a non-hydrostatic mesoscale model, jointly developed by Météo-France and the Centre National de la Recherche Scienti?que (CNRS) (Lafore et al. 1998). The explicit cloud scheme used here is a bulk mixed-phase microphysical scheme developed by Pinty and Jabouille (1998) which predicts the mixing ratio of six atmospheric water categories: water vapor, cloud and rain water, non-precipitating ice, snow and graupel. Each of the precipitating particles is assumed to follow a generalized gamma distribution, with mass-diameter and fall velocity-diameter relationships expressed as power-laws. The multiple interactions operating between the different water cate-

*Corresponding author address: J.-P. Chaboureau, Laboratoire d'Aérologie, OMP, 14 av. E. Belin, 31400, Toulouse, France; e-mail chajp@aero.obs-mip.fr.

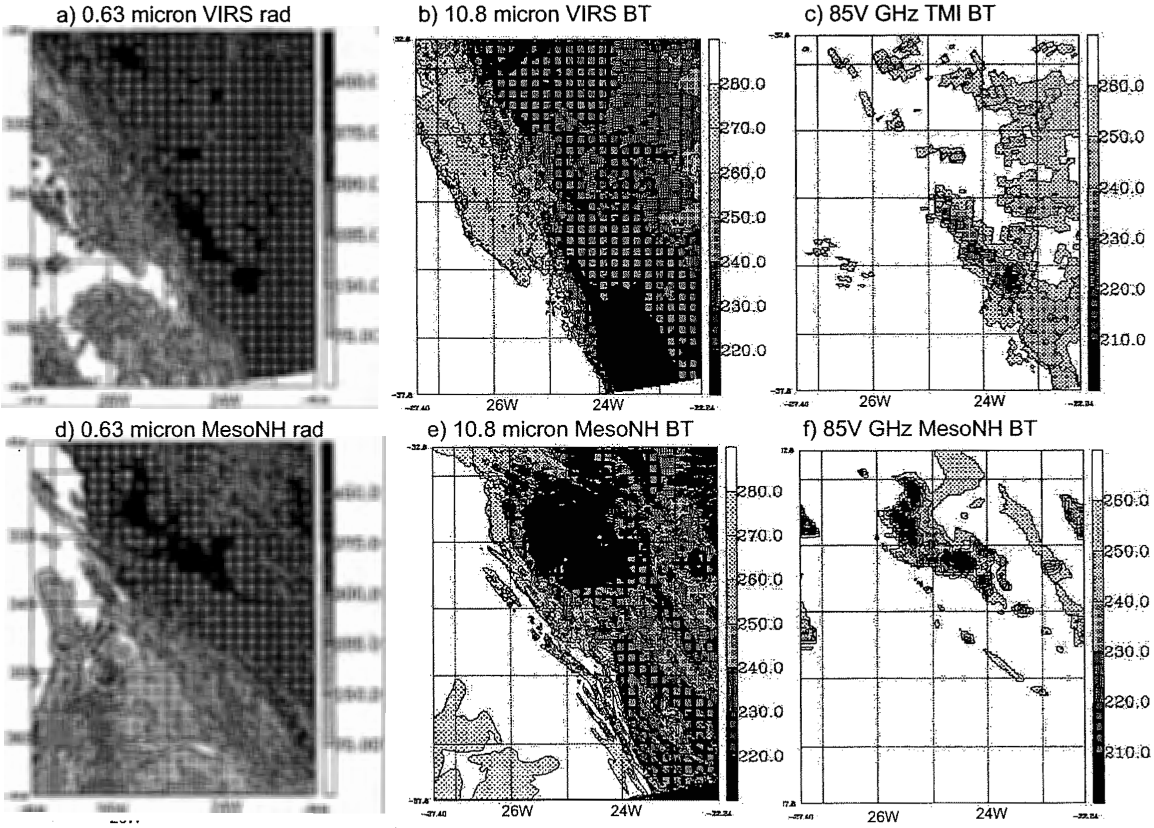

Figure 1: (top) observed and (bottom) simulated (a, d) 0.63 μm radiances (W m^{-2} sr^{-1} μm^{-1}), (b, e) 10.8 μm BTs (K), and (c, f) 85V GHz BTs (K).

gories are accounted for through the parameterization of 35 microphysical processes (nucleation, conversion, riming, sedimentation, etc.).

The SACZ case is simulated with three nested models, using a horizontal grid spacing of 36, 12, and 3 km. The vertical grid has 84 levels with a level spacing stretched from 80 m close to the surface up to 300 m aloft. The inner grid covers 582 km × 726 km. The Meso-NH model is initialized on February 6, 2001, at 1200 UTC and is integrated forward for 27 hours. More details on the setup of the model are given in Wiedner et al. (2004).

2.2 The Radiative Transfer Models

Two radiative transfer models are used, one simulates the VIRS radiances and BTs while the other simulates the TMI BTs. Both assumed the plane-parallel approximation.

The radiative transfer model operating in both the visible and infrared spectrum as measured by VIRS includes scattering, absorption and emission of radiation by clouds, aerosols or molecules using the Discrete Ordinate Method (DOM) (Stamnes et al., 1988). Gaseous absorption is treated with the correlated k-distribution (Lacis et Oinas, 1991). This method allows for a fast and accurate account for gaseous absorption as well as for interactions between absorption and scattering The radiative transfer model has been developed and validated using a reference code (Dubuisson et al., 1996), based on a line-by-line model for gaseous absorption and the DOM for solving the radiative transfer equation with a high spectral resolution.

The Atmospheric Transmission Model (ATM) radiative transfer model (Pardo et al. 2001, Prigent et al. 2001) has been adapted by Wiedner et al. (2004) for simulating the TMI radiances from Meso-NH outputs. Absorption by atmospheric gases is introduced in the model according to Pardo et al. (2001) while diffusion by hydrometeors is computed following the T-matrix approach of Mishchenko (see Prigent et al. 2001). The standard refractive indexes, that change with hydrometeor densities, have been carefully applied to the distribution of hydrometeors predicted by the Meso-NH model.

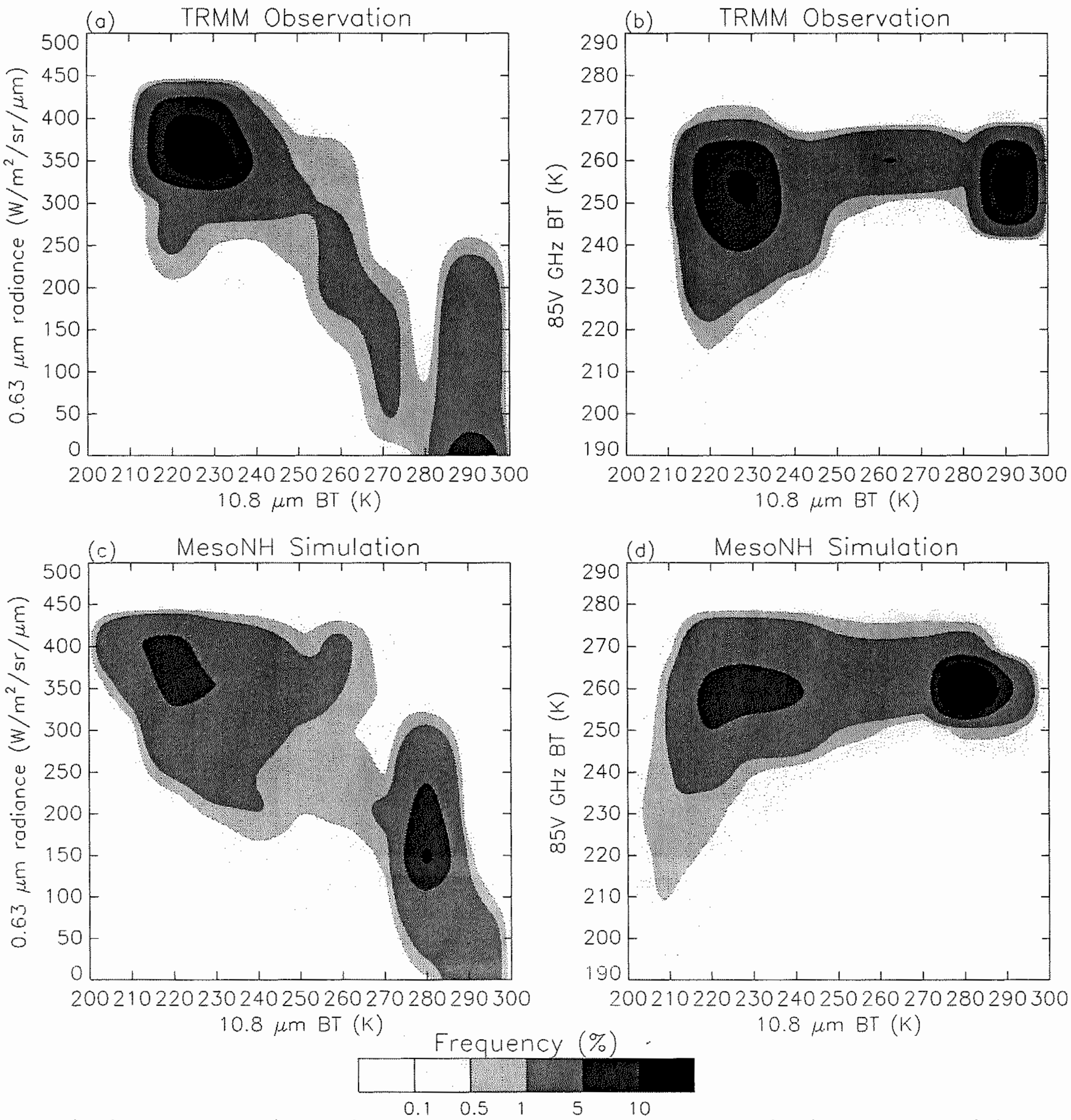

Figure 2: (top) observed and (bottom) simulated bidimensional histograms of (a, c) 10.8 μm BTs (K) against 0.63 μm radiances (W m^{-2} sr^{-1} μm^{-1}), and (b, d) 85V GHz BTs (K) against 10.8 μm BTs (K). Bins are every 50 W m^{-2} sr^{-1} μm^{-1} and 10 K.

2.3 TRMM Observations

TRMM has on board two radiometers, VIRS and TMI. The VIRS is a 5 channel cross-track scanning radiometer, similar to AVHRR, operating at 0.63, 1.6, 3.75, 10.8, and 12 μm, with a spatial resolution of 2.2 km at nadir. TMI measures the microwave radiation at ?ve separate frequencies, 10.65, 19.35, 21.30, 37.00, 85.50 GHz, for both vertical and horizontal polarizations, except for the 21.30 GHz channel that is only observed in vertical polarization. From a satellite altitude of 350 km, TMI has a 780 km wide swath on the surface. The spatial resolution ranges from 36.8 km x 63.2 km at 10.65 GHz to 4.6 km x 7.2 km at 85.50 GHz. We use the 1B01 and 1B11 products which produces calibrated radiances and brightness temperatures for the orbit #18414 on February 7, 2001 between 1346 and 1349 UTC. For sake of concision, only radiances at 0.63 μm, BTs at 10.8 μm and 85.50 GHz (vertical polarization, 85V GHz hereafter) are shown in the following.

3. RESULTS

We start by comparing snapshots of observed and simulated radiances/BTs (?g. 1). Observations from TRMM instruments show high-level clouds with 10.8 μm BTs less than 230 K in the eastern part of the domain and mostly clear sky with 10.8 μm BTs greater than 280 K to the west. Around (36S, 24W), radiances at 0.63 μm larger than 450 W m^{-2} sr^{-1} μm^{-1} indicate dense thick clouds. BTs at 85V GHz, lower than 220

K, result from signi?cant scattering by graupel embedded in the convective clouds. Downstream (the upper-level wind is northeasterly), 10.8 μm BTs lower than 220 K reveal the presence of cirrostratus, a signature of convective out?ows. The Meso-NH simulation well captures the overall situation with high-level clouds to the east and mostly clear sky to the west. The convective system albeit further northwest is also characterized by large 0.63 μm radiances and low 85V GHz BTs in agreement with the observation. The convective out?ow is accordingly further northwest, but located at the top of the convective plume.

The analysis is pursued by looking at the consistency between radiances and BTs for both the observation and the simulation through bidimensional histograms (?g. 2). Observed BTs at 10.8 μm larger than 250 K are accompanied with low-to-moderate radiances at 0.63 μm (?g. 2a) and BTs at 85V GHz larger than 240 K (?g. 2b). Higher cloud with BTs at 10.8 μm less than 240 K are also deep with radiances greater than 250 W m^{-2} sr^{-1} μm^{-1}, but only a small fraction shows low values of BTs at 85V GHz thus denoting the presence of graupel. Histograms from the simulation show a similar distribution of radiances and BTs (?g. 2c, d). They also point out some discrepancies. For example, Meso-NH overpredicts synthetic BTs at 10.8 μm around 280 K compared to the two peaks observed around 270 K and 290 K (Fig. 2a, c). This suggests a misleading representation of low-level clouds. Finally, Meso-NH overpredicts low BTs at both 10.8 μm and 85V GHz (Fig. 2b, d) suggesting too much graupel and a cloud top too high.

4. CONCLUSION

The systematic evaluation of the cloud scheme of the Meso-NH mesoscale model is shown to be very helpful by comparing synthetic radiances to observed ones for the two TRMM radiometers sensing in the visible, infrared, and microwave ranges. A tropical convective situation is examined, showing that the model is able to simulate realistic synthetic radiances using standard parameterizations of the cloud radiative properties. This model-to-satellite approach, which combines an explicit cloud scheme implemented in the mesoscale model with several detailed radiative transfer codes, allows us to examine the vertical distribution of hydrometeors within the cloud systems. In particular, it points out that a simulated cirrostratus out?ow is insuf?ciently exported away from the convective tower. We plan to extend this work to several contrasted meteorological situations.

5. REFERENCES

Chaboureau, J.-P., J.-P. Cammas, P. Mascart, J.-P. Pinty, C. Claud, R. Roca et J.-J. Morcrette, 2000: Evaluation of a cloud system life-cycle simulated by Meso-NH during FASTEX using METEOSAT radiances and TOVS-3I cloud retrievals. *Q. J. R. Meteorol. Soc.*, **126**, 1735-1750.

Chaboureau, J.-P., J.-P. Cammas, P. Mascart, J.-P. Pinty, and J.-P. Lafore, 2002: Mesoscale model cloud scheme assessment using satellite observations. *J. Geophys. Res.*, **107(D16)**, 4301, doi:10.1029/2001JD000714.

Dubuisson P., J.-C. Buriez, and Y. Fouquart, 1996: High spectral resolution solar radiative transfer in absorbing and scattering media: application to the Satellite Simulation. *J Quant Spectrosc Radiat Transfer*, **55**, 103-126.

Lacis A. A. and V. Oinas, 1991: A Description of the correlated k-distribution method. *J. Geophys. Res.*, **96**, 9027-9064.

Pardo, J. R., J. Cernicharo, and E. Serabyn, 2001: Atmospheric Transmission at Microwaves (ATM): An improved model for mm/submm applications, *IEEE Trans. on Antennas and Propagation*, **49/12**, 1683-1694.

Pinty, J.-P. and P. Jabouille, 1998: A mixed-phase cloud parameterization for use in a mesoscale non-hydrostatic model: simulations of a squall line and of orographic precipitations. in *Proceedings of the AMS conference on cloud physics*, Everett, Washington.

Prigent, C., J. R. Pardo, M. I. Mishchenko, and W. B. Rossow, 2001: Microwave polarized scattering signatures in clouds: SSM/I observations interpreted with radiative transfer simulations, *J. Geophys. Res.*, **106**, 28243-28258.

Stamnes K., S. Tsay, W. Wiscombe, K. Jayaweera, 1988: Numerically stable algorithm for discrete-ordinate-method radiative transfer in multiple scattering and emitting layered media. *Appl Opt*, **27**, 2502-2509.

Wiedner, M., C. Prigent, J. R. Pardo, O. Nuissier, J.-P. Chaboureau, J.-P. Pinty and P. Mascart, 2004: Modeling of passive microwave responses in convective situations using outputs from mesoscale models: comparison with TRMM/TMI satellite observations. *J. Geophys. Res.*, **109**, in press, doi:10.1029/2003JD004280

MULTIMODEL ENSEMBLE FORECAST OF PRECIPITATION OVER THE ALPINE REGION DURING THE MAP-SPECIAL OBSERVING PERIOD USING MESOSCALE MODELS

Federico Ceccarelli[1,2], T.N. Krishnamurti[3], B. Mackey[3], C.F. Ratto[1,2]
*

[1]Department of Physics, University of Genova, Italy
[2]INFM, Italy
[3]Meteorology Department, Florida State University, United States

1. INTRODUCTION

Forecasting the exact location and intensity of heavy precipitation events is maybe the most difficult challenge for a numerical weather prediction model. The errors in the forecast of the precipitation field can be a consequence of both errors in the analisys both errors in the model itself. The correct estimation of moisture tranfers and convection in the low atmosphere are crucial for a skillful forecast. Also the resolution of the horizontal computational grid is related to the accuracy of rainfall prediction, especially when the orography of the domain is complex.
In the last few years, in order to improve the rainfall forecast overcoming the errors of the observations and of the single models, ensemble-based predictions have been adopted by several weather services. Many different ensemble techniques exist. In this work is descripted a multimodel-multianalisys ensemble technique, in literature known as *superensemble* technique (Krishnamurti et al. 2000a, 2000b, 2001), applied to limited area mesoscale models.
In the past this methodology was applied only to General Circulation Models at low horizontal resolution. This study aims to understand if this approach can be applied to high resolution mesoscale models in order to improve the forecast of precipitation over the Alpine Region, Europe.
In this study have been chosen as ensemble members different limited area models from the MAP-SOP archive (Mesoscale Alpine Programme, Special Observing Period, September 7th - November 15th 1999). The horizontal resolution of these models ranges from $3km$ to $21km$.
The superensemble forecast has been compared with high resolution observations of precipitation coming from the station-data MAP dataset and SSM/I (Special Sensor Microwave Imager) - TRIMM (Tropical Rainfall Measuring Mission) satellite. These satellite data were originally available at 1° of horizontal resolution.

*Corresponding author's address: Federico Ceccarelli, University of Genova, Phisycs Department, Via Dodecaneso 33, 16146, genova, Italy; E-mail: ceccarelli@fisica.unige.it.

2. THE SUPERENSEMBLE METHODOLOGY

This metodology, at the Meteorology Department of Florida State University, is based on a statistical comparison between forecasts from different models and a dataset of observations.
The dataset has to be divided into two parts, the former for the training of the superensemble and the latter for the forecasts verification. During the first phase a multiple linear regression is performed on the training subset to determine a set of statistical weights for each model that minimizes the error between the combination of the models (the superensemble) and the observed state. Finally, using these weights, the forecasts for the second part of the period are evaluated and verified against the observation subset. The above process is performed separately for every grid-cell of the common models domain, for each variable considered for every timestep. In this study this metodology has been applied only to precipitation. Mathematically:

$$S(t) = \overline{O} + \sum_{i=1}^{n} a_i(F_i(t) - \overline{F_i}) \qquad (1)$$

where S is the superensemble forecast, $\overline{O}$ the observed mean over the training period, N the number of members, a_i the ith model regression weight, $F_i(t)$ the ith model forecast and $\overline{F_i}$ the ith model time mean over the training period. The weights a_i are determined via

Model	Hor. Resolution	Forec. Lenght.
BOLAM21	~ 21km	72h
BOLAM07	~ 7km	36h
Aladin	~ 12km	48h
Lilam	~ 10km	72h
Lokal	~ 7km	48h
Swiss Model	~ 10km	48h
MC2	~ 3km	24h
ECMWF	~ 55km	72h

Table 1: Models used as ensemble members.

the least square minimization of the cost function J:

$$J = \sum_{t=1}^{T} (S(t) - O(t))^2 \tag{2}$$

where $O(t)$ is the observed state and T the lenght of the training period.

3. THE DATASET

In this work the attention is focused on precipitation forecasts for the Alpine Region. Several different superensemble configurations have been tested to understand if this can improve especially the forecast of heavy rainfall events. The period studied is the MAP-SOP extending for about 70 days during the autumn 1999.

In table 1 is reported the list of the mesoscale models (plus one General Circulation Model) used in this work. Before performing the linear regression all the models have been reported by a bilinear interpolation process on the same grid at $21km$ of horizontal resolution.

The observations from ground stations and satellites, used for training and verification, have been combined in a unique field. The ground observations were originally hourly data and have been cumulated in different intervals and reported on the same $21km$ grid used for the models. None interpolation has been performed but it was assigned to every grid cell the rain gauge value obtained averaging the mesurements of the different stations located in that cell. Finally the precipitation field observed from the satellites has been considered as first guess and corrected locally with the station data observations. This technique should permit to keep the high resolution information coming from the station data without introducing in the precipitation field the errors deriving from any kind of interpolation. The dataset covers about 75 days and has been divided in different ways because many training/forecast lenghts have been tested.

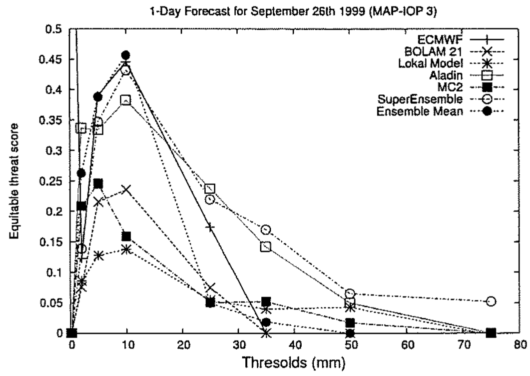

Figure 1: Equitable threat score for day-1 precipitation forecast for 26th September 1999, MAP-IOP 03.

Anyway for the training phase at least 50 days of data have always been used. The number of members for the superensemble ranges from a minimum of 5 to a maximum of 8. It depends on the lenght of the forecast chosen.

4. RESULTS

To verify the skill of the superensemble forecasts have been chosen two skill scores extensively used for this purpose. Equitable threat score (ETS) and Bias score (BS) are defined below:

$$ETS = \frac{H - H_{random}}{H + M + FA - H_{random}} \tag{3}$$

where

$$H_{random} = \frac{(H + M)(H + FA)}{N} \tag{4}$$

In these formulae, H corresponds to a hit, M denotes a miss, FA is the number of false alarm and N is the total number of forecast point. By using the ETS, a forecast is rewarded for predicting precipitation amounts at least equal to the observed values for a given thresold. Anyway a forecast is penalized for forecasting precipitation in the wrong place as well as not forecasting it in the right place for that same thresold. In addition, there is an adjustment for hits associated with random chanche. The ETS may fram from 0 to +1 where one indicates a perfect score.

The bias score compares areas of predicted and observed rainfall. A score of one indicates no bias. Precipitation amounts are said to be underforecasted (overforecasted) for a bias score less than one (greater than one).

$$BIAS = \frac{H + FA}{H + M} \tag{5}$$

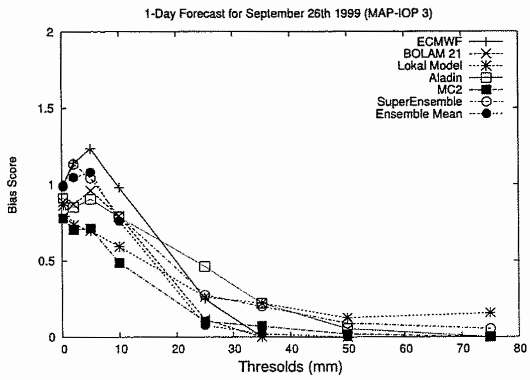

Figure 2: Equitable threat score for day-1 precipitation forecast for 26th September 1999, MAP-IOP 03.

In figure 1 are reported the scores obtained for the day-one forecast of the MAP Intense Observing Period 3 (September, 25th-26th, 1999), a case of heavy orographic rain in the Lago Maggiore Basin, located South of the Alps. In this configuration the training phase lasted 70 days. It is clear that the superensemble forecast shows a better ETS skill compared to ensemble members and ensemble mean for higher thresolds of precipitation.
Also the bias score, reported in fig 2, reveals a good behaviour of the superensamble for high precipitation rates even if Lokal model seems to have a lower bias in this case. In this case bias scores, for high thresolds, gets very low for all of the models showing the difficulty in predicting high precipitation events.
In fig 3 is shown the comparison between observed rainfall and superensamble, ensemble mean and the best model forecasts for the 26th of September. It seems that the superensemble reproduces with more accuracy the location of high precipitation peaks, as it is visible in the maps in the northern part of Italy, close to Garda Lake.

4. SUMMARY

The precedings results and the further tests performed in the whole work and not included in this abstract are encouraging and show that this multimodel-ensemble methodology could be suitable for short-term high resolution precipitation forecasts.
For high thresolds of precipitation the superensemble shows a better skill compared to ensemble members and ensemble-mean. In the next months this work will be extended and completed with other datasets. The final aim is to build an operational superensamble using as ensemble members actual numerical models.

The low computational cost of this postprocessing technique make it suitable for operational forecasting even in smaller meteorological centers.

5. AKNOWDELEGEMENTS

This work was possible thanks to the experience and assistance of Prof. T.N.Krishnamurti and his work group at the Meteorology Department of Florida State University. They gave to the author the support and the codes needed to apply the superensemble technique.
The author would also like to thank the Meteo-Idrological Centre of Liguria Region which gave the acces to the models' database.

6. REFERENCES

Fiordaliso,A.,1998: Nonlinear forecasts combination method based on Takagi-Sugeno fuzzy systems. International Journal of Forecasting, 14, 367-379.
Krishnamurti, T.N., C.M. Kishtawal, T. LaRow, D. Bachiochi, Z. Zhang, C.E. Williford, S. Gadgil and S. Surendran, 1999: Improved skills for weather and seasonal climate forecasts from multimodel superensemble. Science, September 3, 1999.
Krishnamurti, T.N., C.M. Kishtawal, T. LaRow, D. Bachiochi, Z. Zhang, C.E. Williford, S. Gadgil and S. Surendran, 2000: Multimodel superensemble forecasts for weather and seasonal climate. J. Climate, 13, 4196-4216.
Krishnamurti, T.N., C.M. Kishtawal, D.W. Shin and C.E. Williford, 2000: Improving tropical precipitation forecasts from a multianalysis superensemble. J. Climate, 13, 4217-4227.
Krishnamurti, T.N., S. Surendran, D.W. Shin, R.J. Correa-Torres, T.S.V. Vijaya Kumar, C.E. Williford, C. Kummerow, R.F. Adler, J. Simpson, R. Kakar, W.S. Olson, and F.J. Turk, 2001: Real-time multianalysis-multimodel superensemble forecasts of precipitation using TRMM and SSM/I products. Mon. Wea. Rev., 129,2861-2883.
Mitra, A.K., M. Das Gupta, S.V. Singh, 2003: Daily rainfall for the Indian monsoon region from merged satellite and rain gauge values: large-scale analysis from real-time data. J. Hydrometeorology, 4, 769-781.
Tomassetti B., G. Filippo, M.Verdecchia, G.Visconti, 2003: Regional model simulation of the hydrometeorological effects of the Fucino Lake on the surrounding region. Annales Geophys. 2003, 21, 2219-2232.
Williford, C.E., T.N. Krishnamurti, R. Correa-Torres, S. Cocke, Z. Christidis, and T.S.V. Vijaya Kumar, 2003: Real-time multimodel superensemble forecasts of Atlantic tropical systems of 1999. Mon. Wea. Rev., 131, 1878-1894.

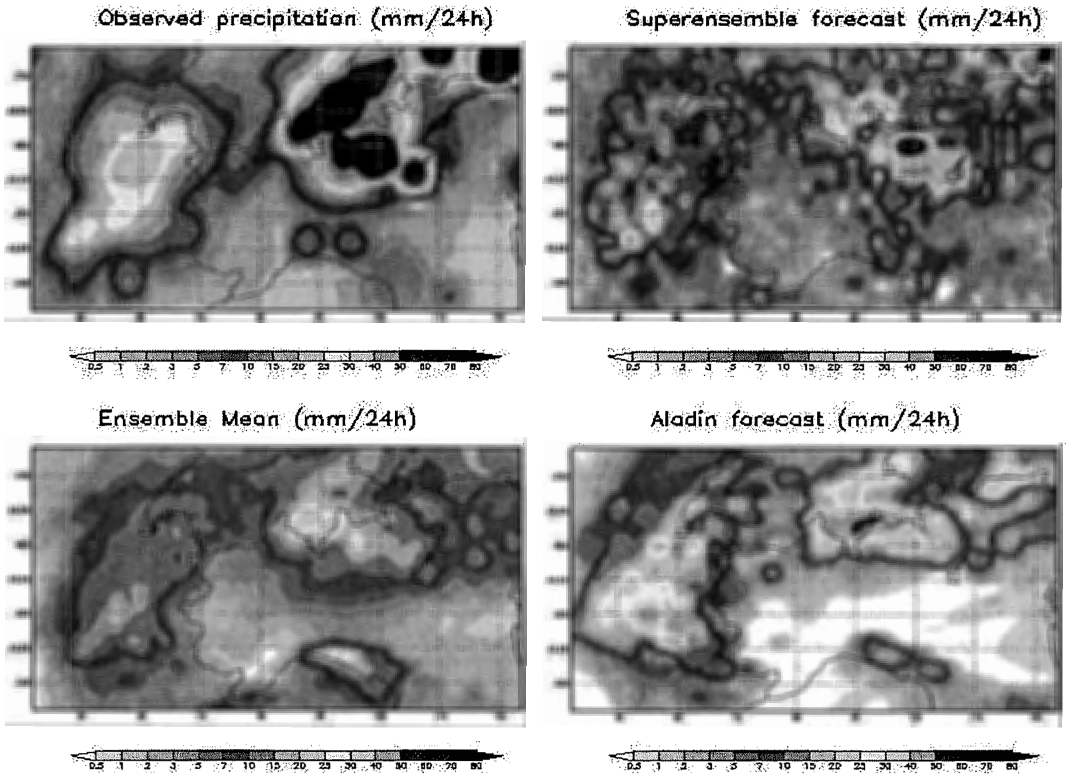

Figure 3: 24h Precipitation pattern observed and forecasted (day-1) for September 26th, 1999. Comparison between the observed precipitation, the superensemble forecast, the ensemble mean forecast and the best ensemble member for that day.

IMPLEMENTATION OF A NEW ICE AGGREGATION AND SEDIMENTATION SCHEME IN A BULK-MICROPHYSICAL MODEL, DERIVED FROM AIRCRAFT OBSERVATIONS

R. J. Cotton,* P. R. Field[1]

1. Met Office, Exeter, UK.

1. INTRODUCTION

Observations using aircraft mounted laser-imaging probes often show bimodal ice particle size distributions (PSDs) with an approximately exponential distribution of small ice crystals combined with a larger ice particle distribution with a discrete mode, (see Heymsfield (1975), Mitchell et al. (1996) and Field (1999)). This bimodality can be explained if aggregation of ice is the dominant process occurring in the larger particle mode, while particle production (nucleation) and diffusional growth dominates the smaller mode (Field 2000). The evolution of the small and large ice modes are therefore controlled by different underlying physics.

This paper describes the implementation of a new ice aggregation and sedimentation scheme in the UK Met Office Large-Eddy Model (LEM), derived from in-situ aircraft observations. The aggregation-sedimentation scheme is tested using two scenarios. The first, which is to validate the operation of the scheme, is the generation of a steady-state cloud element with a constant snow source. The second is the evolution of an idealised cloud layer using both the default and this new aggregation-sedimentation scheme.

2. THE LARGE-EDDY MODEL

The LEM is a high resolution numerical model used to simulate a wide range of turbulent-scale and cloud-scale problems. A large-eddy simulation explicitly resolving the larger scale turbulent motions, leaving only smaller scale (sub-grid) physics to be parametrized. The LEM microphysics is described in Swann (1998).

The basic prognostic variables are the potential temperature (θ), water vapour mass mixing ratio (q_v), and cloud liquid water mixing ratio (q_L). The bulk water cold microphysics scheme is incorporated by the addition of cloud ice (pristine small ice crystals) and snow (low density ice aggregates) hydrometeor categories. When ice particles grow larger, they are reclassified as snow. The ice-phase hydrometeors can be represented by double-moment parametrisations with prognostic variables for the mass mixing ratios (q_I and q_S), and the number mixing ratios (n_I and n_S). The number concentration can be represented by an exponential distribution,

$$n(D) = n_0 \exp(-\lambda D)$$

*Corresponding author: Cloud Physics Research, Met Office, Fitzroy Road, Exeter, Devon, EX1 3PB, UK. e-mail: richard.cotton@metoffice.com

where $n(D)$ is the concentration of particles of a given diameter D, and n_0 and λ are the intercept and slope parameters, and the mass distribution $M(D)$ by a power-law,

$$M(D) = cD^d$$

where c and d are constants which define the particle characteristics. The intercept and slope parameters can then be derived from the n and q bulk water variables.

The sedimentation of the bulk water variables n and q are also parametrised in terms of the intercept and slope parameters. The concentration is advected downward with the number weighted fall speed, V_n, where

$$V_n = \frac{1}{n}\int_0^\infty n(D)V(D)dD$$

The mass mixing ratio is advected downward with the mass weighted fall speed, V_q, where

$$V_q = \frac{1}{q}\int_0^\infty M(D)n(D)V(D)dD$$

For each type of precipitating particle, the terminal fall speed $V(D)$ is

$$V(D) = aD^b$$

where a, b are constants. While these sedimentation equations conserve both mass and number concentration, because of the choice of an exponential size distribution, and because $V_q > V_n$ always, sedimentation can lead to unphysical model responses.

3. AGGREGATION-SEDIMENTATION SCHEME

Field and Heymsfield (2002) show that the large ice PSDs can be scaled onto a single exponential distribution for a wide range of observed conditions. This scaling enables the PSD to be given as a function of the mean particle size, D_1 and the precipitation rate, P. The fallspeed-diameter coefficients (a and b) and the mass-diameter coefficients (c and d) were correlated with P.

By representing the number concentration as an exponential distribution, the PSD can also be given as a function of n_0 and λ, or n and q. This leads to the implementation of the aggregation-sedimentation scheme as a set of functions, which give P, n_0, λ, a, b, c, d ,dn/dt, V_q and V_n all as functions of n and q only. By allowing a—d to vary as functions of the bulk water variables n and q, the effective particle density, or particle shape can vary.

For computational speed, each parameter is incorporated into the LEM using look-up tables. Figs. 1–3 show contour plots over the central high resolution look-up tables, of each parameter. The dashed lines are precipitation isopleths. The discontinuities along the $P = 0.04$ line is due to the step change in the gradient of P at that value.

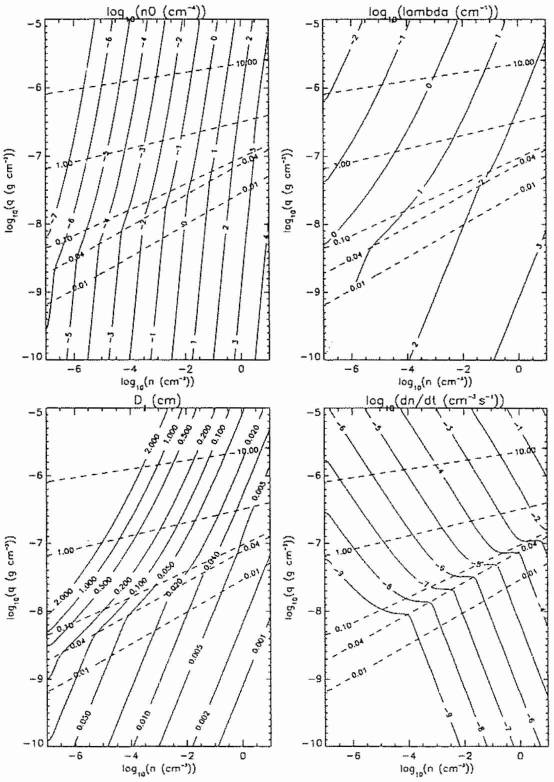

Figure 1: Contours of intercept (n_0) and slope (λ) parameters, mean particle diameter (D_1) and aggregation rate ($\frac{dn}{dt}$). The dashed lines are precipitation isopleths.

4. IDEALISED CLOUD ELEMENT WITH CONSTANT SNOW SOURCE

In order to show the basic operation of the aggregation-sedimentation scheme, a highly idealised test case is used. The aim is to generate a steady-state cloud element throughout the cloud layer depth to validate the aggregation-sedimentation implementation. Cloud elements are steady-state if the ice particle source region varies slowly on timescales relative to fallout. For steady-state aggregating-sedimenting cloud elements, the trajectories in (n,q) and (n_0,λ) space are along lines of constant precipitation. For simplicity, only the snow species is used, there is no ice or IN aerosol, all snow is generated continuously at the top of a deep cloud layer, and snow growth by vapour deposition does not deplete the environmental water vapour, nor contribute to latent heating.

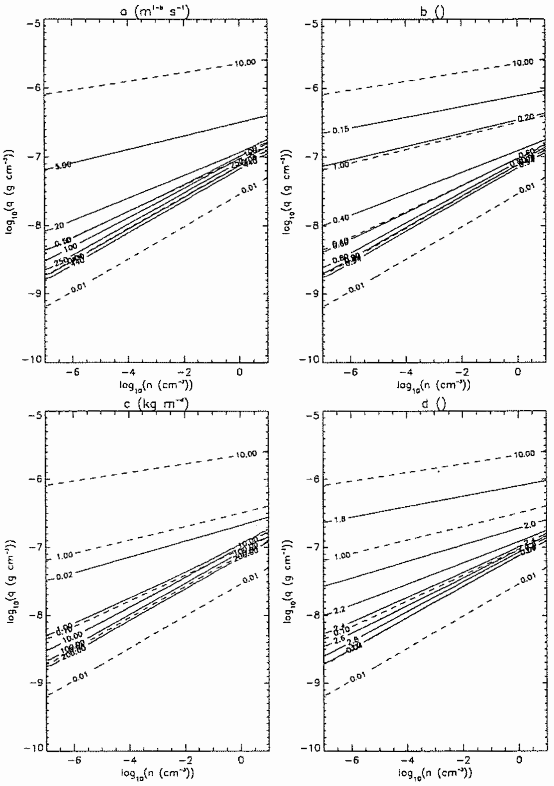

Figure 2: Contours of fallspeed-diameter coefficients (a) and (b), where $V = aD^b$, the mass-diameter coefficients (c) and (d), where $M = cD^d$.

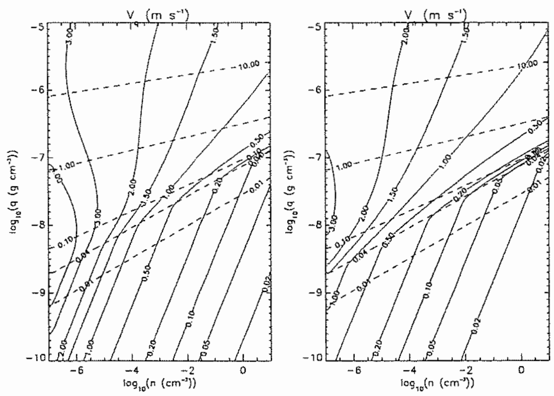

Figure 3: Contours of mass-weighted fallspeed (V_q) and number-weighted fallspeed (V_n).

The LEM is run with a two-dimensional domain 10km horizontally by 10km high. The basic state profiles of potential temperature and relative humidity used to initialise the LEM are shown in Fig. 4. The profiles correspond to neutral stratification for ice pseudoadiabatic processes within the cloud generating layer (4–8 km). Fig. 5 show layer mean profiles once steady-state is reached for two

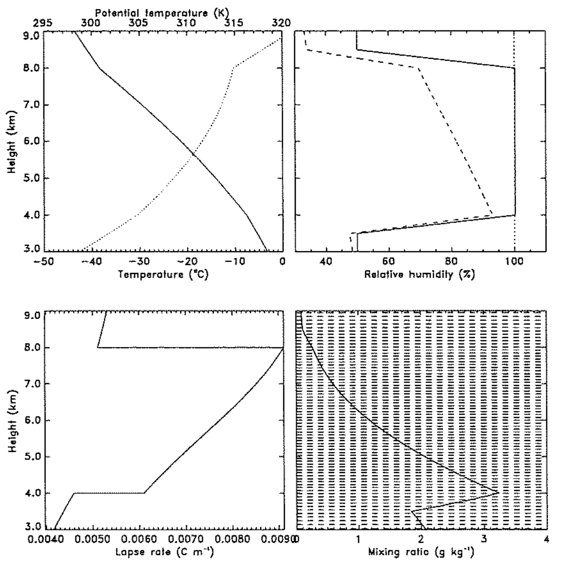

Figure 4: Initially specified thermodynamic profile (with the exception of the idealised infinite supply with diffusional growth, where the ice relative humidity is 100.2%)

model runs. Run 1 has no snow diffusional growth, and sets up an aggregating-sedimenting only cloud element, producing a constant precipitation rate throughout the cloud depth. This constant precipitation rate is just a consequence of conservation of mass. Run 2. has a constant 0.2% ice supersaturation, enabling (arbitrary) snow growth. Fig. 6 show the cloud element grid-box values in (n,q) and (n_0,λ) space.

4. IDEALISED DEEP CLOUD LAYER WITH ICE SOURCE DUE TO NUCLEATION.

The LEM domain and initial thermodynamic profile are as the idealised steady-source test, but now with a more physically realistic ice source and cloud formation. Both ice and snow species are used in double moment parametrisation. The aggregation-sedimentation scheme with coefficients as functions of n and q is applied identically to both ice and snow categories, except that the aggregation of ice is disabled. Within a grid-box, the ice is transfered into the snow category, once the mean diameter of the ice crystals exceeds 20μm. Using both ice and snow categories where the only difference is the mean diameter, and that ice does not aggregate, leads to an obvious seperation of the nucleation and aggregation processes.

Heterogeneous deposition ice nucleation is parametrised using a prognostic variable for the number mixing ratio of ice nuclei (IN) aerosol. There are no other sources of ice. Arbitrarily, all IN activate at a pre-defined ice saturation (2%) and initially have an uniform number mixing ratio (equivalent to 0.1cm^{-3} at 6km. Using a limited supply of IN enables a more realistic cloud evolution. Cloud formation is forced via an imposed di-

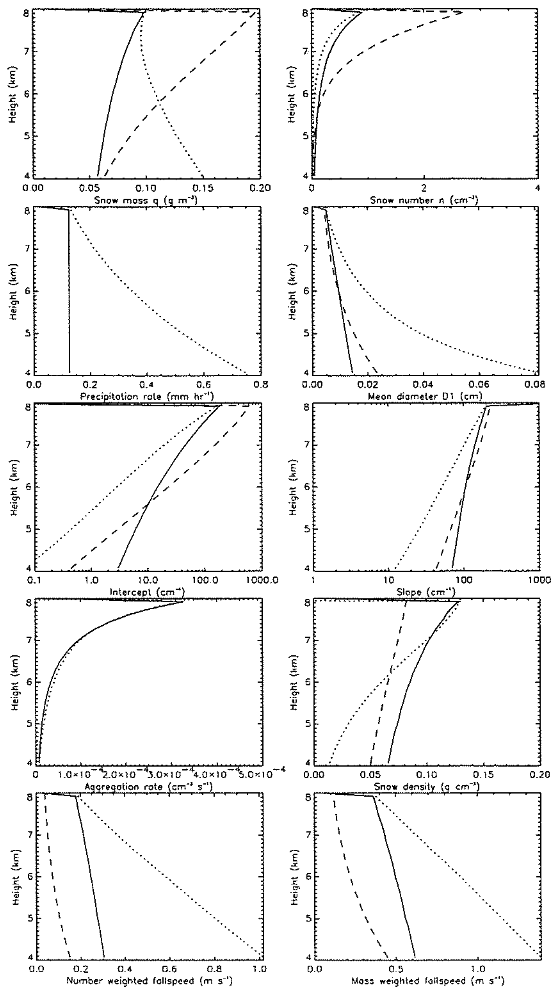

Figure 5: Steady-state cloud element. Solid line: no snow diffusional growth (run 1). Dotted line: with snow mass diffusional growth (run 2).

abatic cooling corresponding to a rate of adiabatic cooling that would be associated with an upward vertical motion of 3cm s^{-1}, applied for two hours. The model is then run for a further four hours during which the cloud slowly dissipates (this phase is more like the idealised cloud element with imposed constant snow source).

During the cooling phase, the cloud structure depends on the initially specified thermodynamic and humidity profiles, and less on the detailed microphysics. The effect of the microphysics of ice nucleation and snow aggregation is more obvious during the cloud dissipation stage. During this phase, a source of new cloud ice is maintained at cloud top by entrainment of unactivated IN from above. This entrainment is due to turbulence driven by LW radiative cooling. The ice crystals fall and grow by vapour deposition, and enventually converted into snow. Fig. 7 show layer mean profiles for two model runs, one with the new aggregation-sedimentation scheme and the other the default (constant coefficient) scheme.

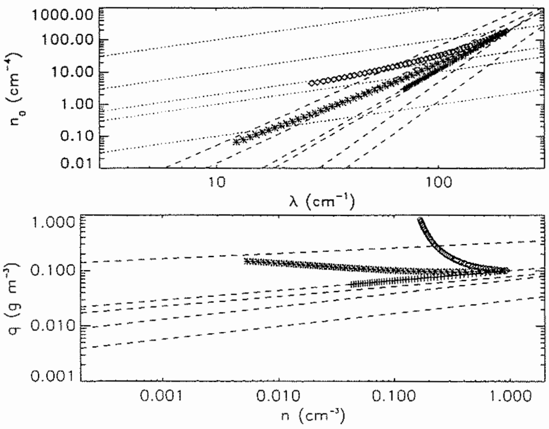

Figure 6: Steady-state cloud element. Plus symbol: no snow diffusional growth (run 1). Cross symbol: with snow diffusional growth (run 2). Diamond symbol: no aggregation (run 4).

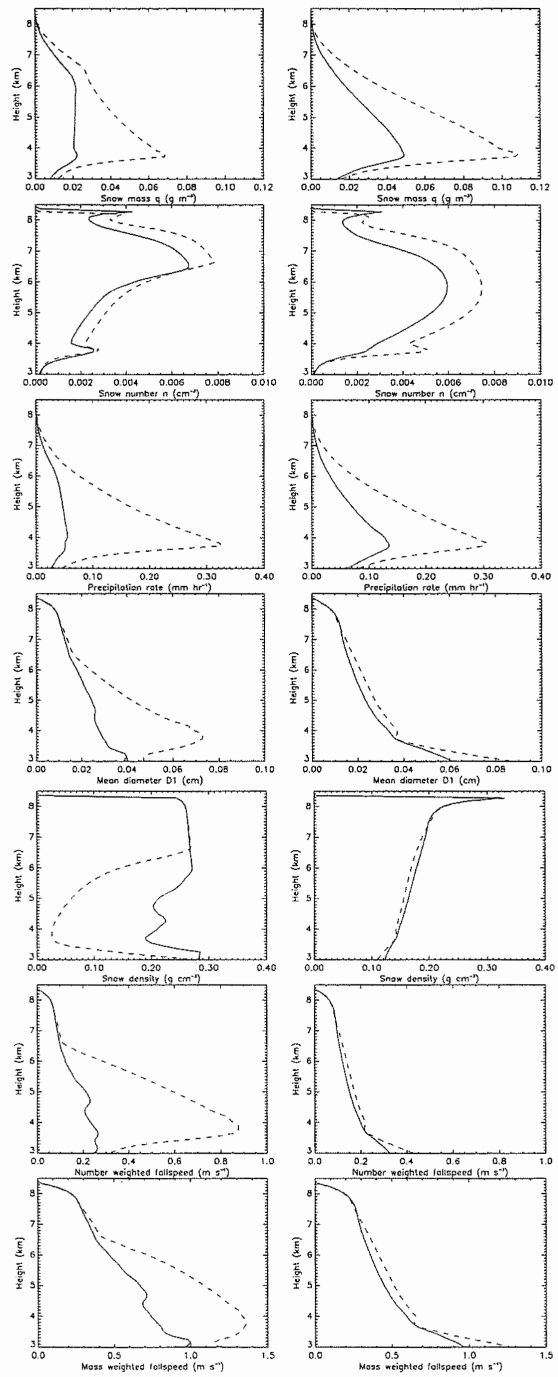

Figure 7: Evolving cloud layer. The left-hand figures are for the new aggregation-sedimentation scheme, while the right-hand ones are for the old. The dashed line is at two hours (just at the end of the cooling phase). The solid line is at three hours (during the cloud dissipation stage).

The profiles are at two hours (at the end of the cooling phase) and at three hours (during the cloud dissipation phase). During the cooling phase, the new aggregation scheme compared to the default scheme tends to produce smaller snow mass (q), higher number and mass-weighted fallspeeds (V_n and V_q) and larger mean diameter (D_1). During the dissipation phase, the new scheme produces more uniform snow mass (q) and more uniform snow density.

5. DISCUSSION AND CONCLUSION .

Observations in layer clouds, of snow mass and density profiles, when there is no large-scale ascent would therefore validate the new aggregation-sedimentation scheme.

REFERENCES.

Heymsfield, A. J., 1975: Cirrus uncirrus generating cells and the evolution of cirroform clouds.Part 1: Aircraft measurements and observations, *J. Atmos. Sci.*,**32,** 799–808

Mitchell, D. L., Chai, S. K., Liu, Y., Heymsfield, A. J. and Dong, Y., 1996: Modeling cirrus clouds. Part 1: Treatment of bimodal size spectra and case study analysis, *J. Atmos. Sci.*, **53,** 1885–1899

Field. P. R., 1999: Aircraft observations of ice crystal evolution in an altostratus cloud, *J. Atmos. Sci.*, **56,** 1925–1941

Field. P. R., 2000:Bimodal ice spetra in frontal clouds,*Q. J. R. Meteorol. Soc.*,**126,** 379–392

Heymsfield, A. J, Bansemer, A., Field, P. R., Durden, S. L., Stith, J. L., Dye, J. E., Hall, W. and Grainger, C. A., 2002: Observations and parametrisations of particle size distributions in deep tropical cirrus and stratiform precipitating clouds: Results from in situ observations in TRMM field campaigns, *J. Atmos. Sci.*, **59,** 3457–3491

Swann, H. A., 1998: Sensitivity to the representation of precipitating ice in CRM simulations of deep convection, *Atmos. Res.,* **47,** 415–435

COMPARISON OF OBSERVED AND SIMULATED DEEP CONVECTIVE CLOUD OBJECTS

Zachary A. Eitzen[1,2] and Kuan-Man Xu[1]

[1]NASA Langley Research Center, Hampton, Virginia, 23681, USA
[2]Department of Atmospheric Science, Colorado State University, Ft. Collins, Colorado, 80523, USA

1. INTRODUCTION

The evaluation of cloud resolving models (CRMs) is an important task, if we wish to use them for purposes such as the study of cloud dynamics. Also, Randall et al. (2003) have recently suggested that CRMs should be used as a replacement for the traditional cumulus parameterizations in general circulation models.

Traditionally, CRMs have been evaluated using case studies that have taken place at over a very limited temporal and spatial scale. While these studies are valuable, it is helpful to have as many cases as possible over as long a time as possible. This allows one to obtain a good measure of the model's current performance, and to verify the robustness of model improvements.

Our approach is as follows (see Fig. 1). First, we diagnose the cloud objects using CERES (Clouds and the Earth's Radiant Energy System) SSF (Single Scanner Footprint) cloud and radiative data. A cloud object is a contiguous region of footprints that fulfills a set of selection criteria. We then match the ECMWF analysis to the same location and closest available time as the cloud object. To initialize the CRM, we use vertical profiles of the temperature, moisture, wind, cooling tendencies and moistening tendencies obtained from ECMWF analyses at the same time and place. Finally, the simulated radiative and microphysical properties can be compared to those of the observed cloud objects.

2. OBSERVATIONS

In this study, we are examining cloud objects diagnosed using the SSF product from the CERES instrument on board the TRMM (Tropical Rainfall Measuring Mission) satellite. A deep convective cloud object is diagnosed with the following selection criteria: cloud optical depth greater than 10, cloud height greater than 10 km, and 100% cloudy conditions within the footprint. In addition, we are limiting ourselves to the 68 large (effective diameter greater than 300 km) cloud objects observed over the tropical (25° S - 25° N) Pacific Ocean in March 1998.

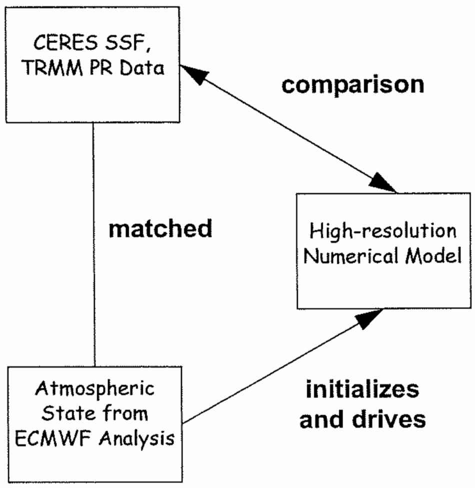

Fig. 1. Schematic diagram of the approach employed in this paper.

Once the cloud object is identified using the CERES instrument, simultaneous observations from the TRMM PR (Precipitation Radar) in the area defined by the cloud object are collected. We are using the corrected reflectivity and near-surface rainfall data from the 2A25 product.

3. MODEL

The CRM that will be used in this study is the Langley Research Center Compressible (LaRC-C) model. This model is based on the Advanced

Corresponding author's address: Zachary A. Eitzen, NASA Langley Research Center, Mail Stop 420, Hampton, VA, 23681, USA; E-Mail: z.a.eitzen@larc.nasa.gov.

Regional Prediction System model (ARPS; Xue et al. 2000), although it has been modified in two areas. The Lin et al. (1983) microphysics have been modified in a manner similar to Krueger et al. (1995). Also, the radiative transfer parameterization follows Fu and Liou (1993).

The LaRC-C simulations were performed in 2-D, with a periodic horizontal domain 512 km wide using Δx = 2 km. The vertical domain was 25 km high (the top 5 km was a sponge layer) and stretched, with an average Δz of 500 m. The initial state of the model atmosphere was horizontally homogeneous, with vertical profiles of wind, temperature, moisture, and the cooling and moistening tendencies calculated from ECMWF analyses over an area that covers the observed cloud objects.

The simulations lasted for 24 hours, the last 12 of which were used for comparison to the observed cloud objects, with a sampling frequency of every 5 minutes.

4. RESULTS

4.1 Comparisons to CERES SSF Data

In the following results, each column of the model domain was tested with the same selection criteria for cloud optical depth and effective cloud height as the observed deep convective cloud objects. Probability density functions (PDFs) were then constructed, with the total number of samples corresponding to the sum of the samples from each of the 68 simulations.

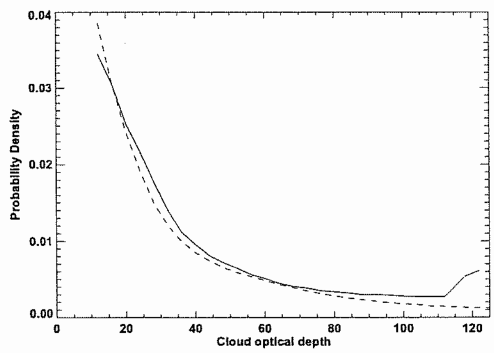

Fig. 2. PDFs of cloud optical depth from the CERES SSF data (solid line) and from the simulations (dashed line).

The observed and simulated cloud optical depth (τ) PDFs are shown in Fig. 2. The model produces a PDF that is quite similar to that observed. Note that the CERES instrument saturates at a value of approximately τ=120, which accounts for the increase in the observed PDF at the tail of the spectrum.

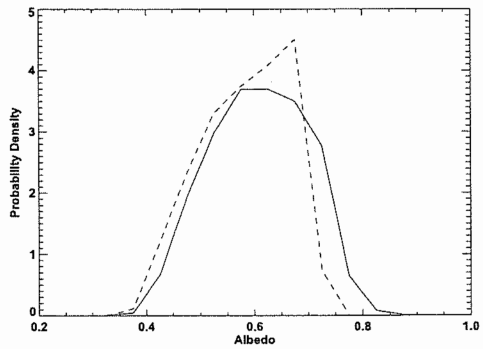

Fig. 3. PDFs of albedo from the CERES SSF data (solid line) and from the simulations (dashed line).

In Fig. 3, the observed and simulated PDFs of albedo are shown. The simulated PDF is similar to that observed. However, the simulated albedos are slightly lower and are distributed less symmetrically than those observed.

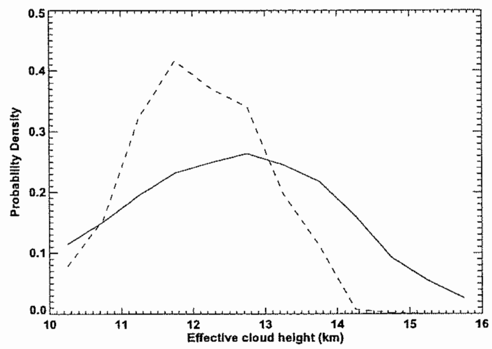

Fig. 4. PDFs of effective cloud height from the CERES SSF data (solid line) and from the simulations (dashed line).

The effective cloud height is the height at which, integrating from the top of the atmosphere, τ=1. PDFs of the observed and simulated effective cloud heights are shown in Fig. 4. We see that the simulated cloud heights are lower than those observed, with very few clouds with an effective height above 14 km.

Since the simulated cloud heights were lower than those observed, we expect the OLR distribution to be skewed towards values that are higher than observed. In Fig. 5, we see that this is indeed the case, with few simulated OLRs occurring at values less than 90 W m^{-2}.

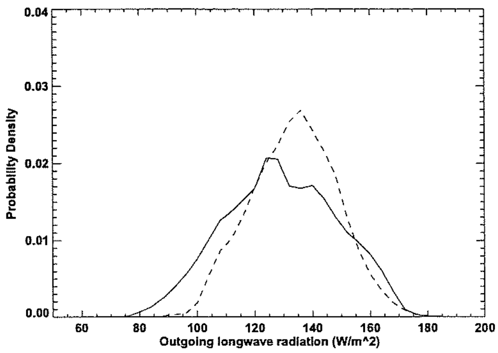

Fig. 5. PDFs of OLR from the CERES SSF data (solid line) and from the simulations (dashed line).

4.2 Comparisons to TRMM PR Data

In Fig. 6, we have calculated contoured frequency by altitude diagrams (CFADs; see Yuter and Houze 1995) for the observed and simulated cloud objects. The simulated reflectivities were calculated using the method of Smith et al. (1975). The bins are 2 dBZ wide, and cover a range from 18-68 dbZ. Note that the only selection criterion for this comparison is a minimum reflectivity of 18 dBZ. This lower threshold was chosen since "the actual minimum detectable Z can be considered to be about 16-18 dBZ" according to the TRMM PR Algorithm Instruction Manual (2000).

Both the observed and simulated CFADs show the presence of a bright band near the freezing level of ~ 5 km. However, we see significant differences between the observed and simulated CFADs. The simulated reflectivities are much more likely to be greater than 40 dBZ in the model than the observations, particularly at altitudes above the freezing level.

Since the Krueger et al. (1995) modification of the Lin et al. (1983) ice microphysics scheme produces much more graupel, we decided to perform a diagnostic test where the simulated graupel was all classified as snow. The results of this test are shown in Fig. 6c. This switch has a large effect at altitudes above 6 km, where "dry" snow (diagnosed when the temperature is less than 0° C) is less reflective than graupel. Conversely, the switch of graupel to snow causes the simulated

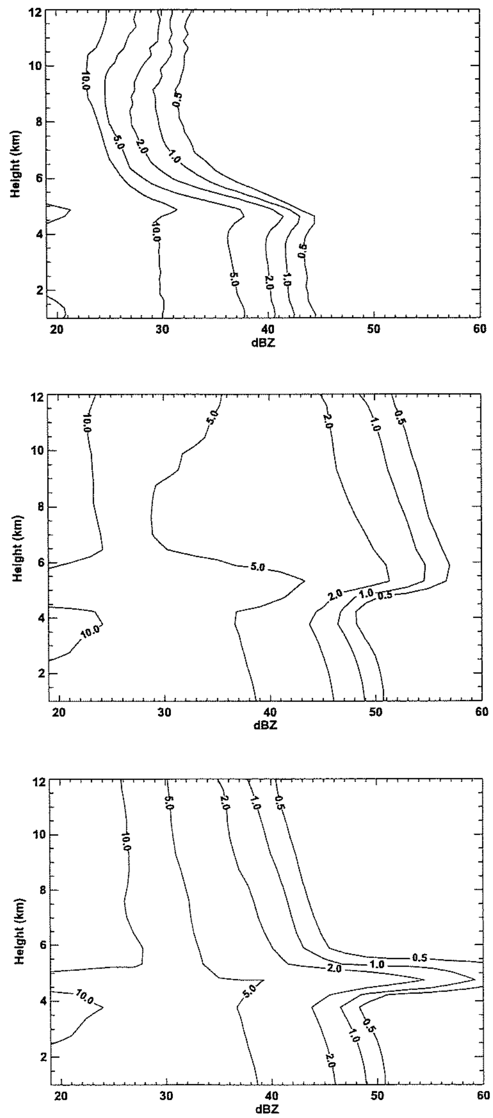

Fig. 6. CFADs for a) the observed TRMM PR reflectivities, b) the simulated reflectivities, and c) the simulated reflectivities with the graupel replaced by snow.

reflectivity to increase near the freezing level, due to the high reflectivity of "wet" snow.

In Fig. 7, we compare the probability density functions (PDFs) of the observed and simulated surface precipitation rates. The only selection criterion for this comparison is that the precipitation rate be greater than 1 mm hr^{-1}. The width of the bins is 1 mm hr^{-1}. We see that both the observed and simulated precipitation rates produce PDFs that are exponential in shape. The simulated dis-

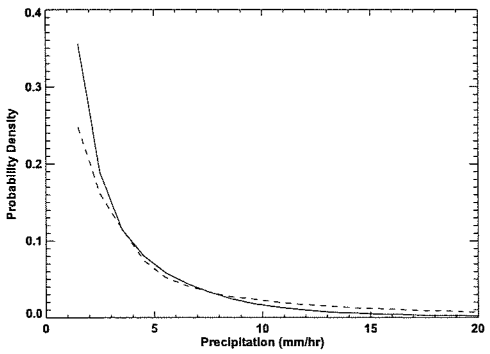

Fig. 7. PDF of surface precipitation rate (mm/hr) from the TRMM PR (solid line) and of the simulated precipitation (dashed line).

tribution is similar to that observed, although it is somewhat flatter, with a lower proportion of precipitation rates in the lowest (1-2 mm hr^{-1}) bin, and a higher proportion of heavy (greater than 10 mm hr^{-1}) precipitation rates than observed. It should be noted that Kummerow et al. (2000) found that the PR underestimated rainfall compared to surface radar stations over the oceans.

5. PRELIMINARY CONCLUSIONS AND FUTURE WORK

We have compared ensembles of observed and simulated deep convective cloud objects. The LaRC-C CRM performed well in simulating the PDFs of several variables: cloud optical depth, albedo, and precipitation rate. The model produced cloud heights that were lower than observed, and OLRs that were higher than observed. The model did not produce a realistic CFAD of reflectivity, but a simple diagnostic test where graupel was treated as snow in the reflectivity calculation indicated that improvements may be made to the model if the model's microphysics code is modified to produce less graupel.

In the future, we will examine the model's ability to simulate smaller deep convective cloud objects. Also, we plan on using TRMM Microwave Imager precipitation data, which has the advantage of sampling a wider swath than the TRMM PR. In addition, we will simulate other types of cloud objects that have been diagnosed from the CERES SSF data, such as boundary-layer stratus, stratocumulus, and shallow cumulus.

REFERENCES

Fu, Q., and K. N. Liou, 1993: Parameterization of the radiative properties of cirrus clouds. *J. Atmos. Sci.*, **50,** 2008-2025.

Krueger, S. K., Q. Fu, K. N. Liou, and H.-N. S. Chin, 1995: Improvements of an ice-phase microphysics parameterization for use in numerical simulations of tropical convection. *J. Appl. Meteor.*, **34,** 281-287.

Kummerow, C., and 26 Coauthors, 2000: The status of the Tropical Rainfall Measuring Mission (TRMM) after two years in orbit. *J. Appl. Meteor.*, **39,** 1965-1982.

Lin, Y. L., R. D. Farley, and H. D. Orville, 1983: Bulk parameterization of the snow field in a cloud model. *J. Climate Appl. Meteor.*, **22,** 1065-1092.

Randall, D. A., M. Khairoutdinov, A. Arakawa, and W. Grabowski, 2003: Breaking the cloud-parameterization deadlock. *Bull. Amer. Meteor. Soc.*, **84,** 1547-1564.

Smith, P. L., Jr., C. G. Myers and H. D. Orville, 1975: Radar reflectivity factor calculations in numerical cloud models using bulk parameterization of precipitation. *J. Appl. Meteor.*, **14,** 1156-1165.

Xue, M., K. K. Droegemeier, and V. Wong, 2000: The Advanced Regional Prediction System (ARPS) - A multiscale nonhydrostatic atmospheric simulation and prediction tool. Part I: Model dynamics and verification. *Meteor. Atmos. Physics.*, **75,** 161-193.

Yuter, S. E., and R. A. Houze Jr., 1995: Three-dimensional kinematic and microphysical evolution of Florida cumulonimbus. Part II: Frequency distributions of vertical velocity, reflectivity, and differential reflectivity. *Mon. Wea. Rev.*, **123,** 1941-1963.

SENSITIVITY OF SIMULATED WARM RAIN FORMATION TO COLLISION AND COALESCENCE EFFICIENCIES, BREAKUP, AND TURBULENCE: COMPARISON OF TWO BIN-RESOLVED NUMERICAL MODELS

Ann Fridlind[1], Axel Seifert[2], Andrew Ackerman[1], and Eric Jensen[1]

[1]NASA Ames Research Center, Moffett Field, CA, USA
[2]National Center for Atmospheric Research, Boulder, CO, USA

1. INTRODUCTION

Numerical models that resolve cloud particles into discrete mass size distributions on an Eulerian grid provide a uniquely powerful means of studying the closely coupled interaction of aerosols, cloud microphysics, and transport that determine cloud properties and evolution. However, such models require many experimentally derived paramaterizations in order to properly represent the complex interactions of droplets within turbulent flow. Many of these parameterizations remain poorly quantified, and the numerical methods of solving the equations for temporal evolution of the mass size distribution can also vary considerably in terms of efficiency and accuracy. In this work, we compare results from two size-resolved microphysics models (Ackerman et al. 1995; Seifert and Beheng 2001) that employ various widely-used parameterizations and numerical solution methods for several aspects of stochastic collection.

2. INITIALIZATION

We perform all of our tests using a box model initialized with a gamma distribution of droplets at the 1000 mb level. Fall velocities are taken from Rogers et al. (1993), where necessary, although evolution in the box model is assumed to proceed without sedimentation removal and results are remarkably insensitive to using a more complicated fall velocity computation method, such as one dependent upon Reynolds number (Pruppacher and Klett 1997). All of our tests are limited to the iteraction of liquid drops.

3. NUMERICAL METHODS

We begin by testing numerical methods used by each model to integrate the stochastic collection equation since errors associated with the numerical method may naturally affect the results of subsequent parameterization tests. We compare two newer methods (Bott 1998; Jacobson et al. 1994) with the classical method derived by Berry and Reinhardt (1978). In subsequent discussion, we refer to these three methods as Bott's, Jacobson's, and Berry's. To compare them most simply, we use the Long (1974) collection kernel, as adjusted by Seifert and Beheng (2001).

The Berry method remains the standard against which other methods can be compared, but is unstable when bin resolution is as coarse as in today's three-dimensional cloud simulations. We find that the Bott method provides an excellent alternative to Berry that is stable at low bin resolution, but predicts some cloud water remaining at the end of the simulation, a feature not produced by the other two methods. We find that the Jacobson method, while also stable, is significantly more diffusive than the other two methods. However, we derive a correction to the Jacobson method that is inspired by Bott's central flux-limiting concept and is equally successful in controlling numerical diffusion. With this correction in place, the Jacobson method provides an accurate and stable alternative to Berry, as well.

4. COLLISION AND COALESCENCE EFFICIENCES

Turning next to the most fundamental parameterization of collision-coalescence, we evaluate the basic gravitational collection kernels. We first compare the Long kernel with that of Hall (1980) and Pinsky et al. (2001) at the 1000 mb level. Whereas the simple analytical Long kernel requires no separate dependence on coalescence efficiencies (or fall velocities), for the latter two we use each model's standard coalescence efficiency parameterization, to which results with most initial size distributions used here are insensitive (future work will further address this matter). Overall, for distributions of drops with mean sizes exceeding ap-

Corresponding author's address: Ann Fridlind, NASA Ames Research Center, Mail Stop 245-4, Moffett Field, CA 94035; E-mail: ann.fridlind@nasa.gov.

proximately 8 micrometers, we find results are surprisingly insensitive to differences in the gravitational collection kernel, with differences often on the order of errors associated with Bott's numerical method versus Berry's.

5. BREAKUP

To test the effect of breakup on the equilibrium box size distribution, we use the Low and List method (List et al. 1987). The two models implement this complicated and computationally expensive parameterization differently owing to its most natural integration with either the Berry and Bott numerical methods or the Jacobson numerical method. While rate of rain formation is not affected by inclusion of breakup, the rain in the box now reaches an equilibrium size distribution determined by the coupling of the collision and breakup kernels. We find that the equilibrium time predicted by the two models is negligibly different, but that the equilibrium mean size is different by almost a factor of two.

6. TURBULENCE

The differences between the gravitational collection kernels pale dramatically when the influence of turbulence is included. Here we compare the method of Saffman and Turner (1956) with that of Pinsky and Khain (2002), which we refer hereafter as the Saffman and Pinsky methods. The Pinsky method is currently only applicable for low-level turbulence intensities of order 100-200 $cm^2\ s^{-3}$ typical of early cumulus clouds. The Saffman method scales with turbulence intensity, but is limited to interaction of drops that differ by less than a factor of two in diameter and drops of significantly different size are not considered. Saffman gives a significantly faster rain formation rate, and the two methods appear similar when the Saffman method is limited to collisions of drops that are within about 20% of one another's size. This points the way to a possible scaling of the Saffman method with the better-established Pinsky method. Results produce somewhat different final size distributions and rain formation rates. However, until better data are available, a parameterization for the impact of turbulence that scales with intensity is highly desirable, especially for deep convection, which may reach turbulence intensities that exceed 2000 $cm^2\ s^{-3}$ or more. We also note that the method of Pinsky, wherein the gravitational kernel is multiplied by a factor that varies with the size of the drops, deviates markedly from the Saffman method, wherein the gravitational kernel is changed by a multiplicative factor as well as an additive factor that allows identically-sized droplets to collide. The potential importance of this to initial spectral broadening and rain formation seems evident.

7. SUMMARY AND CONCLUSIONS

We evaluate the most commonly used means of solving the stochastic collection equation in size-resolved cloud models. We find that numerical method is important and derive a correction to the Jacobson method, bringing results in line with the Bott method. While the choice of collection kernel is not as important, turbulence impacts appear profoundly important to the rain formation rate, although existing parameterizations are lacking in range of applicability. We expect much new research to soon be available to improve representation of turbulence effects in such models.

REFERENCES

Ackerman, A. S., O. B. Toon, and P. V. Hobbs (1995). A model for particle microphysics, turbulent mixing, and radiative transfer in the stratocumulus-topped marine boundary layer and comparisons with measurements. *J. Atmos. Sci. 52*, 1204–1236.

Berry, E. X. and R. L. Reinhardt (1978). An analysis of cloud drop growth by collection: Part I. Double distributions. *J. Atmos. Sci. 31*, 1814–1831.

Bott, A. (1998). A flux method for the numerical solution of the stochastic collection equation. *J. Atmos. Sci. 55*, 2284–2293.

Hall, W. D. (1980). A detailed microphysical model within a two-dimensional model framework: Model description and preliminary results. *J. Atmos. Sci. 37*, 2486–2507.

Jacobson, M. Z., R. P. Turco, E. J. Jensen, and O. B. Toon (1994). Modeling coagulation among particles of different composition and size. *Atmos. Environ. 28A*, 1327–1338.

List, R., N. R. Donaldson, and R. E. Stewart (1987). Temporal evolution of drop spectra to collisional equilibrium in steady and pulsating rain. *J. Atmos. Sci. 44*, 362–372.

Long, A. B. (1974). Solutions to the droplet collection equation for polynomial kernels. *J. Atmos. Sci. 31*, 1040–1052.

Pinsky, M. and A. P. Khain (2002). Effects of in-cloud nucleation and turbulence on droplet spectrum formation in cumulus clouds. *Quart. J. Roy. Meteor. Soc. 128*, 501–533.

Pinsky, M., A. P. Khain, and M. Shapiro (2001). Collision efficiency of drops in a wide range of Reynolds numbers: Effects of pressure on spectrum evolution. *J. Atmos. Sci. 58*, 742–764.

Pruppacher, H. R. and J. D. Klett (1997). *Microphysics of Clouds and Precipitation.* Kluwer Academic Publishers.

Rogers, R. R., D. Baumgardner, S. A. Ethier, D. A. Carter, and W. L. Ecklund (1993). Comparison of raindrop size distributions measured by radar wind profiler and by airplane. *J. Appl. Meteor. 32*, 694–699.

Saffman, P. G. and J. S. Turner (1956). On the collision of drops in turbulent clouds. *J. Fluid Mech. 1*, 16–30.

Seifert, A. and K. D. Beheng (2001). A double-moment parameterization for simulating autoconversion, accretion and selfcollection. *Atmos. Res. 59–60*, 265–281.

NUMERICAL STUDY OF A SEVERE STORM IN BEIJING

Danhong Fu and Xueliang Guo

Institute of Atmospheric Physics, Chinese Academy of Sciences, Beijing 100029, China

1. INTRODUCTION

The severe storm accompanied with strong wind is one of the most severe atmospheric phenomena that always bring many disasters to human activities. Many researchers have investigated the storm in Beijing region by statistical analyses of observational data (e.g. Liu et al., 1996; Ge et al., 1998) and analyzed the formation mechanism of the downburst formation (e.g. Guo et al., 1999; Sun et al., 2003).

A severe convective storm that produced heavy rain, hail, and strong wind and brought serious damage to facilities and electric power of the Beijing city occurred in the evening on 23 August 2001. The peak wind at the surface was more 20 m/s and the hailstone was around 10 mm in diameter.

The main purpose of this study is to understand the mechanism of the downburst formation based on simulation of the cloud microphysics by using numerical simulation in Beijing area and study

2. METHODOLOGY

2.1 The model

The three-dimensional cloud model with hail-bin microphysics (Guo et al., 2001a; Guo et al., 2001b; Guo et al., 2002) was used. The model incorporates time-dependent, nonhydrostatic equations cast in compressible form,

$$\frac{du}{dt}+C_p\overline{\theta}_v\frac{\partial\pi'}{\partial x}=D_u$$

$$\frac{dv}{dt}+C_p\overline{\theta}_v\frac{\partial\pi'}{\partial y}=D_v$$

$$\frac{dw}{dt}+C_p\overline{\theta}_v\frac{\partial\pi'}{\partial z}=$$

$$g\left[\left(\frac{\theta'}{\overline{\theta}}\right)+0.608q'_v-q_c-q_i-q_r-q_s-\sum_{i=1}^{L_h}q_h(i)\right]+D_w$$

Corresponding author's address: Danhong Fu, Institute of Atmospheric Physics, Chinese Academy of Sciences, Beijing 100029, China; E-Mail: fudanhong@mail.iap.ac.cn

$$\frac{d\pi'}{dt}+\frac{\overline{C}^2}{C_p\overline{\rho}\overline{\theta}_v^2}\frac{\partial\overline{\rho}\overline{\theta}_v u_j}{\partial x_j}=-\frac{R_d}{C_v}\pi'\frac{\partial u_j}{\partial x_j}+\frac{C^2}{C_p\theta_v^2}\frac{d\theta_v}{dt}+D_{\pi'}$$

$$\frac{d\theta}{dt}=Q_{fm}+Q_{ce}+Q_{ds}+D_\theta$$

$$\frac{dq_x}{dt}=-D_{q_x}+W_{q_x}+I_{q_x}+\frac{\partial}{\partial x_3}(\rho_0V_xq_x)$$

where π' is non-dimensional pressure. D_u, D_v, D_w, D_θ, Dqx, and D_π are the turbulent fluxes of u, v, w, and θ, respectively. Q_{fm}, Q_{ce}, and Q_{ds} are the latent heating/cooling terms due to melting/freezing, condensation/evaporation and deposition/sublimation produced by microphysical processes, respectively. q_x is one of the mixing ratios of water vapor q_v, cloud water q_c, rain water q_r, cloud ice q_i, snow q_s, and hail-bin water content q_h (i) (i=1, L_h); V_x is the terminal velocity of a hydrometeor.

2.2 Microphysical processes

The model includes the detailed cold and warm microphysical processes, the melting of snow and hail /graupel; evaporation of rain; the accretion of rain by snow and hail; the shedding of water from melting of snow and hail; the sublimation of water vapor from snow and hail/graupel and the evaporation of liquid water from melting of snow and hail/graupel. And hail/graupel is divided into 21 size bins.

The model domain is 36 × 36 km in horizontal and 19 km in vertical. The grid interval is 500 m. The simulation is initialized by thermal bubble placed at the center of model domain. The small time step is 0.125s and the large time step is 5s. The integration time is 80 min. A radiation boundary scheme is used for lateral boundaries. Both the top and bottom boundaries are assumed to be rigid. The model was initiated with rawin sounding at 20:00 BST on 23 August 2001 in Beijing.

3. RESULTS AND CONCLUSIONS

3.1 Results analysis

Table.1 lists the main parameters of the simulated and observed storm.

Fig.1 shows the size distributions of hailstones at the surface. According to the observed data, the maximum diameter of hailstone is about 10 mm. The intensity and accumulated amount of hail increase with time evolution after presenting of hail at the surface.

Table 1 Comparisons of the observed and simulated storm's characteristics

	Simulated	Observed
Lifetime (min)	About 60	About 60
Cloud top (km)	10	----
Max radar reflectivity (dBZ)	70	----
Max updraft (m/s)	48	----
Max downdraft (m/s)	-68	----
Max outflow speed (m/s)	30	>20
Max diameter of hail (mm)	10	10
Precipitation distribution	asymmetry	asymmetry
Precipitation path	Northwest-southeast	Northwest-southeast

By 26 min, the diameter of hailstones in high number concentrations is mainly distributed in the range of less than 2 mm and number of particles decrease with size increase. But the number of particles increases with size for particles larger than 5 mm. The maximum diameter of hailstones is 7mm at this time.

The hail accumulation reaches maximum at 28 min, and the diameter of hailstone in high number concentration is still less than 2 mm, but the number less and larger than 2 mm increases evidently. The maximum diameter of hailstones approaches 10 mm at the surface. By 30 min, the number of hailstones increases, but the maximum diameter of hailstones is still 10 mm. The simulated maximum diameter of hailstone is well consistent with that observed at the surface. By 32 min, the number of larger hail reduces, and that less than 4mm, especially less than 1mm become high.

Fig.2 shows the time evolution of maximum updraft and downdraft. Fig. 2a shows that at 6 min, the simulated maximum updraft is 8 m/s. By 18 min, the maximum value of 48m/s is reached. Due to formation of a great amount of hail, the updraft begins to reduce rapidly due to loading of hail particles. By 40 min, the updraft has already reduced to 8m/s. The simulated downdraft begins to develop after 10 min of updraft forming (Fig. 2b). The downdraft reaches to the maximum value of –68 m/s at 20min later 2min than the present of maximum updraft.

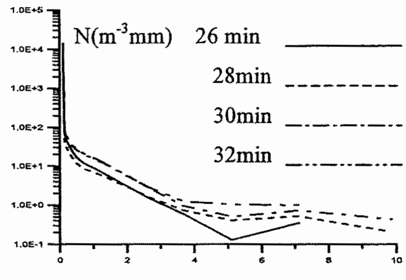

Fig.1 The size distributions of hailstones at the surface

Fig.3 shows the wind vector distribution near the surface associated with the downburst. At 20 min (Fig. 3a), the maximum wind velocity is 8m/s, and the range of divergent outflow presents and it shows a strong wind shear. By 28 min, with the weakening of downdraft and the effect of wind shear, divergent outflow gradually extends and becomes an asymmetric structure, and the maximum value of wind velocity is 30 m/s (Fig.3b).

Fig.4 shows vertical cross section of the simulated radar echo at the mature phase. By 20 min (Fig.4a), the cloud top is about 11 km, and the maximum echo exceeds 70dBZ. At the same time, the strong downdraft is formed in the region of high radar echo. The obvious overhang structure appears at 32min, big-size hail particle is formed, and the top of echo decreases about 10 km (Fig.4b).

In order to understand the contribution of various hydrometeors to the downdraft formation, we calculate the equivalent cooling rates based on methods of Hjelmfelt (1989) and Guo et al. (1999). Fig.5a and b is the time-height distribution of maximum cooling rates due to hail and rain loading, respectively. It shows that the loading of hail greatly influences the development and enhancement of downdraft above the melting level, while the influence of rain loading appear from 12min to 26min, and is weaker than hail loading. At 10 min, the downdraft was primarily produced by rain loading, and the cooling rates (0.05℃/min) is correspond with the downdraft of -4 m/s. With the development of the storm, the downdraft enhances due to the increase of equivalent cooling rate. By 14min the maximum cooling rates of 0.4℃/min is found above the melting level and the downdraft reaches to 10m/s. The downdraft influenced by hail loading above the melting level and rapidly intensifies after 16min. At 20 min, the maximum cooling rates of 18℃ /min is found at 8 km AGL, at the moment, the downdraft reaches the maximum. The downdraft reduces to 20 m/s due to the weakening of hail loading. By 26 min, the maximum value of cooling rates appears again and the downdraft reaches to 40 m/s. It suggests that the loading of hail is the main effect on the downdraft intensity. The loading of rain water presents both above and below the melting level , the maximum cooling rates due to rain loading reaches to 0.5℃ /min, and the influence of rain loading is much weaker than that of hail.

Fig.5c and d is the time-height distribution of maximum cooling rates due to hail melting and rain evaporation, respectively. The phase transformation mainly happens below 0℃ level. The influence of rain evaporation is weak, the maximum cooling rates reaches to 0.24℃/min at 3.5km AGL at 22min , and rain evaporation enhances the downdraft. The hail crossing the melting level begins to melt, and absorb the heat from surrounding air and causes environment cooling in the cloud, and enhances the downdraft by negative buoyancy force induced by cooling. At 22 min, the cooling rates reaches to 5℃/min near the surface due to the melting of hail. It shows that the melting of hail play an important role below the melting level, the maximum region of downdraft is consistent with the maximum cooling rates due to hail melting, and the strong downdraft is produced by hail melting below the melting level.

The strong downdraft produced by these microphysical processes reaches the surface, and forms the strong divergent outflow, and then induces the strong wind at the surface

3.2 Acknowlegements

This research was jointly sponsored by the Chinese Natural Science Foundation (Grant 40175001 and 40333033) and the CAS Innovation Foundation KZCX3-SW-213, and the Key Project of the Ministry of Science and Technology of China (Grant 2001BA610A-06).

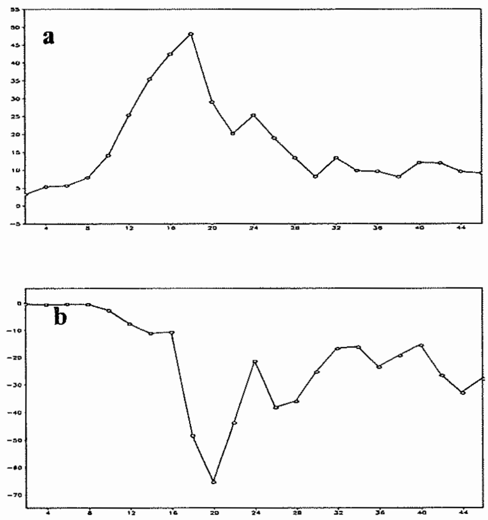

Fig.2 Time series (min) of the maximum simulated vertical velocities a) updraft (m/s), b) downdraft (m/s)

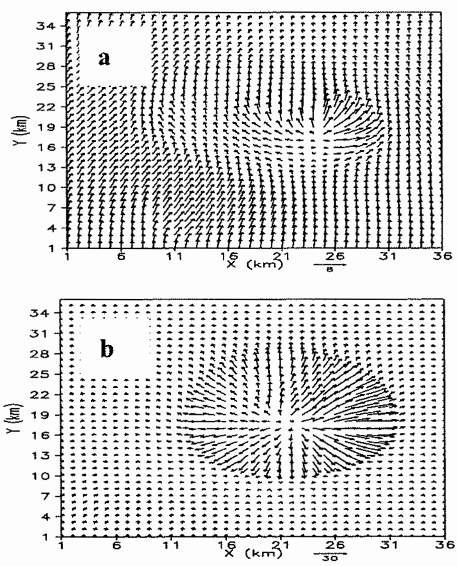

Fig.3 The wind vector distribution near the surface a) 20 min, b) 28 min

3.3 References

Ge Runsheng, Jiang Haiyan and Peng Hong, 1998: Flow structure of hailstorm in Beijing area. *Quarerly J.applied meteorology,* 9(1), 1-7 (in Chinese).

Guo Xueliang and Huang Meiyuan, 2002: Hail formation and growth in a 3-D cloud model with hail-bin microphysics. *Atmos. Res.*, **63**, 59-99.

Guo Xueliang, Huang Meiyuan and Hong Yanchao, 2001: A study of three-dimensional hail-category hailstorm model part I: Model description and the mechanism of hail recirculation growth, *Chin. J. Atmos. Sci.*, **25** (5), 707-720 (in Chinese).

Guo Xueliang, Huang Meiyuan and Hong Yanchao, 2001: A study of three-dimensional hail-category hailstorm model part II: Characteristics of hail-category size distribution, *Chin. J. Atmos. Sci.*, **25** (6), 856-864 (in Chinese).

Guo Xueliang, H. Niino and R. Kimura, 1999: Numerical modeling on a hazardous microburst-producing hailstorm. Towards Digital Earth-Proc. of the International Symposium on Digital Earth, *Science Press*, Beijing, **1**, 383-398.

Hjelmfelt, M. R., R. D. Robert and H. D. Orville, 1986: Observational and numerical study of microburst line producing storm. Joint Sessions of 23rd Conf. on Radar Meteorology and Conf. on Cloud Physics, Snowmass, Amer. Meteor. Soc., J77-J80.

Liu Xiaohong and Hong Zhongxiang, 1996:A study of the structure of a strong wind event in the atmospheric boundary layer in Beijing area. *Chin. J. Atmos. Sci.*, 20(2), 223-228 (in Chinese).

Sun lingfeng , Guo Xueliang, Sun Litan and Fu Danhong, 2003: A numerical study of an airplane disaster-producing microburst on 22 June 2000 in Wuhan. *Chin. J. Atmos. Sci.*, 27(4), 307-323 (in Chinese).

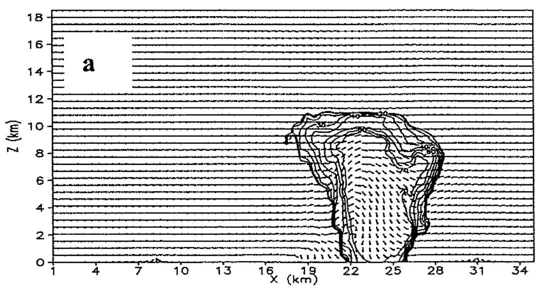

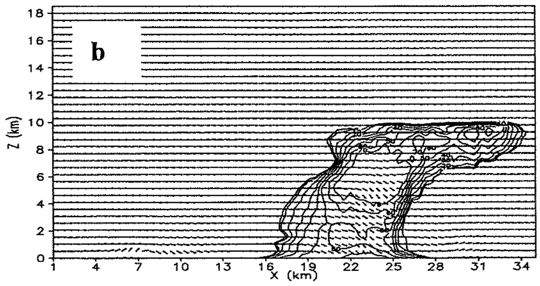

Fig.4 The X-Z cross section of radar reflectivity and wind vector at a) 20 min, b) 32 min

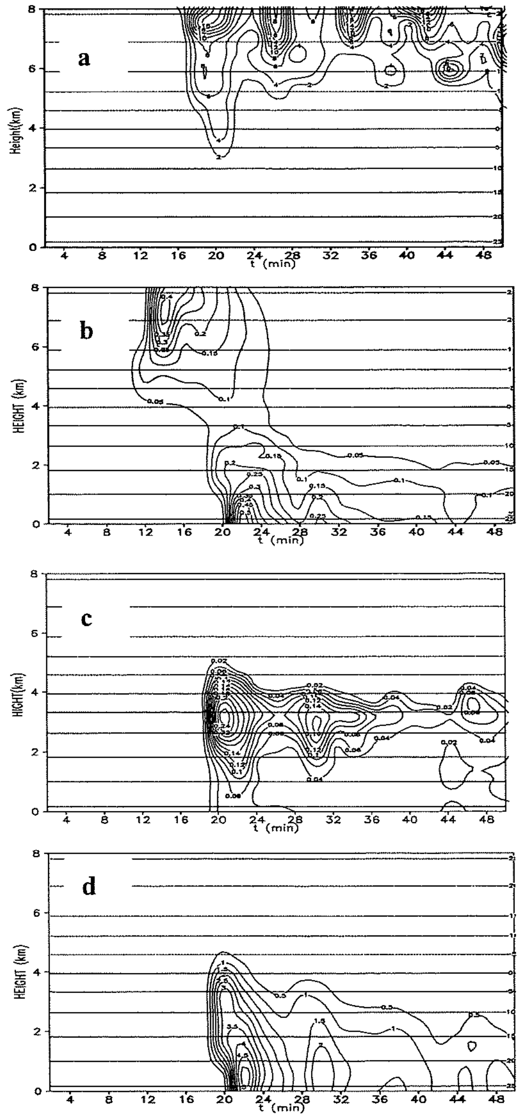

Fig.5 The time-height distribution of maximum magnitude of effective cooling rates for forcing mechanisms due to a) hail loading b) rain loading c) rain evaporation d) hail melting.

UNDERSTANDING OF FOG STRUCTURE, DEVELOPMENT AND FORECASTING, COST 722.

Alan Gadian[1] and Andreas Bott[2] plus many others from 13 European countries

[1]School of the Environment, Leeds University, UK
[2]Meteorological Institute, University of Bonn, Germany

1. INTRODUCTION

In September 2001, the EU initiated a European Concerted Research Action designated as COST Action 722, and entitled "Short range forecasting methods of fog, visibility and low clouds". Currently thirteen European countries participate, Austria, Cypress, Denmark, Finland, France, Germany, Hungary, Poland, Spain, Sweden, Switzerland, UK

The main objective of the Action is to develop advanced methods for very short-range forecasts of fog, visibility and low clouds, adapted to characteristic areas and to user requirements. This overall objective included:

- the development of pre-processing methods of the necessary input data;
- the development of the appropriate forecast models and methods; and
- the development of adaptable application software for the production of the forecasts.

A first phase report, COST722 (2003), an "Inventory" of current science and techniques was completed by Autumn 2003 and is to be followed the second, "Research and Development", phase by 2007, with completion of "Development" and "Dissemination" phases by 2008.

The development of visibility, fog and low clouds is influenced by many parameters (e.g. cloudiness, temperature, humidity, wind speed, topography, vegetation and radiation). Fog is especially very sensitive to small changes in the relevant meteorological parameters in the lowest layers of the atmosphere, so that very high-quality measurements are required. Therefore, high forecast skill is dependent on accurate knowledge of the vertical distribution of the relevant input parameters.

The poster will highlight some of the science relevant to cloud microphysical and meteorological processes relevant for the description of Fog. The work of the initial two working groups is summarised, with a brief outline of future activity

2. ACTIVITIES OF THE WORKING GROUPS

Working Group 1 discussed the evaluation of methods and the need for data set intercomparisons and exchange. Participants presented current activities. The recommendations include a need for sophisticated intercomparisons, more flexibility with models, more details of the science and very importantly, exchange of data sets and evaluation of schemes.

The second working group recommends that an improvement in the models / science is required and that more detailed observations are needed.

Full details and presentations of current observational, modelling and forecasting activity is available in the Phase 1 report, COST722 (2003), and some detail will be available on the poster.

3. PHASE 1 CONCLUSIONS

From the scientific viewpoint, the conclusions emphasise that a deeper understanding of the relevant processes of the development of fog, visibility and low clouds is required. NWP models are able to represent the large scale forcing on most occasions, but are not sensitive to the local meteorological and topographical parameters. 1-D models can be used for local forecasts, but only fine scale 3-D models have the potential to consider all relevant processes. The "inventory" includes a need for increased spatial and temporal data, and an observation that statistical methods can be useful for prediction purposes.

3. PHASE 2

This phase, of three years duration, from October 2003, includes three main areas

- "Initial Data". This area will include a study of incorporating all available surface and remote sensing data, and the ability to differentiate between low cloud and fog.
- "Models". The objective is to examine the potential of different models, investigate the mechanisms and improve model physics, with the possibility of developing probability forecasts and method validation.
- "Statistical Methods". Limitations and potential of existing techniques, data requirements, improvement and portability is an important area.

4. REFERENCES

COST 722, 2003, Phase 1 report.
Very short range forecasting of fog and low clouds: Inventory phase on current knowledge and requirements by forecasters and users.
http://137.248.191.94/cost/publications.html

Corresponding author's address: Alan Gadian, School of the Environment, University of Leeds, LS2 9JT, UK; E-Mail: alan@env.leeds.ac.uk

CONSTANT SLOPE OR CONSTANT INTERCEPT? THE IMPACT ON PRECIPITATION USING SINGLE-MOMENT MICROPHYSICS

Matthew S. Gilmore[1*], Susan C. van den Heever[2], Jerry M. Straka[3], Robert Wilhelmson[1], William R. Cotton[2], and Erik N. Rasmussen[4]

[1] Dept. of Atmospheric Sciences, Univ. of Illinois, Urbana, IL
[2] Dept. of Atmospheric Science, Colorado State University, Fort Collins, CO
[3] School of Meteorology, Univ. of Oklahoma, Norman, OK
[4] Cooperative Institute for Mesoscale Meteorological Studies, Univ. of Oklahoma, Norman, OK

1. INTRODUCTION

The purpose of the current work is to evaluate the differences in precipitation and cold pool characteristics that result when the framework describing the particle size distributions is changed. We compare framework where the mean diameter of each distribution is preserved to a framework where the intercept is preserved. Experiments are compared within each framework using two different models with similar microphysics and initial conditions.

Previous work has shown that the parametric variables describing the hail or hail/graupel category can have a large impact on ground-accumulated precipitation, the size of damaging hail that reaches ground, and cold pool temperature and structure (van den Heever and Cotton 2004, hereafter CV2004; Gilmore et al. 2004,hereafter GSR2004b). However, it is difficult to directly compare those studies because the environmental soundings, microphysics package, particle densities, precipitation distribution description, and models are different (Table 1). Therefore, we embark upon a collaborative microphysical parameter study whereby we make both models more consistent and repeat some of those previous experiments .

Table 1. The parameters previously used by GSR2004b as compared to those used by VC2004. Differences make those study results difficult to compare.

Key Parameters	Previous Studies: Gilmore et al. (2004b)	Previous Studies: van den Heever & Cotton (2004)
Model	SAM	RAMS
Moments	1	1
Microphysics	GSR2004a	Walko et al. (1995)
Ice classes	3	5
qh density	900, 400 (kg m^{-3})	900 (kg m^{-3})
Constant Distribution Parameter	Intercept (m^{-4})	Mean Diameter (m)
Idealized environment	Weisman and Klemp (1984)	Grasso (2000)

* Corresponding Author's Address: Dr. Matthew Gilmore, UIUC Dept. of Atmospheric Sciences, 105 S. Gregory St., Urbana, IL, 61801

2. EXPERIMENTAL DESIGN

Both the Straka Atmospheric Model (SAM; e.g., Straka and Anderson 1993) and the Regional Atmospheric Modeling System (RAMS; Pielke et al., 1992; Cotton et al. 2003) are the three-dimensional, non-hydrostatic cloud models used for the simulations. Grid spacing Δx = Δy = 1000 m are used in both models. SAM uses a 90 x 90 x 22 km^3 domain while RAMS uses 140 x 110 x 22 km^3. SAM uses a constant vertical grid spacing Δz= 500 m while RAMS uses a stretched grid with about the same average grid spacing.

2.1 Initial Conditions

The models are initialized with the idealized temperature and moisture profile described in Weisman and Klemp (1984; hereafter WK84). Environmental CAPE is 2200 J kg^{-1}. The vertical wind shear profile is represented by a half-circle hodograph that traces an arc length of 50 m s^{-1} over the lowest 5 km AGL. Above z = 5 km AGL, the wind speed is held constant. An axially symmetric thermal bubble with maximum temperature (T) excess of +1°C is used to initiate convection in SAM (e.g., Klemp and Wilhelmson 1978). In RAMS, a +3°C maximum T excess is used with a 20% increase in moisture. (Although the different bubble temperatures were unintended, we will show that the qualitative results are similar regardless.)

2.2 The Ice Microphysics Packages

In the RAMS model, the fifth ice category (representing graupel) normally used (Walko et al. 1995) is turned off so that graupel and hail can be represented within a single category and more fairly compared to the 3-ICE scheme of GSR2004a (similar to Lin et al. 1983, hereafter LFO). Three of the ice species in both models are cloud ice (*qi*), snow (*qs*), and hail/graupel (*qh*) while RAMS additionally has an aggregate species. The negligibly precipitating ice and liquid cloud particles are mono-dispersed while the faster precipitating particles are defined by Marshall and Palmer (1948) size distributions wherein the most numerous particles are found at the smallest diameter (*D*) sizes:

$$n_x(D) = n_{ox}\exp\left(-D_x D_{nx}^{-1}\right). \tag{1}$$

In Eq.1, n_{ox} is the intercept parameter and D_{nx} is the mean diameter size of the distribution.

Within both models, one may choose to set n_{ox} and diagnose D_{nx} with the following equation,

$$D_{nx} = \left[\rho q_x / \left(\pi \rho_x n_{ox}\right)\right]^{1/4}, \tag{2}$$

Alternatively, one may set D_{nx} and diagnose n_{ox} by rearranging Eq. 2. In this equation, q_x and ρ_x are the species mixing ratio and particle density, respectively, while local air density is represented by ρ. These selections are then propagated through all of the microphysics equations.

Despite attempts to make both models as similar as possible, both models differ in their representations of evaporation rate (Carver 2001), snow density, rain terminal fall speed, and aggregate species representation. This should prevent both models from producing the same solution. Therefore, *what is sought is to compare general model sensitivities across the parameter space for both the n_{ox} and D_{nx} frameworks.*

2.3 Microphysics Treatments

The sensitivity experiments were designed by varying D_{nh} or n_{oh} individually for the *qh* category. Observations of n_{oh} within hailstorms suggests variations of 10^3 to 10^8 m^{-4} for *qh* (e.g., Knight et al. 1982). Because researchers might not have sampled supercells with extreme hail, we also test 10^2 m^{-4}. Within the n_{oh}=10^3 and 10^8 m^{-4} simulations for SAM, it was found that the maximum D_{nh} at any time in the simulation ranged from about 6 mm to 0.3 mm, respectively. These, along with choices made by VC2004 and GSR2004b, were used as guidance in picking the treatments shown in Table 2. For each framework, there are distributions weighted toward small graupel, large hail, and cases in-between.

Most cases use a *qh* density at 900 kg m^{-3} which is common for hail (Pruppacher and Klett 1978). For the distributions weighted toward small graupel, an additional representative particle density of 400 kg m^{-3} was also tested (similar to GSR2004b).

Table 2. Constant D_{nh} or n_{oh} values defining the *qh* distribution are shown. D.5ρ4 and N8ρ4 use a particle density of 400 kg m^{-3}. Other cases use 900 kg m^{-3}.

	Prescribed D_{nh} Framework	
Case	D_{nh} (mm)	n_{oh} (m^{-4})
D.5ρ4	0.5	diagnosed
D.5	0.5	diagnosed
D1	1.0	diagnosed
D3	3.0	diagnosed
D7	7.0	diagnosed
D10	10.0	diagnosed
	Prescribed n_{oh} Framework	
N8ρ4	diagnosed	4×10^8
N8	diagnosed	4×10^8
N5	diagnosed	4×10^5
N4	diagnosed	4×10^4
N3	diagnosed	4×10^3
N2	diagnosed	4×10^2

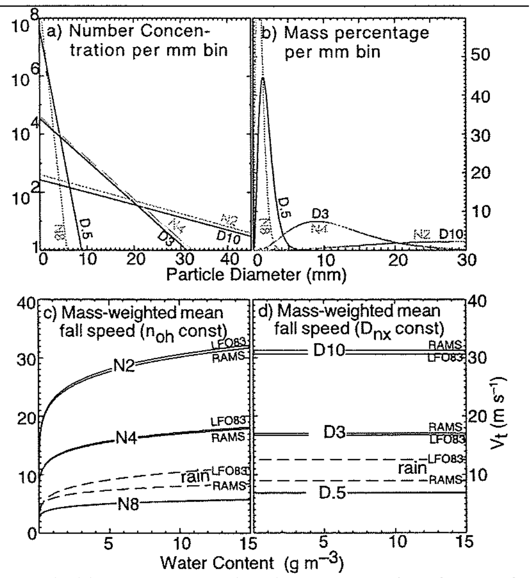

Fig. 1 (a-b) Example *qh* distributions used in this study for the framework descriptions shown in Table 2 and (c-d) corresponding fallspeeds for an assumed total water content of 10 g m^{-3} at an altitude of z = 4.5 km AGL. Plots c and d additionally include rain fallspeed (dashed lines) for both models.

For both models, the particle terminal velocities were computed for several of the cases and those are displayed in Figs. 1c and 1d along with distributions in Figs 1a and 1b. It can be seen that one consequence of prescribing n_{ox} (D_{nx}) is that fall speeds vary (are constant) with mixing ratio. Fall speeds not only impact vertical precipitation flux but also the accretion rates (by qh) and rain evaporation rate.

For the constant n_{oh} cases in SAM, n_{or} and n_{os} are also constants set to 8×10^6 and 3×10^6 m^{-4}, respectively, following LFO. However, for RAMS, the constant N_{oh} framework was used with a constant mean diameter framework for snow and rain (D_{nr} = D_{ns} = 1 mm). Future work is needed to explore the consequences of using different frameworks for different species.

4. RESULTS AND DISCUSSION

The preliminary comparisons between the n_{ox} experiments and D_{nx} experiments for both models are shown below in the form of tables. (Note that many of the n_{oh} cases are also presented within GSR2004b.)

One immediately notices that the RAMS simulations produce colder low-level outflow for every case (Table 3). However, this is believed to be primarily due to the larger storm-initiating thermal perturbation (3°C in RAMS versus 1°C in SAM). Regardless, the coldest low-level outflow in each model appears to occur for an intermediate qh distribution for both the D_{nx} framework and the n_{oh} framework.

Despite the differences between how the SAM and RAMS experiments were conducted, it is remarkable that the qualitative changes across the parameter space are consistent. For instance, the intermediate qh distribution cases have the coldest low-level outflow. Then, as one moves toward a distribution that is weighted either toward small graupel or large hail, the outflow becomes warmer (Table 3). Furthermore, the amount of total precipitation reaching ground (and qh alone) decreases as one moves toward a qh distribution weighted toward smaller particles (Table 4). The reason the outflow is warmer in the D10 and N2 cases is because the qh distribution contains a larger fraction of large hailstones which do not melt as easily thereby limiting subsequent evaporation (VC2004; GSR2004b). In contrast, the outflow is warmer in the D.5ρ4 and N8ρ4 cases primarily because qh falls so slowly that less reaches low levels within 2 hours (also see GSR2004b).

Therefore, the same model sensitivity in cold pools and accumulated precipitation seems to exist regardless of whether D_{nh} or n_{oh} is prescribed. However, we are still analyzing the detailed results and we may find that other differences exist between these frameworks that are not revealed in these tables.

Future work will aim at repeating some of the experiments herein to achieve even greater consistency in model setup between SAM and RAMS. We will also be investigating the consequences of using different terminal fall velocity and evaporation rate equations.

Table 3. The area-averaged perturbation potential temperature (θ') but only for locations cooler than –0.5 °C at the ground (z = 250 m) in the RAMS simulations and SAM simulations. See Table 2 for case definitions. Bold numbers indicate the coldest case at a particular time. ("n/a" indicates that results were not available at time of publication.)

	Area-averaged θ' (°C) at the ground								
	RAMS					SAM			
Time=	30	60	90	120		30	60	90	120
Case	(min)					(min)			
D.5ρ4	n/a	n/a	n/a	n/a		–0.54	–0.73	–0.74	–0.89
D.5	–1.4	–2.3	–3.6	–4.1		–0.56	–0.81	–1.23	–1.29
D1	–1.6	–3.0	**–4.1**	**–4.4**		**–0.57**	–1.04	–1.53	–1.44
D3	–2.3	**–3.6**	–3.9	–3.7		–0.54	**–1.65**	**–2.17**	**–1.82**
D7	**–2.7**	–3.5	–3.4	–3.0	Larger size weighting ↓	–0.54	–1.21	–1.29	–1.37
D10	–2.7	–3.1	–2.9	–2.8		–0.54	–1.04	–1.09	–1.22
N8ρ4	n/a	n/a	n/a	n/a		–0.59	–1.02	–1.24	–1.93
N8	–1.4	–2.1	**–3.3**	**–3.6**		–0.60	–1.19	–2.24	–2.95
N5	n/a	n/a	n/a	n/a		–0.61	–2.18	–3.05	–2.88
N4	n/a	n/a	n/a	n/a		**–0.61**	**–2.50**	**–3.30**	**–3.01**
N3	**–2.8**	**–3.3**	–3.2	–3.0		–0.61	–2.31	–2.77	–2.68
N2	n/a	n/a	n/a	n/a		–0.61	–1.85	–2.06	–2.07

Table 4. Ground-accumulated precipitation mass for $qr + qh$ and qh only for each of the experiments in both the RAMS and SAM model. See Table 2 for case definitions. (N/a indicates that results were not available at time of publication.)

	Accumulated Precipitation			
	RAMS		SAM	
Case	qh+qr (Tg)	qh (Tg)	qh+qr (Tg)	qh (Tg)
D.5p4	n/a	n/a	32.23	0.00
D.5	43.88	0.00	49.31	0.01
D1	52.00	0.00	53.56	0.11
D3	55.80	0.00	53.61	7.22
D7	59.14	7.90	54.85	24.0
D10	59.99	20.1	53.00	28.8
N8p4	n/a	n/a	14.12	0.0
N8	39.78	0.00	29.09	0.0
N5	n/a	n/a	52.06	0.1
N4	n/a	n/a	53.67	1.4
N3	56.03	3.81	51.46	4.0
N2	n/a	n/a	52.05	23.2

Tg = teragrams

5. ACKNOWLEDGMENTS

This research was supported by the National Science Foundation under grants ATM-0003869, ATM-9617318, ATM-99866672, and ATM-9900929. Partial funding for this research was provided by the NSSL under NOAA-OU Cooperative Agreement #NA17RJ1227.

6. REFERENCES

Carver, R. W., 2001: Environmental parameter studies of modelled mesocyclonic supercells: Sensitivity to low-level vertical relative humidity profiles and shear. M.S. thesis, School of Meteorology, University of Oklahoma, 112 pp. [Available from Bizzell Library, University of Oklahoma, 401 W. Brooks St., Norman, OK, 73019–6030.]

Cotton, W.R., and co-authors, 2003: RAMS 2001: Current status and future directions. *Meteor.. Atmos. Phys.,* **82**, 5–29.

Gilmore, M. S., J. M. Straka, and E. N. Rasmussen, 2004a: Precipitation and evolution sensitivity in simulated deep convective storms: Comparisons between liquid-only and simple ice & liquid phase microphysics. *In Press at Mon. Wea. Rev.*

——, ——, and ——, 2004b: Precipitation uncertainty due to variations in precipitation particle parameters within a simple microphysics scheme. Conditionally accepted by *Mon. Wea. Rev.* [Available on-line at http://www.atmos.uiuc.edu/~gilmore1/mwrmicro2/GSR2004b.pdf]

Grasso, L.D., 2000: The dissipation of a left-moving cell in a severe storm environment. *Mon. Wea. Rev.,* **128**, 2797–2815.

Klemp, J. B., and R. B. Wilhelmson, 1978: The simulation of three-dimensional convective storm dynamics. *J. Atmos. Sci.,* **35**, 1070–1096.

Knight, C. A., W. A. Cooper, D. W. Breed, I. R. Paluch, P. L. Smith, and G. Vali, 1982: Microphysics. *Hailstorms of the Central High Plains.,* Vol. 1, C. Knight and P. Squires, Eds., Colorado Associated University Press, 151–193.

Lin, Y.-L., R. D. Farley, and H. D. Orville, 1983: Bulk parameterization of the snow field in a cloud model. *J. Climate Appl. Meteor.,* **22**, 1065–1092.

Marshall, J. S., and W. M. Palmer, 1948: The distribution of raindrops with size. *J. Meteor.,* **5**, 165–166.

Pielke, R.A., and coauthors, 1992: A comprehensive meteorological modeling system –RAMS. *Meteor. Atmos. Phys.,* **49**, 69–91.

Pruppacher, H. R., and J. D. Klett, 1978: *Microphysics of Clouds and Precipitation,* D. Reidel Pub. Co., Dordrecht, Holland, 714 pp.

Straka, J. M., and J. R. Anderson, 1993: Numerical simulations of microburst-producing storms: some results from storms observed during COHMEX. *J. Atmos. Sci.,* **50**, 1329–1348.

van den Heever, S. C., and W. R. Cotton 2004: The impact of hail size on simulated supercell storms. *In press at J. Atmos. Sci.*

Walko, R.L., W.R. Cotton, M.P. Meyers, and J.Y. Harrington, 1995: New RAMS cloud microphysics parameterization. Part I: the single-moment scheme. *Atmos. Res.,* **38**, 29-62.

Weisman, M. L., and J. B. Klemp, 1984: The structure and classification of numerically simulated convective storms in directionally varying wind shears. *Mon. Wea. Rev.,* **112**, 2479–2498.

SUBGRID-SCALE CCN ACTIVATION

Jean-Christophe Golaz[1,2]* Shouping Wang[2] and Vincent E. Larson[3]

[1]National Research Council.
[2]Naval Research Laboratory, Marine Meteorology Division, Monterey, California.
[3]Atmospheric Science Group, Department of Mathematical Sciences, University of Wisconsin – Milwaukee.

1. INTRODUCTION

Cloud droplet number concentration in boundary layer clouds can have a large impact on weather and climate through the so-called "indirect aerosol effect" (e.g. Twomey 1977). In numerical models, accurate activation of cloud condensation nuclei (CCN) to form cloud droplets is a challenging task as it depends on local supersaturation, which can be dif?cult to predict accurately. To circumvent this dif?culty, several parameterizations have been proposed that activate CCN based on the vertical velocity instead (e.g. Ghan et al. 1993; Cohard et al. 1998).

We have implemented one such a scheme in a large eddy simulation (LES) model and present results from two simulations: a nocturnal stratocumulus case and a shallow cumulus case. The purpose of these simulations is to serve as testbeds to investigate possible approaches to the CCN activation in numerical models with coarser grid spacing. These models do not resolve cloud motions explicitly and therefore CCN activation must be treated as a subgrid-scale process.

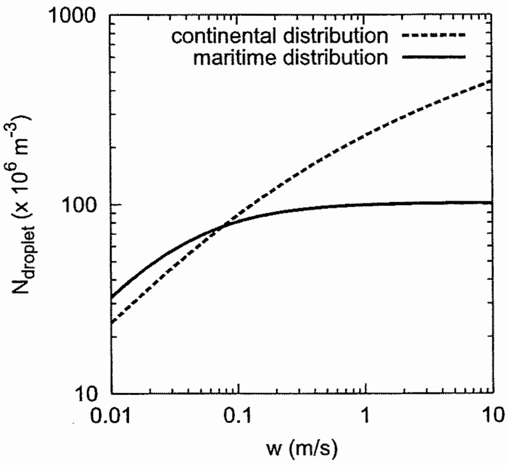

Figure 1: Number of activated CCN as a function of the vertical velocity for the continental and maritime distributions proposed by Cohard et al. (1998).

2. MODEL DESCRIPTION

The model used is based on the Naval Research Laboratory's Coupled Ocean/Atmosphere Mesoscale Prediction System (COAMPS™,[1], Hodur 1987). It has been modi?ed to perform as a LES and tested for a variety of cases. For the results presented here, COAMPS uses a simple microphysics parameterization that predicts two moments of cloud water: the mixing ratio and the droplet number concentration. A saturation adjustment scheme is used to compute the cloud water condensation and evaporation rates and no drizzle is allowed to form. The prognostic equation for the cloud droplet number concentration, N_c, is given by:

$$\frac{\partial N_c}{\partial t} = \underbrace{-u_i \frac{\partial N_c}{\partial x_i}}_{\text{advection}} \underbrace{- \frac{\partial}{\partial x_i} \overline{u_i' N_c'}}_{\text{turbulent mixing}} \underbrace{+ \left.\frac{\partial N_c}{\partial t}\right|_{\text{activation}} - \left.\frac{\partial N_c}{\partial t}\right|_{\text{evaporation}}}_{\text{microphysics}} . \quad (1)$$

The activation and evaporation terms are based on the work of Cohard et al. (1998) and Cohard and Pinty (2000). They propose a formulation to estimate the nucleated cloud droplet concentration based on the vertical velocity. We use two of their CCN activation spectra, one for maritime and one for continental distributions as shown in Figure 1.

*Corresponding author address: Jean-Christophe Golaz, Naval Research Laboratory, 7 Grace Hopper Avenue Stop 2, Monterey, CA 93943-5502; e-mail: golaz@nrlmry.navy.mil.

[1]COAMPS is a registered trademark of the Naval Research Laboratory.

3. REFERENCE SIMULATIONS

Two reference cases have been selected. The ?rst one is a nocturnal stratocumulus cloud (Wang et al. 2003) with near 100% cloud fraction, and the second is a shallow cumulus case (Siebesma et al. 2003) with very low cloud fraction. Two simulations were performed for each case using the maritime and continental CCN distributions. Each simulation is six hours in length and the results shown are horizontally and time averaged over the last two hours when the model is in a near steady-state regime.

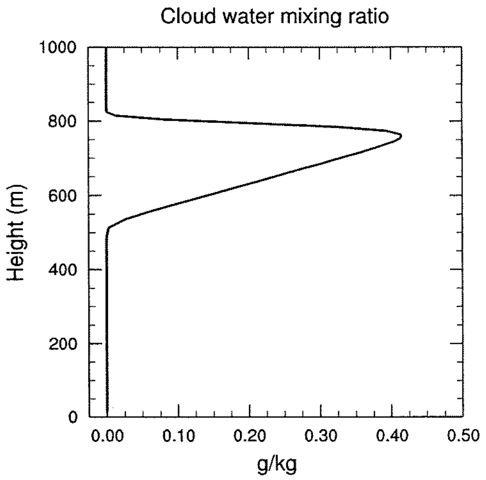

Figure 2: Layer-averaged cloud water mixing ratio for the last two hours of the stratocumulus simulation.

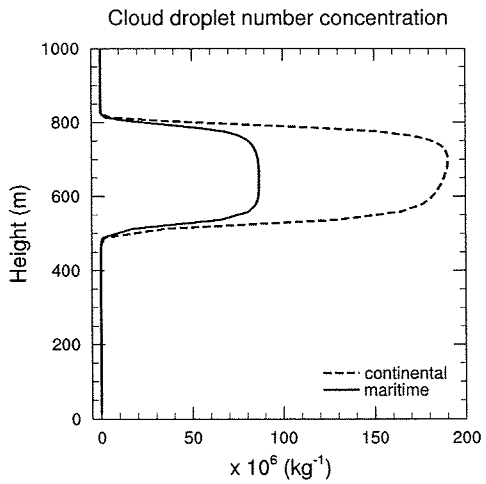

Figure 3: Layer-averaged cloud droplet number concentration for the maritime and continental simulations of the stratocumulus case.

Since no drizzle is allowed to form, simulations with the maritime and continental distributions produce the same cloud water mixing ratio ?eld for a given case but different cloud droplet number concentrations.

3.1 Stratocumulus case

Figure 2 shows the cloud water for the stratocumulus case. Cloud base is located around 500 m and cloud top at 800 m with a liquid water content that increases linearly from cloud base to cloud top, reaching a maximum value of 0.42 g/kg.

The corresponding pro?les of cloud droplet number concentration is displayed in Fig. 3. For the maritime stratocumulus case, the number concentration is almost constant within the cloud layer at 80×10^6 kg^{-1}. This is slightly less that the maximum possible number given by the activation curve in Fig. 1. The simulation with the continental CCN spectrum produces a larger number of cloud droplets, up to 200×10^6 kg^{-1}, and a pro?le that increases slightly within the cloud layer. The number of droplets is also substantially less than the total CCN concentration. This indicates that the relatively weak vertical velocities in this stratocumulus case only activate a fraction of the CCN present.

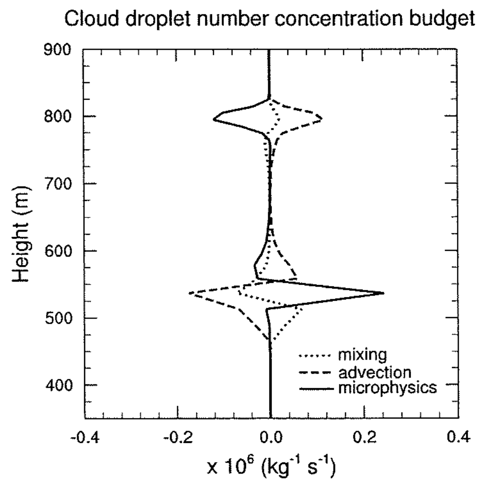

Figure 4: Cloud droplet number concentration budget for the maritime simulation of the stratocumulus case. The terms shown follow Eq. (1).

The cloud number concentration budget for the last two hours of the maritime stratocumulus case is depicted in Fig. 4. The budget shows the terms in Eq. (1). Because the simulation is in near steady-state, the net tendency term is small during this time and is not plotted. The corresponding budget for the continental case (not shown) is qualitatively similar, but with larger tendencies due to the higher number of cloud droplets. The microphysics contributions to the number budget are signi?cant only at cloud base and top. Cloud base is characterized by net activation and cloud top by net evaporation. This is in qualitative agreement with the results of Wang et al. (2003) who used a detailed bin-resolving microphysics with explicit supersaturation to simulate a similar case. We believe that these results validate the approach of Cohard and Pinty (2000) to use the vertical velocity as basis for the CCN activation. The second largest term in the cloud droplet number budget is the turbulent advection which transports droplets upward through the cloud layer, removing them from cloud base where they are activated and replenishing them at cloud top where they are depleted by evaporation in the entrainment zone. The subgrid scale turbulent mixing term contributes only signi?cantly to the budget near cloud base and cloud top due to the presence of strong vertical gradients in cloud number concentration there.

3.2 Shallow cumulus case

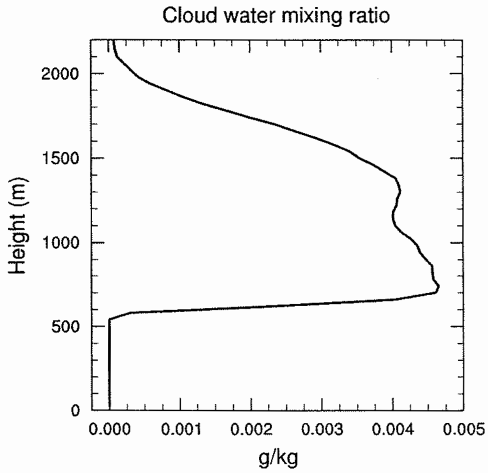

Figure 5: Layer-averaged cloud water mixing ratio for the last two hours of the cumulus simulation.

The layer-averaged cloud water for the shallow cumulus case is much smaller than for the stratocumulus case due to the very low cloud fraction. The maximum value is less than 0.005 g/kg as shown in Fig. 5. As is typical for cumulus layers, cloud water is largest near cloud base and decreases with height. The average cloud droplet number is also extremely small, reaching less than 4×10^6 kg^{-1} for the maritime distribution and 7×10^6 kg^{-1} for the continental case (Fig. 6). The vertical distribution of the cloud droplets actually resembles closely the cloud fraction (not shown) because the in-cloud variability of cloud number is relatively small.

Finally, the number budget for the maritime cumulus case is shown in Fig. 7. (The budget for the continental distribution – not shown – exhibits very similar features.) As was the case for the stratocumulus case, activation occurs in a narrow region around cloud base. Evaporation, however, is spread over a deeper region from 700 m to 2000 m. Turbulent transport nearly balances the microphysics contribution by transporting droplets

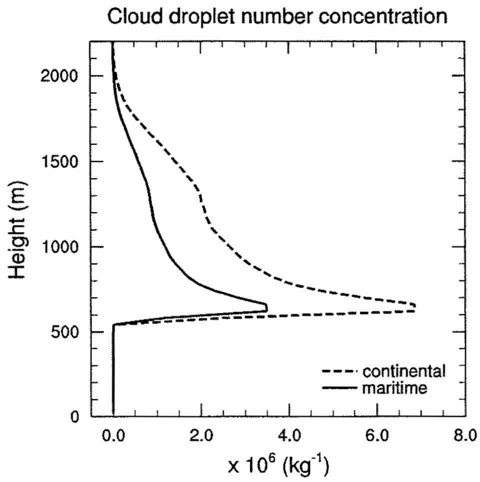

Figure 6: Layer-averaged cloud droplet number concentration for the maritime and continental simulations of the shallow cumulus case.

away from the activation region into the upper portion of the cloud layer where they are progressively evaporated through entrainment of dry environmental air.

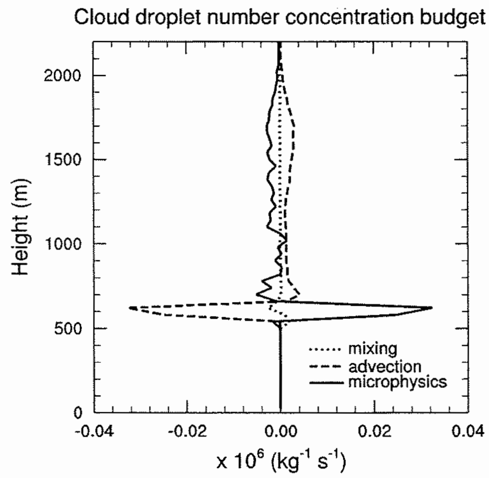

Figure 7: Cloud droplet number concentration budget for the maritime simulation of the shallow cumulus case.

4. SUMMARY AND FUTURE WORK

An activation scheme that uses the vertical velocity to determine the number of nucleated CCN has been implemented in a LES model. Two different boundary layer cloud regimes were simulated. They consist of a stratocumulus and a shallow cumulus case. Each case was run with two different CCN distribution spectra characteristics of maritime and continental environments.

Despite the relative simplicity of the activation parameterization and its lack of explicit supersaturation prediction, the cloud droplet number concentration budgets are in good qualitative agreement with detailed bin-resolving simulations. In particular, activation of new droplets occurs only in a small region near cloud base.

These simulations will serve as reference cases to investigate possible approaches for CCN activation in large-scale models which do not explicitly resolve cloud-scale vertical velocities. Some subgrid-scale models can provide information regarding the the joint probability density function (PDF) of vertical velocity, temperature, and moisture (e.g. Golaz et al. 2002). The basic idea is to use the information contained in the joint PDF, and in particular in the distribution of the vertical velocity, to diagnose the number of nucleated CCN.

5. ACKNOWLEDGMENTS

This work was performed while the ?rst author held a National Research Council Research Associateship Award at the Naval Research Laboratory, Monterey, California. Shouping Wang was supported by the Of?ce of Naval Research and the Naval Research Laboratory through CBLAST project. The third author is grateful for ?nancial support from NSF grant number ATM 0239982.

6. REFERENCES

Cohard, J.-M. and J.-P. Pinty, 2000: A comprehensive two-moment warm microphysical bulk scheme. I: Description and tests. *Quart. J. Roy. Meteor. Soc.*, **126**, 1815–1842.

Cohard, J.-M., J.-P. Pinty, and C. Bedos, 1998: Extending Twomey's analytical estimate of nucleated cloud droplet concentration from CCN spectra. *J. Atmos. Sci.*, **55**, 3348–3357.

Ghan, S. J., C. C. Chuang, and J. E. Penner, 1993: A parameterization of cloud droplet nucleation. Part I: Single aerosol type. *Atmos. Res.*, **12**, 198–221.

Golaz, J.-C., V. E. Larson, and W. R. Cotton, 2002: A PDF based model for boundary layer clouds. Part I: Method and model description. *J. Atmos. Sci.*, **59**, 3540–3551.

Hodur, R. M., 1987: The Naval Research Laboratory's Coupled Ocean/Atmosphere Mesoscale Prediction System (COAMPS). *Mon. Wea. Rev.*, **125**, 1414–1430.

Siebesma, A. P., C. S. Bretherton, A. Brown, A. Chlond, J. Cuxart, P. G. Duynkerke, H. Jiang, M. Khairoutdinov, D. Lewellen, C.-H. Moeng, E. Sanchez, B. Stevens, and D. E. Stevens, 2003: A large eddy simulation intercomparison study of shallow cumulus convection. *J. Atmos. Sci.*, **60**, 1201–1219.

Twomey, S., 1977: The in?uence of pollution on the shortwave albedo of clouds. *J. Atmos. Sci.*, **34**, 1149–1152.

Wang, S., Q. Wang, and G. Feingold, 2003: Turbulence, condensation, and liquid water transport in numerically simulated nonprecipitating stratocumulus clouds. *J. Atmos. Sci.*, **60**, 262–278.

Numerical modeling of microphysical variables using RAMS at Amazonian region, Brazil

Gonçalves, F.L.T., Martins, J.A., Silva Dias, M. A.

Dept. of Atmospheric Sciences, IAG/USP - São Paulo, Brazil

1. Introduction

Amazonian region has been investigated deeply last years as well as the other continental tropics in order to evaluate its importance to the local and global climate. Amazonia is the largest tropical forest in the world and the highest source of energy to the atmosphere from continental origin. Link to that, Amazon region represents also an unequivocal source of humidity to the hydrical resources during wet season. On the other hand, during the dry season, it is a large source of aerosols or particulate matter from biomass burning, which implies in the air quality and indirectly to the regional climate and clearly on cloud microphysics.

Consequently, LBA Project– Large Scale Biosphere Atmosphere Experiment in Amazonia, was developed as an international project initiating during 1998 and being lead by Brazil, with the aim of understanding as a regional entity. The analysis of effect on land use changes is also a goal of the project as well as on climate throughout the physical, chemical and biological mechanisms and interactions. The last Campaign of LBA was based on dry to wet season, on other words, the seasonal transition between the driest season (until September) and the wet season (starting at October). Therefore, the Campaign started at September 15 lasting until November 15, and called by "DRY-TO-WET AMC/LBA Atmospheric Mesoscale Campaign", developed in Rondonia State. The seasonality of the Rondonia region may be identified directly by the surface parameter evolution. For example, the thermal amplitude decreases from the dry season to the wet season.

On the other hand, clouds are also linked to the seasonal transition, which are strictly linked to the surface processes (Betts et al, 1996), through the heat fluxes (sensible and latent) and the composition of aerosols and trace gases. Additionally, clouds are also important to the gases and aerosol transport through a regional or even long distance scale, depending upon their depth (Freitas et al, 2000, 2001).

Corresponding author´s address: F. L. T. Gonçalves - Rua do Matão, 1226 – Cidade Universitária USP 05508-900 São Paulo, SP Brazil e-mail: fgoncalv@model.iag.usp.br

2. Objective

In this article, microphysical variables, particularly droplet size distributions, have been investigated considering a numerical simulation based on RAMS (*Regional Atmospheric Modeling System*), at the Rondonia, Western Brazilian Amazonia with the focus on southwest Amazon Basin during the transition from dry to wet seasons within the scope of LBA. (The Large Scale Biosphere Atmosphere Experiment in Amazonia)

3. Methodology

The numerical simulations had the objective of reproducing as close as possible the microphysical variable spatial distributions in the observed dataset. The dataset included airborne observations with a microphysics airplane measuring cloud droplet content and spectra in several flights; radiosonde launches, a 10 cm Doppler radar visible and IR satellite maps and pluviometer network complete the description of the observed convective systems. All data were obtained during the dry-to-wet campaign from September to November 2003. The data were collected from the LBA Project DRY-TO-WET Campaign. The methodology was based upon the cloud properties and precipitation, which was chosen in order to evaluate the RAMS modeling. It was chosen September 23 rain event to simulate. The main parameterizations were: four grids; topography with 500 m resolution; center of the grid was placed at -10.92° latitude and -62.41° longitude over Fazenda N. Sra., the Weather radar is also located at the same grid center; Cumulus parameterization Grell only at grids 1 and 2; complete microphysical parameterization with GNU variable using two shape parameters: 2 (usually in RAMS default) and 5; cloud water concentrations are chosen 550, 1100 and 3000 droplets per cm^{-3}, and all others with mean diameter $1.e^{-3}$ mm.

4. Results and Discussion

The preliminary modeling results have shown a different cloud patterns using different gamma function and cloud droplet concentration (CDC) initial inputs. Figure 1 shows the RAMS simulation for cloud mixing ratio ($g.kg^{-1}$) at 700 hPa at 19:00 GMT during September 23 event, with CDC 1000 droplets per cm^{-3}. The cloud water contents

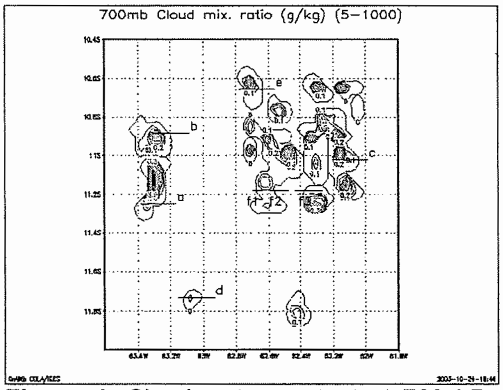

Figure 1. Cloud water content at 700 hPa, with simulation: shape parameter 5 and cloud droplet concentration of 1000 droplets per cm^{-3}, 19Z, showing cloud cuts (***a*** to ***f***) for cloud spectra analysis.

are scattered through the area. That simulation presents similar spatial as well as temporal distributions compared to Weather radar CAPPI (figure 2). Rainfall map distributions during the whole event also show similar patterns. The simulation is comparable to the IR satellite charts, as well. Nevertheless, there are some spatial and, particularly, temporal differences amongst cloud mixing ratio pattern maps, according to the chosen gamma functions and CDC. In order to evaluate that result, it has been chosen a simulated cloud and compared to an observed cloud, from the

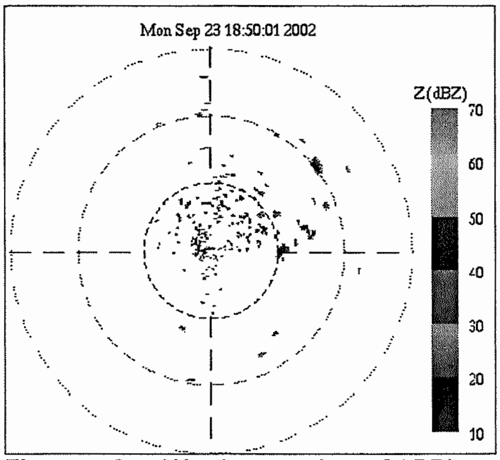

Figure 2. Weather radar CAPPI at September 23, 18:50 GMT. Both Figures have the same geographical center.

aircraft flights, at the same event. From figure 1, the letter '***a***' means the chosen cloud cut for this analysis, which presents similar cloud water concentrations in comparison to the flights. Figures 3 and 4 present the shape parameters adjusted for different cloud water concentrations and their spectra, obtained from the flights. As

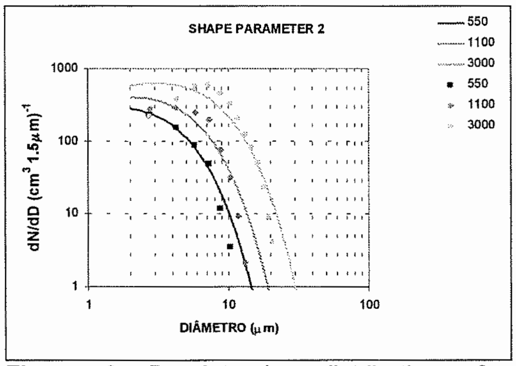

Figure 3. Droplet size distributions for simulated cloud (with cut ***a***) and the observed cloud spectra from the flight and different cloud water contents (550, 1100 and 3000 $droplets.mm^{-3}$), using form gamma function shape parameter 2.

the result obtained from the figures, shape parameter 5 is clearly better fitted, with observed data and presenting square correlation coefficient of 0.95 using CDC 3000 droplets per cm^{-3}, than shape parameter 2 presenting square correlation coefficient of 0.75 (shape parameter 2). That means the gamma function using shape parameter 5 can be a quite useful tool to simulate the cloud spectra in the studied event, instead of the normally used shape parameter 2, for this particular event.

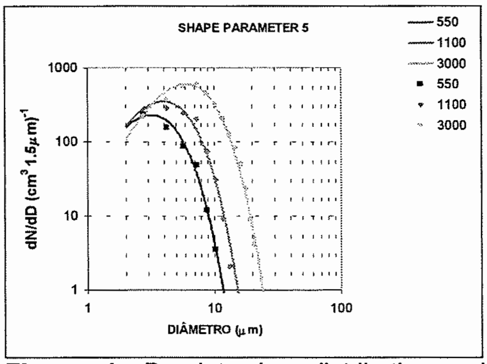

Figure 4. Droplet size distributions with different cloud water contents (550, 1100 and 3000 droplets.cm^{-3}), using gamma functions shape parameter 5.

5. Conclusions

From this preliminary analysis, shape parameters and gamma functions are very important in order to evaluate the spatial and temporal cloud patterns as well as the adjust to the observed cloud spectra, when we are simulating with RAMS.

6. Acknowledgements

We acknowledge CNPq and LBA Project as well as flight for Oliveira, J.C.P. from Universidade Federal do Ceará.

7. References

Betts, A. K., J.H. Ball, A.C.M. Beljaars, M.J. Miller and P. Viterbo, 1996: The land-surface-atmosphere interaction: a review based on observational and global modeling perspectives. J. Geophys. Res., 101, 7209-7225

Freitas, S. R. M. A. F. Silva Dias, P. L. Silva Dias, K. M. Longo, P. Artaxo, M. O. Andreae, H. Fischer, 2000: A Convective Kinematic Trajectory Technique for Low Resolution Atmospheric Models. Journal of Geophysical Research, 105, D19, 24,375-24,386.

Freitas, S R., M. A. F. Silva Dias, P. L. Silva Dias, 2001: Modeling the convective transport of trace gases by deep and moist convection. Hybrid Methods in Engineering, 2, 3, (in press)

RADIATIVE IMPACTS ON THE GROWTH OF DROPS WITHIN SIMULATED MARINE STRATOCUMULUS CLOUDS

Jerry Y. Harrington and Christopher M. Hartman
The Pennsylvania State University, University Park, Pennsylvania

1. INTRODUCTION

Interest in the interaction between a cloud drop and its environment began more than a century ago (1890) when Maxwell formulated his equations for condensation and evaporation. Fuchs (1959) was the first to include a radiative term in the mass growth rate equation; he concluded that influences of infrared radiative processes on the vapor growth of drops are negligible because temperature differences between a drop and its environment inside a cloud are usually small. This conclusion holds true for the cloud interior, but near cloud boundaries there can be a large gradient in incident radiant energy resulting in strong cooling or heating. In the longwave (LW), the net cooling rate of drops in the vicinity of cloud top is generally in the range of 1.5 to 8 K hr^{-1}. This radiative cooling assists the dissipation of warming produced during condensation; consequently, condensation rates are increased. Roach (1976) includes the effects of LW radiation on individual, isolated drops residing at cloud top to show that net radiative cooling enhances condensation and allows larger drops ($r >$ 20 µm) to grow, even in a subsaturated environment.

Radiative effects on droplet populations were first studied by Guzzi and Rizzi (1980), who find a differential impact of radiative cooling on the size spectrum due to the fact that drop absorption coefficients increase rapidly with drop size. Hence, radiative cooling enhances larger drop growth while suppressing the growth of smaller drops, producing spectral broadening. Austin et al. (1995) show that collision-coalescence (collection) is enhanced by radiative cooling such that the time required for the onset of collection, and hence precipitation, may be reduced by as much as a factor of four when radiative cooling occurs.

Since the early 1990s, microphysical-dynamical cloud models have shown that enhanced production of large drops due to radiation occurs within a reasonable time. Bott et al. (1990) include the radiative term in their one-dimensional (1D) fog model and discover that the oscillations of the liquid water content (LWC) observed for their case are only reproducible if the radiative term is included in the drop growth equation. Ackerman et al. (1995) include the radiative term in a 1D stratocumulus model and show a significant influence of the radiative effect on LWC, supersaturation (S_u), and optical depth. Finally, Harrington et al. (2000) use a trajectory ensemble model (TEM) to show that the radiative effect reduces the time required for the onset of drizzle by up to a half hour.

This study uses a Large Eddy Simulation (LES) of a stratocumulus cloud coupled with a TEM that computes detailed bin microphysics in order to address the effects of LW and shortwave (SW) radiation on the growth of drops. Unlike previous studies, this paper addresses the effects of strong solar heating.

2. PROCEDURE

The influences of radiation on drop growth are examined using a TEM that is forced by parcel data generated by the LES option (Stevens et al. 1999) of the Regional Atmospheric Modeling System (RAMS; Pielke et al. 1992). Radiative heating and cooling rates are calculated in the LES by using a two-stream radiative transfer routine that includes six solar and twelve infrared wavelength bands (Harrington and Olsson 2001). The LES model is run with bulk microphysics. For this study, the LES domain covers 6 km by 6 km in the horizontal with grid spacing of 40 m and 3.5 km in the vertical with grid spacing of 20 m. A time step of two seconds is used. After four hours of LES simulation time, at which point the cloud has sufficiently developed, 600 parcels are released into the cloud base and tracked for two hours by the LES code. Output from the LES during the last two hours is used to drive a TEM, which includes liquid phase bin microphysics. This bin microphysical model provides the number concentration and mass of drops in 34 bins at each time step by calculating the rate of transfer of drop concentration and mass between bins due to condensation/evaporation and collection for each parcel. The evolution of the size spectrum is computed by following the method of moments (Tzivion et al. 1987) as modified by Stevens et al. (1996).

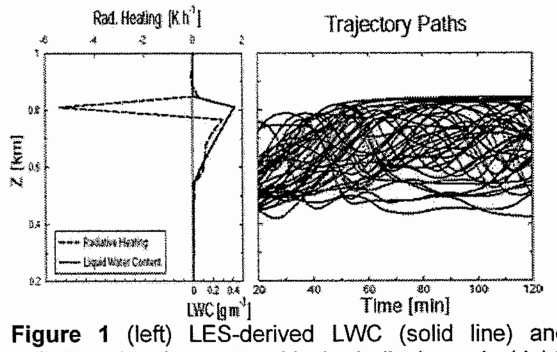

Figure 1 (left) LES-derived LWC (solid line) and radiative heating rate (dashed line) and (right) trajectory paths.

The LES is run for the case of an overhead sun. Included in Fig. 1 are profiles of the LWC and radiative heating rate from the LES. As would be expected, the maximum LWC occurs near cloud top. This maximum LWC corresponds to a maximum in radiative cooling due to the emission of LW radiation by large drops. Radiative cooling is confined to the top 50 m of the cloud, while the lower 250 m of the cloud is warmed by solar heating. Also included in Fig. 1 is a sample (60) of the 600 trajectory paths from the LES. Note that trajectories are confined primarily to the cloud layer. This results from the fact that strong solar heating stabilizes the cloud layer with respect to the sub-cloud layer (e.g., Nicholls 1984).

Vapor depositional growth of drops in the TEM is parameterized by an approximate solution to the mass growth rate equation,

$$\frac{dm}{dt} = 4\pi r G(T,P)\left(S - 1 - \frac{A}{r} + \frac{B}{r^3} - c(r)Q_R\right),$$

where m is the mass of a drop, r is the radius of a drop, S is the environmental saturation ratio, A is a coefficient of the curvature term, B is a coefficient of the solution term, $c(r)$ is a coefficient of the radiation term, and Q_R is the radiative power incident on a drop. Equation (1) shows that drop growth is enhanced by radiative cooling ($Q_R < 0$) and suppressed by radiative heating ($Q_R > 0$). The impacts of the curvature and solution terms are significant at smaller radii ($r < 2$ μm), whereas the impact of the radiative term is significant at radii larger than 10 μm (Roach 1976). Hence, when the solution and curvature effects begin to decrease in importance, radiation becomes important. Output from the LES is then used to drive the TEM, which is run three separate times: once without radiative influences on drop growth (i.e., Q_R = 0), once with only LW radiative influences on drop growth, and once with both LW and SW radiative influences on drop growth.

3. INDIVIDUAL PARCEL RESULTS

Plotted in Fig. 2 is a histogram of the average time parcels spend in the cloud as well as the average time parcels spend at the top of the cloud. For this study, cloud top is defined as the layer where LW cooling occurs. The average time a parcel spends at cloud top is approximately 15 min. Thus, on average, cloud-top radiative effects have about 15 min to influence drop populations when the sun is overhead.

Parcels that spend a significant period of time in the vicinity of cloud top are particularly important for quantifying the effects of radiation on drop growth. Thus a parcel that tracks along the top of the cloud for approximately 50 min is selected for further study. Figure 3 shows the LWC and S_u for this parcel during the last two hours of the simulation. The parcel reaches cloud top just before 300 min, at which

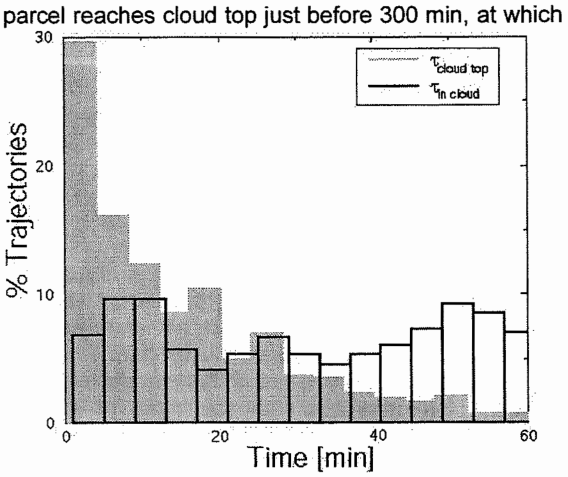

Figure 2 Average in-cloud (open) and cloud-top (shaded) residence times for the case of an overhead sun.

point the LWC reaches a maximum. When LW radiation is included in the radiation term of (1), LWC is increased relative to the no-radiation case. This increase occurs because LW cooling at cloud top enhances the growth of the larger drops. Conversely, the inclusion of LW radiation reduces the S_u to slight subsaturations because the rapid growth of large drops depletes the environment of water vapor. Including SW heating reduces both of the LW effects on LWC and S_u, because SW heating at cloud top reduces the total amount of cooling.

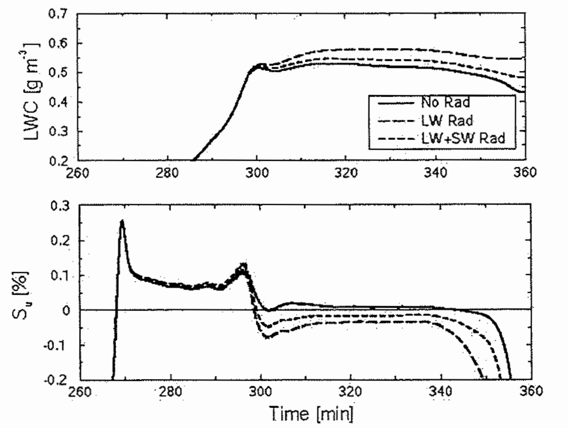

Figure 3 Liquid water content (top) and supersaturation (bottom) of a parcel that tracks along cloud top for approximately 50 min in the no-radiation (solid line), LW radiation (long dashed line), and LW+SW radiation (short dashed line) cases.

The size distribution of the parcel after 15 min at cloud top is plotted in Fig. 4, where 15 min is chosen because this is close to the average time parcels spend at cloud top. The inclusion of LW radiation broadens the distribution with respect to the no-radiation case. With LW radiation, more mass accumulates in the larger drop sizes (r > 50 μm)

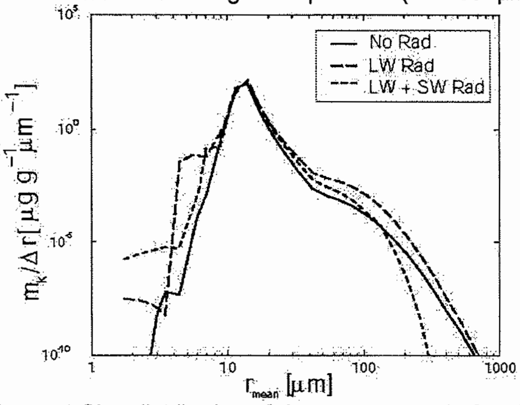

Figure 4 Size distribution of drops in a parcel after 15 min at cloud top for the no-radiation (solid line), LW radiation (long dashed line), and LW+SW radiation (short dashed line) cases.

because the radiative effect increases with drop size beyond r = 10 μm, when drop absorption coefficients become significant. Furthermore, a small drop mode (r ~ 3 to 7 μm) begins to appear. This is due to the fact that small drops (r ~ 8 to 10 μm) are weakly influenced by the radiative effect, and therefore evaporate in the slightly subsaturated environment causing an accumulation of mass at the smallest drop sizes. The addition of SW heating narrows the distribution in Fig. 4 preferentially at drop sizes larger than r = 150 μm after only 15 min at cloud top. In fact, the amount of mass at these sizes is smaller than in the case without radiation. Thus, SW heating dominates over LW cooling for drops with r > 150 μm.

The effects of both LW and SW radiation on drop size spectra may have important implications for the initiation of collection, which often leads to precipitation. With the broadening of the drop size distribution due to LW radiation, the initiation of collection may occur sooner because drops reach larger sizes more rapidly. Finally, the inclusion of SW heating in the drop growth rate equation may result in suppression of the collection process.

4. CONCLUSION

The effects of solar and infrared radiation on the growth of drops within a simulated marine stratocumulus cloud are addressed. Radiative effects are examined by using trajectory datasets produced by a large eddy simulation (LES). A trajectory ensemble model (TEM), which includes detailed bin microphysics, is then used on the LES-derived dataset.

Radiative effects are strongest near cloud boundaries. It is found that most parcels spend less than 20 min at cloud top, with the average being 15 min. Thus, on average, cloud top radiative effects have about 15 min to influence drop populations for the case of an overhead sun. With strong SW heating, cloud base is stabilized. This stabilization of cloud base confines parcels to the cloud layer, resulting in long cloud-top residence times and a greater impact of radiation on vapor depositional growth.

Studies on an individual trajectory show that SW heating has a size-dependent effect on drop growth. For the large drops (r > 150 μm), SW heating has a greater effect on drop growth than does LW cooling even at cloud top. Consequently, the larger drops experience significant heating and evaporate rapidly. This net heating of large drops causes a narrowing of the drop size spectrum even in comparison with the case that excludes the radiative effect.

Ultimately, parcel in-cloud time-scales play an important role in the microphysics of clouds through their indirect impact on the net radiative heating and cooling of individual air parcels. In the future, it would be beneficial to include dynamic feedbacks on the microphysics by running a coupled LES-bin microphysics simulation. Not only would this provide a more realistic view of the simulated cloud, but it would also provide more insight into the complexity of the feedback between the dynamics and microphysics of clouds.

5. ACKNOWLEDGMENTS

The research from which this paper is based upon was supported by an REU under NSF grant numbers ATM01-03815 and ATM-9873643 as well as under an AMS/NASA Earth Science Enterprise Graduate Fellowship.

6. REFERENCES

Ackerman, A.S., O.B. Toon, and P.V. Hobbs, 1995 A model for particle microphysics, turbulent mixing, and radiative transfer in the stratocumulus-topped marine boundary layer and comparisons with measurements. *J. Atmos. Sci.*, **52**, 1204-1236.

Austin, P.H., S. Siems, and Y. Wang, 1995: Constraints on droplet growth in radiatively cooled stratocumulus. *J. Geophys. Res.*, **100**, 14231-14242.

Bott, A., U. Sievers, and W. Zdunkowski, 1990: A radiation fog model with detailed treatment of the interaction between radiative transfer and fog microphysics. *J. Atmos. Sci.*, **47**, 2153-2166.

Fuchs, N.A., 1959: *Evaporation and Droplet Growth in Gaseous Media*. Pergamon Press, New York, NY, 200 pp.

Guzzi, R., and R. Rizzi, 1980: The effect of radiative exchange on the growth of a population of droplets. *Contrib. Atmos. Phys.*, **53**, 351-365.

Harrington, J.Y., G. Feingold, and W.R. Cotton, 2000: Radiative impacts on the growth of a population of drops within simulated summertime arctic stratus. *J. Atmos. Sci.*, **57**, 766-785.

----, and P.Q. Olsson, 2001: A method for the parameterization of cloud optical properties in bulk and bin microphysical models: Implications for arctic cloudy boundary layers. *Atmos. Res.*, **57**, 51-80.

Nicholls, S., 1984: The dynamics of stratocumulus: Aircraft observations and comparisons with a mixed layer model. *Quart. J. Roy Meteor. Soc.*, **110**, 783-820.

Pielke, R.A., and coauthors, 1992: A comprehensive meteorological modeling system – RAMS. *Meteor. Atmos. Phys.*, **49**, 69-91.

Roach, W.T., 1976: On the effect of radiative exchange on the growth by condensation of a cloud or fog droplet. *Quart. J. Roy. Meteor. Soc.*, **102**, 361-372.

Stevens, B., G. Feingold, W.R. Cotton, and R.L. Walko, 1996: Elements of the microphysical sructure of numerically simulated nonprecipitating stratocumulus. *J. Atmos. Sci.*, **53**, 980-1007.

----, C.H. Moeng, and P.P. Sullivan, 1999: Large-eddy simulations of radiatively driven convection: Sensitivities to the representation of small scales. *J. Atmos. Sci.*, **56**, 3963-3984.

Tzivion, S., G. Feingold, and Z. Levin, 1987: An efficient numerical solution to the stochastic collection equation. *J. Atmos. Sci.*, **44**, 3139-3149.

An Improvement for Liquid-phase Microphysics in JMA-NHM.

Akihiro Hashimoto[1], Masataka Murakami[2], Syugo Hayashi[2], Chiashi Muroi[2], Teruyuki Kato[2], Masanori Yoshizaki[2]

[1]Advanced Earth Science and Technology Organization, Tokyo
[2]Meteorological Research Institute / Japan Meteorological Agency, Tsukuba

1. Introduction

We are developing a regional climate model with horizontal resolution of several kilometers on the basis of JMA-NHM (Japan Meteorological Agency NonHydrostatic Model; Saito et al., 2001) in order to study the change of precipitation intensity around Japan under the situation of global warming. Microphysical processes are important for this purpose, because they determine intensity, location and timing of precipitation. For this study, some improvements have been made on the microphysical parameterizations, which include the change of liquid hydrometeor parameterization from 1-memtnt bulk scheme to 2-moment bulk scheme and some modifications of relevant microphysical processes. In order to examine the performance of the improved parameterization, we made the simulations of low-level stratocumulus clouds.

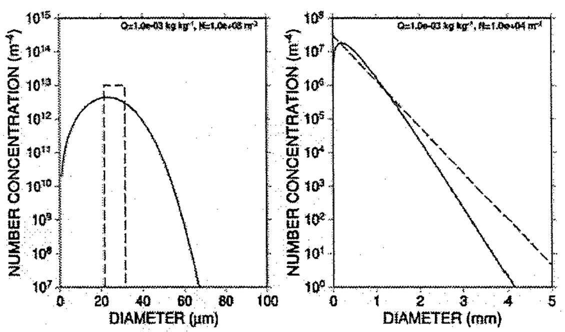

Fig. 1 The size spectra which are assumed in the new (solid lines) and old (broken lines) schemes. (a) and (b) correspond to the size spectra of cloud droplets and rain drops, respectively.

Corresponding author's address: Akihiro Hashimoto, Meteorological Research Institute, 1-1 Nagamine, Tsukuba, Ibaraki 305-0052, Japan, E-Mail: ahashimo@mri-jma.go.jp

Table 1 The major specifications of experiments.

Horizontal resolution: 1 km
Vertical layers (distances): 36 layers (50m near the surface to 220m at the model top)
Basic equations: Full compressible system
Treatment of sound waves: Horizontally explicit and vertically implicit (HE-VI)
Vertical coordinate: Terrain following
Turbulent closure: Level 2.5
Boundary condition: Rayleigh damping is used for lateral and upper boundaries.
Microphysics: 2 liquid (Mixing ration and number densities of cloud droplets and raindrops are predicted.)
Convective parameterization: none
Advection: Second order in conjunction with modified advection scheme
Radiation: Cloud amount is determined by relative humidity.
Surface temperature: 4 layer model

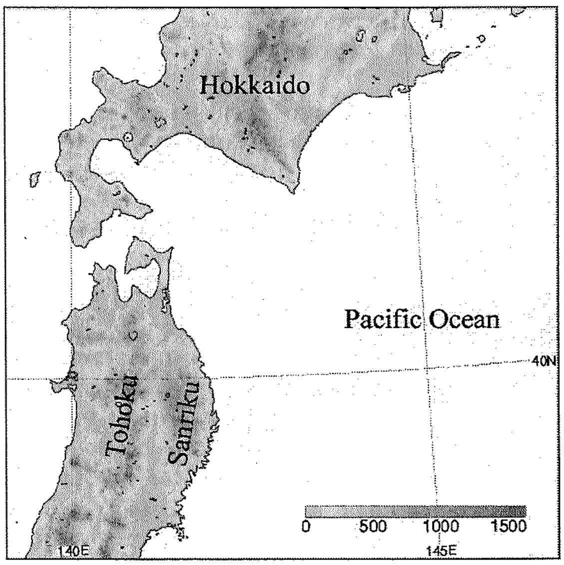

Fig. 2 The model domain and orography.

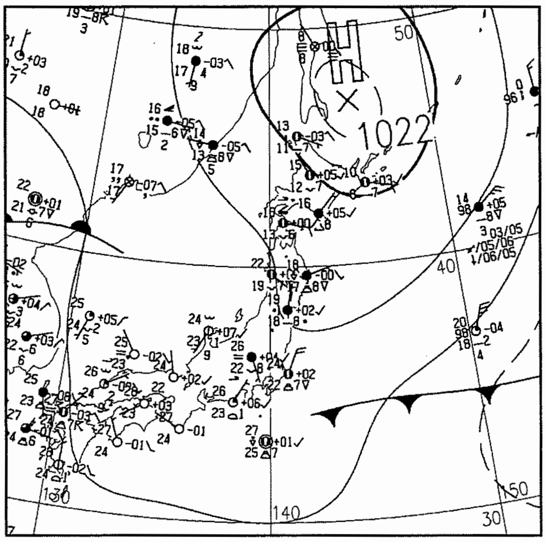

Fig. 3 Surface weather map at 0300 JST, 2 Aug. 2001.

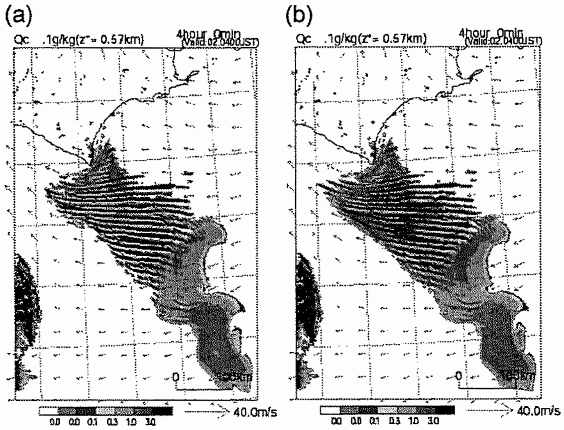

Fig. 4 Mixing ratio of cloud water for (a) new and (b) old schemes at 570-m height.

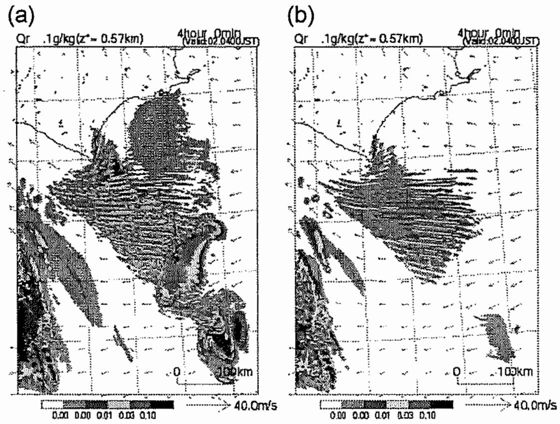

Fig. 5 Mixing ratio of rain water for (a) new and (b) old schemes at 570-m height.

2. Improvements of microphysics in JMA-NHM

The microphysical processes in JMA-NHM are formulated with a bulk parameterization composed of three solid and two liquid water categories. The ice, snow, and graupel categories are represented by a 2-moment parameterization which has two prognostic variables, mixing ratio Q ($kgkg^{-1}$) and number concentration N (m^{-3}), to determine the size spectra of hydrometeors. On the other hand, the cloud and rain categories were represented by a 1-moment parameterization which uses only Q. This old parameterization is improved so as to have 2-moment scheme also for the cloud and rain categories in this study.

In the old scheme, size spectrum of cloud droplets was assumed to be of mono-disperse with constant number concentration 10^8 m^{-3}, while an inverse-exponential function was applied to rain drop size spectrum. On the other hand, a newly-introduced scheme uses gamma functions to represent the size spectra of cloud droplets and rain drops, so as to make them more realistic.

The new scheme has the following improvements in microphysical processes, as compared with the old one. Some processes of warm rain such as auto-conversion, accretion of cloud droplets, and self-collection and breakup of rain drops are introduced based on Cohard and Pinty (2000). Increase in number concentrations of cloud droplets due to CCN (Cloud Condensation Nuclei) activation is diagnostically calculated based on the maximum super-saturation estimated from updraft velocity. Other microphysical processes relating to the liquid hydrometeors are modified so as to reflect the improvements of their size spectra.

3. Designs of numerical experiments

Figure 2 shows the model domain of 640x640 km^2 with horizontal resolution of 1-km. The model Top is located at 4.7 km. Vertically, 36 layers with stretched intervals from 50 m near surface to 220 m near model top are employed. The domain covers around the sea off the coast of Sanriku, the Tohoku, Japan. In this region, the low-level stratocumulus clouds often appear in the cold air mass flowing on relatively warm sea from the northern high pressure in summer. Figure 3 shows the surface weather map at 0300 JST, 2 August 2001. This pressure pattern is typical for the low-level stratocumulus clouds to appear in the model domain. The time integration with Δt=5 sec is started from 2100 JST, 1 Aug, 2001, and continued up to 8640 steps (12 hours). Regional analysis data of JMA are referred to as the boundary condition every hour. The other specifications of the model are shown in Table 1.

According to IR image of GMS, low-level clouds covered the sea off the coast of Sanriku at the present and the next days. We consider only warm rain process in the simulation, because the targeted low-level stratocumulus clouds contain no ice particle.

Simulations with the new and old microphysical schemes are conducted to study the effect of the reformulations in microphysical parameterization on the model results.

4. Simulation results

The low-level stratocumulus clouds simulated by the model covers about 40000-km^2 area with the cloud base at about 300-m height and the cloud top at about 600-m height. For both simulations with the new and old schemes, the amplitudes of vertical velocity are within 0.3 m/s, and the mixing ratios of cloud water are around 0.1 g/kg, as shown in Fig. 4. A difference between the two schemes is apparent in the amount of rain water. Figure 5 shows the mixing ratio of rain water at 570-m height. The simulation with the new scheme produces rain water much more than the old one.

Figure 6 shows the relations between mixing ratio, and number concentration in the different ranges of mean-volume diameter. As shown in Figs. 6a and 6b, the new scheme produces large variations in the number concentration of cloud droplets Ncw, although the old scheme assumes no variation in Ncw. This result indicates that the new scheme can give the larger maximum values of mean-volume diameter (Fig. 6a), and that the new scheme can make the value of auto-conversion rate larger than the old one. Additionally, the number concentration of rain drops Nr is generally much larger for the new scheme, as shown in Figs. 6c and 6d. This enhances the accretion of cloud droplets by rain drops. Therefore, the new scheme produces the greater amount of rain water. The relatively smaller Nr for the old scheme makes the mean-volume diameter in cloud layer larger than for the new scheme so that the fall velocity of rain drops becomes larger for the old scheme. On the other hand, for the new scheme, the mean-volume

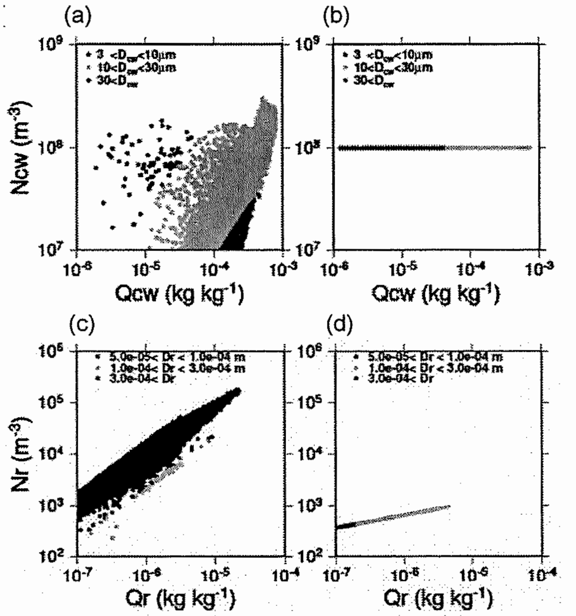

Fig. 6 Relations between mixing ratio Q and number concentration N in the different ranges of mean-volume diameter D which are shown by grey scale. (a) and (b) indicate the relations for cloud water, while (c) and (d) indicate those for rain water. (a) and (c) correspond to the results with new scheme, and (b) and (d) correspond to those with old scheme.

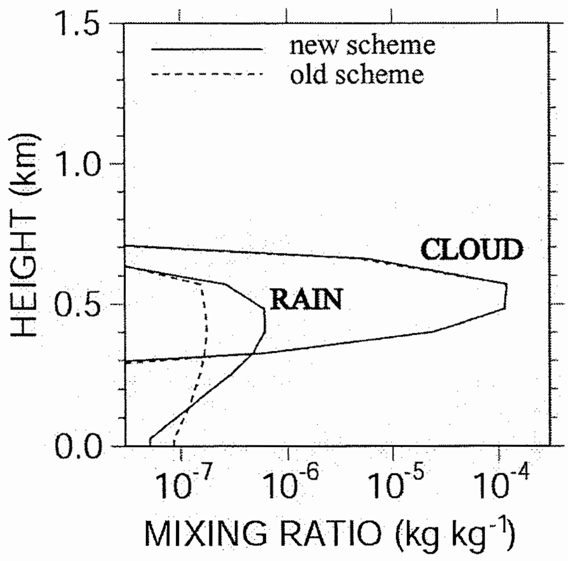

Fig. 7 Averaged profiles of mixing ratio with the new and old schemes indicated by solid and broken lines, respectively.

diameter which is smaller in cloud layer becomes larger with decreasing height by the growth and sorting of rain drops, and the fall velocity also becomes larger. Due to these features, the profiles of mixing ratio of rain for old scheme have smaller gradient, while the mixing ratio of rain water for the new scheme decreases with decreasing of height with greater gradient, as shown in Fig. 7.

5. Summary

The microphysics in JMA-NHM has been improved with respect to the liquid hydrometeors. This effect was examined by the simulations of the low-level stratocumulus clouds in summer.

The new scheme modified the rain water distribution when it is compared with the old scheme. The new scheme produced greater values of the mixing ratio of rain water. This is due to the greater variations in number concentration of Ncw and Nr which are produced in a prognostic manner in the new scheme. The variation in Ncw accelerates auto-conversion, and that in Nr enhances the accretion of cloud droplets by rain drops. The difference in fall velocity of rain drops relevant to Nr between the two schemes makes the gradient of the profile of Qr greater for the new scheme.

Acknowledgements

This study is conducted by the fund of Research Revolution 2002, and the numerical calculations are made by NEC SX-6 on the Earth Simulator.

References

Cohard, J. M. and J. P. Pinty, 2000: A comprehensive two-moment warm microphysical bulk scheme. I: Description and tests. Q. J. R. Meteor. Soc., **126**, 1815-1842.

Saito, K., T. Kato, H. Eito and C. Muroi, 2001: Documentation of the Meteorological Research Institute / Numerical Prediction Division Unified Nonhydrostatic Model. Tech. Rep.of MRI, **42**, p133.

RAPPORT FROM THE WMO INTERNATIONAL CLOUD MODELING WORKSHOP 11-16 JULY 2004

Daniela Jacob[1], Wojciech Grabowski[2], Andreas Chlond[1], Stefan Hagemann[1]

[1]Max-Planck-Institute for Meteorology, Hamburg, Germany
[2]National Center for Atmospheric Research (NCAR),

The International Cloud Modeling Workshop will be hosted by the Max Plank Institute (MPI), in Hamburg, during the week of July 12, 2004. This is the week prior to the International Conference on Clouds and Precipitation to be held in Bologna, Italy. The workshop follows the tradition of such meetings established in late 80ies. The emphasis of this workshop has traditionally been on cloud microphysics and its representation in cloud models. Since the Clermont-Ferrand workshop in 1996, the cloud chemistry topic has also been included.

The tentative list of the cases that will be discussed at the workshop is as follows:

1. Shallow convection case based on BBC (BALTEX BRIDGE Campaign) Cabauw observations. The case leader is Susanne Crewell (University of Bonn and KNMI).

2. The Elbe flooding case. This case involves convection embedded within synoptic-scale frontal precipitation. Daniela Jacob will lead this case.

3. Wintertime orographic precipitation case from December 13/14, 2001 IMPROVE II case. It will be led by Roy Rasmussen (NCAR).

4. Convective snowband case from cold air outbreak over the Sea of Japan. This case involves ice microphysics. Masataka Murakami from Japan's Meteorological Research Institute will lead this case.

5. Cloud chemistry case. This case is being organized by Mary Barth (NCAR).

During this talk a summary of the activities related to the cases mentioned above will be presented.

Corresponding author's address: Daniela Jacob, Max-Planck-Institute for Meteorology, Hamburg, Germany; E-Mail: jacob@dkrz.de.

THE MODELLING OF PROCESS OF RAINFALL FORMATION BY CLOUDS SEEDING

Kadyrov B.Sh.,

Central Asian Research Hydrometeorological Institute (SANIGMI)
72 K. Makhsumov Str., 700052, Tashkent, Uzbekistan
Fax: (998 71) 133-11-50
E-mail: sanigmi@albatros.uz

1. INTRODUCTION

In Uzbekistan, rockets are used for hail suppression. In our opinion, this approach has no future prospective in the in Uzbekistan due to a number of reasons. In this paper, an attempt of a theoretical justification of hail prevention using ground-based generators has been made.

Experimental studying of inner microphysical processes in convective clouds faces to many difficulties concerning secure methods of obtaining necessary information. In particular, for using the direct methods of measuring the microphysical parameters in convective clouds it is necessary to employ extra high durable aircrafts, which are expensive.

Computational modeling of microphysical processes in clouds enables to solve this problem with less expensive methods and to some degree meets a lack in the methods of clouds study.

2. MODEL

The model has been described in the literature, most notably Shiino(1978) and Baranov V. et al.,(1984). A numerical study of precipitation development in cumulus clouds with the use of an Eulerian one-dimensional time-dependent model, which consists of the vertical equation of motion, the mass continuity equation, the thermodynamic equation and parameterized cloud microphysics for liquid and solid water substances is presented. Condensed water substances is classified into three components, cloud droplets (cloud water), raindrops (precipitation water) and frozen raindrops (solid water). The parameterized liquid phase processes include condensation of water vapour, autoconversion of cloud droplets to raindrops, collection of cloud droplets by raindrops and evaporation of cloud droplets and raindrops. The ice phase includes heterogeneous glaciation of raindrops, riming, and sublimation of water vapour, melting of frozen raindrops, evaporation of frozen raindrops and evaporation melting of frozen raindrops. The model also has the capability of simulating seeding processes.

Kadyrov B.Sh. Central Asian Research Hydrometeorological Institute (SANIGMI)/72 K. Makhsumov Str., 700052, Tashkent, Uzbekistan
E-mail: sanigmi@albatros.uz

3. THE METHOD OF CONDUCTING NUMERICAL EXPERIMENTS

Imitation of modification consists in artificial introduction of ice-forming particles of definite concentration in

In the numerical experiments of studying the precipitation formation process in convective clouds a reagent introduction from the ground was imitated with optimal concentration equal to 100 particles per liter at different temperature conditions and at different time moments of the modeled cloud life.

In order to make analyzing numerical experiments more comfortable and to get visual results the temporal sections of the calculated parameters were mapped. The following parameters were calculated: liquid water content (LWC), total water content of a cloud and rainfall fraction, ice water content (IWC) and total water content liquid-drop, rain and ice fractions as well as change in vertical velocity in the course of time.

4. RESULTS

On the base of the numerical experiments at the first phase the optimal concentration of an ice-forming reagent was defined.

At that, according to conducted calculations, this concentration optimum was shown up in the fact that a cloud was staying longer (about 40 min) in the maximal stage of development, whereas under other values of concentration in every 5-10 minutes after reaching the maximal cloud formation, it reduced its thickness up to the values corresponding the case without modification.

The Figure 1 shows the change in time of total LWC of a modeled cloud. As it is seen from the Figure the precipitation out of this cloud began approximately in 20 minutes after starting the model running and the maximum was reached in another 15 minutes. From the Figure 1 one can see that the most LWC is situated at the heights between 2 and 3 km and this zone was formed in 1500 sec after the initiating a cloud model.

Studying the dynamics of LWC change of a cloud drop fraction has shown that there were no liquid drops higher than 6 km. In the process of changing total water content in a cloud life cycle two moments can be distinguished when the maximal water content in a vertical cloud structure was registered. Obviously, the first maximum was related to increase in LWC in the zone of accumulation. The second maximum apparently belonged to the zone of the formation of the particles with rain dimension emerging due to collision of fallen and lifting raindrops.

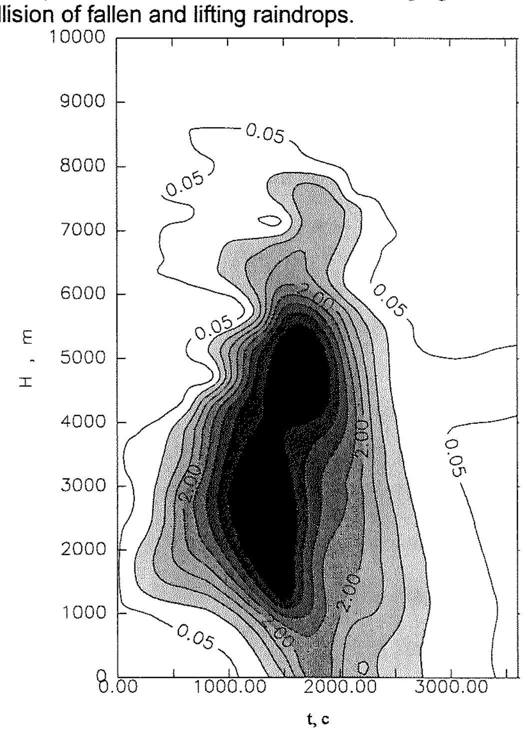

Fig. 1 Change in water content with time (without modification)

The Figure 2 shows the change in time IWC of a cloud. Maximum of ice content was situated at the height of 5-5.5 km and is reached to the 30th minute of initiating a cloud formation.

To out the weather modification technologies numerical experiments were conducted to reveal the peculiarities of running the process of precipitation formation under different seeding schemes and its dependence on the phase of a cloud formation.

Modification has led to full blocking liquid-drop part of water content at the height 4 km (T=-6° C). Influence of seeding by an ice reagent on the vertical distribution of IWC can be defined when comparing the Figures 2 and 3. As a result of modification imitation the zone with IWC maximum went down from 6 km to 4 km, at that the value itself was reduced almost by 3 times. The moment of coming the maximum was shifted for 5-8 minutes forward.

At the height 7-8 km the second, slighter maximum emerged.

The obtained result is of a great importance from the viewpoint of the hail suppression technology.

Namely, such an IWC reduction and the change in the level of maximum localization for a fall enable to decrease amount of precipitation being in solid phase (hail).

In other numerical experiments a reagent introduction from the land was simulated for full localization of liquid-drop part of a cloud lower than the level of the beginning reagent operation at different heights and different character of a reagent introduction (instantly and continuously) .

Differences in temporal changes of vertical structure were shown up as follows: when a reagent introduction at the level of 4 km precipitation started earlier (approximately 50 minutes earlier), precipitation maximum was shifted for 15-17 minutes forward.

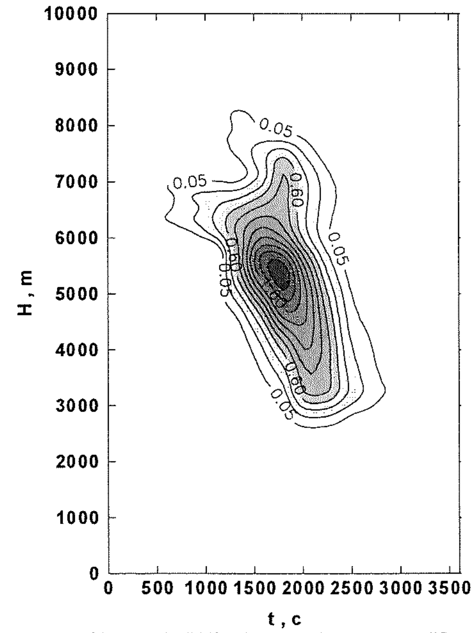

Fig. 2 Change in IWS with time (without modification)

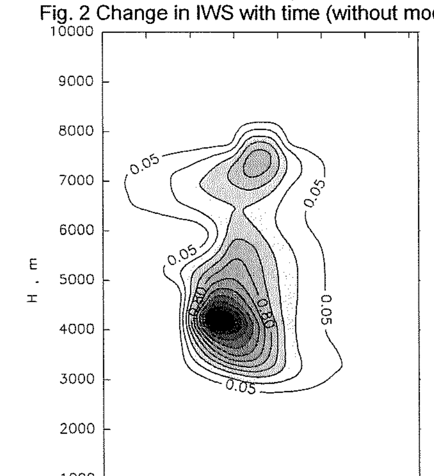

Fig. 3. Change in IWC with time (when modification from land)

The main point, higher than 6 km cloud moisture accumulated three times less than in the case of modification at the level of the isotherm -24°C. Besides the precipitation intensity at the ground layer in the second case was 1.5 times higher. Existing before conception about useless of modification at the level of the isotherm -22°C, which resulted from the suggestion about sufficient amount of natural cores for crystallization at these heights, has turned out to be not quite correct. It follows from the comparing various schemes of the reagents introduction that the value of the water content maximum was reduced and the second, the precipitation maximum was shifted for 5-7 minutes forward.

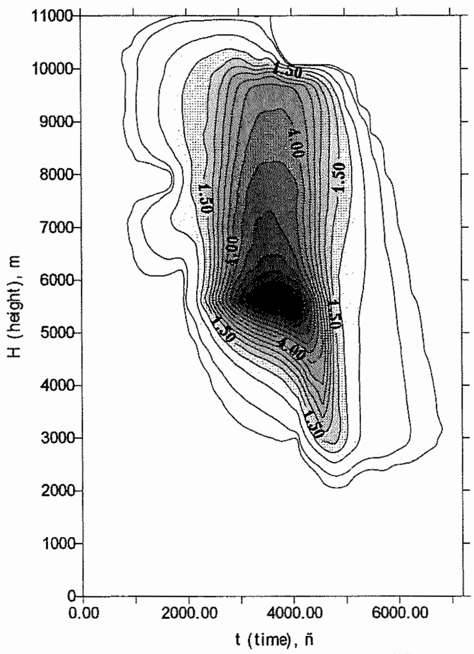

Fig. 4 Change in IWC with time (when modification from land)

Definition of the level of a reagent introduction influence on precipitation intensity at the ground layer can be treated as another important result. So a reagent introduction at the level of the isotherm (-16°C) has led to considerable reduction of precipitation intensity due to a little enlargement of the area with precipitation as comparison with the results of the numerical experiment under which a reagent introduction was implemented to the level of -6 °C.

The Figure 5 presents the change in IWCt when instant reagent introduction at a particular height. This result is of great importance from the viewpoint of influence even short-term impact on the convective cloud formation.

Several numerical experiments were conducted with the purpose of the defining the moment of a reagent introduction, namely, seeding was performed after the cloud reached the maximal accumulation of liquid-drop fraction, and that is, the delay with beginning cloud modification was simulated. The results showed the following: the first, this is the same effect with shifting precipitation maximum at the ground layer and the second unexpected result is a reagent introduction at lower level resulted in higher values of total cloud moisture at the heights of 7-9 km.

5. CONCLUSIONS

Thus the conducted numerical experiments have shown that blocking reagent introduction (introduction into lower part of a cloud) results in sharply reduction of liquid-drop part in the upper part of a cloud and changing precipitation intensity in the ground layer.

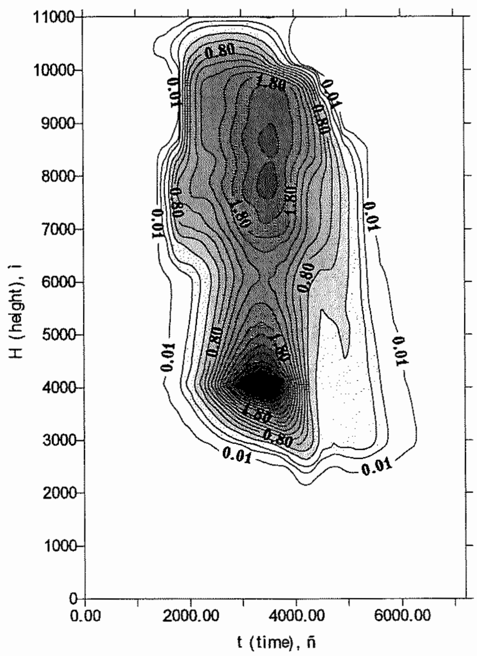

Fig. 5 Change in IWS with time when point modification.

So, if it is necessary to shift the precipitation beginning forward, blocking seeding should be conducted at the levels of the isotherms -4 °C - -6 °C but for reducing precipitation intensity a reagent should be introduced at the level –16 °C. The very interesting result concerns the physical efficiency of modification in the area of low negative temperatures (-22 °C - - 24 °C). Point is that seeding in this area in spite of sufficient amount of ice crystals also permits to regulate the precipitation formation process.

Cloud seeding from the ground (surface based generators) for hail combating purposes, judging by modeling calculations, allows to low the height of the area having the ice-water content maximum values.

References

Baranov V.G., Dovgalyuk Y.A., Stankova E.N.,1984: On the possibility of modeling a convective cloud modification with use of non-stationary model. Proceedings of GGO, Issue 482, 35-42.

Shiino J., 1978: A numerical Study of Precipitation Development in Cumulus Clouds. Papers in the J. Meteor. and Geophysics, **29**. № **4**, 3-37.

THE DERIVATION OF THE GAS DYNAMICS EQUATIONS BY CONSIDERING CHANGES OF THE VELOCITY DISTRIBUTION FUNCTION ON SCALES OF THE MOLECULE FREE PATH

A.V. Kochin

Central Aerological Observatory, Dolgoprudny, Moscow region, 141700, Russia

1. INTRODUCTION

The equations describing gas dynamics are used to study various fundamental and applied problems in many areas of macrophysics. In particular, understanding a number of concrete macroscopic phenomena is based on solutions to Euler or Navier-Stokes equations determining the behavior of the gas velocity field. In contrast with the fundamental Newton dynamics equations, Euler and Navier-Stokes equations are approximate and provide a description of a macroscopic gas system in terms of a reduced number of degrees of freedom. As well known, it is practically impossible to find an exact solution to a system of Newton equations of motion for all interacting gas molecules. Therefore, the equations of gas motion are derived by methods of statistical mechanics, taking into account approximations permitting the description of gas in terms of macroscopic variables such as gas densities or mass velocities.

One of the most widely used approach in statistical mechanics is based on the use of Boltzmann equation of transfer. Euler and Navier-Stokes equations are derived from Boltzmann equation of transfer under certain assumptions (viscosity being taken into account or neglected, respectively). In turn, the formulation of Boltzmann equation is also based on a number of physical hypotheses, which are discussed in detail, for example, in K. Huang (1963).

In particular, one of such hypotheses assumes that for a system, which is close to a locally equilibrium state, the molecules flying into an arbitrary phase volume have the same velocity distribution function as the molecules inside this phase volume. In physical terms, this assumption implies that the molecule velocity distribution function does not change essentially on free-path scales.

This paper aims at deriving the equations of gas motion allowing for the variation of the velocity distribution function on free-path scales. We consider the process of a discrete molecule velocity variation, resulting from intermolecular collisions, as a mechanism responsible for the variation of the distribution function. The conventional definition of the velocity distribution function does not take into account molecule collisions on free-path scales. Therefore, it will be the same for both a dense gas of colliding molecules and a highly rarefied gas without collisions.

Corresponding author's address: A.V. Kochin
Central Aerological Observatory, Dolgoprudny, Moscow region, 141700, Russia; E-Mail: alexkochin@mtu-net.ru

In this paper, we define a velocity distribution function of molecules in a specific form so that only the molecule velocities after intermolecular collisions in a chosen fixed volume contribute to this distribution function. The velocities of the molecules, which pass through the volume without collisions, are not taken into account. The approach developed in this paper, unlike the one based on Boltzmann equation, does not permit the determination of an explicit form of the molecule velocity distribution function. Nevertheless, this method enables deriving the equations of gas motion under the only assumption that the molecule velocity distribution function is spherically symmetric.

2. DEFINITION OF THE PROPER VELOCITY DISTRIBUTION FUNCTION TAKING INTO ACCOUNT THE MOLECULAR COLLISIONS

Usually the velocity distribution function is given by a method which will be referred to as "instant photosnapshot". A virtual camera located inside the volume records all the molecules inside this volume. It is assumed that this camera also measures and records the velocities of all the molecules inside this volume at a given time instant t. Then, one counts the number of molecules with a certain velocity vector (the velocity modulus and the direction) and calculates the velocity histogram of the molecules.

This definition does not take into account the collisions of molecules and will be the same both for gas without collisions, and for gas with collisions. If our purpose is a study of the physical values in a gas for the situations where molecular collisions are essential, we have to find a distribution function containing the effects of molecular collisions in its definition from the very beginning. Therefore, we change the above definition as follows.

Now we use a cinema camera. It fixes on a film a series of consecutive pictures of molecules in the volume during a time interval dt. We separate the molecules, whose images are fixed on the picture area of a film into two groups. The first group contains the molecules, which have taken part in collisions inside the considered volume. Now we assume that the velocities are fixed only after collisions. Velocities of the molecules, which they had before collision, can be quite arbitrary. As a graphic illustration for such a situation we propose that colliding molecules under consideration are painted and become seen to the observer, while the molecules flying without collisions remain colorless and hence are invisible. The observer sees only the painted molecules and therefore only their velocities define the distribution function for him. The second group of molecules which pass through the above volume without collisions, does not contribute to the distribution function.

3. THE DERIVATION OF THE GAS DYNAMICS EQUATIONS

The derivation of the gas dynamics equations by using new velocity distribution function in detail described in paper (Kochin 2003). Only features of this equations here are formulated.

The derivation gives some new terms in comparison with Navier-Stokes equations.

The mass conservation equation can be written in the form

$$\partial\rho/\partial t+\mathrm{div}\,(\rho u)-1/2\,\mathrm{div}(\mathrm{grad}\,\mu)=0$$

where ρ is the density of gas, u is the mass velocity, μ is the gas viscosity.

The momentum conservation equations do not contain the term with volume viscosity but contain dynamical component in the expression for pressure. The mass velocity leads to the change of both values of the momentum and the number of molecules, colliding with the surface. However, this effect works only at distances of the free path. Therefore the value of this dynamic component is given by product of viscosity on the derivative the mass velocity.

The energy conservation equation contains the two terms which describe the process of energy dissipation of the ordering motion into the thermal energy of gas due to the work of forces of viscosity. The energy dissipation can be understood as follows. There are collisions of molecules at each space point. The molecules at a given point have different velocity distributions, in particular, they have different mass velocities. After a collision, the molecules belong to the same velocity distribution. As a result, a part of the energy of the ordering motion will always be used for heating the gas. Hence all processes in the gas resulted from the change of the mass velocity are irreversible processes.

4. Some meteorological aspects – pollution and aerosols transport

It is usually supposed, that under normal conditions air in an atmosphere to be in an equilibrium condition. Hence the mass velocity arise only due to a gradient of pressure. However a vertical gradient of temperature practically always exists in an atmosphere. Thus an atmosphere is constant in nonsteady state. From the point of view of the Navier-Stokes equations there are no new phenomena.

The equations deduced in this work allow to describe new effect. At a derivation of equations we get the expression for flow of mass, a pulse and energy. In particular the equation for a flow of mass looks like

$$J_m=\rho u-1/2\mathrm{grad}\mu$$

where ρ is the density of gas, u is the vector of mass velocity, μ is the gas viscosity

From this equation follows that at presence of a gradient of temperature the mass velocity will be observed. Usually vertical gradient of temperature in an atmosphere is equal 6 degrees /km. That gives the value of the mass velocity about 10^{-10} m/c. At this conditions particles with size less than 10^{-8} m will go in an atmosphere from a surface of the Earth upwards. Thus except for well-known turbulent pollution and aerosols transport the ordered carry of aerosols will be observed due to a vertical gradient of temperature.

5. Conclusion

The new equations of gas dynamics derived here are approximate like Euler and Navier-Stokes equations. We have restricted ourselves to the approximation of small velocities. Nevertheless, we hope that these new equations will be useful for describing nonequilibrium phenomena in various areas of macroscopic physics.

For example, these equations might be applicable for computations of atmospheric processes, like turbulence.

6. Acknowledgements

I am very grateful to prof. I.L. Buchbinder for help in work and useful discussions. Also, I would like to gratitude prof. V.L. Kuznetsov for discussions on various aspects of gas dynamics.

7. References

K. Huang, Statistical Mechanics, John Wiley and Sons, 1963.

A. V. Kochin, New approach to deriving gas dynamics equations, Physics/0305056, 2003.

EVALUATION OF MM5 HIGH-RESOLUTION SUMMERTIME PRECIPITATION FORECASTS OVER THE URBAN AREA OF ATHENS, GREECE

V. Kotroni and K. Lagouvardos

National Observatory of Athens, Institute of Environmental Research, Athens, Greece.

1. Introduction

The assessment of the precipitation forecast skill is a key issue in an operational environment. The verification of precipitation forecasts in this paper focuses on the assessment of MM5 model skill in the prediction of summer thunderstorm activity. The model skill at 2 km horizontal resolution is evaluated over the complex terrain of the Athens Basin. The reasons why we focus on the summer thunderstorm activity during the year 2002 are the availability of a relatively dense raingauge network that was deployed during August and September 2002 in the area, and finally the important thunderstorm activity that occurred during the first two weeks of September 2002. The inability of the model to accurately reproduce summertime convection motivated the performance of some sensitivity tests including the activation/deactivation of the convective parameterisation schemes in both the 8-km and the 2-km simulations in order to assess the model forecast skill at 2-km resolution. The statistical scores have been calculated for three types of simulations: with and without activation of the Kain-Fritch convective parameterisation scheme for the 2-km grid (while convection was activated in the coarse and intermediate grid simulations) and without activation of the Kain-Fritch convective parameterisation scheme for both the intermediate (8-km resolution) and the 2-km grid.

2. Model setup and verification method

In spring 2001, the National Observatory of Athens (NOA hereafter) initiated an activity with the aim to provide accurate very fine resolution weather forecasts over the Athens area, Greece. For that purpose, NOA implemented the MM5 non-hydrostatic primitive equation model (Dudhia, 1993). MM5 is run once per day, following a three- nest strategy with 24-km (Grid 1), 8-km (Grid 2) and 2-km (Grid 3) horizontal grid increment. For the operational setup the combination of the Kain-Fritsch (Kain and Fritsch, 1993) convective parameterisation scheme with the highly efficient and simplified microphysical scheme proposed by Schultz (1995) are used as this combination has been found by Kotroni and Lagouvardos (2001) to give the best precipitation forecast skill over the Greek peninsula.

Corresponding author's address: Vassiliki Kotroni, Institute of Environmental Research, National Observatory of Athens, Lofos Koufou, P. Pendeli, 15236, Athens, Greece; e-mail: kotroni@meteo.noa.gr.

The 0000 UTC Global Forecast System (GFS, NCEP) gridded analysis fields and 6-hour interval forecasts, at 1.25 degree lat/lon horizontal grid increment, are used to initialise the model and to nudge the boundaries of coarse grid during the simulation period. No preforecast spin up period or assimilation of additional observations is used in the operational MM5 model chain.

For the verification of precipitation, the study is focused on the period 2 to 15 September 2002 when almost every day there was some thunderstorm activity in the Athens basin. For that purpose, the four closest grid points to the observational site, weighted by the square of their distance to the station, are considered. The 12-hour accumulated precipitation values are verified (from t+30 up to t+42) for 14 available raingauge stations deployed within the Athens Basin and the following statistical measures are used: bias, threat, quantity bias, and mean absolute error. Bias and threat are calculated for 6 successive thresholds: 0.1, 1, 2.5, 5, 10 and 20 mm. The QB and MAE are calculated for 5 ranges: 0.1-2.5 mm, 2.5-5 mm, 5-10 mm, 10-20 mm and >20 mm. The observations used are provided by 14 automated raingauges, deployed within the Athens area.

3. Discussion of results

Figure 1 gives the bias, threat scores, mean absolute error and quantity bias from the 12-hour forecasts of Grid 3 for the period 2 to 15 September 2002 that included 10 cases of summer thunderstorm activity. The statistical scores have been calculated for three types of simulations:

- Kain-Fritch convective parameterisation scheme activated in Grids 1 and 2 but not in Grid 3 (NCP hereafter);
- convective parameterisation scheme activated in all three grids (CP hereafter);
- convective parameterisation scheme activated only on the coarse grid but not on Grids 2 and 3 (NCP23 hereafter).

Inspection of the bias (Fig. 1a) and threat scores (Fig. 1b) give the overall impression that without activation of the convective parameterisation scheme (NCP) the model fails to reproduce the areal extent of summer thunderstorm activity in the area of Athens. Indeed, the bias score ranges from 0.08 (for the >0.1 mm threshold) to 0 (for the >20 mm threshold) showing that the model dramatically underpredicts the areal coverage of precipitation for all precipitation thresholds. For the bias score the NCP23 is slightly better than the

NCP for the low thresholds (>1mm) and the large thresholds (>20mm) and slightly worse for the medium ones. It should be noted that, for the NCP23 simulations the rainfall fields of Grid 2 (8-km) are unrealistic with the occurrence of "bulls eyes" in the domain of simulation (not shown). On the other hand activation of the convective parameterisation scheme for the Grid 3 simulations (CP experiment) results in much better scores especially for the light and medium precipitation amounts. Namely, the bias for the precipitation thresholds up to >10.0 mm is higher than 0.71 while it drops to 0.5 for the >20.0 mm threshold.

Similar conclusions are drawn from the inspection of the threat scores (Fig. 1b). Both the NCP and NCP23 simulations show almost no skill with threat scores ranging from 0.2 for the >0.1 mm threshold, decaying to 0 (NCP) and 0.1 (NCP23) for the thresholds >10.0 mm. The CP simulations, on the other hand show a fairly good skill for the light rain thresholds with scores of 0.61 and 0.58 for the >0.1 and >1mm threshold. The skill is decaying with increasing threshold values reaching no skill (a score of 0) for the high precipitation threshold (>20.0 mm).

Investigation of the bias of forecast amounts of precipitation is performed through inspection of the mean absolute error (MAE) and the quantity bias (QB), (Figs. 1c-d). The NCP simulations underpredict the amounts of rain for all ranges (negative QB) with the greatest errors being calculated for the large amounts of rainfall (for >20 mm the QB is –44.7 mm) showing that the model at 2-km resolution cannot explicitly predict the local maximum of rainfall during a thunderstorm. The results of the NCP23 experiments are quite close to the results of the NCP simulations. The CP simulations on the other hand show a more realistic and common to limited area models behaviour, overpredicting the light and medium rain amounts (QB ranging from 2.7 to 5.2 mm for the rain amounts less than 10 mm) and underpredicting the large precipitation amounts (with QBs of –9 and –41 for the 10-20 mm and the >20 mm ranges, respectively).

The difficulty of the models to accurately predict summer rainfall activity, and mainly thunderstorms, is documented by Fritsch and Heideman (1989), Stensrud et al. (2000), among others. This is attributed to the fact that a number of physical processes occur on scales too small to be adequately resolved by even the higher-resolution operational models used today. Moreover, during summer, the large scale forcing is weak and the distribution of moisture and mesoscale forcing become very important for the both the spatial and temporal initiation of convection (Stensrud and Fritsch, 1994). Although the increase of the computer resources availability nowadays and in the near future even more allow the use of fine grids, in the operational limited-area weather prediction systems, at resolutions that can explicit resolve convection, there is still a pending question on how and if the increase in horizontal resolution can produce more skilful forecasts mainly precipitation forecasts (Mass et al., 2002; Ducrocq et al., 2002; Lagouvardos et al. 2003). These authors pointed out that the subjective impression of the forecaster is that the fine grid precipitation fields are much closer to the real precipitation fields. Nevertheless, it seems that even when using very fine resolution the models are unable in many cases to reproduce the observed high precipitation amounts and this has been also shown in the present. Indeed, on 3 September 2002 although five stations reported more than 45 mm of rain the CP simulation which gave the best results did not reproduce more than 10 mm in any station in the verified domain.

On the other hand it seems that the use of convective parameterisation on the coarse (Grid1) and intermediate grid (Grid 2) affects the explicit precipitation reproduced by the finer grid (Grid 3). Indeed, Warner and Hsu (2000) have illustrated that the midlevel heating and drying associated with the convective parameterisation scheme used in their coarse (30-km) and the intermediate (10-km) grid produced significant reduction of explicit precipitation of their finer (3.3-km) grid. Colle at al. (2003) also showed that for summertime precipitation, the use of the Kain-Fritch scheme at their 36-km and 12-km grids suppresses the explicit precipitation in their 4-km grid, especially for weak to moderate events. In the present work it has been shown that the model grid at 2-km resolution is unable to reproduce summer thunderstorm activity while the simulations are much more skilful when the convective parameterisation is activated even in Grid 3 (at 2-km resolution). The aforementioned analysis showed that for summertime precipitation the activation of the convective parameterisation even at 2-km resolution, although "uncommon" seems to be necessary in order to reproduce the thunderstorm activity.

4. Concluding remarks

The analysis of a 15-day period of almost everyday summer thunderstorm activity in Athens showed that the 2-km simulations without activation of the convective parameterisation scheme were unable to reproduce the observed thunderstorm activity. Sensitivity tests for the same period with simulations where the convective parameterisation was not activated for both the 8-km and the 2-km simulations were still inaccurate.

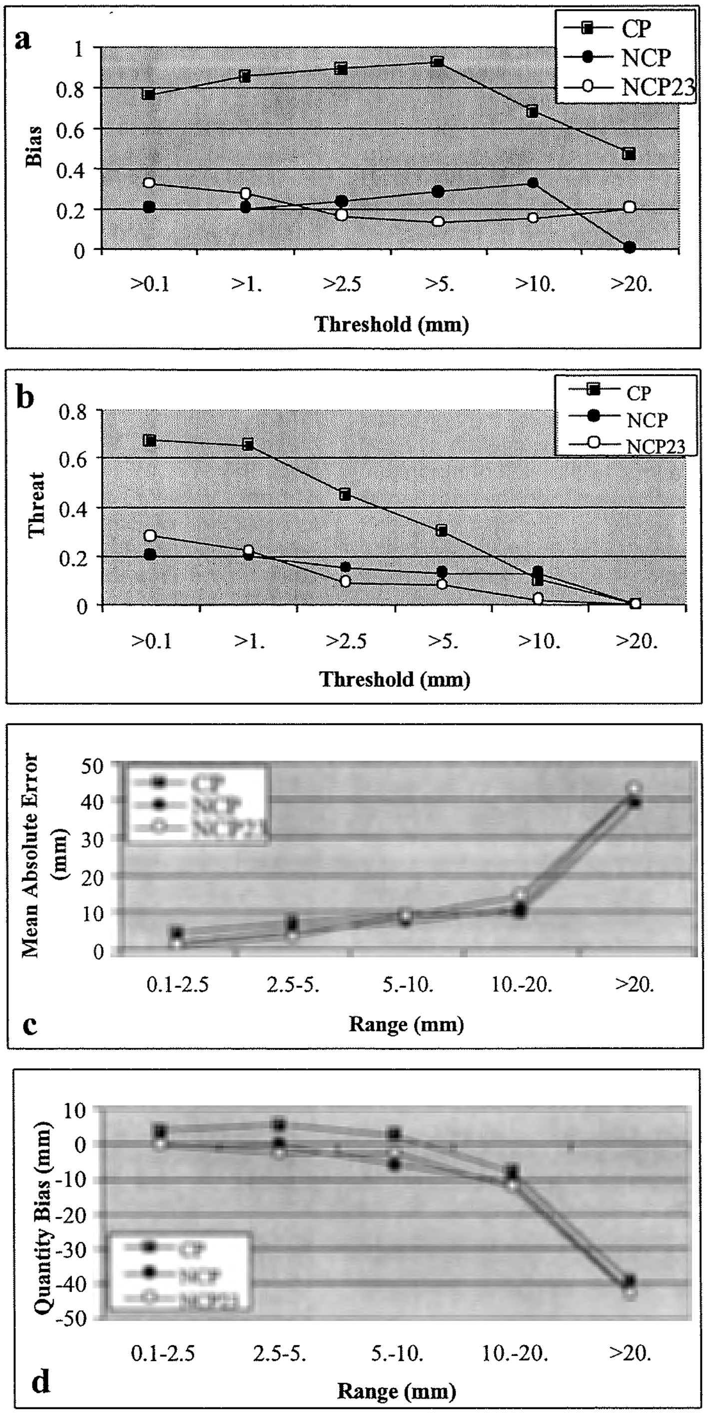

Figure 1: (a) Bias, (b) Threat, (c) Mean Absolute Error (d) Quantity bias, for the 12-h precipitation forecasts of the 2-km grid for the period 2-12 September 2002. CP/NCP denote the simulations where the convective parameterisation scheme was activated/deactivated for the 2-km grid. NCP23 denotes the simulations where the convective parameterisation scheme was only activated for Grid 1.

On the other hand, simulations were the convective parameterisation scheme was activated on all grids (even at the 2-km resolution) increased considerably the precipitation forecast skill at 2-km. Even with this experiment the mean absolute errors and the quantity bias is still very high especially for the observed high precipitation amounts. These last findings raise some further questions. How can one use a convective parameterisation scheme at such fine resolution where convection should be explicitly resolved? How could one use a convective parameterisation scheme that was initially designed and tested for coarser resolutions at such fine resolutions? Is it possible to obtain accurate precipitation forecasts of summer thunderstorm activity only by increasing the horizontal resolution? Which is the role of assimilation of local observations? Is there a limit to the skill of models in predicting summer thunderstorm activity and hence nowcasting techniques would be the best solution? Further investigation in needed on these issues as the increasing computational facilities make more and more possible the operational use of very fine grid resolutions and there is a continuously growing socio-economic demand for more accurate forecasts of thunderstorm activity.

Acknowledgements
This work was supported by the General Secretariat for Research and Technology (Excellence in Research Centers – MIS64563). The Hellenic National Meteorological Service is kindly acknowledged for providing part of the observed precipitation data used in this study. The National Technical University of Athens is also acknowledged for providing raingauge data from their station at Zografou. The authors are also grateful to NCEP (USA) for providing GFS initial and forecast field data that allowed the operational use of MM5 model at NOA.

REFERENCES

Colle, B.A., J.B. Olson and J.S. Tongue, 2003: Multiseason verification of the MM5, Part II: Evaluation of high resolution precipitation forecasts over the northeastern United States. *Wea. Forecasting*, 18, 458-480.

Dudhia, J., 1993: A non-hydrostatic version of the Penn State/NCAR nesoscale model: validation tests and simulation of an Atlantic cyclone and cold front. *Mon.Wea. Rev.,* **121**, 1493-1513.

Ducrocq, V., D. Ricard, J-P. Lafore, F. Orain, 2002: Storm-Scale Numerical Rainfall Prediction for Five Precipitating Events over France: On the Importance of the Initial Humidity Field. *Wea. Forecasting*, **17**, 1236–1256.

Fritsch, J.M., and K.F. Heideman, 1989: Some characteristics of the Limited Area Fine Mesh (LFM) model quantitative precipitation forecasts (QPF) during the 1982 and 1983 warm seasons. *Wea. Forecasting*, 4, 173-185.

Kain, J.S., and J.M. Fritsch, 1993: Convective parameterization for mesoscale models: The Kain-Fritsch scheme. *The Representation of Cumulus in numerical models, Meteor. Monogr.*, No **46**, Amer. Met., Soc., 165-177.

Kotroni, V and K. Lagouvardos, 2001: Precipitation forecast skill of different convective parameterization and microphysical schemes: application for the cold season over Greece. *Geoph. Res. Let.,* Vol. **108**, No 10, 1977-1980.

Lagouvardos K., V. Kotroni, A. Koussis, C. Feidas, ?. Buzzi, P. Malguzzi, 2003: The meteorological model BOLAM at the National Observatory of Athens: assessment of two-year operational use. *J. Appl. Meteor.*, 42,1667-1678.

Mass, C. F., D. Ovens, K. Westrick and B. A. Colle, 2002: Does increasing horizontal resolution produce more skillful forecasts? *Bull. Amer. Meteor. Soc.*, **83**, 407-430.

Schultz, P., 1995: An explicit cloud physics parameterization for operational numerical weather prediction. *Mon. Wea. Rev.*, **123**, 3331-3343.

Stensrud, D. J., J.-W. Bao, and T. T. Warner, 2000: Using initial condition and model physics perturbations in short-range ensemble simulations of mesoscale convective systems. *Mon. Wea. Rev.,* **128**, 2077–2107.

Stensrud, D. J., and J. M. Fritsch, 1994: Mesoscale convective systems in weakly forced large-scale environments. Part III: Numerical simulations and implications for operational forecasting. *Mon. Wea. Rev.,* **122**, 2084–2104.

Warner, T. and H-M Hsu, 2000: Nested model simulation of moist convection: The impact of coarse-grid parameterised convection on fine-grid resolved convection. *Mon. Wea. Rev.*, 128, 2211-2231.

CLOUD WATER AND RAINWATER NUMERICAL SIMULATION WITH LASG-REM MODEL

Shuyan Li[1] and Wenan Xiao[2] and Hengchi Lei[3]

[1]Beijing Weather Modification Office, Beijing, 100089, China
[2]Nanjing Meteorological Institute , Nanjing, 210044,China
[3]Institute of Atmospheric Physics, Chinese Academy of Sciences, Beijing, 100029,China

1. Introduction

Initial model can't describe microphysics process of precipitation. We added explicit predication equations of water vapor, cloud water and rainwater for mesh resolvable systems and parameterization scheme for subgrid cumulus convective systems so that the model can describe the distribution of cloud water and rainwater. In the model the basic thoughts of convective adjustment scheme can be described as following:

There exists special temperature and humidity structure in convective area. When convective activity occurs, convective adjustment makes atmospheric temperature and humidity structure adapt to the special structure. The actual process of adjusting velocity and characteristic structure can be obtained through experiments.

Warm cloud physical process parameterization scheme includes four major processes:

(1) Vapor coagulates into cloud droplet.
(2) Cloud water transforms into rain water automatically.
(3) Rain droplet collects cloud water through collision and combination based on gravity activity.
(4) Rain droplet evaporates in non-saturated area outside cloud.

2. Numerical experiment

The model initial field is to interpolate the data of Europe-Asia upper-air detection message and surface message of 00UTC of July 21st, 1998 in model grid through objective analysis.

Map of actual precipitation from 00UTC of July 21st to 00UTC of July 22nd is showed in figure 1.

From the figure 1 we can see that Wuhan region(115-117°E,27-31°N) which is concerned in the article is a torrential rain center which maximal precipitation reached 150mm. There are another two torrential rain center near three-gorges(109-112°E,27-31°N) which maximal precipitation reached 200mm. Figure 2 is the simulation result of precipitation using improved numerical model. From figure 2 we can see that the forecasting value of Wuhan strong precipitation center reached 200mm but the precipitation center moved almost 1 latitude eastward. On the other hand, the forecasting value of strong precipitation at three-gorge is obvious low that only 25mm precipitation was forecasted there. Compared with actual precipitation, former unimproved scheme forecasted only 25mm precipitation in wuhan district, but it forecasted 100mm strong precipitation center in three-gorge region. Maybe the difference was caused by cloud water and rain water transportation in explicit cloud and rain process.

One of the characters of improved model is to be able to simulate spatial distribution of cloud water and rain water. Figure 3 shows spatial distribution of cloud water at 700hPa using improved numerical model. Looking at the ultrared cloud image on 00UTC of July 22nd(figure 4), We can see that there was a meso-scale cloud cluster near launching out region of Yangtse river, a meso-scale cloud cluster near Wuhan region in Hubei province and a meso-scale cloud cluster at conjunctive region of Sichuan province and Guizhou province. The three meso-scale cloud cluster were simulated very well through cloud water distribution at 700hPa(Fig.3)

Shuyan Li: No.44, zizhuyuan road, haidian district Beijing weather modification office., Beijing, 100089, china.e-mail: lw1024@263.net

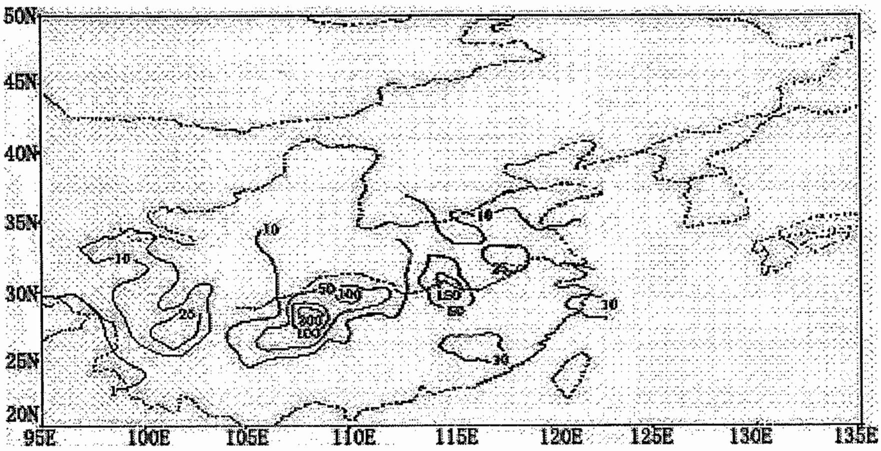

Fig.1 Actual precipitation(24h) at 00(UTC) from21 to 22 July, 1998 (unit: mm)

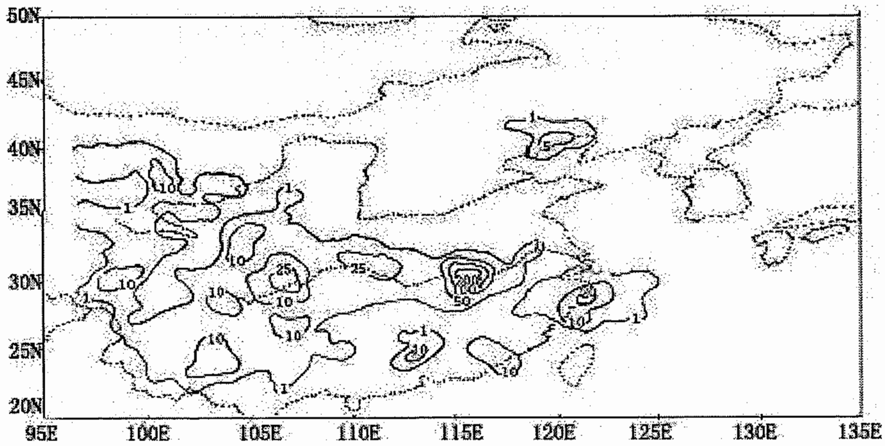

Fig.2 Forecast precipitation(24h) using Improved model at 00(UTC) from 21 to 22 July,1998 (unit: mm)

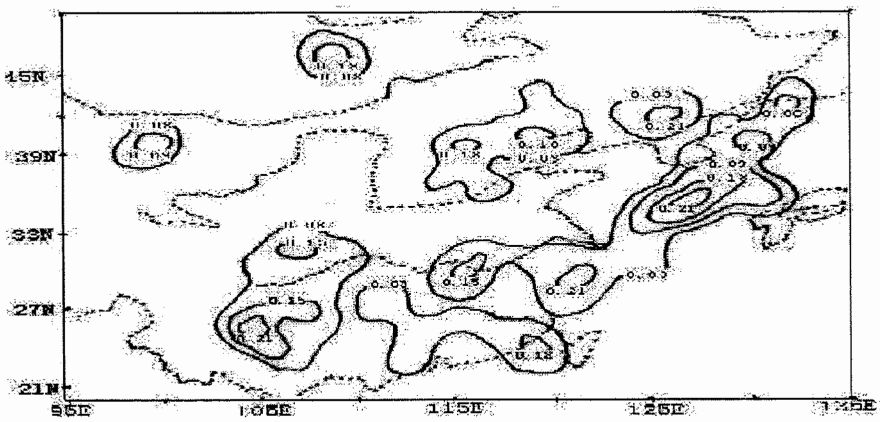

Fig.3 Using improved model to forecast the distribution of cloud water in upper air at 00 （UTC） on July 22, 1998(unit: g/kg)

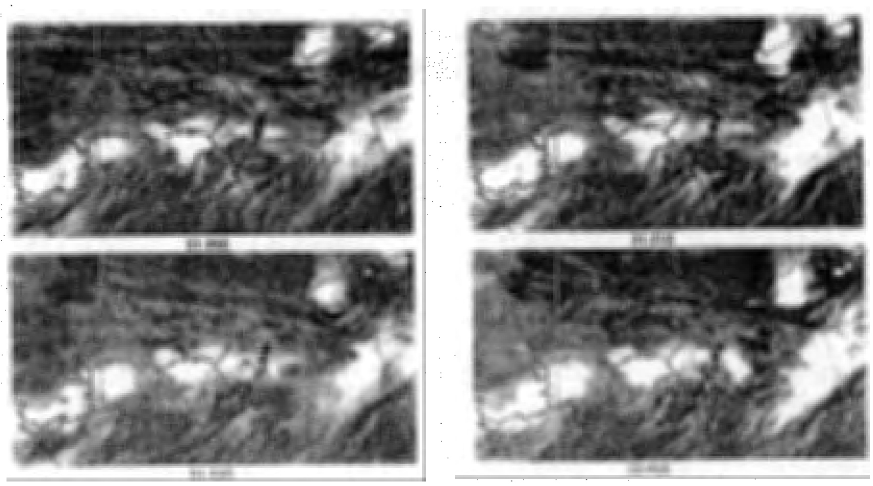

Fig.4 Infrared nephogram from 20 :00 on July 21 to 22:00 (UTC) on July 22, 1998

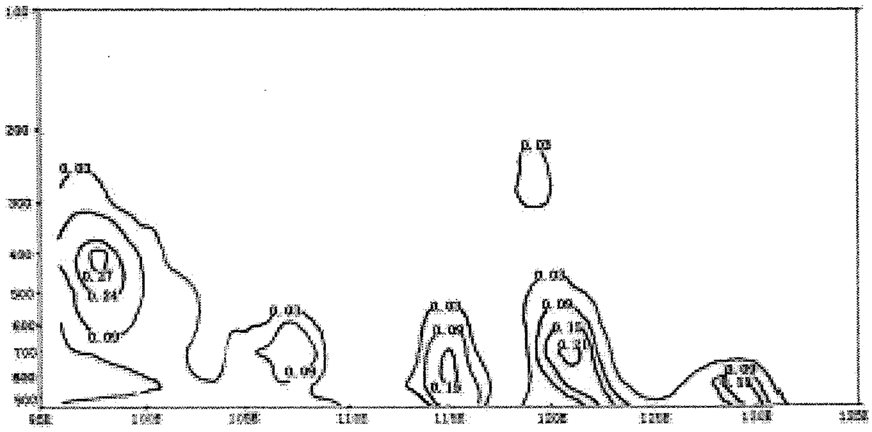

Fig.5 Cross section of cloud water using improved model at 00(UTC) on July 22, 1998(unit: g/kg).

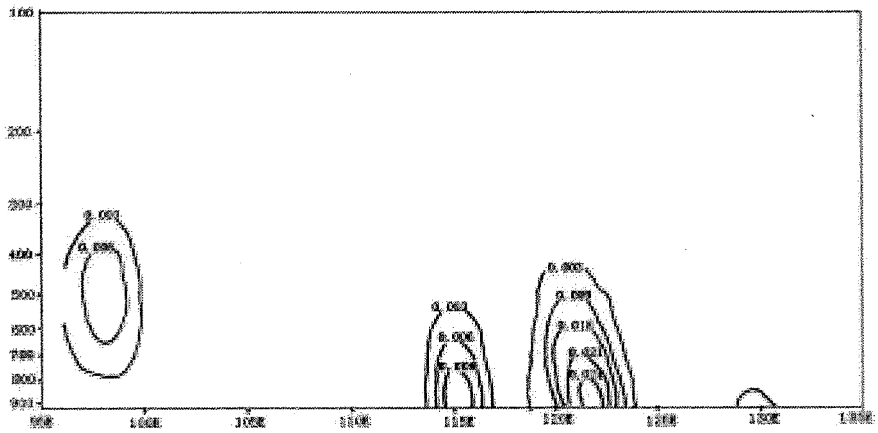

Fig.6 Cross section of rainwater using improved model at 00(UTC) on July 22, 1998(unit: g/kg)

From figure 5 we can see that the top of Wuhan cloud cluster(115-117°E) is quite low, the value is very high, the cloud top at 120°E where is nearby launching out region of Yangtse river just reaches 400hPa, cloud water content center locates at 700hPa and maximal value is 0.21g/kg. The cloud top at 115°E just reaches 400hPa, cloud water content center locates between 700hPa and 800hPa and maximal value is 0.15g/kg. Simulation result about the height of clod top can also be approved by radar observation.

But the content of rain water is lower than that of cloud water. Near Wuhan region（115°E）, maximal cloud water content value is 0.15g/kg, but rain water content value is only 0.009g/kg.

For more detail information about precipitation of Yangtse valley, the cross section of cloud water (figure 5) and rain water (figure 6) was provided along 29°N. the vertical structure of several cloud clusters can be seen from cross section of cloud water and rain water along east-to-west direction.From cross section of specific humidity of cloud water（q_c）(Figure 5) and specific humidity of rain water （q_r）(Figure 6) we can get the conclusion that the improved numerical model can be used to simulate specific humidity of cloud water distribution and specific humidity of rain water distribution at Wuhan region and launching out region of Yangtse river

Conclusion

1) Based on unimproved LASG-REM numerical mode, We added explicit calculating scheme of cloud water and rain water successfully. The dynamic process of cloud water and rain water process can harmonized well with primary dynamic frame. The rational cloud water and rain water physical parameterization scheme and small computing amount ensure the time spending on simulation not to be obviously increased.
2) The numerical model can simulate torrential rain and cloud cluster in Wuhan region and describe the specific humidity of cloud water and specific humidity of rain water spatial distribution. The convective parameterization scheme of LASG-REM numerical model is simple, so we need to further improve the convective parameterization process according to weather characteristic of different regions.

reference

[1] Betts,A.K.. A new convective adjustment scheme. Part 1: Observational and theoretical basis[J]. Quart.J.R.Met.Soc.,1986,VOL.112,P677-691.
[2] Marshall J S, Palmer W M. The distribution of rain drops with size.J.Meteor.,1948,5(2),P165-166.
[3] Kessler,E.,1969:On the distribution and continuity of water substance in atmospheric circulation, Meteor. Monogr.,No.32,Amer.Meteor.Soc., P84

MULTI-DIMENSIONAL LONGWAVE RADIATIVE FORCING OF PBL CLOUD SYSTEMS

D. B. Mechem[1], M. Ovtchinnikov[2], Y. L. Kogan[1], K. F. Evans[3], A. B. Davis[4], R. F. Cahalan[5], E. E. Takara[6], and R. E. Ellingson[6]

[1]University of Oklahoma, Norman, OK, USA
[2]Pacific Northwest National Laboratory, Richland, WA, USA
[3]University of Colorado, Boulder, CO, USA
[4]Los Alamos National Laboratory, Los Alamos, NM, USA
[5]NASA/GSFC, Greenbelt, MD, USA
[6]Florida State University, Tallahassee, FL, USA

1. INTRODUCTION

Numerical cloud models nearly universally employ one-dimensional (1D) treatments of radiative transfer (RT). Radiative transfer is typically implemented as a 2- or 4-stream approximation to the explicit radiative transfer equation. One dimensional RT is computationally attractive relative to Monte Carlo methods or solving the full radiative transfer equation explicitly. However, 1DRT neglects horizontal photon transport, which may be important for situations of complex cloud geometry and internal cloud structure. The I3RC (Intercomparison of 3D Radiation Codes) project has demonstrated that 1DRT sometimes introduces systematic bias that can lead to significant errors in domain-average shortwave heating rates.

Recent studies (e.g. Zuidema and Evans 1998, Di Giuseppe and Tompkins, 2003) have explored the multi-dimensional (MD) effect on albedo for boundary layer stratocumulus cloud fields. These studies typically calculate MD and independent pixel approximation (IPA, effectively 1D) radiative transfer and obtain estimates of the plane-parallel albedo bias (Cahalan et al. 1994), which is an important parameter in computing the shortwave radiation budget for the global energy balance. The MD-IPA bias is generally related to the degree of heterogeneity in the cloud field, with broken cloud systems exhibiting greater bias than solid cloud fields.

These previous studies are mainly concerned with how the cloud spatial structure modulates the radiative characteristics of a cloud system and do not address the direct influence of MD effects on the cloud dynamics. For example, how does using a full MD radiative forcing relative to 1D forcing affect cloud system evolution as measured by such quantities as buoyancy flux or entrainment? Guan et al. (1995) demonstrate that longwave MDRT can produce different stratocumulus cloud top cooling rates depending on whether the cloud top is flat or undulating. Their results suggest an interactive feedback between MDRT and cloud dynamics, though their experimental framework is not able to address the ultimate effect of such a feedback. Guan et al. (1997) show that longwave cooling on the sides of a small, slab-symmetric cumulus strengthens the cumulus downdraft and promotes new development near cloud base. Guan et al. include MDRT effects in their simulation but do not isolate the forcing arising from horizontal photon flow from the total radiative forcing.

Applying incorrect radiative forcing, either in magnitude or in distribution, has the potential to bias cloud system evolution. Boundary layer stratocumulus are the most obvious example of a cloud system predominantly driven by radiative processes, namely longwave cooling at cloud top. At first glance, 1DRT seems reasonable for clouds like stratocumulus that are to a great extent horizontally uniform. However, undulations in cloud top can result in radiative forcing different from the horizontally uniform value that 1DRT produces. Furthermore, the MD effect on the forcing becomes more pronounced as the cloud fraction decreases.

We apply the multi-dimensional radiative transfer scheme of Evans (1998; Spherical Harmonics Discrete Ordinate Method — SHDOM) to cloud fields produced by large eddy simulation (LES) in order to produce longwave MD and 1D fluxes and heating rates. The heating rate difference field ($HR_{MD} - HR_{IPA}$) is analyzed in the context of LES dynamic fields in order

Corresponding author address: David B. Mechem, CIMMS/University of Oklahoma, 100 East Boyd, Room 1110, Norman, OK, 73019-1011

to infer feedbacks onto the cloud-topped boundary layer dynamics and cloud field structure relative to the 1D forcing. Next, we couple SHDOM to a large eddy simulation model to address the interactive and evolutionary behavior of the MD-1D bias and to quantify its importance. Fully interactive MD radiative transport enables us to evaluate the effect horizontal photon transport has on cloud system dynamics and evolution.

2. METHODOLOGY

The Cooperative Institute for Mesoscale Meteorological Studies (CIMMS) LES (Kogan et al. 1995, Khairoutdinov and Kogan 1999) supplies the cloud field liquid water content (LWC) data for the radiative transfer calculation. Cloud optical properties first are calculated, and then SHDOM uses a correlated k-distribution to compute longwave RT in 12 bands from 4 μm to 100 μm. SHDOM accounts for emission, absorption, and scattering of longwave radiation. Initial conditions for the LES are derived from the ASTEX A209 case simulated by Khairoutdinov and Kogan (1999). The initial CCN concentration exerts a strong influence on the ultimate cloud fraction. The unbroken cloud field in Section 3 corresponds to a heavy aerosol load, while the interactive case simulates a relatively low aerosol concentration in order to induce cloud breakup and enhance the MD effects. The LES is configured in a two dimensional geometry (1000×126 points) with 10 m grid spacing both in the horizontal and vertical.

For the interactive simulations, SHDOM periodically calculates the radiative forcing, which the LES then applies. Two interactive simulations are compared: one with the heating rates calculated using full MDRT, and one that subtracts the horizontal flux convergence, the cooling rates associated with horizontal photon transport. The IPA (1D) heating rate is thus related to the MD heating rate by

$$HR_{IPA} = HR_{MD} - \left(-\frac{1}{\rho c_p}\frac{\partial F_x}{\partial x}\right).$$

3. IMPLIED MDRT FEEDBACK

Figure 1 shows that for an unbroken cloud the differences between MD and IPA heating rates are most prominent near cloud top undulations. Regions of high cloud tops are generally associated anomalous cooling ($HR_{MD} - HR_{IPA} < 0$), while low cloud tops are associated with anomalous warming ($HR_{MD} - HR_{IPA} > 0$). The shape of the undulating cloud top is largely dictated by the eddy structure, with billows (high cloud tops) associated with updrafts and valleys (low cloud tops) with downdrafts. Probability distribution functions (PDFs) corresponding to the regions of anomalous heating and cooling rates are shown in Figure 2. The PDFs illustrate that the occurrence of positive and negative regions of $HR_{MD} - HR_{IPA}$ are very nearly equal. It is thus not surprising that the vertical profile of mean $HR_{MD} - HR_{IPA}$ is very nearly zero (not shown).

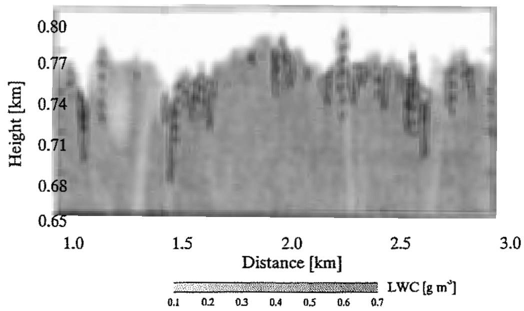

Figure 1. Vertical cross section of LWC [g m^{-3}] over the upper portion of the cloud for a subset of the calculation domain. Contours of $HR_{MD} - HR_{IPA}$ (1.0 K h^{-1} interval) are superimposed.

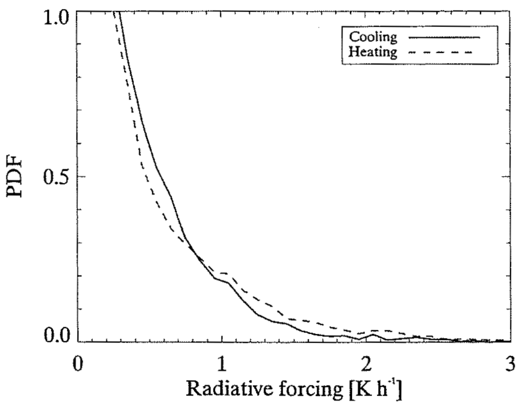

Figure 2. Probability distribution functions (PDFs) of positive and negative regions of $HR_{MD} - HR_{IPA}$. In order that the PDF correspond directly to energetic units, the PDFs are expressed as a function of flux convergences normalized to a heating rate by a constant density.

Since the mean radiative forcing is quite small because of the cancelling effect of positive and negative anomalies, we might be tempted to conclude that any MD effect would be insignificant. However, the regions of anomalous cooling are generally associated with cloud top billows that are typically associated with updrafts. Similarly, anomalous warming is present in cloud top valleys, which are normally in downdraft regions. For this reason, the covariance,

$$\overline{w'\left(\left.\frac{dT}{dt}\right|_{MD}-\left.\frac{dT}{dt}\right|_{IPA}\right)},$$

tends to be mostly negative in the upper region of the cloud, as seen in Figure 3 and confirmed by the mean profile in Figure 4. Figure 3 also contains regions of positive covariance that arise because of multiple scales of variation in the cloud top structure. The cloud top variability scale that most closely matches the boundary layer eddy structures tends to be reliably associated with negative values of covariance. Although the covariance does not correspond rigorously to any term in the governing equations, notions of thermal buoyancy dictate that this negative correlation might tend to damp the PBL energetics.

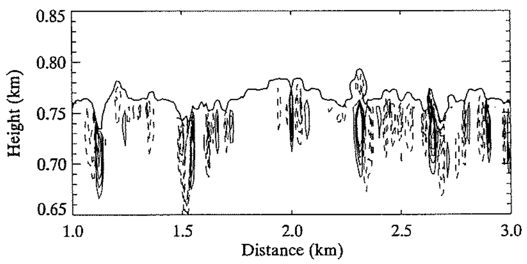

Figure 3. Vertical cross section of mean covariance of vertical velocity and $HR_{MD}-HR_{IPA}$. The contour interval is 3×10^{-5} m K s^{-2}.

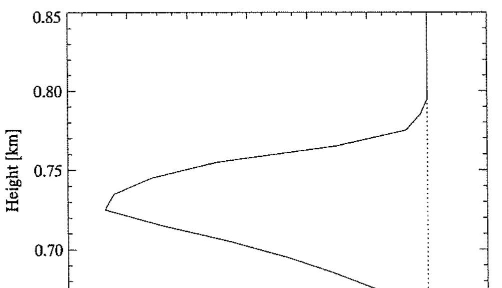

Figure 4. Vertical profiles of mean covariance of vertical velocity and $HR_{MD}-HR_{IPA}$.

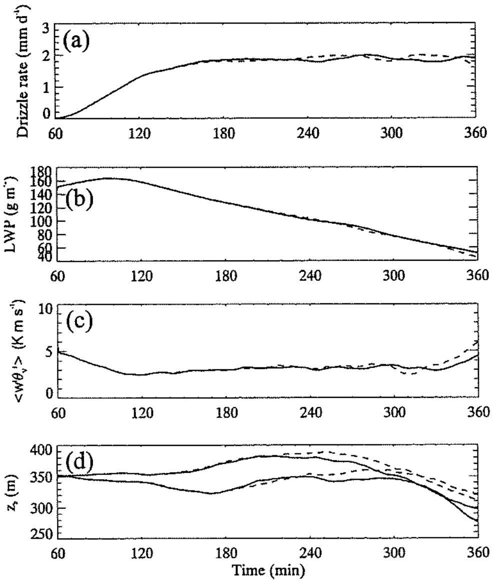

Figure 5. Time series of mean LES quantities from 1-6 h comparing MDRT (solid) and IPA (dashed) simulations. (a) Surface drizzle rate [mm d^{-1}]. (b) LWP [g m^{-2}]. (c) Buoyancy flux [K m s^{-1}]. (d) Updraft and downdraft cloud base heights [m].

4. INTERACTIVE MDRT FORCING

In the fully interactive simulations, the longwave MD effect is realized via the manner in which the MD heating rates modify the thermal buoyancy field relative to the 1D RT solution. This mechanism is the direct radiative-dynamic feedback of interest. The LES is run for an hour using its own two-stream RT scheme to establish a reasonable boundary layer structure. Then, two simulations are conducted using the MD and IPA heating rates from SHDOM, as described in Section 2. Because of computational expense, the RT calculation is performed every 10 timesteps. Relative to calculating RT every timestep, we estimate that calculating every 10 timesteps introduces an RMS error of ~3% in heating rates.

Figure 5 shows the evolution of mean boundary layer statistics for the broken cloud (low CCN concentration) case. Differences between MD and IPA experiments develop but do not appear to exhibit any systematic bias in this relatively short simulation (5 h). Furthermore, as the cloud field breaks apart, the limited number of drizzle cells (realizations) in the domain introduces significant noise in the evolution statistics.

The vertical profile of cloud fraction at hourly intervals in Figure 6 also shows little change between MD and IPA simulations. The slight reduction of cloud fraction in the IPA simulation at 6 h seems opposite to the sense the MD cooling rates would imply, since the cloud top lateral cooling should enhance the negative buoyancy there and enhance cloud breakup. In any case, the difference between MD and IPA cloud fractions are of the same magnitude as the cloud fraction from different LES realizations.

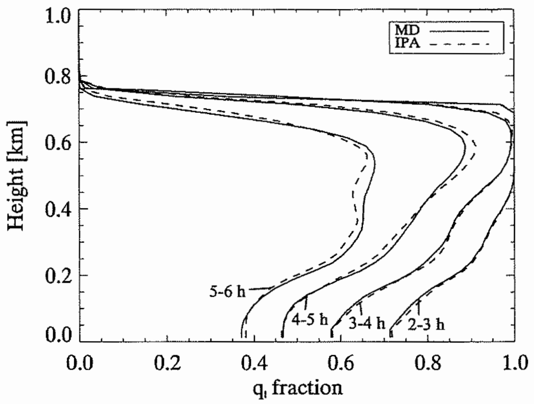

Figure 6. Hourly mean cloud fraction profiles for MDRT and IPA simulations.

5. DISCUSSION AND CONCLUSION

Although not shown, drastic differences in the evolution of specific cloud and eddy structures between the MD and IPA simulations are visible. This is to be expected, since small perturbations in a turbulent flow can have a dramatic impact on the final solution. However, despite a strong correlation between MD-IPA heating rate anomalies and eddies that implies a negative feedback on the boundary layer energetics, statistics for the interactive simulations show little difference between the MD and IPA simulations. This result indicates that the typical 1D, plane-parallel methods of radiative transfer nearly universally applied in numerical models may be sufficiently accurate for longwave forcing of cloud topped boundary layer dynamics.

The reasons for the small differences between the MD and IPA simulation statistics are unclear, but several possibilities may be the cause. First, the horizontal flux convergence may be only a minor contribution to the total energetics; or in other words, the overall forcing from vertical flux divergence is greater than the forcing from the cloud lateral cooling. Second, clouds that are spaced widely apart tend to exhibit a prominent MD effect but also tend to be associated with boundary layer decoupling and perhaps energetics that are more surface based in nature. Finally, weak warming between clouds has been neglected in our inferences, though the interactive MD simulation does take it into account.

ACKNOWLEDGEMENTS

This research was supported by the Environmental Sciences Division of the U.S. Department of Energy (through Battelle PNR Contract 144880-A-Q1 to the Cooperative Institute for Mesoscale Meteorological Studies) as part of the Atmospheric Radiation Measurement Program, and by ONR N00014-96-1-0687 and N00014-03-1-0304.

REFERENCES

Cahalan, R. F., W. Ridgeway, W. J. Wiscombe, and T. L. Bell, 1994: The albedo of fractal stratocumulus clouds. *J. Atmos. Sci.*, **51**, 2434-2455.

Di Giuseppe, F., and A. M. Tompkins, 2003: Effect of spatial organization on solar radiative transfer in three-dimensional idealized stratocumulus cloud fields. *J. Atmos. Sci.*, **60**, 1774-1794.

Guan, H., R. Davies, and M. K. Yau, 1995: Longwave radiative cooling rates in axially symmetric clouds. *J. Geophys. Res.*, **100**, 3213-3220.

Guan, H., M. K. Yau, and R. Davies, 1997: The effects of longwave radiation in a small cumulus cloud. *J. Atmos. Sci.*, **54**, 2201-2214.

Khairoutdinov, M. P., and Y. L. Kogan, 1999: A large eddy simulation model with explicit microphysics: Validation against aircraft observations of a stratocumulus-topped boundary layer. *J. Atmos. Sci.*, **56**, 2115-2131.

Kogan, Y. L., M. P. Khairoutdinov, D. K. Lilly, Z. N. Kogan, and Q. Liu, 1995: Modeling of stratocumulus cloud layers in a large eddy simulation model with explicit microphysics. *J. Atmos. Sci.*, **52**, 2923-2940.

Zuidema, P., and K. F. Evans, 1998: On the validity of the independent pixel approximation for boundary layer clouds observed during ASTEX. *J. Geophys. Res.*, **103**, 6-59-6074.

PARAMETERISATION OF NON-INDUCTIVE CHARGING IN THUNDERSTORM REGIONS FREE OF CLOUD DROPLETS

R. Mitzeva[1], C.Saunders[2] and B.Tsenova[1]

[1]Sofia University, Faculty of Physics, Sofia-1164, Bulgaria
[2]UMIST, Manchester M60 1QD, United Kingdom

1. INTRODUCTION

In numerical models concerning simulations of thunderstorm electrification the assumption is that there is no charge transfer at *LWC*=0, based on the limited numbers of laboratory experiments showing that the charge transfer separated at *LWC*=0 is two orders of magnitude smaller than in the presence of cloud water. However, taking into account that about 30% of the upper part of the updraughts in some severe thunderstorms are free of cloud droplets, it is worth testing if this small charge influences the distribution of charge in thunderstorms. Moreover, recent laboratory experiments showed that the charge separated in non-inductive interactions of graupel and ice crystals at *LWC*=0 is larger than the charge registered in previous experiments, depending on the cloud supersaturation.

The aim of the present study is to test if the small charges separated in the absence of cloud droplets influence the distribution of charge density in the upper part of the thunderstorms. Parameterisations concerning charge transfer during non-inductive interactions between ice crystals and graupel in cloud regions free of cloud droplets are developed and incorporated into our numerical model of a thunderstorm. The charge distribution in two simulated thunderstorms with the new parameterisations are compared and contrasted with the case for zero charge transfer at *LWC*=0.

2. MODEL DESCRIPTION

According to the model, convective clouds are composed of active and non-active cloud masses (Andreev et al.,1979). The active mass is modelled by successive ascending spherical thermals, while the non-active cloud region is formed by thermals that have previously risen and stopped at their convective levels. One can speculate that the ascending thermals represent the updraught region of convective clouds, while non-active masses represent the environment of the updraughts. The model uses bulk microphysical parameterisations with five classes of water substance - water vapour, cloud water, rain, cloud ice, and graupel. Precipitation fallout is calculated in the same manner as in Cotton (1972), and comprises that portion of raindrops and graupel, that have terminal velocities greater than the updraught speed. The magnitude of the charge per crystal separation event depends on the crystal size and the impact velocity, according to the formulation of Brooks et al. (1997).

For the purposes of modelling cloud electrification in the regions free of cloud droplets (*LWC*=0) three different types of parameterisation of charge q acquired by graupel per ice crystal separation event are used:

1. q = 0 when *LWC*=0;
2. q=+0.1 fC when the cloud is supersaturated with respect to ice, and q=-0.1 fC when the cloud is subsaturated with respect to ice. This parameterisation is based on the hypothesis that in the absence of cloud droplets if there is sublimation/deposition of vapour to the graupel surface the graupel charges negatively/ positively respectively. We will notify this variant of the parameterisation as S/D. This situation accords with laboratory studies such as those of Jayaratne et al. (1983) in which an ice target is artificially heated or cooled during ice crystal collisions in the absence of riming.
3. q=-0.1 fC (acquired by graupel) in supersaturated cloud when the crystal surface is growing faster by vapour deposition than the graupel. Also, q=+0.1 fC when the crystals are sublimating faster than the graupel. This parameterisation is based on the Relative

[1]Corresponding author's address: R. Mitzeva,
Sofia University, Faculty of Physics, Sofia-1164, Bulgaria,
E-Mail: rumypm@phys.uni-sofia.bg

Growth Rate hypothesis of Baker et al. (1987). Since ice crystals are smaller than graupel, the crystals will grow, or sublimate, faster than the graupel according to standard theory. In this manner the sign determined by this variant of the parameterisation (we will call it RGR) will be opposite to the sign determined according to the S/D hypothesis.

Ice crystals and graupel in the ascending thermals, together with falling graupel, are the charge carriers in the model cloud. It is assumed that graupel capture of ice crystals and growth by autoconversion conserves the (average) charge on the crystals (from earlier interactions) when it becomes the initial graupel charge and is added to the total graupel charge density.

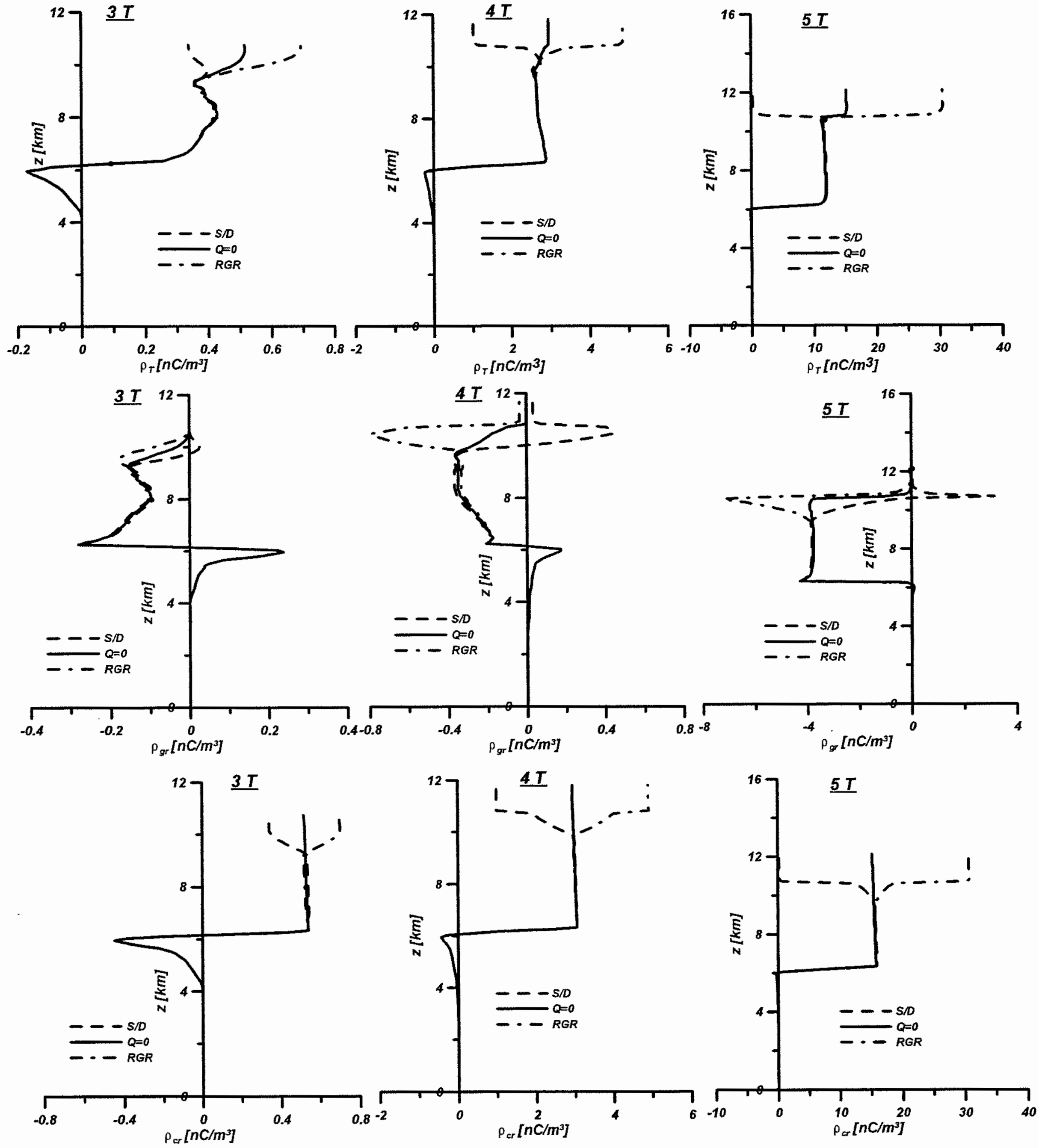

Fig.1. *Total charge density, ρ_T (top panel), charge carried by graupel, ρ_{gr} (middle panel), charge carried by ice crystals, ρ_{cr} (bottom panel) during the ascent of the third (3T), fourth (4T) and fifth (5T) COLO thermals*

The reduction of charge density in ascending thermals due to entrainment is taken into account. The charging rate per unit volume of model cloud is calculated as in Mitzeva and Saunders (1990). The net (total) charge density in ascending thermals, ρ_T is established by summing the charges on the ice crystals ρ_{cr} and on the ascending graupel ρ_{gr}. The net charge density in the non-active part of the cloud is the sum of the charge on falling graupel and on the ice crystals present.

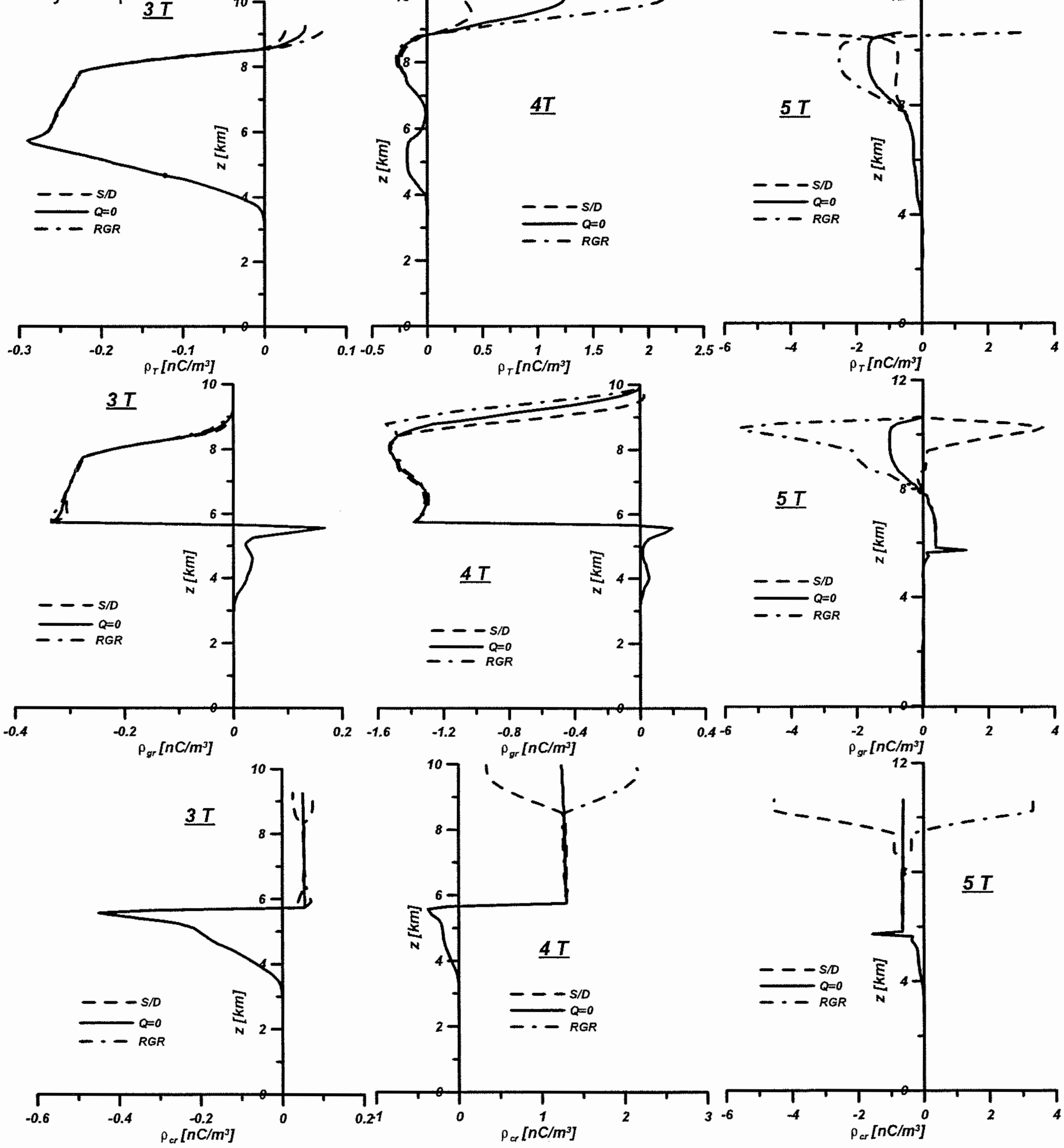

Fig.2. Total charge density, ρ_T (top panel), charge carried by graupel, ρ_{gr} (middle panel), charge carried by ice crystals, ρ_{cr} (bottom panel) during the ascent of the third (3T), fourt h(4T) and fifth (5T) NDTP thermals

3. NUMERICAL SIMULATIONS AND RESULTS

The model has been run using temperature and moisture profiles observed on 24 June 1992 when a multicellular storm developed over the northern Colorado Rocky Mountains (*COLO* cloud) and on 28 June 1989 when a large mesoscale convective system with updraught greater than 30 m s^{-1} developed over much of North Dakota (*NDTP* cloud).

Because one-dimensional models are limited in their simulation of large mesoscale convective systems, the model results for the simulated clouds have to be considered as a simulation of an isolated cumulus cloud developing in the same environmental conditions as the observed multicellular clouds. Since the present study is directed to the comparison between the results of charge density with the three variants of parameterisations mentioned above for thunderstorm charging in the regions where *LWC*=0, one has to consider the charge density in the updraught and in the non-active cloud regions as well. Only the charge density in the updraught will be presented here.

The total charge density ρ_T, the charge carried by graupel ρ_{gr}, and the charge carried by ice crystals ρ_{cr} calculated for the ascent of thermals in the COLO and NDTP thunderstorms are shown in the three panels of Figures 1 and 2 respectively. The results show that the use of the RGR parameterisation leads to an increase of positive charge carried by ice crystals ρ_{cr} (lower panels of Figures 1 and 2) and negative charge carried by graupel ρ_{gr} (middle panels). As a result, the total charge density ρ_T (top panels) is more positive close to the cloud top; it even changes sign from negative to positive during the ascent of the 5-th *NDTP* thermal. The use of the S/D parameterisation leads to changes in opposite direction.

4. CONCLUSIONS

The present study shows that the charge separated by non-inductive interactions of graupel and ice crystals in cloud regions free of cloud droplets influences to some extent the charge density in the upper part of the updraughts of severe thunderstorms. Based on the analyses of these preliminary results one can conclude that the parameterisation of thunderstorm charging in the regions free of cloud droplets based on the RGR hypothesis seems more plausible than the S/D parameterisation, which leads to negative charge on ice crystals during the ascent of some thermals in the higher levels in contrast with field measurements. Of course, the main conclusions to be drawn await the analyses of the impact of the proposed parameterisation on the charge density distribution in the whole volume of the thunderstorms.

5. ACKNOWLEDGEMENTS

This work is supported partially by the Royal Society and the Science Foundation of Sofia University (grant 64/2004).

6. REFERENCES

Andreev, V., Syrakov D. and Mitzeva, R., 1979: Modelling of convective cloud formation in successive ascending thermals. Bulg. Geophys. J., 1, 3-9.

Baker, B., Baker, M. B., Jayaratne, E. R., Latham J., and Saunders, C. P. R., 1987: The influence of diffusional growth rates on the charge transfer accompanying rebounding collisions between ice crystals and soft hailstones, Quart. J. R. Met. Soc., 113, 1193-1215.

Brooks M., Saunders, C. P. R., Mitzeva, R. P. and Peck, S. L., 1997: The effect on thunderstorm charging of the rate of rime accretion by graupel: J. Atmos. Res, 43, 277-295.

Cotton W., 1972: Numerical simulation of precipitation development in super-cooled cumuli - Part II, Mon. Weather Rev.,100 764-784

Jayaratne, E. R., Saunders, C. P. R., and Hallett, J, 1983: Laboratory studies of the charging of soft-hail during ice crystal interactions, Quart. J. R. Met. Soc., 109, 609-630.

Mitzeva R. P. and Saunders C. P. R., 1990: Thunderstorm charging: Calculations of the effect of ice crystal size and graupel velocity. J. Atmos. Terr. Phys., 52, 241-245.

INNER STRUCTURE AND PRECIPITATION MECHANISM IN OROGRAPHIC SNOW CLOUDS OVER THE COMPLEX TERRAIN IN CENTRAL JAPAN

Masataka MURAKAMI*, Narihiro ORIKASA*, Ken-ichi KUSUNOKI* Kazumasa MORI, Akihiro IKEDA** and Mitsunori SAITO***

[1]Meteorological Research Institute, Tsukuba, JAPAN
[2]Metocean Environmental Inc., Yokohama, Japan
[3]Tone River Dams Integrated Control Office, Maebashi, Japan

1. INTRODUCTION

In winter, a cold airmass from Eurasian Continent receives a great amount of heat and moisture and forms a convective mixed layer while it crosses the warmer surface of Japan Sea. Snow clouds developed in the mixed layer land the west coast of Japan Island and bring snowfall. And the airmass is forced up over the divide of Japan Islands with the peak of 2,000 m, producing further condensate and snowfall. The mountain area (windward slopes of the divide in northern and central parts of Japan Islands) is one of heaviest snowfall areas in the world. Although orographic modifications of snow clouds are clearly responsible for the heavy snowfall, and should be investigated to improve the precipitation forecasts in mountainous area and to determine the design of seeding experiments, no systematic study on orographic snow clouds, which covers microscale and mesoscale aspects, has been carried out so far.

Meteorological Research Institute, Japan Meteorological Agency and Tone River Dams Integrated Control Office, Ministry of Land, Infrastructure and Transportation have been carrying out the orographic snow cloud project over the western slope of the Echigo mountain (the divide of central part of Japan Island) since 1994.

In this paper, thermodynamic, kinetic and microphysical structures in vertical cross sections of snow clouds modified by a complex terrain, the Echigo Mountain, are described on the basis of observation data collected by an instrumented aircraft, hydrometeor videosonde, X-band and Ka-band Doppler radar, ground based microwave radiometers, etc.

2. OBSERVATION FACILITIES

Field program on orographic snow cloud study was carried out around the divide in the central part of Japan Island. The topography is not simple like an isolated mountain and two-dimensional one, but of complicated and three-dimensional. Windward slope of the mountain are very steep, with altitude increasing from 300 m MSL to 2,000 m MSL within 20 km of horizontal distance. In order to make measurements of vertical cross section of orographic snow clouds, we flew the instrumented aircraft at several heights over a V-shaped valley (see Fig. 1).

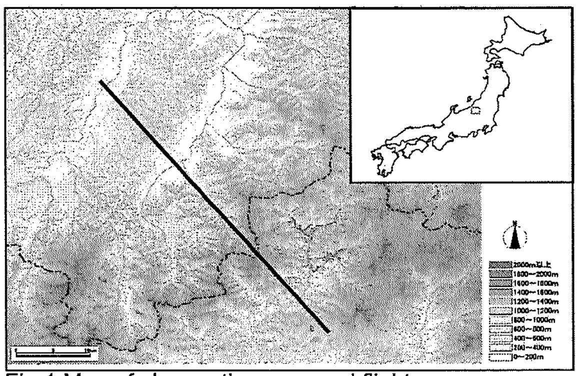

Fig.1 Map of observation area and flight course.

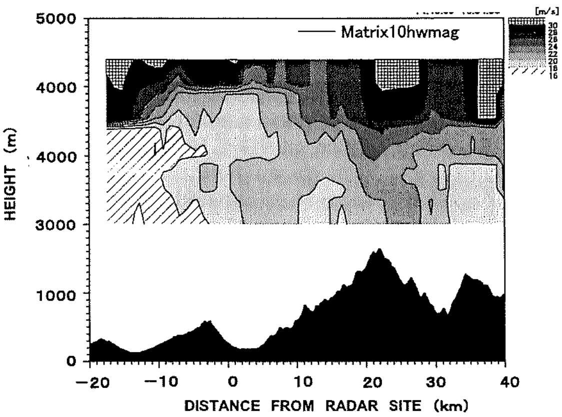

Fig.2 Vertical cross section of horizontal wind speed.

The primary instrumentation is an instrumented aircraft, which provides us with microphysical, thermodynamic and kinetic measurements. On the ground, we deployed X-band and Ka-band Doppler radar, three ground-base and one automobile microwave radiometers, hydrometeor videosonde and rawinsonde system.

3. OBSERVATION RESULTS

Corresponding author's address: Masataka MURAKAMI; Meteorological Research Institute, Tsukuba, Ibaraki 305-0052, Japan E-Mail: mamuraka@mri-jma.go.jp.

3.1 A Case Study

Vertical cross sections of orographic snow clouds observed on 3 December 2001 is shown as an example. The top height of the clouds was about 3.8 km and started to decrease 10 km windward of the mountain peak. Vertical cross sections of physical parameters presented hereafter derived by interpolating the data along the flight tracks at 5 different heights.

Horizontal winds were roughly WNW over most of the domain although they changed to NW leeward of the mountain (Fig.3). Wind speeds increased over the windward slope and the peak of the Echigo Mountains due to a vertical convergence of horizontal wind. Over the leeward slope, wind speed increased due to momentum transport of stronger wind at higher levels by downdraft (Fig.2). Gentle updraft regions extended 20 km windward of the peak and maximum values of 1 ~ 2 ms^{-1} were found around 10 km windward of the peak. Airflow was much more turbulent leeward of the mountain with the main downdraft of more than 2 ms^{-1} followed by the strong updraft.

Vertical cross section of potential temperatures shows a general tendency of higher values leeward and lower values windward. Also evident is regions with lower potential temperatures by ~1 K over the peak (Fig.5). Thermal stratification below 3.5 km gradually destabilized over the windward slope due to lifting aloft and consequent adiabatic temperature decrease. Pressure perturbation, which is the difference between heights calculated from integration of hydrostatic equation and GPS heights. A main low-pressure region with dp = –1 hPa is collocated with major downdraft region just behind the mountain peak.

Spatial distributions of cloud water contents almost coincide with those of updrafts and relatively large values (0.1 – 0.7 gm^{-3}) were found windward of the peak below 3.5 km. High concentrations (-30 particles/L) of ice crystals and snow particles larger than 25 um (measured with 2D-C probe) are distributed windward and over the peak.

3.2 Dependence on Froude Number and Stability

We analyzed many vertical cross sections of snow clouds with top heights of 3 ~ 5 km that were observed over the V-shaped valley for the last 6 years and obtained general characteristics of orographic modification.

Horizontal winds accelerated over the windward slope and the peak due to vertical convergence and over the leeward slope due to momentum transport of stronger winds at higher levels by downdraft. Horizontal winds increase by 30 ~ 50 %. Horizontal winds veer clockwise by 10 ~ 30 degrees during passage over the mountain.

With decreasing Froude number (wind speed), the gentle updraft regions extend up to ~20 km windward of the peak due to the blocking effect of the mountain

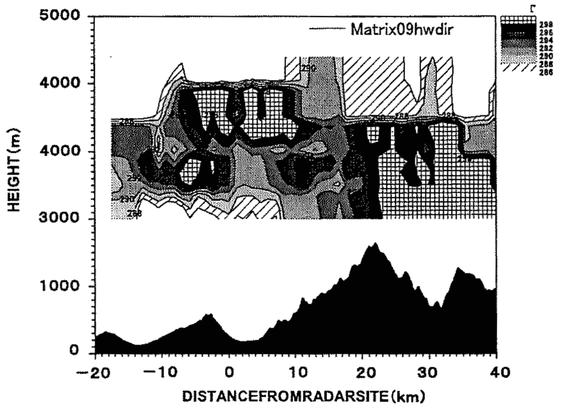

Fig.3 The same as Fig.2 except for horizontal wind direction.

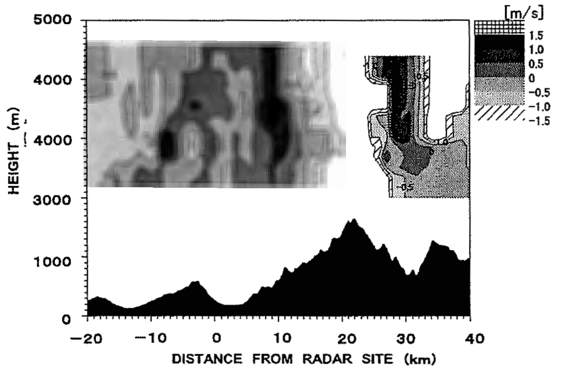

Fig.4 The same as Fig.2 except for vertical wind speed.

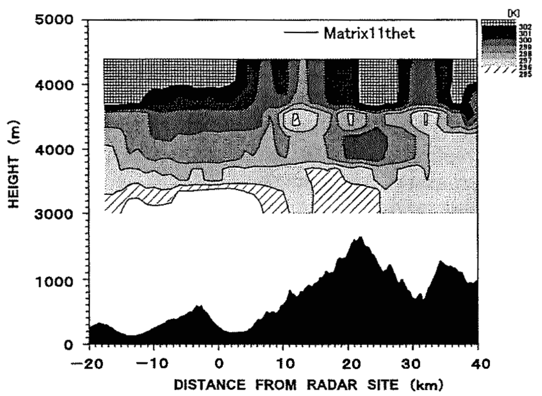

Fig.5 The same as Fig.2 except for potential temperature.

barrier. The gentle updraft regions shift toward the peak and shrink, but intensify with increasing Froude number. Cloud water regions with water contents of 0.1 ~ 1.0 gm^{-3} are almost collocated with the updraft regions. Downdraft and updraft over the leeward slope also intensify up to 5 ms^{-1} or more with increasing Froude number, resulting in temperature rise of 10 C.

Thermal stratification gradually destabilizes toward the mountain peak and finally weak convections occur in orographic clouds. Whether convections occur or not and where convections occur depends upon the upstream thermal stratification. However, week convective cells are embedded in most of orographic snow clouds.

Spatial distributions of ice crystal concentrations suggested that ice nucleation likely occurred near the cloud tops over the windward slopes of the Uonuma Hill and the Echigo Mountains. From the fact that high concentrations of ice crystals occurred in coexistence with supercooled cloud droplets, most likely mechanism of ice nucleation in the clouds was the freezing of cloud droplets (condensation-freezing and/or immersion freezing mechanisms). Ice crystals generated in upper parts of clouds rapidly grew by vapor deposition and accretion of cloud droplets in the cloud water regions with horizontal scale of ~ 20 km during their descent. Assuming horizontal wind speed of 20 ms^{-1} snow particles could continue the rapid growth for 17 ~ 18 min.

The blocking effect of the mountain barrier on lower level winds can extend updraft regions due to the mountain topography to the windward and allowed snow particles to continue the rapid growth for longer time in coexistence of supercooled cloud droplets. Thus it is suggested that the blocking effect could further strengthen the precipitation enhancement due to orographic updrafts.

5. CONCLUSION

The thermodynamic, kinematic and microphysical structures of orographic snow clouds were investigated over the Echigo Mountains with peak height of 2 km, in central Japan with an instrumented aircraft (B200), hydrometeor videosonde, microwave radiometer, X-band Doppler radar, Ka-band Doppler for the last six years.

Most of snow clouds had their top heights of 3 to 4 km and were confined to below a strong temperature inversion. Airflow structures are rather smooth with maximum updraft of 1-2 m/s over the windward slope while they are rough with strong downdraft and updraft of 5 m/s or more over the leeward slope. Horizontal winds are accelerated and veered clockwise passing over the crest line.

With larger Froude numbers, gentle updraft and supercooled cloud water regions exist over rather narrow region of windward slope and crest line. However, they extend windward up to 20 km from crest line with decreasing Froude number.

Ice and snow particle concentrations gradually increase over the windward slope, suggesting that ice nucleation occurs there due to a gradual decrease of cloud top temperature. Higher concentrations are

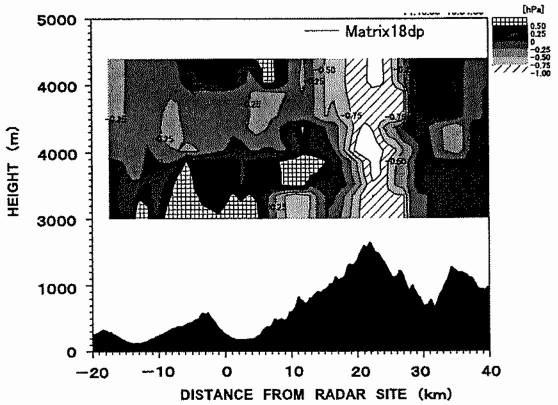

Fig.6 The same as Fig.2 except for pressure perturbation.

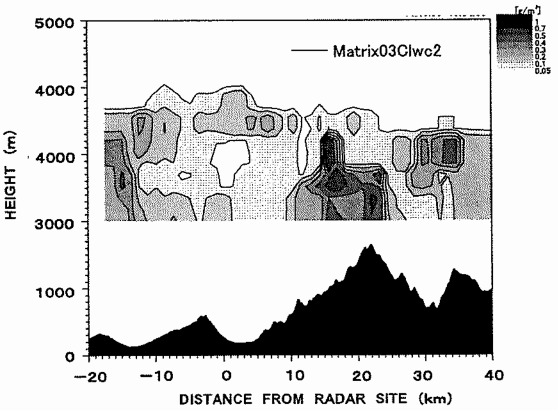

Fig.7 The same as Fig.2 except for cloud water content.

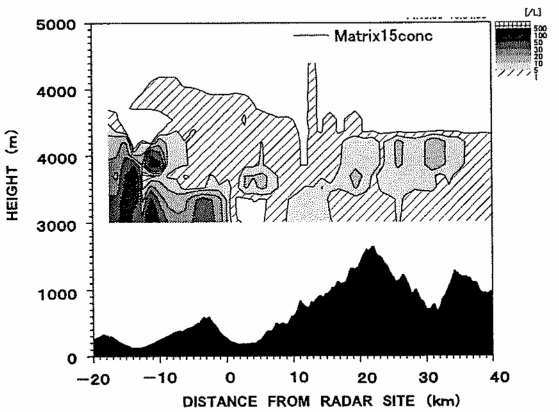

Fig.8 The same as Fig.2 except for number concentration of ice crystals and snow particle measured with 2D-C probe.

sometimes found in convective clouds over the leeward slope. Ice crystals initiated over the windward slope grew rapidly by vapor deposition and accretion during their descent through supercooled cloud droplet regions. An increase in spillover ratio with large Froude numbers is caused by high wind speeds which advect precipitation particles far downwind and by supercooled cloud water region closer to the crest line where precipitation particles falling down to leeward slope are allowed to spend much more time and grow farther.

NUMERICAL STUDY ON STRUCTURE AND MAINTENANCE MECHANISM OF TYPHOON SPIRAL BANDS USING THE CLOUD RESOLVING STORM SIMULATOR

Mitsuharu Nomura and Kazuhisa Tsuboki

Hydrospheric Atmospheric Research Center, Nagoya University, Nagoya, 464-8601, Japan

1. INTRODUCTION

Spiral bands are one of the characteristic meso-beta-scale structures of a typhoon in mature stage. Observational studies showed that spiral bands cause strong rainfall. It is, however, still unknown what dynamics and physical processes work to produce the strong rainfall within spiral bands, because it is difficult to perform an in-situ observation of a typhoon in its mature stage. Previous numerical studies have simulated the typhoon-scale distributions of spiral cloud bands. Detailed three-dimensional mesoscale structure, physical processes within the typhoon spiral band, and interactions of two neighboring spiral bands located near the typhoon center, however, are little unknown, because huge memories and high speed CPU are necessary for the numerical experiment of three-dimensional typhoon with resolving individual clouds. In order to simulate the detailed structure of spiral bands within a typhoon and to reveal dynamics and cloud physical process of the spiral band, we performed the typhoon simulation with fine mesh grid spacing using the Cloud Resolving Storm Simulator (CReSS)(Tsuboki and Sakakibara, 2002) and Earth Simulator.

In this study, we show detailed three-dimensional mesoscale structure of the typhoon spiral band, cloud microphysics processes of strong rainfall within the spiral band, and the effect from the inner spiral band to the outer neighboring spiral band when two spiral bands are located within a distance of a few tens kilometers near typhoon center.

Corresponding author's address: Mitsuharu NOMURA, Hydrospheric Atmospheric Research Center, Nagoya University, Nagoya, Aichi, 464-8601, Japan; E-Mail: nomura@rain.hyarc.nagoya-u.ac.jp

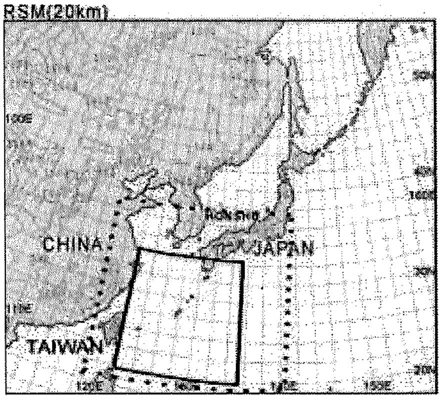

Fig. 1. Map of domains for JMA-RSM, CReSS-5km, and CReSS-2km. CReSS-5km is the area surrounding dotted lines and CReSS-2km is surrounding solid lines.

2. MODEL AND DATA

We used the Cloud Resolving Storm Simulator (CReSS) in this study. CReSS is a three-dimensional cloud resolving numerical model which formulated in the non-hydrostatic and compressible equation system with the cold rain bulk parameterization of the microphysics. In order to understand detail structure and physical process within the spiral band, two numerical experiments were conducted; one is an experiment with a horizontal resolution of 5km (CReSS-5km) and the other is of 2km (CReSS-2km). Vertical resolution in both experiments is stretched from 100m at the lowest level to 400m with height. The initial data for CReSS-5km is the Regional Spectrum Model by the Japan Meteorological Agency (JMA-RSM) at 00UTC September 4, 2002. In this data, T0216 (SINLAKU) in mature stage located near Okinawa, Japan. CReSS-5km ran for 24 hours. In CReSS-2km, this typhoon was simulated for 10hours from 06UTC using CReSS-5km outputs.

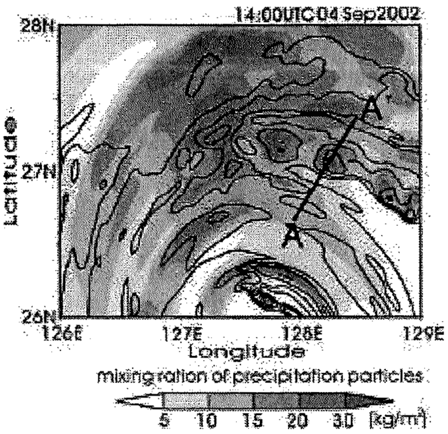

Fig. 2. Vertically integrated mixing ratios at 14UTC. Shadings are mixing ratio of precipitation particles. Contours are mixing ratio pf cloud particles every 1.5 kg m^{-2} from 1.0 kg m^{-2}.

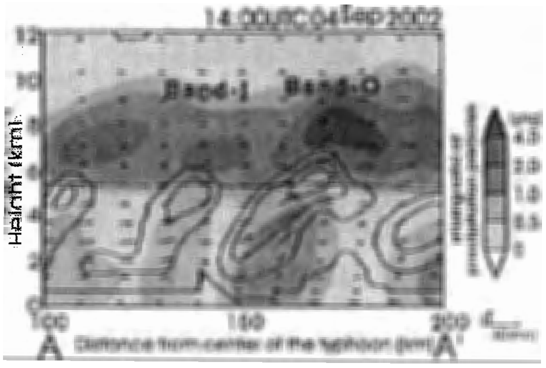

Fig. 3. Vertical cross-section of mixing ratios along AA' in Fig.2. Shadings are mixing ratio of precipitation particles. Contours are mixing ratio of cloud particles every 0.3 g kg^{-1} from 0 g kg^{-1}. Dotted line is 0 degree line.

We used CReSS-2km outputs for analysis of the structure of spiral band and cloud microphysics within the spiral band. For the back trajectory analysis, CReSS-5km outputs were used. JMA-RSM and calculation domains are shown in Fig.1.

3. RESULTS

3.1 Structure of the typhoon spiral band

Large amounts of cloud particles are mainly present in the central part of the spiral band (Figs. 2, 3). They are transported along the axis of the spiral band from lower level to upper level, and generated from water vapor transported

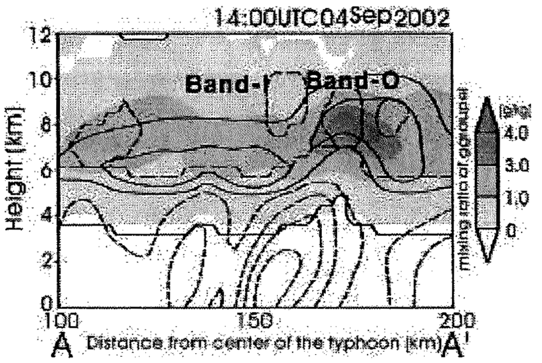

Fig. 4. Vertical cross-section of mixing ratio of precipitation particles along A-A' in Fig.2. Shadings are mixing ratio of graupel. Solid lines are mixing ratio of snow every 0.3 g kg^{-2} from 0 g kg^{-1}. Dotted lines are mixing ratio of rain water every 0.4 g kg^{-1} from 0 g kg^{-1}.

from lower level by condensation. Large amounts of precipitation particles are present in the outermost part of the spiral band. In particular, the maximum mixing ratio of precipitation particles is present on the outer side of the maximum mixing ratio of cloud particles, because wind over about 2km height is outward flow.

Examining more detailed distribution of precipitation particles in the spiral band, we show the vertical cross-section of spiral bands in Fig. 4. There are large amounts of graupel above strong rainfall areas in band-O. Snow is present mostly in the area between band-I and band-O, while a small amount of graupel exists there. This result shows that strong rainfall in the spiral band is caused by collecting cloud water by graupel.

3.2 Cloud microphysics within the spiral band

The strong rainfall process within the spiral band is clarified by investigating cloud microphysics. In particular, we investigate generation and growth of precipitation particles by collecting cloud particles. In the spiral band, large amounts of snow collect cloud water and grow to graupel by riming (Fig. 5a). Little snow grows to graupel between band-I and band-O, because there is small amount of cloud particles there. Therefore, there are larger amounts of snow between bands than in a spiral band. Large amounts of snow grow to graupel within spiral bands. Graupel grows larger by riming within Band-O (Fig.5b). Comparing riming by snow within Band-O with that of Band-I, riming by snow occurred to the same extend (Fig. 5a).

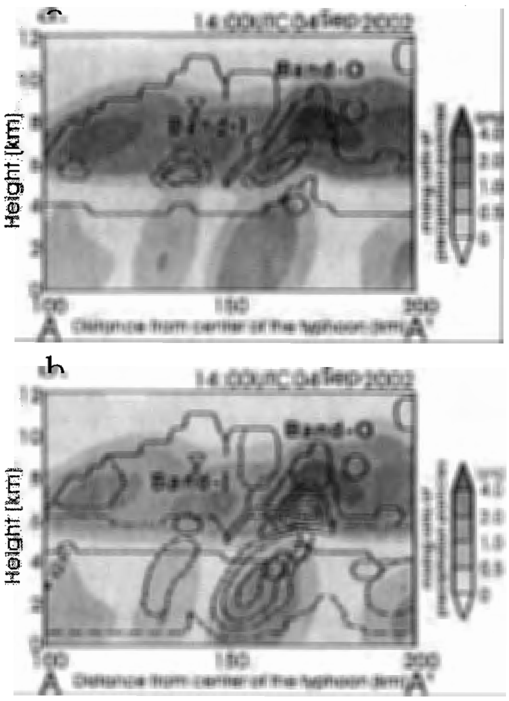

Fig. 5. Vertical cross-section of cloud microphysics processes along A-A' in Fig.2. a.: Dotted lines are riming by snow every $2*10^{-3}$ g kg^{-1} s^{-1}. Solid lines are growth from snow to graupel every $5*10^{-3}$ g kg^{-1} s^{-1}. Shading are mixing ratio of precipitation particles. b.: Dotted lines are collection of cloud water by rain water every $10*10^{-3}$ g kg^{-1} s^{-1}. Solid lines are riming by graupel every $10*10^{-3}$ g kg^{-1} s^{-1}.

Above the melting layer, cloud water within Band-O is larger than that of Band-I (Fig.3). Riming by graupel occurs more strongly by providing large amounts of cloud particles above the melting layer within the spiral band. It is necessary to produce or provide large amounts of cloud particles over the melting layer for strong rainfall within the spiral band. Therefore, it is found that riming by graupel is the most effective process for strengthening of rainfall within a spiral band.

3.3 Effect from the inner spiral band of two neighboring bands to the outer band

When two spiral bands are located within a distance of a few tens kilometers near typhoon center, it is often observed that rainfall of the outer band becomes intense. In Fig. 4, there are large amounts of snow between Band-I and

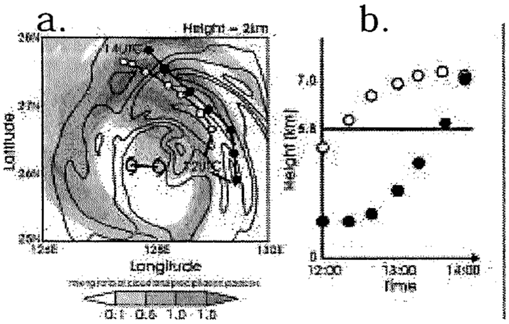

Fig. 6. Projection of trajectories set at 7km height from 12UTC to 14UTC. Horizontal track is a. Vertical track is b. The closed circle supposes cloud water, and the open circle is snow. Typhoon center moves from east to west. In a., shaded is mixing ratio of precipitation particles at height = 2km at 14UTC. Contours are mixing ratio of precipitation particles at 12UTC Contour levels are same as shaded levels. 0 degree line is at about 5.8km height.

Band-O. For generating graupel within Band-O, Snow between two bands is generated in Band-I and transported from Band-I to Band-O. Because there is little source for generating snow between two bands (Fig. 3). For understanding the effect of intensifying precipitation from the inner band to outer band, we used back trajectory technique (Golding, 1984). The back trajectory analysis is performed using the following algorithm

$$\mathbf{x}^{n-1/2}=\mathbf{x}^{n}-\mathbf{u}^{n}(\mathbf{x}^{n})*\Delta t/2$$
$$\mathbf{x}^{n-1}=\mathbf{x}^{n}-\mathbf{u}^{n-1/2}(\mathbf{x}^{n-1/2})*\Delta t$$

where $\mathbf{x}$ is position, $\mathbf{u}$ ($\mathbf{x}$) is the interpolated mode velocity at position $\mathbf{x}$ and n is the time level. For the back trajectory analysis, CReSS-5km output every 5 minutes from 14UTC to 12UTC was used.

Origins of the back trajectories of snow and cloud water are edge of Band-O where riming by snow occurred and the place of the most generating graupel, respectively. Horizontal projection of trajectories set at 7km height is shown in Fig. 6a, and vertical projection is shown in Fig. 6b. In Fig. 6a, trajectory of cloud water (closed circles) moves along Band-O. Trajectory of snow (open circles) which suited Band-O at 14UTC has reached band-I at 12UTC. In Fig. 6b, moreover, it is shown that cloud water is transported from a height of about 2km to 7km.

The open circle is above the melting layer until 14UTC which reach Band-O from 1220UTC which comes out to the outside of band-I. This indicates that snow generated within Band-I is transported to Band-O by the outward flow. For generation and growth of graupel to intensify precipitation within Band-O, snow transported from Band-I becomes seeder, cloud water produced from lower level within Band-O is feeder.

4. CONCLUSIONS

Detail three-dimensional structures of the typhoon spiral band and cloud microphysics process for strong rainfall within the spiral band were studied by the numerical simulation with fine mesh. Large amounts of cloud particles and precipitation particles are present within the spiral band. Cloud water and water vapor are transported along the axis of the spiral band from lower level to upper level. Above the melting layer, there are large amounts of graupel above strong rainfall areas in a spiral band. Snow exists mostly in the area between bands.

In the spiral band, large amounts of snow transported from inside of the band by outflow collect cloud particles and grow to graupel. Generated graupel grows larger by riming, when there are large amounts of cloud water above the melting layer. Within spiral bands, generation and growth of graupel are the most effective processes to produce intense rainfall. There results show that cloud rain processes with the spiral band are important to intensify the rainfall within the spiral band.

When two spiral bands near typhoon center are located within a distance of a few tens kilometers, the conceptual model of mechanism of intensifying rainfall within the outer spiral band is shown Fig. 7. Snow particles generated within the inner band are transported to the outer band by outflow. And they become seeds for graupel generating within the outer band. Providing large amounts of cloud water over the melting layer by updraft within the outer band, generated graupel grows larger and falls down.

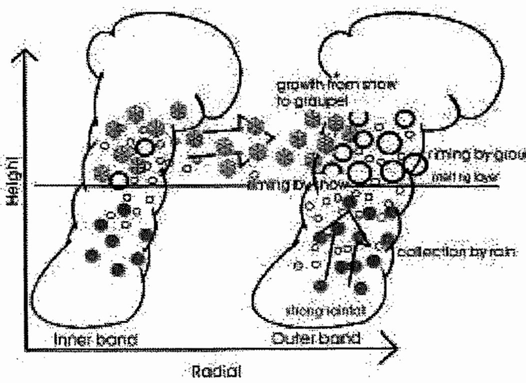

Fig. 7. Conceptual model of mechanism of intensifying rainfall within the outer spiral band. Small circles are cloud water White and gray big circles are graupel and rain.

Acknowledgements

The authors would like to express their special thanks to Professor Uyeda, Dr. Shinoda, Nagoya University, and Mr. Sakakibara, Chuden CTI Co., Ltd., for their assistance in model setup and the analysis, and the Meteorological Research Institute for providing JMA-RSM data. The numerical calculations were preformed using Earth Simulator at the Earth Simulator Center and HITACHI SR-8000 at the University of Tokyo.

References

Golding, B. 1984: A study of the structure of mid-latitude depressions in a numerical model using trajectory techniques I: Development of idea baroclinic waves in dry and moist atmospheres. *Mon. Wea. Rev.*,**127**, 2044-2061

Tsuboki and Sakakibra, 2002: Large-scale Parallel computing of cloud resolving Storm simulator. *High Performance Computing*, Springer, 243-359

NUMERICAL SIMULATION OF THE WARM-SEASON FRONTAL CLOUD SYSTEMS WITH STRONG PRECIPITATION

Pirnach A.M.

Ukrainian Hydrometeorological Research Institute, Kyiv, 03028, Ukraina

1. INTRODUCTION

The 3-D nowacasting and forecasting models that have been developed in UHRI for modeling of the winter and summer frontal cloud systems were modified by orography and carried out for numerical simulation of warm-season frontal clouds (see Pirmach, 1998, , Pirnach et al.1994, 2000 etc). Three-dimension numerical models with detail description of an evolution of cloud particles (cloud drops, rain drops, crystals, cloud and ice nuclei, etc.) are used to study the microphysical processes into widespread and convective frontal clouds. The nowacasting and forecasting models of the warm-season frontal rainbands and convective cloud clusters were constructed for two cases of the severe weather connected with occluded and cold fronts passed over mountain and plain reliefs.

2. GOVERNING EQUATIONS

The formation and development in space and time of atmospheric front and its cloud system are simulated by integration of the following set of the primitive equations and kinetic equations for the cloud particle sizes distribution functions modified by orography.

$$\frac{dS_i}{dt} = F_i + \Delta S_i , \quad (1)$$

$$\frac{\partial \rho u}{\partial \xi} + \frac{\partial \rho v}{\partial \eta} + \frac{\partial \rho \breve{w}}{\partial \varsigma} = 0 \quad (2),$$

$$\rho = \frac{p}{RT}, \quad (3)$$

where

$$S_i = (u, v, \breve{w}, T, q, f_k), \quad i = 1,2,...,8; \quad k = 1,2,3,$$

$$\frac{d}{dt} = \frac{\partial}{\partial t} + u\frac{\partial}{\partial \xi} + v\frac{\partial}{\partial \eta} + \breve{w}\frac{\partial}{\partial \zeta}, \quad (4)$$

$$\Delta S_i = k_\xi (S_{\xi\xi} + S_{\eta\eta}) + k_\varsigma S_{\varsigma\varsigma}, \quad (5)$$

$$F_1 = lv - \frac{1}{\rho}\left[\frac{\partial p}{\partial \xi} - \rho g G_1\right] + \Delta u, \quad (6)$$

$$F_2 = -lu - \frac{1}{\rho}\left[\frac{\partial p}{\partial \eta} - \rho g G_2\right] + \Delta v,$$

$$F_3 = -g - \frac{1}{\rho}\left[\frac{\partial p}{\partial \xi}\frac{1}{G_0}\right] + \Delta \breve{w},$$

$$F_4 = \sum_{k=1}^{3} \alpha_k \varepsilon_k + \alpha_p \frac{dp}{dt} + \Delta T, \quad F_5 = -\sum_{k=1}^{3} \varepsilon_k + \Delta q,$$

$$F_6 = -\frac{\partial}{\partial r}\left(\dot{r}_1 f_1\right) + \frac{\partial f_1}{\partial \zeta}\frac{v_1}{G_0} + I_a - I_f - (c_{21} + c_{31}) f_1 + \Delta f_1,$$

$$F_7 = -\frac{\partial}{\partial r}\left(\dot{r}_2 f_2\right) + \frac{\partial f_2}{\partial \zeta}\frac{v_2}{G_0} - I_{f2} - \frac{\partial}{\partial r}\left(\dot{r}_{c21} f_2\right) + \Delta f_2,$$

$$F_8 = -\frac{\partial}{\partial r}\left(\dot{r}_3 f_3\right) + \frac{\partial f_3}{\partial \zeta}\frac{v_3}{G_0} - \frac{\partial}{\partial r}\left(\dot{r}_{c31} f_3\right) + I_S + I_{f1} + I_{f2} + \Delta f_3.$$

There are:

$$\breve{w} = \frac{G_1 u + G_2 v + w}{G_0}, \quad G_0 = 1 - \frac{\Gamma}{H},$$

$$G_1 = \Gamma_x\left(\frac{\xi}{H} - 1\right), \quad G_2 = \Gamma_y\left(\frac{\xi}{H} - 1\right).$$

t is the time; u, v, w are the components of wind velocity along x, y, z axes. Axes x, y and z have been directed across and along the front and perpendicular to the Earth respectively. The new coordinates have been presented as follows:

$\xi = x, \quad \eta = y, \quad \varsigma = \dfrac{z - \Gamma}{H - \Gamma} H$, where x. y, z are Cartesian coordinates, ξ, η, ς are z-sigma orographic coordinates. Γ $(x.y)$ –relief function, H is z-maximum. Γ_x, Γ_y are first order derivatives of the function Γ with respect to x, y. k_ξ, k_ζ are the coefficients of horizontal and vertical diffusion; $S_{\xi\xi}, S_{\eta\eta}, S_{\xi\zeta}$ are the second order derivatives of the functions with respect to x, y, z respectively; γ is dry-adiabatic gradient; ρ is the density of air; l, g are the Carioles parameter and free fall acceleration; p, T is the pressure and temperature of air; R is the gas constant of dry air; q is the specific humidity of air. f_k are cloud particle size distribution functions (small drops, rain drops, crystals), r is the radius of cloud particle. Functions $I_a, I_s, I_f, I_{f1}, I_{f2}$ describe the nucleation, sublimations and freezing processes. $\dot{r}_{cik}, c_{ic}$ presented coagulation processes, $\dot{r}_k, \xi_k$ described condensation (see Pirnach et al., 1994, 2000).

3. NUMERICAL EXPERIMENTS

The number of simulations have studied the impact on the development of clouds and precipitation of different microphysical processes (such as nucleation, condensation, sublimation, collection, riming, etc) and thermodynamical conditions (such as surface pressure, temperature, updrafts, etc) have been carried out (see Pirnach et al.,2000, Belokobylski et al., 2000, etc).

In this paper numerical experiments were conducted with convective and wide spread clouds passed over mountain and plain relief. Atmospheric state over Ukraine on August 5 1995 was selected for presentation. On August 4-5 the occluded frontal system with secondary cold fronts in it slowly crossed Ukraina in north-west direction and was accompanied by cloudiness, showers and thunder-storms.

Over north Ukraina and the Kiev region widespread precipitation have place on August 5 at 00 GMT (see Fig.1). Over west Ukraina the several showers have been fixed. At 09 GMT two second cold front determined weather in Kiev region. A second cold front with its cloud system reached Lviv region. More detail description of the initial atmospheric state and it temporal and spatial development is described in Pirnach et al., 2000.

State of atmosphere at 00 GMT on August 5 was selected as initial data for modeling cloud and precipitation development. Lviv sounding station was selected as initial coordinate point.

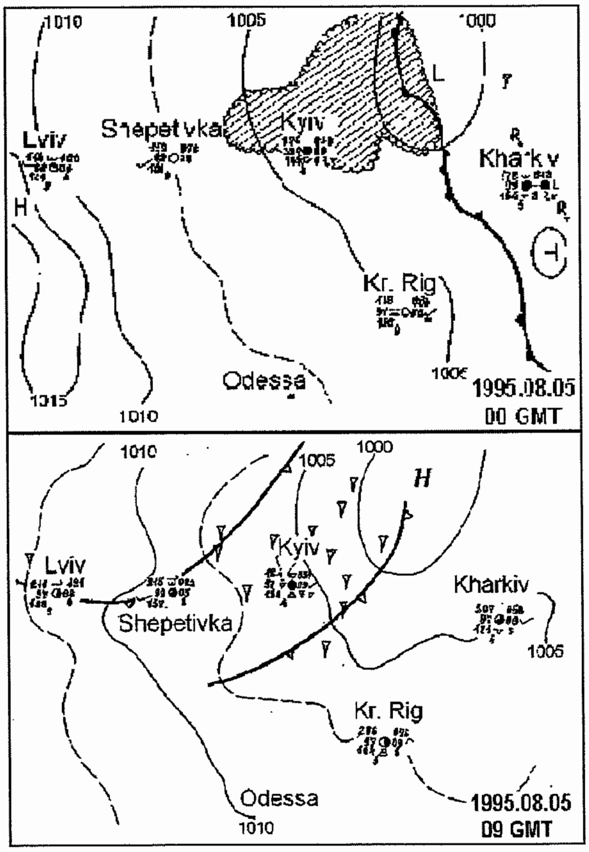

Figure 1. Part of surface synoptic map with Ukraina for 5 August 1995 at 00 GMT and 09 GMT.

There will be presented some numerical experiments estimated the influence on the time and space precipitation core development of rain production mechanisms and relief. Spatial distribution of cloud characteristics will be presented in the ξ,η,ζ coordinate system but in next text the coordinate ξ,η,ζ were renamed as x, y, z.

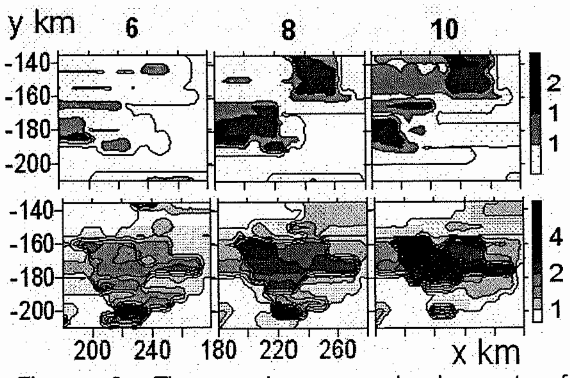

Figure 2. Time and space development of precipitation intensity, mm/h. First row: plain relief (Case 1); second row: real relief (Case 2). Digits in tops indicate time, h. There are ξ,η renamed as *x, y*.

Temporal and spatial development of modeled precipitation intensity is shown in Fig.2. Precipitation in it presented both cases with including and no including relief in calculation Precipitation cover consisted from several clusters with some precipitation cores in them in both cases. Account of relief (Case 2) appreciably had changed the picture of cloud cover at different time its development. Additional precipitation cores appeared in cloud cover and precipitation intensity maxima increased (see Fig.3).

First precipitation core was found near by point *(x,y)*= (220, -200 km). In Case 1 it existed about 2 hours. In Case 2 it maintain a position about 6 hours and there had been fixed precipitation intensity *(x, y)* -maxima (see Fig.3, Case 2 and 3).

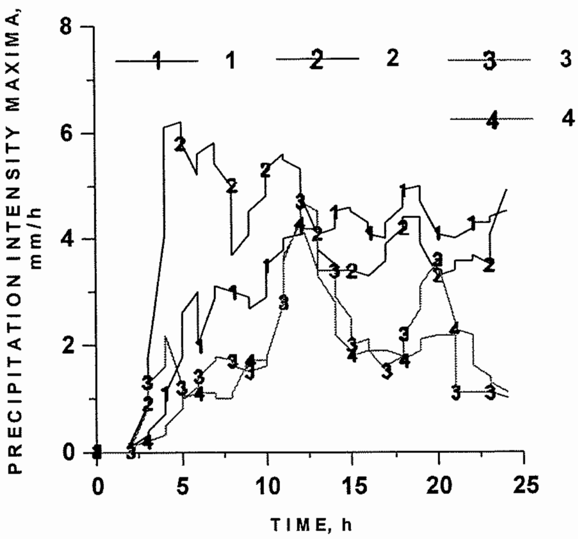

Figure 3. Time and space development of precipitation intensity maxima, mm/h. 1) orography included and coagulation processes have not been included; 2) as 1, coagulation have place; 3) as 2, no orography; 4) as 1, no orography

As can see from Fig.3 precipitation intensity maxima slowly grow if coagulation processes absence. This increasing indicated presence of the free to sublimate water vapor and cloud moisture that is necessary for cloud and precipitation production. Including of coagulation processes in calculation strongly increased precipitation maxima during first 6 h cloud development in first precipitation core. Oscillation structure is common feature for all precipitation production mechanism if they have sufficient intensity to realize free for sublimate water vapor.

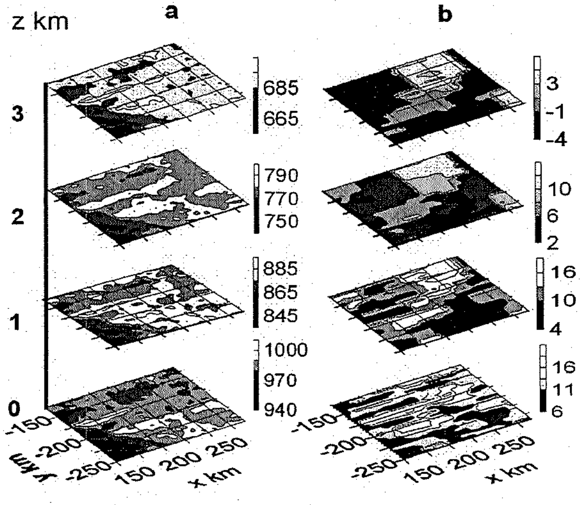

Figure 4. Space distribution of pressure, mb, (a) and temperature, °C (b) at $t = 5$ h. Case 2: orography and coagulation processes included.

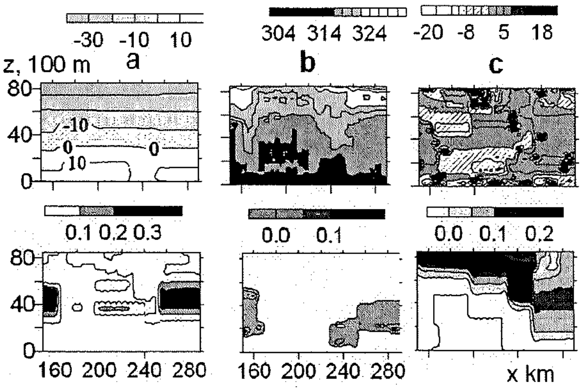

Figure 5. The (x, ζ) cross-section at $t = 6$ h and $y = -200$ km. First row: a) temperature, °C; b) pseudo-equivalent temperature, K; c) w cm/c. Second row: a) ice supersaturation, g/kg; b) liquid water content, g/kg; c) ice content, g/kg. There are η rename as z.

Spatial distribution of pressure and temperature in target area at $t = 5$ h (see Fig.4) shown presence of bands of warm and cold air mass and band of high pressure crossed them with a great angle. This condition indicated baroclinity in air mass and was favorable to next development of rainbands as well as rain spots with precipitation cores in them. In region of first precipitation core the warm air and relatively high pressure have place. The high pressure and temperature gradients result in significant updraft, clouds and precipitation.

Vertical cross-section at $y = 200$ km of temperature and pseudo-potential temperature (see Fig.5) sown that significant horizontal temperature gradients and instable air mass have place near point $(x, y) = (220, -200$ km). There were: typical "seeder" and "feeder" zones with high ice cloud tops and mixed cloud layers under; large supersaturation regions; large updraft zones. Near-by the colum x = 220 km mixed clouds absent and supersaturation have the layer structure. Those absolute values were lees than they were in environment near-by. It declared the intensive absorption of the air moisture by precipitation in precipitation core located near-by this column.

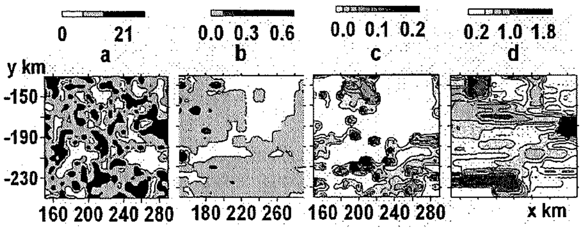

Figure 6. Integral cloud features at t = 6 h in Kiev region. a) updraft z-maxima, cm/s; b) ice supersuturation z-maxima, g/kg; c) water content z-maxima, g/kg; d) ice content z- maxima, g/kg.

State of integral cloud characteristics at $t = 6$ h for Case 2 shown in Fig.6. There are the updraft z-maxima, that have a mosaic picture as will as the water content z-maxima; the ice supersaturation and ice content z-maxima that occupied the large area. The spatial distribution of ice supersuturation, liquid water and ice content for Case 2 confirmed presence of liquid water and free for sublimation water vapor that did not disappeared if even most strong precipitation production mechanisms were included.

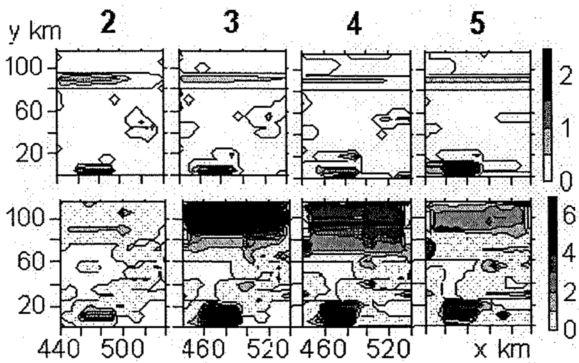

Figure 7. Time and space development of precipitation intensity, mm/h. Digits are as Fig.2 for Kyiv region.

This moisture sources should be a cause of subsequent increasing of precipitation.

Fig.7-9 presented temporal and spatial distribution of cloud and precipitation features for frontal cloud system in Kyiv region. The time development of precipitation in target area sees in Fig.7. During first 6 h two precipitation cores were fixed clearly for both plain and real reliefs (Case 1 and Case 2) but in Case 2 precipitation intensity was more strong. They located in the south and north parts of target area. In last case absolute maxima of precipitation intensity were fixed at t = 3 h for both precipitation cores. North precipitation core was large but south core existed longer.

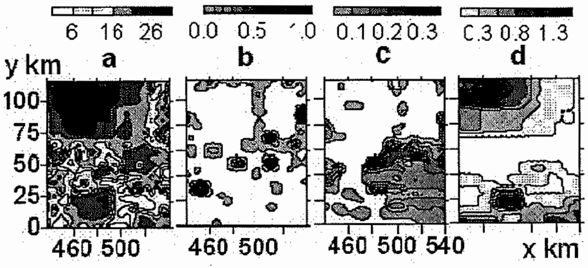

Figure 8. Integral cloud features at t = 3 h in Kiev region. a) updraft z-maxima, cm/s; b) supersaturation z-maxima, g/kg; c) water content z-maxima, g/kg; d) ice content z- maxima, g/kg. Kiev region

Spatial distribution of ice supersaturation at t = 3 h for Case 2 shown in Fig.8. Rare spots of its positive values indicate a lack of cloud moisture for additional precipitation production in some regions as well as in north precipitation core. Precipitation maxima development have an oscillate structure (see Fig.9).

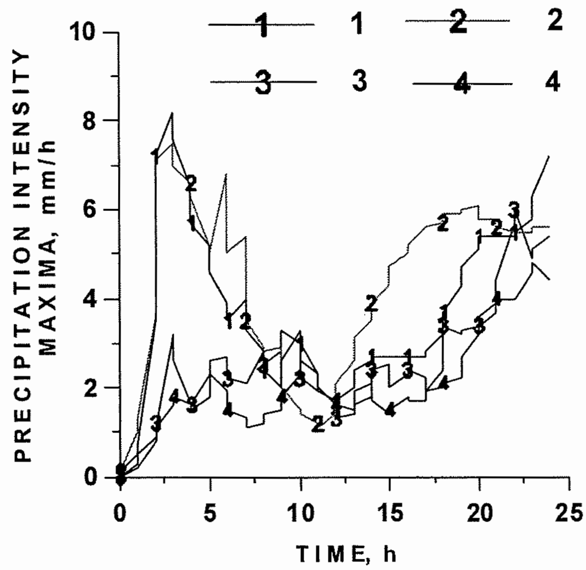

Figure 9. As Fig.3 for Kyiv region

Coagulation processes in this case did not cause a strong increasing of precipitation. It seem to be that the sublimation and glaciating processes successfully realized all cloud moisture and vapor that ably for precipitation production. Absent of additional cloud moisture did not allow increase above precipitation maxima by coagulation. Consequently, the coagulation processes are necessary for realization cloud moisture if the other mechanisms are not able to precipitate the suitable for precipitation cloud moisture.

4. CONCLUSIONS

Numerical model of frontal cloud system modified by orography was developed. Numerical experiments have revealed that including of relief in model caused deepening of cloud cover, increasing of number and intensity of precipitation cores. It intensified coagulation and sublimation processes and led to increasing of precipitation maxima if the free for sublimation water vapor was present in clouds

Numerical experiments for different warm rain production mechanisms (sublimation and droplet collection by raindrop and ice particles) were conducted and comparison between precipitation intensity for them was given.

There are found that increasing of activity of coagulation and sublimation processes can to increase strong precipitation as well as decrease it. Presence of free for sublimation vapor caused increasing nucleation and coagulation activity and increasing of precipitation maxima. In this case it is probably that even a very strong ice nucleation activity can not to realize all precipitate moisture. There is necessary to include the coagulation processes. Sometime the sublimation processes may be able to realize all precipitable moisture in warm-season clouds. If the free vapor is absent, increasing of the ice nucleation activity result in depression of precipitation and coagulation processes change intensity of precipitation insignificantly.

If this free vapor presence in clouds, best favorable influence on precipitation maxima have coagulation processes. The depression of precipitation have place if ice nucleation concentration exceeded the concentration that most favorable for cloud and precipitation production. This concentration was determined by conditions of cloud formation and, as rule, exceeded the statistical experimental values.

5. REFERENCES

Pirnach, A., 1998: Construction and application of the various numerical models for study the cloud dynamics and structure of the frontal rainbands. J. Atmos. Res., 45-47, 356- 376.

Pirnach, A., Krakovskaia, S., 1994: Numerical studies of dynamics and cloud microphysics of the frontal rainbands. J. Atmos. Res., **33**, 333-365.

Belokobylski A., Pirnach A. 2000: Numerical simulation of the warm-season frontal clouds over Ukraine. Proceedings of 13th ICCP. Reno, Nevada, USA. 2000, 1165-1169.

Pirnach, A. and Belokobylski, A. 2000: Numerical simulation of the summer frontal clouds. Trudy UHRI, **248**, 5-21.

CELL MERGER SIMULATIONS WITH THREE-DIMENSIONAL ENVIRONMENTAL DATA

Diana R. Pozo[1], Israel Borrajero[1], Julio C. Marín[1], Graciela Raga[2], Daniel Martínez[1]

[1] Institute of Meteorology, Cuba
[2] Centro de Ciencias de la Atmósfera, UNAM, Mexico

1. INTRODUCTION

Cloud merger is a phenomenon of great complexity hat has been studied with the aid of numerical models to achieve a better understanding of its nature. Many works have been focused on the conditions that favor the occurrence of mergers and whether this process causes the weakening or not of merged cells after it has taken place (Orville et. al, 1980; Turpeinen, 1982; Tao and Simpson, 1989, Kogan and Shapiro, 1996; Stalker and Knupp, 2003). All these simulations have been initialized with homogeneous horizontal environments and in conditions of calm.

On July 21st of 2001 several severe storms occurred over the region of Camaguey, Cuba, which were detected by radar. Some of these storms merged giving place to a great hailstorm over the area. With the aid of a three-dimensional model a simulation (**Sim1**) was carried out utilizing an external three-dimensional field as input data to reproduce the formation and development of the storms in the most realistic way possible, avoiding the inclusion of forced initial perturbations. Among the simulated storms two cases of merger were reproduced that were also detected by radar, one between cells at different stages, referred to as case **A** and other between cells with approximately the same state of development, referred to as case **B**.

2. NUMERICAL MODEL

The numerical model chosen for this study was ARPS (Advanced Regional Prediction System), which is a three-dimensional, non hydrostatic and compressible model (Xue, 1995). Second order momentum advection was used as well as a sub-grid turbulence parameterization of order 1.5 which is carried through the solution of an additional forecast equation for the turbulent kinetic energy. Kessler's (1969) microphysics parameterization scheme for liquid phase and Lin et al. (1983) for solid and mixed phase processes were also included. The later uses a variant of Berry's (1967) parameterization for rain autoconversion. The effects of orography, land-use and radiation were also included.

3. SIMULATION USING AN EXTERNAL THREE-DIMENSIONAL FIELD AS INITIAL CONDITIONS (SIM1)

Diana R. Pozo, Institute of Meteorology, la Habana, Cuba. E-Mail: dpozo@met.inf.cu

For this simulation the 18:00 GMT sounding at Camagüey location and data from surface meteorological stations over the chosen area were used. Synoptic scale information was obtained from the mesoscale model MM5, run for a domain that included Cuba and its neighboring zones and using as initial and boundary conditions output data from AVN global model. MM5 was not included originally among the models available to be used as input to ARPS, so that some additional code had to be written into ARPS. With all this information the initial three-dimensional field was arranged with the aid of the objective analysis system (ADAS), incorporated in ARPS. With this generated three-dimensional field an intermediate simulation with ARPS of 3 and 1.5 km of horizontal and vertical resolution respectively was initiated with the aim of supplying the initial and external boundary conditions data to Sim1every half an hour. Sim1 was run during 4 hours on a grid of 95 x 95 x 70 points with a distance of 1.5 km in the horizontal and 0.5 km in the vertical direction (**Fig 1**).

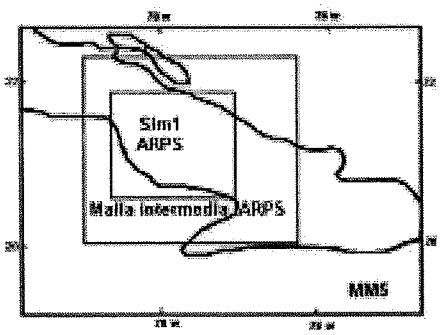

Fig. 1. Domains used in the simulations. Outer domain: MM5, intermediate domain: simulation with ARPS that supplied initial and boundary conditions data for Sim1, inner domain: Sim1

Comparison between results of Sim1 and radar images shows that in both cases of merger analyzed (A and B) the state of development of each cloud, the moments at which merger took place, the direction of motion of the storms and the increase of precipitation due to the increment of area after the merger were correctly reproduced. **Figs. 2-3** show two instants of this process, before the merger, at 21:56 GMT (10200 s of simulation) and 20 minutes later, when it occurred. Simulation output figures and radar images have a horizontal resolution of 1.5 and 1.3 km respectively, making it easier to do comparisons between them.

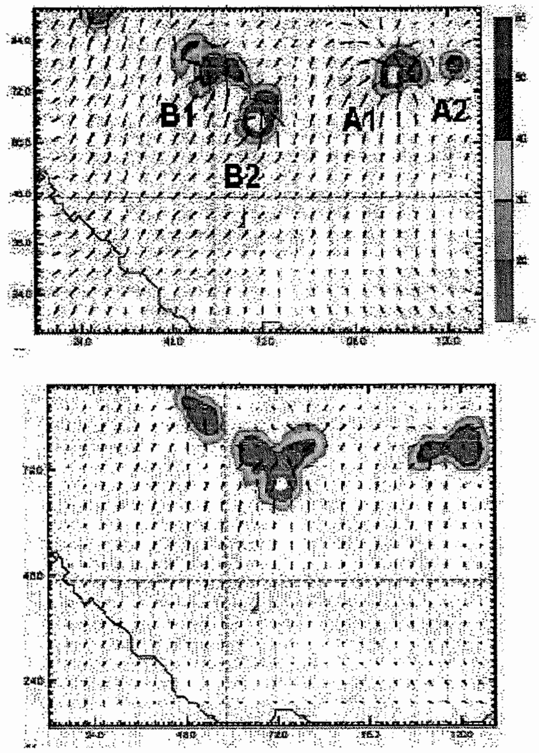

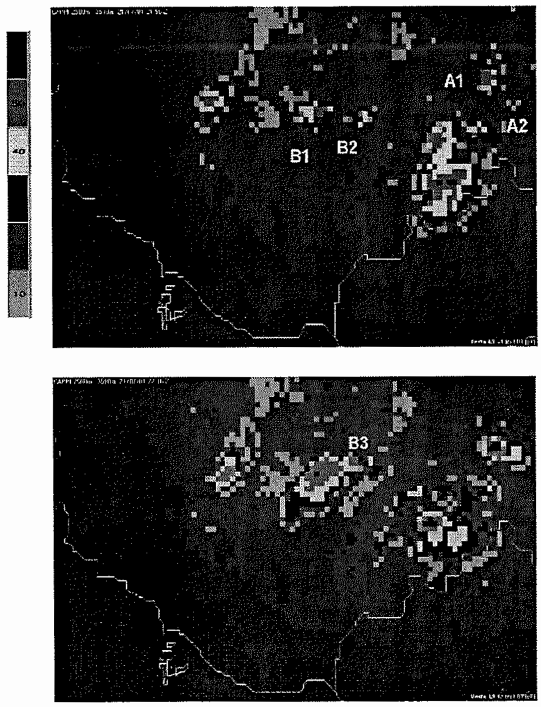

Fig. 2 Temporal evolution of the merger of cells A1+A2 and B1+B2 in July 21, 2001. Simulation figures at 10200 and 11400 s. The reflectivity isolines start at 10 dBz with 10dBz increments.

Fig. 3 Temporal evolution of the merger of cells A1+A2 and B1+B2 in July 21, 2001. Radar images for that day at 2156 and 2216 GMT. The reflectivity isolines start at 10 dBz with 10dBz increments.

Table 1. Cell parameters in the simulation (10200s) and detected by radar at 2156 GMT before the merger occur. Htop: cloud top height, Rmax: maximum reflectivity, Hrmax: height at which the maximum of reflectivity is located, Area: Area occupied by the cells.

	Sim1			
cells	***Htop (km)***	***Rmax (dBz)***	***Hrmax (km)***	***Area (km^2)***
A1	16	60	7-8	181.5
A2	6.7	51	3-4	55.5
B1	14.5	63.5	0-1	180
B2	15	63	7-8	180
	Radar			
A1	9-10	51	3-4	101
A2	3-4	38	6-7	15.6
B1	9-10	53	4-5	137
B2	8-9	55	3-4	50.7

Table 2. Cell parameters in the simulation (11400s) and detected by radar at 2216 GMT after the merger occur. Htop: cloud top height, Rmax: maximum reflectivity, Hrmax: height at which the maximum of reflectivity is located, Area: Area occupied by the cells.

	Sim1			
cells	***Htop (km)***	***Rmax (dBz)***	***Hrmax (km)***	***Area (km^2)***
A1+A2	14	50	0-1	283.5
B1+B2	11.7	60	1-2	263.2
	Radar			
A1+A2	11-12	60	4-5	167.7
B1+B2	11-12	55	3-4	228.8

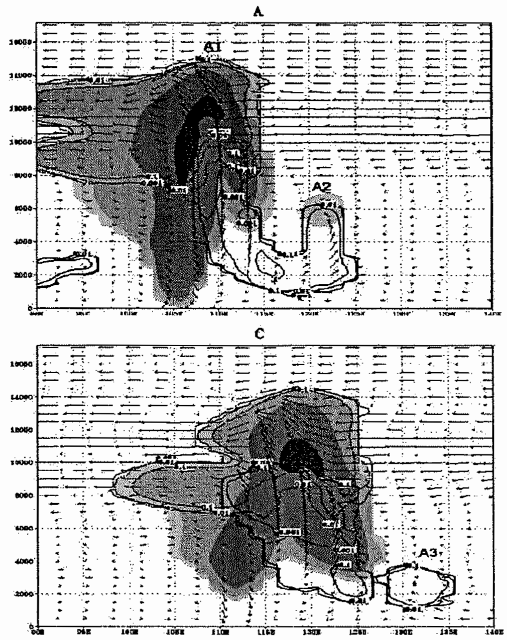

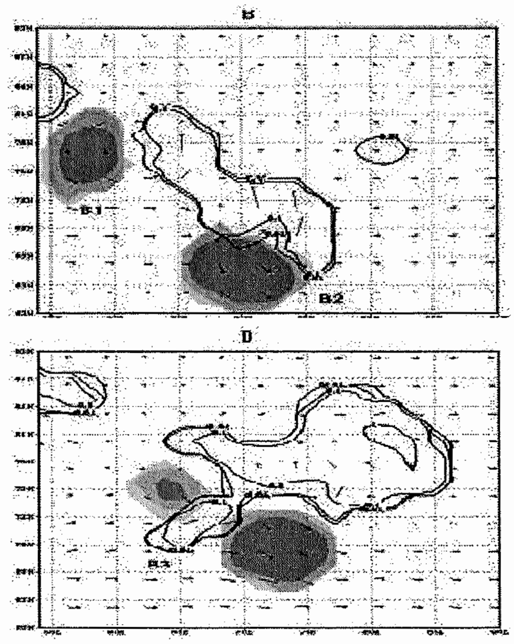

Fig. 4. Vertical cross section in zone A In figs. A and C the shading area represents qr + qh, solid lines qc, dashed lines qi, arrows represent wind velocity
A: zone A at 10200 s of simulation.
C: zone A at 11400 s of simulation

Fig. 5 Horizontal plane in zone B.. In figs. B and D the shading area represents reflectivity and the isolines represent qc.
B: zone B at 10200 s of simulation
D: zone B at 11400 s of simulation

Figures show reflectivity above 10 dBz, which is the lowest value observed in the images. To facilitate the description, cells were labeled as A1 and A2 in case A and B1 and B2 in case B. tables 1 and 2 show some important parameters of simulated and observed clouds. Taking into account the nature of the experiment and that data are derived from radar observations, it may be considered that the agreement Fig. 4-5 show the vertical structure of clouds A1 and A2 at 10200 s. The sum of rainwater and hail contents is represented by shading while cloud water and ice are represented by isolines, continuous and discontinuous respectively. Vectors indicate the components of the wind speed in the X-Z plane. The most developed cloud A1 expanded vertically until 16 km and horizontally until 20 km. A2 appears in the right side of A1 with a weak updraft and a total absence of downdraft; its horizontal width did not exceed 4 km. Both clouds were joined by a bridge of cloud water. Studies of observed cases and numerical simulations have detected this bridge that precedes the merger (Simpson et al, 1980 and Tao and Simpson, 1984). These authors associated this cloud bridge to convergence at the lower levels. This bridge could not be detected in the radar images since it has very low levels of reflectivity. In figure 4C, a single updraft exists accompanied by a maximum of the reflectivity core, confirming that merger has occurred according the criteria of Stalker and Knupp (2003). In low levels, downdrafts predominate and a new cell (A3) appears in the side of A2 favorable to the wind shear.

In case B the appearance of a new cell between B1 and B2 was observed, taking part of the cloud bridge between them. Figure 5 hows this new cell (B3) appearing between the old cells in a horizontal plane. The new updraft formed product of the outflow convergence of the mature cells which incorporated a moister air than the environment, containnig precipitation drops. By this reason, B3 exhibited greater values of reflectivity in its early stage of development, consistent with the observed by Byers and Braham (1949), Goff (1976), among others. In this case, the system resulting from the merger presented characteristics of maturity. The corresponding radar echoes of B3 reached a top height of 6 km, presenting at that moment a relatively high reflectivity maximum of 40 dBz between 3 and 4 km (Fig. 3) Over all, a good correspondence between the general characteristics of simulated clouds and the observed echoes was obtained, although in some cases cloud top heights, cell areas and maximum values of reflectivity were overestimated.

4. EXPERIMENTS WITH A HOMOGENEOUS FIELD AS INPUT DATA

In spite of the fact that in the simulated mergers some characteristic elements show that have been reported both in observational studies and in much more detailed numerical simulations, it is known that fictitious mergers can develop in simulations due to insufficient resolution, depending on the distance between cells and their position with respect to the wind shear. In this case distances were such that no "attraction" due to interaction between cells could exist, so no merger should have taken place in the absence of other local environmental conditions that favored their approximation. As Sim1 was made with a horizontal resolution of 1.5 km it becomes necessary to determine wheter the simulated merger it is due to a real mechanism

To determine whether simulated mergers were an adequate reproduction of reality or a coincidental effect of the coarse resolution, new simulations (**Sim2**) were made keeping the original resolution, soil and orographic data but considering only the horizontally homogeneous field supplied with the sounding. In order to run these simulations, some changes were made to the ARPS source code that allowed the insertion of more than one bubble at start time and the initialization with an external field together with new bubbles. The results of these new runs showed that no merger occurred when the three-dimensional input field was replaced by an initial homogeneous field generated by the sounding data. This endorsed the criterion that mergers were product of the adequate reproduction of the environmental conditions.

Among the main factors that favor the occurrence of merger processes are the position of clouds relative to the wind shear and the horizontal inhomogeneities of the wind field that can produce the approximation of cells. Besides, there are atmospheric factors that can contribute to the horizontal development of individual cells until its approximation, such as moisture. In order to clarify which of these factors could have produced the merger, another simulation (**Sim3**) was made. The sounding used in Sim2 was taken from a meteorological surface station placed at more than 20 km so as the sounding data at the point were cells merged is a weighted combination of the real sounding and the three-dimensional field supplied by MM5, some differences can be expected between the soundings at both points. If the sounding was less favorable for the development of merger conditions this could lead to the no occurrence of merger in Sim2. For this reason Sim3 was initialized with a sounding extracted from the initial three-dimensional field of Sim1 at a point near the place where the merger occurred and all the other parameters as in Sim2.

Despite the homogeneous three-dimensional field in Sim3, merger did occur. This result showed that it is not necessary the presence of the factors associated to the three-dimensional non homogeneous field to produce cell merger. The two main reasons for the occurrence of merger in Sim3 contrary to Sim2 are thought to be that the relative humidity is considerably higher at all levels producing cells with larger and higher cores and a more favorable position of the wind shear relative to the position of cells.

5. REFERENCES

Berry, E. X., 1967: Cloud droplet growth by collection. *J. Atmos. Sci.*, 24, 688-701.

Byers, H. R. and R. R Braham, 1949: The Thunderstorm. U.S. Weather Bur., Washington D. C. 287 pp.

Goff, R. C., 1976. Vertical structure of thunderstorm outflows. *Mon. Wea. Rev.*, 104, 1429-1440.

Kessler, E., 1969: On the distribution and continuity of water substance in atmospheric circulation. *Meteorol. Monogr.* 10.

Kogan, Y. L., and A. Shapiro, 1996: The simulation of a convective cloud in a 3D model with explicit microphysics. Part II: Dynamical and microphysical aspects of cloud merger. *J. Atmos. Sci.,* 53, 17, 2525-2545.

Lin, Y. L., R. D Farley and H. D Orville, 1983: Bulk parameterization of the snow field in a cloud model. *J. Clim. Appl. Meteor.*, 22, 1065-1092.

Orville, H. D., Y-H, Kuo, R. D. Farley, and C. S. Hwang, 1980: Numerical simulation of cloud interactions. *J. Rech. Atmos.,* 14, 499-516.

Simpson, J., N. E., Westcott, R. J. Clerman and R. A. Pielke, 1980: On cumulus mergers. *Arch. Meteor. Geophys. Bioklim.*, 29A, 1-40.

Stalker, J. R., and K. R. Knupp, 2003: Cell merger potential in multicell thunderstorms of weakly sheared environments: Cell separation distance versus planetary boundary layer depth. *Mon. Wea. Rev.,* 131, 1678-1695.

Tao, W. K., and J. Simpson, 1984: Cloud interactions and merging: Numerical simulations. *J. Atmos. Sci.,* 41, 2901-2917.

Tao, W. K., and J. Simpson, 1989: A further study of cumulus interactions and mergers: Three dimensional simulations with trajectory analyses. *J. Atmos. Sci.*, 46, 2974-3004.

Turpeinen, O., 1982: Cloud interactions and merging on day 261 of GATE. *Mon. Wea. Rev.*, 110, 1238-1254.

Xue, M., K. K Droegemeier, V. Wong, A Shapiro, and K. Brewster,,1995: ARPS Version 4.0 user's guide. Center for Analysis and Prediction of Storms, Univ. of Oklahoma, 380 pp. [Available from CAPS, 100 E. Boyd St., Norman, OK 73019.]

MODELING TROPICAL ATMOSPHERIC CONVECTION IN THE CONTEXT OF THE WEAK TEMPERATURE GRADIENT APPROXIMATION

David J. Raymond* and Xiping Zeng

New Mexico Tech, Socorro, NM, USA
Laboratory for Atmospheres, NASA/GSFC, Greenbelt, MD, USA

1 INTRODUCTION

One of the most important unsolved problems in the atmospheric sciences to understand how deep moist convection interacts with the large scale atmospheric circulation, particularly over tropical oceans. Cumulus ensemble models which impose vertical advection equivalent to that observed in some environment are useful for many things. However, they get causality backwards, because in reality vertical motion over tropical oceans is largely a *result* of deep convection, not a cause.

On small scales, various mesoscale dynamic processes such as lifting of surface parcels by gust fronts are the operative mechanisms for releasing conditional instability over tropical oceans. Backing off to larger scales, one more profitably focuses on those mechanisms which produce and maintain the conditional instability in the first place. Foremost among these is the surface flux of moist entropy. This increases with increasing sea surface temperature (SST) and boundary layer wind speed. Thus, strong winds over warm water are likely indicators of strong deep convection.

An additional factor has been uncovered in recent observational and numerical work, namely the humidity of the free troposphere, with higher humidity resulting in more precipitation.

Temperature profiles in the tropics are strongly clamped to a tropics-wide value due to the tendency of gravity waves to disperse buoyancy anomalies over wide regions. Thus, a useful approximation in cumulus ensemble models is to assume that the environmental temperature profile is fixed, or at least approximately fixed. This is the essence of the weak temperature gradient (WTG) approximation of Sobel and Bretherton (2000). A cumulus ensemble model can easily be set up to employ this approximation by relaxing the mean profile in the model to the desired profile.

*Corresponding author address: David J. Raymond, Physics Department and Geophysical Research Center, New Mexico Tech, Socorro, NM 87801, USA; E-Mail: raymond@kestrel.nmt.edu.

In the real world, the net heating due to latent heat release, turbulent fluxes, and radiation results in vertical motion w_D given approximately by

$$w_D = -\frac{\overline{E}_\theta}{\partial\overline{\theta}/\partial z}, \qquad (1)$$

where E_θ is the adiabatic cooling needed to keep the latent heating in the modeled clouds from increasing the environmental temperature, θ is the potential temperature, and the overbar is an average over the horizontal area of the cumulus model. This vertical velocity is responsible, among other things, for the vertical advection of moisture. The quantity E_θ is estimated by a relaxation technique which drives the potential temperature toward an assumed reference profile $\theta_0(z)$:

$$E_\theta = \lambda_t \sin(\pi z/h)[\overline{\theta} - \theta_0(z)], \qquad (2)$$

where λ_t is an assumed relaxation rate and h is the depth of the troposphere. E_θ is assumed to be zero above the tropopause. The sine function makes the relaxation strongest in the mid-troposphere and zero at the surface and the tropopause.

Equation (1) breaks down near the surface due to the generally low static stabilities there. One assumption which fixes this problem is to assume that below some elevation b the vertical velocity tapers linearly to zero from its value at that elevation.

The full treatment of environmental moisture depends on one's assumptions about the environment of the convection. One could, for instance, assume that entrainment from surrounding regions instantly relaxes the cloud environment to the moisture environment of the surroundings. An alternative hypothesis is that the region of convection is extensive enough that surrounding environmental air doesn't penetrate to the region of interest, which means that upward advection results in unchecked moistening of the local environment. An intermediate treatment, which we employ, adds a tendency to the moisture equation of the cumulus ensemble model of the form

$$\left(\frac{\partial \rho r_t}{\partial t}\right)_{env} = -(\overline{r}_t - r_x)\frac{\partial \overline{\rho} w_D}{\partial z} - \overline{\rho} w_D \frac{\partial \overline{r}_t}{\partial z}, \quad (3)$$

where ρ is the air density, r_t is the total advected water (vapor plus advected condensate) mixing ratio, and r_x equals the assumed environmental mixing ratio profile in regions of entrainment ($\partial \overline{\rho} w_D / \partial z > 0$) and $\overline{r}_t$ otherwise. The first term to the right of the equals sign represents lateral entrainment of environmental air into the cumulus ensemble domain, while the second term represents vertical advection of water vapor.

The goal of this study is to determine how convection reacts to varying surface moist entropy fluxes under the WTG approximation. Observational results of Raymond (1995) and Raymond et al. (2003) lead us to believe that the amount of convection and the precipitation rate should be quite sensitive to variations in these fluxes.

2 OUR MODEL

We developed a cumulus ensemble model incorporating the additional WTG terms in the potential temperature and moisture equations represented by equations (2) and (3). The model can be used in two or three-dimensional mode, though we use it exclusively in two-dimensional mode for this work. The computational domain is 50 km by 20 km, with 500 m resolution in the horizontal and 250 m resolution in the vertical. Periodic lateral boundary conditions and a sponge layer above 16 km are imposed. A radiative cooling rate of 2 K d^{-1} is imposed in *equivalent potential temperature* up to 12 km, with a linear taper to zero at 16 km. Model details are available at the web site `http://www.physics.nmt.edu/~raymond/`. See also Raymond and Zeng (2004).

The model was run to radiative-convective equilibrium with the additional terms turned off in an environment with no wind shear, but with a 5 m s^{-1} wind imposed normal to the plane of the two-dimensional calculation. The SST was set at a uniform value of 303 K. The resulting profiles of dry, moist, and saturated moist entropy are shown in figure 1.

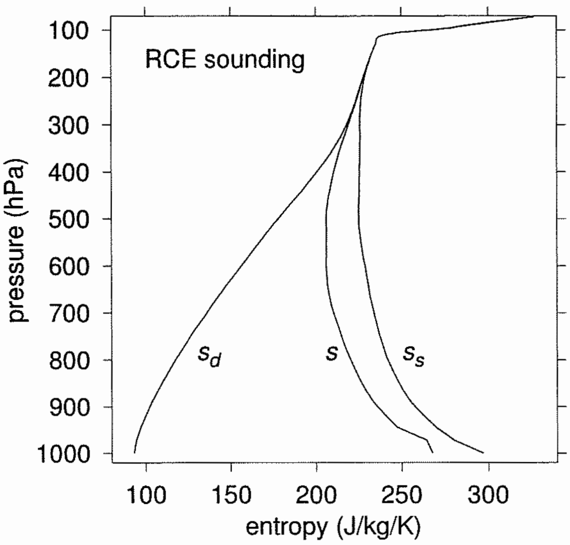

Figure 1: Dry entropy (s_d), moist entropy (s), and saturated moist entropy (s_s) as a function of pressure for radiative-convective equilibrium sounding.

Starting with the above radiative-convective equilibrium profiles, further calculations were done with the WTG terms turned on. We set the temperature relaxation rate to $\lambda_t = 1.5 \times 10^{-4}$ s^{-1} and varied the wind speed imposed normal to the calculation plane between zero and 20 m s^{-1} in order to vary the strength of the surface moist entropy fluxes. The calculations were then allowed to run to statistical equilibrium.

3 RESULTS

Figure 2 shows how the surface moist entropy flux and the mean precipitation rate vary in response to varying imposed wind speeds in the WTG approximation case. The points in this plot result from averages taken after the model reached a state of equilibrium in response to the imposed wind.

Precipitation rate is indeed a strong function of the imposed wind, with wind speeds less than the 5 m s^{-1} value imposed in the radiative-convective equilibrium case yielding essentially zero rainfall. The bottom panel shows that the surface entropy flux is essentially in balance with the radiative loss

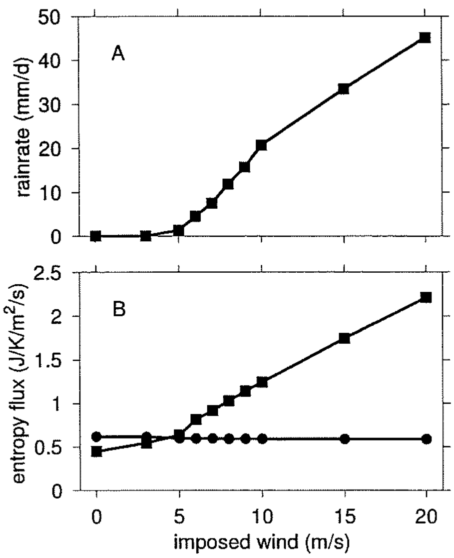

Figure 2: Equilibrium plots of (a) rainfall rate versus imposed wind speed and (b) surface entropy flux (filled boxes) and radiative entropy sink (bullets) as a function of wind speed.

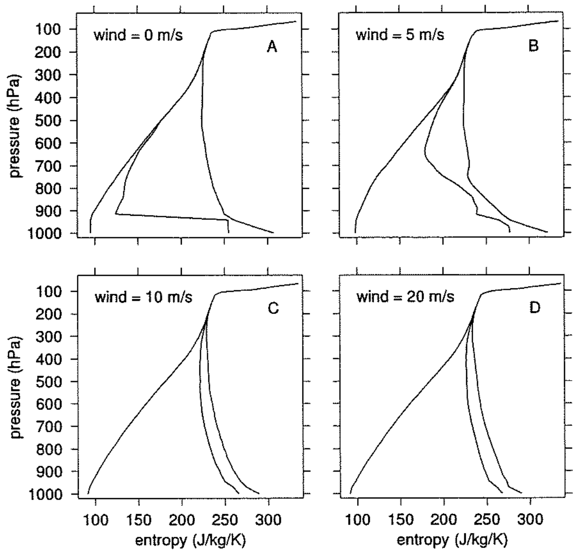

Figure 3: Mean soundings for the last 6 d of four WTG simulations. See figure 1 for meanings of variables.

at 5 m s^{-1}, as it should be in radiative-convective equilibrium.

Figure 3 shows that stronger wind speeds result in in moister soundings. Turning on the WTG terms in the case with at 5 m s^{-1} yields a drier sounding and less precipitation than the corresponding radiative-convective equilibrium case. We believe that this occurs because the WTG calculation, by virtue of the relaxation constraints imposed on the potential temperature and mixing ratio profiles, does not reproduce the full *ensemble* of states occurring in the radiative-convective equilibrium calculation.

The precipitation rate in the model does not adjust instantly to a change in the wind speed. In particular, starting with a dry environment and a high wind speed results in a significant lag in the onset of precipitation as the troposphere moistens. Figure 4 shows the rainfall rate as a function of saturation fraction of the troposphere (precipitable water divided by saturated precipitable water) for transient as well as equilibrium situations. Though not perfect, the precipitation rate appears to be almost uniquely related to the saturation fraction in the troposphere. This suggests that the surface fluxes affect precipitation rate in this model primarily via their indirect effect on the tropospheric humidity, and hence the saturation fraction.

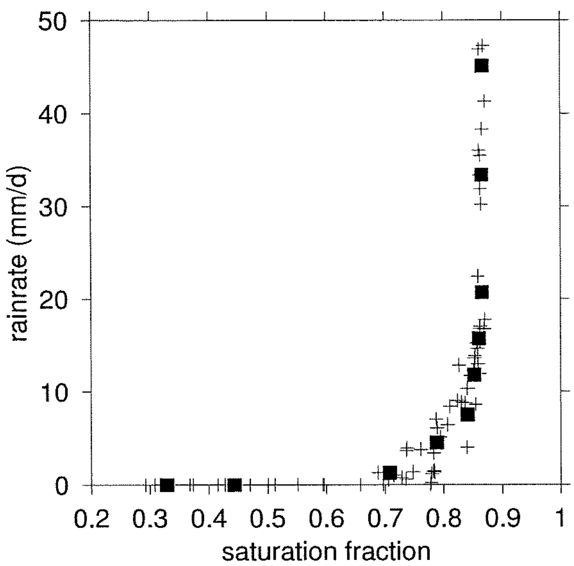

Figure 4: Plot of smoothed rain rate versus smoothed saturation fraction. The filled boxes show the respective values in the WTG equilibrium state for various imposed wind speeds and the pluses show transient values occurring during the relaxation toward equilibrium in the WTG calculations.

4 CONCLUSIONS

In agreement with many recent results, e. g., Sobel et al. (2004), our computations suggest that deep moist convection in the atmosphere is extremely sensitive to tropospheric humidity. If anything, our results show a sensitivity which is even greater than observed. However, these results are for two-dimensional simulated convection in a small domain with no wind shear. It would be surprising if relaxing these constraints did not result in at least some sensitivity to environmental variables besides saturation fraction.

5 ACKNOWLEDGMENTS

This work was supported by U. S. National Science Foundation grant ATM-0079984.

6 REFERENCES

Raymond, D. J., 1995: Regulation of moist convection over the west Pacific warm pool. *J. Atmos. Sci.,* **52,** 3945-3959.

Raymond, D. J., G. B. Raga, C. S. Bretherton, J. Molinari, C. López-Carrillo, and Ž. Fuchs, 2003: Convective forcing in the intertropical convergence zone of the eastern Pacific. *J. Atmos. Sci.,* **60,** 2064-2082.

Raymond, D. J., and X. Zeng, 2004: Modeling tropical atmospheric convection in the context of the weak temperature gradient approximation. *Quart. J. Roy. Meteor. Soc.,* in review.

Sobel, A. H., and C. S. Bretherton, 2000: Modeling tropical precipitation in a single column. *J. Climate,* **13,** 4378-4392.

Sobel, A. H., S. E. Yuter, C. S. Bretherton, and G. N. Kiladis, 2004: Large-scale meteorology and deep convection during TRMM KWAJEX. *Mon. Wea. Rev.,* **132,** 422-444.

NUMERICAL STUDY ON SNOW CLOUD STREETS IN COLD AIR STREAM OVER THE SEA USING THE CLOUD RESOLVING STORM SIMULATOR

Atsushi Sakakibara[1] * and Kazuhisa Tsuboki[2]

[1]Chuden CTI Co., Ltd., Nagoya, 450-0003, Japan

[2] Hydrospheric Atmospheric Research Center, Nagoya University, Nagoya, 464-8601, JAPAN

1. INTRODUCTION

When outbreak of a cold and dry polar airmass occurs over the sea, many cloud streets or cloud bands form in the polar air stream. Large amounts of sensible heat and latent heat are supplied from the sea to the atmosphere. Intense modi?cation of the airmass results in development of the mixing layer and convective clouds develop to form cloud bands along the mean wind direction.

The clouds bands in the cold polar air stream are frequently observed in high latitude. Their length reaches an order of 1000 km while individual bands have a horizontal scale ranging from a few kilometer to a few tens kilometers. Convective cells composing individual bands have a horizontal scale of an order of 10 km. A large computation is, therefore, necessary to perform 3-dimensional simulation of snow cloud bands.

In order to perform simulations and numerical experiments of storms and cloud systems, we have been developing a cloud-resolving numerical model named **"the Cloud Resolving Storm Simulator" (CReSS)**. In the present study, we performed a 3-dimensional simulation using CReSS on the huge parallel computer, Earth Simulator, to study the detailed structure of convective cells and their organized cloud bands or cloud streets developed in cold air streams over the sea.

2. DESCRIPTION OF CReSS

The basic formulation of CReSS is based on the non-hydrostatic and compressible equation system with terrain-following coordinates. Prognostic variables are three-dimensional velocity components, perturbations of pressure and potential temperature, sub-grid scale turbulent kinetic energy (TKE), and cloud physical variables. A ?nite difference method is used for the spatial discretization. The coordinates are rectangular and dependent variables are set on a staggered grid: the Arakawa-C grid in horizontal and the Lorenz grid in vertical. For time integration, the mode-splitting technique is used.

Cloud physical processes are formulated by a bulk method of cold rain, which is based on Lin et al. (1983), Cotton et al. (1986), Murakami (1990), Ikawa and Saito (1991), and Murakami et al. (1994). The bulk parameterization of cold rain considers water vapor, rain, cloud, ice, snow, and graupel. The microphysical processes implemented in the model are described in Fig.1.

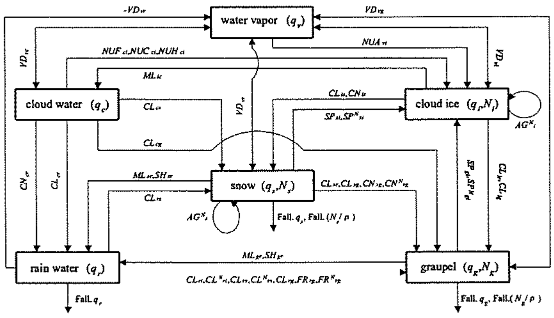

Fig. 1: Diagram describing of water substances and cloud microphysical processes in the bulk scheme of CReSS.

Parameterizations of the sub-grid scale eddy motions in CReSS are one-order closure and the 1.5 order closer with turbulent kinetic energy (TKE). In the latter parameterization, the prognostic equation of TKE is used. CReSS implemented the surface process formulated by a bulk method.

Several types of initial and boundary conditions are available in CReSS. For a numerical experiment, a horizontally uniform initial ?eld provided by a sounding pro?le will be used with an initial disturbance of a thermal bubble or random noise. Boundary conditions are rigid wall, periodic, zero normal-gradient, and wave-radiation type.

CReSS enables to be nested within a coarse-grid model and performs a prediction experiment. In the experiment, initial ?eld is provided by interpolation of grid point values and boundary condition is provided by coarse-grid model. For a computation within a large domain, conformal map projections are available. The projections are the Lambert conformal projection, the polar stereo-graphic projection and the Mercator projection.

For parallel computing of a large computation, CReSS adopts a two dimensional domain decomposition in horizontal (Fig.2). Parallel processing is performed using the Massage Passing Interface (MPI). Communications be-

*Corresponding author's address: Atsushi Sakakibara, Chuden CTI Co.,Ltd., Meieki-Minami, Nakamura-ku, Nagoya, 450-0003, Japan;
E-mail: Sakakibara.Atsushi@cti.co.jp.

tween the individual processing elements (PEs) are performed by data exchange of the outermost two grids. The OpenMP is optionally available.

The readers can ?nd the more detailed description of CReSS in Tsuboki and Sakakibara (2001) or Tsuboki and Sakakibara (2002).

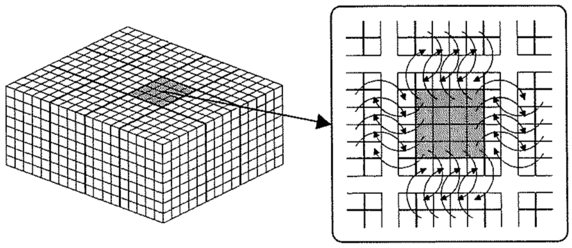

Fig. 2: Schematic representation of the two-dimensional domain decomposition and the communication strategy for the parallel computing.

3. OPTIMIZATION FOR EARTH SIMULATOR

Since the CReSS model is originally designed for parallel computers, no essential modi?cation of the code was necessary to be optimized for Earth Simulator. We, however, updated CReSS from the code of Fortran 77 to Fortran 90. Communication procedures between nodes using MPI were also improved to be more ef?ciently. For the intra-node parallel processing, the OpenMP was introduced.

We evaluated the performance of CReSS on Earth Simulator. The result is summarized in Table 1. The parallel operation ratio was measured using 128 nodes (1024 CPUs) and 64 nodes (512 CPUs) of Earth Simulator.

Table 1: Evaluation of the performance of CReSS on Earth Simulator.

Vector Operation Ratio	99.4 %
Parallel Operation Ratio	99.985 %
Node number to use	128 nodes
Parallel ef?ciency	86.5 %
Sustained ef?ciency	33 %

After the performance test of CReSS, we performed the simulation experiment of snow cloud bands in the cold air stream.

4. EXPERIMENTAL DESIGN

The design for the experiment is summarized in Table 2. The initial condition was provided by a sounding observed on the east coast of Canada at 06 UTC, 8 February 1997.

The calculation domain in this simulation is 457 km and 153 km in x- and y-directions, respectively with a horizontal grid spacing of 300 m. Sea ice is placed on the upstream side. Each grid is occupied by ice or open sea according to the probability of sea ice or sea ice density. According to the sea-ice density χ, an index $\bar{\chi}$ is de?ned as follows which determines each grid is covered with sea ice or is water surface.

Table 2: Experimental design of the snow cloud bands in the cold air stream.

domain	x 457 km, y 153 km, z 11 km
grid number	x 1527, y 515, z 73
grid size	H 300 m, V 50 ~150 m
integration time	20 hrs
node number	32 nodes (256 CPUs)

$$\bar{\chi} = \begin{cases} 1, & Rn/10 < \chi \\ 0, & Rn/10 \geq \chi \end{cases} \tag{1}$$

where Rn is a uniform random number of a single digit $0 \sim 9$. If $\bar{\chi} = 0$, then, the gird is the water surface, if $\bar{\chi} = 1$, it is covered with sea ice completely. Using the index $\bar{\chi}$, albedo, roughness length and evapotranspiration ef?ciency of the grid will be determined at each grid.

In the experiment of the preset study, the probability or density of sea ice is 100 % for $x = 0 - 30$ km and decreases linearly to 0 % at $x = 130$ km and open sea of 1°C extends for $x = 130 - 457$ km (Fig.3). Since the surface is not uniform, no initial disturbance is necessary. The sounding of a cold air outbreak is used for the horizontally uniform initial condition.

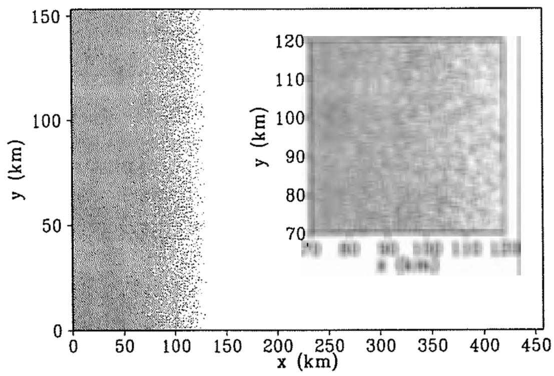

Fig. 3: Model domain and sea ice distribution. The marginal sea ice region is enlarged within the ?gure. Shadings indicate sea ice and no shading regions are open sea.

5. RESULTS

When the dry continental air ?ows over sea, a mixing layer develops in the lower atmosphere owing to large amounts of latent and sensible heat ?ux from the sea. The vertical cross sections along the basic ?ow show the modi?cation of the cold air and development of the mixing layer (Fig.4).

The atmosphere over the packed ice is stably strati-

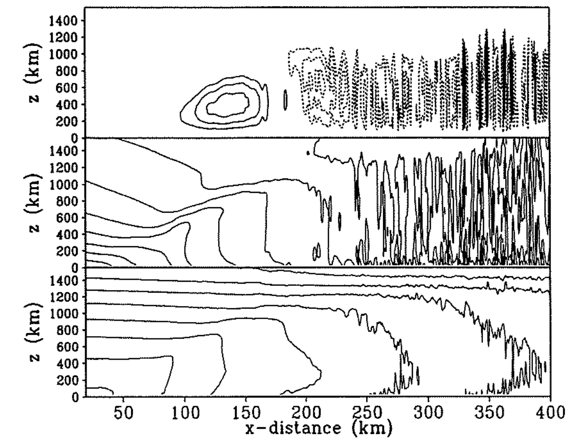

Fig. 4: Vertical cross sections of vertical velocity (upper panel), x-component of horizontal velocity (middle panel) and potential temperature (lower panel).

?ed and the vertical shear is large. Vertical gradient of the potential temperature becomes small with the distance from the edge of the packed ice. Vertical shear also decreases with the distance and it almost vanishes on the downstream side of x=200 km. These indicate that intense vertical mixing occurs over the sea. Vertical motion is uniformly upward for x=100–170 km while it is highly ?uctuating to the downstream of x=170 km. These show the development of the mixing layer.

The cloud bands develop within the mixing layer. Figure 5 shows formation and development of cloud bands over the sea. They begin to form the region of sea ice density of 50−70 % and intensify with a distance and with time. A large number of cloud bands form on the upstream side. Some cloud bands merge each other and selectively develop. Consequently, the number of lines decreases with the distance along the basic ?ow.

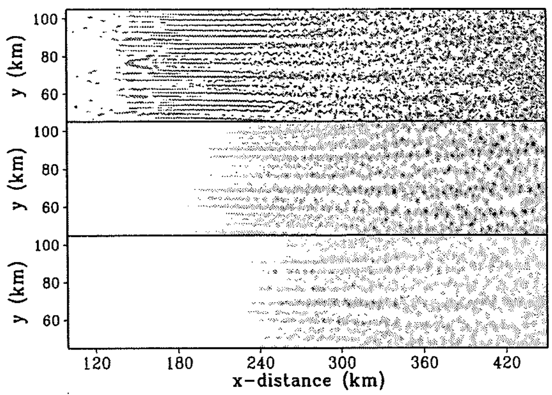

Fig. 5: Horizontal cross sections of vertical velocity (upper panel), mixing ratio of precipitation (snow, graupel and rain) (middle panel) at 1000 m in height and mixing ratio of cloud ice at 1300 m in height (lower panel) for x=100–450 km.

Close view of the upstream region (Fig.6) shows upward and downward motions are almost uniform in the x-direction. As a result, cloud ice and precipitation extend in the x-direction uniformly. This indicates that the convections are the roll convection type in the upstream region.

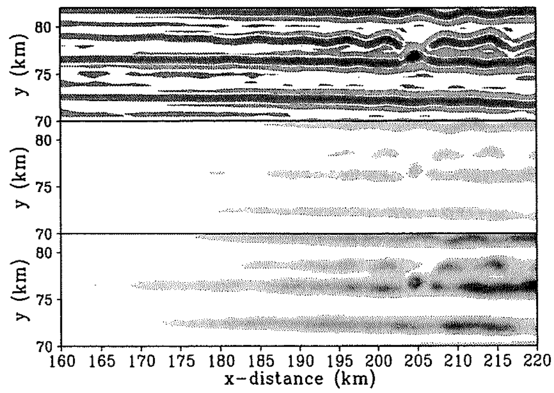

Fig. 6: Horizontal cross sections of vertical velocity (upper panel), mixing ratio of precipitation (middle panel) at 900 m in height and mixing ratio of cloud ice at 1100 m in height (lower panel) for x=160–220 km.

The vertical cross section normal to cloud bands (Fig.7) shows that the roll convections form regularly in y-direction. Clouds form in the upper part of upward motions. Cloud ice (bottom panel) spreads from the top of upward motions and is lifted downward by the downward motions. As a result, it shows a bow shape.

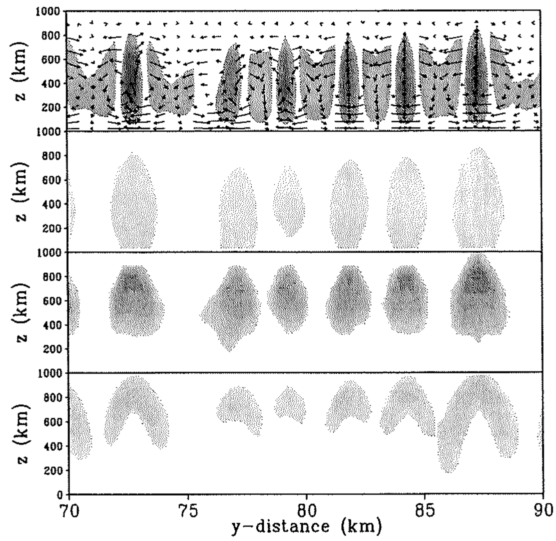

Fig. 7: Vertical cross sections normal to the cloud bands at x= 140 km of vertical velocity (top panel), mixing ratio of graupel (second panel), cloud water (third panel) and cloud ice (bottom panel).

In the downstream region, the roll convections change to alignment of cellular convections (Fig.8). While the upward motions are centered and downward motions are located on their both side, cloud and precipitation show cellular pattern. In this region, the mixing layer fully developed and the vertical shear almost vanishes in the mixing layer.

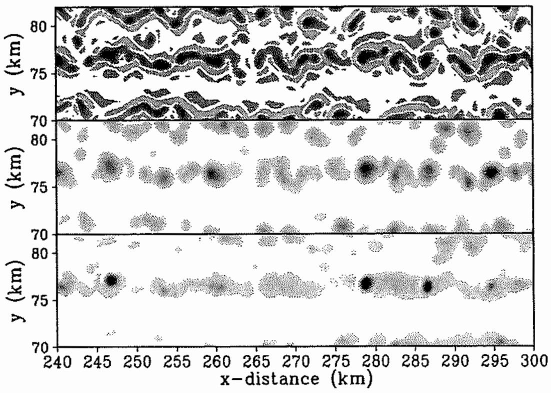

Fig. 8: Horizontal cross sections of vertical velocity (upper panel), mixing ratio of precipitation (middle panel) at 1000 m in height and mixing ratio of cloud ice at 1300 m in height (lower panel) for x=240–300 km.

Vertical cross sections around the region (Fig.9) show that convections develop to the height of 1400 m and precipitation intensi?es. The distance between the cloud bands becomes large and non-uniform, and different development stages of convective cells are present simultaneously. Cloud ice and cloud water extend widely in the upper level of convection.

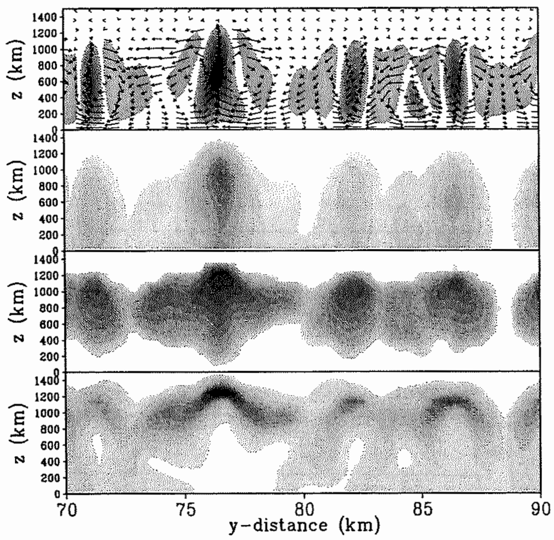

Fig. 9: As in Fig.7, but for x=240 km.

In the region of far downstream, convections change to randomly distributed cells (Fig.10). Band shape of cloud almost disappears and convections become closed cell type. The morphological transformation from alignment of cells to random cells is often observed by satellite. The morphological transformation of clouds in the numerical experiment successfully simulates that of observed cloud bands.

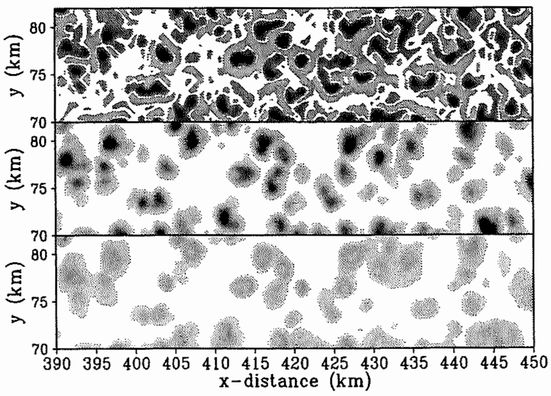

Fig. 10: As in Fig.8, but for x=390–450 km.

6. SUMMARY

The experiment showed formation and development of cloud bands or cloud streets developed over the sea. They begin to form the point of sea ice density of 50–70 % and intensify with a distance and with time. The morphology of convection in the cloud bands changes with the distance along the stream. The cloud bands are roll convections in the upstream region. Then, they change into lines of cellular convections. Finally they become randomly distributed convective cells in the far downstream region. The formation process of the cloud bands, their extension and merging are successfully simulated in the experiment using CReSS.

References

Cotton, W. R., G. J. Tripoli, R. M. Rauber and E. A. Mulvihill, 1986: Numerical simulation of the effects of varying ice crystal nucleation rates and aggregation processes on orographic snowfall. *J. Climate Appl. Meteor.*, **25**, 1658–1680.

Ikawa, M. and K. Saito, 1991: Description of a nonhydrostatic model developed at the Forecast Research Department of the MRI. *Technical Report of the MRI*, **28**, 238pp.

Lin, Y. L., R. D. Farley and H. D. Orville, 1983: Bulk parameterization of the snow ?eld in a cloud model. *J. Climate Appl. Meteor.*, **22**, 1065–1092.

Murakami, M., 1990: Numerical modeling of dynamical and microphysical evolution of an isolated convective cloud — The 19 July 1981 CCOPE cloud. *J. Meteor. Soc. Japan*, **68**, 107–128.

Murakami, M., T. L. Clark and W. D. Hall 1994: Numerical simulations of convective snow clouds over the Sea of Japan; Two-dimensional simulations of mixed layer development and convective snow cloud formation. *J. Meteor. Soc. Japan*, **72**, 43–62.

Tsuboki, K. and A. Sakakibara 2001: CReSS User's Guide 2nd Edition.

Tsuboki, K. and A. Sakakibara, 2002: Large-scale parallel computing of Cloud Resolving Storm Simulator. *High Performance Computing, Springer*, H. P. Zima et al. Eds, 243–259.

Radiative and Microphysical Properties of Mixed-Phase Altocumulus: A Model Evaluation of Supercooling Effects

Kenneth Sassen[1] and Vitaly I. Khvorostyanov[2]

[1] Geophysical Institute, University of Alaska Fairbanks, Fairbanks, AK, USA

[2] Central Aerological Observatory, Moscow, Russian Federation

Using a cloud model with explicit microphysics and radiation, we evaluate the changes in mixed phase clouds caused by increasing ice content until glaciation occurs. The properties of the ice and water particle constituents are resolved independently, revealing the relative radiative contributions from the water phase source cloud versus the ice phase virga. Cloud contents are also converted to remote sensing variables to shed light on the ability of radar/lidar and passive measurements to study these ubiquitous clouds.

1. Introduction

The genera of altocumulus (Ac) clouds are typically thin, water-dominated cloud layers that occur at middle levels in the troposphere in all climatic regimes of our planet. Visually, they can be opaque or semi-transparent to sunlight (Gedzelman 1988). In the infrared, although their emittances depend on temperature, thin AC layers on the order of a few hundred meters will, like cirrus, behave as gray bodies (Sassen et al. 2001). Because of their basic mixed-phase nature, Ac frequently generate ice crystal virga that trails below the supercooled source cloud. Much of what is known of the microphysical composition and thermodynamics of Ac clouds has come from a limited number of research aircraft missions (e.g., Heymsfield et al. 1991; Fleishauer et al. 2002), and from ground-based polarization lidar (Sassen 1991; Demoz et al. 2000; Sassen et al. 2003) and lidar-radiometer (Wang et al. 2003) studies.

Since Ac tend to be relatively optically thin, they are difficult to detect through satellite radiance methods (Sun 2003). Cloud radar probing has difficulties detecting the cloud droplets in Ac, although the larger ice crystals in mixed clouds are easily detected. Importantly, it is uncertain how their radiative properties depend on the relative ice and water contents, and thus, how Ac altered by human-induced changes in cloud-forming particles may affect climate. In this work we use results from a sophisticated cloud model to begin investigating these issues.

2. Model description and initialization

The cloud model used in this study includes explicit bin microphysics for both liquid and crystalline phases with 30 size classes for each phase, along with the supersaturation equation (Khvorostyanov, 1995, Khvorostyanov and Sassen, 1998; 2002; Khvorostyanov et al. 2001, 2003). The model contains six basic units: 1) dynamics (hydrostatic or non-hydrostatic); 2) cloud microphysics (kinetic equations for the droplet and crystal size spectra); 3) thermodynamics (temperature, humidity and supersaturation); 4) aerosols, including transport, deliquescence of the aerosol and nucleation of the liquid and ice phases; 5) longwave and shortwave radiation; and 6) heat and moisture exchange with the underlying surface.

The model can be configured as 1D, 2D or 3D. For this study of Ac clouds, we used the 2D and 1D (single-column) versions of the model in the following manner. First, the 2D simulations of the mixed-phase Ac with 128 horizontal grid points and 61 vertical grid points were performed under various conditions, and sensitivity of the horizontally averaged cloud properties to the input parameters was studied. Then the 1D model was tuned so that it was able to reproduce these averaged profiles and was configured so that the main computational domain from 5 to 8 km in vertical contained 61 vertical steps by 50 m. For radiative calculations, we used the additional 7 levels below the main domain (0 - 5 km) and 9 levels above (8 - 24 km). This 1D (single-column) configuration allowed fast calculation of Ac properties under variable initial conditions.

The situation simulated correspond to some extent to the observations of Ac in July 2002 during CRYSTAL-FACE campaign (Sassen et al. 2003). Although the simulations are based mostly on generic initial conditions, we used the initial temperature profile close to sounding data on 13 July 2002 at 2044 UT, with the temperature of -12.3°C in the middle of the future liquid Ac at a height of ~6.8 km. This is denoted further as "-00", and the temperature effects on Ac phase state were studied by the shift of the entire T-profile to the lower temperatures by 7°, 12° and 18°C, with the corresponding notations further.

The cloud was initiated by imposing a parabolic profile of the vertical velocity w (the source of cooling) in the layer 6.4-6.9 km with a maximum of 12 cm s^{-1} in the middle, which is comparable to the w used in simulation of Ac in Heymsfield et al. (1991). The initial relative humidity with respect to water (RHW) was chosen 60 and 50 % below and above this layer and 98 % inside it. Since Ac clouds often form with the advection of humidity, this process was parameterized also with a parabolic profile for the advection rate of specific humidity in the same layer with a maxima comparable to the values simulated by ECMWF model for the SHEBA case 8 July 1998, when an As cloud was observed. These advection rates allowed simulating this As with a single-column version of the model (Khvorostyanov et al. 2001) and appeared to be sufficient for the maintenance of Ac in this work.

The drop nucleation was parameterized here as in Khvorostyanov et al. (2001). This model includes several schemes of ice nucleation (e.g., homogeneous nucleation from Khvorostyanov and Sassen, 1998, 2002; heterogeneous nucleation from Khvorostyanov and Curry, 2000, 2003), which allows their comparison. For this work, ice formation was assumed to be heterogeneous (occurring on IN) and was calculated using the simple parameterization from Meyers et al. (1992).

The SW fluxes and heating rates were calculated for a midlatitude location (40.8 N) in mid-April.

3. Cloud microstructure

The model runs were performed to 1-h, after which time the cloud approaches a quasi-steady state in agreement with Starr and Cox (1985). Figures 1 and 2 depict vertical profiles of the cloud microstructure that illustrate the effects of the gradual cloud glaciation to be expected with decreasing temperature.

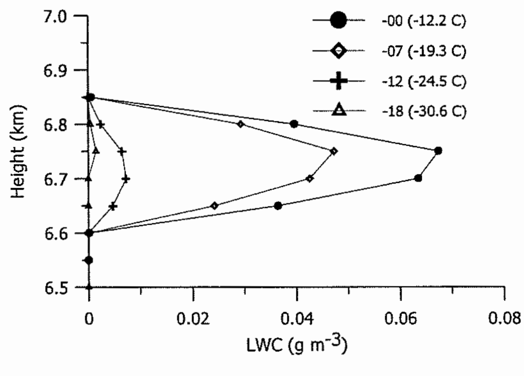

Figure 1. Vertical profiles of liquid water content (LWC) as a function of temperature. Temperatures in parentheses give the actual cloud base temperatures.

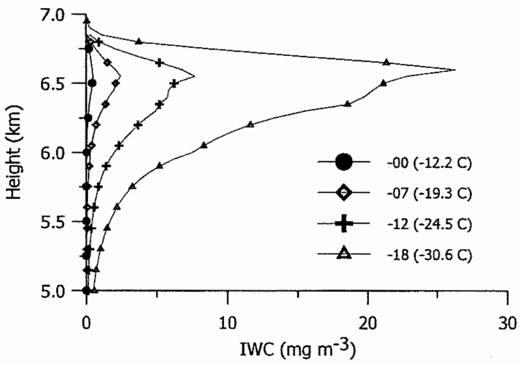

Figure 2. Vertical profiles of ice water content as a function of temperature, as in Figure 1.

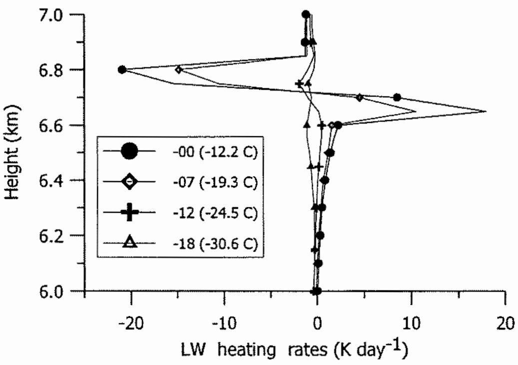

Figure 3. Effect of temperature and cloud glaciation on the longwave heating rates in Ac with the microphysics profiles shown in Figures 1 and 2.

Comparison of the liquid and ice water contents shows that with decreasing cloud temperature the liquid phase suffers from the more significant ice water production, in keeping with the workings of the Wegener-Bergeron-Findeison mechanism. The corresponding maximum mean droplet radii (not shown) near cloud top decrease from ~6 μm to 2 μm as the temperature decreases. In comparison, the maximum ice crystal mean radii in the supercooled liquid cloud vary from ~70 μm to 50 μm.

In terms of how these microphysical contents affect Ac remote sensing with radar, computed radar reflectivity factors (Z) are in compliance with expectations based on earlier parcel modeling and millimeter-wave radar field studies. That is, the Z from the ice content of mixed phase clouds is typically significantly greater than that from the much smaller (but far more numerous) cloud droplets because of the importance of the sixth moment of the size distribution in determining Z. For example, for the –19.2°C liquid cloud base simulation, the maximum radar reflectivities are –4 dBZ from the crystals compared to –30 dBZ from the droplets.

Ultimately, we are interested in converting the model results to the radiative impact as supercooled clouds evolve toward glaciation. For example, we provide in Figure 3 the variations in longwave heating rates related to increasing (decreasing) ice (water) content in mixed phase clouds. It is clear that the infrared heating at cloud base and cooling at cloud top is far stronger when cloud droplets dominate the radiative transfer process. Similar results are found in terms of the net (solar plus infrared) heating rate, which is in agreement with results simulating the insertion of a narrow supercooled liquid cloud at the base of a cirrus cloud (Sassen et al. 1985).

4. Conclusions

We have performed numerical experiments to simulate how the microphysical contents of supercooled altocumulus clouds change with increasing ice content. These results are applied to examining how remote sensing observations respond to these variations, and assessing the radiative transfer impacts in terms of heating rates. Because the total cloud radiative impacts decrease as clouds glaciate, indirect cloud effects caused by increased ice formation from enhanced ice nuclei can have significant climate effects.

This research has been supported by NASA grant NAS-71407 from the CloudSat program.

References

Demoz, B., D. O'C. Starr, D. Whiteman, K. Evans, D. Hlavka, and R. Peravali, 2000: Raman lidar detection of cloud base. *Geophys. Res. Lett.*, **27**, 1899-2002.

Fleishauer, R. P., V. E. Larson, and T. H. Vonder Haar, 2002: Observed microphysical structure of midlevel, mixed-phase clouds. *J. Atmos. Sci.*, **59**, 1779-1804.

Gedzelman, S. D., 1988: In praise of altocumulus. *Weatherwise*, **41**, 143-149.

Heymsfield, A. J., L. M. Miloshevich, A. Slingo, K. Sassen, and D. O'C. Starr, 1991: An observational and theoretical study of highly supercooled altocumulus. *J. Atmos. Sci.*, **48**, 923-945.

Khvorostyanov, V., I. and K. Sassen, 1998: Towards the theory of homogeneous nucleation and its parameterization for cloud models. *Geophys. Res. Lett.*, **25**, 3155-3158.

Khvorostyanov, V. I., and K. Sassen, 1998: Cirrus cloud simulation using explicit microphysics and radiation. Part I: Model description, and Part II: Microphysics, vapor and ice mass budgets, and optical and radiative properties. *J. Atmos. Sci.*, **55**, 1808-1821, and 1822-1845.

Khvorostyanov, V. I., and J. A. Curry, 2000: A new theory of heterogeneous ice nucleation for application in cloud and climate models. *Geophys. Res. Lett.*, **27**, 4081-4084.

Khvorostyanov, V. I., J. A. Curry, J. O. Pinto, M. Shupe, P. Lawson, and K. Sassen, 2001: Modeling with explicit spectral water and ice microphysics of a two-layer cloud system of altostratus and cirrus observed during the FIRE Arctic Clouds Experiment. *J. Geophys. Res.,* **106**, 15099-15112.

Khvorostyanov, V. I., and K. Sassen, 2002: Microphysical processes in cirrus and their impact on radiation: a mesoscale modeling perspective. In: *"Cirrus",* Oxford, D. Lynch et al., Eds, pp. 397-432.

Meyers, P. J., P. J. DeMott, and W. R. Cotton, 1992: New primary ice-nucleation parameterizations in an explicit cloud model. *J. Appl. Meteor.*, **31**, 708-721.

Sassen, K., 1991: Aircraft produced ice particles in a highly supercooled altocumulus cloud. *J. Appl. Meteor.*, **30**, 765-775.

Sassen, K., K. N. Liou, S. Kinne, and M. Griffin, 1985: Highly super-cooled cirrus cloud water: Confirmation and climatic implications. *Science*, **227**, 411-413.

Sassen, K., J. M. Comstock, and Z. Wang, 2001: Parameterization of the radiative properties of midlatitude high and middle level clouds. *Geophys. Res. Lett.*, **28**, 729-732.

Sassen, K., P. J. DeMott, J. M. Prospero, and M. R. Poellot, 2003. Saharan dust storms and indirect aerosol effects on clouds: CRYSTAL-FACE results. *Geophys. Res. Lett.*, **30**, doi:10.1029/2003GL 017371.

Starr, D. O'C., and S. K. Cox, 1985: Cirrus clouds. Part I: A cirrus cloud model. J. *Atmos. Sci.*, **42**, 2663-2681.

Wang, Z., K. Sassen, D. Whiteman, and B. Demoz, 2004: Studying altocumulus with ice virga using ground-based active and passive remote sensors. *J. Appl. Meteor.*, **43**, (in press).

ON THE DEPENDENCY OF PRECIPITATION FROM MIXED-PHASE CONVECTIVE STORMS ON VERTICAL WIND SHEAR, BUOYANCY AND CLOUD CONDENSATION NUCLEI

AXEL SEIFERT[1] AND KLAUS D. BEHENG[2]

[1]National Center for Atmospheric Research, Boulder, CO, USA

[2]Institut für Meteorologie und Klimaforschung, Universität/Forschungszentrum Karlsruhe, Germany

1 Introduction

More than 20 years ago Weisman and Klemp (1982) published their now classic study on numerically simulated convective storms. Today, the numerical simulation of these convective phenomena, especially when considering the various highly non-linear cloud microphysical processes, is still a challenge for state-of-the-art atmospheric models and one of the unsolved problems in quantitative precipitation forecast. In addition, recent observations have shown evidence that atmospheric aerosols affect the precipitation formation in convective systems (Rosenfeld 2000). Therefore the dependency of convective storms on buoyancy and wind shear is revisited, but now adding ambient atmospheric aerosol characteristics as third external factor. Following Weisman and Klemp the environmental conditions like buoyancy and vertical wind shear are varied to simulate different storm types like ordinary single cells, multicells and supercells. The aerosol characteristics are taken into account in form of different relations between activated cloud condensation nuclei (CCN) and supersaturation, ranging from maritime to continental conditions. Thus, this study serves, on one hand, for investigating aerosol effects on the storms' dynamics and, on the other hand, to related effects on precipitation evolution.

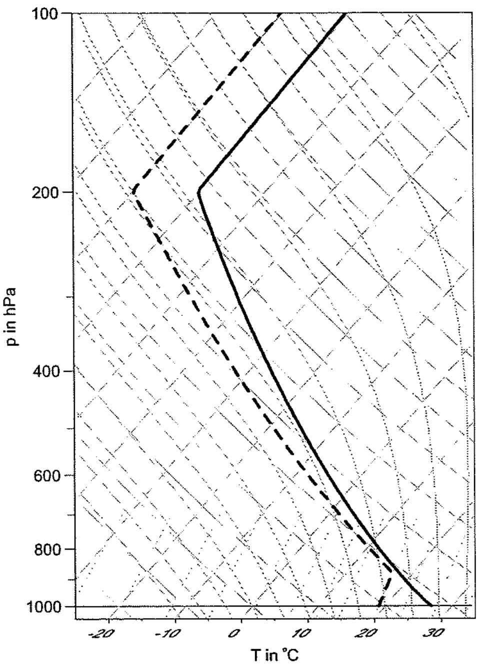

Figure 1: Skew-T-log-p diagram of temperature and dew point pro?les used in the numerical experiments (here with $q_{v0} = 14$ g/kg).

2 Model and experiment description

The 3-dimensional compressible version of the Karlsruhe Mesoscale Model (KAMM2) has been used in a cloud resolving mode, i.e. with a horizontal grid resolution of 1 km, to simulate the evolution of individual storms in detail. To represent the cloud microphysics a novel two-moment scheme has been applied which includes an explicit treatment of cloud droplet nucleation and full mixed-phase microphysics of cloud droplets, raindrops, cloud ice, snow and graupel (Seifert and Beheng 2004). An important ingredient is the autoconversion scheme of Seifert and Beheng (2001). Moreover, in order to predict the number concentration of cloud droplets, an empirical activation relation is applied parameterizing the number of activated nuclei N_{ccn} as a

Corresponding author's address: Axel Seifert, National Center for Atmospheric Research; P.O. Box 3000 Boulder, CO 80307, E-Mail: seifert@ucar.edu. NCAR is sponsored by the National Science Foundation.

function of the supersaturation S. For continental CCN $N_{ccn}(S) = CS^{\kappa}$ with $C = 1260$ cm^{-1}, $k = 0.308$ is assumed, while maritime CCN are described by the parameters $C = 100$ cm^{-1}, $k = 0.462$. To allow a continuous transition between these extreme CCN spectra a linear interpolation of C and κ is performed as a function of a dimensionless continentality parameter α_{CCN} (maritime: $\alpha_{CCN} = 0$; continental: $\alpha_{CCN} = 1$).

The initial conditions used for all simulations are the same as suggested by Weisman and Klemp (1982). An example of an idealized sounding for a boundary layer water vapor mixing ratio of $q_{v0} = 14$ g/kg is shown in Fig. 1. The initial wind pro?le is given by $u = u_{\infty} \tanh(z/z_s)$ with $z_s = 3$ km. Convection is initiated by a 2 K warm bubble of 10 km radius.

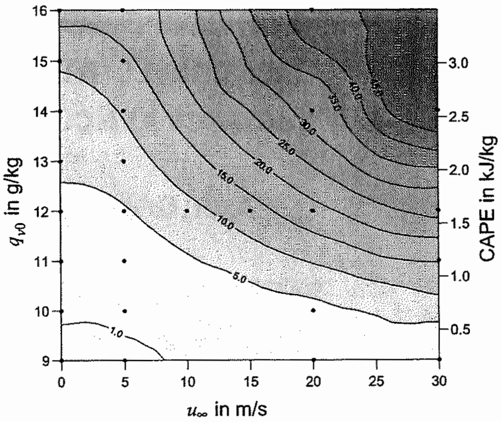

Figure 2: Total accumulated precipitation in 10^6 m^3 for maritime CCN as function of CAPE and wind shear. Black dots indicate simulations performed for this study.

3 Results

The ?ndings of Weisman and Klemp (1982) can be summarized as follows: Increasing buoyancy (or CAPE) leads to more vigorous convection, higher vertical velocities and the formation of secondary convective cells, i.e. multicell formation. Higher wind shear leads to an increased vorticity of the storm's dynamics due to the twisting effect. In general, this results in a longer lifetime of the convective updraft and the individual storm. Strong wind shear induces a pair of quasi-stationary supercells.

These overall ?ndings could be reproduced by our simulations although application of KAMM2 produced slightly weaker updrafts. Further differences depend on the application of the various nucleation modes used.

As the main aim of this study is on elucidating aerosol effects on precipitation evolving under very different convective situations, the following discussions mostly concentrate on comparisons of precipitation amounts varying in effect of changing ambient conditions.

Figure 2 shows the sensitivity of the total domain integrated, 3h-accumulated precipitation amount to changes in buoyancy and wind shear for maritime CCN (the size of model domain was chosen large enough to include all storms completely). Obviously, the total precipitation increases with CAPE and wind shear, as described above both leading to more intense convective systems. The strongest precipitation (exceeding 45 million m^3) occurs when high CAPE is combined with strong shear leading to the formation of multicell systems with embedded supercell storms.

The relative change of the total precipitation for continental CCN (vs maritime) is presented in Fig. 3a. For weak ordinary cells developing at a CAPE below 1500 J/kg we ?nd a reduction of the surface precipitation by some 20 percent. This is caused by the slower coalescence process of the smaller cloud droplets resulting in the formation of fewer and smaller raindrops. Therefore a large amount of supercooled water ends up in higher levels and forms small ice particles which do not contribute to surface precipitation. In case of supercell storms (strong wind shear together with intermediate or high CAPE) the precipitation formation becomes more or less independent from the CCN assumption. To some extent this might be caused by a recirculation of small precipitation sized particles into the updraft region. An unexpected effect is found for multicell systems at high CAPE, low shear condition: In this part of the parameter space the continental storms produce more precipitation as their maritime counterparts, thus revealing an inverse CCN effect. Since the increase of precipitation is strong, exceeding a factor of two for some cases, the reasons cannot be found in the microphysics alone.

An effect of CCN on the cloud dynamics, especially for multicell storms, is obvious from Fig. 3b showing the difference of the maximum updraft velocities in the parameter space. Again different regimes are found for ordinary single cells and supercells in contrast to multicells: Ordinary cells show a negative aerosol effect and the strongest reduction of vertical wind speed for low CAPE, while for multicells the continental aerosol leads to higher updraft velocities showing a maximum (at $q_{v0} = 14$ g/kg) exactly where the relative change in precipitation due to aerosol attains also a maximum (cf. Fig. 3a).

As mentioned above, microphysical reasons alone cannot be responsible for the unexpected precipitation features of multicells storms. In anticipation it can be stated that the effects of CCN characteristics on the dynamics can to a certain degree be explained by a different amount and vertical distribution of the latent heat release by freezing, e.g., of liquid drops to ice. Assuming maritime aerosol precipitation is effectively produced at subfreezing levels (and rains out) such that less wa-

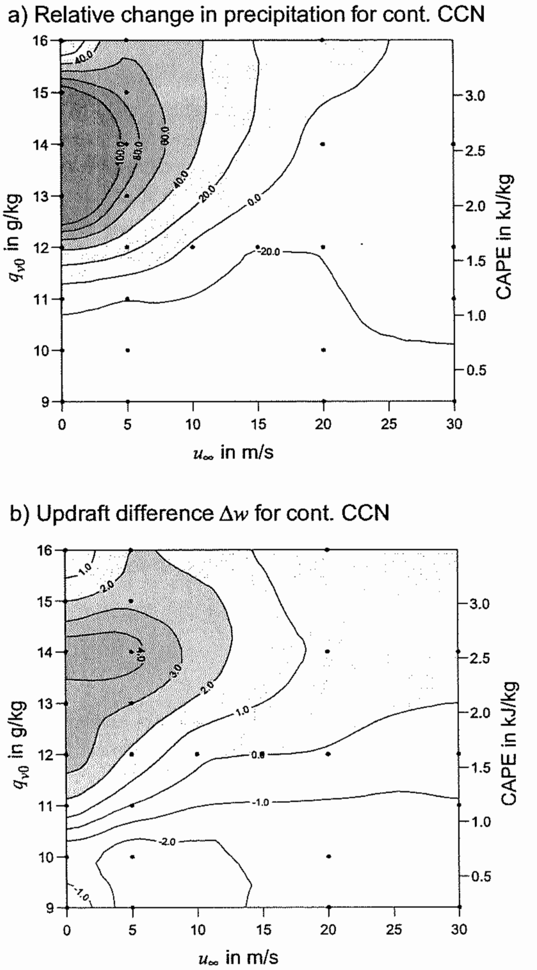

Figure 3: Relative change in total accumulated precipitation in % (a) as well as difference of maximum updraft velocities in m/s (b) between continental and maritime CCNs as a function of buoyancy and vertical wind shear (see text for details).

ter reaches the freezing level, while for a continental aerosol almost all particles are transported beyond the freezing level where they turn to ice, at least temporarily. Thus, assuming continental CCN the amount of latent heat released by freezing is larger and shifted to higher levels. This effect easily explains the higher updraft velocities in continental clouds for high CAPE, and it may also be the reason the higher updraft velocities found in small maritime clouds compared to their continental counterparts, since for small maritime clouds the release of latent heat at lower levels boosts the dynamics more ef?ciently. In other words, in small continental clouds many particles freeze above the level of the maximum updraft, so that a large part of the latent heat release does not contribute to an increase of the maximum updraft velocity, but only has an effect on the dynamics at higher levels as, e.g., by triggering gravity waves. For high CAPE, i.e. strong multicell convection, the additional latent heat release, which is typical for continental CCN, can contribute to the maximum updraft velocity, since maximum updraft speed is attained at higher levels compared to the low CAPE ordinary cells. In addition, cloud water content is much higher leading to a faster formation of raindrops compared to the smaller clouds and consequently these raindrops freeze at lower levels compared to cloud droplets. For very high CAPE the difference between the effects of maritime and continental CCN decreases, since for this condition very high cloud water contents lead to a rapid rain formation even for continental CCN. The abovementioned hypotheses, namely that the vertical distribution of the latent heat release is important, might therefore also explain the maximum of the increase of the updraft velocity found in the present study for a mixing ratio of 14 g/kg.

To support this explanation of the CCN effects on cloud dynamics several simulations have been performed arti?cially turning off latent heat release of freezing and/or melting. These experiments revealed that the decrease of the maximum updraft velocity for the continental ordinary cells (at low CAPE) is caused by the different vertical distribution of latent heat of freezing, while the effects on the amount of precipitation are in fact independent for the latent heat of freezing and therefore based on 'purely' microphysical reasons. The multicell regime is more complicated insofar as both freezing and melting, and consequently the according latent heat releases, are very important for the dynamics of the cloud system. Turning off both latent heat effects makes the difference between continental and maritime aerosol vanish and suppresses also all secondary convection. The total amount of precipitation decreases strongly for these simulations and is identical for maritime and continental CCN. Turning off the latent heat of melting alone, while keeping the latent heat of freezing, suppresses also the formation of secondary cells, but the difference in the maximum updraft velocity and some of the difference in the amount of precipitation, however, remains. This shows clearly that in the multicells regime both effects, freezing and melting, are both very important for cloud dynamics and precipitation formation.

Figure 4 shows the relative change in precipitation and the difference of the maximum updraft velocity as a function of CAPE and the continentality parameter α_{CCN}, whose variation from 0 to 1 describes a linear transition of the activation relation from maritime to continental. The background wind shear was constant at $u_\infty = 5$ m/s. Again the results show a good correlation

a) Relative change in precipitation

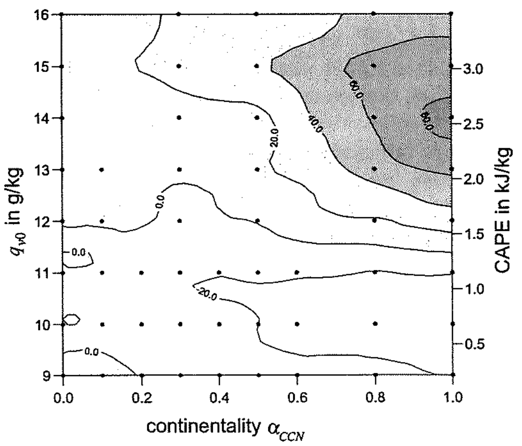

b) Updraft difference Δw

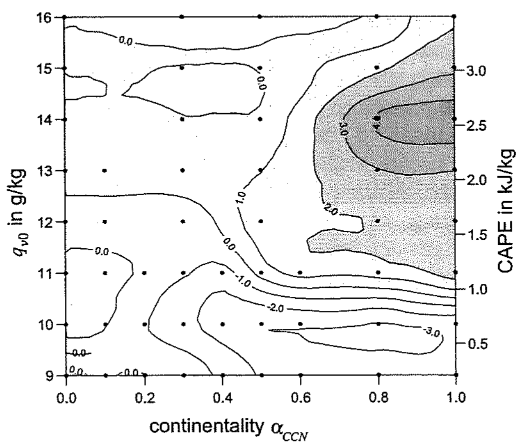

Figure 4: Relative change in total accumulated precipitation in % (a) as well as difference of maximum updraft velocities in m/s (b) as a function of buoyancy and continentality ($u_\infty = 5$ m/s, see text for details).

between surface precipitation and maximum vertical updraft. The ?ndings are that, for $u_\infty = 5$ m/s, the transition from a negative to a positive aerosol effect is more or less independent from the continentality parameter (near $q_{v0} = 11$ g/kg corresponding to a CAPE of 1000 J/kg).

In detail it can be seen that the decrease of the precipitation ef?ciency for the ordinary cells starts at relatively low α_{CCN}. In contrast, the inverse CCN feedback found for multicell storm seems to be a property of the extremely continental CCN-conditions, since only small changes in total precipitation and updraft velocity occur up to $\alpha_{CCN} = 0.5$ which indicates an already continental CCN.

4 Summary and conclusions

The results of this numerical sensitivity study reveal very different effects of CCN-continentality on the cloud microphysics and dynamics of the different storm types. While a negative feedback on total precipitation and maximum updraft velocity is found for ordinary single cells and supercell storms, a positive feedback exists for multicell cloud systems. The most important link between CCNs, microphysics and dynamics is the release of latent heat of freezing.

The study has implications for future cloud-scale quantitative precipitation forecasts (QPF), since it has shown that using ensemble techniques is mostly needed for multicell cloud systems which are most sensitive to the CCN assumptions. The study might also be useful for the interpretation of aerosol-cloud interaction studies as well as cloud seeding experiments. In addition, CCN effects should be considered in parameterizations of deep convection for use in large scale models.

References

Rosenfeld, D. (2000). Suppression of rain and snow by urban and industrial air pollution. *Science 287*, 1793–1796.

Seifert, A. and K. D. Beheng (2001). A double-moment parameterization for simulating autoconversion, accretion and selfcollection. *Atmos. Res. 59-60*, 265–281.

Seifert, A. and K. D. Beheng (2004). A two-moment cloud microphysics parameterization for mixed-phase clouds. Part I: Model description. *submitted to Meteorol. Atmos. Phys.*

Weisman, M. L. and J. B. Klemp (1982). The dependency of numerically simulated convective storms on vertical wind shear and bouyancy. *Mon. Wea. Rev. 110*, 504–520.

CLOUD-ENSEMBLE SIMULATIONS OF TROPICAL CONVECTION UNDER DIFFERENT MICROPHYSICAL REGIMES

Antonio Charles Silvério[1,2], Alexandre Araújo Costa[3,4], José Carlos Parente de Oliveira[1], Gerson Paiva de Almeida[2], Sergio Sousa Sombra[1]

1-Departamento de Física, Universidade Federal do Ceará, Fortaleza, CE, 60455-760, Brazil
2 –Curso de Física, Universidade Estadual do Ceará, Fortaleza, CE, 60740-000, Brazil
3-Department of Geology and Geophysics, Yale University, New Haven, CT, 06520-8109, USA
4- Fundação Cearense de Meteorologia e Recursos Hídricos, Fortaleza, CE, 60115-221, Brazil

1. INTRODUCTION

The Amazonian basin has an area of $6.3{\cdot}10^6$ km^2, most of which (approximately $5{\cdot}10^6$)km^2 pertaining to Brazil. The remaining territory is divided among Bolivia, Colombia, Ecuador, Venezuela, Peru, Suriname and Guyana.

During the last decades, the Amazon region passed through significant changes in land use, including deforestation, forest fires, agriculture, reforestation and other processes (Nepstad et al., 1999; 2002). All those processes are related to an intensive human occupation at that region (Nobre et al., 1991, 2001).

During the transition period between the dry to rainy season, farmers usually deforest and burn the biomass with the objective of substituting forests into plantation areas or pastures. The fires release gases and aerosols in the atmosphere, which can lead to reduced precipitation over the Amazon (Rosenfeld et al., 1999; Williams et al., 2002). In fact, *in situ* observations of aerosol and cloud microphysics over the Amazon show that convective clouds have different behavior depending on the environment where they are formed (Andreae et al. 2004, Costa et al. 2004).

The substitution of forest by pasture can also make the environment drier, through changes in the evaporation, evapotranspiration and surface albedo, which may also contribute to inhibit the precipitation. Hence, deforestation and aerosol loading associated with biomass burning may have catastrophic environmental consequences, including changes in climatic patterns at least on a regional scale.

In the present work, we use a cloud ensemble numerical model (CEM) to study how the modifications in the cloud microphysical structure by forest fires can affect the distribution of the water substance in the atmosphere and the precipitation patterns. Distinct simulations of two regimes in an idealized forest have been made: clean and polluted.

2. THE CLOUD ENSEMBLE MODEL

According to Randall et al. (1996), a CEM is an atmospheric model which grid spacing is fine enough to allow the representation of individual cloud scale circulations. The domain must be large enough to contain many clouds and simulation times must be long enough to span many cloud life cycles. Due to its characteristic, CEMs can furnish information concerning the statistics of cloud systems that cannot be gattered via *in situ* or remote observations.

The atmospheric model used in this study is a two-dimensional version of the *Regional Atmospheric Modeling System* (RAMS, Pielke et al. 1992), similar to that described in Costa et al. (2000). RAMS is non-hydrostatic, with different numerical scheme and physical parameterization options. Microphysical processes are represented following a single-moment scheme, in which water is partitioned in seven categories: vapor, cloud water, rain water, ice crystals, snow, aggregates, graupel and hail (Walko et al. 1995). In each category, the hydrometeors follow a gamma distribution.

A radiation scheme coupled to microphysics was used, following Harrington (1997) and Olsson et al. (1998).

The surface parameterization follows Louis (1981) and includes 12 soil categories and 18 of vegetation. Soil and vegetation properties may be calibrated for a realistic representation.

3. MODEL SETUP

To simulate the two regimes, the model was initialized with a horizontally-homogeneous typical tropical sounding, and forced by imposed idealized large-scale tendencies of ice-liquid potential temperature and total water mixing ratio, representing large-scale cooling and moistening. A non-local nudging was applied to the wind. The model grid comprised 400 points in the horizontal, with a 2-km spacing, and 45 vertical levels, with variable resolution (finer at low levels). The model top was at 22 km, a 10-s timestep and a 60-day integration period were used for the two simulations. Outputs were taken after one month of simulation, when quasi-equilibrium was reached.

In order to represent the two microphysical regimes, we prescribed diferent values for droplet concentration: 200 cm^{-3} for the clean case versus 2000 cm^{-3} for the polluted case.

4. RESULTS

Figures 1 to 5 show vertical profiles of several variables, averaged over time and over the horizontal model domain for the two simulations. In all figures, the clean regime is represented by the thin line and the polluted regime, by the thick line. Figure 1 shows the liquid water mixing ratio. Because precipitation formation is limited by low autoconversion rates, clouds tend to be more persistent and the liquid water increases.

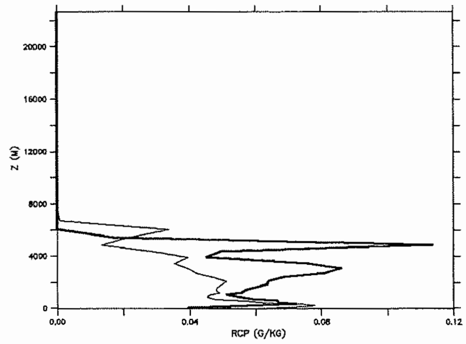

Figure 1. Cloud water mixing ratio, for the two regimes (see text for more details).

Figure 2 depicts the rainwater mixing ratio for the two simulations. On average, the clean case shows about 20% more precipitation than the polluted case. poduced is more intense thand the others cases. It is also noticeable that, although the cloud bases are at about the same height in both simulations (going downward, it corresponds to the level in which rainwater mixing ratio starts do decrease, i.e., slightly below 2000 m), rainwater occurs at lower levels in the polluted case, for which ice processes are supposed to be more important.

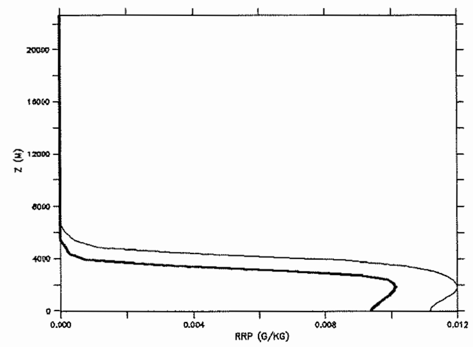

Figure 2 – Same as Figure 1, except for the rainwater mixing ratio

In Figure 3, we present the comparison of the low-density ice (i.e., pristine ice plus snow plus aggregate) mixing ratio for the two simulations. The ice phase formation in the polluted case is initiated at lower levels than in the clean case and the ice mass is larger.

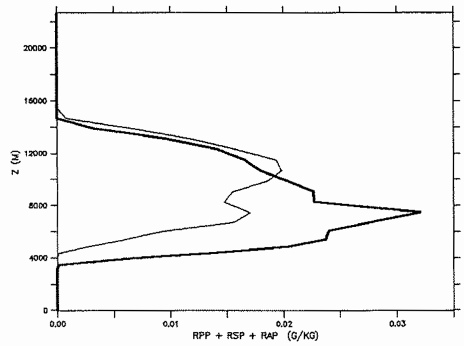

Figure 3. Same as Figure 1, except for the low-density ice mixing ratio.

The high-density ice (i.e., graupel plus hail) mixing ratio fo rthe two regimes is depicted in Figure 4. Again, it is clear that ice processes are more important in the development of precipitation in the polluted case.

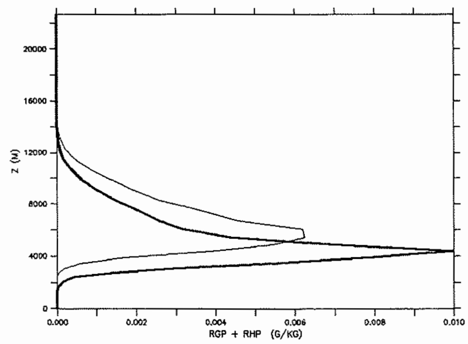

Figure 4. Same as Figure 1, except for the high-density ice mixing ratio.

5. CONCLUSIONS

In this work we presented preliminary results of cloud microphysical sensitivities in tropical convection Simulations of cloud ensemble model are performed for two idealized situations, i.e., clean, and polluted, were performed.

The results suggest that the microphysical processes, including precipitation formation are strongly modified when clouds form under different regimes. The population of cloud formed in polluted air masses has a greater amount of cloud water and produces a small quantity of rainwater, compared to clouds that are formed in clean air masses. In the polluted case the onset of ice formation occurs at lower levels than in the clean case, suggesting that the mechanism of warm rain formation is suppressed in the polluted case.

ACKNOWLEDGEMENTS

A. C. Silvério and G. P. Almeida thank the financial support by the Fundação Cearense de Apoio ao Desenvolvimento Cientifico e Tecnológico (FUNCAP), UECE and UFC

REFERÊNCES

Costa, A. A., W. R. Cotton, R. L. Walko, R. A. Pielke Sr., and H. Jiang, 2001: SST sensitivities in multi-day TOGA-COARE cloud-resolving simulations. *Journal of the Atmospheric Sciences*, **58**, 253-268.

Harrington, J. Y., 1997: The effects of radiative and microphysical processes on simulated warm and transition season Arctic stratus. Ph.D. dissertation, Atmospheric Science Paper No. 637, Colorado State University, Dept. of Atmospheric Science, 289 pp.

Louis, J. F., M. Tiedtke, and J. F. Geleyn, 1981: A short history of the PBL parameterizations at ECMWF. Proceedings, Workshop on Planetary Boundary Parameterization, Reading, United Kingdom, ECMWF, 59-79.

Nepstad, D. C., Moutinho, P., Dias-Filho, M. B., Davidson, E., Cardinot, G.Markewitz, D., Figueiredo, R., Vianna, N., Chambers, J., Ray, D., Guerreiros, J. B., Lefebvre, P., Sternberg, L., Moreira, M., Barros, L., Ishida, F. Y., Tohlver, I., Belk, E., Kalif, K., Schwalbe, K., 2002: The effects of partial throughfall exclusion on canopy processes, aboveground production, and biogeochemistry of an Amazon forest. *J. Geophys. Res.*, **107**, 8085.

Nepstad, D.C., Verissimo, A., Alencar, A., Nobre, C., Lima, E., Lefebvre, P., Schlesinger, P., Potter, C., Moutinho, P., Mendoza, E., Cochrane, M., Brooks, V., 1999: Large scale impoverishment of Amazonian forests by logging and fire. *Nature*, **398**, 505-508.

Nobre, C.A., Sellers, P.J., Shukla, J., 1991: Amazonian deforestation and regional climate change. *J. Climate*, 4, 957-987.

Nobre, C.A., Wickland, D.E., Kabat, P., 2001: The Large Scale Biosphere-Atmosphere Experiment in Amazonia (LBA). *IGBP Global Change Newsletter* LBA - Special Issue, 01-08.

Olsson, P. Q., J. Y. Harrington, G. Feingold, W. R. Cotton, and S. M. Kreindenweis, 1998: Exploratory cloud-resolving simulations of boundary-layer Arctic stratus clouds. Part I: Warm season clouds. *Atmos. Res.*, **47-48**, 573-597.

Pielke, R. A., W. R. Cotton, R. L. Walko, C. J. Tremback, W. A. Lyons, L. D. Grasso, M. E. Nicholls, M. D. Moran, D. A. Wesley, T. J. Lee, and J. H. Copeland, 1992: A comprehensive meteorological modeling system - RAMS. *Meteorol. Atmos. Phys.*, **49**, 69-91.

Randall, D. A., K.-M. Xu, R. J. C. Sommerville, and S. Iacobellis, 1996: Single-column models and cloud ensemble models as links between observations and climate models. *J. Climate*, **9**, 1583-1697.

Rosenfeld, D., 1999: TRMM Observed First Direct Evidence of Smoke from Forest Fires Inhibiting Rainfall. *Geophys. Res. Lett.*, **26**, 3105-3108.

Walko, R. L, W. R. Cotton, J. L. Harrington, M. P. Meyers, 1995: New RAMS cloud micro-physics parameterization. Part I: The single-moment scheme. *Atmos. Res.*, **38**, 29-62.

Williams, E., Rosenfeld, D., Madden, N., Gerlach, J., Gears, N., Atkinson, L., Dunnemann, N., Frostrom, G., Antonio, M., Biazon, B., Camargo, R., Franca, H., Gomes, A., Lima, M., Machado, R., Manhaes, S., Nachtigall, L., Piva, H., Quintiliano, W., Machado, L., Artaxo, P., Roberts, G., Renno, N., Blakeslee, R., Bailey, J., Boccippio, D., Betts, A., Wolff, D., Roy, B., Halverson, J., Rickenbach, T., Fuentes, J., Avelino, E., 2002: Contrasting convective regimes over the Amazon: Implications for cloud electrification. *J. Geophys. Res.*, **107**, 8082 - 9001.

Cirrus Simulations of CRYSTAL-FACE 23 July 2002 Case

David Starr[1], Ruei-Fong Lin[2,1], Belay Demoz[1] and Andrew Lare[3,1]

[1]NASA Goddard Space Flight Center, USA
[2]Goddard Earth Sciences and Technology Center, University of Maryland, Baltimore County, USA
[3]L-3 Communications Government Services, Inc., USA
[4]Joint Center of Earth Systems Technology, University of Maryland Baltimore County, USA

Introduction

A key objective of the Cirrus Regional Study of Tropical Anvils and Cirrus Layers - Florida Area Cirrus Experiment (CRYSTAL-FACE) is to understand relationships between the properties of tropical convective cloud systems and the properties and lifecycle of the extended cirrus anvils they produce. We report here on a case study of 23 July 2002 where a sequence of convective storms over central Florida produced an extensive anvil outflow. Our approach is to use a suitably-initialized cloud-system simulation with MM5 (Starr et al., companion paper in this volume) to define initial conditions and time-dependent forcing for a simulation of anvil evolution using a two-dimensional fine-resolution (100 m) cirrus cloud model that explicitly accounts for details of cirrus microphyisical development (bin or spectra model) and fully interactive radiative processes. The cirrus model follows Lin (1997). The microphysical components are described in Lin et al. (2004) – see Lin et al (this volume). Meteorological conditions and observations for the 23 July case are described in Starr et al. (this volume).

The goals of the present study are to evaluate how well we can simulate a cirrus anvil lifecycle, to evaluate the importance of various physical processes that operate within the anvil, and to evaluate the importance of environmental conditions in regulating anvil lifecycle. CRYSTAL-FACE produced a number of excellent case studies of anvil systems that will allow environmental factors, such as static stability or wind shear in the upper troposphere, to be examined. In the present study, we strive to assess the importance of propagating gravity waves, likely produced by the deep convection itself, and radiative processes, to anvil lifecycle and characteristics.

David Starr, NASA Goddard Space Flight Center, Code 913, Greenbelt, MD, 20771, USA, David.Starr@NASA.gov

Initializing the Cirrus Model

We utilize the output of a reasonably good MM5 simulation of the convective cloud system that occurred on 23 July 2002 to initialize and force our high-resolution 2-D cirrus cloud model. The model is then used to simulate the evolution of the anvil cirrus over a 2-hour time period. The MM5 simulation captured many of the important features of this case including generation of a significant anvil system, albeit somewhat displaced in location and time. We select an MM5 grid column located just downwind of the convective core at 2200 UTC which is 35 min after peak intensity (updraft of 26 m s^{-1} at 13 km). The core dissipated rapidly (peak vertical velocity less than 3 m s^{-1} by 2200 UTC). Back trajectories were calculated at each upper tropospheric level to confirm that the air in the selected grid column was indeed vented from the convective core. Forward trajectories were also used to assess the sensitivity of the trajectory to variations in location (and horizontal wind) of the selected point, the degree to which the column was deformed by wind shear, and to derive the forcing (vertical motion) along that trajectory.

The time-dependent vertical motion forcing along the trajectory is used to drive the cirrus model and is applied uniformly over the entire model domain (6 km in the horizontal and 4 km in the vertical from 11- to 15 km). The forcing is comprised of a series of 4 wavelike oscillations (Fig. 1) over the 2 hours. We interpret these as propagating gravity waves. The magnitude of the imposed forcing reaches +20 cm s^{-1} in the first 15 minutes, and –20 cm s^{-1} just after 2300 UTC. The former is sufficient (adiabatic cooling of 1°C in 10 min) to force significant cloud generation in an ice-saturated environment. The standard deviation is 10.2 cm s^{-1}. The mean forcing is just more than 3 cm s^{-1}, close to values from NCEP North American Re-analysis (32 km resolution) for this location.

The thermodynamic and microphysical profiles extracted from MM5 for the initial anvil-outflow grid point are also used to initialize the cirrus cloud model. Thereafter, the cirrus simulation is independent of the MM5 conditions in the advecting column, except for the vertical motion forcing described above. The upper troposphere is stably stratified (Fig. 2). This is conducive to propagating gravity waves. Conditions are less stable in the layer from 12.9 to 13.5 km. Weak thermal perturbations are randomly prescribed within 12.5-14 km layer to initiate motions.

For the initial microphysical profiles, the ice content (ice and snow mixing ratios) at each level from MM5 is converted to an ice particle size distribution (PSD) using a gamma distribution as:

$$N(D) = \frac{N_t}{\Gamma(v) D_n} \left(\frac{D}{D_n}\right)^{v-1} \exp\left(-\frac{D}{D_n}\right),$$

where $v = 1$, $D_n = 20\ \mu\text{m}$, and $\rho_i = 917$ kg m^{-3} for ice category, and, $v = 3$, $D_n = 200\ \mu\text{m}$, and $\rho_i = 100$ kg m^{-3}. for the snow category. Given the mixing ratios, N_t(D) can be calculated for each category. The 2 PSDs are then added together and discretized into the predefined PSD mass bins of the model. These are interpolated in the vertical from the coarse MM5 grid to the much finer cirrus model grid. Aerosol size distributions, and homogeneous and heterogeneous nucleation processes are explicitly represented in the model but homogeneous freezing is not activated. The initial ice water mixing ratio profile is shown in Fig. 2. The shape of the profile indicates that the anvil outflow occurred predominantly in the 12-14 km layer. Significant ice mass was also found in the 14-15 km layer. Overshooting tops were observed to 15 km in this case. The anvil from an earlier cell along the aircraft flight track was already a multi-layered system by the time it was sampled by the aircraft. There was a tenuous cirrus layer sloping downward in the downwind direction across the 14-15 km layer with a much denser cirrus layer from 7-12 km (see McGill et al. 2004). Another convective core was captured at the mature stage. Near the core, the cirrus anvil extended from 7 to above 14 km.

Results

Results from three cirrus anvil simulations are discussed here. Each simulation is of 2-hour duration. Effects of solar radiation are not included here as the time period corresponds to just before and after local sunset. The simulations are a control run (CTRL) using the time-dependent MM5-derived vertical motion forcing and a run where this forcing is held fixed (CW) to its time-averaged value. In both these cases, an optically dense underlying cloud layer is assumed which acts to shield the cirrus layer from upwelling infrared radiation from the warm surface and moist lower troposphere. This dramatically suppresses infrared radiative heating of the lower cloud layer by absorption. The third simulation (NLC) does not include this underlying cloud layer.

In Fig. 1, the time-dependent, horizontally-averaged, ice water path (IWP) over the model domain (11-15 km) is shown. The IWP decreases substantially over the 2-hour time period. It is evident from the vertical profile (Fig. 2) that this is mostly driven by the "precipitation" process, i.e., sedimentation of ice mass out of the lower model boundary. The effects of the gravity wave forcing are relatively slight by comparison. For the CTRL and NLC simulations, a small undulation of IWP occurs roughly 90° out of phase (lagged) with the wave pattern of the forcing.

Except for the NLC simulation, the cirrus anvil cloud layer remained highly stratified (horizontally homogeneous) throughout the simulation. In the NLC simulation, however, significant motions developed as indicated by the perturbation turbulent kinetic energy (Figs. 1), mostly in the 11.5 to 13.5 layer (Fig.2). Recall that the initial static stability was not so great in the layer from 12.9 to 13.5 km. The cloud ice field was correspondingly structured with cellular organization at a 2-km horizontal scale. The motions and cloud structure are a direct result of "cloud-base" radiative heating (Fig. 2) associated with absorption of upwelling infrared radiation originating from the warm surface and lower troposphere leading to a well-mixed stratification (Fig. 2). We were surprised by the strength of this destabilizing effect.

Discussion – Ice Water Path

Remote sensing measurements of ice water path (IWP) for the thick portion of anvil system on this day indicated mean values of 202, 212 and 225 g m-2 from a combined lidar-mm-radar algorithm (provided by L.Li/GEST/GSFC), submillimeter radiometer observations (SMR, after Evans et al. 2002, JGR), and retrievals using the standard MODIS algorithm applied to MODIS Airborne Simulator (MAS) observations (provided by T.Arnold/JCET/GSFC). MAS and the active sensing systems were on NASA's high-altitude ER-2 aircraft while the SMR was on the high-altitude Proteus aircraft which flew the same lines over the axis of the anvil system and also over the convective core. IWP for the near-core column used to initialize the cirrus model were about 4 times larger. Even after 2 hours, the simulated IWP is more than twice the observations. Horizontal wind speeds at these levels were about 15 m s^{-1} such that the 2-hour simulation can be interpreted as ending at a distance of about 100 km from the convective core

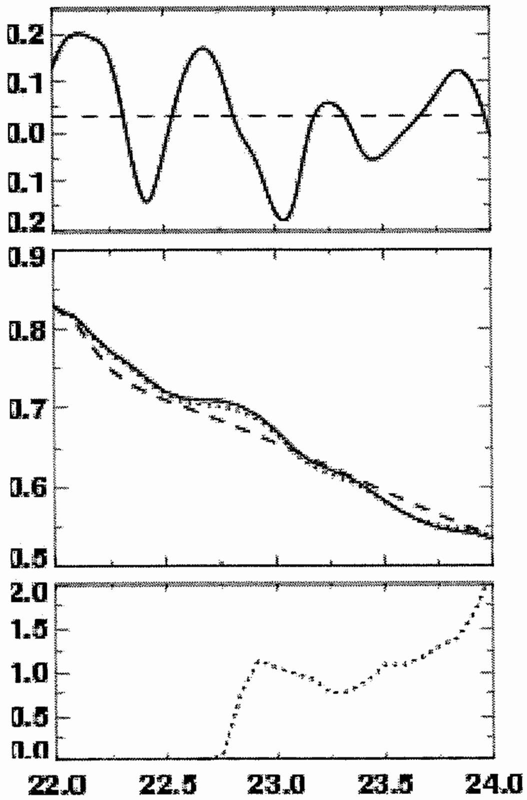

Figure 1: From top to bottom: Time evolution of prescribed vertical motion forcing (m s^{-1}) with time-mean value indicated by dashed line, IWP (kg m^{-2}), and domain-average perturbation TKE ($m^2 s^{-2}$). Simulations start at 2200 UTC and end at 2400 UTC. CTRL is indicated by solid curves, CW by dashed, and NLC by dotted curves. See text for definitions.

-----

that produced the anvil. The observations showed that the anvil became considerably less dense over this distance, much as in the cirrus model simulations here. While the IWP observations are uncertain, probably more so than indicated by the close agreement apparent among the estimates reported here, it is evident that MM5 produced too much ice outflow.

Peak IWP for the updraft core in MM5 (2-km x 2 km grid cell) was about 4600 g m-2. Retrieved values from radar-lidar, SMR and MAS were 373 and 1044 and 2092 g m^{-2}. Again, MM5 is much larger though we here find considerable diversity in the estimate from observations. While questions about timing and location are obviously very important when considering the core overflights with nadir viewing instruments (e.g., Did the aircraft go directly over the

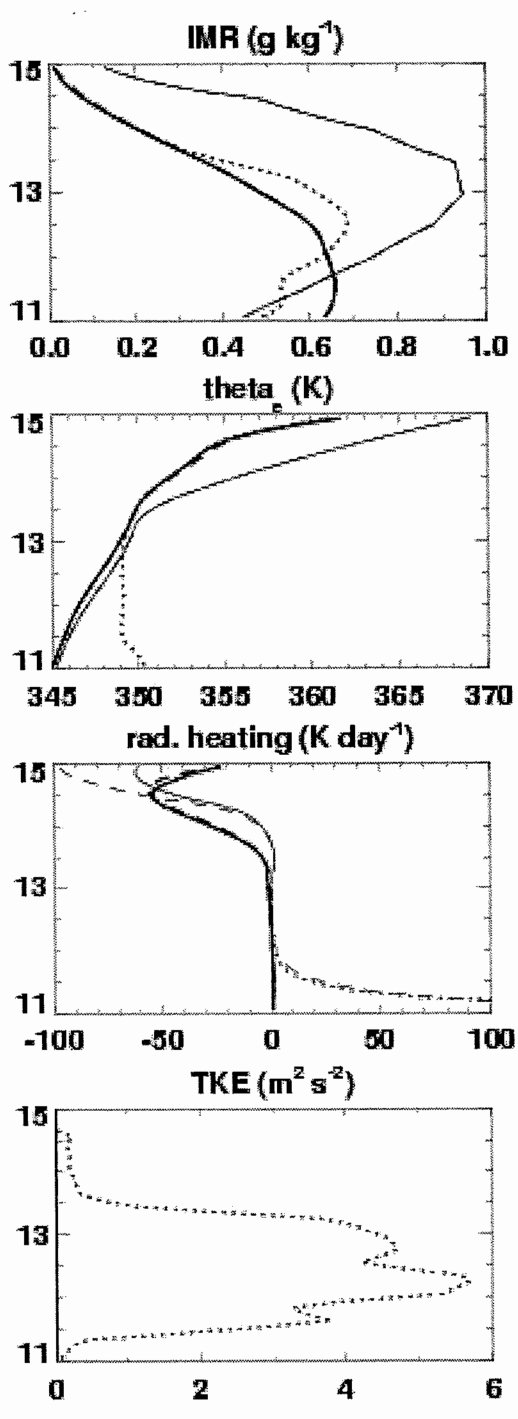

Figure 2: Horizontally-averaged profiles of ice mixing ratio (IMR), equivalent potential temperature (θ_e), infrared radiative heating rate, and perturbation turbulent kinetic energy for simulations in Fig.1. Thin curves indicate the initial profiles while the thick curves denote the profiles 2 hours later at the end of the simulation. Curves for CW may overlay CTRL.

core when it was at peak intensity?), it seems reasonable to conclude that MM5 IWP path was overly large for the core.

Lastly, the sedimentation rate may be too low, or correspondingly the initial PSD too narrow in the cirrus model, such that the precipitation process is too slow in removing ice from the layer. Qualitative comparison to the observations, and published studies, would seem to support a conclusion that this is so, at least during the first 30 minutes or so.

Discussion – Vertical Motions

We have examined the vertical motion observations obtained by the NASA WB-57F aircraft (provided by P. Bui/NASA Ames) along the anvil axis on 23 July, 2002. After application of a low-pass filter, the time series along flight legs in the anvil, when converted to the spatial domain, look very similar in terms of wave scales and amplitudes, to the constant-level plots of MM5 vertical motion fields along a similar line at about the same altitude. Flight-leg statistics of observed vertical motions are shown in Fig. 3 both for the total (raw) and low-pass filtered (5-km scale) time series. The low-frequency variability depends only weakly, if at all, on height in the anvil and represent the dominant component at most levels. However, a few legs around the 13 km level show a strong, even dominant, contribution from smaller scale motions, suggestive of the NLC simulation here.

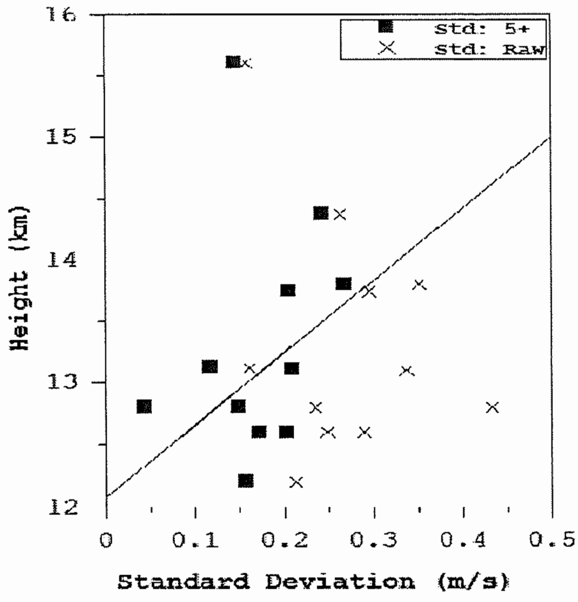

Figure 3: Standard deviation of vertical air motions observed along WB-57F flight legs in cirrus anvil at indicated altitudes on 23 July, 2002.

We also analyzed the vertical motion statistics from MM5 at 2200 and 2400 UTC, at the beginning and end of our cirrus model simulations. The results are shown in Fig. 4 for the inner MM5 domain. Greatest variability is found in cloudy air from 8-13 km and are reasonably consistent with the observed variability at comparable scale (low-pass filtered). The motion fields dampen appreciably over this 2-hour period.

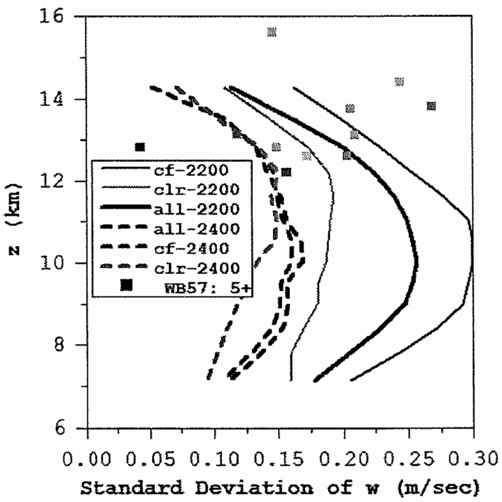

Figure 4: Standard deviation of vertical motions in MM5 simulation as function of height at 2200 (solid) and 2400 (dashed) UTC for cloudy (rightmost) and clear (leftmost) grid points. Observations as in Fig. 3.

Summary and Outlook

While we are generally pleased by the results to date, it is fairly clear that MM5 outflow to the anvil system is either too strong or not well-handled by the cirrus model. It is likely that a much more rapid fallout process occurs for large, precipitation-sized ice particles near the core much like observed by McFaquhar and Heymsfield (1996) during CEPEX that is not well-captured by either MM5 or the cirrus model. Alternative means of accounting for this process will be explored. Further analysis of the cloud-scale (small-scale) motion fields and cloud property statistics from the cirrus model and in-situ observations will also be reported.

References

Lin, R.-F., 1997: A numerical study of the evolution of nocturnal cirrus by a two-dimensional model with explicit microphysics. Ph.D. thesis, Pennsylvannia State University, 199 pp.

Lin, R.-F., D.O'C. Starr, J. Reichart and P.J. DeMott, 2004, *J. Geophys. Res.* (in review). Abstract in this volume.

McFarquhar, G.M., and A.J. Heymsfield, 1996, *J. Atmos. Sci.*, 53 2401-2423.

Starr, D.O'C., R.-F. Lin, A. Lare, B. Demoz, T. Rickenbach, D. Wang, L. Li, G.T.Arnold and Y. Wang 2004, (this volume)

Mesoscale Simulations of CRYSTAL-FACE 23 July 2002 Case

David Starr[1], Ruei-Fong Lin[2,1], Andrew Lare[3,1], Belay Demoz[1], Thomas Rickenbach[4,1], Donghai Wang[5], Lihua Li[2,1], G. Thomas Arnold[3,1], and Yansen Wang[6]

[1]NASA Goddard Space Flight Center, USA
[2]Goddard Earth Sciences and Technology Center, University of Maryland, Baltimore County, USA
[3]L-3 Communications Government Services, Inc., USA
[4]Joint Center of Earth Systems Technology, University of Maryland Baltimore County, USA
[5]NASA Langley Research Center, USA
[6]U.S. Army Research Laboratory, USA

Introduction

A key objective of the Cirrus Regional Study of Tropical Anvils and Cirrus Layers - Florida Area Cirrus Experiment (CRYSTAL-FACE) is to understand the relationships between properties of tropical convective cloud systems and the lifecycle of the extended cirrus anvils they produce. We report here on a case study of 23 July 2002 where a line of land-based convective storms was generated between Lake Okeechobee and the Florida east coast as a result of complex interactions between lake and sea breeze fronts and outflow boundaries. A central goal of this study is to develop a description of convective input to the anvil system and to quantify the ongoing dynamical forcing of anvil processes by mesoscale and large-scale dynamics. This information is then used to force high-resolution cloud simulations with a model that explicitly resolves cloud microphysical processes (bin model, Lin et al. 2004 and in this volume) for study of cirrus anvil microphysical development (companion paper, Starr et al.).

Meteorology Overview

The prevailing wind in the boundary layer was southeasterly (Fig. 1), but backed to easterly from 2 km to 5 km in association with a region of high pressure located to the north. At 10-14 km, wind speeds were 10-15 m s^{-1}, peaking at about 12.4 km. At Miami, CAPE was 2442 J kg^{-1} at 1200 UTC, and 2953 J kg^{-1} by 1500 UTC – very unstable. The upper troposphere was quite moist, likely a result of earlier maritime convection that occurred upwind (NE) of the area. Weak precipitation systems started to form along the east coast in the early morning between 26 and 27°N (Fig. 2) and then migrated inland.

Convection near the south rim of Lake Okeechobee began around 1620 UTC and went through two cycles of development, dissipation and regeneration, ending about 2000 UTC. A convective line (about 30 km in length in the mature stage) developed northeast of the lake around 1920 UTC and lasted for about 2 hrs. Aircraft (NASA ER-2 and Proteus as remote sensing platforms and NASA WB-57 as in-situ platform) were flown roughly along the axis of the anvil generated by these two systems (Fig. 3). The first major cell on the line achieved strong intensity and cloud top reached 15 km (overflown by NASA ER-2). The cirrus anvil(s) advected from the convective cores toward the southwest. Anvils from at least two separate convective cores occurred roughly along the same axis.

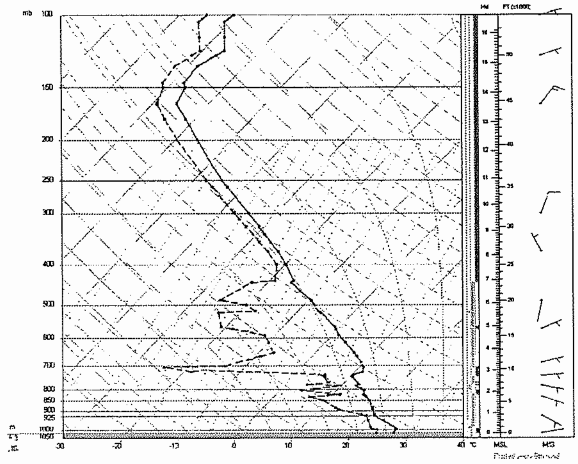

Fig. 1: Miami sounding plotted on a skew T-log p diagram, for 1100 UTC 23 July 2002.

Mesoscale Simulations

Simulations of the cloud systems for 23 July 2002 are compared, including (S1) MM5 initialized using Eta analyses, and (S2) the Advanced Regional Prediction System (ARPS) that also assimilated hourly data from

NEXRAD, surface, satellite and radiosonde observations. Model configurations are described in Table 1. Timing, location and strength of the convective cells, and associated anvil dynamics are of particular interest here.

Simulation S1 successfully captured the development of convective cells along the southern shore of Lake Okeechobee and later to the east and northeast of the lake, albeit delayed by as much as 2 hrs. These were the systems whose anvil outflow was sampled by the aircraft. The area coverage and principal outflow direction of the simulated anvil cloud agree reasonably well with observations. East of the lake, the convective line matured around 2200 UTC in the simulation. The line was not as organized or intense, and did not exhibit

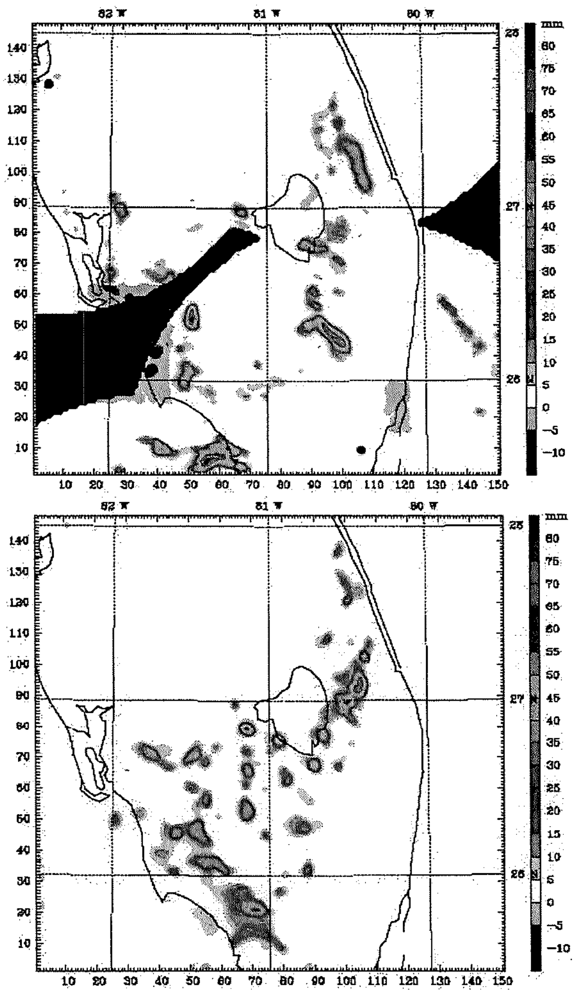

Fig. 2: (a) Cumulative rainfall from 1800 to 2400 UTC estimated from 10-min regional rain maps derived using four NOAA NEXRAD (Key West, Miami, Melbourne and Tampa) and the NASA Polarimetric Radar (NPOL). Negative values indicate no radar coverage. (b) Cumulative precipitation simulated by S1 for the same period.

Table 1. Summary of the two simulations.

Simulation	S1	S2
Model used	MM5 v3.5	ARPS v5.0IHOP_2
Nested domains	2	2
Coarse Domain		
Resolution (km)	6	15
Domain size (km)	540 X 540	2175 X 2175
Cumulus Parameterization	none	Kain-Fritch
Fine Domain		
Resolution (km)	2	3
Domain size (km)	300 X 294	600 X 600
Cumulus Parameterization	none	none
Bulk microphysics	GSFC-3 ice	GSFC-3 ice
PBL parameterization	Blackadar	1.5-order closure

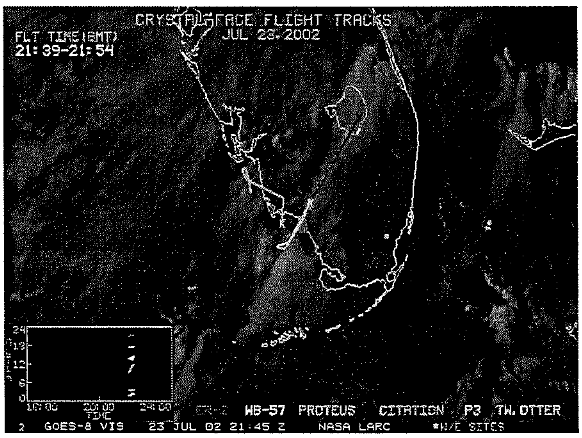

Fig. 3: GOES-8 visible image with aircraft flight tracks for 2139-2154 UTC on 23 July 2002 (from P.Minnis and L.Nguyen, NASA Langley Research Center).

the same orientation as seen in NEXRAD and NPOL observations. The S1 simulated convection in southwest Florida was overly active with more individual cells than observed (Fig. 2) and S1 missed the strong system located at 80.6W, 26.3N during the afternoon (not sampled by the aircraft). Additional simulations using North American Regional Re-analyses for initial and boundary conditions are underway.

The location and timing of the convective cells by S2 agree better with the observations. This is undoubtedly aided by the ingest of observations every hour. One negative consequence is the introduction of artificial discontinuities in the field variables at times of data ingest when the model tries to rapidly adjust the dynamic and thermodynamic fields. This limits the usefulness of the assimilated output for trajectory or time series analysis. Also, despite the success in timing of the convective events, the convective cores and associated stratiform precipitation from S2 covered a much larger area and persisted for a much longer period of time in comparison to the observations.

We intend a rigorous comparison of our 2-D high-resolution bin-microphysics cirrus model and in-situ observations. Selection of a "most-comparable" time-dependent vertical cross section of S1 output with which to force the high-resolution model is therefore a key objective. We first examine the relationship between flight paths and actual locations of the convective cores and anvils (as determined via NEXRAD, satellite and airborne remote sensing data), and then analyze the relationship between the actual locations of the convective features and the simulated ones. The "most-comparable" line for S1 is about 25 km south of the flight tracks in the east and about 10 km south at the western end. Thus, the orientation of the "most-comparable" line is also different than observed in this weak flow situation where the convective influence on the flow field is significant.

Shown in Fig. 4a is the vertical cross-section of simulated total cloud hydrometeor content (g kg^{-1}) and vertical motions (m s^{-1}) from S2 at 2150 UTC. The convection is just beginning to dissipate in the S2 simulation at this time. Fig. 4b is from S1 at the same time but along the "most-comparable" line. Here, the S1 simulated convective intensity is already declining from earlier when updrafts reached 26 m s^{-1} at 2125 UTC which is more than an hour after peak convective intensity was achieved in the actual cloud system. Cloud boundaries at about this time determined from airborne lidar (CPL) and mm-radar (CRS) observations (McGill et al. 2003) are also shown for comparison. The S1 simulated anvil reasonably conforms to the observations, e.g., versus CPL cloud top. For comparison, a vertical cross section of NEXRAD reflectivity at 2148 UTC is shown in Fig. 5 (Rickenbach et al. 2003). This also shows the upward sloping lower anvil boundary in the downwind direction roughly comparable to the S1 results (Fig. 4b).

Both simulations predicted overshooting convective cores into the lower stratosphere when the convection was most intense (S2 was more energetic). The horizontal extent of the cirrus anvil of S2 along the flight path is somewhat smaller than indicated by aircraft observations.

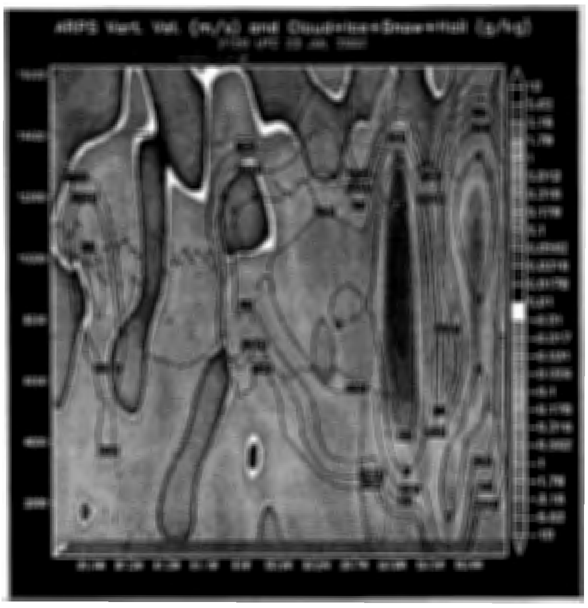

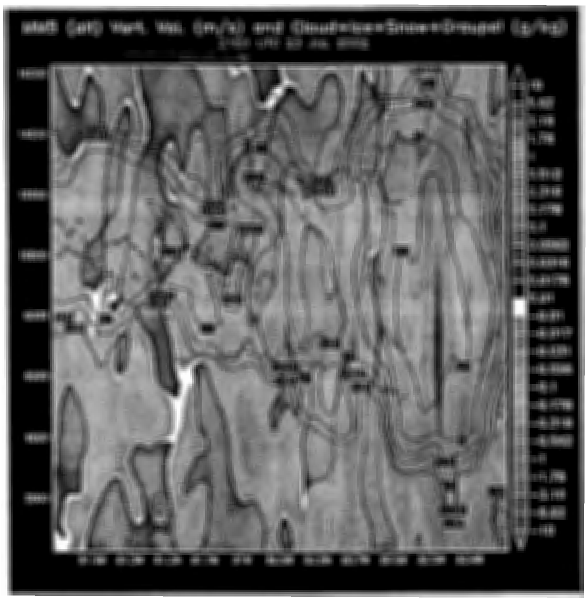

Fig. 4: (a) S2 simulated vertical cross-section of total hydrometeor content in g kg^{-1} (contours) and vertical velocity in m s^{-1} (color coded) at 2150 UTC on 23 July 2002 along the aircraft flight path. Locations of the ER-2 (red) and Proteus (green) above the system, and the WB-57 (cyan, extreme left) are shown for the previous 5 minutes (X indicates current location). Cloud boundaries determined from CRS (magenta) and the merged CRS-CPL (orange) sensors on the ER-2 are also shown. (b) Same as (a) except for S1 and using the most comparable line.

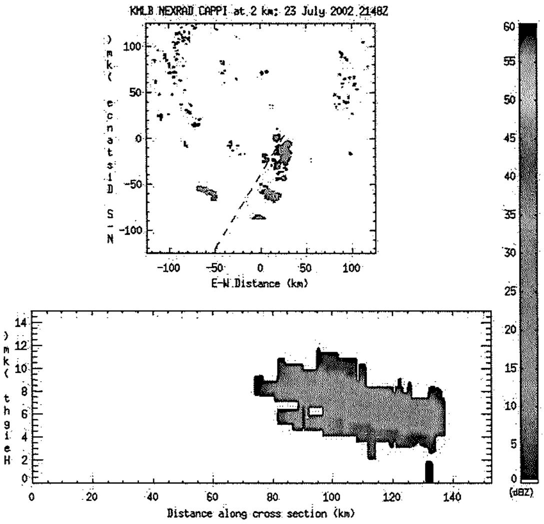

Fig. 5: (a) NEXRAD CAPPI radar reflectivity (dBZ) at 2 km height for 2148 UTC and (b) NEXRAD vertical cross-section of reflectivity along aircraft flight path (indicated by dash line in CAPPI panel).

To estimate the area coverage of the cirrus outflow associated with the convective cores near the lake, parcels were tracked in S1 from low levels in the cores(defined using a threshold updraft speed 5 m s^{-1}) using forward trajectory calculations. More than 5000 parcel trajectories were calculated and allow us to distinguish the source of the outflow mass in the trailing anvil shield. By 2200 UTC, 71% of the parcels had detrained at an altitudes between 10.8 km and 13.9 km and 17% of the released parcels detrained between 8.7 to 10.8 km. About 5% exceeded the 13.9 km level. These estimates reinforce the finding by an independent analysis based on NEXRAD observations of a single cell, where about 70% of the convective mass was determined to be transported into the anvil.

The ice water contents produced by S1 just outside the convective core are used to initialize a high-resolution 2-D cirrus cloud model with explicit bin microphysics in Starr et al. (companion paper in this volume). In addition, that model is forced by the mesoscale vertical motions produced by S1 along a parcel trajectory in time and space. Further illustration of the vertical motion fields produced by S1 may be seen in Fig.6. These fields are along the "most-comparable" line at 2150 and 2250 UTC. S1-resolved (2 km horizontal resolution) vertical motions reach 1 m s^{-1} near the dissipating core but are less than 0.5 m s^{-1} further away in the extended anvil. The motions give the impression of wave-like undulations,

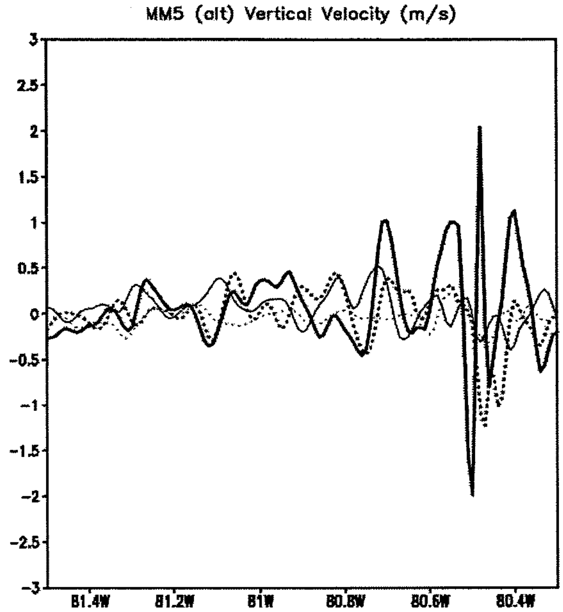

Fig. 6: Vertical velocity along the most comparable line in S1 at 11250 m (solid) and 13250 m (dotted) at 2150 UTC (thick) and 2250 UTC (thin). Peak cell intensity as simulated by S1 occurred at 2125.

such as would be produced by propagating gravity waves. Except near the core, the strength of the undulations does not appreciably decline during the 1-hour time period shown in Fig.6.

Summary

The S1 simulation realistically captured several main features of the 23 July 2002 case. While the timing was delayed and the location offset, the simulation produced outflow from multiple cells into an aggregate anvil system roughly comparable in appearance and extent to that observed. Outflow from the convective cores was predominantly into the high troposphere above about 11 km. The output of S1 is further analyzed and compared to in-situ observation in the companion paper and used to drive a cirrus model with bin microphysics.

References

Lin, R.-F., D.O'C. Starr, J. Reichart and P.J. DeMott, 2004: *J. Geophys. Res.* (in review). Abstract in this volume.

McGill, M., L. Li, G.M. Heymsfield, D.L. Hlavka, W.D. Hart, D.M. Winker and M.A. Vaughan, 2004, *J. Geophys. Res.* (in press).

Rickenbach, T.M., L. Belcher, P. Kucera, L. Carey, J. Halverson and D. Starr, 2003, *Preprints*, 31st Conference on Radar Meteorology, Seattle, AMS.

Starr, D.O'C., R.-F. Lin, B. Demoz, and A. Lare, 2004: Cirrus simulations of 23 July 2002 CRYSTAL-FACE case. (this volume)

A COMPARISON OF CONSERVATION PROPERTIES OF MICROPHYSICAL PARAMETERIZATIONS: CONTINUOUS GAMMA DISTRIBUTION FUNCTION WITH FIXED SHAPE PARAMETER

Jerry M. Straka[1], Matthew S. Gilmore[2], Erik N. Rasmussen[2], Katharine M. Kanak[2]

[1]School of Meteorology, University of Oklahoma, Norman, Ok, USA 73019
[2]CIMMS, University of Oklahoma, Norman, Ok, USA 73019

1. INTRODUCTION

The equations which represent one of many microphysical processes, for which total number concentration N_t should be conserved, is integrated over sizes of hydrometeor diameters D (0,∞) for one- and two-moment methods. The gamma distribution function is assumed and incorporates total mixing ratio q, N_t, and mean diameter D_n, (inverse of the distribution slope λ]. In all the methods, the slope intercept, n_o, is diagnosed or specified but not predicted. The moment methods explored include;

the one-moment method where q is predicted, n_o is specified, and N_t and D_n are diagnosed,

the one-moment method where q is predicted, D_n is specified, and N_t and n_o are diagnosed,

the two-moment method where q and N_t are predicted, and n_o and D_n are diagnosed, and

the two-moment method where q and D_n are predicted, and N_t and n_o are diagnosed.

In order to more easily discern the strengths and weaknesses of each moment method, it would be desirable to evaluate more than on process but owing to space constrains we will focus on vapor diffusional growth with no introduction of new particles (dN_t/Dt = 0). It is demonstrated for the process examined that all of the schemes fail to conserve N_t and have other unphysical attributes, except the two-moment method where q and N_t are predicted.

With the increase of the inclusion of more sophisticated microphysical parameterizations in mesoscale models, it is important for a model user to be cognizant of the strengths and weaknesses of the available parameterizations. With this understanding a modeler can make informed decisions when specifying which microphysical parameters will be predicted, specified, or diagnosed. This knowledge is also important to facilitate the most accurate interpretation of the results.

Corresponding author's address: Jerry M. Straka, School of Meteorology, Univ. of Oklahoma, Norman Oklahoma, 73019, USA; E-Mail: jstraka@ou.edu

It should be made clear to the reader that even this method is not perfect as it is presented as the shape parameter and mode may be in error making the mixing ratio in error.

However we will fix the mixing ratio growth rate and the scheme where we predict Nt and q should be perfect in many regards.

2. VAPOR DIFFUSION GROWTH AND NO NUCLEATION.

First, we examine scheme-E (All schemes described in Table 1), with predicted (q, D_n), analytically. We consider vapor diffusion growth, assuming no particles nucleated. The equation for D_n is

$$\frac{dD_n}{dt} = \frac{D_n}{\beta q}\left[\frac{2\Gamma(\beta+\nu+\delta)\Gamma(\beta+\nu)}{\Gamma(\nu+\delta)\Gamma(2\beta+\nu)} - 1\right]\frac{dq}{dt} \quad (1)$$

$$\frac{dD_n}{dt} = \frac{D_n G}{\beta q}\frac{dq}{dt}$$

where G is just the term in square brackets.
The total number concentration rate can be computed to be

$$\frac{dN_t}{dt} = H\frac{(1-G)}{D_n^{\beta}}\frac{dq}{dt} \quad (2)$$

where H is just

$$\mathrm{H} = \rho_o\Gamma(v)/[\alpha\ \Gamma(\beta+v)].$$

The equation for the slope intercept N_o (3) is

$$\frac{dn_o}{dt} = [1-\nu G]\frac{J}{D_n^{\beta+\nu}}\frac{dq}{dt} \quad (3)$$

where J is

$$J = \frac{\rho_o}{\alpha\Gamma(\beta+\nu)}$$

Consider a sphere where δ = 1, β= 3, v = 1, b = 0.8, and α = 842. (inverse-exponential distribution), constant ventilation f = 1, and v = 1 (D to the power 1; Mitchell 1988, 1994), we find that the following can be computed as constants: G = - 0.6 and (1 - G) = 1.6. Assuming a constant, positive dq/dt, integration of (1) always results in a decrease in the mean diameter D_n for a sphere. In addition, (2) always results in an increase in N_t.

The conservation of N_t is exceptionally important in this analysis, as it implies the equations do not develop new particles. Unfortunately, in general, integration of (1) through (3) do not conserve N_t. Moreover, integration of of an equation for n_o (3), always results in an erroneous increase in n_o, (an increase in smaller particles). In addition, there also is a gain in N_t (non-conservation) and n_o when D_n is held constant in (1) and (3) as would also be the case for scheme-B. This again is unphysical for the physics prescribed for growth of an initial distribution of hydrometeors and employing growth equations used in this paper.

Analytically, the drawbacks of scheme-E do not occur when using scheme-F, that is, predicting q and N_t using (4 & 5) and diagnosing D_n and n_o , from the basic equations of the spectrum equations we can get results, which at least have tendencies in the correct direction, physically, (q trends upward, N_t trend is zero, D_n trends upward, and n_o trends downward.)

We numerically integrate the vapor diffusional growth equation (symbols and values can be found in LFO and Pruppacher and Klett 1981, 1997) for the interval over D (0,∞) using the following equations,

$$\frac{dq_x}{dt} = \int_0^\infty \frac{1}{\rho_o} \frac{4\pi \; C \; N_t \; f \; (S_x - 1)}{\left(\dfrac{L_x^2}{KR_v T^2} + \dfrac{1}{\rho_o q_{xs} \varphi_v} \right)} n(D) dD.$$

The symbol x is used to indicate ice x=i (i=ice) or liquid x=l (l=liquid).

$$\frac{dq_x}{dt} = \frac{4\pi \; C_n \; N_t \; f \; (S_x - 1)\Gamma(\nu+1)}{\rho_o \Gamma(\nu) \left(\dfrac{L_x^2}{KR_v T^2} + \dfrac{1}{\rho_o q_{xs} \varphi_v} \right)} \qquad (4)$$

where for a sphere $C_n = D_n/2$, and for a disk $C_n = D_n/\pi$ (a disk might be an ice plate, broad branch sector, or dendrite; Pruppacher and Klett 1981, 1997). Other shapes are more complicated and are not considered here. The time rate of change of N_t is

$$\frac{dN_{t,x}}{dt} = 0 \qquad (5)..$$

Four of the schemes in Table 1 (schemes-A, -B, -E, and -F) are examined numerically by integrating The latter equations forward in time for 1200 s, using a 1 s time step for an ice sphere undergoing vapor deposition. The time step is kept small so that time truncation error is minimized. To compare solutions for schemes-A, -B, and -E against scheme-F, we assume dq/dt = constant and that $dN_t/dt = 0$ as discussed previously. Specifically, we assume, dq/dt = constant = $5\text{x}10^{-7}$ kg kg^{-1} s^{-1}

- q_i = $1.0\text{x}10^{-3}$ Kg Kg^{-1} for cloud ice at time t = 0
- n_o = $1.0\text{x}10^{8}$ ms$^{\nu)}$ at time t = 0
- f=1 and δ=1 (Mitchell 1988, 1994)
- S_i = 1.05 for all times

Sample values at t = 1200s of dq/dt, q, D_n, □, N_t, and n_o from (1, & 3) for schemes-A, -B, -E and -F, for diffusional growth of a sphere for constant q growth. Relative-differences (RDs) against scheme-F and -E also are shown. The RDs range from O(10)% to O(100)%!

Scheme-F is examined to determine if it is producing consistent solution trends and provides a reasonable comparison solution. With scheme-F we find that dq/dt > 0 as prescribed and dN_t/dt = 0 as it physically should be. Also, with scheme-F, we find with that D_n increases with time (larger mean diameter with time), which is realistic, and with that n_o decreases with time fewer small particles and more large particles with time), which also is correct. Having q and N_t correct (at least the direction) provides a guarantee that the direction of change with time of D_n and n_o are also correct, as they are mathematically related through the fundamental definitions for the distribution variables.

With regard to N_t and n_o, examination of all the other schemes (Table 2) show values and / or trends in error compared to scheme-F, although for scheme-A the mere specification of a constant n_o is incorrect. Scheme-B and -E schemes produce a larger number of particles and therefore imply the existence of more, smaller particles (the increase in n_o) than with scheme-F, with which the number of particles N_t is constant and n_o decreases. In accordance with the increase in N_t and n_o, mean diameters D_n for schemes-A, -B, and -E are all smaller at t = 1200 s than for scheme-F. Even though scheme-A has an increasing D_n and by definition Scheme-B has a constant D_n with time, neither is large enough compared to scheme-F. On the other hand, scheme-E produces smaller D_n (smaller mean diameter) than the initial value using (1) which is even more flawed. These trends for schemes-A, -B and -E violate what should occur physically.

3. CONCLUSIONS

With the rapid increase of microphysical parameterizations in numerical models we felt compelled to evaluate the veracity of some commonly used microphysical moment schemes in an idealized controlled manner (holding the rate of the third moment dq/dt constant).

From the results owing to numerical integration of (1) to (2), one might conclude that a double-moment method where N_t is explicitly predicted is the best form to use (though we have not investigated if D_n behaves correctly for scheme-F.) All of these results suggest that a new way to specify and / or predict (q, D_n, N_t) Lo (1988), or predict (q, N_t), is needed. Further information about the first moment D, is required for cloud physics parameterizations if one does not want to resort to using a bin model, which can be very expensive in large three-dimensional models. In a subsequent paper we will show though that the prediction of (q, D_n, N_t) is not the best choice of methodologies in that there are potential problems with D_{mod} and q. Alternatively, a scheme that uses multiple basis functions (Feingold et. al. 1998) might be of great use. A strong motivation for doing so would be to more accurately simulate N_t or D_n, as they are both essential to conserve electrification charging rates and precipitation rates, for example, let alone microphysical processes.

It has been shown that schemes-A, -B, and -E (Table 1), which are often used in numerical cloud models, do not conserve the important moment N_t when they physically should do so for the processes of vapor diffusional growth (Table 2). In particular, schemes-A,-B, and-E 'artificially nucleate' particles during processes that should conserve N_t. In other words, the number of particles increase for schemes-A, -B, and -E, and the larger diameters get smaller than initial values at some diameter D (scheme-B and -E) as the distribution slope awkwardly becomes more negative (larger) with time. However, the scheme that predicts (q, N_t) preserves N_t by the nature of its design (scheme-F); thus it contains enough information for comparison purposes for cases considered in this paper. Even so, we are not sure any scheme predicts n_o with any great fidelity. This is disheartening as n_o-jumps (Pruppacher and Klett 1981, 1997) as observed with disdrometers and dual-polarimetric radar (Straka et al. 2000) are not even slightly well described in numerical simulations, if at all. Bin models usually show that distribution complexities are oversimplified with the schemes examined in this study. In addition, perhaps not surprisingly, adding moments or complexity does not guarantee better solutions. If given a choice of moment schemes such as those presented herein, the results make it impossible to say which scheme really is the most physically consistent, though a strong case could be made that a scheme that predicts (q, N_t), a two-moment method (scheme-F), is least suspect.

ACKNOWLEDGEMENTS

This work was supported by NSF grants, ATM-9617318, ATM-99866672, ATM-0003869, ATM-0119398, and ATM-0135510. Partial funding for this research was provided by the National Severe Storms Laboratory under NOAA-OU Cooperative Agreement #NA17RJ1227. Katharine M. Kanak was supported by the Cooperative Institute for Mesoscale Meteorological Studies (CIMMS) at the University of Oklahoma. The authors are grateful to Steve Nelson at the National Science Foundation for his long term support of our work.

Table 1

C or P Scheme	q	Nt	No	Dn	# Mom
A	P		C		1
B	P			C	1
C	P	C			1
D	P		P		2
E	P			P	2
F	P	P	·		2

Table 1: P = predicted, C = Constant

Table 2.

scheme	A	B	E	F	
Inititiak conditions/Final values (1200 s)					
q_BEG	1	1	1	1	x10e-3
q_END	1.6	1.6	1.6	1.6	x10e-3
qRD_F	0	0	0	--	%
qRD_E	0	0	--	0	%
Nt_BEG	22	22	22	22	#/me3
Nt_END	28	25	47	22	#/me3
NtRD_F	27	60	113	-	%
NtRD_E	40	24	--	52	%
Dn_BEG	2	2	2	2	1/me4
Dn_END	28	25	47	22	#/me4
DnRD_F	7	14	22	--	(more)
DnR D_E	91	10	--	28	(more)
No_BEG	1	1	1.6	2..2	#/me8+v
No_END	1	1	2	1	#/me8+v
No-RD_F	17	87	172	--	(more)
NoRD_E	57	31	--	63	(more)

Table 2

All the RDs are = relative differences in % (x 100)

A MICROPHYSICS PARAMETERIZATION SCHEME FOR RADAR DATA ASSIMILATION

W.Szyrmer[1], I. Zawadzki[1] and S. Laroche[2]

[1]McGill University, Montreal, H3A 2T5, Canada
[2]Meteorological Service of Canada, Montreal, Quebec, H9P 1J3, Canada

1. Introduction

A growing number of modeling and observational studies point to the importance of an accurate representation of cloud and precipitation microphysics in atmospheric numerical models. The microphysical calculations, describing the evolution of the spectra of different types of hydrometeors, determine the integral latent heat exchange that has an impact on the dynamics, and allow interpretation of measurements from radar or other remote sensing instruments. The major unresolved question is: what degree of complexity is necessary in the microphysical module, particularly in the context of data assimilation into a numerical model. Moreover, with the application of multi-parameter radar techniques (Doppler, polarization and multi-wavelength), the number of potential microphysical variables that may be inferred and used to maximize agreement between model solution and observations has become much larger. The microphysical representation has to be easily adaptable to allow the use of these different sources of data and increase the accuracy of the radar derived information.

Due to the great complexity of the microphysical interactions, the hydrometeor spectra are generally characterized in terms of a few bulk quantities that represent the distribution of moments or their combination, that substitute the spectral parameters. In the commonly used single- and double-moment bulk microphysics schemes, the number of prognostic moments is not sufficient to include the evolution of the shape/curvature of the hydrometeor distribution. This may lead to important errors in the microphysical calculations responsible for an inadequate model representation of radar observables; such model representation is imperative for data assimilation. In this paper we present a three-moment scheme that largely eliminates the errors resulting from the assumption of the fixed curvature particle size distribution (PSD) and assures more accurate radar reflectivity description.

2. Integral variables of particle size distributions

If $y(D)$ is the kernel function that describes a specific property of an individual particle as a function of particle equivalent spherical diameter, the corresponding PSD integral/bulk variable is defined as

Corresponding author's address: Wanda Szyrmer, Department of Atmospheric and Oceanic Sciences, 805 Sherbrooke St. West, Montreal, P.Q., H3A 2K6 Canada; E-Mail: wanda@zephyr.meteo.mcgill.ca.

$$Y \equiv \int_0^\infty y(D)N(D)dD. \qquad (2.1)$$

For $y(D)$ expressed as a power of D, $y(D)=a_y D^{b_y}$, the bulk quantities of distribution (e.g. water content, radar reflectivity factor) are directly related to the distribution moments defined by

$$\mathrm{M}_p \equiv \int_0^\infty D^p N(D)dD. \qquad (2.2)$$

Other variables that are used to describe the whole distribution, are various characteristic sizes (e.g. mass-weighted mean diameter) that essentially can be expressed in terms of two moments as: $D_{i,j} \equiv (\mathrm{M}_j/\mathrm{M}_i)^{1/(j-i)}$.

3. Scaling approach

The scaling normalization approach applied to a PSD is based on the assumption that the relative number concentration of particles for a given size distribution $N(D)$, is a function only of particle size D, normalized by scaling reference variables. This approach implies the occurrence of power law relationships between different integral quantities of the PSD. A reference variable represents the scaling quantity relating all integral quantities to each other. If the scaling PSD is known for a given distribution, the actual PSD at any time can be calculated if the reference variable is known. The normalization procedure, based on the concept of scaling applied to the hydrometeor distribution, namely rain drop size distribution (DSD), was first introduced by Sempere-Torres et al. (1994). Using the normalization approach with the scaling reference variable taken as the i^{th} moment of the distribution, all distribution related variables are expressed in terms of M_i. The expression relating any p^{th} moment to the moment used as scaling parameter is:

$$\mathrm{M}_p = C_{1,p}^{(i)}\, \mathrm{M}_i^{1+(p-i)\beta_i}, \qquad (3.1)$$

where the normalization constant, $C_{1,p}^{(i)}$, is a p^{th} moment of a general distribution function of the normalized diameter $x \equiv D\mathrm{M}_i^{-\beta_i}$, independent of the value of M_i and common to all DSD under consideration. This one-moment normalization approach (1-M), using one integral quantity, implies the interdependence of all distribution parameters.

To capture some of the variability of the general distribution function, Lee et al. (2004) have generalized this approach to two-moments scaling normalization (see also Lee & Zawadzki, these proceedings). In two-moment scaling normalization (2-M), the general form of the moment of the p^{th} order is expressed in terms of the two scaling moments as a double power law:

$$M_p = C_{2,p}^{(i,j)} M_i^{(j-p)/(j-i)} M_j^{(p-i)/(j-i)}, \quad (3.2)$$

where $C_{2,p}^{(i,j)}$ is defined as the p^{th} moment of a general PSD function, as in 1-M, but with a normalized diameter given by $x \equiv D(M_i/M_j)^{1/(j-i)}$.

The normalization of the PSD is a very promising method for modeling of bulk properties of the PSD in the bulk microphysics scheme, not only for DSD of rain, but also for any other hydrometeor category. The predictive moments are the scaling reference moments and their evolution is calculated by the model. All other PSD moments can be retrieved using the normalization relationships. On the other hand, taking the bulk quantities from the remote sensing measurements as the scaling quantities, and retrieving the other quantities based on the concept of scaling is a very useful technique.

The use of the normalization overcomes to some extent the dependence on the variability of the shape of the PSD, expressed via the form of the general scaling function. Its functional form remains free, but has to be imposed and the results are limited by an inherent assumption of a fixed shape for the function. The sensitivity to this fixed shape becomes larger for the moments of the orders more different from the reference moments. To make the results less dependent of the shape of the PSD, we further extend the two-moment normalization to three-moment scheme (3-M).

4. Construction of the three-moment scheme

If i, j and k are the orders of the three scaling moments, any moment p^{th} is calculated using (3.2) as

$$M_p = \left[C_{2,p}^{(i,j)} M_i^{(j-p)/(j-i)} M_j^{(p-i)/(j-i)}\right]^{1-x_p} \cdot \left[C_{2,p}^{(i,k)} M_i^{(k-p)/(k-i)} M_k^{(p-i)/(k-i)}\right]^{x_p} \quad (4.1)$$

In the above relation, the term depending on the shape of the PSD function may be written as

$$\left[C_{2,p}^{(i,j)}\right]^{1-x_p} \cdot \left[C_{2,p}^{(i,k)}\right]^{x_p}. \quad (4.2)$$

We search for the value of x_p^* for each needed order p, integer or not, that makes the expression (4.2) the least dependent on the shape parameter(s) of the most general functional form of PSD (in Section 6 we chose the generalized gamma function). Calculations are done by searching the couple (x_p^*, $C_{3,p}^{(i,j,k)}$) corresponding to a minimum of :

$$\sum_{\mu} ... \sum_{\gamma} \left| C_{3,p}^{(i,j,k)} - \left[C_{2,p}^{(i,j)}\right]^{1-x_p^*} \cdot \left[C_{2,p}^{(i,k)}\right]^{x_p^*} \right| = \min. \quad (4.3)$$

$\mu, ..., \gamma$ are all the shape parameters of the generic function. Their number is not limited to one, as in the case of the procedure where the shape parameter has to be retrieved explicitly. Some forms of shape may be not well represented if the evolution of their shape has to be described only by one parameter. The values of the shape parameters taken into account are the ones that span the range normally observed. Depending on the category of hydrometeors or other information the range of the shape parameters may be reduced relatively to the very general distribution. With the values of x_p^* and $C_{3,p}^{(i,j,k)}$ obtained by requiring that (4.3) be minimum for each moment

$$C_{3,p}^{(i,j,k)} = \left[C_{2,p}^{(i,j)}\right]^{1-x_p^*} \left[C_{2,p}^{(i,k)}\right]^{x_p^*} \approx const, \quad (4.4)$$

we write an approximate relation :

$$M_p = C_{3,p}^{(i,j,k)} M_i^{(1-x_p^*)(j-p)/(j-i) + x_p^*(k-p)/(k-i)} \cdot M_j^{(1-x_p^*)(p-i)/(j-i)} M_k^{x_p^*(p-i)/(k-i)} \quad (4.5)$$

for any p^{th} moment retrieved from three independent moments. The coefficient $C_{3,p}^{(i,j,k)}$ is approximated by a constant since it is much more independent of the shape of the function than in 2-M.

In this approach, in contrast with standard modeling bulk scheme, we obtain a representation of the PSDs by the moments of the size distributions alone, without representing the functional form of the size distribution itself. The functional form is used only as "a bridge" to find the minimizing couple, x_p^* and $C_{3,p}^{(i,j,k)}$. Hence, we avoid the retrieval of the shape parameter that is, in general, very sensitive to uncertainties in the reference moments, and thus impacts the other retrieved moments.

5. Unified representation for one-, two- and three-moment schemes

The number and order of the independent moments necessary to describe accurately enough the evolution of the PSD of the given hydrometeor population, depend on the microphysical processes that are active, the moments of interest, the observed moments that are combined with the model, the spatial and temporal scale, etc.. The proposed unified scheme of the moment's calculations can be used within the one-, two- or three-moment scheme for various selected reference moments.

Let $\Omega \equiv \{i, j, ...\}$ be the set of orders, including non-integer values, of reference moments. The number of elements, n_m is one, two and three for 1-M, 2-M and 3-M schemes, respectively. The moment of the p^{th} order is determined from the set of the reference moments from the general relation:

$$M_p = C_{n_m,p}^{(\Omega)} \prod_{\Omega} M_m^{e_{mp}^{(\Omega)}}, \quad (5.1)$$

where the values of $e_{mp}^{(\Omega)}$ depend, only on the orders of p^{th} and reference moments, and for the 3-M scheme contains a constant x_p^*. The coefficients $C_{n_m,p}^{(\Omega)}$ also depend on the moment orders, and in addition, change with the functional form and its shape parameters. This dependence is the most important for 1-M scheme, is much reduced in 2-M. In 3-M, the coefficients $c_{3,p}^{(\Omega)}$ are considered as constants. (In 1-M scheme, $C_{1,p}^{(\Omega)}$ and $e_{mp}^{(\Omega)}$ are determined in terms of an additional free parameter: λ and β, respectively.) The relation (5.1) is the unified representation of (3.1), (3.2) and (4.5).

The tendency of each independent moment of order $m \in \Omega$ is calculated from a separate predictive equation obtained by multiplying the conservation equation for PSD by D^m and integrating over the entire PSD:

$$\frac{d\mathrm{M}_m}{dt} = \int_0^\infty D^m \frac{\partial N(D)}{\partial t} dD. \qquad (5.2)$$

The rate of change of M_m due to any microphysical process (*PRC*) is

$$\left.\frac{d\mathrm{M}_m}{dt}\right|_{PRC} = \int_0^\infty D^m \left.\frac{\partial N(D)}{\partial t}\right|_{PRC} dD. \qquad (5.3)$$

The expressions on the RHS of (5.3) have been developed in terms of the other moments, integer or not, and without explicit dependence on the PSD. The general form of (5.3) is

$$\left.\frac{d\mathrm{M}_m}{dt}\right|_{PRC} = f\left(\mathrm{M}_{\max(m-3,0)},\ldots,\mathrm{M}_{m+3}\right). \qquad (5.4)$$

The moments on the RHS of (5.4), if not known, are calculated from the independent moment as given in (5.1).

6. Errors due to PSD shape variability

The dependence on the shape of PSD in (5.1) is expressed in terms of the coefficients $c_{n_m,p}^{(\Omega)}$. Taking them as constants means that it is supposed that the variability of the distribution shape has a negligible impact on the values of the retrieved moments. Here, we examine the errors of the retrieved moments caused by the fixed values of $c_{n_m,p}^{(\Omega)}$ for the three schemes.

To represent the observed Gaussian-type cloud droplet distribution, or an exponential DSD in stratiform rain, or a Gaussian-type DSD resulting from drop sorting in updrafts, etc., the general formulation of the true PSD distribution of different hydrometeor categories has to show considerable flexibility of shape. The generalized gamma (GG) function (Lee et al. 2004), compared to other probabilistic functions, appears to be sufficiently general to model PSDs of different hydrometeor categories from a variety of situations. There are two parameters which shape the GG function differently: μ and *c*. To retain all versatility both parameters must be allowed to change.

We assume that the PSDs conform to GG distribution. The uncertainties of the retrieved moments due to the changes described by the two shape parameters of the GG function are

$$\frac{\Delta\mathrm{M}_p}{\mathrm{M}_p} = \frac{\Delta C_{n_m,p}^{(\Omega)}}{C_{n_m,p}^{(\Omega)}} = \frac{C_{n_m,p}^{(\Omega)}(\mu,c) - C_{n_m,p}^{(\Omega)}}{C_{n_m,p}^{(\Omega)}(\mu,c)} \qquad (6.1)$$

where $C_{n_m,p}^{(\Omega)}(\mu,c)$ are coefficients in (3.1), (3.2) and (4.5), for the particular case of GG distribution. They are:

<u>for 1-M scheme</u>

$$C_{1,p}^{(i)}(\mu,c) = \left(\Gamma_p/\Gamma_i\right)\cdot \lambda_i^{i-p} \text{ with } \lambda_i = cst, \qquad (6.2)$$

<u>for 2-M scheme</u>

$$c_{2,p}^{(i,j)}(\mu,c) = \left(\Gamma_p/\Gamma_i\right)\left[\left(\Gamma_j/\Gamma_i\right)^{1/(j-i)}\right]^{i-p}, \qquad (6.3)$$

<u>for 3-M scheme</u>

$$c_{3,p}^{(i,j,k)}(\mu,c) = \left[c_{2,p}^{(i,j)}(\mu,c)\right]^{1-x_p^*}\cdot\left[c_{2,p}^{(i,k)}(\mu,c)\right]^{x_p^*}, \qquad (6.4)$$

where $\Gamma_q \equiv \Gamma(\mu + q/c)$. In 1-M and 2-M, $c_{n_m,p}^{(\Omega)}$ are calculated using (6.2) and (6.3) with $\mu = c = 1$ as it is common for precipitation particles, assuming the inverse exponential form. For 3-M scheme, we put for each p^{th} moment the constant value found by minimization of (4.3) with the values of shape parameters corresponding to a regime of variability: $\mu \in [0.1, 4.]$ and $c \in [1., 2.]$.

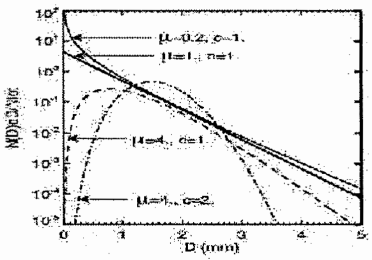

Fig. 1: *Four forms of the generalized gamma (GG) function that represent different naturally occurring DSDs of rain.*

To compare the errors caused by the shape variability in the calculations of the three schemes, we select four different forms of GG distributions described by four couples of μ and c, that represent various observed forms of the DSD of rain and are shown in Fig. 1. For the three forms, different from exponential inverse, the errors (6.1) are presented in function of the order p^{th} of the retrieved moment in Fig. 2. In Fig. 2a, the sets of independent moments are: $\{3\}$, $\{0,3\}$ and $\{0,3,6\}$ for 1-M, 2-M and 3-M schemes, respectively. These sets of moments may represent the model predictive moments for each microphysics scheme. On the other hand, in Fig. 2b, we use the set of independent moments that are related to observational data: 2nd (optical extinction), 6th (radar reflectivity in Rayleigh approximation), and 6.67th (approximated precipitation fall-speed weighted by reflectivity from Doppler radar). The used reference moments are: $\{6\}$, $\{3,6\}$ and $\{2,6,6.67\}$ for 1-M, 2-M and 3-M schemes, respectively.

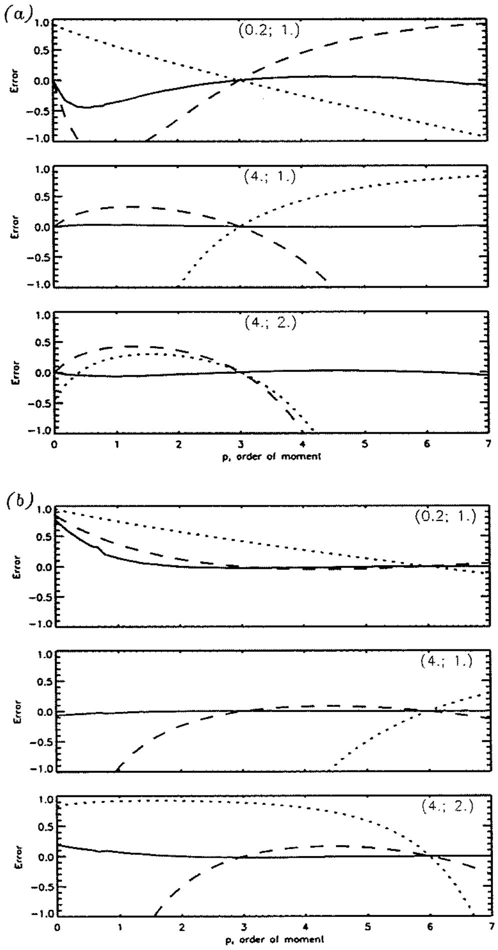

Fig. 2: Error as defined in (6.1) in moment estimation for the three forms shown in Fig. 6.1 as a function of the retrieved moments. The couple (μ, c) for each form is specified for each plot. The three curves describe the results for one- (dashed), two- (long-dashed) and three- (solid) moment schemes obtained from the sets of the reference moments: (a) {3}; {0,3} and {0,3,6}; (b) {6}; {3.6} and {2,6,6.67}.

In general, the new three-moment retrieval, gives the error for all evaluated moments smaller than 5%, except for the lower moments essentially in the case of very super-exponential form with $c\mu - 1 = -0.8$. The reduction of the errors in the 3-M scheme, relatively to the 2-M scheme is rather significant. For cloud droplet distributions represented by the GG with μ and c greater than 1, the accuracy of this 3-M retrieval is, in general, very high.

Another evaluation of our power-law relations between any moment and the three known moments is done using raindrop observations at the ground. The data used here represent 23678 observed DSDs in Montreal over a 5 year period, including all types of rain. (See Lee & Zawadzki in these proceedings for more details about the data). To estimate the accuracy of the proposed relationship between the moments with respect to the observed spectra, we use the efficiency defined for any moment p, as

$$E(p) \equiv 1 - \sum_{n=1}^{Nobs}\left[M_p(i) - M_p^{ret}(i)\right]^2 \Big/ \sum_{n=1}^{Nobs}\left[M_p(i) - \overline{M_p}\right]^2$$

where $M_p^{ret}(i)$ is the value of the M_p moment retrieved from the moments: 0th, 3rd and 6th of the ith observed DSD, while $M_p(i)$ is the actual moment. $\overline{M_p}$ is the average value of the true p^{th} moment. The retrieval using 3-M scheme gives E>0.99 for all retrieved moments up to 8th, while for 2-M, with 0th and 3rd taken as known moments and the exponential form, the efficiency is between 0.8 and 0.9 for p=1,2 and becomes negatives for $p \geq 5$.

7. Concluding remarks

The bulk quantities of hydrometeor PSD are important with respect to remote sensing and numerical modeling, two aspects involved in data assimilation. Here, we propose a unified treatment of bulk microphysics scheme that may be used for microphysics modeling under general conditions, with one-, two- or three- independent moments in normalized form. The time rates of change of arbitrary moments of the PSD are derived from the general evolution equation for the particle distribution in terms of the distribution moments (one, two or three) without the explicit dependence on the assumed general distribution function. This dependence is contained in the relationships between the moments; the uncertainties are generally very small in three-moment scheme with no need for a priori assumption about the form of the distribution, and become larger for the lower number of independent moments. The effectiveness of different schemes has been tested on individual microphysical processes and their results will be shown.

8. References

Lee, GW, I. Zawadzki, W. Szyrmer, D. Sempere-Torres & R. Uijlenhoet, 2004: A general approach to double-moment normalization of drop size distributions. *J. App. Meteor.*, **43**, 264-281.

Sempere-Torres, D., J.M. Porrà, J.-D. Creutin, 1994: A general formulation for raindrop size distribution. *J. App. Meteor.*, **33**: 1494-1502.

FORMATION OF A FIRE-INDUCED CONVECTIVE CLOUD: A MODEL STUDY OF THE CHISHOLM FIRE, 28 MAY 2001

J. Trentmann[1], T. Winterrath[2], G. Luderer[2], C. Textor[3], M. D. Fromm[4], R. Servranckx[5], D. Rosenfeld[6], P. K. Wang[7], P. V. Hobbs[1], M. O. Andreae[2]

[1]Dept. Atmos. Sciences, University of Washington, Seattle, WA, USA
[2]Max Planck Institute for Chemistry, Mainz, Germany
[3]LSCE, CEA Saclay, Gif-sur-Yvette, France
[4]Computational Physics, Inc. Springfield, VA, USA
[5]Meteorological Service of Canada, Montreal, Canada
[6]Institute of Earth Sciences, Hebrew University, Jerusalem, Israel
[7]University of Wisconsin-Madison, Madison, WI, USA

1. INTRODUCTION

Gaseous and particulate emission products from vegetation fires have been found in the upper troposphere and in the lower stratosphere. One potential vertical transport mechanism, which has the ability for cross-tropopause transport, is fire-induced convection. Fires are often associated with strong convection and the formation of convective clouds, so-called pyro-clouds, especially in boreal regions. Here, the vertical transport and the formation of a pyro-cloud related to an intense boreal vegetation fire near Edmonton, Alberta, Canada, in May 2001 (Chisholm fire) is investigated. Satellite observations show that emissions from the Chisholm fire were transported into the stratosphere by the fire-induced convection on 28 May 2001 (Fromm and Servranckx 2003). The active tracer high resolution atmospheric model (ATHAM) is used to simulate the intense convective event and to investigate the sensitivity of the model results with respect to the release of latent heat.

2. OBSERVATIONS AND MODEL

The Chisholm fire (55°N, 114°W), approx. 200 km north of Edmonton, Canada, burned an area of approx. 100,000 ha between 23 May and 29 May 2001. It was one of the the most devastating fire events in Alberta (Quintilio et al. 2001). Satellite and ground-based observations show the formation of a vigorous convective cloud above the Chisholm fire during the afternoon of 28 May 2001. Figure 1 shows a black-and-white AVHRR satellite image

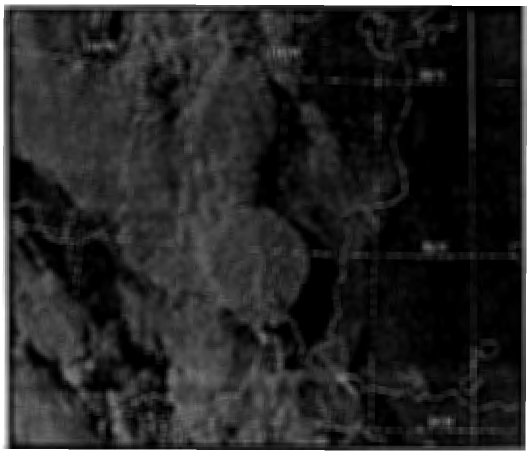

Figure 1: Black-and-white satellite image based on AVHRR data taken on 29 May 2001 at 0200 UTC.

taken at 0200 UTC (= 8 pm local time, MDT) over the location of the fire. The hot spot of the fire can be seen slightly below the center of the image, with a huge convective cloud forming north of it. Cloud top features include significant overshooting well above the altitude of the anvil and gravity wave structures. While the fire has been already burning for a number of days, the onset of the severe convection above the fire was correlated with the approach of a band of convective clouds associated with a cold front.

The ATHAM model is a three-dimensional atmospheric plume model, which has been designed and employed for the simulation of strong convective events, e.g., volcanic eruptions (Graf et al. 1999; Herzog et al. 2003; Textor et al. 2003) and vegetation fires (Trentmann et al. 2002). ATHAM solves the Navier-Stokes equations based on external forcings (e.g., heating from a fire) and calculates the transport of the emitted species

[1]Corresponding author's address: Jörg Trentmann, Dept. Atmos. Sciences, University of Washington, Box 351640, Seattle, Washington 98195, USA, jtrent@atmos.washington.edu

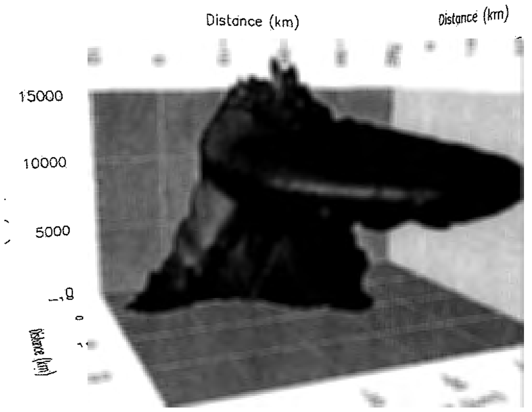

Figure 2: Isosurface of the simulated aerosol mass concentration (50 μg m^{-3}) at 25 minutes after the start of the fire.

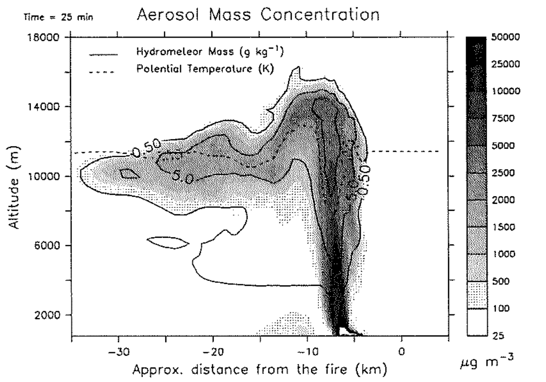

Figure 3: Simulated aerosol mass concentration (gray scale) along the main plume axis at 25 minutes after the start of the fire. Also indicated are the contours of the hydrometeor mass mixing ratio (thick line) and the tropopause (potential temperature 335 K) (dashed line).

with the simulated wind field. Cloud microphysics is treated with a two-moment scheme, predicting the mass of hydrometeors and aerosols, and the particle number concentration. in two liquid and two frozen size classes. Each class of hydrometeors is represented by a gamma distribution. The size cut between the small and large classes of hydrometeors is 40 μm.

3. MODEL SIMULATIONS

In the following we present results from model simulations designed to resemble the situation of the Chisholm fire during the time of the onset of the severe convection on the afternoon of 28 May 2001.

3.1 Model Initialization

The initial meteorological conditions were taken from a radiosonde launched at 0000 UTC 29 May 2001 from 53.55°N, 114.10°W. The convective available potential energy (CAPE) for this background profile was 350 J kg^{-1}, which is not particularly favorable for severe atmospheric convection. A rather large vertical wind shear in the lower atmosphere led to a bulk Richardson Number of 18, which is characteristic for the formation of supercell convection. In the model simulations, the fire was represented by fluxes of heat, water vapor, and aerosol into the lowest model layer. The calculation of these fluxes was based on information on the amount of fuel burned, the fuel moisture content, and the size and speed of the fire front (Quintilio 2001). The amount of dry biomass burned and the fuel moisture content were determined to be 7.6 kg m^{-2} and 88 %, respectively. The fire front was assumed to be 15 km wide and 300 m deep, the rate of spread was determined to be 1.5 m s^{-1}. This results in an energy flux of 710 kJ m^{-2} s^{-1} (50 % of which was assumed to contribute to the convection, the remaining energy was assumed to be released as radiative energy and was neglected in the present study). The emission of water vapor from the fire through production of H_2O in the combustion process (35 % of the total water vapor release), and the release of fuel moisture (65 %), accounts for a potential latent energy flux of 147 kJ m^{-2} s^{-1}, which is released during condensation and freezing at higher levels in the atmosphere.

An aerosol emissions factor of 17.6 g kg(dry mass)$^{-1}$ was used, resulting in average mass and particle number concentrations of 6200 μg m^{-3} and 10^6 cm^{-3} (the latter under the assumption of a volume mean radius of the emitted smoke of 0.1 μm) at cloud base (approx. 2500 m), respectively. It was assumed that 0.3 percent of the emitted aerosol formed cloud droplets under these conditions. The number of cloud droplets formed in the background air when supersaturation occurs is assumed to be 200 cm^{-3}.

The model simulations were performed on a spatial grid domain of x = 60 km, y = 60 km, and z = 28 km, using 80 x 90 x 90 cells on a stretched grid with a minimal grid size of 500 m x 100 m x 50 m. The dynamical time step was set to 1 s, the evolution of the cloud microphysical properties were calculated with a time step of 0.5 s.

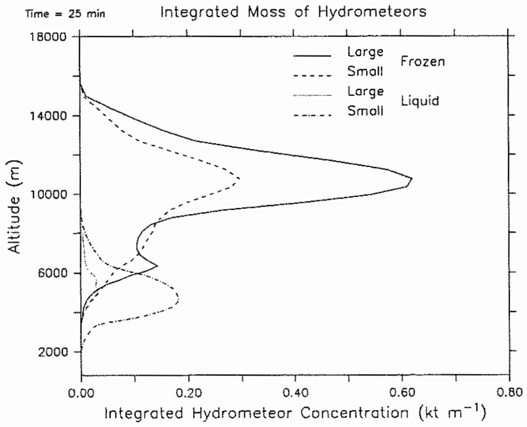

Figure 4: Horizontally integrated mass of the four classes of hydrometeors after 25 minutes of model simulation.

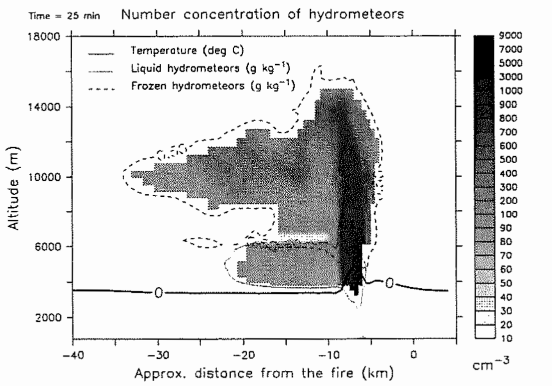

Figure 5: Simulated sum of the number concentrations of all four hydrometeor classes after 25 minutes of model simulation. The solid line represents the local temperature of 273 K, the dotted and dashed lines represent mixing ratios of 0.5 g kg^{-1} of liquid and frozen hydrometeors, respectively.

3.2 Model Results

In the following we will present model results from the reference simulation initialized according to Section 3.1.

The heat release from the fire results in a heating of the lower atmospheric model layer by about 40 K in the region of the fire. The updraft velocity reaches up to 70 m s^{-1} at 10 km. Figure 2 shows the isosurface of the simulated aerosol mass concentration after 25 minutes of simulation time. In the simulations, the fire generates strong convection, which overshoots into the stratosphere above the fire and develops an anvil at the tropopause level comparable to the observations (Figure 1). The cross section along the main plume axis is shown in Figure 3 (gray scale) together with the isolines of the mass mixing ratio of hydrometeors (thick lines) and the potential temperature of 335 K as an indicator for the tropopause. In the convective updraft the release of latent heat lead to a significant deformation of the isoline of the potential temperature. Significant aerosol mass is transported across the 335 K isosurface and up to the 400 K potential temperature level within the updraft region above the fire. This compares well with the potential temperature levels (380 K to 460 K) of stratospheric aerosol layers observed in 2001 (Fromm and Servranckx 2003). Downwind of the fire, a considerable amount of aerosol mass remains in the stratosphere. However, due to the comparatively short simulation time, no conclusion on irreversible cross-tropopause transport can yet be drawn from these results.

As can be seen from Figure 3, the simulations show that in addition to the pyro-cloud a secondary cloud is formed downwind of the fire between approx. 4000 m and 6000 m. This cloud consists of smoke-free background air inflowing on the lee side of the fire and lofted due to the fire induced convection, but without mixing into the smoke plume.

In the simulation, the hydrometeor mass mixing ratio in the cloud is dominated by the large, frozen hydrometeor class (Figure 4) with a volume mean radius of about 100 μm. The ice phase of the hydrometeors starts to dominate the total hydrometeor mass at an altitude of about 6 km. No significant amount of large, warm hydrometeors (warm precipitation) is formed. Despite their dominance of the mass concentration, the large, frozen hydrometeors only make a minor contributions to the number concentration in the cloud, which is dominated by the small, frozen hydrometeors class. Figure 5 shows the total number of hydrometeors in all four classes. The simulated average cloud droplet number concentrations at cloud base is approx. 14,000 cm^{-3} (the simulated updraft velocity at cloud base is approx. 25 m s^{-1}), the number concentration of hydrometeors in the anvil of the convective cloud lies between 200 and 600 cm^{-1}. The local minimum in the number concentration at about 6000 m is related to the dominance of the large, frozen hydrometeor class in this region.

4. IMPACT OF LATENT HEAT RELEASE

To differentiate the impact of the energy release by the fire and the release of latent heat during condensation and freezing, we neglected the release of

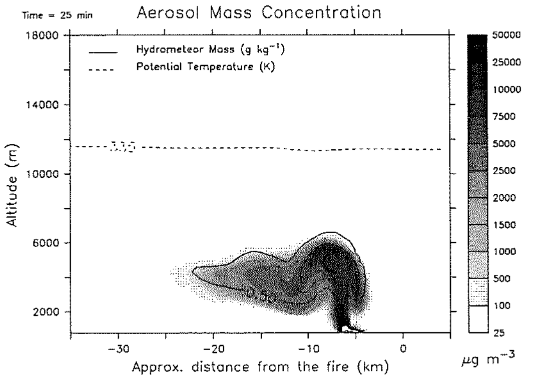

Figure 6: Results from the sensitivity study neglecting the release of latent heat. Simulated aerosol mass concentration (gray scale) along the main plume axis at 25 minutes after the start of the fire. Also indicated are the contours of the convective cloud (thick line) and the tropopause (potential temperature 335 K) (dashed line).

latent heat in a sensitivity study. The formation of hydrometeors was included in these model simulations, but no heat release by condensation and freezing was taken into account.

Figure 6 presents the simulated aerosol mass concentration (gray scale) of the sensitivity simulation along the main plume axis together with the isolines of the mixing ratio of hydrometeors (thick lines) and the potential temperature of 335 K. This figure can be compared with Figure 3, which shows results from the reference simulation. Even though the energy released by the fire leads to significant convection and vertical transport of the smoke emissions up to about 6000 m altitude, the convection is significantly reduced compared to the reference simulation, which includes the release of latent heat. This result indicates the potential importance of processes that modify the release of latent heat (e.g., condensation versus freezing) on the dynamical evolution of pyro-clouds, e.g., the release of water vapor from the fire and aerosol-cloud interactions.

Future studies will investigate the contributions to the latent heat flux from the different sources of water vapor, i.e., the background humidity, the release of the fuel moisture, and the production of water vapor in the combustion process. In addition, the impact of the smoke aerosol on the dynamical cloud evolution will be studied. It has recently been shown, that smoke aerosol modifies the cloud droplet spectrum and its evolution in convective clouds, potentially resulting in more vigorous convection, and thereby enhancing the possibility of cross-tropopause transport of fire emissions (Andreae et al. 2004).

5. ACKNOWLEDGMENTS

We thank Mark Stoelinga, Dean Hegg, and Gretchen Mullendore for helpful and stimulating discussions. J.T. thanks the Alexander von Humboldt-Foundation for support through a Feodor-Lynen fellowship.

6. REFERENCES

Andreae, M. O., D. Rosenfeld, P. Artaxo, A. A. Costa, G. P. Frank, K. M. Longo, and M. A. F. Silva-Dias, 2004: Smoking Rain Clouds over the Amazon, *Science,* **303**, 1337–1342.

Fromm, M. D. and R. Servranckx, 2003: Transport of forest fire smoke above the tropopause by supercell convection, *Geophys. Res. Lett.,* **30**(10), 1542, doi:10.1029/2002GL016820.

Graf, H.-F, M. Herzog, J. M. Oberhuber, and C. Textor, 1999: The effect of environmental conditions on volcanic plume rise, *J. Geophys. Res.,* **104**(D20), 24309–24320.

Herzog, M., J. M. Oberhuber, and H.-F. Graf, 2003: A Prognostic Turbulence Scheme for the Nonhydrostatic Plume Model ATHAM, *J. Atmos. Sci.,* **60**, 2783–2796.

Quintilio, D., B. Lawson, S. Walkinshaw, and T. Van Nest, 2001: Final Documentation Report Chisholm Fire (LWF-063, Publ. No. I/036, ISBN 0-7785-1841-8 (on-line edition)), Alberta Sustainable Resource Development, Forest Protection Division, Edmonton, AB.

Textor, C., H.-F. Graf, M. Herzog, and J. M. Oberhuber, 2003: Injection of gases into the stratosphere by explosive volcanic eruptions, *J. Geophys. Res.,* **108**(D19), 4606, doi:10.1029/2002JD002987.

Trentmann, J., M. O. Andreae, H.-F. Graf, P. V. Hobbs, R. D. Ottmar, and T. Trautmann, 2002: Simulation of a biomass-burning plume: Comparison of model results with observations, *J. Geophys. Res.,* **107**(D2), 4013, doi:10.1029/2001JD000410.

EVALUATION OF CLOUDS AND PRECIPITATION FROM A GLOBAL NWP MODEL

Paul A. Vaillancourt*, Stéphane Bélair, Michel Roch, and Anne-Marie Leduc

Meteorological Service of Canada, Dorval, Quebec, Canada

1. INTRODUCTION

In an effort to improve medium-range weather forecasting in Canada, a mesoscale version of the Global Environmental Multi-scale (GEM) model is now being developed at the Meteorological Research Branch (MRB) in collaboration with the Canadian Meteorological Center (CMC). The proposed configuration (**GEM-meso**) has twice the horizontal resolution and doubles the number of levels in the vertical compared to the present operational configuration (**GEM-op**). Major changes to the physical parameterizations are also proposed; namely to the vertical diffusion in the boundary layer as well as to the shallow and deep convective parameterizations.

Before operational implementations, any new model undergoes an extensive objective and subjective evaluation. The objective evaluation generally consists of rms and bias statistics of the wind, geopotential height, temperature and dew point depression as compared to the global synoptic network of radiosondes. Precipitation over North America is evaluated by comparing the model accumulations to the observed accumulations from the synoptic surface stations as well as from the SHEF (Standard Hydrologic Exchange Format) surface network. These evaluations have revealed significant improvements of most verified variables over most regions of the globe, in particular over Asia and the Tropics. However, given the scarcity of these types of observations over vast regions of the globe (e.g. oceans and the southern hemisphere), efforts have been made to make use of existing data sets which offer a more uniform and global coverage.

Two series of 132 hour simulations were conducted spanning the winter season of 2001-2002 and the summer season of 2002. These simulations were analyzed with special emphasis on determining the physical realism of the global-scale distribution and variability of precipitation, humidity, cloud cover, cloud water content as well as on top of atmosphere and surface radiative fluxes. This is accomplished by comparing the model output to observations provided by GPCP (Global Precipitation Climatology Project), ARM (Advanced Radiation Measurement Program), CERES (Cloud's and the Earth's Radiant Energy System), the CAVE (Ceres ARM Validation Experiment) surface network and SSM/I and TRMM satellites.

In this conference paper, the dynamical and physical configurations of the proposed model are first briefly described. Preliminary results of the study described above are then given.

* Corresponding author address: Paul A. Vaillancourt, RPN, Meteorological Service of Canada, 2121 Trans-Canada Highway, Montreal, Quebec, Canada, H9P 1J3; e-mail: paul.vaillancourt@ec.gc.ca

2. DYNAMICAL CONFIGURATION

The GEM model (Côté et al. 1998 a, b) has been in operational use for short, medium, and long-range weather forecast at CMC since 1998 (1997 for short range). The attributes of the uniform resolution **GEM-op** model as well as those of the proposed numerical (or dynamical) configuration are listed in Table 1. The main differences are related to the horizontal and vertical resolutions. The uniform horizontal grid spacing is decreased from 0.9° to 0.45°, whereas the number of levels goes from 28 to 58. Most new levels were added in the lowest two km and near the tropopause level. The timestep is decreased from 45 to 15 min In both configurations, the model top is at 10 hPa.

TABLE 1

	Current	*Proposed*
Model	**GEM-op**	**GEM-meso**
Horizontal resolution	0.9°	0.45°
No. of vertical levels	28	58
Timestep	45	15

Other aspects with limited impacts on the meteorological response of the model were also modified. For instance, the numerical "computational" poles are now collocated with the geographical poles instead of being located in the Pacific and Atlantic oceans (i.e., the integration grid was rotated).

3. PHYSICS PACKAGE

Practically every aspect of the condensation and convection package is being revisited for this new version of the global forecasting system. Our aim is to include condensation and convective parameterizations which are more appropriate for mesoscale resolution. The configuration of this new physics package is very similar to what is proposed for the short-range regional forecast version of GEM (resolution of 15 km over North America). This new physics package allows the representation of four distinct types of clouds; deep convective precipitating clouds (subgrid), shallow convective non-precipitating clouds (subgrid), boundary layer non-precipitating cumulus and strato-cumulus clouds (subgrid) as well as stratiform precipitating clouds (subgrid or grid scale). Bélair et al (2004) have investigated the impact of the improved representation of boundary layer and shallow convective clouds resultant from this new physics package. They have found an improved realism of the cloud distribution associated with a mid-latitude large scale weather system over the Pacific Ocean.

The parameterizations that differ from the current operational configuration are briefly described below.

3.1 Boundary-layer cloud scheme

An improved formulation of the cloudy boundary layer using a unified moist turbulence approach, following the strategy of Bechtold and Siebesma (1998) has been developed. In this formulation (Mailhot and Bélair, 2002), the vertical diffusion associated with boundary layer turbulence is done on the conservative variables.

3.2 Kuo Transient shallow convective scheme

The Kuo transient shallow convection scheme is a modified version of the Kuo scheme for deep convection. This scheme, specifically made to represent shallow and intermediate cumulus activity, was developed and tested by C. Girard and his colleagues (see Bélair et al. 2004, Mailhot et al. 1998). The shallow cloud model is driven at its base by turbulent boundary layer fluxes, i.e. the humidity "accession" is given by the tendencies from the vertical diffusion scheme.

3.3 Deep convection

The Kain and Fritsch (KF, 1990) scheme is proposed for the implicit condensation related to convective activity. In this scheme, the intensity of parameterized deep convection is proportional to the convective available activity (CAPE). Based on Fritsch and Chappell (FC, 1980), deep convection is triggered only if low-level upward motion is sufficient to overcome the convective inhibition, i.e., the negative energy between the lifting condensation level and the level of free convection on a log p - skew T diagram. The main improvement over the FC scheme comes from the one-dimensional entraining/detraining plume model for the updrafts and downdrafts introduced in KF (1990), and from more detailed microphysics.

4. PRELIMINARY RESULTS

4.1 Precipitation

The Global Precipitation Climatology Project (GPCP) combines data from polar orbiting and geostationary satellites as well as from rain gauge data to produce global lat-lon maps of precipitation estimates (Hufmann et al. 2001).

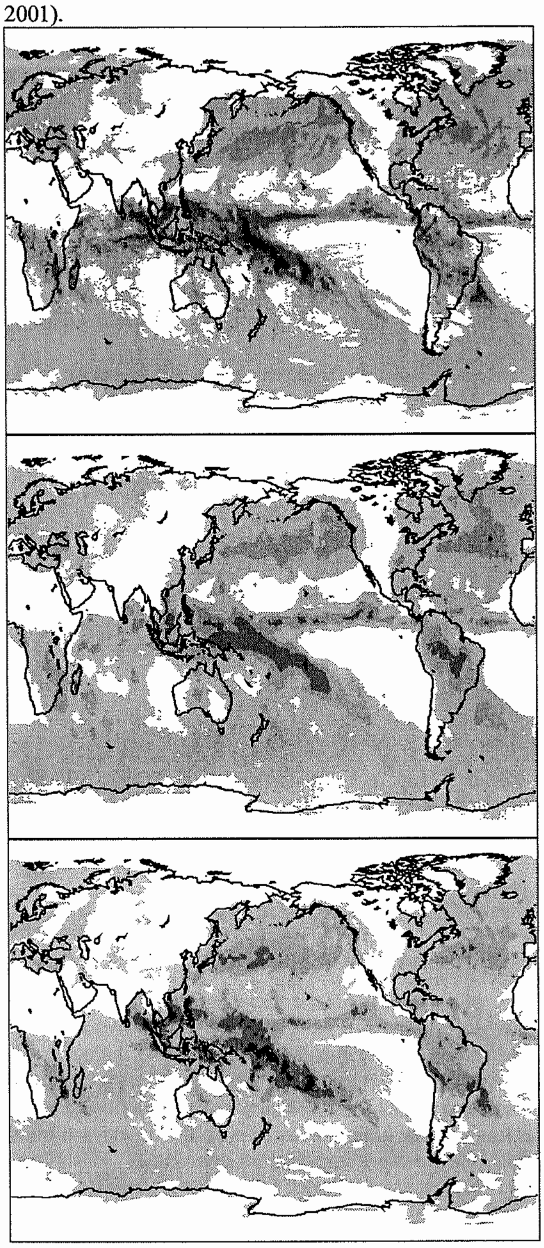

Figure 1: Monthly precipitation for December 2001. Top panel: GEM-meso, middle panel: GPCP, bottom panel: GEM-op. Contours from 0-1, 1-5, 5-10, 10-20, 20-50 mm/day.

Several products of different resolutions are available: monthly averages at 2.5 by 2.5°, daily averages at 1 by 1° and 3 hour averages at 0.25° resolution. For this study, we have mostly made use of the 1 by 1° product. Côté et al. (2003) showed 40 month long time series of monthly average precipitation over various geographical domains. The output of the **GEM-op** model was compared to the GPCP data. This study showed that the **GEM-op** model has a clear tendency to over-estimate the precipitation accumulation, in particular over the oceans. The first objective of the current study is to verify whether this problem persists within the **GEM-meso** model. Fig. 1 shows lat-lon maps of monthly averages of precipitation for both models as well as from the GPCP data. Several improvements in the **GEM-meso** model (top panel) are apparent. The areas with very low precipitation accumulation in the subtropical high pressure regions of the eastern Pacific and eastern Atlantic compare better to what can be seen in the GPCP analysis (middle panel). Furthermore, the ITCZ over the equatorial Atlantic of the **GEM-meso** model is very similar in intensity to that of the GPCP analysis, whereas it is very weak in the **GEM-op** model.

However, several features of the **GEM-meso** model can be identified that could be improved. Namely, the areas of strong precipitation over the North Atlantic and over Brazil.

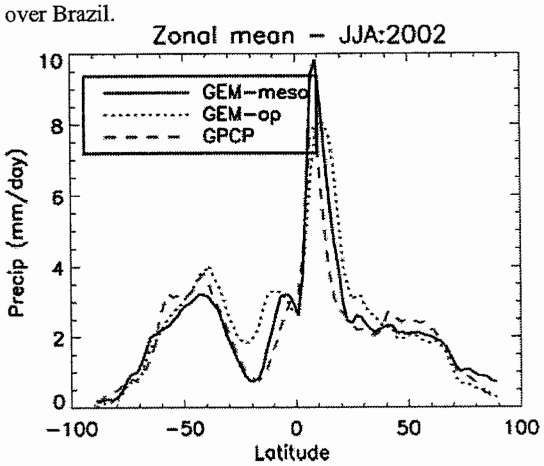

Figure 2: Zonal mean (averages over 2°) of precipitation over the period June to August 2002.

A more quantitative comparison of the precipitation fields is provided in Fig. 2. This figure shows a seasonal (June to August 2002) zonal average of precipitation. This figure confirms that the strong precipitation associated with the upward branch of the Hadley cell circulation as well as the low precipitation associated with the downward branch is much better represented in the new model. However, an over-estimation in the peak of the ITCZ can also be seen. Fig. 3 shows the time series, for the NH summer season, of the global average precipitation. The **GEM-meso** model shows a significant improvement in the global average of precipitation for both seasons (NH winter not shown). An examination of such time series over various geographical domains has led us to conclude that the over estimation seen in the tropical latitudes (Fig. 2) can be mostly traced to the West Pacific area.

4.2 Precipitable water

The model precipitable water (PW-vertical integration of the specific humidity) was evaluated using data from the SSM/I instruments carried onboard a series of polar orbiting satellites. This data was processed by Remote Sensing Systems (RSS) to provide monthly global maps (only over oceans) of PW (Wentz, 1997) from each SSM/I instrument (F13, F14, F15 for 2001-2002).

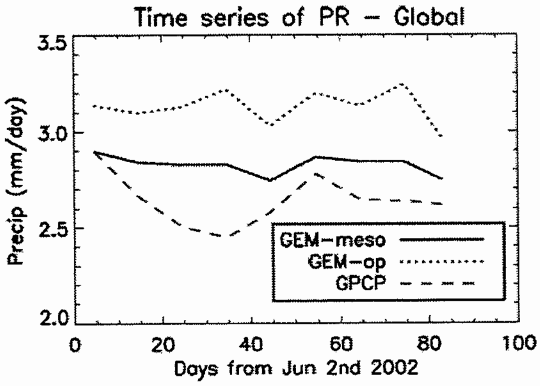

Figure 3: Time series of global precipitation

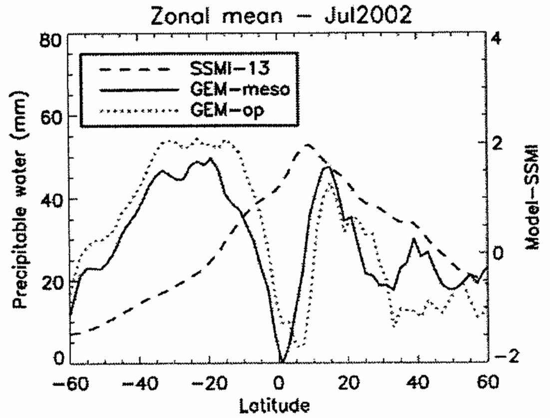

Figure 4: Zonal mean of precipitable water for July 2002.

Fig. 4 shows the zonal mean (over oceans) of the observed PW (left y-axis) as well as the model PW, from which the observed value was subtracted (right y-axis), for the month July 2002. Only the observations from the F13 satellite are shown. The three satellites available for this time period generally agree within less than 0.5 mm. It can be noted that for both models, the strongest biases are positive and are found in the winter hemisphere (NH winter not shown). Furthermore, the bias for the **GEM-meso** model is generally less that that of the **GEM-op** model.

4.3 Integrated cloud liquid water

The SSM/I instruments also allow the retrieval of the vertically integrated cloud liquid water content (IC). This data was also obtained from RSS has global (excluding land) monthly maps. Fig. 5 shows the zonal mean (over oceans) of IC for the month of December 2001. It can be seen that the **GEM-meso** provides a significant improvement in this quantity over the whole globe and in particular over the tropical regions. This is also true for every month of the period under study (not shown). The difference between the two models cannot be explained by a difference in the liquid versus solid partition of the condensate but is rather due to a significant increase of the cloud condensate in the tropical regions of the **GEM-meso** model (not shown).

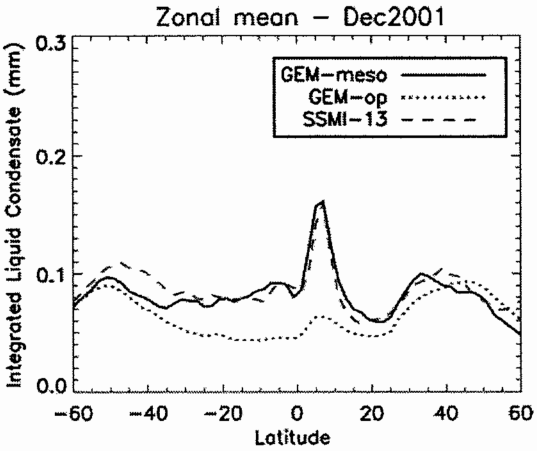

Figure 5: Zonal mean of the vertically integrated cloud liquid water content for December 2001.

4.4 OLR and cloud top pressure

Some preliminary work was done on the verification of the OLR of the **GEM-meso** model. By comparing the model values to observations obtained from NOAA-CIRES, it was found that the model OLR has a positive bias of the order of 15 Wm^{-2}. Furthermore, the global average cloud top pressure is significantly higher (lower clouds) than climatological values obtained from ISCCP. These two results point to a possible under estimation of high clouds in the model.

5. CONCLUSIONS AND FUTUR WORK

In this paper we have focused on evaluating and comparing the large scale features of the proposed **GEM-meso** model to the current operational NWP **GEM-op** model in terms of precipitation, precipitable water and integrated cloud water condensate. It was found that the proposed model provides improved precipitation fields (reduced biases and improved position of ITCZ), reduced biases of precipitable water and significantly improved integrated cloud liquid water in the tropical regions.

This is the first part of a study which also aims at evaluating the variability of the variables mentioned above as well as the biases and variability of the cloud spatial distribution, the outgoing longwave radiation at the top of the atmosphere and the longwave and shortwave radiative fluxes at the surface. Some of this future work will be presented at the conference. Furthermore, work is still needed to understand the weaknesses identified and to provide focused guidance for the efforts that will follow to correct these weaknesses.

6. ACKNOWLEDGEMENTS

SSM/I data and images are produced by Remote Sensing Systems and sponsored by the NASA Pathfinder Program for early Earth Observing System (EOS) products.

7. REFERENCES

Bechtold, P., and P. Siebesma, 1998: Organization and representation of boundary layer clouds. *J. Atmos. Sci.*, **55**, 888-895.

Bélair, S., J. Maihot, C. Girard and P.A. Vaillancourt, 2004: Boundary layer and shallow cumulus clouds in a medium range forecast of a large scale weather system. Submitted to *Mon. Wea. Rev.*

Côté, J. S. Bélair, P A. Vaillancourt, A. Erfani, and U. Gramann,2003: The Canadian global environmental multiscale model: development and applications. Proceedings of the International Workshop on NWP Models for Heavy Precipitation in Asia and Pacific Areas, Tokyo, Japan, 18-24.

Côté, Jean, Gravel, Sylvie, Méthot, André, Patoine, Alain, Roch, Michel, Staniforth, Andrew. 1998: The Operational CMC–MRB Global Environmental Multiscale (GEM) Model. Part I: Design Considerations and Formulation. *Monthly Weather Review*: Vol. **126**, No. 6, pp. 1373–1395.

Côté, Jean, Desmarais, Jean-Guy, Gravel, Sylvie, Méthot, André, Patoine, Alain, Roch, Michel, Staniforth, Andrew. 1998: The Operational CMC–MRB Global Environmental Multiscale (GEM) Model. Part II: Results. *Monthly Weather Review*: Vol. **126**, No. 6, pp. 1397–1418

Fritsch, J.M., and C.F. Chappell, 1980: Numerical prediction of convectively driven mesoscale pressure systems. Part I: Convective parameterization. *J. Atmos. Sci.*, **37**, 1722-1733.

Huffman, G.J., R.F. Adler, M. Morrissey, D.T. Bolvin, S. Curtis, R. Joyce, B McGavock, J. Susskind, 2001: Global Precipitation at One-Degree Daily Resolution from Multi-Satellite Observations. J. Hydrometeor., **2**, 36-50.

Kane, J.S., and J.M. Fritsch, 1990: A one-dimensional entraining/detraining plume model and its application in convective parameterization. *J. Atmos Sci.*, **47**, 2784-2802.

Mailhot J, and S. Bélair, 2002: An examination of a unified cloudiness-turbulence scheme with various types of cloudy boundary layers. Preprints, 15th symposium on Boundary Layer and Turbulence, 15-19 July 2002, Wageningen, The Netherlands, American Meteorological Society, 215-218.

Mailhot J, and Coauthors, 1998: Scientific description of RPN physics library. Version 3.6, Recherche en Prévision Numérique, 188pp. [available online at http://www.cmc.ec.gc.ca/rpn/physics/physic98.pdf]

Wentz F. J. 1997: A well-calibrated ocean algorithm for SSM/I. J. Geophys. Res., Vol. **102**, No. C4, pg. 8703-8718.

INCORPORATION OF A 1D ACOUSTIC-ELECTROSTATIC COALESCENCE MODEL INTO THE 3D CLOUD MODEL

Zlatko R. Vukovic[1] and Mladjen Curic[2]

[1]Meteorological Service of Canada, Toronto, Ontario, M3H 5T4, Canada
[2] Institute of Meteorology, University of Belgrade, Serbia and Montenegro

1. INTRODUCTION

Model simulations of lightning's influence on the redistribution of mass among cloud hydrometeors show very fast, compared to gravitational coalescence almost instantaneous, transformations in size, number, and phase composition in the vicinity of a lightning channel (Moore and Vonnegut, 1964; Curic and Vukovic, 1991; Carey and Rutledge, 1994; Vukovic and Curic, 1996,1998,2000). The intensity of such a sudden change could vary with cloud conditions and is localized in a relatively small part of the cloud. The real impact of the acoustic-electrostatic coalescence (AEC) due lightning could be seen only in interaction with other complex microphysical and dynamical processes that are included in 3D models.

A prime objective of this study is to establish a procedure for the incorporation of the 1D acoustic-electrostatic coalescence model into the 3D model without electrification scheme.

2. MODEL CHARACTERISTICS

2.1 3D ARPS model

The Advanced Regional Prediction System (ARPS) nonhydrostatic model is used for numerical simulation of life cycle of convective clouds (Xue et al., 2001).

The ARPS model has the bulk, mixed-phase microphysical parameterization, which includes the Kessler (1969) two-category liquid water scheme and modified three-category (cloud ice, snow, and hail) ice scheme of Yuh-Lang Lin et al. (1983). For calculation of hydrometeors' terminal velocity, the scheme assumes that the particle-size distribution functions for rain, snow, and hail have an exponential form and that all the ice particles have a spherical shape.

2.2 1D AEC model

The 1D AEC model (Curic and Vukovic, 1991; Vukovic and Curic, 1996,1998,2000) does not deal with the mechanism of electrical discharge in a cloud. The model only observes the moment when it takes place. The lightning channel is considered vertical and the cloud characteristics are axial-symmetrical around the lightning channel. It is also assumed that before the electrical discharge, the cloud is composed of four uniformly distributed negatively charged hydrometeor categories (cloud water, rain, cloud ice, and hail) that belong to a horizontal layer of unit thickness with constant temperature. The cloud-water and ice spectra are parameterized by the Khrgian-Mazin distribution, and the rain and hail with the Marshall-Palmer distribution function.

The lightning channel produces positive ions around the channel (Moore et al., 1964). Those ions, carried by a shock-wave front, will be moved away from the channel and collected by negative hydrometeors. Due to the shock-wave stress, the supercooled droplets could be partially transformed into frozen drops. The result is that air motion caused by the acoustic wave suddenly increases the velocity of differently charged hydrometeors. Faster drops collide with the slower ones and create conditions for coalescence growth. Since the hydrometeors are charged, the electric forces play an important role in coalescence efficiency and stability in newly created droplets. Also, very fast-moving water drops will be unstable, and they will be broken into smaller, stable ones. This growth of frozen and unfrozen drops, as well as a mass transfer from liquid to ice-phase spectra, is called acoustic-electric coalescence with phase transformation (AECT).

3. AEC-ARPS INCORPORATION SCHEME

To include 1D AEC model into the 3D ARPS model we had to solve two main differences between the models:

- time – space resolution and
- bin – bulk representation of hydrometeors.

Also we had to find for both models a suitable lightning parameterization.

3.1 Time – space resolution solution technique

The AEC model requires time and space resolution more than two orders higher than a typical ARPS model setup. A synchronized run of the AEC model inside the ARPS model would be extremely expensive in terms of computer time and memory. Therefore we created a file table where we stored the new values of mixing ratios as output from AEC runs for different initial conditions

For each AEC run all parameters were the same, except for the combination of temperature, cloud water, rain, cloud ice, and hail mixing ratios.

The temperature parameter (T) had three values: 0°C, -10 °C, and -20°C, for three parameterized cloud conditions: T>0 °C, 0 °C >T $\geq$ -15 °C, and T<-15 °C.

Corresponding author's address: Zlatko R. Vukovic, Meteorological Service of Canada, Toronto, Ontario, M3H 5T4, Canada; E-Mail: zlatko.vukovic@ec.gc.ca.

Each of the cloud-water (q_c) and ice-mixing-ratio (q_i) parameters had six values: 0, 0.01, 0.02, 0.03, 0.04, and 0.05 g/kg; while the rain (q_r) and hail (q_h) parameters had an order greater values.

The new mixing ratio values were calculated as AEC space domain averaged values (with the grid span of 10m). Since AEC is axial-symmetric model, the domain was chosen to be equal to the half of the ARPS horizontal grid. The lookup table was organized in a suitable way for fast location of the new mixing ratio values for certain combinations of original q_c, q_r, q_i, q_h, and temperature.

3.2 Bin - bulk hydrometeor representation

For the AEC model, bin representation of hydrometeors is essential, since the different sizes of elements receive different initial velocity due to the acoustic shock wave. Therefore the incorporation of the AEC model into the ARPS model requires a bin decomposition of the ARPS's bulk representation of hydrometeors. For a similar reason, but for obtaining mass-weighted fall speed, the ARPS model assumes exponential particle size distribution of rain and hail. For the cloud droplets and ice particle that is not the case and the ARPS cloud particles have a single size (mono-disperse) with diameter of 0.002cm.

In our bin representation of cloud water, cloud ice, rain, and hail we use a generalized gamma distribution function:

$$n(D) = \frac{N_t}{\Gamma(\nu)}\left(\frac{D}{D_a}\right)^{\nu-1}\frac{1}{D_a}\exp\left(-\frac{D}{D_a}\right), \qquad (1)$$

where $n(D)$ is the number of particles of diameter D, N_t is the total number of particles, ν is the distribution shape parameter, and D_a is the distribution average diameter.

For hail and rain we use the same assumed exponential distribution as in ARPS, i.e. ν=1. The relation between our gamma distribution and ARPS parameters is:

$$N_t = N_o/\lambda, \qquad (2)$$

where N_o is the intercept parameter (0.08 cm^{-4} for rain and 0.0004 cm^{-4} for hail), and λ is the slope of the rain/hail size distribution given by:

$$\lambda = (\pi\rho_x N_o/\rho_a q_x)^{0.25}, \qquad (3)$$

where ρ_x and q_x are density and mixing ratio of rain and hail, respectively, while ρ_a is air density. Using Eq. (1) for obtaining average diameter and comparing with Eq. (3) we obtain:

$$D_a = 1/\lambda. \qquad (4)$$

For cloud water and ice particles we use the Khrgian-Mazin distribution function, i.e. ν=3. The relation between our gamma distribution and the ARPS cloud water and cloud ice parameters is:

$$N_t = \rho_a q_x/(20\pi\rho_x D_a^3) \qquad (5)$$

where q_x is mixing ratio of cloud water or cloud ice, and the average diameter D_a has the same value as in ARPS, i.e. 0.002 cm.

From the set of (1)-(5) equations, we are able to convert ARPS bulk parameterization into the bin representation of hydrometeors: $n_x(D)= f_x(q_x)$.

3.3 Lightning parameterization

For our purposes, the most suitable lightning parameterization without electrification has been developed and described by Price and Rind (1994). The parameterization is based on observations that show thunderstorm electrification to be closely linked to the updraft intensity in the cloud, which in turn is linked to the vertical development of convective clouds. For continental thunderstorms the relationship is:

$$F_c = 3.44 \times 10^{-5} H^{4.90}, \qquad (6)$$

where, F_c is the lightning frequency (flashes per minute) and H is the cloud-top height above ground (km).

In the ARPS-AEC model we need flashes per big time step, $f_c(t)$:

$$f_c(t) = \begin{cases} \mathrm{int}(F_c/t_{mx})+1 & ; for\ t \le t_s \\ \mathrm{int}(F_c/t_{mx}) & ; for > t_s \end{cases} \qquad (7)$$

where t is time index inside one minute of simulation, t=1,2,...,t_{mx}, $t_{mx}=int(60/\Delta t_{big})$, and $t_s=int(F_c)-t_{mx}int(F_c/t_{mx})$. The $int()$ function converts an argument to an integer by truncating. During time iterations the new calculation of F_c was applied only every minute.

The parameterization of the lightning position in the cloud is based on the results of location relations of lightning centers and radar echoes studies (Chagnon, 1992, Lopez, 1997). It is found that flashes tend to cluster away from main reflectivity areas and occurred in regions of high gradients. According to this results, the lightning channel is parameterized as a set of the model points (I_f,j_f,k_f) that belong to the vertical line that passes through one of randomly chosen surrounding points from the point of maximum radar reflectivity in the layer between –10°C and –25°C isotherms.

3.4 Incorporation scheme

In the ARPS-AEC model the incorporation scheme of synchronization of ARPS and AEC models has several stages:

a) finds a possible number and location of lightning (f_c,I_f,j_f,k_f);
b) at the beginning of ARPS time loop, the AEC model takes the mixing ratio values of cloud

water, rain, cloud ice, and hail from each of the selected grid points that represent the lightning channel, $q_x(I_f,j_f,k_f)$;

c) determines which of three temperature regimes is representative for each of (I_f,j_f,k_f) the grid points, and read from the lookup table (for the closest combination of q_x) the new values of the mixing ratios, $q_x^{AEC}(I_f,j_f,k_f)$;

d) replaces the original $q_x(I_f,j_f,k_f)$ values with the new mixing ratio values, $q_x^{AEC}(I_f,j_f,k_f)$;

e) continues with the ARPS simulation;

f) repeats procedures a-e during each big time-step iteration.

The described procedure enables the AEC model to use ARPS current hydrometeor mixing ratios as input, while it's output the ARPS model uses as the new changed mixing ratio field.

4. CASE STUDY

To demonstrate the ARPS-AEC model, comparison between simulations with and without AEC are made for the well-documented and extensively studied storm of 20 May 1977 in Del City, Oklahoma (Ray et al., 1981; Ying Lin et al., 1993). Both model simulations were run for 60 minutes.

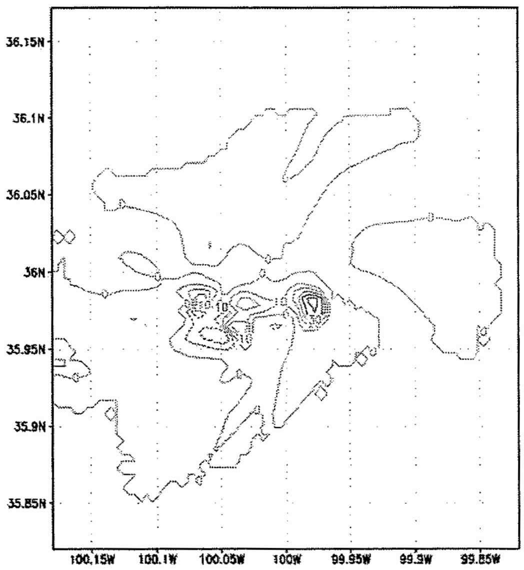

Fig. 1. The surface cross section of difference of rainfall (mm) between runs with and without AEC, t=45min.

For both experiments, the horizontal grid spacing is 500m and the vertical grid is 200m. The domain is 40x40x15km^3 in size. The storm was initiated by a 3.2C^o ellipsoidal thermal bubble centered at x = 48km, y = 16km, and z = 1.5km, and with radii of 10km in x and y directions and 1.5km in the vertical direction. The large and small time-step sizes are 3s and 1s, respectively.

The examples in Fig.1 and Fig.2 reveal the spatial effects of AEC on total surface rainfall and rain intensity. Fig. 3 shows an example of hail differences in vertical cross-section.

The clear effects of differences in dynamics and microphysics between the two simulations, without the effects of spatial shift, are visible in time-series differences in the maximum vertical velocity (Fig. 4) and radar reflectivity (Fig. 5).

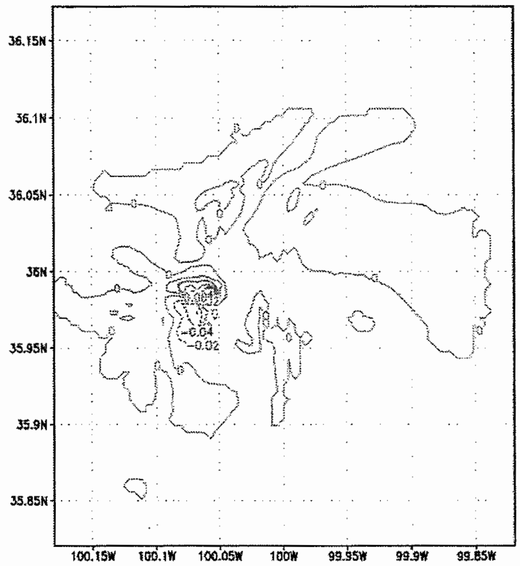

Fig. 2. The surface cross section of rain-rate difference (mm/min) between runs with and without AEC, t=45min.

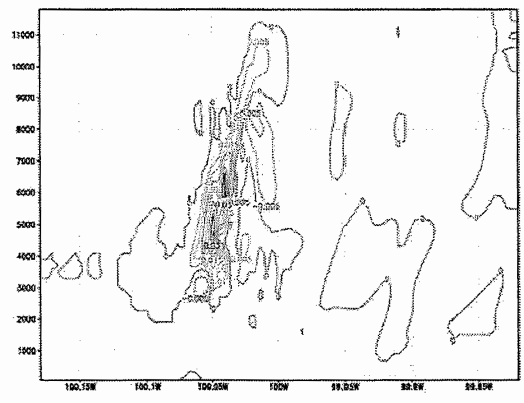

Fig. 3. Vertical cross section, x-z plane, of hail difference (g/kg) between runs with and without AEC, in t=45 minute, y=18.5km (35.957N).

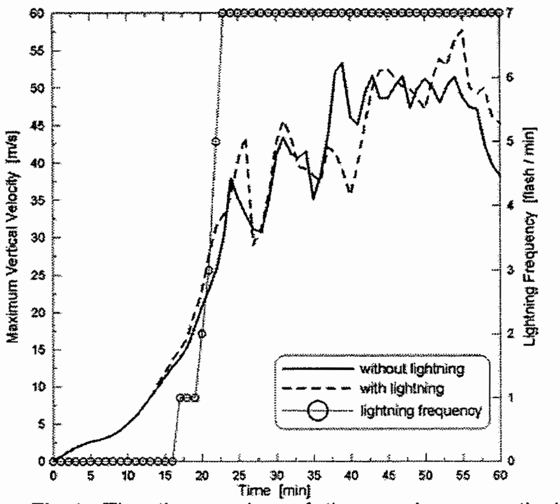

Fig.4. The time series of the maximum vertical velocity for simulations with and without lightning for Del City, OK, storm.

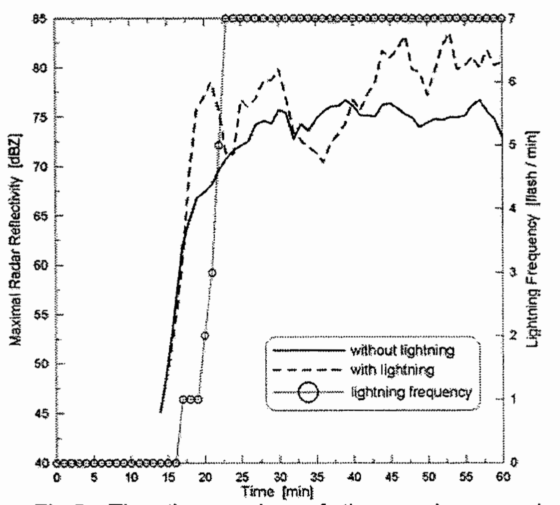

Fig.5. The time series of the maximum radar reflectivity for simulations with and without lightning for Del City, OK, storm.

5. CONCLUSION

To include a lightning parameterization in any numerical model is important not only from the aspect of cloud electrification, but also for studying

- the effects of lightning on the coalescence and faze transformations of hydrometeors; and
- the influence of lightning on cloud dynamics.

The suggested scheme for incorporating the AEC model into the ARPS model gives a good starting point for further, more sophisticated methods of incorporating AEC not only in a 3D model with much higher resolution, but also in a model with an explicit electrification scheme. In the latter case the obtained results would have not only a demonstration purpose but also quantitative importance.

6. REFERENCES

Changnon, S. A., 1992: Temporal and spatial relations between Hail and Lightning. J. Appl. Meteor., 31, 587-605.

Carey, Lawrence D., Rutledge, Steven A. 2000: The Relationship between Precipitation and Lightning in Tropical Island Convection: A C-Band Polarimetric Radar Study. *Mon. Wea. Rev.,*128, 2687–2710.

Curic, M. and Z. R. Vukovic, 1991: The intfluence of thunderstorm genereted acoustic waves on coagulation. Part one: Mathematical formulation. *Z.Meteor.* 41, 164-169.

Kessler, E., 1969: On the Distribution and Continuity of Water Substance in Atmospheric Circulation, Meteor. Monogr., 32, Amer. Meteor. Soc., 84 pp.

Lin, Yuh-Lang, Farley, Richard D., Orville, Harold D. 1983: Bulk Parameterization of the Snow Field in a Cloud Model. *J. Appl. Meteor.,* 22, 1065–1092.

Lin, Ying, Ray, Peter S., Johnson, Kenneth W. 1993: Initialization of a Modeled Convective Storm Using Doppler Radar–derived Fields. *Mon. Wea. Rev.,* 121, 2757–2775.

Lopez E.R. and Jean-Pierre Aubagnac 1997: The lightning activity of a hailstorm as a function of changes inits microphysical characteristics inferred from polarimetric radar observations. *J.G.R.* V102, No. D14, 16779-16813.

Moore, C.B., Vonnegut, B.,Vrablik, E .A., 1964: Gushes of Rain and Hail After Lightning. *J. Atmos. Sci.,*21, 646-665.

Price, Colin, Rind, David. and McCaig,A.D. 1994: Modeling Global Lightning Distributions in a General Circulation Model. *Mon. Wea Rev.,*122, 1930–1939.

Ray, P.S., Johnson, B.C., Johnson, K.W., Bradberry, J.S., Stephens, J.J., Wagner, K.K, Wilhelmson, R.B., Klemp, J.B.. 1981: The Morphology of Several Tornadic Storms on 20 May 1977. *J. Atmos. Sci.,*38, 1643–1663.

Vukovic, R.Z. and Curic M. 1996: A possible relationship between lightning discharge in cloud and gushes of rain. *Pro 12. ICCP*, Zurich, Switzerland.

Vukovic, R.Z. and Curic M.1998: The acoustic-electric coalescence and the intesification of precipitation radar echoes in clouds. *Atm.Res.* 47-48, 113-125.

Vukovic, R.Z. and Curic M. 2000: The ice initialisation by the acoustic-electrostatic coalescence. *Pro 13. ICCP*, Reno, Nevada, USA.

Xue M, K.K. Droegemeier, V. Wong, A. Shapiro, K. Brewster, F.Carr, D. Weber, Y. Liu, and D. Wang, 2001: The Advanced Regional Prediction System (ARPS) – A multi-scale nonhydrostatic atmospheric simulation and prediction tool. Part II: Model physics and applications. *Met. Atmos. Phys.* 76, 143-165.

THE IMPACT OF EXTREME WATER VAPOR SUPPLY ON OROGRAPHIC-CONVECTIVE-STRATIFORM MIXED CLOUD

WANG, Weijia[1] and TAO, Xialing[2]

[1]Artificial Precipitation Stimulation and Hail Suppression Office of Sichuan Province, Chengdu, 610071, China
[2]Nanjing Institute of Meteorology, Nanjing, 210044, China

1. INTRODUCTION

Water vapor supply is an important factor in yielding precipitation. China is abundant in heavy rainfall, which has both good and bad impact on China's fragile agriculture and other respects of the economy. And past studies reveal that most heavy rainfall in China is produced by convective-stratiform mixed cloud systems and orographic-convective-stratiform mixed cloud systems. The latter produced heavy rainfall that does even greater damage. Since Hu et al. studied stratiform clouds using 1-D model in 1986, many cloud models have been presented, from 1-D to 3-D. However, those numerical models suffer from high performance demanding on computer speeds and cannot easily be used in operational work. Then we develop a $1\frac{1}{2}$ dimensional non-constant model in this paper to simulate the orographic-convective-stratiform mixed cloud system and study the impact of extreme water vapor supply on orographic-convective-stratiform mixed cloud.

2. DESIGN OF THE NUMERICAL MODEL

To simulate the orographic-convective-stratiform mixed cloud system with extreme water vapor supply (cloud system A) and the orographic-convective-stratiform mixed cloud system without extreme water vapor supply (cloud system B), a $1\frac{1}{2}$ dimensional non-constant model of microphysical processes in orographic-convective-stratiform mixed clouds is developed. 18 physical variables are studied here. They are mixing ratio of liquid water(unit: g $\cdot$kg^{-1})— Q_v, Q_c, Q_r, Q_i, Q_g, Q_S, maximum velocity of precipitation(unit: m $\cdot$s^{-1})— V_r, V_i, V_g, V_s, radius of water contents(unit: μ m)— X_r, X_i, X_g, X_s, numerical density(unit: kg^{-1})— N_r, N_i, N_g, N_s. In this $1\frac{1}{2}$ D model, the transformation rates of the specific water contents of cloud droplets, raindrops, ice crystals, snowflakes and graupels are deduced based on theoretical and experimental results for 16 microphysical processes. The 16 microphysical processes are illustrated with Fig. 1.

Corresponding author's address: WANG, Weijia, Artificial Precipitation Stimulation and Hail Suppression Office of Sichuan Province, Chengdu, Sichuan Province, 610071, China; E-Mail: wjwang999@sohu.com.

With this model, the main evolution processes, structure and precipitation features of cloud system A and cloud system B are studied; the physical reasons of producing heavy rainfall are analyzed. We have to leave out the 22 basic equations of the numerical model according to the page limit. In the vertical direction, the atmosphere is divided to 21 layers, with heights being 0, 200m, 400m, 600m, 800m, 1000m, 1200m, 1400m, 1600m, 2350m, 3100m, 3850m, 4600m, 5350m, 6100m, 6850m, 7600m, 8350m, 9100m, 9850m, 10600m. As for the time grid, the variables are calculated every 4 min, from 4 min to 240 min.

Two experiments were performed based on this model. The only difference is that extreme water vapor supply was added in experiment A, which simulates the processes of cloud system A, and removed in experiment B, which simulates the processes of cloud system B. The input data are based on the analysis of standard meteorological elements, satellite maps and sounding balloon data. Both experiments were run for 240 minutes.

3. NUMERICAL RESULTS

3.1 Comparison of Rainfall Amount

Table 1 below shows that rain reaches the earth both at 28 min. However, accumulated rainfall amount of cloud system A increases quicklier than that of cloud system B. Experiment A yielded heavy rainfall more than 700 mm, while experiment B yielded small rainfall a little more than 1 mm.

Table1. Comparison of the accumulated rainfall amounts of cloud system A and cloud system B

Time (min)	Cloud system A (mm)	Cloud system B (mm)
4	0	0
24	0	0
28	0.14492	0.00002
64	50.67188	0.37996
84	118.2668	0.57118
104	206.4985	0.73863
240	702.6633	1.23048

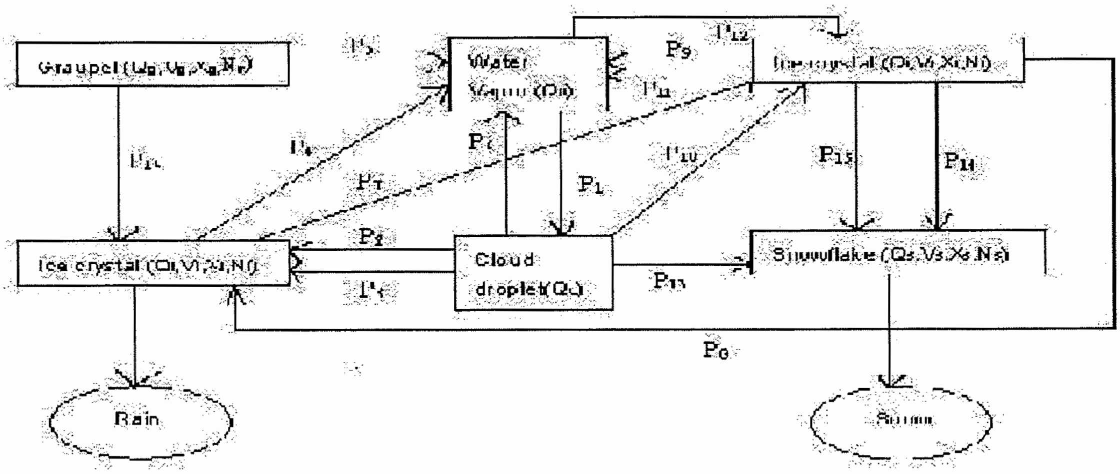

Fig. 1. Cloud Microphysical processes. In this model, the transformation rates of the specific water contents of cloud droplets, raindrops, ice crystals, snowflakes and graupels are deduced based on theoretical and experimental results for 16 microphysical processes. The symbol "P" here stands for both the microphysical process and the velocity of the change of mixing ratios of water contents in each process. P_1:condensation of water vapor, P_2:autoconversion from cloud droplets to raindrops, P_3: accretional growth of coalescence of raindrops and cloud droplets, P_4:evaporation of raindrops, P_5:melting-and-evaporation of graupels, P_6:evaporation of cloud droplets, P_7:freezing of raindrops, P_8:melting of ice crystals, P_9:melting-evaporation of ice crystals, P_{10}:coalescence-and-rimming of ice crystals and cloud droplets, P_{11}:evaporation of ice crystals, P_{12}:sublimation from water vapor to ice crystals, P_{13}:coalescence of snowflakes and cloud droplets, P_{14}:coalescence of snowflakes and ice crystals, P_{15}:conversion from ice crystals to snowflakes, P_{16}:melting from graupels to raindrops.

Because the only difference between two experiments is that extreme water vapor supply was added in experiment A, we can conclude that extreme water supply will make orographic-convective-stratiform mixed clouds yield great heavy rainfall.

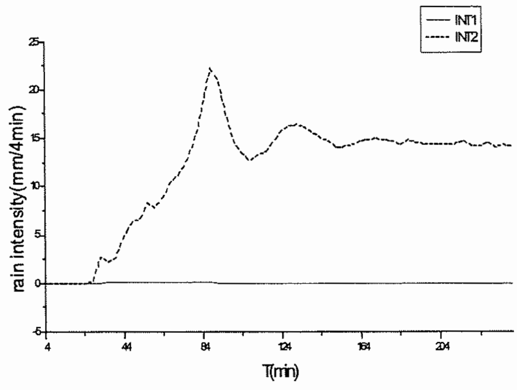

Fig 2. Comparison of changes of rain intensity in experiment A and experiment B. The unit of rain intensity here, is "mm/4min". INT1 stands for rain intensity of cloud system B, while INT2 stands for rain intensity of cloud system A.

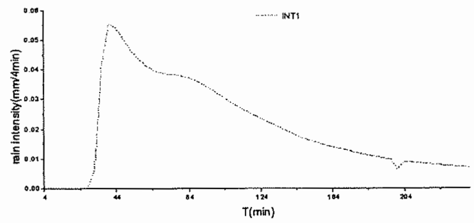

Fig 3. Change of rain intensity in experiment B. The unit of rain intensity here, is "mm/4min". INT1 stands for rain intensity of cloud system B.

Referring to Fig. 2 and Fig. 3, in experiment A, the rain intensity increased to 73.5 mm · h^{-1} at 44 min., then mounted rapidly to the apex — 333 mm · h^{-1} at 88 min., and undulated later, finally reached 211.5 mm · h^{-1}, and kept this value steadily with a little wave in the left time. In experiment B, the rain intensity reached the apex — 0.83 mm · h^{-1} at 40 min., then kept decreasing in the left time.

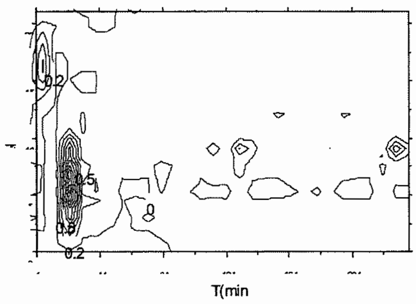

Fig 4. Variation of the mixing ratio of liquid water of clouds in experiment A. The maximum ratio is 5.225 $g \cdot kg^{-1}$.

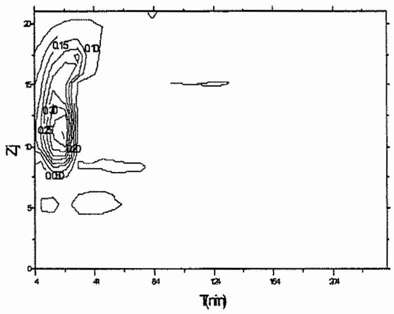

Fig 5. Variation of the mixing ratio of liquid water of clouds in experiment B. The maximum ratio is 0.580 $g \cdot kg^{-1}$.

Clouds begin to form at the same time in Fig 4. and Fig. 5 so that no revisal in drifting should be done. The height of cloud base in cloud system A and cloud system B is respectively 200m, 1000m. The maximum mixing ratio of liquid water of clouds of cloud system A is 5.225 $g \cdot kg^{-1}$, which is at 800m high, 600m higher above the cloud base, at 24 min; while that of cloud system B is 0.580 $g \cdot kg^{-1}$, which is at 3100m high, 2100m higher above the cloud base, at 24 min. Both cloud systems clearly show characteristics of mixed clouds; they have obvious cylinder and layer structure. In both cloud system, cylinder structured clouds form at the stage of highly development. Different from cloud system B, there are many convective clouds in the evolution process of cloud system A. In cloud system B, there are mainly cylinder-structured clouds in first 30 minutes, which distribute mostly from 1200m to 9850m; then the maximum mixing ratio of liquid water of clouds emerges at 24 min, and clouds mount their acme of development; later clouds evolve from convective to stratiform and decrease at 30 min; stratiform clouds become dominant at 50 min and clouds decrease quickly; finally all clouds disappear at 136 min. While in cloud system A, there are mainly cylinder-structured clouds all along in the 240-min-experiment; there are dense isolines, formed respectively at the height from 4000m to 9850m, from 4 min to 15 min, and at the height from 300m to 3100m, from 18 min to 38 min; then stratiform clouds begin to form at 30 min and clouds decrease a little, however, clouds still form at the height from 600m to 2350m; there are still clouds at the end of the 240-min-experiment. These analyses are strongly supported by figure 6 and figure 7.

4. SUMMARY

This study addresses the impact of extreme water vapor supply on orographic-convective-stratiform mixed clouds. With the simulated $1\frac{1}{2}$ D non-constant model developed in this paper, two experiments were performed. The numerical experiments show that if plus extreme water vapor supply then the orographic-convective-stratiform mixed cloud system becomes a very effective precipitation system. The evolution processes of cloud system A and cloud system B are dramatically different. In simulated cloud system B, there were mainly convective clouds at first, then mainly stratiform clouds, later all disappeared at 136 min; while in simulated cloud system A, there were mainly convective clouds all along in the 240-min-experiment. Experiment A yielded heavy rainfall more than 700 mm, while experiment B yielded small rainfall a little more than 1 mm. In experiment A, the rain intensity increased to 73.5 $mm \cdot h^{-1}$ at 44 min., then mounted rapidly to the apex — 333 $mm \cdot h^{-1}$ at 88 min., and undulated later, finally reached 211.5 $mm \cdot h^{-1}$, and kept this value steadily with a little wave in the left time. In experiment B, the rain intensity reached the apex — 0.83 $mm \cdot h^{-1}$ at 40 min., then kept decreasing in the left time. Extreme water vapor supply provides a more saturated environment for clouds, the convergence field lasting much longer, and much more coalescence of ice-phase particles. These are major physical factors for heavy rain formation.

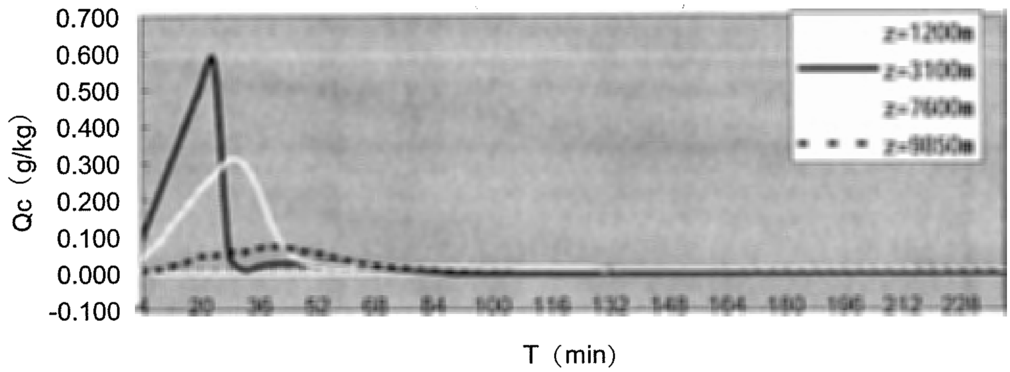

Fig 6. Variation of the mixing ratio of liquid water of clouds in experiment B at specific heights. We choose the height a little higher than cloud base(1200m), the height a little lower than cloud top(9850m), the height which contains the maximum of the mixing ratio of liquid water of clouds (3100m), the height where posterior clouds mainly distribute(7600m).

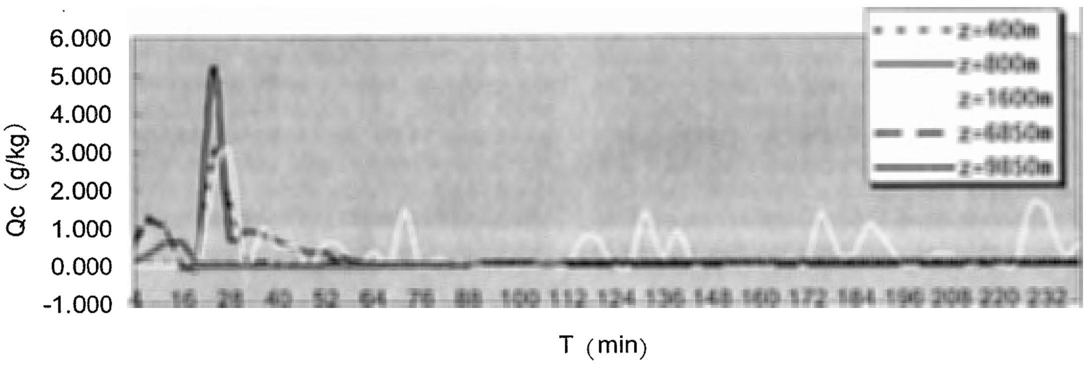

Fig 7. Variation of the mixing ratio of liquid water of clouds in experiment A at specific heights. We choose the height a little higher than cloud base(400m), the height a little lower than cloud top(9850m), the heights which contains the maximum of the mixing ratio of liquid water of two convective cloud sectors(6850m, 800m), the height where posterior clouds mainly distribute(1600m).

Acknowledgements. We thank LUO, Yongping, LIU, Jianxi, and TAO, Yue for comments on our manuscript.

REFERENCES

Ding, Yihui, 1993: The study of continual heavy rainfall over Changjiang-Huaihe River Basin in 1991. China Meteorological Press, 255. (in Chinese)

Hong, Yanchao, 1996: The numerical simulation study of convective-stratiform mixed cloud, part (I) — the model and parameterization of microphysical processes. Acta Meteor. Sinica., 5, 544-557. (in Chinese)

Hong, Yanchao, 1996: The numerical simulation study of convective-stratiform mixed cloud, part (II) — interaction of clouds and formative mechanism of the heavy rain. Acta Meteor. Sinica., 6, 661-674. (in Chinese)

Hu, Zhijin et al, 1986: Numerical simulation of microphysical processes in stratiform clouds (I) — microphysical model. J. Acad. Meteor. Sci. S. M. A. China., 1, 37-52. (in Chinese)

Hu, Zhijin et al, 1987: Numerical simulation of microphysical processes in cumulonimbus clouds (I) — microphysical model. Acta Meteor. Sinica., 4, 467-484. (in Chinese)

Xue, Jishan, 1999: The study of heavy rainfall in South China in the summer of 1994. China Meteorological Press, 7. (in Chinese)

THREE-DIMENSIONAL NUMERICAL SIMULATION OF TORRENTIAL RAINSTORMS IN WUHAN

Hui XIAO, Xiaobo WANG, Feifei ZHOU, and Yanchao HONG

Institute of Atmospheric Physics, Chinese Academy of Sciences, Beijing 100029, P.R. China

1. INDRODUCTION

The Yangtze (Changjiang) River valley is an important economic area of China. The local severe rainstorm frequently occurs in summertime and has taken great effect on the national economy. The continuously torrential rain disaster occurred in the regions of Wuhan, Huangshi, and so on, Hubei Province, during the two successive days of 20-22 July 1998, had made the province lost up to 7300 million yuan RMB (US$ ~880 million). Some studies (Tao *et al.*, 1998, 2001; Xu, 2000; Zhao *et al.*,1998) on the background of macroscale circulation and mesoscale convective system brought about this event have been done, but few studies on its detailed cloud physical processes are made. So in this paper, we will use a three-dimensional convective cloud model to simulate the torrential rainstorm occurred in Wuhan only on 21 July 1998 (abbreviated to Wuhan Case), focused on analyzing the development of cloud and the cloud-physical mechanism of rainstorm formation from microphysical aspect. As a comparison, another case occurred in Xunyi County in the north of Shaanxi Province on the night of 20 July 1999 (abbreviated to Xunyi Case) was chosen.

2. CLOUD MODEL, DATA AND SYNOPTIC PATTERN

The cloud model used in the simulations of torrential rainstorms is the second version of three-dimensional Convective Storm Model (IAP-CSM3D) developed successively by the Institute of Atmospheric Physics (IAP), Chinese Academy of Sciences (Kong et al., 1990; Hong et al., 1999a,b). The model is the one with non-hydrostatic and fully elastic equations, more detailed double-parameter (i.e., specific content Q and specific concentration N) and bulk-water parame-terized microphysics for water vapor, cloud drops, rain drops, ice crystals, snowflakes, graupels, frozen drops, and hailstones.

Weather analyses (Tao *et al.*, 1998, 2001; Xu, 2000; Zhao *et al.*, 1998) show that a shear line was located in the Yangtze River valley from 20 to 22 July 1998. On this line a low pressure system kept stable. The Yangtze River valley lied in the northwest of the southwest low-level jet, while Wuhan lied in the zone of its maximum wind speed. Therefore low-level jet zone maintained over Wuhan Area and water vapor was continuously transported to the torrential rainstorm area. At the same time severe rainfall system appeared in the area of low-level convergence and high-level divergence, and the convergence value of water vapor flux was great (Bei, 2000). As a result, the severe rainfall process began from 05:30 July 21 and lasted approximately two to three hours. The rainfall center was located in Wuhan City and its nearby regions. In Wuhan the maximum hourly rainfall observed was 107.6 mm and maximum 10-min rainfall was 22mm (Deng *et al.*, 1999) during the time of 06:00 to 07:00 (Beijing Time) on the morning of July 21.

On July 20 08:00 in 1999 the surface situation was that the low-pressure center located in the boundary of Xinjiang, Xizang (Tibet), and Gansu Provinces, two high-pressure centers were respectively situated in North Xinjiang and Japan Sea, and Xunyi was in the warm area of the front low-pressure zone. A 500hPa high-level Mongolia cold vortex was located in the Great Bend of Yellow River. And there was a closed low-pressure system in the boundary of Ningxia, Inner Mongolia, and Gansu Provinces. Until 20:00 July 20, the two low-pressure systems merged into a trough. In high-level chart Xunyi located in the front of it, and the trough line passed through to trigger the local severe convection. The real rainfall observed was 72mm during 90 minutes.

As for the Wuhan case, the model is initialized by the local sounding data at Hankou Weather Station of Wuhan on the morning of 21 July 1998, with a proper rectification in the surface layer for simulating the rainstorm event at 05:00. The low-level humidity was very high. The convective cloud is triggered by a warm bubble mode with a maximum of 3°C in the center of axisymmetric potential temperature perturbation. The coordinate of the perturbation zone center is at the grid point of the model domain with a horizontal width of 16km and a vertical thickness of 6 km. The time of simulation is 120 minutes. As to the Xunyi case, the sounding profile conducted at Xunyi, Shaanxi Province, at 20:00 on 20 July in 1999 was used in the simulation. The profile shows that the air humidity of Xunyi was lower than that of Wuhan. A warm-moist bubble was also used to trigger off the convective cloud, with a maximum equivalent potential temperature of 3.5°C and a horizontal perturbation zone width of 10km.

3. ANALYSIS OF SIMULATION RESULTS

3.1 Comparison of Simulation Results with Real Observation

Corresponding author's address: Hui XIAO, Institute of Atmospheric Physics, Chinese Academy of Sciences, Beijing 100029, China; E-mail: hxiao@mail.iap.ac.cn

Fig. 1 shows that the maximum cloud-top depth of the simulated rainstorm for the Wuhan case was 11km, and the maximum echo intensity located in 5.5km approximately on the 0°C (freezing) level was 55 dBz, and the 45 dBz echo-top was at 7-8 km in height. The simulated maximum 10-minute rainfall was 21.6 mm and the hourly rainfall was 91 mm. These results have a good accordance with the real values. On the morning of 21 July 1998 in Wuhan the radar echo-top of real observation reached 9-11 km in height. Its horizontal size was from 30 km× 60 km to 40 km× 60 km, and the strong echo center was at 5-6 km in height, and its maximum echo intensity was 55 dBz.

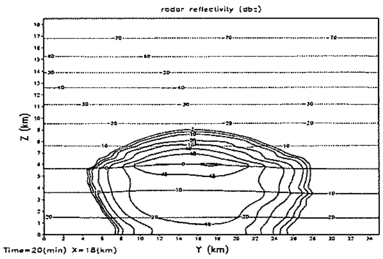

a

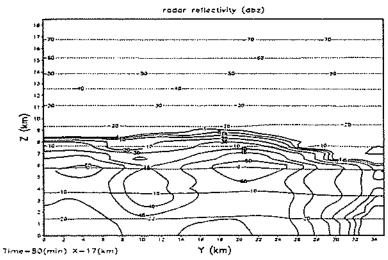

b

Fig. 1 Simulated radar echo chart for Wuhan case (a. 20min, b. 80min)

Fig. 2 indicates that the maximum radar echo-top depth observed was 14 km for the Xunyi rainstorm case at 21:30 on July 21 in 1999, with a strong echo center at 4-5 km in height and the maximum intensity of 55-60 dBz. The 45 dBz strong echo-top was higher than 8 km. According to the new criterion of earlier identification of strong hailstorms from thunder- clouds (Xiao et al., 2003), it can be forecasted that the storm will become a strong hailstorm soon. Actually, the real rainfall observed was 72 mm during 90 minutes with hail falling of 25 mm in maximum diameter. For this case, the simulated maximum radar echo height is 13-14 km. In its mature stage, its height of strong center goes down to 5 km and its maximum echo intensity is up to 60 dBz with the 45 dBz echo-top depth of 8 km. The hourly rainfall was 52mm with hail falling of 20 mm in size. Therefore, the simulated values in the top height and intensity of radar echo, hail-falling, and hourly rainfall have a good agreement with the observation.

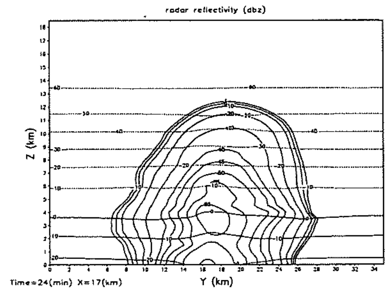

a

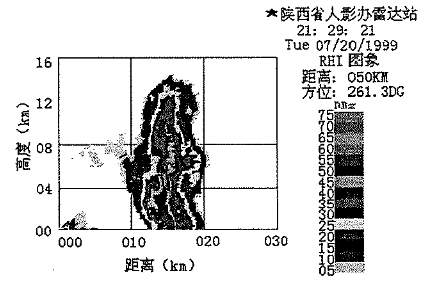

b

Fig. 2 Radar echo chart of Xunyi case (a: simulated; b: observed, ordinate: height, abscissa: distance)

Comparison of the simulated and real cases indicates that the model has a good ability to simulate the two severe rainstorms.

The simulated storm of Xunyi Case develops quickly, its updraft velocity reaches to its peak of 15 $m \cdot s^{-1}$ at 15 min and precipitation brings about on the ground at the same time (Fig. 3). Subsequently, it diminished quickly after keeping for ten more minutes in rather big updraft. At 32 min later, its updraft velocity drops down to 4m/s and lower. While for the storm of Wuhan Case the updraft velocity reaches to 5-6 $m \cdot s^{-1}$ in the first 10 min, and then keeps a slow growth. After 60 min it has developed to the maximum value of 7 $m \cdot s^{-1}$. And then, the updraft velocity weakens slowly. As a comparison, the storm in Xunyi develops quickly and dissipates rapidly as well. So its lifetime was short. Although the storm in Wuhan case develops more slowly than that in Xunyi, it keeps in a steady speed and its lifetime is longer.

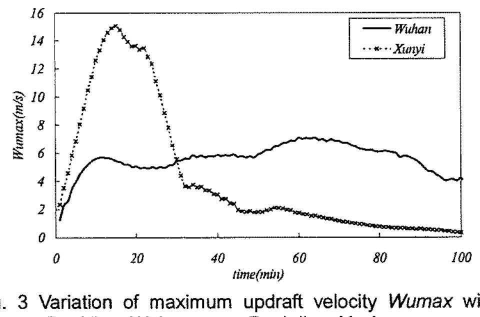

Fig. 3 Variation of maximum updraft velocity *Wumax* with time. Real line: Wuhan case; Dash line: Xuyi case

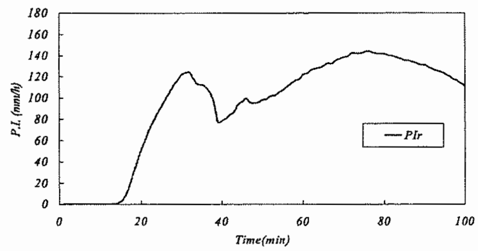

a

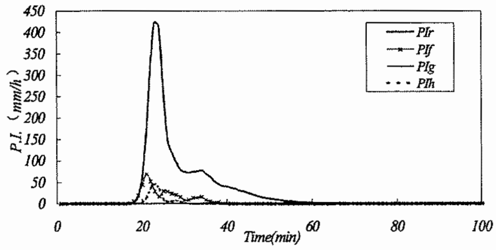

b

Fig. 4 Variation of maximum precipitation intensity (P.I.) of various precipitation particle on ground with time in (a) Wuhan and (b) Xunyi. Pir: raindrop, Pif: frozen drop, Pig: graupel, and Pih: hail

Fig. 4 shows the variation of maximum water content and ground maximum precipitation intensity of all kinds of solid and liquid particles in the Wuhan case and Xunyi case, respectively. In the Wuhan case the ground rainfall undergoes two phases of development. Before 32 min of simulation (as the first period), the storm attains to its first instantaneous maximum rainfall intensity and then diminishes a little. After 40 min (as the first period), it develops again and reaches the second peak value at 76 min. Without exception the surface precipitation is liquid and always keeps in quite steady rainfall intensity. Until the end of simulation the simulated storm still keeps a bigger intensity. These results are in agreement with the observation (Xu, 2000). In the Xunyi case the simulated precipitation intensity changes sharply. When the storm grows for twenty minutes and more it comes to its instantaneous maximum. This value is much larger than that in Wuhan, but it decreases quickly after it reaches its peak. And it does not develop again like that in Wuhan. Besides rainfall there exists other kind of solid precipitation, such as frozen droplet, graupel, and hailstone, on the ground.

According to the above, the cloud of Wuhan case developed more stable. The ground rainfall was liquid. Although the peak value of each quantity is not too big comparing with the Xunyi case, the rainfall can keep for a long time. So the cumulative rainfall is very big. While the storm of Xunyi case develops quickly and dieds out after a short time. Moreover, a little liquid precipitation falls to the ground besides solid one.

3.2 Microphysical Analyses on the Torrential Rainstorms

Table1 gives main microphysical processes of rain water production. It is learned from Table 1 that in the Wuhan case the rain formation is mainly from warm-rain processes (Acr+CLcr). The rainwater from the processes accounts for about 80% to the total rainwater production in which CLcr process is prominent. Although the rainwater by Acr process occupies lower than 1%, the rainwater in initial stage of cloud formation comes mainly from it. So it can not be ignored. The rainwater formed by cold-rain processes accounts for about 20% which is mostly from melting of graupel and from collecting of graupel with cloud water below 0°C level. The cold-cloud processes accelerate the formation of rain water, though the rainfall in it is relatively less. In the Xunyi case, among the amount of rain water formation the warm-rain processes occupies less than 37% in which CLcr process is the most. The rainwater formed by cold-cloud processes occupies 63% and a half of which is from the melting frozen drops and the collection of frozen drop and cloud water (32%) in which the melting frozen drop plays a quite important role (29%). The melting graupel and its collecting with cloud-water provides another 28%, and similarly melting graupel is dominant (26%).

The main reason led to this phenomenon is high humidity of low-level atmosphere, which makes the convective rainstorm develop more stably and longer.

Table 1 Total amount of rain water converted from varied microphysical processes and their percentages respectively in the first hour of simulation

Case		Acr	CLcr	CLcgr	CLcfr	CLchr	CLcsr	MLgr	MLfr	MLhr	MLsr*
Wuhan	Conversion (kt)	121	14672	1152	8	0	<1	2610	30	0	<1
	Percentage (%)	<1	79	6	<1	0	<1	14	<1	0	<1
Xunyi	Conversion (kt)	21	1086	71	106	12	<1	796	890	53	<1
	Percentage (%)	<1	36	2	3	<1	<1	26	29	<2	<1

* Note: Acr: auto-conversion of cloud water into rain water; CLcr: collections of rain water with cloud water; CLcfr, CLcgr, CLchr, CLcsr,: collections of frozen drop, graupel, hailstone, snowflake, respectively, with cloud water becoming into rain water below freezing level; MLgr, MLfr, MLhr: melting of graupel, frozen drop, hailstone into rain water below freezing level.

4. CONCLUSIONS

A three-dimensional numerical model of severe convective rainstorm was used to evaluate its stability and validity on two cases of torrential rainstorms occurred in Wuhan and Xunyi. The formation mechanism of the heavy rainfall has also been analyzed. Comparing with real observation and radar echo data, it can be learned that the model has good ability to simulate convective rainstorm structure and its heavy rainfall. Comparison and analysis of the precipitation cloud in Wuhan and Xunyi indicate that: it is quite different between convective severe rainfall of Mei-yu front in Wuhan and common convective severe rainfall. The rain in this case derives mainly from warm-rain process. In cold-cloud process it mostly depends on melting of graupel. The ground precipitation is liquid and the diameter of raindrop is bigger. The speed of the instantaneous maximum updraft, the water content of all the particles and the rainfall intensity are not bigger than that in Xunyi. But the cumulative rainfall is so much because of long precipitation time. In terms of analysis about low-level atmospheric humidity the flush water vapor is one of the important reason of long-term precipitation.

Acknowledgements

This work was supported by Chinese National Science Foundation under Program Grants 40333033 and 40175001, Chinese National Scientific Key Program under Grants 2001BA610A-06-05 and 2001BA904B09, the Key Foundation of Chinese Academy of Sciences under Grant Y2003002, and the Key Foundation of IAP/CAS under Grant 8-4605.

References

Bei, N.F., 2000: Diagnoses and Simulation Study about Mesoscale System of Gusty Severe Rainstorms, Ph.D. Dissertation, Institute of Atmospheric Physics, Chinese Academy of Sciences, 10-17.(in Chinese)

Deng H.Q., D.Y. Wang, Z.Y. Huang, Q.C. Song, J. Zhang, 1999: Analysis on lasting strong rainstorm in the southeast of Hubei in July of 1998, Rainstorm and Disaster, Vol.3, 115-124.(in Chinese)

Hong Y.C., 1998: Three-dimensional hailstorm numerical model with artificial seeding, Acta Meteorologica Sinica, 57(1), 30-44. (in Chinese)

Hong, Y.C. and P. Fan, 1999a: Numerical simulation of hail cloud--Part I. The numerical model, Acta Meteorologica Sinica, 13(2), 188-199. (in Chinese)

Hong, Y.C. and P. Fan, 1999b: Numerical simulation of hail cloud--Part II. Mechanism of hail formation and hail suppression with seeding, Acta Meteorologica Sinica, 13(3), 331-346. (in Chinese)

Huang, M.Y. and A.S. Wang, 1980: Introduction on Hail Suppression, Science Press, Beijing, 83-104. (in Chinese)

Kong, F.Y., M.Y Huang, and H.Y. Xu, 1990: There-dimensional numerical simulation of ice phase process in convective cloud, Part I: Model establishment and ice phase process parameterization, Chinese J. Atmos. Sci., 14(4), 441-453. (in Chinese)

Tao, S.Y., Q.Y. Zhang, S.L. Zhang, 1998: Climate background and macrosale circulation condition of flood- waterlogging damage of Yangtze River Valley in 1998, Research on Climate and Environment, 3(4), 290-299. (in Chinese)

Tao S.Y., Y.Q. Ni, S.X. Zhao, et al., 2001: Formation Mechanism and Forecast Research about Chinese Rainstorm in the Summer of 1998, Beijing, Meteorological Press. (in Chinese)

Xiao, H., Y.X. Wu, L. Zhou, H.Y. Li, et al., 2003: New Criteria of Earlier Identification of Hailstorms occurring in Xunyi Region, Preprints -- 8th WMO Scientific Conference on Weather Modification, Casablanca, Morocco, 7-12 April 2003, WMO/TD – No.1146, 259-262

Xu, S.Z., 2000: Mesoscale analysis on severe rainstorm in Wuhan, Rainstorm and Disaster, Vol.4, 111-117.(in Chinese)

Yang, J., P.Y. Wang, S.Z. Yang, B.X. Xu, 2002: Photo-sounding observation and analysis of coud physical structure about Meiyu Front precipitation, J. Weather, 28(2), 3-8.(in Chinese)

Zhao S.X., J.H. Sun, H. Chen, F. Zhang, 1998:The analysis and research on the property of storm in the course of severe flood of Yangtze River valley, Research on Climate and Environment, 3(4): 368-381. (in Chinese)

CHARACTERISTIC ANALYSES OF THE CONCENTRATIONS OF ATMOSPHERIC ICE FORMING NUCLEI IN THE SOURCE AREA OF YELLOW RIVER

Hui XIAO [1], Yuxiang HE [1], Bojie CHEN [2], and Zhanyu YAO [3]

[1] Institute of Atmospheric Physics, Chinese Academy of Sciences, Beijing 100029, P.R. China
[2] Guangxi Office for Artificial Modification, Naning City, Guangxi 530022, P.R. China
[3] Chinese Academy of Meteorological Sciences, Beijing 100081, P.R. China

1. INTRODUCTION

Supercooled water in cloud converted to ice particles is a very important physical process of cold cloud precipitation. In cold cloud precipitation, ice nuclei (IN) is one of the important factors forming ice particles which has the effect of inspiring supercooled water in cloud converted to ice particles and it was the basic start point of seeding cold cloud. Observations show that there is a considerable discrepancy in different areas as far as the relationship of atmospheric ice nucleus concentration and its activated temperature is concerned (e.g. You and Shi, 1964; Wang *et al.*, 1965; You *et al.*, 1982; Hundson, 1993; Rogers, 1993; Zhao *et al.*, 2000; Li and Huang, 2001) indicating that it was highly necessary to conduct observation concerning atmospheric IN concentration. The weather modification synthesis experimental base located in Henan County, Qinghai Province of west China, was established in 2002. The experimental base is in the source area of the famous Yellow (Huanghe) River. In order to probe into the influence of background condition of atmospheric IN on the weather modification operation effect and the relationship of variation characteristics of atmospheric IN concentration with weather conditions, an autumn weather modification synthesis field observational experiment in the Qinghai experimental base was implemented in September 2002. In the paper synthesis analyses about atmospheric IN data were performed as well as related meteorological observational data that were obtained from the observation.

2. BRIEF INTRODUCTION OF OBSERVATION AND ANALYSIS METHODS

The observation station of IN was set up on a lawn in the vicinity of Henan County Weather Bureau of Qinghai Province. The station is at 3500m above sea level. IN was observed by adopting a Bigg's mixing-type IN counter. Main body of the instrument is a mixing cold cloud chamber with its volume 3.05 L. The threshold limit value for the instrument detecting ice nuclei is 0.16 L^{-1}. Measurement of activated IN concentration was sequentially carried out from low to high temperature according to -30, -25, -20, -15°C in the chamber.

Corresponding author's address: Hui XIAO, Institute of Atmospheric Physics, Chinese Academy of Sciences, Beijing 100029, China; E-mail: hxiao@mail.iap.ac.cn.

During 6 - 25 September 2002, observation was conducted three times a day and the times were 09:00, 14:30 and 20:00 (Beijing Time) that represent morning, afternoon and night instances of the experimental base, respectively. There are 52 effective samples in total. At the same time, corresponding meteorological observation data from the local meteorological observation station of Henan County Weather Bureau were collected.

3. RESULT ANALYSES

3.1 Main Characteristics of Atmospheric IN Concentration during the Experiment

Table1 shows average characteristic quantities of the observed concentrations of IN activated under various temperatures. The lower the temperature, the higher the concentration of activated IN on an average basis. The average value of IN concentration activated under -30°C is 193.6 L^{-1} which is as 2.4, 10.5, 84.2 times as that under -25, -20, -15°C, respectively. The lower the temperature, the smaller the discrete coefficient indicating discrete extent of IN concentration distribution is smaller. Daily changing of IN concentration activated under various temperature was significant by and large especially that of under high temperature. In view of the fact that the size of IN particles activated under higher temperature is relatively big which probably come from wind blew dust, ambient wind field exerts great effect on them and the dust sediment easily leads to short stay period in the air. In result, the IN concentrations change vigorously against time. As to IN activated under lower temperature, vice verse.

Comparing above results with the observations in other regions (like Maqu, Xining, Yinchuan) of west China and Beijing (Zhao *et al.*, 2000; Niu *et al.*, 2000; Li and Huang, 2001, You *et al.*, 2002), we can find that in the experimental area, except that IN average concentration activated under lower temperature (-30°C) is slightly smaller than that of Maqu, the average concentrations of IN activated under higher tempera-tures (-20°C, -15°C) are higher than those of Maqu, Xining and Yinchuan, which perhaps reflects the IN sizes in the experimental area are larger than those of Maqu, Xining, and Yinchuan. However, They are much lower than those observed at Beijing in the

Table 1 Statistical characteristics of the atmospheric concentrations of ice nuclei activated under different temperatures, the observation was conducted in September 2002.

Temperature (°C)	-30	-25	-20	-15
Average concentration (L^{-1})	193.6	79.1	18.3	2.3
Maximum value (L^{-1})	243.9	185.6	68.4	12.5
Minimum value (L^{-1})	134.1	16.2	2.5	0.3
Standard error (L^{-1})	27.9	43.2	16.1	2.6
Discrete coefficient	0.14	0.55	0.88	1.17

springtime of 1995 and 1996.Generally speaking, larger particles activated into IN easily under higher temperature.

3.2 Relationship of IN Concentrations and Wind

Wind rose figure of IN concentration activated under different temperatures (Figure omitted) indicates that various wind directions exert different effect on IN concentration. IN concentration is the highest when wind is from north-west and then lowers when wind is between south-west and south-east at temperature between -15°C and -25°C. At -30°C, IN concentrations have little discrepancy when wind direction changed, indicating that IN activated under lower temperature is isotropy.

Ground surface wind velocity also has great influence on IN concentrations. IN activated at -15°C have high concentration when wind is calm and the concentration first lowers a little then becomes high rapidly with wind velocity increasing (Figure omitted). This illustrates that when wind is calm, IN of -15°C come mainly from local source and large amounts of local source are blew away by wind with its velocity increasing to 2 ~ 3 $m \cdot s^{-1}$ and ground surface roughness results in that wind blew dust does not come into forth at the time so that IN concentrations are the lowest at the wind velocity. With wind velocity further increasing, wind blew dust begins to form with the consequence that this kind of IN concentration increases sharply. The distribution of IN concentration with wind velocity under -20°C, -25°C and -30°C has similar pattern as under -15°C with the exception that the argument is small.

3.3 Relationship of IN Concentration and Ambient Atmospheric Temperature and Humidity

Ambient atmospheric temperature during observation also has great influence on the IN concentration. The concentration of Ice nuclei activated under -15°C ~ -25°C obviously displayed increase trend with ambient temperature increasing while those under -30°C has little change with ambient temperature (Fig. 1). This is mainly on the ground that local atmospheric condition with lower temperature that usually comes along with overcast and rainy day with higher atmospheric humidity is going against the production of higher-temperature IN.

Ambient atmospheric relative humidity (RH) is a reflection of atmospheric wet degree, especially high-humidity atmosphere come along with overcast and rainy weather. Fig.2 suggests that IN concentration activated under different temperatures is small at large when RH is 20% ~ 40%, and it increases slightly with humidity increasing. IN concentration activated under different temperatures has insignificant variant with ambient atmospheric humidity when RH is 40% ~ 80%. In high-humidity environment of RH greater than 80%, IN concentration of low temperature at -30°C has little change with ambient humidity, but high-temperature IN concentration reduced rapidly showing that overcast and rainy weather exerts strong rain-scavenging and washout effect on this kind of IN.

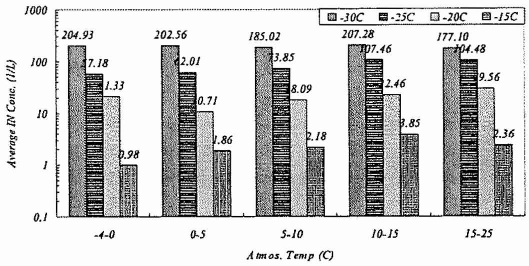

Fig.1. IN concentration activated under different temperatures against ambient atmospheric temperature

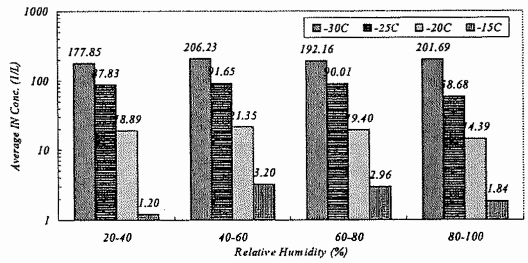

Fig.2. IN concentration activated under different temperatures against ambient atmospheric relative humidity

3.4 Relationship of IN Concentration and Ambient Pressure

Generally speaking, surface low pressure area corresponds with air convection which is in favor to atmospheric IN accumulation near ground surface while high pressure area with high-level atmosphere sinking and ground surface air stream diverging. For higher-temperature IN, the concentrations increase rapidly with pressure decreasing while those of lower temperature (-30°C) have a reverse trend (Figure omitted) showing the former comes probably from source in the vicinity and the latter may mostly come from transportation of source of long distance.

3.5 Influences of Different Weather Pattern to IN Concentration

The concentrations of IN activated under a variety of temperature all have the highest value in clear and part cloudy day while lowest in rainy day, the average value is very close to that in cloudy and overcast day (Table 2). For the concentration of IN activated under -30°C, the change is negligible in different weather pattern relatively. The IN concentration of -25°C decreases sharply from 112.2 L^{-1} of clear and part cloudy sky to 76.6 L^{-1} of cloudy and overcast sky, with a decrease rate up to 32%, and then further decreases to 55.6 L^{-1} with a decrease of 27%. As far as IN of -20°C and-15°C are concerned, the concentration decreases at a rate as great as 32% ~ 37% from clear and part cloudy to cloudy and overcast sky then to 57% ~ 65% for rainy sky. These results illustrate that overcast and rainy sky exerts very significant effect on high-temperature IN in the atmosphere through wet scavenging while the effect is very little to -30°C low-temperature IN. Composite wind direction depicts that high concentration of IN mainly come from north-west in clear and party cloud day, indicating an important source of IN probably exists in somewhere of the windward which greatly impact the weather modification experiment base.

Table 2. Statistical relationship of ice nuclei (IN) concentration and atmospheric characteristic parameters in different weather pattern during September 2002

Weather pattern	Sample number	IN (L^{-1})				Atmos. temp.	Atmos. press.	RH	Ground surface temp.	Vapor press.	Wind velocity	Wind direction
		-30°C	-25°C	-20°C	-15°C	(°C)	(hPa)	(%)	(°C)	(hPa)	(m s^{-1})	(deg)
clear, part cloudy	9	193.8	112.2	29.0	3.4	13.2	667.1	48.8	22.0	7.1	1.3	303
cloudy, overcast	34	194.0	76.6	18.2	2.3	7.3	668.5	67.7	12.9	6.9	1.0	300
rainy	9	191.7	55.6	7.8	0.8	3.8	668.5	82.6	6.3	6.7	1.5	238
average	52	193.6	79.1	18.3	2.3	7.7	668.2	67.0	13.4	6.9	1.0	288

Table 3. Statistical relationship of ice nuclei (IN) concentration and atmospheric characteristic parameters in different daytime during September 2002

Time	Sample number	IN (L^{-1})				Atmos. temp.	Atmos. press.	RH	Ground surface temp.	Vapor press.	Wind velocity	Wind direction
		-30°C	-25°C	-20°C	(°C)	(hPa)	(%)	(°C)	(hPa)	(m s^{-1})	(deg)	(deg)
09:00-11:00	17	197.0	75.5	17.3	1.6	3.9	669.4	82.7	9.4	6.7	0.7	304
14:00-18:00	17	175.9	63.6	13.6	1.8	11.6	667.4	50.8	23.4	6.9	0.6	342
20:00-21:00	18	207.0	97.3	23.6	3.4	7.7	667.9	67.4	7.6	7.1	2.1	270
average	52	193.6	79.1	18.3	2.3	7.7	668.2	67.0	13.4	6.9	1.0	288

3.6 Comparison of IN Concentrations during Different Timespan of Day

The IN concentration under different temperature was the lowest in the morning (09:00-11:00), the highest at night (20:00-21:00) and the middle in the afternoon (14:00-18:00) averagely (Table 3). Average wind velocity has similar pattern. These results indicate that some dust particles on ground surface were raised into atmosphere due to the fact that wind velocity increased in the afternoon in the experimental area and part of the aerosol particles acted as atmospheric IN which were at the bottom of the IN concentration at their highest value during the time period from afternoon to night.

4. CONCLUSIONS

The concentrations of atmospheric ice forming nuclei (IN) activated under different temperature were conducted by a Bigg's mixing-type cloud chamber in the Qinghai Experimental Base of Weather Modification located in the source area of Yellow River during September 2002. The variation features of the concentrations of the activated IN under different environmental condition in the experimental base were analyzed statistically. The results of statistical analysis show that the average concentrations of IN activated under higher temperature are higher than those observed in other regions in west China, which may image the sizes of the IN concentration in this experimental base are larger than those in the other regions. In the experimental base the average concentration of IN activated under lower temperature is higher than that under lower temperature. The IN of higher concentration mainly come from the direction of northwest, indicating that there exists an important source of IN in somewhere of the windward direction, which greatly impact the experiment base. The weather pattern has a very important influence on the IN concentration. The average IN concentration is the highest in the weather of clear and partly cloudy sky and the less in the rainy weather. The mean concentration of ice nuclei is very close to the average situation of cloudy and overcast days. In the overcast and rainy days the wet scavenging plays a great role in the IN concentration activated under higher temperature, but has a less impact on the IN concentration activated under lower temperature (at -30°C).

Acknowledgements

This work was supported by Chinese National Scientific Key Programs under Grants 2001BA610A -06-05 and 2001BA904B09, Chinese National Science Foundation under Program Grants 40333033 and 40175001, the Key Foundation of Chinese Academy of Sciences under Grant Y2003002, and the Key Foundation of IAP/CAS under Grant 8-4605. We thank the scientists and engineers of Qinghai Province Meteorological Bureau and Weather Modification Office for assisting with collecting the related meteorological data of the observation.

References

Hundson, J.G., 1993: Cloud condensation nuclei. J. Appl. Meteor., 32(4), 596-607.

Li, J. and G. Huang, 2001: Observation and analysis of the content of atmospheric ice nuclei in the upper reaches of Huanghe (Yellow) River, J. Weather, 27(11), 8-12. (in Chinese)

Niu, S.J., X.L. An, Y. Chen, and S.H. Huang, 2000: Measurements and analysis of concentrations of atmospheric ice nuclei in the Helanshan Mountain area, J. of Nanjing Institute of Meteorology, 23(2), 294-298. (in Chinese)

Rogers, D.C., 1993: Measurements of natural ice nuclei with a continuous flow diffusion chamber, Atmos. Res., 29(2), 209-228.

Wang, X.L., W.J. Zhang, and S.Q. Xiong, 1965: Atmospheric ice nuclei in Baicheng Area of Jlin Province during springtime, Acta Meteorological Sinica, 35(3), 273-279. (in Chinese)

You, L.G. and A.Y. Shi, 1964: You, L.G. and A.Y. Shi, 1964: The measurement and analysis of ice nucleus concentrations in Beijing during the springtime of 1963, Acta Meteorological Sinica, 34(4), 548-554.(in Chinese)

You, L.G., S.Z. Yang, X.G. Wang, J.X. Pi, 2002: Study of ice nuclei concentration in Beijing during the springtime of 1995 and 1996. Acta Meteorologica Sinica, 60(1), 101-109. (in Chinese)

Zhao, S.X., J.M. Dang, and J. Zhou, 2000: Analyses of atmospheric ice nuclei in Xining Area, in Deligeer (ed.), Study on Cloud and Precipitation Weather Modification on Qinghai-Xizang Plateau, China Meteorological Press, Beijing, pp.24-30. (in Chinese)

NUMERICAL SIMULATION OF THE INFLUENCE OF ATMOSPHERIC ICE NUCLEI DISTRIBUTION ON CONVECTIVE CLOUD SEEDING EFFECT

Hui XIAO[1], Shuyan LIU[1], Zhaoxia HU[1], and Qiang ZHANG[2]

[1] Institute of Atmospheric Physics, Chinese Academy of Sciences, Beijing 100029, P.R. China
[2.] Beijing Office for Weather Modification, Beijing 100089, P.R. China

1. INTRODUCTION

Ice nuclei (IN) are one of the important factors that form ice crystals in cold cloud. IN can inspire conversion of supercooled water into ice particles, and IN concentration in cloud is a basic start point of supercooled cloud seeding up to now. Presently, the activated IN concentration, N_I, in the simulation of supercooded cloud usually is calculated by the following formula of average IN concentration with temperature, T, as given by Fletcher (1962):

$$N_I = N_{I0} \exp[B\,(273.15-T)]. \qquad (1)$$

However, observations indicate that IN concentration has very strong local feature, reflected in the difference of the two parameters, N_{I0} and B, in the relationship. The weather modification synthesis experimental base located in Henan County, Qinghai Province of west China, was established in 2002. The experimental base is in the source area of the famous Yellow River, located in the west of Loess Plateau. The local IN situation (N_{I0} and B) analyzed by Xiao *et al.* (2004a) has a very big difference from that by Fletcher (1962). Observations also show that Loess Plateau of China is an important source area of natural atmospheric IN (Zhao *et al.*, 1965; Wang et al., 1965; Feng et al., 1994). The laboratory study by Feng *et al.* (1994) indicates that the loess particles from Loess Plateau have a large effectiveness reached up 4×10^6 per gram of loess at –15 °C, which can provide abundant IN for the downward area. Therefore, it is very important to study the influence of local IN on precipitation effect of cloud seeding in the experimental base.

A three-dimensional convective cloud model is used to evaluate numerically the influence of atmospheric ice nuclei on precipitation enhancement effect of convective cloud seeding with silver iodide (AgI) agent in this paper.

2. SEEDING METHODS OF MODELING CLOUD

A three-dimensional compressible non-hydrostatic cloud model with a modification of seeding processes of AgI by rocket has been developed based on the second version of three-dimensional convective cloud model (IAP-CSM3D) developed successively by the Institute of Atmospheric Physics (IAP), Chinese Academy of Sciences (Kong *et al.*, 1991; Hong *et al.*, 1999a,b; Xiao *et al.*, 2004b). The simulated domain of the IAP-CSM3D model is 36 km(*X*) × 36 km(*Y*) × 18.5 km(*Z*) with horizontal 1.0 km and vertical 0.5 km grid resolution.

The model is initialized by the local sounding data of the noon of 3 September 2002. The convective cloud is triggered by a warm-moist bubble mode with a maximum of 1.5°C in the center of axisymmetric potential temperature perturbation. The coordinate of perturbation zone center is at the grid point of the model domain with a horizontal width of 10km and a vertical thickness of 6 km. The time of simulation is 120 minutes.

As to the numerical seeding AgI with rocket, supposed that each rocket contains 10 grams high efficient AgI pyrotechnics, and 10 rockets, i.e. total 100 grams of AgI, are delivered into the maximum updraft level (at about -10°C zone) of the cloud during 10 minutes after running 15 min of the storm evolvement at a shooting rate of one rocket per minute.

3. BRIEF INTRODUCTION OF THE REAL OBSERVEATION

In the afternoon of 3 September 2002, there was a strong convective weather event with local hailfalling, occurred in the experimental base. According the Doppler radar observation data, the top heights of convective clouds reached to 13-14 km, the maximum echo intensity was 55 dBZ and its height was at 6 km.The height of 45 dBZ echo top was located at 9 km. The whole event lasted about two hours in the experimental base.

4. NUMERICAL EXPERIMENTAL SCHEME

Six numerical experimental cases listed in Table 1 were conducted, with the concentration under -20°C for comparison. In Table 1, Case Exp-1 stands for the average IN distribution observed in the Qinghai experimental base (Xiao *et al.*, 2004a), as the base case; Case Exp-2 for Beijing's case observed in 1963 (You *et al.*, 1964); Case Exp-3 is from Fletcher (1962). Cases Exp-2 and Exp-3 are usually used in present cloud models established by Chinese cloud modelers. When temperature is higher than -27°C, the IN concentration of Exp-1 is the maximum, that of Exp-3 is the minimum and that of Exp-2 is the middle, but when the temperature is lower than -27°C, vice verse.

Corresponding author's address: Hui XIAO, Institute of Atmospheric Physics, Chinese Academy of Sciences, Beijing 100029, China; E-mail: hxiao@mail.iap.ac.cn.

Table 1 Six numerical experimental schemes

Case	N_{I0} (m^{-3})	B (K^{-1})	N_{-20} (L^{-1})	AgI seeding doze (g)	Note
Exp-1	538	0.197	27.66	--	As the base case, from the average IN distribution observed in the Qinghai experimental base (Xiao *et al.*, 2004a)
Exp-2	2.05	0.398	5.87	--	Beijing's case observed in 1963 (You *et al.*, 1964)
Exp-3	0.01	0.600	1.63	--	Fletcher's (1962) case
Exp-1R	538	0.197	27.66	100	With seeding AgI under the base case
Exp-2R	2.05	0.398	5.87	100	With seeding AgI under Beijing's case
Exp-3R	0.01	0.600	1.63	100	With seeding AgI under Fletcher's case

5. SIMULATION RESULTS

5.1 Influence of Different IN Distribution on the Natural Convective Cloud Development

Fig.1 gives the time variation of the maximum updraft velocity, Wup, of the simulated convective clouds under different natural IN distributions of Exp-1, 2 and 3. It can be seen that a systemic updraft in the strong convective cloud appears at 4^{th} min. The updraft velocities of Exp-1, 2 and 3 reach their maximum with a little difference at 21 – 23 min. In their dissipative stage, the updraft velocities have a great difference, with a sharp decrease in Exp-1 case. But Case Exp-2 and Exp-3 have a second maximum during the stage. The results indicate that the difference of initial IN distribution may affect the dynamic structure of storm, especially in the dissipative stage.

Fig.2 gives the variation of maximum content of hydrometeors of cloud under different IN distributions of Exp-1 to 3. It can be seen from Fig. 2 that the initial IN distribution has great influence on the content of

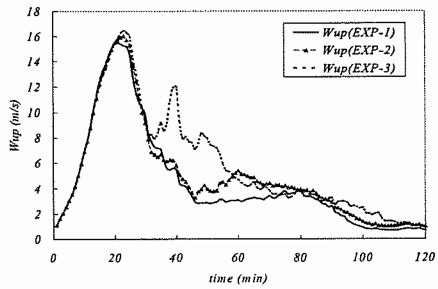

Fig.1. Variation of maximum updraft *Wup* velocity under different IN distribution with time.

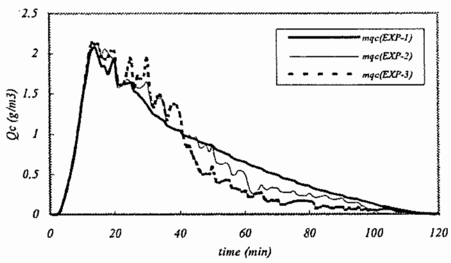

a. cloud water content Qc

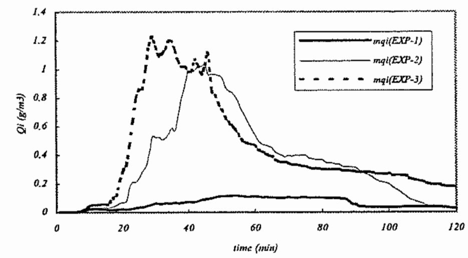

b. ice crystal content Qi

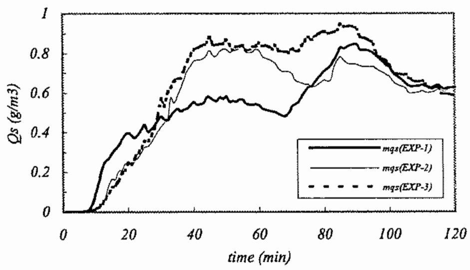

c. snowflake content Qs

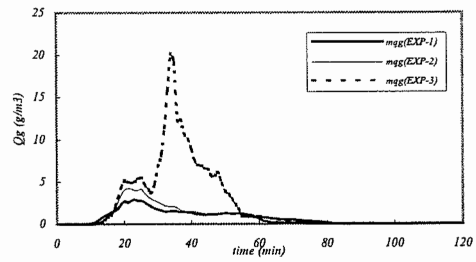

d. graupel content Qg

Fig.2. Time variation of maximum content of hydrometeors of cloud under different IN distribution

hydrometeors of cloud. In the development stage, the larger the initial IN concentration is, the faster the liquid water content depletes, especially for rain water Qr. At 50 min, Qr of Exp-3 cloud appears a second peak, which is mainly caused by the melting of large graupel under freezing level. The initial IN distribution also has great influence on ice crystals (Qi) and snow flakes (Qs), indicating that large initial IN concentration is unfavorable to the growth of ice particles in cloud, the reason being mainly *completion effects*. All the results indicate that the initial IN distribution has a great influence on the microphysical structure of cloud, especially the growth of ice particles.

5.2 Comparison of Surface Accumulative Rainfall of Natural Cloud under Different IN Distribution

Table 2 gives surface accumulative precipitation amount of natural clouds under different IN distribution and its variation rate relative to that of the average IN distribution (base case) observed in the Qinghai experimental base. It can be seen from Table 2 that the surface accumulative precipitation amounts of different phases all have a reverse relation to initial IN concentration activated under high temperature. The smaller the high-temperature IN concentration, the larger the precipitation amount is. Certainly, surface precipitation of different phase has different relative addition.

Table 2 Surface accumulative rainfall of natural cloud under different IN distribution

Prec. type	EXP-1	EXP-2		EXP-3	
	(kt)	(kt)	(%)	(kt)	(%)
Spt	891.93	1016.62	13.98	1320.91	48.10
Spr	802.33	907.16	13.07	1166.94	45.44
Spf	17.17	26.58	54.79	34.53	101.09
Spg	70.92	80.84	13.99	116.76	64.63

5.3 Comparison of Surface Accumulative Rainfall of Natural Cloud with AgI Seeding under Different IN Distribution

Table 3 gives the surface accumulative precipitation amount of natural cloud with AgI seeding under different IN distribution and its variation rate relative to that of the natural (i.e. unseeded) IN distribution. It can be seen from Table 3 that the surface accumulative precipitation amounts of cloud seeded with AgI rocket under the three natural IN distributions (Exp-1, 2, and 3) and their relative increment percentages are quite different. The seeding of AgI can cause a great decrease in ice-phase precipitation, which plays the role of decreasing hail disaster. On the other hand, the seeding can also increase liquid-phase precipitation. The rocket seeding can add an addition precipitation of 2.56%, 17.75%, and 1.10% to their total precipitation amount under the condition of IN distribution of Exp-1, Exp-2, and Exp-3, respectively. From the result, it can be learn that if we still use Beijing's IN distribution as shown by You et al. (1964) to substitute for the real situation of the Qinghai experimental base in model simulations, the simulated seeding effect would be overestimated. Therefore, clearly to know local atmospheric situation, like IN concentration, is the precondition to properly evaluate the precipitation enhancement effect of cloud seeding

Table 3 Surface accumulative rainfall of natural cloud with AgI seeding under different IN Distribution

Precipitation type	EXP-1	EXP-1R		EXP-2	EXP-2R		EXP-3	EXP-3R	
	(kt)	(kt)	(%)	(kt)	(kt)	(%)	(kt)	(kt)	(%)
Spt (total)	891.93	914.74	2.56	1016.62	1176.73	15.75	1320.91	1335.47	1.10
Spr (rain)	802.33	842.47	5.00	907.16	1077.55	18.78	1166.94	1211.27	3.80
Spf (frozen drop)	17.17	7.05	-58.96	26.58	14.41	-45.80	34.53	22.37	-35.21
Spg (graupel)	70.92	64.96	-8.41	80.84	84.71	4.78	116.76	101.78	-12.83

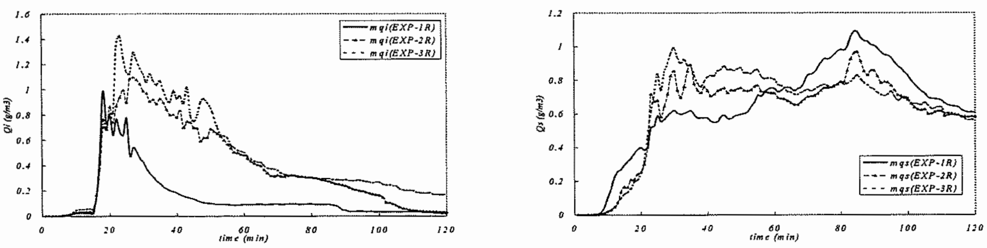

a. Qi b. Qs

Fig.3. Time variation of maximum content of hydrometeors of cloud with AgI seeding under different IN distribution

in different region.

Analyses on cloud physical processes indicate that after seeding, the maximum updraft velocity of cloud increases and its lasting time prolongs, indicating that the seeding has dynamical effect. Seeding of AgI can cause in varying degrees the change of the hydrometeor distribution in cloud, especially ice crystals, snowflakes, and graupels. Meanwhile, the content and concentration of ice crystals sharply increase. The growth of ice particles and freezing of raindrops increase the content and concentration of snowflakes, comparing Fig.3 with Fig.2. The ice crystals and snowflakes further are conversed into graupels. However, seeding can also decrease the conversion rate of raindrop into frozen drop because of depletion of raindrop after seeding. The changes in micro- physical and dynamical processes finally make a change of surface precipitation distribution and structure.

4. CONCLUSIONS

This simulated results indicate that the initial IN distribution highly impact the structure of dynamical field in cloud, especially in its dissipative stage. The initial IN distribution also greatly influence microphysical structure of cloud, especially on the ice particles, and hence the distribution of surface rainfall.

The accumulative precipitation amount has a reverse relation to initial concentration of IN activated under higher temperature whether the cloud is seeded or not. The smaller the high-temperature IN concentration, the larger precipitation amount is. Therefore, if we still use Beijing's IN distribution as shown by You *et al.* (1964) to substitute for the situation of the Qinghai experimental base in model simulation, the seeding effect would be overestimated.

Cloud seeding can decrease surface ice-phase precipitation for all the three types of initial IN distribution and meanwhile increase liquid-phase precipitation at a different extent, hence, cloud seeding can play the role of increasing rainfall and decreasing hail disaster.

Under the condition of different natural IN distribution, cloud seeding has some influence on the development of convective cloud. After seeding, the peak updraft velocity increases and its lasting time prolongs, indicating that cloud seeding causes dynamical effects. Seeding can also change the distribution of hydrometeors (especially ice crystals, snowflakes and graupels) in cloud at varying degrees. After seeding, the content and concentration of ice crystals rapidly increase. Then, the growth of the ice crystals and freezing of raindrops become into snowflakes. It further increases their conversion into graupels. The change in cloud microphysical and dynamical processes finally results in change of the surface rainfall.

In addition, it is quite important to clearly know local atmospheric situation, like IN distribution, before making numerical evaluations on the precipitation enhancement effect of cloud seeding in different region.

Acknowledgements

This work was supported by Chinese National Scientific Key Programs under Grants 2001BA610A-06-05 and 2001BA904B09, Chinese National Science Foundation under Program Grants 40333033 and 40175001, the Key Foundation of Chinese Academy of Sciences under Grant Y2003002, and the Key Foundation of IAP/CAS under Grant 8-4605.

References

Feng, D.X., R.Z. Chen, G.W. Jiang, 1994, A laboratory study on the role of the Loess particles as natural ice nuclei, Quart. J. Applied Meteor.,5(2),129-134. (in Chinese)

Fletcher, N.H., 1962, Physics of Rain Clouds, Cambridge University Press, London, 390p.

Hong Y.C., 1998: Three-dimensional hailstorm numerical model with artificial seeding, Acta Meteorologica Sinica, 57(1), 30-44. (in Chinese)

Hong, Y.C. and P. Fan, 1999: Numerical simulation of hail cloud--Part I. The numerical model, Acta Meteorologica Sinica, 13(2), 188-199. (in Chinese)

Kong, F.Y., M.Y Huang, and H.Y. Xu, 1990: There-dimensional numerical simulation of ice phase process in convective cloud, Part I: Model establishment and ice phase process parameterization, Chinese J. Atmos. Sci., 14(4), 441-453. (in Chinese)

Kong, F.Y., M.Y. Huang, H.Y. Xu, 1991: Three-dimensional simulation on the role of ice-phase processes in the development of convective cloud. Science in China (Series B), 1991(9),1000-1008. (in Chinese)

Wang, X.L., W.J. Zhang, S.Q. Xiong, 1965, Atmospheric ice nuclei in Beicheng Region of Jilin Province during springtime. Acta Meteorologica Sinica, 35(3), 273-279. (in Chinese)

Xiao, Hui, Y.X. He, Z.Y. Yao, and F.F. Zhou, 2004: Characteristic analyses of the concentrations of atmospheric ice forming nuclei in the source area of Yellow River, Proceedings - 14th International Conference on Clouds and Precipitation, Bologna, Italy, 18-23 July 2004.

XIAO, Hui, F.F. ZHOU, X.B. WANG, and Y.C. HONG, 2004: Three-Dimensional Numerical Simulation of Torrential Rainstorms in Wuhan, Proceedings -- 14th International Conference on Clouds and Precipitation, Bologna, Italy, 18-23 July 2004.

You, L.G. and A.Y. Shi, 1964: The measurement and analysis of ice nucleus concentrations during the springtime of 1963 in Beijing, Acta Meteorologica Sinica, 34(4), 548-554.(in Chinese)

You, L.G., S.Z. Yang, X.G. Wang, J.X. Pi, 2002: Study of ice nuclei concentration at Beijing in the springtime of 1995 and 1996. Acta Meteorologica Sinica, 60(1), 101-109. (in Chinese)

Zhao, J.P., M. Zhang, Y.X. Wang, et al., 1965, Observations and analyses of atmospheric ice nuclei in North China, Acta Meteorologica Sinica, 35(4), 416-422. (in Chinese)

Determining Cloud Scaling Anisotropy Exponents using Directional Structure Functions Applied to MODIS Satellite Images

Jean-Bernard Addor*

Physics Department, McGill University, Montréal, Québec, H3A 2T8, Canada

1. INTRODUCTION

A quantity is said to be scaling when it is proportional to the scale raised to a power over a given range of scales. Here, this concept will be used in the context of 2D spatial analysis. In two dimensions, the properties of a ?eld can be different depending on the direction analysed: this is anisotropy. In this presentation, we will look at how a scaling quantity can be anisotropic, i.e. how its scaling exponent will be a function of direction. In order to do this, we propose a simple tool for a quantitative estimation of the scaling anisotropy. This is a statistical method which

*Corresponding author's address: Jean-Bernard ADDOR, Physics Department, McGill University, 3600 University St., Montréal, Québec, H3A 2T8, Canada; E-Mail: jean-bernard.addor@mail.mcgill.ca.

Figure 1: ***MODIS cloud image***

Cloud structures with different sizes and orientations are seen in this image (620-670 nm, 1250x2000 km, sensitive to land, cloud and aerosols). For example, on the top part of the image, large bands are North-South oriented. On the bottom part small scale stripes are EastSE-WestNW oriented, and in the middle a pattern of small scale patchy structure is observed. The image is oriented with NorthNNW on top. There is a 14 degree tilt due to the AQUA satellite's trajectory (South to North); it is not reprojected. On the Eastern and Western side, the image appears compressed. This is due to the detector rotation. Tests have been performed to verify that this compression has little effect on the results. The image was taken on August 23rd, 2002 at 13h45 GMT over the southern Atlantic at latitude -40 and longitude 0 degrees.

describes, on ensemble average, the data over a range of scales, without to explain all details of all scales. We will also provide some insight into how scaling anisotropy can be related to the meteorological situation or some other parameters of a cloud's image (Lewis et al. 1999, P?ug et al. 1993).

2. MOTIVATION

We test for scaling anisotropy in cloud images (Figure 1). Although these images look apparently much the same in all directions, differences are found depending on the scale being observed and the area we look at. For example, small (13 km) bands of clouds tend to be East-West oriented and larger sized (130 km) bands tend to be more North-South aligned. Moreover, cloud structures can have any orientation, so one may test for possible alignment of the direction of scaling anisotropy with the direction of the cardinal points. For example, if it is aligned, this would enable us to suggest that the origin of the scaling anisotropy may be related to the rotation of the Earth.

3. DATA

MODIS satellite images are used to measure scaling anisotropy on cloud ?elds. Two bands available at a resolution of 250 m are used; the images are 1250 by 2000 km (5000 x 8000 pixels) wide. The radiometric sensitivity is 12 bits. The two bands available at that resolution are used; they are primarily designed for use on land, cloud and aerosol boundaries. Band 1 (visible) has a bandwidth of 620-670 nm and is sensitive to land cover and vegetation (chlorophyll). Band 2 (near infra-red) has a bandwidth of 841-876 nm and is sensitive to cloud amount, vegetation, and land cover. The selected images are located over the southern Atlantic, mostly at mid-latitude. Islands, continents, and icebergs have been avoided (in order to reduce the effect of topography on cloud statistics) and bad pixels have been ignored. Figure 1 shows a typical MODIS image.

4. METHOD

4.1. Structure function analysis

All the analysis presented here is based on the *second order structure function* calculated on satellite images. The structure function $S(\vec{r})$ is a quantity which represents a difference in statistical behaviour between the values of a scalar ?eld at two points as a function of the detector projected vector separation. We used the following formula to compute it:

$$S(\vec{r}) = \left\langle \left(f(\vec{r}+\vec{r}') - f(\vec{r}')\right)^2 \right\rangle,$$

where $\vec{r'}$ and $\vec{r'}+\vec{r}$ are two points separated by $\vec{r}$, $f(\vec{r}')$ and $f(\vec{r}+\vec{r}')$ are the value of the ?eld or image at those points, and <> means *ensemble average*, i.e. an average over all possible pairs of values. An important point to note is that the structure function is *centro-symmetric*:

$$S(\vec{r}) = S(-\vec{r}).$$

The most interesting point with the structure function is how it behaves as a function of the scale $|\vec{r}|$. We call the *scaling range* a range of $|\vec{r}|$ values over which we can model the structure function as some power of distance ($S(\vec{r}) \propto |\vec{r}|^e$). We usually estimate the e-exponent by a ?t of the slope of the structure function in a log-log plot.

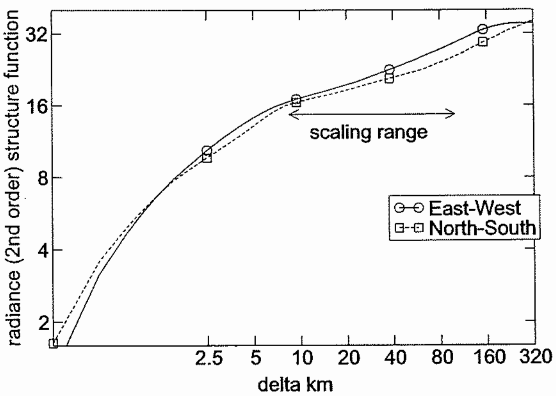

Figure 2: Scaling range of radiance structure function

Figure 2 shows the structure function computed on the satellite image (Figure 1). The structure function computed in both the East-West and the North-South axes of the image are presented in this log-log scale plot. Below 10 km, the structure function is not really straight and cannot be used for a scaling analysis. From 10 to 200 km we have a scaling range. It has been chosen for analysis because it was the longest to be present in the set of images considered. For scales larger than 200 km there is not enough data for the structure function to be reliable. If we now observe the differences between the East-West and North-South structure functions, below 5 km the North-South has a slope that is slightly less steep. From 10 to 200 km the slope of the North-South (0.18) is also less steep than the East-West (0.23). These results suggest that the structure function may be computed in many different directions in order to see whether there is a smooth trend in the variation of the structure function exponent with position angle.

4.2. Scaling anisotropy measurement

We propose a simple method to visualise and measure basic exponents of scaling anisotropy in all directions. One may even use isotropic methods, provided that the anisotropy is weak enough. Considering the fact that very few anisotropic analyses have been reported to date (see Lewis et al. 1999, P?ug et al. 1993), in a ?rst stage, we prefer using as much as possible proved isotropic methods and analysing nearly isotropic data, before going to cases considered to be highly anisotropic for which we may have to validate completely new methods involving many parameters. This way, isotropic scaling analysis methods can be used for determining the scaling range and simple anisotropic scaling analysis will show if there is any anisotropy and allow to measure its main parameters.

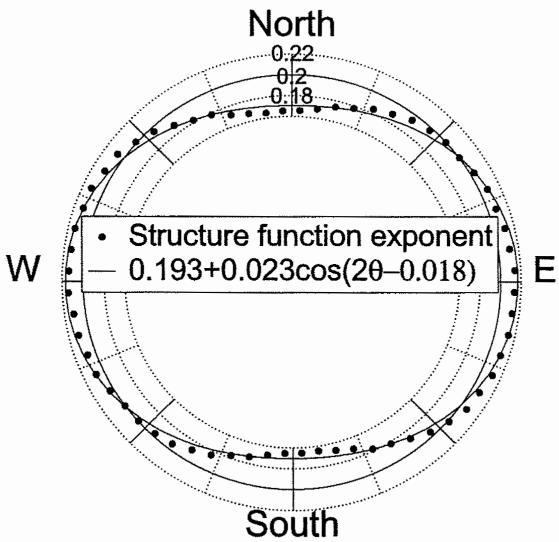

Figure 3: Scaling anisotropy: polar representation of the scaling exponent as a function of direction (the exponents values go from 0.16 to 0.22)

Figure 3 illustrates the scaling anisotropy. Each dot represents the exponent of the structure function computed in the corresponding direction in the satellite image. Remember that the structure function is centro-symmetric, therefore the value of its exponent is also centro-symmetric. The two exponents we computed in Figure 2 could be associated with the dots at 0 and π on a trigonometric circle for the East-West structure function and at $\frac{\pi}{2}$ and $\frac{3\pi}{2}$ for the North-South. The curve ?ts the dots with the function $e = a_0 + a_1 \cos(2\theta - a_2)$, where e is the exponent of the structure function in the direction θ, θ the direction of interest, and a_0, a_1, a_2 are the ?tted constants. $a_0$corresponds to the mean scaling exponent; a_1 measures the strength of the anisotropy (a_1= 0 means isotropy), and a_2 gives the main direction of the anisotropy.

5. MAIN RESULTS

In the analysed scaling range (10-200km), there is a clear difference between the exponents in the North-South and East-West directions. The variation in the value of the exponent between the two axes is one quarter of the exponent, with a higher exponent in the East-West axis. The alignment with cardinal directions is very close: the tilt is only 0.018 rad or 1 degree. This work is an exploratory one and was not focused on ?nding the widest scaling range: a broader one could be made available in further works.

The structure function exponents we give in ?gure 3 show a smooth variation with the geographic direction. This smoothness ensures that the result has not been contaminated by the noise or slow convergence of the statistical estimators. The data ?ts well with the function $a_0 + a_1 \cos(2\theta - a_2)$. The latter point supports the hypothesis of an anisotropy characterised by the following scale function:

$$\sqrt{\left(\frac{|x|}{s}\right)^{2+\epsilon} + \left(\frac{|y|}{s}\right)^{2-\epsilon}},$$

where $(x, y) = \vec{r}$ are the rectangular coordinates, s is a characteristic scale length and ϵ an exponent measuring the strength of the anisotropy. This is because the ?tted function can be analytically derived from such a scale function. As a consequence, the anisotropy of the structure function can be well modeled by the above proposed scale function over the 10 - 200 km scaling range.

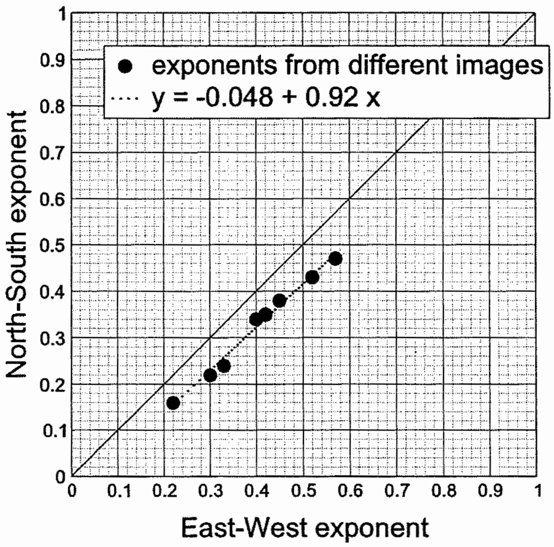

For different analysed mid-latitude images, a circle has been plotted at a position corresponding to its East-West and North-South exponent. As they are almost aligned a linear ?t has been performed. In all cases, the East-West exponent is higher by about 0.05.

Figure 4: East-West and North-South exponents for 8 MODIS images.

Repeating the analysis for different images, even if the values of the exponents vary, the orientation of the scaling anisotropy remains East-West. This led us to plot Figure 4, where every image corresponds to a circle whose coordinates indicates its East-West and North-South exponent. The resulting alignment of the circles is very good which suggests that it is systematic. For all analysed images, the East-West exponent is larger by about 0.05. The results obtained for the two analysed bands are very similar.

6. WHERE DOES HORIZONTAL SCALING ANISOTROPY THE IN ATMOSPHERE COMES FROM?

6.1. Forcing and Coriolis

The possible sources for this scaling anisotropy between North-South and East-West directions are the forcing (i.e. the difference in insolation between the equatorial area and the poles) and the Coriolis force (which causes the beta effect). Note that this last effect is not expected to be large because our scaling range (13 km to 130 km) spreads over scales where the beta effect is almost negligible (Rhines 1975).

6.2. Instabilities

The major meteorological instabilities encountered at those scales are the conditional and the symmetric instabilities (Holton, 1992).

REFERENCES

Holton, J.R., 1992: An Introduction to Dynamic Meteorology. *Academic Press.*

Lewis, G. M., S. Lovejoy, D. Schertzer, and S. Pecknold, 1999: The scale invariant generator technique for quantifying anisotropic scale invariance. *Computer and Geosciences*, **25**, 963-978.

P?ug, K., S. Lovejoy, and D. Schertzer, 1993: Generalized Scale Invariance, differential rotation and cloud texture. *Journal of the Atmospheric Sciences*, **50**, 538-553.

Rhines, P.B., 1975: Waves and Turbulence on a beta-plane. *Journal of Fluid Mechanics*, **69**, 417-443.

THE LIQUID WATER/ICE CONTENT IN MID-LATITUDE CONVECTIVE STORMS

Ingo Bertram*, Axel Seifert and Klaus D. Beheng

Institut für Meteorologie und Klimaforschung, Forschungszentrum Karlsruhe, Germany

1 INTRODUCTION

Deep convection is an important process in the mid-latitude troposphere transferring momentum, mechanical and thermal energy as well as mass from the boundary layer to higher atmospheric levels. According convective transports have to be considered in every atmospheric model. In weather prediction models the description of convective vertical transport mostly relies on simple parameterizations. To check and improve these parameterizations was a major task of the German AFO2000-project VERTIKATOR (Vertical Exchange and Orography). This study contributes to that task by at ?rst deriving liquid water/ice contents from re?ectivity data and then by estimating the mass budget of a speci?c storm.

In literature only a few relations between radar re?ectivity Z and liquid water/ice content L can be found, valid almost for only one kind of hydrometeors. Deep convective clouds, however, contain a mixture of different hydrometeors, rising the question for a suitable Z/L-relation. Since the liquid water/ice contents can not be directly inferred from radar re?ectivity data themselves results from simulations with the Karlsruhe mesoscale model (KAMM2) operated in a cloud-resolving mode are used to derive a new relation between Z and L. As well the method to establish the new relation as a ?rst application to radar data will be described.

2 SIMULATIONS WITH KAMM2

KAMM2 operates with fully compressible dynamics allowing the simulation of meso- and microscale phenomena without scale limitations (Baldauf, 2003; Seifert and Beheng, 2003b).

In contrast to other mesoscale models, KAMM2 includes a sophisticated two-moment bulk microphysical cloud scheme based on speci?c parameterizations. This scheme predicts besides mass densities as usual also number densities of ?ve hydrometeor types (cloud droplets, raindrops, cloud ice, snow and a combined graupel/hail class). The warm phase microphysics' parameterization is based on Seifert and Beheng (2001) whereas a description of the complete mixed-phase cloud scheme can be found in Seifert (2002); Seifert and Beheng (2003a).

The advantage of this microphysical scheme is that size distributions of all hydrometeor types can be inferred from the number and mass densities available at each grid point and at each instant. This allows consequently calculation of according radar re?ectivities. For the radar backscattering cross sections of large precipitation particles (graupel and raindrops) Mie-theory is considered whereas for snow and cloud ice Rayleigh approximation is used. The re?ectivity of a mixture of hydrometeor types is the sum of the speci?c re?ectivities (Seifert, 2002).

In a ?rst step a few convective cells were simulated for typical environmental conditions as observed in southwestern Germany during convective situations. For model initialization radio soundings were used. Usually only soundings almost performed at some distance to observed storms and not simultaneous are available. In the case of the 5th of August 2003 (Fig. 1 lower row) the radio sounding of Stuttgart at 14 LT, about 100 km east of the observed storm's location was used. In the 19th of June 2002-case (Fig. 1 upper row) a couple of soundings and eleven drop sondes released in the vicinity of convective cells were at hand, so that the initial conditions could be determined much more detailed.

The storms were initialized over a plane surface by a warm bubble. An outstanding high resolution (grid distance of 250 m) was chosen to ensure, that the dynamical and microphysical structure inside the storms was well resolved including up- and down drafts as well as the formation of large precipitation particles at the outer ?anks of the major updraft.

Comparison of examples of radar observations and according simulations (Fig. 1) shows that KAMM2 reproduces the main features of deep convection like precipitation area and anvil quite well. On the 5th of August 2003 the observation and the simulation refer to only a single cell. In the 19th of June 2002-case the anvil has a large extension due to strong southwesterly ?ow in the upper troposphere. The observed anvil was longer than the simulated one, as smaller cells, existing before the depicted one, contributed to the anvil.

Since at each grid point of the simulations the radar re?ectivity as well as the liquid water content are known, Z/L-relations can be established by means of this data.

*Corresponding author address: Ingo Bertram, Institut für Meteorologie und Klimaforschung, Forschungszentrum Karlsruhe, Postfach 3640, D-76021 Karlsruhe; E-Mail: ingo.bertram@imk.fzk.de

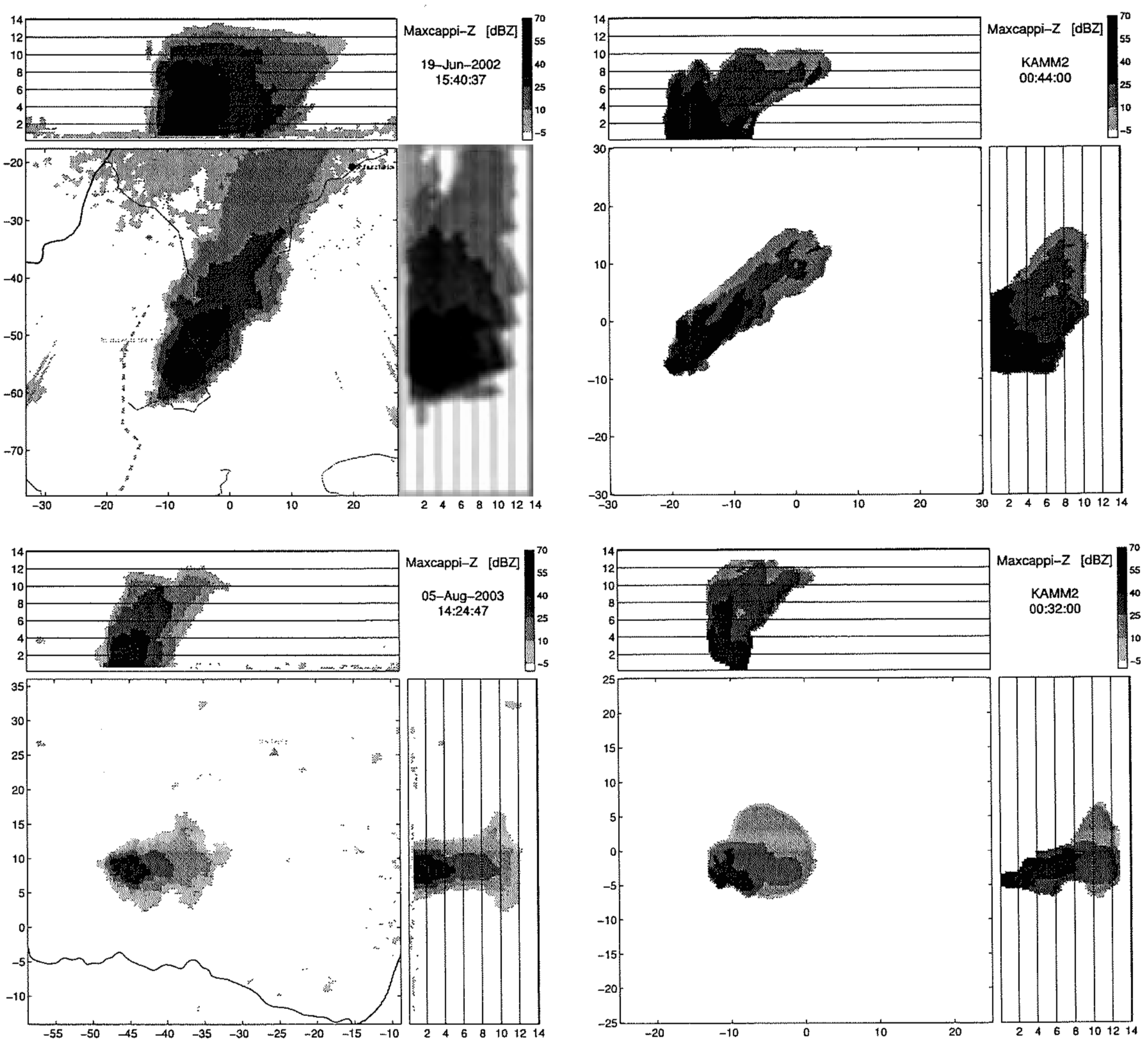

Figure 1: Radar re?ectivities in dBZ as observed (left column) and as simulated by KAMM2 (right column) for 19th, June 2002 (upper row) and 5th, August 2003 (lower row).

3 INDIVIDUAL Z/L-RELATIONS

The next step was the derivation of Z/L-relations for each individual simulation. A detailed inspection of KAMM2 results showed, that the hydrometeor characteristics differ markedly inside the cloud volume. In the lower cloud portions rain dominates whereas above the zero degree level a mixture of graupel, ice, snow and rain prevails. Cloud droplets are also present, but were excluded in this study as they are not detectable for a C-band radar.

To determine the liquid water/ice content as accurately as possible, the cloud would have to be divided into a lot of small portions with equal hydrometeor properties so that many different Z/L-relations would have to be used. As simpli?cation a two layer concept was introduced where the melting layer, assumed to be 1000 m thick and determined by the sounding's temperature, separated both. For many simulation times best straight lines were ?tted by the least square method in logarithmic L-Z diagrams (cf. Fig. 2, e.g.). Their average refers to two Z/L-relations for the modeled cell under consideration: one valid in the mixed region above and one in the rain region below the melting layer. Inside the melting layer a smooth transition between the two relations is chosen.

It turned out that the two distinct Z/L-relations have necessarily to be applied since considering only one mean relation (for all hydrometeor types) results in strong over/underestimation of L or Z in those parts of the clouds whose hydrometeor characteristics deviate more or less from the mean. Therewith Z/L-relations for an individual simulation are known, that can be used to calculate a water/ice content from the modeled Z data, that on average yields the water/ice contents of the model.

4 GENERALIZED Z/L-RELATIONS

The purpose was to ?nd Z/L-relations valid for convective clouds in general. Hence, two respective relations were derived in the described way for 24 individual simulations carried out under different, but for convective events typical conditions. At last two averaged relations were derived as

$$L_r = 2.3 \times 10^{-3} Z^{0.58} \quad \text{for rain region} \quad (1)$$

$$L_m = 3.0 \times 10^{-2} Z^{0.61} \quad \text{for mixed-phase region} \quad (2)$$

with L in g/m^3 and Z in mm^6/m^3.

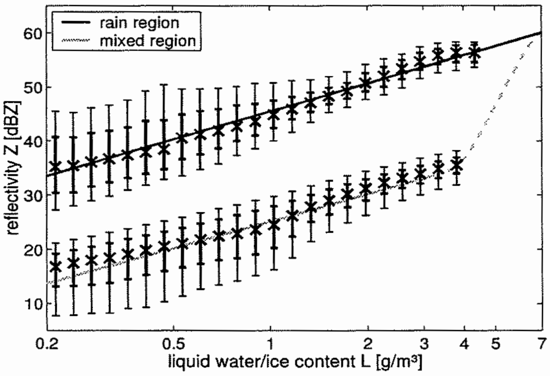

Figure 2: Generalized Z/L-relations consisting of the relation for the rain region (black line) and the relation for the mixed region (grey line). Medians (black crosses) as well as 50 and 80 percent percentiles for different classes of liquid water content are indicated.

The data of the L-Z diagrams of the different simulations showed large scatter at most simulation times. In order to condense the data all pairs of L and Z, that were involved (about 600 000 data points), were assigned to distinct L-classes. For each class medians and percentiles were calculated (Fig. 2). Note that grid points of same L-class can exhibit very different Z-values. The range containing 80% of the data covers partly 15 dBZ, especially for small water contents. At higher L values the scatter is reduced. At 2 g/m^3, e.g., 80% of the data have Z-values between 26 and 34 dBZ in the mixed region and between 48 and 54 dBZ in the rain region.

Since the described procedure in ?nding Z/L-relations averages over many simulations times and extended cloud portions, large differences may occur on single grid points. To quantify this differences, for each individual simulation, liquid water/ice contents extracted from the original model data were compared to those as obtained from applying (1) the generalized and (2) the corresponding individual Z/L-relations at every grid point.

Using the generalized relations the averaged relative error on a single grid-point amounts to 36% in the mixed and 47% in the rain region. With the individual relations 30% and 47%, respectively, result.

Despite these large differences on single grid points, the liquid water/ice contents of the total cloud can be determined much more accurately. A calculation of errors (method of quadratic sums) results in differences of only 0.5% (for the total mass in the mixed region) and 1.2% (total mass in the rain region) if the individual relations are used. These values are averages over all 24 simulations.

Clearly the generalized relations are valid on average but their application to the individual cases (one of all 24) might exhibit considerable differences as well if the total cloud mass is considered. While concentrating so far to Z/L-relations and their differences to model-derived values we now compare results obtained from the generalized relations (Eqs. 1 and 2) to those considering the 24 individual cases. This is done by investigating the time evolution of the total mass, i.e. sum of liquid water and ice contents, of a single cloud out of the 24 cases.

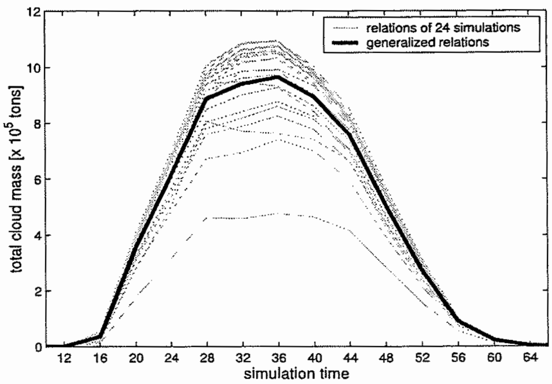

Figure 3: Total mass of a simulated convective cell between 12 and 64 minutes after model initialization using the generalized Z/L-relations (black line) and individual Z/L-relations of 24 simulations (grey lines).

Thus, all the individual Z/L-relations resulting from the different simulations were applied to one of the simulated clouds. Therewith it is shown how large the differences can be estimating the whole cloud mass with an improper Z/L-relation. Assume that the total cloud mass was calculated with the generalized Z/L-relations (black line in Fig. 3), but one of the other relations was valid. Then the difference is in the worst case more than 50%. On average the generalized relations cause an error of 11% with respect to the cell's mass maximum. This uncertainty is important for the mass budget (Section 5).

The comparison of Z/L-relations (Fig. 4) shows, that the new relation for the rain region agrees to those published in literature (Douglas, 1964; Hagen and Yuter, 2003). Hail causes comparatively high re?ectivities and the other ice phase hydrometeors low re?ectivities. Our relation for the mixed region, where graupel, snow, ice and rain occurs, is similar to the relation for storm anvils

(Heyms?eld and Palmer, 1986), but not to the relations for graupel (Kajikawa and Kiba, 1978) and snow (Herzegh and Hobbs, 1980). Note that the relations in literature are almost derived using ground-based precipitation observations.

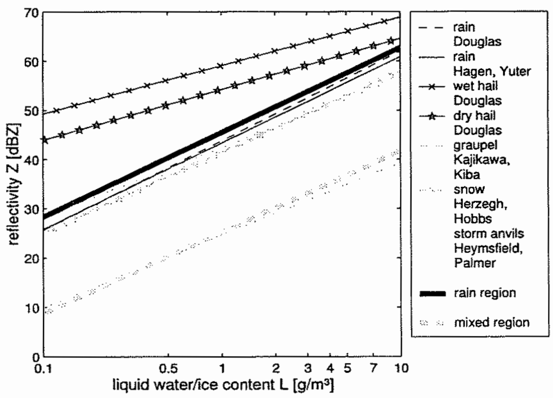

Figure 4: Z/L-relations for speci?c kinds of hydrometeors from different authors and the two generalized Z/L-relations (indicated by thick lines).

5 MASS BUDGET (19.6.02)

The total cloud mass can be estimated much more exactly than the mass at a special time and a special location in an arbitrary convective cell. This enabled our next step: The mass of radar observed convective cells was calculated by the generalized Z/L-relations. Additionally the mass of precipitation leaving the clouds was calculated by a relation between radar re?ectivity and rain rate. It was derived using the generalized Z/L-relation for rain (Eq. 1) and appropriate assumptions.

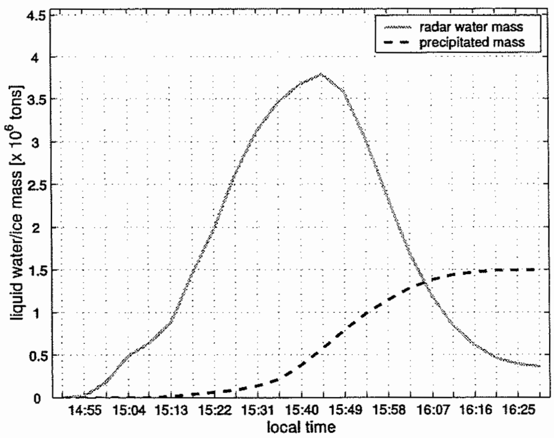

Figure 5: Water/ice mass of the radar-observed convective cell on 19th of June 2002 as function of local time (grey solid line) and cumulative precipitation mass (black dashed line).

Figure 5 shows the results for the 19th of June 2002-case. First radar detectable masses occurred at 15 LT and culminated with maximum values M_{max} of about 3.8×10^6 tons at 15:45 LT. At this time the mass M_p, about 0.6×10^6 tons, had left the cloud as precipitation. Totally the mass $M_{p,total}$, about 1.5×10^6 tons, precipitated. The precipitation ef?ciency $PE = M_{p,total}/(M_{max} + M_p)$ was about 34 percent, an upper estimate, as the maximum cell mass M_{max} excludes cloud droplets, not detectable by a C-band radar. From this budget considerations follows, that about 2.9×10^6 tons of the cell did not contribute to precipitation reaching the ground. This mass remained in the atmosphere as moisture source. Other case studies showed, that the typical maximum condensate mass of mid-latitude thunderstorms ranges from 10^6 to 10^7 tons whereof about 40 percent precipitates.

References

Baldauf, M., 2003: Das mesoskalige Simulationsmodell KAMM2. Internal report (in German), Institut für Meteorologie und Klimaforschung, Karlsruhe.

Douglas, R. H., 1964: Hail size distribution. *Proceedings of the 11th radar weather conference*, Boston, 146 – 149.

Hagen, M. and S. Yuter, 2003: Relations between radar re?ectivity, liquid-water content, and rainfall rate during the MAP SOP. *Quart. J. Roy. Met. Soc.*, **129**, 477–493.

Herzegh, P. H. and P. V. Hobbs, 1980: The mesoscale and microscale structure and organisation of clouds and precipitation in midlatitude cyclones. Part II: Warm frontal clouds. *J. Atmos. Sci.*, **37**, 367 – 381.

Heyms?eld, A. J. and A. G. Palmer, 1986: Relationship for deriving thunderstorm anvil ice mass for CCOPE storm water budget estimates. *J. Climate Appl. Meteor.*, **25**, 691 – 702.

Kajikawa, M. and K. Kiba, 1978: Observation of the size distribution of graupel particles. *Tenki*, **25**, 390 – 398.

Seifert, A., 2002: Parametrisierung wolkenmikrophysikalischer Prozesse und Simulation konvektiver Mischwolken. Dissertation, Institut für Meteorologie und Klimaforschung, Karlsruhe.

Seifert, A. and K. D. Beheng, 2001: A double-moment parameterization for simulating autoconversion, accretion and selfcollection. *Atmos. Res.*, **59**, 265 – 281.

— 2003a: A two-moment cloud microphysics parameterization for mixed-phased clouds. Part I: Model description. *submitted to Meteorol. Atmos. Phys.*.

— 2003b: A two-moment cloud microphysics parameterization for mixed-phased clouds. Part II: Deep convective storms. *submitted to Meteorol. Atmos. Phys.*.

THE DIURNAL CYCLE OF SOUTHEAST PACIFIC STRATOCUMULUS DYNAMICS AND ENTRAINMENT OBSERVED IN EPIC 2001

C.S. Bretherton, P. Caldwell, and R. Wood

Department of Atmospheric Sciences, University of Washington, Seattle, Washington 98195 USA

1. INTRODUCTION

Subtropical stratocumulus exhibit a pronounced diurnal cycle that affects their daytime-mean albedo. Past satellite and surface climatologies have shown the diurnal cycle of cloud liquid water path and fractional coverage is particularly strong over the southeast Pacific Ocean (Wood et al 2002). During a two week October cruise during EPIC 2001, the NOAA ship *Ronald H. Brown* gathered an unprecedented dataset in this region combining shipboard remote sensing including mm and 5 cm radars, microwave radiometer and ceilometer, three-hourly rawinsondes, and surface meteorology and flux observations (Bretherton et al. 2004).

The ship was stationed at 20°S, 85°W for six days, where it sampled a 1300 m deep, fairly well-mixed stratocumulus-topped boundary layer capped by a 10 K inversion overlaid by consistently dry air (Fig. 1). One way of assessing the well-mixedness of the PBL is to compare the ceilometer-inferred cloud base with a ship-based estimate of the lifted condensation level at the top of the surface layer. These track particularly well in the early evening, and deviate by less than 250 m at other times of day. A remarkably regular diurnal cycle was seen, characterized by 200 m fluctuations in the inversion height and cloud thickness, nocturnal drizzle, and partial afternoon cloud breakup.

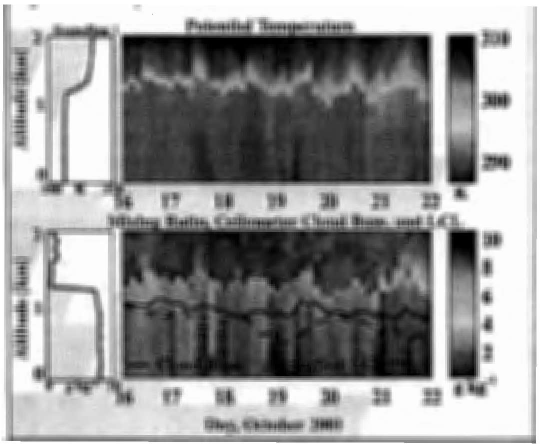

Fig. 1: Time-height plot of soundings at buoy. Line plots of the first sounding are shown at left.

Corresponding author's address: Christopher S. Bretherton, Dept. of Atmospheric Sciences, Box 351640, University of Washington, Seattle, WA 98195, USA; E-Mail: breth@atmos.washington.edu.

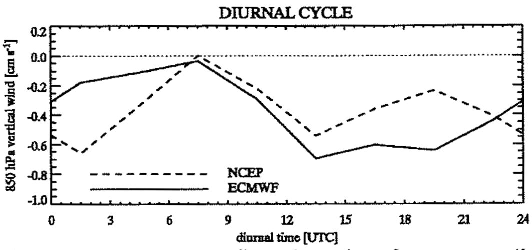

Fig. 2: 6-day mean diurnal cycle of mean vertical velocity at 20°S, 85°W from two large-scale analyses.

2. SUBSIDENCE DIURNAL CYCLE

The diurnal cycle in inversion height is too large to be easily explained by local processes such as entrainment. Martin Koehler provided us with high time resolution output from the ECMWF operational forecast models, which show a pronounced diurnal cycle in 850 mb vertical velocity during this six-day period (Fig. 2), with mean radiatively-driven subsidence amplified during the day, but reduced to zero around midnight. NCEP analyses from Hua-Lu Pan have a qualitative similarity to the ECMWF diurnal cycle, but with more noise and a larger semidiurnal component. A strong diurnal cycle in subsidence was a major contributor to the inversion height and cloud thickness fluctuations, likely reducing the daytime-mean cloud albedo and the magnitude of their climatically important TOA net cloud radiative forcing.

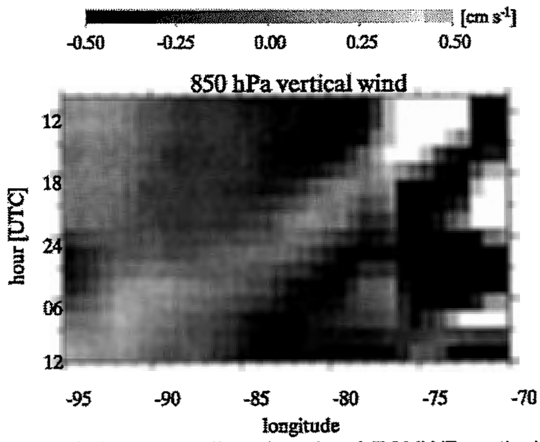

Fig. 3: 6-day mean diurnal cycle of ECMWF vertical motion at the inversion level along an ENE-WSW transect through the buoy. The S American coast is at about 75 W.

The diurnal cycle in subsidence is associated with a gravity wave of half-vertical wavelength 6 km driven by daytime heating on the Andean slopes 1500 km away, elegantly simulated using a mesoscale model by Garreaud and Munoz (2004). Fig. 3 shows the mean diurnal cycle of 850 mb vertical velocity from ECMWF along a transect between the buoy and the Peruvian Andes, showing a wave of 'upsidence' starting at 18 UTC (12 LT) and propagating southwestward at 30 m s^{-1}, arriving at the buoy at midnight.

3. PBL BUDGETS

We calculated diurnally-varying 6 day mean mass, heat and moisture budgets for the boundary layer. Entrainment rate w_e can be inferred from the mass budget. The heat and moisture budgets can be used as independent checks on w_e. They can also be used to infer the buoyancy flux profile that would be required to keep the PBL well mixed, with implications for turbulence and decoupling.

The mass budget is:

$$\partial z_i / \partial t = w_e + \bar{w} - \mathbf{u} \cdot \nabla z_i$$

where $\bar{w}(t)$ is the mean vertical motion at the inversion base height $z_i(t)$, and the final term is horizontal advection of inversion height. For each 3-hourly sounding, z_i was chosen as the local temperature minimum, the subsidence was interpolated to this height using the ECMWF analyses, and $\partial z_i / \partial t$ was computed via centered differencing. From satellite-derived cloudtop brightness temperature, the inversion generally appears to be relatively flat in this region. For the horizontal advection, we used Wood and Bretherton (2004)'s climatological estimate of -0. 45 mm s^{-1} based on two months of MODIS-derived z_i estimates.

The dot-dashed line in Fig. 4 shows the diurnal cycle of w_e estimated in this way. The 6-day mean w_e = 0.4 cm s^{-1}, consistent with climatological estimates of Wood and Bretherton (2004). As expected, w_e has a nighttime maximum when the cloudtop longwave radiative cooling is unopposed by solar absorption, leading to more vigorous turbulence. During the daytime, w_e falls nearly to zero. The 'error bars' are based on the day-to-day standard deviation of the estimated diurnal variation of we, and do not include other possible sources of systematic and random errors.

The heat budget was calculated using the liquid static energy $s_l = c_pT+gz-Lq_l$, where T is temperature and q_l is liquid water content. s_l is conserved within adiabatic vertical displacements and phase changes. For simplicity, the budget assumes a mixed-layer structure within the PBL. For our case, with careful definitions of all the budget terms, this is a quantitatively accurate approximation. The budget is phrased in terms of the PBL mass-weighted average

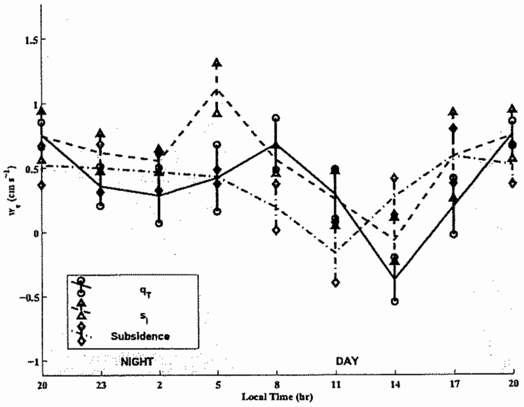

Fig. 4: 6-day mean diurnal cycle of entrainment rate from ECMWF subsidence (mass budget), and derived as a budget residual in the heat and moisture budgets.

$\overline{s_l}$ and PBL mass per unit area $M(t) = \int_0^{z_i} \rho dz$:

$$M\left(\partial \overline{s_l} / \partial t + \mathbf{u} \cdot \nabla \overline{s_l}\right) = \rho_i w_e \Delta s_l - \Delta F_R + SHF + LP(0)$$

The RHS includes entrainment warming, radiative flux divergence, sensible heat flux, and latent heating from surface precipitation. Each term was estimated for three hour intervals centered on sonde launch times.

The tendency terms and PBL mass were computed from the soundings, with the liquid water correction in $\overline{s_l}$ computed from the microwave radiometer derived liquid water path. Since $\overline{s_l}$ tendencies were small and one sounding gives an imperfect estimate of the horizontal mean $\overline{s_l}$ at the sounding time, the tendency term was subject to large random errors. Time-dependent horizontal advection was estimated from ECMWF analyses.

Entrainment warming was estimated from the mass-budget derived $w_e(t)$ and the jump $\Delta s_l(t)$ from $\overline{s_l}$ to the above-inversion s_l^+. We estimated s_l^+ as sl(zi + 150 m) – 600 J kg^{-1}, since the temperature sounding immediately above the inversion was compromised by some mixture of sensor wetting and delayed response. The 600 J kg^{-1} correction was based on a calculation of the radiative cooling a typical air parcel would experience as it subsided from 150 m above the inversion into the entrainment zone.

The Fu-Liou radiative transfer scheme was applied to the observed temperature and moisture soundings to calculate the radiative flux divergence. The observed cloud fraction and PBL cloud liquid water path were also used as inputs to this calculation (no free-tropospheric clouds were observed above the ship during the period). Surface radiative fluxes computed using this approach agreed well with ship observations.

Sensible heat flux was measured on the ship using a bulk aerodynamic approach. Surface precipitation was computed from EPIC-specific Z-R relations derived using a combination of C-band and K-band radar observations (Comstock et al. 2004). While this method has factor-of-two uncertainties, little surface precipitation was observed so this uncertainty has a minimal effect on the heat budget.

The 6-day mean heat budget was a balance between cooling due to radiation (-49 W m^{-2}) and horizontal advection (-19 W m^{-2}), and warming due to entrainment (34 W m^{-2}) and sensible heat flux (14 W m^{-2}), with a 4 W m^{-2} contribution from precipitation, leaving a 17 W m^{-2} residual, which is within our margin of error. Only radiative cooling and entrainment warming had large diurnal variations; these had daytime minima and nighttime maxima that balanced in our budget to within the large 30-40 W m^{-2} margin of error of our diurnally-segregated computations. The diurnally varying entrainment rate deduced as a heat budget residual (Fig. 4) has qualitatively the same structure as the subsidence-derived estimate, but is slightly larger on average, and phased slightly later.

The moisture budget was phrased in terms of total humidity $q_t = q_v + q_l$:

$$M\left(\partial\overline{q_t}/\partial t + \mathbf{u}\cdot\nabla\overline{q_t}\right) = \rho_i w_e \Delta q_t + LHF - P(0)$$

The terms were computed analogously to the heat budget. The inversion humidity jump was very sharp (Fig. 1); the humidity 50 m above the inversion was used for computation of Δq_t.

The 6-day mean moisture budget was a balance between moistening due to latent heat fluxes (99 W m^{-2}) and drying due to entrainment (-70 W m^{-2}), horizontal advection (-26 W m^{-2}), and precipitation (4 W m^{-2}), with a 5 W m^{-2} tendency and a 6 W m^{-2} residual, again well within our margin of error. Only storage and entrainment drying had large diurnal variations that again balanced in our budget to within our margin of error. The moisture budget residual estimate of entrainment rate (Fig. 4) also has qualitatively the same structure as the estimates from the mass and heat budgets.

4. BUOYANCY FLUXES

Given the mixed layer assumption, one can derive the vertical turbulent fluxes of s_l and q_t, and from them, the buoyancy flux (see, e. g. Bretherton and Wyant 1997). To do this we must specify the vertical profile of radiative cooling (from the Fu-Liou scheme) and of precipitation flux (from Comstock et al.), and specify at what levels the PBL is cloud-filled (from the ceilometer observations). Fig. 5 shows the derived diurnal cycle of buoyancy flux. A region of negative buoyancy flux below cloud base develops in the early morning due to extensive evaporating drizzle, and persists throught he morning due to solar heating of the clouds. As a consistency check, these are the periods where the difference of the cloud base and the near-surface LCL

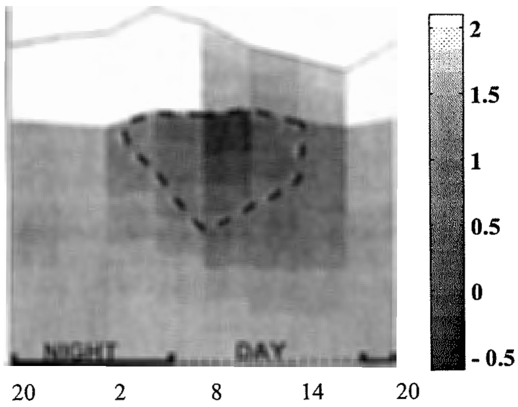

Fig, 5: Buoyancy flux implied from qt and sl flux profiles. Note the discontinuity at cloud base, with strong positive fluxes above that mainly drive the PBL turbulence. Dashes surround region of negative buoyancy flux.

is largest. However, the buoyancy fluxes nowhere become hugely negative, consistent with the nearly well-mixed structure observed throughout the six day period. It is plausible that any decoupling was only partial, and that some turbulent mixing persisted throughout the boundary layer at all times of day.

One can vertically integrate the buoyancy flux profiles to obtain a diurnal cycle of convective velocity w_* and compute an entrainment efficiency $A = w_e \Delta b / w_*^3$, where Δb is the buoyancy jump across the inversion (which is largely independent of time of day). This calculation has many potential sources of error, but our results suggest $A \sim 1$, which is consistent with Stevens et al. (2003) but lower than many earlier published estimates based on aircraft observations. Of course, entrainment closures typically predict that A depends on the thermodynamic sounding and forcings, but our EPIC budgets might be a useful constraint on stratocumulus entrainment closures even though no direct measurements of turbulence profiles or entrainment were made.

5. CONCLUSIONS

In the SE Pacific, a continentally-modulated diurnal cycle of subsidence reinforces the tendency of stratocumulus to thicken at night and thin during the day, perhaps explaining the large diurnal cycle of cloud cover and liquid water path in this region and reducing the climatically important surface ant TOA shortwave cloud forcings in this region. The heat and moisture budgets are pleasantly consistent with the diurnal cycle of entrainment rate estimated from the ECMWF-derived subsidence. Mixed-layer buoyancy flux estimates seem consistent with the tendency of the PBL to be better mixed early at night than in the morning, and are imply more turbulence at times of day with more entrainment, but less efficient entrainment than found in many other past studies.

6. ACKNOWLEDGMENTS

The authors are grateful to Sandy Yuter, Chris Fairall and Taneil Uttal, and to the crew of the RHB for their assistance in collecting the data. This project is funded through NSF Grant ATM-0082384 and NASA grant NAGS5-10624.

7. REFERENCES

Bretherton, C. S., and M. C. Wyant, 1997: Moisture transport, lower tropospheric stability and decoupling of cloud-topped boundary layers. *J. Atmos. Sci.*, 54, 148-167.

Bretherton, C. S., T. Uttal, C. W. Fairall, S. E. Yuter, R. A. Weller, D. Baumgardner, K. Comstock, and R. Wood, 2004: The EPIC 2001 stratocumulus study. *Bull. Amer. Meteor. Soc.*, accepted.

Comstock, K. K., R. Wood, S. E. Yuter, and C. S. Bretherton, 2004: Reflectivity and rain rate in and below drizzling stratocumulus *Quart. J. Roy. Meteorol. Soc.*, submitted 9/03.

Garreaud, R. D., and R. Munoz, 2004: The diurnal cycle in circulation and cloudiness over the tropical southeast Pacific: A modeling study. *J. Climate*, accepted.

Stevens, Bjorn, and coauthors, 2003: On entrainment rates in nocturnal marine stratocumulus. *Quart. J. Roy. Meteor. Soc.,* in press.

Wood, R., C. S. Bretherton, and D. L. Hartmann, 2002: Diurnal cycle of liquid water path over the subtropical and tropical oceans. *Geophys. Res. Lett.*, **29**(23),2092, doi:10.1029/2002GL015371.

Wood, R., and C. S. Bretherton, 2004: Boundary layer depth, entrainment and decoupling in the cloud-capped subtropical and tropical marine boundary layer. *J. Climate*, in press.

CAN THE FRACTAL DIMENSION OF CLOUDS BE MEASURED?

Joe Brewer and Larry Di Girolamo

Department of Atmospheric Sciences, University of Illinois, Urbana, IL 61801, USA

1. INTRODUCTION

Fractal models are commonly used to simulate cloud structures because clouds have been observed to exhibit scaling properties inherent in fractal geometry. These models are parameterized with fractal dimensions calculated from observational data like satellite and in situ measurements. This paper will demonstrate that fractal dimension estimation is unreliable and depends upon many factors including instrument resolution, sun-view geometry, spectral channel, averaging techniques, number of data points, and estimation algorithm used. The relevance of these factors as possible sources of error has been largely overlooked in previous studies of the scaling behavior of cloud structures. Here we review and assess previous work and show that the retrieval of cloud scaling properties is not straightforward.

2. SURVEY OF PREVIOUS WORK

Power spectra were calculated for radiance measurements of marine stratocumulus by Cahalan & Snider (1989) that illustrated a scale break (i.e. change from one power law scaling exponent to another) that was also observed in Barker & Davies (1992), Barker (1996), Davis et al. (1997), and Oreopoulus & Davies (1998). Each of these studies found evidence for a scale break, but the location was different in each report. Table 1 shows that the location of observed scale breaks follow a trend with instrument resolution and the number of pixels used in each scan line analyzed.

One of the physical explanations used to justify the scale-break was radiative smoothing, a phenomenon that claims the structure in a cloud radiance field will appear smooth at horizontal scales comparable to the mean-free path between scattering events in visible portions of the electromagnetic spectrum. One notable inconsistency with this explanation is the discovery of a scale break at 5 km in the 11.5 μm spectral region reported in Barker & Davies (1992). In this spectral region, scattering has a negligible effect on the radiances emerging into space. Thus, another explanation must be sought for the observed scaling behavior. This paper will present an alternative perspective, focusing on the scaling estimation procedure instead. The discussion that follows will further emphasize the limitations of past scaling studies of cloud radiance properties.

Corresponding author's address: Joe Brewer, Department of Atmospheric Sciences, University of Illinois, Urbana, IL 61801, USA; E-mail: jabrewer@atmos.uiuc.edu.

Paper	Instrument Resolution (km)	Scale Break (km)	Pixels per Scan Line
Davis et al. (1997)	0.0285	0.2-0.4	4096
Barker (1996)	0.0285	0.5	2048
Cahalan & Snider (1989)	0.12	0.5	2048
Barker & Davies (1992)	1.1	5	256
Oreopoulus & Davies (1998)	1.1	7	256

Table 1. Summary of observed scale breaks presented in the literature.

3. WHAT IS FRACTAL DIMENSION?

3.1 In Theory

One principle characteristic of fractal geometry is scale invariance. Simply stated, a data set is scale invariant if its statistical properties are the same at different scales. In order for scale invariance to occur, the relationship between scales must produce a power law. Typically the scaling exponent is non-integer, leading to the term "fractional dimension" coined by Mandelbrot (1977), or "fractal" for short. Hausdorff (1919) defined the scaling behavior according to the Hausdorff Dimension, $D_H=\log(N)/\log(r^{-1})$, where N is the number of self-similar parts and r is the scale. This definition only holds in the strict case where the data set is identical at different scales, a condition that is never met with physical objects from the real world.

3.2 In Practice

Because the strict requirement of self-similarity is never met, it is necessary to approximate the fractal dimension defined by Hausdorff. This can be done in a number of ways, each resulting in a different definition and corresponding algorithm. As is usually the case, not all algorithms are created equal. This results in a variety of methods for estimating scaling behavior, each having its own caveats and limitations.

A thorough discussion of four different fractal dimension estimation algorithms (box counting, horizontal structuring element method, variation method, and power spectrum) and their limitations is given in Brewer and Di Girolamo (2004). The main conclusion drawn from that study is that no estimation algorithm considered works reliably well. The power spectrum, used exclusively in the cloud scaling studies described above, is very unreliable and generally is biased toward higher fractal dimensions for Brownian motion fractal types, which are commonly used for generating "realistic" cloud fields.

Errors in the estimation process are the compound result of finite resolution, fractal type and dimension, and estimation algorithm used. The estimation process to derive cloud scaling properties is further complicated in practice by the additional difficulties inherent in remote sensing.

4. ASSESSMENT OF PREVIOUS WORK

In the consideration of scaling exponents and potential scale breaks for cloud radiance fields, only the power spectrum was used. This is very problematic because the power spectrum performs poorly in the determination of scaling exponents. Figure 1 shows the range of estimated values for scaling exponents of three different types of fractal curves with prescribed scaling behaviors. Notice how the performance is generally poor for each fractal type and also shows a strong dependence upon which type of fractal model is chosen. The power spectrum is also strongly dependent upon resolution (Brewer & Di Girolamo 2004).

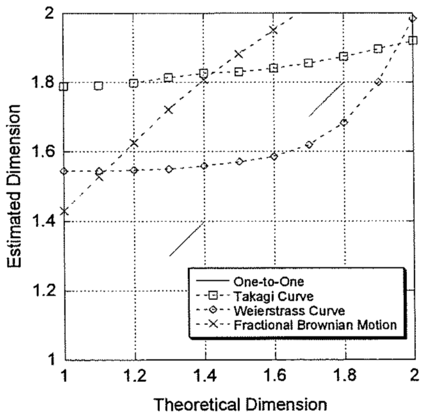

Figure 1. Estimated versus theoretical dimension for power spectrum of three different types of fractal curve, each having 512 data points.

The scale breaks reported in Table 1 were found by calculating the power spectrum for individual scan lines of a satellite radiance image, then averaging several spectra to reduce noise. However, no consideration was given for the effect of averaging power spectra on the location of scale breaks and the estimation of scaling exponents. In order to address this question, several realizations of fractional Brownian motion (Varnai 1996) were generated randomly with the same prescribed scaling exponents and power spectra were calculated and averaged, with and without scale breaks. The scaling exponents were found to be robust against averaging. For 1, 256, 512, and 1024 spectra averaged, the change in estimated scaling exponent was less than 1%. The location of scale breaks was found to be similarly reproducible, suggesting that averaging is not the culprit for the low quality performance of the power spectrum.

Using scaling exponents estimated from power spectra to simulate cloud fields can result in large errors. In order to appreciate the extent of the biases induced from using power spectra, a simple experiment was performed with cloud fields simulated using fractional Brownian motion. The scaling exponents reported in Davis et al. (1997) were input into the model, producing the scene in Figure 2(a). Then another scene was generated with higher scaling exponents so that the estimated values from the power spectrum were consistent with those reported in the literature. This "corrected" scene is shown in Figure 2(b). Note how it looks more like real clouds.

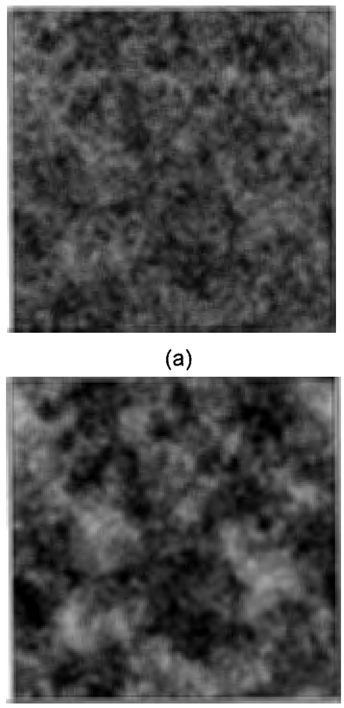

(a)

(b)

Figure 2. Cloud scenes generated (a) with scaling exponents (β = 2, 3.4) reported in the literature and (b) with scaling exponents (β = 2.9, 4.3) that have been corrected for biases in the power spectrum method.

5. REMOTE SENSING PRODUCES MORE ERRORS

Not only are there problems with the estimation of scaling behavior for simulated fractal curves, but also additional complications arise when using remotely sensed data to understand cloud structure. Challenges frequently arise in the remote sensing community with respect to the effect of sun-view geometry and spectral response of the region under scrutiny. Fractal analysis (and implications for cloud structures) is not immune to these complications.

To illustrate the difficulties in applying fractal analysis to satellite imagery, scenes were chosen from the MISR and MODIS instruments for the same marine stratocumulus deck over the Southern Indian Ocean on November 18, 2001. MISR has the unique feature of viewing the Earth from nine different camera angles in the along-track orbital direction, so that all nine cameras scan the same region within a seven minute period. Each camera has four spectral channels located in the blue, green, red, and near infrared regions of the electromagnetic spectrum. The nadir camera, viewing the Earth at an angle of 90° relative the surface, has 275 meter resolution. The camera in the foremost direction views the Earth at an angle of 70.5° relative to nadir with 1.1 kilometer resolution (except for the red channel, which has 275 meter resolution). MODIS has 36 spectral channels in the visible and infrared regions of the electromagnetic spectrum with some channels having 250 meter resolution and others having 1 kilometer resolution. Both instruments are on the EOS-TERRA platform, thus both instruments view the Earth simultaneously. The selected images are shown in Figures 3 and 4.

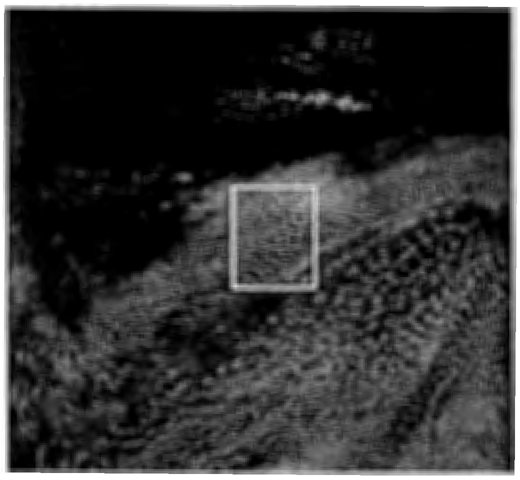

Figure 3. MODIS image from blue channel of a marine stratocumulus cloud deck over the Indian Ocean. The sub-region represents the area depicted in the MISR image below.

Individual scan lines were extracted from the MISR scene for the nadir view and the 70.5° forward view in order to see the effect of sun-view geometry on fractal dimension for the four estimation algorithms presented in Brewer and Di Girolamo (2004). The nadir view data was also coarsened from 275 m to 1.1 km to demonstrate the effect of data resolution. Scan lines were also extracted for these scenes from the blue channel and 11 µm channel of MODIS to see the effect of spectral channel on the estimation of fractal dimension. The results are summarized in Table 2.

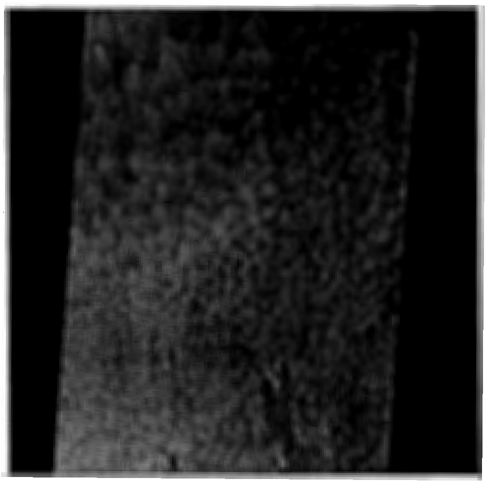

Figure 4. MISR image from 70.5° forward view blue channel for a subset of the MODIS scene shown above.

For each scan line, all four estimation algorithms give different results. Also, each algorithm is dependent upon resolution, view angle, and spectral channel. This highlights that the definition of fractal dimension (scaling exponent) is not for cloud structure, but that of the spectral radiance field, and therefore depends on factors affecting the radiance field, with a significant spread across estimators.

	HR Nadir	LR Nadir	Forward Direction	MODIS Blue	MODIS Infrared
D_B	1.34	1.31	1.18	1.39	1.11
D_H	1.27	1.37	1.29	1.33	1.24
D_V	1.45	1.63	1.55	1.55	1.36
D_P	1.41	1.50	1.26	1.47	1.33

Table 2. Estimated fractal dimension from four different algorithms (box counting, horizontal structuring element method, variation method, and power spectrum) for high (HR) and low (LR) resolution nadir views, the forward view of MISR, and both MODIS channels.

An additional comment should be made regarding the existence of scale breaks in these data sets. Figure 5 shows the power spectrum for the nadir view blue channel from the MISR instrument. A scale break exists near wave number 256, corresponding to roughly 3 km. This is about one order of magnitude above the data resolution of 275 m. The estimated scaling exponents are –1.9 above the break and –3.4 below the break, which are consistent with the values reported in Davis et al. (1997). Thus, this analysis fits within the trends in Table 1. Figure 6 shows similar scaling behavior for the MODIS 11 μm channel with scaling exponents of –2.0 and –3.1, respectively. (Comparable results were found for the blue channel.)

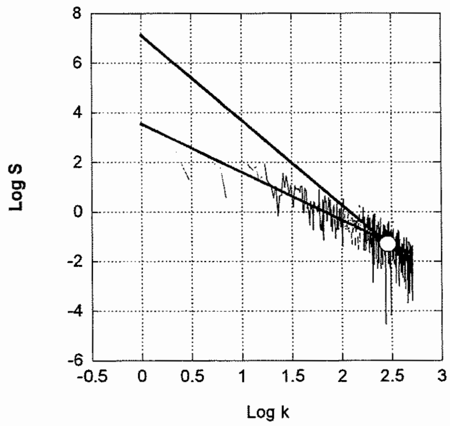

Figure 5. Power spectrum for MISR nadir view blue channel, showing a scale break (white circle) at approximately 3 km.

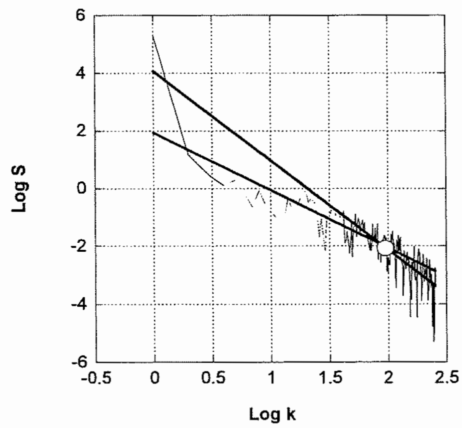

Figure 6. Power spectrum for MODIS 11 μm channel showing a scale break (white circle) at approximately 7 km.

6. RECONSIDERING CLOUD SCALING BEHAVIOR

Answering the question in the title of this paper, the fractal dimension cannot be measured for a cloud with confidence. The definition is ambiguous because the perceived structure depends upon instrument resolution, sun-view geometry, spectral channel, and estimation algorithm. The power spectrum, ubiquitous in previous studies, is not a useful tool for determining scaling exponents. However, it is robust against averaging for determining the location of scale breaks. Caution is recommended when interpreting the scale break until the relationship between location and instrument resolution is more thoroughly investigated. Thus, the power spectrum cannot be used solely for the sake of determining scaling properties of cloud fields. Alternative methods for determining scaling behavior of cloud radiance fields need to be sought.

7. ACKNOWLEDGEMENTS

We would like to acknowledge Tamas Varnai for providing the fractional Brownian motion code used extensively in this research and for helping with the validation of the power spectrum code. Partial funding was provided by the Diffenbaugh Fellowship Program. Additional support was provided by the National Aeronautics and Space Administration's New Investigator Program in Earth Science with the NASA NAG 5-12633 grant. These contributions are gratefully acknowledged.

8. REFERENCES

Barker, H. W., 1996: A parameterization for computing grid-averaged solar fluxes for inhomogeneous marine boundary layer clouds. Part I: Methodology and homogeneous biases. *J. Atmos. Sci.*, **53**, 2289-2303.

_____, and J. A. Davies, 1992: Cumulus cloud radiative properties and the characteristics of satellite radiance wavenumber spectra. *Rem. Sens. Environ.*, **42**, 51-64.

Brewer, J. A., and L. Di Girolamo, 2004: Limitations of fractal dimension estimation algorithms. *IEEE Trans. PAMI*, Submitted.

Cahalan, R. F., and J. B. Snider, 1989: Marine strato-cumulus structure. *Rem. Sens. Environ.*, **42**, 95-107.

Davis, A., A. Marshak, R. Cahalan, and W. Wiscombe, 1997: The Landsat scale break in stratocumulus as a three-dimensional radiative transfer effect: Implications for cloud remote sensing. *J. Atmos. Sci.*, **54**, 241-260.

Hausdorff, F., 1919: Dimension und auberes mass. *Mathematische Annalen*, **79**, 157-179.

Mandelbrot, B. B., 1977: *Form, Chance, and Dimension.* W. H. Freeman & Co., 365 pp.

Oreopoulus, L., and R. Davies, 1998: Plane parallel albedo biases from satellite observations. Part I: Dependence on resolution and other factors. *J. Climate*, **11**, 919-932

Varnai, T., 1996: Reflection of solar radiation by inhomogeneous clouds. Ph.D. dissertation, McGill University, 149 pp.

CHARACTERIZATION OF MESOSCALE FEATURES IN SE PACIFIC STRATOCUMULUS

K.K. Comstock, C.S. Bretherton, S.E. Yuter, and R. Wood

Department of Atmospheric Sciences, University of Washington, Seattle, Washington 98195 USA

1. INTRODUCTION

Large regions of stratocumulus (Sc) clouds significantly affect global albedo. The solar reflectance properties of stratocumulus are influenced by the complex interplay between cloud thickness, horizontal inhomogeneity, and local patterns of drizzle. Two of the key components needed to estimate the albedo are the mean cloud thickness and the horizontal variability of the Sc layer.

Horizontal variability within Sc sheets resembles the hexagonal "open cell" and "closed cell" mesoscale patterns that appear in regions with large heat fluxes (e.g. Agee 1984). These patterns are called mesoscale cellular convection (MCC), where mesoscale variability takes place on scales of roughly 10-100 km. In Sc, the cells are driven by cloud-top cooling rather than surface heating. Closed cells are cloudy regions typically around 30 km in diameter, surrounded by narrow thin-cloud or clear regions. Open cells, conversely, consist of broad clear or thin-cloud areas ringed by cloud elements. It has been suggested that higher drizzle rates in Sc are found in open, rather than closed cellular regimes (Stevens et al. 2004).

Drizzle affects boundary layer dynamics, and it is related to the mesoscale horizontal variability of Sc cloud thickness and extent (see ICCP abstract by Wood et al.). Drizzle is also modulated by the diurnal cycle. To better understand these relationships, it is useful to examine the structure and life cycle of individual drizzling Sc elements.

Observations obtained in the SE Pacific stratocumulus region during the Eastern Pacific Investigation of Climate (EPIC) 2001 stratocumulus cruise are uniquely suited for addressing the spatial and temporal dynamics of Sc (Bretherton et al. 2004). In this study, we used ship-based data obtained during six days in October 2001 at 20°S, 85°W off the coast of Peru. Meteorological time series data were used to characterize the Sc boundary layer. Ship-based radar data were used to associate drizzle with enhanced mesoscale variability. We also identified and composited cellular features in scanning C-band radar data, and used these to determine the characteristics of drizzle cell structure and lifetime.

2. STRUCTURE AND LIFE CYCLE OF SC

The high-resolution C-band data set, which provided reflectivity in a 30-km radius around the ship every five minutes, enabled us to observe the evolution of drizzle cells as they passed by the ship. Drizzle cells were found to range in size up to 100 km^2 in area. Some drizzle cells were observed to form, while others dissipated. Some of the cells split and others merged.

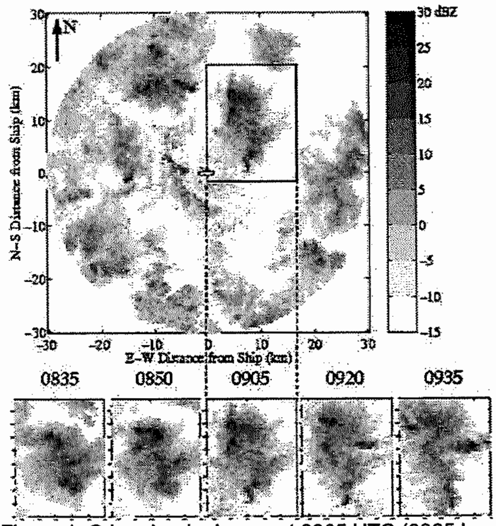

Figure 1. C-band radar image at 0905 UTC (0305 local time) on 21 October 2001 and evolution of boxed drizzle cell between 0835 and 0935 UTC. The 2-D reflectivity map shown has been averaged through the cloud layer.

An example of the evolution of a drizzle cell is shown in Figure 1. The drizzle cell that is boxed in the top panel has been identified and "cut out" of each C-band image throughout its lifetime in the C-band field of view. Five of these individual snapshots are displayed at the bottom of the figure. This cell began to split and to fade during the hour shown. The entire set of these drizzle-cell cut-outs was composited.

Within the 1.5-2 hours it takes to advect through the C-band field of view, no sizable drizzle cell was observed to go through an entire life cycle, from development through dissipation. Although no complete lifecycle was observed, different cells represent different portions of drizzle-cell evolution. The average reflectivity was calculated over time for eight example cells. The examples, shown in Figure 2 indicate that a typical drizzle cell lifetime is about two hours.

The mean e-folding distance in reflectivity (dBZ) for the example cell in Figure 1, and for the other

Corresponding author's address: Kimberly K. Comstock, Atmospheric Sciences, Box 351640, University of Washington, Seattle, WA 98195, USA; E-Mail: kcomstock@atmos.washington.edu.

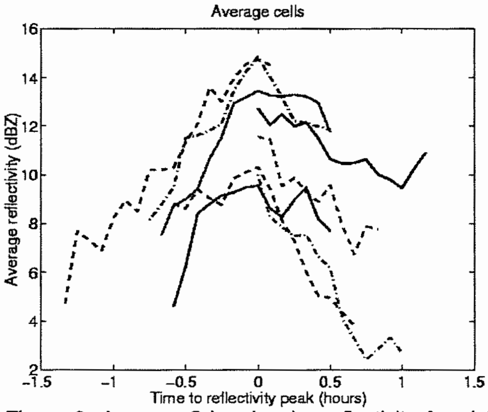

Figure 2. Average C-band radar reflectivity for eight example cells on three days, using data interpolated to 500 m by 500 m pixels. All series are normalized with respect to the time at which the cells reach their peak average reflectivity.

examples, was about 2.5 km. This indicates the rapid drop-off of reflectivity within a drizzle cell, as well as the degree of patchiness of the drizzle signal. This result supports the observation that drizzle is associated with more variable conditions.

3. BOUNDARY-LAYER CHARACTERIZATION

In the SE Pacific, cloud thickness varies diurnally with cloud top height (Bretherton et al. 2004). At night, long-wave cooling is able to drive mixing throughout the boundary layer, so the surface and cloud layers are coupled. This mixing increases the entrainment at cloud top and causes the cloud top to rise, thereby thickening the cloud during the night. If the cloud is thick enough and large drops are present, these can fall through the cloud, collect smaller drops, and eventually fall out as drizzle. Drizzling periods occur most often during the early morning. During the day, short-wave absorption within the cloud layer offsets some of the long-wave cooling at the cloud top so mixing is inhibited between the surface layer and the layer above, and the boundary layer becomes decoupled. This pattern of *coupled-drizzling-decoupled* is not entirely predictable because MCC patterns are superimposed upon the diurnal cycle.

To explore the mesoscale variability of Sc, we examined the dynamics involved in each of the three boundary layer categories just mentioned. We first subdivided the six-day EPIC Sc time series into coupled, decoupled and drizzling categories. When the area-averaged reflectivity from the C-band radar was greater than -5 dBZ the boundary layer was classified as drizzling. Otherwise, if the difference between that hour's cloud base height from the ceilometer (z_{CB}) and the lifting condensation level (LCL) was less than 300 m, the boundary layer was coupled. If the difference was greater than 300 m the boundary layer was decoupled.

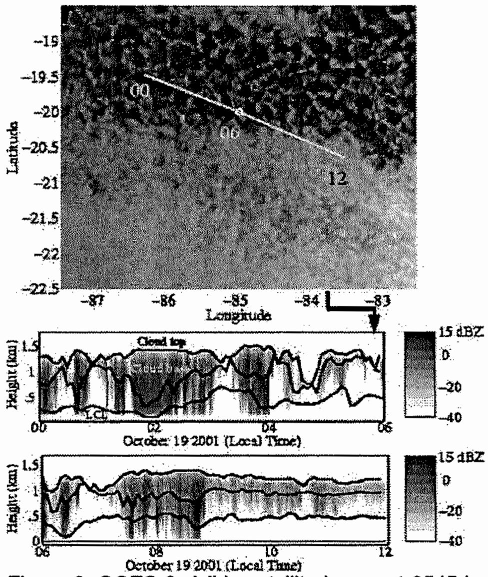

Figure 3. GOES-8 visible satellite image at 0545 local time on 19 October 2001, with estimated advection for the previous and following six hours indicated by lines. The circle is the 0600 position of ship. Corresponding MMCR time-height sections are below for the previous and following six-hour time segments, with overlayed lines of hourly cloud top (from the MMCR), hourly cloud base (from the ceilometer) and hourly LCL (calculated from surface measurements). Local time is used in this figure.

Several time series used in the analysis (temperature, water vapor mixing ratio, wind speed, cloud base, top and thickness, LCL and long-wave radiation) were band-pass filtered. The filter was designed to keep frequencies between 25 min and about 6 hours, corresponding to horizontal features of 10-100 km advecting past the ship at a typical wind speed of 7 m/s. This was done to isolate the mesoscale and to remove the effects of the diurnal cycle.

Computing the variances for the band-passed series in each category, we found that the drizzling boundary layer had the highest variance for each examined parameter. For example, the mean standard deviations of the coupled, decoupled, and drizzling boundary layers are 60, 111, and 151 m, respectively. The drizzling boundary layer is therefore the most horizontally inhomogeneous on the mesoscale. The coupled boundary layer is the most horizontally homogeneous, and the decoupled boundary layer falls in between.

Figure 3 shows a GOES-8 visible satellite image taken at 0545 local time on 19 October 2001. The circle in the center shows the ship location at 0600. The lines extending to the NW and SE indicate the approximate advection during the previous and following six hours. The two vertically-pointing millimeter-wavelength cloud radar (MMCR) time-height sections also correspond to the previous and following six hours, respectively. Between midnight and 0900 local time, the boundary layer cloud field appears quite patchy and variable in both the horizontal and vertical images. There is also a significant amount of drizzle during these hours. After 0900, the cloudiness smoothes out and drizzle ceases, although mesoscale features are still visible. We can clearly see the association between mesoscale variability and drizzle in this example, although we do not know if the drizzle enhanced the horizontal variability or vice versa.

The C-band radar data from this time period (not shown) also indicates a transition from high reflectivity drizzle cells in open-cell type patterns to a smoother field of low reflectivity. Note that "drizzle cell" refers to the drizzling portion of either the closed cell or open cell cloud formation. When using C-band radar data, we refer simply to the precipitating region because this radar does not detect clouds.

4. CONCLUSIONS

We have found a loosely diurnal pattern of coupled, decoupled and drizzling conditions in the Sc boundary layer in the SE Pacific, which is modulated by open and closed-cell MCC patterns. Drizzle often appears in distinct cellular structures, and it is associated with enhanced mesoscale variability. These drizzle cells during EPIC Sc tended to last about two hours, with sizable drizzling areas. Future modeling studies will be necessary to fully explore the cause-and-effect relationship between drizzle and enhanced variability, but the models will need to be constrained with analyses based on observations.

5. ACKNOWLEDGMENTS

The authors are grateful to Chris Fairall, Taneil Uttal, Paquita Zuidema, and Duane Hazen of NOAA ETL for providing meteorological and MMCR data, and to the crew of the RHB for their assistance in collecting the data. This project is funded through NSF Grant ATM-0082384 and a NDSEG fellowship.

6. REFERENCES

Agee, E. M., 1984: Observations from space and thermal convection: A historical perspective. *Bull. Amer. Meteor. Soc.*, **65**, 938-946.

Bretherton, C. S., T. Uttal, C. W. Fairall, S. E. Yuter, R. A. Weller, D. Baumgardner, K. Comstock, and R. Wood, 2004: The EPIC 2001 stratocumulus study. *Bull. Amer. Meteor. Soc.*, accepted.

Stevens, B., G. Vali, K. Comstock, R. Wood, M. C. vanZanten, P. H. Austin, C. S. Bretherton, and D. H. Lenschow, 2004: Pockets of open cells (POCs) and drizzle in marine stratocumulus. *Bull. Amer. Meteor. Soc.*, submitted.

VELOCITY FIELDS IN CUMULUS DERIVED FROM AIRBORNE DUAL-DOPPLER MEASUREMENTS

R. Damiani, Samuel Haimov and Gabor Vali

Department of Atmospheric Science, University of Wyoming, Laramie, WY, 82071, USA

1. INTRODUCTION

High resolution airborne dual-Doppler analysis of cloud kinematics for selected cases of developing cumuli over the southeastern Wyoming plains was performed. The data were collected during the *'High-Plains Cumulus Experiment'* (HiCu) in the summer of 2003.

The 95 GHz Wyoming Cloud Radar (WCR) on-board the University of Wyoming KingAir (UWKA) research aircraft (Vali et al., 1998) was used in dual-antenna (dual-beam) con?gurations. The two beam directions are at about 35° to each other. Aircraft motion provided for scanning the same sample volume from the two directions within 1 to 15 seconds. From the analyses of the independent radial velocity components, two-dimensional (2-D) horizontal or vertical plane velocity vector ?elds were retrieved across the clouds. Data spatial resolution is $\sim 30 \times 45$ m^2.

Section 2 describes the WCR antenna setup and the technique to retrieve 2-D kinematic ?elds. In Sections 3 and 4 we report results for cloud cases investigated with vertical and horizontal radar scans, followed by a summary in Section 5. Our observations shed light on the kinematic structure and internal circulation of growing clouds. They may constitute a basis for quantitative de?nitions and validation of model parameters. The results are consistent with experimental and numerical simulation evidence that cloud-scale vorticity plays a primary role in the dynamic evolution and entrainment processes of convective clouds and thermals. Vertical plane circulations are often associated with episodic ascending thermals and hydrometeor re-ingestion at their base. Horizontal kinematics exhibits magnitudes and gradients of the velocity comparable to those observed in the vertical.

2. DUAL-DOPPLER SETUP AND RETRIEVAL

Figure 1 shows a schematic of the radar antenna con?gurations available on the UWKA. Four antennas are mounted on the aircraft: two point down along a vertical plane and the other two point sideways. The ?rst pair allows for the retrieval of velocities in a vertical plane aligned with the aircraft track (Vertical Plane Dual-Doppler, *VPDD*, Fig. 1a); the second scans a horizontal plane (Horizontal Beam Dual-Doppler, *HBDD*, Fig. 1b). One of the horizontal beams can also be redirected upward and used in combination with the nadir-pointing one to provide single-Doppler vertical scans above and below ?ight level (*up/down pro?le mode*).

Corresponding author's address: Rick Damiani, Department of Atmospheric Science, University of Wyoming, Laramie, WY, 82071, USA; E-Mail: rickdami@uwyo.edu

In Figure 2 the basic concept of the airborne dual-Doppler is illustrated. The radial velocities from any antenna pair are ?rst corrected for the aircraft motion contribution, unfolded, and then combined to provide independent components of the scatterers' re?ectivity-weighted mean velocity in a given illuminated volume.

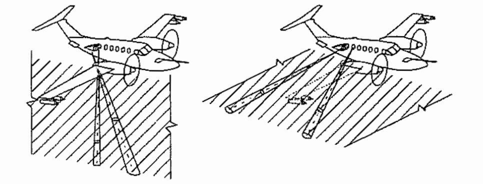

Figure 1. WCR antenna con?gurations on the UWKA. The effective plane of scan also depends on the aircraft actual attitude.

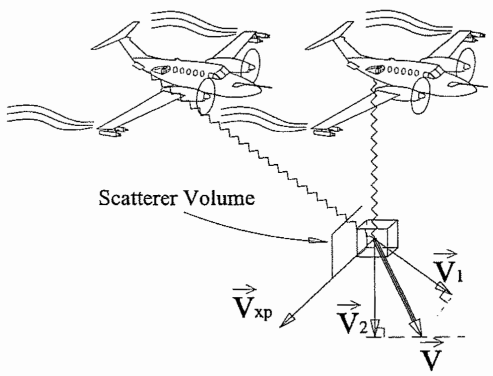

Figure 2. Dual-Doppler concept: a given scatterer volume is illuminated successively by two beams. $\vec{v}_1$ and $\vec{v}_2$ are the unfolded mean Doppler radial velocities corrected for aircraft motion; $\vec{v}_{xp}$ denotes the 'cross-plane' component, *i.e.* the non-measured component of the velocity normal to the plane of the beams.

In order to accomplish these tasks, merging of the radar dual-antenna data onto a common spatial gridded geometry is necessary. A full description of the grid construction is beyond the scope of this article. It will suf?ce to state that the grid, with the desired grid-cell dimensions, is built based on the aircraft trajectory relative to an advecting reference frame (mean wind). Data points coming from the two antennas are then assigned to the grid cells based on their spatial position and weighted according to selected criteria. A variety of weighting functions can be applied.

Mathematically the velocity retrieval for each grid cell is given by: $$[B]\,\vec{v} = \{c\}, \qquad (1)$$

where $\vec{v}$ is the unknown 3-D velocity vector; $[B]$ is the n(>2)-by-3 beam-pointing-unit-vector matrix; c are the n measured radial velocities from the two beams belonging to the generic cell.

System (1) yields the vector $\vec{v}$ in a ground-?xed reference frame. In order to gain insight in the cloud kinematics, the velocity ?elds presented in this paper are relative to an estimated horizontal mean-wind.

Since the sought velocity is a 3-D vector, but only two independent measured components are available, one may hope to resolve with suf?cient accuracy its projection on the plane of the beams. However, to achieve a good determination of this 2-D vector, an estimate of the *'cross-plane'* component (see Fig. 2) is necessary. For this purpose an assumed horizontal wind vector (usually based on *in situ* measurements in the vicinity of the observed clouds) is also employed.

To solve the overdetermined and rank-de?cient system (1), a weighted least-square method is adopted providing the minimum norm solution. The employed method also provides a basis for the null-space of (1), which can be used to add external wind data to the solution and improve the overall accuracy. Information about the null-space basis and other calculated statistical data allow to evaluate the quality of the airborne dual-Doppler. A software package to perform the described analysis is available.

This technique is feasible as long as the volume scanned by one of the beams is observed by the other after a time interval shorter than the characteristic evolution time-scale of the scatterer volume. This hypothesis is generally satis?ed at 90 m/s UWKA airspeed and at the typical WCR spatial resolution (30-40 m) and 3-4 km WCR range. The overall uncertainty associated with the evaluation of the 'cross-plane' component contribution, beam pointing angles and removal of the UWKA motion is estimated in the order of 1 m/s at WCR signal-to-noise ratio (SNR) larger than 0 dB.

3. VERTICAL PLANE DUAL-DOPPLER

Two VPDD passes at an isolated Cu performed on Aug. 26th, 2003 during HiCu are presented. The estimated cloud base pressure altitude is approximately 4400 m. Mean winds in the cloud depth layer (~2 km) were weak and slowly veering from south-westerly to westerly between the level of the base and top, with an approximate shear of 1 ms^{-1} km^{-1}.

Figures 3-4 show ?lled contours of radar re?ectivity factors (Z, mm^6m^{-3} in dBZ) and the calculated 2-D velocity vectors. No correction for attenuation or terminal velocity has been performed. During a previous pass the UWKA penetrated the very top of the cloud recording in-cloud thermodynamic and microphysical quantities. The PMS FSSP showed narrow spectra with mode at 15 μm and total number concentration in excess of 1000 cm^{-3}. The measured liquid water content was 1.8 g/m^3 and the OAP 2D-C recorded ice-crystals at ~0.2 L^{-1} (temperatures ranged around -20 °C).

In the central and lower portion of the cloud the radar is at its sensitivity limit likely due to the presence of small droplets and the attenuation by liquid water content. This region is collocated with the updraft main core. Higher values of re?ectivity, on the other hand, show evidence of ice formation and rapid growth near the summit and edges of the rising thermal. During the last phase of the cumulus evolution, the regions of strong re?ectivity progressively became larger, with values increasing from about -8 to 0 dBZ in ~10 min.

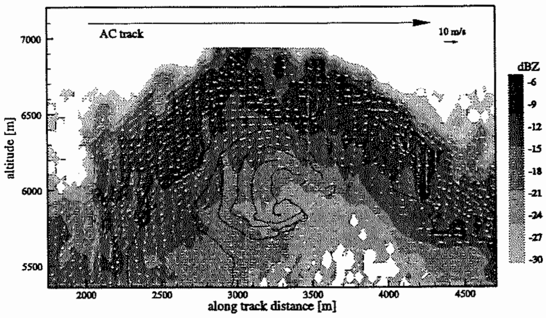

Figure 3. VPDD results for a growing Cu on 20030826 at 18:20 UTC. Vectors plotted every other grid point in the along-track direction. Flight level indicated by *'AC track'*. Solid lines represent selected streamlines.

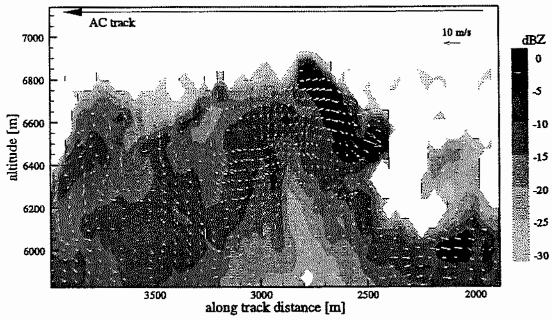

Figure 4. As in Figure 3 for a subsequent pass at 1823 UTC. The horizontal axis has been reversed to align observations between the various scans.

From the velocity ?elds 2-D (meridional) sections of a toroidal circulation are evident: upward motion in the center of the cloud, overturning and horizontal divergence at the top and descending ?ow carrying larger hydrometeors along the sides. The arching pattern in the re?ectivity structure can be partly due to the lateral displacement of previously formed hydrometeors caused by the divergence at the top of the thermal. Figure 3 is a representative image of a vortex ring dominating the kinematics of the cumulus. Due to the lack of sensitivity in the lower portion of the cloud, the clockwise section of the circulation is poorly rendered in this 2-D transect. Figure 5, showing the derived horizontal component of the vorticity, however, clearly exhibits two areas of well de?ned and opposite vorticity. The enhancement of the counterclockwise circulation may be the result of the ambient vertical shear. The vector rendering of the vortex ring in a reference system not moving in the vertical direction is justi?able by its modest overall rate of rise and by the hydrometeor fall-speed contribution to the Doppler velocity.

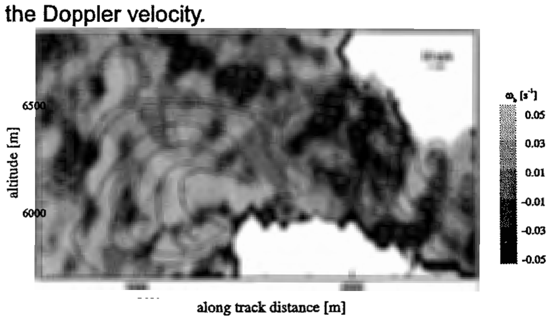

Figure 5. Horizontal vorticity contours near the main circulation zone of Figure 3 (low-SNR zone removed).

The vortex-tube radius is about 200 m (calculated as the distance from the vortex center to the circumferential belt of null vorticity); its characteristic rotational velocity and average vorticity magnitude are ~0.01 rad/s and 0.02 s^{-1} respectively. The associated revolution time would be approximately 10 min. This time scale is relevant if entrainment, mixing, and precipitation development are believed to be affected by the vortical dynamics of the thermal. In laboratory experiments, for example, ?rst mixed parcels were found in the center of thermals after about one vortex revolution (Johari, 1989). Furthermore, the higher re?ectivity patch, located in the lower sector of the counterclockwise circulation and departing from the precipitating region on the left in Fig. 3, shows how some hydrometeors are being captured and recycled into the base of the ascending bubble. This mechanism of hydrometeor re-ingestion, visible in other scans not reported here, may accelerate the generation of precipitation.

During the pass shown in Fig. 4, new stronger upward motion developed in the central part of the Cu topped by two counter-rotating circulations: the typical 2-D signature of a vortex ring. The dip in the re?ectivity at cloud top, on the left of the vortex ring, may be the result of dry environmental air intrusion induced by the vortical kinematics. In the convergence zone at the bottom of the vortex pair, the re?ectivity again shows a hint to hydrometeors being drawn towards the center of the updraft.

The described circulations have features analogous to those revealed in recent Large-Eddy-Simulations carried out by Zhao and Austin (2004). The authors described the rising vortex ring, within the ascending cloud-top (ACT), as being tilted in its ascent by the action of shear, with strong divergence at the top, convergence at the bottom, mixing and downdrafts enhanced on the downshear side of the cloud and weakened circulation on the upshear one.

Figures 3-4 also show instabilities at the cloud/environment interface. They appear as protrusions of cloudy material into the environment, often exhibiting an overturning character. The protrusion at 2100 m along the track and at 6500 m altitude in Fig. 3, for instance, exhibits a clockwise circulation. These structures are likely responsible of erosion of the cloud at the top via incorporation of dry air.

These observations are consistent with an entrainment mechanism beginning at the ACT summit, continuing along the sides of the circulation and mixing occurring in the ACT lower portion (Carpenter et al., 1998).

4. HORIZONTAL BEAM DUAL-DOPPLER

An example of HBDD scan of a young Cu investigated on July 13th, 2003 is offered in Fig. 6. Cloud base was estimated at 6200-6500 m and the wind shear across the cloud layer was roughly 4 ms^{-1} km^{-1}.

From the kinematic ?eld in Fig. 6 a clockwise circulation is visible with center at 2500 m along and at a distance of 700 m to the right of the UWKA track. Calculated vorticity values exceed 0.05 s^{-1}. The vortex diameter is ~800 m, determined by a sign reversal in the vorticity ?eld (not shown). In the upper-right portion of the plot, a counterclockwise circulation is also present. The two vortices induce an in?ow from the edge of the cloud (visible between the two circulations). A notch in the re?ectivity structure at the cloud boundary and lower Z values (-25 to -19dBZ) are associated with that kinematic feature.

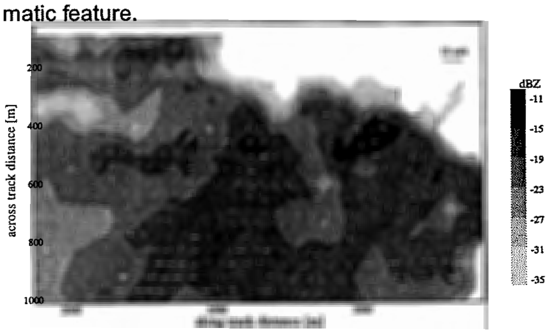

Figure 6. As in Figure 4 for an HBDD scan of an isolated Cu, conducted on 20030713 at 20:55 UTC. Flight altitude is ~7300 m, approximately at half the depth of the cloud.

Figure 7 presents *in situ* and WCR measurements during an aircraft penetration at the same cloud in up/down pro?le mode. Density temperature (Emanuel, 1994), DMT liquid water content (lwc) and air vertical velocity (w) are reported together with one-second gust vectors. The mean horizontal wind has been removed from the data.

The Doppler ?eld shows an updraft located in the central portion of the cloud, near its base, and tilted to the left in the upper levels. Vertical plane gust vectors reveal the overturning of the thermal: a counterclockwise meridional circulation is visible in the leftmost sector of the cloud with convergent ?ow towards the center. Stronger re?ectivity echoes are evident within the downward motion region, but some dry air may be captured by the circulation and intrude the cloud from the side and bottom, just below ?ight level. Notice how, associated with a patch of low-Z values (at ~3700 m along the track), the lwc drops to 0 g/m^3. The proposed vortical kinematics might then explain the overall mushroom shape of the cloud.

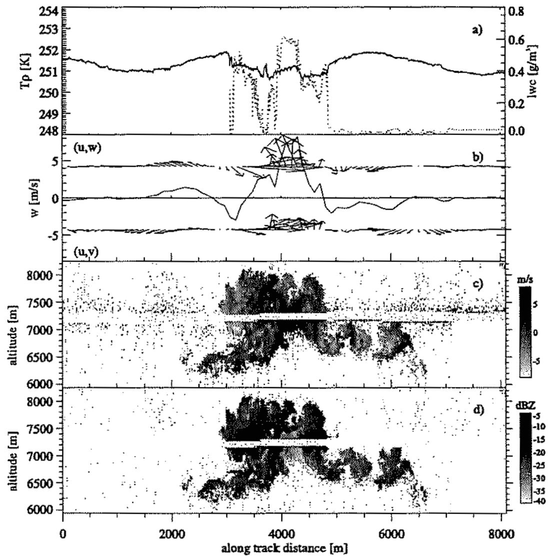

Figure 7. WCR and *in situ* data from an up/down pro?le pass, time 20:58 UTC; a) Density Temperature (T_ρ) and liquid water content (dotted line, lwc); b) air vertical velocity (w) and 1-s gust vectors (deviations from a mean horizontal wind); c) Doppler vertical velocity ; d) re?ectivity. Flight level is in the middle of the WCR blind zone.

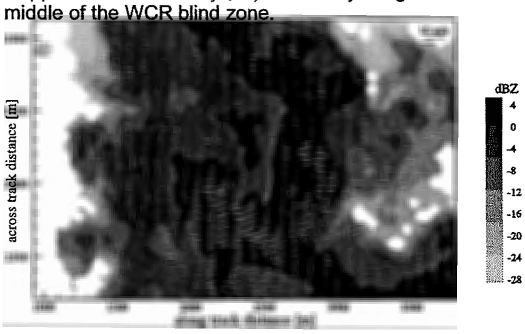

Figure 8. As in Fig. 6 for a subsequent pass, time 21:04 UTC.

Change in cloud-top height between subsequent passes (not shown) indicated a rate of rise of ~3.5 m/s, approximately half the measured updraft core vertical velocities. Meanwhile, the re?ectivity at the top decreased to values below -15 dBZ from -10 dBZ in about 2 min. This may imply either transport and fall of large hydrometeors towards and along the sides of the Cu or evaporation following entrainment at the top.

A later HBDD scan (Fig. 8) reveals the persistence of the major clockwise circulation and the development of stronger Z echoes with maxima grown by more than 15 dBZ in about 10 min. The horizontal plane kinematics is characterized by complex convergence/divergence patterns and the velocity gradients are comparable to those pertaining to the vertical plane.

5. CONCLUSIONS

This article reports observations of the kinematics of new updrafts rising into already formed cumuli, collected during the HiCu experiment in the summer of 2003. The WCR data have been used to retrieve 2-D velocity ?elds across the clouds. Support to some of the conceptual interpretations comes from *in situ* measurements and WCR pro?les from cloud penetrations.

Cloud-scale circulations are often identi?able with ascending thermals. Vertical plane vortical dynamics is responsible for recycling hydrometeors into the bubble core. This can affect the production rate of the precipitation. Vorticity visualizations provide a tool to investigate the length-scales of the main eddies and interpret their possible role on the cloud microphysics.

Downdrafts are located at the edges of the main updraft, carrying the bulk of the precipitating hydrometeors. Instabilities are visible in the re?ectivity ?elds at the cloud/environment interface; characterized by overturning motions they may lead to dry air engulfment.

The horizontal kinematics shows length scales and gradients of the velocity comparable to the vertical plane counterparts. Vertical motion in the horizontal plane may have consequences on the stability of the updrafts as well as on entrainment processes.

Extending these results to the initial growth phase, assuming that bubbles evolve in the same manner, entrainment is thought to occur both at the top and the sides of the rising ascending cloud top region, the internal vortical circulation playing a fundamental role. Entrained air, engulfed by instabilities at the upper boundary, may be carried downward along the side, but cannot penetrate directly in the ascending core hampered by the strong horizontal divergence at the top. The mixed parcel can then be transported into the center of the thermal through its bottom. In the process dry ambient air can be captured and directly brought towards the middle of the thermal by the strong convergent ?ow at the base of the vortex ring.

6. ACKNOWLEDGMENTS

This study was supported by NSF Grant ATM-0094956. We appreciate the contributions from the colleagues and the UWKA facility team involved in the HiCu experiment.

7. REFERENCES

Carpenter, R. L. Jr., K. K. Droegemeier, and A. M. Blyth, 1998: Entrainment and detrainment in numerically simulated cumulus congestus clouds. Part III: Parcel analysis. *J. Atmos. Sci.*, **55**, 3440–3455.

Emanuel, K. A., 1994: *Atmospheric Convection*. Oxford, 580 pp.

Johari, H., 1989: *An experimental investigation of mixing in buoyant ?ows*. Ph.D. thesis, University of Washington, available from University Micro?lms, 300 N. Zeeb Rd., Ann Arbor, MI 48106, 110 pages.

Vali, G. et al., 1998: Finescale structure and microphysics of coastal stratus. *J. Atmos. Sci.*, **55**, 3540–3564.

Zhao, M. and P. H. Austin, 2004: Life cycle of numerically simulated shallow cumulus clouds. Part II: Mixing dynamics. *J. Atmos. Sci.*, submitted.

FACTORS CONTROLLING THE FORMATION AND EVOLUTION OF CUMULONIMBUS ANVILS OVER SOUTHERN FLORIDA

Ann Fridlind[1], Andrew Ackerman[1], and Eric Jensen[1]

[1]NASA Ames Research Center, Moffett Field, CA, USA

1. INTRODUCTION

It is widely recognized that inadequate representation of cloud processes is the greatest source of uncertainty in the numerical prediction of climate sensitivity to changes in atmospheric radiative forcings, as due to the buildup of greenhouse gas concentrations (Intergovernmental Panel on Climate Change 2001). Among myriad cloud processes, tropical deep convection is expected to play a major role in global climate sensitivity (Hartmann et al. 1992; Del Genio and Kovari 2002), but exactly what that role will be remains an open question. Over the last 15 years, satellite data has been used to develop competing hypotheses that tropical deep convection over warmer oceans will lead to either greater numbers of thicker anvil clouds whose brightness will cool the surface (Ramanathan and Collins 1991) or fewer anvil clouds whose *absence* will allow the surface to cool more efficiently (Lindzen et al. 2001). More recent analysis of lengthening satellite records indicates that surprising shifts in tropical cloud coverage patterns are now occurring on decadal timescales, apparently in association with changes in the tropical Walker and Hadley circulations, and that these are not captured by current general circulation model (GCM) simulations (Chen et al. 2002; Wielicki et al. 2002).

GCM predictions of global temperature response to radiative forcings have demonstrated sensitivity to predicted changes in predicted tropical cloud coverage (Yao and Del Genio 1999), but tropical clouds are not well represented in current GCMs because many fundamental aspects of deep convection remain poorly understood and therefore cannot be properly simplified. At the storm macroscale, for instance, it is not well known how much lofted water is precipitated at low levels versus detrained at upper levels (Del Genio and Kovari 2002), where it forms anvil cirrus that may be exceedingly long-lived and also contributes to chemically and climatically important water vapor concentrations in the upper troposphere and lower stratosphere. At the storm microphysics scale, more fundamentally, it is also not well known how ice is generally initiated during deep convection (Beard 1992; Rosenfeld and Woodley 2000) or how aerosols may impact anvil ice crystal concentrations (Sherwood 2002).

To help develop the level of understanding required to study deep convection effects on chemistry and climate, the U.S. National Aeronautics and Space Administration (NASA) funded the Cirrus Regional Study of Tropical Anvils and Cirrus Layers-Florida Area Cirrus Experiment (CRYSTAL-FACE), which took place in southern Florida during July 2002. CRYSTAL-FACE has provided the most extensive available data set with which to study cumulonimbus anvil formation and evolution, including in situ and remote-sensing data from six aircraft, three ground stations, and multiple satellites. In previous work, we have found that the number and size distribution of anvil crystals is strongly dependent upon entrainment of midtropospheric aerosols into updraft cores (Fridlind et al. 2004). In this work, we broaden our previous study to focus on the response of anvil properties and evolution to five factors: (i) aerosol and ice nuclei profiles, (ii) updraft strength and frequency, (iii) relative humidity profiles, (iv) wind shear profiles, and (v) radiative fluxes. With a 3-dimensional large-eddy simulation with size-resolved distributions of aerosols, cloud droplets, and ice particles, we simulate anvil formation and evolution on seven days during the CRYSTAL-FACE experiment (July 3, 11, 16, 19, 21, 28, and 29), using extensive in situ observations to constrain model performance.

2. MODEL DESCRIPTION

The model we use, the Distributed High-resolution Aerosol-Radiation-Microphysics Application (DHARMA) (Ackerman et al. 2000), aims to resolve as completely as possible the coupling of cloud motions and aerosol-cloud microphysics within a domain that remains large enough to encompass a single small cumulonimbus system. DHARMA treats atmospheric and cloud dynamics with a large-

Corresponding author's address: Ann Fridlind, NASA Ames Research Center, Mail Stop 245-4, Moffett Field, CA 94035; E-mail: ann.fridlind@nasa.gov.

eddy simulation code (Stevens and Bretherton 1996) and treats microphysics and two-stream radiative transfer with the Community Aerosol-Radiation-Microphysics Application (CARMA), a model that has been developed over many years at NASA Ames (Jensen et al. 2001; Ackerman et al. 2003). The model transports size-resolved mass distributions of aerosols, liquid drops, and ice particles, and accounts for activation, condensational growth, evaporation, sedimentation, and melting (Pruppacher and Klett 1997); gravitational collection (Pruppacher and Klett 1997; Hall 1980; Jacobson et al. 1994); spontaneous and collision-induced drop breakup (Hall 1980; List et al. 1987); homogeneous and heterogeneous freezing of aerosols and drops (Pruppacher and Klett 1997; Meyers et al. 1992); and Hallett-Mossop rime splintering (Pruppacher and Klett 1997). Radiation is treated by dividing solar and infrared radiation into 26 and 18 respective wavelength bins and using Mie theory to calculate particle scattering and absorption coefficients and an exponential sum formulation to calculate gaseous absorption and emission.

To simulate CRYSTAL-FACE case studies, we initialize the model domain (96-km square footprint by 24-km height) with a meteorological profile derived from local rawinsonde measurements an aerosol profile derived from aircraft measurements on each day. Surface heat and moisture fluxes are assimilated from mesoscale weather forecasts of NASA Langley's Advanced Regional Prediction System (ARPS) mesoscale model (Xue et al. 2003), which was initialized at 12:00 UTC on each day. The simulations performed here used 500-m horizontal resolution and either 375-m or stretched-grid vertical resolution, with a simple Smagorinsky sub-grid scale turbulence closure scheme.

3. RESULTS AND CONCLUSIONS

Preliminary results indicate that bulk anvil properties are controlled by surface fluxes, wind shear, and lower-level moisture. Initial storm dynamics and early stages of anvil evolution are little affected by variations in aerosols and ice nuclei. Overall, ice nuclei decrease numbers of anvil ice crystals in these simulations, which may be in contrast to results obtained with some other models.

REFERENCES

Ackerman, A. S., O. B. Toon, D. E. Stevens, and J. A. Coakley, Jr. (2003). Enhancement of cloud cover and suppression of nocturnal drizzle in stratocumulus polluted by haze. *Geophys. Res. Lett. 30*, 10.1029/2002GL016634.

Ackerman, A. S., O. B. Toon, D. E. Stevens, A. J. Heymsfield, V. Ramanathan, and E. J. Welton (2000). Reduction of tropical cloudiness by soot. *Nature 288*, 1042–1047.

Beard, K. V. (1992). Ice initiation in warm-base convective clouds: An assessment of microphysical mechanisms. *Atmos. Res. 28*, 125–152.

Chen, J., B. E. Carlson, and A. D. Del Genio (2002). Evidence for the strengthening of the tropical general circulation in the 1990s. *Science 295*, 838–841.

Del Genio, A. D. and W. Kovari (2002). Climatic properties of tropical precipitating convection under varying environmental conditions. *J. Climate 15*, 2597–2615.

Fridlind, A. M., A. S. Ackerman, E. J. Jensen, A. J. Heymsfield, M. R. Poellot, D. E. Stevens, D. Wang, L. M. Miloshevich, D. Baumgardner, R. P. Lawson, J. C. Wilson, R. C. Flagan, J. H. Seinfeld, H. H. Jonsson, T. M. VanReken, V. Varutbangkul, and T. A. Rissman (2004). Evidence for the predominance of mid-tropospheric aerosols as subtropical anvil nuclei. *Science*. in press.

Hall, W. D. (1980). A detailed microphysical model within a two-dimensional model framework: Model description and preliminary results. *J. Atmos. Sci. 37*, 2486–2507.

Hartmann, D. L., M. E. Ockert-Bell, and M. L. Michelsen (1992). The effect of cloud type on Earth's energy balance: Global analysis. *J. Climate 5*, 1281–1304.

Intergovernmental Panel on Climate Change (2001). *Climate Change 2001: The Scientific Basis*. Cambridge University Press. (J. T. Houghton, Y. Ding, D. J. Griggs, M. Noguer, P. J. van der Linden, X. Dai, K. Maskell, and C. A. Johnson, Eds.).

Jacobson, M. Z., R. P. Turco, E. J. Jensen, and O. B. Toon (1994). Modeling coagulation among particles of different composition and size. *Atmos. Environ. 28A*, 1327–1338.

Jensen, E. J., L. Pfister, A. S. Ackerman, O. B. Toon, and A. Tabazadeh (2001). A conceptual model of the dehydration of air due to freeze-drying by optically thin, laminar cirrus rising slowly across the tropical tropopause. *J. Geophys. Res. 106*, 17,237–17,252.

Lindzen, R. S., M.-D. Chou, and A. Y. Hou (2001). Does the earth have an adaptive infrared iris? *Bull. Amer. Meteor. Soc. 82*, 417–432.

List, R., N. R. Donaldson, and R. E. Stewart (1987). Temporal evolution of drop spectra to collisional equilibrium in steady and pulsating rain. *J. Atmos. Sci. 44*, 362–372.

Meyers, H. P., P. J. DeMott, and W. R. Cotton (1992). New primary ice-nucleation parameterizations in an explicit cloud model. *J. Appl. Meteor. 31*, 708–721.

Pruppacher, H. R. and J. D. Klett (1997). *Microphysics of Clouds and Precipitation.* Kluwer Academic Publishers.

Ramanathan, V. and W. Collins (1991). Thermodynamic regulation of ocean warming by cirrus clouds deduced from observations of the 1987 El Niño. *Nature 351*, 27–32.

Rosenfeld, D. and W. L. Woodley (2000). Deep convective clouds with sustained supercooled liquid water down to -37.5°C. *Nature 405*, 440–442.

Sherwood, S. C. (2002). Aerosols and ice particle size in tropical cumulonimbus. *J. Climate 15*, 1051–1063.

Stevens, D. E. and C. S. Bretherton (1996). A forward-in-time advection scheme and adaptive multilevel flow solver for nearly incompressible atmospheric flow. *J. Comp. Phys. 129*, 284–295.

Wielicki, B. A., T. Wong, R. P. Allan, A. Slingo, J. T. Kiehl, B. J. Soden, C. T. Gordon, A. J. Miller, S.-K. Yang, D. A. Randall, F. Robertson, J. Susskind, and H. Jacobowitz (2002). Evidence for large decadal variability in the tropical mean radiative energy budget. *Science 295*, 841–844.

Xue, M., D.-H. Wang, J.-D. Gao, K. Brewster, and K. K. Droegemeier (2003). The Advanced Regional Prediction System (ARPS), storm-scale numerical weather prediction and data assimilation. *Meteor. Atmos. Phys. 82*, 139–170.

Yao, M.-S. and A. D. Del Genio (1999). Effects of cloud parameterization on the simulation of climate changes in the GISS GCM. *J. Climate 12*, 761–779.

CHARACTERISTICS OF PRECIPITATING CLOUDS OVER ASIA DURING SUMMER AS DERIVED FROM TRMM PR AND TMI

Yunfei Fu [1] Rui Li[1] Guosheng Liu [2] Jinli Liu[3] Daren Lu[3]
[1]School of Earth and Space Sciences, University of Science and Technology of China
Hefei, Anhui 230026, P.R. China
[2]Department of Meteorology, Florida State University, Tallahassee, FL 32306, USA
[3]Institute of Atmospheric Physics, Chinese Academic Sciences, Beijing 10029, P. R. China

1. INTRODUCTION

Clouds and precipitation play an important role in determining regional and global climate by redistributing water and heat in the atmosphere (Simpson et al. 1988; Tao et al. 1993). Studies showed that precipitation may be divided into two main types: convective and stratiform (Houze 1993). On one hand, the two rain types produce distinctively different latent heating profiles due to the different microphysical processes associated with precipitation formation. On the other hand, the type of rain is a reflection of atmospheric stability and large-scale dynamical conditions. By understanding the precipitation characteristics, we can get better insight to the interrelation among dynamical, thermo- dynamical and precipitation processes.

Understanding precipitating cloud characteristics is also important for developing satellite rain retrieval algorithms. Physical retrieval of rainfall rate from satellite microwave measurements requires the knowledge of the vertical distributions of hydrometeors because microwave brightness temperatures are very sensitive to these profiles (Kummerow and Giglio 1994; Smith et al. 1994; Evans et al. 1995).

In this paper, GPCP data, NCEP data, together with three-dimensional rainfall rate (2A25) and microwave brightness temperature data (1B11) derived from precipitation radar and microwave imager boarded on Tropical Rainfall Measuring Mission (TRMM) satellite are used to study precipitating cloud distributions and their structures in the region of Asia (0° - 40°N, 60° - 140°E) during summer months of 1998 through 2000.

2. RESULTS

The surface rainfall distribution during summer from June to August averaged from 1980 to 2000 is shown in Fig.1, which is gene [1] rated from the Global Precipitation Climatology Project (GPCP) archived by NASA. The 21 years' mean wind vector (Fig.1a) and mean water vapor flux (Fig.1b) in 850 hPa derived from NCEP data are overlapped upon the mean rainfall distribution. The Fig.1 expose an important rainfall climatological distribution in Asia during summer monsoon period, i.e. six heavy rainfall centers in Asia. They are located in the western coast of Indian

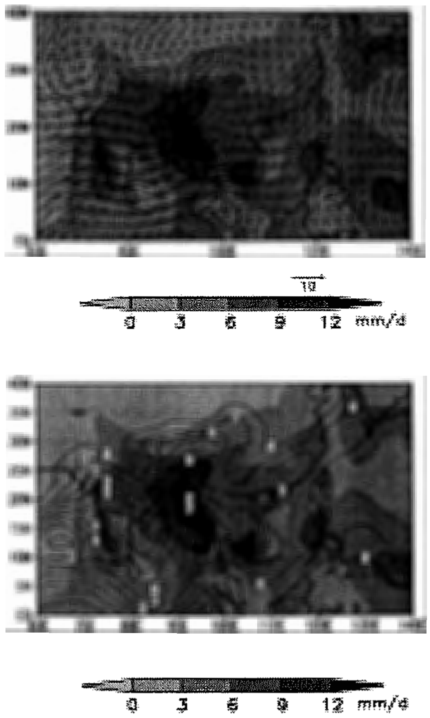

Fig.1 Distributions of 21 years' mean surface rainfall (shadowed), wind vector (upper panel Fig.1a) and water vapor flux (below panel Fig.1b) in 850 hPa.

Peninsula, the eastern coast of Bangladesh, the southern part of Indochina, Philippine and her east ocean, the southeastern coast of China, and the southern part of Japan, respectively, which is formed by the effect of topographic forcing on wet fluid from

---

[1] Corresponding author's address: Yunfei Fu, School of Earth and Space Sciences, USTC; Email: fyf@ustc.edu.cn

ocean. Against the heavy rainfall centers, there are two regions, the western Indian Ocean near Sri Lanka and the South China Sea near the eastern coast of Vietnam, with significant scattered rainfall due to dry fluid blows from land.

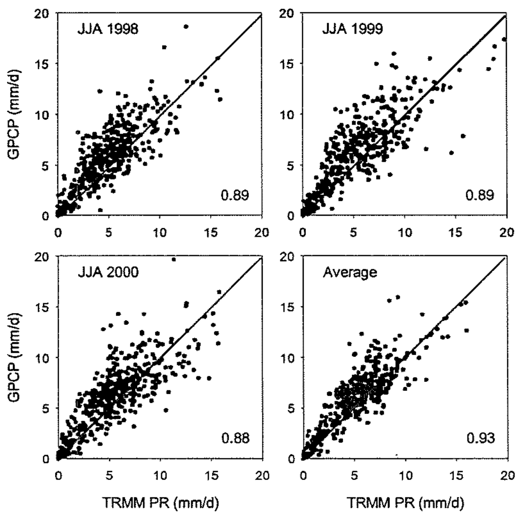

Fig.2 Scattering points of rainfall rate derived from GPCP and TRMM PR. Number in right below of each panel is correlation coefficient.

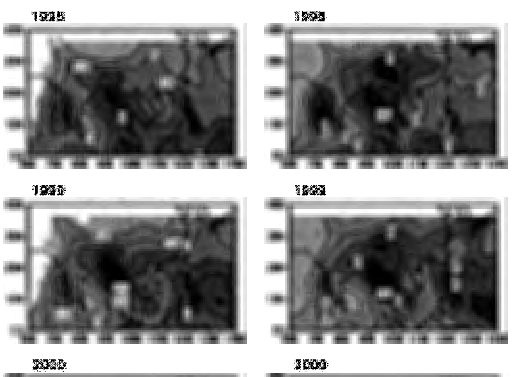

Fig.3 Area fractions of deep convective rains (left panel) and stratifrom rains (right panel)

In order to understand how difference of rainfall rates between GPCP output and TRMM PR measurements, we compared both rainfall rates and plotted the scattering point distributions in Fig.2. It shows a consistent tendency of both rainfall rates in summer although a little bit over estimate by GPCP. The correlation coefficient of both rainfall rates is grater than 0.85 in each summer, and three years' mean correlation coefficient is over 0.90.

The area fraction distributions of convective rains and srtatiform rains are shown in Fig.3, which indicates predominating stratiform rains in Asia as in tropics and East Asia (Liu and Fu, 2001; Fu et al. 2003; Fu and Liu, 2003). Usually, the amount of Stratiform rains is at least four times as large as that of deep convective rains. However, the latter contributes more rainfall to rain total due to its heavy rainfall rate in Asia.

To investigate precipitating cloud structures and microwave brightness temperatures in Asia, we selected ten regions, land (L1, L2, and L3), ocean (O1,O2,and O3), coast (C1, C2, and C3), and marine (M1), as shown in Fig.4 basis on the rainfall climatological distribution in Fig.1.

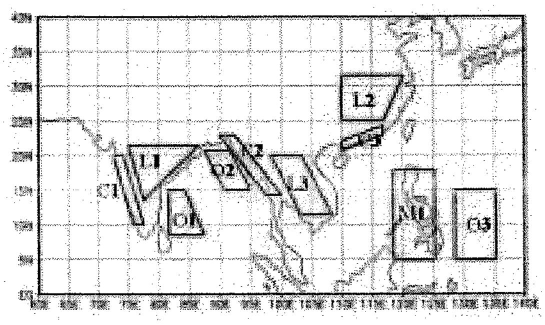

Fig.4 The selected investigating regions in Asia

The vertical structures of stratiform rains (Fig. 5a) and convective rains (Fig. 5b) as displayed in normalized profiles indicate that profile differences between Land and ocean, land and coast, ocean and coast, ocean and marine, apart from profile difference between convective and stratiform.

The normalized vertical precipitation profiles showed that the stratiform rains have a near constant rainfall rate below freezing level, about 5 km in altitude, (especially over land and marine regions) and a sharp drop-off above, regardless over land, coast, or ocean. Profiles of startiform rains display strong rainfall rate variations near the altitude of freezing level, which implies complicated physical process occurring in the layer. Stratiform profiles are also shown unique increase rainfall rate near surface over the coast regions (C1, C2, and C3).

Generally, convective precipitation profiles often have a maximum rainfall rate below the freezing level,

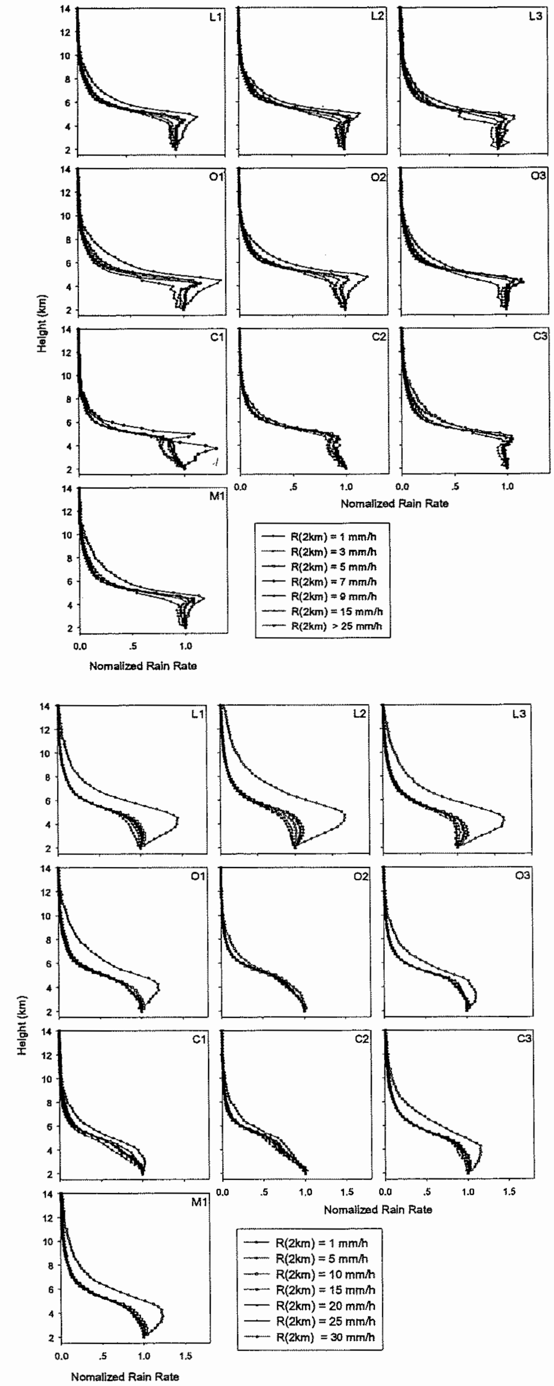

Fig.5 Normalized profiles over land (L1, L2, and L3), ocean (O1, O2, and O3), coast (C1, C2, and C3), and marine (M1) regions (upper panel for stratiform profiles, below panel for convective profiles)

implying a significant growth of raindrops by warm microphysical processes, such as coalescence. Above the freezing level, precipitation layer for convective rains is thicker than for stratiform rains. Comparing differences between regions, the vertical structures of convective rains are deeper over land and marine than over ocean and coast. The maximum rainfall rate of convective profiles over land is located at altitude of 3~4 km, while it is near surface for the other regions, which means only coalescence process existing over ocean, marine and coast regions. In the three land regions (L1, L2 and L3), convective precipitating clouds have almost a same deep in the region L2 and L3, and both are deeper than in the region L1.

For considering on the climatology of microwave brightness temperatures with rainfall pixels, we collocated rainfall pixels detected by TRMM PR with TMI pixels in each TMI channel resolution. Figure 6 shows the mean microwave brightness temperatures at 10.7 GHz, 19.4 GHz, 37 GHz and 85 GHz in both vertical and horizontal polarization for the two rain types averaged in the studied regions.

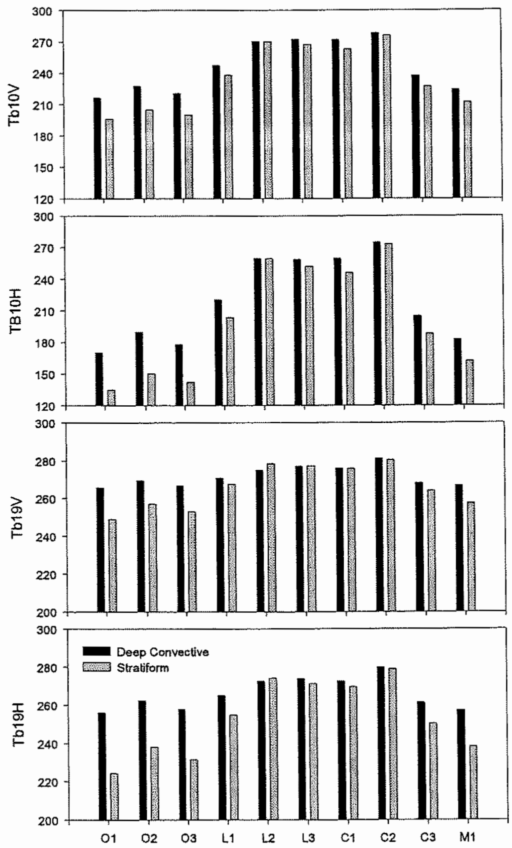

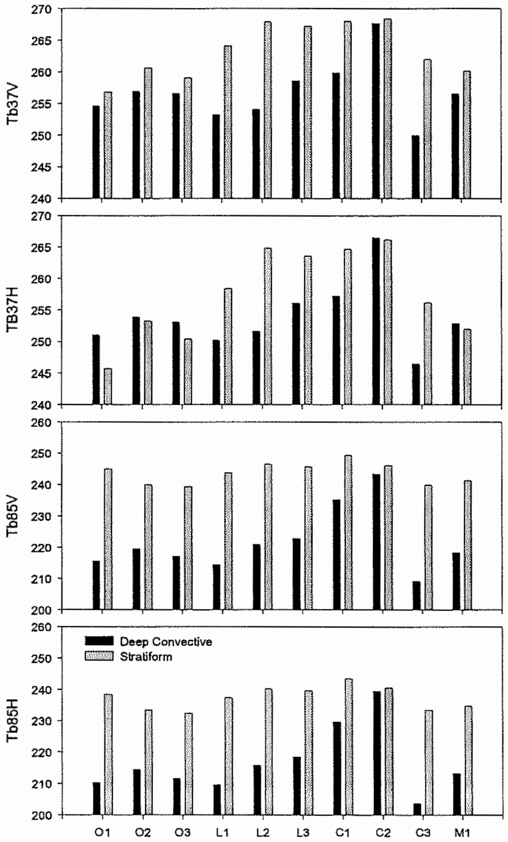

Fig. 6 Mean microwave brightness temperatures at 10.7 GHz, 19.4 GHz, 37 GHz and 85 GHz in both vertical and horizontal polarization averaged in the studied regions.

Figure 6 shows a much lower value at 85 GHz for convective rains than for stratiform rains in each region except in the coast region C2. That illustrates more ice contents inside convective precipitating clouds in these regions, while a small different ice content between convective and stratiform in C2 region. The largest difference value of 85 GHz between convective and stratiform in C3, L1, and O1 regions indicates the former rain type contain much more ice particles in the southeastern coast of China, Indian Land, and the western Indian Ocean near Sri Lanka. At low frequency channels, such as 10.7 GHz and 19.4 GHz, it is found that higher brightness temperatures for convective precipitating clouds than stratiform precipitating clouds, especially over ocean and marine regions, which says more liquid water contents inside convective precipitating clouds. Although high emission background over land at lower frequency, the mean microwave brightness temperatures from convective at 10.7 GHz is higher than these from stratiform over land and coast regions.

3. Acknowledgements

Satellite radar data were provided by NASDA/EORC and NASA Goddard Space Flight Center through TRMM project. This research has been supported by NASA TRMM grant NAG5-8647 to G. Liu, and NSFC grant (No.40175015, 40375018, and 40233031), CAS grant (No.KZCX2-208 and No.ZKCX-SW-210), NASDA (No.206) and USTC grant (No.CX0766) to Y. Fu.

4. REFERENCES

Evans, W.F.J. and E. Puckrin, 1995: The Extraction of the Thermal Emission Band of Methane from the Longwave Spectrum of the Atmosphere. J. Climate, 8, 3091–3095.

Fu, Y., Y. Lin, G. Liu, et al., 2003: Seasonal Characteristics of Precipitation in 1998 over East Asia as Derived from TRMM PR, Adv. Atmos. Sci., Vol. 20, 511-529.

Fu, Y. and G. Liu, 2003: Precipitation characteristics in mid-latitude East Asia as observed by TRMM PR and TMI, J. Meteor. Soc. Japan, 81, 1353-1369

Houze, R. A., Jr., 1993: Cloud Dynamics. Academic Press, Inc., New York, 573pp.

Kummerow, C., and L. Giglio, 1994: A passive microwave technique for estimating rainfall and vertical structure information from space. Part I: Algorithm description, J. Appl. Meteor., 33: 3-18.

Liu, G., and Y. Fu, 2001: The characteristics of tropical precipitation profiles as inferred from satellite radar measurements, J. meteor. Soc. Japan, 79: 131-143

Simpson, J., R. F. Adler, and G. R. North, 1988: A proposed Tropical Rainfall Measuring Mission (TRMM) satellite. Bull. Amer. Meteor. Soc., 69, 278-295.

Smith, E.A., X. Xiang, A. Mugnai, R.E. Hood, and R.W. Spencer, 1994: Behavior of an Inversion-Based precipitation Retrieval Algorithm with High-Resolution AMPR Measurements Including a Low-Frequency 10.7-GHz Channel. J. Atmos. Ocea. Tech., 11, 858–873.

Tao, W.-K., J. Simpson and R.F. Adler, 1993: Retrieval algorithms for estimating the vertical profiles of latent heat release: Their applications for TRMM. J. Meteor. Soc. Japan, 71, 685-700

CLOUD HOLES

H. Gerber [1], G. Frick [1], S.P. Malinowski [2], J.-L. Brenguier [3], and F. Burnet [3]

[1] Gerber Scientific Inc., Reston, VA, 20190, U.S.A.
[2] Warsaw University, Warsaw, Poland
[3] Meteo-France, Tolouse, France

1. INTRODUCTION

The Dynamics and Chemistry of Marine Stratocumulus-II (DYCOMS-II) study was held in July of 2001 when NCAR C-130 aircraft measurements were made during 9 flights in mostly unbroken and primarily nocturnal stratocumulus clouds (Sc) off the southern California coast. The measurements were unique in that three fast microphysics and thermodynamic probes were co-located on an aircraft for the first time: The UFT (ultra-fast thermometer; Haman et al., 2001) and the PVM-100A (Gerber et al., 1994) measured respectively incloud temperature and LWC with a maximum horizontal resolution of 10cm, and the FFSSP (Brenguier et al., 1998) measured the droplet spectra at 2-m resolution. The initial analysis of those measurements is given in Gerber et al. (2002), and a more thorough analysis is given in Gerber et al. (2004). This paper describes some of the analyses' results which are based on the conditional sampling of entrainment events in the Sc that are here called cloud holes.

2. CLOUD HOLES

The cloud holes in Sc are defined as sharp deviations near cloud top of LWC from approximately constant background LWC values. Figure 1 gives an

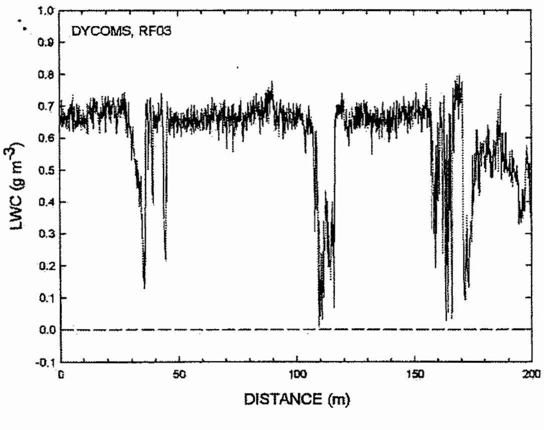

Fig. 1 - Cloud holes during level flight in Sc.

Corresponding author's address: H. Gerber, Gerber Scientific Inc., 1643 Bentana Way, Reston, VA, 20190, USA; E-Mail: hgerber6@comcast.net

example of 10-cm resolution LWC data near cloud top on flight RF03. The background LWC shows some Poissonian sampling noise, while the holes are sharply defined. We assume that the holes are a result of the evaporation of water due to the entrainment of dryer air from above the Sc. The holes are just as clearly evident in the rest of the flights, and form the "indicator variable" (Khalsa, 1993) for locating cloud parcels that have been affected by the entrainment process. The conditional sampling technique applied to the LWC data to identify holes is described in Gerber et al. (2004). Cloud holes have been described in part in the literature as "turbules" (Rogers and Telford, 1986); "downdraughts" (Nicholls, 1989); "wisps" (Krueger, 1993); and "entrainment events" (Khalsa, 1993; Wang and Albrecht, 1994).

3. HOLE PROPERTIES

The conditionally sampled holes are used to estimate composite hole statistics. Figure 2 gives the frequency distribution of hole lengths (distances of aircraft within the holes), and the number concentration of holes as a function of hole length. The hole widths

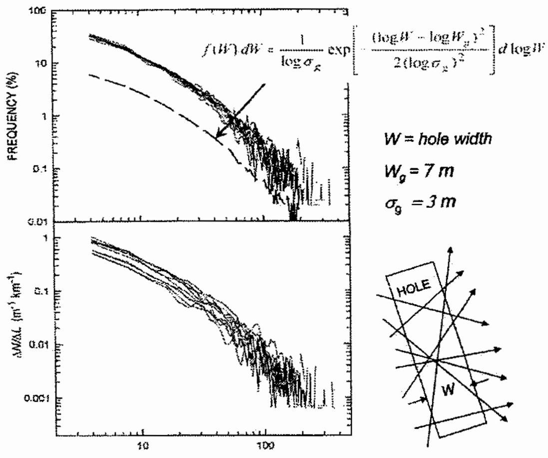

Fig. 2 - Frequency and number distribution of hole lengths 100-m below cloudtop. ΔL= 4m.

are the narrowest dimension of the holes that are known to be long, narrow, and sinuous; and widths can only be estimated from the length data. By assuming that the hole geometry is a rectangle, that the widths are distributed lognormally, and that the aircraft flies at random angles with respect to the rectangle, the Monte Carlo approach can be used with variable geometric mean and standard deviation of the widths to determine a length distribution that agrees best with the measured distribution (dashed line, top panel, shifted for clarity). The best fit of the geometric mean width is 7m, showing that the hole widths are surprisingly narrow. At cloud top the widths are even smaller. The top panel shows a composite for all 9 flights, and indicates that the relative frequency distribution is nearly constant. The bottom panel shows some variability for the flights; integration of the curves yields about 6 to 12 holes per km, which shows that numerous entrainment episodes occur on the upwelling Sc domes that span about 1km - 2km.

The vertical distribution of holes (not shown) shows a gradual decay of the holes as they are carried downward with the larger-scale cellular flow. They gradually mix with adjacent unaffected cloud, and some can penetrate hundreds of m deep into the Sc before they are dissipated.

The temperature and LWC in holes is compared to adjacent values in Fig. 3. The

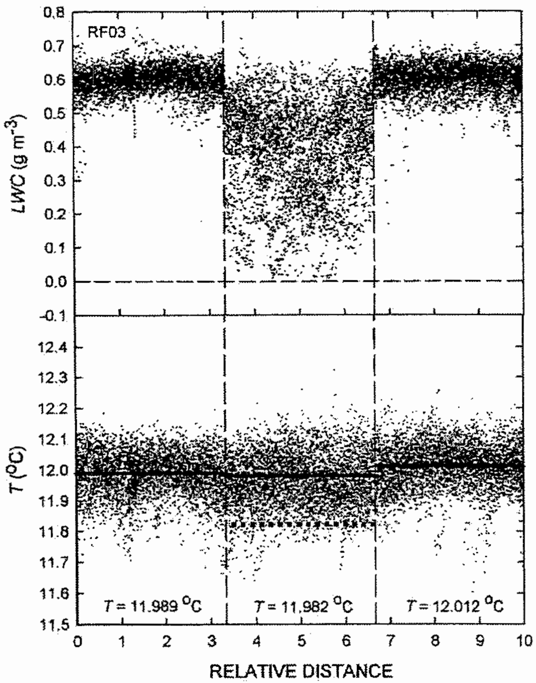

Fig. 3 - Composite of conditionally sampled hole LWC and T data (1000-hz) normalized to fit in the relative distance enclosed by the vertical lines.

difference in the mean temperature of 0.018C between the holes and adjacent cloud is significantly smaller than the maximum 0.16C cooling the holes should show (horizontal dashed line) if evaporative cooling plays a prominent role during entrainment.

4. ENTRAINMENT VELOCITY

A primary goal of DYCOMS-II was to measure the average entrainment velocity, w_e, (rate) into the top of the Sc. This measurement has proved to be difficult to make; DYCOMS-II promised improvements given new developments in conserved scalar measurements such as DMS. The "flux-jump" method applies measures of scaler fluxes, and is described in Faloona et al. (2003) and Stevens et al. (2003). We applied the conditional sampling approach to estimate w_e. The equation relating w_e to the LWC holes is given by (Nicholls, 1989) as

$$w_e = \frac{A_1}{A_1 + A_2}\frac{<w'\times q_T'>}{\Delta q_T} = \overset{\mathbf{1}}{A_r}\,\frac{<\overset{\mathbf{2}}{w'\times[(LWC'/\rho)} + \overset{\mathbf{3}}{q_v'}]>}{\underset{\mathbf{4}}{\Delta q_T}}$$

where A_r is the area ratio of holes at cloud top to the total cloud area, w' x LWC' and w' x q_v' are the fluxes of reduced LWC and vapor mixing ratio in the holes and Δq_T is the total water mixing ratio jump at cloud top. The bold numbers indicate the parameters that must be established to determine w_e. Figure 4 illustrates term **2** of the above equation. High correlation is seen between the downward velocity in the holes and the depleted LWC'.

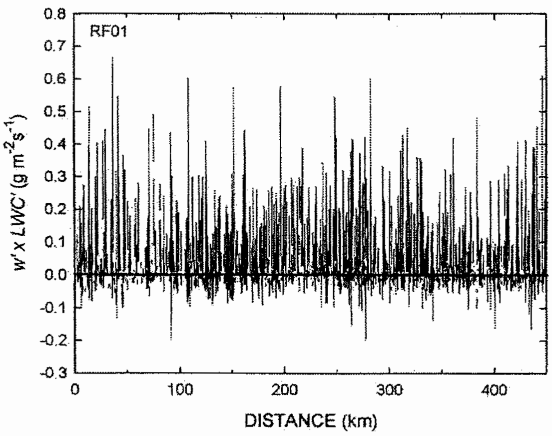

Fig. 4. - Depleted flux of LWC in holes during the 1-hr horizontal flight 100-m below cloud top on flight RF01.

The terms of the above equation are evaluated for all flights which had approximately 1-hr horizontal flight segments about 100-m below cloud top. Rapid changes are noted in the terms with height near cloud top so that scaling of w_e calculated for those segments needed to be done to get cloud-top w_e values. Each flight had about 8 profiles through the Sc from which scaling constants were determined for all the terms in the equation. The mean value of w_e determined in this manner is shown in Fig. 5 for all 9 flights.

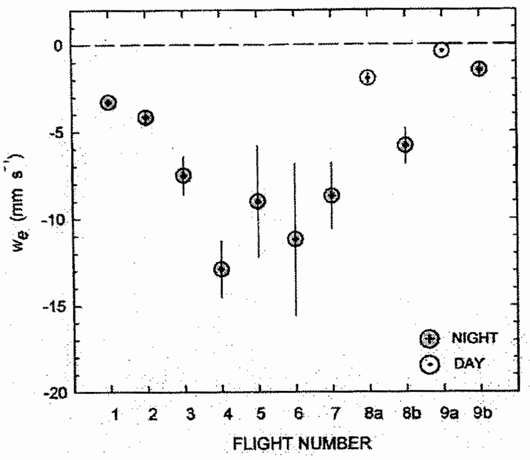

Fig. 5 - Mean entrainment velocity for each DYCOMS-II flight. Flights 8 and 9 have both afternoon and evening segments.

The values of w_e ranging over about an order of magnitude for the nocturnal flights are related closest to the temperature (and virtual potential temperature) jumps at cloud top. The evening portions of flights 8 and 9 give values of w_e about 3 times larger than the sunlit afternoon portions. This illustrates the diurnal effect where solar absorption apparently strongly affects Sc dynamics.

These conditionally sampled w_e values from the cloud hole data are about a factor of 1.9 times larger the "flux-jump" w_e values determined simultaneously on the C-130 by using measures of DMS, ozone, and total water fluxes (Faloona et al. 2003). The reason for the disagreement is not apparent, but suggests that the reliability of w_e measurements for Sc might still not be better than a factor of 2 or 3.

5. ENTRAINMENT PROCESSES

The high resolution data collected on the C-130 during DYCOMS-II permitted some new speculation on physical mechanisms related to the entrainment process in Sc. Figure 6 shows a conceptual sketch of what this data suggests. The entrainment interface layer (EIL; Caughey et al., 1982) sits just above cloud top and consists of cool, moist, and cloud-free air. Intuitively, the EIL must be formed by detrainment of cloud, with the sensible heat causing most of the cooling. The data shows that multiple mixing episodes occur between the cloud and EIL, causing a gradual reduction in the excess buoyancy of

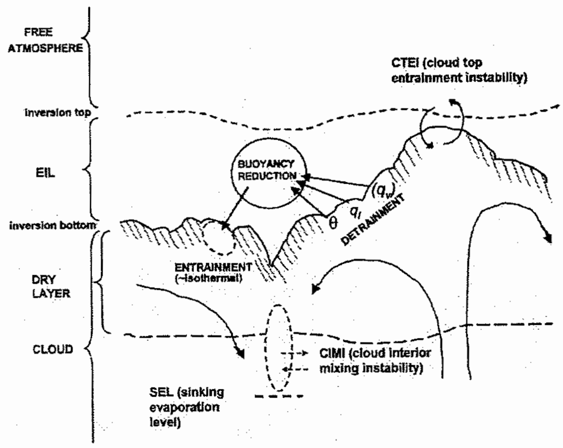

Fig. 6. - Conceptual sketch of mechanisms associated with the entrainment process.

the air in the EIL. Obviously, the other ingredient of the EIL is some air from the free atmosphere which energetic cloudy updrafts must engulf. The scales and mixing processes between the free atmosphere, EIL, and cloud are not well understood. However, the end result is that air entrained into the cloud comes in nearly isothermally as the UFT measurements show, and causes primarily inhomogeneous mixing as the FFSSP measurement show, where the cloud is diluted rather than causing droplet size changes.

Thus it appears that LWC near cloud top may only slightly cool the EIL, rather than causing buoyancy reversal by cooling due to LWC evaporation. This means that the cloud-top entrainment instability (CTEI) concept does not function for these Sc, which has also been observed previously for other Sc. For all the present flights the stability parameter of CTEI predicts thinning and breakup of the Sc. This does not happen. Instead, these nocturnal Sc thicken, even though entrainment velocities are enhanced.

The measurements suggest that the holes are transported towards the major convergence zones at the top of the Sc, where they are then carried downward into the Sc with the larger-scale eddy circulation. Given that the holes can have small values of LWC, their motion downward can only follow the moist adiabat while they retain some LWC. When they reach the level where all the LWC has evaporated (termed SEL, sinking evaporation level) they will attempt to follow the dry adiabat. This would cause significant temperature gradients between the holes and the adjacent unaffected cloud, and potentially cause more LWC evaporation and buoyancy reversal. This affect we have termed CIMI (cloud interior mixing instability). Whether CIMI is important for Sc is unknown. The rate at which holes mix with adjacent cloud is the crucial parameter, because if the rate is fast enough then SEL will not be reached and CIMI will not occur,

6. CONCLUSIONS

6.1- The general behavior of the Sc and entrainment holes in DYCOMS-II is similar to that described by Nicholls (1989). This includes the dominance of radiative cooling over evaporative cooling at cloud top.

6.2- The high resolution temperature (UFT) and LWC (PVM) measurements show hole widths much smaller than previously estimated. The geometric mean of the widths is about 5m near Sc top, and the entrainment flux at Sc top has a dominant width scale of about 10m.

6.3- Holes are strongly correlated with Sc downdrafts and can persist hundreds of m below cloud top until they are mixed with adjacent cloud. This raises the possibility that additional LWC evaporation occurs within the Sc due to this mixing, and causes buoyancy reversal as suggested by Krueger (1993).

6.4- Entrainment at cloud top is nearly isothermal, showing significantly smaller cooling than expected from the evaporation of droplets. It is hypothesized that this observation is a result of detraining cloud cooling the cloud-free EIL with multiple mixing events until a near buoyancy match is reached with the cloud, at which time entrainment commences.

6.5- The nocturnal Sc thicken on the average even though entrainment rates increase substantially at night. The enhanced top-down convection due to radiative cooling at night must increase the vertical flux of water vapor from the sea surface to more than compensate for the increased entrainment drying.

6.6- The physical mechanism by which air is entrained into Sc top remains unknown. Large changes in the entrainment rate over relatively small horizontal distances at constant height in unbroken Sc has no explanation. The effect of the vertical coherence of updrafts in Sc with shear, and the role of drizzle on the entrainment rate also require clarification.

6.7- The use of the high resolution LWC data for conditionally sampling cloud holes proved to be a practical approach for calculating the entrainment rate into the Sc. Accuracy of the calculations can be significantly improved with a future aircraft deployment strategy optimized for conditional sampling near cloud top.

7. ACKNOWLEDGMENT

One of us (H.G.) was supported by the National Science Foundation (ATM-0107738).

8. REFERENCES

Brenguier, J.-L., et al., 1998: Improvements of droplet size distribution measurements with the Fast-FSSP (Forward Scattering Spectrometer Probe). *J. Atmos. Sci.*, **55**, 1077-1090.

Caughey, S.B., B.A, Crease, and W.T. Roach, 1982: A field study of nocturnal stratocumulus II. Turbulence structure and entrainment. *Quart. J. Roy. Meteor. Soc.*, **108**, 125-144.

Faloona, I., et al., 2003: Observations of entrainment in Eastern Pacific marine stratocumulus using three conserved scalars. *J. Atmos. Sci.*, accepted.

Gerber, H., B.G. Arends, and A.S. Ackerman, 1994: A new microphysics sensor for aircraft use. *Atmos. Res.*, **31**, 235-252.

Gerber,H., S.P. Malinowski, J.-L. Brenguier, and F. Burnet, 2002:On the entrainment process in stratocumulus clouds. *Preprints, 11th Conf. On Cloud Physics*, Ogden, UT, AMS, CD-ROM, paper JP7.6.

Gerber, H., S.P. Malinowski, J.-L. Brenguier, and F. Burnet, 2004: Holes and entrainment in stratocumulus. *J. Atmos. Sci.*, accepted.

Haman, K.E., S.P. Malinowski, B. Strus, R. Busen, and A. Stefko, 2001: Two new types of ultra-fast aircraft thermometer. *J. Atmos. Oceanic. Technol.*, **18**, 117-134.

Khalsa, S.J.S., 1993: Direct sampling of entrainment events in a marine stratocumulus layer. *J. Atmos. Sci.*, **50**, 1734-1750.

Krueger, S., 1993: Linear eddy modeling of entrainment and mixing in stratus clouds. *J.Atmos. Sci.*, **50**, 3078-3090.

Nicholls, S., 1989: The structure of radiatively driven convection in stratocumulus. *Quart. J. Roy. Meteor. Soc.*, **115**, 487-511.

Rogers, D.P., and J.W. Telford, 1986: Metastable stratus tops. *Quart. J. Roy. Meteor. Soc.*, **112**, 481-500.

Stevens, B., et al., 2003: Dynamics and chemistry of marine stratocumulus - DYCOMS-II. *Bull. Amer. Meteor. Soc.*, **84**, 579-593.

Wang, Q., and B.A. Albrecht, 1994: Observations of cloud-top entrainment in stratocumulus clouds. *J. Atmos. Sci.*, **52**, 2778-2787.

CENTRIFUGAL PRECIPITATION TRANSPORT IN TORNADIC SUPERCELLS: AN ALGORITHM CONSISTENT FOR USE WITH BULK MICROPHYSICS SCHEMES

Matthew S. Gilmore[1*], Robert P. Davies-Jones[2], Jerry M. Straka[3], Erik N. Rasmussen[4], and Robert B. Wilhelmson[1]

[1] Dept. of Atmospheric Sciences, Univ. of Illinois, Urbana, IL
[2] NOAA/National Severe Storms Laboratory, Norman, OK
[3] School of Meteorology, Univ. of Oklahoma, Norman, OK
[4] Cooperative Institute for Mesoscale Meteorological Studies, Univ. of Oklahoma, Norman, OK

1. INTRODUCTION

Traditional three-dimensional nonhydrostatic cloud models do not include the outward centrifuging of precipitation where the flow curvature is large (e.g., Klemp and Wilhelmson 1978). These models assume that the precipitation moves precisely with the airflow except in the vertical where a downward precipitation flux is allowed. This approximation may be acceptable for coarsely resolved storms with broad regions of rotation and small flow curvature. However, now that scientists are simulating tornado-like vortices with horizontal gridspacings of 100 m or less (e.g., Wicker and Wilhelmson 1995), the effects of centrifuging precipitation can no longer be neglected. In strong vortices, centripetal accelerations may exceed gravitational accelerations by a factor of 10.

Mobile radar observations reveal that tornadoes typically have central weak-echo holes with a void of precipitation (e.g., Wurman et al. 1996; Dowell et al. 2004). However, our preliminary three-dimensional tornado simulations reveal that a model without centrifuging results in large amounts of precipitation directly in the center of the tornado.

Aside from the precipitation structure within the tornado appearing unrealistic, the lack of centrifuging has two potentially adverse side effects:

- reduced buoyancy in the tornado updraft, and,
- enhanced scavenging of cloudwater from the tornado funnel.

While the results of centrifuging have been demonstrated with idealized axisymmetric models (e.g., Dowell et al. 2004), the work herein is the first known attempt to include such an algorithm within a three-dimensional cloud model.

2 DERIVATION

Once its weight is balanced by the drag (air-resistance) force, a precipitation particle falls at a terminal (downward) velocity, which can be calculated from the force balance (e.g., Rogers and Yau 1989). In many bulk models with Marshall Palmer (1948; hereafter MP) precipitation distributions, the terminal fall velocity actually applied is weighted by the mass of each particle in the distribution (e.g., Lin et al. 1983, hereafter LFO). This mean terminal velocity is then applied to the precipitation so that it is transported relative to the vertical airflow.

A similar balance can be equated between the air drag and centrifugal forces acting upon precipitation-sized particles within very curved and high-speed flow (e.g., see Dowell et al. 2004).

In order to apply this principle to a bulk model, we integrate the effects of the centrifugal force (F_C) and the drag force (F_D) for each particle within the MP distribution. Consider a force balance only in the cross-streamline direction and only in the horizontal direction. Those forces are

$$\sum F_c = \int_0^\infty \left[\frac{\pi D_x^3}{6} \rho_x \frac{V_t^2}{R} \right] n_{ox} \exp(-D_{nx}^{-1} D_x) dD_x \,, \quad (1)$$

and

$$\sum F_D = \int_0^\infty \left[\frac{\pi D_x^2}{8} \rho_{air} C_D \Delta U_x^2 \right] n_{ox} \exp(-D_{nx}^{-1} D_x) dD_x \,. \quad (2)$$

In (1) and (2), x represents rain, snow or hail/graupel, D_x is the diameter of the particle, D_{nx} is the mean diameter of the distribution (inverse of the slope parameter – see LFO), ρ_x and ρ_{air} are the particle and air densities, respectively. Also, n_{ox} (m^{-4}) is the intercept parameter and C_D is the drag coefficient.

R is the radius of curvature of the airflow horizontal velocity, V_t (which is also the tangential particle velocity). U_x is the horizontal velocity component of the particles directed normal to the horizontal streamline of the air and in the opposite direction to the radius of curvature.

U_x is brought outside the integral by assuming that all particles in the bulk distribution travel at the same velocity following Wisner et al. (1972). (The same simplifying assumption is applied when deriving the

* Corresponding author's address: Dr. Matthew Gilmore, UIUC Dept. of Atmospheric Sciences, 105 S. Gregory St., Urbana, IL, 61801; E-Mail: gilmore@atmos.uiuc.edu

terminal fall velocity in bulk schemes.) Note that the nth moment is given by $\int_0^\infty D_x^a \exp(-D_{nx}^{-1} D_x) dD_x = \Gamma(a+1) D_{nx}^{a+1}$ and note that $\Gamma(4) = 6$. After integrating, we are left with

$$\pi n_{ox} \rho_x |\kappa| V_t^2 D_{nx}^4 = \frac{\pi}{4} C_D n_{ox} \rho_{air} U_x^2 D_{nx}^3, \qquad (3)$$

where κ is the local radius of curvature along the streamline. Although the actual airflow streamline does not fall precisely in a horizontal plane, we make this simplifying approximation for the purposes of presentation and reducing computational expense.

One may then solve for the mean outward particle velocity, U_x, giving

$$U_x = 2|V_t| \sqrt{\frac{|\kappa| \rho_x D_{nx}}{C_D \rho_{air}}}. \qquad (4)$$

The sign of U_x in (4) depends on whether U_x is along $+\hat{n}$ or $-\hat{n}$ to the streamline in right-handed (s, n, z) coordinates.

Consider the outward radial velocities owing to centrifuging for precipitation located at a core radius of 500 m from the center of a tornado with tangential wind of 50 m s^{-1}. Assume ρ_{air} = 1 kg m^{-3} for simplicity. Consider mean diameters of ~1 mm for rain, snow, and hail/graupel distributions. Such a D_{nx} is reasonable given numerous observational studies and similar values have been used (preset or diagnosed) in cloud models with LFO-like single-moment microphysics schemes (e.g., Gilmore et al. 2004a, 2004b, 2004c; van den Heever and Cotton 2004). Using drag coefficients of .45, 3.0, and 0.4, and particle densities of 1000, 100, and 400 kg m^{-3} for rain, snow, and hail/graupel, respectively (e.g., LFO and Rutledge and Hobbs), one finds $U_r = -6.7$, $U_s = -0.8$, and $U_h = -4.5$ m s^{-1} using Eq. 4 which seem reasonable. If instead the median size by mass ($3.672 D_X$) is used in place of D_x, the outward radial velocities nearly double: $U_r = -12.7$, $U_s = -1.5$, and $U_h = -8.5$ m s^{-1}. In either case, notable centrifuging of rain and hail/graupel precipitation would be expected to occur within this tornado even when using bulk microphysics.

2. APPLICATION

The most computationally expensive part of this calculation within the three-dimensional cloud model involves diagnosing the curvature along a streamline for grid cells containing precipitation. Weightless parcel trajectories are employed to diagnose the change in the tangent along a streamline (which defines its curvature). The trajectory calculations are also used to define the sign of the curvature and the unit normal direction.

For simplicity, we assume that the curvature of an instantaneous streamline approximates the curvature of a flow trajectory over 1 model timestep. This approximation is probably reasonable over small model timesteps on the order of 1 s, and a trajectory timestep of 10% the model timestep. This assumption also simplifies calculations if there is only a single time level of air velocities in memory. We have found that a simple Euler method is sufficient, however, accuracy can be improved at the expense of more steps for 3rd or 5th order Runge-Kutta methods.

Once the curvature and unit normal are diagnosed, it is straightforward to break (4) into Cartesian component centrifuging velocities for use within an advection scheme for lateral precipitation flux. It is performed each model timestep - similar to the vertical precipitation flux. An upper limit is also applied on calculated U_x values so that the model stability is not violated.

To reduce computational expense, one might only make curvature calculations where precipitation is present and windspeeds are high.

3. DEMONSTRATION

A demonstration of this scheme within a numerically simulated tornado and its parent thunderstorm will be presented at the conference.

4. REFERENCES

Dowell, D. C., C. R. Alexander, J.M. Wurman, and L. J. Wicker, 2004: Reflectivity patterns and wind measurement errors in high-resolution radar observations of tornadoes. *Submitted to Mon. Wea. Rev.*

Gilmore, M. S., J. M. Straka, and E. N. Rasmussen, 2004a: Precipitation and evolution sensitivity in simulated deep convective storms: Comparisons between liquid-only and simple ice & liquid phase microphysics. *In Press at Mon. Wea. Rev.*

——, ——, and ——, 2004b: Precipitation uncertainty due to variations in precipitation particle parameters within a simple microphysics scheme. Conditionally accepted by *Mon. Wea. Rev.* [Available on-line at http://www.atmos.uiuc.edu/~gilmore1/mwrmicro2/GSR2004b.pdf]

——, S. C. van den Heever, J. M. Straka, R. Wilhelmson, W. R. Cotton, and E. N. Rasmussen, 2004c: Constant slope or constant intercept? The impact on precipitation using single-moment microphysics. *14th International Conf. on Clouds and Precip.*, Bologna, Italy. This volume.

Klemp, J. B., and R. B. Wilhelmson, 1978: Simulations of right- and left-moving storms

produced through storm splitting. *J. Atmos. Sci.*, **35**, 1097-1110.
Lin, Y.-L., R. D. Farley, and H. D. Orville, 1983: Bulk parameterization of the snow field in a cloud model. *J. Climate Appl. Meteor.*, **22**, 1065–1092.
Marshall, J. S., and W. M. Palmer, 1948: The distribution of raindrops with size. *J. Meteor.*, **5**, 165–166.
Rogers, R. R., and M. K. Yau, 1989: *A Short Course in Cloud Physics. Third Edition.* Pergamon Press, New York, 293 pp.
van den Heever, S. C., and W. R. Cotton 2004: The impact of hail size on simulated supercell storms. *In press at J. Atmos. Sci.*
Wicker, L. J., and R. B. Wilhelmson 1995: Simulation and analysis of tornado development and decay within a three-dimensional supercell thunderstorm. *J. Atmos. Sci.,* **52**, 2675–2703.
Wisner, C., H. D. Orville, and C. Myers, 1972: A numerical model of a hail-bearing cloud. *J. Atmos. Sci.,* **29**, 1160–1181.
Wurman, J., J. Straka, and E. Rasmussen, 1996: Preliminary radar observations of the structure of tornadoes. *Preprints, 18th Conference on Severe Local Storms*, San Francisco, CA, 17-22.

SMALL SCALE MIXING PROCESSES AT THE TOP OF A MARINE STRATOCUMULUS - A CASE STUDY.

Krzysztof E. Haman[1], Szymon P. Malinowski[1], Joanna Remiszewska[1], Marcin Kurowski[1], Hermann Gerber[2], Jean-Louis Brenguier[3].

[1]Warsaw University, Institute of Geophysics, Warsaw, Poland
[2]Gerber Scientific Inc. Reston, VA, USA
[3]CNRM, Météo-France, Toulouse, France.

1. INTRODUCTION

One of the main aims of the DYCOMS II experiment, performed in July 2001 over Eastern Pacific (Stevens et al., 2003), was study of entrainment and mixing processes in marine stratocumulus. NCAR C-130 aircraft, richly equipped in various instruments measuring dynamic and thermodynamic parameters of clear and cloudy air was an unique platform for realizing such task.

Among instruments installed on the board of this plane were Ultrafast Aircraft Thermometer UFT-F (version with two sensors for measurements of temperature in warm clouds) delivered by Warsaw University (Haman et al., 2001), and Particle Volume Meter PVM-100A delivered by Gerber Scientific Inc (Gerber et al., 1994) and Fast FSSP (Brenguier et al., 1998). 5 mm long and 2.5 µm thick resistance sensor of UFT-F has time constant of order 10^{-4}s, while PVM-100A can measure liquid water content (LWC) with about 10 cm spatial resolution and 2 kHz sampling rate. FFSSP allows for measurements of droplet interarrival times. Simultaneous measurements with these instruments supplemented with data from more conventional slower units like Lyman-α hygrometer, Rosemount thermometer, 5 hole turbulence probe, pressure and GPS altimeters etc., were expected to give new information on entrainment and mixing processes in decimeter scales.

Initially, UFT, PVM and FFSSP had to be installed close together on one pod under the right wing of C-130 aircraft. Unfortunately, due to technical reasons (interference with some other instruments) UFT was finally shifted to the tip of the wing, what resulted in ca 6 m separation from PVM and FFSSP instruments and made comparison of their indications much less informative. Additionally, strong vibrations of the tip of the wing had negative effect of performance of UFT and even caused a serious mechanical damage to one of the two sensors. In result only few flights of nine DYCOMS II missions yielded fully valuable data. Fragment of one of them Research Flight 05, performed on 18 July 2001, 6:25-15:40 UTC (night and early morning local conditions) is analyzed in this paper.

Corresponding author address:
Krzysztof E. Haman, Warsaw University, Institute of Geophysics, ul. Pasteura 7, 02-093 Warsaw, Poland;
e-mail: khaman@fuw.edu.pl

2. GENERAL ATMOSPHERIC CONDITIONS AROUND THE STRATOCUMULUS TOP LAYER

The investigated fragment presents a flight along a circle of ca 60 km diameter, localized approximately at 30N, 120,5W (about 600 km WSW from San Diego), at 12:01- 12:29 UTC. The flight was conducted in a porpoising manner about the cloud top, consecutively climbing over the cloud and descending into it with vertical velocity about 2m/s with true airspeed in range 90-125 m/s.

The cloud was a typical marine stratocumulus with base presumably about 600m (not observed directly) and top varying between 900m and 1000m. The cloud was capped by a strong and extremely sharp inversion layer. Typical temperature at the cloud top was about 8.5°C, while in the dry air above the cloud temperature was about 15°C. Mixing ratio derived from Lyman-α was respectively 7.5g/kg in cloud and 2.5g/kg above. Typical LWC at the cloud top was about 0.6g/m^3, presumably close to its adiabatic value. There were no direct vertical soundings during the considered fragment of the flight, but soundings made earlier or later showed a well mixed layer below and inside the cloud with surface air temperature about 2°C below SST. Potential temperature in the subcloud layer fluctuated within about 0.4°C range, dew point within about 0.2°C, what could result in about 50m local variations in cloud base height. At least 500m thick layer above the inversion had a nearly isothermal stratification, but layer of low humidity was thinner, varying from few tens to about 200m, above which mixing ratio became close to the in cloud values. The cloudy air was fairly turbulent with irregular vertical updrafts and downdrafts (detected by the five hole probe) in range of few dm/s (occasionally up to +/-1.5m/s) and typical horizontal size 50-200m. Above the inversion the air was very calm with weak wavy motions (usually not exceeding +/- 20cm/s) and wavelength 200-1000m. Transition layer between cloud and dry air was usually very sharp (Fig.1 - more than 2°C jump over about 20 cm or even much less, accounting for possible inclination of the aircraft path to the cloud edge).

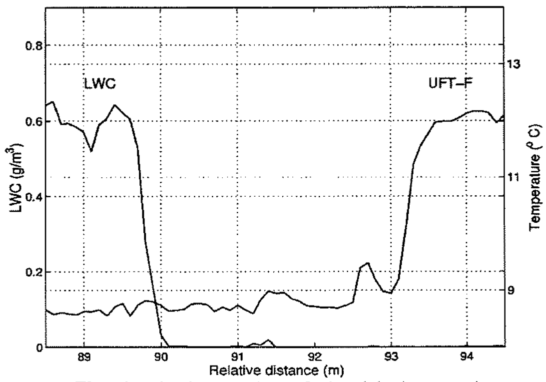

Fig. 1. A sharp edge of cloud in temperature and LWC records. Notice a shift between temperature and LWC resulting from 6m separation between the instruments.

3. PATTERNS OF MIXING IN TEMPERATURE AND LWC RECORDS

During the discussed flight UFT temperature and PVM LWC were recorded with 1kHz sampling rate, while Lyman-α mixing ratio, and other auxiliary data with 25 Hz. The main subject of the present study is temperature and LWC structure in transition layer between pure cloudy air and dry, warm air from above the inversion. Because of porpoising pattern of the flight and wavy shape of the inversion, thickness of this layer is difficult to determine but as it will be shown later, its vertical extent is presumably not more than several meters. Following typical patterns of temperature and LWC in this layer can be identified:

1. Intrusions of cloudy air into "pure" dry air (i.e. unmixed warm, dry air from above the inversion) environment; temperature and LWC typical to "pure" cloudy air (i.e. unmixed air from inside the cloud) (Fig. 2).

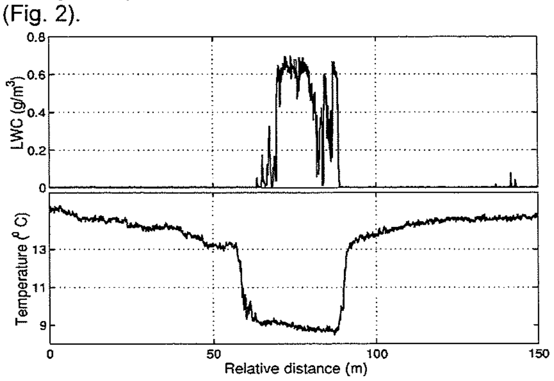

Fig. 2.

2. Intrusions of cloudy air into "pure" dry environment; LWC reduced below that of "pure" cloudy air, temperature intermediate between those of "pure" cloudy and "pure" dry air (Fig. 3).

3. Intrusions of cloudless air into "pure" dry environment; temperature intermediate between that of "pure" dry and "pure" cloudy air (Fig. 4).

4. Intrusions of cloudy air with reduced LWC into "pure" cloudy environment; temperature intermediate between that of "pure" cloudy and "pure" dry air (Fig. 5).

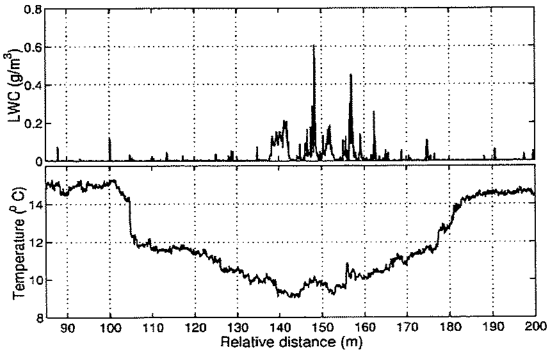

Fig. 3.

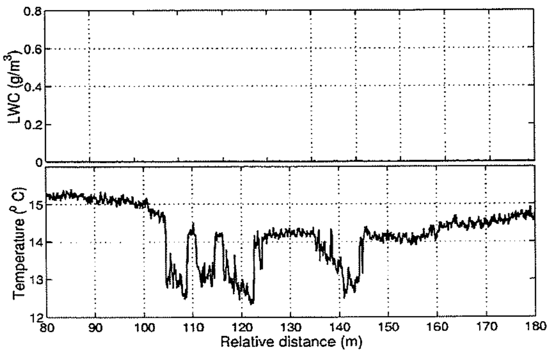

Fig. 4.

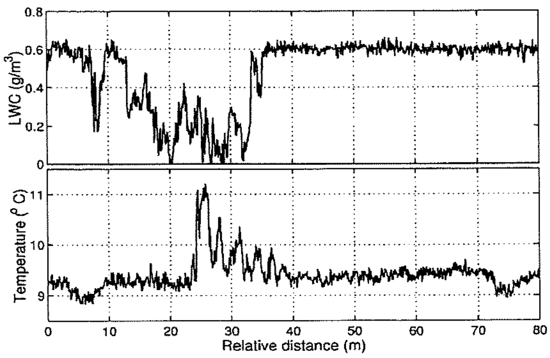

Fig. 5.

5. Intrusions of cloudy air with reduced LWC into "pure" cloudy environment; temperature close to that of "pure" cloudy air (Fig. 6).

6. Intrusions of cloudless air into "pure" cloudy environment; temperature close to that of "pure" cloudy air (Fig. 7).

7. Intrusions of cloudless air in "pure" cloudy environment, temperature intermediate between those of "pure" cloudy and "pure" dry air (Fig. 8).

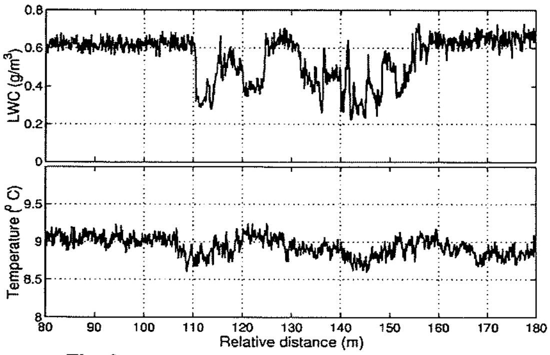

Fig. 6.

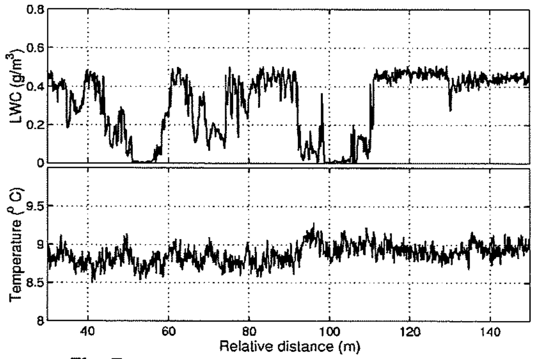

Fig. 7.

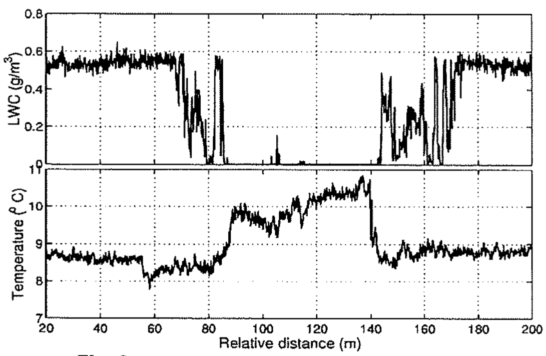

Fig. 8

Horizontal extent of intrusions listed above varies from decimeters to few hundreds meters. Sometimes intrusions of various types form bundles in which identifying the "environment" may be uneasy, otherwise certain intermediate forms of intrusions appear. Interpretation of size of intrusions must be made with caution; one should remember that observed are only random linear cross sections of cloud features. In case of narrow and long structures directed under small angle to the flight direction width of the structure can be strongly overestimated (see e.g. Gerber et al 2004).

A wavelet multiscale analysis of mixing patterns has been performed. Temperature and LWC signals has been decomposed in Haar wavelet basis, then selected wavelet components has been plotted separately in order to get idea about characteristic scales of mixing pattern (cloudy and clear air filaments. An example result of this study is plotted in Figs. 9 and 10 as a function of the vertical distance from the cloud top. It is interesting, that LWC in the uppermost part of the cloud is slightly (about 1g/kg) larger, than just few meters below. Similar behaviur of LWC has been observed in many other penetrations of the cloud top. Inspection of Figs 9 and 10 indicates significant LWC fluctuations in scales 1, 10 and 100m through the whole 100m deep penetration inside the cloud. In contrary largest temperature fluctuations are located close to the cloud top, with significant variability above the cloud.

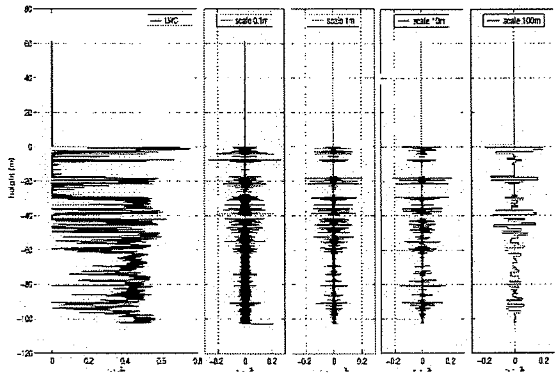

Fig. 9. *In the left panel: LWC recorded during slantwise penetration of the stratocumulus plotted as a function of height (0 corresponds to the cloud top). In the consecutive panels Haar wavelet components corresponding to wavelet lengths 10cm, 1m, 10m and 100m respectively are presented.*

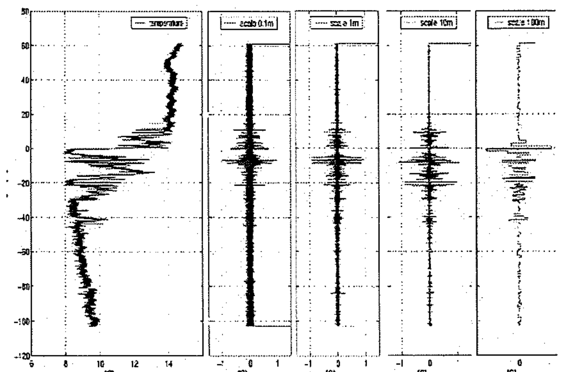

Fig. 10. *Temperature record from the same penetration as in Fig 9a presented in the similar manner.*

4. HYPOTHETICAL MECHANISMS RESPONSIBLE FOR VARIOUS PATTERNS OF MIXING

Though available data are insufficient for exhaustive and fully credible description and explanation of the process of mixing at the top of stratocumulus cloud, some speculation concerning the physical mechanisms responsible for formation of the observed patterns of temperature and LWC can be made. First let us notice, that with observed values of temperature jump (ca 6^{0}C), and velocities of vertical drafts (ca 1,5 and 0.2m/s respectively) between "pure" cloudy and "pure" dry air, inertial penetration of cloud into the dry air hardly can exceed 5m, while for dry air descending into the cloud it will be of order of centimeters. Thus initial stages of mixing presumably took place between intrusions of cloud into the warm, dry air.

An isobaric homogeneous mixing analysis corresponding to typical conditions of the discussed flight shows, that homogeneous mixture containing less than critical amount of ca 18% of dry air has temperature not exceeding that of "pure" cloudy air, with minimal depression of ca 0.3^{0}C at ca 14% of dry air. This corresponds to a weak CTEI (cloud top entrainment instability) effect. For smaller proportion of dry air the parcels contain liquid water and are slightly cooler than "pure" cloud.

The fact that homogeneously mixed parcels containing liquid water have to be cooler than the "pure" cloud suggests that patterns No 2 and 4 (intrusions containing liquid water but having temperature higher than that of "pure" dry air) present inhomogeneous mixtures of dry and cloudy filaments of scales smaller than resolution of UFT and PVM records. Parcels of such nature should presumably tend to hydrostatic equilibrium level at the temperature discontinuity surface, eventually undergoing homogenization and forming transition layer of the inversion. The same behavior should be observed with parcels corresponding to pattern No 3 , (representing presumably later stages of mixing between intrusions of cloud tops into the dry, warm layer) and No 7 (presumably parcels of mixed air engulfed by rising cloud or inertially penetrating cloud from above).

One can suspect that pattern No 1 presents a young inertial intrusion of cloud into the dry air, which can be treated as an initial stage of any other pattern. Patterns No 5 and 6 (reduced or no LWC, close to thermal equilibrium with cloudy environment) present presumably homogeneously (or nearly homogeneously) mixed parcels containing less than critical fraction of "pure" dry air and subsiding due to marginally negative buoyancy down to its hydrostatic equilibrium level inside the cloud. During subsequent mixing with surrounding cloud content of "pure", dry air must remain subcritical and the parcel may continue to subside in a quasisteady way close to hydrostatic equilibrium, with vertical velocity controlled by the speed of mixing and homogenization. Such parcels are presumably the source of "holes" observed as a rule through whole thickness of typical stratocumulus clouds (Nichols, 1989; Khalsa, 1993; Wang and Albrecht 1994, Gerber et.al 2004). Let us notice that such permanent subsidence is possible, provided that the stratification in cloud is at least wet adiabatic, what seems to occur often, particularly in nocturnal stratocumulus, which undergoes radiative cooling from the top. Such subsidence can be additionally enhanced by larger scale cellular convection or gravitational wavy oscillations of the inversion.

5. ACKNOWLEDGMENTS

Participation of Atmospheric Physics Division in DYCOMS II was supported by the National Science Foundation. Data processing was made with statute support from the Polish State Committee for Scientific Research.

6. REFERENCES:

Brenguier, J.-L., et al., 1998: Improvements of droplet size distribution measurements with the Fast-FSSP (Forward Scattering Spectrometer Probe). *J. Atmos. Sci.*, **55**, 1077-1090.

Gerber, H., B.G. Arends, and A.S. Ackerman, 1994: A new microphysics sensor for aircraft use. *Atmos. Res.*, **31**, 235-252.

Gerber, H., S.P. Malinowski, J.-L. Brenguier, and F. Burnet, 2004: Holes and entrainment in stratocumulus. *In this volume.*

Haman, K.E., S.P. Malinowski, B. Strus, R. Busen, and A. Stefko, 2001: Two new types of ultra-fast aircraft thermometer. *J. Atmos. Oceanic. Technol.,* **18**, 117-134.

Khalsa, S.J.S., 1993: Direct sampling of entrainment events in a marine stratocumulus layer. *J. Atmos. Sci.*, *50*, 1734-1750.

Nicholls, S., 1989: The structure of radiatively driven convection in stratocumulus. *Quart. J. Roy. Meteor. Soc.*, **115**, 487-511.

Stevens, B., et al., 2003: Dynamics and chemistry of marine stratocumulus - DYCOMS-II. *Bull. Amer. Meteor. Soc.*, **84**, 579-593.

Wang, Q., and B.A. Albrecht, 1994: Observations of cloudtop entrainment in stratocumulus clouds. *J. Atmos. Sci.*, **52**, 2778-2787.

IMPACTS OF UNIFORM FLOW ON THE DIFFUSION OF THE ICE NUCLEI IN STRATUS

Hui He[1] and Wankui Chen[2]

[1] Beijing Weather Modification Office, Beijing, 100089, China
[2]Chinese Academy Meteorology of Science, Beijing, 100081, China

1. INTRODUCTION

In this paper, the uniform flow was considered to ameliorate the probability equation of the catalyst particle that remains in the nucleation layer of the cloud .It is concluded that the remaining probability of particle in the cloud have been influenced by different uniform flow, and the effect of the thickness of the nucleation level on the remaining probability of the particle in the cloud, the relation between this effect and the uniform flow. simultaneously ,it is also discussed the influence of remaining time when seeding artificial ice nuclei in the different ascending-velocity and altitude by the change of the initial field of the ameliorated diffusivity equation ,and elicits the proper seeding altitude of the catalyst.

2. THE EFFECT OF THE UNIFORM FLOW ON THE REMAINING PROBABILITY OF THE PARTICLE IN NUCLEATION LAYER OF THE CLOUD

2.1 The equation to the effect of the uniform flow on the remaining probability of the particle in the nucleation layer

Ice crystal is the particle that moves in the medium. The origin of coordinates is the center of the nucleation layer in the upper level of the cloud. The particle located initially in the middle of the layer. Particle will be absorbed if it reached the upper or lower boundary of the layer which act as an absorption wall. Here $W^*(z,t)$ is defined as the probability of the particle that locate at the altitude of z from the origin.The equation of Einstein-Fokker is as followings:

$$\frac{\partial w^*}{\partial t} = D^* \frac{\partial^2 w^*}{\partial z^2} \qquad (1)$$

where $D^*=(1/2)N^*l^2$ is the coefficient of diffusion, N^* is motion number of the particle within unit time ,and l is the free path. Boundary condition is $z=\pm z_0$,$W^*(z,t)=0$(B.J.Mason 1960); When the uniform flow is considered ,the equation (1) should be

$$\frac{\partial w^*}{\partial t} = -w\frac{\partial w^*}{\partial z} + D^* \frac{\partial^2 w^*}{\partial z^2} \qquad (2)$$

Corresponding author's address: Hui He, Beijing Weather Modification Office, No.44, Zizhuyuan Road, Haidian District, China; E-Mail: hehui307@yahoo.com.cn.

The probability of the crystal remains in the nucleation layer is:

$$p(t) = \int_{-z_0}^{z_0} w^*(z,t)dz$$

so we can get:

$$\begin{aligned} p(t) &= \frac{1}{2}[erf(\frac{wt+z_0}{2\sqrt{D^*t}}) - erf(\frac{wt-z_0}{2\sqrt{D^*t}})] + \frac{1}{2} \\ &\times \sum_{n=1}^{\infty}(-1)^n \exp(\frac{nz_0w}{D^*})\{erf[\frac{(2n+1)z_0+wt}{2\sqrt{D^*t}}] \\ &- erf[\frac{(2n-1)z_0+wt}{2\sqrt{D^*t}}]\} + \frac{1}{2}\sum_{n=1}^{\infty}(-1)^n \exp(-\frac{nz_0w}{D^*}) \\ &\times \{erf[\frac{(2n+1)z_0-wt}{2\sqrt{D^*t}}] - erf[\frac{(2n-1)z_0-wt}{2\sqrt{D^*t}}]\} \end{aligned} \qquad (3)$$

2.2 The relation between uniform flow and the remaining probability of particle when z_0=500m.

With the parameter D^*=95m^2/s, z_0=500m and w varies among 0, 10, 20, 30, 40 , 50cm/s, the remaining probability could be calculated during different period of time by equation (3) . Figure 2.1 illuminates the result where the horizontal coordinate is time and the vertical coordinate is probability.

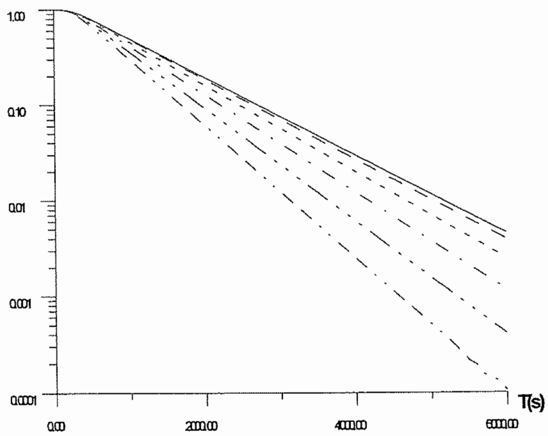

Fig.2.1 the temporal evolution of the remaining probability of the particle seeded in the middle of the nucleation layer.
(Lines from the top to bottom separately implies w=0, 10, 20, 30, 40, 50cm/s)

When the particle is seeded in the middle of the nucleation layer , from the figure above, we can come to some conclusions as the followings:

(1)The remaining probability of the particle in the cloud descends and it is also decreasing faster with the time increasing when the velocity of the uniform flow is larger ;

(2)The difference of the remaining probability in different uniform flow will be small when the period of time is short. Otherwise, the difference will be larger ;

2.3 The effect of the thickness of nucleation layer on the remaining probability of the particle and the relation between this effect and the uniform flow

The effect of different uniform flow on the remaining probability of the particle in the condition of different thickness nucleation layer is discussed below , it is discussed when z_0 varies among 250m, 500m, 750m, the equation to be calculated is (3). The result is plotted as the following figures:

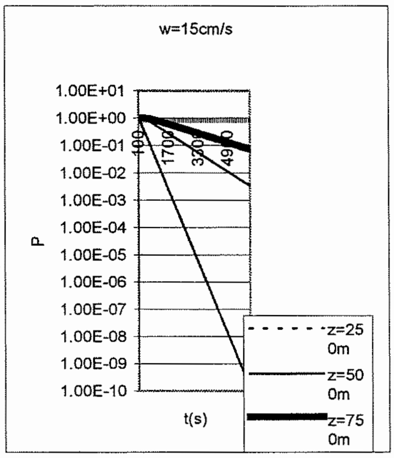

Fig.2.2 W=15cm/s, the variation of the remaining probability with the time in different thickness of layer

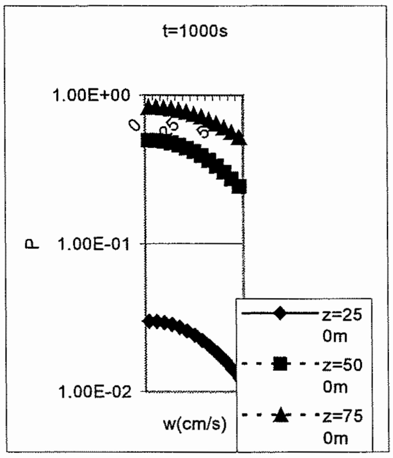

Fig.2.3 t=1000s, the variation of the remaining probability with the w in different thickness of layer.

It can be concluded from the figure 2.2 and 2.3 that the remaining probability of the particle in the nucleation layer will be smaller when the layer changes thinner. With the passing of the time,the remaining probability with thinner nucleation layer decrease faster .In addition, the rising of the uniform flow would decrease the remaining probability ,but this effect is smaller in thicker layer and it is larger in thinner layer.

3. THE SPECTRUM DISTRIBUTION OF ICE CRYSTAL

3.1 The formula to calculate parameter N_0 of the crystal spectrum

The spectrum distribution of the crystal size in cloud is:

$$n(r)dr = Nbre^{-\frac{1}{2}br^2}dr \qquad (4)$$

Where n(r)dr is the number of the crystal with the diameter between r and r+dr in unit volume of air. , b=λ ρ/D Δ ρ , ρ is the density of crystal and N is the number concentration of the crystal. In sheet cloud, the vapor source is the condensation G(g · cm^{-3} · s^{-1}) result from ascending motion w(cm · s^{-1}).Elliott(1958) has reported G = κ w and the κ =1.5×10^{-11}g · cm^{-4}, .In the upper level of cold cloud, G is the main supporter that maintains and raises the crystal spectrum and activated ice nucleus when the nucleation layer is stable, we can get the balance equation below :

$$G = \Delta M_0 \qquad (5)$$

and the increasing equation of crystal mass is :

$$\frac{dm(r)}{dt} = 4\pi r D\Delta\rho \qquad (6)$$

The spectrum distribution of crystal is $n(r) = N_0 bre^{-\frac{b}{2}r^2}$ The mass addition of the spectrum distribution of crystal within unit time is:

$$\Delta M_0 = \int_0^{r_R} n(r)\frac{dm}{dt}dr = 4\pi D\Delta\rho N_0[\sqrt{\frac{\pi}{2b}}erf\sqrt{\frac{b}{2}}r_R - r_R e^{-\frac{b}{2}r_R^2}] \qquad (7)$$

Based on the formula above ,we can get

$$\kappa w = 4\pi D\Delta\rho N_0[\sqrt{\frac{\pi}{2b}}erf\sqrt{\frac{b}{2}}r_R - r_R e^{-\frac{b}{2}r_R^2}]$$

that is:

$$N_0 = \frac{1.5\times10^{-11}w}{4\pi D\Delta\rho[\sqrt{\frac{\pi}{2b}}erf\sqrt{\frac{b}{2}}r_R - r_R e^{-\frac{b}{2}r_R^2}]} \qquad (8)$$

3.2 The effect of different supersaturation and uniform flow on the crystal spectrum distribution

When ρ_i=1g/cm^3 and D=0.2cm^2/s, The effect of the uniform flow on the crystal spectrum will be studied in case of the different supersaturation . The relation between the spectrum distribution and uniform flow velocity while the supersaturation is the same is shown in figure 3.1. And in figure 3.2, the relation between the spectrum distribution and the difference of supersaturation is illuminate while the uniform flow velocity is the same.

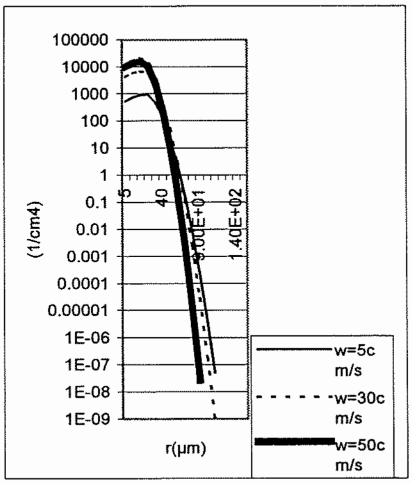

Fig.3.1 Δ ρ =1.0E-8g/cm^3, the spectrum distribution when the velocity of the uniform flow is different.

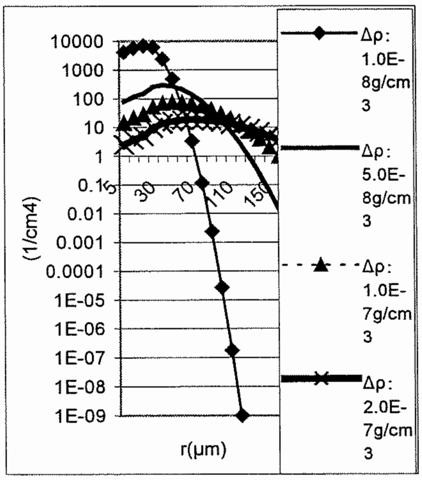

Fig.3.2 w = 30 cm/s, the spectrum distribution when Δ ρ is changing.

It can be found in these two figures that types of the spectrum are all unimodal distribution . With the enhancing of the supersaturation , the spectrum of crystal is widening while the density of the peak is lessening at the same time .Also we can see in Figure 3.1, if the supersaturation is the same, the peak density rises with the enhancing of the uniform flow.

4. THE REMAINING PROBABILITY OF PARTICLE IN NUCLEATION LAYER WHEN IT IS SEEDED AT DIFFERENT ALTITUDE.

The original location is in the middle of the nucleation layer in the model above we discussed . To study the remaining probability of particle in the cloud when the catalyst is seeded in different altitude, it is assumed that the seeding altitude is h ($-z_0<h<z_0$) and the thickness of nucleation layer is $2z_0$ ..The factor of uniform flow is considered and the origin of coordinate locates in the middle of nucleation layer.The initial condition of equation (2) is:

When $z\neq h$, $W^*(z,0)=0$

$$\int_{h-\Delta}^{h+\Delta} w^*(z,0)=1$$

$W^*(z,t)$ can be obtained from the equation above. Therefore, the remaining probability is:

$$p(t)=0.5\times\left[erf\left(\frac{z_0+h+wt}{2\sqrt{Dt}}\right)+erf\left(\frac{z_0-h-wt}{2\sqrt{Dt}}\right)\right]+0.5$$

$$\times\exp\left(\frac{2nz_0w+(-1)^n hw}{2D}\right)\times\left[\begin{matrix}erf\left(\frac{z_0-wt-2nz_0-(-1)^n h}{2\sqrt{Dt}}\right)-\\ erf\left(\frac{-z_0-wt-2nz_0-(-1)^n h}{2\sqrt{Dt}}\right)\end{matrix}\right]+0.5$$

$$\times\exp\left(\frac{-2nz_0w+(-1)^n hw}{2D}\right)\times\left[\begin{matrix}erf\left(\frac{z_0-wt+2nz_0-(-1)^n h}{2\sqrt{Dt}}\right)\\ -erf\left(\frac{-z_0-wt+2nz_0-(-1)^n h}{2\sqrt{Dt}}\right)\end{matrix}\right]$$

The origin of coordinate locates in the middle of nucleation layer and the z_0=500m . The altitude will be minus when seeding at the lower level of the layer. The seeding altitude in layer varies between -400 ,200m, and the uniform flow velocity changes among 0,20,40cm/s. The result of calculating is plotted in the figure as followings.

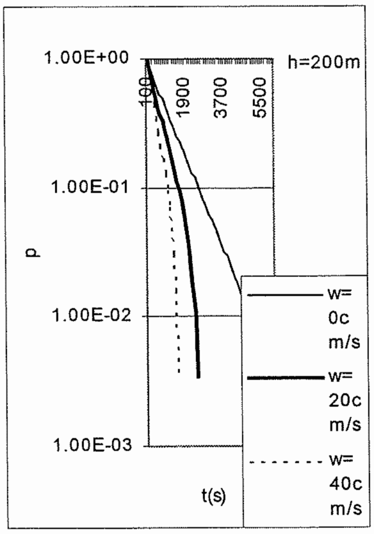

Fig.4.1 when the seeding altitude is 200m, the variation of the remaining probability of crystal with the time in different uniform flow velocity

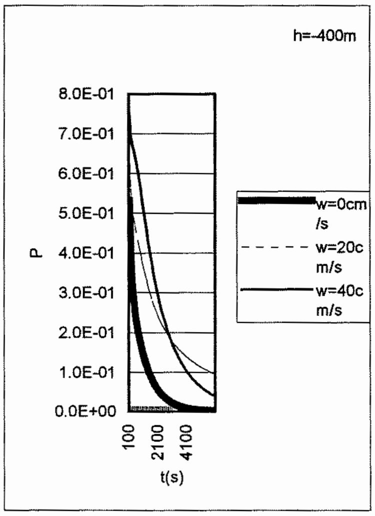

Fig.4.2 when the seeding altitude is -400m, the variation of the remaining probability of crystal with the time in different uniform flow.

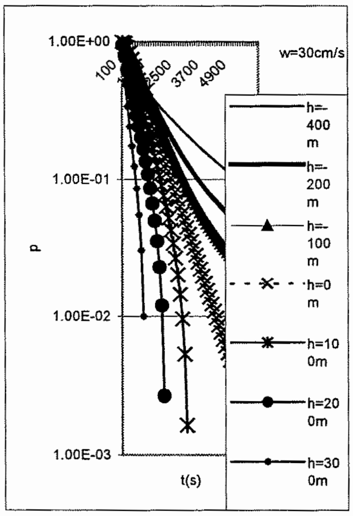

Fig.4.3 when the w= 30 cm/s, the variation of the remaining probability of crystal with the time in different seeding altitude.

Based on figures above, we can come to some conclusions as followings:

(1) Within certain range of the uniform flow velocity and period of time, the remaining probability of the particle in nucleation layer will be enhanced with the uniform flow velocity rising when seeded at the vicinity of the bottom of nucleation layer.

(2) The remaining probability of the particle in nucleation layer will be lessen with the uniform flow velocity rising when seeded at the middle or upper level of layer.

(3) when the uniform flow velocity is 30cm/s ,It can be found from figure 4.3 that the remaining probability of the particle decrease gradually in the seeding altitude -400, -300, -200, -100, 100, 200 and 300m. That is : the lower is the seeding altitude, the larger is the remaining probability of particle.

5. CONCLUSION

The main conclusion of this paper is as followings:

When the particle is seeded in the middle of the nucleation layer ,the remaining probability of particle in the cloud varies with the velocity of the uniform flow varying When the uniform flow grows larger, the remaining probability of the particle in the cloud deceases faster with the time increasing. However , the effect of rising of the uniform flow on the remaining probability of particle changes in different nucleation layer. This effect is smaller in nucleation layer with thicker thickness and it is larger in nucleation layer with thinner thickness.

With the enhancing of the supersaturation , the spectrum of crystal is widening while the density of the peak is lessening at the same time. Also we can observe, if the supersaturation is the same, the peak density rises with the enhancing of the velocity of the uniform flow.

Within certain range of the uniform flow velocity and period of time, the remaining probability of the particle in nucleation layer will be enhanced with the uniform flow velocity rising when seeded at the vicinity of the bottom of nucleation layer. The remaining probability of the particle in nucleation layer will be lessen with the uniform flow velocity rising when seeded at the middle or upper level of nucleation layer. The remaining probability of the particle in cloud decrease gradually with the rising of altitude when the uniform flow exists.

The result in this paper is remained to be examined by the planned field experiment.

REFERENCE

Mason.B.J, 1960: Cloud physics, The science press,138-140

STRUCTURES OF CLOUDS AND PRECIPITATION PRODUCING MECHANISMS

Peter V. Hobbs and Arthur L. Rangno

Department of Atmospheric Sciences, University of Washington, Seattle, WA, 98195, U.S.A.

1. INTRODUCTION

Over the past 25 years the Cloud and Aerosol Research Group at the University of Washington has obtained extensive and detailed in situ airborne measurements of the microstructures of a variety of clouds in several regions of the world, including continental and maritime clouds in mid-latitudes, clouds in the tropics and the Arctic, and in orographic cloud systems. These measurements have revealed some important common features of cloud structures, the mechanisms by which cloud particles grow to precipitable sizes, and insights into some recently suggested mechanisms for the rapid growth of precipitable particles.

2. ICE PARTICLE CONCENTRATIONS IN CLOUDS (*J. Atmos. Sci., 42,* 2523–2549 (1985))

Measurements on the development of ice in cumulus, cumulonimbus and stratiform clouds show ice particle concentrations significantly in excess of those to be expected from ice nucleus measurements. For clouds several kilometers in width, the maximum concentrations of ice particles (I_{max} per liter) are essentially independent of cloud top temperature (T_T) ($r = 0.32$). However, I_{max} is strongly dependent on the broadness of the cloud droplet size distribution near cloud top. If the breadth of the droplet size distribution is measured by D_T, such that the cumulative concentration of droplets with diameters $\geq D_T$ exceeds a prescribed value, then for $-32^{\circ}C \leq T_T \leq -6^{\circ}C$:

$$I_{max} = \left(\frac{D_T}{D_0}\right)^n$$

where $n = 8.4$ and $D_0 = 18.5$ µm for cumuliform clouds and $n = 6.6$ and $D_0 = 19.4$ µm for stratiform clouds.

When $D_T > D_0$ and $T_T \leq -6^{\circ}C$ ice first appears near the tops of clouds in the form of clusters about 5–25 m in width. These clusters form strands of ice which, with increasing distance from cloud top, widen and merge and may eventually appear as precipitation trails (virga) below cloud base.

We postulated that ice enhancement is initiated during the mixing of cloudy and ambient air near the tops of clouds and that it is associated with the partial evaporation and freezing of a small fraction (~0.1%) of the droplets $\gtrsim 20$ µm in diameter. Contact nucleation could be responsible for the freezing of these droplets. Under suitable conditions, this mechanism for ice enhancement may be augmented by other ice-enhancement mechanisms (e.g., ice splinter production during riming, and crystal fragmentation).

Corresponding author's address: Professor Peter V. Hobbs, Department of Atmospheric Sciences, University of Washington, Seattle, WA, 98195-1640, U.S.A.; E-Mail: phobbs@atmos.washington.edu.

3. CRITERIA FOR ONSET OF ICE MULTIPLICATION (*Atmos. Res., 22,* 1–13 (1988))

We have used our measurements from many locations around the world to deduce the cloud depths (and cloud top temperatures) required for the Onset of Significant Concentrations of Ice Particles (OSCIP) in cumulus clouds. The results show that for clouds with base temperatures $\geq 5^{\circ}C$ the OSCIP will generally occur if cloud top temperatures are between about -4° and $-10^{\circ}C$.

4. SMALL POLAR MARITIME CUMULUS CLOUDS (*J. Atmos. Sci., 47,* 271–2722 (1990); *Quart. J. Roy. Meteor. Soc., 117,* 207–241 (1991))

Increases in the concentrations of ice particles, as well as precipitation development, can proceed very rapidly in even quite small maritime cumuliform clouds. In the upper portions of these clouds, ice particle concentrations can increase from <1 per liter to >100 per liter in ~10 minutes, even when cloud tops are warmer than $-12^{\circ}C$. Just prior to the onset of high ice particle concentrations in the upper regions of these clouds, a few liquid and frozen drizzle drops appear; these are followed almost immediately by high concentrations of largely vapor-grown ice crystals. Subsequently, the ice particle concentrations gradually decline as the ice particles grow, aggregate and fall out. Crystal habits and sizes indicate that nearly all of the ice crystals encountered in the upper regions of these clouds form in situ, rather than being transported from below.

Prior to the formation of high ice particle concentrations, the clouds generally contain, near cloud top, droplets >30 µm diameter in concentrations >1 cm^{-3}, and often drizzle drops (100–400 µm diameter) in concentrations >1 per liter. For maritime and continental cumuliform clouds with widths $D \gtrsim 3$ km, the breadth of the droplet spectrum near the cloud top is a better predictor of the maximum ice particle concentrations that will develop in this region than is cloud top temperature.

Exceptions to the general picture described above are very narrow ($D < 3$ km), 'chimney-type', maritime cumuliform clouds with tops that quickly subside after reaching their maximum altitudes. For cloud-top temperatures between −7 and −13ºC these clouds produce fewer ice particles (~1–20 per liter), even though droplets with diameters >30 μm are present in concentrations >1 cm^{-3} and drizzle drops are often present in concentrations >1 per liter.

Ice particle concentrations produced by the ejection of ice splinters during riming appear to be about an order of magnitude less than the ice particle concentrations measured in the upper regions of broad maritime clouds. The freezing of evaporating drops by contact nucleation could be responsible for the frozen drops that precede the high concentrations of vapor-grown ice crystals. The latter could be produced in localized regions of unexpectedly high supersaturation that may be produced when drops begin to grow by collisions. This explanation is consistent with several findings concerning the conditions under which high concentrations of vapor-grown crystals appear almost spontaneously in maritime clouds. There are similarities between these natural crystals, and the conditions under which they appear, and those produced artificially by dry-ice seeding and by aircraft flying through supercooled clouds (Rangno and Hobbs, 1983).

5. SMALL CONTINENTAL CUMULUS CLOUDS (*Quart. J. Roy. Meteor. Soc., 120,* 573–601 (1994))

Maximum ice particle concentrations (I_M) in modest ≤3.7 km deep) continental cumuliform clouds, with tops with temperatures between −6 and −25ºC, are better correlated with the broadness of the droplet spectrum near cloud top (r = 0.78) than with cloud-top temperature (r = 0.58). The broader the droplet spectrum the warmer is the cloud top at which ice first appears.

Stratification into three cloud-base-temperature (T_B) categories, cool (0ºC ≤ T_B ≤ 8ºC), cold (−8ºC < T_B < 0ºC), and very cold (T_B ≤ −8ºC), results in correlations between I_M and cloud-top temperature (T_T) of 0.71, 0.88, and 0.89, respectively. The best-fit lines for these relationships shift to higher I_M values as T_B increases; this reflects the effect on I_M of the broadness of the droplet spectrum, since the size of the largest drops increases as T_B increases. When clouds contain drops with diameters ≳ 25 μm, ice particle formation is sudden and prolific. High concentrations of ice particles appear coincident with, or very soon after, the formation of graupel; these high concentrations occur at ambient temperatures between −11 and −28ºC, including some clouds with T_B < 0ºC.

For clouds with similar droplet spectra and T_T values, the width of the cloud also affects I_M; narrow clouds (<2 km wide) form less ice than wider, multi-turreted clouds.

Continental cumulus clouds have to be about 50% wider and about 5ºC colder at their tops than maritime cumulus to have the same chance of producing a radar echo. However, the difference in width to produce a radar echo disappears for clouds with widths >4 km, although continental clouds still need to be about 5ºC colder at cloud top than maritime clouds if they are to produce a radar echo.

6. STRUCTURES OF CLOUDS OVER THE BEAUFORT SEA (*Quart. J. Roy. Meteor. Soc., 124,* 2035–2071 (1998))

Airborne measurements in low and middle-level clouds over the Beaufort Sea show that these clouds often have low droplet concentrations (<100 cm^{-3}) and relatively large effective droplet radii. The highest average droplet concentrations are in altocumulus clouds that form in airflows from the south that pass either over the North American continent or from Asia. Droplet concentrations in low clouds tend to be higher in April than in June. The low clouds in June occasionally contain drops as large as 35 μm diameter; in these clouds the collision-coalescence process is active and produces regions of extensive drizzle. Cloud-top droplet concentrations are significantly correlated with aerosols beneath their bases, but appear to be relatively unaffected by aerosols above their tops. Anthropogenic sources around Deadhorse, Alaska, increase local cloud droplet concentrations.

Ice particle concentrations are generally low in April; they are high in June, when cloud-top temperatures are considerably higher. Tens per liter of columnar and needle ice crystals were measured in stratocumulus with top temperatures between −4 and −9ºC. Ice particle concentrations were poorly correlated with cloud top temperature (r = 0.39), but the concentrations of ice particles tended to increase with *increasing* temperature from −30 to −4.5ºC. Ice particle concentrations correlate better with the size of the largest droplets (r = 0.61).

The most common mixed-phased cloud structure over the Beaufort Sea are clouds topped by liquid water that precipitates ice. Liquid-water topped clouds were observed down to temperatures of −31ºC.

Temperature lapse rates in these clouds are generally complex, reflecting either layering, due to differential advection, or radiational effects. In these cases, vertical profiles of liquid-water content and effective cloud droplet radius do not vary systematically with height above cloud base, as they do in well-mixed clouds. However, when the temperature in a cloud decreases with height at or very near the pseudo-adiabatic lapse rate, the cloud liquid-water content (and various measures of the broadness of the cloud droplet size distribution) generally increase monotonically with height up to near cloud top.

For clouds consisting entirely of droplets, or droplets and ice crystals, cloud coverage increases by about 10% if the definition of a cloud is changed from 10 to 5 droplets per cubic centimeter. For clouds containing ice particles, cloud coverage and/or cloud depth increases by about 40% if the definition of a cloud is changed from 1 to 0.1 ice particle per liter.

7. ICE PARTICLES IN STRATIFORM CLOUDS IN THE ARCTIC AND POSSIBLE MECHANISMS FOR UNUSUALLY HIGH ICE PARTICLE CONCENTRATIONS (*J. Geophys. Res., 106,* 15,065–15,075 (2001))

High ice particle concentrations occur often in slightly to moderately supercooled clouds in the Arctic. Data collected in a common type of ice-producing arctic cloud (cumulus), and calculations based on laboratory experiments, were used to elucidate mechanisms that might be responsible for the ice. Ice splinters produced during riming could account for the relatively high concentrations of ice particles in clouds that encompass temperatures between –2.5ºC and –8ºC. However, it has generally been assumed that ice splinters grow into pristine ice crystal habits, whereas detailed measurements in an arctic stratocumulus cloud showed that only 32% of the ice particles are pristine crystals (needles, sheaths, short columns, and plates), while 10% are broken pieces of needles or sheaths. Thirty-seven percent of the ice particles are not identifiable crystal types, 20% are frozen drops, and 1% are aggregates and graupel. Large numbers of unidentifiable ice particles might originate from the fragmentation of delicate ice crystals and the shattering of some drops during freezing in free fall. These two mechanisms may also play a role in the production of relatively high ice particle concentrations in moderately supercooled arctic clouds that lie outside of the temperature zone where ice splinter production by riming is thought to occur.

8. STRUCTURES AND PRECIPITATION DEVELOPMENT IN CUMULIFORM CLOUDS OVER THE TROPICAL PACIFIC OCEAN (Rangno and Hobbs, *Quart. J. Roy. Meteor. Soc.,* submitted (2004))

In situ airborne measurements in convective clouds in the vicinity of the Marshall Islands have revealed the microphysical structures and precipitation producing mechanisms in these clouds. The liquid water contents of the clouds are generally well below adiabatic values, even in newly risen turrets. This is attributed to the entrainment of ambient air and to the very efficient removal of cloud water by the collision and coalescence of drops. The formation of raindrops begins when the concentration of droplets with radii >15 μm exceeds ~1 cm^{-3}, or equivalently when the effective cloud drop radius reaches ~13 μm. Clouds rain when their depths exceed ~1.5 km.

Extremely high concentrations of ice particles (often >500 per liter) form very rapidly at temperatures between –4 and –10ºC. High resolution imagery of these particles, which are primarily sheaths, needles and irregular ice fragments, indicate that the high concentrations of ice are initiated by the freezing of individual drops, followed or accompanied by ice splinter production during riming (e.g., Mossop, 1985).

Narrow (10–50 m wide) streamers of precipitation (see Hobbs and Rangno, 1985), containing large (>3 mm diameter) solid and liquid particles are common in growing tropical clouds.

Our observations of bursts of extraordinary large raindrops and large graupel particles, located in vertical filaments, support the mechanism of formation of very large precipitation particles suggested by Rauber et al. (1991) and Szumoski et al. (1997). These researchers surmised that a few drops that descend within narrow channels containing above average liquid water content grow exceptionally fast. The low concentrations of such drops would make drop breakup by collisions with other millimeter-sized raindrops unlikely.

Recently, there have been several studies of clustering of precipitation particles and its effects on precipitation processes and the interpretation of radar data (Shaw et al., 1998; Jameson and Kostinski, 1999; Kostinski and Jameson, 1997, 2000). Pinsky and Khain (1997, 2001) attributed the clustering of drizzle-sized drops to an inherent property of cumulus dynamics that organize drops into clusters, a phenomenon they call "self concentration." Their model results appear to be consistent with the observations of Hobbs and Rangno (1985) and Rangno and Hobbs (2004) of localized concentrations of drizzle drops and ice particles in filaments a few meters to tens of meters wide.

Convective clouds consisting entirely of liquid water produced rain rates that are similar to those of deep convective clouds containing ice. This finding, which is similar to that of Saunders (1965) in the Bahamas, attests to the efficiency of growth by collection, whether it be water or ice particles.

Since the concentration of raindrops within a few kilometers of cloud base are highly correlated with cloud depth, and therefore cloud top temperature, the concentration of raindrops in the clouds studied by us in the tropical Pacific could be inferred from satellite measurements of cloud top temperatures.

9. ACKNOWLEDGEMENTS

The research summarized here was supported by a series of grants from the U.S. National Science Foundation and NASA.

10. REFERENCES

Hobbs, P. V., and A. L. Rangno, 1985: Ice particle concentrations in clouds. *J. Atmos. Sci.,* **42**, 2523–2549.

Hobbs, P. V., and A. L. Rangno, 1990: Rapid development of high ice particle concentrations in small polar maritime cumuliform clouds. *J. Atmos. Sci.,* **47**, 2710–2722.

Hobbs, P. V., and A. L. Rangno, 1998: Microstructures of low and middle-level clouds over the Beaufort Sea. *Quart. J. Roy. Meteor. Soc.,* **124**, 2035–2071.

Jameson, A. R., and A. B. Kostinski, 1999: Fluctuation properties of precipitation. Part V: Distribution of rain rates–theory and observations in clustered rain. *J. Atmos. Sci.,* **56**, 3920–3932.

Kostinski, A. B., and A. R. Jameson, 1997: Fluctuation properties of precipitation. Part I: On deviations of single drop counts from the Poisson distribution. *J. Atmos. Sci.,* **54**, 2174–2186.

Mossop, S. C., 1985: Secondary ice particle production during rimer growth: the effect of drop size distribution and rimer velocity. *Quart. J. Roy. Meteor. Soc.,* **111**, 1113–1124.

Pinsky, M., and A. P. Khain, 1997: Formation of inhomogeneity in drop concentration induced by drop inertia and their contribution to the drop spectrum broadening. *Quart. J. Roy. Meteor. Soc.,* **123**, 165–186.

Pinsky, M., and A. P. Khain, 2001: Fine structure of cloud droplet concentrations as seen from the fast-FSSP measurements. Part I: Method of analysis and preliminary results. *J. Appl. Meteorol.,* **40**, 1515–1537.

Rangno, A. L., and P. V. Hobbs, 1983: Production of ice particles in clouds due to aircraft penetrations. *J. Climate Appl. Meteor.,* **22**, 214–232.

Rangno, A. L., and P. V. Hobbs, 1988: Criteria for the onset of significant concentrations of ice particles in cumulus clouds. *Atmos. Res.,* **22**, 1–13.

Rangno, A. L., and P. V. Hobbs, 1991: Ice particle concentrations and precipitation development in small polar maritime cumuliform clouds. *Quart. J. Roy. Meteor. Soc.,* **117**, 207–241.

Rangno, A. L., and P. V. Hobbs, 1994: Ice particle concentrations and precipitation development in small continental cumuliform clouds. *Quart. J. Roy. Meteor. Soc.,* **120**, 573–601.

Rangno, A. L., and P. V. Hobbs, 2001: Ice particles in stratiform clouds in the Arctic and possible mechanisms for the production of high ice concentrations. *J. Geophys. Res.,* **106**, 15,065–15,075.

Rangno, A. L., and P. V. Hobbs, 2004: Microstructures and precipitation development in cumuliform clouds over the warm pool of the tropical Pacific Ocean. *Quart. J. Roy. Meteor. Soc.,* submitted.

Rauber, R. M., K. V. Beard, and B. A. Andrews, 1991: A mechanisms for giant raindrop formation in warm shallow convective clouds. *J. Atmos. Sci.,* **48**, 1791–1797.

Saunders, P. M., 1965: Some characteristics of tropical marine showers. *J. Atmos. Sci.,* **22**, 167–173.

Shaw, R. A., W. C. Reade, L. R. Collins, and J. Verlinde, 1998: Preferential concentration of cloud droplets by turbulence: Effects on the early evolution of cumulus cloud droplet spectra. *J. Atmos. Sci.,* **55**, 1965–1976.

Szumowski, M. J., R. M. Rauber, H. T. Ochs III, and L. J. Miller, 1997: The microphysical structure and evolution of Hawaiian rainband clouds. Part I: Radar observations of rainbands containing high reflectivity cores. *J. Atmos. Sci.,* **54**, 369–385.

A 3D STOCHASTIC CLOUD MODEL FOR INVESTIGATING THE RADIATIVE PROPERTIES OF INHOMOGENEOUS CIRRUS CLOUDS

Robin J. Hogan* and Sarah F. Kew†

Department of Meteorology, University of Reading, Reading, Berkshire, United Kingdom

1 INTRODUCTION

The importance of ice clouds on the earth's radiation budget is well recognized (Liou 1986), and studies have shown that ice cloud inhomogeneity can have a strong effect on mean ?uxes in both the shortwave (Carlin et al. 2002) and longwave (Pomroy and Illingworth 2000). Stochastic models capable of simulating realistic cloud structures are very useful for quantifying this effect, and several such models exist for boundary layer clouds, such as those of Cahalan et al. (1994) and DiGuiseppe and Tompkins (2003) for stratocumulus, and Evans and Wiscombe (2004) for cumulus. In this paper we present the ?rst stochastic model capable of representing the important structural properties unique to cirrus: fallstreak geometry and shear-induced mixing. The model essentially takes 1D power spectra of ice water content obtained from cloud radar, and performs a 3D inverse Fourier Transform with random phases for the Fourier components to obtain an isotropic 3D fractal ?eld with the same spectral properties as the original data. Each vertical layer of the ?eld is then manipulated in various ways to generate a realistic cirrus cloud.

In section 2 we show how cloud radar data are analysed to extract the parameters describing the 3D structure of cirrus. In section 3 the formulation of the model is outlined. Then in section 4, radiation calculations are performed to demonstrate the sensitivity of the ?uxes to fallstreak orientation, which is determined by wind shear.

2 ANALYSIS OF CLOUD RADAR DATA

We use data recorded by the vertically pointing 94-GHz *Galileo* radar located at Chilbolton in Southern England. The approach is initially similar to Hogan and Illingworth (2003); radar re?ectivity factor is converted to ice water content (IWC) using a power-law expression derived from aircraft data. Figure 1 shows a 2-hour time-height cross section of IWC through a cirrus cloud with a pronounced fall streak structure.

2.1 Probability density function

Hogan and Illingworth (2003) showed that the PDF of IWC tended to be well represented by a lognormal distribution, and characterised the horizontal variability in terms of the fractional variance of IWC, f_{IWC}, which may be regarded as the variance of ln(IWC). We therefore constrain the stochastic model to produce lognormal IWC distributions with mean and fractional variance at each height derived from the radar data. Where there are gaps in the radar data due to re?ectivities below the instrument sensitivity threshold, the data are analysed in such a way as to obtain the parameters of an "underlying" lognormal distribution which best ?ts the observed PDF in the upper part of its range.

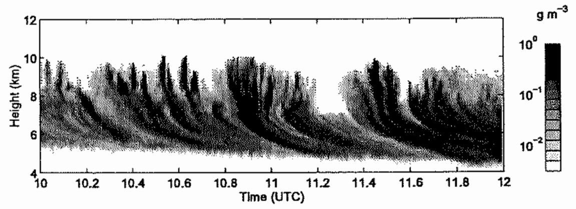

Figure 1: Ice water content derived from 94-GHz radar re?ectivity on 26 December 1999.

2.2 Vertical structure

A striking feature of radar images of ice clouds is the fallstreak structure, whereby horizontal inhomogeneities caused by convective overturning at cloud top (the "generating level") are carried down with the falling ice, but displaced horizontally with respect to cloud top due to the presence of vertical wind shear. Marshall (1953) showed that consideration of the pro?le of horizontal wind and mean particle fallspeed cloud be used to predict cirrus fallstreak geometry, and that constant vertical wind shear and constant fallspeed led to parabolic fallstreaks. We use essentially the same formulation as Marshall (1953), with the wind pro?le taken from the Met Of?ce forecast model and a prescribed fallspeed. In principle the velocity measured by a Doppler radar could be used for fallspeed.

2.3 Horizontal structure

The radar data are ?rst transformed from time to horizontal distance using the wind at cloud top, which in the case shown was 55 m s^{-1}. The horizontal structure is then characterised by taking power spectra of ln(IWC) at each height. Gaps in the radar data are replaced by a constant value below the radar sensitivity threshold. This does not signi?cantly affect the resulting spectra, provided that the gaps do not constitute more than about 25% of the ?eld.

*Corresponding author address: Robin J. Hogan, Department of Meteorology, University of Reading, Earley Gate, PO Box 243, Reading RG6 6BB, UK; E-mail: r.j.hogan@reading.ac.uk.

†Current af?liation: Institute for Atmospheric and Climate Science, ETH, Zürich, Switzerland.

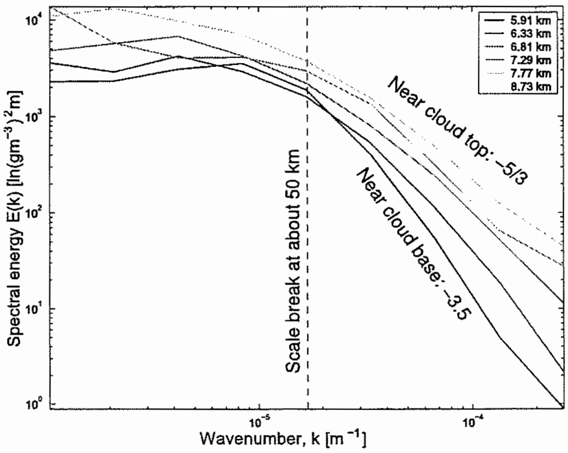

Figure 2: Power spectra of ln(IWC) as a function of height for the data shown in Fig. 1. The raw spectra have been averaged such that there are around four points per decade of wavenumber.

The results for the cloud in Fig. 1 are shown in Fig. 2. It can be seen that near cloud top a spectral slope of −5/3 is evident. This indicates that here IWC is acting as a tracer of a turbulent ?eld, presumably originating from convective overturning in the generating region. The fact that this behaviour is seen up to scales of 50–100 km indicates a 2D upscale cascade of energy (e.g. Lilly 1983) rather than 3D turbulence in the inertial subrange, although interaction with gravity waves could play a part. The reason for a scale break at 50–100 km is not certain, although it was clearly also evident in the f_{IWC} results of Hogan and Illingworth (2003), obtained from 18-months of data. Below cloud top there is a distinct steepening of the power spectra, indicating the suppression of structure preferentially at small scales. An explanation for this is variable particle fall speeds in the presence of vertical wind shear leading to different horizontal displacements (as predicted by the Marshall 1953 model) and hence a horizontal homogenisation.

The parameters of the spectrum provided to the stochastic model are simply the slope of the power spectrum at each height and the position of the scale break (which is assumed constant with height). At scales larger than the scale break, the power is taken to be constant with wavenumber. It should be noted that the absolute value of spectral energy does not need to be recorded, as this is implicitly provided by f_{IWC} which, by Parseval's Theorem, is simply the area under the power spectrum.

3 FORMULATION OF STOCHASTIC CLOUD MODEL

3.1 Generation of an isotropic fractal ?eld

The ?rst step is to generate a 3D isotropic ?eld with a Gaussian PDF and a spectral slope of our choosing. Suppose that we wish the 1D power spectrum $E_1(k)$ through this ?eld to have a single slope μ at all scales:

$$E_1(k) = \hat{E}_1 k^{\mu}, \qquad (1)$$

where k is wavenumber and $\hat{E}_1$ is the spectral energy density at $k = 1\ \mathrm{m}^{-1}$. Now, for the 3D ?eld we are to generate there exists a 3D spectral energy density matrix $E_3(k_x, k_y, k_z)$, which is found by taking the 3D Fourier Transform of the ?eld and multiplying each Fourier component by its complex conjugate (i.e. taking the square of the amplitude and discarding the phase information). Our approach is to reverse this process: if we can generate E_3 somehow then by assuming random phases for each of the Fourier components, a 3D inverse Fourier Transform will yield the required fractal ?eld. A different set of random phases will produce a different realisation of the cloud ?eld, but with the same statistical properties. For our ?eld to be isotropic, E_3 must be a function of absolute wavenumber $k = (k_x^2 + k_y^2 + k_z^2)^{1/2}$ only. A 1D power spectrum through the ?eld in the x-direction will satisfy

$$E_1(k_x) = \int_{-\infty}^{\infty} \int_{-\infty}^{\infty} E_3(k_x, k_y, k_z)\, dk_y\, dk_z. \qquad (2)$$

With the constraint that the ?eld is isotropic and that there is a single spectral slope, it can be shown that

$$E_3(k) = \hat{E}_3 k^{\mu - 2}, \qquad (3)$$

i.e. the 3D power spectrum is a simple power law and is steeper than E_1 by two powers of k. If there is a scale break in the 1D spectrum then this may be included at the same place in the 3D spectrum, but ensuring that the spectrum to each side of the break is still steeper than E_1 by k^2. It should be noted that the value of $\hat{E}_3$ is arbitrary as the variance of the ?eld will be later scaled by f_{IWC}.

The procedure described here is only really valid for cubic domains with the same grid spacing in the horizontal and vertical, whereas for cirrus we typically require a domain of around $L_x = L_y = 200$ km in the horizontal but only $L_z = 5$ km in the vertical, and similarly a vertical resolution of around $\Delta z = 100$ m compared with only $\Delta x = \Delta y = 1$ km in the horizontal. When (2) is reduced to a discrete summation this necessitates the introduction of two additional arti?cial scale breaks in E_3 (at Δx and L_z), in order that the 3D ?eld has the required spectral properties. The details are unfortunately too involved to describe here.

3.2 Conversion to a realistic cloud ?eld

The resulting 3D fractal ?eld is then manipulated in various ways to simulate a realistic cirrus cloud. The ?rst two steps, horizontal displacement (to simulate fall-streaks) and adjustment of the slope of the power spectrum (to simulate shear-induced mixing) are performed in the wavenumber domain. At each height a 2D Fourier Transform is performed. To simulate a horizontal translation of $(\delta x, \delta y)$, the Fourier coef?cients are multiplied by $\exp(i\theta)$ where $\theta = 2\pi(k_x \delta x + k_y \delta y)$. To change the slope of the power spectrum from μ_1 to μ_2, the Fourier components are then multiplied by $k^{(\mu_2 - \mu_1)/2}$, where k is the absolute wavenumber in 2D space. An inverse 2D Fourier Transform is then performed to recover the modi?ed ?eld.

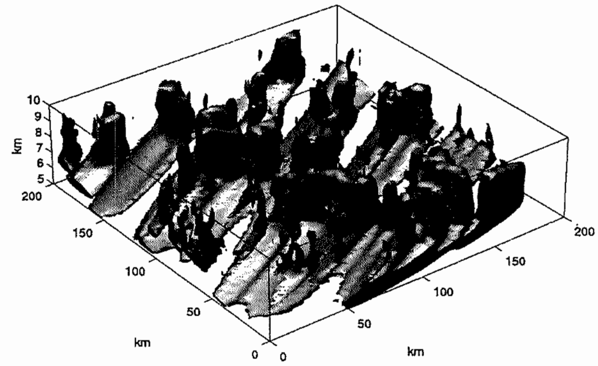

Figure 3: 3D visualisation of the 0.2 g m^{-3} IWC isosurface, for a simulation of the 26 December 1999 case.

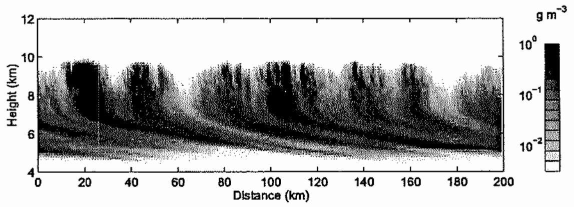

Figure 4: Cross-section of IWC through a simulation of the 26 December 1999 case; to be compared with Fig. 1.

At this stage the ?eld has an approximately Gaussian distribution with a mean of zero and an arbitrary variance. The ?nal step is to scale and threshold it. We scale each 2D slice of the ?eld in order that that it has the variance f_{IWC} obtained from observations, then exponentiate it to yield a lognormal distribution. The resulting ?eld is scaled again to obtain the required pro?le of mean IWC with height, and ?nally values below a certain threshold may be rejected to represent gaps in the cloud.

3.3 Example simulation

The model has been applied to the 26 December 1999 case discussed in section 2, and Figure 3 shows a 3D visualisation of the result. The fallstreak structures characteristic of cirrus are clearly evident, and a cross-section through the domain in Fig. 4 exhibits encouraging similarity to the original radar image in Fig. 1. Power spectra through the simulated cloud ?eld are very similar to those in Fig. 2. It is evident in Fig. 3 that near cloud top the ?eld is horizontally isotropic, while in real cirrus, gravity waves and shear can lead to roll-like structures in this region. While the model does not currently represent these anisotropic effects, the results of Hinkelman (2003) suggest that manipulation of E_3 could enable them to be simulated.

4 RADIATIVE PROPERTIES OF INHOMOGENEOUS CIRRUS CLOUDS

We now demonstrate how the stochastic model may be used to investigate the effect of cloud inhomogeneity (speci?cally fallstreak orientation) on the radiative properties of cirrus. An optically thinner cloud from 17 July 1999

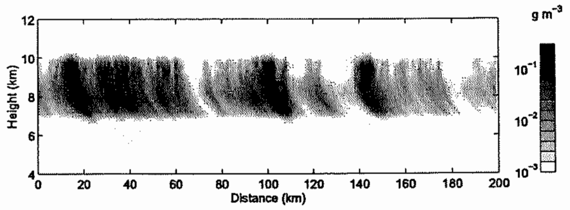

Figure 5: Cross-section of IWC through a simulated cirrus cloud based on observations from 17 July 1999, when the mean vertical shear through the cloud was 2 m s^{-1} km^{-1} (low shear case).

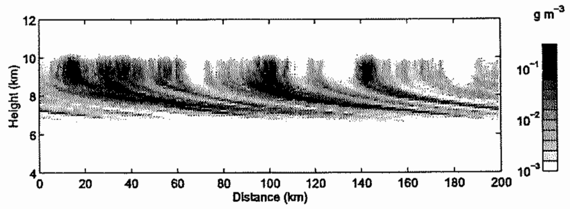

Figure 6: Cross-section through the same cloud as in Fig. 5, but with the wind velocity multiplied by 10 (high shear case).

is used, at which time the wind shear according to the Met Of?ce model was low at around 2 m s^{-1} km^{-1}. The simulation was performed on a domain measuring 200 km horizontally, with a resolution of 780 m in the horizontal and 50 m in the vertical. A cross-section through the domain is shown in Fig. 5. Figure 6 shows a second simulation performed with the same input parameters as the ?rst (and with the random number generator seeded by the same value), except with the wind speed (and hence shear) a factor of 10 higher. This results in much more horizontally aligned fallstreaks, similar to those in Figs. 1 and 4. It should be stressed that the two ?elds have the same mean IWC at each height, and hence the same mean optical depth.

The effects of these ?elds on radiative ?uxes are best illustrated by consideration of the shortwave albedo and longwave emissivity. Assuming a constant effective radius of 50 μm the vertically integrated IWC may be converted to shortwave optical depth, and assuming no horizontal transport of photons, to albedo. Figure 7 shows the albedo of the low and high shear cases, assuming a solar zenith angle of 60° and a surface albedo of 0.2, calculated using the Edwards-Slingo radiation code. These images are similar to what would be seen by a visible satellite imager. The fallstreaks are clearly visible in the second panel, and importantly there is an increase in the mean albedo of the ?eld of 0.04, corresponding to an increase in re?ected shortwave ?ux of around 25 W m^{-2} at this solar zenith angle. This represents a 20% increase in the top-of-atmosphere shortwave effect of the cloud.

Assuming the longwave extinction coef?cient to be half the visible extinction coef?cient, the corresponding emissivity of the cloud may be estimated, and is shown in Fig. 8. While emissivity is a rather crude parameter for describing the longwave properties of a cloud 3 km deep, it clearly illustrates how the horizontal alignment

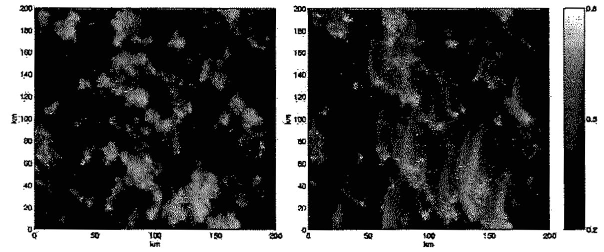

Figure 7: Albedo of simulated cloud in the low (left) and high (right) shear cases, the domain-mean albedos being 0.37 and 0.41 respectively.

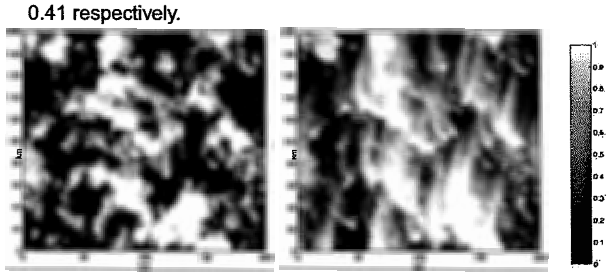

Figure 8: Emissivity of simulated cloud in the low (left) and high (right) shear cases, the domain-mean emissivities being 0.52 and 0.66 respectively.

of fallstreaks in high wind shear conditions leads to a greater fraction of the domain covered by "near black-body" clouds. For a mean cloud temperature of -50°C and a surface temperature of 10°C, the increase of mean emissivity from 0.52 to 0.66 corresponds to a reduction in outgoing longwave radiation of around 30 W m^{-2}, i.e. 30% of the top-of-atmosphere longwave effect of the cloud.

The reason for the effect on mean ?uxes is that the relationships between optical depth and both albedo and emissivity are not linear, so even though the mean optical depth stays constant, the mean albedo and mean emissivity will change as the PDF of optical depth changes. The main curvature in the relationships occurs at lower optical depths in the case of emissivity, so longwave ?uxes will tend to be more sensitive to the inhomogeneities of optically thin clouds than shortwave ?uxes, with the converse being the case for optically thick clouds.

5 CONCLUSIONS

In this paper a stochastic model has been described for generating realistic 3D cirrus cloud ?elds from radar-derived power spectra. Simple radiative transfer calculations using the independent column approximation have demonstrated the strong effect of fallstreak geometry (which is in turn governed by wind shear) on both shortwave and longwave ?uxes, highlighting the importance of cirrus inhomogeneity for climate and the need to represent it adequately in large-scale models. It should be noted that, by contrast, in the study of the effects of stratocumulus inhomogeneity, longwave ?uxes are of little interest because the temperature contrast with the ground is much less, and because the higher optical depth means that most of the cloud ?eld behaves as a black body.

Future analysis will address some of the simpli?cations made here in estimating cloud radiative properties. The assumption of constant effective radius may be relaxed in two ways, either by applying the method of Evans and Wiscombe (2004) to generate an effective radius ?eld simultaneously with IWC (with a speci?ed correlation between the two), or by directly simulating extinction coef?cient rather than IWC, as extinction is much more directly related to the radiative properties of the cloud in both the shortwave and longwave. Three-dimensional radiative transfer calculations will also be performed.

Another use for the model is in testing the performance of satellite retrieval algorithms, particularly those which involve the synergy of multiple instruments where coincident sampling of the cloud is important (such as spaceborne radar and lidar).

ACKNOWLEDGEMENTS

We are grateful to the Rutherford Appleton Laboratory for the use of the Galileo radar, to Malcolm Brooks for assistance in running the radiation code and to the Met Of?ce for the model data. SFK was supported by a NERC studentship.

REFERENCES

Cahalan, R. F., W. Ridgeway, W. J. Wiscombe, T. L. Bell and J. B. Snider, 1994: The albedo of fractal stratocumulus clouds. *J. Atmos. Sci.,* **51,** 2434–2455.

Carlin, B., Q. Fu, U. Lohmann, G. G. Mace, K. Sassen and J. M. Comstock, 2002: High-cloud horizontal inhomogeneity and solar albedo bias. *J. Climate,* **15,** 2321–2339.

DiGuiseppe, F., and A. M. Tompkins, 2003: Effect of spatial organisation on solar radiative transfer in three dimensional idealized stratocumulus cloud ?elds. *J. Atmos. Sci.,* **60,** 1774–1794.

Evans, K. F., and W. J. Wiscombe, 2004: An algorithm for generating stochastic cloud ?elds. *Submitted to Atmos. Res.*

Hinkelman, L. M., 2003: *The effect of cumulus cloud ?eld anisotropy on solar radiative ?uxes and atmospheric heating rates.* PhD Thesis, The Pennsylvania State University.

Hogan, R. J., and A. J. Illingworth, 2003: Parameterizing ice cloud inhomogeneity and the overlap of inhomogeneities using cloud radar data. *J. Atmos. Sci.,* **60,** 756–767.

Lilly, D. K., 1983: Strati?ed turbulence and the mesoscale variability of the atmosphere. *J. Atmos. Sci.,* **40,** 749–761.

Liou, K.-N., 1986: In?uence of cirrus clouds on weather and climate processes: A global perspective. *Monthly Weather Rev.,* **114,** 1167–1199.

Marshall, J. S., 1953: Precipitation trajectories and patterns. *J. Meteorol.,* **10,** 25–30.

Pomroy, H. R., and A. J. Illingworth, 2000: Ice cloud inhomogeneity: Quantifying bias in emissivity from radar observations. *Geophys. Res. Lett.,* **27,** 2101–2104.

A NUMERICAL STUDY OF THE SNOWFALL AROUND THE NIIGATA REGION

Katsushi Iwamoto[1] , Sento Nakai[1], Masaaki Ishizaka[1], Masujiro Shimizu[1], Atsushi Sato[1], and Toshisuke Maruyama[2]

[1]Snow and Ice Research Group, National Research Institute for Earth Science and Disaster Prevention (NIED), Nagaoka, 940–0821, Japan
[2]Niigata electric Co., Ltd., Nagaoka, 940–1101, Japan

1. Introduction

In winter, the northwestern monsoon with cold and dry air frequently blow out from the Eurasian Continent to Japan. Snow clouds develop as heat and moisture supply from the warm sea surface over the Japan Sea in this time, and often bring about heavy snowfall over the coastal area in Japan. Concerning the principal cloud structure there are both cloud streets running parallel to and at an angle with the mean wind direction. Additionally, the horizontal convergence, generated by the mountain chain near the Japan Sea coast of the Eurasian continent, often produces big snow clouds. Many researchers have investigated the dynamical and thermodynamical structure of these cloud systems over the Japan Sea using doppler radar or numerical modeling (e.g., Asai and Miura 1981; Miura 1986; Yamada *et al.* 1992).

Niigata region is one of the heaviest snowfall areas in Japan, and is sometimes subject to snow disasters. In order to prevent these, it is important to know not only about the dynamic and thermodynamic structure of the cloud systems but also about the distribution and amount of the snowfall related to different types of cloud systems and orographic effects. For this purpose, we performed the numerical simulation of a snowstorm hitting the areas of the Niigata region close to the coast in January 2003. This was done, using Non-Hydrostatic Model (NHM) developed by the Japan Meteorological Agency (JMA). In this paper, we show the preliminary results of the study.

2. Numerical Experiment

The domain of the numerical experiment is shown in Fig. 1. Initial and boundary conditions were given by the grid point values of the Regional Spectrum Model (RSM) provided by JMA with the horizontal resolution of about 40km. The NHM simulation utilized a nested grid system with an outer grid of 10km spacing and an inner grid of 2km including the area from the Japan Sea to the mountain range of the water divide between the Japan Sea region and the Pacific Ocean region of Japan. In order to remove the effect on the cloud systems caused by the time evolution of the boundary condition, boundary condition is fixed to the initial state.

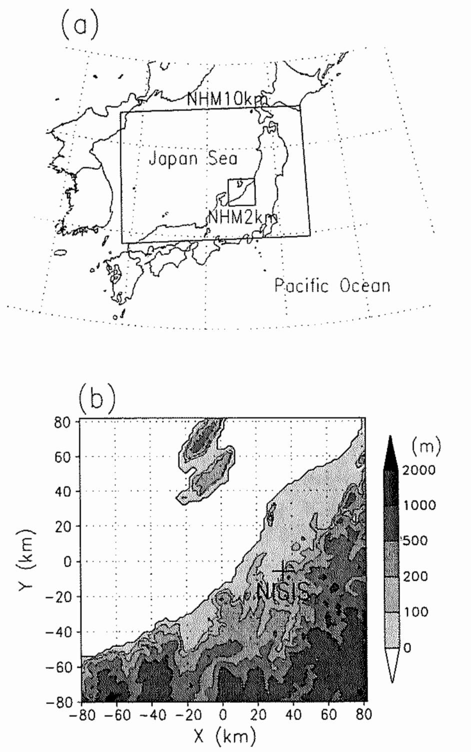

Figure 1: (a): Outer grid of the numerical experiment using the NHM (Non-Hydrostatic Model), and (b): orography of the nested grid. The position of the Nagaoka Institute of Snow and Ice Studies (NISIS) is marked.

[1]Corresponding author's address: Katsushi Iwamoto, Nagaoka Institute of Snow and Ice Studies, Nagaoka, 940–0821, Japan; E-Mail: katsu@bosai.go.jp.

3. Results

In January 2003, four large snowfall events related to the cold-air outbreaks occurred at Niigata region. To perform the NHM experiment, we chose the period from 4 to 6 January 2003 which generated the heaviest snowfall of that winter. At the beginning of this event, several vortex-structured radar echos were observed by the doppler radar established at the Nagaoka Institute of Snow and Ice Studies (NISIS; Fig. 1b) while heavy snow fell over this area.

The total precipitation after 48 hours integration by NHM under the boundary condition of 00 UTC 5 January is shown in Fig. 2. Heavy snowfall occurred at the coastal area around y = -10km and the sea–facing slope of the mountain range, partly explicable by orographic lifting. This feature is consistent with the surface observation. (not shown here).

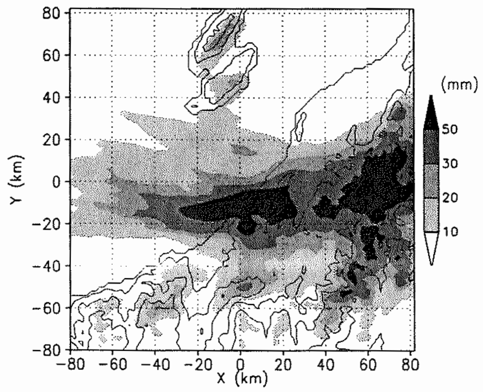

Figure 2: Horizontal distribution of precipitation during 48 hours model run from 00 UTC 5 January.

The snapshot of the precipitating water amount (sum of the rain, snow, and graupel) at 520m level after the 48 hours integration is shown in Fig. 3a. At y = -20km, precipitating clouds with a scale of about 10 km are alligned (Fig. 3a), corresponding to a street of positive and negative vorticity maxima (Fig. 3b). Since the horizontal wind shear over this area exists(not shown here), the vorticity street seems to be the wave generated by shear instability. Its wave length is about 10 km at the western boundary of the domain and about 20 km near the coast. Over the land, the wave–like structure is indistinct.

4. Concluding remarks

The numerical experiment using NHM was performed focussing on a snowstorm hitting the Niigata region in Japan. Horizontal distribution of precipi-

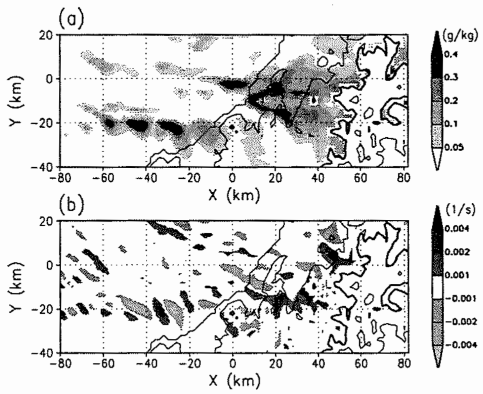

Figure 3: Horizontal distribution of (a): the amount of total precipitating water (sum of the rain, snow, and graupel) and (b): the vertical component of vorticity at the level of 520m above mean sea level. The inside of the thick line is undefined.

tation was in good agreement with the surface observations. Several vortex-like snow clouds were observed by the doppler radar at NISIS at this time. In the model, marked snow clouds with a wave–like wind distribution with a length from 10 to 20km appeared along the shear line of the horizontal wind. The clouds were moving eastward, and decaying over the land.

The next step of this study is to investigate the relationship between the wave over the Japan Sea and the vortex–like radar echo observed by doppler radar. Moreover, we have to simulate other types of cloud systems and investigate the differing orographic effects related to each of these.

References

Asai, T. and Y. Miura, 1981: An analytical study of meso–scale vortex–like disturbances observed around wakasa bay area. *J. Meteor. Soc. Japan*, **59**, 832–843.

Miura, Y., 1986: Aspect ratios of longitudinal rolls and convection cells observed during cold air outbreaks. *J. Atmos. Sci.*, **43**, 26–39.

Yamada, Y., T. Matsuo, M. Murakami and H. Mizuno, 1992: Structure of mesoscale snow bands over the sea of japan. *Proceedings 11th International Conf. on Clouds and Precipitation*, 605–608.

INVESTIGATION OF THE EVOLUTION OF RELATIVE HUMIDITY DURING TURBULENT MIXING USING PDF METHODS

Christopher A. Jeffery*
Los Alamos National Laboratory (ISR-2), Los Alamos, New Mexico

1 INTRODUCTION

Early convective cloud parameterizations assumed that cloud interiors were well mixed—the so-called "homogeneous mixing" approximation (Jonas and Mason, 1982). This assumption was challenged by Baker et al. (1980) who first pointed out that the actual mixing of two fluid elements with different relative humidity, RH, occurs via diffusion across narrow centimeter-scale filaments with advection controlling the contact rate of unmixed fluid elements. The converse of this statement—fluids remain unmixed in the absence of diffusion—is a consequence of the well-known phase preservation property of Louiville equations.

Based on this phenomenological picture, Baker et al. proposed that turbulent mixing in clouds is either "inhomogeneous" or "extreme inhomogeneous" in nature as illustrated in Fig. 1. During inhomogeneous mixing [Fig. 1b)] cloud droplets experience a range of subsaturations in filaments with different ratios of cloud/environmental air. The net result is a broadening of the size-spectrum to smaller sizes. In contrast, during extreme inhomogeneous mixing [Fig. 1c)] some fraction of droplets completely evaporate in subsaturated filaments and thereby restore RH to unity—the size of the remaining droplets are unchanged but the number concentration decreases.

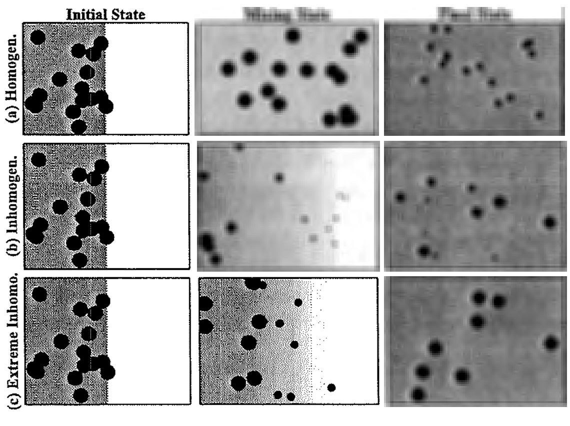

Figure 1: Schematic of different mixing scenarios: (a) Homogeneous, (b) Inhomogeneous and (c) Extreme Inhomogeneous.

* *Corresponding author address:* Christopher Jeffery, Los Alamos National Laboratory (ISR-2), PO Box 1663, MS D-436, Los Alamos, NM 87545; E-Mail: cjeffery@lanl.gov.

In this work, we consider the isobaric evolution of clear and cloudy air during turbulent mixing in the absence of secondary nucleation and we study the broadening of the droplet size spectrum to smaller sizes due to evaporation. Baker et al. introduced three characteristic time scales: an entrainment time, the time for molecular diffusion across filaments and the evaporation time for a single droplet. For the present scenario, I demonstrate that the nature of mixing [e.g. homogeneous vs inhomogeneous] is primarily determined by the Damköhler number (Damköhler, 1940):

$$\mathrm{Da} \equiv \mathrm{t_{eddy}}/\mathrm{t_{react}},$$

the ratio of turbulent ($\mathrm{t_{eddy}}$) and reactive ($\mathrm{t_{react}}$) time scales, where—for cloud evaporation—$\mathrm{t_{react}}$ is given by the characteristic time for phase change (Austin et al., 1985) such that

$$\mathrm{Da} = 4\pi N D_v \mathrm{t_{eddy}} \left\langle r^2/(r+a)\right\rangle_{t=0} \qquad (1)$$

where N is the initial droplet number density in the cloudy air, D_v is the diffusivity of water vapor, r is droplet radius, $a = 2$ μm is an accommodation length, and $\langle\cdot\rangle_{t=0}$ is an ensemble average at time zero. For the present mixing scenario and typical atmospheric conditions Da is large, in the range 10–1000.

Evaluation of the impact of Da on the evolution of RH is complicated by the non-linear nature of mixing and evaporation. Moment formulations suffer from the well-known closure problem that information about statistical moments of every order is needed to have closed non-linear terms. Probability density function (PDF) methods offer a distinct advantage over moment approaches since non-linear reaction terms like evaporation are more easily evaluated. The PDF equation for advection-diffusion requires evaluation of the conditional Laplacian. However, evaluation of this statistic using a Gaussian mixing assumption leads to unphysical behavior in the evolution of the scalar PDF unless the PDF is strictly Gaussian itself.

In this study I use a technique called "mapping closure" (Chen et al., 1989) to evaluate the conditional Laplacian, that does not suffer from the deficiencies of a purely Gaussian closure. The PDF-equation for RH is introduced in Sec. 2 and Chen et al.'s mapping closure is briefly summarized. In Sec. 3 I introduce a linear droplet number mixing model for the conditional evaluation of N, and Sec. 4 summarizes the impact of Da on the evolution of RH and the droplet size distribution, $f(r)$. Sec. 5 discusses total droplet evaporation during mixing and Sec. 6 contains a brief summary.

2 PDF-EQUATION FOR RH

In analogy with the well-known equation for $f(r)$, the equation for the RH-PDF is given by:

$$\frac{\partial \mathrm{P(RH)}}{\partial t} = -\frac{\partial}{\partial \mathrm{RH}}\left[\left\langle \frac{\partial\widetilde{\mathrm{RH}}}{\partial t}\middle|\widetilde{\mathrm{RH}}=\mathrm{RH}\right\rangle \mathrm{P(RH)}\right] \tag{2}$$

where $P(\mathrm{RH})d\mathrm{RH}$ is the probability that RH is in the range $[\mathrm{RH}, \mathrm{RH}+d\mathrm{RH}]$, $\widetilde{\mathrm{RH}}(\boldsymbol{x},t)$ is the RH field and $\langle\partial\widetilde{\mathrm{RH}}/\partial t|\widetilde{\mathrm{RH}}=\mathrm{RH}\rangle$ is the conditional derivate of $\widetilde{\mathrm{RH}}$ evaluated on level sets of RH.

For temperature differences between the cloud/environmental air that are small compared to the Clausius-Clapeyron temperature† R_vT^2/L_v and assuming equality of the diffusivities of water vapor and temperature, $\widetilde{\mathrm{RH}}$ obeys the usual advection–diffusion equation with an evaporative source term. Substitution of the diffusive contribution to the conditional derivative of $\widetilde{\mathrm{RH}}$ gives the conditional Laplacian describing the impact of diffusion on P(RH):

$$D_*\left\langle \nabla^2\widetilde{\mathrm{RH}}\middle|\widetilde{\mathrm{RH}}=\mathrm{RH}\right\rangle \tag{3}$$

where D_* is the vapor/temperature diffusivity.

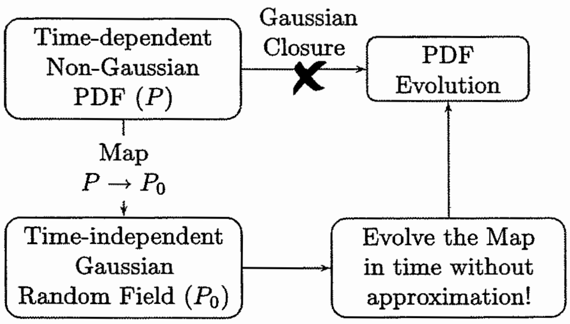

Figure 2: Schematic of mapping closure.

Evaluation of Eq. (3) is the fundamental closure problem in the evaluation of PDFs describing advection-diffusion systems. Gaussian closure results in an advection equation for the PDF that does not give the expected relaxation toward Gaussian statistics unless the PDF is strictly Gaussian itself. Chen et al. (1989) proposed a technique called mapping closure to evaluate Eq. (3) that exhibits realistic relaxation for strongly non-Gaussian PDFs and will be used in the present study. In this new approach, illustrated in Fig. 2, a time-dependent non-Gaussian PDF is mapped to a time-independent Gaussian random field. Once the mapping is established, the map can be evolved in time without approximation since the statistics of the Gaussian random field are known.

3 LINEAR MIXING MODEL

Equating the conditional derivative in Eq. (2) to the sum of diffusive and evaporative contributions and introducing the non-dimensional time scale $\tau = t/\mathrm{t_{eddy}}$ gives

$$\begin{aligned}\partial \mathrm{P}/\partial\tau \;&=\; -(\partial/\partial\mathrm{RH})\left[D_*\mathrm{t_{eddy}}\left\langle\nabla^2\widetilde{\mathrm{RH}}\right\rangle_\tau \mathrm{P}\right] \\ &+ \mathrm{Da}\frac{\partial}{\partial\mathrm{RH}}\left[\frac{\langle N\rangle_\tau}{N}\left\langle\frac{r^2}{r+a}\right\rangle_\tau\left\langle\frac{r+a}{r^2}\right\rangle_{\tau=0}\times\right. \\ &\left.(\mathrm{RH}-1)\mathrm{P}\right]\end{aligned} \tag{4}$$

where it is implicit in the notation that ensemble averages are evaluated on level sets of relative humidity, e.g. $\langle N\rangle_\tau$ expands to $\langle N(\widetilde{\mathrm{RH}},\tau)|\widetilde{\mathrm{RH}}=\mathrm{RH}\rangle$. Note that $\langle\nabla^2\widetilde{\mathrm{RH}}\rangle_\tau$ is evaluated using mapping closure in what follows.

The terms in square brackets in Eq. (4) are of order unity. Thus the Damköhler number, Da, determines the relative strengths of the evaporative and advective-diffusive contributions to the RH-PDF evolution as expected. The final closure relations needed are $\langle N\rangle_\tau$ and $\langle r^2/(r+a)\rangle_\tau$. Our present interest is in universal PDF evolution which occurs for small changes in average droplet radius, i.e. $\langle r^2/(r+a)\rangle_\tau = \langle r^2/(r+a)\rangle_{\tau=0}$. This assumption may easily be dropped in future studies.

In order to model $\langle N\rangle_\tau$ we must first specify the present mixing scenario. We consider the mixing of equal volumes of clear and cloudy air with $\mathrm{RH} = \mathrm{RH_{env}}$ in the clear volume and $\mathrm{RH} = 1$ in the cloudy volume. Formally, $\mathrm{P}_{\tau=0} = 0.5\delta(\mathrm{RH}-\mathrm{RH_{env}}) + 0.5\delta(\mathrm{RH}-1)$. The final state is $\mathrm{P}_{\tau\to\infty} = \delta(\mathrm{RH}-1)$. We introduce a linear droplet number mixing model for $\langle N\rangle_\tau$ based on the following considerations. In the limit that droplet and RH trajectories coincide and in the absence of evaporation, $\langle N\rangle_\tau$ is proportional to the relative volume fractions of clear and cloudy air:

$$\langle N(\mathrm{RH})\rangle_\tau/N = (\mathrm{RH}(\tau)-\mathrm{RH_{env}})/(1-\mathrm{RH_{env}}).$$

Evaporation must necessarily modify this relation; as droplets evaporate and local RH increases, the

†T is temperature, R_v is the water vapor gas constant and L_v is the latent heat of vaporization.

relative fraction of drops becomes less than this volume fraction relation indicates.

In the linear droplet number mixing model we preserve the linear structure suggested by the above volume fraction analysis but introduce a time dependent function $F(\tau)$ to account for the effects of evaporation. Specifically, and in what follows, we use

$$\langle N(\mathrm{RH})\rangle_\tau/N = F(\tau)(\mathrm{RH}-\mathrm{RH}_{\mathrm{env}})/(1-\mathrm{RH}_{\mathrm{env}}) \quad (5)$$

where $F(\tau)$ is evaluated at each time step to preserve total droplet number. For our scenario of equal volumes of clear/cloudy air it is easy to show that $F(\tau \to \infty) = 1/2$.

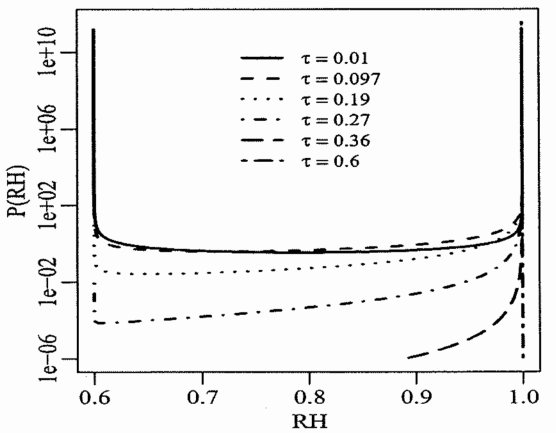

Figure 3: Evolution of P(RH) calculated from Eq. (4) with Da = 100 and $\mathrm{RH}_{\mathrm{env}} = 0.6$.

4 PDF EVOLUTION

The evolution of the PDF of RH is shown in Fig. 3 for Da = 100. At large Damköhler number, the predictions of the present approach are consistent with the phenomenological model of Baker et al.. The relatively low probability of finding RH in the range $0.62 < \mathrm{RH} < 0.98$ illustrates that mixing of fluid elements is confined to narrow filaments with small volume fraction. Restoration of RH to unity in filaments due to evaporation occurs at a faster rate than the diffusive growth of the filament—this is the fundamental nature of hydrodynamic reaction at high Da.

A comparison of the cumulative distribution function (CDF) that $\mathrm{RH} \leq 0.99$ for $\mathrm{Da} \in [10, 1000]$ is shown in Fig. 4. The top figure shows CDF($\mathrm{RH} \leq 0.99$) while the bottom figure depicts the CDF weighted by droplet number as modeled by Eq. (5). The results illustrated in Fig. 4 re-emphasize the fundamental connection between Damköhler number and Baker et al.'s concept of inhomogeneous mixing. Specifically, Fig. 4 demonstrates that the relative fraction of droplets that experience a subsaturated environment decreases with increasing Da.

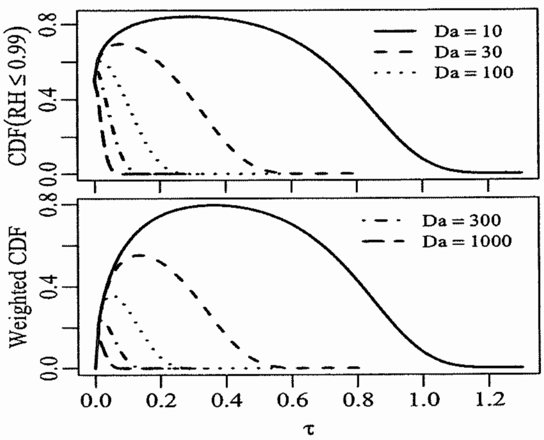

Figure 4: Cumulative probability $\mathrm{RH} \leq 0.99$ (top) and CDF weighted by $N(\mathrm{RH})/N$ (bottom).

Determination of the droplet size spectrum, $f(r)$, requires Lagrangian information of the supersaturation along droplet trajectories. Let

$$(\mathrm{S}_{\mathrm{int}})_A = \frac{1}{\tau(1-\mathrm{RH}_{\mathrm{env}})}\int_0^\infty dt\ \mathrm{RH}_A(t) - 1$$

be the normalized supersaturation integral of the droplet labeled "A" such that $\mathrm{RH}_A(t)$ is the local supersaturation experienced by A at time t. The present approach provides $N(\mathrm{RH})$ but not $\mathrm{S}_{\mathrm{int}}$ without further assumption. We hypothesize that once a droplet has diffused across a filament from a high N/high RH environment to a low N/low RH environment then it will tend to stay in that low N/low RH environment. Mathematically, this assumption corresponds to a set of droplet trajectories that minimize the total RH variance along the trajectories.

The PDF of $|\mathrm{S}_{\mathrm{int}}|$ calculated using Eq. (4) and Lagrangian trajectories that minimize RH variance under the constraints imposed by the model prediction of $N(\mathrm{RH})$ is shown in Fig. 5. Note that $\langle \mathrm{Da}|\mathrm{S}_{\mathrm{int}}|\rangle = 1$. The figure reveals that most droplets do not experience significant subsaturation during mixing at large Da while for smaller Da most droplets experience a subsaturation that is greater than the minimum.

This behavior in $\mathrm{S}_{\mathrm{int}}$ can be seen in the droplet spectrum shown in Fig. 6 and calculated such that 5% of droplets completely evaporate during the mixing process. The figure reveals that decreasing Da broadens the droplet spectrum to smaller sizes.

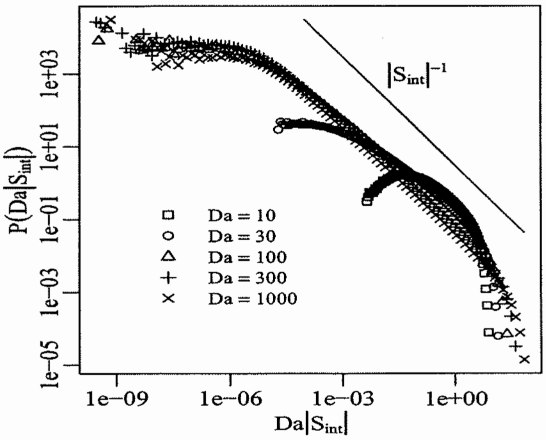

Figure 5: PDF of $Da|S_{int}|$ for $Da \in [10, 1000]$.

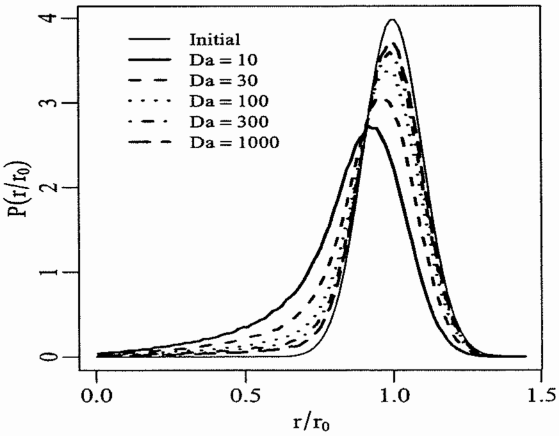

Figure 6: Droplet spectra assuming a Gaussian initial state with $\sigma = 0.1r_0$.

5 DROPLET EVAPORATION

The dependence of total droplet evaporation on Damköhler number is illustrated in Fig. 7. Here, N_i is the initial in-cloud droplet number concentration, N_f is the final concentration after mixing, and ρ_i and ρ_f are the initial and final liquid water densities, respectively. The point $(0.5, 0.5)$ refers to dilution of the cloudy air by an equal volume of environmental air with no change in droplet size or number. The figure reveals that increasing Da increases the number of droplets that evaporate completely.

6 SUMMARY

In this work the PDF equation for RH has been derived and closed using (i) mapping closure to evaluate the conditional Laplacian and (ii) a linear droplet number mixing model to evaluate $\langle N(\widetilde{RH}, \tau)|\widetilde{RH} = RH\rangle$. The central conclusions of this study are summarized in Fig. 8. The concepts of "inhomogeneous mixing" and "extreme inhomogeneous mixing" introduced by Baker et al. are shown to be equivalent to hydrodynamic reaction at $Da = \mathcal{O}(1)$ and large Da, respectively. For the present mixing scenario and typical atmospheric conditions "homogeneous mixing" does not occur. In addition, due to the dependence of Da on N indicated by Eq. (1), we find that increasing N increases Da which thereby decreases the dispersion of the droplet size spectrum to smaller scales and increases total droplet evaporation.

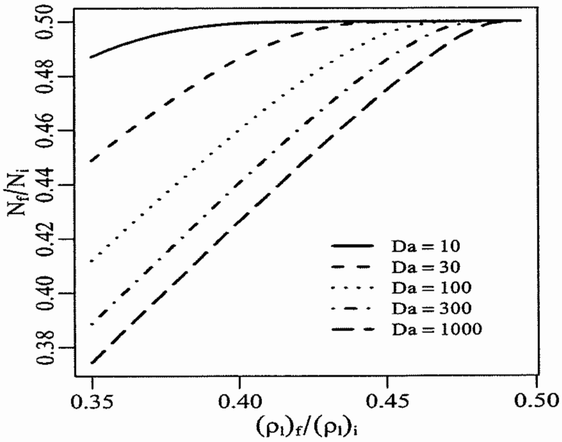

Figure 7: Dependence of droplet evaporation on Da.

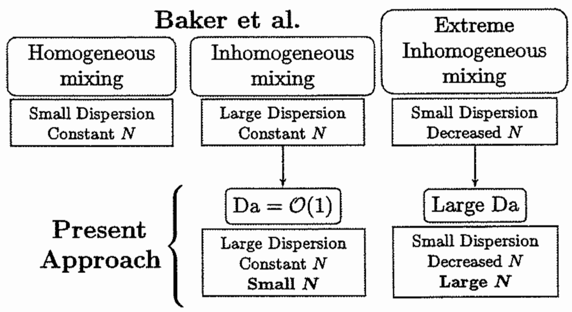

Figure 8: Schematic of present results.

REFERENCES

Austin, P. H., M. B. Baker, A. M. Blyth and J. B. Jensen, 1985: Small-scale variability in warm continental Cumulus clouds. *J. Atmos. Sci.*, **42**(11), 1123–1138.

Baker, M. B., R. G. Corbin and J. Latham, 1980: Influence of entrainment on the evolution of cloud droplet spectra. *Q. J. R. Meteorol. Soc.*, **106**, 581–599.

Chen, H., S. Chen and R. H. Kraichnan, 1989: Probability distribution of a stochastically advected scalar field. *Phys. Rev. Lett.*, **63**(24), 2657–2660.

Damköhler, G. Z., 1940: Influence of turbulence on flame velocity in gaseous mixtures. *ZH Electrochem*, **46**, 601.

Jonas, P. R. and B. J. Mason, 1982: Entrainment and the droplet spectrum in cumulus clouds. *Q. J. R. Meteorol. Soc.*, **108**, 857–869.

STRUCTURE AND EVOLUTION OF LONG-LIVED SLOW-MOVING LINE-SYSTEM IN MOIST AND WARM ENVIRONMENT IN EAST ASIA.

Sachie Kanada[1] , Teruyuki Kato[2] and Masanori Yoshizaki[2]

[1]Advanced Earth Science and Technology Organization, Tokyo
[2]Meteorological Research Institute / JMA, 1-1 Nagamine, Tsukuba, Ibaraki 305-0052 Japan

1. INTRODUCTION

A heavy rainfall is very often caused in subtropical humid-climate region by a meso-scale precipitating convective cloud system. One of the most evident systems is the line-shaped system and it sometimes maintains for a long time in the same place to bring a huge rainfall at limited area. Many long-lived slow-moving line-systems are associated with orographic effect (Fujiyoshi et al. 1992, Kang and Kimura 1997, Kanada et al. 2000).

When south-southwesterly winds are predominant on the southern region of the Baiu front, line-shaped systems are very often formed over Kyushu Island. There are some studies about them (Yoshizaki et al.; 2000), but three-dimensional structures or the intensification/maintenance process of them have not been revealed yet.

The main purpose of this study is to reveal the structure and behavior of the long-lived line-shaped system, which produce a heavy rainfall as one of the process of orographic enhancement of rainfall. The line-shaped system which extends from the Nagasaki Peninsula is investigated in detail, since it observes the most frequent and maintains longer period than other line-shaped systems..

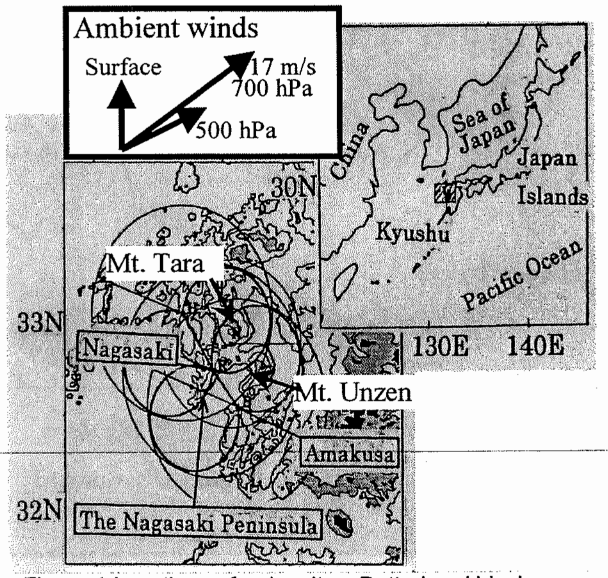

Figure 1 Locations of radar sites. Dotted and black areas indicate areas over 500 and 1000 m, respectively. Wind profile at 1500 LST at Amakusa (left-top).

2. RADAR OBSERVATION

The locations of radar-sites are shown in Fig. 1. There are two high mountains, Mt. Tara and Mt. Unzen, whose tops exceed 1000m around radar sites. Wind profile at 1500 LST at Amakusa was shown in left-top of Fig. 1. Southerly wind was predominant at surface and southwesterly wind which exceeded 15 m/s was seen at 700 hPa level.

On July 11 in 1997 a heavy rainfall was concentrated in the narrow area in the Nagasaki Peninsula. The largest amount of 176 mm was recorded at the base of the peninsula. Total rainfall amounts larger than 10 mm were observed only in the limited area around the base of the peninsula. Another large rainfall amount was observed over Isahaya City and Isahaya Bay. This rainfall was produced by a long-lived line-shaped convective cloud system which maintained for about 18 hours almost in the same place.

Corresponding author's address: Sachie KANADA, Meteorological Research Institute, -1 Nagamine, Tsukuba, Ibaraki 305-0052 Japan: e-mail: skanada@mri-jma.go.jp

Radar-echo analysis reveals that the length and width of its radar-echo band were over 60 km and about 10 km, respectively and its length extended with period of 2 to 3 hours. The system was composed with many convective cells whose echo-tops were about 6 km..

The horizontal distribution of radar-echo averaged from 1648 to 1922 LST on July 11 with the positions of the formation, intensification and disappearance of each cellular-echoes are shown in Fig. 2. The duration time of this radar-echo band (Line-1) is divided into two stages as the developing stage (1648-1805 LST) and the decaying stage (1819-1922 LST). As shown in the figure, most cellular-echoes are formed around the base of the Nagasaki Peninsula. During the developing stage some cellular-echoes are also formed over Isahaya Bay. The formation positions of the developing stage tend to locate in southeastern side of the Line-1, although the formation positions of the decaying stage shift to inland (in the northwestern side of the Line-1) over the base of the peninsula. Cellular-echoes of the developing stage become the most intense between the base of the peninsula and Isahaya Bay, but concentrate in the northwestern side in Line-1.

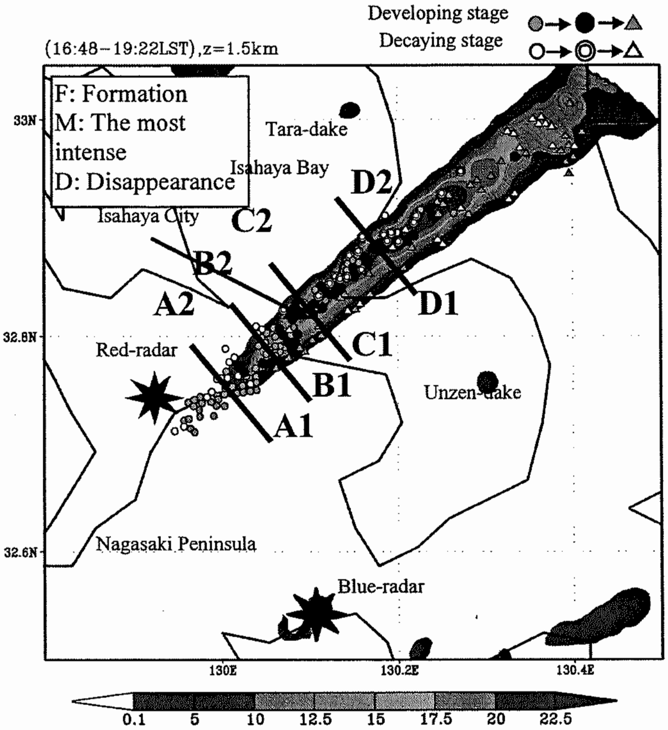

Figure 2 Horizontal distribution of radar-echo averaged from 1648 to 1922 LST on July 11 and positions of the formation, intensification and disappearance of each cellular-echoes. Black circles and dotted-triangles indicate the cellular-echoes of the developing stage and open circles and triangles indicate the cellular-echoes of the decaying stage.

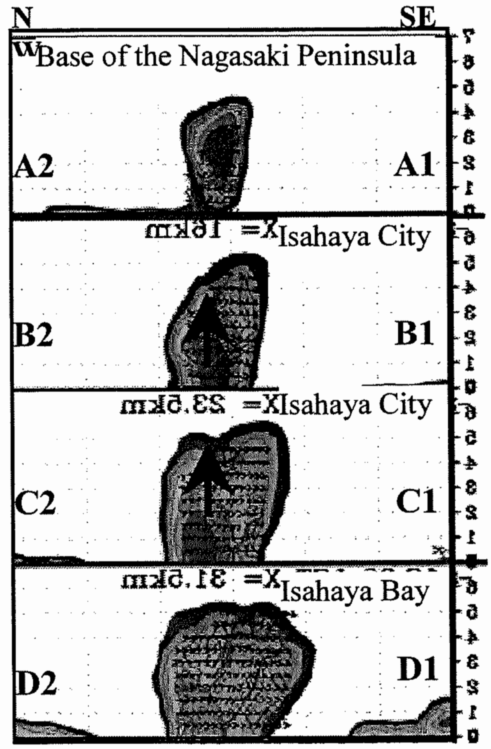

Figure 3 Time variations of the vertical structures of the cellular-echoes normal to the band

Figure 3 shows the time variations of the vertical structures of the cellular-echoes normal to the band. The intense echo regions are almost upright in the northwestern side in Line-1 and updrafts were also seen at the same place. However, there is no evident downdraft in any sections.

Three-dimensional distributions of airflows were observed by the dual-Doppler radars. The convergence and divergence zones extend widely over the several cellular-echoes along the radar-echo band in the northwestern side and the southeastern side, respectively. The distribution of the convergence zone around Isahaya City and Isahaya Bay consists with the formation or the most intense positions of the cellular-echoes. This convergence was evident during the developing stage.

3. NUMERICAL SIMULATION

To investigate the relationship between the structure and time variation of the line-system including its periodicity and the environment conditions, a non-hydrostatic model developed by the Meteorological Research Institute (Saito et al., 2001, JMA-NHM) was employed. The domains are shown in Fig. 4. The outer domain contains a horizontal resolution of 5 km with 500x500 grind points and the inner domain which contains a horizontal resolution of 1 km with 1000x1000 grind points is nested in the outer domain. RSM (Region Spectral Model) data of 0900 LST 11th 1997 is applied for the initial data.

Horizontal distribution of rainfall is shown in Fig. 5. The line-shaped system which extends along the Nagasaki Peninsula is well reproduced in the model. Figure 6 shows the time variations of the vertical structures of the convective clouds normal to the line-system. As shown in Fig. 6a, southerly winds near the surface are lifted along the southern slope of the Nagasaki Peninsula forming the orographic updraft. Fig. 6b and 6c, show that intense updrafts over 50 cm/s are seen in the northwestern side of the line-system. In Fig. 6b, weak downdraft is seen in the southeastern side of the line-system at z=1km level, however it doesn't reach the surface. This feature indicates the moist warm inflow from the south can be provided into the line-system without being cut-off by the downdraft. Another convergence zone is seen around Isahaya City at southern side (=upwind side) of Mt. Tara (Not shown). The upwind effect of Mt. Tara and the confluence of predominant ambient winds diverted by Mt. Tara and Mt. Unzen intensify this convergence zone. This convergence zone consists with the place where most of cellular-echoes observed by Doppler-radar are intensified.

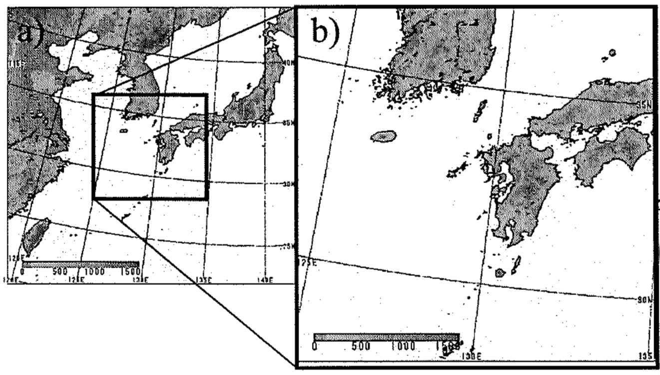

Figure 4 The domains for the numerical simulation. a) Outer-domain and b) Inner-domain.

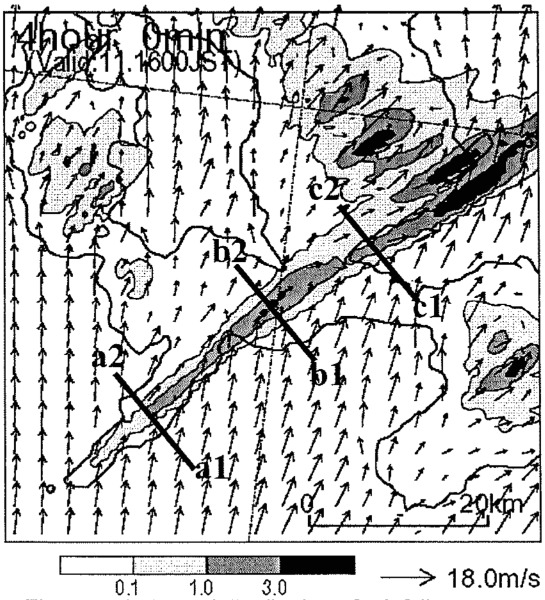

Figure 5 Horizontal distribution of rainfall. (Numerical simulation)

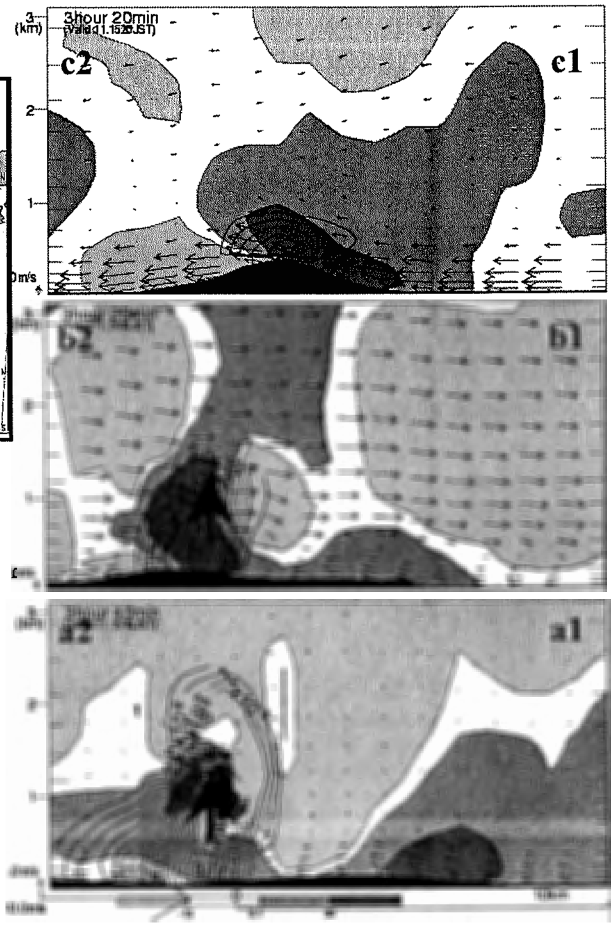

Figure 6 Time variations of the vertical structures of the cellular-echoes normal to the line. Counters indicate Rainwater mixing ratio and dense shaded areas indicate updraft, respectively.

4. SUMMARY

From 0900 LST on July 11 to 0300 LST on July 12, a long-lived line-shaped convective system was observed in the Nagasaki Peninsula. It maintained for about 18 hours almost in the same place to bring a huge rainfall. It had the periodicity of about 2-3 hours.

Three-dimensional structure of the line-shaped system and cellular-echoes of line-shaped system are investigated on the basis of radar-data. The line-shaped system was composed with many convective cells whose echo-tops were about 6 km. Most of them were formed successively around the base of the Nagasaki Peninsula, in the upwind side of the band and moved along its direction at a speed of 17 m/s. They became the most intense between Isahaya City and Isahaya Bay. The intense convergence and divergence zones are observed in the northwestern side and the southeastern side along the line, respectively. No evident downdraft was seen in the line-shaped system.

Numerical simulation reveals two convergence zones are formed at the southern sides of the Nagasaki Peninsula and Mt. Unzen by topography. The formation and intensification processes of the line-shaped system observed around the Nagasaki Peninsula are summarized as bellow.

1) Low-level southerly winds converged in the base of the Nagasaki Peninsula by the upwind effect of the peninsula. New convective clouds were formed and developed in this area and drifted to the downwind side.

2) In Isahaya Bay there was another convergence zone caused by the upwind effect of Mt. Tara and the confluence of predominant ambient winds diverted by Mt. Tara and Mt. Unzen. This convergence zone intensifies the activity of the convective clouds in the line-system.

Interestingly, there is no evident downdraft in the line-shaped system. The evaporation of precipitation near the surface isn't so significant because the lower atmosphere is very humid. This feature means that the moist atmosphere can be supplied into the line-shaped system without being cut-off by the downdraft.

5 ACKNOWLEDGEMENTS

This study is conducted by the fund of Research Revolution 2002, and the numerical calculations are made by NEC SX-6 on Earth Simulator.

6 REFERENCES

Fujiyoshi, Y., K. Tsuboki, S. Satoh and G. Wakahama, 1992: Three-dimensional radar-echo structure of a snow band formed on the lee side of a mountain. J. Meteor. Soc. Japan, 70, 11-24

Kanada, S., H. Minda, B. Geng and T. Takeda, 2000: Rainfall enhancement of band-shaped convective cloud system in the downwind side of and isolated island. J. Meteor. Soc. Japan, 78, 47-67

Kang, S.-D. and Fujio Kimura, 1997: A Numerical Study on the Mechanism of Cloud-Street Formation in the Lee of an Isolated Mountain Near a Coast. J. Meteor. Soc. Japan, 75, 955-968.

Saito, K., T. Kato, H. Eito and C. Muroi, 2001: Documentation of the Meteorological Research Institute / Numerical Prediction Division Unified Nonhydrostatic Model. Tech. Rep.of MRI, 42, p133.

Yoshizaki M., T. Kato, Y. Tanaka, H. Takayama, Y. Shoji, H. Seko, K. Arao, K. Manabe and Members of X-BAIU-98 Observation, 2000: Analytical and numerical study of the 26 June 1998 orographic rainband observed in western Kyushu, Japan. J. Meteor. Soc. Japan, 78, 835-856.

OCEANIC DIURNAL PRECIPITATING SYSTEMS OVER THE TROPICAL WESTERN PACIFIC, NORTH OF NEW GUINEA ISLAND

Masaki KATSUMATA and Kunio YONEYAMA

Japan Marine Science and Technology Center (JAMSTEC), Yokosuka 237-0061 Japan

1. INTRODUCTION

The tropical western Pacific is characterized by a high SST and so-called "warm pool". The accumulated warm water is one of the important factors of ENSO. The large amount of the precipitation over the warm pool provides fresh water and drives the surface water.

The one of the significant and important characteristics of the precipitation in the tropics is the diurnal cycle. Nitta and Sekine (1994) pointed out that the diurnal cycle of the cloud also exists over the tropical western Pacific Ocean. Chen and Houze (1997) pointed that the diurnal cycle is important factor in the MJO convection, which is active over the warm pool.

While many studies regarded the mechanisms of the diurnal cycle as the vertical one-dimensional processes, some other studies reported that the precipitating features propagate from the land to the ocean diurnally (e.g. Houze et al., 1981; Yang and Slingo, 2001; Mapes et al, 2003; Mori et al., 2004). In the tropical western Pacific, Liberti et al. (2001) revealed that the precipitation over the warm pool is affected by the land effect of New Guinea Island and other small islands. However, results of Liberti et al. (2001) were based on the infrared image from satellites, which sometimes do not reflect the behavior of the precipitating systems below the thick cloud.

In the past four years, we JAMSTEC was carried out the observational study of the equatorial precipitating systems and the ambient atmosphere over the warm pool by deploying our research vessel (R/V) *Mirai* at (2N, 138E) stationary for weeks to a month in the every boreal autumn or winter. In the present study, we investigated the diurnal cycle of the precipitating systems over the warm pool by using the data from the shipborne Doppler radar, which can detect the behavior of the precipitating systems directly.

Corresponding author's address:
Masaki KATSUMATA, Japan Marine Science and Technology Center, Natsushima-cho 2-15, Yokosuka 237-0061 JAPAN; E-Mail: katsu@jamstec.go.jp

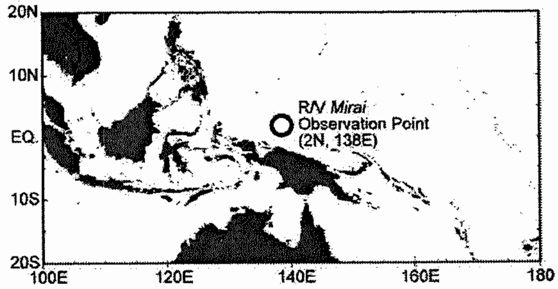

Fig. 1: The map around the R/V Mirai observation point (2N, 138E)

2. OBSERVATION POINTS AND PERIODS

The map around the observation point (2N, 138E) is shown in Fig. 1. The local time of the point is 9 hours ahead of UTC (LST = UTC + 9h).

The stationary observations of R/V *Mirai* at (2N, 138E) have been carried out in four boreal autumn / winter as shown in Table 1. The convectively active periods of MJO appeared in the observation period in MR00-K07, MR01-K05 and MR04-01. The convectively inactive periods appeared in MR00-K07, MR01-K05 and MR02-K06.

Year Code	Start End	Days	Characteristics
2000 MR00-K07	Nov.28 Dec.10	13	Incl. latter half of MJO active period
2001 MR01-K05	Nov.9 Dec.9	31	Incl. former half of MJO active period
2002 MR02-K06	Nov.22 Dec.12	21	All Inactive, but MJO signal passed over
2004 MR04-01	Mar.2 Mar.15	14	Incl. MJO active period

Table 1: The periods of the observations used in this study.

3. OBSERVATION INSTRUMENTS AND DESIGN

The principal meteorological instruments on R/V *Mirai* are a C-band (5-cm in wavelength) Doppler radar and a radiosonde launcher. The continuous observation of the C-band Doppler radar was carried out for every cruise, by repeating a cycle every 10 minutes. The cycle consisted of (1) surveillance PPI (at the elevation of 0.5 degree, for 200-km in range distance, to obtain reflectivity), (2) volume scan (at 21 elevations, for 120-km in range distance, to obtain reflectivity and Doppler velocity), and (3) optional RHIs (for 120-km in range distance to obtain reflectivity and Doppler velocity).

The radiosonde observations were carried out every 3 hours through each observation period. The pre-launch calibration procedures were in Yoneyama et al. (2002).

4. GENERAL DIURNAL CHARACTERISTICS

To extract the general characteristics on the diurnal cycle of the precipitation, we used the radar echo area with the reflectivity stronger than 15 dBZ in the surveillance PPIs at every 1 hour. The diurnal tendency is presented by the ratio of the snapshot echo area to the running mean for 25 hours, i.e.

$$R(h0) = A(h0) / \left(\sum_{h=h0-12}^{h0+12} A(h) / 25 \right) \qquad (1)$$

where *h0* is the target time, *R(h0)* is the ratio to obtain, *A(h)* is the radar echo area at the time *h*.

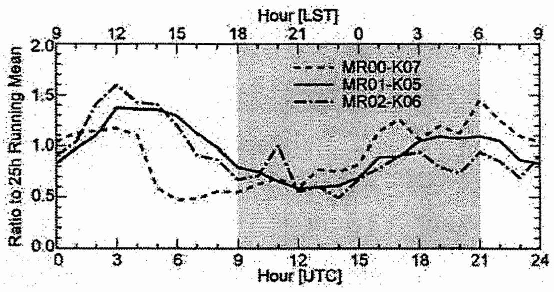

Fig. 2: Diurnal variation of the radar echo area (> 15 dBZ), represented by averaging the ratio to 25-h running mean (R in Eq.(1)) for each hour.

The averaged *R* for each hour and each observation period are in Fig. 2. The figure indicates two peaks at around local afternoon (12-15LT) and local midnight to dawn (3-6LT). Among the peaks, the former is larger in MR01-K05 (including convectively active period) and MR02-K06 (inactive period), while the latter in MR00-K07 (including both active and inactive period).

5. DETAILED CHARACTERISTICS OF THE CONVECTIVELY INACTIVE PERIOD

First we focus on the convectively inactive observation period in MR02-K06. On almost everyday in the period, the GMS (Geostationary Satellite) infrared images show that the clouds initiated from New Guinea Island and moved northward, as shown in Fig. 3. The figure also shows that the diurnal variation is also appeared on the radar echo area, corresponding to the northward-moving cloud.

One typical case is shown as the GMS IR images (Fig. 4) and radar echo images (Fig. 5). The GMS IR images (Fig. 4) indicate that the cloud aligned parallel to the northern coast of the New Guinea Island and moved northeastward. The radar echo images (Fig. 5) show that the organized linear-formed leading edge proceeded northeastward with the trailing stratiform echo. The radar observation revealed that the diurnal peak in the afternoon, at least in MR02-K06, was principally caused by such northward-moving precipitating systems.

In the observation period, the northward-moving precipitating systems did not pass over the vessel. However, the overcastting clouds and the change of wind direction were observed when such precipitating systems reached near the vessel.

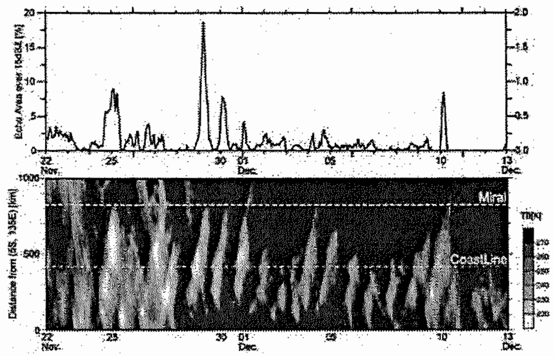

Fig. 3: Time series of the radar echo area (Upper panel), and time series of GMS IR-TB along the line orthogonal to the northern coast of New Guinea Island from (5S, 135E) to north, which averaged for the 500-km width (Lower panel). The time scale is same in both panels, from Nov.22 to Dec.13, in 2002 (MR02-K06). The dotted lines in the lower panel represent the positions of northern coast of New Guinea Island (lower) and R/V Mirai (upper), respectively.

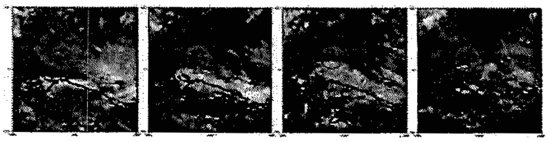

Fig. 4: GMS IR channel images from 18UTC on Nov.28 to 12UTC on Nov.29 with 6-hourly interval. The circle in each panel shows the radar observation range (200 km in radius).

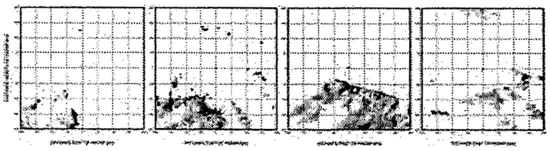

Fig. 5: PPI images for 200-km range (400 x 400 km) at (2N, 138.5E), from 00UTC to 09UTC on Nov.29 with 3-hourly interval (note: the time is not simultaneous to Fig. 4).

6. DETAILED CHARACTERISTICS OF THE CONVECTIVELY ACTIVE PERIOD

The diurnal variation of the precipitating activity was also observed in the MJO convectively active period by the Doppler radar. In MR01-K05, ten organized mesoscale convective systems (MCSs) (Fig. 6) passed over the vessel, with moving northward or eastward. Among these ten MCSs, six passed over the vessel in the afternoon, 12-17LST (03-08UTC), while three in the early morning, 05-08LST (20-23UTC), as shown in Fig. 7. These two time ranges well correspond to the diurnal peaks shown in Fig. 1.

The interesting difference between two groups is found in the internal structure. The results of EVAD analyses (Matejka and Srivastava, 1991) show that the most of the afternoon MCSs have dominant convergence around the 0-degC height, while the dominant convergence is in the lower layer for the other MCSs, as shown in Fig. 7. This difference indicated that the afternoon MCSs have the relatively well-developed melting convergence. The melting convergence is one of the indices of the development of the stratiform precipitating region.

The correspondence between this diurnal MCSs and large-scale disturbances are shown in Fig. 8. For the period, the westward-moving clouds, which are embedded in the eastward-propagating MJO convectively active region, can be seen in the Hovmellor diagram, as same in Chen and Houze (1997). However, four of the six afternoon MCSs did not collocated with the westward-moving clouds. This suggests that the diurnal cycle in the observation point has weak relationship to the westward-moving large-scale disturbances in MJO.

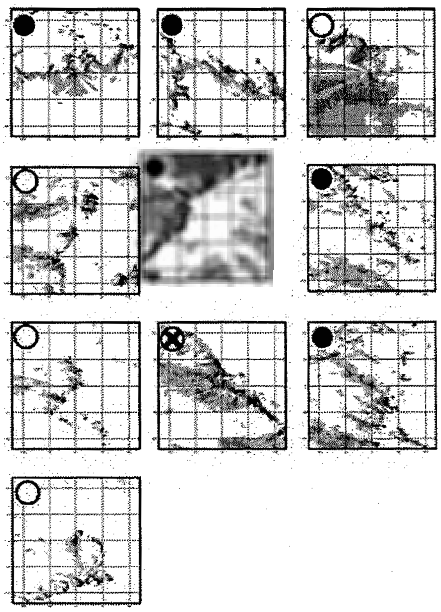

Fig. 6: PPI images for 120-km range (240 x 240 km) at (2N, 138E), for typical scenes of observed MCSs. The black and white circles represent the characteristics of vertical profile of divergence, calculated by EVAD analyses: The black circles are for MCSs which have dominant convergence around the melting level, while the white for others. The white circle with cross indicated the exceptional case, without dominant melting convergence but the time and form is similar to that of afternoon MCS.

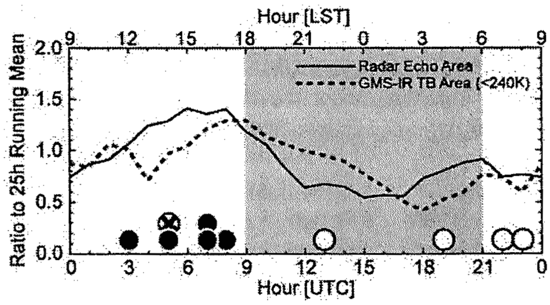

Fig. 7: Same as Fig. 1, but only for MR01-K05 convectively active phase. The solid and broken line are for radar echo area (>15dBZ) and GMS-IR low-TB (<240K) area, respectively. The black and white circles are same to Fig. 6, and are located at the time when each MCS passed over R/V Mirai.

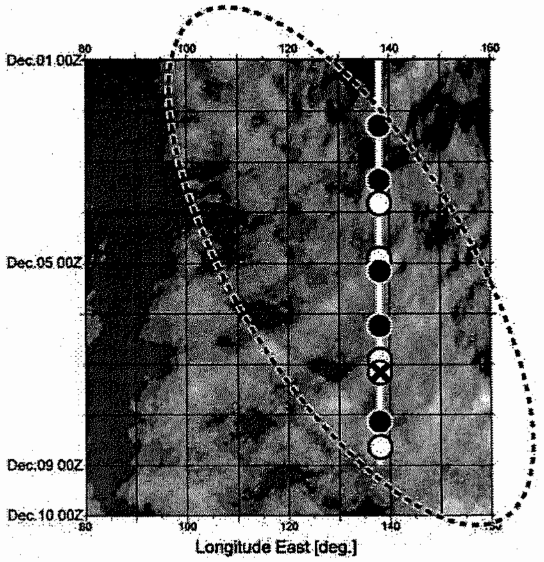

Fig. 8: The Hovmellor diagram of equatorial GMS IR-TB (averaged for 5S to 5N), for longitude in the abscissa (80E to 160E) and the time in the ordinate (downward from 00UTC on Dec.01 to 00UTC on Dec.10). The black and white circles are same to Fig. 6, and are located at the time when each MCS passed over R/V Mirai. The white vertical line indicates the observation point (2N, 138E). The oval indicates MJO signal which propagated eastward.

7. SUMMARY AND DISCUSSION

In the present study, the radar-derived precipitating area shows the diurnal cycle with the dominant peak in the local afternoon, in both convectively active and inactive periods. The afternoon peak was caused by the eastward- to northward-moving precipitating clouds. These are consistent with Liberti et al. (2001).

The diurnal precipitating signal with the afternoon peak was existed within the MJO convectively active period. Because the diurnal peak did not always correspond to the passage of large-scale disturbance, it is implied that the diurnal cycle in the convectively active period also affected by the local effect around the observation point.

The internal structure of the diurnal precipitating clouds in this region, north of New Guinea Island, is also revealed. The afternoon diurnal peak was made by organized MCSs with well-developed strafiform region. The dominating convergence is at the 0-degC height in the afternoon MCSs, while in the lower height in the other MCSs. These imply that the circulation around the stratiform precipitating region is a key in the diurnal precipitating systems in the region.

The further study is required to reveal the mechanism of these propagating diurnal precipitating systems over the warm pool, and in the vicinity of the other landmasses.

[ACKNOWLEDGMENTS]

The authors would like to express their thanks to the Captains M. Akamine and T. Hashimoto and their crews of R/V *Mirai*, and the technical staff of the Global Ocean Development Inc., for their skillful operations of the vessel and the instruments.

[REFERENCES]

Chen, S. S., and R. A. Houze, Jr., 1997: Diurnal variation and life-cycle of deep convective systems over the tropical Pacific warm pool. *Q. J. R. Meteor. Soc.*, **123**, 357-388.

Houze, R. A., Jr., S. G. Geotis, F. D. Marks, and A. K. West, 1981: Winter monsoon convection in the vicinity of north Borneo. Part I: Structure and time variation of the clouds and precipitation. *Mon. Wea. Rev.*, **109**, 1595-1614.

Liberti, G. L., F. Cheruy and M. Desbois, 2001: Land effect on the diurnal cycle of clouds over the TOGA COARE area, as observed from GMS IR data. *Mon. Wea. Rev.*, **129**, 1500-1517.

Matejka, T., and R. C. Srivastava, 1991: An improved version of the extended velocity-azimuth display analysis of single-Doppler radar data. *J. Atmos. Oceanic Technol.*, **8**, 453-466.

Mapes, B. E., T. T. Warner, M. Xu, and A. J. Negri, 2003: Diurnal patterns of rainfall in northwestern South America. Part I: Observations and context. *Mon. Wea. Rev.*, **131**, 799-812.

Mori, S., Hamada J.-I., Y. I. Tauhid, M. D. Yamanaka, N. Okamoto, F. Murata, N. Sakurai, H. Hashiguchi, and T. Sribimawati, 2004: Diurnal land-sea rainfall peak migration over Sumatera Island, Indonesian maritime continent observed by TRMM satellite and intensive rawinsonde soundings. *Mon. Wea. Rev.*, in press.

Nitta, Ts., and S. Sekine, 1994: Diurnal variation of convective activity over the tropical western Pacific. *J. Meteor. Soc. Japan*, **72**, 627-641.

Yang, G.-Y., and J. Slingo, 2001: The diurnal cycle in the tropics. *Mon. Wea. Rev.*, **129**, 784-801.

Yoneyama, K., M. Hanyu, S. Sueyoshi, F. Yoshiura and M. Katsumata, 2002: Radiosonde observation from the ship in the tropical region. *JAMSTECR*, **45**, 31-39.

THE LIFE CYCLE OF CONVECTIVELY GENERATED STRATIFORM CLOUDS

Steven K. Krueger*, Michael A. Zulauf, and Yali Luo

University of Utah, Salt Lake City, Utah, USA

1. INTRODUCTION

Observations show that cirrus clouds are often produced by convective cloud systems. Figure 1 is a schematic of the life cycle of a convective system that is consistent with satellite observations of convective systems. The fraction of a grid cell occupied by anvil clouds is largely determined by the history of the clouds, so that a prognostic cloud fraction parameterization is appropriate. Such an approach was first developed by Tiedtke (1993). To date, these methods have not been examined using cloud-resolving models (CRMs) or tested against observations except indirectly using global, monthly averaged datasets

We used the University of Utah (UU) 2D cloud-resolving model (CRM) to study the cirrus clouds that result from the life cycle of convective cloud systems. (1) We analyzed a 29-day simulation based upon Case 3, a joint GCSS and ARM intercomparison project (Xu et al. 2002, Luo et al. 2003). (2) We performed a variety of idealized 2D and 3D CRM simulations of the life cycle of anvil clouds to study the physical processes that determine the cloud fraction of anvil clouds.

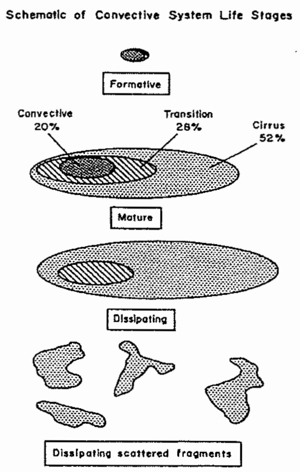

Figure 1: Schematic of the life cycle of a convective system. [From Machado and Rossow (1993).]

*Corresponding author address: Department of Meteorology, University of Utah, Salt Lake City, UT 84112. E-mail: skrueger@met.utah.edu

2. REALISTIC SIMULATION

The UU 2D CRM was used to simulate the full life-cycle of cumulus convection, in which cirrus anvils were generated by deep convection, for Case 3. Figure 2 displays a sequence of hourly simulated hydrometeor reflectivity snapshots that shows the formation of an anvil. Each panel is a $x - z$ cross-section 512 km x 16 km in extent.

Figure 3 is a Hovmuller diagram of ISWP (cloud ice and snow water path) for a 14-h period from the Case 3 simulation. In the simulated anvils, snow represents larger, precipitating ice crystals (Luo et al. 2003). Figure 4 shows the corresponding co-evolution (trajectory) of the cloud fraction and ISWP in the Case 3 simulation.

Pixel-level cloud products for the ARM SGP site (Minnis et al. 2001) provide observational insight into the relationships between cloud amount and large-scale ISWP for anvil cirrus clouds, and are also useful for model evaluation. Figure 5 plots large-scale high cloud amount versus ISWP from the Case 3 simulation and from the corresponding pixel-level cloud products. The results are quite similar, which suggests that the simulation is realistic in this aspect. The results also clearly demonstrate that there is not a general diagnostic relationship be-

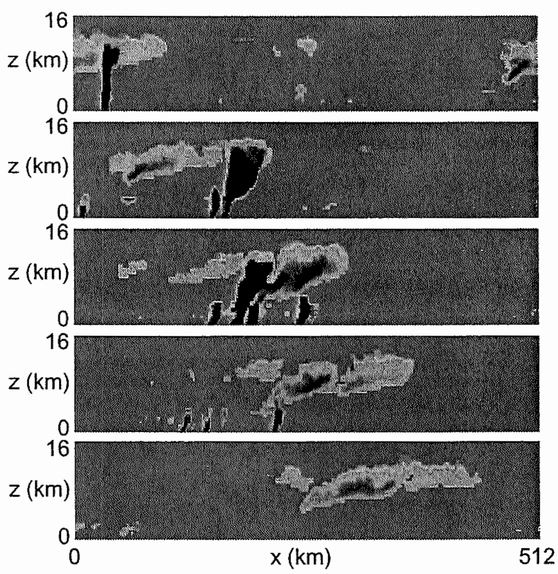

Figure 2: Sequence of hourly simulated reflectivity snapshots of all hydrometeors. Black is > 20 dBZ; the color/grayscale range is from -60 to +20 dBZ.

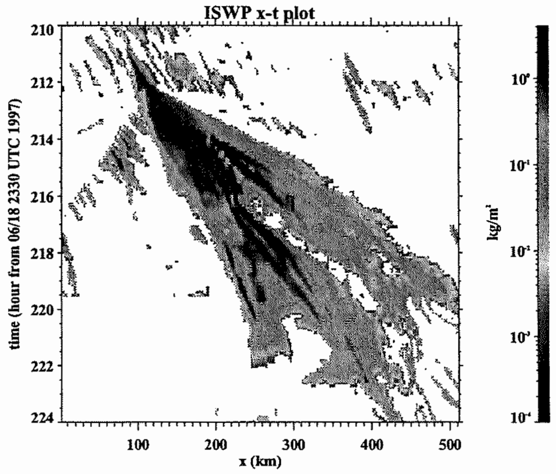

Figure 3: Hovmuller diagram of ISWP for a 14-h period from the Case 3 simulation.

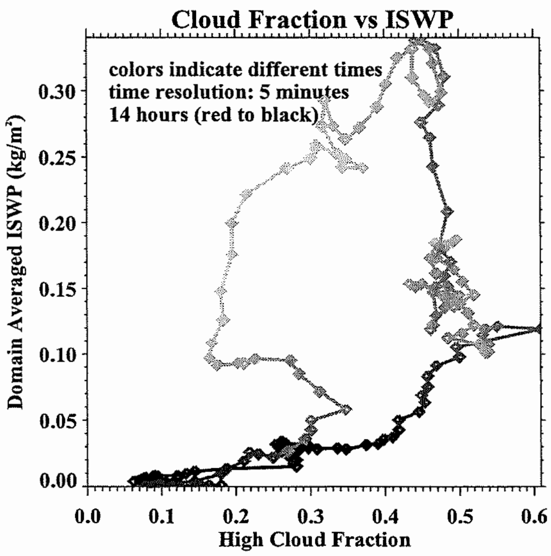

Figure 4: Trajectory of high cloud amount and domain-averaged ISWP for the period shown in Fig. 3.

tween large-scale cloud amount and IWP for anvil cirrus clouds, at least not at these time (3-h) and space (300-km) scales.

3. IDEALIZED SIMULATIONS

In these simulations, we represented the generation of cirrus anvils by detrainment from deep convection by adding ("injecting") cloud ice in a layer between 9 to 11 km height and in a sub-region of the domain over a time period of 6 hours. The horizontally averaged rate of ice addition was 0.067 kg m^{-2} h^{-1} for most runs. We ran

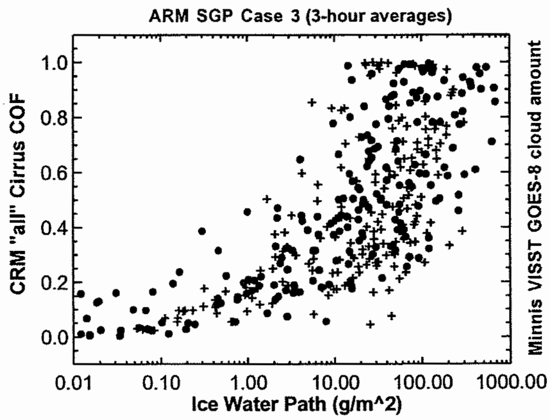

Figure 5: Cloud amount versus ISWP for CRM (blue +) and Minnis pixel-level data (red •) for Case 3.

each simulation for a total of 18 hours. We ran more than 40 2D simulations, with a 200 m grid size in both the horizontal and vertical directions, a spatial domain 51.2 km long and 18.2 km high, and cyclic lateral boundary conditions.

Figure 6 shows that when ice is injected into 25% of the domain, the cloud spreads to cover 50% by 3 h and 90% by 6 h. In a corresponding 3D simulation using the UU 3D CRM (Zulauf 2001), the cloud spread as it did in the 2D simulation. In a 3D simulation with ice injected in a circular region, the cloud spread radially outward.

Figures 7 and 8 show that trajectories of cloud fraction and IWP from ten of the idealized simulations have the same characteristic features as the trajectories in Fig. 4 from the realistic simulation described in the last section. The curves labeled i44 and i45 in Fig. 7 correspond to the results shown in Fig. 6.

The Hovmuller diagrams of ISWP in Fig. 9 show the spread of anvil cloud for 8 idealized simulations. From these results, we conclude that:

- There is no spread without radiative heating, except when vapor instead of ice is injected.
- Mesoscale motions are required for spreading.
- Cloud-scale motions and/or turbulence are NOT required for spreading.
- Solar radiation does not reduce the spreading.

4. CONCLUSIONS

There are two major conclusions from these simulations:

1. A general diagnostic relationship between cloud fraction and ISWP does not exist. However, there is a diagnostic relationship in the final decay stage. This suggests that a prognostic approach is generally required to determine cloud fraction for convectively generated cirrus.

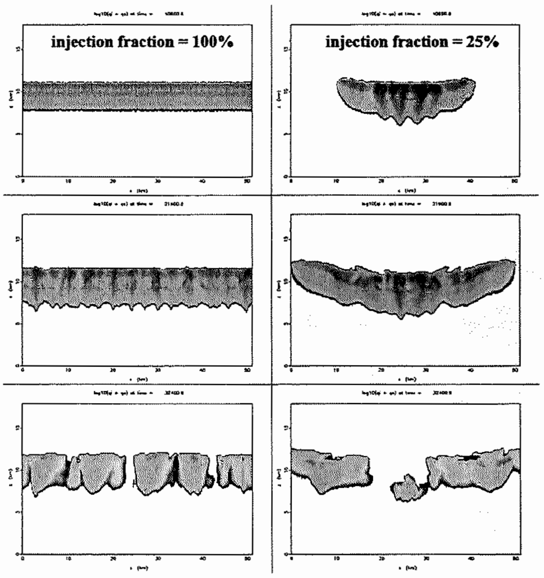

Figure 6: Cloud ice plus "snow" fields at 3, 6, and 9 h for two simulations with different injection fractions.

2. A mesoscale circulation that spreads the cloud horizontally at about 1 m/s is generated within the cirrus anvil by horizontal gradients of radiative heating at the cloud edges. As the cloud spreads due to the mesoscale circulation, the radiative heating gradients also spread. The result is a positive feedback that lasts as long as there is a sufficient cloud ice. This spreading mechanism has not been previously reported.

ACKNOWLEDGMENTS. This research was supported by NASA Grant NAG5-11504 and by the Environmental Sciences Division of the U.S. Department of Energy (DOE) as part of the Atmospheric Radiation Measurement program under Grant DE-FG03-94ER61769.

REFERENCES

Luo, Y., S. K. Krueger, G. G. Mace, and K.-M. Xu, 2003: Cirrus cloud statistics from a cloud-resolving model simulation compared to cloud radar observations. *J. Atmos. Sci.*, **60**, 510–525.

Machado, L. A. T., and Rossow, W. B., 1993: Structural characteristics and radiative properties of tropical cloud clusters. *Mon. Wea. Rev.*, **121**, 3234–3260.

Minnis, P., and 8 coauthors, 2001: A near-real time method for deriving cloud and radiation properties from satellites for weather and climate studies. *Proc. AMS 11th Conf. Satellite Meteorology and Oceanography*, Madison, WI, Oct. 15-18, 477-480.

Tiedtke, M., 1993: Representation of clouds in large-scale models. *Mon. Wea. Rev.*, **121**, 3040–3061.

Xu, K.-M., and 15 coauthors, 2002: An intercomparison of cloud-resolving models with the Atmospheric Radiation Measurement summer 1997 Intensive Observation Period data. *Q. J. Roy. Meteor. Soc.*,**128**, 593–624.

Zulauf, M. A., 2001: Modeling the effects of boundary layer circulations gener-ated by cumulus convection and leads on large-scale surface fluxes. Ph.D. dissertation, University of Utah, Salt Lake City, 177 pp. `<www.met.utah.edu/skrueger/publications/zulauf_dissert_2001.pdf>`

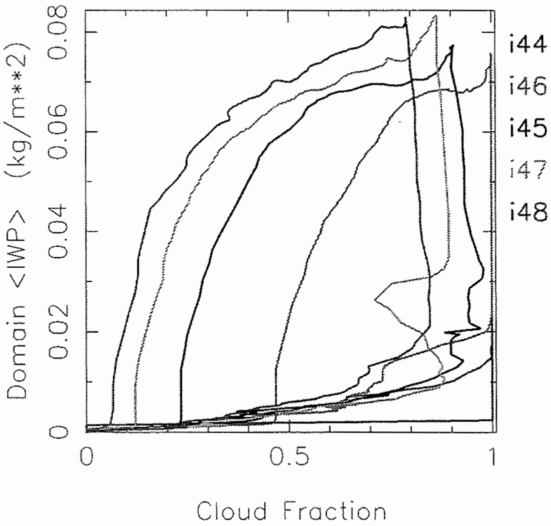

Figure 7: Trajectories of cloud amount and average ice water path for simulations with various injection fractions.

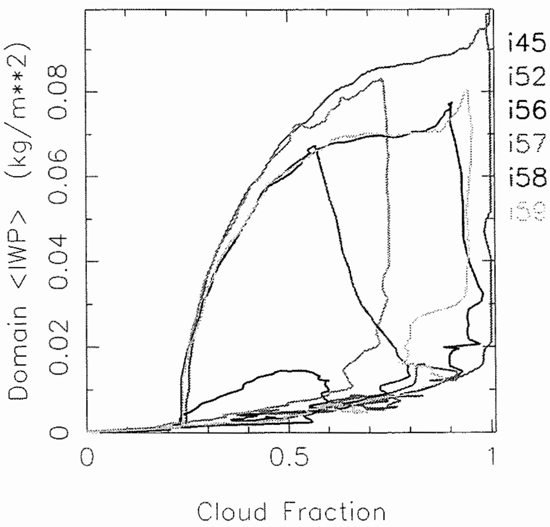

Figure 8: Trajectories of cloud amount and average ice water path for simulations with various injection rates, injection periods, environmental humidity, etc.

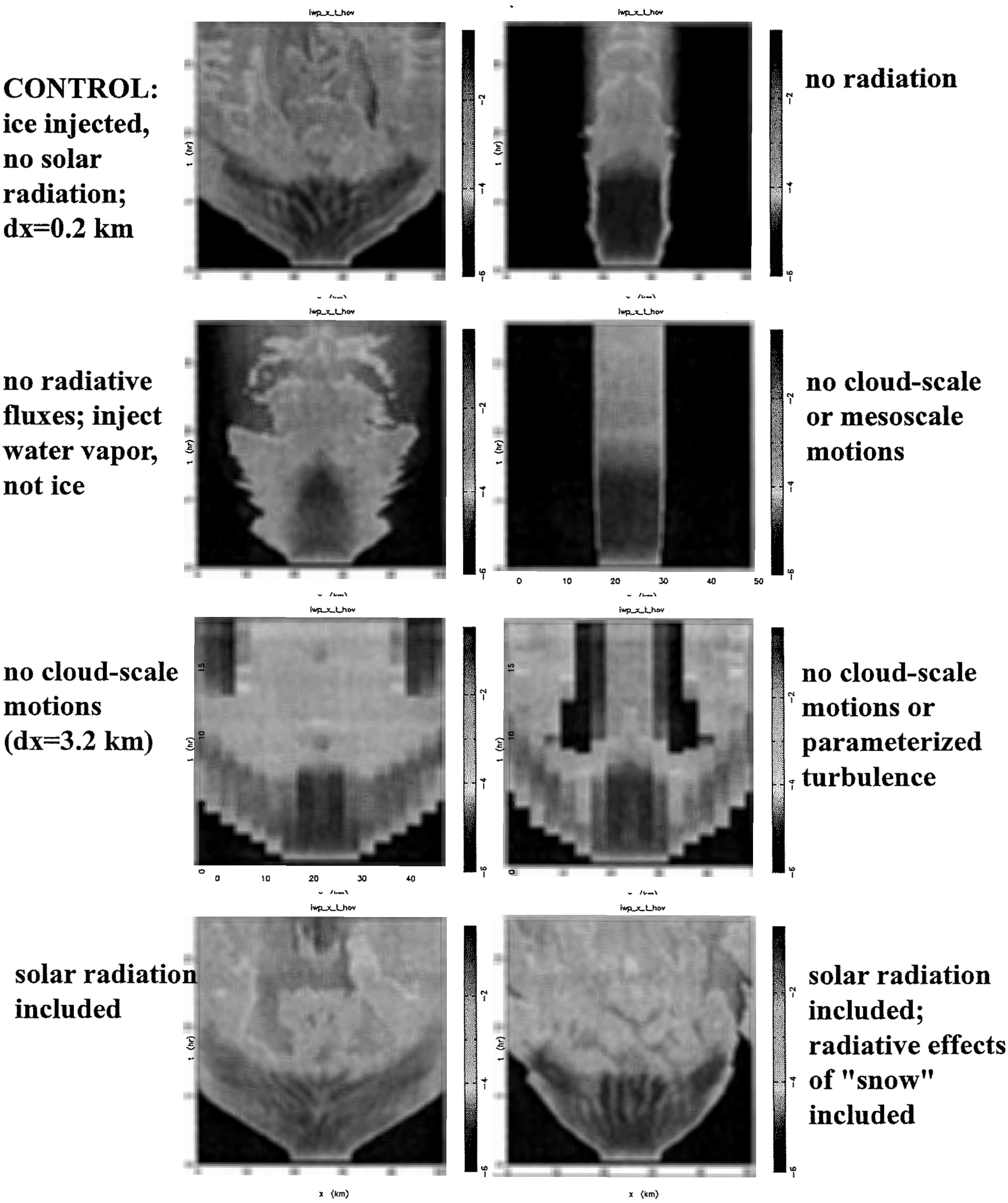

Figure 9: Hovmuller diagrams of ISWP (kg m^{-2}) for 8 idealized simulations.

STRUCTURE OF LWC AND TEMPERATURE FIELDS IN SMALL CUMULUS CLOUDS SEEN FROM STATIONARY (TETHERED BALLOON) AND MOVING (AIRCRAFT) PLATFORMS.

Marcin Kurowski[1], Holger Siebert[2], Krzysztof E. Haman[1] and Szymon P. Malinowski[1]

[1]Warsaw University, Institute of Geophysics, Warsaw, Poland
[2]Institute for Tropospheric research, Leipzig, Germany

1. INTRODUCTION

An intensive field campaign (BBC2) aimed at investigation of microphysical, radiative and dynamical properties of the boundary layer clouds has been performed in Holland in May 2003. Among many in-situ and remote sensing systems participating, there were research aircrafts and a balloon-borne instrumental platform. Meteo-France Merlin V aircraft as well as ACTOS balloon-borne system (Siebert et al., 2003) were equipped with the fast response temperature sensors UFT (Haman et al., 2001) allowing for measurements of temperature fluctuations in cloudy and cloudless air with resolution down to few centimeters. Additionally, high resolution liquid water content (LWC) measurements with PVM-100 probe (Gerber et al., 1994) have been performed. ACTOS platform was also equipped with the ultrasonic anemometer/thermometer, from which high resolution measurements of turbulent flow were possible.

In the present preliminary study we compare high resolution measurements of temperature from the board of the Merlin aircraft and tethered balloon borne ACTOS platform in order to investigate the influence of the platform on the recorded data series. We also analyze high resolution LWC records from ACTOS.

Tethered balloon platform is almost Eulerian in a sense that its position is fixed in space. Usually Taylor "frozen flow" hypothesis is adopted in order to analyze time series from such a platform. In the experimental data investigated here, mean horizontal wind speed calculated from the ultrasonic anemometer was about 8m/s with turbulent velocity fluctuations in range +/- 2m/s. Such big variability of the wind speed suggests, that in this case application of the Taylor hypothesis may be questionable.

Aircraft data, collected at about 100m/s true air speed, value order of magnitude greater than the wind velocity can be treated as surrogates of "snapshots" i.e. Eulerian spatial series.

In the following section results from the statistical analysis of the records is presented. We show power spectral density and 2[nd], 4[th] and 6[th] order structure functions of LWC and temperature fluctuations in clouds from:

a) ACTOS platform, uncorrected for the wind velocity fluctuations (processed with use of Taylor hypothesis;

b) ACTOS platform, corrected for the local fluctuations of the wind velocity

c) Merlin aircraft

Conclusions are presented in the last section of this extended abstract.

Corresponding author address:
Marcin Kurowski, Warsaw University, Institute of Geophysics, ul. Pasteura 7, 02-093 Warsaw, Poland;
e-mail: mkuro@igf.fuw.edu.pl

2. RESULTS.

Due to air traffic limitations and safety reasons simultaneous measurements with aircraft and balloon borne platform were not possible. Thus, there is no data for the direct comparison of the aircraft and ACTOS measurements. The only way to compare platforms is the statistical analysis of fluctuations of temperature and LWC recorded in comparable conditions: shallow boundary layer developing cumuli in cold, marine air entering Holland flatland. For the aircraft measurements the highest quality data were collected during flight 13, May 10[th] around 13:45 local time, for the ACTOS platform best data were collected on May 21[st] around noon local time. These data were chosen to analyze for the purpose of this abstract.

In Fig.1. example result of the statistical analysis of LWC recorded by ACTOS in a small cumulus cloud is presented. In Fig. 2 results of the analogical analysis of temperature fluctuations are given. Both LWC and temperature records have been collected in the same shallow cloud at height of 765+/-10m above the ground level. The sampling frequency of the data was 100Hz, which corresponds to about 8 cm spatial resolution. Environmental temperature at this level was about 6^{0}C, in cloud temperature reached 6.8^{0}C and LWC was 0.4g/kg.

From LWC recordings two data series in the spatial domain were constructed. The first one was obtained with use of Taylor hypothesis, where conversion from temporal to spatial space was obtained by simple multiplication of time intervals by a mean wind speed. Such a series is hereafter referred as TH type. The second series resulting from point after point multiplication of time interval by corresponding actual flow velocity, it is hereafter referred as TR(-ue) type.

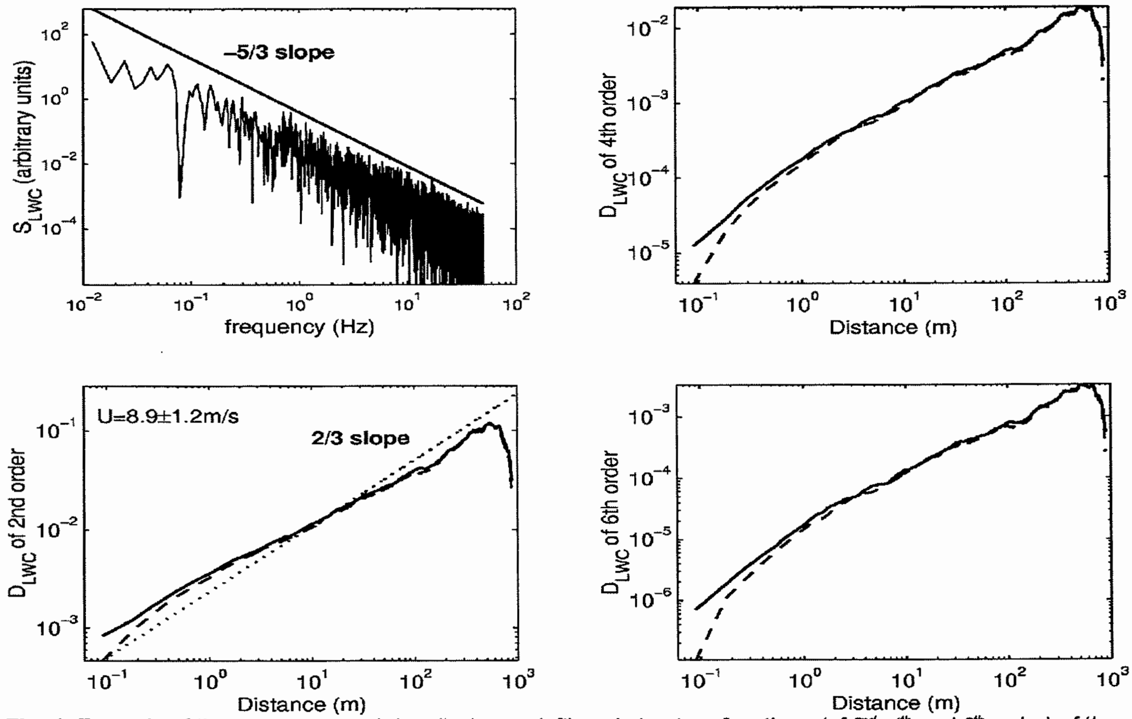

Fig. 1. *Example of the power spectral density (upper left) and structure functions (of 2nd, 4th and 6th order) of the LWC recorded in boundary layer cumuli with ACTOS platform. Continuous lines represent series obtained with use of Taylor hypothesis (TH), dashed lines represent data corrected for turbulent velocity fluctuations (TR). More details in the text.*

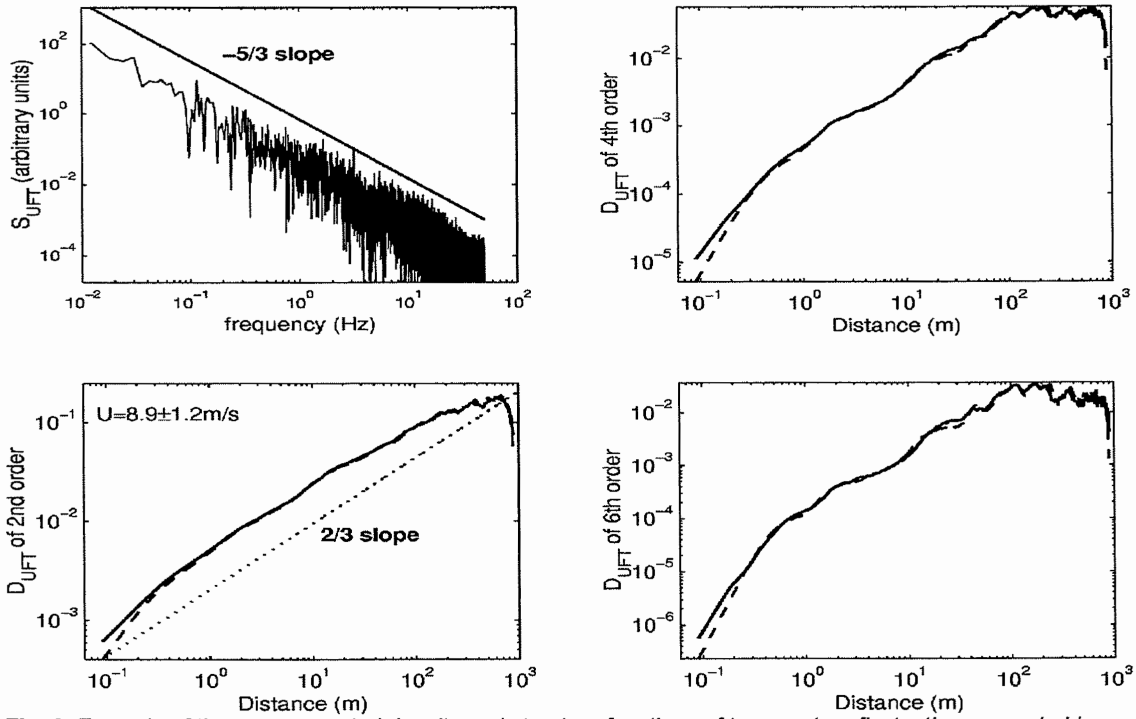

Fig. 2. *Example of the power spectral density and structure functions of temperature fluctuations recorded by ACTOS platform. Plots similar to Fig. 1.*

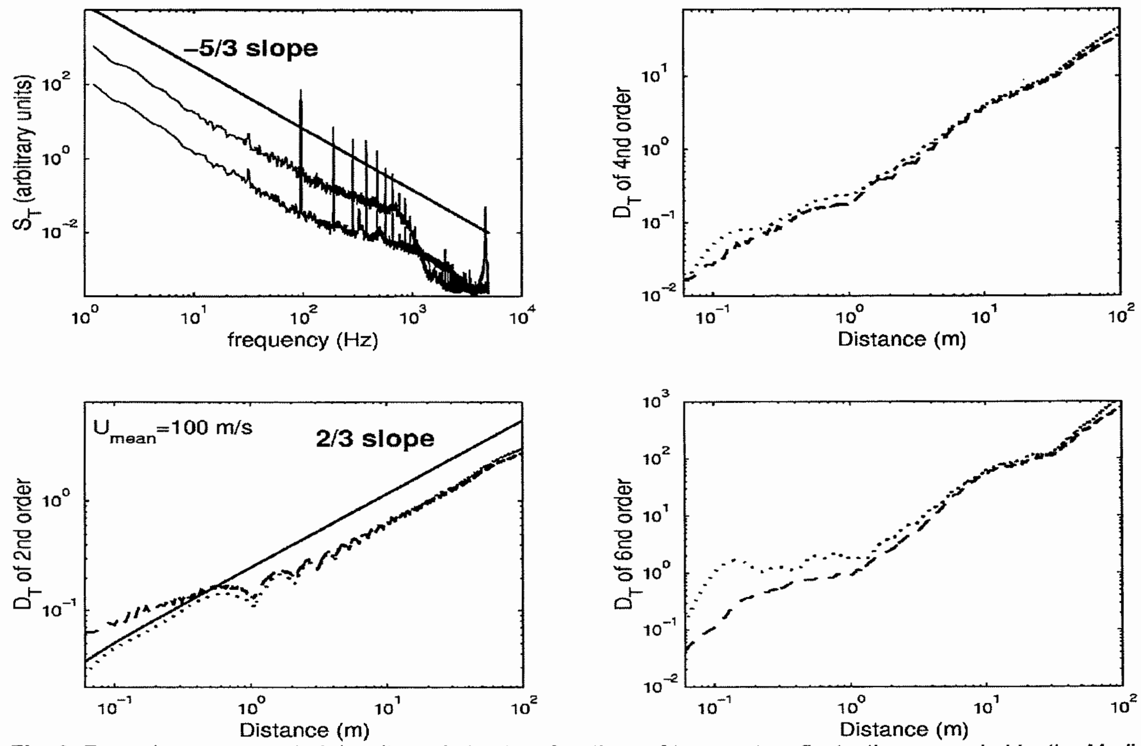

Fig. 3. *Example power spectral density and structure functions of temperature fluctuations recorded by the Merlin aircraft with two UFT sensors: UFT1 (lower line in the upper left panel and dashed lines in other panels) and UFT2 (remaining lines). UFT 2 data are filtered with 1000Hz lowpass filter. Spikes on the power spectrum and corresponding fluctuations in structure functions are artifacts due to the electric noise in the aircraft.*

Then, both series were analyzed with use of Fast Fourier Transform (power spectral density) and structure functions. Results are plotted in Fig.1, with the power spectrum in the upper left corner (1 Hz corresponds to 8m wavelength), second order structure function in the lower left corner, fourth and sixth order structure functions in the upper right and lower right corners, respectively.

Power spectral density of TH and TR type series were almost identical and for the sake of clarity only TH data are plotted in adequate panels in Figs 1 and 2. -5/3 slope is plotted as a reference. The relatively high noise level results from small fluctuations of temperature. It seems, that power spectral density of temperature and LWC is in accordance with -5/3 scaling.

While there was no differences in power spectra, structure functions of TR and TH type exhibit substantial differences in small scales. It seems, that adoption of Taylor hypothesis extends scaling range of structure functions towards small scales. Second order structure function of LWC seems to scale with smaller scaling exponent than temperature. Temperature in the range from 1m to 100m scales according to 2/3 power law.

In Fig.3 aircraft temperature measurements collected at the altitude of about 1900m during penetration of developing cumulus cloud are presented. Liquid water content in this cloud was about 0.4g/kg, the environmental temperature was -2°C, similar to the mean temperature within the cloud. Temperature from two UFT sensors was recorded at 10kHz frequency, giving theoretically 1 cm spatial resolution. Due to thermal inertia of the sensor and lowpass filtering of the output the real spatial resolution was about 5cm, i.e. close to this from the ACTOS platform. In Fig.3 statistical properties of temperature fluctuations are presented.

Effects of electric noise on the board of the aircraft, which in standard low frequency (up to 200Hz) recordings is filtered out, spoils the data in high resolution. However, in the range of scales from 1m to 100m temperature power spectrum scales according to -5/3 power law and the second order structure function scales according to 2/3 power law, like in the data from ACTOS platform. Higher order structure functions of temperature from ACTOS and Merlin have similar bump in few tens of meters.

3. CONCLUSIONS.

Presented results indicate that Taylor hypothesis works in the investigated ACTOS data. Power spectra and structure functions obtained with its use (TH series) and corrected for the velocity fluctuations (TR series) are similar in the scales above 1m. In smaller scales differences between TF and TR series are visible, resulting in smaller scaling range in corrected signal.

Temperature power spectra and structure functions recorded at the ACTOS platform and at the Merlin aircraft have similar properties in the range of scales from 1m to 100m. Due to electric noise problem it is not possible to make valuable comparison in smaller scales.

Scaling properties of LWC observed from the ACTOS platform look very interesting. While power spectra scale with -5/3 power law, the second order structure function scales with the exponent significantly smaller than expected 2/3. Such behavior have been noticed in other data series not presented in this abstract.

4. ACKNOWLEDGMENTS

Participation of the Atmospheric Physics Division, Institute if Geophysics, Warsaw University in BBC2 campaign was supported by European Commission V-th Framework program project EVK2-CT2002-80010-CESSAR. We wish to thank the crew of Meteo-France Merlin aircraft for assistance and help with solving technical problems.

6. REFERENCES:

Gerber, H., B.G. Arends, and A.S. Ackerman, 1994: A new microphysics sensor for aircraft use. *Atmos. Res.*, **31**, 235- 252.

Haman, K.E., S.P. Malinowski, B. Strus, R. Busen, and A. Stefko, 2001: Two new types of ultra-fast aircraft thermometer. *J. Atmos. Oceanic. Technol.,* **18**, 117-134.

Siebert H., M. Wendisch, T. Conrath, U. Teichmann, and J. Heintzenberg, 2003: A new tethered balloon-borne payload for fine-scale observations in the cloudy boundary layer. *Boundary Layer Meteorolol.,***106** (3): 461-482

HUMIDITY CHARACTERISTICS IN THE DETRAINMENT REGION OF SMALL CUMULUS

Neil F. Laird, Robert M. Rauber, and Harry T. Ochs

Department of Atmospheric Sciences, University of Illinois at Urbana-Champaign, Illinois, USA

1. INTRODUCTION

The environment in which cumulus clouds grow is continuously modified by transport of energy, moisture, and aerosol from below cloud base to the detrainment regions of clouds. Significant enhancements to humidity, above that in the undisturbed, cloud-free environment, have been observed in the near-cloud detrainment region of cumulus clouds (e.g., Malkus 1949, Ackerman 1958; Radke and Hobbs 1991; Perry and Hobbs 1996, Lu et al. 2002, Lu et al. 2003). What role might these regions of enhanced humidity play towards providing preferred locations for subsequent cloud development and might they contribute to the processes important to the rapid onset of precipitation in small tropical cumulus clouds? Telford and Wagner (1980) presented some observational evidence that suggested high humidity regions (i.e., cloud halos) represent preferred areas for new cloud development.

Although previous observational studies have established the existence of an enhanced region of humidity in the area surrounding cumulus clouds, a large sample of clouds has not been used to thoroughly characterize the horizontal and radial humidity distribution in the cumulus detrainment region. Using 203 aircraft penetrations of 31 cumulus clouds, the largest sample to date, Perry and Hobbs (1996) found humidity halos broaden with cloud age and their frequency and average size is directly related to the orientation relative to the vertical wind shear.

Using their observations and findings from previous studies (e.g., Malkus 1949, Ackerman 1958), Perry and Hobbs (1996) proposed a conceptual model describing the structure of the detrainment region (i.e., humidity halo) surrounding small to medium cumulus clouds. Initially, air is detrained from the cloud uniformly in all directions at levels where the in-cloud buoyancy decreases with height. However, vertical wind shear results cloud growth on the upshear side and decay on the downshear side. This pattern of growth results in an enlargement of the enhanced humidity region on the downshear side of the cloud and limits the width of the humidity halo on the upshear side. The humidity enhancement regions in the cross-shear directions are equidistant and have radial widths less than the downshear direction.

A goal of our current research is to develop a better understanding of and quantify the moisture and turbulence characteristics of the cumulus detrainment region to provide new information applicable to areas of cloud edge mixing, cloud radiative properties, cumulus exchange with the large-scale ambient environment, and cloud impact on subsequent particle and cumulus formation. This article briefly describes our investigation and results toward understanding the characteristics of the humidity halo of small cumulus clouds using a large dataset of aircraft penetrations from the Small Cumulus Microphysics Study.

2. DATA & METHODS

The Small Cumulus Microphysics Study (SCMS) was conducted in July-August of 1995 along the east-central coast of Florida (i.e., in the vicinity of Cape Canaveral). The objective of SCMS was to investigate the initial development and early evolution of warm cumulus clouds, specifically addressing 1) the onset of precipitation, 2) the evolution of droplet and raindrop size distributions, and 3) the processes of entrainment and mixing. It is important to note that the small cumulus clouds sampled during SCMS developed in similar ambient thermodynamic environments that were systematically documented on each project day using aircraft and rawinsonde measurements. Aircraft soundings collected following take-off and prior to landing on each flight provided vertical profiles of humidity, stability, and wind shear in the undisturbed ambient environment.

Aircraft measurements from 12 flights of the NCAR C-130 during SCMS and a total of 471 cumulus cloud penetrations were used to examine the characteristics of humidity halos. Within the cloud-free detrainment region surrounding a cloud, the humidity approaches the value of the undisturbed environment as the distance from the cloud increases. For purposes of our investigation, the cloud edge is defined using total particle concentration measurements from the forward scattering spectrometer probe (FSSP). A threshold value of 10 cm^{-3} was consided the cloud boundary. Similar to Perry and Hobbs (1996), the horizontal extent of the humidity halo is represented by the e-folding distance prior to and following cloud penetration. The e-folding distance is determined through a comparison of the average in-cloud absolute humidity with the absolute humidity of the undisturbed environment at the height of each aircraft

Corresponding author's address: Neil F. Laird, Dept. of Atmospheric Sciences, University of Illinois, Urbana, IL 61801, USA; e-mail: n-laird@uiuc.edu

cloud penetration. The e-folding distance is defined as the distance from the cloud boundary where the measured absolute humidity decreases to, and remains below, the e-folding absolute humidity (ρve), where ρve is defined by

$$\rho ve(z) = \bar{\rho}vc(z) - \{[\bar{\rho}vc(z) - \bar{\rho}venv(z)] \times (1 - e^{-1})\}$$

and $\bar{\rho}vc(z)$ and $\bar{\rho}venv(z)$ are the average absolute humidities of the cloud and the undisturbed ambient environment at the height of the aircraft penetration (z), respectively. Figure 1 presents an example of data from a SCMS cloud penetration and shows an extension of the cloud humidity halo in the downshear direction with no evidence of a halo in the upshear direction.

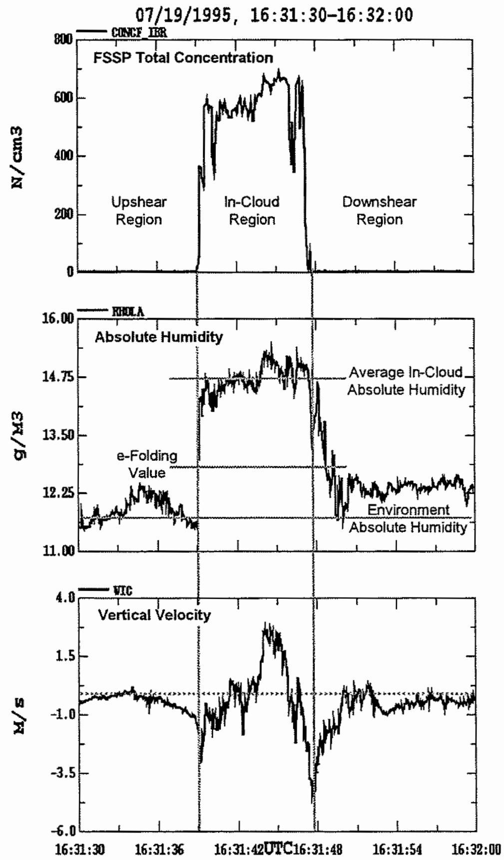

Figure. 1 Sample data from a NCAR C-130 aircraft cloud penetration demonstrating the procedure used to determine the width of the humidity halo in the near-cloud environment.

3. RESULTS

The vertical wind shear within the ambient environment generally had values less than ± 2 m s^{-1} km^{-1} on each of the SCMS project dates used for our analyses. Such weak vertical wind shear environments pose a challenge when examining the relationship of radial distribution of the humidity halo to vertical wind shear. Results suggest that these low values of environmental wind shear may cause the cloud age to be the most significant factor in determining the width of the cloud humidity halo. In a stronger wind shear environment over the Pacific Ocean west of the Washington and Oregon coastlines, Perry and Hobbs (1996) found vertical wind shear to be the most dominant factor in determining halo width and cloud age a secondary factor.

The average humidity halo width for all SCMS clouds was found to be 0.6121, 0.6682, and 0.8396 relative to the cloud radius for upshear, cross-shear, and downshear regions, respectively. These values are similar to those found by Perry and Hobbs (1996) of 0.3, 0.7, and 1.3 for upshear, cross-shear, and downshear regions, respectively. Analysis showed that 44% of the SCMS clouds sampled had no observable humidity halo in the vicinity of a radial cloud boundary. Further details of our analyses examining the influence of cloud age and orientation relative to the vertical wind shear direction will be presented at the ICPP conference. In addition, we will provide a discussion of work to supplement the current SCMS analyses using measurements from the upcoming Rain In Cumulus over the Ocean (RICO) experiment in December 2004 – January 2005.

ACKNOWLEDGEMENT

This research was supported by the National Science Foundation under grant ATM0121517. Any opinions, findings, and conclusions expressed in this material are those of the author and do not necessarily reflect the views of the National Science Foundation.

REFERENCES

Ackerman, B., 1958: Turbulence around tropical cumuli. *J. Meteor.*, **15**, 69-74.

Lu, M-L, et al., 2003: Analysis of humidity halos around trade wind cumulus clouds. *J. Atmos. Sci.*, **60**, 1041-1059.

Lu, M-L, R. A. McClatchey, and J. H. Seinfeld, 2002: Cloud Halos: Numerical simulation of dynamical structure and radiative impact. *J. Appl. Meteor.*, **41**, 832-848

Malkus, J. S., 1949: Effects of wind shear on some aspects of convection. *Trans. Amer. Geophys. Union*, **30**, 19-25.

Perry, K. D., and P. V. Hobbs, 1996: Influences of isolated cumulus clouds on the humidity of their surroundings. *J. Atmos. Sci.*, **53**, 159-174.

Radke, L. F., and P. V. Hobbs, 1991: Humidity and particle fields around some small cumulus clouds. *J. Atmos. Sci.*, **48**, 1190-1957.

Telford, J. W., and P. B. Wagner, 1980: The dynamical and liquid water structure of the small cumulus as determined from its environment. *Pure Appl. Geophys.*, **118**, 935-952.

COMPARISON STUDY OF A TYPHOON PRECIPITATION OVER SOUTH CHINA SEA

Jinli Liu[1], Gang Zhao[1], Jiantong Li[2], Daren Lu[1],Yong Zhang[3] and Ling Zhang[1]
[1]LAGEO, Institute of Atmospheric Physics, Chinese Academy of Sciences, Beijing 100029, China

[2]Xia Men Meteorological Station, Xia Men, Fu Jian, 361012, China
[3]Beijing Institute of Applied Meteorology

1. INTRODUCTION

Since severe weather, strong wind and heavy rain, frequently caused by typhoon, especially at the coast area of China, for avoiding and reducing the large disaster, we have to accurately forecast typhoon, more precise to know its intensity, as well as when and where it will be landfall etc.. In recent years, as the progress of satellite remote sensing and the numerical simulation, more precise information and understanding of typhoon have been given, it was very helpful for us to study typhoon, but it still can't meet the request of the application and research, therefore, to investigate the behavior and the structure of typhoon is still an important and challenging task.

In this paper, we intend to investigate a typhoon, 0102, 'Chebi', it formed in West Pacific Ocean east of the Philippines on June 20, 2001, then moved NW ward to South China Sea and landed at FU Qing (119.23^0 E, 25.43^0 N, Fu Jian Prov., China) on June 23. The strong wind and flood resulted in a big disaster, 216 persons died and missed, total properties loss were more than 45 million RMB (> 5 million US$). By using ground-based S band Doppler weather radar (GR), located at Xia Men Radar Station （118.04^0 E, 24.29^0 N Fu Jian Prov., China）, Chebi was in radar observation range for more than 20 hours in its mature, landfall and decay stages. From this data we may derive the characteristics of the typhoon in more detailed. Also, we have obtained a TRMM PR data at the 20:58 of 23 June 2001. Therefore we may compare instantaneous PR and GR data of Chebi. In addition, for further understanding the characteristics of Typhoon, we also did some numerical simulation of Chebi.

2. DATA AND ALGORITHM

2.1 GR data

From GR (Xia Men Ground-based S band Doppler radar), Chebi firstly was found in the south-east 280 km (coordinated by GR) at 8:31 a.m. (Beijing Standard Time, hereafter BST) of 23 June 2001 over South China Sea. We have tracked this typhoon till it landfall to Fu Qing at 22:00, and finally decayed and went out from radar observation range after 23:30 June 23.

Corresponding author's address: Jinli Liu, Institute of Atmospheric Physics, Chinese Academy of Sciences, P.O. Box. 9804, Beijing, 100029, China; E-Mail: jliu@mail.iap.ac.cn.

2.2 TRMM PR data

There was one Swatch (20:58 23 June 2001) of PR observation of Chebi which matched well in time and space with GR observation. Here TRMM PR 2A25 product was chosen for comparison.

2.3 Numerical simulation

For understanding the structure and evolution of Chebi in more detail, numerical simulation was performed for its lifetime by using Mesoscale Model (MM5)[Grell 1994]. The model initial and boundary conditions were derived from NCEP, grid $1^0 \times 1^0$. Also a bogus vortex was introduced into NCEP analysis at the initial time using a four-dimensional variation technique. It improved the accuracy of track and intensity of Chebi simulation.

2.4 GMS IR, water vapor, VIS data

Each hour data were analyzed in all lifetime of Chebi.

3. RESULTS

In this paper Beijing Standard Time (BTS) was used to describe all the time, BTS= GMT+8 hr

3.1 Behavior of Chebi

Typhoon Chebi formed in West Pacific Ocean east of the Philippines on June 20, 2001, and then moved northwest ward to South China Sea and getting stronger. The minimum center pressure was 955mb, 10- min mean sustained wind reach 40m/s (NMCC) and 1-min MSW reach 50 m/s at 08:00 23 June, the track of Chebi were shown in Fig.1(a). It can be seen that the moving direction changed from NW to NNW at 20:00 22 June, and then suddenly changed to N ward at 08:00 23 June, and landed on Fu Qing at 22:00 23 June, Fig.1(b) was the tract of Chebi derived from GR. It was shown that the moving direction of Chebi basically was N ward, and its moving velocity was changeable. It changed from 14-30 km/hr, the average was 21km/hr. When Cbebi landed, the wind speed of Fu Qing reached 36m/s, and caused large flood, the total rain fall was 112.8 mm in Chebi precipitation.

Accurate forecasting of the landfall time and place of the typhoon is very important, for predicting Chebi when and where it will landfall, we have to understand the behavior of Chebi, especially focus on the big suddenly change of its moving direction and velocity. There are some research work focus on the affected factors on the behavior of Chebi, it was found, the divergence, vorticity fields, Θse fields at different altitudes in Chebi lifetime may influence the behavior of Chebi [Liu Aiming, 2003]and the topographic forcing to the Bay may interpret the suddenly changes of moving direction of Chebi.

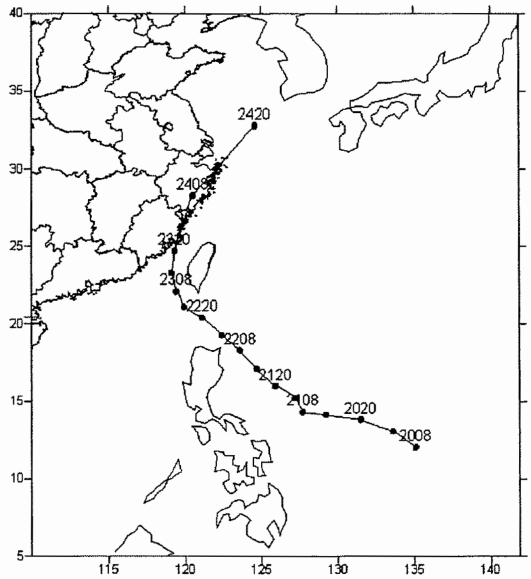

(a)

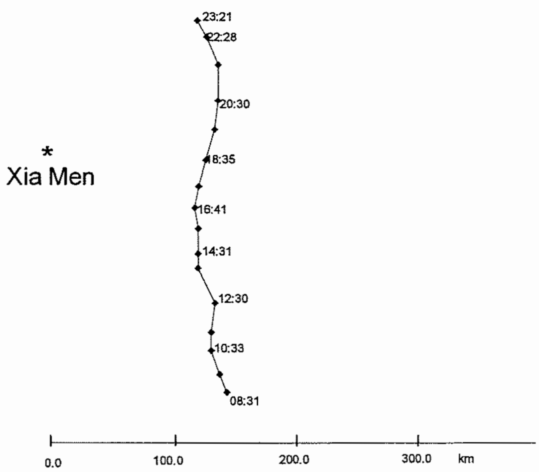

(b)

Fig.1: Track of Typhoon Chebi

(a). 08:00 20 June – 20:00 BST 24 June 2001,
(b). 08:31 23 June – 23:35 BST 23 June 2001

3.2 Structures of Chebi

Chebi has a typical Typhoon Characteristics, from GR we may derived its structures observed from 05:00 23June to 05:00 24June 2001 BST

A. Typhoon eye:
From GR a clear typhoon eye was found in SE, 207 km at 12:29 June 23, its diameter was about 50 km, see Fig.2(a), then the eye wall precipitation echo was spreading), and the eye was getting smaller(Fig.2(b), 13:40); 18:31 the eye is only ten more km diameter (Fig .2(c)), it lasted till the typhoon landed.

B. The eye wall
The eye wall of CHEBI is about 20km width and 8 km height, the average reflectivity was about 25 dbz., the maximum reflectivity was near 40 dbz,

C. Spiral rain band
There were several rain bands as spiral distribution outside the eye wall, and the rain echo area was about 300x200 km^2 .the spiral rain band consisted of many intensive echo cells with about 40 dbz, and these strong cells usually placed in front of the typhoon (relative to it moving direction), and caused a severe damage weather, e.g. within two hours (before and after Chebi landfall) rainfall of Fu Qing reach 97.8mm, 87% of its total rainfall in this typhoon process.

3.3 Comparison study

For comparison, we remapped the PR data set to a GR-centered coordinate system, and compare PR and GR at different height (not shown here). Here we only showed the comparison results of radar reflectivity between PR and GR. Fig.2(d) was the radar reflectivity PPI maps (on surface) derived from GR (Xia Men) and Fig.3 was TRMM PR both at 20:59. It was indicated that the structure and located place of Typhoon Chebi are agree well for GR and PR; Also, it was found that considerable echo intensities difference existed between PR and GR, especially for the surface situation, e.g. the maximum reflectivity difference of spiral rand band reached 10 dbz; For the higher altitude, these differences were getting smaller (less than 5dbz).
The quantitative comparison of PR and GR data is very difficult, the difference between two data sets are resulted from their respective frequency, volume resolution, view angle and calibration error etc. Some evaluation and validation of comparison PR and GR have been made[Bolen 2000], when look at the 8 cases given in Bolen's paper, it was found that the attenuation-corrected reflectivities of PR at near surface (<2km) are agree well with GR (about 1db); Also, we may found that in the higher altitude, 8 cases were very different, some of them also agree well but some of them were very changeable, the maximum

difference between attenuation-corrected reflectivities of PR and GR may reach 6-7 db, probably it is mainly caused by the different vertical structures of different rain type.

In our case study, it was found that the reflectivities of PR were larger than the GR. And the differences were getting smaller as the increase of altitude. It seems that PR attenuation correction may be too strong, especially for near surface situation. This probable interpretation is similar to that mentioned in Ikai [2003]. It is indicated that in convective rain and low freezing level area, PIA $_{2A25}$ (path integrated attenuation derived from PR 2A25) was too large, and may result in over estimate of PR attenuation correction.

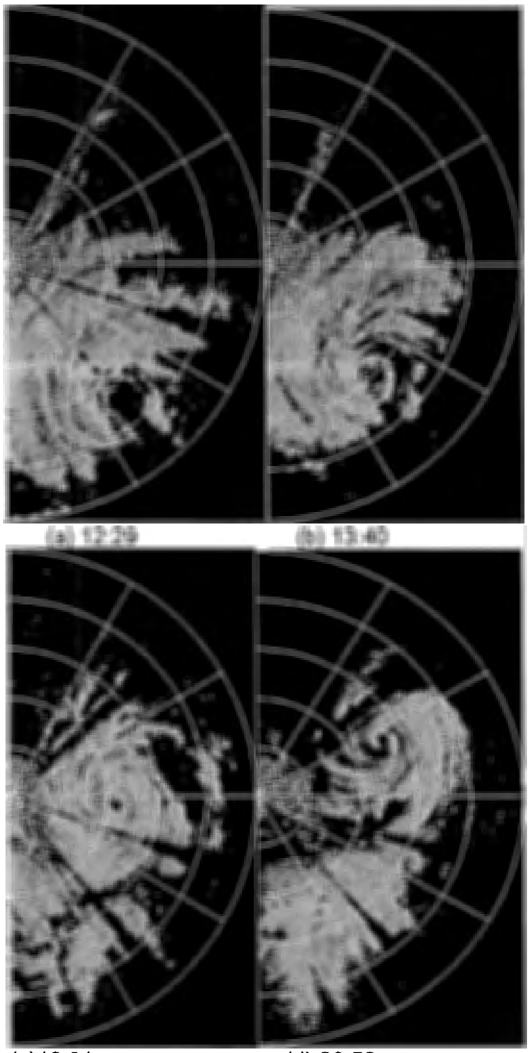

(c)18:31 (d) 20:59

Fig2. GR PPI maps of Chebi: Elevation:0.1^0, Rmax: 300km

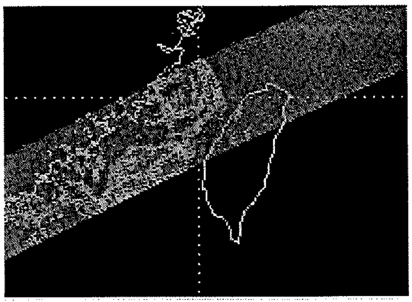

Fig.3 TRMM PR echo intensity data (surface) at 20:59 23 June 2003 BST

3.4 Preliminary results of numerical simulation

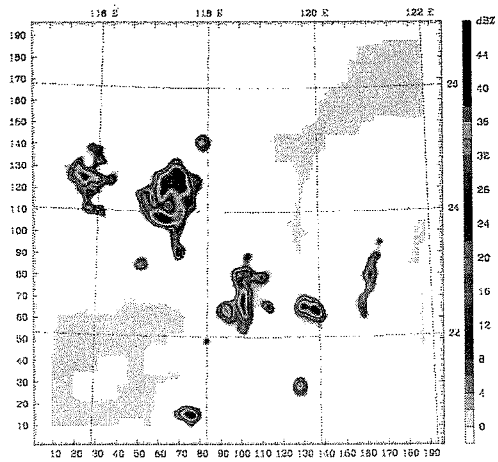

(a) 1000 hpa

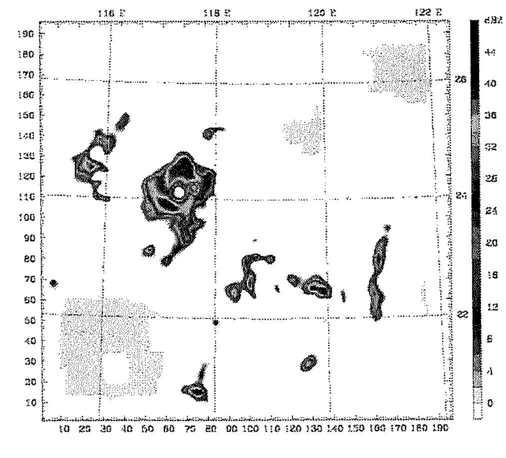

(b) 850 hpa

Fig4. Numerical simulation results of Chebi, 21:00 23 June 2001 BST. Altitude: (a):1000 hpa (b):850 hpa

From analyzing the numerical simulation results of typhoon Chebi the further information of Chebi was Obtained, except the behavior and the general structure of typhoon, we have got vertical profiles of the hydrometeors which play important role on the PR attenuation correction and the rain rate retrieval. Here only two radar reflectivities simulation were given (Fig, 4). Comparing Fig.4 and Fig. 2(d), it can be seen: 1). in typhoon area (around 150 km in Diameter), the eye and the general structure were similar between the simulation and GR observation. (2) The location and the intensity of intensive echo had some difference, simulation showed it was in north of typhoon eye with >40 dbz, for GR and PR they were in east of typhoon eye, and the value of the intensities were different, simulation results were close to the PR (45dbz) and stronger than GR (35 dbz).

4. SUMMARY

1) By using GR (ground-based S band Doppler radar at Xia Men) data and related weather station data we derived the characteristics of Typhoon Chebi when it was near the coast of Fu Jian and landfall in Fu Qing. It may be helpful for forecasting mini typhoon as Chebi;

2) Comparison GR and PR data of Chebi quantitatively showed that there were considerable difference, and the difference was getting smaller in higher altitude. TRMM PR products have given a good precipitation estimation in global area and monthly or seasonally data [Kummerow 2000]. But for short time or instantaneous rainfall estimation it is still a challenging task.

3) For the numerical simulation of Chebi we obtained the preliminary results. Comparison of simulation and ground-based radar indicated that they were basically consistent. For more understanding typhoon forming mechanism, changeable behavior, the dynamic model have to combine with the PR and GR data.

ACKNOWLEDGEMENT: This project is supported by National Basic Research Project Initiative of China ministry of Science and Technology No.2001CCA02200 and the National Natural Science Foundation of China No.40027002 and 40075006

REFERENCE

Bolen S.M., and V. Chandrasekar 2000: Quantitative Cross Validation f Space-Based and Ground-Based Radar Observation, J.Appl. Meteor., 39(2071-2079)

Grell,G.A, J Dudhia, D R Stauffer, 1994: A description of the fifth—generation Penn State/NCAR Mesoscale model(MM5),NCAR Technical Note, 1994, NCAR/TN — 398+STR,138pp.

Ikai.J and K.Nakamura 2003: Comparison of Rain Rates over the Ocean Derived TRMM Microwave Imager and Precipitation Radar,

Kummerow, C. et al. 2000: The status of the Tropical Rainfall Measuring Mission (TRMM) after two years in orbit. J. Appl. Meteor., **39**, 1965–1982.

Liu Ai-ming, Lin yi and Li Honghao 2003: Analysis of Track of Typhoon 0102 "Chebi". J. Oceanography Taiwan Strait 22(1)102-107. (in Chinese).

NUMERICAL SIMULATION OF RETRIEVING THREE-DIMENSIONAL WIND FIELD FROM DUAL DOPPLER RADAR

Shuyan LIU, Hui XIAO, and Yuxiang HE

Institute of Atmospheric Physics, Chinese Academy of Sciences, Beijing 100029, China

1. INTRODUCTION

A simple technique of deriving three dimensional wind fields was investigated from the Dual-Doppler weather radar wind on the ground of certain assumptions. It provides a simultaneous resolution of three wind components and satisfies both the radial velocity equation system and the continuity equation. Choose the strong convective storm that occurred in the northeast of Beijing on June 29, 1996 as the retrieving case and analyze the errors.

2. BRIEF INTRODUCTION OF THE MODEL

The model used to simulate dual-Doppler radar scanning data in this paper is the three-dimensional Convective Storm Model that was established and developed by the Institute of Atmospheric Physics, Chinese Academy of Sciences, (IAP-CSM3D). Introduction in detail of the model please referred to Hong (1998) and Kong (1990).

3. RETRIEVING ALGORITHM

Iterating relative simple mass continuous equation and according to redial velocity projecting relation, u, v, w hence be obtained (Armijo, 1969).

4. NUMERICAL SIMULATION OF THE STRONG CONVECTIVE STORM

Fig.1 is RHI section of observational radar echo along 71° azimuth at 15:14(a) and simulated radar echo (real line), streamline field distribution on X-Z section (b) respectively. Comparison shows that position and height of the simulated echo wall, weak echo region and overhang echo coincide well with those of the observational indicating the model has the ability to simulate strong convective storm (Liu, 2003, 2004).

5. RETRIEVING EXPERIMENT OF THE SIMULATED STORM

5.1 Retrieving Results

Bejing-Gucheng dual-Doppler radar detecting data were simulated. According to the simulation results, the simulated storm began to precipitate at 27min and the updraft in the cloud reached the maximum value, the downdraft reached its maximum value at 36mn. So use the retrieving algorithm mentioned above, choose the two time levels of 27min and 36min to retrieve wind field. Fig.2 is u-w wind vector and w fields on vertical section of 27min and 36min of simulated storm and retrieved results respectively, where (a) is the retrieved results, (b) is the model output results, isoline is the distribution of vertical velocity.

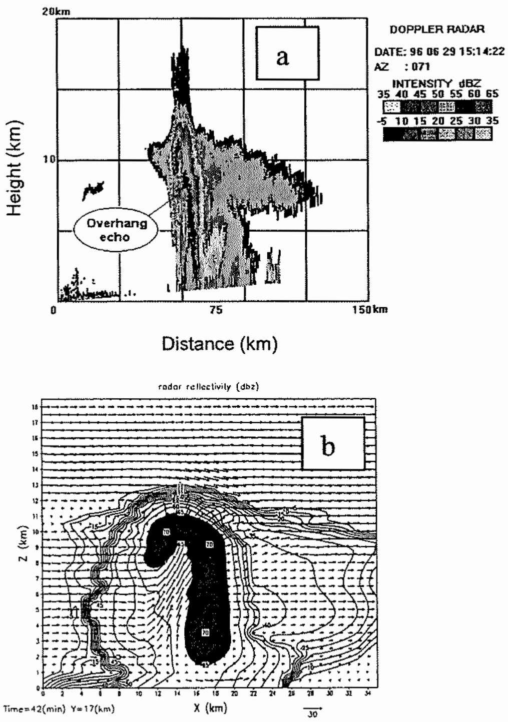

Fig.1 Observational radar echo (a) and simulated streamline field (wind vector) and radar echo (real line) distribution on the *X-Z* section (42min, shaded is strong echo area) (b)

Fig.2 shows that the updraft in the storm behaved as a strong air column and as organized continuous motion. Model simulated results show that updraft

---

Corresponding author's address: Shuyan LIU, Institute of Atmospheric Physics, Chinese Academy of Sciences, Beijing 100029, China; E-Mail: liushuyanhe@sina.com.cn

slant to northeast while for retrieved results, the updraft basically vertical. But the general trend and center position of the retrieved stream field coincide well with the simulated ones at both developing and robust phases, and they have alike updraft and downdraft distributions.

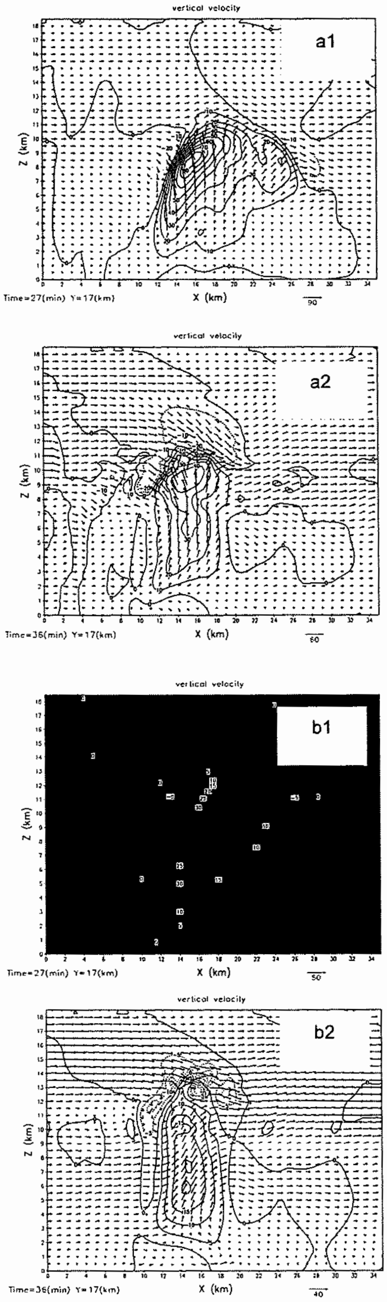

Fig.2 Simulated and retrieved *u-w* fields

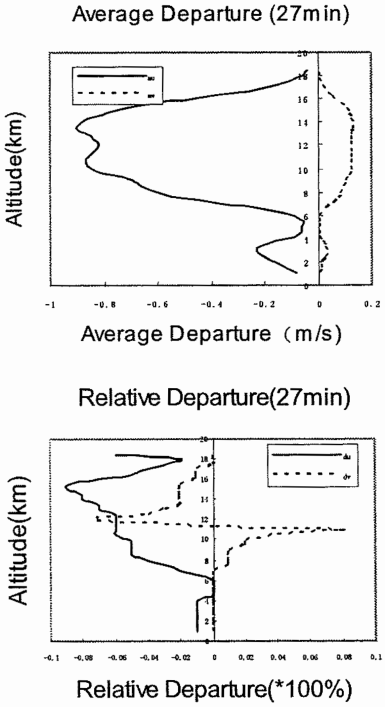

Fig.3. Average and relative departure error of *u.v* at different altitudes(27min)

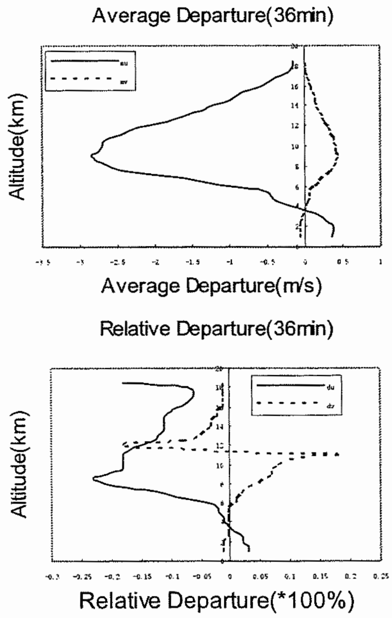

Fig.4 Average and relative departure error of *u,v* at different altitudes(36min)

5.2 Error Analysis

To compare retrieved results, adopt physical quantities of velocity error of average and relative departure errors under rectangular coordination.

Fig.3 and Fig.4 are average and relative departure error distribution of u, v at 27min and 36min on various altitudes. At 27min, average departure errors of u, v are both very small, the maximum departure value of u is -0.9m/s appeared at the altitude of 13.5km , and that of v is 0.14m/s at 14km. As far as relative error concerned, retrieved results are well, the maximum value of u, v relative departure errors are less than 10%. The retrieved results of 36min are not as well as that of 27min, but generally speaking, the errors of u, v are both small indicating well retrieved results. The retrieved effect of 27min is better than that of 36min and that of v is better than u. There exists a best retrieving altitude of about 5.5km at both 27min and 36min.

Fig.5 depicts the average departure error distribution of vertical velocity at different altitudes. Fig.5 shows that the average departure errors are small on each altitude, the maximum error of 27min is -1.15m/s at 17km height and that of 36min is 2.79m/s at 7km height. Vertical velocity retrieving result is also very well and 27min is better than 36min.

Retrieving results of 27min and 36min have difference probably because the storm was at its robust stage at 36min with the most rigorous convective activity while it was at development stage with relatively weak convective motivation at 27min.

Due to use mass continuous equation as retrieve restriction condition, many processes such as vortex, entrainment etc have not been considered in the retrieving algorithm, and the choosing of initial and boundary values as well as error cumulation of continuous equation are one of the causes.

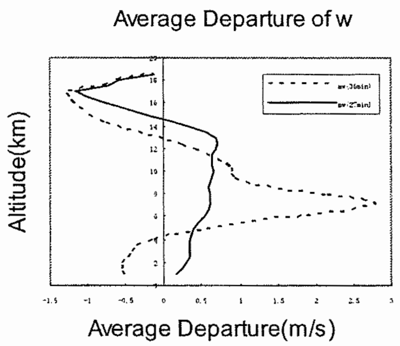

Fig.5 Average departure error of *w* at different altitudes

6. CONCLUSIONS

Numerical experiment results show that the general trend of retrieved and simulated streamline fields are alike and the center positions of the storm are coincide very well, the distributions of updraft and downdraft are resemble. Analyses of average and relative departure of horizontal wind velocities shows that the retrieving errors are small and can reflect the true situation of three-dimensional wind field by and large. At the mean time, analyses average departure of vertical velocity indicates that the errors at various altitudes are all very small and gives satisfactory retrieving effects. While the retrieving effects of 27min are better than that of 36min. Retrieving results of 27min and 36min have difference probably because the storm was at its robust stage at 36min with the most rigorous convective activity while it was at development stage with relatively weak convective motivation at 27min.

Since the retrieving results especially vertical velocity are very well and can reflect the true situation of three-dimensional wind field by and large, and the retrieving results at about 5.5km are the best while the center positions of mesoscale convective systems are mainly at 4-6km height, thus the retrieving algorithm used in the paper can be further developed and applied in future research works.

The observational Doppler weather radar data are more difficult to deal with than the simulated data in the paper, so put the retrieving algorithm to practice has many works to do, we will do further research.

Acknowledgements

This work was supported by Chinese National Scientific Key Program under Grants 2001BA610A-06-05 and 2001BA904B09, Chinese National Science Foundation under Program Grants 40333033 and 40175001, the Key Foundation of Chinese Academy of Sciences under Grant Y2003002, and the Key Foundation of the Institute of Atmospheric Physics, Chinese Academy of Sciences.

References

Armijo L., 1969: A theory for the determination of wind and precipitation velocities with Doppler radar. J Atmos Sci, 26,570-573.

Hong Y.C., 1998: A 3-D Hail Cloud Numerical Seeding Model. Acta Meteorological Sinica, 56(6), 641-653. (in Chinese)

Kong F.Y., M.Y. Huang, H.Y. Xu, 1990:Three-Dimensional numerical simulation of ice phase process in convective cloud I: Model Establishment and Cold Cloud Parameterization. Chinese J. Atmos. Sci., 14(4), 441-453. (in Chinese)

Liu S.Y., H. Xiao, et al., 2004: Numerical Simulations of a Strong Convective Storm in Beijing. Chinese J. Atmos. Sci., 28(2). (in Chinese).

SIMULATIONS OF MEIYU FRONT WITH A NEW MICROPHYSICS SCHEME

Lou Xiaofeng, Hu Zhijin, Wang Penyun, Zhou Xiuji, Shi Yueqing, Sun Jing
Chinese Academy of Meteorological Sciences, Beijing 100081, P.R. China

1. INTRODUCTION

In MM5 most of explicit microphysical schemes only predict the mass contents of water substances, with the number concentrations diagnosed. Further more, descriptions of several microphysics processes should be improved.

Using a quasi-implicit calculation method, a new developed two-moment mixed-phase microphysical scheme with 5 species of water substance is on the basis of Hu (1988 and 1986). The new scheme includes water contents and number concentrations of cloud, ice crystal, snow crystal, rain and graupel, totally 11 cloud variables and 31 microphysical processes. Several microphysical processes are improved comparing with other explicit microphysical schemes of MM5 (Tao, 1993; Dudhia, 1993; Hsie 1980; J.Reisner 1998; Paul 1995), such as deposition, freezing, ice nucleation, autoconversion of cloud to rain, ice to snow and snow to graupel.

Results of one-dimensional model of this scheme using different time steps and vertical velocities show that the quasi-implicit calculation scheme can be run positively, stably and conservatively. It need not use iteration processes to solve the implicit variables, which shortens the running time. A number of sensitivity experiments have been conducted to examine parameters of microphysical processes. Cloud parameters should be changed with maritime clouds or continental clouds. The ice nucleation parameters should be used according to local observations.

Corresponding author's address: Lou Xiaofeng, Chinese Academy of Meteorological Sciences, Beijing 100081, P.R. China; E-Mail: louxf@cams.cma.gov.cn

When coupling the new developed scheme with MM5 V3, four prognostic variables (Nr, Ns, Ng, Fc) are added to the mesoscale model. With the new model, a Meiyu front case is simulated with the integration time of 24 hours.

2. SIMULATIONS OF MEIYU FRONT IN JULY IN CHINA

Experiments in heavy rainfall in the Meiyu front in the downstream of the Yangtze River were carried out in June and July of 2001 and 2002 sponsored by the Ministry of Sciences and Technology of China. The simulated case is during the period of 21–24 July. The accumulated rainfall is up to 120mm within 24 hours. The precipitation area is a narrow-long band with convective cells moving toward northeast, and there are several heavy rain centers of over 100mm. The simulated rain includes two parts: convective and non-convective. The maximum simulated rainfall is 180mm. Though it is larger than observations, the location, width and heavy rain centers of the simulated rain-band are very cloze to observations. The convective cells bringing the stationary rain-band also moves northeast, consistent with observations.

The simulated precipitation of the most complicated explicit scheme of MM5, Reisner scheme, is a very narrow rain-band, and only one center of 100mm. The result of mixed phased scheme, the default scheme of released MM5 and the most widely used scheme, is very similar with that of Reisner scheme, and both of them, the accumulated rainfall reach 180mm. Obviously, the precipitation within 24h of the new scheme is better than those of the most complicated and the most widely used scheme of MM5.

Simulation results with 1.11km grid spacing are compared with Doppler observation. Figure 1 displays the north-south vertical section of simulated reflectivity and Doppler radar echoes of Yichang Station of a cloud cluster. The simulated horizontal scales of convective cells generally are 30km, and the vertical height reaches 12km, which agrees with the observations. The strongest reflectivity of both simulated and observed exceed 45dBz. The model-derived reflectivity values of all four convective cells are bigger than 45dBz, but only one of the three observed three echoes reach 45dBz. Though simulated reflectivity values are bigger than observations, in both of them the strong echoes appear around and below 5km height level (around 0℃ level). Overall, the strength, horizontal and vertical scales of modeled reflectivity of convective cells are consistent with the radar observations of Doppler radar.

In simulation results, as shown in Fig. 2, airflow comes from south, climbs slanting upward and flows out northward. Cold air from rear cloud and downdraft caused by dragging of precipitation raindrops is diffused near the ground layer. This type of airflow of convective cells is in a quasi-steady state which can last for a long time, and is validated by the reflected stream of radar echoes.

3. CONCLUSION

A new developed dual-parameterized mixed-phased explicit scheme with mass contents and number concentrations of cloud drops, ice crystals, snow crystals, rain drops and graupel particles is coupled with MM5. A Meiyu front case is simulated and its results are compared with observations.

With the new cloud resolving model, MM5 runs stably, and simulated dynamic fields and microphysical fields are reasonable.

The simulated accumulated rainfall is improved comparing with the MM5 original schemes. With high horizontal resolution, the strength and scale of model-derived reflectivity of convective cells is consistent with the radar observations of Doppler radar. Airflow of convective clouds is validated by the retrieved vectors of dual doppler radar echoes.

ACKNOWLEDGEMENT

We are grateful to Dr. Liping Liu for figures of radar echoes and retrieved vectors. This work is supported jointly by the National Key Project of Science and Technology during the Tenth Five-Year Plan 2001BA610A-06 and National Natural Science Foundation of China 40305001.

REFERENCES

Dudhia, J.: A nonhydrostatic version of the Penn State-NCAR mesoscale model: Validation tests and simulation of an Atlantic cyclone and cold front. *Mon., Wea. Rev.*, 121, 1493-1513, 1993.

Eirh-Yu Hsie: Richard D. Farley and Harold D. Orville. Numerical simulation of ice-phase convective cloud seeding. *J. Appl. Meteorol.*, 19(8), 950-977, 1980.

Hu Zhijin, and Yan Caifan: Numerical simulation of microphysical processes in stratiform---Part Ⅰ: Microphysical model, *ACTA METEOROLOGIA SINICA*, 1 (1), 37－52, 1986.

Hu Zhijin, and He Guanfang: Numerical simulation of microphysical processes in cumulonimbus---Part Ⅰ: Microphysical model, *ACTA METEOROLOGIA SINICA*, 2 (4), 471-484, 1988.

J.Reisner. R.M.Rasmussen and R.T.Bruintjes: Explicit forecasting of supercooled liquid water in winter storms using the MM5 mesoscale model. *Q. J. R. Meteorol. Soc.*, 124, 1071-1107, 1998.

Paul Schultz: An explicit cloud physics parameterization for operational numerical weather prediction. *Mon. Wea. Rev.*, 123(11), 3331-3343, 1995.

Tao, W.-K., and J. Simpson: The Goddard cumulus ensemble model. Part I: Model description, *Terrestrial Atmospheric and Oceanic Sciences*, 4, 19-54, 1993.

Yubao Liu, Da-Lin Zhang and M.K.Yau: A multiscale numerical study of hurricane Andrew (1992). Part Ⅰ: Explicit simulation and verification. *Mon. Wea. Rev.*, 125(12), 3073-3093, 1997.

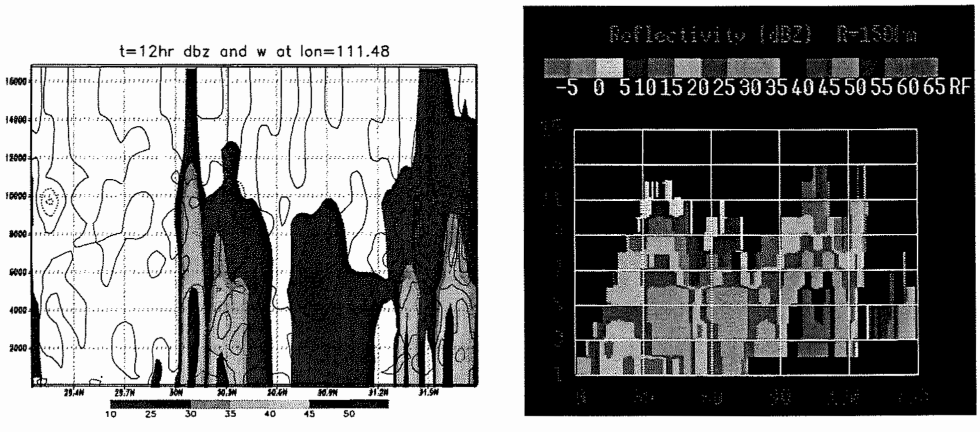

Fig.1. The vertical sections of simulated (left) and observed (right) Doppler echoes of Yichang Station, Hubei Province on 24th July, 2003.

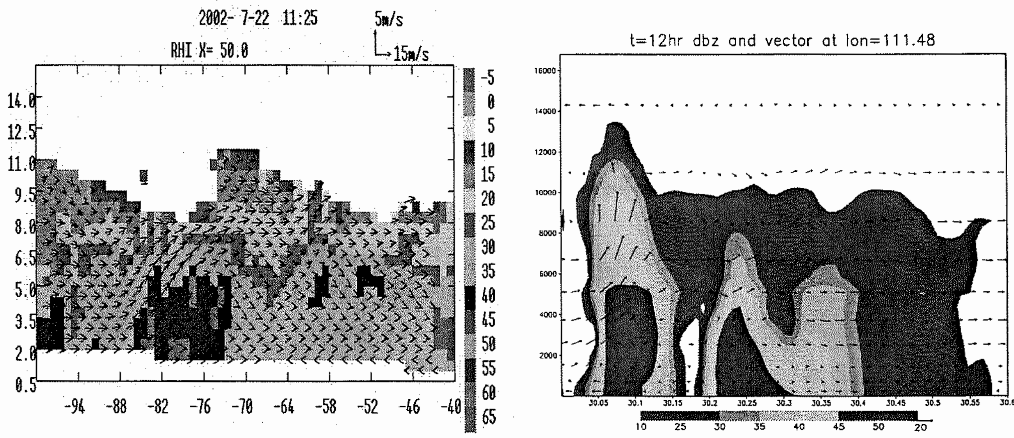

Fig. 2 The vertical sections of observed radar echoes and retrieved vectors (left) and simulated echoes and wind (right).

MIXING OF CLOUD AND CLEAR AIR IN CENTIMETER SCALES OBSERVED IN LABORATORY BY MEANS OF PARTICLE IMAGE VELOCIMETRY

Szymon P. Malinowski[1] Piotr Korczyk[2] and Tomasz A. Kowalewski[2]

[1]Warsaw University, Institute of Geophysics, Warsaw, 02-093 Poland
[2]Institute of Fundamental Technological Research, Polish Academy of Sciences, Warsaw, Poland.

1. INTRODUCTION

The best available airborne instrumentation for turbulence measurements: aircraft- borne BAT probe (Hacker and Crowford, 1999) or balloon-borne ultrasonic anemometer mounted on ACTOS platform (Siebert et al.) due to physical limitation of the sensors can resolve atmospheric flows down to the scale of order of tens of centimeters. This scale, considered small in typical cloud physics research, is still two orders of magnitude greater than Kolmogorov microscale or typical distance between cloud droplets, which both for atmospheric conditions are of order of 1mm. Thus, flow in scales crucial for interactions of cloud microphysics and turbulence cannot be observed in natural conditions.

Interactions between cloud turbulence and microphysics are attach growing attention. Such problems as cloud droplet spatial distribution due to turbulence, droplet growth and evaporation in the course of turbulent mixing of cloud and environment are still poorly understood (see e.g. review papers by Pinski and Khan, 1997, brilliancy's and Ya 2000 and Shaw, 2003).

In many papers about droplet collision probability, due to lacking information about small-scale turbulence in clouds, properties of this turbulence have to be assumed. In recent years, however, articles appeared, showing that in some circumstances a small scale turbulence in clouds may not fulfill the most commonly adopted assumption of uniformity and isotropy. Banal and Malinowski (1999) show, that filaments created in the process of turbulent mixing of cloud and clear air are elongated in vertical. They argue, that the reason of such behavior is buoyancy force resulting from evaporation of cloud droplets at the border of these filaments. Verifying this hypothesis Andrejczuk et al. (2004) prove in high-resolution numerical simulations that in mixing of cloud with clear air turbulent kinetic energy (TKE) is generated in small scales by evaporation of cloud droplets. It is interesting, that even if additional TKE resulting from evaporative cooling and following production by buoyancy forces in small scales is a tiny fraction of TKE coming in the energy cascade from large scales, the resulting small-scale turbulence is highly anisotropic with the preferred direction in vertical. This finding, if confirmed by other studies, may be important for our knowledge on cloud microphysical processes and microphysics-turbulence interactions.

In the present study we verify the above conclusion by Andrejczuk et al. (2004), performing the experiment in a laboratory cloud chamber. Our goal is to measure horizontal and vertical turbulent velocities in a cloud at scale of millimeters. The adopted technique is the Particle Image Velocimetry (PIV) of cloud droplets.

Corresponding author address:
Szymon P. Malinowski, Warsaw University, Institute of Geophysics, ul. Pasteura 7, 02-093 Warsaw, Poland; e-mail: malina@fuw.edu.pl

2. THE EXPERIMENT

The experimental chamber of size 1x1x1.8m and method of generation of the artificial cloud (consisting of droplets with mean diameter of 14μm) are the same as in experiments by Malinowski et al (1998) and Banat and Malinowski (1999). The negatively buoyant cloudy plume enters the chamber through the round opening at the upper wall with velocity of about 10cm/s. Liquid water content of a saturated plume is of order of 4g/kg, its temperature is 22°C, temperature of the unsaturated air in the chamber (relative humidity of 60%) is close to this of a plume. The plume descends slowly when mixing with the environment.

Illumination of the chamber interior with sheet of laser light allows imaging planar cross section of the scene with a high-resolution CCD camera. An example output from the experiment is presented in Fig.1. Inspection of the image, covering area of about 7x4.5cm^2 reveals a very fine filamented structure created in the process of turbulent mixing of cloudy plume with unsaturated environment. One pixel in this image corresponds to the volume of about 55x55μm^2 in the plane of the light sheet and 1.2mm deep. Such elementary volumes occupied by droplets are represented by dark pixels in the presented negative image, light pixels correspond to volumes with no droplets.

Identification of patterns in the two consecutive images separated by a known time interval allows for determination of two components of velocity. This technique widely adopted in experimental fluid dynamics and is known under name of Particle Image Velocimetry (PIV). A special, precise. multiscale PIV algorithm, searching firstly for motion of large structures, then for the motion within these structures has been developed for a purpose of this study. Its details are given in paper by Korczyk et al. (2004). Application of this algorithm allows for measurement

Fig.1. Negative image from the cloud chamber showing small-scale structures created in a process of cloud-clear air mixing. Imaged area corresponds to 7cm x4,5cm in physical space.

of two components of velocity vector in the plane of the image with spatial resolution of about 1.2mm, i.e. close to the Kolmogorov microscale (Fig.2).

3. RESULTS AND DISCUSSION.

In this section we present statistical properties of horizontal and vertical components of turbulent velocity vector resulting from analysis of 21 pairs of images (scenes). Due to the details of the velocity retrieval procedure its large scale downward component is substracted in each scene (pair of images). Additional spatial averaging of each velocity component was performed over the scene in order to retrieve turbulent velocities according to the equations:

$$u' = u - \langle u \rangle \;, \qquad (2.1)$$

$$w' = w - \langle w \rangle \;. \qquad (2.2)$$

Here u and w are horizontal and vertical velocities, respectively, <> denotes spatial averaging over the scene and u' w' are turbulent velocity components. Additionally, a vorticity component perpendicular to the plane of the image was calculated with use of the Stokes' theorem.

Application of equations (2.1) and (2.2) ensures that mean turbulent velocity components for each of 21 scenes as well as for the whole ensemble is equal to zero. This is nicely confirmed in Fig.2 where histograms of u' and w' are plotted. Inspection of the figure shows, that probability distributions of horizontal and vertical velocity components differ significantly: histogram of a vertical velocity component has a greater span and longer tails than histogram of a horizontal component. This is more evident when investigating second, third and fourth statistical moments. Standard deviations are calculated according to the formula:

$$\sigma_u = \sqrt{\langle (u')^2 \rangle} \;, \qquad (3.1)$$

$$\sigma_w = \sqrt{\langle (w')^2 \rangle} \;, \qquad (3.2)$$

skewnesses are calculated as:

$$S_u = \frac{\langle (u')^3 \rangle}{\sigma_u^3} \;, \qquad (3.3)$$

$$S_w = \frac{\langle (w')^3 \rangle}{\sigma_w^3} \;, \qquad (3.4)$$

Fig. 2. Another example image from the experiment with superimposed retrieved two components of velocity field.

while kurtosis of both components is calculated according to the following pair of formulas:

$$K_u = \frac{\langle (u')^4 \rangle}{\sigma_u^4} , \tag{3.5}$$

$$K_w = \frac{\langle (w')^4 \rangle}{\sigma_w^4} . \tag{3.6}$$

In equations (3.1)-(3.6) <> denotes averaging over all points in which velocity is calculated and over all scenes. Calculated values of statistical moments are presented in a table below:

	u'	*w'*
Standard deviation	1,9	2,4
Skewness	0,39	0,17
Kurtosis	3,9	3,5

Above results reveal anisotropy of small-scale turbulent motion in scale of millimeters: velocity fluctuations in vertical are significantly stronger than fluctuations in horizontal. This finding is in agreement with results of Andrejczuk et al. (2004). Small scale mixing patterns created by such anisotropic velocity distribution can be elongated in vertical, as present Banat and Malinowski (1999). This vertical elongation can be observed in Fig.1 and in many other images from the experiment.

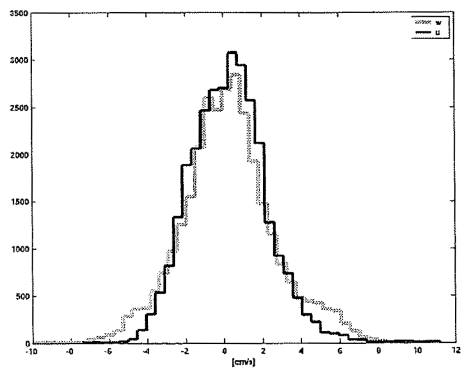

Fig. 3. Histogram of horizontal and vertical turbulent velocities.

An additional comment and analysis is required in order to understand the positive skewness of both distributions of u' and w'. Due to technical reasons, imaged fragment from the cloud chamber was shifted right from the axis of the chamber. This means, that the field of view of the camera was close to the right edge of the negatively buoyant cloudy plume. Such plumes are characterized by a gradient of the mean velocity and development of vortices at the edge. In order to verify, that this could influence turbulent velocity distributions an additional analysis of a vorticity component perpendicular to the plume was performed. Results, presented in Fig. 4. indicate dominating positive vorticity , which is consistent with location of the imaging area and is responsible for the skewness of the velocity components.

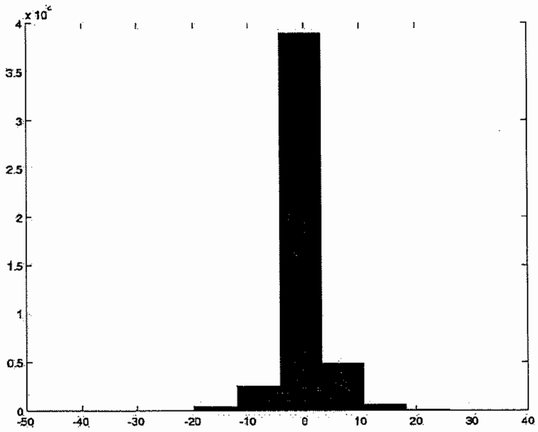

Fig.4. Histogram of vorticity.

Finally, in order to describe more precisely small-scale properties of the observed flow, Taylor microscales (horizontal and vertical) have been calculated according to the following equations:

$$\lambda_u = \frac{\left\langle (u')^2 \right\rangle^{\frac{1}{2}}}{\left\langle \left(\frac{\partial u'}{\partial x} \right)^2 \right\rangle^{\frac{1}{2}}} , \quad (3.7)$$

$$\lambda_w = \frac{\left\langle (w')^2 \right\rangle^{\frac{1}{2}}}{\left\langle \left(\frac{\partial w'}{\partial z} \right)^2 \right\rangle^{\frac{1}{2}}} . \quad (3.8)$$

In order to calculate velocity derivatives a simplest two-point algorithm has been used. The resulting values of Taylor microscales are:

$$\lambda_u = 5{,}83 \pm 0{,}23 \ mm ,$$

and

$$\lambda_w = 6{,}92 \pm 0{,}36 \ mm .$$

Similar difference between horizontal and vertical microscales, with larger values resulting from the resolution of the grid used in the the numerical experiment, has been reported by Andrejczuk et al. 2004.

Acknowledgments.

This research was supported by a research grant No 5 T07A 052 24 of the Polish Committee for Scientific Research.

References:

Andrejczuk M, W.W. Grabowski, S.P. Malinowski and P.K. Smolarkiewicz 2004. Numerical simulation of cloud/clear air interfacial mixing *J. Atmos. Sci.*, accepted for publication.

Banat P. and Malinowski S.P. 1999. Properties of the turbulent cloud-clear air interface observed in the laboratory experiment. *Phys. Chem. Earth (B),* 24, 741-745.

Hacker, J. M. and T. L. Crawford, 1999 The BAT-probe: The ultimate tool to measure turbulence from any kind of aircraft (or sailplane), J of Technical Soaring, XXIII:2, 43-46

Korczyk P.M., Malinowski S.P. and Tomasz A. Kowalewski, 2004: Particle image velocimetry of cloud droplets in the process of turbulent mixing. *In this volume.*

Korolev A.V and G.A. Isaac, 2000: Drop growth due to high supersaturation caused by isobaric mixing. *J. Atmos. Sci.* **57** (10): 1675-1685

Malinowski S. P., Zawadzki I., and Banat P. 1998. Laboratory observations of cloud-clear air mixing in small scales. *J. Atmos. Oceanic Technol.* 15, 1060

Pinsky, M.B. And A.P. Khain, 1997: Turbulence effects on droplet growth and size distribution in clouds – a review. *J. Aerosol. Sci.*, **28**, 1177-1214.

Siebert H., M. Wendisch, T. Conrath, U. Teichmann, and J. Heintzenberg, 2003:A new tethered balloon-borne payload for fine-scale observations in the cloudy boundary layer. *Boundary Layer Meteorolol.*,**106** (3): 461-482

Shaw R. A. 2003. Particle-turbulence interactions in atmospheric clouds. *Annu. Rev. Fluid Mech.* 35, 183-227, 2003.

Vailancourt P. A. and Yau M. K. 2000. Review of Particle-Turbulence interactions and Consequences for Cloud Physics. *Bull. Am. Meteorol. Soc.* 81, 285-98

Effects of mesoscale convergence on convective rainfall simulated with an axisymmetric cloud model with detailed microphysics

Ryohei Misumi, Ken-ichi Maruyama Masayuki Maki, Koyuru Iwanami, Sang-Goon Park and Mihoko Suto

National Research Institute for Earth Science and Disaster Prevention, Tsukuba 305-0006, Japan

1. INTRODUCTION

It is well known that mesoscale convergence intensifies convective rainfall. In Japan heavy rainfall is sometimes observed in a mesoscale convergence zone of the order of 10^{-4} s^{-1} (Matsumoto and Akiyama 1969). Similar problems have been studied on the initiation and the development of convective rainfall in Florida in the United States (Shepherd et al. 2001).

A numerical simulation is one of the useful methods to understand how convergences intensify convective precipitation. Some researchers have studied the dynamic effects using two or three dimensional models (Chen and Orville 1980; Tripoli and Cotton 1980; Xin and Reuter 1996). However, in previous simulations, cloud physics are highly simplified with the use of bulk cloud parameterizations. It is necessary to use more detailed microphysical models to understand the rainfall-enhancement process deeply.

In this study we make use of an explicit microphysical model including ice-phase processes based on Reisin et al. (1996) with an axisymmetric 2-dimensional dynamic framework to understand how mesoscale convergence intensifies precipitation of convective clouds.

2. NUMERICAL MODEL

2.1 Model

The microphysics are represented with a four class (drops, ice crystals, snow and graupels) explicit model constructed based on Reisin et al. (1996). The sizes of particles in each class are divided into 34 categories from 3.1 μm to 8.1 mm in melted diameter. The processes included in the model are nucleation of CCN and IN, diffusion growth and evaporation of drops and ices, collision coalescence and breakup of drops, aggregation of ices and riming of drops on ice particles, ice multiplication due to Hallet-Mossop mechanism, drop freezing, ice melting and sedimentation. The variations of size spectrum are calculated with the two-moment scheme to achieve high accuracy. The dynamic framework of the model is a non-hydrostatic 2-dimensional axisymmetric cloud model as in Soong and Ogura (1973). The effects of mesoscale convergence are superimposed by the same technique as Chen and Orville (1980). The domain is 20 km in the horizontal direction and 16 km in the vertical direction. Mesh sizes are $\Delta r=\Delta z=400$m and the time step is fixed as 2 s.

2.2 Initial conditions

As the initial conditions of the atmosphere, two typical situations in East Asia are considered. One is the condition in Baiu (Mei-yu) frontal zone, which is a stationary precipitation area extending from China to Japan in early summer. In this situation heavy rainfall sometimes occurs associated with mesoscale disturbance and causes flood disasters (Watanabe and Ogura, 1987). A sounding data near Baiu frontal zone used as the initial condition is shown in Fig.1(a). The low-level air is very moist and atmosphere is potentially unstable below the 5km level. The Showalter stability index (SSI) in this case is -0.3 K. The other condition is the atmosphere under subtropical high, in which thunderstorms are likely to develop because of heating of the surface by solar radiation. A sounding data used in the model is shown in Fig.1(b). The atmosphere is very unstable (SSI=-3.1K) but low-level air is relatively dry.

The profile of the mesoscale convergence is shown in Fig.2. The convergence of 10^{-4} s^{-1} is a characteristic value for disturbances causing heavy precipitation (Matsumoto and Akiyama, 1969). Positive divergence exists above the 5 km level to satisfy the mass conservation. The convergence field is assumed not to change with time.

Corresponding author's address: Ryohei Misumi, National Research Institute for Earth Science and Disaster Prevention, Tsukuba 305-0006, Japan;
Email: misumi@bosai.go.jp

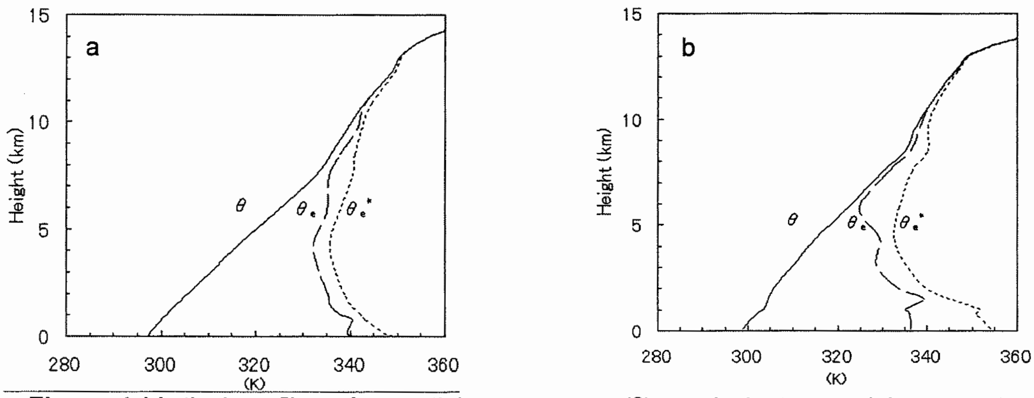

Figure 1 Vertical profiles of potential temperature (θ), equivalent potential temperature (θ_e) and saturated equivalent potential temperature (θ_e^*) at (a) 00UTC on 24 June 2000 at Kagoshima (near Baiu frontal zone) and (b) 12UTC on 3 July 2000 at Tateno (under subtropical high).

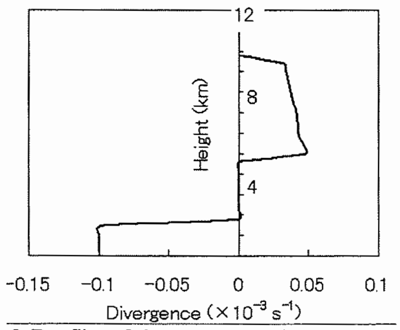

Figure 2 Profile of the mesoscale convergence.

Table 1 Cases for calculation.

Case	Atmospheric condition	Mesoscale convergence
F1	Frontal zone	No
F2	Frontal zone	Yes
S1	Subtropical high	No
S2	Subtropical high	Yes

Four cases of calculations are made (Table 1). In all calculations the numbers of the initial CCN are assumed to be 250 cm^{-1} (reflecting maritime clouds). As an initial perturbation a warm and moist bubble is put in the lower layer and the integration is made for 120 minutes.

3. RESULTS

3.1 Cases F1 and F2

In both cases the initial perturbations developed and formed convective cells. Only one convective cell developed in F1, while a secondary cell appeared in the vicinity of the first cell in case F2 (Fig.3). As a result, strong rainfall continued for longer time and the area of rainfall was wider in case F2. Water budgets (not shown) indicate that the difference of total amount of rainfall between F1 and F2 is almost equal to the amount of water vapor supplied by the mesoscale convergence. This result is reasonable because the atmosphere of frontal zone is so moist that the evaporation is restricted and almost all the supplied water reaches ground as rainfall.

Table 2 compares the production amount of precipitable water (defined as the hydrometeors larger than 100 μm in melted diameter) in the first and the second cells in F1 and F2. Here the first cell and the second cell are defined based on the range of the radial distance (r) and the time (t) as follows:

First cell: r = 0 - 1.6 km, t = 0 - 40 min
Second cell: r = 1.6 - 4.0 km, t = 40 - 80 min

In F1 the warm rain processes, such as coalescence of drops and condensation, are dominant. On the other hand, the ice-phase processes, especially riming on graupels, are very active in F2. This is because the updrafts of convective cells in F2 are more vigorous and reach higher level due to the effects of mesoscale convergence, thus more ice particles are nucleated in this case. The second cell in F2 produces similar amount of precipitating water to the first cell, although the condensation amount is very small. This indicates that the precipitating water is formed efficiently in the second cell. It is also notable that the amount of riming in the second cell is the greatest.

Figure 4 shows the trajectory of an air parcel and the size distribution of hydrometeors in the second cell of F2. It is very interesting that the drop size distribution is bimodal even at the root of the updraft (40 min). Obviously the large drops are provided by the first cell which has already reached its mature stage. The broad drop size distribution is favorable for an efficient raindrop formation. Graupels larger than 1000 μm, which are also provided by the first cell, appear just above the melting level (50 min). Drops rime on the graupels and the mass of particles larger than 1000 μm rapidly increases (55 min). These facts suggest that the large particles provided by the first cell interact with the small droplets formed in the second cell and efficiently produce precipitating water.

3.2 Cases S1 and S2

In case S2 the amount of rainfall was higher and the rainfall area was wider than S2. However, the difference of rainfall amount between S1 and S2 was almost half of the amount of water supplied by the convergence. The rest of water was used to moisten the air. A secondary convective cell developed in S2, but the convection of the second cell was too shallow to produce strong rainfall. Therefore, strong rainfall did not continue for long time in S2. It is considered that mesoscale convergence intensifies thunderstorm rainfall under subtropical high but does not sustain heavy rainfall for long time.

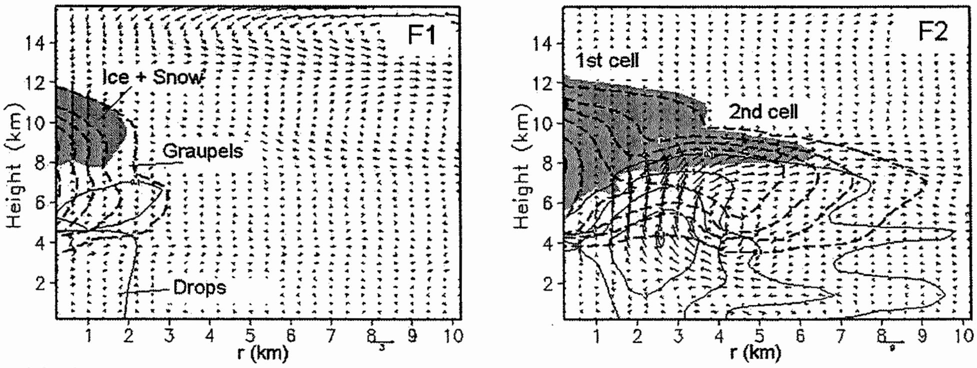

Figure 3 Vertical sections of mixing ratio of hydrometeors and wind vectors at 60 min for F1 and F2. Outermost contours indicate 0.1 gkg^{-1} and other contours are drawn every 1 gkg^{-1}.

Table 2 Amount of precipitable water (hydrometeors greater than 100 μm) produced in the convective cells. Units are mm.

	Case F1	Case F2	
	1st cell	1st cell	2nd cell
Raindrops	30.4	40.0	26.3
Condensation	*12.1*	*18.5*	*36.2*
Coalescence	*27.0*	*46.9*	*22.4*
Evaporation	*-2.7*	*-4.9*	*-8.9*
Riming	*-6.0*	*-20.4*	*-23.3*
Ice crystals	0.5	1.5	0.4
Deposition	*0.9*	*5.2*	*1.8*
Collision with drops	*-0.1*	*-0.1*	*-0.2*
Sublimation	*0.0*	*-0.5*	*-0.2*
Collision with ice particles	*-0.3*	*-3.1*	*-0.9*
Snowflakes	0.1	0.8	0.2
Deposition	*0.0*	*0.6*	*0.2*
Riming	*0.0*	*0.0*	*0.0*
Aggregation	*0.1*	*0.3*	*0.0*
Sublimation	*0.0*	*-0.1*	*0.0*
Graupels	7.5	27.6	27.3
Deposition	*0.8*	*2.5*	*2.9*
Riming	*6.5*	*22.3*	*24.0*
Aggregation	*0.2*	*3.1*	*0.9*
Sublimation	*0.0*	*-0.2*	*-0.4*
Total production of precipitable water	38.5	69.9	54.3
Total condensation	51.9	88.1	58.7

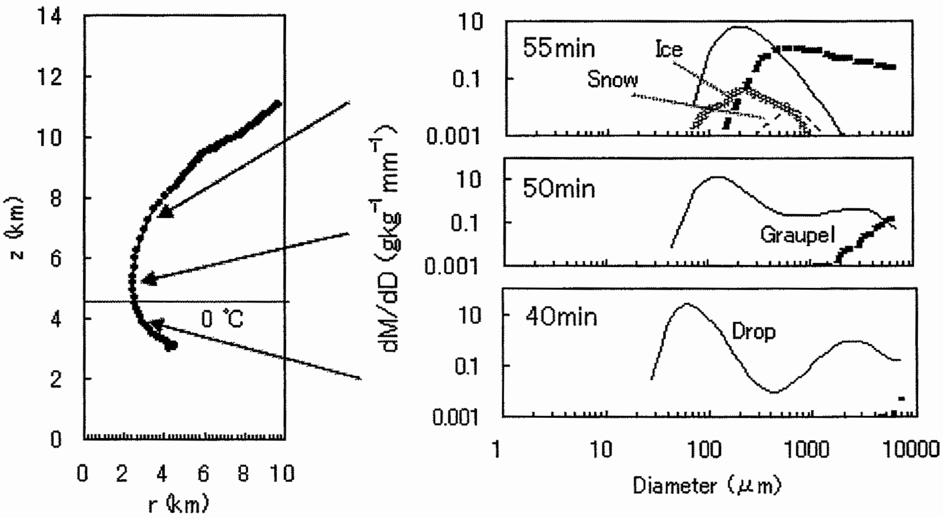

Figure 4 Trajectory of an air parcel and the size distribution of hydrometeors rising in cell 2 of F2.

4. CONCLUSIONS

1) By the effects of mesoscale convergence secondary convective cells develop in the vicinity of the first cell and the rainfall area extends if enough water vapor is supplied.

2) Total amount of rainfall enhanced by mesoscale convergence is almost equal to the supplied water in the condition of the Baiu frontal zone (very moist and less unstable), while it was almost half amount of the supplied water in the condition of thunderstorms under subtropical high (very unstable and relatively dry).

3) In Baiu frontal zone a secondary convective cell produces so strong rainfall that intense precipitation continues for long time in mesoscale convergence field.

4) In the secondary convective cell, precipitable water is produced efficiently by the interaction with the first cell: raindrops efficiently grow by the coalescence of droplets with large drops provided by the first cell, and large graupels rapidly form by the riming of drops on the ice particles given by the first cell.

REFERENCES

Chen, C. H. and H. D. Orville, 1980: Effects of mesoscale convergence on cloud convection. *J. Appl. Meteor.*, **19**, 256-274.

Matsumoto, S. and T. Akiyama, 1969: Some characteristic features of the heavy rainfalls observed over the western Japan on July 9, 1967. Part 1: Mesoscale structure and short period pulsation. *J. Meteor. Soc. Japan*, **47**, 255-266.

Reisin, T., Z. Levin and S. Tzivion, 1996: Rain production in convective clouds as simulated in an axisymmetric model with detailed microphysics. Part I: Description of the model. *J. Atmos. Sci.*, **53**, 497-519.

Shepherd, J. M., B. S. Ferrier and P. S. Ray, 2001: Rainfall morphology in Florida convergence zones: a numerical study. *Mon. Wea. Rev.*, **129**, 177-197.

Soong, S. T. and Y. Ogura, 1973: A comparison between axisymmetric and slab symmetric cloud model. *J. Atmos. Sci.*, **30**, 879-893.

Tripoli, G. J. and W. R. Cotton, 1980: A numerical investigation of several factors contributing to the observed variable intensity of deep convection over south Florida. *J. Appl. Meteor*, **19**, 1037-1063.

Watanabe, H. and Y. Ogura, 1987: Effects of orographicallly forced upstream lifting on mesoscale heavy precipitation: a case study. *J. Atmos. Sci.*, **44**, 661-675.

Xin, L. and G. W. Reuter, 1996: Numerical simulation of the effects of mesoscale convergence on convective rain showers. *Mon. Wea. Rev.*, **124**, 2828-2842.

AN OBSERVATIONAL STUDY OF THE NIIGATA SNOWSTORM OF 4-6 JANUARY 2003

S. NAKAI[1], M. ISHIZAKA[1], K. IWAMOTO[1], M. SHIMIZU[1], A. SATO[1] and T. MARUYAMA[2]

[1]Snow and Ice Research Group, National Research Institute for Earth Science and Disaster Prevention (NIED), Nagaoka, 940-0821, Japan
[2]Niigata Electric Co., Ltd., Nagaoka, 940-1101, Japan

1. INTRODUCTION

On 4-6 January 2003, heavy snowfall occurred in the Niigata prefecture. The new snow depth and the precipitation amount from 0900 JST (Japan Standard Time; JST=UTC+9 hours) 4 January to 0900 JST 5 January were 55 cm and 52 mm, respectively, at Nagaoka Institute of Snow and Ice Studies (NISIS). Many trees were broken because of snow accretion. More than one thousand telephone lines in total were dead because telephone wires were destroyed by the weight of accreted snow. The snowstorm accompanied the Japan Sea Polar- airmass Convergence Zone (JPCZ).

In general, the spatial variation of the snowfall amount is large (*e.g.,* Higuchi 1963) and strongly affected by the topography (Nakai and Endoh 1995; Kodama et al. 1999) and the land breeze (*e.g.,* Tsuboki et al. 1989; Ohigashi and Tsuboki 2003). Therefore, it is important to investigate the snow cloud structure in relation to the surface snowfall in a meso-γ scale.

In the following sections, we will describe the results of the intensive observations using a Doppler radar and other facilities. The observation and data processing are described in Section 2; synoptic conditions are shown in Section 3; the results are presented in Section 4. Section 5 is the summary.

2. OBSERVATION AND ANALYSIS METHODS

During the Niigata snowstorm of 4-6 January 2003, we made intensive observations at the Nagaoka Institute of Snow and Ice Studies / National Research Institute for Earth Science and Disaster Prevention (NISIS/NIED) using an X-band Doppler radar (X-POL), the Snow Particle Observatory, and automatic weather stations (AWSs). The observation area of the X-POL was a semicircle with a radius of 64 km, mainly located on the coastal side of the NISIS. The topography is shown in Fig. 1.

The radar operation schedule included twelve steps of conical (PPI) scans, repeated in about 7.5-minute intervals. Three-dimensional distributions of the equivalent radar reflectivity factor (Ze) and the radial velocity (Vr) were obtained. The spatial

Corresponding author's address: Sento Nakai, Nagaoka Institute of Snow and Ice Studies, Nagaoka, 940-0821, Japan; E-mail: saint@bosai. go.jp

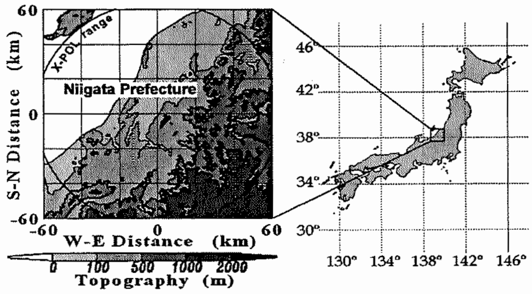

Fig. 1 Topography of the analysis area. The NISIS (37°25'N, 138°53'E) is located in the center of the left-hand square. The large solid circle indicates the X-POL observation range (64 km from the NISIS).

resolution of the raw data was 0.703° and 250 m, respectively, in tangential and radial directions.

The conical scanning data were analyzed in a conventional method of CAPPI as performed in Nakai et al. (2003). The three-dimensional data on the polar coordinate were converted into a three-dimensional Cartesian grid system with resolutions of 1 km and 500 m, in horizontal and vertical directions, respectively. A Cressman function (Cressman 1959) was used for the coordinate conversion. An animation movie of Ze and Vr at a height of 1.5 km was produced to examine the time change of the Ze distribution.

As for surface meteorological data, we operated two AWS stations. We also used the data of 11 AMeDAS (Automated Meteorological Data Acquisition System) stations operated by the Japan Meteorological Agency (JMA). Data of other AMeDAS raingauge stations were also used to examine the precipitation distribution. We also utilized the objective analysis data (Regional Spectral Model initial data).

3. SYNOPTIC CONDITION

According to the objective analysis data, a JPCZ had been formed on 2100 JST 04 January 2003 between a west-northwesterly flow from the Korean Peninsula and a northwesterly flow from the Maritime Province of Siberia (not shown). The former flow was more westerly near the coast of the Japan

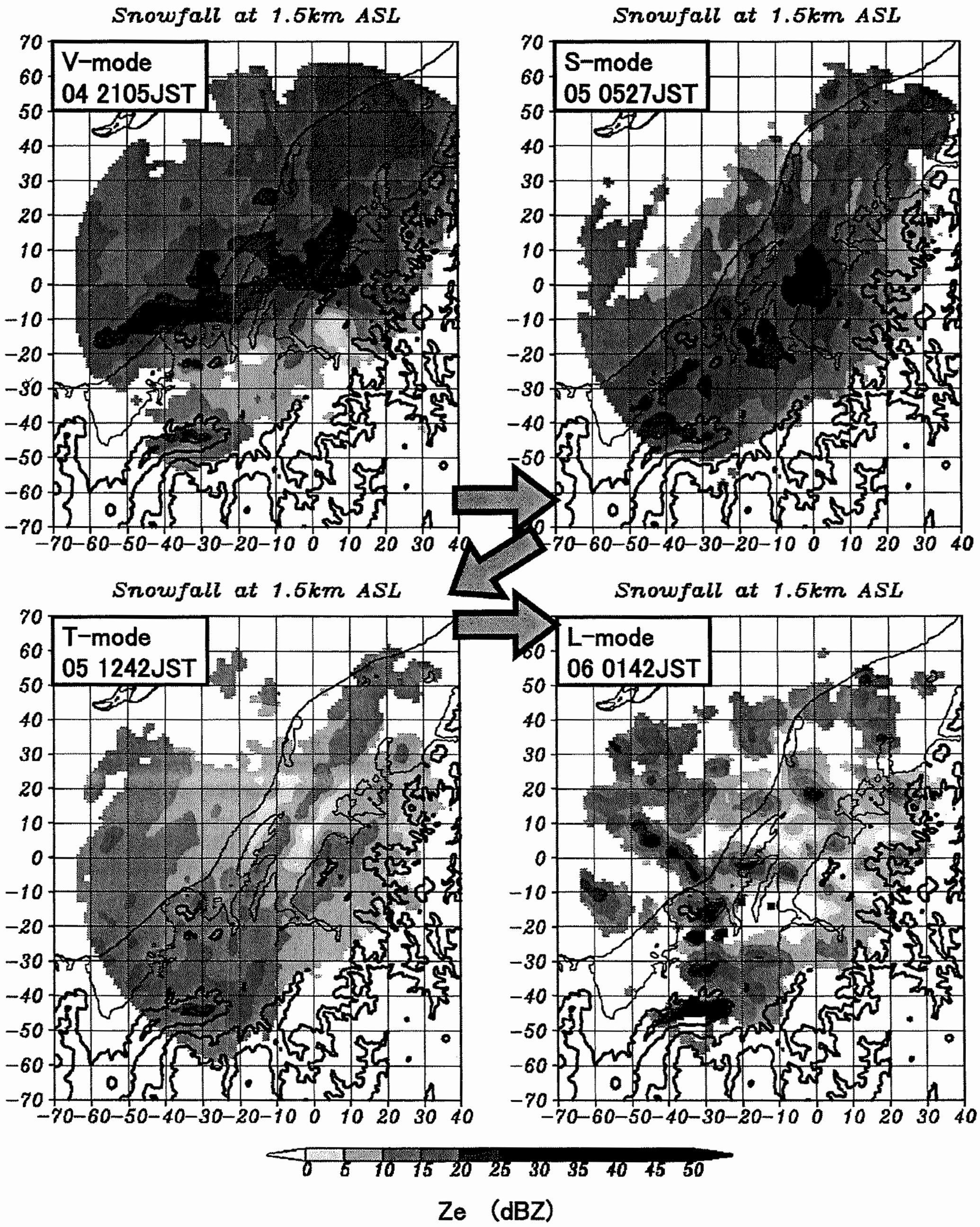

Fig. 2 Snowfall modes as a classification of snowfall distribution. Ze at a height of 1.5 km is shown in each panel by shading. The abscissa and the ordinate are the distance from the NISIS in km. Contours indicate 0, 100 (thin lines), 500, 1000 and 2000 (thick lines) meters.

Islands. The westerly wind proceeded to the east over the Main Island of Japan, and the convergence zone extended toward the Niigata Prefecture. Most of the Japan Sea was covered by a cold airmass less than -39 °C at the 500 hPa level at 21 JST 04 January. The cold airmass moved slowly eastward across the Japan Islands till 0900 JST 06 January.

4. CHARACTERISTICS OF THE SNOWSTORM

Table 1 Characteristics of the snowfall modes during the Niigata snowstorm of 4-6 January 2003.

Snowfall mode	V-mode	S-mode	T-mode	L-mode
Duration	>5.5 hours	5 hours	16 hours	20 hours
Total precipitation #	11.39 mm	9.82 mm	7.77 mm	6.78 mm
Mean surface precipitation intensity *#	2.14 mm h^{-1}	1.96 mm h^{-1}	0.49 mm h^{-1}	0.34mm h^{-1}
Echo top height	5 km	4 to 4.5 km	3 km	2 to 3 km
Snowfall enhancement ratio #	5.10	1.64	1.29	0.97
Surface temperature *#	-0.86 ^{o}C	-1.40 ^{o}C	-1.61 ^{o}C	-0.60 ^{o}C
Surface wind speed *#	2.14 m s^{-1}	2.13 m s^{-1}	5.25 m s^{-1}	4.35 m s^{-1}
Snow echo motion	East-northeast	Stationary	East-southeast	East-southeast
Prevailing wind at 1.5 km	West-southwest	Northwest	West-northwest	West-northwest
Snowfall particles	Rimed snowflakes and graupels	-	Mostly graupels	-

* Averaged for the duration.

\# Arithmetric mean of 13 surface stations.

4.1 Snowfall modes

The snowstorm was mainly composed of four periods of the characteristic snowfall distribution, "snowfall modes." The snowfall modes were defined using the Ze movie at a height of 1.5 km. Examples of the snowfall distribution of the four snowfall modes are shown in Fig. 2. V-mode indicates echo vortices. S-mode means the widely-spreading echoes. T- and L- modes are snow-echo streets aligned transversal and longitudinal to the prevailing wind, respectively.

The intensive observation started at 2105 JST 4 January, when V-mode snow clouds already existed. The snowfall mode changed from V-mode to S-mode at 0227 JST 5 January. The S-mode snowfall continued until 0712 JST 5 January. The T-mode snowfall was from 0727 JST to 2305 JST 5 January. Finally, the snowfall mode changed into L-mode at 2312 JST 5 January, which persisted until 1905 JST 6 January.

The prevailing wind direction was estimated using Vr fields at a height of 1.5 km. For the V-mode snowfall, it significantly changed from west-southwest to northwest. It is inferred that the echo vortices were generated in the synoptic-scale shear zone between the westerly flow and the northwesterly flow (not shown). The prevailing wind direction of the S-mode was northwest and the wind speed was slightly weaker than in the other snowfall modes. The prevailing wind in the T- and L- modes were strong west-northwesterly, which is the most typical wind direction around Niigata prefecture when the cloud street accompanying the cold-air outbreak appears.

4.2 Characteristics of the snowfall modes

The V-mode snowfall tended to concentrate on the northern slope of the mountains. The intensity of V-mode snowfall was often very strong with Ze more than 30 dBZ (Fig. 2). The echo-top was the highest among the four snowfall modes (see Table 1). The S-mode snowfall had a maximum between the coastal area and high mountains, corresponding to the location of stationary radar echoes. The intensity of S-mode snowfall was almost as strong as that of V-mode, with the echo-tops in S-mode being slightly lower than those in the V-mode. The surface snowfall of T- and L- modes increased with the distance of the station from the seashore. These modes were related to large wind speeds: 5ms^{-1} on the ground and more than 20ms^{-1} at a height of 1.5 km. The echo tops of these snowfall modes were low, and the surface precipitation intensity was weak, however, the total precipitation amount was comparable to that of the V- and S- modes because of the long duration.

Snowfall at a height of 1.5 km and the surface snowfall were compared using Ze (Fig. 2) and the surface precipitation. We adopted $Z_{ice}=554R^{0.88}$ (Fujiyoshi et al. 1990) as a Z-R relation. This relation was obtained by a careful comparison of the radar data and the snowfall weight measured by an electronic balance, and considered to be appropriate. As for the surface precipitation amount, temperature and wind speed were used for the snow-rain distinction and the correction of the catch ratio of the raingauge (Yokoyama et al. 2003). The lower-tropospheric enhancement ratio of the snowfall (ER) was defined by

$$ER = R_{surface} / R_{1.5}$$

where $R_{surface}$ was the corrected surface precipitation (in mm) and $R_{1.5}$ was the precipitation above (in mm) calculated from Ze. The ER was large in the V-mode and much smaller in the S-, T- and L- modes (Table 1). The difference may be attributed to orographic effects and the variability in Z-R relations as well as the inherent vertical structure of the snow clouds.

In the V-mode period, many rimed snowflakes and graupels were observed at NISIS using the Snow Particle Observatory (Fig. 3a). However, only graupels appeared in the T-mode period (Fig. 3b), and the number concentration of the snow particles

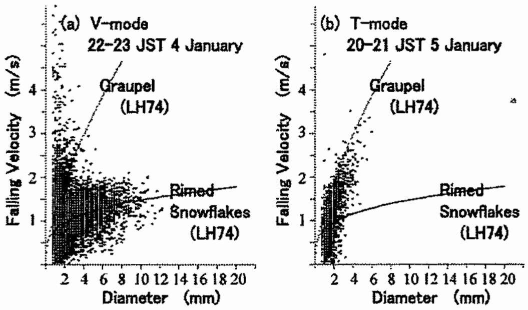

Fig. 3 Diameter-falling velocity scattergram of snow particles observed in the V- and T- modes derived at the Snow Particle Observatory of NISIS. LH74: Locatelli and Hobbs (1974).

was one order smaller than that in the V-mode period. The mean temperature of the V-mode was higher than that of the T-mode. Concerning the V-mode snowfall, it is suggested that the high echo-top resulted in the high number concentration of the ice crystals by natural seeding (Saito et al. 1996), and that there were enough supercooled cloud droplets for the riming growth of the snow particles with the high number concentration.

5. SUMMARY

The Niigata snowstorm of 4-6 January 2003 was observed and analyzed mainly using a Doppler radar, AWSs and the Snow Particle Observatory of NISIS. The "snowfall modes" were deduced from a sequence of Ze fields as shown in Fig. 2. The investigated storm was mainly composed of a sequence of V-, S-, T- and L- modes. The V- and S- modes showed large precipitation intensities, while the precipitation of the T- and L- modes was characterized by the relatively small precipitation intensities and long durations. The snowfall enhancement ratio was largest in the V-mode.

The V-, S- and T- modes were the internal structure of the band cloud accompanying the JPCZ. The evolution mechanism of a sequence of the snowfall modes is one of the remaining problems. The snowfall enhancement ratio is expected to be high when orographically forced lifting processes are important.

At this point, we are executing the quantitative data analysis using a nonhydrostatic numerical model.

ACKNOWLEDGMENTS

This work is supported by the NIED project "Research on a probability prediction system for snow disasters." The Regional Spectral Model (RSM) initial data and AMeDAS data were provided by JMA. DRAFT was used for the X-POL data analysis. The authors are grateful to Yoshinobu Tanaka of the Meteorological Research Institute and to other researchers who made efforts to develop and maintain DRAFT. We also thank Gerald Spreitzhofer for his helpful comments. GrADS was used for the construction of the figures.

REFERENCES

Cressman, G. W., 1959: An operational objective analysis system. *Mon. Wea. Rev.*, **87**, 367-374.

Fujiyoshi, Y., T. Endoh, T. Yamada, K. Tsuboki, Y. Tachibana and G. Wakahama, 1990: Determination of a Z-R relationship for snowfall using a radar and high sensitivity snow gauges. *J. Atmos. Sci.*, **29**, 147-152.

Higuchi, K., 1963: The band structure of snowfalls. *J. Meteor. Soc. Japan*, **41**, 53-70.

Kodama, Y.-M., M. Maki, S. Ando, M. Otsuki, O. Inaba, J. Inoue, N. Koshimae, S. Nakai and T. Yagi, 1999: A weak-wind zone accompanied with swelled snow clouds in the upstream of a low-altitude ridge — Single Doppler radar observations over the Tsugaru District of Japan —. *J. Meteor. Soc. Japan*, **77**, 1039-1059.

Locatelli, J. D. and P. V. Hobbs, 1974: Fall speeds and masses of solid precipitation particles. *J. Geophys. Res.*, **79**, 2185-2197.

Nakai, S. and T. Endoh, 1995: Observation of snowfall and airflow over a low mountain barrier. *J. Meteor. Soc. Japan*, **73**, 183-199.

————, K. Iwanami, R. Misumi, S.-G. Park, M. Shimizu and T. Kobayashi, 2003: Relation between snow-cloud mode and snowfall distribution observed in central Niigata prefecture (in Japanese with English abstract). *Report of the National Research Institute for Earth Science and Disaster Prevention*, No.64, 9-17.

Ohigashi, T. and K. Tsuboki, 2003: Structure and maintenance process of stationary snowbands along coastal region observed by Doppler and dual-polarization radars. *The 31st International Conference on Radar Meteorology*, 6-12, August 2003, Seattle, Washington, P5C.3.

Saito, K., M. Murakami, T. Matsuo and H. Mizuno, 1996: Sensitivity experiments on the orographic snowfall over the mountainous region of northern Japan. *J. Meteor. Soc. Japan*, **74**, 797-813.

Tsuboki, K., Y. Fujiyoshi and G. Wakahama, 1989: Structure of a land breeze and snowfall enhancement at the leading edge. *J. Meteor. Soc. Japan*, **67**, 757-770.

Yokoyama, K., H. Ohno, Y. Kominami, S. Inoue and T. Kawakata, 2003: Performance of Japanese precipitation gauges in winter (in Japanese with English abstract). *Seppyo*, **65**, 303-316.

INSIGHTS ON THE UPDRAUGHT EXTINCTION BY SATELLITE OBSERVATIONS AND CLOUD MICROPHYSICAL MODEL

Alvise Papa[1], Federico Porcù[1], Alessandro Battaglia[1] , Pao K Wang[2], Stefano Natali[3] and Franco Prodi[1,4]

[1]Dept of Physics, University of Ferrara, Ferrara, 44100, Italy
[2]Dept of Atmospheric and Oceanic Sciences, University of Wisconsin, Madison
[3]Nubila s.a.s., Bologna, Italy
[4]ISAC-CNR, Bologna, Italy

1. INTRODUCTION

The current knowledge on thunderstorms dynamics and structure is strongly based on radar observation (see Atlas, 1990 for a summary). In parallel, numerical simulations with different degree of microphysical treatment are providing interpretation tools of field data (Klemp and Wilhemson, 1978; Tripoli, 1992; Straka, 1989, among others). Satellite observations at visible-infrared wavelengths are limited by several shortcomings: lack of adequate resolution (time and/or space), cloud top/side-view, cloud envelop sensing. Passive microwave space-borne sensors, even if provide signals from lower cloud layers, are currently limited by coarse ground resolution and poor time coverage.

Nevertheless, satellite data contributed to the understanding of large scale convective cloud features, integrating radar information to some extent (Maddox, 1980; Morel et al., 1999 among others). In the last decade satellite capabilities increased: GOES, MSG, MTS and the low earth orbit Terra, Aqua, TRMM, are enhancing the role of satellite in cloud physics studies, given the high amount of spectrally detailed data.

In this work observations from the Moderate-resolution Imaging Spectro-radiometer (MODIS, on board low earth orbit satellites Terra and Aqua) are used to recognize and classify cloud top structures on mid-latitude thunderstorms: a sensitive number of observed events shows a warm ring-shaped signature in the IR data, which exceed the phenomenology of cloud top features already observed on large anvils such as V-shape, warm core (Negri, 1982; Heymsfield and Blackmer, 1988) and plumes (Levizzani and Setvak, 1996). In this study a multi-channel analysis has been performed to try an interpretation of this features in terms of radiative properties of the cloud particle at VIS-NIR-IR wavelengths. Geostationary infrared sequences are used to estimate cloud lifetime and cloud top divergence. In parallel, cloud microphysical model output are used to explore possible mechanisms producing the observed ring, and conclusion are drawn relating the cloud top depression with the updraft extinction.

Corresponding author's address: Federico Porcù, University of Ferrara, Dept. of Physics, Ferrara, I-44100, Italy; E-Mail: porcu@fe.infn.it.

2. DATA AND MODEL

Two convective seasons (April-July 2000 and 2001) in Europe were observed by MODIS and Meteosat data. In the 2000 summer Europe was particularly stroked by convective systems, causing, in some regions, an increase of the average monthly precipitation of a factor of two. Terra satellite overpasses continental Europe between 9:00 and 11:00 UTC and 21:00 and 23:00 UTC: unfortunately, such schedule doesn't allow the observation of the smaller scale convective development (taking usually place in the afternoon). Nevertheless, long lasting systems were observed by the evening overpass during their mature/decaying stage. Meteosat dataset were also available, allowing the IR monitoring of the cloud life and the estimate of the cloud top divergence.

The microphysical model used in this work is a reviewed version of the WISCDYMM model developed by Straka (1989), where time-dependent, energy conserving, and non-hydrostatic primitive equations are cast in quasi-compressible form. The model utilizes six different types of water substance: water vapor, cloud droplets, cloud ice crystals, rain drops, snow, crystals and aggregates, graupel/hail. There are a total of thirty-eight microphysical processes incorporated in the model including nucleation, condensation, evaporation, freezing, melting, sublimation, deposition, auto-conversion and accretion. For this study the WISCDYMM exponential size distributions for rain, snow and graupel/hail, and monodispersed distributions for cloud water and cloud ice) has been used.

Since there are no limitations in vertical and horizontal spatial resolution, and the lower limit for temporal resolution is 2 seconds, a compromise among simulations definition (spatial and temporal as well) and computational resources, sets spatial resolution at 1 km, and temporal resolution at 2 minutes. A horizontal grid spacing of 1 Km and vertical spacing of 0.5 Km over 20 Km depth and over a 56x56 Km horizontal domain is found to adequately resolve the dynamics of all storms here analyzed. To keep the storms near the center of the domain, a mean horizontal wind is removed from the base state wind profile and is frequently adjusted to accommodate changes in the storm propagation. To initiate convection in the model, a technique similar to Klemp and Wilhelmson (1978) is used. A warm thermal bubble is placed in the center of the domain, which is 20 Km wide, 4 Km deep, and is centered 2 Km above ground level in horizontally homogeneous environment. The maximum thermal perturbation is 4.5° C in the center of the bubble, and the mixing ration is adjusted to keep the relative humidity the same as that in the undisturbed soundings.

3. WARM RING SATELLITE VIEW

A total of about 60 ring shaped structures were detected during the two observation periods. The main characteristics were:

- occurrence over mature anvils, in the last part of the cloud life;
- no sensitive temperature difference alongside IR spectrum (8.5, 10, 11 μm);
- temperature difference of several degree between overshooting top, ring and anvil.

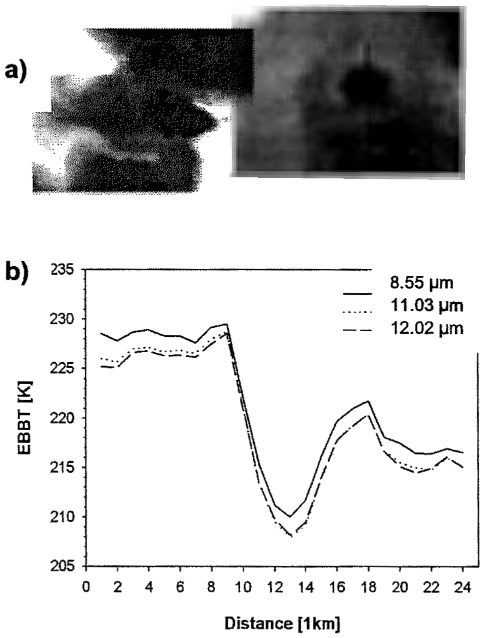

Figure 1. a) MODIS IR image of warm ring over a mature anvil; b) EBBT cross section along the black line on the image of EBBT in three IR channels

In figure 1a, the IR 11 μm MODIS image of a thunderstorm cluster over central Europe is shown, and in fig 1b the equivalent black body temperature (EBBT) cross sections alongside the two directions sketched in fig.1a, in three IR channels. Since no marked differences in the radiative properties of the particles appear, the temperature increase seems to correspond to an effective depression of the cloud top surface. For other daytime events was also possible to make an estimate of cloud top particles effective radius (Rosenfeld and Lenski, 1998), and negligible differences in effective radius among ring, over- among ring, overshooting top and anvil were noted.

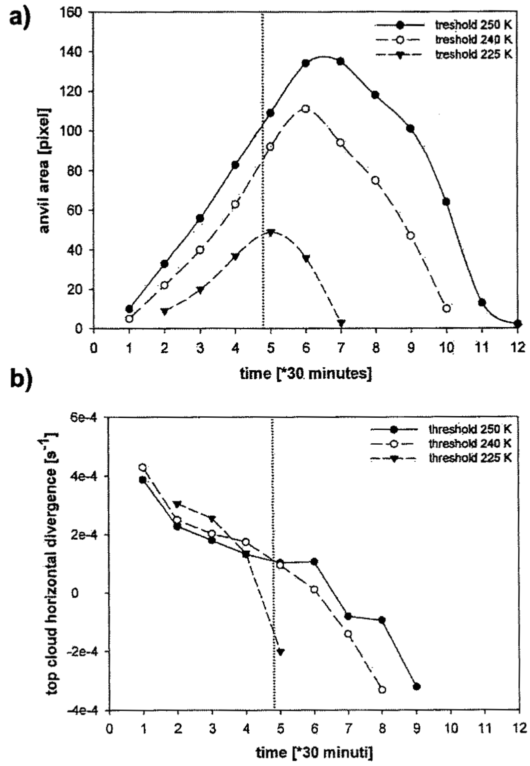

Figure 2. a) Time evolution of cloud areas at different EBBT thresholds by Meteosat IR, the vertical line shows the time of MODIS observation; b) cloud top divergence at different thresholds

The mesoscale organization of thunderstorms made difficult the estimate of cloud lifetime and cloud top divergence by means of Meteosat IR sequences. Usually convective cells merge and it is not possible to follow the cloud evolution beyond some initial stage. For few isolated storms was nevertheless possible to evaluate cloud areas at different EBBT thresholds and cloud top divergence as function of time: in fig 2a and 2b is shown the time evolution of cloud areas (in pixel) and divergence (computed as $1/A_c\ dA_c/dt$, where A_c is the cloudy area extent at three different thresholds) for the 25/07/2001 event occurred over central Mediterranean.

At the time of satellite overpass (01:10 UTC) (black vertical line), when the warm ring feature was detected, the 225 K area is in the last growing stage, when the updraft starts weakening. Warmer thresholds areas continue to grow for few hours, indicating the spreading of cloud top particles driven by upper level winds. The divergence analysis shows the change of the sign at the coldest threshold in correspondence to the warm ring observation, and one hour later also the warmer anvil is decaying. This suggests that the ring feature occurrence is related to the stage when the updraft start weakening and thus to the decaying of the thunderstorm. Since such feature is not frequently observed, we suppose that is a rather short living phenomenon, occurring close to the last stage of the cloud life.

The more direct way to assess these suppositions would be a in-situ observations of the updraft, for instance by a ground Doppler radar, not available for this study. To provide an indirect assessment of the consistency of our interpretation of the warm ring meaning with respect to the dynamics of the cloud, we analyzed the output dataset of WISCDYMM.

4. MODEL SIMULATIONS

Two WISCDYMM runs of deep convective clouds were analyzed looking for warm ring signatures on cloud tops: both simulations show a clear ring-shaped depression around overshooting top in the 90% RHI isosurface.

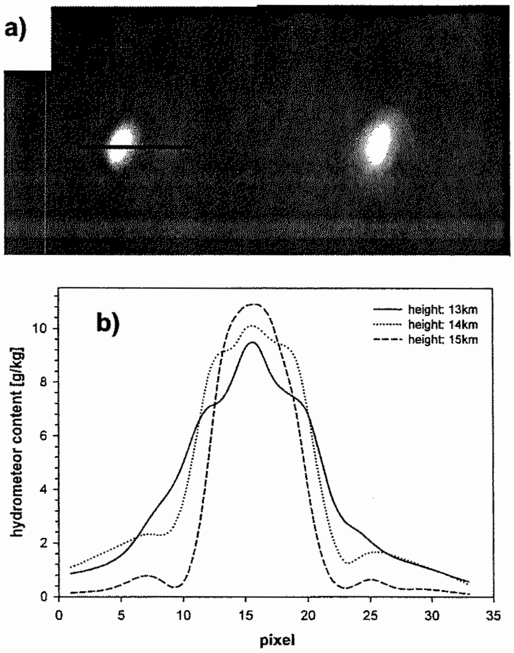

Figure 3. a) Horizontal cross sections of ice content a two cloud levels: 15 km (left) and 13 km (right) for the Nashville WISCDYMM simulation; b) cross section of ice content along the line on the image at three levels.

This feature shows up rather weak at different stages of the cloud life, but becomes deeper and more evident close to the end of the convective development. Only one simulation is shown and discussed here, relative to the 25-May-2000 storm, occurred near Nashville (TN). The environment of the simulated storm is very different from the continental Europe where we observed the warm ring features: e.g. CAPE values are larger of a factor of two in U.S. plains and also the wind shear is stronger. Nevertheless we assume that the differences in the severity of the storm, don't prevent the comparison of cloud top features in simulated and observed clouds.

In figure 3 the evidence of the occurrence of a warm-ring on the anvil of the simulated cloud is shown, considering horizontal cross sections of the hydrometeors content at different heights of the cloud volume. Figure 3a shows in gray shades, the total content of the three hydrometeor species (ice crystals, snow and graupel/hail) at two different levels: 15 km (left) and 13 km (right). In the center of the domain the updraft is characterized by high ice content at both the considered levels, while, surrounding the updraft, the ring of very low hydrometeors content is found only at the higher level. At 13 km, the content decreases with the distance from the center of the overshooting top. The total content along a line at three levels is shown in fig. 3b: the ice content at the highest level shows a local minimum symmetric to the maximum, while one or two kilometers lower, the decrease in ice content is monotonic, and a not negligible ice content is present on the anvil.

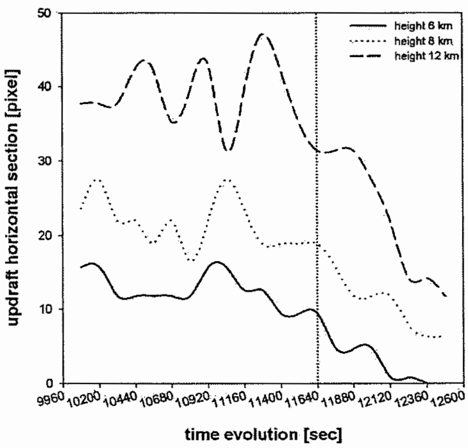

Figure 4. Time evolution of the horizontal section of the updraft current with vertical velocity higher than 25 m/s, at three cloud levels, for the Nashville simulation. Vertical line indicates the occurrence of the ring shaped depression on the anvil.

The stage of the cloud life represented in fig. 3 was after 11640 seconds (about 3 hours) after the convective initiation, being about 4 hours the total duration of the simulation. To assess the dynamics of the clouds at the time of the ring-shaper depression at the top, we considered, as indicator of the updraft strength, the horizontal section of the vertical velocity field exceeding a fixed threshold. During the cloud life, the updraft speed reached 50 m/s as maximum close to the center of the vertical current: we choose 25 m/s as threshold velocity to define the horizontal size of the updraft current.

In figure 4 the evolution of the size of horizontal cloud section with vertical velocity greater than 25 m/s is shown. The areas at three levels are plotted as function of time around the 11640 time step of the simulation, when the ring showed up. The size of the updraft is stationary, with fluctuation, at all levels, till about the 11160^{th} seconds of cloud life, when it starts decreasing at the lower levels. The shrinking of the updraft current propagates vertically in few time steps, and reaches the cloud top at the time of the ring features occurrence around the overshooting top. After this time, the areas of strong vertical velocity vanishes at all levels in few minutes of the simulation, indicating the cloud collapse.

This analysis confirms the link between the occurrence of the warm ring on the cloud top, and the last stage of the cloud life.

5. DISCUSSION AND CONCLUSIONS

In this work two convective seasons over Europe were analyzed by MODIS and Meteosat infrared data, in order to detect the occurrence and classify cloud top features over isolated thunderstorms. A ring shaped feature is found over mature anvils around the overshooting top, several degree warmer than the anvil and the top. The analysis of cloud top divergence, as estimated by Meteosat sequences, shows the occurrence of this feature close to last stage of the cloud life, induced by the collapse of the updraft. To confirm this hypothesis, we analyzed the microphysical output of the WISCDYMM, in order to verify if such feature is present also on the modeled convective cloud and to study the dynamic of the cloud at the time of the warm ring occurrence.

Model simulated hydrometeors content shows the occurrence of a ring-shaped depression on the anvil around the overshooting top, close to the extinction of the updraft current. A detailed analysis of the vertical velocity field shows that the warm ring occurrence on the cloud top is related to the shrinking of the updraft current, as the convective cell starts decaying. The larger hydrometeors lifted by the updraft precipitate as the vertical speed decreases and, since the vertical velocity decreases radially, this result in a cloud top depression un the external border of the overshooting top.

To further assess these findings two main lines have to be pursued: to run the model on a European environment and to look into in-situ measurements (such as radar data) coincident to satellite overpasses.

6. REFERENCES

Atlas, D. (Ed.), 1990: *Radar in Meteorology*, American Meteorology Society, Boston, 806 p.

Klemp, J. B. and R. B. Wilhemson, 1978: The simulation of three-dimensional convective storm dynamics. *J. Atmos. Sci.*, **35**, 1070-1096.

Heymsfield, G. M., and R. H., Blackmer, 1988: Satellite-observed characteristics of Midwest severe thunderstorm anvils. *Mon. Wea. Rev.*, **116**, 2200-2224.

Negri, A. J., 1982: Cloud-top structure of tornado storms on 10 April 1979 from rapid scan and stereo satellite observations. *Bull. Am. Met. Soc.*, **63**, 10, 1151-1859.

Levizzani, V., and M.Setvák 1996: Multispectral, high-resolution satellite observations of plumes on top of convective storms. *J.Atmos.Sci.*, **53**, 361-369.

Maddox, R., 1980: Mesoscale Convective Complexes, *Bull. Am Met. Soc.*, **61**, 1374-1387.

Morel C., S. Senesi, K.A. Browning and P. Panagi, 1999. A climatology of European mesoscale convective systems using Meteosat images and NWP analysis, COST78-Final Seminary-ECAM99.

Rosenfeld D. and I. Lenski, 1998: Satellite-based insights into precipitation formation processes in continental and maritime convective clouds, *Bull. Am. Met. Soc.*, **79**, 2457-2476.

Straka, J. M., 1989: Hail growth in a highly glaciated central High Plains multi-cellular hailstorm. Ph.D. Diss., Dept. Meteorology, Universitiy of Wisconsin, Madison, 413 pp.

Tripoli, G.J., 1992: A nonhydrostatic mesoscale model designed to simulate scale interaction. *Mon. Wea. Rev.*, **120**, 1342-1359.

7. AKNOWLEDGEMENTS

This work has been jointly funded by the Italian National Group for Prevention from Hydro-Geological Disasters (GNDCI), and within the framework of EURAINSAT a shared-cost project (contract EVG1-2000-00030) co-funded by the Research DG of the European Commission within the RTD activities (5th Framework Program).

ANVIL CIRRUS STRUCTURE

J. M. Petre and J. Verlinde

Department of Meteorology, Pennsylvania State University, University Park PA 16803

1. INTRODUCTION

Tropical anvils are frequently considered to be well-mixed layers (Lilly, 1988), with radiative cooling at cloud top providing the mixing mechanism (Ackerman et al, 1988). Contrary to this assumption, after dusk on 21 July 2002, a vertically pointing radar at the Tamiami Airport in Miami detected persistent shear instability, also known as Kelvin-Helmholtz instability, in a convective outflow anvil. To our knowledge, the observations presented in this paper are the first documented large-amplitude, embedded Kelvin-Helmholtz billows inside a tropical anvil and point to a distinct layering in the anvil.

Radar has been used before to detect shear instability in the atmosphere. The early work of Gossard and Richter (1970) and Gossard et al. (1971) described the detailed structures of shear instability in clear air using a vertically-pointing, frequency-modulated, continuous-wave radar system operating at a wavelength of 100 mm. Browning (1971) conducted radar observations of shear instability in Britain and documented numerous episodes, mostly in clear-air turbulence near the jet stream. This phenomenon also occurs in clouds; for example, Chapman and Browning (1997) captured radar imagery of Kelvin-Helmholtz billows near the surface in clouds associated with a warm front over southwestern England. In either case, a distinct interlaced double-sinusoidal structure first described by Kelvin (1880) characterizes this type of instability and allows for easy identification.

2. DATA AND METHODS

The cloud radar data presented in this paper were collected by the University of Miami Radar Laboratory Group at the Kendall-Tamiami Executive Airport in Miami, Florida, on 21/22 July 2002 as part of the Cirrus Regional Study of Tropical Anvils and Cirrus Layers-Florida Area Cirrus Experiment (CRYSTAL FACE). The University of Miami radar is described in detail by Lhermitte (1987). The data collection occurred between 01:00 and 05:00 Universal Time Coordinate (UTC) on 22 July 2002, or 21:00 to 01:00 Eastern Daylight Time (EDT, local time) 21 22 July 2002. The life cycle of an anvil was sampled from shortly after its initiation by convection through its detached anvil stage; afterward, the anvil advected eastward, away from the radar site.

Corresponding author's address: Hans Verlinde, Dept. of Meteorology, Penn State University, PA 16803, USA; E-Mail: Verlinde@ems.psu.edu.

The radar system recorded calibrated in-phase and quadrature values from every pulse and range gate from the surface to an altitude of 15,210 m with a vertical resolution of 30 m. These low-level measurements were processed to provide velocity power spectra for every range gate every 2 to 3 s (Kollias et al., 2001). Because most spectra exhibited a sharp drop-off in power at their slow-falling edges—indicative of low turbulence conditions—the volume-mean air velocity was taken as the velocity of the slowest-falling particles with signal above the noise (Babb et al., 1999; estimated error < ±0.1 ms^{-1}). In addition to the volume-mean air velocity, the total reflectivity and Doppler spread were calculated.

3. RESULTS AND DISCUSSION

The Fig. 1 presents time-height evolutions of the radar reflectivity, the volume mean air velocity, and the Doppler spread. The left-hand side of each image

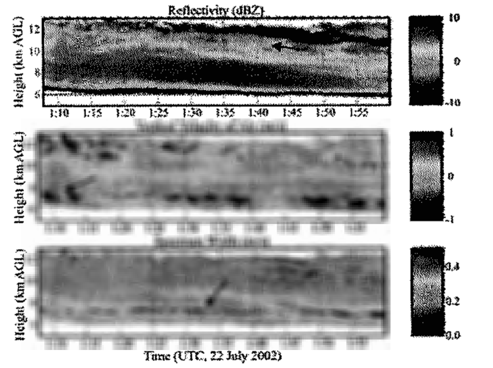

Figure 1 : Radar reflectivity (dBZ), vertical velocity of the air (m s-1), and Doppler spread (m s-1) from the University of Miami vertically-pointing cloud radar. The arrows point an embedded generating cell (top panel), and a long-lasting shear line (lower two panels).

represents the time when convection was still active close to the radar, the right-hand side the detached anvil. The reflectivity image (top) reveals a descending pattern throughout the period, associated mostly with precipitation, leaving smaller, low-reflectivity particles at cloud top. The radar-resolved cloud top region exhibits mostly upward air motion (center), varying between 0 ms^{-1} and 1 ms^{-1} over brief periods, indicative of generating cells. The method used to determine the air motion likely results in an overestimation of the velocity in this turbulent region

(Giangrande et al., 2001). As the anvil matures, these generating cells gradually sink deeper into the anvil, eventually becoming deeply embedded in the anvil (indicated by the arrows, more than 2 *km* below cloud top). The lower part of the anvil exhibits predominantly descending motion, consistent with expectations for anvil regions on mesoscale convective complexes.

The most notable feature in these images can be seen in the velocity and Doppler spread fields at 7 *km*, a closer view of which is presented in Fig.2. In addition to this feature, several other similar though less conspicuous features can be found in the velocity and Doppler spread fields (e.g. at 9 km early in the period). An understanding of the causes of high spread in profiling Doppler spectra is critical for the interpretation of these features.

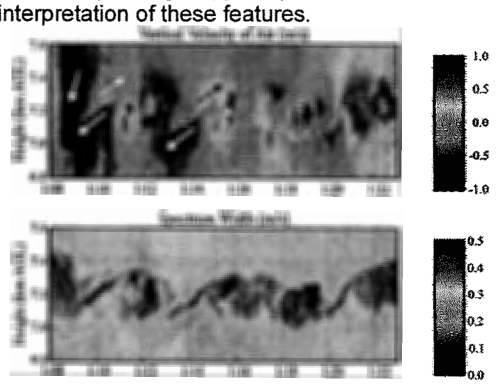

Time (UTC, 22 July 2002)

Figure 2 High resolution view of the vertical velocity of the air (m s^{-1}) and Doppler spread (m s^{-1}) fields of the well-developed shear instability. The white dots track the axis of the maximum Doppler spread

Wide spectra can be produced by either 1) hydrometeors within the radar volume with wide-ranging fall velocities, or 2) sub radar-volume velocity fluctuations. An example of the first can be seen at the high Doppler spread associated with the embedded generating cell. The fall streak emanating from the generating cell represents a region where precipitating hydrometeors fall through the population of otherwise smaller hydrometeors, producing a wide Doppler spread.

Looking at the feature at 7 *km*, a clearly different pattern is discernable. Here the Doppler spread feature is frequently only a single range gate (30 *m*) wide and is situated in an almost uniform reflectivity field. Velocity fluctuations within the radar volume, therefore, must produce the high Doppler spread. At times (Fig. 2, 1:10 UTC, 1:14 UTC), this turbulence is confined to a layer less than 30 meters in depth, the narrowness of which suggests that the velocity fluctuations result from turbulence generated by vertical shear of the horizontal wind confined to a very narrow layer. At other times, however, the sharply defined line broadens into a diffuse, turbulent structure through the entire 300 *m* depth of the feature.

To highlight better the structure of the shear layer, we added white markers on both the volume-mean air vertical velocity and Doppler spread images in Fig. 2. These markers represent local maxima of the Doppler spread fields in each profile; they serve to indicate the axis of maximum shear or "boundary" between the two cloud layers on the velocity plot. Each of these points satisfies a set of objective criteria applied to its respective vertical profile: 1) all spectra within 100 *m* vertical separation of the point must have sufficient signal to process; 2) must be primary maximum, defined as having no higher Doppler spread within 100 m; and 3) must exceed the minimum Doppler spread within 100 m by at least 0.0652 ms^{-1}. Taken as a whole, the structure of this shear layer resembles a breaking wave with interlaced sinusoids, reminiscent of Kelvin's (1880) "cat's eye" vortices, long associated with shear instability (see further Browning 1971; Reiss and Corona 1977).

To further illustrate the resemblance to Kelvin-Helmholtz billows, arrows of the relative air motion, deduced from the vertical velocity pattern, have been drawn on the velocity image. These velocity vectors generally support a hypothesis that the air in the lower layer below the shear axis moves (relatively) to the left while the air in the upper layer moves to the right. Kelvin-Helmholtz instability occurs when two layers of different densities experience a relative shear across the density interface. The deduced flow field, with shear across the Doppler spread maximum, is consistent with that expected in developing shear instability. We then conclude that these observed features in the velocity and Doppler spread fields indicate shear instability in the interior of the anvil. This shear instability occurs within the cloud; lidar observations confirmed that the visible cloud base was at approximately 6 *km*, 1 *km* below the shear instability.

Theory suggests that the instability occurs when the layer gradient Richardson number drops below a critical value. Although no sounding passed through these particular anvils during the measurement period, the National Weather Service office in Miami released a balloon-based radiosonde that penetrated another anvil about an hour and a half before these radar observations. The anvil penetrated by this sounding extended from cloud base, just above 7 *km*, to a cloud top well above 11 *km*. Computation using centered differences reveals no Richardson number less than 0.25, the presumed critical value. The critical Richardson number, however, depends significantly on the resolution of the measurements used to calculate it. In his half-year study of Kelvin-Helmholtz billows in Britain, Browning (1971) observed five events with Richardson numbers greater than 0.5 based upon hourly radiosonde data with a 400 *m* vertical resolution. Using the criterion that $Ri < 1$ indicates possible conditions for shear instability, the National Weather Service sounding shows that conditions conducive to shear instability may have existed at altitudes of 7.1 *km*, 7.6 *km*, and 9.7 *km*.

The shear instability at 7 *km* lasted for the full hour presented here (Fig.1); observations not presented show that it lasted for an additional 2.5 hours, slowly descending about 1 km to the cloud base. When the shear instability reached cloud base, the radar operators made visual observations of mammatus (Jo et al. 2003). Martner (1995) hypothesizes that the mamma clouds that he observed west of Thompson, Manitoba formed from a Kelvin-Helmholtz billow or another wave phenomenon within the interior of the cloud.

In his long-term study of Kelvin-Helmholtz billows in Britain, Browning (1971) noted sixteen shear-instability events. A quarter of these appeared for less than 2 minutes; half of the events lasted 10 minutes or less, and only one endured more than 18 minutes. This long-duration event of Browning (1971) lasted more than four hours, occurring near the tropopause along the axis of the jet stream as clear-air turbulence. Another long-lasting event of Kelvin-Helmholtz billows was described by Chapman and Browning (1997). In this case, the billows were associated with a warm front approaching southwestern Britain and persisted for three hours near the surface.

The vertical mixing associated with Kelvin-Helmholtz instability tends to weaken the shear that defines this phenomenon sufficiently to cause its demise; therefore, hours-long episodes of Kelvin-Helmholtz billows require a continuous shear-generating mechanism, such as a frontal boundary. With a vertical mixing depth of 300 m and a maximum vertical speed of 1 ms^{-1} (Fig. 2), the eddy associated with the shear instability overturns completely within 300 s or 5 minutes. The Kelvin-Helmholtz billows, despite this continuous turbulent destruction of shear, endure for more than an order of magnitude longer than the eddy-overturning timescale. The synoptic conditions over Florida do not suggest the existence of any synoptic-scale shear-generating phenomenon. Some local mechanism of the internal cloud dynamics, therefore, must provide this generating mechanism.

During the first half-hour of radar observations, the outflow from the quasi-stationary thunderstorm a few kilometers west of the radar site may have contributed to the generation of shear; however, these storms weakened quickly after dusk. Active lines of thunderstorms oftentimes contain rear-inflow jets that descend beneath the trailing anvil into the storm (Houze et al. 1989), with a front-to-rear flow within the cloud itself. A shear layer must lie between these two air currents; if they occur in sufficient proximity to one another, then shear instability may result. The rear inflow jet develops internal to the anvil (Houze 1993, p 385) such that the shear axis will be some distance above the cloud base. We hypothesize that such an anvil internal circulation was responsible for the persistence of the shear instability for the case presented here. The fact that the embedded Kelvin-Helmholtz billows lasted for more than an hour after the demise of the convection requires that an internal circulation within this anvil persisted for the same period.

4. CONCLUSIONS

Embedded Kelvin-Helmholtz billows occurred within an anvil over Miami on the evening of 21 22 July 2002. Although previous studies associate large-amplitude shear instability with Kelvin-Helmholtz billow clouds along frontal zones (Chapman and Browning 1997), to our knowledge, these are the first documented large-amplitude, embedded Kelvin-Helmholtz billows inside a tropical anvil. The duration of this phenomenon—more than three hours—suggests that internal anvil circulations played a role in continuously regenerating the instability, even more than an hour after the demise of all deep convection. The analysis demonstrates that the frequent assumption of an anvil as a well-mixed layer does not hold generally. In addition to the main shear axis along which the Kelvin-Helmholtz instability developed, several identifiable weaker shear layers existed in the anvil, evident in the Doppler spread, especially of the aged anvils. will be printed on both sides of the paper to commence on the next available page. No guarantee can therefore be given that particular pages will be printed to face each other. Figures, which must be viewed together, should be displayed on the same page.

Acknowledgements
Special thanks to Dr. Pavlos Kollias for providing the data and to the Miami Radar Laboratory for collecting the data. This work was supported by the National Science Foundation under grant ATM-0127360.

References

Ackerman, et al., 1988, *J. Atmos. Sci.*, **45**, 1606-1628.
Babb, et al., 1999, *J. Atmos. Oceanic. Technol.*, **16**, 489-503.
Browning, K.A., 1971, *Quart. J. Roy. Meteor. Soc.*, **97**, 283-299.
Chapman, D., and K.A. Browning, 1997, *Quart. J. Roy. Meteor. Soc.*, **123**, 1433-1439.
Giangrande, et al., 2001, *J. Atmos. Oceanic. Technol.*, **18**, 1577-1583.
Gossard, E.E. and J.H. Richter, 1970, *J. Atmos. Sci.*, **27**, 903-913.
Gossard, et al., 1971, *J. Atmos. Sci.*, **28**, 794-807.
Houze, R. A., 1993: *Cloud Dynamics*. Academic Press, 573 pp.
Houze, et al., 1989, *Bull. Amer. Meteor. Soc.*, **70**, 608-619.
Jo, et al., 2003, 31st AMS Int. Conf. Radar Meteor.
Kelvin, W. T., 1880, *Nature*, **33**, 45-46.
Kollias, et al. 2001, *J. Atmos. Sci.*, **58**, 1750–1766.
Lhermitte, R., 1987, *J. Atmos. Oceanic Technol.*, **1**, 36–48.
Lilly, D. K., 1988, *J. Atmos. Sci.*, **45**, 1594-1605.
Martner, B. E., 1995, *Mon. Wea. Review*, **121**, 3115-3121.
Reiss, N. M. and T. J. Corona, 1977, *Bull. Amer. Meteor. Soc.*, **58**, 159-162.

THE INFLUENCE OF MELTING ON THE PRECIPITATION PRODUCTION IN A MARITIME STORM-CLOUD

V.T.J. Phillips[1] and Alexander Khain[2]

[1] Atmospheric and Oceanic Sciences (AOS) Program , Princeton Unversity, Princeton, USA
[2]Institute of the Earth Science, Hebrew University of Jerusalem, Jerusalem, Israel

1. INTRODUCTION

The process of melting is not instantaneous: latent heat of melting must be provided, and this heat can only be supplied at a finite rate. At a steady state, the rate of heat transfer through the water layer to the ice core is balanced by the net rate of supply of heat to the surface by forced convection and by evaporation (or condensation). Consequently, smaller ice particles melt more quickly than larger ones.

There are some curious physical phenomena that occur during melting. Firstly, the onset of melting is delayed if particles fall through the 0 degC level in a subsaturated environment. This is due to evaporation temporarily absorbing all the heat supplied by forced convection from the environment. For instance, at a relative humidity of 50%, melting only begins at 4 degC, i(Pruppacher and Klett 1997). Secondly, the terminal velocity of graupel and hail is increased by the initial wetting of the surface of the particle, but can be subsequently reduced if a 'meltwater torus' develops around the equator of the particle.

A new melting procedure has been implemented in the Hebrew University Cloud Model (HUCM), by extending the scheme applied by Phillips *et al.* (2003). The procedure takes into account processes of diffusion of heat into the melting particles, and the modification of the terminal velocity of particles during melting, as well as shedding of water.

Accurate representation of melting is important for simulating the radar 'bright band' that characterizes stratiform melting layers. This will facilitate interpretation of radar observations of cloud. The radar reflectivity is high in the bright band partly because melted drops tend to be larger than simple raindrops. In the present paper, the impact from inclusion of this detailed melting scheme is examined.

2. MODEL DESCRIPTION

The HUCM is a two-dimensional non-hydrostatic model. The equations for velocity components, and the continuity equation, are expressed in terms of the vorticity and stream function. Thermodynamic equations include the equations for the potential temperature and water vapor-dry air mixing ratio.

Size distributions for several microphysical species are predicted in the HUCM, with 33 mass doubling categories for each microphysical species. These species are:- water drops, ice crystals, aggregates, graupel, frozen drops/hail, and CCN. Further details about the HUCM are given by Khain and Sednev (1996).

The new detailed melting scheme in the HUCM is based on models by:- (1) Rasmussen *et al.* (1984a) and Rasmussen and Heymsfield (1987) for graupel/hail; and (2) Mitra *et al.* (1990) for crystals/snow. For graupel and hail, meltwater initially accumulates in the interior of the ice particle, soaking up air-spaces (except for particles with a bulk density > 910 kg m^{-3}). When all air-spaces are filled up, meltwater begins to accumulate on the exterior of the particle. Shedding of raindrops occurs when the meltwater mass on the exterior of the particle exceeds a critical equilibrium value that depends on the mass of the ice particle. Shed drops have a size that is dependent on the Reynolds number (Rasmussen *et al.* 1984b). The heat budget of the particle determines its melting rate and includes diffusion of heat and (vapor) mass to and from the particle, with latent cooling from evaporation of meltwater. For Reynolds numbers < 3000, circulation of the meltwater is assumed to occur and the ice core is embedded in a spherical shell of meltwater. For the largest hail/graupel particles (Reynolds numbers > 20000), the heat transfer coefficient for rough spheres is applied (Bailey and Macklin 1968). When the surface of the ice particle is dry, (Eg. before the delayed onset of melting), sublimation occurs.

Snowflakes and crystals are assumed to have an ice skeleton structure that is incollapsable but of varying axial ratio during melting. Their capacitance and axial ratio are interpolated with respect to liquid fraction towards "totally melted" values of 80% of the dry value and 0.3 respectively. Empirical functions for the capacitance and axial ratio of dry ice particles are those given by Pruppacher and Klett (1997) for columns, dendrites, plates and snow. Whereas for snow and crystals there is a monotonic increase of the

Corresponding author's address: Vaughan T.J. Phillips, Princeton University, AOS Program, Geophysical Fluid Dynamics Laboratory (GFDL), Princeton, PO Box 308, New Jersey, NJ 08542-0308 USA; E-Mail: vaughan.phillips@noaa.gov

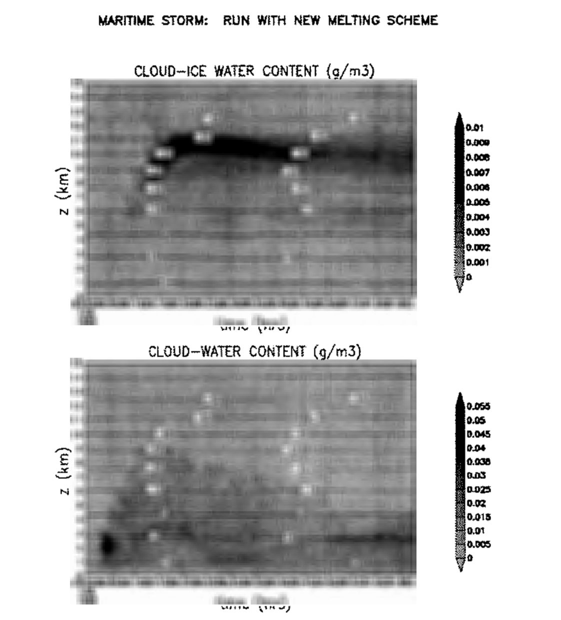

Figure 1. Cloud-ice and cloud-water contents (g/m^3) from the new melting case. H orizontal contours are isotherms (degC).

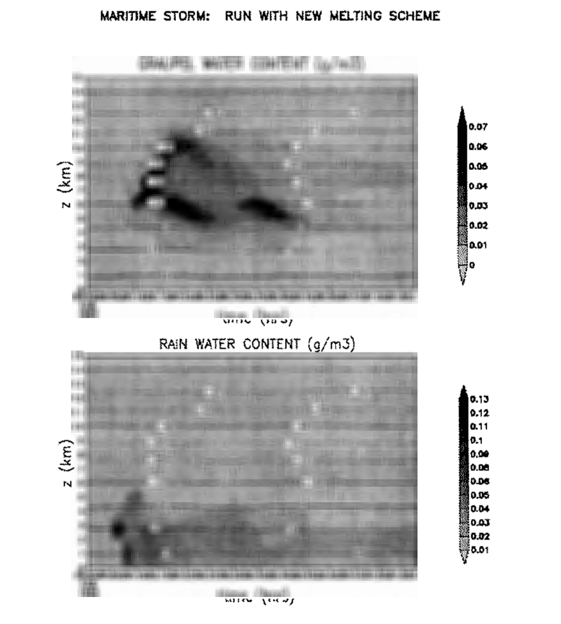

Figure 2. Graupel and rain contents plotted as in Fig. 1.

terminal velocity with liquid fraction during melting, the situation is more complex for hail and graupel. At the onset of melting, hail and graupel with Reynolds numbers < 4000 experience a sudden increase in terminal velocity because the drag coefficient becomes that of a smooth sphere as the ice surface becomes wet. But after the ice particle is fully soaked with meltwater, the shape of the particle is affected by meltwater being aerodynamically molded. The buildup of a meltwater torus tends to reduce the fall-speed.

A melted liquid fraction in each mass bin of ice particles is advected with the particles. If an ice particle with a non-zero liquid fraction penetrates into the region of subzero temperatures, the liquid fraction is set to zero (ie. the water is frozen). Adjustment of the ambient temperature and humidity is performed by the melting scheme as a result of the phase changes of melting, sublimation and evaporation.

3. SIMULATION WITH DETAILED MELTING SCHEME

The case simulated is a maritime storm observed on 1 July 1995. Figures 1 and 2 show the domain-averaged time-height maps depicting the evolution of the different microphysical species from the simulation with the new detailed melting scheme (the 'new melting case'). The storm's cloud-top ascends from 2 km MSL up to 11 km MSL from 00:00Z to 00:15Z. There are two ascending 'bubbles' of maximum cloud-water content that go through the freezing level at about 00:10 and 00:25Z. These bubbles produce copious graupel which falls out in two distinct episodes during the simulation. This graupel is partially converted to hail as it approaches the freezing level.

Most of the mass of snow, graupel, and hail melts within a few degrees of the freezing level. There is a maximum of rain created by the first graupel fallout. However, a small fraction (< 10 %) of the total original mass of ice penetrates up to about 1 km below the freezing level.

4. RESULTS FROM SENSITIVITY TESTS

4.1 Inclusion of Detailed Melting Scheme

The new melting case is compared with a simulation that is identical except that it is without the new melting scheme (the 'control'). In the control, all melting occurs instantaneously at the freezing level.

Figures 3, 4 and 5 show the difference maps depicting the effect of inclusion of the detailed melting scheme on the domain-averaged water contents of hydrometeor species and on the average temperature and humidity. In the new melting case, the snow, graupel and hail water contents are about 1 - 5 mg/m^3 over most of the layer 200-300 m below the freezing level during fall-out episodes. This compares to zero in the control. The water contents at the freezing level are of the order of 10 mg/m^3. Most of the mass of ice melts over this narrow layer in the new melting case. However, a small fraction (< 10%) penetrates down to the 10 degC level. This fraction corresponds to the few largest particles that take a long time to melt.

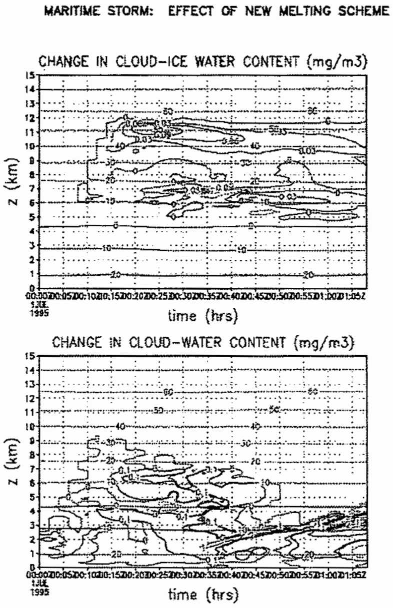

Figure 3. Change in cloud-ice and cloud-water contents (mg/m^3) due to inclusion of detailed melting scheme (new melting case minus control). Horizontal contours are isotherms.

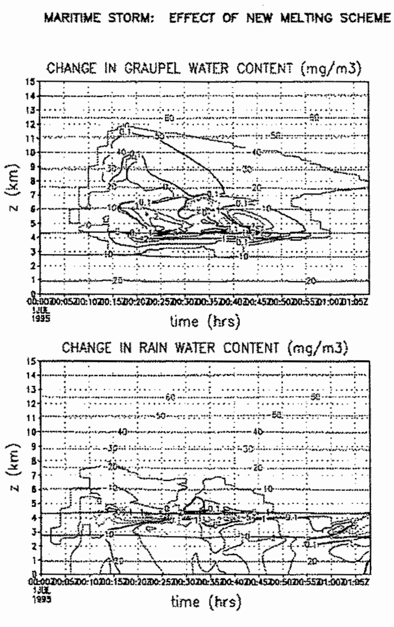

Figure 4. As for Fig. 3, except for graupel and rain.

During both episodes of fallout of graupel through the freezing level, the rainwater content is reduced by up to 5 mg/m^3 in the layer 200–300 m below the freezing level, as the melting of ice is prolonged in the new

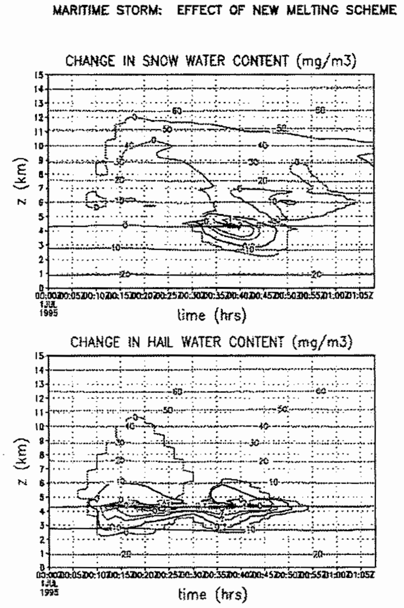

Figure 5. As for Fig. 3, except for snow and hail.

melting case relative to the control. Intensification of the graupel water content aloft by inclusion of the melting scheme accompanies the enhancement of rainwater content at all levels below this layer by up to about 1–2 mg/m^3 relative to the control.

Finally, inclusion of the detailed melting scheme is found to spread the latent cooling from melting over a much deeper layer than in the control. At the freezing level, the average temperature is increased by 0.02 K because all the ice no longer melts instantaneously there. The temperature is reduced by up to about 0.01 K between a level that is about 200 m below the average freezing level and the surface relative to the control.

4.2 <u>Terminal Velocity Adjustment During Melting</u>

The new melting case was compared with a run in which realistic adjustment of the terminal velocity during melting was prohibited, with melting particles falling at their dry fall-speeds (the dry fall-speed case').

Figure 6 depicts the difference in snow and hail water contents between the new melting and dry fallspeed cases. Inclusion of the variation of terminal velocity during melting was found to cause a general increase of the snow water content by up to 2 mg/m^3 over the 1 – 2 km layer below the freezing level throughout the snow fall-out event at 00:30 Z relative to the dry fallspeed case. This is because the gradual increase of fallspeed of each snow particle towards its final raindrop value during melting causes more overall penetration of snow mass towards the surface in the

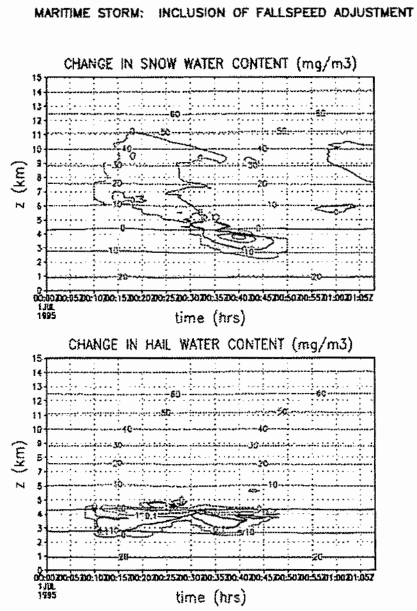

Figure 6. Change in snow and hail water contents (mg/m^3) due to inclusion of a realistic fallspeed adjustment during melting (new melting case minus dry fallspeed case). Horizontal contours are isotherms (degC).

new melting case. The layer over which 90% of the snow melts in the fallout event at 00:30 Z appears to be about twice as deep as in the dry fallspeed case.

Compared to snow, there is a qualitatively similar response of the hail and graupel water contents with respect to inclusion of the variation of terminal velocity during melting, except the over the 200-300 m layer immediately below the freezing level. Over this layer, they are up to about 2 mg/m^3 lower during fallout episodes. This temporary reduction in the hail and graupel water contents during melting may reflect a sudden increase in fallspeed linked to the surface of ice particles becoming wet as soon as melting begins (see Sec. 2).

5. CONCLUSIONS

Inclusion of the detailed melting scheme appears to produce a major impact on the distribution of snow, graupel and hail over the few hundred metres below the freezing level. It also enhances the rain water content during the fallout events documented here.

There is some qualitative agreement between the new melting case and aircraft observations of stratiform melting layers described by Willis and Heymsfield (1989), insofar as in this simulation:-

- most of the mass of ice melts over quite a narrow layer that is about 300 m deep;
- the layer of complete melting is much deeper than this;
- melting processes cause a significant impact on the ambient temperature profiles.

The duration of this simulation is probably insufficient for a consistent dynamical response to the detailed melting to become established. Over a longer time period of simulation, the detailed melting scheme might be expected to deepen the layer destabilized by melting.

Finally, the terminal velocity adjustment during melting (compare Figs 5 and 6) is a major contribution to the overall sensitivity with respect to inclusion of the detailed melting scheme.

6. REFERENCES

Bailey, I.H. and W.C. Macklin, 1968: Heat transfer from artificial hailstones. *Q. J. R. Met. Soc.*, **94,** 93-98

Khain, A. P., and I. Sednev, 1996: Simulation of precipitation formation in the Eastern Mediterranean coastal zone using a spectral microphysics cloud ensemble model. *Atmos. Res.,* **43**, 77-110.

Mitra, S.K., Vohl, O., Ahr, M., and H.R. Pruppacher, 1990: A wind tunnel and theoretical study of the melting behavior of atmospheric ice particles. IV: Experiment and theory for snow flakes. *J. Atmos. Sci.*, **47,** 584-591.

Phillips, V.T.J., Choularton, T.W., Illingworth, A.J., Hogan, R.J., and P.R. Field, 2003: Simulations of the glaciation of a frontal mixed-phase cloud with the Explicit Microphysics Model. *Q. J. R. Meteor. Soc.*, **129,** 1351-1371

Pruppacher, H. R., and J. D. Klett, 1997: *Microphysics of clouds and precipitation.* 2nd edition, Oxford Press.
Rasmussen, R.M., and A.J. Heymsfield, 1987: Melting and shedding of graupel and hail. Part I: model physics. *J. Atmos. Sci.,* **44,** 2754-2763

Rasmussen, R.M., Levizzani, V. and H. R. Pruppacher, 1984a: A wind tunnel and theoretical study of the melting behavior of atmospheric ice particles. II: A theoretical study for frozen drops of radius < 500 μm. *J. Atmos. Sci.,* **41,** 374-380

Rasmussen, R.M., Levizzani, V. and H. R. Pruppacher, 1984b: A wind tunnel and theoretical study of the melting behavior of atmospheric ice particles. III: Experiment and theory for spherical ice particles of radius > 500 μm. *J. Atmos. Sci.,* **41,** 381

Willis, P.T., and A.J. Heymsfield, 1989: Structure of the melting layer in mesoscale convective system stratiform precipitation. *J. Atmos. Sci.,* **46,** 2008-2025

EVALUATION OF VERTICAL AIR VELOCITY AND ITS DISTRIBUTION IN FOUR OPERATIONAL FORECAST MODELS USING CONTINUOUS DOPPLER CLOUD RADAR MEASUREMENTS

Alain Protat[1]*, Dominique Bouniol[1] and Martial Haeffelin[2]

[1]Centre d'étude des Environnements Terrestre et Planétaires, CNRS, Vélizy, France

[2]SIRTA, IPSL, Palaiseau, France

1. INTRODUCTION

In operational forecast and climate models, the life cycle of a cloud is strongly linked to its internal dynamics (sedimentation of cloud particles), to the environmental air dynamics (wind) and to the feedbacks between dynamics and microphysics. In a model, this essentially translates into two dynamic parameters that must be accurately represented: the terminal fall speed of the cloud particles, and the vertical air velocity. Vertically-pointing cloud radars measure the sum of these two quantities. As will be shown in what follows, these two components can be separated using simple statistical considerations. Such a method is applied in the present paper to continuous vertically-pointing Doppler cloud radar observations collected from the ground since October 2002 at three instrumented sites over Europe in the framework of the CloudNET European project (the SIRTA site in France, the Chilbolton Observatory in England, and the Cabauw site in the Netherlands). The vertical profiles of four operational forecast models (ECMWF, and the operational models from the meteorological offices of France, England and Netherlands) are also recorded over these three sites, which offers an unique opportunity to evaluate these models using active remote sensors. This paper reports the results for the vertical air velocity magnitude and statistical distribution in terms of probability density functions. It is clearly seen that the broad structures of vertical air velocity are generally well captured by the models. However the statistical distribution of vertical velocity is much narrower in the models than in the radar velocities computed at the model resolution.

2. RETRIEVAL OF THE DYNAMIC PARAMETERS

The method to recover the dynamic properties of clouds makes use of both the reflectivity factor Z and Doppler measurement V_D of a 95 GHz vertically-pointing cloud radar. The Doppler measurement is the sum $(V_t + w)$ of terminal fall speed of the hydrometeors and vertical air velocity. In order to estimate the terminal fall velocity, a statistical approach has been proposed in the case of frontal cyclones and weakly-precipitating ice clouds (Protat *et al.*, 2002, Protat *et al.*, 2003). It consists in developing statistical relationships between terminal fall speed and radar reflectivity. Terminal fall velocity and reflectivity are integral parameters of the particle size distribution (PSD). Ulbrich (1983) for a Gamma-type PSD, and Testud *et al.* (2001) for a normalized PSD, established that the relationships between integral parameters were represented by power-law relationships, which, in the case of the V_t-Z relationship, can be written as $V_t = aZ^b$, where Z is expressed in mm^6m^{-3}, and V_t in ms^{-1}. Within weakly-precipitating clouds, the vertical air motions are generally small, even at small scales of motion, as opposed to the case of convective systems. In any case, however, the vertical air motions are not negligible with respect to the terminal fall speed. For a long time span however (a few hours), the mean vertical air motions should vanish with respect to the mean terminal fall speed, which is much less fluctuating. A statistical power-law relationship between the terminal fall speed and radar reflectivity may therefore be derived from this statistical approach. This hypothesis has been recently validated in the case of frontal cyclones sampled during FASTEX (Protat et al. 2003). A more thorough validation of this assumption will be performed in a near future using high-resolution numerical simulations of cirrus clouds. Once the $V_t = aZ^b$ statistical relationship is obtained the radar reflectivity is easily translated into terminal fall velocity at each radar gate. Finally, this terminal fall velocity is subtracted from the Doppler velocity in order to access the vertical air velocity.

An illustration of this method is given in Fig. 1, which shows a plot of $V_D = (V_t + w)$ as a function of Z for 3 hours of cloud radar data collected in an ice cloud over the SIRTA. On this scatterplot a clear trend for an increase of negative Doppler velocity with reflectivity is obtained, which likely reflects the increase of terminal fall velocity and reflectivity with cloud particle diameter. A least-squares fitting has

*Corresponding author address: Alain Protat, CETP/CNRS, 10/12 avenue de l'Europe, 78140 Vélizy, France; *e-mail*: alain.protat@cetp.ipsl.fr

been carried out in order to derive the $V_t = aZ^b$ statistical relationship. At this step the hypothesis that the mean vertical air velocity is negligible with respect to the mean terminal fall velocity is applied. Most of the scatter around the fitted curve (order of magnitude of 20 cms^{-1}) is most likely attributable to the individual vertical air velocity contributions. It could also be argued that some of this scatter might be due to changes in the cloud microphysics but this cannot be checked out in the present case. The respective orders of magnitude of changes in cloud microphysics versus the vertical air velocity contributions will be evaluated in a near future using high-resolution numerical simulations of cirrus clouds.

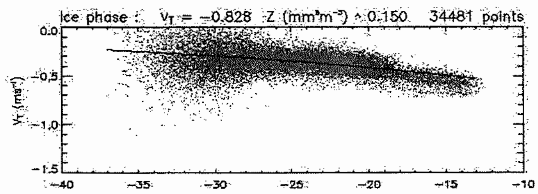

FIGURE 1: Statistical relationship $(V_t + w) = aZ^b$ obtained in an ice cloud sampled on 27 March 2003 from 0830 UTC to 1130 UTC over the SIRTA by the RASTA 95 GHz radar in a vertically-pointing configuration

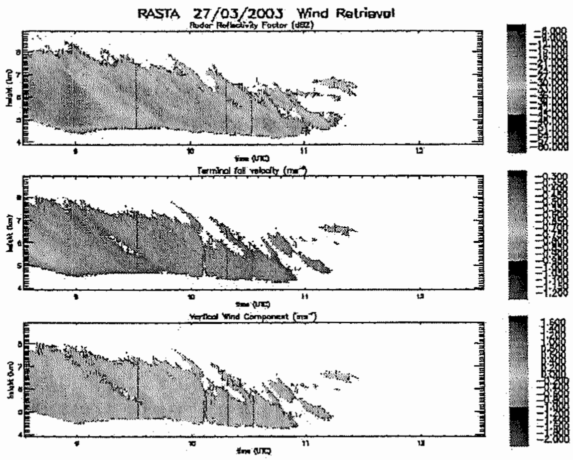

FIGURE 2: Time-height cross-sections of (a) radar reflectivity (dBZ), (b) terminal fall velocity (ms^{-1}), and (c) vertical air velocity (ms^{-1}) in the same ice cloud as that of Fig. 1.

This statistical relationship is then used to translate the time-height cross-sections of reflectivity into terminal fall velocity. This process is illustrated in Fig. 2. Fig. 2a shows the radar reflectivity, which is translated into terminal fall velocity (Fig. 2b) using the statistical relationship of Fig. 1. Terminal fall velocity values ranging from -0.8 to -0.4 ms^{-1} are obtained within this ice cloud, with the highest negative V_t values clearly correlated with the core of highest reflectivities in Fig. 2a. The last step of this retrieval of the dynamic properties consists in subtracting the terminal fall velocities from the Doppler velocity measurements, in order to access the time-height cross-section of vertical air velocity. This w cross-section is given in Fig. 2c, which shows the spatial distribution of updraft and downdraft within the ice cloud.

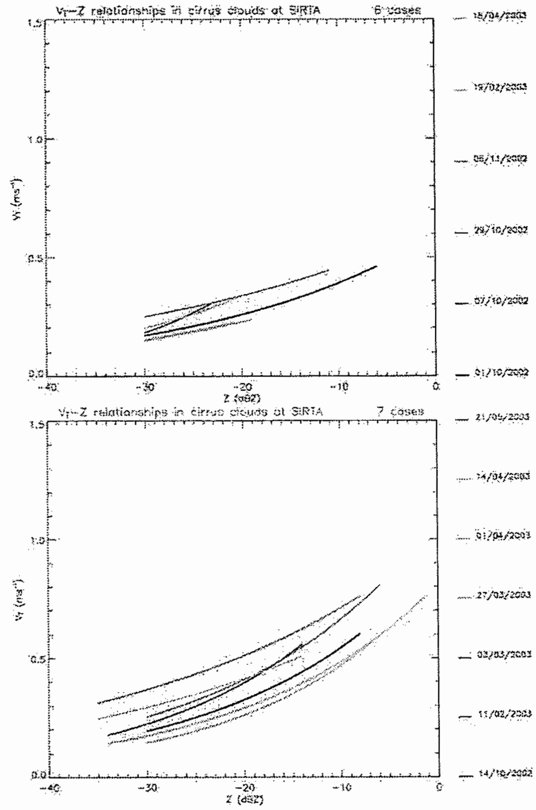

FIGURE 3: Statistical $V_t = aZ^b$ relationships for (a) thin cirrus clouds and (b) thick cirrus clouds sampled over the SIRTA with the RASTA 95 GHz cloud radar.

This method has been applied to one year of cirrus clouds in the CloudNET/SIRTA database. The obtained $V_t - Z$ relationships have been all displayed together in Fig. 3 for the thin cirrus cases and the thick cirrus cases (thin cirrus clouds are defined as having a cloud base upper than 8 km and a depth less than 2 km, thick cirrus are below 8 km altitude and deeper than 2 km). It is observed that the relationships for both the thin and thick cirrus categories are not very different from one case to another, with differences in V_t less than +-5 cms^{-1} for the thin cirrus clouds, +-15 cms^{-1} for the thick cirrus clouds, in the [-40,0] dBZ reflectivity range. However, it is clearly observed that the change in V_t as a function of reflectivity is clearly not the same for these two categories, with a faster increase in V_t as a function of reflectivity within the thick cirrus clouds. This likely reflects the fact that crystal densities/shapes are not the same in both types of clouds. In a near future, this method will be systematically applied to the databases from the three CloudNET sites, which will allow new parameterizations of the sedimentation of ice crystals to be developed. These new parameterizations derived from active remote sensing observations will help validate/improve the existing parameterizations within GCMs that were essentially derived from in-situ microphysical sensors (e. g., Heymsfield and Iaquinta, 2000).

3. Case study analysis of the accuracy of vertical air velocity in NWP models

In this section the time-height cross-section of vertical air velocity w retrieved using the method described in Section 2 is compared with those diagnosed by three operational forecast models. The analyses from these three models are indeed recorded hourly over the three CloudNET sites, which allow straight comparisons between the radar-derived and model estimates of w. Only one case will be shown for illustration in what follows, but the conclusions drawn from this case holds for most of the ice cloud cases that have been investigated in this study. The time-height cross-section of cloud radar reflectivities is shown in Fig. 4.

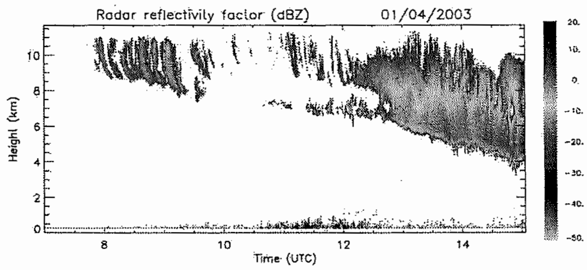

FIGURE 4: Time-height cross-section of radar reflectivity (dBZ) in a frontal passage over SIRTA on 1 April 2003. This case has been objectively selected for its scientific interest, although it also corresponds to the day the daughter of the first author is born.

This case corresponds to a typical prefrontal situation with high-altitude cirrus clouds passing first above the SIRTA, followed by a front with ice clouds progressively subsiding and ultimately producing precipitation at ground. This feature is a particularly

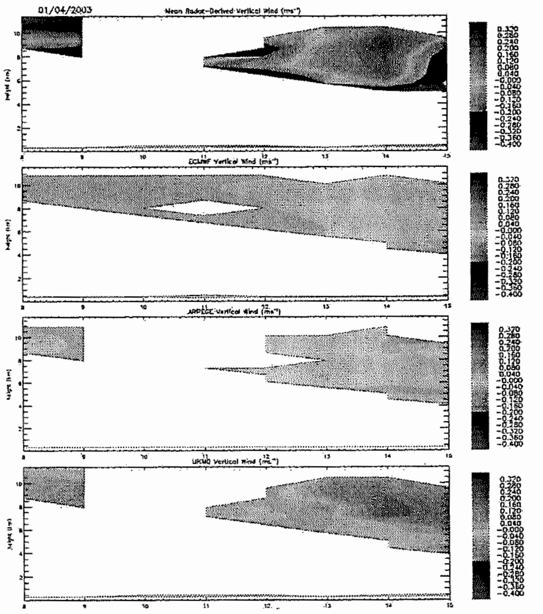

FIGURE 5: Time-height cross-section of vertical air velocity from (a) the cloud radar retrieval, w is averaged at the scale of the UKMO model, (b) ECMWF, (c) ARPEGE, and (d) UKMO. The case under study is that described in Fig. 4.

common situation in France and UK. A straight comparison of the performances of the three models as compared to the cloud radar retrieval (Fig. 5) highlights the importance of horizontal grid resolution in the representation of cloud dynamics. Indeed, it appears clearly in Fig. 5 that only the UKMO model is able to reproduce the updraft/downdraft structures within the clouds at its scale, and it is the model that has the highest horizontal resolution (UKMO grid is 12 km, while ECMWF and ARPEGE grids are 40 and 20km, respectively). It is noteworthy that in Fig. 5 the radar-derived w has been averaged at the UKMO scale, which may explain the differences between the other models and the radar-derived w. However, when averaging at the scale of the ECMWF model (40 km), the same conclusion still holds (not shown). Histograms of w values averaged at the scale of each model have been computed from the cloud radar retrieval of w. These distributions are displayed in Fig. 6, together with the histograms of w from the model outputs. This figure clearly indicates that the ECMWF and ARPEGE models do not fully represent the variability of vertical air velocity at their scale, while the UKMO has a broader distribution, in better agreement with the radar-derived distribution. This narrower distribution of vertical air motions in models may have a strong impact on the life cycle of the cloud. An in-

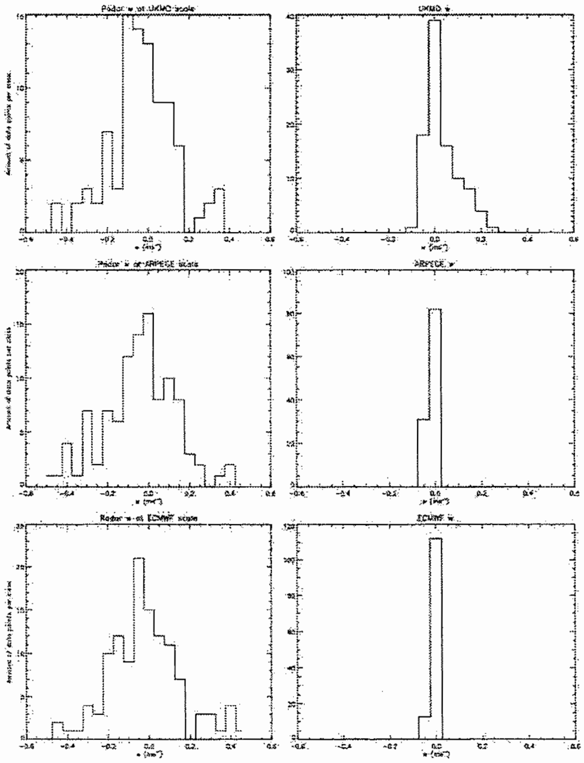

FIGURE 6: Histograms of vertical air velocity from the cloud radar, averaged at the scale of the three models (left) and the same histograms from the model outputs.

spection of the precipitation forecast by the ECMWF and UKMO models over the Cabauw site indicates that precipitation at ground, which occurred at 1330 UTC, was forecast at 1400 UTC by the UKMO model and 1800UTC by the ECMWF model. This large difference in timing of the frontal passage could be explained by the representation of vertical air velocity in the model, although other reasons could be invoked (the sedimentation parameterization, for instance, which has not been compared yet with the radar retrieval, but will be in a near future). It has to be mentioned that more generally the comparisons for other cases always indicate this behaviour of the ECMWF and ARPEGE models, and sometimes indicate that even the UKMO model fails to reproduce the radar observations. A more thorough statistics is under construction, but this preliminary study seems to indicate that the horizontal grid resolution has to be increased if the cloud life cycle is to be fairly reproduced by NWP models.

4. Conclusions and Outlook

In this paper, we propose and apply a method to separate the vertical air motion and terminal fall velocity contributions from vertically-pointing Doppler cloud radar measurements. This method has been applied to one year of cirrus clouds sampled over the SIRTA. Statistical relationships between terminal fall velocity and radar reflectivity are found to be fairly comparable for 'thick' and 'thin' cirrus clouds categories, but the 'thick' cirrus relationship is characterised by a sharper increase of terminal fall velocity as a function of reflectivity. The radar-derived vertical air motion has then been compared with the vertical air motion field of three operational forecast models. It is found that the model which has the highest horizontal grid resolution is the only model that broadly represent the natural variability of w at its own scale. It is therefore stressed that an inaccurate representation of w will impact the simulation of the cloud life cycle. It is therefore suggested that this problem be addressed by NWP modellers.

5. Acknowledgements

The RASTA 94 GHz radar has been developed with support from Centre National d'Etudes Spatiales and Institut des Sciences de l'Univers. Thanks go to the technical staff that helped develop the radars and conduct the CloudNET operations. This research received funding from the European Union CloudNET project (grant EVK2-CT-2000-00065).

6. References

Heymsfield, A. J., and J. Iaquinta, 2000: Cirrus crystal terminal velocities.J. Atmos. Sci., 57, 916-938.

Protat, A., C. Tinel and J. Testud, 2002: Dynamic properties of water and ice clouds from dual beam cloud airborne radar data : the CARL2000 and CARL2001 validation campaign, 11^{th} Conference on Cloud Physics, 3-7 June 2002, Ogden, UT, USA

Protat, A., Y. Lemaitre, and D. Bouniol, 2003: Terminal fall velocity and the FASTEX cyclones. Quart. J. Roy. Meteor. Soc., 129, 1513-1535.

Ulbrich, C. W., 1983: Natural variations in the analytical form of the drop size distribution. J. Cli. and Appl. Meteor., 22, 1764-1775.

Testud, J., S. Oury, R. A. Black, P. Amayenc, X-K Dou, 2001: The Concept of Normalized Distribution to Describe Raindrop Spectra: A Tool for Cloud Physics and Cloud Remote Sensing. J. Appl. Meteor., 40, 1118-1140.

Tinel, C., J. Testud, J. Pelon, R. Hogan, A. Protat, J. Delanoë and D. Bouniol,2004 : The retrieval of ice cloud properties from cloud radar and lidar Synergy. Submitted to J. Appl. Meteor, december 2003.

STRUCTURE AND LENGTH SCALES OF A STRATOCUMULUS FIELD DEVELOPING UNDER CONTINENTAL INFLUENCE: THE BBC CASE 23.09.01

M. Quante, J. Meywerk, and D. Nagel

GKSS Research Center, Institute for Coastal Research, Geesthacht, Germany

1. INTRODUCTION

A stratocumulus topped boundary layer is a feature of many marine and coastal as well as of some continental environments. During the Baltex Bridge Campaign (BBC) in 2001 (Crewell et al. 2004) the development of a stratocumulus field over the experimental site of Cabauw, NL, has been extensively observed by remote sensing instruments as well as by *in situ* measurements. The clouds developed under continental influence before they reached the observational site closer to the coast, where around noon a transition into a cumulus field organized in band like structures could be observed.

We report on internal structure of the stratocumulus and its break-up through convection in the developing boundary layer as deduced from high resolution reflectivity and Doppler measurements obtained by a vertically pointing cloud radar and from airborne microphysical observations.

The assessment of inhomogeneities within the cloud layers is of importance for radiative transfer calculations and the structure of embedded convection could well be significant for the transport of constituents to the free atmosphere.

2. METEOROLOGICAL SITUATION

The data presented here were collected on 23 September 2001. The extended cloud field was advected into the measurement area by a North-Easterly flow. A three day back-trajectory analysis (Boers and Krasnov, 2004) revealed that the air mass originated from central Europe with only a short fetch over the south western tip of the Baltic Sea before it turned counter clockwise towards the Cabauw area. Therefore, the attribute continental is justified for these clouds.

Vertical profiles of the potential temperature obtained from local radiosonde ascents, as displayed in figure 1, indicate an inversion during the morning hours until about 11 UTC capping the boundary layer at an altitude of about 700 m to 800 m. As data of the KNMI RASS profiler revealed the inversion weakened just after 11 UTC and the mixing layer height increased from about 500 m to about 1 km.

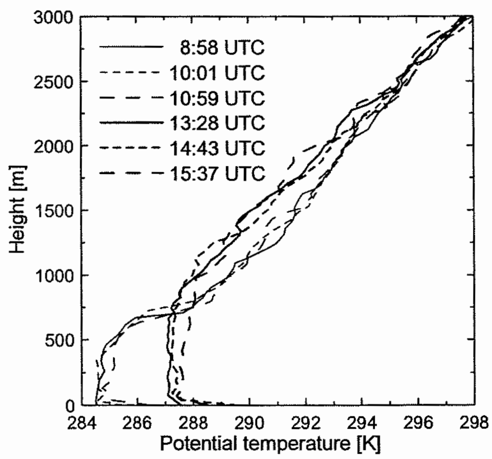

Figure 1: Potential temperature profiles obtained from radiosondes released at the Cabauw site on 23 September 2001.

Wind velocities at the boundary layer top measured by the KNMI 1290 MHz profiler were around 8 to 9 ms^{-1} with the general tendency to decrease slightly in the course of the afternoon.

During the entire morning until about 10 UTC a stratocumulus layer of about 300 m thickness was observed underneath the inversion. Cloud base heights measured by a Vaisala CT75 ceilometer increased from about 200 m at 6 UTC to 400 m at 10 UTC, and to about 800 m after the stratocumulus layer broke up into bands of cumuli. During the transition cloud top heights increased from about 700 m to 1.3 km. Radar

Corresponding author's address:
Markus Quante, GKSS Research Center, Institute for Coastal Research, D-21502 Geesthacht, Germany;
E-Mail: markus.quante@gkss.de

and airborne observations confirmed that for the entire morning and early afternoon no further cloud layers were present above the boundary layer clouds. The freezing level was at about 2 km altitude, well above the top of the clouds considered here, which can safely be considered as water clouds.

3. INSTRUMENTATION

Cloud radar MIRACLE: For the BBC campaign the transportable 95-GHz cloud radar operated by GKSS was set up at Cabauw. The pulsed-Doppler radar is fully polarimetric and has a peak power of 1.7 kW. Selectable pulse lengths allow for a range resolution between 7.5 m and 82.5 m up to a range of 15 km. The beamwidth of the center-fed Cassegrain antenna of 0.17° leads to a range cell diameter of 30 m at a distance of 10 km. During the measurements discussed here the radar was operated in a vertically upward pointing mode with a range gate resolution of 37 m. A more comprehensive description of the radar is provided in Quante et al. (2000).

Cloud microphysical measurements: During the BBC campaign the research aircraft MERLIN IV of Meteo France was additionally equipped with microphysical sensors of GKSS. Cloud particle number concentrations and sizes were measured with a FSSP-100-ER, a 2D2-C, and a 2D2-P probe, covering the relevant size range for water cloud droplets and precipitation size particles. A Nevzorov probe (Korolev et al., 1998) was used to assess the integral LWC and the total water content (TWC). LWC measurements were also made using a particle volume monitor, PVM-100A (Gerber et al., 2001), operated by Meteo France. This probe allows for fast sampling rates, the data used here was available with a time resolution of 0.005 s.

4. RESULTS

During the early morning hours of the 23rd of September 2001 the stratocumulus passing the observational site showed in general a closed appearance with some internal structure indicating weak convective activity. A transition to a

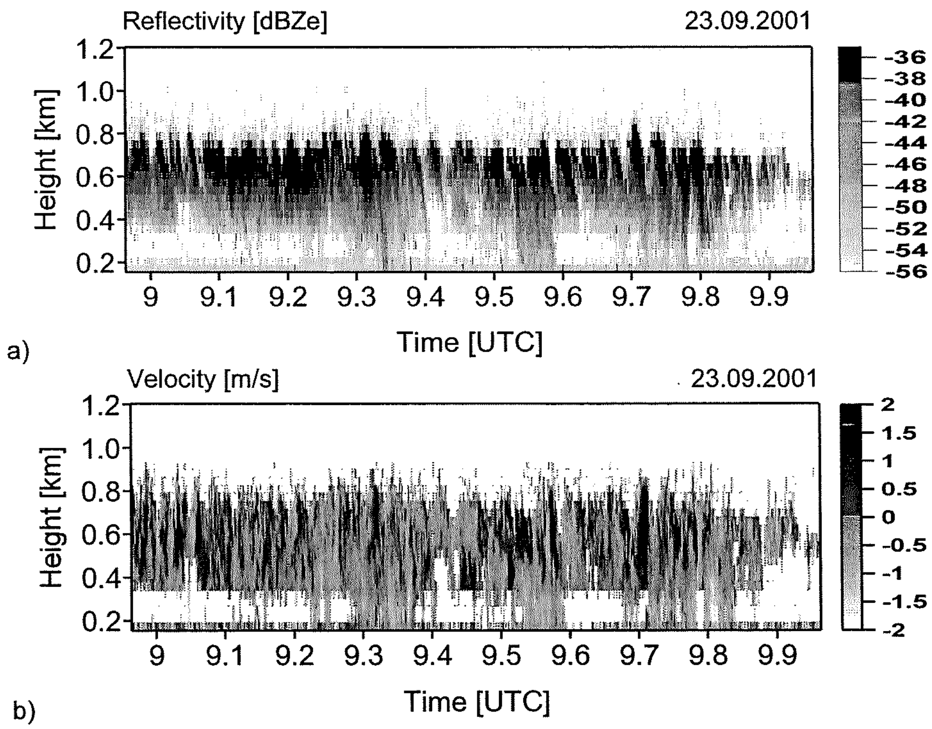

Figure 2: Height time cross-sections of the equivalent radar reflectivity factor (a) and Doppler velocity (b) measured by the GKSS cloud radar for a segment of a stratocumulus layer passing Cabauw on 23 September 2001. Negative velocities indicate downward motion.

more cellular sub-structure could be observed between 9 and 10 UTC. Cloud radar data for this time interval, representing about 30 km of the cloud field, is shown in figure 2 a) and b). In general, the radar reflectivities, with maximum values of about –35 dBZ near cloud top, were quite low, as it can be expected for continental stratiform clouds. Only very weak drizzle activity was observed. At about 9.4 UTC the cloud layer starts showing a more cellular appearance, indicating the break up of the stratus field, most probably due to convective activity in the clouds and the underlaying boundary layer. Accordingly, more vertically extended and intense up- and downdrafts (±1 ms^{-1}) developed.

In-situ measurements of LWC in the cloud top region for this time interval range between 0.2 to 0.5 gm^{-3}, in agreement with LWC deduced from combined microwave radiometer and cloud radar measurements (Meywerk et al., 2004). Typical effective radii varied between 5 and 8 μm. Maximum droplet concentration in the embedded cellular elements were found in the range of 300 to 600 cm^{-3}.

A comparison of maximum entropy power spectra of radar reflectivities at an altitude around 600 m for the first and second half of the data displayed in figure 2 shows a general increase in PSD below a frequency of 0.06 Hz, corresponding to a spatial scale of about 150m. Both spectra show a peak at 0.008 Hz (about 1 km spatial scale), marking the basic cell size, which became more distinct in the course of the morning. The higher spectral amplitude for the data segment starting at 9.48 UTC is due to sharper gradients at the edges of the more isolated cloud elements. The spectrum obtained in a train of cumulus elements after the break up of the stratus (12.32 UTC, 1.1 km altitude) shows no obvious single peak, there is no dominant cloud element size present any more.

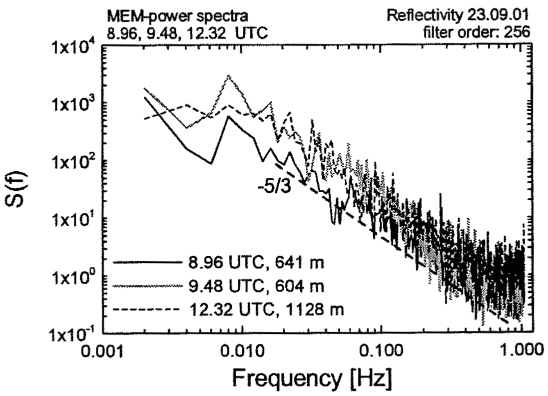

Figure 3: Maximum entropy power spectra of the radar reflectivities from the indicated range gate heights for 30 minute segments starting at the given times.

For all times before 9.48 UTC the spectra of radar reflectivities and Doppler velocity (not displayed here) at scales below 150 m roll off with a –5/3 slope down to the noise level, indicating that inertial subrange turbulence was organizing the clouds on the smaller scales. Later, when stronger convective activity was present, the –5/3 spectral roll off started at about 300 m (0.03 Hz).

In the scalogram of the squared wavelet coefficients of radar Doppler velocities from the range gate centred at about 680 m altitude and the time interval from 8.96 to 9.8 UTC, as displayed in figure 4, the more intense relative up- and downdrafts in the second half of the record due to stronger convection are obvious. With a few exceptions the dominant features have periods between 64 s to 128 s corresponding to spatial scales of about 550 m and 1.1 km in accordance with the cloud cell size deduced from the reflectivity data.

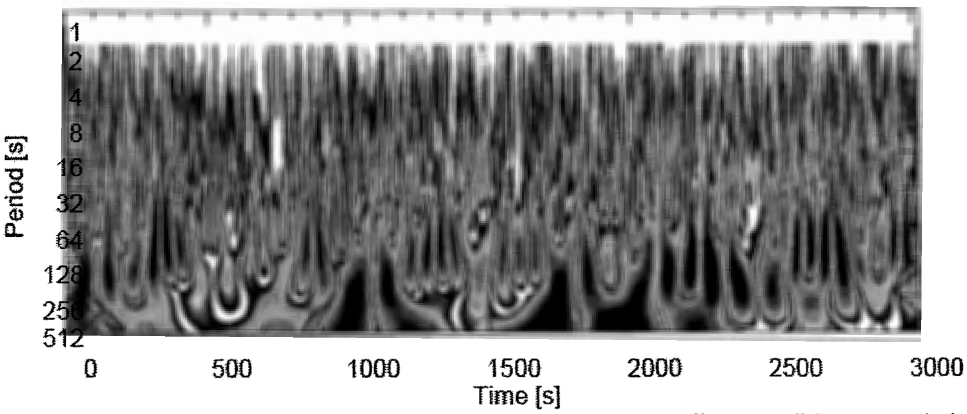

Figure 4: Scalogram (time/period) of the squared wavelet coefficients (Marr wavelet) of the Doppler velocity signals from the range gate at an altitude of 678m; the time period is 8.96 to 9.8 UTC. The wavelet variance is colour coded increasing from blue to red with a lower threshold of 0.05 m^2s^{-2} and an upper bound of 20 m^2s^{-2}.

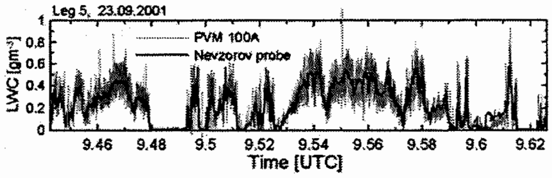

Figure 5: LWC measured with a Nevzorov probe (1 Hz res.) and a PVM 100A (200 Hz res.) along a 60 km cross wind flight leg at an altitude of 580 m. The leg started at 9.45 UTC over Cabauw.

During the time interval discussed above the Merlin IV aircraft flew several horizontal legs almost perpendicular to the mean flow. As an example the LWC measured by the Nevzorov and the PVM probes for a flight leg at an altitude of 580 m is shown in figure 5. Note the variability on the large scale as well as the strong fluctuations of the PVM measurements around the 1 Hz signal of the Nevzorov probe.

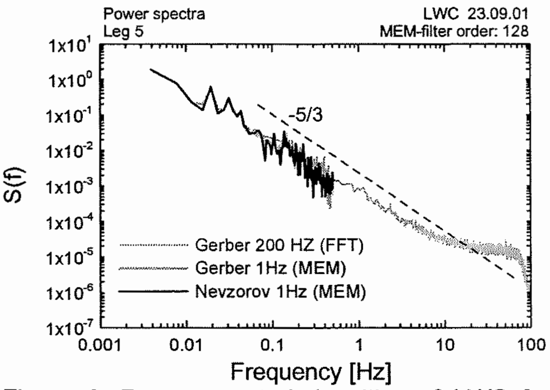

Figure 6: Power spectral densities of LWC for the data segment displayed in figure 5. The dashed line marks a –5/3 spectral slope.

The corresponding power spectra of the LWC data are plotted in figure 6. The fluctuations below 0.05 Hz are due to the irregular appearance of the cloud elements in the cross stream direction at a time when the cloud field was in transition to a more band like organisation (according to the corresponding cloud video). A small plateau around 0.1 Hz (about 950 m) marks the scale of the cellular structures which are visible in figure 5 especially in the cloud element between 9.53 and 9.59 UTC. This indicates that the basic convective elements which appeared in the radar data are also found at a similar scale in the cross flow direction. At frequencies higher than about 0.12 Hz (800 m spatial scale for an aircraft speed of 95 ms^{-1}) the spectrum rolls off with a slope close to –5/3, again indicating the influence of turbulence at these scales. The obvious deviation from the –5/3 scaling at high frequencies, showing enhanced LWC variance, is believed to have a physical and not an instrumental reason; this phenomenon is discussed by Davis et al. (2000) and Gerber et al. (2001). The "scale break" which in our data occurs at scales between 2 and 10 m could be the result of the mixing of cloudy air with entrained cloud free air leading to sharp microphysical gradients at small scales.

5. CONCLUSIONS

The internal structure of a continental strato-cumulus was observed by cloud radar and *in situ* microphysical measurements. The typical size of the convective elements embedded in the sc was found to be of the order of 1 km. At the meter-scale, 2 to 5 m, a "scale break" was found in LWC spectra.
For the future a more detailed analysis of the microphysical structure in relation to cloud dynamics as well as dynamical modelling of the introduced case is planned.

6. REFERENCES

Boers, R. and O. Krasnov, 2004: A note on the microphysical properties of boundary layer clouds over the Netherlands. *Submitted to Atmos. Res.*

Davis, A.B., H. Gerber, and A. Marshak, 2000: Marine boundary-layer cloud structure from cm- to km-scales. Proceedings of the 13th International Conference on Clouds and Precipitation, Reno, Nevada, USA, 803-806

Crewell, S. et al., 2004: The BALTEX Bridge Campaign – An integrated approach for a better understanding of clouds. *Submitted to Bull. Amer. Meteorlo. Soc.*

Gerber, H., J.B. Jensen, A.B. Davis, A. Marshak, and W.J. Wiscombe, 2001: Spectral density of cloud liquid water content at high frequencies. *J. Atmos. Sci.*, **58**, 497-503.

Korolev, A. V., J. W. Strapp, G. A. Isaac, and A. N. Nevzorov, 1998: The Nevzorov airborne hot-wire LWC-TWC probe: Principle of operation and performance characteristics. *J. Atmos. Oceanic Technol.*, 15, 1495-1510.

Meywerk, J., M. Quante, O. Sievers, 2004: Radar based remote sensing of cloud liquid water – application of various techniques – a case study. *Submitted to Atmos. Res.*

Quante, M., H. Lemke, H. Flentje, P.Francis and J. Pelon, 2000: Boundaries and internal structure of mixed phase clouds as deduced from ground based 95 GHz radar and airborne lidar measurements. *Phys. Chem. Earth* (b), Vol. **25**, No.10-12, 889-895.

MAINTENANCE MECHANISM OF CONVECTIVE CELLS
WITHIN MESOSCALE CONVECTIVE SYSTEM IN HUMID SUBTROPICAL REGION

S. Shimizu[1], H. Uyeda[1], T. Shinoda[1], K. Tsuboki[1],
H. Yamada[2], B. Geng[2], and T. Kato[3]

[1]Hydrospheric Atmospheric Research Center, Nagoya University, Nagoya, Aichi, 464-8601, Japan
[2]Frontier Observational Research System for Global Change, Yokohama, Kanagawa, 236-0001, Japan
[3]Meteorological Research Institute, Japan Meteorological Agency, Tsukuba, Ibaraki, 305-0052, Japan

1. INTRODUCTION

The relation between environment and types of Mesoscale Convective System (MCS) has not been documented well in a moist environment such as that of East Asia. On the contrary, in a dry environment such as that of the Great Plains in U.S., it is well known that Convective Available Potential Energy (CAPE) and vertical wind shear are important environmental parameters for determining formation types of MCS (Bluestein and Jain, 1985). In a moist environment, a humidity distribution, as well as CAPE and vertical wind shear, is now focused as an important parameter for maintenance of convective cell within MCS.

In order to reveal maintenance mechanism of convective cells within linear MCS in a moist environment, we selected two back-building rainbands with distinct characteristics of convective cells observed during a field experiment in the downstream region of Yangtze river during Baiu/Meiyu season in 2001 (Geng et al., 2002 and Yamada et al., 2004). We investigated the lifetime and downdraft strength of convective cells within the two back-building rainbands by dual-Doppler analysis, and estimated three-dimensional humidity distribution by using Regional objective ANALysis (RANAL) and Regional Spectral Model (RSM), which are produced by the Japan Meteorology Agency.

2. DATA

Two X-band Doppler radars (at Wuxian and

Corresponding author's address: Shingo Shimizu, Hydrospheric Atmospheric Research Center, Nagoya University, Nagoya, Aichi, 464-8601, Japan;
E-Mail:shimizu@rain.hyarc.nagoya-u.ac.jp

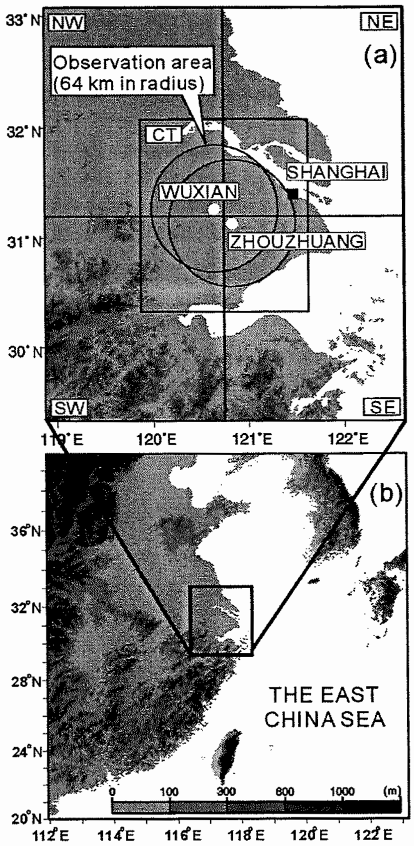

Fig. 1. The observation field around two X-band Doppler radars at Wuxian and Zhouzhuang (Fig. 1a). Two circles in Fig. 1a show the radar observation area (64 km in radius). Five of 2° x 2° regions (NW,NE,SW,NE,and CT) in Fig. 1a indicate analysis regions for estimating environmental parameters using RANAL. The RSM calculated the parameters within the 10° x 10° region shown in Fig. 1b.

Zhouzhuang, covering the downstream of Yangtze river with 64 km in radius) obtained sets of volume scan data of reflectivity and Doppler velocity every six minutes.

We analyzed lifetime and three dimensional structure of convective cells within two back-building rainbands by using dual-Doppler radar analysis with variational method (Gao et al.,1999) within the overlapped radar observation area of the two radars (Fig. 1a).

In order to evaluate the environment around the observation area, humidity distribution is investigated in the five regions (2°×2° regions: NE, NW, SE, SW, and CT (covering the radar observation area)) using RANAL data (Fig. 1a). The time resolution of RANAL is 6 hours (02, 08, 14, 20 LST (LST = UTC + 8 hours)). The horizontal resolution of RANAL is 20 km. In the vertical direction, RANAL contains 20 levels. The mean value of environmental parameters in the each region is calculated: vertical integrated specific humidity deficit from 850 hPa to 500 hPa (HUDE), and vertical integrated vapor flux convergence from surface to 850 hPa (VFC), vertical integrated specific humidity from surface to 850 hPa (VISH), CAPE and CIN. HUDE is an index for dryness of midlevel layer. In order to investigate the time variation of humidity distribution, we used the forecast of RSM within 10° × 10° region (Fig. 1b). The time resolution of RSM is 1 hour. The horizontal resolution is 20 km. The RSM was run for 24 hours from 20 LST 18 Jun and 20 LST 23 Jun.

3. RESULTS

3.1 Dual-Doppler analysis

We investigated lifetime and the maximum downdraft velocity of convective cells within two back-building rainbands (CASE1: 0348 LST 24 June, CASE2: 0118 LST 19 June). We defined lifetime of convective cell as the period when the maximum reflectivity at 4 km above sea level (ASL) was over 30 dBZe. The longest lifetime of convective cell was 90 minutes in CASE1 (0318 LST - 0448 LST), and 42 minutes in CASE2 (0106 LST - 0148 LST). The maximum reflectivity during the lifetime was 39 dBZe at a height of 4 km ASL in CASE1, and 44 dBZe at a height of 2 km ASL in CASE2 (not shown). We named the back-building rainband with long-lived convective cells as BBL, and the back-building rainband with short-lived convective cells as BBS. The BBL consists of steady convective cells. On the contrary, the BBS was maintained by repeated replacement of the

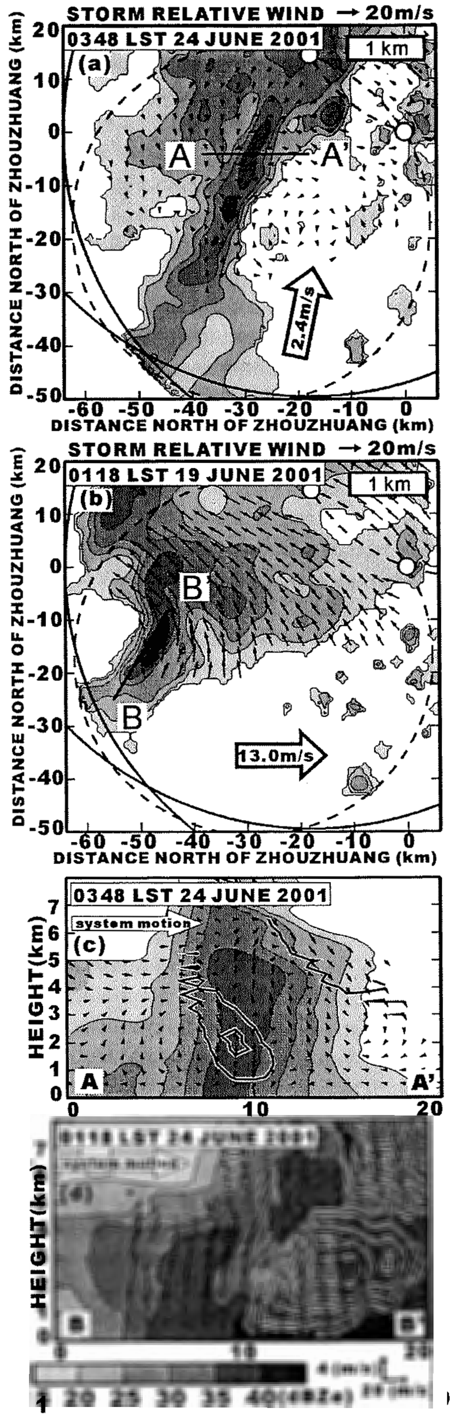

Fig. 2. The radar reflectivity overlaid with storm-relative wind vectors at a height of 1 km ASL of CASE1 (a), CASE2 (b). Vertical cross sections along A-A' (Fig. 2c) and B-B' (Fig. 2d) lines are indicated. Thick contours show downdraft every 1 m s^{-1}. Open arrows show system movement speed.

convective cells.

We observed a remarkable difference in the maximum downdraft velocity. Reflectivity at a height of 1 km ASL of CASE1 and CASE2 is shown in Fig. 2. Vertical cross sections along the A-A' and B-B' lines in Fig. 2a and Fig. 2b are shown in Fig. 2c and Fig. 2d, respectively. The maximum downdraft velocity at 2 km ASL was 2.0 m s^{-1} (CASE1) and 5.0 m s^{-1} (CASE2), respectively. The location of downdraft core differed from the location of the reflectivity core in two cases (not shown). The cause of the downdraft seems to be mainly due to evaporative cooling in two cases because the downdraft core located at the confluence of the wind at a height of 4 km ASL and the edge of strong echo in two cases (not shown).

It is known that a strong downdraft of a convective cell causes a strong outflow cutting warm and moist air supply to an updraft of the convective cell (Weisman and Klemp, 1982). In present cases, actually short-lived convective cells were observed corresponding to the strong downdraft in CASE2, and long-lived cells were obserbed corresponding to the weak downdraft in CASE1.

3.2 Environments of two rainbands

We investigated the environment around the two rainbands, in order to find environmental parameters to determine lifetime and downdraft velocity of convective cell, and to understand the maintenance mechanism of convective cells within a rainband in a moist environment. We compared the two cases, and calculated the mean value of HUDE in the region where the storm-relative wind at 4 km ASL blew from. The other parameters were calculated in CT region. In Fig. 3, HUDE distributions in two cases are indicated. In CASE1, low CAPE (0 J kg^{-1}) in CT region and large CIN (104 J kg^{-1}) over the ocean restrained vertical transport of vapor, thus abundant vapor in lower layer (VISH in SE region was 24.1 kg m^{-2}) was horizontally transported from ocean to the observation area. The transported abundant vapor was accumulated in lower layer because the VFC had high value (6.95×10^4 kg $m^{-1} s^{-1}$). In the middle layer, a moist air (HUDE was 3.14 kg m^{-2}) existed over the windward region of storm-relative wind at the mid-level (Fig. 3a). In CASE2, CAPE (777 J kg^{-1}) and HUDE (9.99 kg m^{-2} in Fig. 3b) were higher, and VFC (3.66×10^4 kg m^{-1} s^{-1}) was lower than that of CASE1. A mid-level layer in CASE2 was drier than that of CASE1 (Fig. 3b).

CAPE was important parameter to transport vapor from lower layer to middle layer in CASE2. In

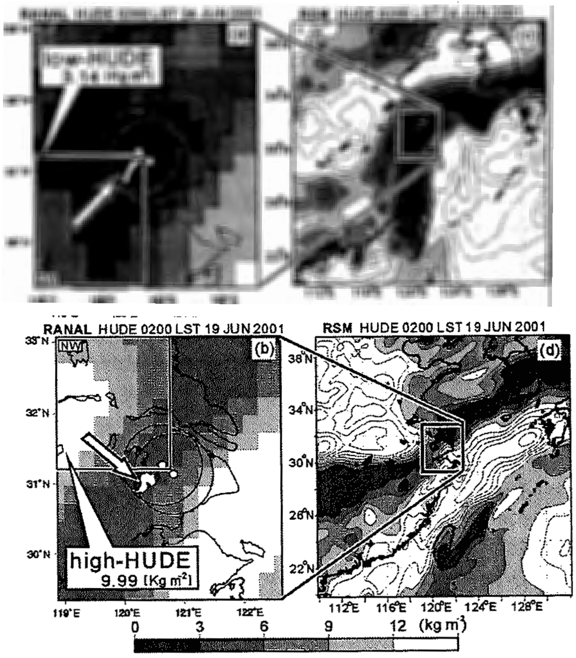

Fig. 3. The distribution of HUDE on 19 Jun (a) and on 24 Jun (b) calculated by RANAL data, and those of 19 Jun (c) and 24 Jun (d) estimated by RSM. In Fig. 3a and Fig. 3b, the locations of two rainbands are shown by open area within radar range (over 30 dBZe). Open arrows indicate storm-relative wind at 4 km ASL estimated by dual-Doppler analysis. The mean value of HUDE is calculated in SW (a) and NW (b) region. Contours in Fig. 3c and Fig. 3d show HUDE every 3 kg m^{-2} estimated by RSM.

fact, maximum updraft in CASE2 was more that 7 m s^{-1}, and maximum reflectivity was more than 42 dBZe (Fig. 2d) corresponding to high CAPE. On the contrary, in CASE1, VFC, instead of CAPE, was important parameter to transport vapor vertically. The maximum updraft was less than 2 m s^{-1}, and maximum reflectivity was less than 40 dBZe (Fig. 2c) corresponding to low CAPE. The weak updraft was quasi-steady during 90 minutes. It caused a large amount of rainfall (Geng et al., 2002) corresponding to high VFC.

Distributions of HUDE in Fig. 1b are shown in Fig. 3c and Fig. 3d, respectively. The belt of HUDE less than 6 kg m^{-2} from east to west (Fig. 3a and Fig. 3b) approximately corresponded to the Baiu/Meiyu frontal zone. In both north and south sides of the Baiu/Meiyu front, HUDE was more than 20 kg m^{-2}. From 23 LST 23 Jun to 05 LST 24 Jun (three hours before and after Fig. 3c), a dry air (HUDE was more than 5 kg m^{-2}) advected from northwest to the NW region in Fig. 3b. On the contrary, from 23 LST 18 Jun to 5 LST 19 Jun (three hours before and after Fig. 3d), a moist air (HUDE was less than 5 kg m^{-2}) advected from southwest to SW region (Fig. 3a.).

4. DISCUSSION

We summarized our results in Fig. 4. In a dry mid-level environment (high HUDE environment (Fig. 4b)), the vapor was evaporated well and caused strong downdraft in CASE2. The strong downdraft cut off warm and moist air supply to the updraft of convective cells in the lower layer, and caused the short-lived convective cells in CASE2. The vertical vapor transportation in CASE2 is explained by high CAPE. On the contrary, in a moist mid-level environment (low HUDE environment (Fig. 4a)), the evaporative cooling is inactive, therefore, long-lived convective cells with weak downdraft velocity were observed in CASE1. The vertical vapor transportation in CASE1 is explained by high VFC in spite of low CAPE.

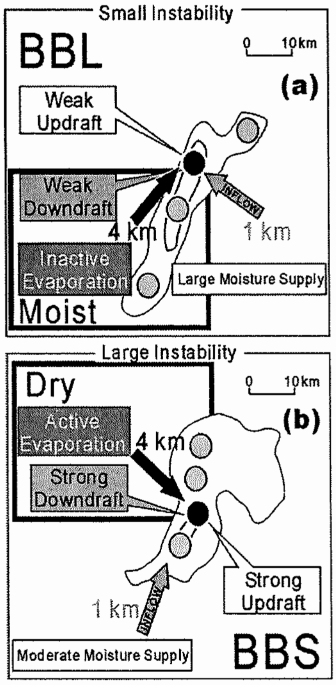

Fig. 4. Characteristics (lifetime and downdraft velocity) and schematic model of two rainbands developed in different distribution of mid-level humidity on 24 Jun 24 (CASE1: Fig. 4a) and 19 Jun (CASE2: Fig. 4b), 2001. Black dot indicates the longest-lived convective cell (90 min in CASE1, 42 min in CASE2). In a moist mid-level environment (CASE1), evaporative cooling was inactive and a weak downdraft could not cut off warm and moist air supply to the convective cell.

We propose that HUDE is a parameter to determine the lifetime of convective cells within MCS and the strength of downdraft caused by evaporative cooling of rain. CAPE and VFC would be important environmental parameters to determine the amount of vertical vapor transportation.

The research on environmental parameters focused on mid-level humidity (HUDE and VFC), such as these two case studies, gives us strong possibility to understand the maintenance mechanism of MCS in a moist environment.

5. CONCLUSIONS

We investigated the humidity distribution for determining the lifetime of convective cell within two rainbands observed near Shanghai during Baiu/Meiyu period in 2001 by using dual-Doppler radar analysis with variational method, RANAL, and RSM. We propose that mid-level dryness between 850hPa and 500 hPa (HUDE) behind a rainband determines the maximum downdraft velocity and lifetime of convective cell within MCS. More observational and numerical study on the relation between this HUDE and MCS would lead to a clear understanding of maintenance mechanism of MCS in a moist environment.

References

Bluestein, H. B. and M. H. Jain. 1985:Formation of Mesoscale Lines of Precipitation: Severe Squall lines in Oklahoma during the Spring. J. Atmos. Sci.,**42**, 1711-1733.

Gao, T., M. Xue, A. Shapiro, K. K. Droegemeier 1999: A variational method for the analysis of three-dimensional wind fields from two Doppler radars. Mon. Wea. Rev.,**127**, 2128-2142.

Geng, B, H. Yamada, K. K. Reddy, H. Uyeda, Y. Fujiyoshi, 2002: Diurnal variations of precipitation system and mesoscale environment in the downstream of Yangtze river. Proc. International Conference on Mesoscale Convective System and heavy Rainfall/Snowfall in East Asia,131-133.

Weisman, M. L., J. B. Klemp, 1982: The dependence of numerically simulated convective storms on vertical wind shear and buoyancy. Mon. Wea. Rev.,**110**, 504-520.

Yamada, H., B. Geng, K. K. Reddy, H. Uyeda and Y. Fujiyoshi 2003: Three-dimensional structure of a mesoscale convective system in a Baiu-frontal depression generated in the downstream region of the Yangtze river. J. Meteor. Soc. Japan, **81**,1243-1271.

THE BALTEX BRIDGE CAMPAIGNS – A QUEST FOR CONTINENTAL CLOUD STRUCTURES

C. Simmer[1], V. Venema[1], M. Diederich[1], S. Crewell[2], Arnout Feijt[3], and Jean-Louis Brenguier[4]

[1]Meteorological Institute, Bonn University, Germany
[2]Meteorological Institute, Munich University, Germany
[3]Royal Netherlands Meteorological Institute (KNMI), De Bilt, the Netherlands
[4]MeteoFrance, Toulouse, France

1. INTRODUCTION

In 2001 und 2003 two large field experiments were conducted around the central meteorological measurement facility of the Dutch Meteorological Service (KNMI) at Cabauw, the Netherlands. BBC1 (First BALTEX BRIDGE Campaign) ran for two months covering August and September 2001, while BBC2 (Second BALTEX Bridge Campaign) lasted for roughly one month, May 2003. Both campaigns were devoted to continental clouds with a focus on boundary layer clouds, their spatial variability, vertical structure, and diurnal cycle. Especially in BBC2 precipitation and its small scale variability influencing weather radar returns, has been an additional focus.

Both field experiments have been conducted in the framework of BALTEX (Baltic Sea Experiment), the European continental-scale experiment within GEWEX (Global Energy and Water Cycle Experiment) as a sub-programme of the World Climate Research Programme (WCRP). BRIDGE was the central field campaign within the first phase of BALTEX, which included several field experiments within a Central European modeling region with the Baltic Sea catchment area within its centre. The BBCs were funded from many national and international projects and organisations – the pillars being KNMI, which contributed with large internal funds and personnel, the Fifth Framework European Commission (EC) project CLIWA-Net (Cloud Liquid Water Network, www.knmi.nl/samenw/cliwa-net) and the 4DClouds project (www.meteo.uni-bonn.de/projects/4d-clouds/) in the AFO2000 (Atmosphärenforschungsprogramm 2000) research programme of the German Ministry of Research and Education (BMBF). Important contributions came also from the CAARTER-programme of the EC, MeteoFrance, the MetOffice and the military of the Netherlands and many university groups from the Netherlands, France, Poland and Germany. All in all about 25 research groups were involved with roughly 100 scientists.

Corresponding author's address: Clemens Simmer, Meteorological Institute of the Rheinische Friedrich-Wilhelms-Universität Bonn, Auf dem Hügel 20, 53121 Bonn, Germany; E-Mail: csimmer@uni-bonn.de.

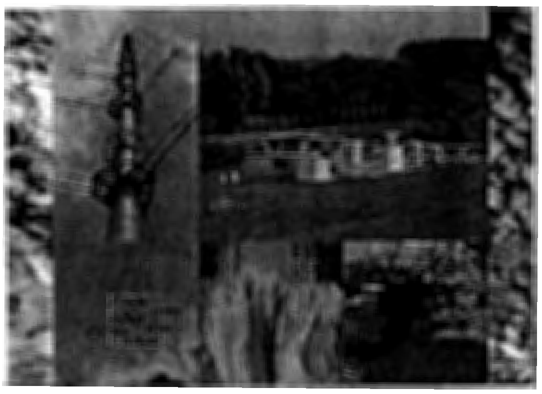

Figure 1. Schematic overview of the BBC components: Ground-based observations from the main experimental site at Cabauw, satellite observations from AVHRR, the regional network spread in an approx. 100x100 km^2 area and the three aircrafts based in Rotterdam. Cabauw is characterized by the high measurement tower and its green polder landscape. The three pictures at the bottom of the figure are the orographic map of the Netherlands with the stations of the regional network, a radar measurement of a cumulonimbus, and a cloud classification from AVHRR. The vertical stripes with *casi* cloud measurements at 753 nm depict the airborne component of the campaign.

2. GOALS OF THE BBCs

The focus of both BBCs was experimental research on the cloudy continental troposphere. Spurred by the large deficiencies in climate and weather forecast models related to clouds and precipitation (IPCC 2001) and the many boundary layer cloud experiments conducted already over ocean regions, the coordinators of the BBCs selected a continental site to deliver data for research on the following goals:

- Assessment of the quality of modeling the vertically integrated cloud liquid water in weather and climate models, which is the link between dynamic cloud processes and cloud radiation effects

- Assessment of the spatial variability of clouds in three dimensions and time to allow for the analysis of three-dimensional effects in cloud radiative transfer and to aid in the development of cloud parameterizations in weather and climate models

- Assessment of the spatial and temporal variability in number and size of precipitating particles below clouds to allow for the analysis of non-linear effects on the relation between radar reflectivity and precipitation intensity.

While the first goal has by large parts already been accomplished with the data in the framework of CLIWA-Net (see contribution by Crewell et al. 2004 in this issue) the other goals are currently being addressed. Some detailed results on the second topic can be found in Venema et al. 2004 (this issue).

3. EXPERIMENTAL SITE

The BBC campaigns were performed around the experimental facility at Cabauw (51°58.2' N, 4°55.6' E), The Netherlands. Cabauw was in both campaigns part of a regional network consisting of ten remote sensing stations covering a region of 100 by 100 km^2 in the central Netherlands. All the aircraft observations, satellite analysis and atmospheric modeling for the BBCs (Fig. 1) were centered around Cabauw. BBC 1 began with a Microwave Intercomparison Campaign (MICAM) at Cabauw in the first two weeks. Then the microwave radiometers were distributed over the regional network. The network stations performed continuous cloud and radiation observations using lidar ceilometers, infrared-radiometers and pyranometers. In contrast to BBC1 during BBC2 the regional network did not host passive microwave radiometers,but three microwave radiometers were operating at Cabauw.

4. INSTRUMENTAL SETUP

During both campaigns a multitude of measurements of different cloud parameters and the cloudy atmosphere in general were taken by various instruments deployed both at the ground and air born (see Table 1 and 2 for details). The backbone of the measurements were provided by three cloud radars at different frequencies and a suite of different microwave radiometers, the combination of which allow for the quantitative estimation of cloud liquid water profiles. Backscatter lidars and lidar-ceilometers aided in accurately determining the cloud base development and gave valuable information to constrain profiling the atmosphere when precipitating particles were present below the clouds. A new fast Oxygen-A-Band spectrometer estimated solar photon path length distributions to evaluate the influences of cloud structures on the multiple scattering statistics of inhomogeneous clouds in order to challenge our current understanding of radiative transfer in the cloudy atmosphere. Four upward looking Mircro Rain Radars were deployed in array to cover roughly a signal return volume of the nearby DeBilt weather radar.

Table 1: List of instruments including home institutions deployed during BBC1

Radars: 1.29 GHz windprofiler + RASS (KNMI), 3 GHz radar TARA (TU Delft), 35 GHz radar (KNMI), 78 GHz radar (UKMO), 95 GHz radar MIRACLE (GKSS)
Lidars: 1064nm, 532 nm backscatter lidar (RIVM), CT75K ceilometer (KNMI), LD40 ceilometer (KNMI), CT25K ceilometer (U Bonn)
Microwave Radiometers: 22 channel MICCY (U Bonn), MARSS (UKMO), 24+37 GHz DRAKKAR (CETP), 24+31 GHz WVR 1100 (DWD), 12 channel WVP/TP 3001 (DWD), 21+31 GHz (Chalmers), Asmuwara (U Bern), 13+22+37+89 GHz (St. Petersburg)
Radiation: SW in & out, SW direct & diffuse, LW in & out (KNMI), Oxygen-A band spectrometer (U Heidelberg), IR radiometer (KNMI, U Bonn, (U Bern), Albedometer (IfT Leipzig), Sunphotometer (IfT Leipzig), CM21, LXG500, Metek USA1, Campbell KH2O, 8 channel interferometer (TU Dresden)
Cabauw 200 m tower (KNMI): temperature, dew point temperature, wind
Tethered balloons: pressure, temperature, humidity, wind (U Utrecht, 0 - 1.4 km), in-situ particle measurements (IfT+German army)
Radio soundings: 0,3,6,9,12,15,18,21 UTC (Cabauw or De Bilt; KNMI, UKMO or National Army)
Other instruments: GPS receiver (TU Delft),10 m meteo tower, sonic, Ly-a, SW, LW (U Utrecht), digital video cameras (KNMI, TU Dresden)
Cessna C207 T (FU Berlin): radiation, CASI (imaging spectrograph), FUBISS (spectrograph), MIDAC (FTIR)
Partenavia (IfT Leipzig): PCASP-X Nephelometer, PSAP, CPC 3010, CPC 3025, Fast FSSP (GKSS), OAP (GKSS) 2D-C, PVM-100A (GKSS), Albedometer
Merlin IV (MeteoFrance): Cloud m-physics (GKSS) FSSP 100, extended range Fast FSSP, 2D-C, 2D-P, Nevzorow, PVM

In both campaigns three aircrafts were employed for coordinated flights to measure in-situ cloud microphysical parameters and radiation below, inside, and on top of the clouds. A tethered balloon also equipped with cloud microphysics probes and radiation sensors was used to take vertical and horizontal profiles through the clouds. Wind profilers, temporally dense radiosonde ascents, a multitude of ground-based standard meteorological sensors including radiation measurements and turbulent flux devices, and last not least the 200 m meteorological tower completed the efforts to describe as good as possible the properties of the cloudy sky.

Table 2: List of instruments including home institutions deployes during BBC 2

Radars: 1.29 GHz windprofiler + RASS (KNMI), Sodar/RASS (IfT), 3 GHz radar TARA (TU Delft), 35 GHz radar (KNMI), 95 GHz radar MIRACLE (GKSS), C-band weather radar, 4 Micro Rain Radars (U Bonn, U Wageningen, U Marburg)
Lidars: Raman Aerosal Lidar ARAS (GKSS), HTRL backscatter lidar (RIVM), CT75K ceilometer (KNMI), LD40 ceilometer (KNMI), CT25K ceilometer (U Bonn)
Microwave Radiometers: 22 channel MICCY (U Bonn), 20+30 GHz HATPRO (U Bonn, RPG), 36+95 GHz radiometer (Attex)

Radiation: Operational and Quasi-BSRN SW and LW: SW in & out, SW direct & diffuse, LW in & out (KNMI), Oxygen-A band spectrometer (U Heidelberg), IR radiometer (KNMI, U Bonn), IR rad.meter downward looking (KNMI), IR Imager (CELAR), UV Spectrometer (RIVM), Albedometer (IfT Leipzig), Sunphotometer (IfT Leipzig), FUBISS (standard, ASA, Polas) (FU Berlin), Sunphotometer CIMEL (TNO), Total Sky Imager (KNMI)
Cabauw 200 m tower (KNMI): temperature, pressure dew point temperature, wind
Tethered balloons: pressure, temperature, relative humidity, wind (U Utrecht, 5 Heights between 0 - 1.4 km); in-situ particle measurements (IfT, German army)
Other instruments: GPS receiver (TU Delft), 10 m meteo tower, sonic, Ly-a, SW, LW (KNMI), Aerosol counters (TNO), rain gauges (U Wageningen), Video Disdrometer (U Wageningen), present weather sensor (U Wageningen), Video camera (KNMI), ground-water level (KNMI), soil heat-flux (KNMI)
Radio soundings: RS90 (Cabauw and De Bilt (KNMI), Dutch Army
Dornier (NERC): CASI (imaging spectrograph, FU Berlin), FUBISS (spectrograph, FU Berlin), IR-camera (FU Berlin), Airborn POLDER (U Lille), POLIS (Lidar, U Munich)
Partenavia (IfT Leipzig) : Albedometer (290-1000 nm), AFDM (305-700 nm; 2-3 nm), PCASP-X (Aerosol m-physics), Fast FSSP (GKSS), PVM-100A (GKSS)
Merlin IV (MeteoFrance): FSSP 100, extended range (GKSS), Nevzorow (GKSS), OAP 2D2-C, OAP 2D2-P (GKSS), fast temperature probes (U Warsaw), DIRAM (Multidirectional radiances; U Utrecht), King probe, PVM, Fast FSSP, Various pressure, temperature, humidity

All quality-controlled measurement data are stored in a central data base at KNMI. Fig. 2 shows an example of quicklooks for some of the ground-based sensors. Higher-level products, e.g. liquid water profiles derived from synergetic use of several sensors are also available. Requests to access to the data should be sent to one of the campaign coordinators

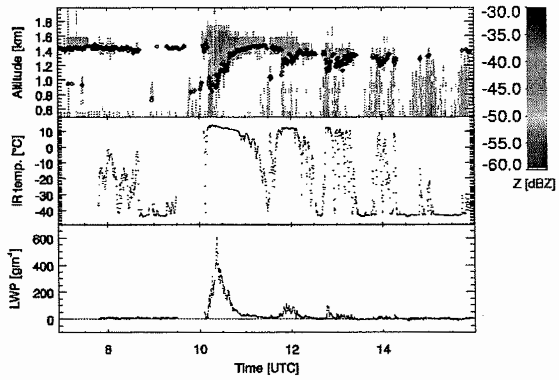

Figure 2. Time series of radar reflectivity, cloud base height derived from lidar ceilometer measurements (black dots), infrared temperature and liquid water path (LWP) measured at Cabauw on August 1, 2001 (BBC 1). The radar reflections below cloud base height are probably caused by insects because the radar signal is dominated by backscattering from larger targets. Hence, cloud base information from lidar is necessary to screen the radar measurements below the cloud

5 HIGH-LEVEL PRODUCTS

In the following we show some higher level products related to cloud and precipitation structurestill in an experimental stage obtained from the BBCs.

5.1 Scanning Microwave Measurements

Probably for the first time a microwave radiometer (MICCY, Crewell et al. 2001) was operated in a scanning mode in order to measure the spatial variability of cloud liquid water (Fig. 3). Both zenith and azimuth of MICCY can be controlled by software and the high spatial and temporal resolution of MICCY allows to scan the sky in minutes. Thus we have a closer look to spatial variability of clouds compared to time series from a radiometer with a fixed viewing angle

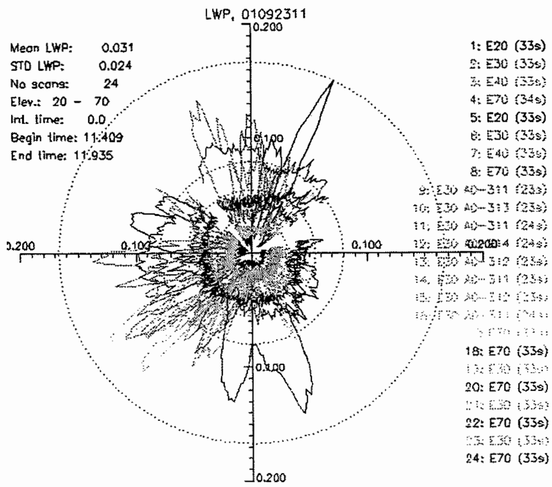

Figure 3: A set of 24 azimuth scans of the Liquid Water Path (LWP) measured by MICCY; plotted like a wind rose. At the origin the LWP is zero, at the top the direction is North, to the right is east. The azimuth scans were made at various elevations, the blue scans with 30 degree elevation and the red ones with 70

5.2 Spatial Cloud Structures and Surrogate Clouds

By no means can microphysical parameters of clouds be monitored directly. Any sensor, measuring directly or remotely, either from airplanes or from ground, probes only a very small volume of the cloudy atmosphere. For evaluation the radiation interaction of clouds or for parametrisation of clouds in dynamic models the three dimensional distribution of cloud microphysical parameters must be known. A way to obtain such cloud descriptions are so-called surrogate clouds. These are artificial clouds which share the statistical characteristics with the probed real clouds. Fig. 4 shows 3D example-surrogate cloud fields made from measured BBC-data. The surrogate cloud fields (middle) have the same horizontally isotropic power spectrum and LWC distribution as LWC profile retrievals (left). These LWC profiles (and corresponding R_{eff} (effective radius) profiles, which are not shown) were derived using an optimal estimation technique (Löhnert et al., 2003) which combines microwave radiometer brightness temperatures, with other measurements and with a priori information from a microphysical cloud model. To generate these surrogate clouds the iterative amplitude adapted Fourier transform algorithm was used, which is described in Venema et al. (2004; this volume). The 3D effective radius fields were created by permutating the R_{eff} values from the profile measurements just like the liquid water content values were permuted. The profile measurements of half an hour is converted in a distance scale in km by the wind speed at cloud height as measured by radiosondes.

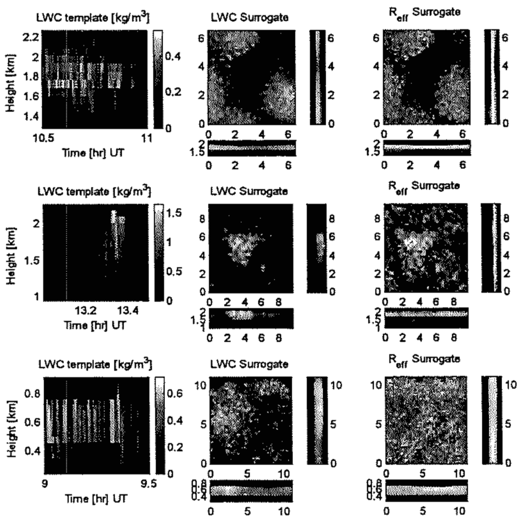

Figure 4: Three examples of 3D surrogate clouds (liquid water content, LWC) and effective radius (R_{eff}) derived from time series of liquid water profiles and effective radii inferred from a synergetic algorithm using passive microwave radiometry and cloud radar data.

6.3 Sub-Pixel Variability of Precipitation

Variability in raindrop size distribution inside the pixel or illuminated volume of a weather radar leads to greater ambiguity and to an often cited but till now unpredictable error when deriving rain rates from radar reflectivity. The vertical profile of raindrop spectra can be measured by vertically-looking so-called Micro Rain Radars, which analyze the spectral distribution of the Doppler return of radio waves. During BBC 2 we distributed four MRRs over an area roughly equivalent to the return volume of the DeBilt weather radar. Using the wind advection information from the nearby wind profiler the time series of the vertical profiles obtained from the MRRs could be transformed into slices of droplet size spectra, which represent the true spatial distribution of the measured raindrops. Fig. 5 shows one example exemplifying the large variability of radar reflectivity possible within a sub-resolution weather radar volume.

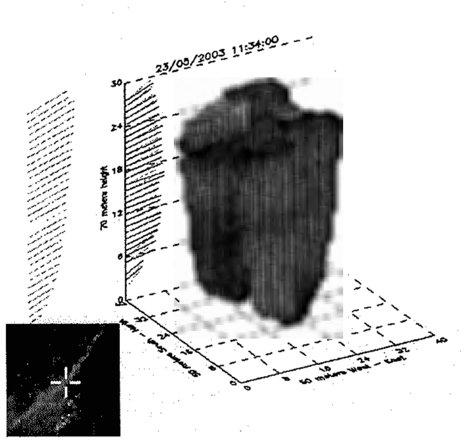

Figure 5: Slices of radar reflectivity measured with three Micro Rain Radars within a signal return volume of the DeBilt weather radar. The lower left sub-picture shows the PPI of the DeBilt weather radar indicating a highly convective situation. The cross gives the location of the three MRRs within the radar image. The usual assumption of equally distributed drops inside the volume (2 x 2 kilometers) will cause significant measurement errors.

ACKNOWLEDGEMENTS

Part of the work presented in this paper was funded by the EC 5th Framework CLIWA-NET project, The German AFO2000 4DClouds project and the EC CAARTER programme. We thank KNMI for hosting and co-coordinating both campaigns, and we want in particular to acknowledge the help of the fabulous site manager Willem Hovius of KNMI.

REFERENCES

Crewell, S., H. Czekala, U. Löhnert, C. Simmer, T. Rose, R. Zimmermann and R. Zimmer-mann, 2001: Microwave Radiometer for Cloud Carthography: – A 22 channel ground-based microwave radiometer for atmospheric research, *Radio Sci.*, 36, 621-638.

Crewell, S., U. Löhnert, and E. van Meijgaard, 2004: Evaluating cloud liquid water in NWP and climate models using measuremenst from the BALTEX Cloud Liquid Water Network: CLIWA-NET. *Proceedings of the 14th International Conference on Clouds and Precipitation*, Bologna, Italy, 18-23 July 2004 (this issue).

Löhnert, U., S. Crewell, and C. Simmer, 2004: An integrated approach towards retrieving physically consistent profiles of temperature, humidity and cloud liquid water. Accepted by *J. Apply. Meteor.*

Venema, V., St. Meyer, S. Gimeno Garcia, C. Simmer, S. Crewell, U. Löhnert, and Th. Trautmann, 2004: Iterative amplitude adapted Fourier transform surrogate cloud fields. *Proceedings of the 14th International Conference on Clouds and Precipitation*, Bologna, Italy, 18-23 July 2004 (this issue).

Cu OF NORTH-WEST OF RUSSIA (GENERALIZED CHARACTERISTICS)

A.A.Sinkevich, Y.A. Dovgaluk, Y. Ph. Ponomarev, V.D. Stepanenko and N.E.Veremey

Department of Cloud Physics, Cloud Seeding and Solar Radiation Studies, A.I.Voeikov Main Geophysical Observatory, Karbyshev str. 7, St.Petersburg, 194021, Russia

1. INTRODUCTION

To obtain cloud characteristics instrumented aircrafts and radars have been used during a lot of years by Main Geophysical Observatory (Sinkevich (2001), Stepanenko (1973), Zvonarev et al. (1986), Begalishvily et al. (1993)). The following characteristics were measured – clouds sizes, temperature excess in clouds, LWC, vertical flows, electrical field strength. Results of these measurements have been analyzed in dependence on Cu living stage and height over cloud base. The analyzed data include the results of aircraft measurements carried out in the north-west of Russia in warm seasons during 1977-1987. More than 1000 clouds were studied. Synoptic-meteorological conditions were typical for convective clouds development. Most of the experiments (more than 70%) were carried out on the peripheral parts of cyclones with cold fronts and occluded fronts. Depth of investigated (by instrumented aircrafts) convective clouds was usually less than 4-5 km.

3 cm radar was used to obtain Cu characteristics also. Measurements were carried out in north-west of Russia.

Generalized characteristics of Cu are presented below.

2.CLOUDS SIZES

Clouds sizes were measured during aircraft traverses through Cu. As aircraft had made traverses not through central cloud part (though pilots tried to cross through mentioned cloud part) measured sizes in general are less than real sizes of the clouds. We consider that this decrease in sizes is 10-20% for Cu hum-Cu med, 20-30% for Cu cong – Cb. Here we present data without any corrections.

Mean horizontal length (L) of Cu hum-Cu med was near 1 km. There is dependence of L from cloud living stage. Maximum L=1.3 km was registered in dissipating stage when clouds were diffluent.

Horizontal length is nearly 2 times greater than vertical cloud depth.

Cu cong have horizontal length nearly 2 times greater than Cu hum-Cu med. Relation of clouds length to cloud depth was near 1 in most cases. The dependence of horizontal length L(km) from cloud depth ΔH(km) can be presented by the following equation:

$$L=1.4+0.4\,\Delta H.$$

Horizontal length of Cu cong in mature living stage was higher than in developing or dissipating stages.

Cb have L greater than Cu cong, in most cases it equals to 4.0-4.4 km. These data was obtained with the help of instrumented aircraft.

Radar data was used to study dangerous for aircrafts Cb (Cb(p)- clouds with intensive precipitation and Cb®- clouds with thunderstorms). 282 cases were analyzed. Results of this analysis had shown that mean clouds depths were the following: ΔH(Cb(p))=8km and ΔH(Cb(®))=10 km, at the same time mean horizontal length of precipitating Cb was equal to 60 km and it was significantly greater than Cb with thunderstorms which equals to 32 km (these measured Cb, having rather large sizes, could be either multicell clouds or even some cloud clusters). Results of the presented investigations clearly show that Cb sizes varies in rather wide limits in investigated region.

3. INCLOUD TEMPERATURE

To carry out measurements IR radiometer was used Sinkevich (2001). Most airborne temperature measurements carried out earlier have been collected using "immersion thermometers", which employ a sensing element that is immersed into the ambient air stream. The errors are mostly associated with the uncertainties in quantifying the effect of cloud drops impacting the sensor and or its housing.

Radiometric measurements of temperature in clouds do not suffer from most of the problems associated with sensor wetting that confound immersion temperature sensors (Lawson and Cooper 1990). In this sense, radiometric thermometry can be an inherently improved methodology for measuring temperature in cumulus clouds.

Measurements of temperature excess ΔT in small depth convective clouds (Cu hum-Cu med) had shown that maximum number of mean ΔT is observed in developing clouds (0.4 °C) and the minimum (0.0 °C) - in dissipating clouds (ΔT was calculated for every cloud as difference between

---

Corresponding author's address: Andrei A.Sinkevich, Cloud Physics Department, A.I.Voeikov Main Geophysical Observatory, Karbyshev str.7, St.Petersburg, 194021, Russia, E-Mail: sinkev@main.mgo.rssi.ru

averaged temperature in cloud and temperature of ambient air). More than 50% of ΔT are within the limits 0.4-1.6 °C for clouds in developing and mature stages of life. The maximum numbers exceed 2 °C. The maximum temperature difference T^+ between cloud air and ambient air is rather great and is equal on the average to 1.0°C in Cu hum-Cu med in developing stage. In dissipating stage T^+ decreases in comparison with developing and mature stages of life. The minimum negative temperature differences T^- between cloud and ambient air increases and its mean number equals to –0.5 °C .

Mean temperature excess ΔT in developing Cu cong (Fig.1) depends on the height over cloud base and reaches maximum in our experiments at the height of 2-3 km (ΔT=0.7°C). Considerable

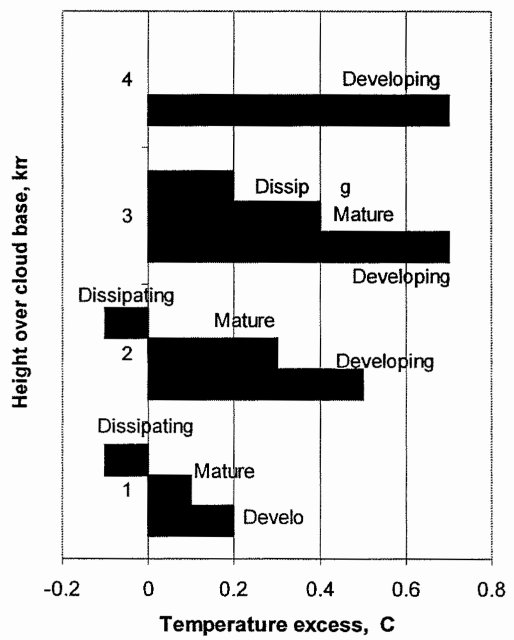

Fig.1. Mean temperature excess in Cu cong

temperature excess is observed there; for example, in more than 10% of cases ΔT exceeds 2.0°C. The maximum (among all measurements of incloud temperature) temperature excess T^+ was registered there and it was equal to 4.1 °C. There is no increase of ΔT at the height of 3-4 km over cloud base. It can be explained by the fact, that measurements have been made in most cases in the upper parts of Cu cong, while the development of the latter were limited by intercepting layers. The minimum averaged values of ΔT were observed in the lower part of cloud at the height 0-1 km over the cloud base.

Temperature excess in Cu cong being in mature stage of life also depends on the height over cloud base and maximum is observed at the height 2-3 km. ΔT is 2-3 times lower in this stage of live in comparison with developing clouds. Mean numbers of T^- equals here –0.4 - -0.5 °C. Minimum numbers of T^- attain –2 - -4 °C.

Dissipating clouds are on average colder than ambient air. Mean ΔT is qual to –0.1 °C for heights 0-2 km over cloud base. Here, $T^-<-0.5$ °C in more than 50% of cases. Positive temperature excess (ΔT=0.2°C) is observed for dissipating clouds at the height 2-3 km over cloud base, it may be the result of crystallization processes going on in clouds.

Cb being in developing or mature stages, have ΔT>0 in more than 85% of cases (only the upper part of cloud was examined). Developing clouds practically have no areas where temperature is lower than that of the ambient air. The maximum temperature difference between incloud and ambient air T^+ exceed 1.0 °C in 45% of cases. The cloud temperature excess ΔT depends on cloud living stage and decreases during cloud transition from developing to dissipating stage (ΔT=0.9 °C for developing clouds and ΔT=0.2°C for dissipating clouds). One can observe the decrease of ΔT by the factor of 2-3 in mature stage of life in comparison with developing. Similar to Cu cong (for heights 2-3 km over cloud base) positive temperature excess (ΔT=0.2°C) is observed in dissipating stage of live, it may be the result of crystallization processes going on in clouds.

Measurements of temperature under Cb in the areas of precipitation had shown that there is significant reduction of temperature in some its parts. Mean T^- was equal to –0.9 °C, minimum registered number of T^- was equal to –2.4 °C.

4. VERTICAL FLOWS

Velocity of vertical flows was measured with the help of ultrasonic anemometer installed on boards of aircrafts Dracheva and Sinkevich (1995).

Averaged over clouds passes vertical flows velocity $\bar{V}$ in Cu hum-Cu med equals 0.7 m/s in developing clouds and -0.1 m/s - in dissipating (V -averaged over cloud pass vertical flows velocity) . Amplitudes of updrafts $\bar{V}^+$ and downdrafts $\bar{V}^-$ velocities were not too great and lie within the limits of -2 - +2 m/s. Maximum registered updraft velocity was 10 m/s in developing Cu med.

Developing Cu cong have mean V>0 for all clouds parts (see Fig.2). Maximum of averaged $\bar{V}$ was registered in upper cloud parts. There, V was greater than 0.5 m/s in 70% of cases. Mean number of V^+ equals 6.0 m/s in this cloud part.

Maximum registered updraft velocity was equal to 12 m/s and downdraft velocity –10m/s.

Mean vertical velocity in mature clouds is very near to 0 m/s. V is within the limits –2 – 2 m/s in more than 70% of cases. Maximum registered updraft and downdraft velocities were as high as 20 and –18 m/s. They were registered in middle cloud part.

Downdrafts dominate in dissipating clouds. Mean V is within the limits –0.8 - -0.6 m/s. Amplitudes of downdraft and updrafts velocities are usually smaller than for clouds in developing or mature stages of life.

cloud LWC reduces and mean number of LWC was 0.4 g/m^3 in the middle part of a cloud and 0.2 g/m^3 - in the lower cloud part.

For clouds in mature living stage maximum mean LWC was discovered to be in the middle cloud part (0.4 g/m^3). Averaged LWC exceeds 0.6 g/m^3 in more than 65% of cases and maximum LWC in cloud exceeds 1.0 g/m^3 in more than 50% of cases. One can observe rather big numbers of LWC in the middle cloud part, LWC was greater 2 g/m^3 in 23% of cases.

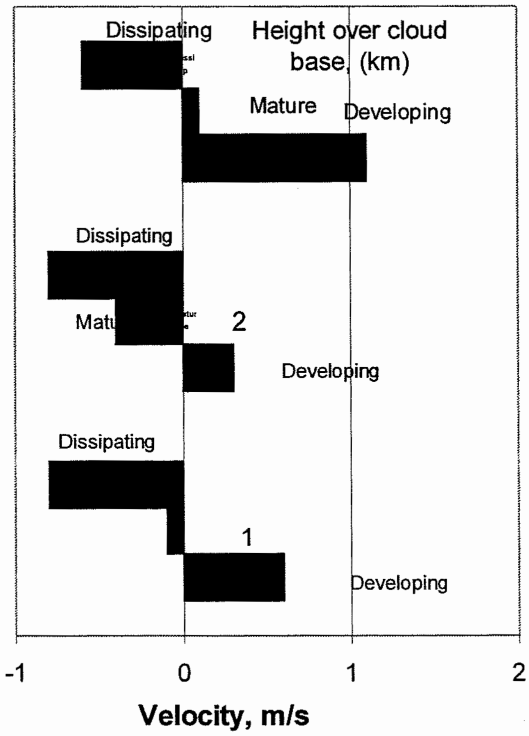

Fig.2. Mean vertical flows velocity in Cu cong

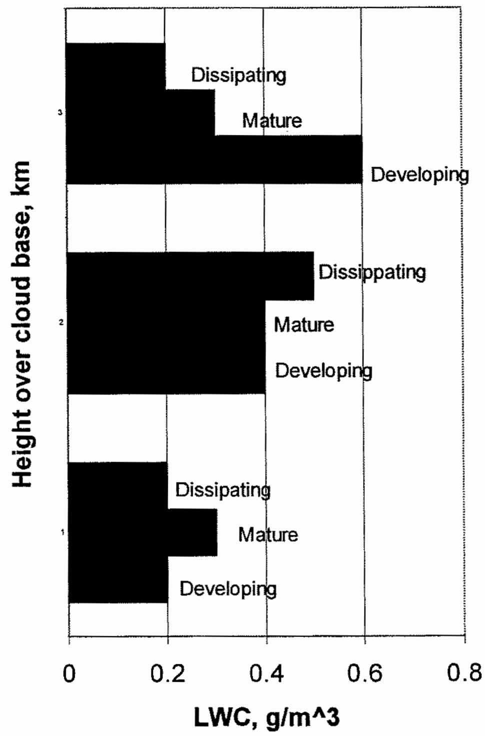

Fig.3. Mean LWC in Cu cong

5. LWC

Hot wire instrument was used to measure LWC Ponomarev et al. (1991).

Mean LWC of Cu hum-Cu med was equal to 0.2 g/m^3. Mean LWC of the clouds do not exceed 0.4 g/m^3 in 80% of cases. Maximums of LWC within the clouds do not exceed 0.6 g/m^3 in 80 % of cases also.

Results of LWC measurements in Cu cong are presented in Fig. 3.

Maximum numbers of mean LWC have been registered in upper part of developing clouds. Here LWC was equal to 0.6 g/m^3. Averaged LWC exceed 1.0 g/m^3 in 39 % of cases. Averaged maximums of LWC was equal to 1.7 g/m^3. While descending in

Dissipating clouds also have maximum mean LWC in central cloud part (mean LWC=0.5 g/m^3). LWC reaches rather big numbers in this living stage (maximum LWC exceeds 1.5 g/m^3 in 25% of cases).

LWC of upper cloud part depends on cloud living stage and decreases while cloud transforms from developing to dissipating stage. No similar regularity was discovered for lower and middle cloud parts.

6. ELECTRICAL FIELD STRENGTH

Electrical field strength was measured by 4 rotating probes installed on board of aircrafts Begalishvily et al (1993). Here we present data on vertical component of electrical field strength E. Maximum numbers of E registered in clouds are analyzed below.

Investigations of Cu med had shown that mean E is nearly the same for developing clouds and clouds in mature stage 240-260 V/m. Electrical field strength varied from 90 to 600 V/m and in every case was a positive value that means that positive charges were in cloud tops. Greater E values were registered near central cloud part in comparison with their boundaries.

Results of measurements in Cu cong - Cb show that mean number of electrical field strength depends on cloud living stage and relative height over cloud base. Maximum E numbers are usually registered in clouds in mature living stage and in dissipating clouds. Averaged E amounts up to 16-20 kV/m at relative height 2-3 km over cloud base, at the same time in developing clouds it equals nearly 2 kV/m

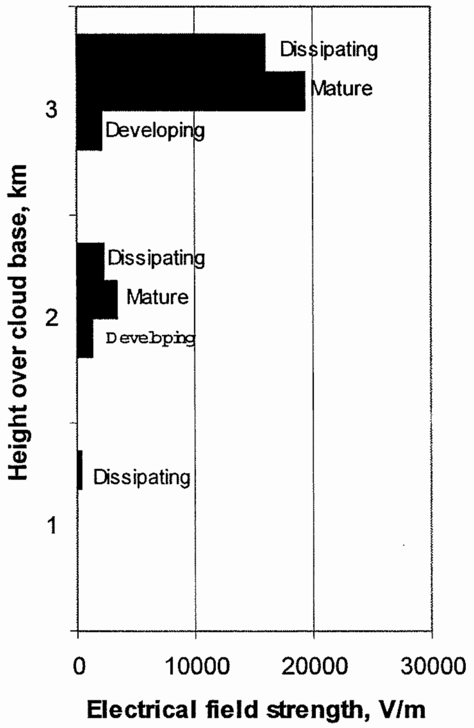

Fig.4. Mean Electrical Field Strength (vertical component) in Cu cong-Cb

(Fig.4). We would like to mention that rather great electrical fields can present in dissipating clouds - E>30 kV/m in 28% of cases, in 22% of cases such fields were registered in clouds being in mature stage. At the same time mode of electrical field strength varies usually within the limits 1.2-4.0 kV/m. It means that such clouds are not dangerous for aircrafts in most cases. Electrical field strength was a positive value in 96% of cases. It means that positive charge was higher than aircraft.

Electrical field strength numbers were less at heights 1-2 km over cloud base in comparison with height 2-3 km. Mean E varies from 1.2 to 3.4 kV/m. Electrical field strength mode equals 2.0-2.5 kV/m. Only 12% of clouds in mature and dissipating stages had electrical field strength greater than 10 kV/m.

Developing clouds have lower numbers of electrical field strength. Maximum E do not exceed 6.5 kV/m. Negative E numbers were registered with probability less than 5%. Small E numbers were the result also of the fact that clouds with smaller heights were included in this group in comparison with the group discussed above.

We obtain data only for dissipating clouds for lower layer. Registered E are small here and do not exceed 1 kV/m.

7. Conclusion

Clouds sizes, incloud temperature excess, velocity of vertical flows, LWC and electrical field strength being measured in Cu in north – west of Russia are presented in the paper.

Clouds sizes varies in rather large range but for individual cloud they are mostly within the limits 1- 4 km. Mean temperature excess varies from –0.2 up to 0.7 °C. Mean velocity of vertical flows is not too large and varies from –1 up to 1 m/s in dependence on cloud living stage. Maximum numbers of mean LWC have been registered in upper part of developing clouds. Here LWC was equal to 0.6 g/m^3 . Maximum E numbers are usually registered in clouds in mature living stage and in dissipating clouds. Averaged E amounts up to 16-20 kV/m at relative height 2-3 km over cloud base.

8. Acknowledgements

Experiments were supported by Rosgidromet Department of Cloud Seeding. Data analyze and preparation of the paper were supported by Russian Fund of Basic Investigations and ICCP.

9. REFERENCES

Begalishvily, N. A., Ponomaryov, Yu. F., Sinkevich, A. A., Stepanenko, V. D., 1993: Aircraft Laboratory Yak-40. Meteorology and Hydrology, 4, 102-108.

Drachyova, V. P., Sinkevich, A. A., 1995: Investigation of vertical Fflows in Cu in North-Western European Part of USSR. VNIGMI MCD, , dep.N1181, gm 95, 94-102.

Lawson, R. P., and Cooper, W. A., 1990: Performance of some airborne thermometers in clouds. J. Atmos. Oceanic Technol., 7, 480-494.

Ponomarev, Yu. F., Sinkevich, A. A., Tolkachev, V. K., 1991: Results of LWC studies in Cu cong in North-West of the European Territory of the USSR. Gidrometeoizdat, Trudy MGO, 534, 10-17.

Sinkevich, A. A., 2001: Cu of North-West of Russia. Hydrometeoizdat, , 157 p.

Stepanenko, V. D., 1973: Radiolocation in meteorology. Hydrometeoizdat, 342 p..

Zvonarev, V. V., Lyadov, V. S., Ponomarev, Yu. F., Sinkevich, A. A., Stepanenko, V. D. 1986: Peculiarities of the MGO Aircraft Laboratory IL-14, Leningrad, Gidrometeoizdat, Trudy MGO, 497, 51-52.

Vertical motions at cirrus altitudes

Johan Ström

[1] ITM, Air Pollution Laboratory, Stockholm University, Sweden

1. INTRODUCTION

Clouds usually form in ascending air. For low level clouds the knowledge about updraft motions and their typical scales in time and space are fairly well known. However, for high altitude clouds there are yet some gaps to fill. The evolution of the microphysical properties in lee wave clouds and the importance of turbulence in cirrus have been demonstrated in several studies, but what does the trajectory look like in the vertical for an air parcel at cirrus altitudes? In this study we have made an attempt to recreate vertical motion experienced by air parcel in cirrus altitudes by use of data form the experiment INCA (Interhemispheric differences in cirrus properties from anthropogenic emissions).

2. METHODOLOGY

2.1 Basic concepts and assumptions

The vertical trajectory *z(t)* experienced by an air parcel can not be measured directly from a moving aircraft, but if the temporal variation of the vertical wind, *w*, was know for a specific air parcel one could simply integrated *w* over time to retrieve the vertical trajectory of that air parcel. Normally, *w* is only measured along a constant altitude or pressure level and not known for a specific air parcel, thus we need to make a number of assumptions about the ambient conditions to get the information we need.

The first assumption is that the observed vertical wind is representative over some altitude range, which is at least of the same characteristic depth as the vertical displacement made by the air parcel. For instance, if an air parcel typically moves up-and-down by 50 m, then the whole column of air with this characteristic depth moves up-and-down. The second assumption is that the changes in the vertical wind field are small over the time it takes an air parcel to travel a given distance flown by the aircraft. For instance, if the aircraft makes a 55 km flight track it will take approximately 30 minutes for the air to travel this distance with a horizontal wind speed of 30 m s^{-1}. Hence, over this half hour the wind field remains unchanged.

Moreover, the analysis will only make sense if flight is performed parallel to the horizontal wind; with the wind or against the wind.

Corresponding author's address: Johan Ström, Institute of Environmental Research, Stockholm University, Frescativägen 52, S-106 91 Stockholm, Sweden; E-Mail: johan@itm.su.se

in addition, the integration of *w* must be performed along the direction of the horizontal wind, which implies that the integration must begin at the end of the flight leg (performed against time) if the aircraft flew against the wind. The calculations will result in an inverted or mirrored vertical trajectory if the integration begins at the wrong end of the flight leg.

We also must consider the fact that it takes the aircraft less time to traverse a given distance than it takes the wind to move the same distance. The observed vertical wind velocity represents an average over the distance flown by the aircraft during one second as in the case of the INCA data. Therefore, the integration must be scaled by the time it takes the air parcel to travel this distance. In one second the Falcon aircraft moves approximately 180 m, and it takes an air parcel 6 seconds to travel the same distance at a typical horizontal wind speed of 30 m s^{-1}.

2.2 Selection procedure

To be considered a parallel flight segment the angle between the flight track and the horizontal wind had to be within ±15°. Typically the mean deviations were around 5 to 10 degrees for the selected segments. Only straight and level flights segments longer than two minutes were accepted. Data collected below 6 kilometer altitude and temperatures warmer than 235K were excluded. The selection procedure resulted in 26 segments from the NH and SH campaign, respectively. In the next section we will illustrate this method to retrieve the vertical trajectory by applying it on two example segments, one from the NH campaign and one from the SH campaign. No distinction was made regarding cloudy or non-cloudy air.

3. RESULTS

3.1 Example Segment A

This flight was conducted 01 October, 2000 just north of Ireland. The wind was from south-southwest at more than 30 m s^{-1} throughout much of the free troposphere. From this flight we have selected a 10 minute segment performed at temperature of approximately -37°C. The observed *w* is plotted in Figure 1a as function of the distance covered by the aircraft. The vertical wind exhibits a very pronounced wave pattern with peek amplitudes near 1 m s^{-1}. Six main wave structures can be identified over the 80 km stretch. Our aim is to retrieve the vertical trajectory performed by air parcels around the flight path by using the observed vertical wind velocity. Since the aircraft flew into the wind the integration must begin at the end of the flight segment. That is from right to left in Figure 1a. The resulting trajectory is presented in Figure 1b.

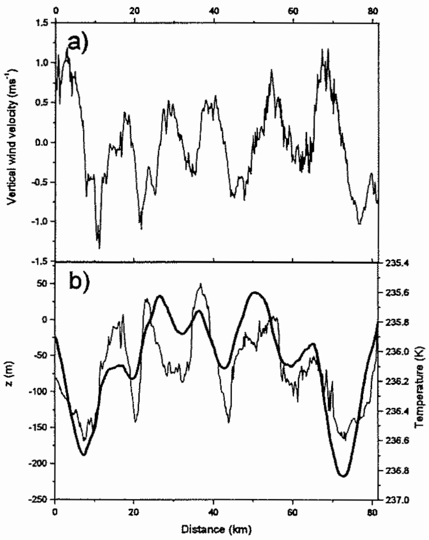

Figure 1. Example segment A from the NH-campaign at a temperature of -37°C. The top panel shows the vertical wind as function of distance traveled by the aircraft. The bottom panel shows the observed temperature (thin line) and the derived vertical trajectory (thick line).

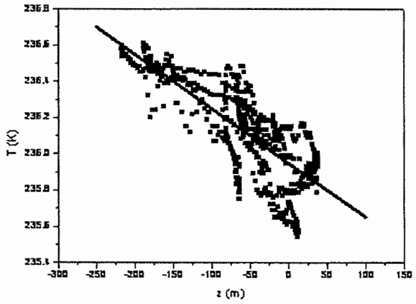

Figure 2. Scatter plot between the observed temperature and the derived vertical displacement of the air

If changes in temperature experienced by the air parcel were due to adiabatic processes we would expect the temperature to be anti-correlated with the trajectory. For comparison the observed temperature is included in Figure 1b as well, but the temperature scale is inverted to make the relationship more clear. The anti-correlation between the vertical motion of the air parcel and temperature is obvious, but the wave structure in the temperature is more accentuated. From top to bottom the air parcel moves ca 250 m over the flight segment, whereas the temperature changes by approximately one degree. Estimated from these values the temperature would change 0.004 K for every meter the air parcel moved in the vertical. This is significantly less than the dry adiabatic temperature change of 0.01 K m^{-1}. We investigate this further by presenting the observed temperature and the vertical trajectory as a scatter plot in Figure 2. A linear fit to the data gives a slope of -0.003 K m^{-1} and an r^2 value of 0.6.

It is important to remember that the observed temperature is not from a single air parcel but represents an ensemble of air parcels originating from different levels above and below the flight track. In an isothermal atmosphere we would expect the slope in Figure 2 to be -0.01 K m^{-1}. Usually, the temperature change with altitude in the troposphere is less than the dry adiabatic laps rate. Thus, the slope in Figure 2 is dependent on the ambient temperature stratification. A slope of -0.003 K m^{-1} as in Figure 2 would then imply an ambient temperature stratification of -0.007 K m^{-1}. It is interesting that, although the aircraft is flying on a constant altitude level the vertical movement by the air provides us with information about the surrounding temperature stratification.

3.2 Example Segment B

This flight was conducted on 05 April, 2000 over the southern most tip of Chile. The wind was from the west at around 20 m s^{-1}. From this flight we have selected a ca 18 minute segment performed at a temperature of approximately -46°C. The observed *w* is plotted in Figure 3a as function of the distance covered by the aircraft. In this example the wave structure is not very pronounced except for a period in the middle of the 220 km long segment. The flight was conducted along the wind and the integration is made from the left to the right in the figure. The resulting vertical trajectory and observed temperature is presented in Figure 3b.

From top to bottom the air parcel moves ca 700 m in the vertical over the flight segment, whereas the temperature changes approximately by half a degree. The two parameters really do not present any convincing relation, which is clear from the scatter plot in Figure 4a. The r^2 value for a linear fit is zero in this case.

Measurements of vertical wind from aircraft are difficult and subject to uncertainties especially in the mean values. Within a flight path of 200 km an uncertainty of 10 cm s^{-1} is well within the expected accuracy (R. Baumann, personal communication). We therefore adjust the vertical wind measurements by applying an offset to the observed *w*. The offset is change successively by 1 cm s^{-1} until a maximum in the r^2 value is reached. Figure 4b shows the scatter plot between the vertical trajectory and temperature after applying an offset of 0.13 m s^{-1} giving an r^2 value of 0.73 for the linear fit. The difference between Figure 4a and 4b is rather dramatic, and the effect is clearly seen in the relation between the vertical trajectory calculated with the adjusted wind data and the change in temperature presented in Figure 5.

The appearance of the vertical trajectory in example B is very different from example A both in form and amplitude. In A the wave structure was very pronounced

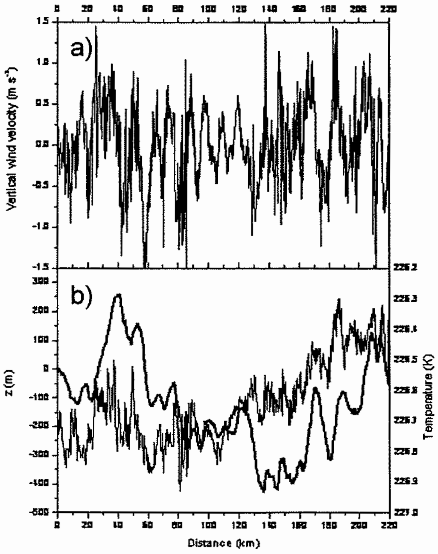

Figure 3. Example segment B from the SH-campaign at a temperature of -46°C. The top panel shows the vertical wind as function of distance traveled by the aircraft. The bottom panel shows the observed temperature (thin line) and the derived vertical trajectory (thick line).

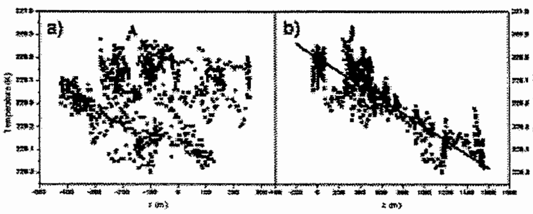

Figure 4. Scatter plot between the observed temperature and the derived vertical displacement of the air using the observed vertical wind velocities a). Figure b) is same as a) but an offset of 0.13 m s^{-1} was applied to the vertical wind velocity measurements.

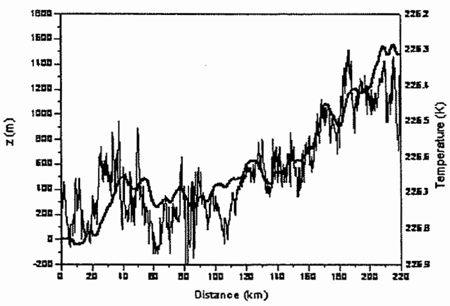

Figure 5. Same as Figure 3b, but after applying an offset of 0.13 m s^{-1} to the vertical wind data.

and the amplitude on the order of hundred meters, whereas in A the motion is dominated by a strong ascent over 1.5 km in altitude. The linear fit in Figure 4b gave a slope of 0.0003 K m^{-1}. This implies that the ambient temperature stratification in example B is almost neutral with respect to the dry adiabatic laps rate. We will return do this difference in amplitudes and ambient stratification below.

3.3 <u>All data</u>

The offset adjustment procedure to find the best r^2 value was applied to all 52 segments. The adjustments were typically small, less than 0.1 m s^{-1}, but in two occasions the offset was as large as 0.25 m s^{-1}. In a few cases r^2 was originally small and did not improve by applying an offset. Because we are interested in the temperature stratification in the vicinity of the aircraft, segments where r^2 was less than 0.5 were excluded from the subsequent analysis. After using this criterion 32 segments from 12 different flights remained and equally distributed between the two campaigns. The reasons for the low r^2 on ca 40% of the original 52 segments may be many. Obviously, if the ambient conditions do not match the assumptions described above we must expect that the procedure will have difficulties to capture the vertical trajectory. However, low r^2 do not necessarily imply that the relation between the vertical trajectory and the temperature are entirely bad.

We noted that the excursion in the vertical made by the air parcel in example B was very large and that the deduced vertical stratification was near neutral in that case. Example A presented smaller vertical displacements for a more stable atmosphere. It is well known that a very stable atmosphere suppress vertical motions. In the following we wish to investigate if it possible to relate a characteristic vertical motion with the temperature stratification. In want of a more appropriate measure to describe the vertical motions with one single number we decided to experiment with the standard deviation of the vertical trajectory. In example A, the standard deviation of the trajectory was 66 m and in example B, the value was 413 m.

Figure 6 presents the standard deviations as function of the absolute value of the laps rates. Absolute values are used because of the apparent non-linear relation between these two parameters. The data follows the excepted general trend of a decreasing standard deviation with increasing atmospheric stability. One data point obviously falls outside of the general trend and is excluded from the analysis for no other reason than being an outlier. The fitted power distribution gives an r^2 value of 0.68.

In a stably stratified atmosphere an air parcel forced from its point of dynamical equilibrium will begin to oscillate around this level with the so called Brunt-Vaaisala frequency. A stable atmosphere causes the oscillations to be faster than in a more neutral atmosphere. In other words the period, time between upward and downward motion, will be longer if the frequency is smaller. Power-spectra for each of the remaining segments were computed to investigate if this phenomenon is present in our data. Five frequencies with the largest amplitudes were selected and a mean amplitude weighted frequency was calculated from these. This frequency was inverted to a period. A curve ws fitted, which provides a relation between the derived period and the static stability. A comparison shows that the derived relation follows the so called Brunt-Vaaisala frequency well, but underestimates the period with between 30 and 60%.

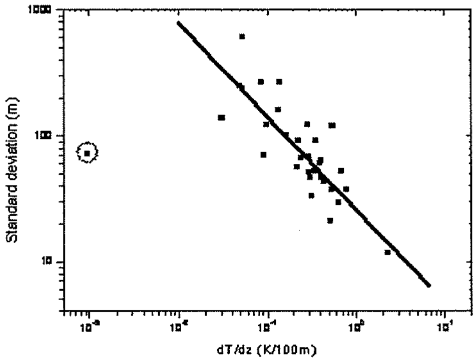

Figure 6. Standard deviation for the different flight segments discussed in the text as function of the fitted slope between the observed temperatures and derived vertical displacement of the air. The fitted curve is SD = $28(-100\ dT^{*}/dz)^{-0.73}$, r2 = 0.68. The encircled data point is excluded from the curve fitting. Note that dT^{*}/dz here is observed and not the ambient laps rate.

As a final exercise we try to make a qualitative comparison between the derived vertical trajectories and a harmonic wave motion based on the fitted expressions of the period and vertical displacement. The amplitude is given by the fit for the standard deviation and the period is given by the fit for the weighted frequency. In the example we have assumed a horizontal wind speed of 30 m s^{-1}. Three different temperature stratifications were selected to illustrate the influence by the atmospheric stability on the appearance of the trajectories. The three ranges representing stable, intermediate and near neutral conditions are: -0.2 to – 0.6, -0.75 to – 0.85, and -0.95 to -0.98 K per 100 m. For this comparison we also allowed derived trajectories where the r^2 was less than 0.5 to get more cases to compare with. The data is presented in Figure 7 with the most stable conditions on top and the near neutral conditions in the bottom panel. The thick lines in each panel are the trajectories using the fitted expressions calculated for the *dT/dz* limits listed above. The more stable of the two limits present a smaller amplitude and shorter period. Figure 7 shows that it is possible to get a feeling for the type of vertical motions that is going on at cirrus altitudes based simply on the atmospheric stability.

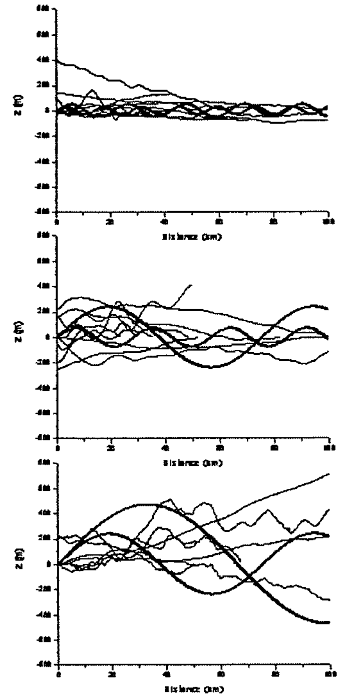

Figure 7. Qualitative comparison between the derived vertical trajectories and trajectories using the fitted expressions, see text. Derived trajectories are shown by thin lines. Trajectories given by the fitted expressions are shown by thick lines. The top panel shows trajectories for laps rates between -0.2 to – 0.6 K per 100 m. The middle panel shows trajectories between -0.75 to – 0.85 K per 100 m. The bottom panel shows trajectories between -0.95 to -0.98 K per 100 m.

4. CONCLUSIONS

The study shows that it is possible to retrieve a convincing vertical trajectory experienced by an air parcel based on aircraft measurements on a single flight level given some simple assumptions about the wind field. The vertical excursions made by an air parcel is related to the atmospheric stability and for typical values of the laps rate the characteristic vertical motions are in the range 30 to 80 m. The period or the characteristic time it takes for the air parcel to move in the vertical is related to the atmospheric stability as well. This deduced dependence resembles very much what is given by the Brunt-Vaaisala frequency. We therefore conclude that bouncy or gravity waves are important components in understanding vertical motions at cirrus altitudes.

5. ACKNOWLEDGMENTS

This work was funded by the European Commission through the projects INCA. Thanks to everyone involved in that project.

Cirrus cloud occurrence as function of ambient relative humidity: A comparison of observations obtained during the INCA experiment

J. Ström[1], M. Seifert[1], B. Kärcher[2], J. Ovarlez[3], A. Minikin[2], J.-F. Gayet[4], R. Krejci[1], A. Petzold[2], F. Auriol[4], W. Haag[2], R. Busen[2], U. Schumann[2], and H. C. Hansson[1]

[1] ITM, Air Pollution Laboratory, Stockholm University, Sweden
[2] DLR, Institut für Physik der Atmosphäre, Oberpfaffenhofen, Germany
[3] LMD, Ecole Polytechnique, CNRS-IPSL, Palaiseau, France
[4] LAMP, Universite Blaise Pascal, Aubiere, France

1. INTRODUCTION

Studying a possible anthropogenic effect on clouds involves the detection of subtle but systematic differences between the properties of clouds formed in a pristine environment and those formed in a perturbed environment. The possible anthropogenic influence on warm clouds has been studied extensively and covers a range of environmental conditions in both hemispheres. However, until recently all in-situ measurements of midlatitude cirrus had been performed in the Northern Hemisphere. With the project INCA (Interhemispheric differences in cirrus properties from anthropogenic emissions) the first observations of cirrus properties in the Southern Hemisphere midlatitudes became available, allowing clouds that formed under comparable meteorological conditions in two very different regions of the world to be compared with each other with an identical set of in situ instruments.

2. METHODOLOGY

2.1 Instruments

Although a cloud is something known to everyone, it may sometimes be difficult or even impossible to provide a simple definition for when a cloud is actually present or not. What is the minimum crystal number density or horizontal and vertical extent necessary for an ensemble of hydrometeors to be called a cloud? Is a 1 m thick layer or a particle number density of 1 m^{-3} sufficient? We can raise similar questions for observable parameters obtained by in-situ or remote sensing methods alike. Because of theses difficulties, the presence or non-presence of a cloud is usually determined by the detection limit of the particular sensor used to observe the cloud. What is interpreted as a cloud by one sensor might be interpreted as cloud-free air by another.

Corresponding author's address: Johan Ström, Institute of Environmental Research, Stockholm University, Frescativägen 52, S-106 91 Stockholm, Sweden; E-Mail: johan@itm.su.se

In this study we will make use of four different cloud sensors to investigate the presence or non-presence of cirrus clouds as function of ambient relative humidity. These instruments are the Counterflow Virtual Impactor (CVI), the PMS FSSP-300, the PMS 2D-probe, and the Polar Nephelometer. The same instruments were used in both INCA campaigns, which permits a direct comparison of the observations with respect to an unchanged payload configuration. The afore-mentioned cloud probes were mounted on the research aircraft Falcon operated by Deutsches Zentrum für Luft- und Raumfahrt (DLR). All probes have different advantages and limitations and provide information about different aspects of the cloud, as explained below. With the term "cloud particles" used hereafter we mean "particles measured in the presence of cirrus clouds".

Relative humidity was measured using a cryogenic frost point mirror (Ovarlez and van Velthoven, 1997). The unheated inlet, a modified Rosemount-Goodrich temperature housing, was located on the top of the fuselage. The relative humidity is determined from the Sonntag saturation vapor pressure formula (Sonntag, 1994), using the air temperature data provided by the standard instrumentation on board the Falcon. The relative uncertainty in observed relative humidity is estimated to be better than 7% (2 standard deviations).

2.2 Cloud Presence Fraction

We define cloud occurrence as the ratio between the number of in-cloud data points versus all data points at any given RHI and call this ratio the cloud presence fraction (CPF). A substantial part of the paper deals with the question of how to decide whether a data point represents cloudy or cloud-free air.

The expected CPF as function of relative humidity over supercooled liquid water for warm clouds consisting of supercooled water droplets is illustrated in Fig.1a. Such clouds form and disappear at essentially the same relative humidity marked X_1 and X_2. Actually, a small supersaturation, typically a fraction of a percent, is necessary to activate aerosol particles into cloud droplets. However, within measurement capabilities of relative humidity, the CPF can be approximated as unity at and above water saturation and zero at humidities below. Solution droplets may be in equilibrium with ambient water vapor even at relative humidities well below 100%. These particles are not activated into cloud droplets in the traditional sense.

Ice clouds are more complicated than their liquid counterparts since they may form at one RHI substantially (many tens of percent) above saturation and dissolve completely at much lower (few tens of percent) values below saturation; see Sect.3. The rate at which water molecules are transferred between the different phases at cold temperatures is slower than in warm clouds, which is why a cirrus cloud can persist for some time in air subsaturated with respect to ice and give rise to their often fuzzy appearance especially around cloud edges.

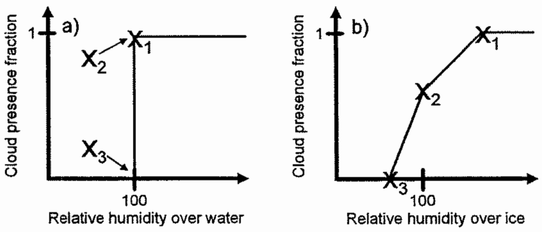

Figure 1. Schematic illustration of the cloud presence fraction as a function of the relative humidity for liquid clouds (a) and ice clouds (b). All data points above X_1 are in-cloud data points. The point where clouds start to dissolve and where cloudy and non-cloudy air parcels coexist is marked X_2 and the point where the cloud has completely disappeared is marked X_3.

A possible scenario is illustrated in Fig.1b. At some relative humidity over ice, X_1, ice crystals appear in any given air parcel. In this case we do not care about their size and number density, we simply acknowledge the presence of cloud. The relative humidity may still increase after crystals initially appear. This increase in relative humidity continues until the formation phase is completed and all crystals have formed. In our case this does not change the presence or non-presence of the cloud and the CPF=1 at X_1 and humidities above. At X_2 (near ice saturation), CPF is less than unity since this point represents a mixture between air parcels that contain cloud particles and where the humidity is perhaps decreasing, and air parcels that have not yet formed a cloud and where the humidity might still be increasing. To the left of X_2 (below ice saturation), ice crystals begin to evaporate. Once below saturation, all clouds will eventually have disappeared at some humidity X_3. Because of the slower evaporation processes in cold clouds the relative humidity at X_3 is different from X_2. The details about X_1, X_2 and X_3 for cirrus clouds are not well known.

3. OBSERVATIONS

Our study is limited to observations performed above 6 km altitude and temperatures below 235 K. Under these conditions, clouds will consist of ice crystals and interstitial aerosol particles (sometimes referred to as supercooled haze droplets), as liquid water droplets would freeze spontaneously. Although the different cloud probes are based on different working principles and have different detection limits it is interesting to compare the consistency between the probes for a subset of the data where there is an overlap in cloud detection. The FSSP-300 is able to detect clouds when particles are smaller than the aerodynamic cut-off of the CVI, but the CVI is able to detect clouds with a much lower particle number density than the FSSP-300 is capable of. If a subset of the FSSP-300 data is selected to emulate a CVI with respect to the size cut-off, and a subset of the CVI data is selected to emulate the FSSP-300 with respect to the number density detection limit, the two instruments should detect clouds with similar efficiency.

3.1 Transition between clouds and cloud-free air

Figure 2 shows observed CPFs as a function of RHI from both INCA campaigns (SH in Fig.2a and NH in Fig.2b) taken with the CVI (dotted curves) and the FSSP-300 (dashed curves).

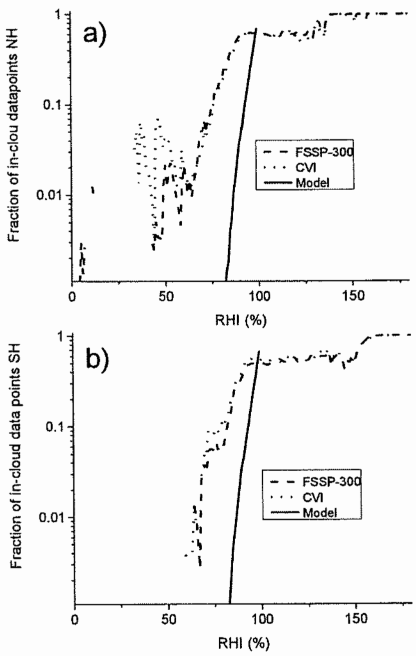

Figure 2. Observed cloud presence fractions as a function of relative humidity over ice using similar detection thresholds for the two probes (CVI: dotted curves, FSSP-300: dashed curves) with respect to particle size (> 4 μm) and number density (> 0.3 cm^{-3}). Data from the SH campaign (a) and from the NH campaign (b). The solid curves are corresponding model results taken below ice saturation and exclusively count ice crystals.

To enable a direct comparison, we have used similar detection thresholds for both instruments: particle size > 4 μm and particle concentration > 0.3 cm^{-3}. Given these thresholds, we expect the detected particles to be mostly ice crystals, as such high number densities of large aerosol particles are hardly found in cirrus levels (Kärcher and Solomon, 1999). For example, in situ measurements over continental Europe revealed the presence of coarse-mode aerosol in the tropopause region, but only at low concentrations (Schröder et al., 2002, their Fig.3b). The measured CPFs show more structure than suggested by the schematic in Fig.1b. We observe a plateau region between 90-130% (NH) and 90-150% (SH), a transition region between 70-90%, and a dry region < 70%.

The comparison of CPF data from both campaigns shows an excellent agreement between the CVI and FSSP-300 over several orders of magnitude in CPF. Typically, the difference between the two cloud probes is in the range of percent. The CPF is plotted on a logarithmic scale to highlight the agreement even down to RHI = 70-80%. Before the CPFs rapidly decrease around 80%, they stay elevated over a wide range of RHI up to about 130% (NH) and 150% (SH). Recall that the CVI counts residual particles from evaporated crystals, whereas the FSSP-300 detects the scattered light from the crystals in the ambient air. Although their working principles are completely different, Fig.2 proves that the two instruments perform as expected within at least the overlapping range in particle number density and size.

In what follows, we compare the findings shown in Figs.2 with model simulations described in full detail by Haag et al. (2003), whose principal goal is to infer freezing thresholds and nucleation modes from the observed distributions of RHI above ice saturation. Here, it is sufficient to note that the microphysical trajectory model roughly captures the typical environmental conditions (temperatures, cooling rates, mesoscale wave amplitudes and frequencies) that prevailed during the NH and SH campaigns and uses a fairly detailed microphysical scheme to predict the formation and disappearence of cirrus clouds. The prescribed aerosol freezing properties provide a consistent explanation of the SH data in terms of homogeneous freezing, and of the NH data in terms of homogeneous freezing competing with a small number of efficient ice nuclei (cases HOM and MIX0.001 of Haag et al. (2003), respectively).

We present model-derived CPFs computed from the distributions of RHI inside and outside of cirrus clouds. The calculated CPFs do not include aerosol particles, in contrast to the observations that make no distinction between these two types of particles. They are plotted as solid curves in Figs.2, using the same criteria to define cloud as in the observations with the CVI and FSSP-300 probes. The model curves show the same characteristic transition regime as the measurements at roughly comparable RHIs (see below). The reason for the strong decrease of CPF in the model is that the evaporation of water molecules from the ice crystals is kinetically limited. The time needed to (almost) completely evaporate water from ice crystals can be longer than the time in which air parcels experience (significant) subsaturation due to warming, especially at low temperatures and in the presence of temperature oscillations.

3.2 Onset of freezing in cirrus clouds

In Fig.3, cloud data points are defined as having an extinction coefficient of 0.05 km^{-1} or larger as measured by the Polar Nephelometer. In addition, this criterion had to be fulfilled during at least four consecutive seconds in order to be considered an in-cloud data point. A microphysical equivalent of this optical threshold corresponds to ice crystals of ~ 5 μm diameter at a number density roughly between 0.05 and 0.1 cm^{-3}. The criteria used to define Polar Nephelometer in-cloud data points presented in Fig.3 are the same as used by Ovarlez et al. (2002). Whereas previous CPFs were calculated for each percent of RHI, the Polar Nephelometer data are averages over 10% increments.

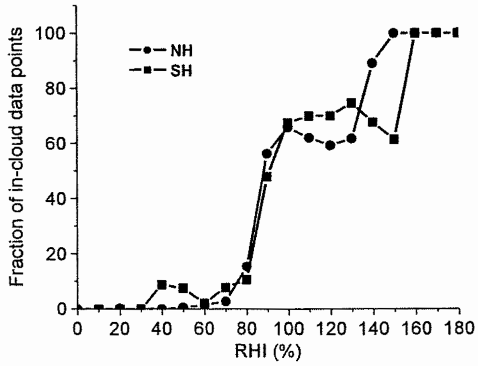

Figure 3. Cloud presence fractions as a function of relative humidity over ice measured by the Polar Nephelometer. If the probe, at a given RHI, observes an extinction coefficient exceeding 0.05 km^{-1} during four consecutive seconds, the data point is considered a cloudy data point. This criterion roughly corresponds to particle size and concentration thresholds of 5 μm and 0.05-0.1 cm^{-3}, respectively, indicating that mostly ice crystals are detected. Only data during straight and level flight segments are included.

Values of CPF near zero in the dry region below 70% support the notion that the Polar Nephelometer has exclusively probed ice crystals. (The origin of the hump at RHI between 40-50% in the SH data set is not known.) In contrast to what is expected from the schematic shown in Fig.1b, however, the CPF curves in Fig.6 do not increase monotonically to unity when RHI rises, but exhibit local minima centered at 120% (NH data) and 150% (SH data). This feature can also be traced in the data of the other probes presented in Figs.2, but the extent of the minimum depends on the threshold used to characterize in-cloud and out-of-cloud data points.

As the Polar Nephelometer detects ice crystals in cirrus when they return an extinction signal > 0.05 km^{-1}, a sufficient number of crystals must have nucleated and grown to certain sizes in order to produce such large extinction values. The very first, freshly nucleated crystals are certainly not detectable by the Polar Nephelometer probe. When all ice crystals have formed at RHI > 130% (NH) and > 150% (SH), they grow and thereby reduce RHI and become detectable by the Polar Nephelometer when crossing again the RHI-regions containing the local minima. The same reasoning can be applied to the other probes.

This provides an explanation for the distinct minima observed in the Polar Nephelometer data presented in Fig.3. Thus, the interpretation of the local minimum in observed CPF above ice saturation is that it approximates the range in RHI where the onset of cloud formation occurs. The comparison of the NH and SH cases strongly suggests that the mode of nucleation was different during the respective campaigns.

The study of Haag et al. (2003) investigates this difference in ice nucleation in cirrus in more detail by analyzing the distributions of RHI taken outside of and inside cloud with the help of microphysical model simulations.

4. CONCLUSIONS

In this study we employed different cloud probes to determine the presence or non-presence of cirrus clouds as function of relative humidity over ice during the INCA campaigns. The observed cloud presence fractions showed a characteristic behavior when plotted as a function of relative humidity over ice: a flat, plateau-like region between RHI = 90% and values close to the cloud formation thresholds above which CPF = 1; a transition region between 70-90% where the bulk of the ice crystals evaporate and the cloud dissolves; and a dry particle region < 70% where eventually all ice particles disappear.

The CPF derived from the Polar Nephelometer data exhibits a distinct local minimum between 140-155% RHI in the SH data set when plotted as a function of RHI. A less pronounced local minimum in CPF is also suggested in the NH data set between approximately 115-130% RHI. Our interpretation of these features is that they correspond to the preferred ice nucleation thresholds during the respective campaigns. The SH threshold is consistent with homogeneous freezing, whereas the NH threshold indicates heterogeneous ice formation.

5. ACKNOWLEDGEMENTS

This work was funded by the European Commission through the projects INCA and PARTS. It also contributes to the project "Particles and Cirrus Clouds" (PAZI) supported by the Helmholtz-Gemeinschaft Deutscher Forschungszentren (HGF). The Swedish Research Council is sponsoring this work by supporting ITM in airborne aerosol and cirrus activities. We thank the entire INCA team for help in collecting the data.

6. REFERENCES

Haag, W., Kärcher, B., Ström, J., Minikin, A., Ovarlez, J., Lohmann, U., and Stohl, A.: 2002 Freezing thresholds and cirrus cloud formation mechanisms inferred from in situ measurements of relative humidity, Atmos. Chem. Phys., 3, 1791–1806.

Kärcher, B. and Solomon, S.: 1999, On the composition and optical extinction of particles in the tropopause region, J. Geophys. Res. 104, 27 441-27 459.

Ovarlez J. and van Velthoven, P.:1997, Comparison of water vapor measurements with data retrieved from ECMWF analyses during POLINAT experiment, J. Appl. Meteor., 105, 1329-1335.

Ovarlez, J., Gayet, J.-F., Gierens, K., Ström, J., Ovarlez, H., Auriol, F., Busen, R., and Schumann, U.: 2002, Water vapour measurements inside cirrus clouds in Northern and Southern hemispheres during INCA, Geophys. Res. Lett., 29, 1813-1817.

Schröder, F., Kärcher, B., Fiebig, M., and Petzold, A.: 2002, Aerosol states in the free troposphere at northern midlatitudes, J. Geophys. Res., 107, 8126, doi:10.1029/2000JD000194

Sonntag, D.: 1994 Advancements in the field of hygrometry, Meteorol. Z., 3, 51–66.

AIRBORNE RADAR OBSERVATIONS OF NON-DRIZZLING MARINE STRATOCUMULUS

Gabor Vali

Department of Atmospheric Science, University of Wyoming.

1. INTRODUCTION

Since drizzle is nearly ubiquitous in marine stratocumulus, observations are sparse from situations where drizzle was absent. The case here described fits in that category and is interesting to examine because the Doppler radar data allows air motions to be diagnosed without serious contamination by the fallspeed of precipitation.

As part of the Dynamics and Chemistry of Marine Stratocumulus-II (DYCOMS-II) experiment in July 2001, nighttime observations were made in the vicinity of 31°N latitude and 122°W longitude. Main features of the study are given by Stevens et al, 2003. Observations were made with the NSF/NCAR C-130 aircraft carrying cloud physics probes, aerosol and trace gas (O_3, DMS) instrumentation, the SABL lidar and the Wyoming Cloud Radar (WCR). This paper focuses on information derived from the radar data on one flight,18 July, 2001 0619-1541UTC; flight RF05. The flights pattern consisted of circles of 60 km diameter at various altitudes while allowing the aircraft to drift with the ambient winds, hence approximately tracking a given cloud region.

2. GENERAL CHARACTERISTICS

During the 7-h study period, the sampled area moved a total distance of 200 km with the mean boundary layer flow. Cloud depth was near 250 m under a temperature inversion of about 8°C. The average depth of the boundary layer remained relatively constant near 820 m during the first 3.5 h of the flight, then increased to 960 m during the next 3.5 h, accompanied by an apparent thickening of the cloud layer. In addition to smaller-scale variations, the top of the boundary layer was tilted, by up to 150 m over the 60-km dimension of the observation area; the direction of the tilt changed on the scale of hours. The following discussion refers to observations made at about the mid-point of the total study period, i.e. prior to the onset of BL deepening. At that time, the BL was relatively uniform in depth, with <50 m variation, over the 60-km study area.

Corresponding author's address: Gabor Vali, Dept. Atmospheric Science, 1000 E. Ivinson Ave. Laramie, WY 82070, USA; E-Mail: vali@uwyo.edu.

The cloud layer was 95 to 98% unbroken. Cloud base[1] measurements from detectable amounts of LWC during soundings range between 590 and 705 m; inferred upper limits from adiabatic LWC assumption indicate lower values near 580 - 600 m. From uplooking SABL data (during the circle flown 1300 - 1350 UTC), the average cloud base altitude was 596 m. Liquid water content maxima were near 0.5 g m^{-3}; highest droplet concentrations were about 150 cm^{-3}. At about mid-level in the cloud, the in situ probes detected only a few dozen drizzle drops (>50 μm diameter) dispersed during nearly 1000 km of sampling; the maximum sizes detected were 200 μm early in the flight and 400 μm near the end. Halfway between cloud base and the ocean surface, no drizzle drops were detected. Based on this, and on evidence from the radar, it is justified to refer to this case as a non-precipitating stratocumulus layer, though more precise characterizations will be attached to that definition in the following.

Much detail about the observations for this case is available on the web page http://www-das.uwyo.edu/ ~vali/dycmos/dy_rept/rf05_part1.html, and in Part 2 which is accessible from there via a link. Only the main features of the findings are summarized here. In addition, some new material is presented.

3. REFLECTIVITY PATTERNS AND ECHO TOP VARIATIONS

Radar data from the full cloud depth was obtained during the 10:30-10:58 UTC circle flown at 998 m MSL above the cloud.

The dominant pattern in radar reflectivity is an upward gradient, from values near -30 dBZ at the base to values near -15 dBZ at the top of the cloud layer. This is consistent with the upward gradient in liquid water content, and with the assertion that the radar reflectivity is dominated by populations of cloud droplets, not drizzle drops. In many other cases drizzle is observed to produce strong vertical striations in reflectivity.

Since the strongest reflectivities are at cloud top, the echo top is well defined in the data; comparison

[1] All altitudes quoted are from radar altimeter data.

with lidar data shows that the lidar-detected mean cloud top is 11 m higher than the mean echo top over a 200-km sample (10:30-10:58 UTC). In the following, echo top and cloud top are used almost interchangeably. Both measurements show cloud top altitude to be strongly skewed (S_k = -1.1) with a long tail toward low values. The standard deviation of cloud top altitude is 35 m. Associated with the variations in cloud top altitude, there is a well-correlated variation in the maximum local reflectivity: for 1-km horizontal averages r=0.84, with roughly 10 dBZ higher values for each 50 m increase in the altitude of the echo top.

Interestingly, the reflectivity pattern is neither uniformly flat independently of variations in echo top (implying a uniform cloud base altitude), nor is it a simple parallel variation with the echo top altitude. Taking the -21 dBZ level as a mid-cloud value (at a mean altitude of 727 m, 101 m below the mean echo top) it is seen to vary parallel to the echo top on the large scale and out of phase on the scale of kilometers. On the 20-km scale, the two altitudes have r=0.8, while deviations from the 20-km means show no correlation at all (r=0.014). The implications of these results will be further elaborated later on, when discussing reflectivity gradients.

4. ECHO BASE

Most complete radar data from the lower portions of the cloud, and corresponding in situ measurements, were obtained from two circles flown in cloud during 11:08-11:30 and 11:33-12:03 UTC.

With the mean *cloud base altitude* (**CB**) just about 180 m below the flight level, the resulting greater radar sensitivity benefits examinations of reflectivity near cloud base. After careful (but nonetheless still subjective) noise thresholding, the mean *echo base altitude* (**EB**) was found to be 545 m with standard deviations of 42 m for 30-m horizontal averages, and 30 m for 0.6-km averages. The distribution of **EB** is negatively skewed (S_k = -0.5), i.e. toward lower values. The best data for **CB** is from SABL during a period two hours later than the **EB** data. It yields **CB** = 596 m, and, for 110-m horizontal averages, has a standard deviation of 36 m and no skewness. This value for **CB** (reasonably well supported by other determinations from earlier periods) is roughly 50 m higher than the mean **EB**. The difference, even if not precisely known, indicates that in fact there were radar-detectable hydrometeors present of the order of 50 m below the cloud base, and that these were, most likely, small drizzle drops of perhaps 50-100 μm diameter which are difficult to measure with the in situ probes. Also, these drizzle drops were evidently evaporating and only extending to about something like 50 to 100 m below cloud base.

When **EB** is stratified by the Doppler velocity measured near cloud base, a strong correlation is found for velocities <1 m s^{-1}: **EB** = 517 m for -2 m s^{-1} and **EB** = 557 m for +1 m s^{-1}. There is no change in the mean **EB** for vertical velocities >1 m s^{-1}. The coincidence of lower echo bases with downward velocities supports the idea that these echoes are due to larger drops which are evaporating slower in moistened downward plumes.

There is additional evidence for lower values of **EB** to be associated with drizzle in the strong negative correlation (r = -0.7) observed between **EB** and the 90-percentile reflectivity directly above the given **EB** location. The lowest echo bases correspond to reflectivities near -20 dBZ, while the highest ones correspond to -30 dBZ. This also implies the presence of negative vertical velocities at the echo base at locations where the reflectivity above is stronger, and vice versa, though the direct correlation between the reflectivity and the velocity at the base is weaker.

Reflectivity gradients in the lowest 75 m of the observed echoes have also been stratified by the vertical velocity measured in the same location. The gradients for velocities >1 m s^{-1} are near 14 dBZ per 100 m. For velocities in the range -1.75 ± 0.25 m s^{-1}, it is near 8 dBZ per 100 m. The values of these gradients can be best judged when compared to results from parcel model calculations (Snider and Petters - <http://www-das.uwyo/ccp/web/model.html>). With C=250 cm^{-3}, k=0.3, cloud base (defined as 50% final drop concentration) at 590 m and for updrafts in the range 1 to 4 m s^{-1}, the model indicated that by the time reflectivity values reach -34 dBZ (comparable to the observed values near **EB**) the rate of increase of reflectivity is between 12 and 18 dBZ per 100 m of lift. These values bracket the observed 14 dBZ per 100m for upward vertical velocities. The implication is that the reflectivity gradient, for updrafts, is dominated by the condensation of droplets, but with the absolute value of the reflectivity increased from -34 to about -29 dBZ (at 590 m altitude) by recirculating drizzle drops. Admittedly, this is not a fully developed description. To firm up these ideas, it will be necessary to collect simultaneous data, at a minimum, on **CB**, **EB** and vertical velocities.

5. VERTICAL VELOCITIES

In contrast with the horizontal stratification of reflectivity, vertical velocities[2] vary predominantly along the horizontal, and exhibit greatest variation near cloud base. Images accessible from the web page cited at the beginning of this paper demonstrate

[2] The measured Doppler velocities are affected by the fall velocities of droplets to a minor extent, comparable to the estimated 0.2 m s^{-1} accuracy of the measurements. Hence, for simplicity, Doppler velocities and air velocities are referred to here, interchangeably, as "vertical velocities".

this pattern quite clearly. For both positive and negative values near **EB**, the velocity diminishes toward zero at cloud top.

Frequency distributions of vertical velocity at given altitudes are symmetrical and quite broad. Using 10-m resolution data, the range of values at the 0.01 percentile level extend to ±3.5 m s^{-1}. At the echo base, the 1, 5, 10, 90, 95 and 99-percentile values are [-2.1, -1.4, -1.1, +1.1, +1.4, +2.2], and at cloud top these values are [-1.5, -0.80, -0.57, +0.42, +0.60, +1.3]. Mean values are very close to zero at all levels.

Perhaps the most important aspect of the vertical velocity observations is the patchiness of updraft and downdraft regions in the lower part of the cloud. Again, the best way to see this is from the images. The size distributions of regions of given velocity thresholds (variously defined) are all exponentially decreasing. Yet, contiguous regions of larger sizes can be seen to have the greatest significance in terms of upward penetration, correspondence with echo top altitude (both of these indicating longevity), and in terms of drizzle development. Thus, it is worth quoting that 100-m patches of vertical velocities exceeding 1 m s^{-1} (either positive or negative) are about 3 km apart and 200-m patches are on the average 30 km apart. For >0.5 m s^{-1}, 200-m patches are 3 km apart. These numbers relate to sampling along a line (a circle) so the dimensions quoted are random sections of patches of yet unknown shapes.

6. COMMENTS

Not surprisingly, even in this simplest of the stratucumulus cases from the DYCOMS experiment, rich structure has been revealed by the data so far examined. Perhaps the key deduction at this point is that updrafts are modest in horizontal extent (very few are large) but are relatively vigorous, and that they appear to penetrate cloud regions already containing low concentrations of small drizzle drops. From the point of view of drizzle growth, this implies that the residence time of droplets is lengthened by updrafts for some unknown fraction of the total cloud volume. This is not re-circulation in the sense that other cases suggest, but a simpler floatation of the cloud volume, more the way repeated parcels have been modeled for cumulus. The drizzle drops evaporate within about 100 m of cloud base, and so play a different role in sub-cloud forcing of circulations than in cases with more profuse drizzle.

The proposition for re-lifting of growing drizzle drops is neither really surprising, nor novel. It has also been made by Vali et al. (1998) on the basis of a positive correlation between velocities and reflectivity in the upper parts of coastal Sc, and similar ideas have been expressed by others. It is the specific form and documentation of the process that is the contribution made here. The plausibility of this model could be countered by recognizing that divergence at cloud top is associated with updrafts and that this flow might transport drizzle, or incipient drizzle, away from the updraft. Resolution of these two notions depends on the steadiness of the updrafts, i.e. on the likelihood of persistent circulations throughout the boundary layer. For the current case, images from dual-Doppler analysis presented at http://www-das.uwyo.edu/~vali/dycoms/dy_rept/rf05_sixplot.pdf show that divergence is on fact found in some cases, but most updrafts, even some of stronger ones, while they push the cloud top higher, do not have clear divergence associated with them This is most likely a consequence of diminishing updraft velocities with height. So, it may be appropriate to think of the updrafts as pulses (of only moderate energy) which do not have longer lifetimes than a single rise to cloud top.

There are, of course, weaknesses in the data from which the foregoing construct was drawn. Worst of all, aircraft data provide snapshots of the cloud, from which the time evolution on the scales kilometers and tens of minutes cannot be evaluated. Neither can three-dimensional features be well observed. A more specific weakness, whose importance is well demonstrated by the analyses here given, is the lack of simultaneous data on cloud base (lidar seems the best tool of observation), radar data from the full cloud depth and in situ data from at least one level in the cloud. Such data sets can be generated with currently available tools. Further quantitation of the data here presented (such as the spectral characteristics of fluxes at the base of the cloud) and comparisons with chemistry data are yet to be performed. The analysis of similar cases (RF01) can also be expected to be helpful in refining or modifying the picture here discussed. Clearly, this is just a progress report.

Finally, a reminder: referring to this case as non-drizzling (in the title and elsewhere) is only an approximation.

7. References

Stevens, B. et al., 2003: Dynamics and chemistry of marine stratocumulus -- DYCOMS II. *Bull. Amer. Meteor. Soc.*, **84**, 579-593.

Vali, G. et al., 1998: Finescale structure and microphysics of coastal stratus. *J. Atmos. Sci.*, **55**, 3540-3564.

Acknowledgements: Much credit is due to the NCAR/ATD/RAF staff for the conduct of the DYCOMS field experiment and to JOSS for data management. Thanks to Drs. Lenschow and Stevens for organizing the field project and for many fruitful ideas, to D. Leon for data processing and refinement, and for helpful discussions, to S. Haimov for preparing and operating the radar. Dr. Bruce Morley (NCAR) is thanked for providing SABL data. Funding for this work was provided by NSF grant ATM-0094956 and by ONR.

ITERATIVE AMPLITUDE ADAPTED FOURIER TRANSFORM SURROGATE CLOUD FIELDS

Victor Venema[1], Steffen Meyer[2], Sebastián Gimeno García[3],
Clemens Simmer[1], Susanne Crewell[1], Ulrich Löhnert[1], Thomas Trautmann[4,3]

[1]University of Bonn, Germany
[2]University of Kiel, Germany
[3]University of Leipzig, Germany
[4]German Aerospace Center, Oberpfaffenhofen, Germany

1. INTRODUCTION

It is not possible to measure a 3D field of cloud properties. The best measurements available are 2 dimensional, e.g. a horizontal field or a vertical cross cut. Therefore, cloud fields for research into cloud structure are often either simulated by physical cloud models or they are surrogate cloud fields. Surrogate cloud fields are fields that share certain (typically statistical) properties with real cloud field.

Most methods to make such surrogate fields assume an ideal fractal structure and each method has its own typical shape of the PDF. For example, surrogate cloud fields made with the standard Fourier method typically have linear power spectrum with a -5/3 slope and a Gaussian PDF. The Bounded Cascade algorithm makes fractal fields with a discontinuous structure (Cahalan, 1994) and a 'log-normal-like' PDF. This paper introduces a new method to generate surrogate cloud field that allows presetting both the power spectrum as well as the shape of the cloud water distribution. This method can use measured cloud water distributions; there is no need to fit this to some theoretical distribution. The algorithm uses the full power spectrum; it does not have to be approximated by a linear power law. Thus this method allows for surrogate cloud fields that have a very close agreement with a specific cloud measurement. The algorithm is based on the Iterative Amplitude Adapted Fourier Transform (IAAFT) method to generate surrogate time series by Schreiber and Schmitz (2000) and has been extended to fields.

The original time series or field on which the statistics are based is called the template. We will only consider water clouds in this paper, which are described in terms of their Liquid Water Content (LWC) or, the Liquid Water Path (LWP).

2. THE IAAFT ALGORITHM

From a measured time series a sorted list is made of all values, to be used in the amplitude conversions. Furthermore, the power spectrum of the measurement is calculated. For theoretical studies, the power spectrum and the values of the amplitude distribution can be predefined. The algorithm starts with a random shuffle of the data points. Then, in each iteration, the Fourier spectrum is adjusted first and secondly the amplitudes. To get the desired power spectrum, the Fourier transform of the iterated time series is calculated and its squared coefficients are replaced by those of the original time series. The phases are kept unaltered. After this step the amplitudes of the iterated time series will no longer be the same. Therefore in the second step the amplitudes are adjusted by sorting their values and replacing the values of the surrogate by the values of the template having the same ranking. Calculation times, for the examples in this paper, range from seconds to several hours, depending on the matrix size.

Corresponding author's address: Victor Venema, Auf dem Huegel 20, 53121 Bonn, Germany, victor.Venema@uni-bonn.de.

3. SURROGATE FIELDS FROM MEASUREMENTS

3.1. 1D LWP surrogate

As a first example, we took a 1 Hz LWP time series measured with the microwave radiometer MICCY. From this LWP time series template (Fig. 1a) we made a 1D surrogate (Fig. 1b) for comparison which shows a very similar structure. However, in the template there are only spikes (which are associated with the fall streaks) in the high LWP part. The surrogates have spikes everywhere, and in a larger number. Figure 1c shows that the power spectra of the template and the surrogate are (almost) identical.

3.2. 2D LWP surrogate field

We can make a 2D LWP field from a 1D LWP time series by assuming horizontal isotropy and rotating and rescaling the 1D Fourier coefficients around the origin in the 2D wavenumber-space, see Fig. 2a. Assume we have an isotropic 2D field with a linear power spectrum with slope $-\gamma$ and we extract a 1D time series from this field. The linear power spectrum of this time series will have a slope $(-\beta)$ given by: $\gamma = \beta + 1$ (Austin et al., 1994). In other words, a measured time series where the power is proportional to the wavenumber (k) to the power $-\beta$, i.e. $k^{-\beta}$, was taken from a field with a 2D power spectrum that is proportional to $k^{-\gamma}=k^{-\beta-1}=k^{-\beta}/k$. This relation was derived for a linear power law, and should be a good approximation for isotropic clouds.

This rotation and scaling method seems to work well. In Fig. 1c we find that the average 1D power spectrum, calculated from the rows and columns of the

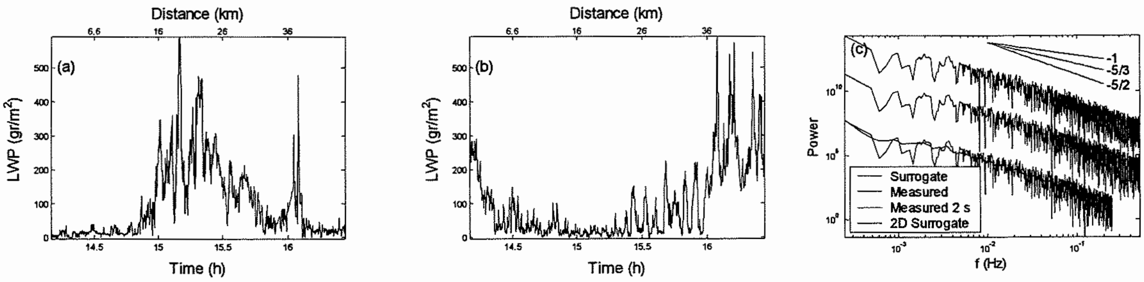

Figure 1. a) Microwave radiometer LWP time series (template) which was measured at Cabauw, The Netherlands, during the BALTEX Bridge Campaign (BBC) on the 5th of September 2001. b) Iterative Fourier (IAAFT) surrogate of the same measurement. c) Power spectrum of the 1D template (black, noisy) and the 1D surrogate (offset 30 dB, upwards, grey). Furthermore, the power spectrum of a 0.5 Hz version of the 1D template (offset -30 dB, downwards, grey) and on top of this, in black, the scaled average 1D power spectrum calculated from the 2D surrogate shown in Fig.2, which was generated based on the 0.5 Hz template.

2D surrogate field, is almost the same as the power spectrum of the 1D template. Only the typical Fourier noise is missing. Evans and Wiscombe (2004) use an optimizing method to find a 2D horizontally isotropic power spectrum that has the same 1D power spectrum as the template. This may provide a more accurate power spectrum as fewer assumptions have to be made.

One of the resulting surrogate time series of the IAAFT algorithm can be seen in Figure 2b.

The strongly correlated cloud time series are not stationary, i.e. the fields are inhomogeneous. Thus a local sample from a non-stationary data set will on average have a smaller width of the amplitude distribution. Imagine, a line measurement going through the maximum of a 2D field. Due to the strong correlations, also a large part of the other values will be higher than average. Thus the width of the PDF of this 1D measurement will be lower than that of the 2D field.

As an illustration, consider the standard deviation of the LWP cloud field (Fig. 2b). The standard deviation of the entire 2D field is 109 g m^{-2}, but the average standard deviation of the 1D vectors of this field is only 90 g m^{-2}. Thus if we would have made a zenith pointed measurement of this correlated field we would found a 17 % smaller width of the LWP distribution.

3.3. LWC profiles

In this section we will make 3D LWC fields from 2D LWC profiles, i.e. a vertical 2D space height field (see Figure 3). These LWC profiles were derived using an optimal estimation technique (Löhnert et al., 2003) which combines microwave radiometer brightness temperatures, with other measurements and with a priori information from a microphysical cloud model.

This vertical LWC field is clearly anisotropic and we would like the surrogate to have exactly the same LWC amplitude distribution at every height level. Thus not one sorted vector with all LWC values is used, but rather this operation is carried out for every height level, i.e. we utilize a 2D sorted LWC field.

The mean LWC profile was subtracted from the template before a 2D Fourier transform was utilized to calculate the 2D power spectrum. The structure is thus

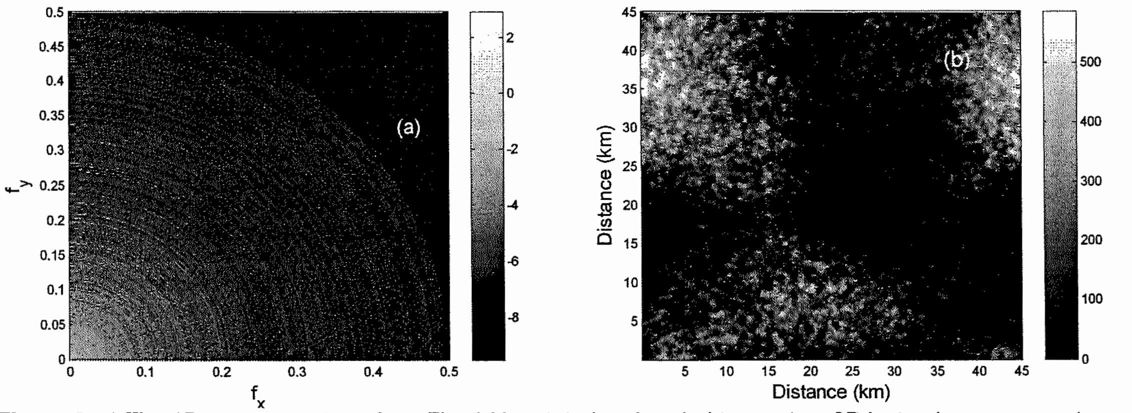

Figure 2. a) The 1D power spectrum from Fig. 1d is rotated and scaled to create a 2D isotropic power spectrum. The values for the upper right corner are set to zero. b) 2D surrogate calculated using the 1D LWP time series of Fig. 1 as a template for the statistics. The temporal scale was converted into this spatial scale using a wind speed of 5.5 m/s, taken from a close by radiosonde. The high peaks are due to the fall streaks in the virga.

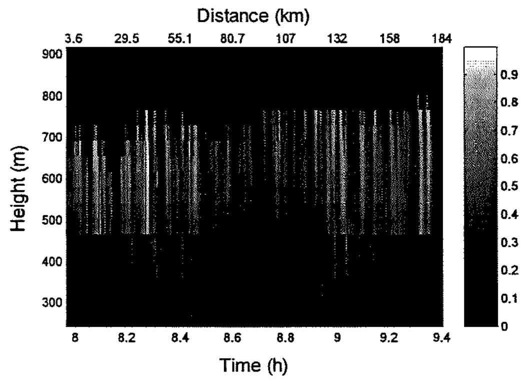

Figure 3. Retrieval of liquid water content profiles of a cloud field made during the BBC campaign on the 23rd September 2001.

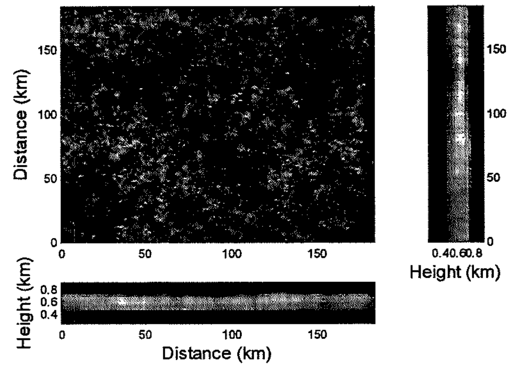

Figure 4. 3D surrogate LWC cloud field made from the 2D template shown in Fig. 3. The 2D fields should be interpreted as the integrated values of the 3D field as seen from the top (large picture), the side (right picture) or the front (bottom).

defined globally, whereas the amplitudes are defined per height level. The 2D Fourier coefficients are rotated cylindrically around the vertical wavenumber axis and scaled to make a 3D horizontally isotropic field. Figure 4 shows a 3D surrogate field made from the 2D template from Fig 3.

3.4. 3D LES stratocumulus field

The limitation of the IAAFT statistics become apparent when stratocumulus and altocumulus are considered that often display beautiful cell structures, similar to Bénard convection. Figure 5a shows a stratocumulus calculated with a Large Eddy Simulation model (Schroeter and Raasch, 2002), with these Bénard cells. The 3D IAAFT surrogate calculated from this cloud does not show cell structures. Nevertheless, the radiative properties of IAAFT stratocumulus are good.

4. VALIDATION

The most prominent application of 3D surrogate cloud fields is the study of 3D radiative transfer. In order to verify the suitability of our surrogates for this purpose, we used 3D LES cloud fields as templates for 3D LWC surrogates. The difference in the radiative properties between such cloud pairs shows the quality of surrogates with the conserved statistical properties. In other words, we want to know how good a cloud field is described with only an amplitude distribution and a power spectrum, with respect to its radiances and irradiances. As input templates, we used two sets of LES clouds: 33 stratocumulus LWC fields and 52 cumulus LWC fields.

Duynkerke et al. have modeled maritime stratocumulus clouds (P.G. Duynkerke et al., 2004) These LES clouds have a resolution of 50 m horizontally (52 grid boxes) and 10 m vertically (122 grid boxes). Drop sizes were calculated for each cloud box by assuming a monospectral distribution (i.e. one drop size) with 300 drops per cm^3. The average reflectance was 0.66.

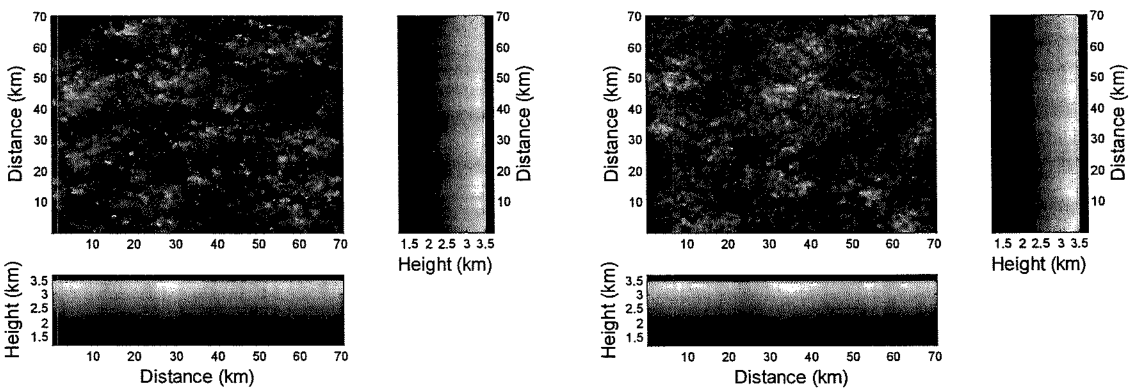

Figure 5. The left picture is a 3D LWC field from a stratocumulus that was calculated by an LES model. The right picture is its surrogate

The cumulus case represents the diurnal cycle of cumulus over land (Brown et al. 2002). The clouds have a resolution of 100 m in the horizontal and 40 m in the vertical. The number of grid boxes is 66x66 horizontally with 112 height levels. Drop sizes were calculated from these clouds by assuming a monospectral distribution with 1000 drops per cm^3, resulting in an average reflectance of 0.08.

All calculations are made assuming the wavelength of the incoming monochromatic solar radiation to be 550 nm and a solar zenith angle of 60°. The radiances were calculated with the Monte Carlo model MC-UNIK (Macke et al., 1999). These radiances were calculated in all four wind directions and at four zenith angles: 0, 30, 45, and 60 degrees. This results in total 16 calculations for each cloud field. The upward and downward flux densities were calculated with Leipzig Monte Carlo Model (LMCM; Gimeno and Trautmann, 2003). The results of the calculation can be found in Table 1. The radiative properties of the surrogates are very similar to LES clouds. Especially, the radiative budget is matched very well: within 0.5 % of the incoming radiation.

Concluding, the radiative properties of the surrogate fields are close to those of the original fields. Best results are achieved for the stratocumulus fields and the flux densities. The deviation of the radiances of surrogate cumulus fields are probably mainly due to insufficient convergence, not the insufficiency of the statistical description.

5. OUTLOOK

The cloud properties that we impose do not have to be purely statistical. In future we want to try if it is possible to include spatial constraints, e.g. a cloud mask. With scanning LWP measurements one can improve the estimate of the LWP distribution and generate anisotropic surrogate LWP fields

The code of all methods is available on our website: http://www.meteo.uni-bonn.de/victor/themes/surrogates/

Acknowledgements. This research was carried out in the framework of the 4D clouds project, which is sponsored by the German ministry of research, BMBF, in the AFO2000 program on atmospheric research.

6. REFERENCES

Austin, R.T., A.W. England, and G.H. Wakefield, Special problems in the estimation of power-law spectra as applied to topographical modeling, IEEE Trans. Geosc. Remote Sensing, 32(4), 928 939, 1994.

Brown, et al., Large-Eddy Simulation of the Diurnal Cycle of Shallow Cumulus Convection over Land, *Q. J. R. Meteorol. Soc.*, Vol. **128**, no. 582, pp. 1075-1093 Part B, Apr. 2002.

P.G. Duynkerke et al., Observations and numerical simulations of the diurnal cycle of the EUROCS stratocumulus case, submitted to the Q. J. R. Met. Soc., 2004.

Evans, K.F., and W.J. Wiscombe, An algorithm for generating stochastic cloud fields from radar profile statistics, accepted by Atmospheric Research special issue on Clouds and Radiation, 2004.

Gimeno García, S., and T. Trautmann, Radiative transfer modeling in inhomogeneous clouds by means of the Monte Carlo method, Wissenschaftliche Mitteilungen aus dem Institut für Meteorologie der Universität Leipzig, no. 30, Meteorological Institute of Leipzig University, Germany, ISBN 3-9808822-0-9, 2003.

Löhnert, U., S. Crewell, and C. Simmer, An integrated approach towards retrieving physically consistent profiles of temperature, humidity and cloud liquid water, submitted to J. Appl. Meteor., 2003.

Macke, A., D. Mitchell, and L. von Bremen, Monte Carlo radiative transfer calculations for inhomogeneous mixed phase clouds, Phys. Chem. Earth, 24(3), 237-241, 1999.

Schreiber T, and A. Schmitz, Surrogate time series, *Physica D*, Vol. **142**, no. 3-4, pp. 346-382, 2000.

Schroeter, M and S. Raasch, Broadening of convective cells during cold air outbreaks: A high resolution study using a parallelized LES model, in: *Proceedings of 15th Symposium on Boundary Layers and Turbulence*, AMS, July 15-19, 2002 Wageningen, The Netherlands, pp. 45-48, 2002.

Cloud type	Parameter	Mean value[1]	Number of fields	Relative bias (%)	RMS error (%)	Slope linear regression	Offset linear regression
Stratocumulus	Transmittance	0.34	33x2	0.031	0.040	1.0001	-0.0001
	Reflectance	0.66	33x2	-0.016	0.020	1.0001	0.0000
	Radiance(0°)	51	4x33x2	-0.13	0.76	0.9980	0.0000
	Radiance(30°)	55	4x33x2	0.056	0.71	1.0039	-0.0002
	Radiance(45°)	60	4x33x2	0.0094	0.75	1.0012	-0.0001
	Radiance(60°)	72	4x33x2	0.076	0.87	1.0038	-0.0002
Cumulus	Transmittance	0.92	49x2	0.44	0.35	1.0489	-0.0491
	Reflectance	0.080	49x2	-5.1	4.0	1.0489	0.0001
	Radiance(0°)	4.0	4x52x2	3.2	3.8	1.0359	0.0000
	Radiance(30°)	4.8	4x52x2	4.7	5.2	1.0493	0.0000
	Radiance(45°)	5.9	4x52x2	7.1	7.8	1.0803	-0.0001
	Radiance(60°)	8.8	4x52x2	11	12	1.1287	-0.0002

[1] The unit of the radiances is W m^{-2} sr^{-1}, using a solar intensity of 1000 W m^{-2}.

Table 1. Comparison of the radiative properties of LES template clouds and their surrogates.

SIZE DISTRIBUTIONS OF SNOW AND AEROSOL PARTICLES IN A CONTINUOUS PRECIPITATION WITH A CHANGE OF SURFACE OZONE CONCENTRATION AT NY-ÅLESUND, ARCTIC

M. Wada[1], Hiroyuki Konishi[2], Shinji Morimoto[1] and Takashi Yamanouchi[1]

[1]National Institute of Polar Research, Itabashi, Tokyo, 173-8515, Japan
[2]Osaka kyoiku University, Kashihara, Osaka, 582-8582, Japan

1. Introduction

Discussions about roles of aerosol for forming cloud are prosperously in climate research field recently (e.g. IPCC, 1990). Surveys of aerosol, cloud particles, cloud condensation nuclei and ice forming nuclei have been carried out by using aircraft (e.g. Curry, 2001; Raes et al., 2000). Understanding of forming mechanisms of cloud and ice particles, however, has not been clear still now.

The characteristics of cloud and precipitation in an airmass are due to aerosol features such as size distribution and composition together with meteorological factors such as water vapour content, air temperature, vertical wind velocity and so on.

Understanding characteristics of an airmass, we have measured surface ozone concentration. Understanding also characteristics of precipitation and aerosol, we have observed them using several instruments. They were an ultraviolet absorption photometer for measuring ozone concentration, a vertical pointing radar and a low power bi-static doppler radar for observing precipitation, a dual frequency microwave radiometer for measuring column water vapour and cloud liquid and an optical particle counter for measuring size distribution of aerosol at Ny-Ålesund, Svalbard, Arctic. In my presentation we introduce 2 case studies. Two different airmass types were found in one case and three different airmass types were classified in another case.

2. Instrumentation

Precipitation Occurrence Sensor System (POSS) made by Andrew Inc., Canada can measure precipitation rate and size distributions of precipitation particle. The POSS is a low power, X-band, bi-static doppler radar with a scattering angle defined by the axis of transmitter and receiver (Sheppard, 1990). A dual frequency microwave radiometer with 23.8 GHz and 31.4 GHz by Radiometric Co., U.S.A. can measure column water vapour and column liquid water in the atmosphere.

An ultraviolet absorption photometer by Dasibi measures surface ozone concentration (Yamanouchi, 1996). Optical particle counter (OPC) by Rion Inc., Japan measures number densities of aerosols which are larger than 0.3 µm, 0.5 µm, 1 µm, 2 µm and 5 µm in diameters.

A vertical pointing radar records radar echo intensities in the atmosphere. Precipitation rate can also be estimated using the echo intensities. The vertical pointing radar is a X-band pulse radar (Wada and Konishi, 1992).

Basic meteorological instruments, recording air temperature, relative humidity, atmospheric pressure, wind speed and wind direction, have been also installed there. Weather charts from Deutscher Wetterdienst and NOAA satellite quicklook images from Dundee University, U.K. were used for examining synoptic condition.

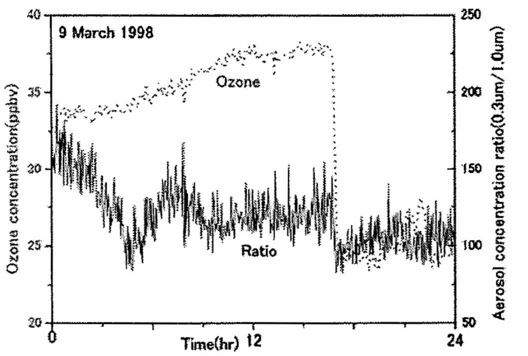

Fig. 1: Size distribution of snow particles between 16:30 and 17:12 on 9 March 1998.

Corresponding author's address: Makoto Wada, National Institute of Polar Research, Itabashi, Tokyo, 173-8515, Japan; E-Mail: wada@pmg.nipr.ac.jp

3. Results

3.1 Case study on 9 March 1998

A cloud area accompanied by a cyclone covered over Svalbard on 9 March 1998. Details of this cloud over sea were reported by Asuma et al. (2002). Cloud area sometimes covered over Ny-Ålesund around 03UTC on 9 March, viewing

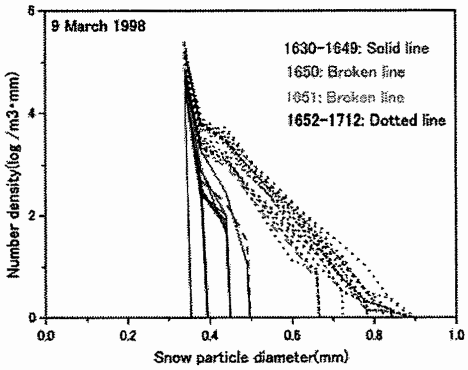

Fig. 2: Ozone concentration and aerosol concentration ratio on 9 March 1998 at Ny-Ålesund.

from NOAA satellite images. Then, the cloud area passed over Ny-Ålesund between two satellite images at 17:06 UTC on 9 March and 2:53 UTC on 10 March from west to east. The wind direction and wind speed of basic meteorological data at just before 18:00 UTC changed rapidly. Wind direction changed from SW to NNW around 16:50 UTC. Air temperature, relative humidity and atmospheric pressure data also changed at the same time.

Ozone concentration data, moreover, shows a big depression shown in Fig. 1. But other data, which are precipitation rate, radar echo, column water vapour and column liquid water, show no remarkable change at the time. The big ozone depression, about 13 ppbv, occurred between 16:49 UTC and 17:04 UTC according to more detailed data.

Size distributions of snow particles by POSS were investigated between 16:30 UTC and 17:12 UTC, which includes the period above. Aerosol concentration ratios of a size larger than 0.3 μm to a size larger than 1.0 μm were also plotted in Fig.1. Figure 2 shows the size distributions of snow particles. Their size distributions indicate that snow particles after 16:52 UTC were relatively larger than those before 16:51 UTC. The graph of aerosol in Fig. 1 indicates that a change of aerosol was occurred together with ozone depression.

3.2 Case study on 31 December 1998

Southerly wind in the 1st period shown in Fig. 3, easterly wind in the 2nd period and northerly wind in the 3rd period were the prevailing wind at Ny-Ålesund (not shown). The variation suggests a low pressure moved from west to east around Spitsbergen although air pressure did hardly change for whole day of 31 December.

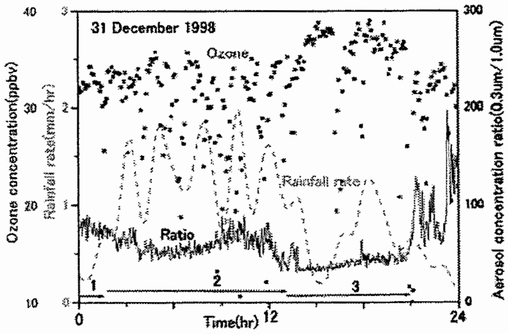

Fig. 3: Ozone concentration, aerosol concentration ratio and rainfall rate on 31 December at Ny-Ålesund.

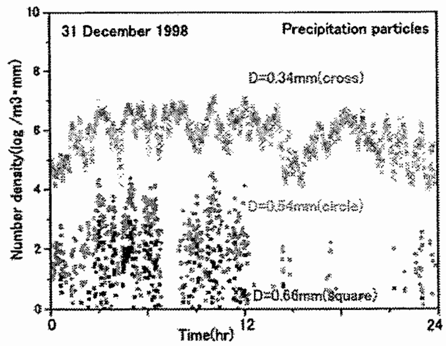

Fig. 4: Number density of precipitation particle of each size (0.34, 0.54 and 0.66 mm in diameter).

Figure 3 shows rainfall rate, ozone concentration and aerosol concentration ratio of a size larger than 0.3 μm to a size larger than 1.0 μm. We classified ozone variation data into 3 periods for the reason that the data scattered and were often very small in the 2nd period (shown as 2 in Fig. 3) comparing to the 1st and the 3rd periods. The ozone concentration was higher in the 3rd period than in the others. The ozone data did not scatter in the 1st period and the no scatter variation had continued from 12 UTC of the previous day.

The rainfall rate was stronger in the 2nd period than in the others, was weak in the 1st period and was relatively strong around 18 UTC only in the 3rd period.

The aerosol concentration ratio was relatively small and its variation was seemed to be almost flat in the 3rd period. In addition the aerosol concentration ratio was minimum around a boundary between the 2nd and 3rd periods.

Figure 4 shows daily variations of precipitation particles depended on sizes in diameter. The concentration of small size particle (0.34 mm) did not change largely, but the concentration of large size particles (0.54 and 0.66 mm) was low in the 3rd period and still low in the period of relatively strong rainfall rate, which means around 18 UTC.

4. Discussions

Two cases are reported in previous session. We infer from the variation of the ozone concentration that characteristics of the airmass over Ny-Ålesund changed around 16:50 UTC of the case on 9 March and characteristics of the airmass changed around 2 UTC and 13 UTC of the case on 31 December.

First of all we discuss about the case on 9 March. The characteristics in the first period, before 1650 UTC, are summarized that the ozone concentration was normal, the aerosol concentration ratio was relatively high and relatively small snow particles were counted. In other word, relatively large aerosol and snow particles were found in the latter period. It is imagined that the latter precipitating cloud was formed with relatively large aerosols such as sea-salt particles and grew up to relatively large snow particles and precipitation rate was relatively strong. The former one would be formed with relatively small aerosols and did not grow up to large snow particles. The latter airmass, in addition, would be affected by bromide ion released from sea surface because of low ozone concentration.

Next, we discuss about the case on 31 December. The characteristics are summarized below: The ozone concentration changed violently and the rainfall rate was relatively strong in the 2nd period, The ozone concentration hardly scattered in the 1st period and scattered slightly in the 3rd period. The aerosol concentration ratio was the lowest and relatively large snow particle was hardly counted in the 3rd period, but relatively small snow particles were counted with almost same value in the 2nd period. The precipitation in the 2nd period was fairly strong, about 1.5 mm/hr. The precipitation rate changed at the boundaries between 1st and 2nd periods, and 2nd and 3rd periods. The precipitation of the case on 9 March was comparably weak, about 0.5 mm/hr.

It is a possibility that the strong precipitation in the 2nd period affected ozone and the ozone concentration changed violently. A period of the strong rainfall rate was found in the 3rd period, but the ozone concentration did not change violently in the period. Large snow particles such as 0.54 and 0.66 mm in diameters, moreover, were not found in the period in spite of fairly strong precipitation rate. Namely it is inferred that the severe variations of ozone concentration were promoted by relatively large snow particles.

5. Concluding remarks

Elements and factors which change ozone concentration are few in the polar region, especially in the dark season because of remote area from anthropogenic emissions and no sunrise. Studies on formation process of cloud and precipitation and a role of snow particles in scavenging process in each airmass were described in this paper on the basis of the detailed data of ozone concentration, which is a good marker for classifying each airmass in polar region.

6. References

Asuma Y., Fukuda, Y., Kikuchi, K., Shiobara, M., Wada, M. and Moore G.W.K., 2002: Airborne measurements of a polar low over the Norwegian Sea(in Japanese). Antarctic Record, 46 1A, 234-260.

Curry, J.A., 2001: Introduction to special section: FIRE Arctic Clouds Experiment. J. Geophy. Res., D14, 106, 14985-14987.

Hobbs P.V., 1993: Aerosol-cloud interactions. In Aerosol-cloud-climate interactions. Edited by P.V. Hobbs. Academic Press, 33-73.

IPCC, 1990: Climate change. Edited by Houghton J.T., Jenkins G.J. and Ephraums J.J., Cambridge Univ. Press, 364p.

Raes, F., Bates, T., McGovern, F. and Liedekerke, M.V., 2000: The 2nd aerosol

characterization experiment(ACE-2): general overview and main results. Tellus, 52B, 111-125.
Sheppard, B. E., 1990: Measurement of raindrop size distributions using small doppler radar. J. Atmospheric and Oceanic Tech., 7, 255-268.
Wada, M. and K. Konishi, 1992: A study of precipitation in the coastal area of Antarctica as observed at Syowa Station using a vertical pointing radar. Antarctic Record 36, 341-349.
Wada, M., Konishi, H. and Yamanouchi T., 1996: Variation of monthly precipitation and frequency of radar echo existence at some altitudes in Ny-Ålesund, Svalbard, Arctic. Mem. Natl Inst. Polar Res. Spec Issue, 51, 239-246.
Yamanouchi, T., Aoki, S., Morimoto, S. and Wada, M., 1996: Report on atmospheric science observations at Ny-Ålesund, Svalbard. Proc. Int. Symp. Env. Res. in the Arctic, 153-163.

PRECIPITATION TYPE CLASSIFICATION IN THE BALTIC AREA IN RADAR OBSERVATIONS AND IN REMO

Andi Walther[1] , Jürgen Fischer[1] and Ralf Bennartz[1,2]

[1]Institut für Weltraumwissenschaften, Freie Universität Berlin , Berlin, Germany, D-12165 Berlin
[2] Atmospheric & Oceanic Sciences, University of Wisconsin, Madison, WI , USA

1. INTRODUCTION

The overall objective of the BALTIMOS project is the development of a coupled model system for the Baltic Sea and its drainage basin in order to understand and model exchange processes between atmosphere, sea, land surface, and lakes including hydrology. BALTIMOS is a contribution to the BMBF research program DEKLIM.

Observations and modeling of spatial and temporal variability of precipitation are an important factor for understanding the water cycle. *Sumner (1988)* classifies precipitation as an expression of origin and considered three main types: convectional, cyclonic and orographic. One focal point of this presentation is the application of a method to divide precipitation in frontal and non-frontal fraction.

Models simulate the diurnal cycle of precipitation often wrongly. Operational models tend to produce the maximum of precipitation over land at about local noon, corresponding to the time of maximum heating (*Trenberth et al.* 2003). Observations have shown that this timing is a few hours before. One further goal of this study is to compare the diurnal cycle of REMO simulations with observations from radar data.

2. CLIMATE MODEL REMO

The regional climate model REMO that will be used in this study was developed by the Max Planck Institut for Meteorology (MPI) in Hamburg (e.g. *Jacob and Claussen,M..* (1995)). It is a three-dimensional, hydrostatic atmosphere model, that is based on the DWD physical parameterization model. The horizontal resolution is 1/6° or in a grid size equal of about 18 x 18 km². Our investigations were processed in the "climate" modus.

Corresponding author's address: Andi Walther, Institut für Weltraumwissenschaften, Freie Universität Berlin, D-12165 Berlin, Germany; E-Mail: andi.walther@wew.fu-berlin.de

3. RADAR DATA SOURCE

The primary data used in our study are the BALTRAD composite radar reflectivity data set. The properties of this product include 2 km spatial grid with 15 minutes temporal resolution and 8-bit dBZ converter. The BALTRAD data are gauge-adjusted and can be transformed into rain intensity information with two fixed seasonal-dependent Z-R relations. This procedure was undertaken by the Swedish Weather service (SMHI) and introduced by *Michelson et al.* (1999).

In order to compare with REMO output it was necessary to transform the data from a 2 km spatial grid into REMO grid (1/6 ° - about 18 km spatial resolution). The rain rates of all BRDC-pixel, rain or non-rain pixel inside a REMO pixel are averaged.

4. FRONTAL/NON-FRONTAL DISTINCTION

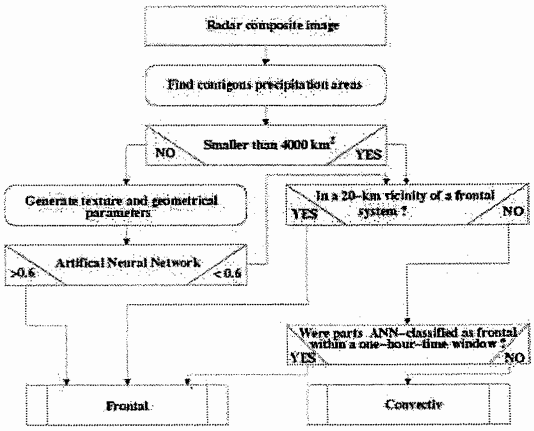

Figure 1: Data flow for Frontal/Non-frontal (convective) partitioning.

The main attribute is to classify contiguous precipitation systems in contrast to classification of each individual pixel in other investigations (e.g. *Steiner et al.* (1995)). That means, that

each pixel of a contiguous rain area gets a common classification, frontal or non-frontal.
Figure 1 illustrates the processing scheme. Threshold for rain pixel was defined as 0.1 mm/hr. First, contiguous precipitation areas are identified in the radar data. Any rain areas smaller than 4,000 km² are initially considered, by virtue of their space scale, to be non-frontal. Larger echoes are subject of a classification algorithm with help of an artificial neural network (ANN) algorithm. Input parameters of the ANN are 9 texture and shape information. Texture information is a result of statistical analysis of spatial rain rate differences and gives a hint of homogeneity and the inner structure of the rain field. Shape parameters are the size of the major axis, the eccentricity and the size of the area. 400 scenes from the available dataset of BALTRAD network were randomly selected to classify manually with help by weather reanalysis maps. Both, the calculated parameters of a rain area, and the corresponding classification represent one vector of the training dataset of the ANN.
The resulting algorithm are applied to BALTRAD as well as REMO products. Figure 2 shows the fraction of frontal rain events for BALTRAD data in 2000.

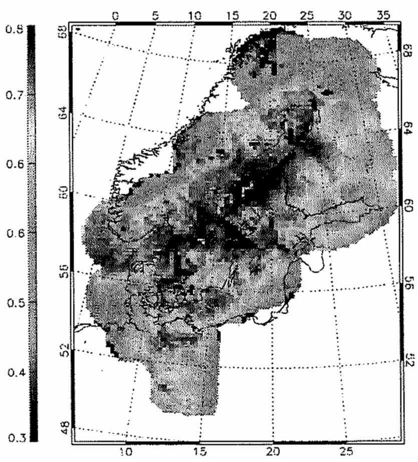

Figure 2 Spatial distribution of the fraction of frontal rain events in 2000 for radar data.

Figure 3 shows the dependency of frontal fraction on the rain intensity. That means, for example, that about 58% of all pixel with a rain intensity of 1mm/hr are frontal classified. Non-frontal events have over-averaged fraction at low (up to 0.2 mm/hr) and high (from about 8 mm/hr) intensities.

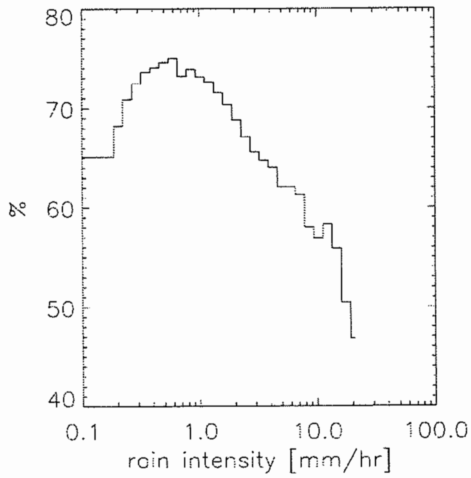

Figure 3 Frontal fraction in dependency to rain intensity.

4. DIURNAL CYCLE

Diurnal variations were analyzed by Fourier decomposition. For expediency, both, the radar and REMO products were grouped by the hour. Instead of using the rain rate and averaging, the final field is the fraction of time that a rain intensity exceeds a threshold of 0.1 mm/hr at each grid point. The amplitude of the first harmonic refers to the significance of the diurnal variability, the phase shift to the time of the peak in the diurnal cycle.

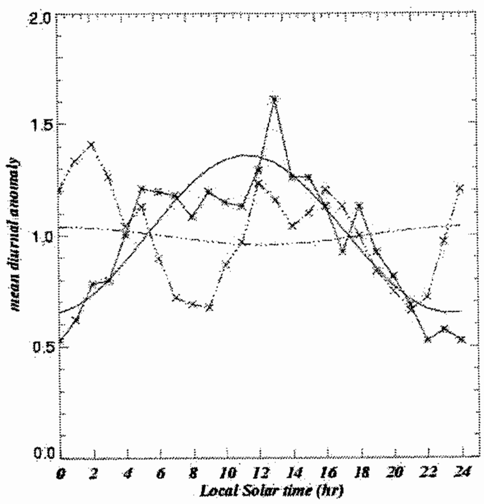

Figure 4: Example for diurnal cycle. Solid lines represent a pixel over land, dashed lines over sea. Graphs with asterixes or crosses show results of radar measurements, without the first harmonics.

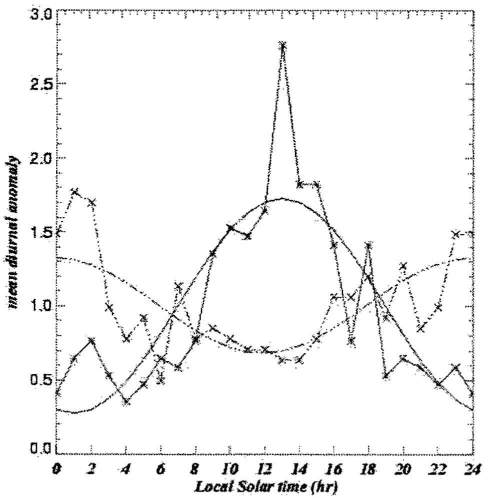

Figure 5: Same as figure 4, but only for non-frontal events.

We applied this method to all rain events and to only non-frontal rain events. Figure 4 and 5 show examples of normalized diurnal cycles of all rain events (Fig.4) and non-frontal (Fig.5) for one pixel above sea and one above land. It can be seen that while the diurnal variability with peaks at afternoon hours dominates over land, the rain frequency is less strong over sea and has a noctuanal maximum.

Figure 6 shows the normalized amplitude of the first harmonic of non-frontal events. There is a high dependency on the surface type. The diurnal variability over land is much higher than over sea.

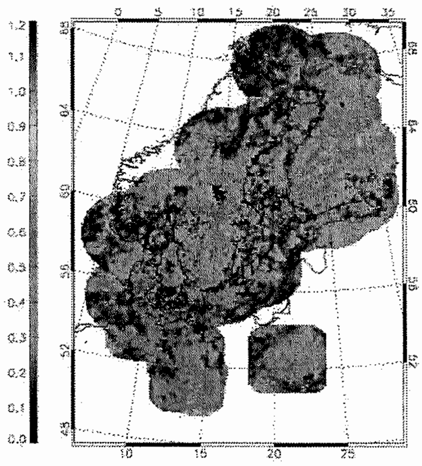

Figure 6: Spatial distribution of normalized amplitude of the first harmonic of non-frontal events in summer.

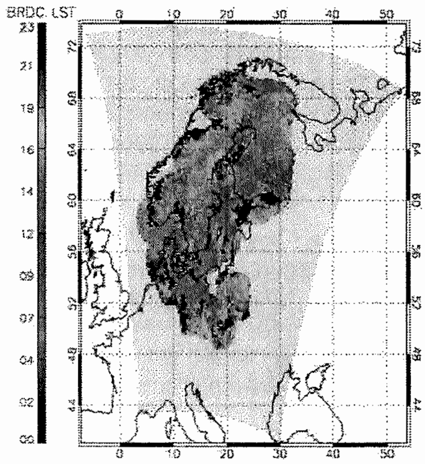

Figure 7 Local solar time for peak of first harmonic derived from hourly time series of percentage time with rain rate >= 0.2 mm/hr for June, July and August of 2000-2002 in radar data. Note that blue and red color stand both for nocturnal peaks.

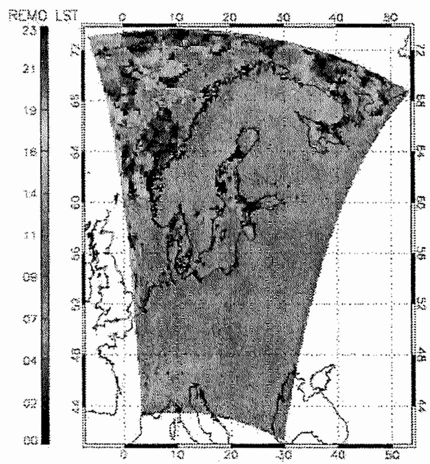

Figure 8 Same as Figure 7 for REMO output

Figure 7 and 8 show the transformation of the phase shift into hour of the day with highest precipitation activity in radar data (Fig.7) and REMO (Fig.8).

While the average time point of the peak in REMO over land is more than 1 hour ahead of the radar observations, the general pattern are in a good agreement.

REFERENCES

Jacob, D., and M. Claussen, REMO-A Model for Climate Research and Weather Forecast, *First Study Conference on BALTEX (ed. A.Omstedt)*. International BALTEX Publication No.3, International Baltex Secretariat, GKSS-Research Center. P.O. Box 1160 D-21494

Michelson, D., Andersson, T., Koistinen, J., Collier, C., Riedl, J., Szturc, J., Gjertsen, U., Nielsen, A., and Overgaard, S., BALTEX Radar Center Products and their Methodologies. RMK 90, SMHI, SE-60176 Norrköping, Sweden. 76pp., 2000

Steiner, M., Houze JR, R. A., and Yuter, S., Climatological characterization of three-dimensional storm structure from operational radar and rain gauge data., *Journal of Applie Meteorology*, 34, pp. 1978-2007, 1995

Sumner, G., Precipitation Process and Analysis, *John Wiley & Sons Chichester*, 1988

Trenberth, K. E., Dai, A., Rasmussen, R. M., and Parsons, D. B., The changing character of precipitation, *Bulletin of American Meteorological Society*, 84, pp. 1205-1217, 2003

OBSERVATION OF A MESOSCALE CONVECTIVE SYSTEM IN A BAIU-FRONTAL DEPRESSION GENERATED NEAR THE EAST COAST OF THE EURASIAN CONTINENT

Hiroyuki Yamada[1], Biao Geng[1], K. Krishna Reddy[1], and Hiroshi Uyeda[2]

[1]Frontier Observational Research System for Global Change (FORSGC), Yokohama, 236-0001, Japan
[2]FORSGC / Hydrospheric Atmospheric Research Center, Nagoya University, Nagoya, 464-8601, Japan

1. INTRODUCTION

The formation of a Baiu front, and the development of mesoscale convective systems (MCSs) along the front, are the peculiar phenomena to the East-Asian summer monsoon (e.g., Ninomiya and Akiyama 1992). Several previous studies point out that a MCS, causing a disastrous heavy rainfall in the western Japan, often forms and develops near the east coast of the Eurasian Continent (Takeda and Iwasaki 1987; Iwasaki and Takeda 1993; Hasegawa and Ninomiya 1984). It is an interesting point that there is no significant mountain along the coast along 30-35 °N. This suggests the small orographic effect on the development of a MCS.

To clarify the mechanism of the development in the coastal region, field experiments using three Doppler radars were performed in the downstream region of the Yangtze River, in China. This paper describes the structure of a MCS that formed near the coast, and reveals that low-level convergence due to a local wind system assisted the MCS in its evolution.

2. OBSERVATIONS

The field experiment consisted of two observational networks with different horizontal scale. Figure 1 shows the maps of the mesoscale and intensive observational network. The aim of the mesoscale network is to reveal the overall structure of a meso-α-scale convective system of a MCS, and the aim of the intensive network is to reveal the detailed meso-β-scale three-dimensional structure of convective areas within the MCS. The observations were performed during Baiu seasons (June and July) of 2001 and 2002.

Corresponding author's address: Hiroyuki Yamada, Frontier Observational Research System for Global Change, Yokohama, 236-0001, Japan; E-Mail: yamada@jamstec.go.jp.

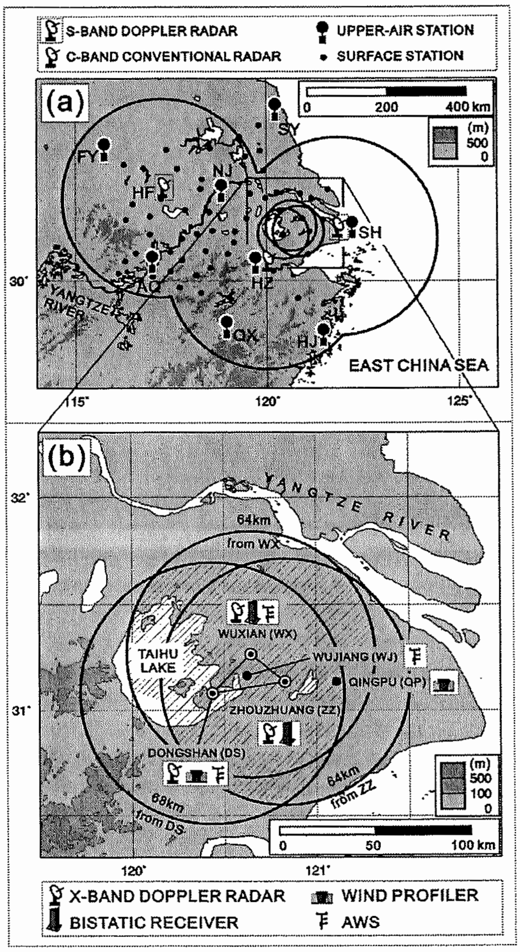

Fig. 1. (a) The map in the mesoscale observational network. Radar range circles are drawn by bold lines. (b) The map in the intensive observational network. The dual-Doppler analysis area is hatched.

3. OVERVIEW OF THE CASE

In this study, an MCS observed on 18 June 2001 are examined in detail, because this case related to the torrential rain in the western Japan on the next day. The sequence of surface

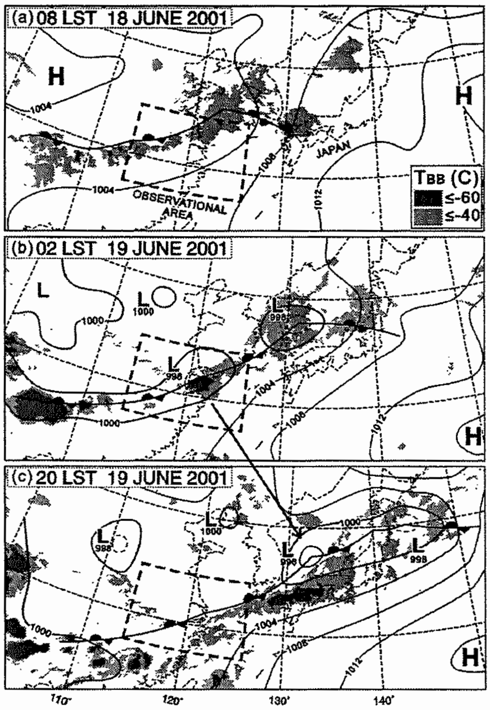

Fig. 2. Series of surface weather map at 18 hour intervals from 0800 LST 18 June to 2000 LST 19 June 2001 (LST = UTC + 8 hours). The T_{BB} distribution is superimposed on each panel. A rectangle drawn by bold broken line shows the area of the mesoscale observational network.

weather maps (Fig. 2) shows that a depression was formed within the observational area (Fig. 2b). This depression moved north-eastward along the stationary front (i.e., Baiu front), and reached over the Japan Sea (Fig. 2c) when the torrential rain occurred. The daily rainfall amount in the western Japan reached 350 mm due to this rain event. The distribution of cloud-top black-body temperature (T_{BB}) at the developing stage (Fig. 2b) shows that this depression was accompanied by a MCS with an oval-shaped high-cloud area (T_{BB} < -60 °C).

4. STRUCTURE OF THE MCS

The distribution of radar reflectivity (Fig. 3) shows that this MCS was composed of several meso-β-scale convective groups. They were band-shaped echoes (labeled '*Cb*') near the depression center, cellular echoes ('*Fa*', '*Fb*', and '*Ca*') ahead of the center, and band-shaped echoes ('*Ra*', and '*Rb*') in the rear portion. These

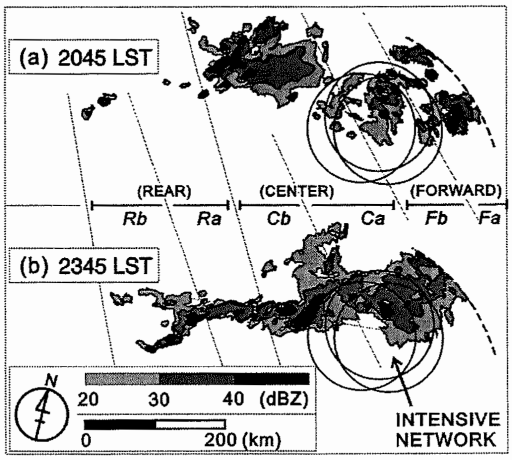

Fig. 3. Horizontal distributions of radar reflectivity in the MCS at 3 km ASL on (a) 2045 LST, and (b) 2345 LST 18 June.

echoes extended more than 600 km from the west to the east.

An important point to emphasize is the fact that the cellular echoes in the forward portion (*Fa*, *Fb*, and *Ca*) were formed one after another within the intensive network. This fact can be easily recognized from the trajectory of these echoes on the longitude-time cross section (Fig. 4). These echoes began to appear near 120.5°E.

5. THE ROLE OF A LOCAL WIND SYSTEM

To reveal the mechanism of these echoes' formation, flow patterns and thermodynamic features in and around the cellular convective echoes were examined. Surface wind distribution in Fig. 4 shows that easterly wind occupied the intensive network area when the cellular echoes developed (i.e., 1800-2300 LST 18 June). This easterly is recognized as a local wind system near the coast, because this wind had different wind direction and thermodynamic features from two synoptic-scale wind systems near the front: the warm southwesterly in the south side, and also from the cold northwesterly in the northern side.

The relationship between the local easterly and the warmer southwesterly was examined by dual-Doppler radar analysis. Figure 5 shows the flow pattern in the vertical section penetrating the convective echoes in '*Ca*' part (from the southwest to the northeast). It is seen that the easterly intruded below the southwesterly. Convective updrafts and strong echoes located where air parcel in the southwesterly was lifted

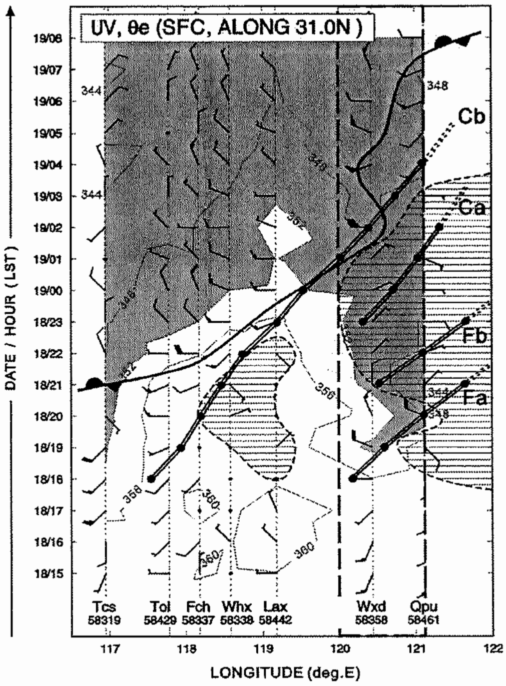

Fig. 4. Longitude-time cross section of equivalent potential temperature (contour) and wind barb at surface between 1500 LST 18 June and 0800 LST 19 June. A half-barb and a full-barb represent 1.0 and 2.0 ms^{-1}, respectively. The easterly-wind areas are hatched. The shearline corresponding to the Baiu front, and the trajectory of convective echo parts (Fa, Fb, Ca, and Cb) are superimposed. A rectangle drawn by a broken line shows the intensive observational network.

up to 1.5 km above sea level (ASL). This height corresponded to the level of free convection (LFC), which was estimated from the upper-air observations (not shown). It is, therefore, found that the easterly wind played the role to uplift the warm-moist air and to form the convective updraft in the forward portion of the Baiu-frontal depression.

6. DISCUSSION

6. 1 Structure of the MCS

The schematic illustration of the overall three-dimensional structure of the MCS is shown in Fig. 6. It is the common features among all convective echoes within the MCS to have formed where the warm-moist southwesterly wind was lifted up to the LFC. There was,

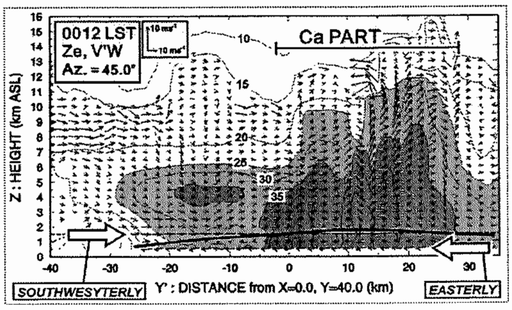

Fig. 5. Reflectivity and system-relative flow pattern in the vertical section penetrating the strong echo in the 'Ca' part from the southwest to the northeast. The shearline between the easterly and the southwesterly is shown by a bold line. The broken line at 1.5 km ASL shows the LFC, which was estimated from the upper-air observations.

however a difference in the mechanism of this uplift.

In the rear part (*Rb*), this lift resulted from the intrusion of synoptic-scale northwesterly wind associated with a midlatitude trough (described in Yamada et al. 2003). This suggests that the depression and convective echoes in the rear part were initially formed under the influence of a large-scale upward motion ahead of the midlatitude trough.

In contrast, the uplift in the forward part (*Ca*) was due to the intrusion of the local easterly wind, as described in this paper. This fact suggests that the local circulation near the coast played a role in assisting the MCS in its evolution.

6. 2 Mechanism of the Local Wind

It is suggested that the local easterly wind was formed both by heat contrast between land and sea, and by pressure gradient. There was large difference in temperature between ground (30.5 °C) and surface over the East China Sea (22 °C). The pressure gradient at that time was 0.8 hPa, and was due to the formation of the Baiu-frontal depression in the observational area. The observed wind speed of the easterly wind (1-2 ms^{-1}) is roughly consistent with an estimated wind (about 4 ms^{-1}) from the pressure difference between land and sea. Therefore, it is reasonable to explain that the cold airmass of the local wind system was formed due to the cold sea surface, and that this air was moved to the land by the pressure gradient due to the formation of the depression.

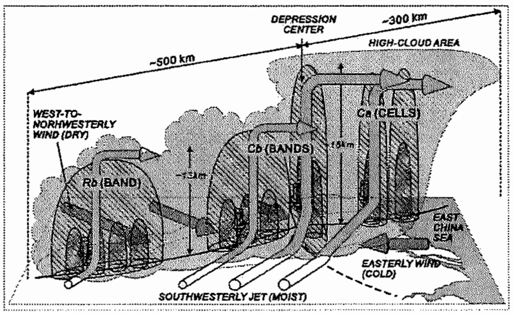

Fig. 6. Schematic illustration of the three-dimensional structure of the MCS examined in this study.

3. SUMMARY

The structure of a MCS, which developed near the east coast of the Eurasian continent, was examined using observational data in the downstream region of the Yangtze River. This study revealed the role of a local wind system in the coastal region for the development of the MCS, and for the evolution of the Baiu-frontal depression that was the cause of torrential rainfall over Japan. It is suggested that the convergence due to local wind system is one of the causes for the occasional development of a MCS near the east coast of the continent during Baiu seasons.

ACKNOWLEDGEMENTS

The data used in this study were obtained from the field experiments in the downstream region of the Yangtze River, which were carried out under the cooperative project between FORSGC and 'China Heavy Rainfall Experiment and Study (CHeRES)'. The satellite images were provided from Dr. T. Kikuchi, Kochi University, Japan. The information on the torrential rainfall in the western Japan was provided from Dr. M. Ushiyama, Graduate School of Engineering, Tohoku University, Japan.

REFERENCES

Hasegawa, R. and Ninomiya, K., 1992: Features of Nagasaki Heavy Rainstorm of 23 July 1982 as revealed GMS observation data. *Tenki*, **31**, 565-572, (in Japanese).

Iwasaki, H., and T. Takeda, 1993, Structure and behavior of mesoscale cloud clusters traveling over the Baiu-frontal zone, *J. Meteor. Soc. Japan*, **71**, 733-747.

Ninomiya, K., and T. Akiyama, 1992: Multi-scale features of Baiu, the summer monsoon over Japan and the East Asia. *J. Meteor. Soc. Japan*, **70**, 467-495.

Takeda, T., and H. Iwasaki, 1987, Some characteristics of meso-scale cloud clusters observed in East Asia between March and October 1980, *J. Meteor. Soc. Japan*, **65**, 507-513.

Yamada, H., B. Geng, K. K. Reddy, H. Uyeda, and Y. Fujiyoshi, 2003: Three-dimensional structure of a mesoscale convective system in a Baiu-frontal depression generated in the downstream region of the Yangtze River. *J. Meteor. Soc. Japan*, **81**, 1243-1271.

The analysis of precipitation characteristics in Hebei Province

Wu Zhihui[1], Duan Ying[1], Wang Xiaobin[2], Shi Lixin[1] and Zhang Xinmin[1]

[1]Weather Modificationh Office of He'Bei Province, Shijiazhuang, 050021,China
[2]Institute of Weather Modification, CAMS, BeiJing, 100081, China

1.Introduction

Weather Modification Office united Chinese Academy of Meteorological Sciences and Peking University to develop the rainfall enhancement field experiment in spring from 1990 to 1994. Mostly importance precipitation systems were observed by the ground rainfall observation, the high frequency sounding balloon, the aircraft, the ground microwave radiometer and so on, and had gotten plenty of production, as Qian Chunsheng(1994), Shi Lixin(1994), Duan Ying(1994). The precipitation enhancement field experiment is held in the four seasons every year from 2000 to meet the combating droughts, to develop the water reservation in reservoirs and to improve the Hebei Province's entironment, etc. It was analyzed that the precipitation regime in Hebei province based on the 101 weather observation data from 1981 to 2000. The feature of the 24 category precipitation systems was analyzed accorded to the different seasons in Hebei Province. And combined the summarize precipitation model made by the high frequency sounding balloon data, the observation by the ground weather radar, the rainfall density observed data, the ground microwave radiometer observed result and the aircraft observed data from 1981 to 2000, the feature of the 2 kind of the significant category precipitation system in Hebei province was analyzed in this paper.

Corresponding author's address: Wu Zhihui, Weather Modification Office of Hebei Province, Shijiazhuang, Hebei, 050021, P.R.China; E-Mail: wuzh98@yahoo.com.

2. The precipitation regime of 40 annual variety

The precipitation regime in Hebei province is shown in Table 1. It was based on the 101 weather observation data from 1981 to 2000. The average precipitation in Hebei Province is 521mm from 1981 to 2000 and is 557mm from 1961 to 1980 based on the ground precipitation observation. The total annual mean precipitation of the former 20 years is higher 36 mm than the later 20 years'. And the seasonal precipitation in the later 20 years' rainfall is less than the former 20 years' in summer, autumn and winter, but it is increase in spring.

Table 1: The average seasonal precipitation in HeBei Province in the past 40 years (mm)

	Spring	Summer	Autumn	Winter
1961-1980	58.9	391.0	91.1	16.3
1981-2000	71.0	355.4	85.1	9.5
increase	12.1	-35.6	-6.0	-6.8

3. The feature of the 24 category precipitation systems

The feature of the 24 category precipitation systems was analyzed accorded to the different seasons in HeBei Province from 1981 to 2000. Table 2 is the frequency of the 24 category precipitation systems in a year. The percentage of the seasonal mean precipitation in the annual precipitation is 13.6%, 68.2%, 16.3% and 1.8% respectively spring, summer, autumn and winter. The seasonal mean rainfall day of a year is 25.4%, 43.3%, 21.5% and 9.8% to the different season.

Table 2: The appear frequency of the 24 category precipitation systems in the different seasons

Weather system	precipitation				rainfall day			
	spring	summer	autumn	winter	spring	summer	autumn	winter
westerly trough	27.1	127.5	30.2	2.9	10.6	21.1	11.9	4.8
north-westerly trough	7.0	11.3	4.7	1.3	4.9	3.4	3.4	2.0
southerly trough	0.8	5.1	3.4	1.2	0.5	1.0	1.3	0.4
easterly Mongolia vortex	2.5	12.8	5.4	0.0	1.5	3.9	1.2	0.1
north-easterly vortex	0.7	8.8	0.3	0.0	0.4	2.4	0.3	0.0
northerly vortex	5.0	51.6	8.0	0.5	1.9	8.1	3.0	0.5
westerly vortex	1.3	13.7	0.7	0.2	0.5	1.5	0.3	0.1
south-westerly vortex	0.0	1.7	0.0	0.0	0.1	0.3	0.0	0.0
Yellow River cyclone	0.1	0.0	1.3	0.0	0.1	0.0	0.2	0.0
westerly cyclone	0.1	1.0	0.0	0.0	0.1	0.2	0.0	0.0
Mongolia cyclone	1.5	0.2	0.0	0.0	0.5	0.2	0.0	0.0
Jiang'Huai cyclone	0.8	2.0	0.0	0.4	0.4	0.4	0.0	0.1
typhoon inverted trough	0.0	8.9	0.0	0.0	0.0	0.7	0.0	0.0
inverted trough	1.3	0.0	1.1	0.1	0.3	0.0	0.3	0.1
cold front	14.7	31.7	14.7	1.6	7.8	7.7	6.0	2.7
returning air-mass	1.8	0.9	0.5	0.5	0.9	0.3	0.5	1.0
transversal trough	0.7	4.9	2.6	0.3	1.3	1.2	0.9	0.6
shear line	3.9	26.8	5.9	0.2	7.0	7.8	2.0	2.0
the back of the horse latitude high	0.0	32.4	1.4	0.0	0.0	3.8	0.3	0.0
weaken cold air mass	1.6	3.6	2.6	0.1	0.9	1.4	1.3	0.5
north vortex -south trough	0.1	3.9	0.1	0.0	0.1	1.2	0.2	0.0
typhoon	0.0	5.9	0.0	0.0	0.0	0.7	0.0	0.0
high front area	0.0	0.2	1.5	0.0	0.1	0.2	0.6	0.3
others	0.0	0.6	0.9	0.2	0.1	0.4	0.5	0.2
total	71.0	355.4	85.1	9.5	39.5	67.3	33.4	15.3

Summer is the biggest amount of precipitation season in the annual rainfall distribution in He'Bei province. The amount of precipitation in summer is decrease from 1981 to 2000, and it has a biggish change if some precipitation systems with plenty of water vapor move on He'Bei province. Westerly trough is the first precipitation system on the rainfall day and the amount of precipitation of a year except summer in He'Bei province, and the cold front precipitation system is the second. North-westerly trough is one of the signify precipitation systems too. Northerly vortex is the most importance precipitation in summer and autumn. And the back of the horse latitude high (the subtropical high pressure zone) and shear line are the importance rainfall systems in He'Bei province.

Some of the precipitation systems (as typhoon inverted trough, the back of the horse latitude high, typhoon, Yellow River cyclone and westerly cyclone) are infrequency, but they have the notability offer on the annual precipitation. The amount of precipitation from these weather systems above usually is notable in summer and autumn. For example, the daily mean precipitation of typhoon inverted trough is 2.5 billion cubic meter rainfall. These weather systems should pay more attention to analyze the condition of rainfall enhancement to lighten water-stressed in North China.

Most of the precipitation system in the 24 category weather systems occurred in su trough from 1981 to 2000. It was 18 category precipitation systems occurred in spring and autumn. The number of the precipitation systems in winter is the least. It only 13 category precipitation systems occurred in winter in Hebei Province in the past 20 years.

4. The summarize precipitation model of westerly trough weather system

Westerly trough precipitation system in Hebei province is the most important precipitation as the result above. It is the feasible weather system for the aircraft enhancement due to its stability. Fig. 1 is the summarize precipitation model of westerly trough weather system based on the aircraft observation, the ground weather radar observed, the high frequency sounding balloon data, and the ground microwave radiometer. It is the spatial and temporal variability of the cloud system in Hebei province and its hydrometeor image. Abscissa is the time (BST). Ordinate is the height (km) in Fig.1（A） and rainfall intensity (mm/hour) Fig.1（B） respectively. Fig.1（B）is the time-varying precipitation intensity. J is the jet current and the number is the wind velocity (m/s) in Fig.1 (A). The short line athwart represents ice crystal region, and the dot is the cloud droplet region in the hydrometeor image of Fig.1 (A). The obvious distinction exists in the hydrometeor image that in the different period of the westerly trough development. The amount of precipitation is decided by the collocation of the cloud system. The stronger rain comes from the high cloud to seed the lower feed cloud with the plenty vapor. It is only small amount of rainfall while the seed cloud without the feed cloud collocation in the former period. The amount of precipitation is high while the high cloud with the low feed cloud to afford the sufficient growth condition in the middle period. The rain decreases while the seed cloud drop to the feed by a long dry layer in the terminal stages.

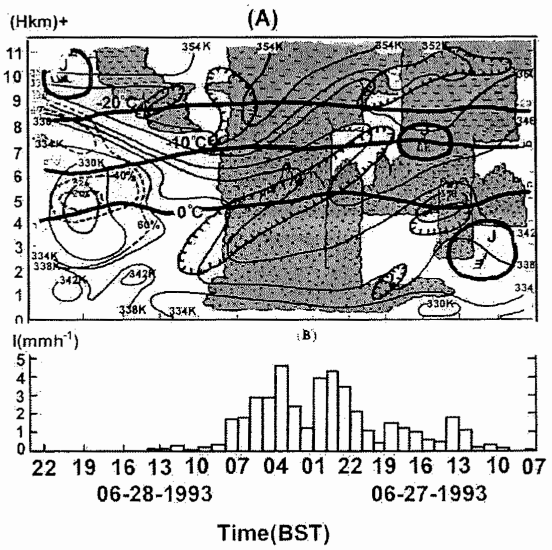

Fig.1The spatial and temporal variability of westerly trough weather system and the cloud geometry

5. The spatial and temporal variability of the phenomena and the hydrometeor geometry for cold front weather system

Cold front precipitation system is the second weather system in Hebei province. Fig. 2 is the spatial and temporal variability of the phenomena and the hydrometeor geometry for cold front weather system based on the various observation data. Abscissa is the time (BST) as above. Ordinate is the height (km) in Fig.2 (A) and rainfall intensity (mm/hour) Fig.2 (B) respectively. Fig.2 (B) is the time-varying precipitation intensity too. J is the jet current and the number is the wind velocity (m/s) in Fig.2 (A). The short line athwart represents ice crystal region, the dot is the cloud droplet, and the vertically line is the rainfall respectively in the hydrometeor image of Fig.2 (A) It is the spatial and temporal across section of the cold front cloud system in Hebei province and its hydrometeor image. The obvious distinction exists in the hydrometeor image that in the different period of cold front development.

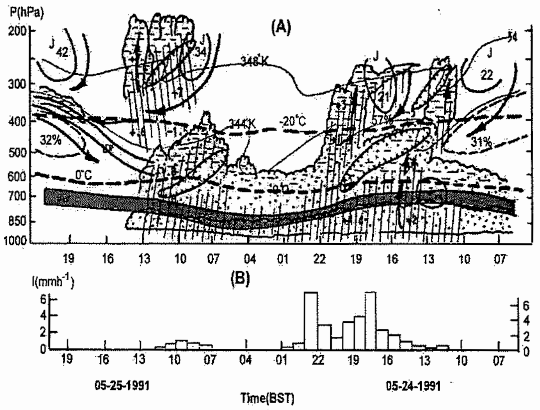

Fig.2 The spatial and temporal variability of the phenomena and the hydrometeor geometry for cold front weather system

6.Summary

1) The annual mean precipitation in He'Bei Province is decrease from 1981 to 2000 than that from 1961 to 1980, but the seasonal precipitation is increase in spring .

2) Summer is the biggest amount of precipitation season in the annual rainfall distribution in Hebei province. Westerly trough is the first precipitation system on the rainfall day and the amount of precipitation of a year except summer in Hebei province, and the cold front precipitation system is the second.

3) Some of the precipitation systems (as typhoon inverted trough, the back of the horse latitude high, typhoon, Yellow River cyclone and westerly cyclone) are infrequency, but they have the notability offer on the annual precipitation. These weather systems should pay more attention to analyze the condition of rainfall enhancement to lighten water-stressed in North China.

4) The obvious distinction exists in the hydrometeor image that in the different period of westerly trough and clod front development. The stronger rain comes from the high cloud to seed the lower feed cloud with the plenty vapor.

Reference

Duan Ying, et al., 1994: Observational reseach on cloud seedable conditions of aircraft artificial precipitation, The study of the cloud and precipitation physics and the rainfall enhancement technique, Meteorological Press, 11-22.

Meteorologocal Bureau of Hebei Province, 1987:Handbook of weather forecast in Hebei Province, Meteorological Press, 10-12.

Qian Chunsheng, et al., 1994: The classification of weather systems in spring and their artificial precipitation conditions, The study of the cloud and precipitation physics and the rainfall enhancement technique, Meteorological Press, 11-22.

Shi Lixin, Duan Ying, Sun Yuwen, 1994: The macro-characterisrics of the stratiform clouds in artificial precipitation operation in Hebei Province, The study of the cloud and precipitation physics and the rainfall enhancement technique, Meteorological Press, 53-62.

MODELLING THE IMPACT OF URBAN AREAS ON PRECIPITATION INITIATION

M.G.D. Carraça[1,2] and C.G. Collier[2]

[1]Department of Physics, University of Évora, Évora, 7000, Portugal
[2]School of Environment and Life Sciences, University of Salford, Greater Manchester, M5 4WT, U.K.

1. INTRODUCTION

Among the causes ascribed to the modifications of precipitation induced by urbanisation (Shepherd *et al.*, 2002), most studies suggest that dynamic forcing-destabilisation associated with the heat island and surface roughness- is the most significant, more so than microphysical or moisture enhancement. Urban areas modify boundary layer processes mostly through the production of an urban heat island, and by increasing turbulence through locally enhanced roughness.

Recent results of numerical studies (see Thielen *et al.*, 2000, and Shepherd, 2002, for example) show the impact of the surface sensible heat flux and roughness of urban surfaces on convective rain.

Thielen and Gadian (1999) presented a numerical study of the influence of topography and urban heat island effects on the outbreak of convective storms under unstable meteorological conditions. Analysis of observational data of convective storms in Northern England confirm that the particular combination of effects such as sea breezes, elevated terrain and the presence of large cities has an influence on the initiation and development of convective storms. The results of the numerical study show that the presence of the Pennines, a north–south orientated ridge, could influence the initiation of convection due to its long sun-facing slopes, and to a lesser degree forced lifting along the slopes. The inclusion of urban heat island effects produces enhanced and prolonged convection, particularly downwind of the major urbanised areas, including Greater Manchester.

On the other hand, comparison of the two average annual rainfall maps covering NW England for 1941-1970 and 1961-1990 (Met. Office, UK), suggests an increase of precipitation over some particular south west suburbs of Greater Manchester. Considering the expansion of urbanisation during the past fifty years or so, with a significant increase on high rise buildings in the early 1970s, it is reasonable to consider whether or not those differences in rainfall may be due to the urban development, noting that it may be due to some other reason such as different rainfall regimes, or even global climate change.

Corresponding author's address: M.G.D. Carraça, School of Environment and Life Sciences, University of Salford, Greater Manchester, M5 4WT, U.K.; E-Mail: M.G.Carraca@pgr.salford.ac.uk.

An estimate, based on the analysis of Shaw (1962) of the origins of precipitation in Northern England, shows that a considerable proportion (34% - 50%) of the total precipitation over the region of Manchester is of convective origin.

In this paper are presented some steps of a study of the influence of an urban area on convective clouds and precipitation. Of particular interest is the degree to which spatial variations of surface heterogeneity impact these phenomena, and whether the processes involved can be represented appropriately within a single-column model of surface energy balance applied on a rectangular grid. Here, are presented preliminary results of a numerical scheme based upon several published systems and developed to derive fields of surface sensible heat flux, for a range of wind, temperature and roughness inputs, over an urban area.

The next step of our study is to implement the model for Greater Manchester in order to look for any patterns that may indicate areas of increased sensible heat flux, which might be related to downwind convective initiation. In order to do this the model estimates of sensible heat flux will be used to instigate ascent of a parcel of air, and, depending upon atmospheric stability, subsequent condensation and rainfall production downwind of areas of increased roughness within the urban area. This procedure is outlined.

2. MODELLING

The model is formulated initially for Greater Manchester, in a large study area of 24km x 24km, with a grid resolution of 1km x 1km, or finer, where the model parameters are specified as averages over each grid square and the bulk equations will be used.

The surface sensible heat flux, Q_H, over the urban area is calculated by a resistance-type formulation using the difference between the radiometric surface temperature, T_R, and air temperature, Ta.

$$Q_H = \rho\, c_p \frac{(T_R - T_a)}{r_h} \tag{1}$$

$$r_h = \frac{1}{k\,u_*}\left[\ln\left(\frac{z_s - z_d}{z_{0m}}\right) - \Psi_H\right] + \frac{1}{k\,u_*}\ln\left(\frac{z_{0m}}{z_{0hR,T}}\right) \tag{2}$$

$$L = \frac{-u_*^3 \rho c_p T_a}{k g Q_H} \quad (3)$$

$$u_* = k u \left[\ln\left(\frac{z_s - z_d}{z_{0m}} \right) - \Psi_M \right]^{-1} \quad (4)$$

Where:
Q_H ≡ sensible heat flux
r_h ≡ resistance to heat transfer from a surface at T_R to an atmospheric level at T_a
L ≡ Moni-Obukhov length
u_* ≡ friction velocity
u ≡ wind speed
T_a ≡ air temperature,
T_R ≡ radiometric surface temperature
z_d ≡ zero-plan displacement length
z_{0h} ≡ roughness length for heat
z_s ≡ level above the surface where the wind speed, u, and the air temperature, T_a, are measured
z_{0m} ≡ roughness length for momentum
$z_d + z_{0m}$ ≡ level at which the wind speed extrapolates to zero, u=0, via the logarithmic wind profile
Ψ_H ≡ stability correction function for heat
Ψ_M ≡ stability correction function for momentum
$g = 9{,}8\ m\ s^{-2}$.
ρ ≡ air density (=1,2 kg m^{-3})
c_p ≡ specific heat of the air, at constant pressure (=1004 J kg^{-1} K^{-1})
k ≡ von Karman's constant (= 0,4)

Input meteorological variables used in the model are T_R, T_a, and the wind velocity, u. T_a and u are typically measured several metres above the surface, in the inertial sub-layer where the Monin-Obukhov Similarity Theory is valid. Although the validity of Monin- Obukov similarity theory (MOST) in the atmospheric boundary layer has being questioned, the surface sub-layer is usually studied within the framework of MOST. This will form the basis of the model which will be used later to explore the impact of the heterogeneity of the urban canopy.

Input roughness parameters are the building height, z_H, and the frontal area index, λ_F. Roughness parameters zero-plan displacement length, zd, and roughness length for momentum, z_{0m}, are estimated as a function of building height, z_H, and frontal area index, λ_F, using Raupach's (1994) method, as reported by Grimmond and Oke (1999a).

Roughness length for heat, z_{0h}, is determined as a function of z_{0m}, using the formulation proposed by Brutsaert (1982) for bluff-rough surfaces.

Stability corrections for momentum, Ψ_M, and heat, Ψ_H, are the Paulson (1970) stability functions. The Hogstrom (1988)- modified Dyer (1974) equations are used to calculate Ψ_M, when L<0, and Ψ_H. The Ulden and Holtslag (1985) equation is used to calculate Ψ_M, when L>0.

Q_H, u_* and L (or the stability functions) are determined by an iteration of equations (1)- (4).

3. PRELIMINARY RESULTS

3.1 Sensitivity and convergence tests of the numerical model

The model has been evaluated regarding the main situation of interest: atmospheric convective conditions over Manchester region, which occur during the daily period, typically on springtime and summer. The examples studied were the following:
(A) 0.01≤ λ_F ≤0.47, and z_H=6m, u=1.5m/s, T_R=303K, T_a=293K;
(B) 0.5m≤ z_H ≤12m, and λ_F=0.2, u=1.5m/s, T_R=303K, T_a=293K;
(C) 274K ≤ T_R ≤320K, and λ_F= 0.2, z_H=6m, u=1.5 m/s, T_a= 293K;
(D) 280K ≤ T_a ≤ 303K, and λ_F= 0.2, z_H=6m, u=1.5 m/s, T_a= 303K;
(E) 0.5m/s ≤ u ≤12m/s, and λ_F=0.2, z_H=6m, T_R=303K, T_a=293K. In all cases, the measurement height has been considered z_S = 20m.

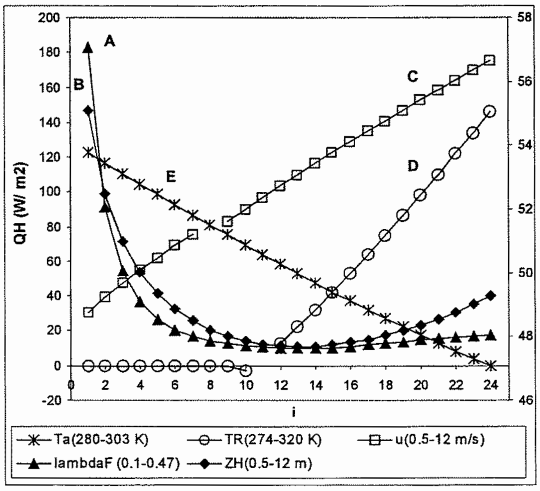

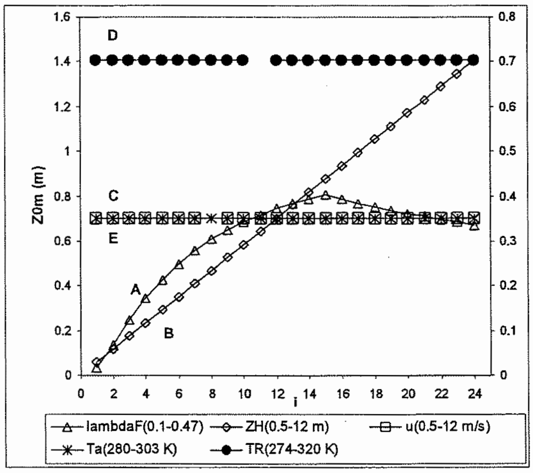

Figure 1 - Some model results, z_{0m}, and Q_H , as functions of the input values. Each curve relates to a different input variable, λ_F, z_H, u, T_R, or T_a, where all the other are constant. [Filled symbols: right y-axis.]

For the range of typical input values used, the model behaves reasonably for slightly stable to unstable conditions. However, as expected, the model fails for the stable conditions represented in points D1-D9, where z_S >>L, and does not converge for points C8 and D11, which are cases where there is a discontinuity of the stability functions. These discontinuities are a consequence of the established criteria for being near neutral stability: $|\zeta=(z_S-z_d)/L| < 0.1$, where $\Psi_M = \Psi_H = 0$.

A discontinuity is also observed between points A15 and A16, in this case, due to the different behaviour of the roughness parameter z_{0m} for values of $\lambda_F > 0.29$. The value λ_{Fmax} (=0.29) can be interpreted as the onset of "over-sheltering", the point at which adding further roughness elements merely shelters one another (Raupach, 1994). After this point the roughness z_{0m} is seen to decrease, yet the heat flux increases (z_{0h}, Q_H).

3.2 Experiments on Spatial Variations of Urban Roughness

In order to more clearly identify the comparative impact of surface roughness versus local heating effects, some experiments using a stylised representation of the urban area have been carried out (see Figure 2).

Initial model results (Figure 2) show the impact of roughness and vertical temperature gradient on the spatial distribution of the surface sensible heat flux, Q_H. The area of uniform low buildings (C) has a lower sensible heat flux than those areas (A and B) which have higher roughness. However, interestingly, the area of high rise buildings close together (A) produces almost the same sensible heat flux as the area (B) having lower buildings covering a larger area than the high rise buildings (A).

Future work will investigate this further, and use actual roughness distribution.

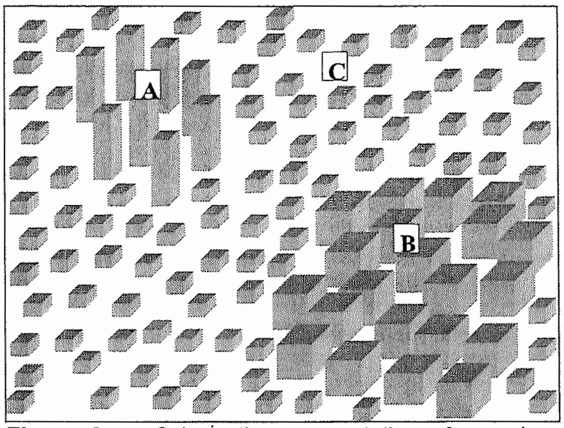

Figure 2.a - Schematic representation of an urban area (5km x 5km): distribution of roughness.

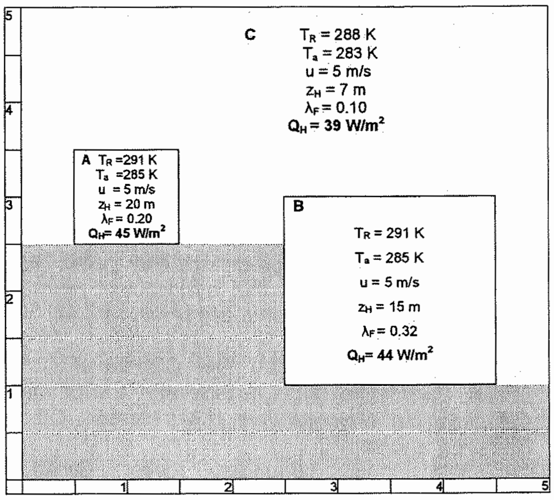

Figure 2.b - Schematic representation of an urban area (5km x 5km): model input parameters and resulting surface sensible heat flux.

4. CONCLUDING REMARKS AND FUTURE WORK

The sensitivity of Q_H to the different model parameters, T_R, T_a, u, z_H, and λ_F, has been investigated. Initial experiments aimed at examining the impact of spatial variations of roughness and stability have shown that significant variations in sensible heat flux may occur. Such variations may lead to the initiation or enhancement of convection has been observed in some cities. This will be subject to further investigation.

References

Arnfield, A.J., 2003: Two Decades of Urban Climate Research: A Review of Turbulence, Exchanges of Energy and Water, and the Urban Heat Island, Int. J. Climatology, **23**, 1-26.

Bornstein, R.D. and K.J. Craig, 2002: Survey of the history of the urbanization of numerical mesoscale models. *Proc. Fourth Symposium on the Urban Environment*, Norfolk, Virginia, USA, Amer. Meteor. Soc..

Brutsaert, W., 1982: *Evaporation into the Atmosphere*, D. Reidel, 229 pp.

Dyer, A.J., 1974: A review of flux-profile relationships. *Bound.-Layer Meteor.*, **7**, 363-372.

Grimmond, C.S.B. and T.R. Oke , 1999a: Aerodynamic properties of urban areas derived from analysis of surface form. *J. Appl. Met.*, **38**, 1262-1292.

Grimmond, C.S.B. and T.R. Oke, 1999b: Heat storage in urban areas. Local-scale observations and evaluation of a simple model. *J. A. Met*, **38**, 922-940.

Grimmond, C.S.B. and T.R. Oke, 2000: A Local-scale Urban Meteorological Pre-processing Scheme (LUMPS). *Proc. Workshop on Preparation of* *meteorological input data for urban site studies,* Prague, Czech Republic, COST Action 715, 87-98.

Grimmond, C.S.B. and T.R. Oke, 2002: Turbulent Heat Fluxes in Urban Areas: Observations and a Local-Scale Urban Meteorological Parameterization Scheme (LUMPS*). J. Appl. Meteor.*, **41**, 792-810.

Grimmond C.S.B. and C. Souch, 1994: Surface description for urban climate studies: a GIS based methodology. *Geocarto Int.*, **1**, 47-59.

Högström, U., 1988: Non-dimensional wind and temperature profiles in the atmospheric surface layer:A re-evaluation. *Bound.-Layer Meteor.*, **42**, 55–78.

Meteorological Office, 1983: *The Climate of Great Britain. Lancashire and Cheshire and Isle of Man. Climatological Memorandum 130.* Meteor. Office, Bracknell, Cronw.

Oke, T.R., 1987: *Boundary Layer Climates,* Routledge, 435 pp.

Paulson, C.A., 1970: The mathematical representation of wind speed and temperature profiles in the unstable atmospheric surface layer. *J. Appl. Meteor.*, **9**, 857-861.

Raupach, M.R., 1994: Simplified expressions for vegetation roughness length and zero-plane displacement as functions of canopy height and area index. *Bound.-Layer Meteor.*, **71**, 211-216.

Raupach, M.R., 1995: Corrigenda. *Bound.-Layer Meteor.,* **76**, 303-304.

Sabatino, S. di, Ratti, C., and Bitter, R., 2002: Modelling the urban flow field and pollution dispersion using digital elevation models. *Proc. Fourth Symposium on the Urban Environment,* Norfolk Virginia, USA, Amer. Meteor. Soc., 198-199.

Shaw, E.M., 1962: An analysis of the origins of precipitation in Northern England, 1956-1960. Quart. J. Royal Meteor. Soc., **88**, 539-547.

Shepherd, J.M., 2002: An investigation of the influence of urban areas on rainfall using a cloud-mesoscale model and the TRMM satellite. *Proc. Fourth Symposium on the Urban Environment*, Norfolk, Virginia, Amer. Meteor. Soc.,1-2.

Shepherd, J.M., H. Pierce and A.J. Negri, 2002: Rainfall Modification by Major Urban Areas: Observations from Spaceborne Rain Radar on the TRMM Satellite. *J. Appl. Meteor.*, **41**, 689-701.

Thielen, J. and A.Gadian, 1996: Influence of different wind directions in relation to topography on the outbreak of convection in Northern England. *Annales Geophysicae,* **14**, 1078-1087.

Thielen, J. and A. Gadian, 1997: Influence of topography and urban heat island effects on the outbreak of convective storms under unstable meteorological conditions: a numerical study. *Meteor. Applic.*, **4**, 139- 149.

Thielen, J., W. Wobrock, A. Gadian, P.G. Mestayer and J.-D. Creutin, 2000: The possible influence of urban surfaces on rainfall development: a sensitivity study in 2D in the meso-γ-scale. *Atmos. Res.*, **54**, 15-39.

van Ulden, A.P. and A.A.M. Holtslag, 1985: Estimation of atmospheric boundary layer parameters for diffusion applications. *J. Climate Appl. Meteor.*, **24**, 1196-1207.

Voogt, J.A. and C.S.B. Grimmond, 2000: Modeling Surface Sensible Heat Flux Using Surface Radiative Temperatures In a Simple Urban Area. *J. Appl. Meteor.*, **39**, 1679-1699.

TROPOSPHERIC DRYNESS AND CLOUDS OVER TROPICAL INDIAN OCEAN.

G.L: Liberti[2], F. Cheruy[1], and C.Iori[2]

[1] LMD-CNRS, UPMC, 4 pl. Jussieu;75252 Paris-cedex05, France, cheruy@lmd.jussieu.fr
[2] ISAC-CNR, Via Fosso del Cavaliere 100, I-00133, Roma, Italy.

1. INTRODUCTION

Dry layers have been frequently observed in atmospheric soundings from the climatologically humid warm pool region (Mapes and Zuidema, 1996). They received a great deal of interest from the TOGA-COARE community because of their impact in the convective activity (e.g. Yoneyama and Parson 1999, Sheu and Liu 1995, Yoneyama and Fujitani 1995, DeMott and Rutledge 1998, Parsons et al. 2000,). Among the processes involved in the recovery from dry to normal status radiation may play an important role. As a consequence, the possible presence of clouds must be characterized as much as possible. Liberti et al. (1994), by combining SSM/I and GMS/IR data over the TOGA-COARE area, observed that quite often low total precipitable water vapour content (TPWV), as retrieved from SSM/I measurements, occurred in cloudy sky. Brown and Zhang (1997) examine the variability of the midtropospheric moisture and its effect on the cloud type distribution during TOGA-COARE. They note that during dry events, substantial amount of mid-level clouds is present. The cloud level is inferred from hourly IR brightness temperature averaged over 4 pixels center at each ISS site. However they do note that in the case of thin high cirrus overlaying thick middle cloud, cloud top height for the later could be overestimated. Both studies used single channel IR measurements with which cirrus clouds can be also misinterpreted as middle level clouds.

Narrow band radiometers data (TMI and VIRS) from the TRMM mission, unavailable during TOGA-COARE, represent a unique data set for such a kind of study. In fact, TMI observations allow the retrieval of total precipitable water vapor (TPWV) content also for non-precipitating cloudy conditions while the set of wavelengths of the VIRS radiometer allows the detection of cloud as well as the inference of some microphysical characteristics of the clouds such as the phase, the cloud optical thickness and the cloud top level.

This study is based mostly on the analyses of one month (March 1999) of TRMM data over the Indian Ocean (40°E-80°E, 30°S-30°N) during the INDOEX experiment (Ramanathan et al. 1996). A study area and period different from TOGA-COARE one have been selected to take advantage of any possible ancillary observations, especially in situ ones, that over tropical oceans are available almost uniquely during international experiments.

Within this frame the objectives of this study are the following:

- document the occurrence of *dry layers* in this part of the Tropical Oceans;
- confirm the existence of clouds during such events, try to characterize them and their link with the dry event occurence.

In addition to TRMM data, observations from radiosounding stations as well as from METEOSAT 5 have been included in the analyses in order to help in the description of the dry tongues and the associated cloudiness occurrence.

TRMM data processing including the algorithms used for the detection of the dry events and clouds are described in section 2 where also results for March 1999 are repoted and discussed. Section 3 contains the detailed multi-instrument description of one of these events including the preliminary results of the retrieval of cirrus characteristics. Section 4 reports preliminary efforts to demonstrate that the study case analysed is somehow representative of similar cases.

A discussion of possible link between dry layer and cirrus is contained in section 5.

2. DATA PROCESSING AND RESULTS

TRMM data have been analysed using the following procedure:

- match-up of MW and VIS-IR observations
- definition of TPWV (Dry/moist) and cloudy (Cloud/clear) thresholds for 2.5°x2.5° boxes.
- Definition of cirrus thresholds (Cirrus/other clouds)
- detection of interesting cases.

Figure 1 shows, for each box, a summary of the results of the processing and the position of Seychelles and Vacoas radiosounding stations. As expected there is a strong latitudinal gradient of the TPWV threshold as a consequence of the effective TPWV distribution. In the following, the location of the maximum value is assumed to be representative of the position of the ITCZ.

The majority of the boxes reporting significant percentages of dry and cloudy pixels (black area) are located N and S of the ITCZ. In terms of occurrence of cirrus for dry pixels (red area), two distinct zones are identified:

Corresponding author's address: Frederique Cheruy, 4 pl. Jussieu;75252 Paris-cedex05, France
E-Mail: , cheruy@lmd.jussieu.fr

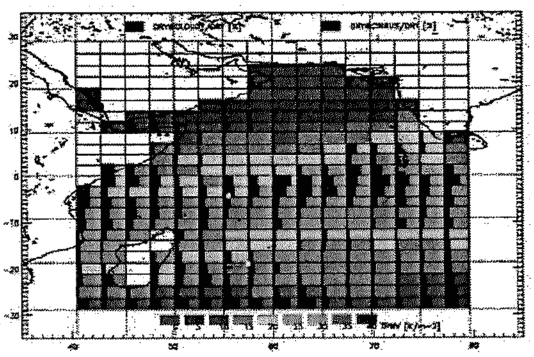

Fig.1: *March 1999 analyses results.*
- *Colour background: TPWV value used as threshold for the definition of dry events.*
- *Black area: % (e.g. 50% half of the box is black) of dry observations classified as clouy.*
- ***Red** area: % of dry observations classified as cirrus.*
- ***Withe dots:** Radiosounding stations.*

1. South of the ITCZ, dry and cloudy pixels are seldom classified as cirrus. From the analyses of VIRS data, dry and cloudy pixels, in this zone, seem to be associated with clouds with increasing optical depth and with a 280 K cloud top temperature. This is coherent with the Vacoas (20.S, 57.5E) soundings which show a persistent inversion for a temperature of about 280K. This behaviour is representative of the whole southern part of the zone.
2. North of the ITCZ. In this region almost the whole set of dry and cloudy pixels is associated with cirrus clouds.

3. THE 15th OF MARCH STUDY CASE

We focus now on the characterization of the cirrus observed N of the ITCZ, during the occurrence of a dry event. From the analysis of daily mean TPWV maps (not shown), it is possible to identify anomalies in the TPWV distribution. During the analysed period a dry anomaly is observed, roughly along the equator (N of ITCZ) and from 50 to 70 East, lasting from the 13th until the 17th of March. The same area is also mostly classified as cloudy. The analysis of the measurements taken at the Seychelles sounding station, located in the area interested by the previously detected dry event confirms the occurrence of a dry tongue: Figure 2 (upper panel) shows the time series for the month of March of the profile of water vapour mixing ratio while in the lower panel the time series of TPWV as derived from the radiosounding at the Seychelles station. The presence of relatively dry air mass is observed between 600 and 800 hPa from the 13th to the 15th of March. In the TPWV time series the dry event is evident too. It is interesting that the dry event follows a very moist period around the 10th of March when relatively high water vapour mixing ratio values are reported between 400 and 600 hPa.

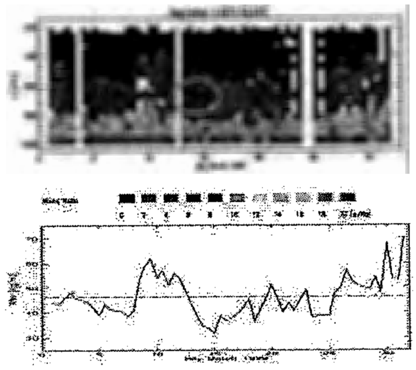

Fig.2 March 1999 Seychelles radiosounding time series:
- upper panel: water vapour mixing ratio profile
- lower panel: TPWV (___) and mean value (----)

To examine the relevance of taking into account the cirrus clouds, observed during the dry event, in the current non-cloud resolving and highly parameterized numerical models, it may be useful to characterize them in terms of some relatively simple spatial and temporal relationship with respect to the main core of the convective system. In order to do that, a synoptic view is needed and for this reason time series of METEOSAT5 IR and WV channel images have been qualitatively analyzed together with TRMM derived products (TPWV and Cloud classes). For the case of the 15th of March such qualitative analysis, shows that the observed cirrus clouds were produced by the main convective system and extend as filaments for more than 1000 km of length and about 50 to 100 km of width.

To characterize the cirrus the minimum set of information needed includes:
- the altitude/pressure of the cirrus top (Z_{top})
- its optical depth τ (or the emissivity) at a given wavelength: in this case 10µm.
- the microphysical properties (habit and size distribution) to compute radiative properties over the whole spectrum.

By using the sensitivity of the split window difference (T4 (10.8µm)-T5(12µm)) and of the T4 value to the above variables (see for example Wu 1987), it is possible to retrieve with narrow band observations a set of parameters that can be used to describe the above variables, assuming the following:
- cirrus particles as spherical;
- ice particle size distribution log-normal with a fixed σ=2µm and therefore represented uniquely from a single parameter: for example the modal radius r_{modal}.
- plane parallel infinite and vertically homogeneous (i.e. same size distribution) single layer cirrus;

Using a detailed RTM (MODTRAN (Berk et al. 1983) to compute spectrally detailed atmospheric gas extinction profiles and POLRAD (Evans and Stephens 1991) to solve the multiple scattering) a series of curves, each one representing a given cirrus cloud top height and size distribution and a varying optical depth, were build on the space T4-T5 vs T4 using temperature and water vapour profile from the corresponding radiosounding at the Seychelles.

The retrieval of 3 cirrus parameters (i.e. τ, Z_{top} and r_{modal}) from only 2 observations (T4 and T5) per pixel, even assuming clear sky as known from the radiosounding and the hypothesis on surface temperature and emissivity as correct, requires some additional information. Consequently, within a given box, the detected cirrus is assumed to have its top at a constant height and particles with a constant size distribution, only the optical thickness is allowed to vary. Given the above assumptions, observations of the 15th of March, over the box including the Seychelles location, have been compared against the RTM simulations by computing, for each Z_{top} and r_{modal} combination, Bias and RMS between observed and simulated Tb's.

The set of Z_{top} and r_{modal} values that minimizes the distance between the observation and the RTM simulations is the result of the retrieval. In addition the average τ, for the whole cirrus is a third retrieved parameter. For the study case we obtain r_{modal}=14 μm and Z_{top} around 10-11 km (200-250 hPa), well above (see fig.2) the level of the mixing ratio negative anomaly (600-700 hPa). The retrieved average cirrus optical thickness is about 0.8 at 10μm. While it is very difficult to quantitatively evaluate the accuracy of the retrieved parameters, from a qualitative point of view:

- the potential temperature lapse rate of the Seychelles radiosounding is relatively low at the level of the layer where the retrieval would **put** the cirrus
- the modal radius correspond quite close to the value reported, as a summary of several in situ observations, by McFarquhar and Heymsfield (1996), for dissipating cirrus at the temperature of the retrieved cirrus pressure height.

In addition, even is the accuracy of the results may not be quantitatively evaluated the sensitivity of the results to the different hypothesis and inputs may be characterized. In any case, if an estimation of the radiative impact of such cirrus is required, to have developed such a method.

4. REPRESENTATIVENESS OF THE STUDY CASE

Having analysed in some detail the case of the 15th of March 1999 over the Seychelles the next step will be to demonstrate that such case is somehow representative for such dry intrusion events.

During the same period, unfortunately due to the incomplete coverage of the TRMM instrument, it was not possible to extract from the radiosoundings recorded during the ship cruises (Ron Brown, Sagar Kanya) useful information. The radio-sounding of Male (73.5E, 4.18N) associated with VIRS observation shows evidence of dry layers covered with cirrus clouds.

In order to avoid to process large amount of TRMM data to identify similar cases, time series (1989-2003) of radiosoundings at the Seychelles have been preliminarily analysed to identify similar cases, at least from the point of view of vertical distribution of water vapour and temperature.

An automatic procedure to select cases with dry event occurrence has been developed. This method search for an at least 100 hPa width layer such that the water vapour mixing ratio in the layer is lower than the value in its upper (lower pressure) boundary. This search is performed from 400 to 825 hPa with a 25 hPa step.

With such a definition it was found that the largest amount of cases occurs during the months of June July August (JJA) in the layers between 400 and 450 hPa while a relative maximum of cases occurs during the months of March April May (MAM) in the layer between 600-650 hPa. Given the fact that during the JJA period there is the minimum of the water vapour small changes in the water vapour mixing ratio can be detected as a dry layer, moreover the impact of a dry layer at such altitude should be less important for convective processes than events occurring at lower layers. We analysed therefore all cases, in the MAM period with a dry layer detected at 600-650 hPa. It is interesting to notice that in addition to some similarity among the selected profile, expected by the selection criteria, it was found that the average mixing ratio profile corresponding to 5 days before the dry events is 5 to 10% more humid that seasonal average.

In order to test how often, for a dry event as defined from the above method, cirrus clouds are observed too, for a preliminary set of 16 randomly selected cases TRMM data have been analysed. For such preliminary data set in 12 cases cirrus clouds are detected.

5. CLOUD DRY LAYER RELATIONSHIP.

This section contains few preliminary ideas on possible relationship(s) between the presence of cirrus and the occurrence of dry air column.

From a qualitative analysis of the time series of METEOSAT IR images it is evident that the cirrus are generated by a large convective system while the TPWV maps indicates that a dry air mass is of extra-tropical origin. The observed presence of cirrus during the occurrence of anomalously dry air column can be interpreted as no directly related because in a relatively convectively active region cirrus clouds could be somehow imagined as a persistent characteristic as a result of aging convective active systems. In such scenario the presence of dry layer would inhibits the development of low/middle troposphere clouds, making the cirrus 'visible' with the adopted technique.

Nevertheless we discuss the hypothesis that the presence of the dry layer may be responsible for a longer lifetime of the observed cirrus. Two possible physical mechanisms, that could relate the presence of the dry layer with the cirrus observed above, are proposed and are object of future analyses.

From a radiative point of view, because of the presence of a relatively dry layer in the middle troposphere, the flux emerging from the warm lower levels will not be absorbed by the dry layer but mostly at the boundary between the latter and the upper layer. Such absorption would be quite localized because of the relative abundance of water vapour in the lowest levels of the upper boundary. As a consequence, the atmospheric levels below the cirrus base would have IR cooling rate close to 0. This is confirmed by computations of the cooling/heating rates for the profile of the 15th March with the Chou et al. (2002) radiative transfer model. Also Fig. 11 from Mapes and Zuidema, (1996) shows the same behavior. The evolution of the temperature profile from a 12 hours period due to vertical radiative exchanges is computed. This leads to buoyancies close to zero at middle/upper troposphere interface is while for the rest of the profile it is clearly negative. This relative decrease of inhibition at upper levels may helps in the surviving of the cirrus.

In addition turbulence generated by a strong wind shear at the interface between mid and upper troposphere can be put forward as a second mechanism helping the cirrus to maintain.

6. CONCLUSIONS

In this study, we demonstrated that dry cloudy atmospheres occur also in the tropical Indian Ocean. During dry events, cirrus clouds are observed N of the ITCZ, Shallow Cumulus S of it. Focusing on the cirrus clouds, while the one month-long dataset includes only one event, the extension and lifetime of the clouds observed during this single event make them probably relevant to understand the interactions between tropospheric water vapor and convection and consequently relevant for the weather and climate modelers. Qualitative study based on multi-satellite approach seems to indicate that the cirrus are generated by the convective systems. The next step is to estimate how the cirrus observed during the dry events act in the recovery process to the moist and convectively active period. A first step in this direction consists in retrieving the microphysical properties of the cirrus in order to compute their radiative impact (cooling/heating profiles). While ancillary information is needed, preliminary results appear encouraging in a successful retrieval of parameters such as the cloud top level, particle size distribution and optical thickness.

References

- Berk, A., L.W.Bernstein and D.C. Robertson 1983. MODTRAN: a moderate resolution model for LOWTRAN7 -AFGL- TR-83-0187, 261 pp., 1983.
- Brown,R.G. and C.Zhang 1997: Variability of midtropospheric moisture and its effect on cloud top height distribution during TOGA-COARE. J. Atmos. Sci., 54, 2760-2774
- Chou,M-D., M.J.Suarez, X-Z.Liang, M.M.-H.Yan 2002. Thermal infrared radiation parametrization for atmospheric studies, NASA/TM-2001-104606, vol 19 pp55
- DeMott, C.A., and S.A.Rutledge, 1998: The Vertical Structure of TOGA-COARE Convection. Part II: Modulating Influences and Implications for Diabatic Heating. J. Atmos. Sci., 55, 2748-2762.
- Evans,K.F. and G.L.Stephens 1991: A New Polarized Atmospheric Radiative Transfer Model. J. Quant. Spectrosc. Radiat. Transfer, 46, 5, 413-423.
- Liberti G.L., I.Jobard and M.Desbois. 1994. Multispectral (IR-MW) analysis of the TOGA COARE Intensive Observation Period. Satellite data: Preliminary Results. Summary Report of the TOGA-COARE International Data Workshop. Published by TCIPO, UCAR, Boulder, Col., USA. 127.
- Mapes,B.E. and P.Zuidema, 1996: Radiative-Dynamical Consequences of Dry Tongues in the Tropical Troposphere. J.Atmos. Sci., 53, 620-638.
- McFarquhar, G.M. and A.J.Heymsfield 1996, Microphysical characteristics of three cirrus anvils sampled during the Central Equatorial Pacific Experiment (CEPEX). J.Atmos.Sci. 52,4143-4158.
- Parsons,D.B., K.Yoneyama and J.L.Redelsperger, 2000: The evolution of the tropical Western Pacific atmosphere-ocean system following the arrival of a dry intrusion. Q.J.R.M.S., 126, 517-548.
- Ramanathan et al. 1996: Indian Ocean Experiment (INDOEX): a multi-agency proposal for a field experiment in the Indian Ocean. C4 Pub. 162, Scripps Inst. of Oceanogr., La Jolla, Calif., June 1996.
- Sheu,R.-S. and G.Liu 1995. Atmospheric humidity variations associated with westerly wind bursts during TOGA-COARE. J. Geophys. Res.,100, D-12, 25759-25768.
- Wu, M.C., 1987: A method for remote sensing the emissivity, Fractional cloud cover and cloud top temperature of high level, thin clouds. J. Climate Appl. Meteor. 26, 225-233.
- Yoneyama, K. and T. Fujitani, 1995: The behavior of the dry westerly air associated with convection observed during the TOGA-COARE R/V Natsushima Cruise. J. Meteor. Soc. Japan, 73, 291-304.
- Yoneyama, K. and D.B.Parson 1999: A proposed mechanism for the intrusion of dry air into the Tropical Western Pacific Region. J. Atmos. Sci., 56, 1524-1546.

CLOUDS SPACE AND TIME SCALE IN THE MEDITERRANEAN AREA:CLIMATE MODEL AND OBSERVATIONS.

F. Chéruy[1], G.L: Liberti[2]

[1] LMD/IPSL/CNRS, UPMC, Case 99, 4 pl. Jussieu;75252 Paris-cedex05, France, cheruy@lmd.jussieu.fr
[2] ISAC-CNR, Via Fosso del Cavaliere 100, I-00133, Roma, Italy.

1. INTRODUCTION

The need to produce reliable climate simulations over the south Europe-Mediterranean region makes essential to evaluate the performances of the parameterizations which govern humid processes at regional scale. The goal of our work is to characterize process aspects of clouds at this particular regional scale, both in the observations and in numerical model simulations.
In this abstract, preliminary results concerning the methods developped to compare climate model simulations against geostationnary satellite observations are described. The relative restricted dimensions of the region of interest allows to refine the data processing and to use higher resolution data than usually done when considering global applications. The method is designed both to evaluate the cloud representation in the climate model and to support improvement or developpement of a locally optimized parameterization. The model used is briefly described in section 2. Section 3 describes the processing of the satellite data. The problem of numerical model generated cloud parameters and satellite brightness temperature comparisons is introduced in section 4. Section 5 describes comparisons of cloud parameters for a test dataset. Some conclusions and prospectives are drawn in section 6.

2. THE LMDZOR MODEL

The LMDZOR model is a numerical tool resulting from the coupling between the atmospheric GCM, LMDZ3.3 and the land surface scheme ORCHIDEE. LMDZ uses finite difference (Sadourny and Laval, 1984). The horizontal grid can be streched in order to increase the resolution in a particular region of the globe. There are 19 vertical layers, unequally spaced. The convection parameterization is based on the K. Emanuel scheme (1991). A prognostic scheme is used to parameterize the large-scale condensation and clouds (Le Treut and Li, 1991). The cloud fraction is predicted from 2 large scale variables of the model: the mean value of the total water in the grid mesh, and the saturation humidity, assuming that the sub-grid repartition of the water follows a probality distribution function. In the general case the PDF is a rectangle, in the case of convection the scheme uses log-normal generalised PDF, in addition it accounts for the amount of condensate produced at sub-grid scale by the convection (Bony and Emanuel, 2001). The parameterization of radiation transfer is from Fouquart and Bonnel (1980) and Morcrette (1991), the clouds are assumed to overlap in a maximum-random way. The boundary layer is parameterized by an eddy diffusivity formulation. The ORCHIDEE scheme is the result of the coupling of the SECHIBA (Ducoudré et al., 1993) land-surface scheme, which is dedicated to the surface energy and water balances, and the carbon and vegetation model STOMATE (Krinner et al., 2003). In the work presented here, only the SECHIBA module is actived. Meteorological simulations (Hourdin et al., 1999) are performed for the whole month of october 2000: the wind and temperature fields are relaxed 4 times a day toward the ECMWF analysis with a time constant of 3 hours, actually constant over the whole domain. For the mediterranean zone [10W:40E,26N:50N], the variables of the model are archived every 30mn. This corresponds both to the time step of the evolution equations for the physics and to the observation interval of METEOSAT. The simulation is initialized the 24th of september to avoid for spin-up problems. The grid has 192 points along the latitude direction and 145 along the longitude one. It is streched with a zoom of factor 4, centered at 40N,15E; in the mediterranean area, the resolution is of about 30km by 50km, while it reaches 600 km outside.

Corresponding author's address: Frédérique Chéruy, 4 pl. Jussieu, Case 99 ;75252 Paris-cedex05, France
E-Mail: , cheruy@lmd.jussieu.fr

3. SATELLITE DATA PROCESSING AND SUB-REGIONS DEFINITION

The restricted dimensions of the mediterranean area and its high degree of heterogeneity make suitable to use full-resolution METEOSAT data; along the Mediterranean coasts it is very common to pass within 100 km from relatively deep sea to a mountain region. However, since the scope of the study is the evaluation of the GCM simulations at regional scale, it is relevant to look for a partition of the data in sub-region where local forcings and processes can be identified if not isolated. Note that, such a partitionning would probably be meaningless if we were concerned with a NWP model where the spatial resolution is essential. The adopted definition of the sub-regions is based on literature, experience, surface type and elevation. The regions are not

always of comparable size, some of them are relatively small sized but their signal, when included in largest region appeared to induce considerable distortion: this is the case of the Balearic islands that when included in a pure ocean region induced considerable deviation from the pure ocean behaviour.
Each METEOSAT pixel has been assigned to one of the mediterranean sub-region. Because of the relatively high resolution of the model, it has been possible to assign each model grid box to a sub-region corresponding to the one of the majority of the METEOSAT pixels within the mesh.
Satellite data used in this study are the full resolution B-format METEOSAT data of the archive of the PDUS receiving station of the University of Ferrara and ISAC-CNR. Standard EUMETSAT suggested processing and coefficients have been used to produce brighness temperature geolocated maps.
The period used to develop and test the presented comparison methodologies is the month of October 2000. Several data gaps are found in this time series. No attempt to fill such data gaps, for example with interpolated estimations, was done. We plan to fill such gaps, when possible with data for more complete archives (e.g. the EUMETSAT one).

Fig.1 reports the sub-regions identified in the Mediterranean area as defined for the model. To test the independence of the selected regions the correlation coefficient of the diurnal cycle of frequency occurrence for 1K width classes for all possible sub-regions combinations of was computed. It shows that generally regions are uncorrelated.

4-GCM CLOUD PARAMETERS AND SATELLITES

The basic problem of such a comparison exercise is that the GCM most general cloud product is the cloud cover, for a certain grid size for each model level while the geostationary satellite data from the broadband IR window channel, gives an instantaneous measure of the radiance reaching the satellite sensor from a given FOV. Such radiance can be converted into brightness temperature that, only in the case of optically thick and high cloud, can be assumed, with negligeable error, to be the temperature of the cloud top. Briefly, neglecting the spatial resolution and the temporal aspects, the model gives a 3D representation of clouds while at the best a 2D representation of the cloud top can be inferred from IR satellite data.

Three different approaches have been identified to perform such comparison and applied to the month of October 2000 in order to identify problems and information content:
-The "model to satellite" method (Morcrette, 1991, Bonnazola et al., 1999, Chevallier et al., 2001) uses highly parametrized RTM coupled with overlapping models to compute radiances from the GCM parameters (surface parameters, temperature, water vapor, cloud profiles) as they would be observed by the satellite radiometer. Such a method tests not only the single layer cloud information but also the models (RTM, overlapping ...) included in the processing. Given the fact that temperature dependence is close to the 4[th] power, for example, the sensitivity to any error in the surface temperature or emissivity will be very large. We consider therefore such an approach as a method to validate the overall performances of a model but very difficult to use when testing a single part of the model.
-An alternative approach consists in adding somehow a vertical information to the satellite data by considering relatively large areas (sub-regions). This method assumes that there is an equivalence between the vertical distribution of clouds within a column and the horizontal distribution of cloud top properties. Fig.2 shows an example for a particular sub-region of time series of histograms for averaged (computed over the whole sub-region) model cloud cover (upper panel) and for occurrence of the brightness temperatures (lower panel). The sub-region is the easterm Mediterranean region (grey zone of Fig.1), the model shows very persistent high level clouds layers (levels 10, 11, about 350hPa), not revealed by the satellite observations; the later reache 240K only from time to time. In the second part of the period (days 282,283) from the METEOSAT data it seems that low clouds are deepening reaching higher tops,

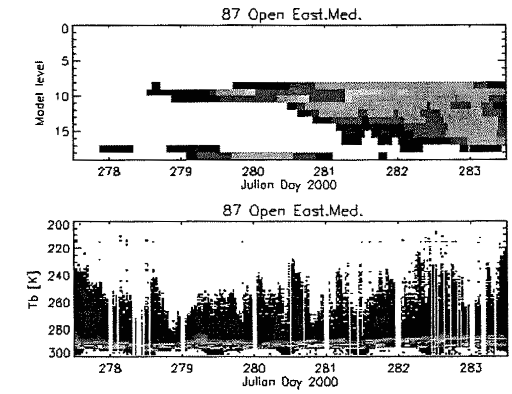

Fig. 2, time series of the histograms for the averaged model cloud cover (upper panel) and for the occurrence of brightness temperature (lower panel)

while the model seems to indicate that the lowest clouds arise after the highest. This behavior is observed for other sub-regions and seems to be consistent in the simulation. At this stage of the study no explanation is provided. Such comparison method appears to be rich in qualitative informations because the only reduction of information is the actual geographical position of both data. Converserly it is very difficult to design a quantitative estimation of the skill. This could be useful when the method is used to test and evaluate modified versions. For this reason, we seek for a less subjective and more quantitative method even if less general.

-The quantitative method adopted again consider regions and it consists in classifying each satellite pixel into cloudy or clear, then compute the surface covered by clouds, loosing any information on the cloud height, and compare such value against the maximum and minimum cloud cover from the model. As stated before such method looses in generality and can test only the hypothesis of underestimation (if maximum overlapping is imposed) or overestimation (in case minimum overlapping is imposed) of cloudiness by the model.

Other tests under examen concern specific aspect of cloud characteristics. In particular the ability of the model to reproduce observed diurnal variability of cloudiness is tested. Such a test is again a very powerfull method to test the overall performances of most of the parametrizations, and their mutual coupling, included in the model. In fact the diurnal cycle of cloudiness would depend, in terms of parameterization, not only on the moist processes parametrization but also in the PBL and radiation parameterizations.

5. CLOUD COMPARISON METHOD

5.1 The water vapor issue

The quality of a numerical model cloud representation depends not only on the efficiency of the parameterizations but also on the quality of the input variables. Availability of water vapor is one of the most important conditions for the model to generate a cloud. Comparison between water vapor inferred from SSMI as well as TRMM/TMI observations (where possible) with the LMDZOR water content is performed. Results show that the model agrees quite well with the observations over most part of the sub-regions. The comparisons with radiosoundings is more delicate. Discrepancies occur which require to be analysed.

5.2 Clouds

For each sub-region and each 30' a model estimation of maximum and minimum possible coverage have been defined and compared with two cloud covers derived from the satellite observations. In the first case a pixel is classified as cloudy when its temperature is colder than 280K. In the second case, each METEOSAT pixel is classified as cloudy if its brightness temperature is colder than a given dynamically determined threshold, distinctive of the particular sub-region, and, to take into account of the surface temperature diurnal cycle, on the slot number in the case of land sub-regions. Such threshold is defined as follow:

- the histogram of the distribution of all brightness temperature for a sub-region in the studied period is computed. The moda (T_{moda}) value of the distribution and the lower boundary of 5% warmest part of the distribution (T_{max}) are identified. The moda is assumed to represent the clear sky and the clear sky variability is supposed to be symetric with respect to the moda value. With such hypothesis the threshold temperature is defined as:

$$T_{th}=T_{mod}-(T_{max}-T_{moda})$$

Concerning the model cloud cover, the minimum value is computed assuming the maximum overlapping hypothesis: in each box and at each time step, the maximum value of cloud cover among all vertical levels is defined as the minimum box cloud cover. Converserly, the maximum cloud cover is given by the sum (until it reach 1) of the cloud covers in each single layer.

Time series of the cloud covers are produced for every sub-region. Three examples are plotted in Fig. 2. for: the Mediterranean area north of Atlas (upper panel), the Greek peninsula (middle panel) and the north Italian peninsula (lower panel) In the following figures, the lines represent the 2 model cloud cover estimations: minimum overlapping (thick line) and maximum overlapping (thin line). Symbols are the METEOSAT cloud cover estimations: for the fixed 280 K threshold (red plus +) and for the dynamic threshold described above (purple diamond ◊).

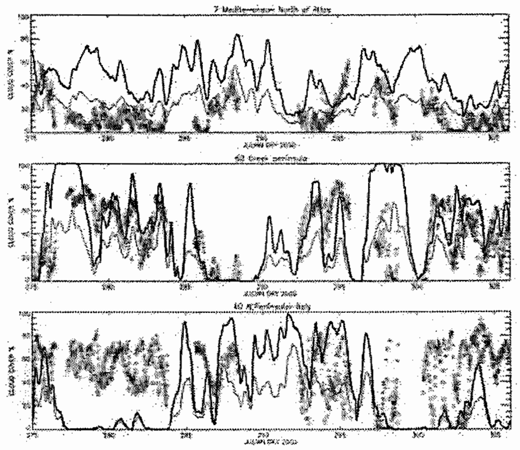

Fig.3 *Examples of time series of model and satellite derived cloud covers for three sub-regions (see text)*

For the upper panel (Mediterranean North of atlas), the model slightly overestimates the cloud cover. For middle panel (Greek peninsula), the results are in overall good agreement. The lowest panel (North Italy), the tendency is an underestimation of the cloud cover by the model. A skill score, S, is tentatively defined in order to summarize the results. A bias B is defined as the ratio of the model to the satellite cloud cover.

B_{min}=model_min/satellite, B_{max}=model_max/satellite

For each slot in a particular region, S is set equal to 1 if B_{min} and B_{max} are both greater than 1 (overestimation of the model), it is set to -1 when both are smaller than 1 (underestimation), the zero value is attributed to S, when B_{min} is less than one and B_{max} is greater than one (correct). The overall skill is the mean of the S values over the month for each sub-region.

Figure 4 shows the distribution, over the subregions of the S parameter, for the 2 different thresholds adopted for the METEOSAT data processing: 280K (lower panel) and dynamic threshold (upper panel)
While both methods show consitent results for some regions (France, most of the north Africa, eastern part of the Mediterranea), they diverge for several regions (e.g. Central Europe). This shows that work has to be done to improve the threshold definition for the cloud cover calculation with the METEOSAT data.

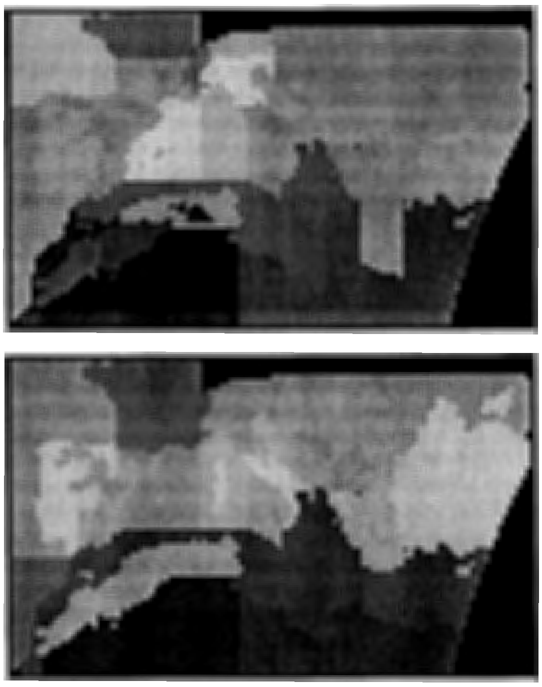

Fig.4 *Distribution, over the subregions of the S skill parameter (see text), for the 2 differrent thresholds adopted for the METEOSAT data processing: 280K (lower panel) and dynamic threshold (upper panel).*

6. CONCLUSIONS AND PERSPECTIVES

A preliminary set of tools, for the quantitative as well as qualitative, validation of model cloud cover with satellite observation have been presented. The developed methodology needs to be refined in particular the definition of satellite cloudy pixels over land regions.
Other tests, not described here, have been developed and are being analysed in order to assess their contribution to final task. They include:

- capability of the model to reproduce diurnal cycle of cloudiness
- analyses of the capability of the model to reproduce observed cloud cover temporal evolution characteristics through comparison of cloud cover time derivatives
- specific analyses on the model cloud convective scheme using additional information as CAPE. Preliminary tests have been performed by simply comparing the convective cloud cover as produced by the model with the sub-region area portion with brightness temeprature colder than 250 K. However a more detailed, and sub-regional, definition of satellite convective cloud cover are in progress.

References

- Bonazzola M., et al. , 2001, Retrieval of large-scale wind divergences from infrared Meteosat-5 brightness temperatures over Indian Ocean, J.G.R, 106, D22, 28113-28128
- Bony S and K.A. Emanuel, 2001, A parameterization of the cloudness associated with the cumulus convection: Evaluation using TOGA-COARE data, J. Atmos Science, 58, 3158-3183
- Ducoudé, N., Laval, K. and Perrier, A. (1993) SECHIBA, a new set of parametrizations of the hydrologic exchanges at the land/atmosphere interface within the LMD atmospheric general circulation model. *Journal of Climate* 2(9):248-273.
- Emanuel K., 1991: A scheme for representing cumulus convection in large scale models, 1991, J. Atmos. Science, 48, 2313-2335
- FouquartY and Bonnel, 1980: Computation of solar heating of the Earth's atmosphere: A new paramterization. Beitr. Phys. Atmos., 53, 35-62
-Krinner G. et al., 2003: A dynamic global vegetation model for studies of the coupled atmosphere biosphere system. Submit. to global biogeochemical cycles.
- Hourdin F., J.P. Issartel, B. Cabrit, A. Ideladi : Reciprocity of atmospheric transport of trace species. CRAS
- LeTreut, H. and L.Li: Sensitivity of an AGCM to prescribed SST changes feedback effects associated with the simulation of cloud optical properties, Climate dynamics, 5, 175-187
- Morcrette J, Evaluation of model generated cloudiness:Satellite observed and model generated diurnal variability of brightness temperature, 1991 Mont. Weather Rev., 119, 1205-1224
-Morcrette, 1991: Radiation and clouds radiative properties in the ECMWF system. J. Geophys. Res, 96, 9121-9132
- Sadourny R., and. K. Laval, 1984, January and July performance of the LMD general circulation model, in New Perspectives in Climate modelling, edited by A Berger and C. Nicolis, pp 173-198, Elsevier Sci., New-york.

OBSERVATIONS OF CLOUDS AND PRECIPITATION OVER THE ARCTIC OCEAN BY USING THE RESEARCH VESSEL "MIRAI"

Y. Fujiyoshi[1] , K. Yoshida[2], H. Kasuya[2], O. Tsukamoto[3], H. Okamoto[4], H. Horie[5]

[1]Inst. Low Temp. Sci., Hokkaido University, Sapporo 060-0819. Japan
[2]Graduate School of environmental Earth Science, Hokkaido University, Sapporo 060-0819, Japan
[3]Department of Science, Okayama University, Okayama 700-8530, Japan
[4]Center for Atmospheric and Oceanic Studies, Tohoku University, Sendai 980-8577, Japan
[5]Communications Research Laboratory, Tokyo 184-8795, Japan

1. INTRODUCTION

Amplification of greenhouse warming in the Arctic is predicted. Ikeda et al. (2003) suggest that the decaying trend of sea ice in last 40 years in the Arctic Ocean closely relates with clouds and radiation. Although SHEBA and FIRE III Arctic Clouds Experiment produced the wealth of data on arctic clouds and radiation, further observations and analyses are indispensable to understand the current climate variability in the Arctic.

We joined the Arctic cruise of the research vessel "MIRAI" (Japan Marine Science and Technology Center) in 1999 (Sep.), 2000 (Sep.), and 2002(Sep.-Oct.). Main purposes of our study are to study formation and organization processes of marine boundary layer clouds and mesoscale cloud systems, precipitation mechanism, aerosol-cloud interaction, and to make ground truth data of many remote sensors. As shown later, "MIRAI" has a C-band Doppler radar. Since its detection range is 250 km, we were able to study radar echo structures of storms (including Polar lows) that developed in higher latitude than 70 degree.

2. OBSERVATION

In 1999 and 2000, we analyzed the data of standard instruments of MIRAI, that is, upper air sounding data, C-band Doppler radar data, ceilo-meter data, meteorological components and oceanological components. In 2002, in addition to the above instruments, we deployed new instruments, that is, a polarized LIDAR, a 95GHz Doppler radar, a microwave radiometer, a turbulent latent and sensible heat flux meter, a Doppler sodar, and a tethered balloon up to 1000 m. Figure 1 shows the ship trucks of "MIRAI".

3. TURBULENT HEAT FLUXES

We calculated the turbulent latent and sensible heat

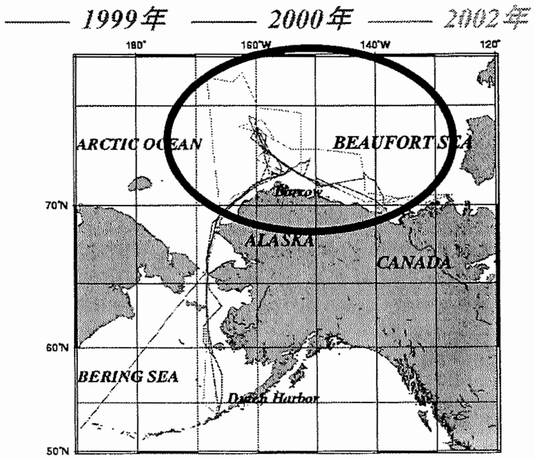

Figure 1: Ship trucks of "MIRAI" in 1999, 2000, and 2002.

fluxes by using the bulk method. The maximum, minimum and mean heat fluxes (latent + sensible) (W/m^2) are (203.7, -3.0, 33.2) in 1999 (14-23 Sep.), (128.6, -25.3, 36.4) in 2000 (7-29 Sep.) and (216.9, -25.3, 26.4) in 2002 (5 Sep. – 7 Oct.). In short, mean turbulent heat flux and Bowen ratio were about 30 W/m^2 and 1.3, respectively.

In 2002, we were able to measure turbulent heat and CO2 fluxes by using eddy correlation method. When temperature difference between air and sea surface was small (before 21 Sep.), both turbulent heat and CO2 fluxes were small (Fig. 2). However, these fluxes became larger after 21 Sep., when cold air outbreak occurred, that is, net CO2 flux from atmosphere to the sea was positive.

4. ARCTIC STRATUS CLOUD

4.1 Optical properties

Since turbulent heat fluxes were very small as shown above, radiative heat budget and the Arctic stratus cloud (ASC) play an important role in net heat balance in the Arctic Ocean.

Comparing the theoretical and observed intensity of solar radiation, we found that about 30 % of solar

Corresponding author's address: Yasushi Fujiyoshi, Insti. Low Temp. Sci., Hokkaido Univ., Sapporo 0606-0819, Japan; E-Mail: fujiyo@lowtem.hokudai.ac.jp

radiation was absorbed or scattered by aerosols and gases. When the depth of ASC was larger than 500 m, 60 % of solar radiation was absorbed by ASC. The transmittance of ASC changed rapidly below the depth of ASC is smaller than 500 m. On the other hand, the IR emissivity of ASC was about 0.9 regardless its depth. Therefore, the vertical and horizontal structure of ASC with smaller depth than 500 m is very important to elucidate the heat budget and study the climate in the Arctic region.

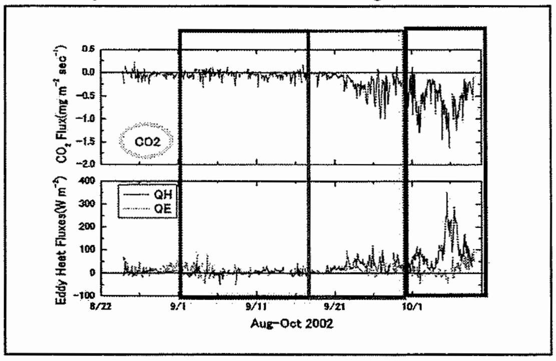

Figure 2: Turbulent heat (lower panel) and CO2 (upper panel) fluxes from 22 August to 10 October, 2002, calculated by the eddy correlation method.

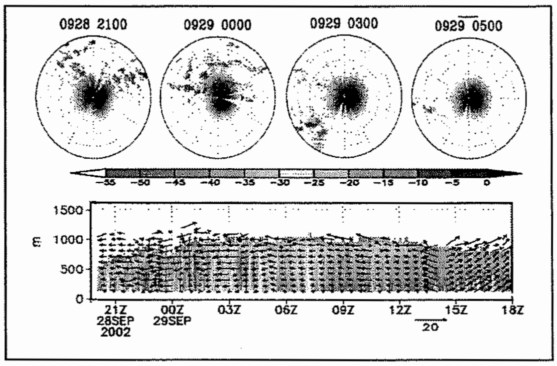

Figure 3: Time series of PPI C-band radar echo patterns (upper panels) and the time-height cross section of radar echo intensity (95GHz cloud radar) and horizontal wind vectors derived by the C-band Doppler radar of typical ASC from 15Z on 28 Sep. to 21Z on 29 Sep., 2002 (lower panel).

4.2 Radar echo structure

ASC often appeared after the passage of a cold front. Figure 3 shows the horizontal and vertical radar echo structures of typical ASC. There were the strong temperature inversion and humidity gap near the cloud top (not shown). Radar echo intensity was strong and showed organized line-structure composed of small convective clouds when vertical wind shear was large. When the horizontal wind speed near the sea surface was large, the convection within ASC was strong because turbulent heat fluxes were large (Fig. 4). As shown in Fig.4, LWP (liquid water path) was also large when wind speed was large.

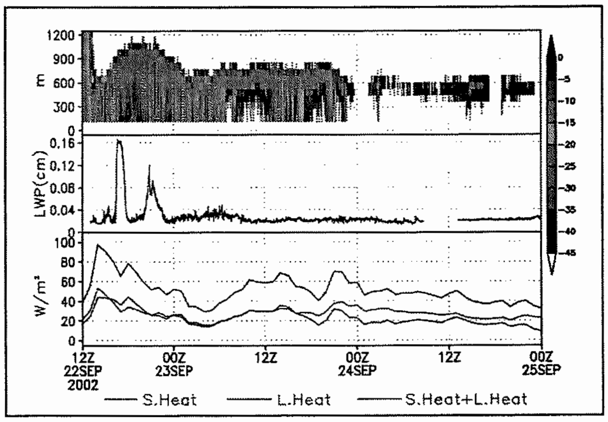

Figure 4: Time-height cross sections of radar echo intensity, change with time of LWP and turbulent heat fluxes from 12Z on 22 Sep. to 00Z on 25 Sep., 2002.

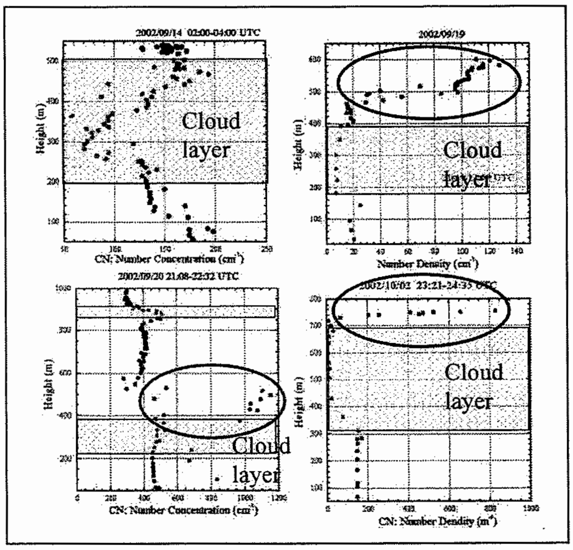

Figure 5: Vertical profiles of total number density of CN measured by using a tethered balloon from the sea surface to the level of cloud top of ASC.

4.3 Number density of aerosols below and above ASC

The calculated LCLs were almost the same with the level of cloud base measured by the ceilo-meter when ASC appeared. This result suggests that the CCN near the sea surface would be the source of cloud droplets of ASC.

We measured vertical profiles of total number density of CN by using a tethered balloon when ASC appeared (4 times) (Fig. 5). Except for the case of 14

Sep., the number densities of CN were almost constant below the cloud base. On the other hand, the number densities of CN above the cloud top were much larger than those below the cloud base. This fact indicates that the source of aerosols above ASC was different from that below ASC.

5. CLOUD SYSTEMS

To study the vertical distributions of precipitation particles, we made time-height cross-sections of radar echo intensity measured by C-band Doppler radar in 1999, 2000 and 2002 (Fig. 6). Synoptic-scale disturbances with very strong radar echo and high level of radar echo top passed over "MIRAI" about a few days interval. Most of precipitation was brought by these disturbances It is to be noted that some radar echoes did not reach to the ground surface, that is, the amount of evaporation of precipitation particles is not negligibly small in the Arctic Ocean.

Figure 7 shows the appearance frequency of the level of cloud top measured by the 95 GHz cloud radar. Three peaks (1000m, 5000m and 7500m) are found in the figure. The peak at 1000 m corresponds to ASC. Other two peaks correspond to synoptic scale disturbances. ECMWF synoptic surface weather charts show that warm air was advected from south when the disturbances existed over the bay of Alaska. In these cases, the level of echo top was higher than 7500 m. On the other hand, cold air was advected from north when Polar lows passed over "MIRAI" and the level of echo top was as low as 5000 m. Although the highest levels of radar echo top were different between these disturbances, the iso-thermal line of –40 °C well corresponds with the level of echo top as seen in Fig. 6(d).

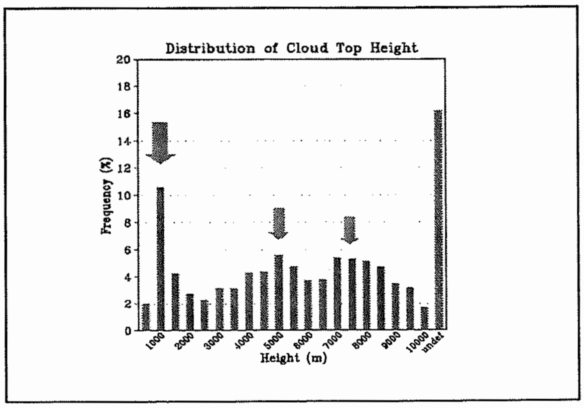

Figure 7: Appearance frequency of the level of cloud top measured by 95 GHz cloud radar in 2002.

6. SUMMARY

Major findings are as follows: Comparing the theoretical and observed intensity of solar radiation, we found that about 30 % of solar radiation was absorbed or scattered by aerosols and gases. When the depth of ASC was larger than 500 m, 60 % of solar radiation was absorbed by ASC. The transmittance of ASC changed rapidly below the depth of ASC is smaller than 500 m. On the other hand, the IR emissivity of ASC was about 0.9 regardless its depth. Number density of aerosols above the low level cloud was much larger than that below it. Usually sensible and latent heat fluxes near the sea surface were very small. However, both upward turbulent heat fluxes and downward CO2 flux increased very large when the cold air outbreak occurred. From the C-band Doppler radar data, which is the most unique data sets, we studied mesoscale features of precipitation cloud systems and vertical distribution of precipitation over the Arctic Ocean.

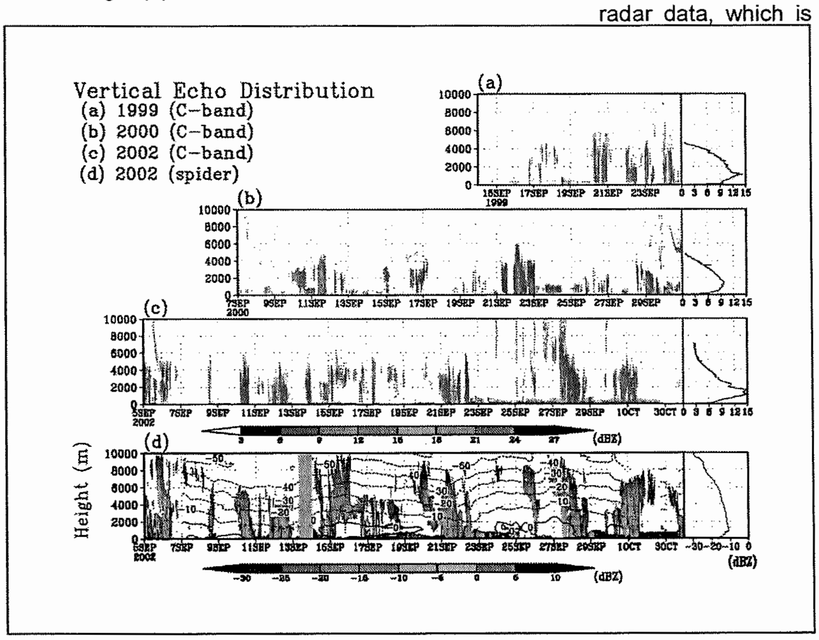

7. REFERENCES

Ikeda, M., J. Wang, and A. Makshtas, 2003: Importance of clouds to the decaying trend and decadal variability in the Arctic ice cover. J, Meteor. Soc. Japan, 81, 179-189.

Figure 6: Time-height cross-sections of radar echo intensity measured by C-band Doppler radar in 1999 (a), 2000 (b) and 2002 (c). That measured by the 95 GHz cloud radar is also shown in the lowest panel (d). Air-temperature is shown by contours in the lowest panel (d).

Environmental Variables Affecting the Hailstone's Size Distribution

Dario B. Giaiotti and Fulvio Stel

OSMER - ARPA FVG Regional Meteorological Observatory, Italy

1. Introduction

Since 1988 in the plain of Friuli Venezia Giulia a network of polystyrene hailpads for the monitoring of hail frequency and intensity is active. With this network, managed by volunteers and active from April to September, a preliminary climatology of hail falls (Giaiotti et al, 2003) and hailstone size distributions (Giaiotti et al, 2001) has been determined, highlighting some aspects that still need a physical interpretation. One of these features is the observed statistical increase of hailstone's diameter during the local night-time (nearly between 00 and 06 local time, see Fig. 1).

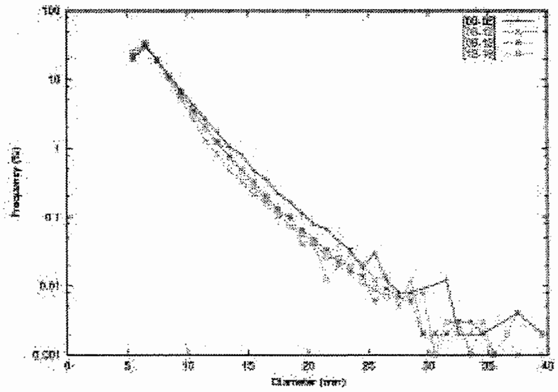

Fig. 1 Times-of-the-day hailstones size distributions.

This work is voted to face the interpretation of this observation. Being the water vapor amount in lower levels one of the fundamental ingredients for the hailstone growth, because of its direct (Prodi and Wirth, 1973; Danielsen, 1977) and indirect (Fabush and Miller, 1953; Morgan, 1970) effects, in this work its daily variability is analyzed using the upper level data retrieved from the Campoformido atmospheric sounding (WMO code 16044), which is carried out every six hours by the Italian Airforce in the middle of the Friulian plain.

2. The daily trend of water vapor in lower levels

The data obtained trough the Campoformido atmospheric soundings from 1988 to 1998, the same range of years analyzed in Giaiotti et al (2001) to determine the hailstone's size distribution, are used in this work to compute the average vertical profile of mixing ratio in the four different times-of-the-day (00, 06, 12, 18, UTC) and for the different months (April, March, June, July, August, September). This analysis shows that the amount of mixing ratio is systematically higher (difference of nearly 0.5 g/kg) during night-time (00 UTC, i.e. 02 local time), especially in July, August and September (see Fig. 2 for the August case).

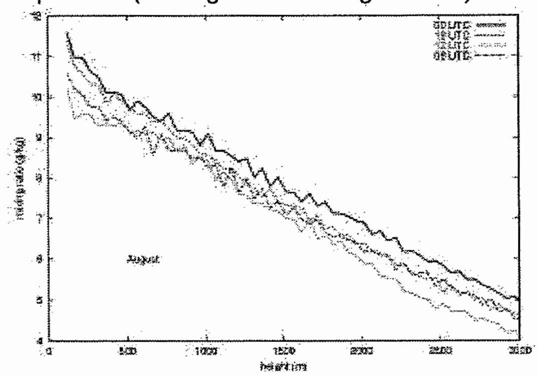

Fig. 2. Vertical profile of the average mixing ratio in the four times-of-the-day for August

To test if this observation is due only to a measurement bias connected with radiative effects, we computed the average vertical profile for the four times-of-the-day in January (Fig. 3) and February (not shown).

For these two months there is almost no difference between the four vertical profiles, difference that, on the contrary, should be expected if due to a measurement bias. For this reason the hypothesis of the measurement bias is rejected and the difference in the vertical profile is considered as a real effect. Further studies will be carried out to test further this hypothesis.

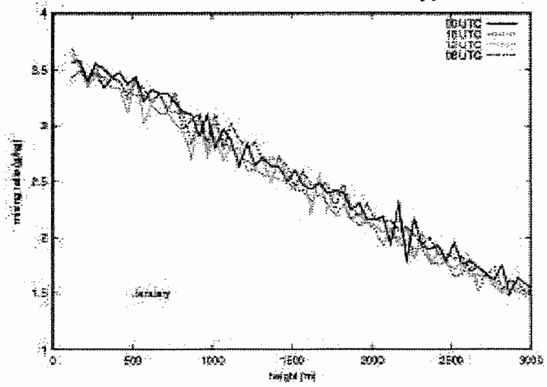

Fig. 3. Vertical profile of the average mixing ratio in the four times-of-the-day for January

To test if the observed differences are due mainly to a relatively small number of outlier soundings we computed the cumulative distribution of the average mixing ratio computed between 1000 and 2000 m, range that encompasses the mean cloud base height in the Friulian plain (Morgan, 1992). The results reported in Fig. 4. show that the observed differences are not due to a small number of soundings, but affect the whole cumulative distribution.

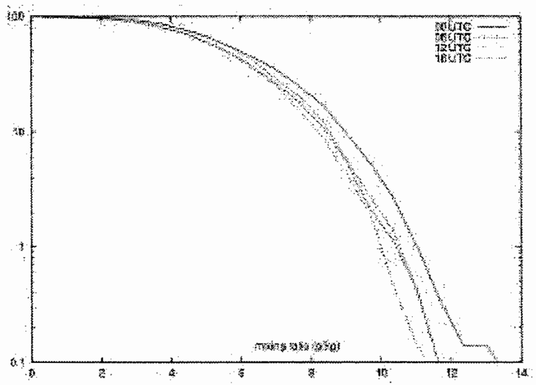

Fig. 4. Cumulative distribution of the average mixing ratio in the four times-of-the-day in the level between 1000 and 2000 m.

3. The effects of the mixing ratio on hail growth

The effects of the increased mixing ratio during night-time on hail growth are studied using the following simple equation (Knight and Knight, 2001)

$$\frac{dD}{dt} = V_\infty \cdot LW \cdot E \cdot \frac{\rho_w}{2\rho_i}$$

with *LW* the liquid water content of the cloud, *E* the collection efficiency, ρ_a the air density, ρ_w the water density, ρ_i the ice density and V_∞ the hailstone terminal velocity given by the formula

$$V_\infty = \left(\frac{4g\rho_i D}{3C_d\rho_a}\right)^{0.5}$$

where C_d is the drag coefficient.

It is possible to show that inserting the explicit form of the terminal velocity in the growth equation, assuming a diameter for the hail embryo D_e = 5 mm and using an average air density $\rho_a = \overline{\rho_a}$, the final diameter reached after a time interval Δt is given by the expression

$$D^{0.5} - D_e^{0.5} = \left(\frac{g\rho_w^{\ 2}}{3C_d\overline{\rho_a}\rho_i}\right)^{0.5}\frac{LW}{2}\cdot E\cdot\Delta t$$

If we assume that the liquid water content is equal to the difference between the observed mixing ratio x at the cloud base and the saturation mixing ratio $x_s(T)$ at T=-15 °C, average temperature of the level in which hail grows (Knight and Knight, 2001), that is

$$LW = x - x_s(T)$$

we have

$$D^{0.5} - D_e^{0.5} = \left(\frac{g\rho_w^{\ 2}}{3C_d\overline{\rho_a}\rho_i}\right)^{0.5}\frac{(x - x_s(T))}{2}\cdot E\cdot\Delta t$$

If we take the ratio between the diameter obtained after a same interval Δt but in environments that differ for their mixing ratio at cloud base, that is x_a and x_b with $x_a > x_b$, we have

$$\frac{D_a^{0.5} - D_e^{0.5}}{D_b^{0.5} - D_e^{0.5}} = \frac{(x_a - x_s(T))}{(x_b - x_s(T))}$$

This equation, even if obtained by crude assumptions, shows that the difference in diameter for hailstones that grow in environments which differ for the amount of mixing ratio is a nonlinear function of this difference and of the diameter itself, that is

$$\Delta D_{a-b} = \left[D_e^{\ 0.5} + \frac{(x_a - x_s(T))}{(x_b - x_s(T))} \left(D_b^{\ 0.5} - D_e^{\ 0.5} \right) \right]^2 - D_b$$

As a result of this equation, the hailstone's size distribution for hail grown in an environment characterized by an average mixing ratio x_a at cloud base is related to an hailstone's size distribution given by an environment characterized by an average mixing ratio x_b according to the relationship

$$N(D_a) = N(D_b)$$

This means that the number of hailstones with a diameter D_b in an environment characterized by the mixing ratio x_b becomes the number of hailstones with a diameter D_a in an environment characterized by a mixing ratio x_a. Because, thanks to the nonlinear relationship between the final diameter and the mixing ratio, hailstones with a greater diameter become larger than those smaller, the result of this transformation is a stretching of the distribution which enlarges its cue when the mixing ratio increases. If we transform the afternoon distribution into the night distribution according to the observed average differences in the mixing ratio, these almost coincide, as shown in Fig.5.

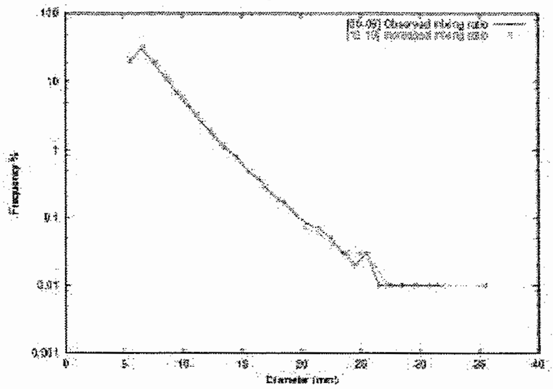

Fig 4. Observed size distribution during night-time ([00-06[local time) and evening size distribution ([18-24[local time) obtained keeping into account a night-time vertical mixing ratio.

4. Conclusions

The results obtained using this simple analytical model implementing the observed differences in night-time mixing ratio, show that the difference between the observed hailstone's size distributions in the different times-of-the-day can be explained taking into account the observed differences in the vertical mixing ratio amount. Being these results obtained only using general physical considerations, it is expected that similar observations could be found even in other areas and regions.

5. References

Danielsen, E., F., 1976: Hail: a Review of Hail Science and Hail Suppression, Meteor. Monog., 38, 135-143.

Fawbush, E., F. and Miller R., C., 1953: A method for forecasting hailstone size at the earth's surface. Bull. Amer. Meteor. Soc., 34, 235-244.

Giaiotti, D., B., Nordio, S. and Stel, F., 2003: The climatology of hail in the plain of Friuli Venezia Giulia. Atmos. Res., 67-68, 247-259.

Giaiotti, D., B., Gianesini, hailstone's size distribution E. and Stel, F., 2001: Heuristic considerations pertaning to the hailstone size distributions in the plain of Friuli Venezia Giulia. Atmos. Res., 57, 269-288.

Knight, C., A. And Knight N., C., 2001: Hailstorms. Meteor. Monog., 50, 223-249.

Morgan, G., M., Jr., 1970: An examination of the wet bulb zero as a hail forecasting parameter in the Po valley, Italy. J. Appl. Meteor., 9, 537-540.

Morgan, G., M., Jr., 1992: Some results of aircraft investigation of internal properties of thunderstorm cloud systems in northeastern Italy with an interpretation for hail prevention. Atmos. Res., 28, 259-269.

Prodi, F. And Wirth E., 1973: Mesoscale and Microphysical Investigation of an Isolated Hailstorm. Rivista Italiana di Geofisica, XXII 3-4, 165-185.

A STUDY ON PRECIPITATION FORMATION MECHANISM OF COLD FRONTAL CLOUD SYSTEM IN HENAN PROVINCE

Hong Yanchao[1] Liu Zhongxiu[2] Taoyue[1]

1: Institute of Atmospheric physics, CAS, 100029, Beijing; China
2: Chinese Meteorological Society, 100080, Beijing, China

1. INTRODUCTION

In artificial precipitation, frontal cloud system is an important seeding object and its various studies and understanding, especially studies of microphysical structure and mechanism of rainfall are the bases. In this paper, a cold frontal stratiform cloud system that move pass on Henna province on April 5, 2002 is simulated by cloud numerical model containing detail microphysical processes to study the precipitation mechanism, chain of precipitation formation and to analyze condition for artificial precipitation.

2. NUMERICAL SIMULATION ON CLOUD MICROPHYSICAL STRUCTURE

There is asymmetry radar echo which contains strong echo cores with reflectivity of 25-30dBz in the cold frontal cloud system; It can be seen on RHI echo that the top height of the echo is about 8km and radar bright band is located in about 3km level and with reflectivity of 30-40dBz. Over the bright band, there is an inhomogeneous radar echo with reflectivity of 0-20dBz, so that the structure of the bright band is to correspond the cloud protuberance (fig.1). The radar bright band indicates contributing of ice phase microphysical in the cloud to precipitation formation.

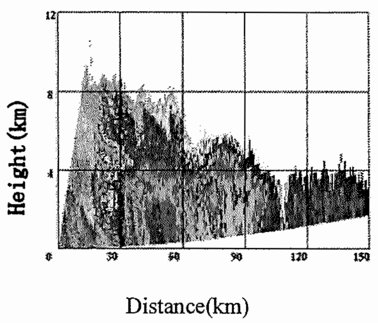

Fig.1 RHI echo from the cloud system at Zhengzhou station on April 5, 2002(time 07：06，azimuth 214°)

Corresponding author's address: hong Yanchao, Institute of Atmospheric Physics, CAS, Bejing, China; E-Mail: hyc@mail.iap..ac.cn

Using the radio-sounding at 05:00 on Zhengzhou station to be located in the frontal zone and 1-D stratiform cloud numerical model, which is the a predigest version from 2-D mixed cloud mode(Hong,1997) and with detail microphysical processes including condensation(VD), collection(CL), nucleation(NU), multiplication(P), melting(ML), auto-conversion(CN) processes, vertical structure of the cloud system is simulated.

Vertical distribution of radar reflectivity of simulation cloud is showed in fig.2. The top height of OdBz and 10dBz radar echo, height and intensity of radar bright band are consistent with that of observation (Fig1).

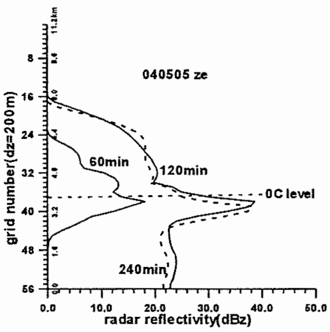

Fig.2 vertical distribution of radar reflectivity for thesimulation cloud.

3. CLOUD MICROPHYSICAL STRUCTURE CHARACTERISTIC

It can be seen from fig.3 that ice crystal and snow only exist in region over 0°C level，and graupel particle can descent to 3km level and melting of graupel has contribution to formation of rainwater; on the other hand, high graupel water content area is consistent with cloud water zone，it shows that formation of graupel is relatve to supercooled cloud water. It is obvious that in stratiform cloud, microphysical structure has remarkably stratificating characteristic: the upper part of the cloud consist of ice articles, nearby 0°C level exist mixed layer consisting of ice and liquid water, and under the 0°C level only liquid water. This is typical "seeder-feeder" cloud structure.

4. MECHANISM OF PRECIPITATION FORMATION IN STRATIFORM CLOUD

4.1 'Seeder-feeder' Cloud Precipitation Formation Mechanism

It can be seen from table 1 that In the stratiform cloud located in frontal zone, Ice crystal grows mainly by sublimation, total mass of ice crystal (TQi) almost equals to sublimation amount (TVDvi).

Snow particles are produced by auto-conversion of ice crystal (CNis) and grow by three microphysical processes which are: collection of ice particles by snow (CLis), collection of cloud droplets by snow (CLcs), deposition of water vapor on snow (VDvs). The appearing heights of different growing process of snow are different. From the maximum value, growing rate of snow by accretion of cloud water is bigger than that by deposition. But total masses of snow growing by deposition and collection are all higher than that by accretion. 77 % of the snow mass is by CLis and VDvs process. Owing to influence of microphysical processes on snow growing, the maximum producing rate of snow is about at the height of 4.4km.

Graupel particle is formed by conversion (CNsg) of snows, which grow by accreting supercooled cloud water. Because the accretion takes places in a narrow vertical region and conversion to graupel particles also occurs in this region. After graupel particles form, theygrow mainly by accretion of cloud water (CLcg) and collection of snow (CLsg). Producing amount of CNsg, CLcg and CLsg process account for 94 % of the total mass of graupel.

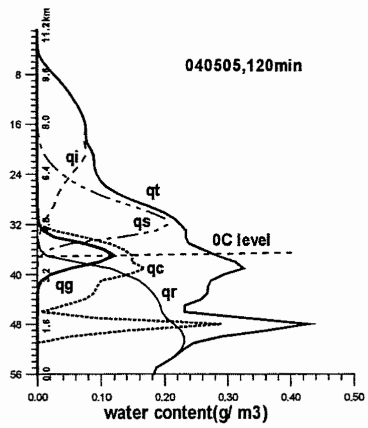

Fig.3. Distribution of water content of various particles with height at 120min in the simulation cloud.. The subscript stands for particle types: c cloud water,i ice crystal, s snow, g graulel ,r rainwater. Qt is total water content of various particles.

Rain is produced by three microphysical processes, which are collection of cloud water by rain (CLcr), melting of ice particles in warm region (MLxr), and collection of cloud water by melting ice particle (CLcxr) in warm region. Figure 3 shows that the melting of graupel particles (MLgr) contributes a lot to rain, and the total amount of producing rain by MLgr process accounts for 57 percent of the total amount of producing rain. Below 2.8km, rain droplets grow mainly by collection of cloud water (CLcr). The contribution of MLxr process on rain also cannot neglect. The melting and collection of cloud water in warm sector by melting ice particle accounts for 70.3% of rain water amount.

Table1. At 300 min, the total amount (unit: kg/m2) of source terms of all particles in simulated cloud

TQi	TVDvi	TPci	TCLci	THNUci		
4.05	4.03	0.00	0.02	0.00		
TQs	TCNis	TCLcs	TCLis	TVDvs	TCLii	
4.21	0.20	0.76	1.65	1.59	0.00	
TQg	TCNsg	TCLcg	TCLig	TCLsg	TCLrg	TVDvg
5.89	1.52	1.63	0.02	2.33	0.22	0.17
TQr	TCNcr	TCLcr	TMLsr	TMLgr	TCLcxr	
9.94	0.00	2.93	0.02	5.68	1.31	

Note: Q stands for mass. Capital letter T expresses mass total amount.

4.2 Precipitation formation mechanism in different position of the cloud system

At 20:00 April 5, 2002, Yingchuan station was located in post-frontal area far from the frontal zone, precipitation forms mainly by ice-phase process, in which snow water content is the largest. There are only ice crystals, snow and a few graupel particles in the cloud, while not cloud water. Snow is from conversion of ice crystals, and grows mainly by deposition. Therefore deposition is primary growth way of ice-phase particles in the cloud due to be short of supercooled cloud water. Formation Process of graupel is different from that in frontal and pre-frontal area, is not by conversion of snow but by freezing of small supercooled raindrops and they grow mainly by collection of snow but also not by accretion. Within cloud, rain comes from melting of snow and graupel without warm cloud process.

At Zhengzhou station in pre-frontal area, while ice-phase particles don't appear, rainwater is formed by warm cloud process, rain water content increases suddenly from 0.15g/m3 to 0.4g/m3 with water contents of ice crystals, snow, and graupel increase. These mean that cold cloud process contributes a lot to precipitation. Formation process of snow and graupel is identical with that in frontal area. On the other hand, collection of cloud water by melting ice particle contributes a lot to rain formation in warm region. Upper precipitation particles may further grow by collection of cloud water in warm region. In contrast to frontal area, warm-cloud processes contribute a lot to precipitation formation, 60% of rainwater amount is generated by warm-cloud process.

Therefore precipitation formation mechanism differs from one location to another in the frontal cloud system. So cloud seeding technique for precipitation enhancement should be different, it cannot use only one method, and seeding technology is further studied on the basis of studying precipitation formation mechanism.

5. CONTRIBUTION OF VARIOUS CLOUD LAYER IN "SEEDER-FEEDER" CLOUD ON RECIPITATION

According to the microphysical structure, simulated cloud may be divided into three layers: ice phase layer, ice and water mixed layer and liquid water layer. From vertical distribution of precipitation amount of simulated cloud (Figure 4), total precipitation amount increases with decrease height above cloud base, but increase speed of precipitation amount is different, that means different layer of cloud contributes differently to precipitation. The particles falling into the mixing layer from ice phase layer are mostly snow. Snowfall intensity (Ps) is 0.67mm/h, and snow amount is about 2.51kg/ m2. In this layer, 90 percent of snow is converted into graupel, and supercooled water is consumed mainly by snow and graupel. Therefore particles fall into liquid water layer are mostly graupel. Graupel fall intensity (Pg) is 1.29mm/h, and graupel amount is about 5.59kg/ m2. It indicates that ice phase particles fall into the mixing layer grow by deposition and accretion, which increases 3.08 kg/ m2 in precipitation amount. In warm region of 'feeder' cloud, graupel particles melt into rain, and at the same time cloud water to be collected by graupel convert into rain. In rainwater amount of 9.94kg/m2 in warm sector, contribution amount of melting graupel is 6.99 kg/m2. At the cloud bases, rain intensity (Pr) is 2.26mm/h. Owing to evaporation of precipitation below cloud bases, rain intensity at the ground decreases to 1.72mm/h.

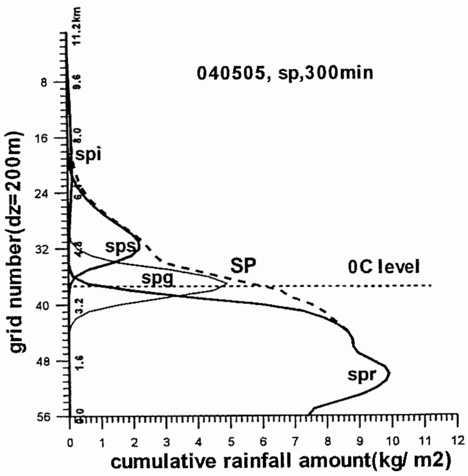

Figure 4. At 300 min, the distribution of cumulative rainfall amount with height in stimulated cloud at 05:00 on 5 April 2002 at Zhengzhou station.

It is seen from figure 5 that contributions of ice phase layer, mixing layer, and liquid water layer within stimulated cloud to precipitation are about 25.5 percent, 31.3 percent, and 43.1 percent, respectively. That means contribution of 'feeder' cloud on precipitation is about 74.4 percent. Furthermore, contribution of graupel on precipitation is 70 percent, which means cold-cloud process has an important effect on precipitation and ice particles grow in the mixing layer are also significant to precipitation formation.

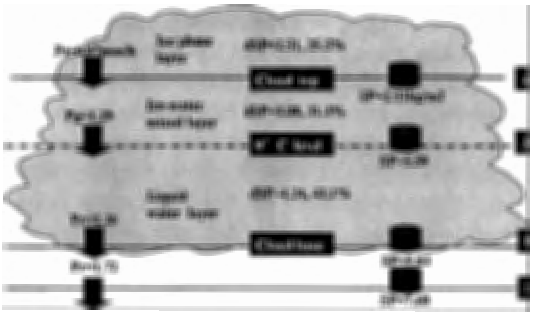

Figure5. Contribution rate of each layer on precipitation (SP is precipitation amount, dSP is increased precipitation amount)

6. ANALYSIS OF ARTIFICIAL PRECIPITATION CONDITIONS

Analysis of formation process of stratiform cloud precipitation shows that cold-cloud process has a very important effect on precipitation. Deposition and accretion are main growing processes of ice particles. So that vapor and supercooled water content is important condition of natural precipitation formation and artificial precipitation.

whether effect of vapor or supercooled cloud water on rain formation is the biggest? The amount of producing rain by deposition is as follows:

((VDvi.Pis+VDvs)Psg+CLig)PMLgr=3.05 (kg/m2)

In which Pis=(TCNis+TCLis)/TQi; Psg=(TCNsg+TCLsg)/TQs; PMLgr=MLgr/TQg

Rain amount produced by the accretion is as follows:

(CLcs.Psg+CLcg) PMLgr=2.24 (kg/m2)

As we know the amount of producing rain by graupel melting is 5.68 kg/m2, in which the rainwater amounts by conversion of vapor and supercooled cloud water are 3.05 and 2.2.4kg/m2. That means contribution rate of the vapor is 54 percent and supercooled cloud water is 39 percent. Therefore not only supercooled cloud water is an important seeding condition but also vapor in artificial precipitation for stratiform cloud.

On the other hand, ice crystals are important particles to start precipitation formation and contribution of 'feeder' cloud on precipitation is about 74.4 percent. Furthermore, Therefore, if water content within 'feeder' cloud is very low, large precipitation doesn't form in stratiform cloud, in which exists 'seeder-feeder' mechanism of precipitation formation. In turn, without seeding of ice particles in upper level, large precipitation also doesn't form only by depending on middle and low cloud. 'Seeder-feeder' cloud process should be one of artificial precipitation conditions. Furthermore, no doubt supercooled cloud water content in 'feeder' cloud is an important precipitation enhancement condition but study of precipitation mechanism shows that melting ice particle grows by collection of cloud water in warm region of 'feeder' cloud and contribution of growth amount of it on precipitation enhancement is 10 percent. Therefore cloud water content and cloud thickness in warm region of 'feeder' cloud can also be considered as precipitation enhancement condition.

7. CONCLUSION

Generally, there are ice phase layer, ice - water mixed layer and liquid water layer in typical "seeder-feeder" stratiform cloud system. The ice-water cloud, as a seeding cloud, has a contribution of 25.5% to rainfall, the mixed layer 31.3% and liquid water layer 43.1%, i.e., contribution of the feeding cloud to precipitation is about 74.4%.

In different position, the precipitation formation mechanisms are different. At the position behind and far from frontal zone, there is no liquid water and very low condensation rate in the cloud, so that graupels are produced by freezing of little raindrops, but in other zones, from auto-conversion of snow.. In front part of the frontal zone, contribution of warm cloud processes to rainfall is large and in the frontal zone cold cloud processes.

"Seeder-feeder" system is an important structure condition for artificial precipitation. The sublimation and collecting cold water are main growing processes for ice particles and important processes to producing precipitation; as same as supercooled cloud water, water vapor is also an important condition for artificial precipitation because it and supercooled water almost have a same contribution to rainwater.

Acknowledgement: The paper was subsidized by Chinese study item (2001BA610-06-03).

REFERENCES

Hong Yanchao, 1997, A numerical model of mixed convective-stratiform cloud, Acta Meteorologica Sinica, .11,,489-502.

STRUCTURE AND DYNAMICS OF THE DEVELOPMENT AND CLASSIFICATION OF THE HAIL-STORM PROCESSES IN UZBEKISTAN

Imamdzhanov Kh.A.

Main Administration of Hydrometeorology
at the Cabinet of Ministers of the Republic of Uzbekistan

INTRODUCTION

The conditions of the hail-storm processes development are determined by a set of circulation and thermal-and-dynamic characteristics of the atmosphere, which, as the other climatic phenomena are subjected to the laws of the latitudinal zonality and vertical extension. However, the effect of these factors is mainly corrected by the peculiar features of the geographic position of the region and its relief.

Hail-storm processes have a numerous regional features. The structure and dynamics of their development, direction and moving velocity are mainly being transformed under the impact of the effect of the underlying surface. Nevertheless, the hail-storm processes, which are being observed in very different physical-and-geographical conditions, can have their characteristic features, different frequency of occurrence, etc.

CLASSIFICATION OF THE HAIL- STORM PROCESSES

The following specific features are used in the classification of the hail-storm processes:

- Cell structure of the hail-storm process
- Dynamics of the development of the convective hail-storm cloud system and separate convective cells
- Form (symmetric, asymmetric) of individual convective cells
- Regularities of the extension of the cloud processes and precipitation formation in space (discrete, discrete-permanent, permanent)
- Direction and velocity of movement of separate convective cells in relation to the transport of the processes relating the clouds and precipitation-formation and the vector of dominant flow (along the flow, to the left or right from the flow).

In [1, 2] the description of the slightly idealized features of the hail-storm processes are presented. The types of the hail-storm processes which are being observed in a real life are much more diverse and complicated.

THE AREA OF STUDIES

The Fergana valley which occupies the eastern part of Uzbekistan (which can be compared with the typically hail-prone areas of CIS states in relation to the frequency of hail phenomenon) is the most interesting region in this concern. The surface area of this valley is 18, 2 thous. km^2. The range of the spectrum of the forms and shapes of the hail-stones is rather wide. The diameter of the hail-stone can be 0,5<d<12,0 cm while in the majority of cases it was 0,5<d<2,0 cm. The total area of the territory under the hail-protection activities is 741 000 he where 57 points of missile means are installed. In this area the basic studies and investigations of the structure and dynamics of the development of the hail-storm processes were carried out.

TYPES OF THE HAIL-STORM PROCESSES

The results of investigations of the hail-storm processes carried out in Fergana valley have shown that by the thermodynamics conditions of atmosphere, synoptic situation and physical and geographic characteristics of the region the following types of the hail-storm processes can be distinguished:

1. One-cell hail-storm processes
2. Multi-cell hail-storm processes
3. Super-cell hail-storm processes
4. Frontal band of the hail-storm processes, i.e., squall-line.

The results of studies [3-6] have shown that numerous hail-storm processes observed in Fergana valley depending on the wind-regime and thermodynamic characteristics can be defined as follows:

- Organized multi-cell hail-storm processes – right-hand moving processes with the cell-formation on the right side and moving to the left from the direction of the process development, but to the right from the dominant flow
- Non-organized multi-cell hail-storm processes – right-hand moving processes with the cells which are chaotically formed in different parts of the hail-storm process and chaotically moving to the left from the dominant flow and process.

ONE-CELL HAIL-STONE PROCESSES

One-cell hail-storm processes are observed during the days with convective instability: W_{max} = 10^m/sec with the wind velocity V_w = 4^m/sec and wind shift $2 \cdot 10^{-4} sec^{-1}$ in the atmosphere. As a rule, the wind in a surface layer (up to 2-2.5 km) has the eastern or south-eastern direction; upper than 3 km – it is mainly western or north-eastern. The liquid content of the atmosphere is $q \le 28$ kg/m^2 while the relative humidity is ~ 35%.

One-cell hail-storm processes involve several simultaneously existing and usually axis-symmetric convective cells with the different stage of their development (development stage, maturity stage or quasi-stationary state, dissipation stage). Axis-symmetric convective cell is fast developing acquiring the maximum radar characteristics without the stage of quasi-stationary stage and begins to collapse. The stage of development and dissipation is 5-20 min. The existence of insignificant wind shear (less than $1 \cdot 10^{-4}$sec^{-1}) provides for the slope of the cloud axis and, due to this, a certain spatial separation between the updrafts and falling precipitation and, consequently, the increase of the life-time of convective cell.

The horizontal size of the one-cell hail-storm processes is ~ 10 – 20 km.

It is difficult to predict the area of the convective cells origination in the one-cell hail-storm processes, because it has a random character and is determined by the local orography. One-cell hail-storm processes develop over the mountains up to the middle of the day, and during the second half of the day they move into the foothills and plains. Being collapsed in one location, they immediately appear in the other one with a weak drift. Hail and rainfall events cause the fast natural destruction of these clouds. Afterwards, because of the short life-time and low cell mobility the hail precipitation is formed and falls as localized spot, which is being observed in 10% of cases.

ORGANIZED MULTI-CELL HAIL-STORM PROCESSES

The organized multi-cell hail-storm processes are being developed during the days of a high convective instability with the high position of the maximum velocity level of the up-draughts. The processes of this type are intensive and long and are observed in 50% of cases. The direction of trajectory of the organized multi-cell storm-hail processes is declined on 10-80° to the right from the trajectory of the dominating flow, while the convective cells move on 0-80° to the left from the dominant flow. As a rule, the new convective cells are formed on the right side of the windward part of the cloud system. The velocity of separate convective cells movement is:

$$0{,}3\, V_d < Vc < 1{,}5\, V_d$$

V_d - velocity of the dominant flow.

New cells are formed on the windward side of the hail-storm process in the "hook" of a radar echo which restricts the zone of up-draughts. It is worth to mention that the field of the up-draughts develops in time around the centre of the mass of the cloud being fed in a clock-wise direction. Besides, in the hail-storm process the cell is turning round its axis. This is because the right front of the hail-storm process spreads faster than the left one, as the velocity of its movement is formed of the velocities V_c of the cells movement, V_r of uninterrupted extension of radar echo at the expense of the increase of the area of the newly formed and developing young cells on the right front and V_d - of the discrete extension at the expense of the formation of new cells at the right front, close to the front margin of the hail-storm process.

At the same velocity of the convective cells movement on the right front, in the centre and on the left front we have the following expressions for the total velocity of the extension of the above-mentioned components of the hail-storm process:

$$V_r = V_c + V_r + V_d$$

$$V_{cn} = V_c + V_r$$

$$V_l = V_c$$

From this we can make a conclusion about the rotating of the hail-storm process around the mass centre. This rotation is caused only by the big velocity, uninterrupted and discrete extension of the new cells on the right front. I.e., the rotation of cells is determined by the rotation of jets of the up-draughts depending on the Coriolis force from the jet of the up- or down-draught . In this case the direction of the rotation is determined by the directions of the dominating and vertical flows.

NON-ORGANIZED MULTI-CELL HAIL-STORM PROCESSES

Non-organized multi-cell hail-storm processes are observed during the days with the complex wind structure in the atmosphere when its direction and velocity are sharply changed with the altitude. Non-organized multi-cell hail-storm processes develop with the moderate and high instability and with a slightly decreased liquid content in comparison with the organized ones. Non-organized multi-cell hail-storm processes are observed with the western, northern and north-western intrusions of the main and secondary cold air masses and are recorded in 20% of cases. These processes are stronger and last longer.

The longer life-time of convective cells is due to the simultaneous existence of several up-draught zones in the non-organized multi-cell hail-storm processes. In this case, up-draught zones are located on the periphery of the hail-storm process, both at the right and left margins, and front and back ones. The appearance of new cells is recorded above the up-draught zone. The transverse size of the up-draught is 10-15 km.

For the non-organized multi-cell hail-storm processes formed with the complex structure of wind in the atmosphere the chaotic formation of convective cells in different parts of hail-storm process is typical. Different convective cells decline in different directions and move along different directions in relation to the movement of the whole cloud-formation process. In some cases the same convective cell can shift from the initial direction to 60-90° and sometimes – to 160°. The cyclonic rotation is not observed in this process as it is in the multi-cell hail-storm process.

Low-organized multi-cell hail-storm processes

Low-organized the multi-cell hail-storm processes are observed with the north-western and western intrusions of the main and secondary cold air masses in relatively dry in the surface layer and cold air mass with the altitudinal change of the wind direction and shear. Low-organized multi-cell hail-storm processes are short and not so intensive, being observed in 10% of cases. Thermodynamic and wind characteristics, liquid content of the atmosphere are less than in the organized and non-organized multi-cell, super-cell hail-storm process. Hail precipitation is not observed with such processes.

Super-cell hail-storm processes

Super-cell hail-storm processes are observed in 10% of cases. For these processes such conditions as a high potential atmospheric instability, high liquid content, high-altitude cold air masses intrusion (when the south-eastern flows are observed in the surface layer, while the south-western and western ones are observed in the intermediate and upper layers with the velocity increase with the altitude) are favorable. The life-time of the super-cell hail-storm processes is about 1–5 hour. The length of a hail lines is 30-80 km, their width - 3-10 km, hail-stone diameter – 8,0 cm and hail-layer density – 10-15 cm.

The hail-formation process in a super-cell hail-storm cloud is stable and uninterruptedly spreads in the space due to the constant renovation in the front part and disruption in the back one.

Frontal line of a hail-storm line - squall line

Squall-line – hail-storm process is observed very seldom in 2-4 5 of cases. The structure and dynamics of the process development is similar with the organized multi-cell and super-cell hail-storm process. In the course of evolution process one process can transform into the other one.

CONCLUSIONS

The following hail-storm processes are observed in Fergana valley differing by their structure and evolution dynamics: single-cell, organized multi-cell, non-organized multi-cell, low-organized multi-cell, super-cell and squall-lines – hail-storm processes. The following regional features were found out on the base of the hail-storm processes observations:

- Large-scale nature and long life-time
- Relative scarcity of single-cell processes, being formed with the wind shears of $6 \cdot 10^{-5}$ -3 $\cdot 10^{-4}$ sec^{-1} and wind velocity of V_w = 5 m sec^{-1}.
- Development of a large number of convective cells
- Hail-forming convective cells are originated at 4-8km altitude

3 following evolution stages of the convective cells are recognized:
Development stage - 10-20 min period
Stage of quasi-stationary state – 120-180 min. period
Dissipation stage - 10-20 min period.

The stage of quasi-stationary state is absent in single-cell hail-storm processes.

During the evolution phase in the first turn the upper limit height of the zone of the increased reflectivity – H_{zir} gets the maximum value, then – radar reflectivity (η), then – upper limit height of radar echo (H_h) and at last – radar echo area (S_{ra}).

The above mentioned parameters decrease in the same order in dissipation stage.

The differentiated techniques of the weather modification of different hail processes depending on their structure and evolution dynamics is introduced into practice.

The derived regularities can be used in the forecasting of the expected types of the hail-storm processes. The parametric model is developed for the hail-storm processes showing the regional features of their structure and evolution dynamics.

REFERENCES

1. Chisholm A.J. and Renick J.H. Supercell and multicell Alberta hailstorms.//Proc. Intern. Cloud Physics Copnf. – London. – 1972.-P.67-68, 82-85.
2. Marwitz J.D. The structure and motion of severe hailstorms. Parts I-III.//.J. Appl. Meteorol.- 1972. – vol.11. – N 1. – P.166-201, 236-238.
3. Imamdzhanov Kh.A. Parametrical model of hail-storm clouds//Proceed. SANIGMI of Goskomgidromet.-1984.-vol. 100(181).-P.14-21.
4. Imamdzhanov Kh.A. supercell hail process on the north of Fergana valley.//Proceed. SANIGMI.-1990-vol.110(191).- P.78-87.
5. Imamdzhanov Kh.A. Methodical recommendations on weather modification on the hail-storm processes in Uzbekistan.//Tashkent-1985.-20 pp.
6. Imamdzhanov Kh.A., Kamalov b.A. Uzbekistonda ob-khavodga tasir etish.//Tashkent.-2001.-120 pp.

A CLIMATOLOGY OF CONVECTIVE PRECIPITATING PATTERNS IN AFRICA

Arlene G. Laing[1], Richard Carbone[2], Vincenzo Levizzani[3]

[1]Department of Geography, University of South Florida, Tampa, FL USA
[2]National Center for Atmospheric Research, Boulder, CO, USA
[3]CNR-Institute of Atmospheric Sciences and Climate, Bologna, Italy

1. INTRODUCTION

The prediction of precipitation, particularly quantitative precipitation forecasting (QPF) remains one of the greatest problems in weather forecasting. Warm season precipitation presents an even greater challenge as the precipitation forms under relatively benign synoptic conditions and is strongly modulated by diurnal heating. The goal of this study is to develop a climatology for warm-season precipitation in Africa based on the propagation characteristics of convective precipitation. The term "warm season" as applied to Africa, a continent that straddles the equator, is more indicative of the precipitation regime change than the temperature.

In the United States (US), studies of the lifecycles of mesoscale convective systems (MCSs) have found that the majority of these systems initiate in the lee of the Rocky Mountains, move towards the east and produce an overnight maximum in precipitation across the central plains, sometimes while undergoing various cycles of regeneration (Maddox 1980, Fritsch et al. 1986; Augustine and Caracena, 1994; Davis and Anderson and Arritt 1998, Trier et al. 2000). Using Weather Surveillance Radar-88 Doppler (WSR-88D) data, Carbone et al. (2002) found that clusters of heavy precipitation display coherent patterns of propagation across the continental US with propagation speeds for envelopes of precipitation that exceed the speed of any individual MCS. Wang et al. (2003) developed a similar climatology for warm season precipitation in East Asia using infrared brightness temperatures from the Japanese Geostationary Meteorology Satellite (GMS). Their study showed propagation of cold-cloud clusters (or quasi-precipitation episodes) across a zonal span of 3000km with a duration of 45h compared with 60h for the precipitation episodes in the US. The discovery of similar coherence is not surprising as MCSs in both regions have similar properties (Ma and Bosart 1987; Miller and Fritsch 1991).

Given the similarity in the properties of MCSs globally (Laing and Fritsch 1997), coherence in propagating characteristics is expected for precipitation over Africa. For example, the escarpment of South Africa serves as the initiating point for convection that propagates to the east.

Corresponding author address: Arlene Laing, Visiting Scientist, NCAR/MMM, P.O. Box 3000, Boulder, CO, e-mail: laing@ucar.edu

(Garstang et al. 1987; Laing and Fritsch 1993). In Sahelian Africa, the Jos Plateau (west Africa), the mountains of Dafur (western Sudan), and the Ethiopian highlands are regions where squall lines and mesoscale convective complexes originate (Tetzlaff and Peters 1988; Laing and Fritsch 1993). Other studies of west African squall lines and cloud clusters have found that systems are modulated by easterly waves, the low-level jet, and moisture convergence in the lower troposphere (e.g., Payne and McGarry 1977; Frank 1978; Bolton 1984; Machado et al. 1993; Rowell and Milford 1993; Thorncroft and Haile 1995).

Convection and precipitation over Africa also varies inter-annually (Duvel 1989, Ba et al. 1995). Desbois et al. (1988) found that African squall lines had different initiation points, tracks, and speed for July 1983 and July 1985. Those differences are related to the large-scale dynamics like the interannual variability of the Inter-tropical Convergence Zone migration.

2. DATA AND METHODS

Digitized images from the European geostationary satellite (Meteosat) for a multi-year period will be used to document convective precipitation episodes over Africa. The initial study period is May through August of 1999. The infrared (11.5µm) images have a spatial resolution of 5km at the sub-point (0, 0) and are available at 30 minute intervals. A threshold technique is used to identify cold cloud systems that are most likely to be precipitating. For example, Duvel (1989) used 253K as the threshold associated with convection while Arkin (1979) used 233K for identifying accumulated convective precipitation. Mathon and Laurent (2001) used 213K to identify very deep convection over the Sahel. Further discrimination between precipitating and non-precipitating cold clouds is accomplished by comparisons with radar and microwave derived rain rates from the Tropical Rainfall Measurement Mission (TRMM) Precipitation Radar and TRMM Microwave Imager (TMI) respectively. Consideration is also given to techniques for calibrating Meteosat IR with passive microwave measurements from the Special Sensor Microwave Imager (SSM/I) (Levizzani et al. 1996). Comparisons are made with the corresponding water vapor images, which helps to indicate differences between deep layer moisture of precipitating thunderstorms and a layer with mostly cirrus.

Propagation characteristics are determined using a methodology similar to that employed by Carbone et al. (2002) and Wang et al. (2003). Based on the prevailing low-level flow, the continental boundaries, and tracks of mesoscale convective systems, two domains are used for the Hovmoller calculations (Fig. 1). The northern domain covers 5°S to 20°N and 20°W to 40°E from May to September. The southern domain is 35°S to 5°N and 5°E to 40°E from October to April. The second domain includes prevailing easterly flow north of 15°S and prevailing westerly flow to the south.

Global Reanalysis data are used to analyze the large-scale environments associated with deep convective development. Reanalysis pressure level data has a 2.5 degree grid and are provided daily at 0000, 0600, 1200, and 1800UTC.

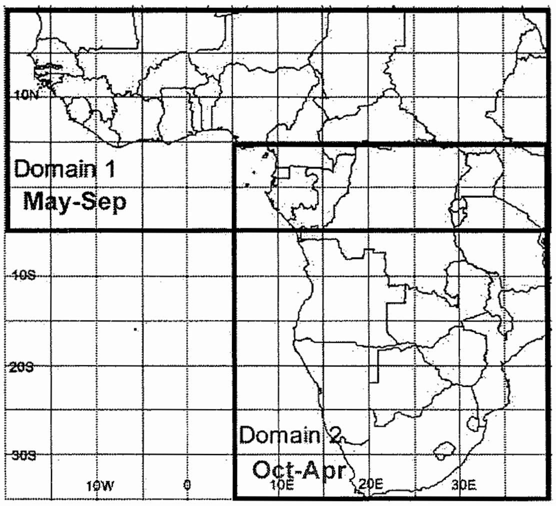

Fig. 1. Domains for the Hovmoller calculations

Results will be presented at the conference.

Acknowledgements

This research is sponsored by National Science Foundation support to the U.S. Weather Research Program. Satellite data are provided by EUMETSAT archives. We appreciate assistance with reading Meteosat data from L Zamboni and F. Torricella.

REFERENCES

Augustine, J. A. and F. Caracena, 1994: Lower-tropospheric precursors to nocturnal MCS development over the Central United States. *Wea. Forecasting*, **9**, 116-135.

Anderson, C. and R. Arritt, 1998: Mesoscale convective complexes and persistent elongated convective systems over the United States during 1992 and 1993. *Mon. Wea. Rev.*, **126,** 578-599.

Arkin, P.A., The relationship between fractional coverage of high cloud and rainfall accumulation during GATE over the B-scale array. *Mon. Wea. Rev.*, **107**, 1382-1387.

Ba, M. B., R. Frouin, S.E. Nicholson, 1995: Satellite-derived inter-annual variability of west African rainfall during 1983–88. . *J. Appl. Meteor*, 34, 411–431.

Bolton, D. A., 1984: Generation and propagation of African squall lines. *Quart. J. Roy. Meteor. Soc.*, **110**, 695-721.

Carbone, R.E., J.D. Tuttle, D. Ahijevych, S.B. Trier, 2002: Inferences of predictability associated with warm season precipitation episodes, *J. Atmos. Sci.*, **59**, 2033-2056.

Desbois, M., T. Kayiranga, B. Gnamien, S. Guessous, and L. Picon, 1988: Characterization of some elements of the Sahelian climate and their annual variations for July 1983, 1984, and 1985 from the analysis of Meteosat ISCCP data. *J. Climate.*, **9**, 867-904.

Duvel, J-. P., 1989: Convection over tropical Africa and the Atlantic ocean during northern summer. Part I: Interannual and diurnal variations. *Mon. Wea. Rev.*, **117**, 2782-2799.

Frank, W. M., 1978: The life cycles of GATE convective systems. *J. Atmos. Sci.*, **35**, 1256-1264.

Fritsch, J. M., R. J. Kane and C. H. Chelius, 1986: The contribution of mesoscale convective weather systems to the warm season precipitation in the United States., *J. Clim.Appl.Meteo.*, **25**, 1333-1345.

Garstang, M., B. E. Kelbe, G. D. Emmitt, W. B. London, 1987: Generation of convective storms over the escarpment of northeastern South Africa. *Mon. Wea. Rev.*, **115**, 429-443.

Laing, A. G. and J. M. Fritsch, 1993: Mesoscale convective complexes in Africa. *Mon. Wea. Rev.*, **121**, 2254-2263.

Laing, A.G. and J.M. Fritsch, 1997: The global population of mesoscale convective complexes. *Quart. J. Roy. Meteor. Soc.*, Jan B, **123**, 389-405.

Levizzani, V., F. Porcu, F. S. Marzano, A. Mugnai, E. A. Smith, F. Prodi, 1996: Investigating a SSM/I microwave algorithm to calibrate METEOSAT infrared instantaneous rain rate estimates. *Meteor. Appl.*, **3**, 5-17.

Ma, K-Y. and L. F. Bosart, 1987: A synoptic overview of a heavy rain event in Southern China. *Wea. Forecasting,* **2**, 89-112.

Machado, L. A. T., J.-Ph. Duvel, and M. Desbois, 1993: Diurnal variations and modulations by easterly waves of the size distribution of convective cloud clusters over West Africa and the Atlantic Ocean. *Mon. Wea. Rev.*, **121**, 37-49.

Mathon, V. and H. Laurent, 2001: Lifecycle of Sahelian mesocale convective cloud systems. *Q.J.R. Meteorol. Soc.*,**127**, 377-406.

Miller, D. and J.M. Fritsch, 1991: Mesoscale convective complexes in the western Pacific region. *Mon. Wea. Rev.*, **119**, 2978-2992.

Payne, S. W. and M. M. McGarry, 1977: The relationship of satellite inferred convective activity to easterly wave over west Africa and the adjacent ocean during Phase III of GATE., *Mon. Wea Rev.*, **105**, 413-420.

Rowell, D. P. and J. R. Milford, 1993: On the generation of African squall lines. *J. Climate*, **6**, 1181-1193.

Tetzlaff, G. and M. Peters, 1988: A composite study of early summer squall lines and their environment over West Africa. *Meteorol. Atmos. Phys.*, **38**, 153-163.

Thorncroft, C. D. and M. Haile, 1995: The mean dynamic and thermodynamic fields for July 1989 over Tropical North Africa and their relationship to convective storm activity. *Mon. Wea. Rev.*, **123**, 3016-3031.

Trier, S. B., C. A. Davis, and J. D. Tuttle, 2000: Long-Lived Mesoconvective Vortices and Their Environment. Part I: Observations from the Central United States during the 1998 Warm Season. *Mon. Wea. Rev.*, **128**, 3376-3395.

Wang, C-C, G. T-J. Chen, R. E. Carbone, 2003: A climatology of warm season cloud patterns over East Asia based on GMS Infrared Brightness Temperature Observations. In review, *Monthly Weather Review.*

Analysis Characteristic of Spring Precipitation Cloud in Shaaxi and Gansu Province

HENG-CHI LEI YU-XIA WU[1] and PENG FAN[2]

[1]Institute of Atmospheric Physics, Chinese Academy of Sciences, Beijing 100029, China
[2]Weather Modification Office of Shaanxi Province, Xi'an 710015, China

1. INTRODUCTION

To increase water supplies in northwest of China, rainfall enhancement through cloud seeding is a possible mean. The stratus cloud is the main operational cloud for weather modification in north of China. To be effective, seeding must be done at the correct time and in the correct manner. Analysis the characteristic of stratus cloud will guide reasonable cloud seeding operation. To analysis the mechanism of precipitation forming and cloud structure for cloud seeding in spring, 711(3 cm) radar was used in Yanan and Xunyi to observe cloud in different synoptic. Numerical simulation of cloud structure was compared with observation. The data we used including radar echo, raindrop spectral data, conventional observation data and satellite images from April to May in 2001 in Xunyi and from March to April in 2003 in Yanan.

2. PRECIPITAION WEATHER SYSTEM AND RADAR ECHO

The precipitation weather system in spring is cold front, cyclone and shear. For 20 precipitation processes, cold font is 14 times which is the dominant weather system, second is the shear which is 4 times, cyclone is only one time. Table 1 gives the precipitation weather system and its characteristic in Xunyi in spring. Rainfall type for cyclone, strong cold front, weak cold front and shear are non-uniformity stratus, hail thunderstorm, uniformity stratus and uniformity stratus shower, respectively.

Table 1 Precipitation weather system and its characteristic in Xunyi in spring.

Weather system	Rainfall duration (h)	Max rainfall (mm)	Max △ T (℃)
Cyclone	>10	19.1	-16.4
Strong cold front	3-4	17.0	-3.8
Weak cold front	>5	1.5	-3.6
Shear	4-5	0.7	-4.9

Table 2 Radar echo characteristic of different weather system

Weather system	Echo max H (km) and T (℃)	Zero level H (km)	Bright band top H (km) and T (℃)	Bright band thickness (m)
Cyclone	7.4(-22.5)	3.3	3.2(0.5)	500
Shear	7.0(-18.5)	3.3	3.1(0.2)	300
Weak cold front	9.0(-30.2)	4.3	4.3(0.2)	600

Table 2 shows the radar echo characteristic of different weather system. Radar echo characteristic for cyclone is two layer, bright band strong core, non-uniformity; for shear is bright band uniformity stratus and for weak cold front is stratus, convective bubble in bright band, two layer, strong core.

Figure 1 (a)-(c) gives the typical radar echo in different weather system.

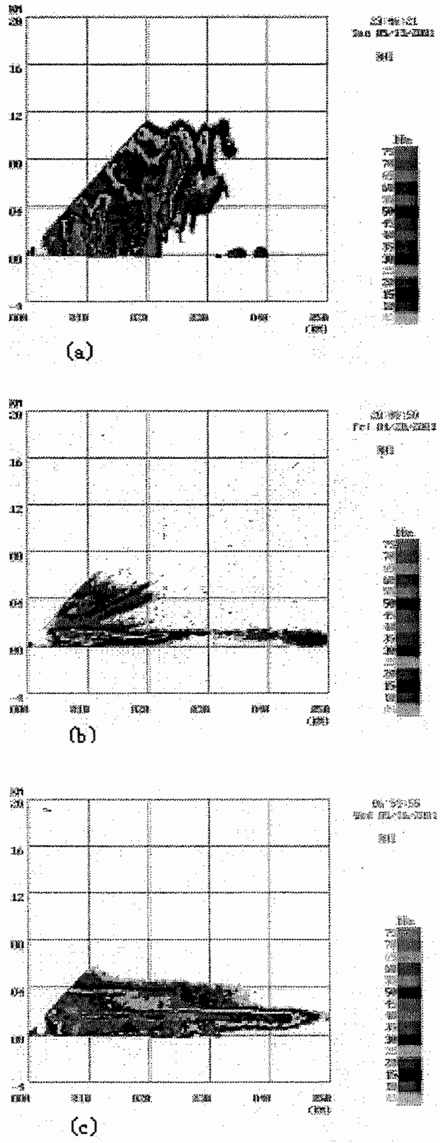

Fig. 1 Typical radar echo in different weather system (a) strong front (b) cyclone (c) shear

3. ECHO CHARACTERISTIC OF FRONT AND STRATUS MODEL SIMULATION

Ahead of front, the radar echo shows bright band, strong core and convective cell, echo height is 7.2 km, bright band height is 4.1 km, water content is 0.04 g/m^3, rain intensity is 0.35 mm/h and spectra width is 0.18mm. Near the front, the radar echo shows strong core, convective bubble and two-layer, echo height is 8.2 km, bright band height is 4.3 km, water content is 0.05 g/m^3, rain intensity is 0.70 mm/h and spectra width is 0.24mm. At the back of front, the radar echo shows uniformity stratus, bright band, not obvious strong core, echo height is 8.2 km, bright band height is 4.3 km, water content is 0.05 g/m^3, rain intensity is 0.70 mm/h and spectra width is 0.24mm. Figure 2 (a)-(c) shows the radar echo at different part of front.

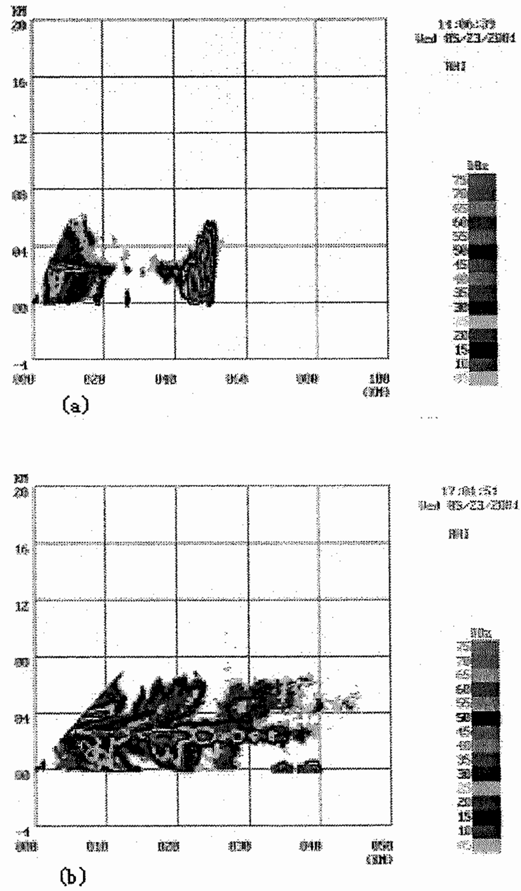

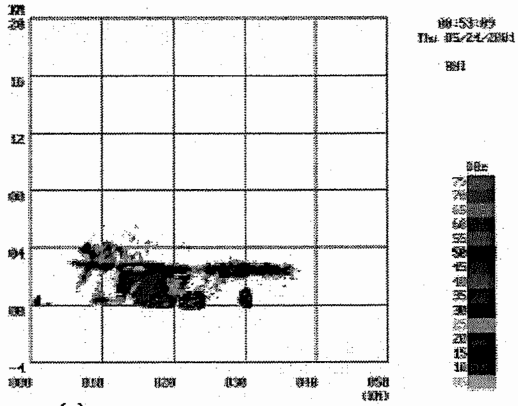

(c)

Fig. 2 Characteristic of radar echo at different part of front (a) ahead of front (b) in the front (c) at the back of front

To simulate the precipitation process on April 1,2003, one dimension stratus model was used. Observation and simulation result shows that the precipitation was formed in cold region and was cold cloud mechanism.

4. CONCLUSION

The ice-crystal process develops stratiform cloud precipitation. A cloud with ice crystals (seeder) moves over the top of a lower, supercooled liquid cloud and precipitates ice down into that cloud (feeder). The supercooled liquid cloud layer with ice will produce snowflakes and ice, and then the ice crystals will melt in the lower, warmer cloud and form precipitation.

5. ACKNOWLEDGEMENTS

Thanks for the support of Weather Modification Office of Shaanxi Province and Yanan city.

6. REFERENCE

Xiao Hui etc., 2002,Earlier identification and numerical simulation of hail storms occurring in Xunyi region, Plateau Meteorology, 21(2), 159-166.

Study of a Typical Cold Front Rain Belt Micro Characteristics, Precipitation Mechanism and Artificial Weather Modification Potential

Liu Jian, Yu Yong, Jiang Tong, Chen Xinzhi

Jilin Province Weather Modification Office, Changchun 130062

1. PREFACE

On May 9, 1995, the central part of our province was impacted by a strong cold front rain belt. The rain started at around 2 am on the morning of May 9th and lasted till the morning of May 10th. It was extensive moderate rain to downfalls. By day of May 9th, our province's artificial precipitation modification planes made three survey flights and obtained quite a lot of macro and micro data about clouds. In order to further understand rail belt characteristics, precipitation mechanism and artificial weather modification potential, we made analyses about this case so as to raise our artificial precipitation operation level. In the analyses, we made use of that day's weather data, satellite and radar data and PMS instrument survey data

2. RAIN BELT WEATHER DYNAMIC CHARACTERISTICS AND CLOUD MACRO FEATURES

This cold front rain belt started from 700 hPa to the lower trough on the ground. Then a 500 hPa strong cold trough from northwest moved east and south, and a 500 hPa strong front zone compounded the impact and generated many rain belts. This process was composed of three rain belts, which affected the central part of our province one after another. The 1st rain belt impact time was from 2 am on the morning to the noon of May 9th; the 2nd rain belt impact time was from 10 am to the dusk of May 9th; the 3rd rain belt impact time was during the night of May 9th. We did not conduct any survey on the night rain belt, so we will only discuss the 1st and 2nd rain belts.

2.1 The First Rain Belt

This rain belt occurred between 700 hPa and the ground cold front, and was intensified with the increase of the correlated front zone grads. On the morning of May 9th, this rain belt moved along the front zone from southwest to northeast and east in the Siping and Changchun in the central part of our province. At 05:30, the provincial radar detected that it was about 400 km long and 200 km wide; the echo top was 7-8 km high; the intensity was 36 db, without convections. At 07:30, the rain belt moved out of Changchun to the east of Changchun and Jilin City, and finally the rain belt disappeared near Jiaohe to the east of Jilin City.

Corresponding author's address: No.653, HePing Street, ChangChun, JiLin Province,130062,China; E-Mail: jlwm@public.cc.jl.cn

Macro features of the clouds: We made two flights to survey this rain belt. The 1st one was between 05:25 and 07:00, and the route was

Changchun-Siping-Shuangliao-Changchun. The 2nd one was between 08:44 and 10:37, and the route was Changchun-Jilin-Changchun. The 1st flight flew to 4229m at elevation, where the temperature was –11.5 °C, and it did now fly out of the clouds. The 2nd flight reached an altitude of 5015m, where the temperature was –14.6 °C, and it nearly flew out of the clouds. To sum up the comprehensive data, the macro cloud structures observed from these two flights did not vary much. According to radar observation, the echo top of the 1st flight was 7-8 km high, which leads to the inference that there was another Cs cloud with plenty of liquid water above; the echo top of the 2nd flight was 5-6 km high, leading to the inference that there was basically no cloud above. The 2nd flight found that the Sc clouds was rising a little and becoming thinner, with thin Fn clouds below.

2.2 The second rain belt:

Created by upper sky strong cold air, this rain belt occurred in the rear part of the 700 hPa trough. It quickly moved to the front part of the 700 hPa trough and continued to impact the central part of our province. It started to rain again in Changchun at 10:00 and the rain lasted till the night. At 14:00, the provincial radar observed that, centering on Changchun, this rain belt was about 300km long and 200km wide. It moved at medium speed toward northeast and east. It disappeared near Dunhua at dusk. Cloud Macro Features: We attempted a flight survey to this rain belt along the route of Changchun-Changling-Tongyu-Changchun between 13:26 and 15:40. from the comprehensive data we could see that the intensity of this rain belt changed quickly. which comprises two graphs, one about the outgoing and the other incoming, and we will see that this rain belt clouds were divided into three layers, respectively over the 850, 700 and 500 Pa front areas. The medium and high layers of the clouds of this rain belt had been integrated into Ns cloud, and the lower Sc cloud went lower. This flight reach its maximum height at 5241m, where the temperature was –22 °C, but it did not get out of the cloud. Actually, the top of the cloud was even higher.

3. RAIN BELTt MICRO FEATURES

We made three flights to explore the above two rain belts and obtained a lot of consecutive micro data. They were two-dimension rain drops image, liquid water content and one-dimension drops. We used three detectors for the sampling. The sampling scopes were 3.0-31.0 microns, 36.15-1860 microns and 180.75-9300 microns. The sampling principles are: dispersion method for the 1st sample and light-array method.

3.1 First Rain Belt

3.1.1 First Flight

Snow crystal features: From 0 °C to –12 °C, basically, the snow crystals were mainly star-shaped, followed by cylinder-shaped. There were not much differences in terms of snow crystal sizes and numbers. Snow crystals with frozen drops were observed. Closely to the –10 °C layer, snow crystal attachments could clearly be observed. Between 0 °C and –10 °C, we also spotted snow crystal attachments.

Liquid Water Content Features: The average liquid water content on the whole layer was $0.076gm^3$. The liquid water contents were scattered in four large value areas at varied altitudes: -10 °C - -12 °C layer, -2 °C - -3 °C layer, 1.2 °C layer, and 7.0 °C – 4.0 °C. They were found correspondingly on over Ns cloud at the highest altitude of the flight, under Ns cloud and near Sc cloud.

Drop Features: Small cloud drop concentration in the Ns clouds had three concentration value areas, in keeping with the large value areas of the liquid water contents. The ice/snow crystal concentration at 4000m (-10 °C) layer had an extremely large value area (19 L^{-1}). Below 4000m the concentration decreased with lowering altitude. At 2300m small value was detected. Between 1400m and 800m we found another two small values, which corresponded to the top and bottom of the Sc clouds. Large cloud drop concentration had two large value areas respectively at 3800m and 3000m. On the whole, near the 4000m layer, the numbers of small cloud drop and ice/snow crystal were many. At the 3800m layer there were many large drops. There were quite a few small cloud drops under the Ns cloud. In the Sc cloud we mainly found large cloud drops and rain drops.

3.1.2 Second Flight

Snow Crystal Features: When the plane flew up into the cold cloud, we found the snow crystals basically star-shaped and cylinder-shaped on the 0 °C - -7 °C cloud layer, basically star-shaped, cylinder-shaped and plate-shaped on the –7 °C - -2 °C layer, and few snow crystals small plate-shaped and cylinder-shaped on the –12 °C - - 14.5 °C layer. During the plane descending, on the –12 °C - -7 °C cloud layer, we did not see star-shaped snow crystals, but small plate-shaped and cylinder-shaped snow crystals with a few needle-shaped ones.

Liquid Water Content Features: On the whole layer, the average liquid water content was $0.1311gm^3$. the large values of liquid water content were scattered on six layers, four in the Ns clouds and each in the Sc cloud and the Fn cloud. The plane ascended and descended rather slowly. During its descending, we found that in the Ns cloud, the water content on the 4700-5000m layer was obviously decreasing, while on the 3500-3600m layer and the 2100-2200m layer, the water content was obviously increasing. On the 2100-2200m layer, the liquid water content rose from $0.12gm^{-3}$ to $0.48gm^{-3}$. At the bottom of the Ns cloud, in particular, the small liquid water content soared to $0.51mg^{-3}$; in the Sc cloud, the liquid water content increased from $0.113gm^{-3}$ to 0.378 general manager^{-3}.

Drop Features. The small cloud drop concentrations increased as altitude rose and they were distributed in multi-peaks. The peak value and the water content large value area agreed to each other well. The biggest concentration was found on the 2700m (-3 °C) and 2000m (-1 °C). There were basically no small cloud drops in the Sc clouds. The ice/snow crystal concentration basically remained unchanged with altitude, averaging about 5 L^{-1}. The extremely large value was found near 0 °C, about 26 L^{-1}. The concentration of large drops was very small, less than 2.5 L^{-1}. A comparative large value zone was detected between –2 °C and –4 °C.

3.2 Second Rain Belt

Snow Crystal Features: During the process in which the plane ascended from 1900 to 5200m, the snow crystals varied much in various types of clouds. In the Cs cloud of –18°C ~ -22°C, we detected star-shaped, plate-shaped and cylinder-shaped snow crystals with comparatively small mass. In the As clouds of –10°C ~ -15°C, on the top, we detected small plate-shaped and cylinder-shaped snow crystals, and at the bottom, we detected ice crystals (whose diameter was estimated to be around 100u). In the Sc cloud of 0 °C ~ -4 °C, we found star-shaped snow crystals with ice blooms, and a few large snow balls. During the descending process, in the Ns cloud of –6.8 °C ~ -20.2 °C, there were basically star-shaped, plate-shaped and cylinder-shaped snow crystals. In particular on the –18 °C ~ -20 °C layer, we found basically star-shaped snow crystals with large measurements. As the plane descended, we found that the snow crystals were becoming smaller and smaller.

Liquid Water Content Features: The liquid water on the whole layer averaged $0.087gm^{-3}$. The large liquid water value, $0.246gm^{-3}$, was located in the middle of the cloud at 2900m (-10 °C). $0.12gm^{-3}$ was located at 3500m (-13.5 °C). On the top of the Sc cloud at 2000m, the large value was $0.29gm^{-3}$.

Drop Features: The small cloud drops concentration had four peak values as altitude rose, one at 4600m in the middle/lower part of the Cs clouds, two at 3700m on the top of the medium cloud zone and 2800m at the bottom of the medium cloud, and one at 1900m in the Sc clouds. We found one large value zone of ice/snow crystal concentration in the lower part of the Cs cloud, another one on the top of the Sc cloud and a third one at the bottom of the Sc cloud. The big drop concentration had a large value zone in the Cs cloud and the As cloud each.

4 Rain Belt Precipitation Mechanism and Artificial Weather Modification Potential

4.1 First Rain Belt

4.1.1 First Flight

This rain belt flight enjoyed fairly good dynamic water and vapor conditions. The top of the cloud was higher than 5000m and the temperature there was lower than –14 °C. The supercooled layer was more than 3000m in thickness. The liquid water extended as far as the vicinity of the cloud top. The liquid water on the whole layer averaged 0.076gm^{-3}. Because of the existence of Cs cloud, the ice crystal concentration was rather large on the top of the cloud. The liquid water on the layer of –10 °C ~ -12 °C, averaged 0.06gm^{-3}, and the ice crystal concentration was rather large too. This layer was the major venue of ice crystal activation and growth. The basic shape of snow crystals was star with a few cylinders. A few had attachments. On the layer of –4.5 °C ~ -10 °C, the liquid water content and the small cloud drop concentration were both low, with little changes in ice crystal concentration. Most of the ice/snow crystals on this layer were condensation growth. On the layer of 0 °C ~ -4.5 °C, the liquid water content and the small cloud drop concentration were both quite big, while the ice/snow crystal concentration became a little smaller. Most of the ice/snow crystals on this layer were ice bloom growth, coupled with attachment growth.

4.1.2 Second Flight

According to the weather conditions, now the rain belt was at its later phase. The radar echo top was dropping, but still, it had quite good dynamic conditions. The cloud top height was more than 5000m; the height at the bottom of the Ns cloud was about 1500m; the 0 °C layer altitude was about 1750m; and the supercooled layer thickness was about 3200m. On the whole layer the average liquid water content was 0.1311gm^{-3}. There was no Cs cloud on the upper layer, compounded by the earlier ice/snow crystal consumption, so the ice/snow crystals in the cloud belt decreased. We found that the ice/snow concentration in the whole supercooled layer averaged about 5 L^{-1}, and no ice/snow crystals were found near the 5000m layer. On the contrary, due to the fact that there were few ice/snow crystals in the cloud belt, which consumed little liquid water, the liquid water content was quite large, especially in the lower part of the cloud. Analyses of the two-dimension drop image and liquid water content vs. one-dimension drop concentration combination show that the ice/snow crystals were mainly condensation growth on the layer of –7 °C ~ -14 °C; the snow crystals were in plate shape and cylinder shape; on the layer of –2 °C ~ -7 °C, mostly were ice bloom growth coupled by attachment growth. The snow crystals were mostly star-shaped, with frozen drops, and large snowballs appeared. From the samples gathered at 378m, 7 °C, we found large snowballs in the rain. At the bottom of the cloud were mainly collisions of melted drops and their growth, and it was the same case in the Sc cloud and the Fn cloud. On the top of the Fn cloud, it seemed that the collision made the rain concentration bigger. At this stage, this rain belt had quite large potential for artificial modification. It would be the best to apply liquid nitrogen near the –12 °C cloud layer.

4.2 Second Rain Belt

This rain belt developed in the three layers of front zones of 850 hPa, 700 hPa and 500 hPa, so there appeared three layers of clouds with rather large spaces in between. Later on, the front zones became intensified and the middle and the high layers of clouds merged. Due to the functions of the strong cold air, this rain belt's temperature was very low. It was about –22 °C at 5200m. The 0 °C cloud layer was at about 1150m. The whole cold layer was about 4000m. the average liquid water content on the whole layer of this rain belt was 0.087gm^{-3}. However, the liquid water content in the middle and the high clouds was quite small, while it was quite big in the low Sc cloud.

From the above, we can see that the liquid water content in the middle and the high clouds was quite small, with little artificial modification potential.

5.BRIEF SUMMARY

(1) The cold front, with the function of the lagging 500 hPa strong front zone, can generate several medium rain belts, one after another. These rain belts' extension is rather high, with low temperature and different micro physical structures. With the folding functions in one region, it can create large ground rain.

(2) High cloud provides large quantities of ice crystals for growth. The ice crystal source zone is in the cloud of lower than –10 °C with supercooled water. Snow crystals are mainly in the shapes of star, followed by cylinder, plate and needle. Ice/snow crystals are mainly condensation growth in the upper part of the cloud and ice bloom growth in the lower part of the cloud. Collision growth is at the bottom and in the warm cloud zones. In large value zone of liquid water content, there are attachment growth processes.

(3) During one cold front rain belt process, the artificial modification potentials vary according to various rain belts. The first rain best had bigger potential for artificial modification, especially in the later phase of the rain belt.

References

1. You Laiguang, "Making Use of UMS to Study Physical Cloud and Artificial Precipitation Modification Conditions", "Artificial Weather Modification", 1993 (6): 73-80
2. Wang Xuelin, Jin Dezhen, Liu Zhiming, "Analyses of Cloud Precipitation Mechanism in Jilin during Spring", "Cloud and Rain Paper Collection", Beijing: China Science & Technology Press, 1987
3. Wang Xuelin, "Preliminary Probe into Precipitation Cloud Micro Physical Features", "Cloud and Rain Paper Collection", Beijing: China Science & Technology Press, 1987

Convective System Area Expansion and its Relationship with precipitation Intensity

Luiz A. T. Machado[1] and Henri Laurent[2]

[1]Centro de Previsão do Tempo e Estudos Climáticos – CPTEC/INPE - Brazil
[2]Institut de Recherche pour le Développement – IRD/LTHE - France

1. Introduction

Convective systems are responsible for most of the rainfall in tropical regions as well as in temperate latitudes during the warm season and they are also responsible for some extreme weather conditions in various regions of the earth. Knowledge of convective system evolution is of fundamental importance for understanding weather and climate, particularly in the tropics, and it is essential to improve forecasting of these systems to reduce vulnerability to extreme weather damage. The identification of predictor parameters for the evolution of a convective system, based on its previous evolution, could make a significant contribution to a nowcasting scheme and provide important information for mesoscale model initialization.

The growth rate of the convective systems can be deduced from their area expansion, which is easily observed from successive satellite images. This area expansion is expected to be associated with the high-level wind divergence and with the rate of condensation/evaporation that is directly related to the mass flux inside the convective system. The objective of this study is to investigate these hypotheses, to examine if the rate of change of area of a convective system can be associated with its lifetime and if this rate can indicate the level of convective activity

2. Data

The WETAMC/LBA allows us to study the three-dimensional structure of convective systems and their associated precipitation using a combination of raingauge network, satellite images and radiosonde data. The GOES-8 satellite images were pre-processed by NASA-GSFC for the entire duration of the experiment at full resolution (every 30 min; pixel size of ~4 km for the infrared channels). The convective systems are detected using the thermal infrared channel (~11 μm) assuming that the convective clouds that are high and thick are those with a small brightness temperature. A convective system is here defined as an area of at least 200 pixels (i. e., area larger than about 3500 km^2) that falls below the temperature threshold. Two thresholds were used: 235 K to identify the whole convective system including the thick cirrus shield, and 210 K to identify the areas of very intense convection that may exist embedded in the convective system. The systems are tracked during their life cycle using the method described by Mathon and Laurent (2001) which determines whether the system initiates spontaneously or from a split, and whether it ends by dissipation or by merging into another system. This objective tracking was performed for the period 11 January-27 February over a window covering tropical South America approximately from 7.5 N to 20 S and from 80 W to 30 W. The total number of systems tracked was 13409 at 235 K and 3867 at 210 K. For comparison with the WETAMC/LBA observations we use a window defined by 12 S-8 S and 64 W-60 W. A more detailed description of the methodology is given in Laurent et al. (2002).

Corresponding author's address: Luiz A. T. Machado Instituto Nacional de Pesquisas Espaciais Centro de Previsão de Tempo e Estudos Climáticos. Rodovia Pres. Dutra, km 40. Cachoeira Paulista/SP - 12630-000. Brazil. e-mail: machado@cptec.inpe.br

3. Area expansion of the convective systems

The convective system area is calculated from the number of pixel with a brightness temperature smaller than the given threshold (235 K or 210 K). The area expansion rate is simply the normalized difference of the system area between two successive images (Machado et al., 1998). The area expansion is closely linked to the phase of the convective system life. At the beginning of its life the convective system presents a large positive area expansion. The area expansion is close to 0 during the mature phase of the system and negative during the dissipative phase. The magnitude of the area expansion may be a good indicator to monitor the convective activity of the convective system, acting as a proxy to quantify the mass flux or the condensation rate inside the convective system.

Machado et al. (1998) discuss the possibility of associating the area expansion of the convective systems with the high-level wind divergence, if condensation and evaporation are neglected, with the following equation:

$$A_e = \frac{1}{A}\frac{\partial A}{\partial t} \approx \nabla.V \qquad (1)$$

Where A is the convective system area and *V* is the horizontal wind vector. A_e is the normalized area time rate of expansion called area expansion hereafter. A negative area expansion corresponds to contraction. Rapid area expansion would correspond to large upper levels wind divergence.

Machado et al. (1998) suggest that the magnitude of the area expansion at the initial time may be related to the total duration of the convective system. They found that the area expansion is systematically larger at the initiation stage for long-lived convective systems. There are two possible reasons for this: (i) the environmental conditions that are needed for vigorous development of convection, such as low level moisture convergence and vertical conditional instability, are likely to persist during the following hours; (ii) A strong area expansion indicates a strong internal dynamic (strong mass flux) of the convective system which will transport energy to the middle to high troposphere, modifying the atmospheric circulation and favouring the low level moisture convergence that will in turn prolong the life of the convective system. This feedback is likely to be activated if the convective system has a strong internal mass flux, in the initial stage. Note that as the convective systems have a size larger than 3500 km^2, they include various convective towers and the satellite analysis is an integration of all small-scale features.

4. Results

4.1 Relationship between area expansion and lifetime

The work of Machado et al. (1998) was based on a low resolution dataset and did not consider the different situations of splitting and merging of convective system. This study aims to test the hypotheses mentioned using high resolution data from various sources. In order to analyze the relationship between the area expansion of a convective system and its lifetime, we only consider here the systems that initiate spontaneously (i.e., not as a result of a split of a former system) and end by dissipation (i.e., not by merging into another system). This ensures that the initial growth of the system is due to its internal dynamics, and that the lifetime is representative of a complete life cycle. The tracking method allows for such a selection; the number of systems is thus reduced to 4240 at 235 K and 2569 at 210 K.

The average relationship between area expansion at the initial time (between t0 and t0 + 30 min) and total lifetime is shown in Figure 1. The plot gives the mean area expansion observed for each life duration and the associated standard deviation. The number of observed convective systems is also indicated. On average, the convective systems with a weak area expansion during the initial phase have a short lifetime. The convective system duration increases as its initial area expansion increases. The fitted curve shows that there is a nearly exponential relationship. For life duration larger than 8 h the function could be asymptotic, however the small number of cases leads to a very noisy and inconclusive relationship. For most cases (lifetime smaller than 8 h) the results show that the area expansion is a good indicator of the lifetime, within error bars, and that the relationship can be approximated by an exponential function.

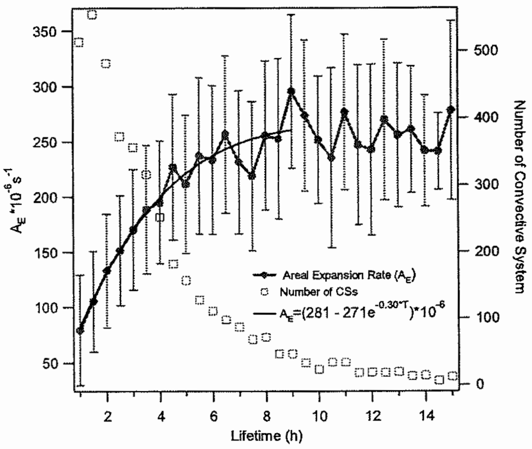

Figure 1. Area expansion (Ae, $10^{-6}s^{-1}$) and associated standard deviation as a function of the convective system lifetime (h). The number of cases is also plotted (right axis).

4.2 Relationship between area expansion and precipitation and cloud cover.

Figure 2 shows the average diurnal cycle of the area expansion, rainfall and 235K area fraction. It can be seen that the maximum area expansion occurs close to the time of maximum precipitation and around 4 hours before the maximum cold cloud fraction defined with the same threshold (235K). This means that, for this region, the area expansion captures the moment of maximum precipitation whereas a traditional approach to estimate the rainfall using brightness temperature would be biased by about 4 hours. As discussed by Machado et al. (2002), precipitation occurs very rapidly in the beginning of the afternoon close to the time of minimum total cloud cover. It is also the time when high and convective clouds have the maximum area fraction increase rate and when the initiation of convective systems and rain cells are the most numerous. These are the characteristics of the convection in the WETAMC/LBA region. However other investigations are needed to determine whether the nearly simultaneous time of maximum precipitation, wind divergence and area expansion could be verified in others regions of Amazonia.

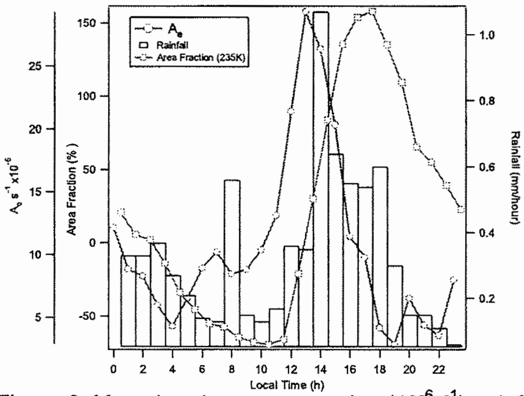

Figure 2: Mean hourly area expansion ($10^{-6}s^{-1}$), rainfall (mmh^{-1}) and 235 K area fraction (%) for the WETAMC/LBA region.

5 Conclusion

The convective system area is calculated from the number of pixel with a brightness temperature smaller than the threshold considered (235 K or 210 K). The area expansion is defined as the system area difference between two successive images, normalized by the mean area. The area expansion is closely linked to the phase of the convective system's life. At the beginning of its life the convective system presents a large positive area expansion. The area expansion becomes close to zero during the mature stage of the convective system and negative in the dissipation stage.

The results demonstrate the ability to predict the probable lifetime of a convective system from its initial area expansion. The physical explanation for this result is founded on the principle that this parameter measures the vigor of the convective forcing indicating the time/space scale of the convective cloud organization. The area of the cloud shield of the convective system changes in association with the upper level wind divergence and with the condensation/evaporation process.

The maximum area expansion occurs close to the time of maximum precipitation and about 4 hours before the maximum cold cloud fraction at the same threshold (235K). It can be concluded that the area expansion could be used to determine the time of maximum precipitation. This approach led to some more results that are described in Machado and Laurent (2004).

The analysis of the area expansion showed that this parameter could be very useful for short-range forecasts, convection diagnostics, and maybe to help improve precipitation estimation from geostationary meteorological satellites.

6 Acknowledgements

This work has received financial support from the Fundação de Amparo a Pesquisa do Estado de São Paulo (FAPESP) grant 01/13816-1 and from CNPq project grant 910153/98-1.

7 References

Laurent H., L. A. T. Machado, C. A. Morales and L. Durieux, 2002. Characteristics of the Amazonian mesoscale convective systems observed from satellite and radar during the WETAMC/LBA experiment. *J. Geophys. Res.* VOL. 107, NO. D20, 8054, doi:10.1029/2001JD000337.

Machado, L. A. T., W. B. Rossow, R. L. Guedes, and A. W. Walker, 1998. Life cycle variations of mesoscale convective systems over the Americas, *Mon. Wea. Rev.*, **126**, 1630-1654.

Machado L. A. T., H. Laurent and A. A. Lima, 2002. The diurnal march of the convection observed during TRMM-WET AMC/LBA. *J. Geophys. Res.*, VOL. 107, NO. D20, 8064, doi:10.1029/2001JD000338.

Machado L. A. T. and H. Laurent, 2004: The Convective System Area Expansion over Amazonia and Its Relationships with Convective System Life Duration and High-Level Wind Divergence. Mon. Wea. Rev., **132**, 714-725.

Mathon V. and H. Laurent, 2001. Life cycle of the Sahelian mesoscale convective cloud systems. *Quart. J. Roy. Meteo. Soc.*, **127**, 377-406.

NUMERICAL SIMULATION OF A SUPERCELL STORM OVER CAMAGÜEY, CUBA.

Daniel Martínez, Diana R. Pozo, Arnoldo Bezanilla, and Sadiel Novo
Instituto de Meteorología, Apdo. 17032, La Habana 17, Cuba

1. INTRODUCTION

Recently, the Advanced Regional Prediction System (ARPS) of the Oklahoma University, was customized for tropical conditions and was applied to the investigation of the development of simple convective cells[1] over Camagüey using a real sounding (Pozo et al., 2001).

In the present paper, ARPS is applied to the simulation of cloud development for the hailstorm, which developed on July 21, 2001 over the region of Nuevitas, in the NE of the Camagüey province. The objective of this paper is to show that the afternoon environmental sounding, and specially the wind profile corresponding to the day of the storm can produce this type of storm, even without considering dynamic forcing produced by sea-breeze convergence. The physical mechanism explaining the development of this storm, its splitting and the prevalence of one of the secondary cells is explained. It is intended also to corroborate the hypothesis that the storm can be classified as a supercell from the point of view of the simulation, and compare this conclusion with the analysis of radar data.

2. NUMERICAL SIMULATION OF THE JULY 21, 2001 HAILSTORM IN NUEVITAS.

2.1 Initial and boundary conditions.

The applied model is version 4.5.1 of ARPS (Xue et al., 2000, 2001). It is a mesoscale, three-dimensional, compressible and non-hydrostatic model.

As domain for the simulation, a 90x96 km mesh was used, with a horizontal step of 1 km, and 40 levels in the vertical, with a resolution of 0.5 km. The center of the mesh was located at nearly 45 km to the East of the Camagüey sounding station, at (21°35'N and 77°33'W, Fig. 1). The time step was 6 s for the calculation of all cloud parameters, and output was produced every 60 s. The simulation time was 3 hours. To initiate convection, an axially symmetric warm perturbation of maximum excess potential temperature of 4 K was applied. The perturbation was centered at x=50, y=37 and z=1.5 km, and its dimensions were 10x30x1.5 km. The form of the perturbation was chosen similar to that of the radar echo of the real storm in an early stage of development.

2.2. Meteorological situation and environment for the simulations.

The 1800 GMT sounding of the Camagüey station (21°25'N and 77°10'W), used as environment for the simulations exhibits a deep moist layer, a well mixed sub-cloud layer and high convective available potential temperature (CAPE), of 3351 J/kg. The low level wind is relatively weak, with variable direction, from the W-SW at low levels, but turning preferentially clockwise until the level of 10 km, which is the base of a jet from the NE, extending to the 16 km level (Fig.1). Three different wind layers can be identified in the troposphere: a low shear layer from the surface to 7 km, and a layer with wind speed increasing with height, from 7 to 12 km, and a higher shear layer with wind speed decreasing with height from 12 to 16 km.

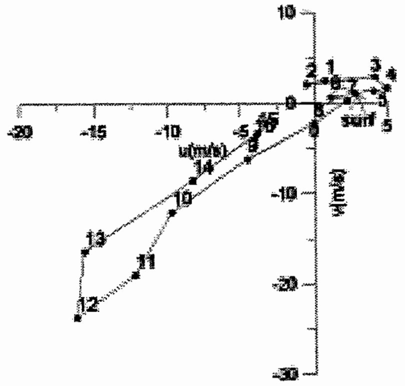

Fig 1 . Camaguey station 1800 GMT hodograph for 7/21/2001

2.3. Results and discussion of the simulation.

The first cell was initiated at 11 min. of simulation, in the coordinates of the initial perturbation. Two vortex centers were then generated by the interaction of the environmental wind shear with the updraft when the horizontal vortex tube is swept into it. The evolution of these vortices has been analyzed for different moments of the simulation (Fig. 2 shows the vorticity and horizontal wind distributions for 50 and 70 min of cloud life and for horizontal cross sections at heights of 4, 6 and 9 km). At 30 min, the updraft at low levels has two cores with vertical velocity greater than 10 m/s, next to two weak centers of vorticity. However, vertical vorticity is much greater at higher levels (Fig 2), showing two well-structured regions of positive and negative vorticity, whose center is located in the periphery of the updraft core, reaching a vertical velocity of 42 m/s in its center. The rapid strengthening of the updraft through the middle troposphere is a consequence of the high CAPE. This can be better observed for the 6 km level, where the high acceleration of the updraft produces an increase in lateral entrainment in early stages of cloud development. The combined effect of entrainment and of the increase in wind shear observed above the 7 km

---

[1] Corresponding author's address: Daniel Martínez. Instituto de Meteorología.. La Habana 17, Cuba. Ap. 17032 E- mail: dan@met.inf.cu)

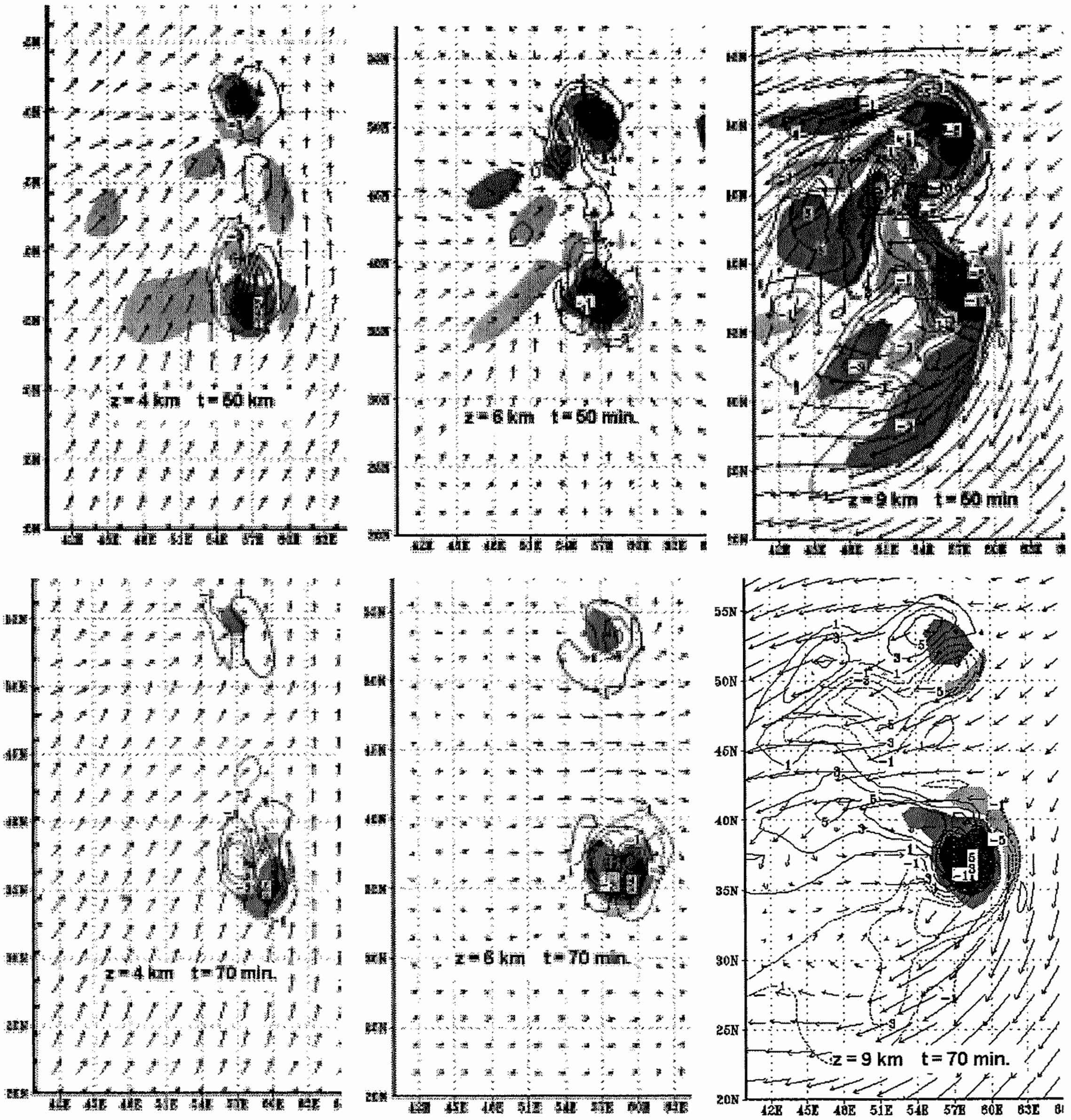

Fig. 2 Horizontal cross sections of vertical velocity (m/s) and vorticity (x 10^{-3} s^{-1}). Shaded: Vertical velocity. Contour: Vertical vorticity.

level (Fig. 1) favors the organization of the vorticity centers at higher levels.

The cyclonic and anticyclonic vortices, in early stages of cloud life are consistent with the conceptual model of a convective simple cell cloud (Houze, 1993), which coincides with the first step of a supercell development. At 50 minutes of simulation, the vortex centers at the north and south of the updraft reinforce at the 9 km level. A central downdraft region divides the updraft for all levels, generating two convective cells. This downdraft overlaps with the southern high water content zone, produced by high rainwater and melting hail content at low levels, and by the formation of hail and snow in the upper levels. The influence of

the loading of this hydrometeors seems to be the major cause of the splitting of the initial updraft, which was a gradual process, occurring progressively from the base to the top of the cloud. The vertical velocity, vorticity and reflectivity patterns are consistent with the conceptual model of a supercell developed by Klemp and Wilhelmson (1978) (Fig. 2). Two pares of cyclonic and anticyclonic vortices, corresponding to the two newly generated convective cells that can be identified as the left moving (LMS) and right moving storms (RMS), according to their movement direction relative to the center of the system. One the storm has split, the internal wind structure shows asymmetry in the sense that LMS entrains downdraft cold air to its southern flank, blundering with the central downdraft, while the right moving storm entrains mainly environmental air into its northern flank (Fig 2)
At 70 min., LMS starts to dissipate at the 4 km level. At 9 km, the system keeps its structure, but the updraft area of LMS is smaller than that of RMS. At 80 min., both cells go on raining on the ground, but the northern cell produces no more hail., while its ice and hail water contents don't reach 1 g/kg.

During its development, the system moved slowly towards the E-NE, approximately in the direction of the average wind, in the 1-7 km layer. The two cells shifted slowly to the northern side (left) and the southern side (south) from the center of the system, being the southern cell (RMS) the one reaching a greater development and lifetime. Fig. 3 shows the paths of the two cells and the approximate center of the system during the first 80 minutes of storm life. Afterwards, LMS accelerates its dissipation, though rain and ice persist for an hour more. RMS remains in the mature stage for approximately two more hours.

In this case, the hodograph turns clockwise with increasing height, and the more developed storm is the right moving one RMS, according with Klemp and Wilhelmson (1978) results. However, in the present simulation, the difference between both storms is no so great in early stages of system development after the splitting. This can be explained from the characteristics of the shear flow at low levels. In the lower 6 km the wind is relatively weak and there is preferential clockwise turning of the hodograph, but it is accompanied by significant variations in wind shear direction, so that the net effect in the difference between the vertical pressure gradients in the southern and northern flanks of the storm in its early stage of development is less than in Klemp and Wilhelmson's simulations. However, between 6 and 12 km, the increment in wind shear intensity is remarkable, while the wind shear vector direction is nearly constant, making possible the development of both cells. The final predominance of RMS may be due to the inclusion of cold air, coming from the central downdraft at middle levels, as can be observed from fig 1. This mechanism was discussed by Grasso (2000) as one of the possible causes of asymmetry in the development of split storms.

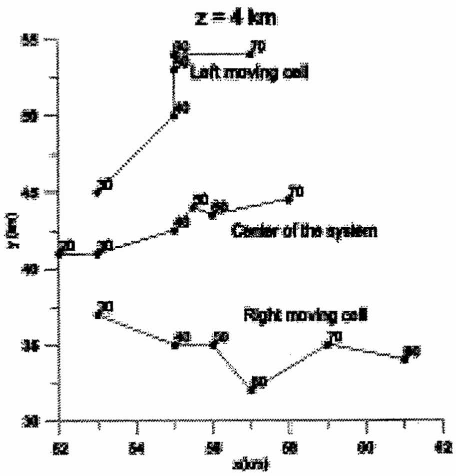

Fig 3. Trajectories of the centers of the left moving cell, the right moving cell and the center of the system at z= 4km. The labels indicate simulation time in minutes.

2.4 Radar Observations

At 22:35 GMT, the "original" cell is observed; showing a reflectivity maximum in its center at both levels, and corresponds to the central downdraft in the simulation. At 22:46 GMT (Fig. 4a) in the lower level the splitting process has begun, while in the upper level, a decrease in reflectivity is observed. Nine minutes later, the cores of both cells are separated in the lower level, and in the upper levels, the cells are totally separated, using the 20 dBZ threshold. At 23:10, the southeastern cell, which deviates gradually rightward, dominates in both levels. This is the time at which hail was detected on the ground. At 23:30, the left cell has practically disappeared, while the right cell continues its development for an hour more.

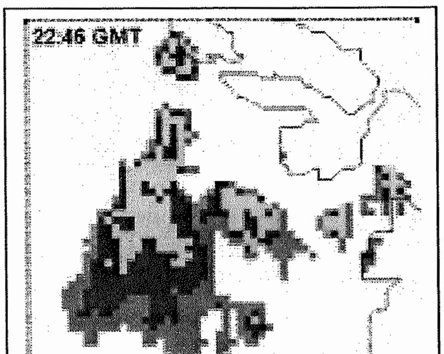

Fig 4 a. 3-4 km CAPPI immage of the radar echoes of the observed cloud system at 22:46 GMT. Threshold: 20 dBZ, Step: 10 dBZ

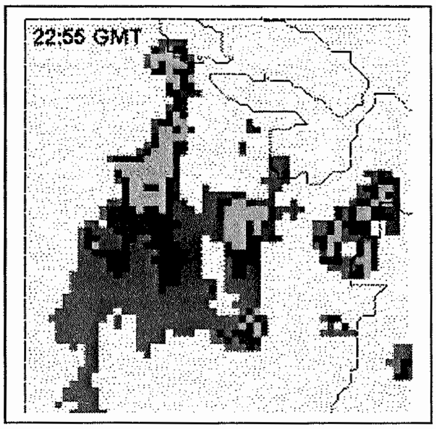

Fig 4 b. 3-4 km CAPPI immage of the radar echoes of the observed cloud system at 22:55 GMT. Threshold: 20 dBZ, Step: 10 dBZ

Radar observations of the Nuevitas storm of July 21, 2001 roughly corroborate the above simulations results, even if there are important differences. As convective development took place in different zones of the province from the early afternoon, the system that was present at the initial simulation time was the result of previous interactions of different systems. The simulation reproduces the main features of the observations, regarding both the general evolution of the system and the range of reflectivity values, showing that the development of a supercell from a simple cell storm is a consequence of the evolution of the system in the environment given by the sounding, even if it does not meet the condition of having large shear at low levels. However, the simulation was unable to reproduce the sizes and lifetimes of the cells resulting from the splitting of the original storm. This partial lack of coincidence is related to some limitations in the application of the model. The first is that the time of the nearest available sounding was some hours before the beginning of the storm, so that two other convective systems had developed in the province before the time chosen as "initial" . On the other hand, the site of the sounding was located nearly 40 km distant from the zone where the studied system developed. Another limitation of the results is the arbitrary selection of the initial perturbation, considering that the real system existed before of the starting time of the simulation, and was the result of merging of preexisting systems.

4. CONCLUSIONS

Numerical simulation results corroborated that the July 21, 2001 Nuevitas severe storm consisted in the right moving cell of a supercell system, generated in an environment of high instability, and a wind profile characterized by clockwise turning hodograph with low wind speeds at the lower levels and strong, and nearly unidirectional wind shear at heights from 6 to 12 km.

The left moving and the right moving cells develop similarly in relatively early stages of storm development, but after 70 min. of simulation, the left cell begins to dissipate, while the right moving one remains stable. The probable reason for the relatively early dissipation of the left moving cell is the entrainment of cold air, generated in the central downdraft at low and middle level, while the right moving cell entrained environmental air, which is conditioned by the wind profile.

The simulation reproduces the main features of the observations, regarding both the general evolution of the system and the range of reflectivity values, showing that the development of a supercell from a simple cell storm is a consequence of the evolution of the system in the environment given by the sounding, even without large shear at low levels.

Acknowledgments. The authors want to thank Felix Gamboa and Roberto Aroche, from the Camagüey Meteorological Center, for organizing the radar observations and part of the meteorological information. Support for this work was provided by the Cuban-Mexican CITMA-CONACyT project E120.1306 and the Cuban CITMA project 49204212. The simulations were made using the Advanced Regional Prediction System (ARPS) developed by the Center for Analysis and Prediction of Storms (CAPS), University of Oklahoma. CAPS is supported by the National Science Foundation and the Federal Aviation Administration through combined grant ATM92-20009.

References

Grasso, L. D., 2000. The dissipation of a left-moving cell in a severe storm environment. Mon. Weather Rev., 128, 2797-2815.

Houze, R. A., Jr., 1993. Cloud Dynamics. . International Geophysics Series. Vol. 53., 573 pp. Academic Press.

Klemp, J. B, and Wilhelmson, R. B., 1978. Simulations of right- and left- moving storms produces through storm splitting J. Atmos. Sci., 35, 1097-1110.

Pozo, D., Martínez, D. and Chac6n, M., 2001. Simulaci6n numérica tridimensional de una celda convectiva simple en condiciones tropicales utilizando el modelo ARPS. Rev. Cub. Meteor., 8, 1, 74-82.

Xue, M., Droegemeier, K.K.and Wong, V., 2000. The Advanced Regional Prediction System (ARPS) – A multi-scale nonhydrostatic atmospheric simulation and prediction model. Part I: Model dynamics and verification. Meteorol. Atmos. Phys. 75, 161-193.

Xue, M., Droegemeier, K.K., Wong, V., Shapiro, A., Brewster, K., Carr, F., Weber, D., Liu, Y. and Wang, D., 2001. The Advanced regional prediction System (ARPS) – A multi-scale nonhydrostatic atmospheric simulation and prediction model. Part II: Model physics and applications. Meteorol. Atmos. Phys. 76, 143-165.

Impact of topography resolution and upper air data on real data thunderstorm simulation using RAMS

P. Mukhopadhyay
Indian Institute of Tropical Meteorology, Pune-411008, India

1. Introduction

The west coast of peninsular India is breeding ground of variety of meteorological phenomena ranging from meso-alpha to meso-gamma scales. During pre-monsoon seasons of March, April and May the coastal state Kerala every year experiences thunderstorm activity frequently. The physiographical feature of the region with Western Ghat hills to the east and Arabian sea to the west of the state has further made the condition conducive for the formation of all these weather systems. Yamasaki (2002) has mentioned in a study that mesoscale weather systems are manifestation of interaction of large scale flow with local heterogeneity. The thunderstorms over the state of Kerala during pre-monsoon months appear to be the ideal example of formation of local thunderstorms by interaction of the large scale flow with the Western Ghat hills. Santosh et al. (2001) has given a detail description of the climatological features of thunderstorms over three airport stations of Kerala namely Thiruvananthapuram, Kochi and Kozhikode. They showed that Thiruvananthapuram has a maximum average thunderstorm frequency of 14.3 days in April, followed by 13.4 days in May. Kochi was found to have maximum average thunderstorms of 15.6 days in the month of May. Kozhikode was found to have an average frequency of 11 days each in May and June. They further showed that 40% storms over Thiruvananthapuram occur during 0900-1200 UTC and highest frequency of storms of duration less than 3 hours was found to be 10.3 over the station in the month of April. Kochi was found to have 22.3% of storms occurring during 1200-1500 UTC and average maximum frequency of thunderstorms of duration less than three hours was 9.0 in May, 8.1 in April and 7.9 in June. They showed in the study that long lasting thunderstorms (> 6 hours) generally start at 0900 UTC over Thiruvananthapuram in March, April and May months. Similarly thunderstorms of longer duration form between 0900-1200 UTC over Kochi in the April, May, June months. Thus it is apparent from the above study that the state of Kerala receives major percentage of thunderstorms during pre-monsoon months and the most preferred time of occurrence is 0900-1200 UTC. The Kerala state has one more advantage of having three upper air stations namely Thiruvananthapuram, Cochin and Panambur (coastal Karnataka) located nearby at a distance suitable for mesoscale resolution. The objective is to study the impact of USGS topography data of 10 min and 30 arc sec resolution and upper air data on the real data simulation of the thunderstorm reported on Cochin stations at 1200 UTC of 20 April 2003. Regional Atmospherc Modelling System (RAMS) with two way interactive nested domain of resolutions 16- and 4-km (Fig. 1) is used to simulate the storm.

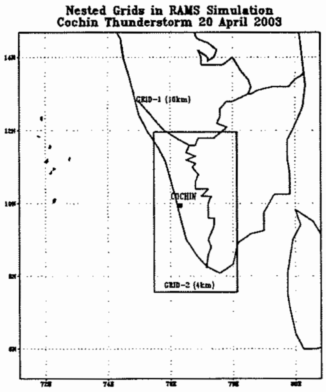

Figure 1.Nested grid

2. Methodology and Data

RAMS is used with two way interactive nested grids of resolutions 16- and 4-km. The domain used in the study is shown in Figure 1. The outer domain in Figure 1 covers 71.1°E to 80.8°E and 5.2°N to14.7°N and inner domain covers 75.5°E to 77.9°E and 8.11°N to 12.0°N. The number of grid points in the east-west and north-south direction for the outer domain is 68 x 68 and that for the inner domain is 66 x 110 and the grids are centered at 76.0°E, 10.0°N. The vertical levels for all the simulations are taken to be 36 with a stretching ratio of 1.1:100; 2000. The Klemp and Wilhelmson (1978) radiative boundary condition is applied in the lateral boundary and Davies (1983) nudging is applied as upper boundary condition. A Modified Kuo convection scheme (Tremback 1990) is used for the large scale precipitation and Bulk microphysics of Walko et al. (1995) is used for prognosing cloud constituents and grid scale precipitation. A two-stream radiation scheme developed by Harrington (1997) and Harrington et al. (1999) is used. It allows interaction of three solar and five infrared bands with model gas constituents and cloud hydrometeors (Cotton et al. 2003). The horizontal and vertical eddy diffusion coefficients are computed as the product of the 3D rate-of-strain tensor and a length scale squared. The length scale is the product of the vertical grid spacing and a constant (CSZ) defined in the namelist as 0.2.

For the simulation, the NCEP/NCAR reanalyses at 2.5° x 2.5° lat x lon at six hourly interval is used for the initial and boundary condition. The 0000 UTC and 1200 UTC upper air data from three nearby stations Thiruvananthapuram (76.95°E, 8.48°N) Cochin (76.27°E, 9.95°N) and Panambur (74.83°E, 12.95°N) are used to incorporate these data in the initial analyses.

The 10 min and 30 arc sec USGS topography data with envelope averaging, is used as ground truth. The envelope topography over the coarse domain (16-km resolution) is shown in Figure 2.

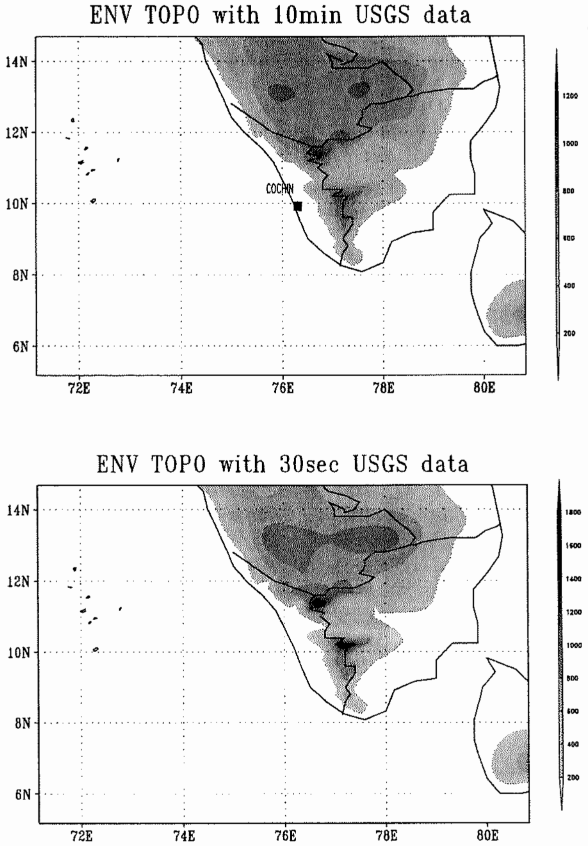

Figure 2: The envelope averaged 10 min topography (upper panel); envelope averaged 30 sec topography (lower panel) in the coarse domain (16-km).

3. Discussion of results

The results of numerical experiments reveal that marginal improvement is achieved by changing topography resolution from 10 min to 30 arc sec. Meteorological parameters namely vertical velocity, total cloud condensate, rainfall are found to be marginally better simulated with 30 arc sec topography data. The 12 hour accumulated rainfall forecast by the two types of topography data sets are shown in Figure 3. This improvement may be attributed to the high resolution (30 arc sec) topography data that resolves the regional heterogeneity better than the coarse resolution (10 min) data. This improvement has led to perform another set of experiments with NCEP/NCAR reanalyses data with which the upper air data at 0000 UTC of 20 April 2003 of Cochin and nearby stations namely Thiruvananthapuram and Mangalore are blended along with 30 sec topography. These simulation results are compared with that obtained without using upper air data. Model simulation suggests that significant improvement is achieved by incorporating upper air data. Meteorological parameters such as wind filed at the surface, wind at 700 hPa, total cloud condensate at 700 hPa, vertical velocity and rainfall (Fig. 4) are found to be well simulated in comparison to the results obtained without upper air data. The gradual development of sea breeze in the eastern side of the Western Ghat hill is also well captured in the model simulation. It appears from the simulation that sea breeze over these coastal stations become stronger with the progress of the day. The stronger sea breeze has caused more moisture incursion over the region. The Western Ghat hill has provided the necessary lifting to the parcel which finally got manifested as the thunderstorm in the evening. Thus it appears that by using upper air data and high resolution topography, RAMS is able to show the genesis, maturity and dissipation of the 20 April thunderstorm over Cochin closer to reality.

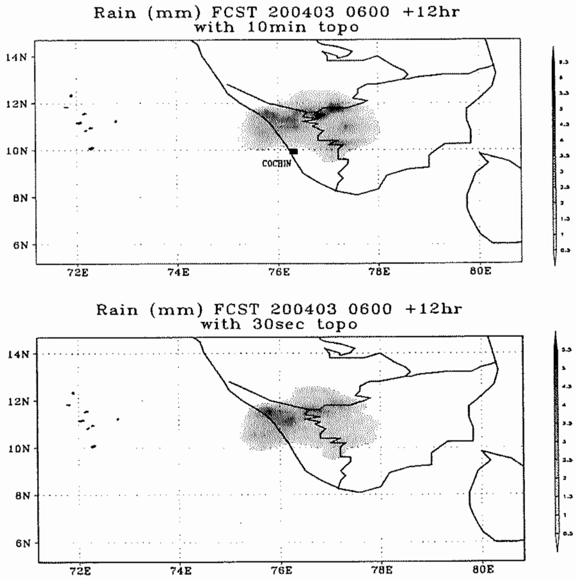

Figure 3: 12 hour accumulated rainfall forecast in the coarse domain (16-km); upper panel with 10 min data and lower panel with 30 arc sec data.

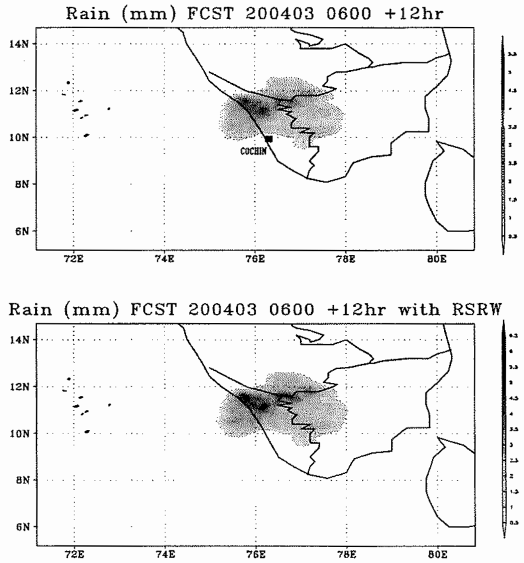

Figure 4: 12 hour accumulated rainfall forecast in the coarse grid domain (16-km); upper panel without RSRW and lower panel with RSRW data.

4. Conclusions

Numerical experiments are carried out to study the effect of topography and RSRW data over coastal city Cochin which is located in the windward side of Western Ghat in the Kerala state. The plot of envelop topography with 10min data shows the highest peak of 1200m as compared to 30s data where the highest value is found to be 1800m. The topography thus is better resolved in the 30 s data. The simulation results suggest 30 s topography has simulated the storm marginally better than that of 10 min. The improvement of simulation with high resolution topography is reflected in the forecast of vertical velocity, relative humidity and rainfall. Evolution of sea breeze has been well simulated by both the experiments. A line of wind convergence is found have developed at 4 hour forecast in both the simulation ENV-10m and ENV-30s. The (%) RH at 700 hPa also is found to be of the order of 80~90% at 4 hour when the genesis of the storm took place. Thus it seems that the high resolution topography with better spatial feature may have better resolved the topographic lifting of the moist parcel to initiate the storm more accurately than the other experiment. The thunderstorm of 20 April is simulated by incorporating three stations data along the west coast which are located at a suitable distance to resolve mesoscale signature of the atmosphere. ith the The lower troposphere appears to be moister after blending the RSRW data. The wind field suggests flow from land towards the sea which is generally expected in the early hours. The comparison of experiments without and with RSRW data, reveals the storm is in general well simulated by the both the experiments. However the evolution of vertical velocity (m s^{-1}) at 850 hPa, total cloud condensate (g kg^{-1}) at 700 hPa and hourly rainfall (mm) appears to have been improved in terms of time and location of the storm with respect to satellite observations. The initiation of the storm and gradual maturity along with its westward movement is well brought out by the simulation experiment ts-rs.

References

Davies, H. C., 1983: Limitations of some common lateral boundary schemes used in NWP models. Mon. Wea. Rev., **111**, 1002-1012.

Klemp, J. B. and Wilhelmson, R. B., 1978a: The simulation of three dimensional convective storm dynamics. J. Atmos. Sci. **35**, 1070-1096.

Klemp, J. B. and Wilhelmson, R. B., 1978b: The simulation of three dimensional convective storm dynamics. J. Atmos. Sci. **35**, 1097-1110.

Santosh, K., Sarasakumari, R., Gangadharan, V., K., and Sasidharan, N. V., 2001: Some climatological features of thunderstorm at Thiruvananthapuram, Kochi and Kozhikode airports, *MAUSAM*, **52**, 357-364.

Harrington, J. Y., 1997: The effects of radiative and micro-physical processes on simulated warm and transition season Arctic stratus. PhD Dissertation, Atmospheric Science Paper No 637, Colorado State University, Department of Atmospheric Science, Fort Collins, CO 80523, 289 pp.

Harrington, J. Y., Reisin, T., Cotton, W. R., and Hreidenweis, S. M. 1999: Cloud resolving simulations of Arctic stratus. Part II: Transition-season clouds. Atmos Res **55**, 45-75.

Tremback, C. J., 1990: Numerical simulation of a mesoscale convective complex: Model development and numerical results. PhD dissertation, Atmos sci Paper No 465, Colorado State University, Department of Atmospheric Science, Fort Collins, CO 80523.

Walko, R. L., Cotton, W. R., Meyers, M. P., and Harrington, J. Y., 1995: New RAMS cloud microphysics parameterization part I: the single-moment scheme Atmos Res **38**, 29-62.

Cotton, W. R., Pielke, R. A. Sr., Walko, R. L., Liston, G. E., Tremback, C. J., Jiang, H., McAnelly, R. L., Harrington, J. Y., Nicholls, M. E., Carrio, G. G., and McFadden, J. P., 2003: RAMS 2001: Current status and future directions. Meteorol Atmos Phys, **82**, 5-29

MESOSCALE AND MICROSCALE STRUCTURES OF PRECIPITATION BANDS ASSOCIATED WITH BAIU FRONT : AIRCRAFT OBSERVATIONS AND NUMERICAL SIMULATIONS

Masataka MURAKAMI[1], Akihiro HASHIMOTO[2], Narihiro ORIKASA[1], Kazumasa MORI[1], Hiroshi KUROIWA[3],Akihide KAMEI[3] and Haruya MINDA[4]

[1]Meteorological Research Institute, Tsukuba, Japan
[2]Advanced Earth Science and Technology Organization, Tokyo, Japan
[3]Communications Research Laboratory, Tokyo, Japan
[4]Nagoya University, Nagoya, Japan

1. INTRODUCTION

Cloud systems associated with Baiu-front are one of typical systems that bring a great amount of precipitation over Japan Islands and their surroundings. Therefore, many studies have been carried out on formation/maintenance mechanisms from the viewpoint of their synoptic-scale features. However, few studies have been done so far from the viewpoint of their meso-scale and micro-scale features although Doppler radar observations of their meso-scale structures were recently made by several researchers.

In this paper, meso-scale and micro-scale structures of precipitation bands associated with Baiu front that were observed with an instrumented aircraft are described and are compared with simulation results of a cloud resolving model.

2. OBSERVATIONS

2.1 Synoptic Scale Features

A stationary front (Baiu front) extended more than 3000 km from the low (32N/139E) to the west over the Pacific ocean south of Japan Islands on 22 June 2002 (Fig.1). Cloud bands with 200 km width formed along the Baiu front are shown in visible satellite imagery (Fig.2). CAPPI at 2 km of JMA's C-band radar shows that precipitation echoes existed between latitudes of 28N and 30N and their intensities were mostly less than 10 mmhr^{-1} except for precipitation cores with 30 ~ 40 mmhr^{-1} (Fig.3).

2.2 Aircraft Observations

We flew the instrumented aircraft (G-II) at 12.5 km level (~ -57C) along the box in Fig.4 , and made downward looking cloud radar measurements and released GPS dropsondes at points of A to F. We also flew the aircraft at different heights (12.6, 7.7, 3.5, 0.5 km) along the line AE and made in-situ measurements of kinetic, thermodynamic and

Corresponding author's address: Masataka MURAKAMI, Meteorological Research Institute, Tsukuba, Ibaraki 305-0052, Japan; E-Mail: mamuraka@mri-jma.go.jp.
four spaces.

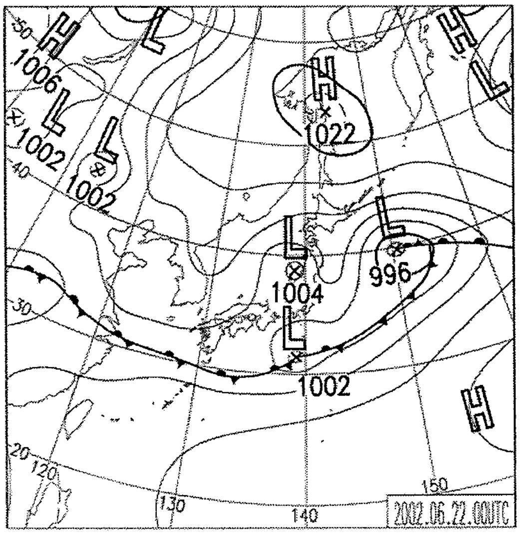

Fig.1 Surface weather map at 09 JST 22 June 2002

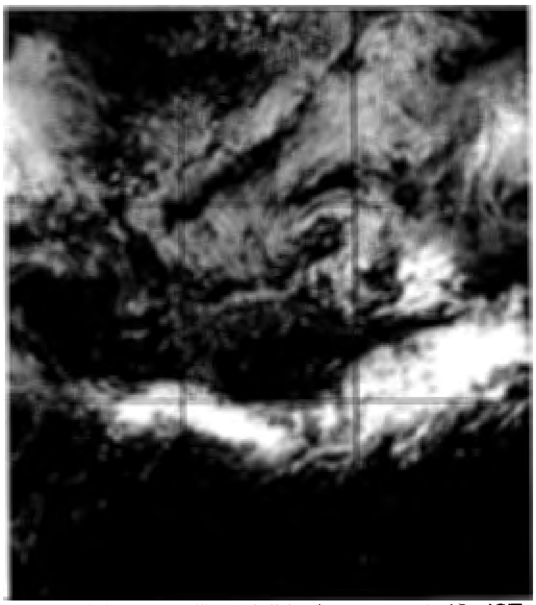

Fig.2 Visible satellite visible imagery at 12 JST 22 June 2002.

microphysical structures in/around the cloud system.

It is shown from the dropsonde observation that convectively unstable stratification was maintained in the precipitation bands by the confluence of warm and humid W ~ WSW below 1.5 km level from the south and colder and drier NW at middle and upper layers from the north. At lower layers, the convergence between strong humid W ~ WSW flow and cooler N ~ NE flow lifted convectively unstable air mass with high equivalent potential temperatures, liberated the instability and produced convective clouds reaching the height of 14 km. Values of CAPE were 2000 ~ 3000 Jkg^{-1} on the south and nearly 0 Jkg^{-1} on the north of the precipitation bands. The vertical profiles of horizontal wind divergence and water vapor flux in the box of Fig.4 showed that airflow and water vapor converged below 600 hPa level and diverged above the level. Vertical integration of water vapor fluxes indicated that water vapor convergence corresponded to mean precipitation rate of 1 ~ 2 $mmhr^{-1}$ over the box area (Fig.5).

Vertical cross section of horizontal wind shows that NW prevailed in middle and upper layers and a combination of W~WSW with a speed of 20 ms^{-1} and N~E with a speed of 10 ms^{-1} produced a strong convergence in lower layers. The vertical cross section suggested that the convergence kicked off the strong convections and transported momentums of horizontal wind in lower levels. Above 3.5 km level, vertical velocities of several ms^{-1} were found where horizontal wind abruptly changed. Even at 12.6 km level, strong updraft of ~10 ms^{-1} was observed. At the lowest level, relatively strong updraft was found in the southern part of the precipitation bands (Fig.6).

Horizontal gradient of air temperatures were remarkable at 0.5 and 12.6 km. At upper levels, the air in the central part of cloud regions was very humid while both sides of it were rather dry and much drier on the northern side than on the southern side. In middle and lower layers, temperature fluctuations up to 3 C accompanied with strong vertical velocity, which is corresponding to changes of equivalent potential temperatures up to 10 K. At the lowest level, horizontal gradients of both temperatures and water vapor mixing ratios were steep and corresponding to a horizontal gradient of more than 10K/200km (Fig.7).

At upper levels, cirrostratus and anvil clouds prevailed. In the central part of developed convective clouds, water substances were blown up to 14 km and maximum number concentration and maximum water content of ice crystals reached 1000 L^{-1} and 0.3 gm^{-3} there. Middle layers on both sides of the precipitation band were very dry. In updraft regions, supercooled cloud water of 0.3 ms^{-1} and snow water content of 0.5 gm^{-3} coexisted. On both sides of the precipitation band, there existed shallow clouds with top height of 5 ~ 6 km that were suppressed by the dry air in middle levels. Below melting level, cloud water contents were 03~0.5 gm^{-3} in most of clouds except for water contents of 1 gm^{-3} in strong updraft (Fig.9).

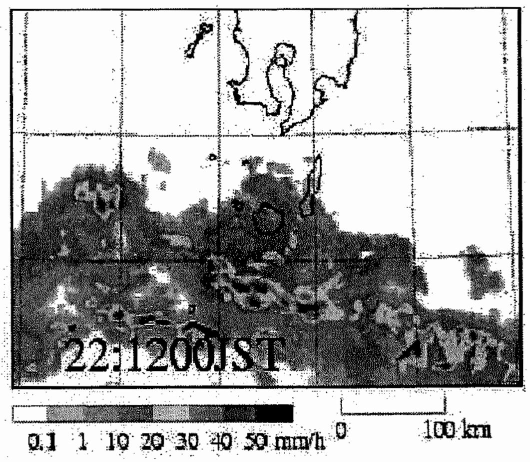

Fig.3 CAPPI at 2 km of JMA conventional radar at 12 JST 22 June 2002

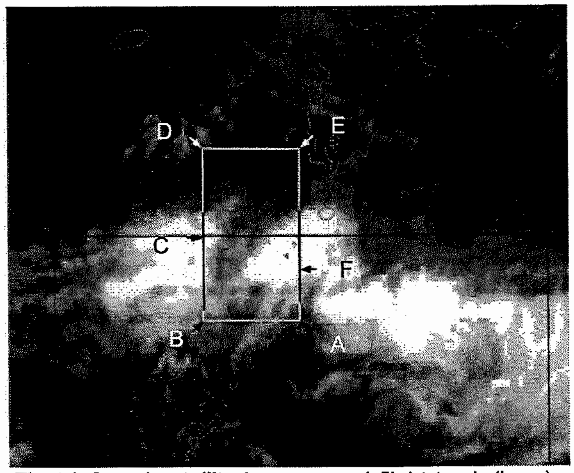

Fig.4 Infrared satellite imagery and flight track (box). Arrows indicate release points of GPS dropsondes

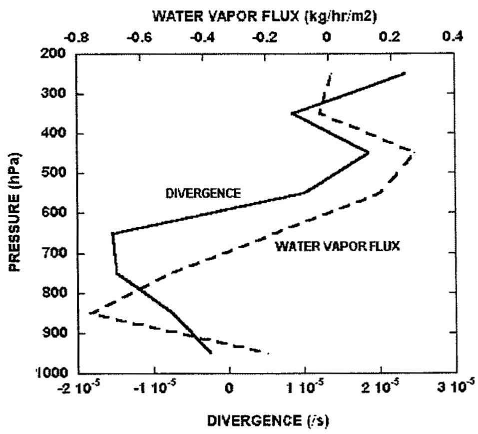

Fig.5 Vertical profiles of divergence and water vapor flux calculated from dropsonde data.

It is thought from these observation results that major precipitation formation mechanisms above freezing level are the depositional growth in most of stratiform clouds and accretional growth in convective clouds whereas accretional growth of rain drops that are produced by melting of snow crystals below freezing level is dominant.

3. NUMERICAL SIMULATIONS

3.1 Model Description

In order to simulate the precipitation bands, we used JMA-NHM (Japan Meteorological Agency Non-Hydrostatic Model) with a fully 2-moment bulk microphysical parameterization. Model domain covers 1500 km x 1500 km in horizontal with resolution of 5 km. The model domain covers 20 km in vertical and consisted of 38 layers with stretched intervals from 40 m near surface to 1096 m near model top. Time integration with dt=12 sec is started from 1800 UTC, 21 June, 2002 and continued up to 12 hours. Forecast of RSM (Regional Spectral Model) of JMA are used as the boundary condition every hour.

3.2 Simulation Results

Figure 10 shows surface precipitation rate at 03 UTC 22 June. The features of surface precipitation, like area, band shape and maximum precipitation rate, are well reproduced as compared with the observation although eastward movement of simulated precipitation bands are ahead of observed one by 3 hours.

Ice crystal concentrations in simulated clouds are mostly less than 30 /L except for high concentrations of ~1000/L in convective cores and are comparable to observed ones although the coverage of ice clouds are much wider than the observations.

Figure 11 shows vertical cross section of hydrometeor mixing ratios and number concentrations along the line CD in Fig.8 at 03UTC (12JST) 22 June, which is corresponding to the location of aircraft vertical cross section measurement along 130E at around 03UTC. Mixing ratio and number concentrations of hydrometeors and their spatial distributions are well reproduced except for wide coverage of cloud ice, higher mixing ratio and number concentration of graupel and its larger spatial extension..

4. CONCLUSION

Precipitation bands associated with Baiu front were investigated with an instrumented aircraft (Gulfstream-II) on 22 June 2002. In-situ measurements of airflow, thermodynamic and microphysical fields in/around the cloud system were made as well as measurements of reflectivity and Doppler velocity with a w-band cloud radar and GPS dropsonde sounding.

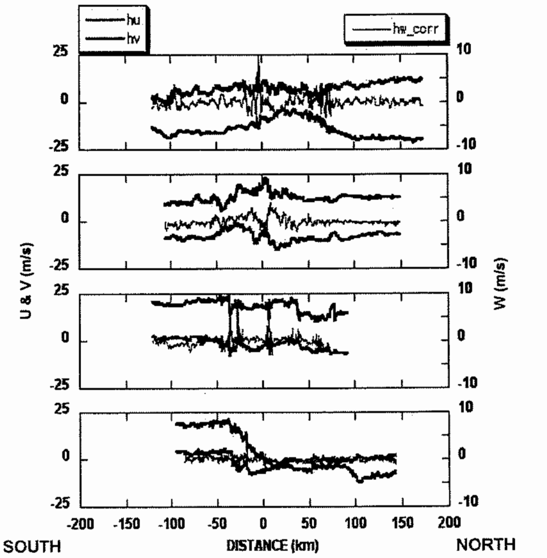

Fig.6 Horizontal distributions of u,v and w components of wind obtained from the instrumented aircraft at 12.6, 7.7, 3.5, 0.5 km along 130E

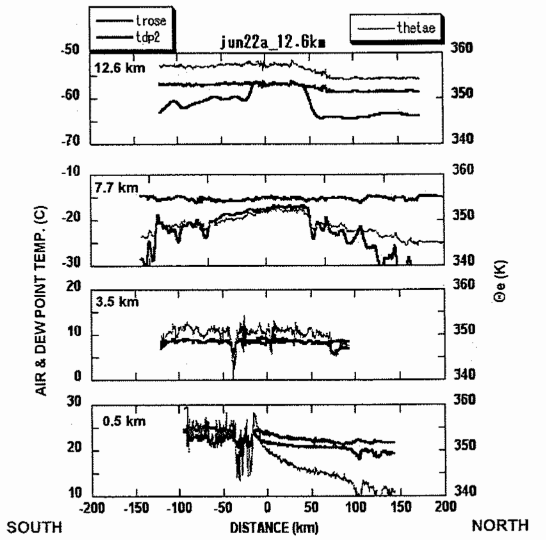

Fig.7 Horizontal distributions of air temperature, dewpoint temperature and equivalent potential temperature at 12.6, 7.7, 3.5, 0.5 km along 130E.

Baiu front formed between warm and humid westerly flow with CAPE values of 2000 to 3000 and cool northerly flow with CAPE values of nearly 0. Such a confluent airflow structure was prominent below the height of 1.5 km. In the center of Baiu frontal zone, the warm and humid airflow from west-southwest induced intense updraft and formed deep (~14 km) convective clouds with top temperature of ~-60C. The strong updraft blew a large amount of hydrometers upward to cloud top. Ice crystal concentration and ice water content near the top were $1000L^{-1}$ and $0.3\ gm^{-3}$, respectively. The northwesterly blew off these ice

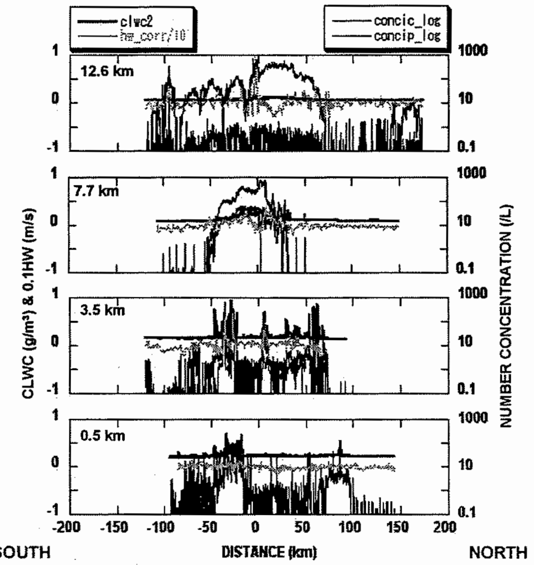

Fig.9 Horizontal distributions of cloud water content(clwc2), vertical velocity(hw_corr/10), 2DC concentration(concic_log) and 2DP concentration(concip_log) at 12.6, 7.7, 3.5, 0.5 km along 130E.

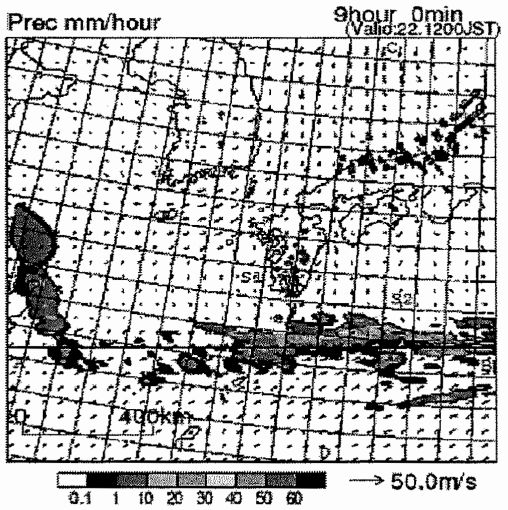

Fig.10 Hourly-accumulated surface precipitation at 12JST 22 June 2002.

crystals downwind and formed anvil clouds. At middle layers above freezing level, snow particles with ice water contents of 0.5 gm^{-3} and supercooled cloud water of 0.3 gm^{-3} coexisted in convective regions. Air on the both sides, especially northern side, of convective regions was dry, and confined clouds below 6 km. Below freezing level (5km), cloud water contents were mostly less than 0.5 gm^{-3} except for high cloud water contents of ~1 gm^{-3} in strong updraft regions. Above freezing level, the precipitation formation mechanisms were primarily depositional and

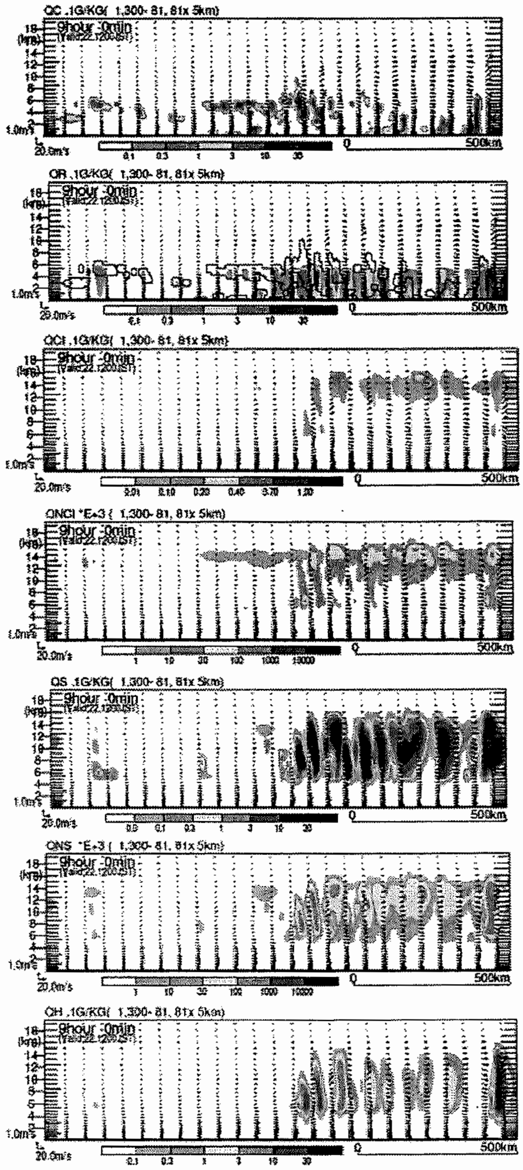

Fig.11 Vertical cross section of Qc, Qr, Qi, Ni, Qs, Ns, Qg along the line AB in Fig.10.

secondarily accretional growth of snow particles. Below freezing level, rain drops produced by melting of snow particles grew through the collection of cloud droplets.

Non-hydrostatic model with 2-moment bulk microphysics parameterization reproduced most of observed features of airflow, thermodynamic and microphysical structures. Deficits in numerical simulation are too much extension of cirrus clouds to the north of the precipitation band and too much formation of graupel in the precipitation band.

THE RELATIONSHIP BETWEEN SOUTH AMERICAN LOW-LEVEL JET EVENTS WITH THE FORMATION AND MAINTENANCE OF MESOSCALE CONVECTIVE SYSTEMS

Matilde Nicolini[1], Paola Salio[1], Juan Carlos Torres, Edward J Zipser[2]
[1]Centro de Investigaciones del Mar y la Atmosfera. CONICET/UBA. Department of Atmospheric and Oceanic Sciences. University of Buenos Aires. Argentina
[2]Department of Meteorology. University of Utah. USA

1. INTRODUCTION

Much of the warm season precipitation in the La Plata Basin is produced by large mesoscale convective systems (MCSs). Improvement of short-term forecast of heavy precipitation and particularly organized convection in this region represents a worthwhile challenge.

Nicolini et al. (2002) and Torres (2003) studied the environmental conditions that support the evolution of these systems using a 5-year period (October to April1988-1993) of ISCCP-DX satellite data base. They selected heavy precipitating episodes (daily precipitation higher than 120 mm at least at one of the stations of the raingauge network) over subtropical South America and composed the corresponding thermodynamic and dynamic fields using the European Centre for Medium-Range Weather Forecasts reanalyses (ERA-15). The results show that the studied MCSs have a tendency to originate in the eastern Andes slopes, northward of 40°S, moving eastward. Both their average lifetime (17.5 hours) and their size at maturity (504000 km^2) largely exceed the magnitudes that characterize the North American mesoscale convective complexes (MCCs). Besides, the MCS composite exhibits a nocturnal phase already found in previous researches (Velasco and Fritsch, 1987).

The results also highlights the importance of the South American Low-Level Jet (SALLJ) immediately east of the Andes (Nicolini et al., 2004) given its role in effecting warm and humid advection and because of the water vapor flux convergence that occurs downstream its core (over northern and central Argentina). This relationship is still more evident as the results demonstrate that the system decay occurs at the same time as the LLJ weakening and consequently in phase with the decay of the moisture flux convergence that is the main source of the convective activity. This is more clearly shown in individual case analysis and confirms that even if synoptic forcing is fundamental for triggering the MCS, once it develops its lifecycle is mainly controlled by the respective SALLJ lifecycle. It is noteworthy that 81% of the MCSs cases included in the sample have at least one of their lifetime stages occurring during strong episodes of low-level jet that penetrates southward of 25°S (denoted Chaco-SALLJ events defined by Nicolini and Saulo, 2000, from now on CJE). CJEs are strong synoptic situations that present statistically significant anomalies respect to mean summer, in the mean only represent 17% of the austral summer days but account for a significant fraction of the precipitation (a maximum of 55%) over South Eastern South America (SESA) (Salio et al., 2002). Also, during CJEs moisture flux convergence at low and mid levels within the SESA area is about ten times more intense than the summer mean with a dominant contribution by the northerly flux. In turn, MCSs are effective in locally perturbing the atmosphere increasing both convergence at low and mid levels and divergence at upper-levels.

The South American Low-Level Jet Experiment (SALLJEX), conducted under VAMOS/CLIVAR was an internationally coordinated effort aimed to monitor, quantify and analyze the low-level circulation over a region enclosing the SALLJ domain. This field experiment featured an enhanced sounding network within which pibals and radiosondes were launched during the Austral summer of 2002-2003 in a region enclosing the SALLJ domain. This enhanced upper-air network and the availability of higher resolution both in time and space IR satellite data allowed addressing the relationship between the timing and intensity of the low-level jet and the MCSs with more reliability. The restriction of heavy precipitation has been released for this MCS higher resolution sample.

Corresponding author's address: Matilde Nicolini. Dep. of Atmospheric Sceince. Ciudad Universitaria. Pabellon 2 - 2 Piso. (1428) Ciudad de Buenos Aires Argentina email: nicolini@cima.fcen.uba.ar

2. DATA AND METODOLOGY

In order to define the position and stage of mesoscale convective systems (MCS) occurred during the SALLJEX period November 15, 2002 to February 15, 2003, 4km horizontal resolution IR brightness temperature data available at http://lake.nascom.nasa.gov/ every half an hour was used. More description about the dataset can be found in Janowiak et. al (2001).

The MCS is defined following a similar criteria to Maddox (1980) and Torres (2003). Size criterion at initiation stage requires an area within the 218°K isotherm larger than 50,000 km^2. Mature stage is attained when that area reaches its maximum size and dissipation stage when the size criterion is no longer satisfied. This criterion must verify for at least 3 hours. Systems that during their life cycle become involved in complex merger or split processes with another MCS and as a result go through more than one growth/decay cycle, attaining sizes smaller than 50,000 km^2, are not included in the sample. These restrictions reduce the sample to a group characterized by large systems.

The FORTRACC program (Machado et al, 1998) determines the position of any cluster that verified the

MCS criterion. This program follows the different systems through their life cycle assuming an areal overlap between an image and the previous one higher than 15%. The spatial domain is limited to Southeastern South America (SESA, 20-40 S and 45-65 W), that mostly include La Plata Basin. Operative analyses produced by NCEP are used in this study to characterize the synoptic and meso-alpha MCS environment.

SALLJEX upper-air data (network information at: http://www.nssl.noaa.gov/projects/pacs/html_files/invehour.html) has been used to analyze the diurnal variability in the vertical structure of the winds.

3. RESULTS

The SALLJEX days have been divided into three different samples using the NCEP operational analyses: days without evidence of SALLJ (NSALLJ), days characterized by SALLJ occurrence penetrating to subtropical latitudes (CJE) and non-Chaco SALLJ days (NCJE).

Nicolini et al. 2004, composited wind profiles for the three samples every three hours to describe the diurnal cycle. Vertical wind structure at three stations located between 15S and 30S, is illustrative of the main signals (not shown). At Santa Cruz, Bolivia (17.75°S, 63.06°W) the wind speed vertical profile shows a strong (~15 m/s) maximum present at all the available hours (except 21 UTC) during NCJEs. This signal is still stronger during CJEs. Mean summer wind profile shows no signal at 12 UTC and during NSALLJ the maximum is much shallower. Over Paraguay (around 22°S), maximum amplitude in diurnal oscillation occurs during CJEs and the strongest jets (>20 m/s) are detected from 06 to 12 UTC (few observations earlier). At Resistencia, Argentina (27°27'S, 59°03'W) a jet is evident only during CJEs.

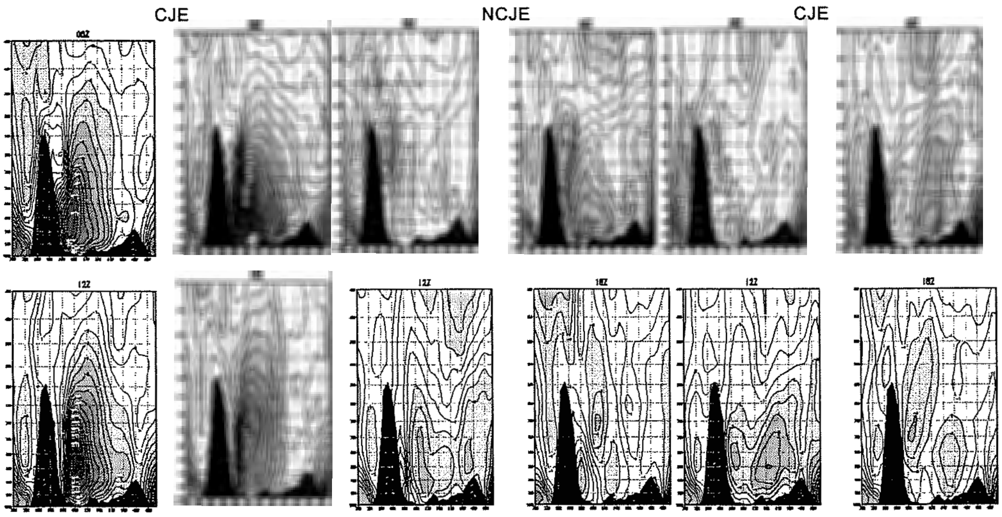

Figure 1: Vertical cross section at 23S of the composites of meridional component of the wind, every 6 hours (00, 06 UTC in the upper panels, 12 and 18 UTC in the lower panels), for the three environmental settings CJE, NCJE and NSALLJ (from left to right) during SALLJEX period. Shaded areas show values higher than 4 ms^{-1} every 2 ms^{-1}. Latitudes progress from 75W to 40W.

Vertical cross sections of meridional component of the wind at 23°S from operative NCEP analysis, composited for the three different synoptic patterns at the 4 synoptic times (Fig. 1), are compared. In particular, differences in vertical thickness, in strength and in horizontal extension in the cross LLJ direction including two wind speed maxima better defined during NCJEs and NSALLJ, are in agreement with SALLJEX observations and clearly emphasize the different potential for fueling long-lived and huge convective systems supported by CJEs, NCJEs and NSALLJ synoptic patterns, respectively.

In order to address the question of what is the role of these SALLJ cases (CJE and NCJES respectively) in triggering and controlling organized convection we analyze some satellite-derived statistics for the 53 MCS cases examined. Figure 3 includes the MCS sample distribution for the whole region of initiation time, maturity time, life cycle duration and area at maximum extension respectively for the three specified environmental condition samples.

For life time analysis purpose we separate the day in two periods: the one between 0000 to 1200 UTC identifies nighttime whereas the one between 1200 to 0000 UTC has been assigned to the daytime period. The organized MCS usually did not occur until 1500 UTC (about local noon) and initiation time maximizes in the 1800-2100 UTC interval (before sunset) during radiational heating hours (Fig. 2a). This behavior is similar for the three environmental condition samples with a more defined

absence of initiation during nighttime hours during NSALLJ events.
As to the distribution of MCS at the time of maximum extent (Fig. 2b) there is an absence of organized mature convection during the 1500-1800 UTC interval when few systems are still increasing in size or dissipating, particularly those with longer duration (>24 hours). The distribution is similar to the one corresponding to initiation time but shifted three hours later maximizing in the 2100-0000 interval of time (early evening). This is consistent with the shorter systems (lasting at least 3 hours as required). However, more mature systems occur during the night and CJEs favor nocturnal organized convection. Average time of maximum extent for nocturnal systems is 0500 UTC (during CJEs is 04:30 UTC).
Distribution of duration (Fig. 2c) shows an expected decreasing number of cases for longer duration, some cases last more than 24 hours and few isolated long systems last more than one and a half day. NCJEs and more clearly CJEs show a tendency to last longer than no-SALLJ cases. Average lifetime duration was about 10.5 hours for the complete MCS sample (the same as the one found by Cotton el al. 1989 for the North America sample) while average longevity was 13.3, 9.0 and 7.5 hours for CJEs, NCJEs and no-SALLJ cases respectively.
Frequency distribution of areas at maximum extent (Fig. 3d) also shows a decreasing dependence with size and a tendency for larger MCS occurring during nocturnal CJEs (average area=366,413 km^2).The average maximum effective radius and size for the 55 MCS sample are 282 km and 249,076 km^2 respectively (34% larger than the 186,000 km^2 found by Cotton et al. 1989). A still more significant difference is found respect to the average maximum size of 504,000 km^2 (400 km radius) found by Torres (2003) for a similar region. McAnelly and Cotton (1989) found that in average, MCCs (larger than 200,000 km^2) produce more precipitation than the smaller ones, requiring a more intense convective activity in meso-β scale at their initiation. They explain this situation, among other mechanisms, by a more important water vapor supply by a low-level jet in its convergence area and more intense large scale lifting at mid levels, both present during CJEs. The requirement imposed by Torres (2003) of a high precipitation threshold in the selection of his MCS sample might have forced a sample of synoptic situations like CJEs particularly favorable for organized and heavy precipitating convection and explains a factor of two in the size values.

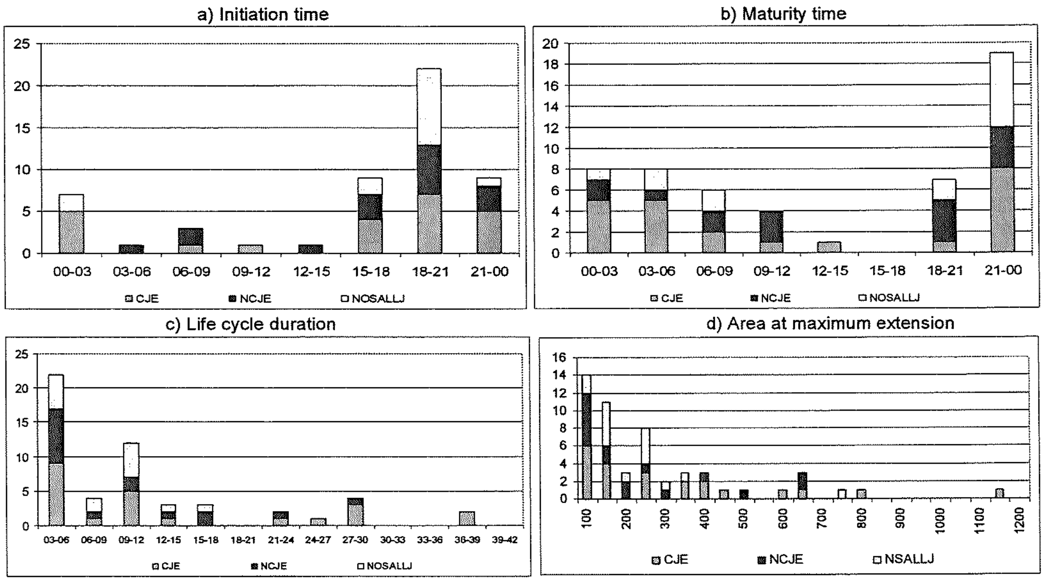

Figure 2: Frequency distributions of MCS (number of cases) for CJE, NCJE and NSALLJ samples of a) initiation time, b) mature time, c) life cycle duration and d) MCS area at maximum extent for the SALLJEX period over the domain 20S, 65W- 40S,40W.

More intense systems in terms of size and longevity corresponds primarily to first day of CJEs and secondarily to NCJEs. Figure 3 shows a map of the region with the location of the centroids of the 3 types of MCS at their mature stage, distinguishing nocturnal from diurnal systems. It is evident the signal of a late afternoon phase during NSALLJ conditions, of a nocturnal phase over the central part of northern Argentina (dominated by the stronger diurnal cycle and nocturnal phase of CJES) and absent over NE

Argentina, the dominance of an opposite phase in a band oriented NW-SE over Brazil parallel to the border with Paraguay and a tendency for daytime mature convection in mountainous regions over Brazil and over sloping terrain in southern Bolivia. This result agrees with previous findings by Nesbitt and Zipser (2003) using TRMM data.

This is also in agreement with the diurnal variability characterization obtained from ETA model 40 km-resolution precipitation forecast products during the warm season 1997-1998 over the same region (Nicolini and Saulo, personal communication). A larger number of systems is located in the northern half of the region, where almost all those occurring during NCJE settings are confined.

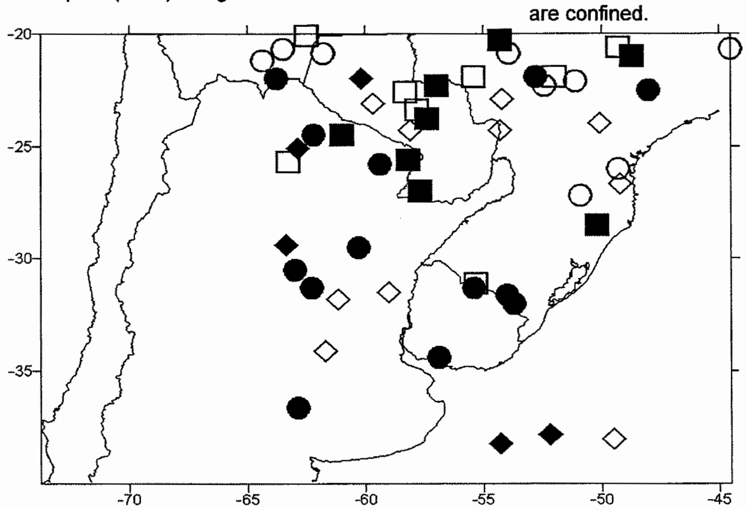

Figure 3: 53 MCS centroids at the time of maximum extent. Circles indicate CJEs' centroid position, squares correspond to NCJEs' and diamonds to NSALLJ events. Daytime convection (white symbols) and nocturnal convection (black symbols).

Acknowlegments

This research is supported by UBA grant TX30 (Argentina), ANPCyT grant PICT N° 07 – 06671 (Argentina), PACS-SONET network, FAPESP grant 01/13816-1 (Brazil), NSF ATM0106776, NASA NAG5-9717 NOAA PID-2207021 and NA03OAR4310096. Thanks to Daniel Vila for his valuable assistance with the FORTRACC program.

References

Cotton, W. R.; M. S. Lin; R. L. McAnelly and C. J. Tremback, 1989: A composite model of mesoscale convective complexes. *Mon. Wea. Rev.*, **117**, 765-783.

Janowiak J., R. Joyce, and Y. Yarosh, 2001: A real time global half hourly pixel resolution infrared dataset and its applications. *B. Am. Met. Soc.*, **82**, N 2.

Machado L.A.T., W.B. Rossow, R.L. Guedes and A.W. Walker, 1998: Life cycle variations of mesoscale convective systems over the Americas. *Mon. Wea. Rev.*, **126**, 1630 – 1654.

McAnelly, R. L. and W. R. Cotton, 1989: The precipitation life cycle of mesoscale convective complexes over Central United States. *Mon. Wea. Rev.*, **117**, 784-808.

Nesbitt S. and E. J. Zipser, 2003: The diurnal cycle of rainfall and convective intensity according the three years of TRMM measurements. *J. of Clim.*, **16**, 1456 – 1475.

Nicolini M. and A.C. Saulo, 2000: ETA characterization of the 1997-1998 warm season Chaco jet cases. *6th International Conference on Southern Hemisphere Meteorology and Oceanography. 3-7 April, Santiago, Chile*, 336 – 337.

Nicolini, M., A.C. Saulo, J.C. Torres and P. Salio, 2002: Enhanced precipitation over Southeastern South America related to strong low-level jet events during austral warm season. *Meteorologica*, Special Issue for the South American Monsoon System, **27**, 59-69.

Nicolini, M., P. Salio, G. Ulke, J. Marengo, M. Douglas, J. Paegle, and E. Zipser, 2004: South American Low-level jet diurnal cycle and three-dimensional structure. *Exchanges*, Special Issue Featuring SALLJEX, 4pp.

Velasco I. y J.M. Fritsch, 1987: Mesoscale convective complexes in the Americas. *J. Geophys. Res.*, **92**, 9591-9613.

Torres, J.C., 2003: Heavily precipitating mesoscale convective systems over Central and Northern Argentina, in spanish, Univ. of Buenos Aires, Ph D dissertation, 132 pp.

NUMERICAL INVESTIGATION OF THE INTER WAVE-ROTOR STRUCTURE OF FRONTAL CLOUDS AT DIFFERENT STAGES OF THEIR DEVELOPMENT

L.V. Palamarchuk[1], A.M. Pirnach[2], V.M. Shpyg.[3]

[1]Cathedra of meteorology, Kiev National Shevchenko University, Vasilkivska 90, Kiev,03022,Ukraine
[2]Ukrainian Hydrometeorological Research Institute, Kiev, 03028, Ukraine
[3]Cathedra of meteorology, Kiev National Shevchenko University

1. INTRODUCTION

Authors continue investigation of the cold- and warm-season frontal clouds in target areas (see Shakina, 1985, Belokobylski et al., 2000, Pirnach et al., 2000, Leskov et al., 2001, etc.).

Three-dimension nowacasting and forecasting numerical models of the frontal cloud systems passing over Crimea have been used for theoretical interpretation of the field measurements in cumulus clouds that were carried out on the hail suppression proving ground. Field experiments have been conducted in eastern Crimea on September 2001. A radar complex "Antigrad" was used for radar measurements. Cross-section area and radio-echo volumes have been received (see Leskov et al., 2001). Investigations of feature of vortical movement in cumulus clouds and nearest environment were basically investigated.

The theoretical interpretation of depicted features has been carried out. Convective sell and raindband formation and development were investigated. Study of dynamical features during the Cb frontal cloud development in the south Ukraina 2001.09.03 and 2001.09.07 was primary task of the next investigation. Second task was assessment a spacing of calculating grid that determined sizes of mesocale formation reproduced correctly. It will be used for cloud and precipitation parameterization in regional forecasting.

Researches of frontal cloud mesoscale were realized by complex approach. It included synoptical analysis, rawinsonding, radar observations and numerical modeling. Instrumental research and visual observation results were compared with numerical experiment results. Results of field and grid measurements were used for construction of diagnostic numerical models and for modeling result verifications.

2. METHODOLOGY OF THE RESEARCH

Numerical experiment with using 3-D diagnostic and prognostic models was put as base for investigations.

Detailed information about system of equations and border conditions is described in Pirnach (1998), Pirnach et al. (2000), etc. Notice only that in diagnostic numerical models frontal clouds was definded by localization positive values of condensation rate. In turn, precipitation was definded by the integral condensation rate:

$$E = -\int_0^H \rho w \frac{\partial q_s}{\partial Z} dz \ .$$

There are: high, z; z-maiximum, H; air density, ?; updraft, w; specific saturated humidity, q_s.

In this paper special attention was given to a vertical vorticity distribution in ?u cong and Cb forming zones. A relationship for calculation was used as follows:

$$\Omega_z = \frac{\partial v}{\partial x} - \frac{\partial u}{\partial y} \ .$$

Ω_z is vertical vorticity, x,y are horizontal coordinates in north and east directions, u, v, are the components of wind velocity respectively.

Analysis was carried out using the precondition: mesoscale formations in the frontal clouds and precipitation bands were generated if an instability expensed in the synoptical scale air currents in direction normal to frontal line. Theoretical researches specify two principal causes of occurrence of such instability in zones of atmospheric fronts: due to vertical shifts of a wind or formation of the high horizontal temperature gradient zones. At the analysis of numerical modelling results it was given more attention to revealing of baroclinic instability zones. The account of a wind shift was spent directly through definition of the Richardson number critical values as in Shakina (1985), Pirnach (1998).

Evolution of frontal nebulosity is accompanied by infringement of uniformity of internal structure of bands most frequently due to strengthening hydrostatical instability along front. As criterion of identification of such zones is a vertical gradient of potential and pseudo-potential temperature. Stable zones of updrafts caused of formation the Cu cells with rotary circulation. A scale of such cells forms tens of kilometers. These structures are accompanied by intensive rotations.

The forecasting models of the warm-season frontal rainbands and convective cloud clusters were constructed for study the severe weather connected with cold front passed over target area on 2001.09.03 (see Pirnach at al., 2000).

Corresponding author's address: Ludmila V. Palamarchuk, Cathedra of meteorology, Kiev National Shevchenko University, Vasilkivska 90, Kiev,03022,Ukraine; E-mail: Hanna@ozsol.kiev.ua

3. NUMERICAL DIAGNOSTIC RESEARCH OF THE FRONTAL CLOUDINESS

Numerical investigation results will be taken below for illustration of the research methodology of nebulosity and precipitation and for study of atmospheric state in the zone of cold front observed in the south of Ukraine on 2001.09.03 and in the warm sector of south-west cyclone observed on 2001.09.07.

On September 03 synoptical situation was definded by cyclone. Its centre was disposed in the Oster region. South-east regions of Ukraine was being under the action of warm cyclon sector. The cold front line passed aproximately along meridian (Smila — Znamjanka — Kherson — Evpatoria). Convection development, showers and thunder-storms were observed before cold front.

Fig.1 presents the modelling results on a regular grid. Spatial space is 30 km. Proving ground was located near point (*x*, *y*) = (340, -630 km). Modeling results allow representing of the surface pressure and temperature field for considered event and display nature of the synoptycal process of the cool air intrusion from north and north-west.

The high temperature horizontal gradient zones were observed in investigation area (see Fig.1d). Their existence promoted formation of instable zones in atmosphere and as result formation of ascending movement cells (see Fig.1e). Maximum updrafts corresponded to zone of the contact of cold air that entered in rearly part of cyclone with air mass its warm sector. Distribution of the potential and pseudo-potential temperature within the framework of investigation region shows an unstable of thermal stratification. A simulated field of thermodynamic condensation rate (see Fig.1a) enables to reproduce a cloud band as well as a cloud cell structure of the cold front. In band disposed in front of frontal line and orientated along maximum updrafts don't exceed 1m/s. Such order were observed for downdraft motion. In accordance with radar observations, maximum updrafts reached 7 m/s. The reduction of the vertical motion velocities is explained by spatial averaging in the numerical modeling. Large grid step causes smoothing of the research charzcteristics.

Cloud system is identified by thermodynamic condensation rate (see Fig.1a). It was characterized by intensive drawing processes of water vapor (see Fig.1b23) identified by occurence of ice supersuturation that practically completely was realized by precipitation. All free for sublimation water vapor completely was realized by precipitation at *t*=11 h. At *t*=23 h in the north-west and south-east part of the calculation area were noted zones with ice supersuturation that did not exceed 0,3 g/kg.

Chains of rotor cells with $\Omega_z > 0$ were formated in initial stage of *Cu* development in prefrontal cloud band. Under proving ground the convective cell identified by cell of updrafts and cyclonic vertical vorticity. The radar observations angular velocity of rotation did not exceed 1 degree per minute. The numerical calculations give value of the vertical vorticity within - $0,5 - 2 \cdot 10^{-3}$ s^{-1}.

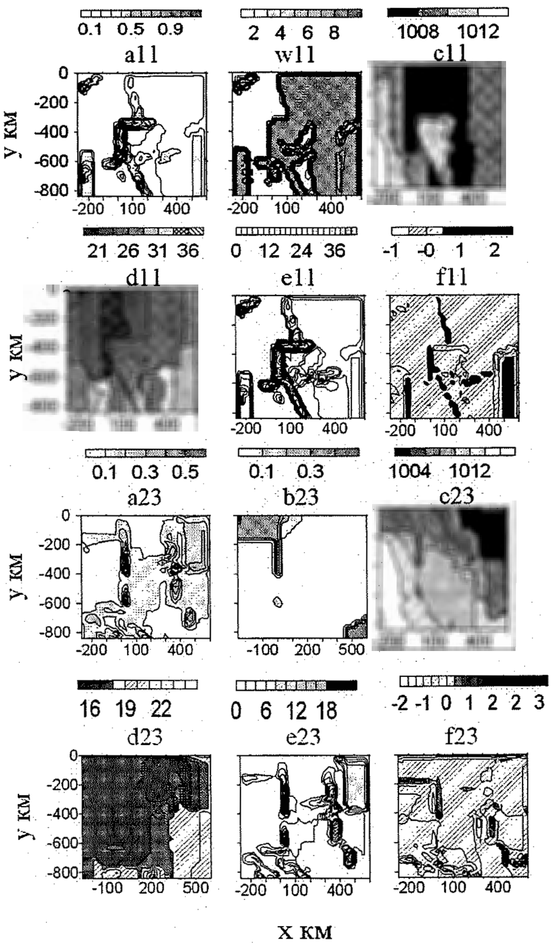

Figure 1. Surface and integral thermodynamic features of atmosphere in the frontal zone on 2001.09.03 at 11 GMT (1-st and 2-nd row accordingly) and 23 GMT (3-rd and 4-th row). Kiev sounding station is initial coordinate point. Integral cloud features: ?11, ?23) condensation rate, mm/h; b23) ice supersaturation, mm (3-rd row); w11) deep of the updraft layers, km (1-st row); ?11, e23) z-maximum updrafts, sm/s. Surface meteorological features: ?11, c23) surface presssure, mb; d11, d23) temperature, ^{o}C; f11, f23) vertical vorticity, 10^{-3} s^{-1} (digits near scale).

The cloud evolution has been accompanied by change of character of the vertical vorticity distribution (see Fig.1f23). At 23 GMT Ω_z changed from $-3*10^{-3}$ to $3*10^{-3}$ s^{-1}. Anticyclonic character of circulation was dominated.

Target nested grid presented in Fig.2. Cross-sections of the thermodynamic features show cell and band structure of the vertical motion in perpendicular to front direction, as well as along it direction. As can see from Fig.2b pseudo-potential temperature can serve as main criterion for finding centre of instability that were identified by this temperature z-decreasing.

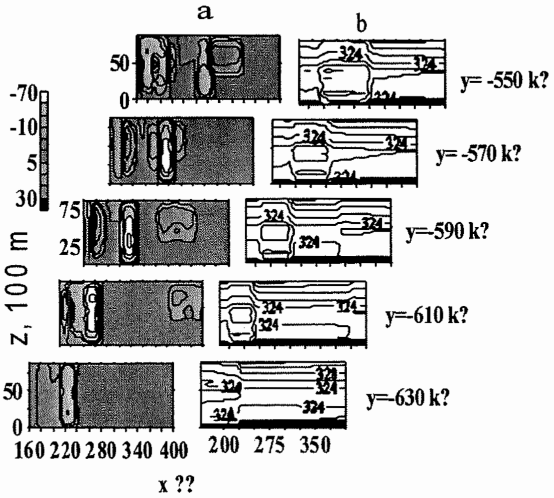

Figure 2. Vertical cross-section of thermodynamic features in the frontal zone on 2001.09.03 (11 GMT) with spatial steps $?x$ = $?y$ =10 km. ?) vertical motion velocity, sm/s (digits near scale); b) pseudo-potential temperature, °K (digits near curves).

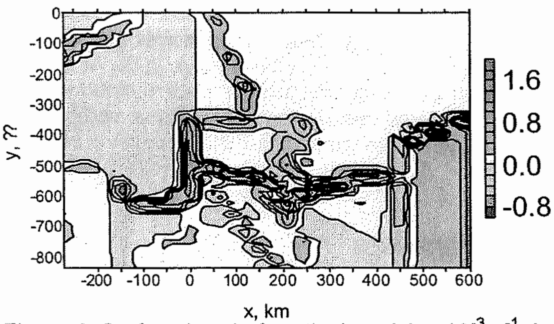

Figure 3. Surface band of vertical vorticity, 10^{-3} s^{-1} in the warm sector of south-west cyclone on 2001. 09. 07. (11 GMT).

As example, distribution of vertical vorticity for warm sector of south-west cyclone observed on 2001.09.07 is shown in Fig.3. It confirms existence paired formations with anticyclonic and cyclonic circulation of air in band of instability (as ex., see 100<x<200 km; -840<y<-740 km). At the area which was disposed on north-east within *Cb* supercells dominated the cyclonic rotation. It confirmed that *Cb* supercells did not reach the stage of its maximum development. Ω_z can be an indirect criterion of identification of the ?b development stage and accompanied above named meteorological phenomena.

4. NUMERICAL STUDY VORTICAL STRUCTURE EVOLUTION

Numerical investigation of the inter wave-rotor structure of frontal clouds at different stages of their development was conducted by numerical model of warm-season frontal cloud and precipitation evolution develop in Pirnach et al. (2000). Field experiment on September 03 was selected for illustration.

Field measurements on August 03 were conducted from11 h 24 min to 13 h. 16 min GMT during lifetime of investigated convective cloud at 0.4<t<1.3 h. t is calculating time.

Numerical modeling of cloud evolution with initial stage t = 0 at 11 GMT depicted that most strong vertical motion, clouds and precipitation have place in band with coordinates 240km < x < 270 km at y=700 km. It was oriented in west-north direction and has 30 km wide. Some precipitation cores in it were fixed. It existed at 0.5<t< 2.5 h. During field measurements the convective cells were fixed nearby the proving ground area.

Numerical simulation of cloud evolution pointed to presence *Cb* supercells, and single-cells, and *Cb* multicells in advance of front line. In the formation region of Cb supercells both anticyclonic and cyclonic formation have place. They can coexist as paired formations or as chaotic formations.

Nested grids with space intervals from 2 to 10 km were used in numerical runs. Spatial distribution of the vertical velocity is shown in Fig.4 in different time of *Cb* development. In it the 10 km spacing is presented. This scale did not allow reproduce vortex for several cloud. It has reproduced the common pictures of above band and some cloud clusters. The cyclonic rotation accompanied above named cloud band during its development and changed by anticyclonic rotation in decaying stage.

In initial stage of frontal cloud band development a relative internal homogeneity of the sign and value of the vertical motion, condensation rate, liquid water content, ice content and etc have place. They evolution is accompanied by infringement of homogeneity of its internal structure and by reinforcement of convection and rotary circulation.

Distribution of vertical vorticity in rainband was not homogeneity. Coupled cyclonic and anticyclonic cells accompanied precipitation cores and gaps between them respectively. Especially it was clear evident from mature to decaying stage cloud development at 1<t< 2.5 h and 3 <z<5 km (see Fig.4).

The most strong cyclonic circulation was depicted at 1<t<1.5 h within prefrontal rainband. Mainly the cell structure of cyclonic vertical vorticity has place under proving ground at 1<t<1.5 h. At t = 2.5 h anticyclone circulation observed at 1<z<5 km. It confirmed

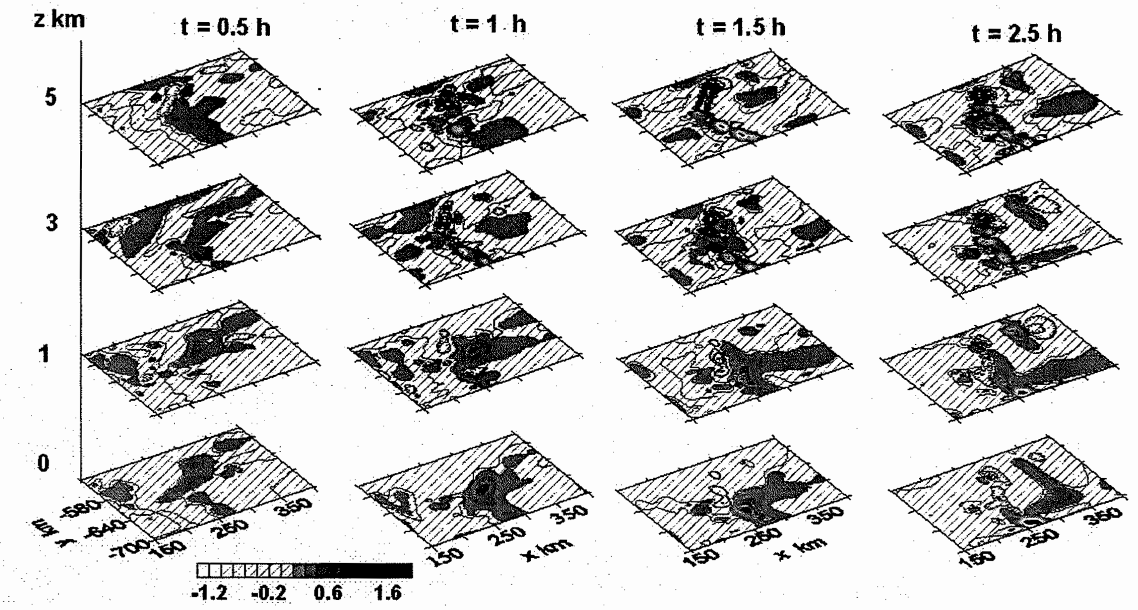

Figure 4. Spatial distribution of vertical vorticity 10^{-3} s^{-1} (digits near scale) at different t (digits at tops)

decaying of convective cloud that has been subject of field experiment. Appearance of new cyclonic cells predicted a new convective cells formation. Decomposition of convective cells was followed by reduction of angular rotation velocity and by anticyclonic circulation.

5. CONCLUSIONS

Three-dimensional nowacasting and forecasting numerical models of frontal cloud systems passing over Crimea have been constructed and theoretical interpretation of field experimental measurements were conducted. Meteorological feature distributions in field experiment zones and interrelation between disturbance zones and features of cloudy formations development is received by numerical modeling. At the analysis of result of numerical modeling high attention was given revealing of baroclinic instability zones. They were promoted formation of sells and bands of frontal ascending movement and were responsible for transportation mechanisms of moisture.

At the analysis of result of numerical modeling high attention was given revealing of baroclinic instability zones. Disturbance in air column it is possible to determine by temperature distribution. Especially pseudo-potential temperature is sensitive. Other available characteristic are shift of wind, ascending movement of significant velocity achieved tens m/s and powerful and homogeneous cyclonic whirlwind.

In initial stage of development of frontal cloud bands is notable relative internal uniformity of vertical movements, thermodynamic condensation rate, cloud and precipitation and etc. Infringement of the internal uniformity of bands, strong convection and formation of cloud cells with rotary circulation accompanied evolution of cloudiness from mature to deceiving stage. The scale of rotary cells is some kilometers. Theoretical interpretation of natural experiments by numerical modeling has shown that cyclonic vertical cells are following the initial stage and stage of maximal development of convective sells. At the stage of maximal development of convective cloud existence of the coupled cyclonic and anticyclonic vertical vortex is possible. Decomposition of convective cells was followed by reduction of angular velocity of rotation and by anticyclonic circulation.

6. REFERENCES

1. Belokobylski, A. V., Pirnach, A. M., 2000: Numerical simulation of the warm-season frontal clouds over Ukraine. Proceedings of 13th ICCP. Reno, Nevada, USA. 2000, 1165-1169.
2. Pirnach, A. M., Krakovskaia, S. V., 1994: Numerical studies of dynamics and cloud microphysics of the frontal rainbands. J. Atmos. Res., **33**, 333-365.
3. Pirnach, A. M., 1998: Construction and application of the various numerical models for study the cloud dynamics and structure of the frontal rainbands. J. Atmos. Res., **45-47**, 356- 376.
4. Pirnach, A. M., Belokobylski, A. V., 2000: Numerical simulation of the summer frontal clouds. Trudy UHRI, **248**, 5-21.
5. Leskov, B. N., Syrota, N. V., Bondarenko, A. V., 2001: About angular velocity and period of Cu rotation. Trudy UHRI, **249**, 35-54.
6. Shakina, N. P., 1985: Dynamics of Atmospheric Fronts and Cyclones, 263.

THREE DIMENSIONAL KINEMATIC AND MICROPHYSICAL EVOLUTION OF MAP IOP3B OROGRAPHIC PRECIPITATION

Olivier Pujol, Jean-François Georgis, Michel Chong and Frank Roux

Laboratoire d'aérologie, CNRS et Université Paul Sabatier, Toulouse, France.

1. INTRODUCTION

Dynamics and microphysics of orographic precipitating systems are investigated through Doppler and polarimetric radar data collected during MAP-IOP3B (25 September 1999) between 1720-1950 UTC in the Lago Maggiore region.

Smith (1979) suggested that orographic effects on the airflow could generate very active convective cells. MAP IOP2B (19-21 September 1999) was a typical example of convective situations; it was studied by Georgis et al. (2003) and Medina and Houze (2003) which proposed a conceptual model of convective orographic precipitation. It is based on the orographic lifting of the moist low-level flow and the subsequent release of potential instability. Microphysics consists in coalescence below the 0° C level, riming and freezing above leading to graupel formation. Moreover, melting through the 0° C isotherm could enhance liquid precipitation.

Strong similarities were pointed out by Medina and Houze (2003bis) between IOP2B and IOP3B. In particular, both are characterized by an unstable moist low-level airflow coming from the Mediterranean sea, because of the presence of a trough in north Atlantic associated with a thalweg extending to north Africa.

We then proposed to verify the model by Medina and Houze (2003) through a complete spatio-temporal investigation of dynamics and microphysics of IOP3B.

2. THE LAGO MAGGIORE TARGET AREA

The Lago Maggiore target area is displayed in Fig.1; it encompasses different terrains with the Pô Valley to the south, the hilly Piedmont to the south-west, the high Alpine mountains to the north with the Lago Maggiore and deep Toce and Ticino valley.

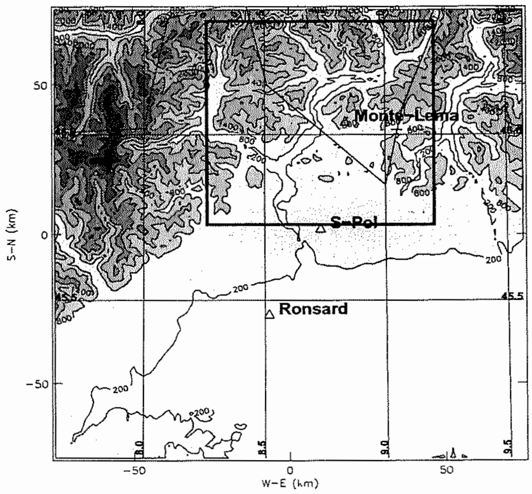

Fig.1: Topography of the observational region with the three ground-based Doppler radars. The black square represents more precisely the Lago Maggiore target area.

More precisely, we focus on the region delimited by the black square which was concerned by the strongest precipitation. Observation were conducted with three ground based Doppler radars: the French RONSARD radar, the Swiss MONTE-LEMA radar and the US SPOL polarimetric radar. Wind field was retrieved from Doppler data by the RAMDAM method developed by Chong et al. (2000). From five SPOL polarimetric parameters (Z, ZDR, LDR, KDP, ρ_{hv}), nine hydrometeor classes (HC) were inferred using the fuzzy logic method by Vivekanandan et al (1999): light, medium and heavy rain (LR, MR, HR), hail (HA), rain-hail and graupel-hail (RH, GH) mixture, wet and dry snow (WS, DS) and ice crystals (IC).

3. TEMPORAL MEAN CHARACTERISTICS

Mean dynamics is characterized by a dominant southerly wind with however a low eastward component. Precipitation correspond to

Corresponding author' s address: Olivier Pujol, Laboratoire d' aérologie, Observatoire Midi Pyrénées, 14 avenue Edouard Belin, 31400 Toulouse, France; e-mail: pujo@aero.obs-mip.fr.

a convective pattern primarily located over the first mountain and on the foothills, over the lake. The next two figures illustrate the temporal mean reflectivity signal and vertical wind velocity for two vertical cross-sections along the dominant wind direction. Figure 2 shows a high reflectivity cell (higher than 34 dBZ) over the lake, upwind of the mountains, with a vertical extension of 3.5 km indicative of a convective pattern; mean updrafts of about 0.5 to 1.5 m s^{-1} are correlated with orography. A more classical structure of upslope convection is observed in Fig. 3: a cell of mean reflectivity equal to 34 dBZ is located just over the first mountain and associated with updrafts higher than 1.5 m s^{-1}.

This mean signal structure is similar to that observed during IOP2B by Medina and Houze (2003). It shows a convective structure over the first peak and a high mean reflectivity cell at low-level upwind of the first mountain.

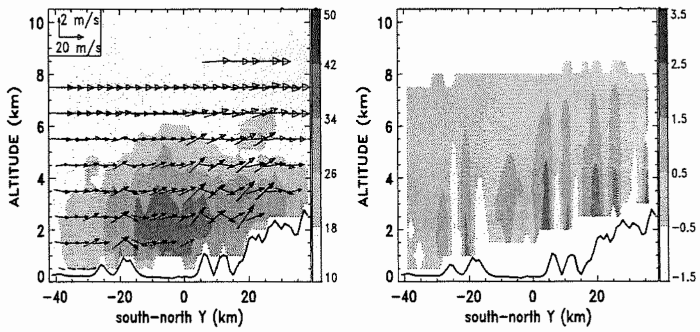

Fig. 2: Temporal mean reflectivity and updraft velocity respectively for a meridional cross section characterized by a variable topography. From south to north, plain, little peaks, the Lago Maggiore and mountains of increasing peaks are observed.
Grey scales represent mean reflectivity (in dBZ) and updraft velocity (in m s^{-1}) respectively.

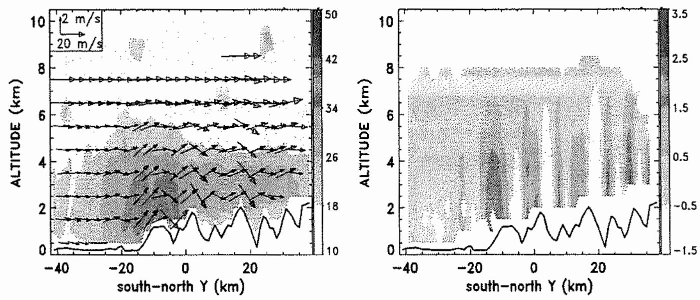

Fig. 3: As Fig 2 except for a meridional cross section with a more marked lake/mountains separation. From south to north, the lake and the high Alpine mountains with a succession of peaks and valleys are observed.

Figure 4 displays the temporal mean vertical distribution of the HC over the whole target area. Each HC is present except HA and RH. LR and DS, formed by condensation and vapour deposition respectively are dominant (below and above the 0° C level respectively). The organization below the 0° C level (i.e below 3.5 km altitude) (stratification) is consistent with coalescence growth processes which occur at positive temperature. The distribution above the 0° C level highly suggests formation of graupel by riming and freezing. Melting during the fall of GH through the 0° C level leads to WS and probably also to HR just below. All these results are consistent with those of Yuter and Houze (2003) and Medina and Houze (2003).

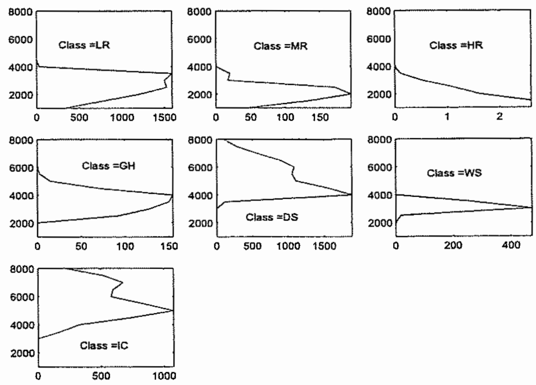

Fig.4: Temporal mean vertical distribution of each HC between 1720-1950 UTC over the whole target area.

4. KINEMATIC AND MICROPHYSICAL TEMPORAL ANALYSES

In order to better understand the different processes implied in the hydrometeor formation, a 3D analysis of dynamics and microphysics between 1720 and 1950 UTC is now presented. As displayed in Fig. 5 and Fig. 6 for the same cross-sections as previously considered, growing and intensification of the system is observed in updrafts over the seeding lake and over the upslope of the first mountainous peak which acts as an efficient instability releaser. High cores of reflectivity (42 dBZ) are observed at 1809 UTC over the lake and associated with updrafts of about 0.5 to 1.5 m s^{-1}. At 1750 UTC, a major convective cell extending up to 6.5 km altitude with a reflectivity core of 42 dBZ is observed over the upslope of the first peak. It is associated with updrafts of 2.5 m s^{-1} around 4 km of altitude. This convective cell results in a release of instability by orography after a development over the lake. These observations indicate efficient microphysical growing processes.

The microphysical evolution of the system is characterized by coalescence processes at low-level (below 0° C level) leading to formation of HR, and by riming and freezing at higher level (above 0° C level) leading to graupel formation. An illustration of the microphysical content of the cells is displayed in the next two figures which correspond respectively to Fig. 5 and Fig. 6.

Figure 7 highlights an hydrometeor column of MR, HR, WS and GH. This configuration can be explained by the lake which acts as a secondary moisture source and by the updrafts which tends to increase the residence time of water in cloud. Water is also carried aloft where freezing and riming can occur by contact with ice particles leading to the observed graupel cap. Moreover, falling through the 0° C level, graupel can participate through melting to the presence of HR, particularly just below the 0° C level. The same microphysical content and organization can be observed on Fig. 8, with a graupel cap inclination corresponding to that of the upslope of the peak.

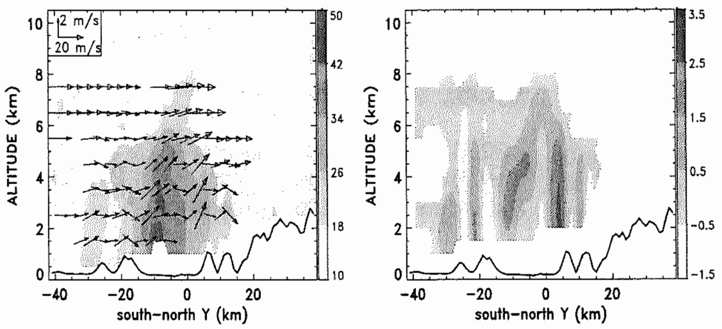

Fig. 5: Reflectivity and wind field at 1809 UTC along the same meridional cross section as in Fig. 2. Grey scale represents reflectivity in dBZ and updraft velocity in m s^{-1} respectively.

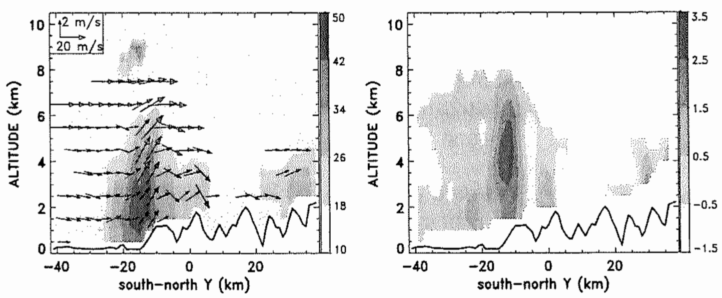

Fig. 6: Reflectivity and wind field at 1750 UTC along the same meridional cross section as in Fig. 3. Grey scale represents reflectivity in dBZ and upraft velocity in m s^{-1} respectively.

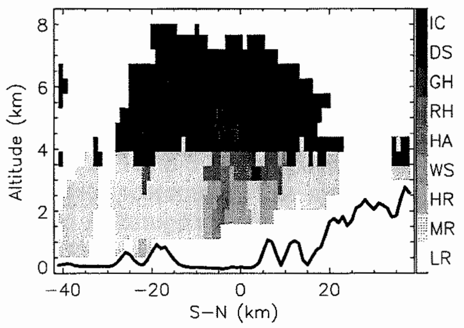

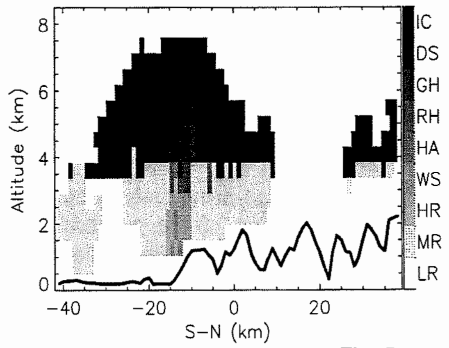

Fig.7 (on the left): Microphysics of the system at 1809 UTC for the same meridional cross section as in Fig. 5.
Fig.8 (on the right): Microphysics of the system at 1750 UTC for the same meridional cross section as in Fig. 6
Grey scales represent the nine HC.

CONCLUSION

Dynamics and microphysics of MAP IOP3B (25 September) orographic precipitation were investigated between 1720 and 1950 UTC using Doppler and polarimetric ground based radar data.

The mean location of the precipitating system is over the first mountain and on the foothills over the lake. The associated mean wind is predominantly southerly.

Microphysics is characterized by convective processes as coalescence below the 0° C level, riming and freezing above. Moreover, melting of graupel during their fall highlights the important ice phase role in the enhancement of liquid precipitation. This microphysics is favoured on the one hand by the presence of the lake which acts as a local moisture source and, on the other hand, by the orography which permits release of potential instability.

All these results are consistent with those obtained in IOP2B.

REFERENCES

Chong, M., Georgis, J-F., Bousquet, O., Brodzik, S., Burghart, C., Cosma, S., Germann, U., Gouget, V., Houze, R., James, C., Prieur, S., Rotunno, R., Roux, F., Vivekanandan, J. and Zeng, Z., 2000: Real-time wind synthesis from Doppler radar observations during the Mesoscale Alpine Program. Bull. Am. Meteor. Soc., **81**, 2953-2962.

Georgis, J-F., Roux, F., Chong, M. and Pradier, S., 2003: Triple-Doppler radar analysis of the heavy rain event observed in the Lago Maggiore region during MAP IOP2B. Q. J. R. Meteor. Soc., **129**, 495-522.

Medina, S., Houze, R., 2003: Air motions and precipitation growth in Alpine storms, Q. J. R. Meteor. Soc., **129**, 341-371.

- 2003 bis: Orographic precipitation in potentially unstable Alpine storms: Map IOPs 2b, 3, and 5. Extended abstract for conference.

Smith, R.B., 1979: The influence of mountains on the atmosphere, Advances in Geophysics, **21**, 87-230.

Vivekanandan, J., Zrnic, D., Ellis, S., Oye, R., Ryzhkov, A., Straka, J., 1999: Cloud microphysics retrieval using S-band dual-polarization radar measurements. Bull. Am. Meteor. Soc., **80**, 381-387.

Yuter, S., Houze, R., 2003: Microphysical modes of precipitation growth determined by S-band vertically pointing radar in orographic precipitation during MAP. Q. J. R. Meteor. Soc., **129**, 455-476.

FORMATION OF THE CONVECTIVE CELL IN SHEET CLOUD AND THE NUMERICAL EXPERIMENTS OF ITS INFLUENCE ON THE PRECIPITATION

Yanbin Qi[1] , Dezhen Jin[1] and Yanli Qi[2]

[1]JiLin Weather Modification Office, Changchun, 130062 ,China
[2]Department of Information Engineering, JiLin Professional Technology Institute of Electronic Information, JiLin,132021,China

1. INTRODUCTION

With the development of exploring, monitoring system and computer technology ,cloud modeling has better simulated the cloud dynamical processes and microphysical processes. Recently, the theory of cloud physics has gradually been improved . The microphysical scheme of parameterization (Kessler and Berry)was widely adopted in a variety of later cloud model. A model including 26 kinds of microphysical processes is developed (Hu Zhijin et al.). Huang Meiyuan et al. research show: the sheet cloud in merging cloud has clearly influence on the development of cumulus. Another model including 37 kinds of microphysical processes is established and developed (Guo Xueliang).Single station sounding data is used in these model. Hence, the effect of the meso-scale vortex energy on convective cloud evolution can not be better simulated .

It has been paid close attention to that the convective cell in sheet cloud have a great action to the distribution and strengthen of precipitation field. Lamb.R.G(1978) and Meong.et al.(1989)have shown some structures and characteristics that convective cell possessed by numerical simulation. Young. (1988) also get the same results by experimental research.

The processing method of Nesting technology have two way. One way is one way interaction , it is that the affect of coarse-grid forecast model in a lager areas on fine grid model is only considered , Time integration in two models is independent. Forecast value in coarse-grid model provide needed boundary value for fine grid model. Another way is two way interaction, it is that interaction during coarse grid and fine grid model is considered , Time integration in two models must be similar time step. In this paper, a nesting method of different model is developed and the effects of meso-scale characteristic field on convective cloud evolution is simulated.

2. MODEL DESCRIPTION

2.1 MM5 meso-scale model

In this paper , MM5 is the Fifth Generation NCAR/Penn State Meso-scale Model. The convective cell in sheet cloud can often lead to larger amount of surface precipitation in JiLin Province , China. In order to look for potential area of precipitation, a new model that MM5 Modeling System nested with a three dimensional numerical model with fully elastic primitive equations is developed. The model is employed the method of one way interactive and the numerical processing technology on the boundary and more detail bulk-water parameterized microphysics are considered .

Corresponding author's address: Yanbin Qi, No.653, HePing Street, ChangChun City, JiLin Province,130062,China;E-Mail:qyb880201@sina.com

2.2 Convective cloud model

A three dimensional numerical model with fully elastic primitive equations is developed, including 38 kinds of microphysical processes. The water material in model is divided into the vapor, cloud water ,rain water ,ice crystal , snow and graupel particle and so on.

3. NESTING SCHEMES OF CONVECTIVE CLOUD MODEL

(a)The forecast result of MM5 model , including T, P, T-Td, U, V field elements, are output in δ t (δ t=1hour) time interval , these data was interpolated into the grid point of convective cloud model by objective analysis.

(b) At δ T time interval, the boundary tendency value in MM5 model is calculated at the grid point of convective cloud model, the formula is as follow:

$$(\frac{\partial\overline{\Phi}}{\partial t})^{(\tau)} = \frac{\Phi(\tau+\delta\tau)+\Phi(\tau)}{\delta T}$$

(c) At T time, as the convective cloud model is integrated till some time step, the physical elements tendency value calculated by above formula in MM5 model will be weighted mean with those in convective cloud model to get new physical elements tendency value at the grid point of convective cloud.

4. RESULTS AND ANALYSIS

The model has been used to simulate the evolution processes of convective cell in sheet cloud occurring in JiLin province ,On July 11th ,2002. Fig.1and Fig.2 show the radar echoes in PPI at 11:16 and in RHI at 11:47, respectively .(Data from meteorological observatory of JiLin Province). Fig.1 indicates that the

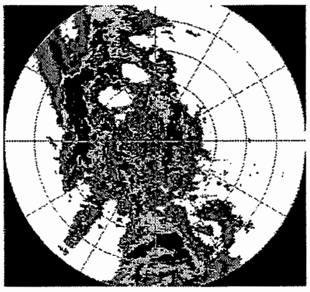

Fig.1 Radar echo PPI, Ang=0.0,11:16 on 11 July 2002.

30dbz echo area was located at 90km from the radar station, with the direction of 245.4^0 , it is a convective cell in sheet cloud.

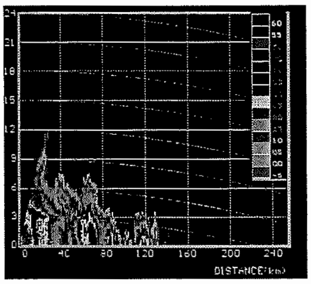

Fig.2 Radar echo RHI,248.1^0 ,11:47 on 11 July 2002.

Fig.2 shows that the width and the height with the 30dbz echo area is approximately 8000m and 1500m, respectively. The top of cloud is about 6000m. From 11:16 to 11:35 (BeiJing time), the echo intensity increased to approximately 35dbz and the echo area extended obviously(its width is approximately 14km). The width of the echo areas with 30dbz is approximately 12000m and its height rises up to 2800m. The top of cloud is approximately 7500m. The echo of convective cell in PPI has get weak at 11:47

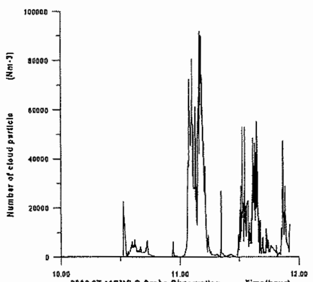

and the areas of precipitation get small, the precipitation ended at 12:02. By means of exploring airplane, macroscopic and microscopic data for the convective cell were detected. The flight started at

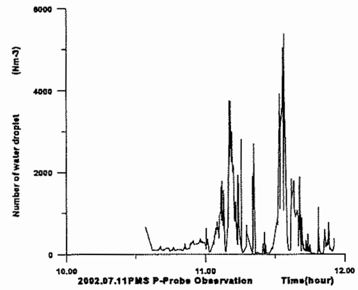

Fig.3 Measure data by PMS

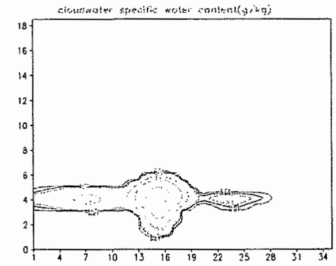

Fig.4 The X-Z vertical section of cloud water mixing ratio at Y=18km at 76 min

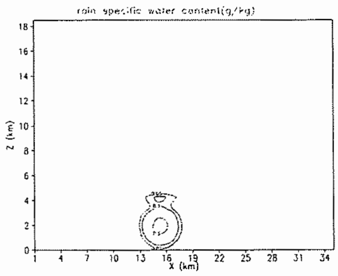

Fig.5 The X-Z vertical section of rain water mixing ratio at Y=18km at 76 min

10:33 in Changchun airport, it was near the convective cell at 11:10 with height of 5000m ,the height of 0℃ level is approximately 4500m. Fig.3 was measure data by PMS (particle measure system). It shows that the content of liquid water at 5000m is approximately 2.5g/m^3 at 11:10, the content of cloud water is 0.68g/m^3 ,the concentration of drop is approximately 3800N/m^3 , the cloud drop is about 90000 N/m^3. The large amounts content of Liquid water shows that ice crystal is major in this layer.

The convective cell occured in JiLin Province on July 11th, 2002. A numerical simulation using MM5 output data , has been employed as initial condition for our nesting cloud model. At initial time ,it is one of main reason that the transformation of the meso-scale vortex energy into turbulent energy trigger the evolution of convective cell . The formation of convective cell lead larger amount of surface precipitation by means of dynamic and thermal change and microphysical action. Fig.4(abb.) (72min) shows the content areas of rain water of 0.1g/kg has been formed during 2200m and 4000m . Fig.5 (76min) indicates the top of cloud continually raise, the content areas of cloud water of 2g/kg has been formed near 4500m . Fig.6 (76min) shows the content areas of rain water of 0.5g/kg was formed near 2000m .At modeling 80min, the content of ice crystal at the top of cloud decrease, so do that of cloud water, the content of rain water rises up to 1g/kg . It is because the convective cell at lower level, lead to the ascending motion inside cloud , the top of cloud is raised, ice crystal are formed above 0℃ level. the top of cloud continually raise, a large amount of ice crystal start to drop, through the processes of sublimation and coherence et al., a large amount of snow crystal are formed, then continue to drop , it melt in melting layer, collection growth in lower sheet cloud. At modeling 96min, the precipitation increase on the ground, appear in a maximum value, and the range of rain region is extended . at modeling 120min , the results show the precipitation have ended , and the content of ice crystal in cloud also decrease ,the development processes of convective cell tendency to end.

5. CONCLUSION

We made use of those data including radar , satellite ,ground live recording of weather, airborne cloud rain sounding data ,the observation of penetration cloud by airplane and numerical modeling to make a calculation and integrated analysis . The results indicate that precipitation close to convective cell has not only characteristic of the sheet cloud precipitation but characteristic of convective precipitation as well. The conclusions show that:

(a)It is one of main reason that the transformation of the meso-scale vortex energy into turbulent energy trigger the evolution of convective cell .

(b) The formation of convective cell lead larger amount of surface precipitation by means of dynamic and thermal change and microphysical action.

(c)The scale of the convective cell is usually related with microscale or mesoscale systems.

(d)The numerical simulated results are basically consistent with the observed results of penetration cloud by airplane.

(e) A lot of ice particle on the top of the convective cell fall down, Because of the effects of wind shear in vertical direction, they were formed snow virga and were playing an important role in natural steering ice crystal seeding.

REFERENCES

Hu Zhijin and He Guanfang ,1987. Numerical Simulation of Cumulonimbus Microphysical Processes, Meteorological Academy. 46(1)28-40.

Klemp.J.B and R.B.Wilhelson.1978:The simulation of three dimensional convective storm dynamics ,J.Atmos.Sci.,35,1070-1096.

Lamb.R.G,1978.A numerical simulation of dispersion from an elevated point source in the convective boundary layer,Atmos.Environ.12,1297-1304.

Meong.C.-H and R.Rotunno,1989,vertical velocity skewness in the buoyancy-driven boundary layer,J.Atmos.Sci.,47,1149-1162.

Phillips N.A. and Shukla, J., 1973. On the strategy of combining coarse and fine grid meshes in numerical weather prediction, J.Appl.Met.,Vol.12,763-770,

Triploli, G. J .,and W.R.Cotton,1982: The CSU three dimensional cloud/ meso-scale model 1982.Part I: General theoretical framework and sensitive experiments,J.Rech.Atmos.,16,185-219.

Zhou Xiuji et al. 1991.Advanced Atmospheric Physics, Meteorological Press.

DIURNAL CYCLE OF MESOSCALE CONVECTIVE SYSTEMS OVER SOUTHEASTERN SOUTH AMERICA

Paola Salio[1] , Edward J Zipser[2], Matilde Nicolini[1] and Chuntao Liuct[2]
[1]Centro de Investigaciones del Mar y la Atmosfera. CONICET/UBA. Department of Atmospheric and Oceanic Sciences. University of Buenos Aires. Argentina
[2]Department of Meteorology. University of Utah. USA

1. INTRODUCTION

The structure and evolution of Mesoscale Convective systems (MCSs) have been studied in several regions of the world, but most extensively over United States of America. Previous studies have identified MCSs following colder areas on IR cloud-top temperatures, Machado et al (1998) and Torres (2003) have shown the MCS structure over South America with an emphasis over the general characteristics of the systems. The goal of the present study is to analyze the diurnal cycle of MCSs over South Eastern South America (SESA – 20-40S – 65-40W) at their mature stage using IR cloud-top temperature over all year and their relationship with the synoptic patterns.

2. DATA AND METODOLOGY

IR brightness temperature data every half an hour available with 4km horizontal resolution at http://lake.nascom.nasa.gov/ is used to determine the position and stage of every mesoscale convective system (MCS) during March 2002 – February 2003. More description about the dataset can be found in Janowiak et. al (2001).
The MCS is defined following similar criteria to Cotton et al. (1989) and Torres (2003). The MCS initiation stage occurs when the -55° C (218 K) isotherm area is greater than 50,000 km^2, the mature stage is attained when the area enclosed by the -55° C isotherm is maximum, and the dissipation stage when this area is smaller than 50,000 km^2. To qualify as an MCS its lifetime has to be longer or equal than 3 hours. Systems that during their life cycle become involved in complex merger or split processes with another MCS and as a result go through more than one growth/decay cycle, attaining sizes smaller than 50,000 km^2, are not included in the sample. These restrictions reduce the sample to a group characterized by large systems.
The FORTRACC program (Machado et al, 1998) determines the position of any cluster that verifies the MCS criterion. This program follows the different systems through their life cycle requiring an areal overlap between an image and the previous one higher than 15%.

Corresponding author's address: Paola Salio. CIMA. CONICET/UBA. Ciudad Universitaria. Pabellon 2 - 2 Piso. (1428) Ciudad de Buenos Aires Argentina email: salio@cima.fcen.uba.ar

We present only the results over the Southeastern South America (SESA, 20-40 S and 45-65 W) in this study. GDAS operational analysis data is used in this study to analyze the synoptic and meso - alpha environment structure.

3. RESULTS

During the one-year period 2002-2003, 130 MCS systems verified the imposed conditions. These systems were located only in their mature stage over SESA area, but could have started to organized or dissipate out of this region. Most of these systems occurred during summer (33%) and spring (32%), still significant portion happened during fall (24%), leaving a smaller portion for the winter (10%).
The mature stage occurrence during the different seasons is shown in Figure 1. SESA region has been divided in four portions to explore different signals in the diurnal cycle. There limits are: region 1 (20-30S, 65-55W), region 2 (20-30S, 55-40W), region 3 (30-40S, 65-55W) and region 4 (30-40S, 55-40W). Maximun frequency of mature stage occurrence is located in region 1 with a 38% over the whole year, followed by region 2 with 32% of occurrence while the other regions show a 15% each one.
For the whole period, over SESA region, the 56 % of the systems had their mature stage during daytime hours while the remaining 44% during nighttime. The mature stage occurrence in summer shows a maximun over region 1 and 2, occurred at late afternoon and early evening (between 21 and 00Z). A dominant and more evenly distributed number of cases happen during the night (between 3 and 12 Z) in region 1. There are no systems between 12 – 18Z in any regions. Region 3 and 4 show maximun frequency during night-time hours. The number of diurnal cases decreases during spring, nocturnal period still dominates in region1 but in region 2 the diurnal cycle weakens and in region3 mature phase dominates during daytime. A similar behavior is present during fall except that region 3 shows (as in summer) a nocturnal prevalence. Diurnal cycle is weak during winter with a dominance of mature MCS in region 4.
The mature size shows huge values during spring with areas lager than 400.000 km^2 in 30 % of the cases, while in the other seasons this occurs in only 15% of the cases.
Most of these characteristics are related to the associated synoptic scale environment in each season. While in summer the MCSs are strongly related to the evolution of a low-level jet just east of the Andes and the convective instability (Nicolini et al 2004, in this issue), in fall the northerly flow is present, but it does not show a low level jet profile and the environment is dominated by

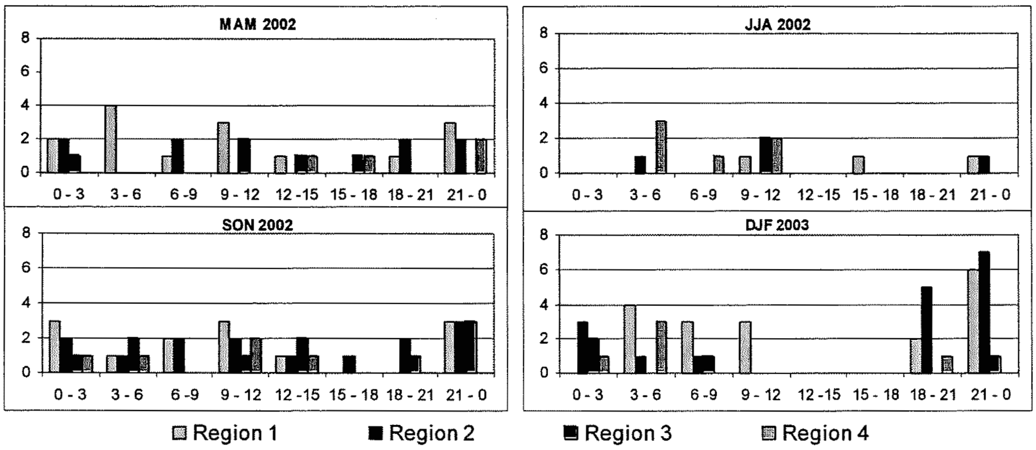

Figure 1: Frequency histograms for mature stage time on region 1 (20-30S, 65-55W), region 2 (20-30S, 55-40W), region 3 (30-40S, 65-55W) and region 4 (30-40S, 55-40W) at different seasons.

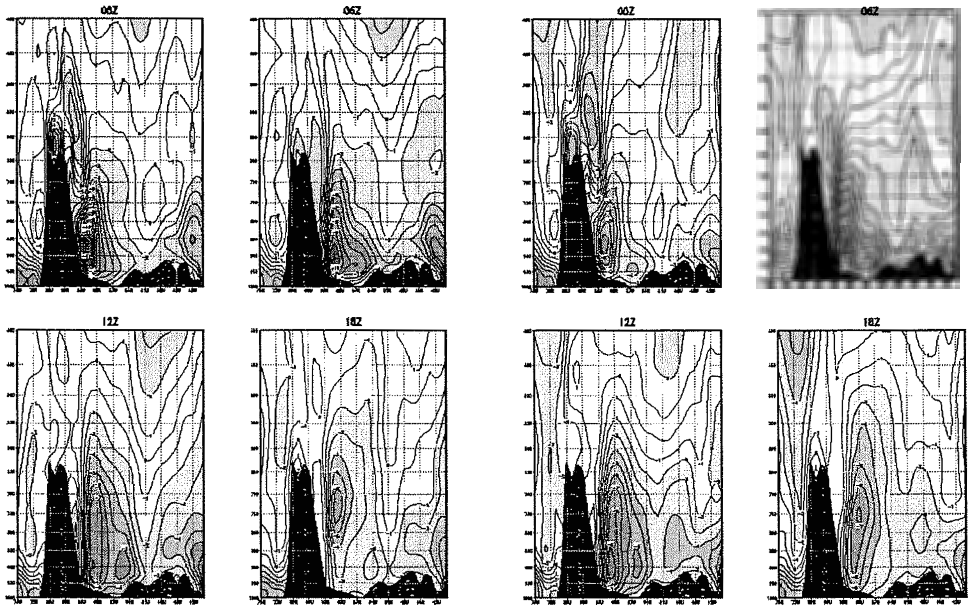

Figure 2: Meridional component of the wind at 20S during summer shaded areas show values higher than 4 ms^{-1} every 2 ms^{-1} for Night composition at left and Day composition at right..

the presence of a strong cold front (Campetella and Vera, 2002).

The low-level jet and cold surges are both present in spring generating strong, huge MCSs, that produce strong precipitation over SESA (Torres, 2003).

In order to give support to these statements, fields from NCEP analysis are composited over all MCS systems that have their mature stage over region 1. This is done separately for daytime (12 to 00Z) and for nighttime (00Z to 12Z) on the different seasons. Winter is excluded of this analysis because of its reduced sample of MCS cases.

The wind field at 850 hPa, according to NCEP analysis (not shown) for the different composition on the MCS day shows no significant difference between the night and day samples during fall. Contrasting with this behavior a diurnal cycle exists during this season supporting the hypothesis of the action of other mechanisms favoring organized convection, not directly related to a low-level jet diurnal cycle.

These results require further insight in identifying synoptic patterns related with these systems.

In spring, the northerly current is stronger than during other seasons, supporting a stronger moisture transport and consequently the formation of stronger MCS respect to fall and winter.

In what follows we concentrate in analyzing the summer season because of the clear diurnal peak in the frequency distribution.

A meridional wind vertical cross section at 20S during summer (figure 2) shows a low level jet profile at 00Z and 06Z in the night time sample stronger than the low level jet in the day time sample. In turn, the day sample shows a stronger and deeper low level jet reaching lower level at 18Z respect to the nocturnal. According with Nicolini et al. (2004) using South America Low Level Jet Experiment (SALLJEX) data, the low level jet diurnal cycle shows strong values at 06-09Z with no presence of low level jet profile at 18Z around 20S. This day time sample shows an unusual low level jet profile at that time, but still weak to generate strong convection.

There is a light difference between night and day time sample in the magnitude of the convective instability in a deep layer above the ground, showing stronger values in the afternoon in the day time sample at 60W (not shown).

The 90% of the systems in the day sample have lower size than 300.000 km^2 while during night the systems are bigger reaching values up to 600.000 km^2. Strong low level jet over this region during the night sample helps to explain the existence of larger systems during nocturnal hours than diurnal time.

Figure 3 shows the centroids of the mature stage at time during the four seasons 2002-2003 over SESA. There is nocturnal phase during fall over northern Argentina that moves to the afternoon in southern Brasil. Most of the systems in winter are close to the sea. The diurnal cycle in spring shows a strong nocturnal pattern over northern Argentina and northern Uruguay and southern Brasil, while on the tropical region all systems have the maximum extent during diurnal time. During summer, close to the mountain all systems show a nocturnal maxima, while there is no systems over the Mesopotamia, this can be related with the small number of low level jet cases that penetrates over this region during this particular summer. Further east and close to the coast the systems show a diurnal maxima. Tropical behavior is shown over Paraguay and Brasil with a maxima of cases during diurnal hours.

Further analysis has to be made over a longer period of time, including initiation and dissipation stages in order to progress in a climatologically characterization of MCSs diurnal cycle.

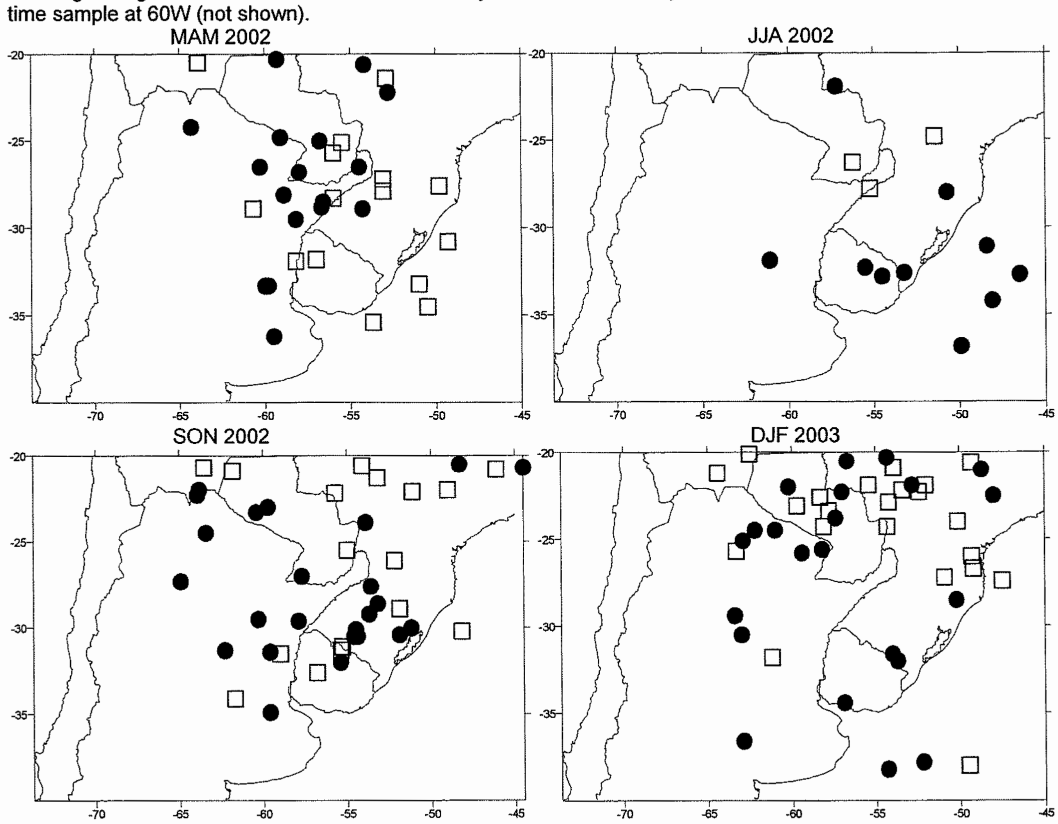

Figure 3: Mature stage centroids during nocturnal (closed circle) and diurnal stage (open box) in the four seasons.

Acknowlegments
This research is supported by UBA grant TX30, ANCyT grant PICT N° 07 – 06671, NASA NAG5-9717 NOAA PID-2207021 and NA03OAR4310096. This research was partially developed during the first and third author visit at University of Utah. Thanks to Daniel Vila for his valuable assistance with the FORTRACC program.

References

Campetella C. and C. Vera, 2002: The influence of the Andes mountain on the South American low-level flow. Geophysical Research Letters. Vol. 29, N°17, 1826, doi: 10.1029/2002 GL015541, 2002.

Cotton, W. R.; M. S. Lin; R. L. McAnelly y C. J. Tremback, 1989: A composite model of mesoscale convective complexes. *Mon. Wea. Rev.*, **117**, 765-783.

Janowiak J., R. Joyce, and Y. Yarosh, 2001: A real time global half hourly pixel resolution infrared dataset and its applications. *B. Am. Met. Soc.*, 82, N 2.

Machado L.A.T., W.B. Rossow, R.L. Guedes and A.W. Walker, 1998: Life cycle variations of mesoscale convective systems over the Americas. *Mon. Wea. Rev.*, 126, 1630 – 1654.

Nicolini M., P. Salio, G. Ulke, J. Marengo, J. Paegle, E. Zipser and M. Douglas, 2004, South American Low-level jet diurnal cycle and three dimensional structure. Clivar Exchange.

Torres J.C., 2003: High precipitationg mesoscale convective complex on Northern and Central Argentina, in spanish, Univ. of Buenos Aires, Ph D dissertation (132pp).

UNIVERSAL LAWS FOR POSTFRONTAL SHOWER CLOUDS

Michael Theusner[1] and Thomas Hauf[1]

[1]Institute of Meteorology and Climatology, University of Hannover, Hannover, Germany

1. INTRODUCTION

Knowledge of the spatial and temporal structure of fields of precipitation, notably the rain area size distribution, is important to many fundamental and applied areas, especially for the parameterization of the water cycle in atmospheric circulation models (eg. Houze, 1993; Cheng and Arakawa, 1997; Mesnard and Sauvageot, 2003).

This study is focused on the structure of post-frontal, small-scale precipitation over Germany, using radar composite images of the German Weather Service (Deutscher Wetterdienst, DWD).

The dataset used for the project is described in section 2. An overview of the methodology is given in section 3. The results are presented in section 4, and the proposed hybrid forecasting scheme for post-frontal convective shower precipitation is described in section 5. The conclusions and summary can be found in section 6.

2. THE DATASET

The radar composite images used for the investigation were provided by the DWD. The national composite (the so-called PC-product) is routinely generated from the radar data of 16 local radar stations within Germany. Each of the radars contributes with the lowest elevation PPI (plane position indicator) which is not obscured by the surrounding terrain. The angle of the lowest elevation varies between 0.5° and 1.8°. The radar images are presented as a six-step scale with a lower cut-off of τ = 7 dBZ (DWD, 1998).

Data were available from 01 May 1997 to 06 September 1997 and 01 June 1998 to 31 August 1998. They have a temporal resolution of 15 minutes and a spatial resolution of 2 x 2 km^2. The composite covers all of Germany and also parts of neighbouring countries. On the whole radar data for an area of approximately 760 000 km^2 are available.

Corresponding authors' addresses: Michael Theusner, Institute of Meteorology and Climatology, University of Hannover, Herrenhäuser Str. 2, 30419 Hannover, Germany; E-Mail: theusner@muk.uni-hannover.de
Thomas Hauf, Institute of Meteorology and Climatology, University of Hannover, Herrenhäuser Str. 2, 30419 Hannover, Germany; E-Mail: hauf@muk.uni-hannover.de

3. METHODOLOGY

3.1 Selection Process

Using a comprehensive set of meteorological data (synoptic observations, radiosonde-data, charts of geopotential, temperature etc. for various pressure levels and satellite images) 39 days were selected which showed convective precipitation structures in the wake of a cold front (Table 1). A boundary line was then manually drawn around the area with convective precipitation using the meteorological data mentioned above. All pixels outside this boundary line were omitted for the subsequent analysis.

Table 1: Days selected for the analysis.

Month	Days
May 1997	07, 09, 10, 21, 28, 30, 31
June 1997	09, 14, 22, 23, 24
July 1997	01, 04, 05, 19, 27, 29
August 1997	01, 29
June 1998	10, 11, 15, 16, 17, 18, 28
July 1998	01, 05, 06, 07, 14, 15, 31
August 1998	05, 22, 23, 27, 29

3.2 Data Analysis

The rain areas were computed using a four-connected-neighbour algorithm. This algorithm labels each rain area with a unique region index. Only pixels with reflectivity $R \geq \tau$ are taken into account. That means that pixels where $R < \tau$ do not contribute to the area A of a rain area.

The perimeter U of each rain area was determined by counting all those sides of the rain area's pixels that bordered pixels where $R < \tau$. Therefore, areas with $R < \tau$ inside the rain area also contributed to the perimeter of that rain area.

The peak number p of a rain area was computed using a 2-dimensional Gauss-filter and counting all pixels which had a higher reflectivity than all their surrounding eight neighbours.

All the above mentioned parameters were also calculated for thresholds greater than τ = 7 dBZ. For the sake of clarity results for τ = 7 dBZ only are presented here. Thresholds with τ > 36 dBZ result in a small number of rain areas. Therefore, they were not considered for the analyses.

4. RESULTS

The analysis of the more than 3500 radar images resulted in a total number of identified rain areas of about 140 000.

4.1 Diurnal Variation

The temporal evolution of the average number of rain areas (without peak number distinction) found in the segmented radar images is displayed in Figure 1. It exhibits a typical diurnal cycle of convective activity. While in the morning hours less than 20 rain areas are present, this number triples until noon and reaches a maximum value of 60 around noon.

In the analysis of rain area distributions and cloud area distributions often a distinction between single-peaked and multi-peaked objects is done. Applying this to the number of rain areas shows that most of the rain areas are single-peaked (about 72 %, Figure 1).

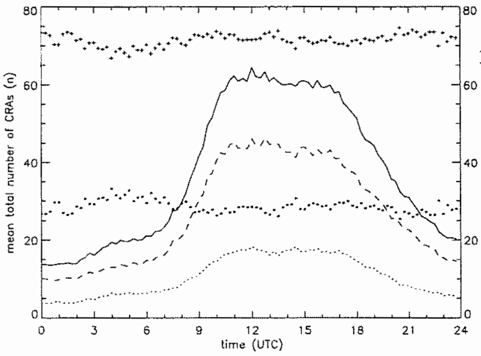

Figure 1: Diurnal variation of the average number of convective rain areas without peak distinction (solid line), single-peaked rain areas (dashed line) and multi-peaked rain areas (dotted line). The relative numbers of single-peaked (crosses) and multi-peaked rain areas (circles) are shown as well.

It is also obvious that the ratio between single- and multi-peaked rain areas does not significantly change during the day.

The diurnal variation of the total area of all rain areas follows a typical cycle of convective activity as well (Figure 2). When a distinction is made between the single- and multi-peaked rain areas it can be noted that, though much smaller in number, the multi-peaked rain areas provide about 80% to 90% of the total rain area (Figure 2).

4.2 Rain Area Size Distribution

The frequency of occurrence of the various rain areas with different peak numbers is displayed in Figure 3. The resulting graph can very tightly be fitted by a power law of the form $N_A = a\,p^b$. The correlation coefficient is 1.0. In this case the relation is:

$$N_A = 0.6p^{-1.92} \qquad (1)$$

This relation also holds for different times of the day. That explains why a constant ratio between single-peaked and multi-peaked rain areas was observed (Figure 1). For $\tau > 7$ dBZ the parameters a and b change. The larger the cut-off the steeper the slope. This is due to the smaller number of rain areas with a large p.

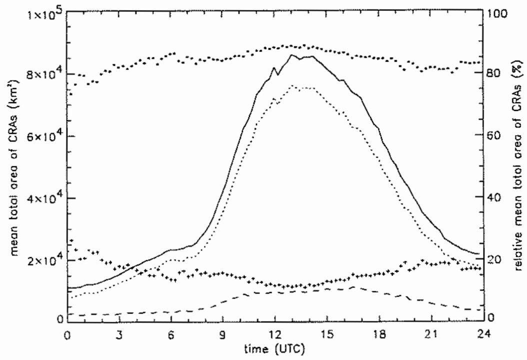

Figure 2: Total area of all rain areas (solid line), single-peaked rain areas (dashed line) and multi-peaked rain areas (dotted line). The relative area of single-peaked rain areas (crosses) and that of multi-peaked rain areas (circles) is shown as well.

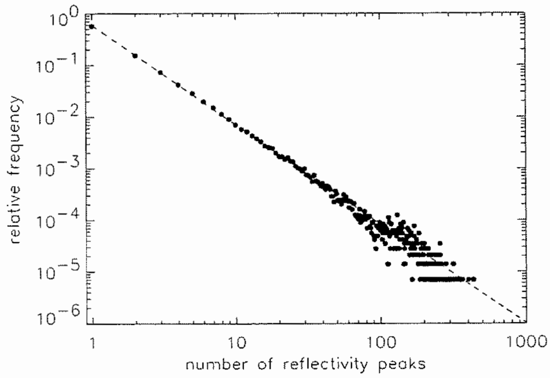

Figure 3: Relative frequency of rain areas as a function of peak number and line of Equation 1.

The frequency of the rain areas as a function of area A cannot be fitted by a power law. But, the population of areas A for a fixed p can be described by a lognormal fitting function. This function is (eg. Crow and Shimizu, 1988)

$$P_p(A) = \frac{1}{\sqrt{2\pi}\,A\sigma_p}\exp\left[-\frac{(\ln A - \mu_p)^2}{2\sigma_p^2}\right]. \qquad (2)$$

It is found that the two parameters σ_p and μ_p, as a function of p, can be tightly fitted by (modified) power laws as well:

$$\sigma_p = 0.76p^{-0.3} \quad \text{and} \qquad (3)$$

$$\mu_p = 6.16p^{0.11} - 1.94p^{-0.89} + 0.072. \qquad (4)$$

For Equation 3 the correlation coefficient is 0.99 and 1.0 for Equation 4.

Equation 1, 2, 3 and 4 can then be used to determine the frequency of rain areas as a function of area A. First the population for each p is computed and then added up for all p. Figure 4 shows that the observed and computed frequency distributions as a function of area A match very well.

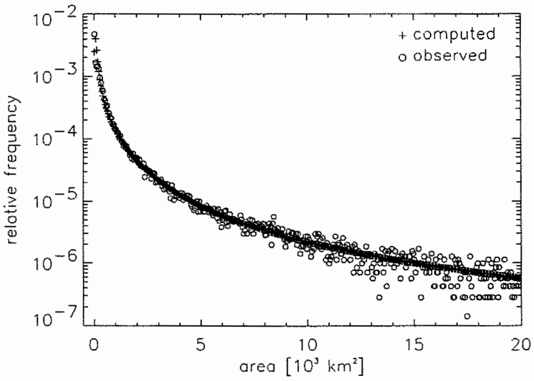

Figure 4: Relative frequency of rain areas as a function of area A.

Figure 5 displays to what extent a certain area class is influenced by a certain class of p. Rain areas with an area A < 100 km^2 are almost entirely single-peaked.

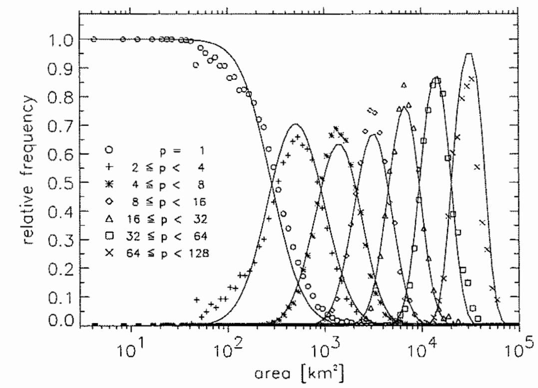

Figure 5: Relative frequency for certain classes of peak numbers as a function of area A. The line represents the corresponding computed values using Equations 1, 2, 3 and 4.

4.3 Area-to-Perimeter Relation

The fractal dimension D of a cloud or a rain area (or any other object) can be calculated using the relation between the perimeter U and the area A (eg. Lovejoy, 1982; Rhys and Waldvogel, 1986; Lawford, 1996): $U = aA^{D/2}$. The fractal dimension can be described as the "wigglyness" of the perimeter in relation to the area A. For the whole data set the resulting D = 1.35.

It can be seen from Figure 6 that the data points can not be tightly fit by a single power relation, though. Instead, two different relations seem to represent best the data below about 300 km^2 and above 3000 km^2. In between, the fractal dimension changes. This change seems to be related to the frequency of single-peaked rain areas. Along with their strong decrease in frequency, the area-to-perimeter relation changes as well. For single-peaked rain areas the fractal dimension is between D = 1.14 and D = 1.2. For rain areas with $p > 16$ it changes to D = 1.74. The change of the fractal dimension points to a break diameter of approximately 30 km.

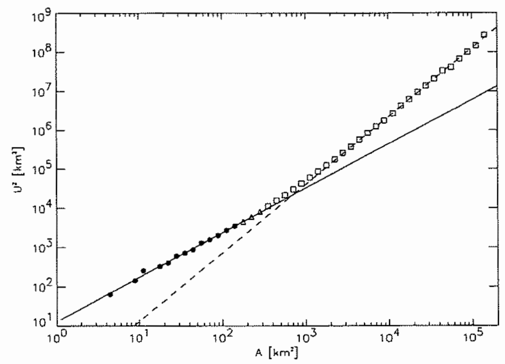

Figure 6: Squared average perimeter U as a function of area A. Black circles denote a relative frequency of single-peaked rain areas of greater than 80 %, triangles of greater than 50 % (solid line fitted to the corresponding data points, D = 1.14). Squares denote a relative frequency of multi-peaked rain areas of greater than 50 % (dashed line fitted to the last 15 data points, D = 1.74)

4.4 Spatial Distribution

The spatial distribution of the frequency of occurrence of rain areas with different p shows some interesting features. Rain areas with p < 10 show a more or less even distribution over Germany. But, they most frequently occur over mountain ranges (not shown). Rain areas with $p \geq 10$ can be found almost exclusively in an area extending 200 km inland from the North Sea coast. This is the area where the location of the sea breeze front is expected (Brümmer et al., 1985).

5. PROPOSAL OF A HYBRID FORECASTING SCHEME FOR POST-FRONTAL CONVECTIVE SHOWER PRECIPITATION

The development of the forecast scheme for postfrontal shower precipitation is based on the assumption that cold fronts and related post-frontal convective precipitation fields can be diagnosed and forecasted to a sufficient degree by conventional numerical weather prediction models (NWP). This assumption appears to be well founded but a closer look at forecast errors of front location, size of PCPF, thermal stability, convection height and wind velocity seems appropriate.

The universal laws of mean statistical properties, derived from the analysis of post frontal shower precipitation, including the diurnal cycle of number of rain areas, size of rain areas and distribution functions seem to show little or no dependency on the synoptic setting and are applicable for all specified post-frontal conditions. If a deeper analysis will reveal a systematic dependency, it is assumed that this dependency can be parameterised and the corresponding sampling error can simultaneously be reduced.

Including the rainfall rates based on *Z-R* relationships would then allow to derive rainfall characteristics such as total area rainfall, distribution of the amount of rainfall, mean rainfall at specific locations etc.

This would be done in two steps:

1. Forecast of cold fronts, related post-frontal convective precipitation fields and mean rain area motion field based on (deterministic) NWP model output.
2. Probabilistic forecast of number of rain areas, total rain area, areal precipitation, local precipitation likelihood, mean maximum local precipitation, mean rain duration and other quantities. A final goal would be the evaluation of the scheme.

6. CONCLUSIONS AND SUMMARY

The analysis of a set of radar images with convective precipitation behind cold fronts shows that the population of convective rain areas can be described by simple power relations and lognormal fitting functions. It confirms and extends results obtained by Mesnard and Sauvageot (2003).

The fractal dimension of this subset of rain areas is in the range observed by other authors (eg. Lovejoy, 1982). A break dimension of approximately 30 km could be observed, obviously connected to the different shapes of single-peaked and multi-peaked rain areas.

Finally, the implementation of these results into a hybrid forecasting scheme for post-frontal convective shower precipitation is described

REFERENCES

Brümmer, B., S. Bakan and H. Hinzpeter, 1985: Kontur – Observations of Cloud Streets and Open Cellular Structures. Dynam. Atmos. Oceans **9(3)**: 281-296.

Cheng, M. D. and A. Arakawa, 1997: Inclusion of rain water budget and convective downdrafts in the Arakawa-Schubert cumulus parameterization. J. Atmos. Sci., **54**: 1359 – 1378.

Crow E. L. and K. Shimizu, 1988: Lognormal Distributions: Theory and Applications. M. Dekker, New York, 378 pp.

DWD, 1998: Der Radarverbund – Informationen zum Wetterradar-Verbundsystem. Deutscher Wetter-dienst, Offenbach.

Houze, R. A., 1993: Cloud Dynamics, Int. Geophys. Ser., vol. 53, Academic, San Diego, California, 570 pp.

Lawford, R. G., 1996: Temporal variations in the scaling properties of rain echoes during development of a cold low in Saskatchevan. J. Appl. Meteorol., **35**, 796-809.

Lovejoy, S., 1982: Area-perimeter relation for rain and cloud areas. Science, **216**, 185-187.

Mesnard, F. and H. Sauvageot, 2003: Structural characteristics of rain fields. J. Geophys. Res., **108(D13)**, 4385-4401.

Rhys, F. S. and A. Waldvogel, 1986: Fractal shape of hail clouds. Phys. Rev. Lett., **56**, 784-787.

WRF SIMULATIONS OF RAINFALL COHERENCE OVER THE CONTINENTAL U.S.

S. B. Trier, C. A. Davis, R. E. Carbone, and S. Frederick

National Center for Atmospheric Research
Boulder, Colorado

1. INTRODUCTION

Recent analyses of radar-rainfall observations have clearly established coherence of propagating warm-season convection over the continental United States having spatial and temporal scales in excess of 1000 km and 1 day (Carbone et al. 2002). However, the propagation mechanisms for these long-lived episodes of organized convection are not well understood, which may partly explain the limited skill of operational numerical models in predicting warm-season precipitation over this region (Davis et al. 2003). In many instances, the phase speed of these convective disturbances exceed those of upper tropospheric forcing mechanisms (e.g., tropopause based short waves) and the midtropospheric steering ?ow (Carbone et al. 2002), suggesting a convectively induced component to the propagation. In the current work we discuss preliminary results from medium range (7-10 day) simulations from a convective active period that occurred across the north central United States during early July 2003. The emphasis is on examining the extent to which a research numerical model is capable of accurately reproducing the statistical behavior of the observed propagating convection. Given similar statistical properties of modeled and observed convection, subsequent studies may employ model diagnostics and sensitivity studies to determine mechanisms responsible for rainfall coherence.

2. CASE SELECTION

We have performed simulations from two separate periods that comprised episodes of long-lived propagating convection and occurred under disparate large-scale forcing regimes. The ?rst was a 10-day period (19-29 July 1998) that occurred during an active southwestern United States monsoon. Here, afternoon convection formed daily over the high terrain of the western United States and consolidated into eastward-propagating mesoscale convective systems (MCSs) over the central Plains overnight, which either persisted or could be linked to subsequent convection east of the Mississippi River the following day. A 7-day period (3-10 July 2003) was also simulated. Convection over the mountains of the western United States was less active during this period, and organized propagating convection occurred farther over the northern plains and upper midwest, often redeveloping the following afternoon downstream over the Ohio Valley region. In both cases, the organized eastward propagating convection was restricted to a relatively narrow latitudinal corridor during the multiday period, where both vertical wind shear associated with moderate midtropospheric ?ow and high θ_e lower-tropospheric southerly ?ow were juxtaposed. In this paper, we discuss results from the 3-10 July 2003 simulations.

Corresponding author address: Dr. Stanley B. Trier, National Center for Atmospheric Research, P.O. Box 3000, Boulder CO 80307-3000

3. METHODOLOGY

The Weather Research and Forecast (WRF) model is the investigative tool used in this study. The 7-day simulations used a single domain with both initial conditions and boundary conditions (updated every Δ t = 3 h) obtained from operational ETA model analyses. In these simulations, the Yonsei University (Korea) planetary boundary layer scheme is coupled to the Noah land surface model (Pan and Mahrt 1987) and a long- and shortwave radiation parameterization (Dudhia 1989) is used. Simulations with 4-km horizontal grid spacing and 22-km horizontal grid spacing have been analyzed. In the 4-km simulations a microphysical parameterization based on the Lin et al. (1983) bulk scheme is used. Here, deep convection develops explicitly and no cumulus parameterization is used. In the 22-km simulations, both the Kain and Fritsch (1990) cumulus parameterization and the simpler NCEP 3-class microphysical scheme are used. The 4-km simulation has grid dimensions of 625 $\times$ 445 $\times$ 35 and is performed over a regional scale domain that covers the central United States and extends westward to the Rocky Mountains. A 22-km simulation with 114 $\times$ 81 $\times$ 28 grid dimensions is run over the same geographical area as the 4-km simulation, whereas an additional 22-km simulation with grid dimensions of 260 $\times$ 164 $\times$ 28 was performed over a domain the encompassed the entire continental United States (CONUS). For comparison purposes, forthcoming analysis of all simulations are presented for only the geographical area that encompassed regional domain used in both the 4-km and smaller 22-km simulations (Fig. 1).

4. PRELIMINARY RESULTS

Figure 2 presents a Hovmoller diagram of the observed rain rate latitudinally averaged from 30 to 48° N for 3 to 10 July 2003. The precipitation rate data was obtained using the empirical relationship Z=300$R^{1.5}$ applied to NOWRAD re?ectivity data, where Z is the radar re?ectivity and R is hourly rain rate. The latitudinal averaging of these data occurred in 0.05°

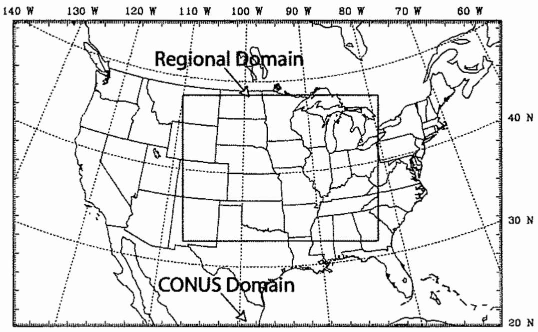

Figure 1. Model domains used for the individual regional-scale (inner) 4 and 22-km simulations and the CONUS (outer) 22-km simulation.

longitudinal strips, as described in Carbone et al. (2002). The numerous downward sloping streaks are indicative of coherent eastward propagating rainfall. The majority of the long-lived rain streaks during the 7-day period originate slightly east of the continental divide (~ 105-110°W) and some progress up to 2000 km (~ 20° LON) eastward. In Fig. 2 there are examples of both continuously propagating (streak A) and intermittent (streak B) rainfall events that occur along coherent phase lines.

Hovmoller plots of latitudinally averaged rain rate from the 4-km (Fig. 3) and 22-km (Fig. 4) regional-domain simulations also exhibit coherent zonally propagating rainfall features (narrow downward sloping streaks). The following semi-objective criteria are used to de?ne the modeled rain streaks. 1) they possess a meridionally averaged rain rate of 0.5 mm h^{-1},

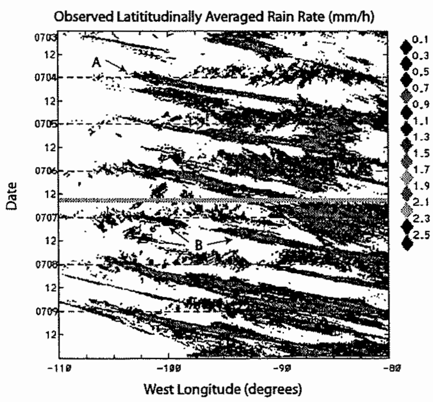

Figure 2. Observed latitudinally-averaged rain rate (mm h^{-1}) during 0000 UTC 3 July to 0000 UTC 10 July 2003. See text for details.

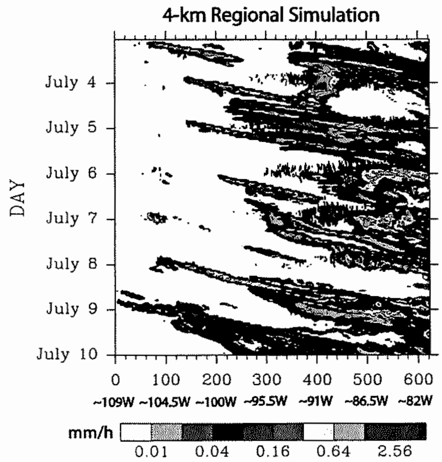

Figure 3. WRF model y-averaged rain rate (mm h^{-1}) for the 4-km regional simulation. Analysis area (Fig. 1, inner rectangle) is approximately equal to that used for observations presented in Fig. 2.

for either 6 h or 500 km and 2) have a time width $\leq$ 6 h. These two criteria applied together eliminate diurnally forced quasi-stationary convection. Comparison of the two simulations (Figs. 3 and 4) and the observations (Fig. 2) reveals an abundance of stationary or very slowly propagating afternoon precipitation in the 22-km simulation (Fig. 4). Excessively heavy and frequent precipitation occurs near the eastern boundary in this simulation that relies on a cumulus parameterization.

Preliminary phase speed statistics for the observed and simulated rain streaks (Fig. 5) de?ned by the above criteria indicate a similar number of rain streaks in the 4-km simulation to those observed. Both the observed and 4-km simulated rain streaks had broad distributions of zonal phase speeds and similar average phase speeds of 18.7 and 19.4 m s^{-1}, respectively. The 22-km had considerably fewer rain streaks than the observations and the 4-km explicit simulations which, on average, had a slightly slower phase speed of 16.9 m s^{-1}. The mean phase speed in the observations and both simulations were greater than the 14 m s^{-1} warm-season climatological average found by Carbone et al. (2002). There are several possible reasons for this difference including the large values of convective available potential energy during this period, which could have enhanced convective downdraft potential and thus resulted in a more rapid convectively-induced component of propagation. Alternatively, the

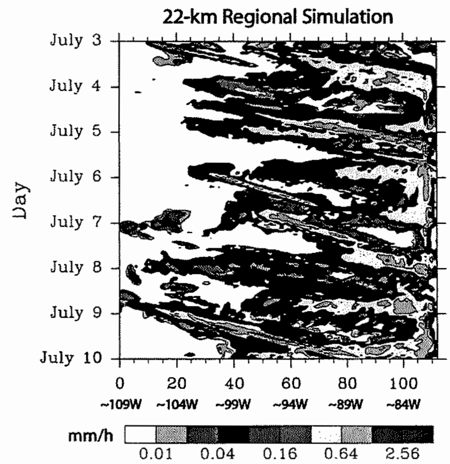

Figure 4. As in Fig. 3 but for the 22-km regional simulation.

Rain Streak Phase Speed Statistics (3 -10 July 2003)

	Number	Mean (m/s)	Distribution 5-10	10-15	15-20	20-25	≥25 m/s
Observations	14	18.7	2	1	4	6	1
4-km Fully Explicit	13	19.4	0	1	6	6	1
22-km Parameterized	6	16.9	0	2	3	1	0

Figure 5. Propagation speed (m s^{-1}) statistics for observed and simulated coherent rain streaks.

preliminary streak de?ning criteria used in the current study differ from those employed in the Carbone et al. study, and may have eliminated some weaker and slowly propagating streaks from the current sample.

The propagating rain streaks were associated with enhanced lower-tropospheric (850 hPa) y-averaged southerly ?ow in both the 4-km and 22-km regional simulations (not shown). This y-averaged southerly ?ow often extended up to 700 hPa. However, there was signi?cant sensitivity in the y-averaged meridional ?ow to domain size. For example, the 22-km regional-scale simulation exhibited meridional ?ow that compared favorably to the ETA analysis, whereas the solution over the larger 22-km CONUS domain exhibited substantial departures from the ETA analysis that developed after several days of simulation. Unlike in the regional domain, the lateral boundaries in the CONUS domain are located a substantial distance from the analysis area (Fig. 1) and thereby may allow too much freedom for the large-scale ? ow to evolve (incorrectly) during a medium range simulation.

5. SUMMARY AND FUTURE RESEARCH

In the current study we have examined characteristics of coherent zonally propagating rainfall over the continental United States, obtained in 7-day numerical simulations, with those found in observations from the same period. Preliminary results indicate that high resolution simulations with with explicit convection are necessary to produce episodes of rainfall coherence with characteristics (e.g., frequency, intensity, propagation speed) similar to the observations. Most of the long-lived zonally propagating rainfall episodes were associated with latitudinally averaged southerly ? ow that often extended into the middle troposphere (e.g., 700 hPa). Their association with southerly lower tropospheric ?ow is not surprising considering the deep moisture transport, large CAPE, warm-advection, and mesoscale ascent that often occurs with lower-tropospheric southerlies over the central United states during the warm season.

Future work will be directed toward better understanding mechanisms responsible for rainfall coherence. A more comprehensive examination of rain streak statistics for the 3-10 July 2003 simulations and for simulations of additional periods comprising different large-scale regimes is planned. We will also further examine the sensitivities to model domain size and examine sensitivities to model physical parameterizations.

REFERENCES

Carbone, R. E., J. D. Tuttle, D. A. Ahijevych, and S. B. Trier, 2002: Inferences of predictability associated with warm season precipitation episodes. J. Atmos. Sci., 59, 2033–2056.

Davis, C. A., K. W. Manning, S. B. Trier, and J. D. Tuttle, 2003: Coherence of warm-season continental rainfall in numerical weather prediction models. Mon. Wea. Rev., 131, 2667–2679.

Kain, J. S., and J. M. Fritsch, 1990: A One-dimensional entraining/detraining plume model and its application in convective parameterization. J. Atmos. Sci., 47, 2784–2802.

Lin, Y.-L., R. D. Farley, and H. D. Orville, 1983: Bulk parameterization of the snow ?eld in a cloud model. J. Climate Appl. Meteor., 22, 1065–1092.

Pan, H.-L., and L. Mahrt, 1987: Interaction between soil hydrology and boundary-layer development. Bound.-Layer Meteor., 38, 185–202.

ON THE FORMATION OF LONGITUDINAL CLOUD MODE IN THE WINTER MONSOON OVER JAPAN

Akira Watanabe

Department of Earth Science, Faculty of Education, Fukushima University
Fukushima, 960-1296, Japan

1.INTRODUCTION

It is well known that the two cloud modes appear over the Sea of Japan in the winter monsoon. One is the transverse cloud mode, and the other is longitudinal cloud mode.

Already, Asai (1964, 1971) indicated that streak clod is formed by roll convection and the mode change by vertical wind shear by the numerical simulation. However, longitudinal cloud mode appears over the inland of the Northeast Japan when the transverse mode cloud has occurred over the Sea of Japan. We studied the occurrence mechanism of longitudinal cloud mode over the inland.

2.OBSERVATION AND OROGRAPHY

We have observed the mesoscale convective system over the Northeast Japan in January 2001. We carried out the intensive observation from Jan. 12 to Jan. 19 and Jan. 25 to Jan. 31. The topography and observation points of the research area are shown in Figure 1. The observation of an upper-atmospheric structure by rawinsonde was conducted four or eight times a day at the 5 stations (over the Sea of Japan, Wajima, Jouetsu, Mikuni, Fukushima). Furthermore, we observed three components of wind with the L-band radar every 1-minute at Fukushima

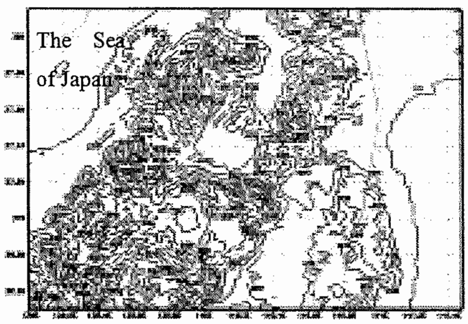

Fig.1 The topography and observation station Contours are at an interval of 200m.

University. We observed an echo with meteorological radar every 10 minutes over Tohoku District of Japan. As a result, we able to obtain the upper observation data for each 3 hours or 6 hours, the echo data for each 10 minutes, and the three components of wind data for each 1 minute in the intensive observation period.

Fukushima University, 1, Kanayagawa, Fukushima, 960-1296, Japan: E-mail: may@educ.fukushima-u.ac.jp

As for in this period especially the winter monsoon was strong for the first time in 63 years. We were able to obtain the good data to research execution.

3. SYNOPTIC SITUATION

The convective mixing layer is 4 km or less. We understand to be corresponding when the longitudinal mode cloud occurs in the front of the cold front and gradually the height of the convective mixing layer is low. Figure 2 shows the time-height cross section for the difference of mixing ratio between Fukushima and Jouetsu. The positive values indicate that the mixing ratio is relatively

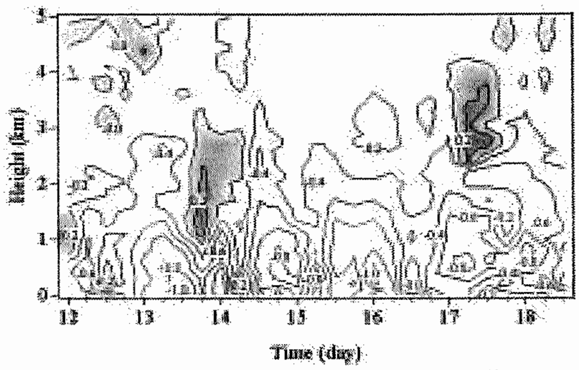

Fig.2 The time-height cross section for the difference of mixing ratio (g/kg) between Fukushima and Jouetsu from Jan.1200Z to Jan.1821Z Contours are at an interval of 0.2g/kg.

large in Fukushima of the leeward. We find that the mixing ratio is large at the leeward during appearance of the echo. Ouu Mountains of 1km or more exists to the north from the south to the research area. The leeward is drying relatively for a winter monsoon. However, we find that the leeward is wet relatively when the longitudinal echo as shown in the Figure 3 is appearing over the Northeast Japan. We find that there are many case the longitudinal echo, appears when the transverse echo is appearing on the side of the Sea of Japan. The echo hardly appears when the longitudinal echo is appearing on the side of the Sea of Japan.

We average the rawinsonde data in the time that the echo is appearing over the Northeast of Japan. There are 9 examples when the longitudinal echo was appearing on the Sea of Japan at the time of rawinsonde observation. And, there are 7examples when the longitudinal echo was appearing over Fukushima Prefecture at the observation.

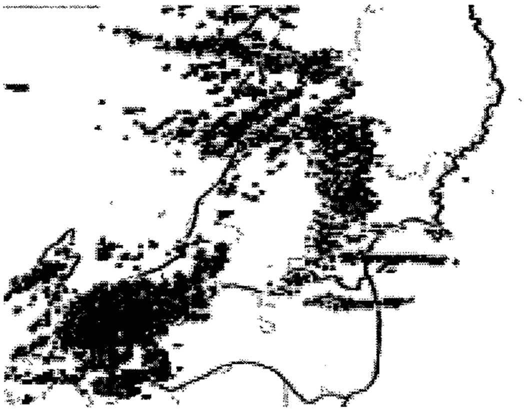

Fig.3 Distribution of echo at Jan. 1209Z, 2001

The blackened areas correspond to the echo (greater than 4mm/h)

Figure 4 shows the vertical distribution of mean equivalent potential temperature of the each case.

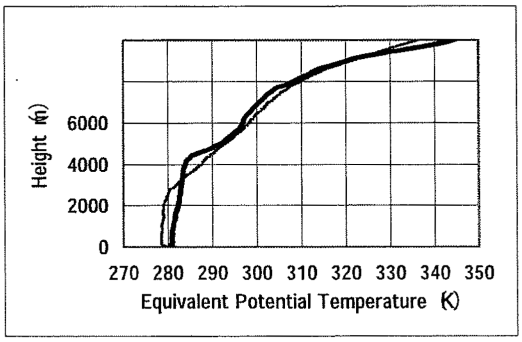

Fig.4 Vertical profile of equivalent potential temperature (K). The thick solid line indicates the mean profile in the time that the echo progressed.

The height of the convective mixing layer at appearing the echo is higher than at the time when the echo does not appear. The water vapor quantity of 4 km or less is increasing at the time of the echo appearance over Fukushima Prefecture. The stable layer is formed by increasing water vapor. The temperature lapse rate in the mixing layer at appearing the echo is bigger than at the time that the echo does not appear. Accordingly, the convective activity is lively at appearing the echo.

Figure 5 shows the vertical distribution of northward component of wind. The both cases are similar with eastward component of wind, but the speed at appearing the echo is larger than at the time that the echo does not appear. The vertical wind shear is large around the stable layer. The southerly wind is blowing in the upper part of mixing layer at the time of the echo appearance. Accordingly, we find that the vertical shear is large at the time of echo appearance. The condition is clearly different from the condition that Asai (1971) pointed out.

Figure 6 shows the time-height cross section of horizontal wind and echo strength of zenith direction.

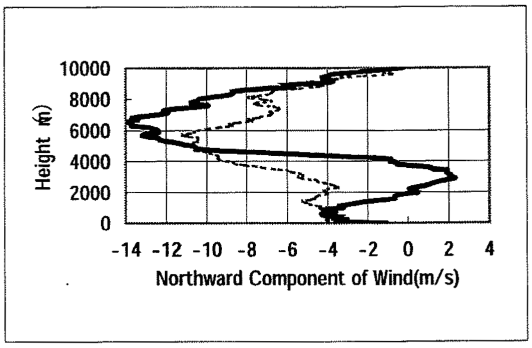

Fig.5 Vertical profile of northward component of wind The thick solid line indicates the mean profile in the time that the echo progressed

A northwesterly wind is excelling for the place in the synoptic situation. It is conceivable that the excellence of the southerly wind is related to the formation of the convection.

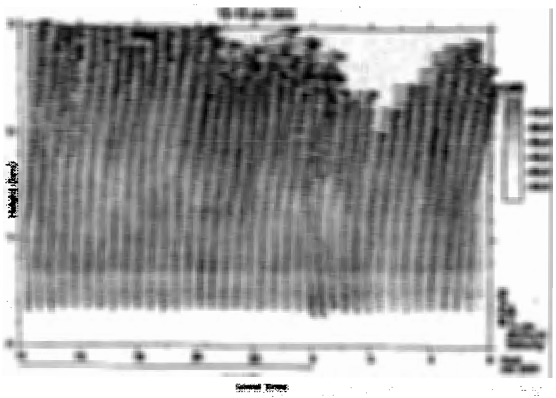

Fig.6 The time-height cross section for the horizontal wind from Jan.1205Z to Jan.1213Z

The blackened areas correspond to the developing echo.

Figure 7 shows the distribution of the deviation of zenith atmospheric delay from Jan. 1209Z to Jan.1212Z by Global Positioning System (GPS). The quantity of the zenith atmospheric delay is related to

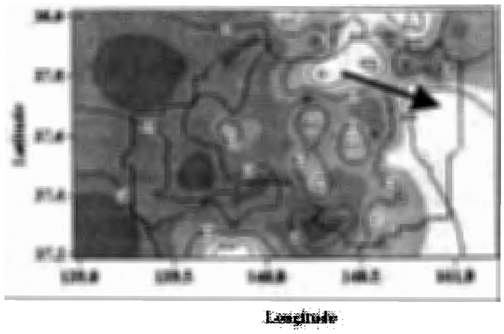

Fig. 7 The distribution of the deviation of zenith atmospheric delay (cm) from Jan. 1209Z to Jan.1212Z

the fluctuation of the water vapor quantity. We find that it is a wet on the west side and a dry on the east side of Ouu Mountains from the distribution of the deviation in 3 hours average of atmosphere delay. Especially, it is a wet in the Sea of Japan side. And the longitudinal echo is formed where it is drying relatively. Accordingly, the mechanism of collected water vapor in the leeward is necessary to develop the convective echo over the Fukushima. We are conceivable as the convergence of water vapor is transported from northeast and southwest from the zenith atmosphere delay distribution by GPS.

4. NUMERICAL SIMULATION

We used the Cloud Resolving Storm Simulator (CReSS) for the numerical experiment. CReSS is developed by Tsuboki and Sakakibara (2001). The model is formulated in the non-hydrostatic and compressible equation system. In order to include the effect of orography, the coordinate system is a terrain-following coordinate in three-dimensional geometry. Prognostic variables are three-dimensional velocity components, perturbations of pressure and potential temperature, subgrid-scale turbulent kinetic energy and mixing ratio for water vapor and several types of hydrometeors. The model is used a finite difference method for the spatial discretization and the leapfrog time integration with the Asselin time filter for time integration. Turbulence is one of the most important physical parameterization in a cloud model. The model includes the 1.5-order closer with turbulent kinetic energy. Cloud physics is formulated by a bulk method of cold rain. Prognostic variables are mixing ratios for water vapor, cloud water, rain water, cloud ice, snow and graupel. Radiation of cloud is not included. Numerical smoothing is the second or forth orders computational mixing.

In the numerical experiment using CReSS, we used the following experimental design. The horizontal grid size was 2km, and vertical grid size was 300m within a domain of 200km X 200km. Cloud microphysics was the cold rain type. An initial condition was provided by the rawinsonde observation and the L-band radar observation at Jan.1212Z on the Fukushima University. The initial condition of the calculation range of the model made uniform with the observation data. The boundary condition was the wave-radiating type In this experiment; the ground condition was not included.

The vertical distribution of eastward and northward component of wind is shown in Figure 8. The height of mixing layer is 5km. The wind shear is large around 5km. The wind velocity is strong as the upper layer in the mixing layer. Especially, a south wind is appearing with the lower layer from 1.5km in L-band radar observation. The vertical profile of the equivalent potential temperature resembles to the profile at the time of the echo occurrence that showed it in Figure 4.

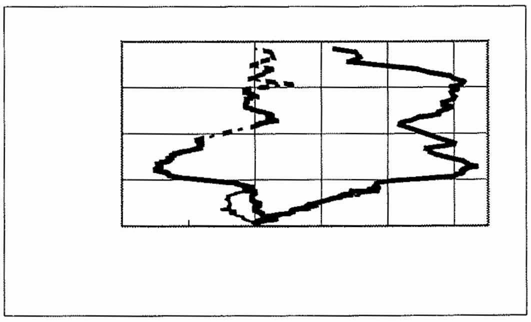

Fig. 8 The vertical distribution of eastward and northward component of wind
The solid lines denote the eastward component of wind and the broken lines denote the northward component of wind. The thick lines indicate the wind speed profile that was observed by the L-band radar.

We considered the result of 4 hours later from the initial condition that was integrated by CReSS. Figure 9 shows the distribution of horizontal wind at 740m above the sea level. The region where there is

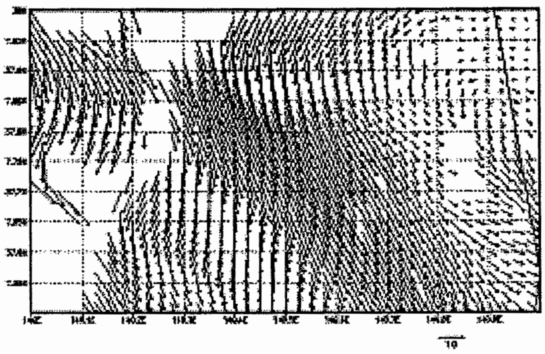

Fig. 9 The distribution of horizontal wind at 740m simulated by the CReSS

not a vector display is corresponding to the mountainous region higher than 740m. The wind velocity has strengthened conspicuously in the leeward of the mountains. We find that the vortex circulation occurs in the northeast side of the gale belt. The vortex appears between 740m and 1360m above the sea level. The upper limit of the vortex corresponds with the south wind region. The Froude number in this time is very small with 0.1 or less. Accordingly, the topographic effect is large for the atmospheric flow. It is conceivable that the detour effect is big. We find that the gale belt in the mountains leeward is formed by the detour effect. Furthermore, it is conceivable that the formation of this gale belt strengthens the horizontal wind shear and that form the horizontal vortex. This vortex is formed to only the north east side of the gale belt and do not appear in the southwest. We think that the south wind that is observed with L-band radar is formed by the vortex that is similar as the vortex of the northeast side. It is conceivable that this vortex collects the horizontal water vapor.

Figure 10 shows the distribution of total mixing ratio of rain, snow and graupel at 740m. The water

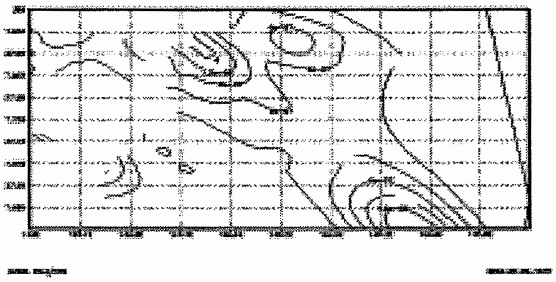

Fig. 10 The distribution of total mixing ratio (kg/kg) at 740m simulated by the CReSS

vapor concentrates along the gale belt. Especially, the convergence of the vapor is admitted between vortex and gale belt. The vertical cross section of vertical flow of the north latitude in 37.85 degrees is shown in Figure 11. The region of the gale belt

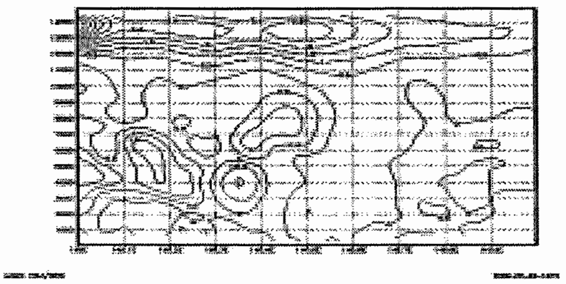

Fig. 11 The vertical cross section of vertical flow of the north latitude in 37.85 degrees simulated by the CReSS

corresponds to the descending flow. Accordingly, we are conceivable that the increase of the water vapor in the gale belt is depended on the horizontal convergence largely. Also, the descending flow and ascending flow are appeared on the west side of the gale belt. This is included even the possibility that the cloud progresses by the jump in the mountains leeward.

Figure 12 shows the distribution of snow fall rate that is calculated with the numerical experiment is few about 0.5 mm in an hour.

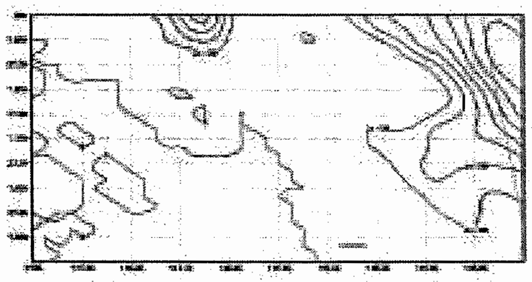

Fig. 12 The distribution of snowfall rate (m/sec) simulated by the CReSS

The snowfall area is inclining in the Pacific shore. And, the snowfall area does not correspond with echo that was observed with the radar. However, the formation of the gale belt and horizontal vortex of the mountains leeward are able to explain the cause that echo progresses.

5. CONCLUSIONS AND DISCUSSION

We have studied the occurrence cause of longitudinal cloud that appears over the land area with observation and numerical experiment. Kuettener (1959,1971) and Plank (1966) pointed out that the formation of streaked cloud is related to the vertical distribution of horizontal wind speed and vertical shear. From those viewpoint, it has been conceivable that the cloud progresses also in Pacific Ocean side because the atmosphere where will pass a valley is maintained the water vapor on the side of the Sea of Japan. Because of this the cloud progresses in the leeward of the valley. However, in fact, the cloud occurs in the leeward of the mountains. And it snows a dozens centimeter. The height of the mixing layer needs to become high, to develop the convection that causes snow fallen. The height is higher than about 4km. It is necessary to develop the convection for the height of the mixing layer. The height is higher than 4km. We found that a Froude number is small (little than 0.1) and wind makes a detour the mountain. And the gale belt formed in the leeward of the mountain. Furthermore, the gale belt forms a vortex circulation by the horizontal shear. The vortex circulation collects water vapor widely and develops the convection near the strong wind band.

ACKNOWLEDGEMENTS

The author would like to thank Dr. Tsuboki in Nagoya University, for permission of the application of CReSS.

REFERENCES

Asai, T., 1964: Cumulus convection in the atmosphere with vertical wind shear; Numerical experiment, J. Meteor. Soc. Japan, 42, 245-259.

Asai, T., 1971: Three-dimensional features of thermal convection in a plane Couette flow, J. Met. Soc. Japan, 48, 18-29.

Kuettener, J. P., 1959: The band structure of the atmosphere. Tellus, 11, 267-294.

Kuettener, J. P., 1971: Cloud bands in the earth's atmosphere: observation and theory. Tellus, 23, 404-425.

Plank, V. G., 1966: Wind conditions in situations of pattern from and non-pattern form cumulus convection, Tellus, 8, 1-12.

Tsuboki, K. and Sakakibara, A., 2001: CReSS user's guide, Second Edition, 1-210.

KEY PARAMETERS AND PROCESSES LEADING TO TORRENTIAL RAINFALL EVENTS IN THE SOUTH – EASTERN MASSIF CENTRAL, FRANCE

W. Wobrock[1], A.I.Flossmann[1], G. Delrieu[2] and S. Anquetin[2]

[1]Laboratoire de Météorologie-Physique, Université Blaise Pascal, OPGC, CNRS, Clermont-Ferrand, France
[2]Laboratoire d'étude des Transferts en Hydrologie et Environnement, BP 53X, Grenoble, France

1. INTRODUCTION

Intense rainfall events with accumulations of 300 mm of rain in 6 h occurred quite frequently over the region of the Cevennes-Vivarais in Southern France (Rivrain, 1998). Next to the considerable devastation in the cities these floodings also come with a great number of human victims.

Heavy rainfall events typically occur in the period between September and December when warm humid air masses in the lower atmospheric levels arrive by a southerly flow in the river Rhone delta. The southeastern rim of the Massif Central and the narrowing Rhone valley force the southerly flow to rise (Miniscloux et al., 2001, Anquetin et al., 2002) which results in combination with the appropriate synoptic conditions in the formation of steady state mesoscale convective systems leading to torrential rain falls in the region between Montpellier, Nîmes and Alès (see Fig.1).

In order to improve our understanding of these rain events the "Cévennes-Vivarais Mediterranean Hydro-meteorological Observatory" (OHM-CV) a research initiative between hydrologists and meteorologists was created. Here, extensive observation is coupled with analysis and modeling. For more information see http://www.lthe.hmg.inpg.fr/OHM-CV/index.htm.

Up to now we simulated different flooding events which occurred between 1995 and 2002 by means of a high resolved cloud scale model. Initially, modeling results were not very promising: the period of heavy precipitation and the rainfall totals were typically underestimated by a factor of 3 and the maximum rain fall locations were more then 25 km displaced. Thus, the necessity for a more thorough analysis became evident.

The present study concentrates on the flash flood of 8/9 Sept. 2002 where precipitation periods and rainfall totals were even significantly stronger than in the previous cases. Due to the shortcomings in the model results of previous flooding events a first objective of this study was to check if model dynamics and microphysics are able at all to simulate the basic characteristics (i.e. very strong rain fluxes during periods of several hours) of the steady state convective systems in the region of the Cevennes-Vivarais. If this prerequisite is achieved a detailed analysis of the modeled atmospheric dynamics and cloud microphysics will allow to better detect key parameters and key processes responsible for these extraordinary atmospheric phenomenon.

Corresponding author's address: Wolfram Wobrock, Lab. de Météorologie-Physique,24 Ave des Landais, F-63177 Aubière: wobrock@opgc.univ-bpclermont.fr

2. OBSERVATIONS

During 8 Sept. 2002 a low pressure system with its center over Ireland and a surface high over Italy and the Ligurian Sea caused a strong southern flow of warm and extremely moist air into the Rhone valley. Convection developed over land in the cyclonic flow of the approaching perturbation, which was supplied in the lower levels by a persistent moist air stream arriving from the Mediterranean Sea.

Observations by means of three weather radars of Météo-France and of a dense network of hourly rain gauges (130 stations) of the OHM-CV are available to resolve the spatial extension of the precipitating cloud fields and the surface rain flux and accumulation.

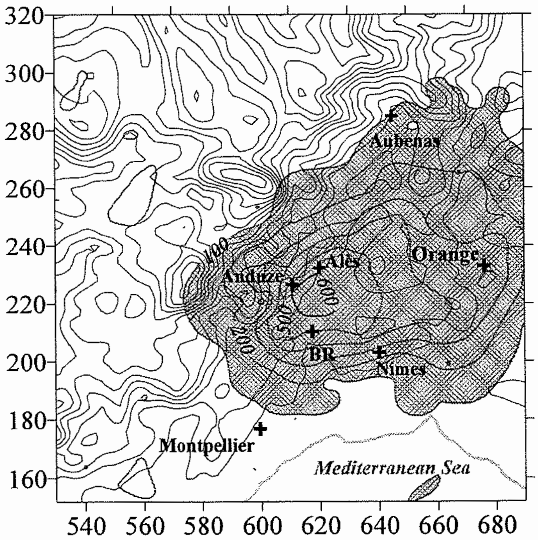

Figure 1: *total rain amounts observed during 8/9 Sept. 2002 over the Gard region, France.*

Fig.1 gives the total surface rain accumulation after 26 hours. Maximum values of 600-700 mm were measured in the region between the city of Alès and

Anduze which are located on the south-eastern rim of the Massif Central. Rain amounts of more then 200 mm cover a surface of 5500 km^2.

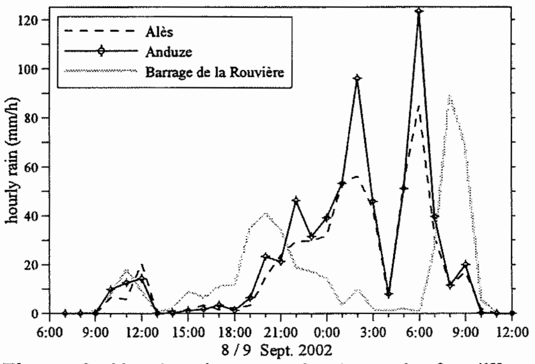

Figure 2: *Hourly rain gauge hyetographs for different locations given in Fig. 1.*

Fig. 2 shows the time evolution of the hourly rain for three locations in the center of the maximum rain accumulation. While *Alès* and *Anduze* have a quite similar time response, *Barrage de la Rouvière* (indicated by BR in Fig.1) which is located 15 km south of Anduze displays an important difference in its temporal evolution. All three stations indicate that the torrential rain rates are characterized by high hourly values (up to 125 mm) and long lasting episodes.

3. NUMERICAL MODELING

In order to understand the atmospheric processes which lead to the important rain events on 8/9 Sept. 2002 we used the NCAR Clark-Hall cloud scale model (Clark et al, 1996) with a two domain setup. The outer domain with a grid resolution of 8 km covers an area of about 1000 x 700 km^2 reaching from the Bay of Biscay in the west to Northern Italy in the east and from the Mediterranean Sea (42°N) in the south to the center of France (47°N).

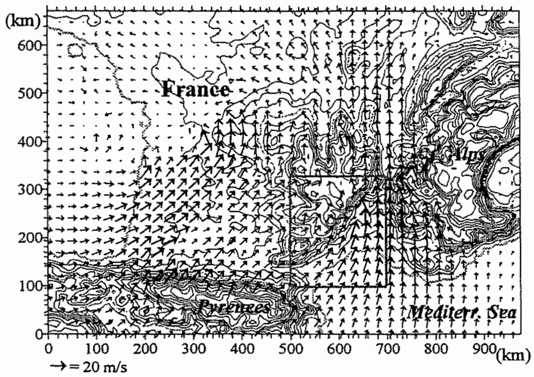

Figure 3: *horizontal wind field in 850 hPa for the outer domain at 0.00 UTC, 9 Sept.2002; the rectangle gives the 2nd model domain.*

The 2nd domain covers the region of the Cevennes – Vivarais (see Fig.4 and 5) and a part of the Mediterranean Sea with a horizontal grid resolution of 2 km. The vertical telescopic grid for both domains has 60 levels and reaches up to 20 km.

Initial and boundary conditions for wind, temperature, geopotential height and humidity were taken from the ECMWF analysis given in a 0.5 degree grid resolution. Weak heat and moisture fluxes were imposed on the land and sea surfaces to speed up the formation of deep convection. The fluxes are kept constant during the entire simulation.

One modeling activity was to test the role of the initial and boundary conditions on the rainfall intensity. Thus, we initialized the model by the field of soundings coming from the ECMWF analysis at 6.00, 12.00, 18.00 on 8 Sept. 2002 and integrated until 12.00 on the following day by adapting the lateral boundaries every 6 hours.

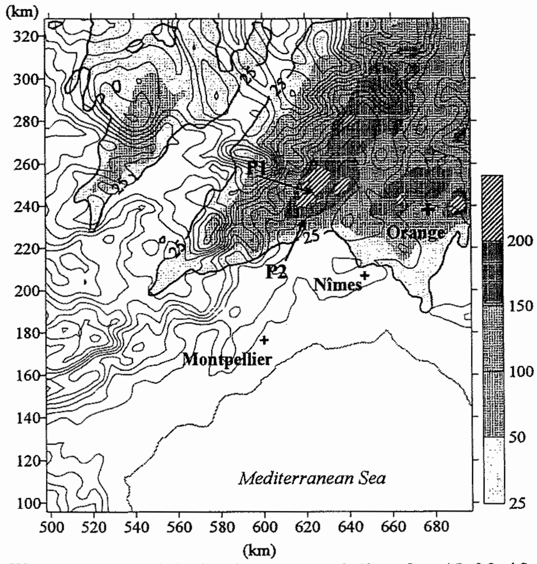

Figure 4: *modeled rain accumulation for 18.00-12.00 UTC, 8/9 Sept 2002*

The highest precipitation rates were modeled when the integration started at 12.00 or 18.00 UTC. The resulting surface rain accumulation after 18h and 24h are illustrated in Fig.4 and in Fig.5, respectively. For the case starting at 18.00 (Fig.4) max precipitation rates of 242 mm were reached about 25 km northeast of the observed rain maximum (see Fig.1). For the other case starting at 12.00 (Fig.5) the precipitation maxima are located 60 km to the east of the mountain rim, south of the city of Orange. Max precipitations modeled are 282 mm.

The hourly rainfall of the modeled maximum precipitation rates are depicted in Fig.5. Point 1 which is located in the maximum rain accumulation (242 mm during 18h) for the18.00 case gives hourly values of 30-40 mm over a period of 5 hours. At Point 3 which is located 12 km south of Point 1 the rain accumulation is already much weaker but a model maximum of 75 mm per hour was achieved.

The time evolution of rain for the maximum accumulation of the 12.00 case is illustrated by Point 3 in Fig.5. Next to the strong precipitation period from 22.00 until 5.00 this location also experiences a second intense period of rain in the morning of 9 Sept. 2002 causing a rainfall total of 282 mm during 17 hours.

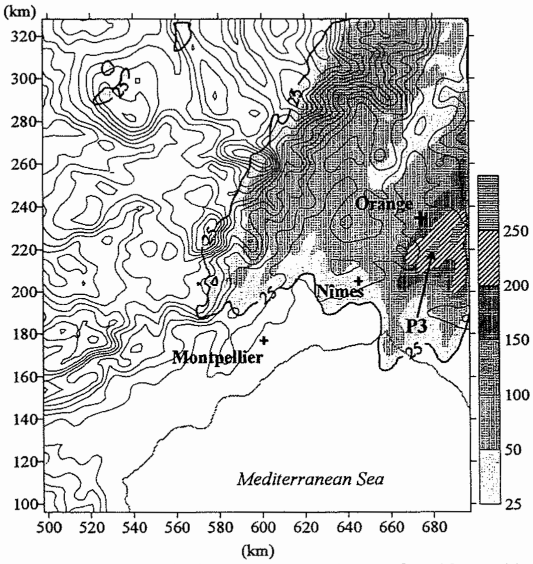

Figure 5: *modeled rain accumulation for 12.00-12.00 UTC, 8/9 Sept 2002*

4. DISCUSSION

The comparison of observed and modeled hourly rain data shows several points of agreement but also of disagreement between both time series. We note that the model is able to resolve the long lasting intense rain period from 22.00 to 5.00 and after a short pause also the second period from 6.00 to 12.00.

It is surprisingly to see that the modeled maximum hourly rainfall intensities of 50 and 75 mm around midnight compare quite well with the maxima observed in this period for Alès and Anduze.

The simulation starting at 18.00 (Fig.4) predicts reasonably well the maximum rainfall intensity for the region next to Alès during the nocturnal period but fails considerably during the morning period (see point 1 and 2 in Fig.6). An accumulation of only 30 mm obtained by modeling is confronted with an observation of almost 200 mm during the morning hours.

The simulation starting earlier at 12.00 predicts significantly weaker rain accumulations (below 100 mm) for the region around Alès (see Fig.5). This is why we refrained from presenting the hyetograph of Alès for this case. The hourly rain curve depicted in Fig. 6 by point 3 for this modeling case represents a location next to the city of Orange in the eastern part of the model domain. Similar to the simulation starting at 18.00 two precipitation episodes can be distinguished, one during nighttime and another very dominant one in the morning hours. The rain gauge measurements in this part of the domain (not presented here) confirm the presence of strong precipitation in the morning hours, however, did not register any rainfall in the period from midnight until 8.00 in the morning.

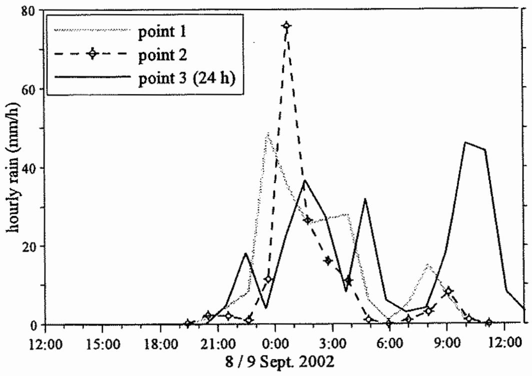

Figure 6: *Modeled hourly rain gauge hyetographs for different locations given in Figs. 3 and 4.*

The strong rain accumulation of more than 300 mm which is visible in the rainfall totals of Fig.1 for the region around Orange results from a first intense precipitation phase which started already at 17.00 and persisted until 22.00. During this period a huge convective rainband brought more than 200 mm of precipitations more southeasterly in the Rhone delta. The rainband was oriented in northeasterly direction starting southwest of Nîmes reaching up to Orange. The strong rainfall during this period is also visible in Fig.2 for the rain gauge observation of the *Barrage de la Rouvière*. Its nocturnal maximum is reached already at 19.00 and thus suggests a convective evolution that developed decoupled from the severe rain storms which started several hours later at the northern locations of Ales and Anduze (Fig. 2).

This initial strong precipitation event could not be reproduced by modeling. Also the change of the initial conditions to the synoptic situation at 6.00 UTC for 8 Sept. 2002 did not effect the development of a similar convective system as observed.

5. PRELIMINARY CONCLUSIONS

The simulations performed for the 8/9 Sept. 2002 show that the Clark-Hall cloud scale model is able to reproduce strong and long lasting rain fall episodes for the Gard region in southern France and can cause 250-300 mm of rain during a 12 h period.

Thus, we can conclude that the model dynamics as well as the model microphysics are well adapted to the mesoscale convective systems occurring in the southeastern Massif Central.

Significant differences with the observations however exist as the observed rain accumulation was by a factor of 2 to 3 stronger. These differences in the rainfall totals result from the fact that the model is only able to simulate one severe and long lasting rainfall episode while most parts of the area of interest were concerned at least by two separate periods of strong precipitation.

This lack of the model to reproduce a second severe rainfall period is very likely caused by the prescribed synoptic fields given by the ECMWF analysis. We can speculate that a) the initial data on a coarse 0.5° grid differed from the true atmospheric conditions and b) that the time changes in the synoptic field took place on time scales significantly faster than the prescribed 6 h interval of the ECMWF analysis.

Sensitivity studies on the role of the initial and boundary conditions were performed by integrating the model from the initial fields at 6.00, 12.00, 18.00 and 0.00 - this time, however, without changing the lateral boundary conditions for the following 18h. The results of these runs indicate that only the ECMWF analysis fields at 0.00 and 6.00 UTC are able to produce rainfall totals of more then 200 mm. Integrating the initial data field at 0.00 over 12 hours yields similar precipitation results as given in the case study of Fig. 4. Starting, however, the model at 18.00 results in rainfall maxima below 50 mm after 12 hours integration under constant lateral boundary conditions.

We can thus conclude that the key information which atmospheric conditions are responsible for the formation of the heavy precipitation can be detected by comparing the model results of these two simulations. This investigation is subject of our ongoing research.

Consequently, we note from the presented modeling studies in Figs. 4 and 5 that the possibility to produce episodes with very strong and long lasting rainfall is dependent on the accurate knowledge of the synoptic situation over southern France and the adjacent Mediterranean Sea. Fast changes in the synoptic field which were not resolved by the ECMWF analysis can effect the revival, the dissipation or any other modifications of the mesoscale convective systems.

Considering this difficulty in the prediction of thunderstorms for southern France improvements in the forecast of the location of the maximum precipitation field for hydrological purposes will be difficult to achieve. Uncertainties of more then 30 km for the prediction of the rain location will further persist also in the future.

6. ACKNOWLEDGEMENTS

The authors acknowledge with gratitude the Institut du Développement et des Ressources en Informatique Scientifique (IDRIS, CNRS) in Orsay (France) for the hours of computer time and the support provided. Furthermore, the authors acknowledge the support provided by the French national program PATOM/PNRH (INSU).

7. REFERENCES

Anquetin S., F.Miniscloux, J.D. Creutinand S. Cosma, 2002: Numerical simulation of orographic rain, J. of Geophysical Res., 108, N0 D8, 8386, doi:10.1029 / 2002JD001593.

Clark, T.L., Hall, W.D., Coen, J., 1996: Source code documentation for the Clark-Hall cloud scale model, code version G3CH01; NCAR/TN-426+STNRCAR Technical Note, 1996, NCAR, Boulder, CO, USA.

Miniscloux F., J.D. Creutin and S. Anquetin, 2001: Geostatitistical analysis of orographic rainbands, J. of Appl. Met., 40, 1835-1854.

Rivrain, J.C, 1998: Storm-floods in the Mediterranean region of Southern France. Phémomèmes remarquables, n° 4, Météo Franc, SCEM, 1998, 93 pp.

DRIZZLE AND CLOUD STRUCTURE IN SE PACIFIC STRATOCUMULUS

R. Wood, K. Comstock, P. Caldwell, C.S. Bretherton, and S.E. Yuter
Department of Atmospheric Sciences, University of Washington, Seattle, WA 98195, USA

1. INTRODUCTION

Drizzle is a common phenomenon (Petty 1995) in marine boundary layer (MBL) cloud, but many questions remain regarding its formation, structural properties, and climatological effects (Bretherton et al. 2004).

Factors leading to the formation of drizzle are poorly understood, and include cloud thickening (increasing liquid water path, *LWP*) and low cloud condensation nuclei concentrations (leading to low values of cloud droplet concentration N_d). The effects of drizzle upon the MBL energy and moisture budgets, and therefore the cloud radiative properties, are largely unquantified. These effects are strongly dependent upon whether drizzle reaches the surface or evaporates below the cloud. Austin et al. (1995) show that drizzle is unevenly distributed in the horizontal and occurs in intermittent patches. The spatial distribution of drizzle may have important consequences for dynamical feedback effects associated with its evaporative cooling below cloud base (e.g. Jensen et al. 2000). Quantifying the structural properties of drizzle in MBL clouds is therefore necessary.

The EPIC (East Pacific Investigation of Climate Processes) field campaign (October 2001) provided an unprecedented dataset of boundary layer clouds over the SE Pacific Ocean, the largest region of stratocumulus on the planet. Data from a number of sources, including shipborne remote sensing, are used to investigate aspects of drizzle formation and structure in this relatively unstudied region of marine boundary layer clouds (Bretherton et al. 2004).

2. DATA and METHODOLOGY

The primary source of data for this study is the R/V Ronald H Brown, a NOAA ship fitted with an array of meteorological instrumentation. Instruments pertinent to this study include a vertically pointing K_a band (8.9 mm) cloud and precipitation radar (MMCR), a scanning C-band (5 cm) precipitation radar, a microwave radiometer (to estimate cloud *LWP*), a ceilometer (to measure cloud base height), and surface meteorological and turbulent and radiative flux measurements. Cloud droplet concentration estimations were made using a combination of shortwave transmittance and microwave *LWP* using the method of Dong et al. (2003).

Corresponding author address: Robert Wood, Atmospheric Sciences, Box 351640, University of Washington, Seattle, WA 98195, USA. Email: robwood@atmos.washington.edu

Radiosonde launches were made every three hours during the cruise, which started in the Galapagos Islands, traveled to the WHOI buoy at 85W, 20S, and ended in Arica, Chile (Figure 1).

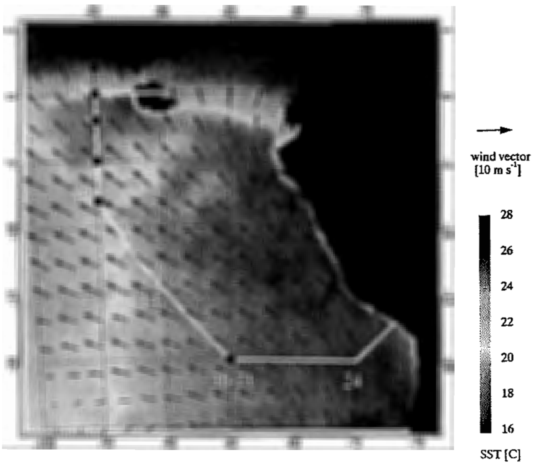

Figure 1. Sea-surface temperature, mean wind vectors, and track of cruise during EPIC 2001. Numbers indicate day in October 2001.

Our methodology is to use the vertically pointing MMCR together with a microphysical model of sedimenting and evaporating drizzle, to determine the two parameters of the drizzle drop size distribution (DSD) at cloud base, and the precipitation rate profile. The drizzle DSD is assumed to be exponential in form, in accordance with recent observations (Wood 2004). The temporal variability in the cloud base drizzle DSD is used to determine a reflectivity-rainrate (Z-R) relationship that is then applied to two dimensional cloud base reflectivity fields from the C-band radar (60 km diameter circle around the ship). These data result in much improved sampling statistics for drizzle, and allow investigation of its spatial structure and variability on the mesoscale. The retrieval of the parameters of the drizzle DSD is described in more detail below.

2.1 Retrieval of drizzle DSD parameters

Our basic assumption is that the cloud base drizzle DSD $N_{CB}(r)$ can be described using a truncated exponential distribution:

$$N_{CB}(r)=[N_D/(\langle r\rangle-r_0)]\exp[-(r-r_0)/(\langle r\rangle-r_0)] \quad (1)$$

where N_d is the drizzle droplet concentration, $\langle r \rangle$ is the mean radius of the DSD, and r_0 is the smallest drizzle drop (r_0=20 μm). Figure 2 indicates how the two drizzle DSD parameters can be obtained from the cloud base radar reflectivity and its decrease due to evaporation below cloud. We have found that although the method is somewhat sensitive to the correlation between turbulent flux and the mean radius of the DSD, the DSD parameters can be retrieved in most instances with reasonable accuracy (Comstock et al. 2004). It is clear from Fig. 2 that there is greater sensitivity to changes in $\langle r \rangle$ for small values of $\langle r \rangle$, i.e. where significant subcloud evaporation is present. Uncertainties in our method are described more completely in Comstock et al. (2004).

Because both drizzle DSD parameters at cloud base are estimated, it is then possible to estimate the fraction of precipitation that reaches the surface.

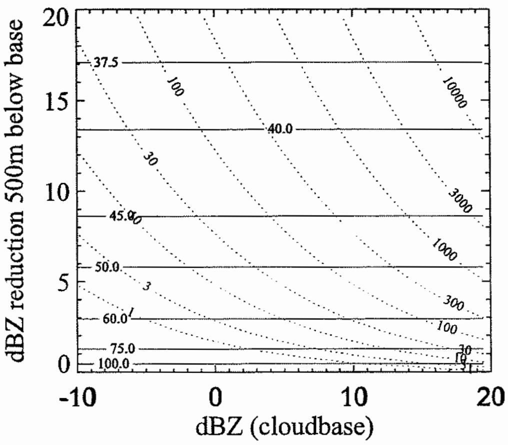

Figure 2. Contour plot demonstrating methodology. Contours show drizzle DSD mean radius (μm, solid) and drizzle drop number concentration (litre^{-1}, dotted) as a function of the reflectivity at cloud base and the reduction of dBZ from cloud base to 500 m below cloud base due to evaporation.

3. MEAN DRIZZLE PROPERTIES

3.1 Evaporation of drizzle

Figure 3 shows time series of cloud base and surface drizzle rate, plus cloud *LWP* and cloud droplet concentration N_d. It is clear that a large fraction of the drizzle evaporates before reaching the surface. This is a result of the elevated cloud bases (800-1000 m) observed during EPIC 2001. Notice also that the cloud base drizzle rates are quite large (mean value of ≈ 1 mm day^{-1}), which is energetically equivalent to around 30 W m^{-2}. The evaporating drizzle could lead to strong dynamical feedbacks upon the MBL. Finally, Fig. 3 reveals that the cloud base drizzle rate is positively correlated with cloud *LWP* and negatively correlated with N_d. The latter correlation is suggestive of an important microphysical control upon drizzle rates.

3.2 What controls the drizzle rate?

Three-hourly averages of MMCR cloud base drizzle rate R_{CB}, cloud *LWP*, and interpolated *cloud* droplet concentration N_d were constructed from the EPIC dataset. We find that the cloud base drizzle rate scales quite well with the ratio of *LWP* and N_d (Figure 3).

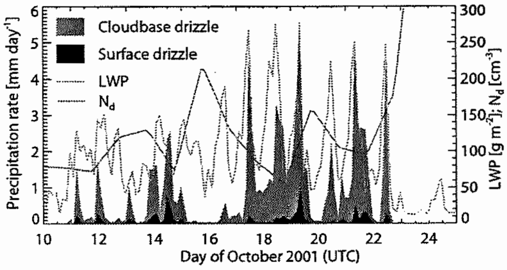

Figure 3. Time series of C-band area mean drizzle rate at cloud base, surface drizzle rate, cloud LWP, and cloud droplet concentration N_d.

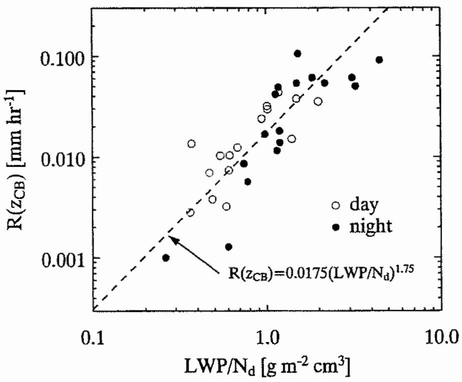

Figure 4. Cloudbase drizzle rate plotted against the ratio of cloud LWP to cloud droplet concentration, for the EPIC 2001 dataset. Night-time droplet concentration estimates were obtained by interpolation.

4. STRUCTURAL PROPERTIES OF DRIZZLE

The C-band precipitation maps permit, for the first time, detailed analysis of the structural properties of precipitation in stratocumulus clouds (see also ICCP 2004 abstract by Comstock et al.). We use these maps to examine the probability density function (pdf) of drizzle precipitation observed during EPIC 2001. Figure 5 shows the pdf of cloud base precipitation rate and the pdf of the total accumulation ($R_{CB}\,dP/dR_{CB}$). In addition, Figure 6 shows a bar chart that shows the contribution to rain accumulation (left) and rain area (right). Together these results paint a picture of drizzle being highly intermittent and patchy. For example, 50% of the total accumulation corresponding to the heaviest drizzle originates from only 3% of the drizzle area, while 56% of the drizzling area containing the lightest drizzle contributes only 2.5% to the total accumulation. Also interesting is the finding that a significant fraction of the accumulation comes from precipitation rates of at least 25 mm day^{-1}. These are extremely high rates for clouds that rarely were thicker than 500 m.

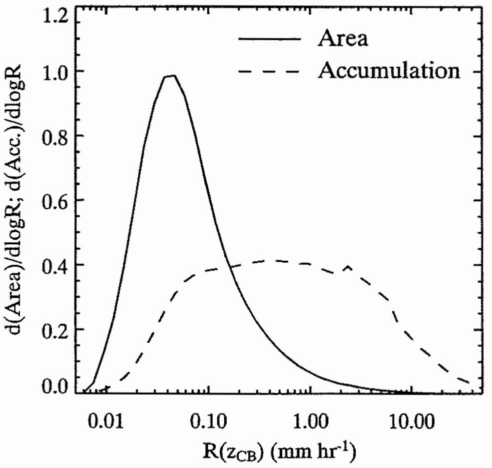

Figure 5. Mean probability density function (pdf) of the cloud base precipitation rate (when drizzling) from the 6 days at the WHOI buoy (85W, 20S) (solid line), and of the accumulation (dashed line). Note that although the median and modal cloud base drizzle rates are quite low (≈ 0.06 mm hr^{-1} ≡ 1.4 mm day^{-1}), around 50% of the accumulation comes from rainrates at least one order of magnitude higher than this.

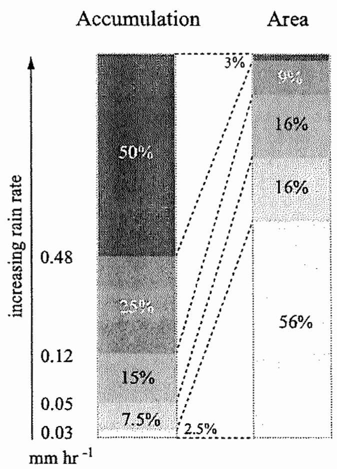

Figure 6. The total accumulation and the corresponding drizzling area for the given rain rates (e.g. 25 % of the rain comes from 0.12 < R_{CB} < 0.48 mm hr^{-1}, and this corresponds to 9 % of the drizzling area).

Figure 7 shows a composite power spectrum of cloud base drizzle rate generated from 6 days of data from EPIC. A C-band rainmap was obtained every 5 minutes during this period. The dotted lines show confidence intervals. The power spectrum peaks at a scale of approximately 10 km and falls off with a power law at smaller scales. The spectral exponent is approximately -1 in accordance with observations using aircraft (Wood, 2004). This is considerably less steep a fall-off than is seen in other cloud parameters such as LWP and cloud base height (exponents close to -5/3), indicating that there is heightened small-scale variability in precipitation compared with other cloud parameters.

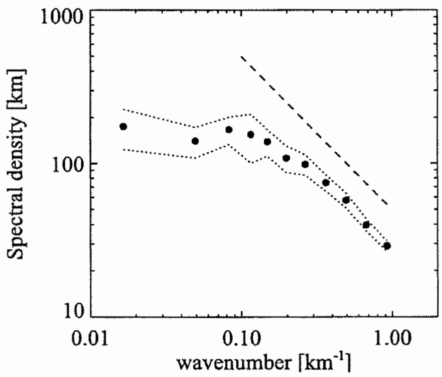

Figure 7: Composite power spectrum of C-band estimate rainrate from 6 days at WHOI buoy during EPIC 2001. The dashed line shows the Power ∝ (wavenumber)$^{-1}$ scaling, also seen in aircraft observations (Wood, 2004).

5. EFFECT OF DRIZZLE UPON BUDGETS

Using the estimated precipitation rate profiles we estimate the effect of drizzle upon the energy and moisture budgets in the MBL. To do this we use a mixed layer formulation and determine the contributions to the budgets of (a) liquid static energy S_L and (b) total water content q_T. Liquid static energy is defined as $S_L=c_pT+gz-L_vq_L$, where T is temperature, z is height, q_L is the liquid water mixing ratio, L_v is the latent heat of condensation, c_p is the heat capacity of air at constant pressure, and g is the gravitational acceleration. In a well mixed layer with moist processes, S_L and q_T are conserved quantities.

A complete budget analysis is presented in more detail in Caldwell et al. (2004). Here, we state some of the conclusions regarding the role of drizzle. Drizzle affects the budgets of the layer as a whole in two ways: first, drizzle reaching the surface has a *direct* effect upon the budgets, by decreasing q_T and increasing S_L (through the latent heating effect); second, the evaporating drizzle below cloud base can *indirectly* affect the budgets, by causing decoupling of the boundary layer, reducing its turbulence and feeding back onto the entrainment rate.

The direct effect of drizzle is small because most of the drizzle evaporates in the layer below cloud, and so the magnitude of the surface drizzle rate is only 4 W m^{-2} when expressed in energy terms. This may be compared with an SL budget that is roughly balanced by the combination of longwave cooling (-79 W m^{-2}), shortwave warming (+30 W m^{-2}) and entrainment of warm air from above the MBL (+34 W m^{-2}), with some advection of low SL air from upstream. Similarly, the total water budget is balanced by latent evaporation (+99 W m^{-2}), entrainment of dry air from aloft (-70 W m^{-2}), and some advection of dry air from upstream (-26 W m^{-2}). Thus, we conclude that drizzle does not seriously contribute to the mean budgets directly.

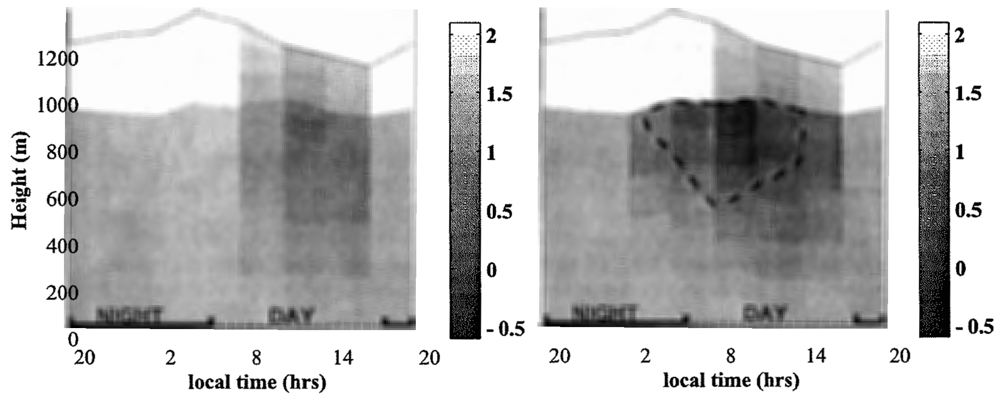

Figure 8. Composite diurnal buoyancy flux profiles estimated using the mixed layer analysis. Units are 10^{-3} m^2 s^{-3}. Left: drizzle assumed to be zero at all levels and times. Right: including observed drizzle rate profiles. The dashed contour contains regions where the buoyancy flux becomes negative.

The *indirect* effect of drizzle upon the MBL budgets can be assessed by constructing buoyancy flux profiles for the MBL using the mixed layer budget analysis (Schubert et al. 1979, Bretherton and Wyant 1997). Stevens (1999), using large eddy simulation (LES), shows that decoupling is initiated when the buoyancy flux profile has any appreciable negative values, and that the decoupling markedly reduces the turbulence in the MBL, and therefore its ability to entrain air from the free troposphere.

Buoyancy flux profiles during EPIC are highly diurnally variable (because shortwave warming and also drizzle have strong diurnal cycles), and so we show these as a composite diurnal cycle in Figure 8. Notice that the buoyancy flux only becomes negative below cloud base when drizzle is included (although it does become small without drizzle), even though the shortwave forcing is strong in this region. This suggests that the inclusion of drizzle is sufficient to initiate decoupling in these clouds. It is not possible to quantify, using this simple mixed layer analysis, how important the drizzle-induced decoupling is on clouds observed during EPIC, but we plan to examine this further using LES.

CONCLUSIONS

The EPIC 2001 dataset has been used to demonstrate the importance of drizzle in the SE Pacific MBL. Important aspects of the dependence of drizzle upon cloud properties, and of its structure have been addressed, and the significance of drizzle in the MBL budgets assessed.

ACKNOWLEDGEMENTS

We thank the staff at NOAA ETL, particularly Chris Fairall, Paquita Zuidema, Pavlos Kollias, Duane Hazen, and Taneil Uttal for their work in obtaining and synthesizing the dataset used in this study. We are also grateful to the crew of the NOAA Ronald H Brown for their assistance in collecting EPIC data. This work was funded by NSF grant ATM-0082384, NASA grant NAG5S-10624 and a NDSEG fellowship.

REFERENCES

Austin, P., Wang, Y., Pincus, R., Kujala, V., 1995: Precipitation in Stratocumulus Clouds: Observational and Modeling Results. *J. Atmos. Sci.*: **52**, 2329-2352.

Bretherton, C.S, and M.C. Wyant, 1997: Moisture transport, lower tropospheric stability and de coupling of cloud-topped boundary layers. *J. Atmos. Sci.*, **54**, 148-167.

Bretherton, C.S., Uttal, T., Fairall, C.W., Yuter, S.E., Weller, R.A., Baumgardner, D., Comstock, K., and R. Wood, 2004: The EPIC 2001 Stratocumulus Study. *Bull. Am. Meteorol. Soc.*, in press.

Caldwell, P., R. Wood, and C. S. Bretherton, 2004: The diurnal cycle of marine stratocumulus in the SE Pacific in a mixed layer context. Manuscript in preparation.

Comstock, K. K., Wood, R., Yuter, S. E., and Bretherton, C. S., 2004: Reflectivity and rain rate in and below drizzling stratocumulus. *Quart. J. Roy. Meteorol. Soc.*, submitted.

Dong, X., and G. G. Mace, 2003: Arctic stratus cloud properties and radiative forcing derived from ground-based data collected at Barrow, Alaska. *J. Climate*, **16**, 445-460.

Jensen, J. B., S. Lee, P.B. Krummel, J. Katzfey, and D. Gogoasa, 2000: Precipitation in marine cumulus and stratocumulus. Part I: Thermodynamic and dynamic observations of closed cell circulations and cumulus bands. *Atmos. Res.*, **54**, 117-155.

Petty, G. W., 1995: Frequencies and characteristics of global oceanic precipitation form shipboard present-weather reports. *Bull. Amer. Meteor. Soc.*, **76**, 1593-1616.

Schubert, W.H., Wakefield, J.S., Steiner, E.J., Cox, S. K., 1979: Marine Stratocumulus Convection. Part I: Governing Equations and Horizontally Homogeneous Solutions. *J. Atmos. Sci:*, **36**, 1286-1307.

Stevens, B., 1999: Cloud transitions and decoupling in shear-free stratocumulus-topped boundary layers. *Geophys. Res. Lett.*, **27**, 2557-2560.

Wood, R., 2004: Drizzle in stratiform boundary layer clouds. Part I: Vertical and horizontal structure. Submitted to *J. Atmos. Sci.*

ON HETEROGENEITY OF DRIZZLE IN A STRATOCUMULUS-TOPPED MARINE BOUNDARY LAYER

Bai Yang and Yefim L. Kogan

Cooperative Institute for Mesoscale Meteorological Studies
University of Oklahoma, Norman, OK 73019, USA

1. INTRODUCTION

Drizzle plays a crucial role in the longevity and fractional cover of boundary layer clouds. Observations show that magnitude of drizzle flux is frequently comparable to or even larger than other water substance fluxes. Wang and Albrecht (1992) using aircraft data from the First ISCCP (International Satellite Cloud Climatology Project) Regional Experiment (FIRE) field experiment concluded that the effect of drizzle is usually localized, so that drizzle patches enhance the horizontal heterogeneity of the cloud-topped boundary layer (CTBL). The surface area covered by drizzle, according to observations, may vary in a rather wide range, from 5% (Brost et al. 1982) to as large as 30% (Paluch and Lenschow 1991). The dependence of drizzle spatial coverage on the large-scale meteorological conditions is not well understood and needs further investigation.

In this paper we investigate drizzle variability in both time and space domains using data from a large eddy simulation (LES) of a stratocumulus-topped boundary layer.

2. MODEL AND EXPERIMENT

This study is based on the Cooperative Institute for Mesoscale Meteorological Studies (CIMMS) LES explicit microphysical model. The size-resolving microphysics predicts distribution function for both cloud condensation nuclei (CCN; 19 bins) and cloud drops (25 bins). Detailed description and verification of the model against observations can be found in Khairoutdinov and Kogan (1999).

The current experiment is initialized with data obtained during the Atlantic Stratocumulus Transition Experiment (ASTEX) flight A209 on 12-13 June 1992. Initial soundings of total water mixing ratio, q_t (g kg^{-1}), and liquid water potential temperature, θ_l (K), are specified in Table 1 at four vertical levels, H (m). An initial CCN concentration of 54 cm^{-3} is prescribed, representing a clean maritime background. The domain size is $3.0 \times 3.0 \times 1.25$ km^3 with $40 \times 40 \times 50$ grid points. The experiment is run for 6 hrs with a 4s time step. Instantaneous, 3-D data sets are produced from t=2 to 5 hr with a 1-min increment.

Corresponding author's address: Bai Yang, CIMMS, University of Oklahoma, 100 E. Boyd Street, Room 1110, Norman, OK 73019, USA. Email: byang@ou.edu.

TABLE 1. Sounding used in the simulation.

H	0.0	662.5	687.5	1687.5
q_t	10.2	10.2	9.1	6.3
θ_l	289.8	289.8	295.0	301.0

3. RESULTS

We analyze two stages in cloud evolution (Fig. 1) which significantly differ in cloud cover and surface drizzle rate (R). The first stage (from t=2 to 3.3 hr) is characterized by solid cloud layer with mean surface drizzle rate of R_m=0.15 mm day^{-1} (light drizzle stage, LD). The cloud layer becomes broken and precipitates more heavily (R_m=0.43 mm day^{-1}) during the second stage (from t=3.5 to 5 hr; heavy drizzle stage, HD).

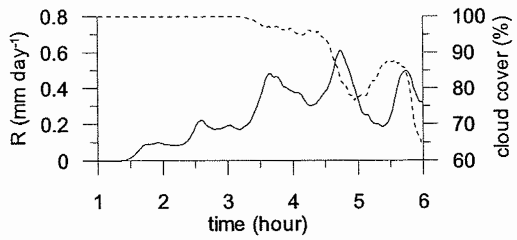

FIG. 1. Evolution of cloud cover (dash line) and mean drizzle rate at surface (solid line).

3.1 Drizzle spatial distribution

Fig. 2 shows drizzle area coverage fraction and drizzle mass fraction as a function of drizzle rate *R*. At the LD stage the area covered by weak drizzle (< 0.3 mm day^{-1}) is 20-30% larger than at the HD stage. At the latter stage about 12% of the area is covered by drizzle stronger than 1 mm day^{-1}. At the LD stage, drizzle at this high rate has negligible area coverage.

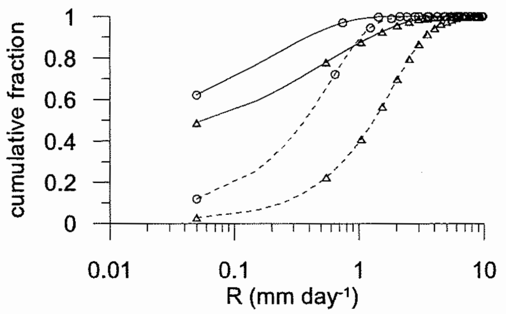

FIG. 2. Cumulative drizzle area (solid) and mass (dashed) fractions; circles and triangles denote LD and HD stages, correspondingly.

By definition, drizzle mass fraction is the area coverage fraction multiplied by R/R_m. The LD stage has a lower R_m (one third of that from HD stage), but higher area coverage (on average 20% higher for weak drizzle <0.3 mm day^{-1}). Therefore the LD drizzle mass fraction is about 3-4 times as high as HD. For strong drizzle > 1 mm day^{-1}, the difference in area coverage is the main reason for the difference in drizzle mass fraction. HD mass fraction is about 6 times larger than that of LD.

Strong drizzle (> 1 mm day^{-1}) occupies a negligible portion of the simulation area at surface, but contributes a significant amount to total drizzle. The opposite is true for weak drizzle (<0.1 mm day^{-1}). For example, cumulative mass fraction for drizzle greater than 1 mm day^{-1} is 0.10 and 0.59 for LD and HD respectively, while corresponding cumulative area fractions are 0.02 and 0.12. In contrast, weak drizzle (< 0.1 mm day^{-1}) covers 77% and 59% of the area for LD and HD, but contributes 25% and 6% to total drizzle.

3.2 Drizzle temporal distribution

Fig. 3 shows spatial distribution of the cumulative surface drizzle mass as a percentage of total drizzle accumulated at each grid point. If drizzle were homogeneous in time, the percentage values would be constant in space and proportional to the drizzle recording time, e.g., all equal to 25% for the first quarter of the drizzle recording period. However, due to intermittent nature of the drizzle process, the cumulative drizzle mass fraction varies in a wide range. The top panel in Fig. 3 shows that during the first quarter of the drizzle recording time, the cumulative mass fraction varies from a few percent to more than 70%. Similarly, for the first three quarters of the drizzling period (bottom panel) most of areas have received about 80-90% of the total drizzle. However, some regions

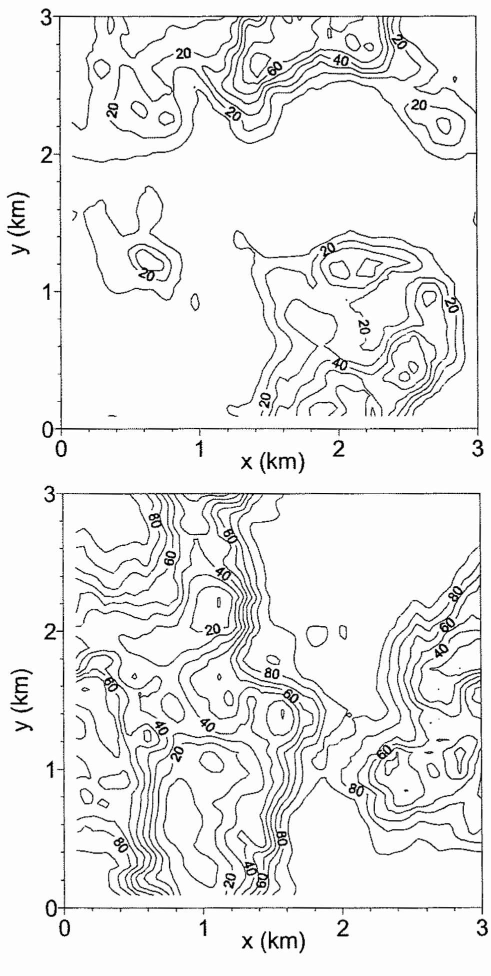

FIG. 3. Cumulative drizzle mass percentage (%) for the first 25% (top panel) and 75% (bottom panel) of simulation time starting from t=2 hr.

(e. g., one bordered by x=0.8 to 1.2 km and y<1.2 km and a second one bordered by x=0.9 to 1.2 km and y=2.0 to 2.4 km) received only less than 20%. In other words, these two regions will receive 80% of the total drizzle in the last quarter of the drizzle recording time.

3.3 Parameterization of drizzle spatial distribution

We now address the question of parameterization of drizzle heterogeneity. For this we show in Fig. 4 cumulative area and mass fractions as functions of normalized drizzle rate, R/R_m. In these coordinates, the two curves representing the two stages of cloud evolution are very close and show similar functional dependency on R/R_m.

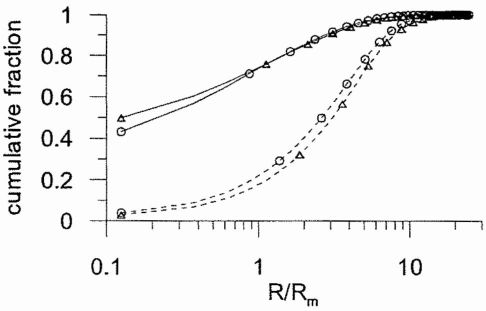

FIG. 4. As in Fig. 2 but now cumulative fraction is computed based on normalized drizzle rate.

We found that a lognormal function can be used to parameterize the area coverage fraction, shown in Fig. 5. It is given by,

$$f(R/R_m) = \frac{\exp\{-[(\ln(R/R_m) - \mu)^2 / 2\sigma^2]\}}{(R/R_m) \bullet \sigma \bullet \sqrt{2\pi}},$$

where μ and σ are the mean and the standard deviation for the logarithm of normalized drizzle rate, ln(R/R_m). And the best fit for drizzle mass fraction in Fig. 5 is produced by (R/R_m)•f(R/R_m). The integrals of area and mass fractions yield the corresponding cumulative fractions.

The best fit for area coverage fraction tends to generally underestimate for R/R_m < 7.5 by 19% on average but overestimate for R/R_m > 7.5 by from 3% to as large as 10 times. This is because occurrence for R/R_m > 7.5 is so rare, indicated by extremely small magnitude for area coverage fraction, that a tiny difference in absolute values between the best fit and the numerical data can result in huge relative deviation. For the same reason, an overestimation by 10 times at this high drizzle rate would not be thermodynamically significant. For area coverage fraction, correlation coefficients are 0.997 between best fit and LD stage, and 0.985 between best fit and HD stage.

The best fit for mass fraction has a similar shape to the numerical data from two cloud stages. However, its peak shifts towards smaller drizzle rate than the latter, which peaks at R/R_m=1 implying the greatest contribution to total drizzle amount at this point. Considering the magnitudes, the best fit for drizzle mass fraction overestimates for weak drizzle ($R/R_m \leq 0.8$) by about 25% and strong drizzle ($R/R_m \geq 7.5$) by from a few percent to 20 times or more, but underestimates at the intermediate drizzle rate by 22% on average. However, this best fit is in general acceptable if we realize that the gaps between the best fit and numerical data for mass fraction are magnified in Fig. 5, as plotted are 5 × (mass fraction). Reasons for the gaps are the uncertainties in the best fit for area coverage fraction and use of middle value as the mean drizzle rate in each bin, which may not necessarily true, when we calculated the best fit for mass fraction. For mass fraction, correlation coefficients are 0.96 between best fit and LD stage, and 0.92 between best fit and HD stage.

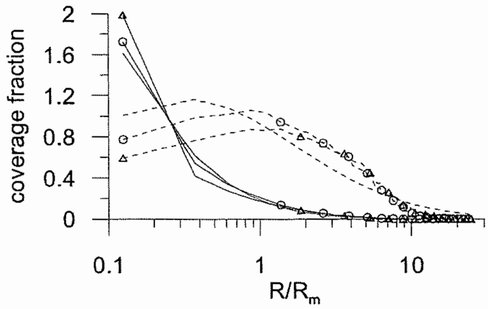

FIG. 5. Drizzle area coverage fraction (solid) and 5 × [mass fraction] (dashed) against normalized drizzle rate; circles and triangles denote LD and HD stages, correspondingly. Lines without symbols denote the best fits.

4. CONCLUSIONS

We study time and space distribution of drizzle from a stratocumulus-topped marine boundary layer. Our major conclusions are as follows.

(1) Clouds of different stages in a marine boundary layer are in great similarities on their drizzle area coverage and mass fractions and the corresponding cumulative fractions, if drizzle rate is properly normalized. Area coverage fraction of drizzle rate can be parameterized by a lognormal function. And then the parameterizations for mass fraction and the corresponding cumulative fraction can be derived accordingly.

(2) Our data show that heavy drizzle patches (R/R_m > 5.0) can contribute 35% to total drizzle mass with only 10% of surface area coverage. The corresponding values are 76% and 22% for R/R_m > 1.0. On the other hand, drizzle-free and extremely slight drizzle areas (R/R_m < 0.125) cumulatively cover 46% of the surface area but only contribute 3.4% to total drizzle.

(3) Drizzle intermittency is illustrated by the fact that as many as 10% of grid points, receive 75% of their total drizzle within one quarter of the total time. Equivalently, less than 25% of the total drizzle is received within three quarters of total time at these grid points.

Our results are preliminary and based on a single simulation. Additional simulations, for example exploring the dependence of drizzle distribution on domain size, thermodynamic conditions etc, are necessary to generalize the results.

ACKNOWLEDGEMENT

This research was supported by the ONR Grants N00014-96-1-0687 and N00014-03-1-0304.

REFERENCES

Brost, R. A., D. H. Lenschow, and J. C. Wyngaard, 1982: Marine stratocumulus layers. Part I: Mean conditions. *J. Atmos. Sci.*, 39, 800-817.

Khairoutdinov, M. F., and Y. L. Kogan, 1999: A large-eddy simulation model with explicit microphysics: Validation against aircraft observations of a stratocumulus-topped boundary layer. *J. Atmos. Sci.*, 56, 2115-2131.

Paluch, I. R., and D. H. Lenschow, 1991: Stratiform cloud formation in the marine boundary layer. *J. Atmos. Sci.*, 48, 2141-2158.

Wang, S., and B. A. Albrecht, 1992: Convective mixing in stratocumulus-topped boundary layers observed during FIRE. Preprints, *11th Int. Conf. on Clouds and Precipitation,* Montreal, ICCP and IAMAP.

Orographic precipitations. Physical processes and contribution to the rainfall regime of the Cévennes - Vivarais region.

E. Yates, S. Anquetin [1], J.-M. Cohard
Laboratoire d'étude des Transferts en Hydrologie et Environnement, Grenoble, France

1 Introduction

Understanding the physical processes that lead to orographic precipitation has its importance in domains such as weather and climate prediction or water management. Mountains affect atmospheric circulation over a wide range of scales, contributing to an uneven repartition of moisture and rain in space and time. Understanding the link between temporal and spatial variations of rainfall distribution over complex terrain is therefore a great challenge for hydrological purposes. The runoff production of mountainous watersheds will be, therefore, very sensitive to this distribution.

Based on the analysis of radar images and non-hydrostatic simulations of a shallow convection case above the Cévennes - Vivarais region in the South-eastern part of France, Miniscloux et al. (2001), Cosma et al. (2002) and Anquetin et al. (2003) have shown that the small orographic features of the topography focus and intensify the precipitation due to the convergence of low level air masses within the succession of oriented ridges and valleys.

Following these previous works, this study is based on ideal atmospherical simulations that aim to understand and highlight the main processes that lead to orographic precipitation organized in bands. The interaction between the atmospherical flow conditions (wind direction) and the resulting precipitation is investigated in terms of localisation of the rain patterns and in terms of water depth at catchment scale. The role of initial soil moisture is also investigated and its contribution to the enhancement of shallow convection is presented in this abstract.

2 Description of the simulations

The domain of simulation is the south-eastern ridges of the French "Massif Central" (Fig.1) called the "Cévennes - Vivarais" region. The Cévennes region altitude ranges from sea level up to 1500 m in roughly 30 km. This region experiences prolonged rain events that may lead to catastrophic floods over the wide range of river basin sizes. In this context, this study aims to analyse the contribution of the shallow convection in the spatial distribution of the humidity at watershed scale. This initial humidity may have a critical hydrological impact once the intense event occurs.

The idealized simulations were carried out with the 3D non-hydrostatic model MesoNH (Lafore et al., 1998). The anelastic system of equation is integrated in the system of curvilinear coordinates with nonuniform grids. The simulations used two domains run in a two-way interactive mode. Only, the high resolution ($\Delta = 1km$) simulated fields are analysed and discussed here.

The ideal simulations used 1.5 TKE turbulence scheme (Bougeault and Lacarrère, 1989), radiative transfer (Mocrette, 1989), soil-atmosphere exchanges (Noilhan and Planton, 1989) and the Kessler warm microphysical parametrization (Kessler, 1969). Ice microphysics are neglected for simplicity and because the cloud tops barely extend the freezing level (Fig.3).

Five ideal simulations are performed and are presented Table 1. The atmospherical inflow is the same for the 5 simulations and is characterized by a two stratified layers atmosphere: the Brunt-Väisälä frequency of the lower layer, up to $z = 4km$, is fixed to $N = 8.10^{-3}s^{-1}$ whereas the upper layer is more stably stratified ($N = 2.10^{-2}s^{-1}$). The relative humidity of the lower layer is fixed to 80 %. The interaction between the modification of the wind direction and the resulting precipitation is analysed through the comparison of the results of the REF simulation (south direction) with the SIM3 (N165^o E), and SIM4 (N195^o E) simulations. The results are not presented in this abstract. This paper aims to highlight the role of initial soil moisture (SIM1 and SIM2) in terms of localisation of the rain patterns and in terms of rain intensity. For these simulations, the humidity of the three layers of the soil is initialized and maintained during the whole simulation to saturation (SIM1) and 50 % of the saturation (SIM2). For the simulations REF, SIM3 and SIM4, the three humidities of the three soil layers are initialized to 50 % of their saturation and are then free to evoluate through the SVAT model.

The simulations are carried out during nine hours, only the two last hours are analysed.

3 Orographic rainbands

The global structure of the simulated rain fields is characteristic of orographic precipitation organized in bands (Fig.2)(Miniscloux et al. (2001), Kirshbaum and Durran (2004)). The precipitation patterns are organized in N-S orientated bands and are confined

[1]Corresponding author's address : Sandrine Anquetin, L.T.H.E., B.P. 53X, 38041 Grenoble Cedex 9, France, E-Mail : Sandrine.Anquetin@hmg.inpg.fr

to the hilly and mountainous areas. The simulations SIM1 and SIM2 (not shown here) present the same type of rainband structure whereas the orientation of the rainbands of the SIM3 and SIM4 simulations are slightly inclined due to the main flux orientation.

Due to the prescribed atmospherical stratification, the vertical extension of the precipitation is limited by the inversion at the altitude of 4 km. The vertical cross section of the cloud mixing ratio within a rainband is shown Fig.3. The cloud is confined to the first five kilometers above the ground. Therefore, the ground forcings (i.e. the topographical disturbances and the surface fluxes) are the only processes that initiate and maintain the precipitation within the domain.

4 Impact of the ground humidity

In this part, the role of initial soil moisture on the rainband localization and intensity is discussed on the base of the REF, SIM1 and SIM2 simulations. The simulated maximum of precipitation slightly increases with the ground saturation. After the 2 last hours of simulation, the maximum of precipitation are 35 mm, 42 mm, and 46 mm for REF, SIM2 and SIM1 respectively. The rain patterns present also some discrepencies. The larger is the humidity amount in the soil, the larger will be the surface of maximum of precipitation. Morevover, the larger latent heat flux at the ground due to the saturated ground (SIM1) leads to a delocalization of approximately 10 km of the rainband compared to the REF simulation in the hilly region. In the mountainous area, where the orographic precipitation is mainly formed by the small scale topographic features, the rainbands remain at the same place (Fig.5).

To investigate the impact of the surface fluxes on the orographic precipitation formation, the water vapour surface flux is plotted along a rainband that remains approximately at the same place for the 3 numerical experiments (Fig.2). The surface flux as well as the 2 hours cumulated rain field and the horizontal wind at the first vertical grid point are plotted Fig.4. Here, the rainband takes place on the leeward of the highest mount of the region (i.e. The Mount Lozère) and is mainly active due to the low level convergence of the air masses (Anquetin et al., 2003). The preliminary results show that the latent heat flux reduces the air warming on the lee side of the mount, leading to the intensification of the valley wind that reduces the uplift of the atmosphere. Therefore, the rain intensity is reduced.

5 Conclusions

The main objective of this study is to highlight the interaction between the local atmospherical flow and the energetic surface forcing on the resulting precipitation over the region of the Cévennes - Vivarais in the southeast of France. These preliminary results must be completed with a geostatistical analysis to further investigate the simulated fields. The role of the microphyics in the formation of orographic rain will be also investigated by the mean of the new microphysical scheme developped by Cohard and Pinty (2000).

Acknowledgements The current study has been supported by the PATOM research programs of the CNRS-INSU, the French Institute for the Universe Sciences. The numerical simulations were carried out on the NEC of the IDRIS (CNRS) computing center.

6 References

Anquetin, S., F. Miniscloux, J.-D. Creutin and S. Cosma, 2003, Numerical simulation of orographic rainbands, *J. of Geophysical Research*, 108(D8), 8386, doi:10.1029/2002JD001593.

Bougeault, P. and P. Lacarrère, 1989, Parametrization of orographic induced turbulence in mesobeta scale model, *Mon. Weather Rev.*, 117, 1872-1890.

Cohard, J.M. and J.P. Pinty, 2000, A comprehensive warm microphysical bulk scheme, Part I: Description and selective tests, *Quat. J. R. Meteoro. Soc.*, 126(566), 1815-1842.

Cosma, S., E. Richard and F. Miniscloux, 2002, the role of small scale orographic features in the spatial distribution of precipitation, *Quat. J. R. Meteoro. Soc.*, 126(566), 1843-1860.

Kessler E., 1969, On the distribution and continuity of water substance in atmospheric circulation, *Meteorol. Monogr*, 32, 84 pp.

Kirshbaum D.J. and D.R. Durran, 2004, Factors governing cellular convection in orographic precipitation, in press *J. of Atm. Scie.*

Lafore, J.P. et al., 1998, The MesoNH atmospheric simulation system, Part I: Adiabatic formulation and control simulations, *Ann. Geophys.*, 16, 90-109.

Miniscloux, F., J.-D. Creutin and S. Anquetin, 2001, Geostatistical analysis of orographic rainbands, *J. of Applied Meteoro.*, 40, 11, 1835-1854.

Mocrette J., 1989, Description of the radiation scheme in the ECMWF model, *ECMWF Tech. Memo. 165*, 26 pp., Eur. Cent. for Medium-Range Weather Forecasts, Reading, UK.

Noilhan J. and S. Planton, 1989, A simple parametrization of land surface processes for meteorological models, *Mon. Weather Rev.*, 117, 536-549.

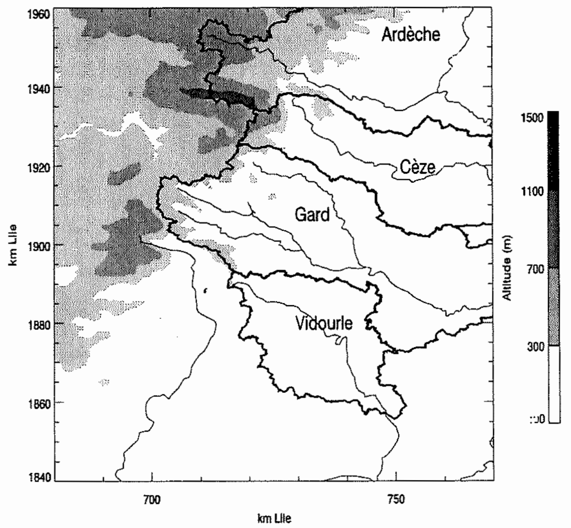

Figure 1: The simulated relief of the Cévennes - Vivarais region

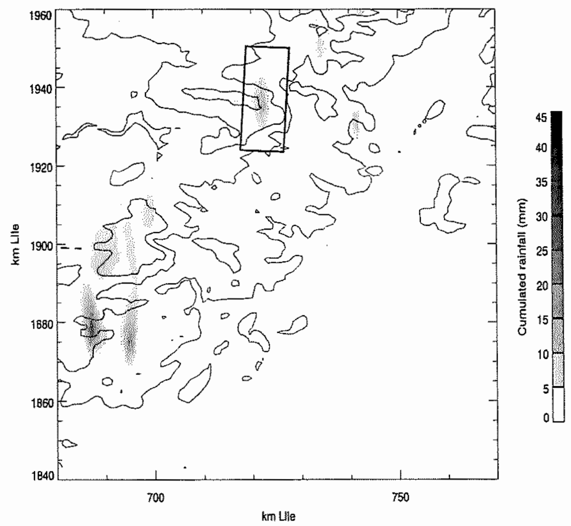

Figure 2: Cumulated rain field patterns for the REF simulation.

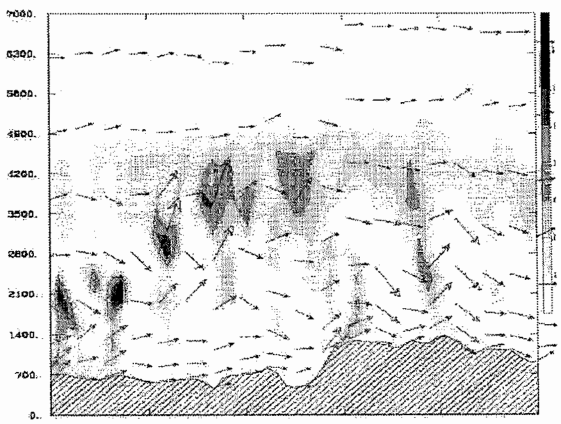

Figure 3: Vertical cross section of the cloud mixing ratio within a rain band

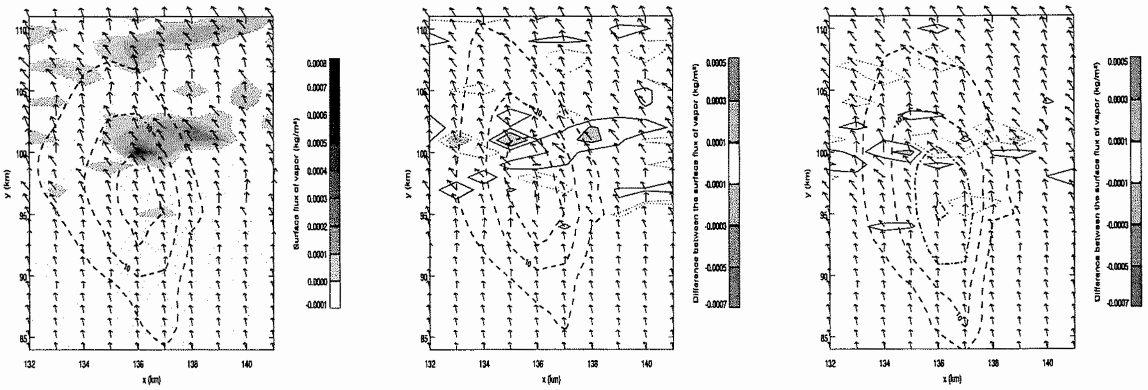

Figure 4: (a)Surface latent heat flux for the REF simulation.(b)Difference of the surface latent heat fluxes (SIM1-REF).(c)Difference of the surface latent heat fluxes (SIM2-REF)

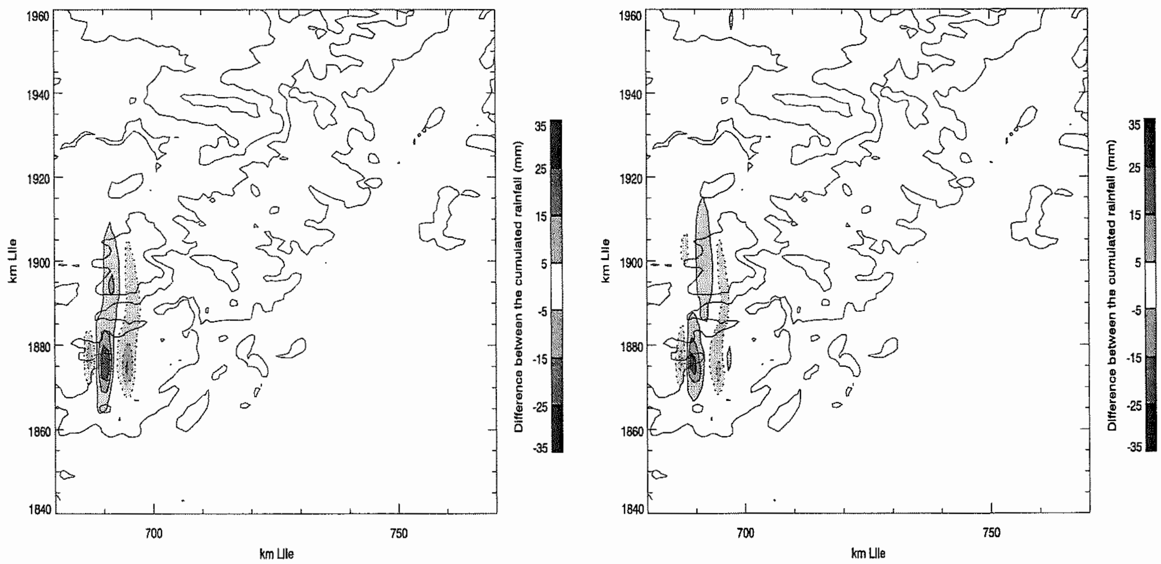

Figure 5: Difference of the cumulated rain fields.(a)SIM1-REF, (b)SIM2-REF

	REF	SIM1	SIM2	SIM3	SIM4
soil humidity	free	100 % sat.	50 % sat.	free	free
wind direction	N180°E	N180°E	N180°E	N165°E	N195°E
wind intensity	$15\ m.s{-1}$				
Larger domain	80 x 90 x 45, Δx = Δy = 4 km, ΔT=16 s				
Inner domain	200 x 200 x 45, Δx = Δy = 1 km, Δt=4 s				

Table 1: Definition of the idealized simulations

A Case Study on the Cold-Front and Cyclone Clouds with Their Multi-Scale Structures and Precipitating Mechanisms in China

Zhou Yuquan[1,3], Hong Yanchao[2], Su Aifang[3], Huang yimei[3] and Zheng Guoguang[4]

[1] Nanjing Institute of Meteorology, Nanjing 210044, China
[2] Institute of Atmospheric Physics, Academia Sinica, Beijing 100029, China
[3] Henan Meteorological Administration Zhengzhou 450003, China
[4] China Meteorological Administration Beijing 100029, China

1. INTRODUCTION

It is well-known that research of the multi-scale structures and their interactions of cloud and rainfall development under the effects of different synoptic systems is of great significance to the understanding of precipitation occurrence and development and hence improving the forecasting and seeding techniques.

This work is devoted to analysis of multiple kinds of observations derived of the cold-front and cyclone precipitating clouds on April 4-5, 2002 together with the numerical study in order to investigate the multi-scale structures and physical mechanisms for rain production and development in such clouds.

2. INTENSIVE OBSERVATION NETWORK AND DATA

A network covering ~100,000 km^2 is operated for intensive observations consisting of 3-hr radiosonde data, 8-station surface raindrop size distribution, 128-station rainfall recordings apart at a short distance, intensive time-level measurements of Doppler radara, bi-channel microwave radiometer data and air-borne PMS (particles measuring system) microphysical observations, with their distributions shown in Fig.1.

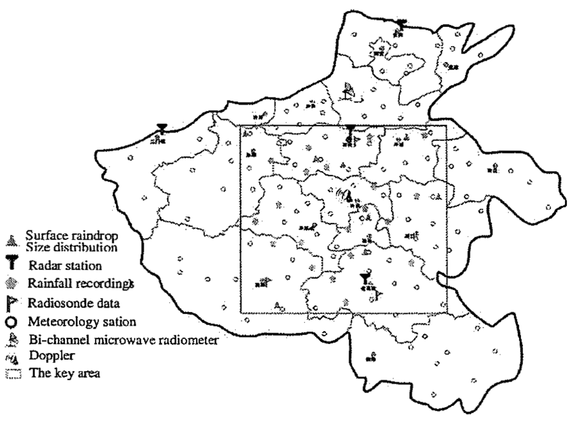

Fig.1. The network for integrative observations in Henan Province, with the key area in box.

Corresponding author's address: Zhou Yuquan
Henan Meteorological Adminstration, Zhengzhou 450003, China; E-Mail: hnzhouyq@371.net

3. Weather Situation

Under the joint impacts of a 500- westerly trough, an east-moving 700- shear line, a 850-hPa easterly flow for vapor transport and a surface cold front and a ground cyclone, a province-wide rainfall event occurred on April 4-5, 2002. At 0500 BT of the 5th day, a cold front passed through Zhengzhou and 3 hr later the front, entering the ground inverted V-shaped trough, generated the surface cold front and cyclone.

4. THEIR MACRO-AND MICROSCOPIC STRUCTURES

4.1 Evolution of the Cloud Systems

As displayed by analysis of the synoptic situation in combination with clouds (Fig.2), under the joint effects of high-level and surface systems, organized was a banded cloud parallel to the trough line between the cold front line and 500-hPa trough and structured unevenly at 0800 BT of April 4. In its movement eastward the cloud band was developing. As vapor transport was reinforced at 700 hPa a cluster of clouds were seen and part of the clouds rose, developed and traveled north. At 0200 BT of the next day the band-form structure exhibited distinct change and at 0800 hr it turned into a precipitating cloud typical of a Jiang-Huai cyclone in the country.

Observations reveal the evolution of the cold front and cyclone clouds, with their combination with their forms as As-Sc-Ns-Fn and Acop-Sc-Ns-Fn.

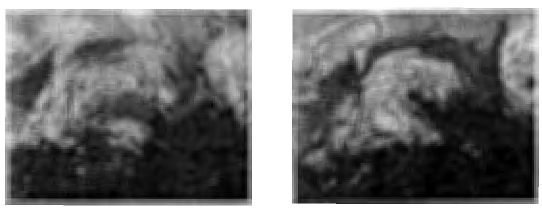

(a) (b)

Fig.2. High- and low-level situations and related clouds at 2000 of April 4(a) and 0800(b)

4.2 Cloud Vertical Structure and Cloud Particles Size Distribution

Analysis of the datasets from the radiosonde stations of Zhengzhou (34045', 133040'E) and

Nanyang (330N, 112040'E) and of radar vertical measurements indicates that the clouds were stratified, following the criterion of $T - Td \le 2^0C$ for a cloud layer. And under different dynamic effects the cloud tops and bases differed in height from one portion to another and so did the temperatures and layering.

Effective radii of cloud particle size spectrum retrieved from GMS-5 images show that the mean effective radii ranged over 6-8 μm, which were 1-2 μm bigger in the cyclone clouds than in the cold front counterpart(Fig.3)

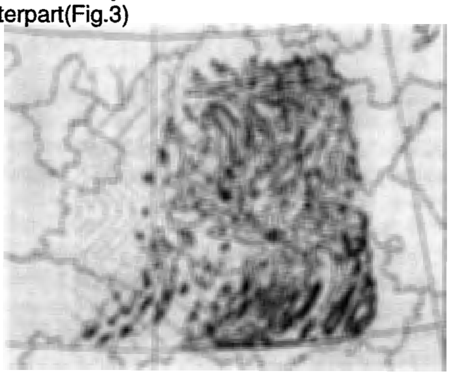

Fig.3. The cyclone and cold front clouds effective radii from GMS-5 imagery

The satellite data-reduced cloud top brightness temperatures ranged over -25~- -40^0C and they dropped while the clouds were developing. The clouds were lifted higher on a continuous basis as observed at Zhengzhou from 0800 hr on April 5 till after they moved out. Evidently, the cyclone could top under development was higher compared to the cold front equivalent.

5. MULTI-SCALE MOISTLY THERMAL AND DYNAMIC STRUCTURES OF THE CLOUDS

In the context of 3-hr apart Zhengzhou soundings on April 4-5 we constructed a diagram for the mesoscale moistly thermal and dynamic structure during precipitation from the cold front and cyclone clouds as shown in Fig.4

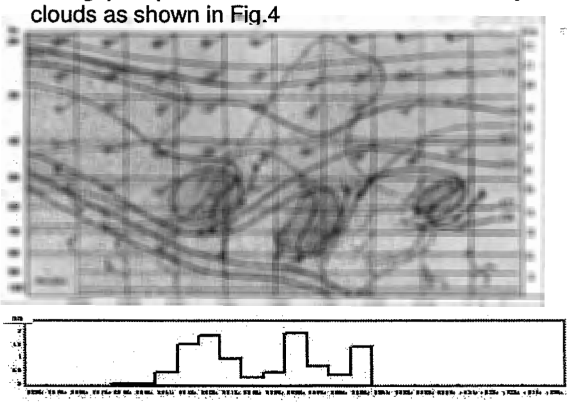

Fig.4. The vertical cross-sections of multi-scale wetly thermal and dynamic structures and time-dependent surface rainfall at Zhengzhou on the study days.

where the pseudo equivalent potential temperature (Qse) is denoted by solid line, the characteristic layer isothermal condition (T) by dashed contour, the potential instability zone is shaded, cloud portion (relative humidity >90%) is stippled, ice-supersaturation vapor band ($e - Ei > 0$) denoted by dotted line, the front line by double full line and the inversion layer by thickened short double solid line.

It is seen therefrom that during the weather event the cold front was located below 2500 m level, acting as a large-scale "cold cushion", with three apparent meso cold surges upon it in good correspondence to as many potential unsteadiness zones of varying intensity. The difference in low level moisture at different time intervals was responsible for the heterogeneous rainfall pattern as observed at Zhengzhou station. During the first cold surge occurring about 4 km ahead of the prefrontal warm sector, was observed stratified clouds from which no distinct rain fell due to dry stratification at lower levels. And with weak cold air incursion another cold surge showed up at 0200 hr of April 5, and the instability zone at 3 km level was in a deep layer of moisture, where the good wetly thermal environment allowed clouds to develop, leading to a first rainfall peak (2.4 mm/h). Furthermore, the ice supersatuation vapor band ($e - Ei > 0$) was sufficiently deep to extend downward as far as 5 km level compared to the 9 km height of cloud top derived from the satellite retrieval, thus providing moistly thermal and dynamic conditions favorable for high-level ice crystals growing during descent, which was a time interval (0200-0800 BT of April 5) conducive to rainfall development. The precipitation diminished while the cold surge was coming to an end. Two hours later a third cold surge emerged in the 5-km level at 1100-1400 BT of April 5, resulting in another ground rainfall peak of 1.9 mm/h on the strength of pretty rich vapor at lower levels despite the instability zone at higher level.

These constitute a good meso wetly dynamic environment for the "seeder – feeder" mechanism. Analysis shows that rainfall would possibly occur in future and last 3-4 hrs (around 0500-0800 and 1100-1500 BT) on April 5 in association with the likely existence of the second and third cold surge so that we made a scheme of catalyzing clouds As and Ac and leaving Sc to act as the vapor supplier.

6. MESO AND SMALL SCALE SURFACE RAINFALL STRUCTURES AND DEVELOPMENT OF RAIN NUCLEI

6.1 Meso-Small Scale Structures of Ground Precipitation

From the analysis of hourly rainfall we see that at the interval of 0200-0800 hr of April 5 rainbands were largely in front of the trough, at the rear of the cold front and in the NW of the cyclone, producing an inhomogeneous rainfall patterns, showing a few 20-50-km-width domains with 1-3 mm/h intensities.

Analysis of the hourly rainfall and radar PPI tracings indicates three belts of rain cores at varying intensity, denoted by A, B and C, moved from SE to NE at the rate, on average, 15 km/10 min, with B and C disappearing earlier than A, the last following a SSE – NNW path (at 170 degrees from the due north) towards Zhengzhou.(Fig.Omit)

6.2 "Seeder-Feeder" mechanism and Development of Rain Core

To examine the mechanism for clouds and rainfall development under the favorable wetly thermal and dynamic conditions we made use of the Zhengzhou 714CD radar to trace the movement of rain nucleus A on a horizontal and vertical basis. Fig.6 gives scanned vertical cross sections and core A-related hourly rainfall at the observing points in the SSE – NNW direction at 0400-0700 hr on April 5.

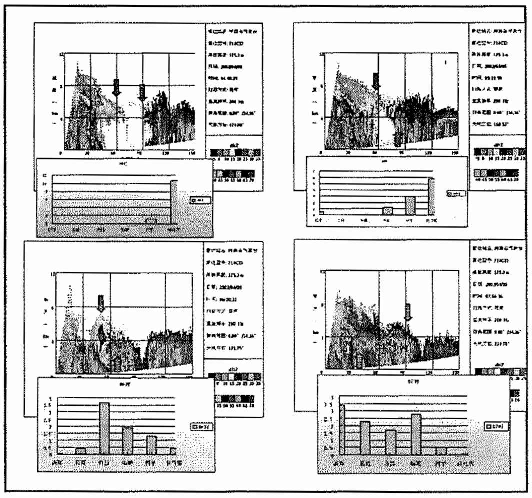

Fig.5. Radar-derived vertical sections and hourly precipitation from 0400- 0800 BT on April 5 in the direction Core A moved.

Fig.5 clearly reveals the unevenly-distributed cloud structure with a few 5-10 km width column-like echoes from the convective cells and part of the clouds were locally composed of two layers, the upper (lower) layer being 6-8 (~4) km in depth, with (ice-phase) particles dropping locally into rich-abundant zones, where they developed into rain, producing more rainfall.

The vertical profile of echoes intensity at 0400-0800 hr April 5, indicating increased rain formation mainly below 3000 m level. Comparison radar soundings indicates that the lower-layer clouds of rich vapor was fairly consistent with the medium-scale potential instability zones on space and temporal basis.

A careful examination of the echoes cross sections shows that from the upper layer of mixed ice and water the ice-phase particles due to seeding fell steadily as seen from a greater to a short distance. Whenever apparent "particles descent" happened at a preceding time interval we notice markedly intensified echoes there at the following time, with a cloud mass or nucleus seen at ground in the right place and a later time. This suggests that the "seeder – feeder" mechanism is the predominant physics for rainfall increase. Also, we see that in the lower clouds of equally rich vapor did not produce considerable precipitation because of no seeding done in the clouds above. Likewise, even with catalysis in the upper layer, the lower cloud, if provided with less water or dry by evaporation, will not generate noticeable rainfall. As a result, to fix on a right interval of time and space with plentiful water available in the lower clouds and determine the presence of possible meso instability-caused dynamic effect represents a necessary condition for artificial rain increase.

6.3 Microphysical Features of Surface Rain Nucleus

To further investigate the microphysical characteristics of local higher rainfall caused by the "seeder – feeder" mechanics, focus was on the analysis of rain nucleus A giving the raindrop size distribution in its northward movement across stations of Xiping, Linying and Xingzheng, indicating that the number density of raindrops was, on average, 10^2 drops/m3, mean water content was 10^{-2} g/m^3, the radar reflectivity is 10^2 mm^6/m^3.

7. NUMERICAL SIMULATION OF MICROPHYSICAL STRUCTURES AND MECHANISM FOR RAIN INCREASE

A stratiform cloud model containing detailed microphysics was adopted to simulate the cloud structure and mechanism for the genesis and development of rainfall in 0500-0800 BT, April 5 at Zhengzhou. Fig.6. presents the vertical distribution of the water content of particles of different kinds

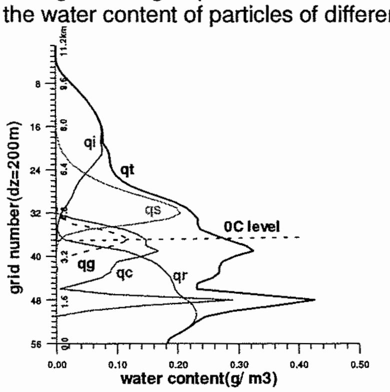

Fig.6 Vertical distribution of particles of all kinds in the clouds.(040505)

Fig.6 portrays the vertical distribution, in a level-descending order, of quantity of ice crystals (qi), snow (qs), graupel (qg) and rain water (qr) below 0^0C level in the seeded clouds, of which the top – mid levels were completely made up of ice-phase particles, the layer around 0^0C comprised mixed ice and water with liquid water below. Ice crystals and snow particles failed to reach the melting layer (warm sector) except graupels that came from ice crystals or snow in collision-coalescence with supercooled cloud water, contributing to the production of rainfall.

From the heights at which maximal water contents of all the kinds of particles are shown we see that ice crystals occurred at >4.8 km level, snow particles emerged at 4.4 km level with the maximum inside the cloud water genesis layer and so did graupels except at 4.3 km level; cloud water emerged dominantly around 3.8 and 1.6 km levels where vapor condensation happened most strongly; rain water was produced largely below 0^0C level, having two maxima, one at 3.4 km height (where rain water maximum was bigger compared to that of high-level cloud water content, maybe in relation to ice-phase particles melting) and the other at 1.6 km level a height that was completely consistent with that at which the low-level maximum cloud water genesis occurred, implying that the rain water at this level had its origin from condensation and collision-coalescence in the warming cloud process.

For"Seeder – Feeder" Mechanism for Rainfall Increaset, simulations indicate that ice crystals were the initiators of rainfall originating from cold cloud, and about 53% of them changed to precipitation-related snow particles, of which, in turn, 90% passed into graupels. Cold cloud rainwater came mainly from melted graupels.

8. CONCLUDING REMARKS

(1). The clouds of the two systems were made up of two layers. The cloud top was at 6-8 km levels with its brightness temperatures of –25~- --40^0C. The 0^0C level was at, on average, 4000 m over surface; the cloud systems combined with forms are given as As (Ac), Sc and Fn.. Mean effective particle radii in the cold-front clouds ranged over 6-8 μm, growing by 1-2 μm after the cyclone clouds were organized.

(2).Rainfall from the cold front and cyclone clouds occurred mainly between the trough and front and in the northwest of the cyclone, the rainbands moving NE with the clouds and the precipitation was distributed unevenly with multiple rain cores embedded therein, 15-50 km wide at 1-3 mm/h, steered by the 3000m winds aloft, and the rainbands were enlarged, when displacing from south to north at the rate, on average, of 15 km/10 min. The mean number density of raindrops was 10^2 drops/m^3; averaged water content of the drops was 10^2 g/m^3.

(3).In the large-scale cold front and cyclone clouds heterogeneous meso- and small scale moistly thermal and dynamic structures were embedded, displayed as a large-scale "cushion" at lower levels, with frequent meso "cold surge" at midlevels and related potential instability zones there, which acted as dynamic condition for vapor transport at lower levels and also as a good environment for "seeder – feeder" mechanism on the space (time) scales of 50-100 km width (3-4 hr).

(4).Precipitation from the clouds was initiated mainly through the clouds cooling. The higher levels comprised ice-phase particles; mixture of ice and water existed around the 0^0C level, with ice crystals generated at >4.8 km level.

(5).The meso- and small scale moistly thermal and dynamic conditions favorable for the rainfall "seeder--feeder" mechanism, the number concentration of ice crystals and contents of vapor and supercooled cloud water were in a good enough combination to constitute the meso microphysical environment for implementing artificial seeding.

ACKNOWLEDGEMENT.

The authors are indebted to Profs. Zheng Guoguang, You Laiguang and Hu Zhijin for their supervision and to the staff of the Henan Experimental Base and also to the team colleagues for their making sounding and compiling data.

REFERENCES

Hobbs, P. V., 1978: Organization and structure of clouds and precipitation on the mesoscale and microscale in cyclone storms, Rev. Geophys. Space Phys., 16, 714-755.

House, R. V. Jr. and P. V. Hobbs, 1982: Organization and structure of precipitating cloud systems, Adv. Geophys., 24, 225-315.

Hu Zhijin and Yan Caifan, 1987: Numerical simulation of microphysics in stratiform clouds. II. Microphysics in Midlatitude Cyclone Clouds, Collection of Papers published by the Chinese Academy of Meteorological Sciences, pp. 133-142 (in Chinese).

Liu Yubao and You Laiguang, 1998: Mesoscale structures of potentials and natural environment of wintertime artificial rain increase of northern Xinjiang, J. Appl. Meteor., 13,31 (in Chinese).

Rurledge, S. A. and P. V. Hobbs, 1983: The mesoscale and microscale structure and organization of clouds and precipitation in midlatitude cyclones. VIII. A model for the "seeder-feeder" process in warm frontal rainbands, J. Atmos. Sci., 40, 1185-1206.

Xu Zixiu and Wang Pengyun, 1989: Medium-scale rainband features in front of cold front clouds with the mechanism study, Acta Meteor. Sinica, pp.198-206 (in Chinese).

You Laiguang, Ma Peimin and Hu Zhijin, 2002: Experimental study on artificial rainfall from strtiform clouds in Beijing, in Meteorological Sci. and Tech. 30 (suppl. issue), 19-56, China Meteorological Press, Beijing (in Chinese).

PROMINENT FEATURES OF THE GRAVITY WAVES GENERATED BY TROPICAL CONVECTION DETECTED BY VHF DOPPLER RADAR: A CASE STUDY.

S. Abhilash[1] and K. Mohankumar[1]

[1]Department of Atmospheric Sciences, Cochin University of Science and Technology, India

1. INTRODUCTION

Vertically propagating gravity waves are known to have a profound effect on the structure and circulation of the atmosphere. One of the important issues on gravity waves is the energy sources and generation mechanisms. Deep convection has also been recognized as a source of gravity waves [Gosard and Hooke 1975]. The forcing mechanisms responsible for generating vertically propagating waves in convective clouds are not well understood. *Fovell et al.,* [1992] demonstrated the mechanical oscillator effect, oscillating updrafts and downdrafts impinging on the tropopause, as a mechanism for generating high frequency waves in Multicell storms. Convective turrets penetrating into an overlying shear layer can also excite waves in a process analogous to orographic forcing. Wave excitation by a transient or steady heat source in a stratified atmosphere is another forcing mechanism [Pandya et al. 1993: Lin and Smith 1986], and certain aspects of this problem can be described via simple analytical models. Understanding the wave forcing mechanisms active in convection, as well as the properties of the storm and atmosphere that control the wave characteristics, are crucial steps toward developing a parameterization of their global effects on the middle atmosphere.

The intermittent nature of the convection in both space and time makes observational studies challenging. Recently advanced MST radars (VHF/UHF clear air Doppler radars) provide wind velocities with fine time and height resolutions, which enable us to investigate detailed structures of small-scale gravity waves in a wide range of frequency and vertical wave number spectra. With the aid of the MST Radars, several kinds of gravity waves were detected and the relation to synoptic-scale atmospherics phenomenon was discussed in some studies. Recent observations using VHF radar and aircraft measurements have shown some evidence of clouds coupled with deep convection resulting in the generation of gravity waves [Fritts and Nastrom, 1992; Sato, 1993; Dhaka et al. 2001].

Corresponding author's address: S. Abhilash, Department of Atmospheric Sciences, Cochin University of Science and Technology, Finearts Avennue, Cochin –682016, Kerala, India.
E-mail:abhimet@cusat.ac.in

Case studies results of the MST radar observations from several sites around the world show enhanced gravity wave activity during convective events [Roettger. 1980, Sato, 1993]. With the aid of the MST Radars, several kinds of gravity waves were detected and the relation to synoptic-scale atmospheric phenomenon was discussed in some studies.

2. OBSERVATIONS AND DATA DESCRIPTION

As part of Convection campaign, VHF radar observations were made at Gadanki (13.5^{0}N, 79.2^{0}E) during 20-29 June 2000 and 10-20 October 2002 to investigate the behavior of vertical wind disturbances during the convection event and its associated energetic. The period of observation was after the onset of South West monsoon and highly convective over the radar site. During the period, radar made observations only with vertical beams, since the buoyancy waves are much more evident in the vertical wind component. The data provide information from heights of 3.6 km above the ground in the vertical direction at a resolution of 150 m. The standard height resolution of the radar is 150 m, but during 20-29 June 2000 only height resolution of 300 m could be obtained due to some technical problem in the radar system. The details of the Indian MST radar system have been given by *Rao et al.,* [1995].

Some results obtained by the preliminary analysis of the data have already been reported by *Dhaka et al.,* [2001]. The continuous observations for a period of 6 hours starting from 19:00–01:00 hrs LT during 21-22 June 2000 and 20:30-00:30 hrs LT during 17-18 October 2002 have been used for the present study.

3. SYNOPTIC OVERVIEW.

Figure 1.a showing the synoptic chart of geopotential height at 12UTC on 1000 hPa level from NCEP/NCAR reanalysis data. On both the days a trough is observed in the contour height at 1000 hPa near the radar site. Figure 1.b shows the precipitation rate at 12UTC from TRMM satellites. The precipitation rates were high near the radar site. Both the conditions clearly showing that the period of observations were highly convective near the radar site.

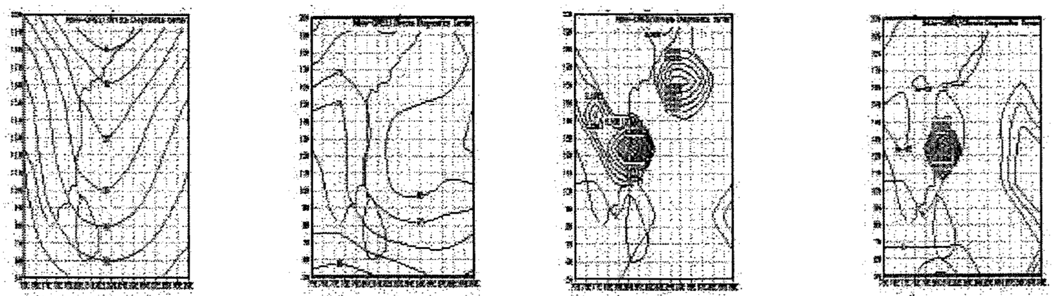

21st Jun 2000 (a) 17th Oct 2002 21st Jun 2000 (b) 17th Oct 2002

FIG. 1. (a) Synoptic chart of Geopotential height in gpm and (b) TRMM rain rate in kg/m^2/s at 12 UTC on 21st Jun 2000 and 17th Oct 2002.

4. RESULTS

4.1 Observed features

Figure 2 presents the details of the radar observation during the convection experiment. Figure 2.a shows the time-height plot of Signal to Noise Ratio (SNR) for vertical beam. Figure 2.b and 2.c showing the Doppler width and intensity of vertical wind observed. The high values of SNR, Doppler width and vertical velocity in the middle troposphere were lasts for a period of 2 hours after the commencement of the observation. The coherence of the high value of SNR and Doppler width is possibly due to the effect of turbulence associated with convection during both the days. A layered structure of enhanced SNR is also noticeable at a height of about 16-17 km, which corresponds to the thermal tropopause altitude derived from Radiosondes measurements at a nearby station Chennai (13.5^{0}N, 80.2^{0}E). This type of layered structure of SNR near the tropopause was also reported by *K. Sato,* [1993]. The small discontinuity of the high value of SNR near 16 km at about 21:30 hrs on 21 Jun 2000 and at 22:30 hrs on 17 Oct 2002 clearly showing the evidence of tropopause weakening. The reappearance of the tropopause after convection at a higher altitude at 18km on 17 Oct 2002 is also noticeable

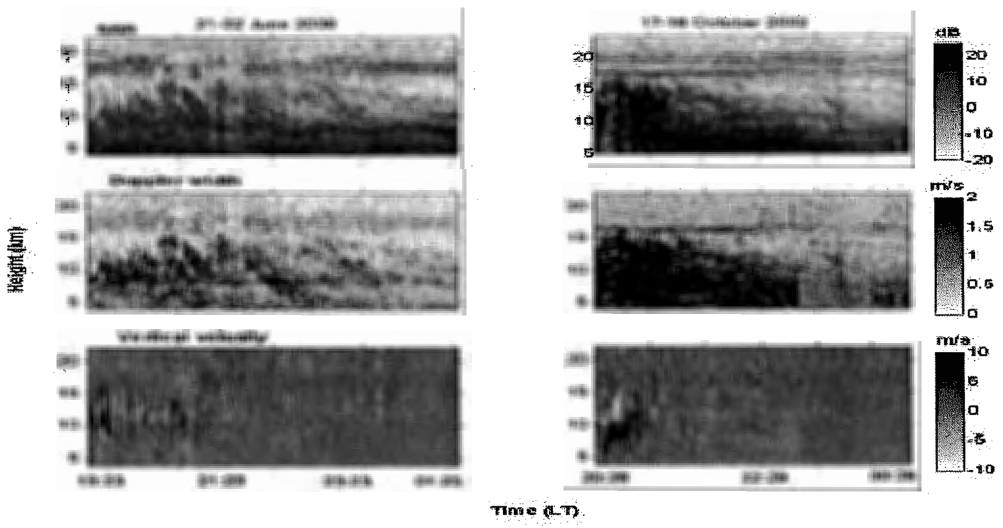

FIG. 2. Time- Height variation of (a) Signal to Noise ratio (SNR) in dB, (b) Doppler width in (m/s) and (c) Vertical Velocity in (m/s) on 21-22 Jun 2000 and 17-18 Oct 2002.

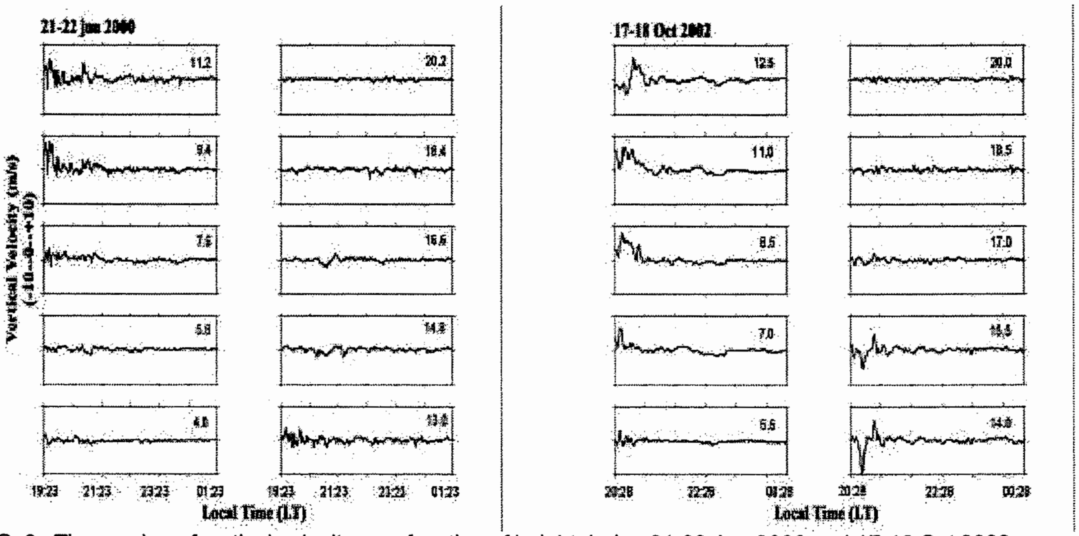

FIG. 3. Time-series of vertical velocity as a function of height during 21-22 Jun 2000 and 17-18 Oct 2002

4.2 Time-series of vertical wind disturbances.

Figure 3 showing the time series of vertical wind observed at different height regions. To remove small-scale wind perturbations having vertical wavelength below 1km, the averaged vertical wind components have been used to produce the wind fields at 900m intervals. To smooth the profile, a three-point running mean is also applied on the time scale.

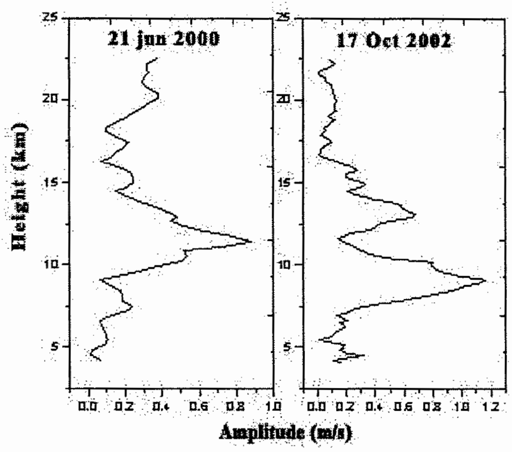

Figure. 4. Amplitude- Height profile of the Vertical velocity obtained from Fourier analysis.

The vertical velocity fluctuate between +8 to –6 m/s only in the height range of 9.3 to 14.7 Km and +3 to – 3 m/s over rest of the troposphere and lower stratosphere for a period of nearly 2 hours on both the days during convection active periods. Rest of the time the vertical winds fluctuate between +2 to –2 m/s in the troposphere and lower stratosphere. These large fluctuations are confined in the middle and upper troposphere during convection active period. These enhanced fluctuations are typically quasi-sinusoidal in nature. Sato et al., 1993 also reported these types of wind fluctuations over Platteville radar site during thunderstorm active periods. The amplitude height profiles in figure 4 shows that the peak amplitude occurs at a height level of 11.5 km on 21 June 2000 and at 9 km on 17 October 2002. A secondary peak is also noticeable at about 20 km on 21 June 2000 and at 14 km on 17 October 2002.

4.3 Frequency-domain analysis

Fourier analysis has been performed on vertical velocity time series data. The perturbations of the respective winds are estimated by subtracting the mean value from each instantaneous value. The power spectrum is obtained at each range bin. Multi-height normalized power against harmonic number in the height region of 18-22 km is shown in the figure 5. From this figure, the dominant wave periods can be easily noticed. Thus, these plots give an overall view of the power spectra in the lower stratosphere.

To identify the dominant time period and characteristics of the wave uniquely, the Power spectrum of the vertical wind perturbations at two levels (14.1 km and 21.0 km) is shown in the figure 6. From this figure it can be noted that the wave having time period 20-25 min and 10-12 min is dominant. It has been noticed that this wave period is dominant in the UT/LS region.

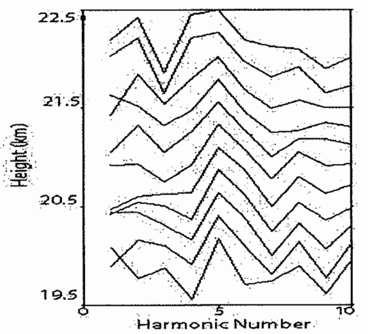

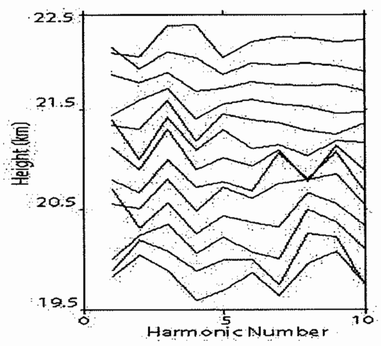

FIG. 5. Multi height normalized power against Harmonic number on (a) 21st Jun 2000 and (b) 17th Oct 2002.

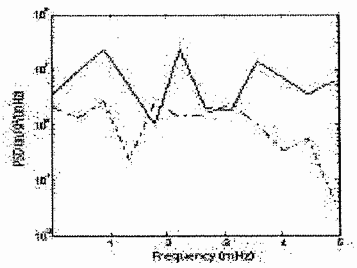

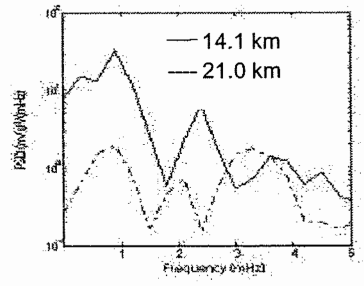

FIG. 6. Power Spectral Density at 14.1 km and 21.0 km during (a) 21-22 Jun 2000 and (b) 17-18 Oct 2002.

5. CONCLUDING REMARKS

Several characteristics of small-scale wind disturbances having periods of several minutes associated with the tropical convection have been revealed here through the detailed analysis of the observation using Indian MST Radar. Dominant time period of the waves observed were 24-28 and 10-15 minutes. Vertical coherence of the spectrum is seen in the UT/LS region. Tropopause weakening is also observed and is possibly due to penetrating convection and gravity waves excited in association with deep convection. The spectral power is more in the upper tropospheric region, which is in agreement with the amplitude peaks near upper troposphere. The gravity waves in the UT/LS region are associated with wind disturbances in the middle and upper troposphere.

Acknowledgments: The Authors would like to thank Dr. D. N. Rao, Director, National MST Radar Facility for providing the data. Financial assistance from SVU-UGC Centre, Tirupati. One of the authors, S. Abhilash, is thankful to CSIR (Council of Scientific and Industrial Research) for Junior Research Fellowship.

References:

Dhaka, S. K., P. K. Devrajan, Y. Shibagaki, R. K. Choudhary and S. Fukao, 2001: Indian MST Radar observations of gravity wave activities associated with tropical convection, *J. Atmos. Solar-Terr. Phys.*, **63**, 1631-1642.

Fovell, R. G., D. Durran, and J. R. Holton, 1992: Numerical simulations of convectively generated gravity stratospheric gravity waves. *J. Atmos. Sci.*, **49**, 1427-1442.

Fritts, D.C., and G. D. Nastrom, 1992: Sources of Mesoscale variability of gravity waves. Part II Frontal, convective, and jet stream excitation. *J. Atmos. Sci.*, **49**, 111-127.

Gossard, E. E., and W. H. Hooke., 1975: waves in the Atmosphere. *Elsevier.*, 456 pp.

Lin, Y. L., and R. B. Smith, 1986: Transient dynamics of airflow near a local heat source. *J. Atmos. Sci.*, **43**, 40-49.

Pandya, R., D. Durran, and C. Bretherton, 1993: comments on Thermally forced gravity waves in an atmosphere at rest. *J. Atmos. Sci.*, **50**, 4097-4101.

Rao, P. B., Jain, A. R, Kishore, P, Balamuralidhar, P, Damle, S. H, Vishwanathan, G, 1995: Indian MST rara, 1, System description and sample vector wind measurement in ST mode. *Radio Science*, **30**, 1125-1138.

Roettger, J., 1980: Structure and dynamics of the stratosphere and mesosphere revealed by VHF radar investigations. *Pure. Appl. Geophys.*, **118**, 496-527.

Sato, K., 1993: small-scale wind disturbances observed by MU radar during the passage of Typhoon Kelly. *J. Atmos. Sci.*, **50**, 518-537.

IMPACT OF HORIZONTAL MODEL RESOLUTION ON CLOUD PARAMETERS FORECASTED BY A NON-HYDROSTATIC MESOSCALE MODEL

F. Ament[1], S. Crewell[2] and C. Simmer[1]

[1]Meteorological Institute, University of Bonn, Germany
[2]Meteorological Institute, University of Munich, Germany

1. INTRODUCTION

The scale of macroscopic cloud processes like stratus clouds or deep convection is in the order of a few kilometers. If the horizontal grid spacing of operational mesoscale weather prediction models is refined to these scales, it is expect that these phenomena can at least partly be resolved explicitly resulting in improved forecasts of cloud related quantities by avoiding uncertainties which are inherent to any parameterization.
To investigate the effect of horizontal refinement on prediction of cloud parameters we have performed integrations using the operational non-hydrostatic mesoscale model Lokal-Modell (LM) of the German weather service with grid spacings of 7km down to 1km. Since high resolution simulations require high computational costs, we were restricted to concentrate on case studies. In the following, the results of six case studies during observation periods of the Cloud Liquid Water Network (CLIWA-NET) project (Crewell, 2002) will be presented.

2. MODEL DESCRIPTION AND EXPERIMENTAL DESIGN

The LM is a fully compressible non-hydrostatic model which is currently operated with a horizontal resolution of 7km. The time integration is implicit in the vertical direction and split-explicit in horizontal directions following the concept of Klemp and Wilhemson (1978).

The model has a generalized terrain-following vertical coordinate, which divides the model atmosphere into 35 layers from the earth's surface up to 20hPa height. The vertical resolution is highest close to the surface with less than 50m vertical grid spacing and increases with altitude. Prognostic model variables are the wind vector, temperature, pressure perturbation, specific humidity, and cloud water of grid scale clouds. Precipitative fluxes of rain and snow become diagnostic quantities by assuming steady state conditions within each atmospheric column.

Grid-scale condensation is parameterized according to the concept of saturation adjustment: Water vapour exceeding saturation is converted into cloud water instantaneously and if a grid point becomes unsaturated, cloud water will be evaporated as long as cloud water is available or until saturation is reached.

The physical parameterization package is completed by a mass flux convection scheme (Tiedtke, 1989), a level-2.5 turbulence parameterization, a delta-2-stream radiation transfer scheme, and a 2-layer soil model. Initial and boundary values are provided by operational nudging LM-analysis of DWD. A detailed model description is given by Doms and Schaettler (1999).

In order to identify effects of horizontal refinements simulations with horizontal grid spacings of 7, 2.8 and 1.1km were performed. To maintain the same numerical accuracy the Courant number was kept constant resulting in decreasing time steps of 60, 25 and 10s respectively. It is essential to use the same model boundaries at all resolution because otherwise effects due to different boundary conditions might have the same magnitude as refinement effects. The target area of the CLIWA-NET campaigns differed and consequently two different model domains, POTSDAM and CABAUW which are centered over the respective measuring site were necessary (see Figure 1). Both domains cover an area of 440x440km^2 with very moderate orographic structures. The CABAUW domain is more maritime influenced since it comprises a significant part of open sea and costal regions.

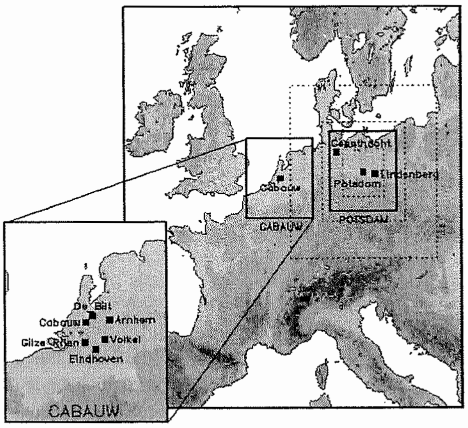

Figure1: Model domains „CABAUW" and „POTSDAM" with corresponding measuring stations.

Corresponding author's address: Felix Ament, Meteorological Institute, University of Bonn, Auf dem Huegel 20, 53121 Bonn, Germany; E-Mail: ament@uni-bonn.de .

Table 1: Fractional deviation of mean quantities (averaged over model domain and 24h) simulated at different resolutions relative to 7km run. Mean values of all six cases in bold letters, smallest (biggest) deviation indicated above (below). Convection scheme is always switched off.

	Integr. water vapour	Liquid water path	Precipi-tation	Total cloud cover	Grid scale cloud cover	Net surface radiation	Sensible heat flux	Latent heat flux
	1,00	1,10	1,26	0,98	0,96	0,95	0,92	0,97
2.8 km	**1,01**	**1,33**	**1,93**	**1,04**	**1,05**	**1,00**	**0,99**	**1,00**
	1,02	1,74	4,26	1,10	1,16	1,05	1,08	1,02
	1,00	1,03	1,36	0,96	0,89	0,94	0,88	0,96
1.1 km	**1,01**	**1,54**	**2,25**	**1,01**	**1,02**	**0,99**	**0,97**	**0,99**
	1,02	2,38	5,49	1,07	1,24	1,09	1,07	1,02

3. RESULTS

3.1 Spatial and temporal averaged quantities

A perfect model will add small scale features without changing the coarse scale structure, if grid spacing is reduced. Consequently area averaged quantities are expected to be insensitivity to changes in resolution. Table 1 summarizes the deviation of averaged quantities observed by simulation without convection parameterization with reference to the 7km run. The integrated water vapour content (IWV), which is one of the key variables defining the probability of cloud formation, obeys this rule very well, since this quantity is mostly determined by large scale advection. In contrast, liquid water path (LWP) and precipitation have significant trends; these quantities increase as grid spacing is reduced. Surprisingly, parameterized as well as resolved cloud cover seems to be consistent in terms of mean values. As a consequence hardly any deviations in the net surface radiation occur, because cloud cover is the most relevant parameter modifying radiative fluxes. Since not only the energy input but also the boundary layer stability remains unchanged, the surface energy budget is not affected by the refinement.

The increase in cloud water can be mostly attributed to the lack of a subgrid condensation scheme. Due to humidity fluctuations saturated areas connected with positive cloud water content may occur within a box, which is on average unsaturated. Since cloud water content is a positive definite quantity, this type of sampling error will result in a systematic underestimation of cloud water content at coarse scales. Derived from the three case studies at the "Cabauw" area, an increase of cloud water content due to resolved water vapour fluctuations in the order of 25% at the 2.8km scale and of 80% at the 1.1km can be expected. Since more cloud water will directly increase precipitation, the observed trend is even stronger here.

It is expected that simulations at 1km horizontal scale can resolve at least deep convection and that therefore a parameterization of convection becomes superfluous or less important. Therefore it is of great interest to compare simulations with and without parameterized convection. As far as mean quantities are considered, IWV, cloud cover and net surface radiation show no sensitivity, small differences occur in sensible and heat flux and significant discrepancies can be observed with respect to LWP and precipitation, as depicted by figure 2. The Tiedtke convection scheme implemented into LM assumes stationarity neglecting all storage terms. Over saturation is directly converted into rain without producing cloud water. Consequently LWP values of simulations with parameterized convection are dramatically reduced. The results concerning precipitation give no clear picture.

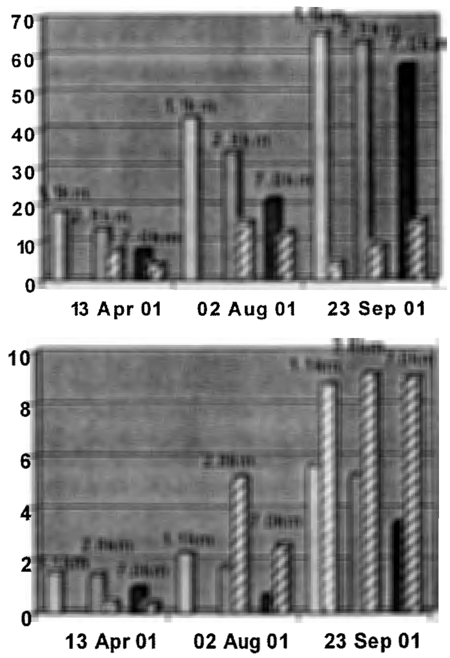

Figure 2: Daily mean values averaged over model domain for all "Cabauw" cases. Solid bars as result of runs without parameterized convection, dashed ones including the Tiedtke convection scheme. Top: LWP [g/m²], Bottom: Amount of rain [mm]

Nevertheless, relying more on the stronger precipitating cases one might assume, that explicitly resolved convection produces less rain but the differences become smaller as the resolution is increased. The remaining gap may be traced back to the lack of subgrid scale condensation at scales smaller than 1km.

3.2 Vertical profiles and fluxes

The most important effect of convection modifying the atmospheric development on longer time ranges is the stabilization due to vertical transport. This transport differs between resolved and parameterized convection. Humidity deviations in the order of 10% appear and differences of potential temperature with the magnitude of 1K can be observed. It is worthwhile to note, that simulations at different resolutions with explicit convection are in much closer agreement than compared to the simulation with parameterized convection.

As already indicated by the analysis of averaged values, less water vapour is converted into rain by simulations without parameterized convection and consequently less latent heat is released in the free atmosphere. This is the main reason, why explicit convection is less efficient in transporting energy from the boundary layer to the free atmosphere.

3.3 Cloud structure

Concerning cloud structures, the size of resolved convective cells seems to shrink systematically as the grid spacing was reduced. The development of an objective cell detection algorithm, which uses certain LWP thresholds to identify pixels in the surrounding of local LWP maxima as part of a convective cell (see Figure 3 as an example), allows quantifying this effect. Normalized cell size distributions plotted in Figure 4 clearly indicate that the size of cells remains nearly constant in number of grid points but not in physicals units. One reason is that the turbulence scheme is based on the boundary layer approximation, which assumes no horizontal exchange. This approximation is well justified as long as the horizontal grid spacing is large compared to the boundary layer height. The lack of horizontal exchange allows the development of

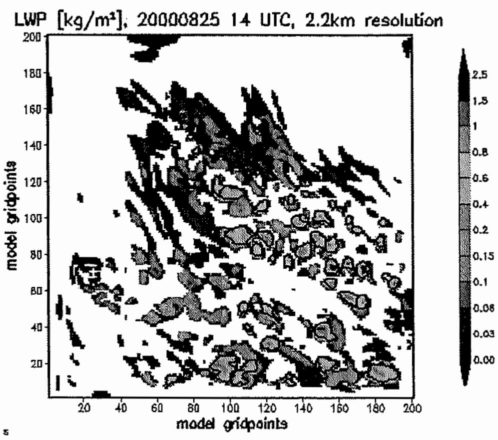

Figure 3: Example of LWP field at one time step. Detected cells are encircled by thick black lines.

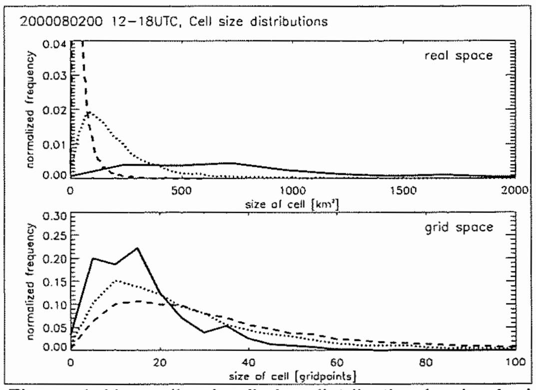

Figure 4: Normalized cell size distribution in physical units (top) and in number of grid points (bottom).7km (solid), 2.8km (dashed), 1.1km (dotted). Convection scheme always switched off.

locally confined convective updrafts at the pixel scale. The only type of horizontal diffusion implemented into the LM is a computational mixing to numerically stabilize the leap-frog integration scheme. A sensitivity study varying the strength of computational mixing proved the dependence between cell size distribution and horizontal diffusion

3.4 Comparison with ground based observations

Figure 5 shows time series with high temporal resolution measured as well as simulated at the CLIWA-NET station Potsdam. In order to compensate the different spatial scales of model and observation, the measurements are filtered with the advective time scale corresponding to each resolution. It is obvious, that simulations with higher horizontal resolution do not predict cloud conditions at a certain time and space more accurately, but the statistical representation of cloud conditions are improved, e.g. as far as intermittence is concerned.

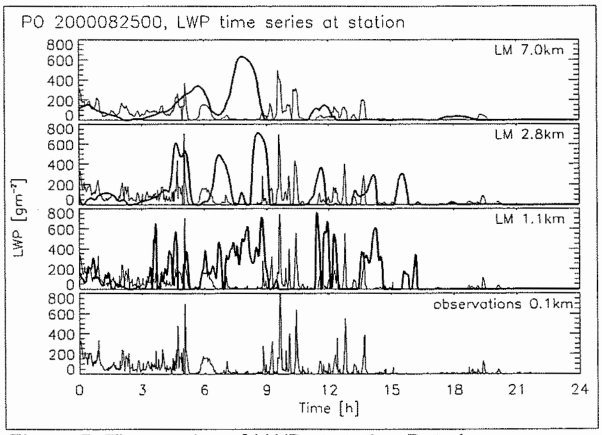

Figure 5: Time series of LWP at station Potsdam. Microwave radiometer measurements (black lines) are filtered with the advective timescale to be representative for each model resolution.

4. CONCLUSIONS

Undergoing a horizontal refinement the nonhydrostatic, mesoscale model LM is consistent in terms of mean IWV, mean cloud cover and averaged surface fluxes. The systematic trends in LWP and rain rate, which occur in simulations without convection scheme, are mainly caused by neglecting subgrid scale variability of water vapour and cloud water. This is an indication that sub-grid scale condensation schemes are required even at horizontal scales of a few kilometers. A comparison between simulations with parameterized and with explicit convection revealed differences concerning the vertical stratification and vertical transport. One important reason is the less efficient conversion of water vapour into rain if the convection scheme is switched off. It is observed that the size convective cells shrinks as the grid spacing is reduced and that no real convergence can be detected at scales larger than 1km. This effect can partly be counteracted by introducing a physical motivated horizontal diffusion. A comparison of time series with high temporal resolution at CLIWA-NET stations showed that the benefit of high resolution modelling can not be expected to be a more accurate deterministic forecast of cloud conditions at a particular time and place but to provide a better characterization of the statistical properties of cloud conditions.

References:

Crewell, S., M. Drusch, E. van Meijgaard and A. van Lammeren, 2002: Cloud observations and Modeling within the European BALTEX Cloud Liquid Water Network, Boreal Environment Research, 7, 235-245

Doms, G. and U. Schaettler, 1999: The Nonhydrostatic Limited-Area Model LM (Lokal-Modell) of DWD, Part 1: Scientific Documentation, (available from http://www.cosmo-model.org)

Tiedtke, M., 1989: A comprehensive mass flux scheme for cumulus parameterization in large-scale models, Mon. Wea. Rev., 117: 1779-1799

RIMING AND OTHER CHARACTERISTICS OF COLUMNS AND ROSETTES OBSERVED IN WAVE CLOUDS

Brad Baker and R. Paul Lawson

SPEC Incorporated, Boulder, CO 80301 USA

1. INTRODUCTION

Wave clouds vary from very smooth and simple to very complex and jumbled. SPEC's Lear jet has collected enough in-situ observations of wave clouds that are sufficiently well structured that basic cloud microphysical processes can be studied. Cloud Particle Imager (CPI) data is used and of such quality that ice crystal habit can be determined for particles larger than 30 μm and individual rime particles can be observed. In this study the basic processes of riming and side-plane growth are examined.

Our results for the onset of riming of columns are consistent with previous results (Ono 1969), while our results for other column characteristics differ from Ono's previous results. Results for the onset of riming of rosette crystals are also presented. Rosettes can be a dominant crystal type in wave and cirrus clouds. No results on threshold sizes for riming of rosettes have previously been reported in the literature.

Observations of side-plane on the wave cloud particles are consistent with the hypothesis that side-plane growth initiates with a rime particle. That is, side-plane was observed only on particles larger than the threshold size for riming.

2. METHODS

The CPI takes high-resolution (2.3 μm) images of cloud particles. Images from wave clouds were manually processed to determine crystal habit and degree of riming and/or side plane growth. **Figure 1** shows examples of columns and rosettes that have various amounts of rime and/or side plane. The data were then analyzed to determine threshold sizes for the occurrence of riming and side plane. Using software written specifically for CPI data, particle length, width and area were automatically calculated. Length is defined as the maximum cord while width is defined as the maximum cord perpendicular to the length cord. For columns, these result in a close approximation to a rectangle's usual length and width. Although other crystal habits (particularly irregular crystals) were present, only results for columns and rosettes are presented.

Corresponding authors address: Brad Baker, SPEC inc., 3022 Sterling Circle, suite 200, Boulder CO 80301, USA; E-Mail: brad@specinc.com

3. WAVE CLOUD STRUCTURE

Wave clouds can be ideal for this type of 'natural laboratory' study because the cloud sits fixed in space while air flows through it first gradually upwards, where condensation of water occurs, and then gradually downwards, where evaporation occurs. The cloud can remain for some time in a somewhat steady state situation. The microphysics of droplet nucleation and growth by condensation and then ice nucleation and growth by vapor deposition and riming progresses in time for a Lagrangian parcel but only in space from a Euclidian point of view. Ideally one therefore has time to map out the cloud with aircraft penetrations, make repeat observations of the same process at the same stage, and follow Lagrangian parcels by following streamlines. Even the effects of the aircraft on the cloud, such as aircraft produced ice particles (Rangno and Hobbs 1983), can be avoided by waiting for new air to flow through the cloud.

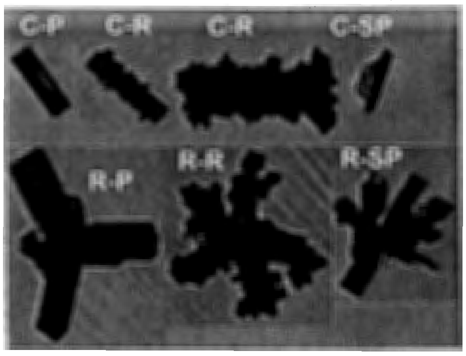

Figure 1: Examples of CPI images used in this study. Each has an accompanying 2-part crystal type designator. The first part, a **C** or **R** designates column or rosette respectively. The second part **P**, **R**, or **SP** designates pristine, rimed, or with side plane respectively.

Two main factors complicate the ideal picture described above. First, it is difficult for an aircraft to follow actual streamlines and thus measurements generally cut across streamlines and observations are not of a Lagrangian parcel. Second, wave clouds often have significantly more internal structure than expected by the above discussion. Clouds are like the ice crystals that make them up. While they can be classified into broad groups, no two are exactly alike.

Figure 2 consists of cloud photographs with the point of showing the variability that exists in the class called wave clouds. The clouds formed over mountains and the basic scenario described above exists. However, one picture shows a simple uniform looking wave cloud while the others show the variability that can exist in the vertical and both horizontal directions.

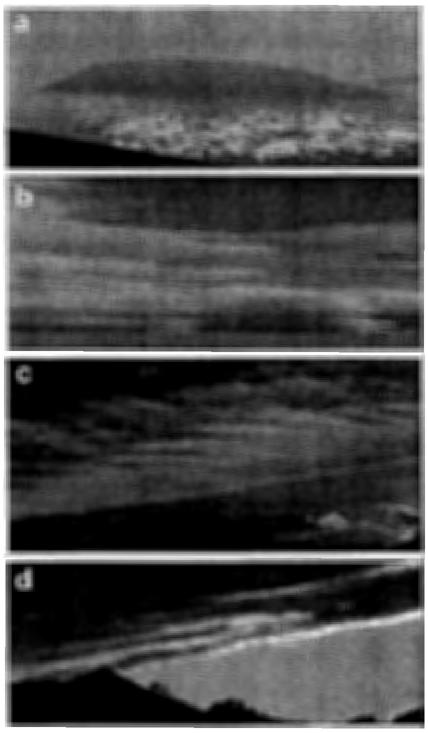

Figure 2: Pictures of mountain induced wave clouds that show the variability that can exist in all 3 spatial directions. a) & b) were taken from an aircraft over Utah. c) and d) were taken from the surface in Boulder CO. In d) scattering of light from the setting sun brings out the wavelike structure near the cloud's leading edge.

Time series of cloud properties reveal the same variety in wave clouds from smooth and simple, as shown for example in **Figure 3**, to very complex and jumbled as shown in **Figure 4.**

For a level penetration through a simple wave cloud the potential temperature should gradually decrease and then increase again while the condensed mass content would increase and then decrease gradually. This picture is close to what is seen in **Figure 3**.

Figure 4 in contrast reveals much more complex structure. There appears to be two waves with about 15 Km lengths. The first large wave seems to have an additional oscillation superimposed with about 1.2 km wavelength. The second large wave, which is primarily glaciated, also has large variations but with less regularity. The wind speed divided by the Brunt-Vaisala frequency, calculated from the sounding, yields a wavelength of about 15 Km in the clear air that may explain the large waves. However, the 1.2 km wavelength oscillation is not easy to explain. The same can be said for most of the variability exemplified in **Figure 2.** Only the vertical structure is easily understood.

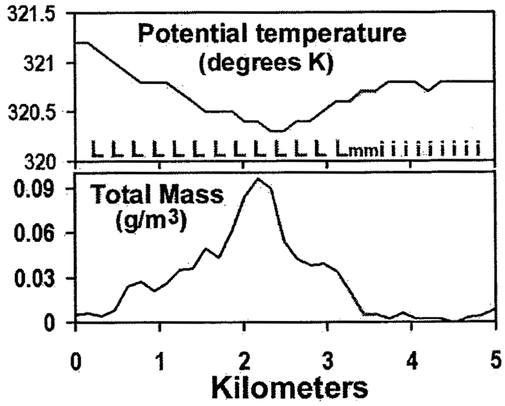

Figure 3: Potential temperature and total condensed mass content as a function of distance downwind of cloud leading edge for a particularly simple wave cloud. The letters L, m, and i designate regions of liquid, mixed, and ice phase cloud respectively. The mixed phase regions are also indicated using gray traces.

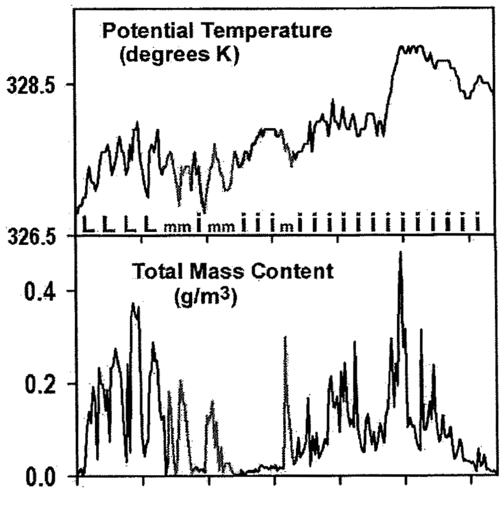

Figure 4: Potential temperature and total condensed mass content, as in Figure 3 above, for a particularly complex wave cloud.

The riming onset results presented below for columns are consistent with the previous results of Ono (1969). However, only data from certain mixed phase regions of cloud were used. If data from glaciated regions are included then the consistent results are lost. This suggests that ice columns can continue to grow in the glaciated region of cloud. Similarly, if mixed regions of the more jumbled clouds (like shown in **Figure 4**) are included, then the consistent results are again lost. This suggests that the jumbled mixed phase regions are too localized. It is possible that particles had grown larger than the threshold size for riming in regions without enough droplets for riming to occur and then fell into the localized mixed phase region where they were observed.

The glaciation characteristics of the wave clouds in this study are very similar to those reported by Heymsfield and Miloshevich (1993) that were attributed to homogeneous nucleation. However, our observations find these characteristics for a wider range of temperatures than Heymsfield and Miloshevich (1993) observed. It remains to be determined whether these additional observations are also consistent with the homogeneous nucleation hypothesis.

4. RESULTS FOR COLUMNS

Ono (1969) presented results on the onset of riming with size of columnar ice crystals in warm (tops –6 and –5 °C, observations at –2 °C) cumulus and stratocumulus clouds. Our results in wave clouds are similar. **Figure 5** shows a transition from pristine to rimed columns at widths between 56 and 81 µm, which is consistent with Ono's result of 50 and 90 µm. Also consistent with Ono's results is the finding that width is a better predictor of the onset of riming than length. Using length, the transition zone is much larger; 117 to 312 µm. Width is also a better predictor of riming onset than particle area (**Fig. 6**). Area however, is better than Length. Using the square root of area, the transition occurs between 73 and 133 µm.

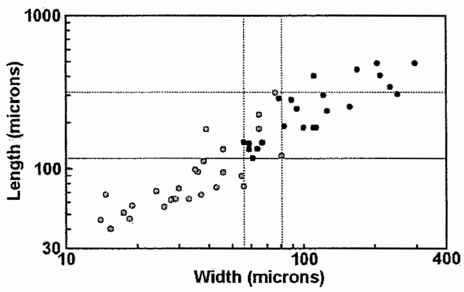

Figure 5: Scatter plot of Length versus width with pristine columns as shaded circles and crystals that are rimed as solid disks.

The physical process of riming should not be very different in wave clouds than in cumulus and stratocumulus and no difference is found in this study. However some other aspects of Ono's results in cumulus and stratocumulus do differ from our results in wave clouds. For example, Ono claims that for warm and cold (-32 °C stratus) columns both axes continue to grow until the minor axis (width in this study) reaches about 90 µm after which growth is confined to the major axis. Also the aspect ratios (length/width) of his columns vary considerably. In **Figure 5** the aspect ratios of the crystals are scattered around 2. This difference from Ono's results

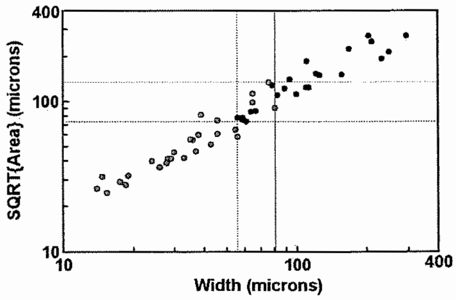

Figure 6: Scatter plot of the square root of particle area versus width with pristine crystals as shaded circles and crystals that are rimed as solid disks.

is emphasized further in **Figure 7,** which shows all the pristine columns regardless of location in cloud instead of all the columns in only the mixed regions (**Fig. 5**). The aspect ratios are still scattered around a value of about 2, crystal widths exceed 90 µm, and show no sign of being limited at any value[1].

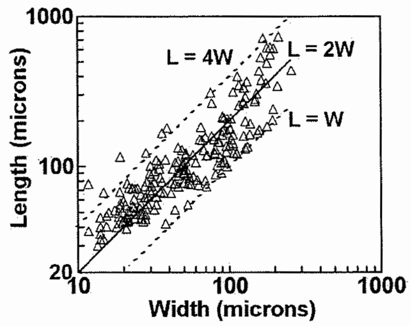

Figure 7: Scatter plot of column length versus column width for all the pristine columns. Dotted lines represent aspect ratios of 4 and 1 while the solid line represents an aspect ratio of 2.

[1] Some values in **Fig 7** are exaggerated by the automatic processing. For example, the column with width of 260 µm was grossly exaggerated by a glitch in the perimeter algorithm and should be 190 µm instead. This however is still much larger than 90 µm.

5. RESULTS FOR ROSETTES

Once the mixed phase regions appropriate for onset of riming studies was determined, using onset of riming results for columns as a litmus test and also cloud property time series (e.g. **Fig. 3 & 4**), results for the onset of riming of rosette type crystals were obtained.

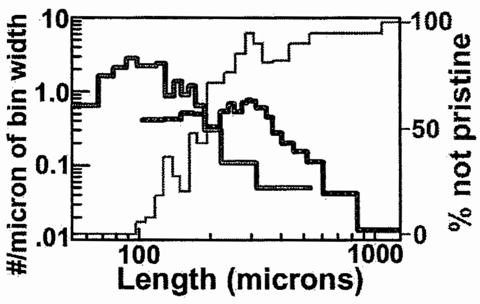

Figure 8: Relative particle size distributions using particle length for size. Pristine rosettes – thick gray, rosettes rimed and/or with side plane – thick gray with black dashes. Also percent rimed and/or with side plane – thin gray.

For rosettes there is also a size range for which riming begins. However of the three size parameters; length, width, and area, none stand out as the dominant controlling factor as width does for columns. This is understandable since the width of the arms is not represented by the width of the rosette and because rosettes do not orient themselves horizontally as falling columns do. Results for length are shown in **Figure 8** since length is the most common parameter used to describe cloud particles. The smallest rimed rosette is about 100 μm long and most rosettes are rimed by about 250 μm in length.

6. RESULTS FOR SIDE PLANE

For both columns and rosettes, side plane was observed either on crystals that were also rimed or if rime was not apparent, the particle was already larger than the threshold size for riming to occur. This result suggests that side plane is continued growth by vapor deposition on rime.

With regard to the crystallographic orientation of side plane growth, Ono (1969) reports, "From an examination of some 200 crystals we conclude that, almost without exception, droplets accreted on the prism faces between −15 and −20°C take the same orientation as the substrate." At the colder temperatures of these wave cloud observations there is either no apparent preferred crystallographic orientation of the side plane relative to the substrate's crystallographic orientation or there may even be a preferred orientation that is perpendicular to the substrate's orientation (**Fig. 1**). The ambiguity is due to the fact that it is difficult to determine full 3D information from 2D images even with high resolution. Random orientation might be explained by the greater fraction of the droplet that freezes upon initial contact with the substrate and also by the more rapid subsequent freezing of the remainder of the droplet.

7. CONCLUSIONS

Wave clouds are interesting in their own right (**Figs 2 – 4**) and because they can provide a natural laboratory for studying basic cloud physical processes. In the presence of sufficient supercooled drops, the onset of riming of columns is primarily controlled by the column width. Riming begins around 55 μm and most columns are rimed by about 80 μm in width, which is consistent with results of Ono (1969). In the absence of droplets sufficient for riming, columns in this study tended to continue growing pristinely in both length and width and maintained aspect ratios scattered around 2, which is contrary to Ono's results.

This is the first reported study of the riming threshold of Rosettes, which appears to begin at about 100 μm in length and most rosettes are rimed by about 250 μm.

Side plane seems to grow only after riming, presumably as vapor deposition on a rime drop. Growth occurs with either random crystallographic orientation or (conversely to Ono's findings) an orientation perpendicular to the substrate.

Acknowledgements

This work was funded by NSF Grant No. ATM-9904710. We extend a big thank you to the SPEC Lear jet personnel for collecting the data and to Beth Ferriter for manually classifying them.

References

Heymsfield, A. J., and L. M. Miloshevich, 1993: Homogeneous ice nucleation and supercooled liquid water in orographic wave clouds. *J. Atmos. Sci.,* **50,** 2335-2353.

Ono, A., 1969: The shape and riming properties of ice crystals in natural clouds. *J. Atmos. Sci.,* **26,** 138-147.

Rangno, A.L. and P.V. Hobbs, 1983: Production of ice particles in clouds due to aircraft penetrations. *J. Clim. Appl. Meteor.*, **22**, 214-237.

RADAR CHARACTERISTICS OF PRECIPITATING CLOUDS IN THE UNITED ARAB EMIRATES

D. Breed[1], R. Bruintjes[1], N. Rehak[1], A. Al Mangoosh[2], and A. Al Mandoos[2]

[1]National Center for Atmospheric Research, Boulder, Colorado, USA
[2]Department of Water Resources Studies, Office of H.H. the President, Abu Dhabi, UAE

1. INTRODUCTION

The United Arab Emirates (UAE) is located at the southeastern end of the Arabian or Persian Gulf (referred to here as simply the Gulf) on the Arabian Peninsula. The atmosphere in the UAE is generally very dry due to the dehydrating effect of upper-level subsidence and limited sources of upper-level moisture. This moisture comes almost exclusively from frontal systems in the winter and tropical monsoon systems in the summer. However, due to the latitude of the UAE, only the fringes of the frontal systems in the winter and the monsoon systems in the summer substantially affect the rainfall in the UAE.

Past climatological studies have identified the winter season as accounting for the bulk of rain in the UAE. These studies were based on reporting stations located primarily along the northern coast or in the Gulf. However, the fact that the monthly standard deviation at these sites typically exceeds the monthly average precipitation for the wettest months (January through March) reveals the extreme year-to-year variation in precipitation. Furthermore, the sparse observational network fails to capture some important mesoscale features that impact local rainfall patterns. For example, convective rainfall over the Oman Mountains (bordering eastern UAE) during the summer season is a phenomenon that is widely known to local meteorologists but is not described adequately in climatological studies.

Under the guidance of the Department of Water Resources Studies (DWRS), the various C-band weather radars that exist in the UAE have been networked over the past three years. Data have been archived continuously as each radar has been added to the network. Here, however, data analysis is focused on the intensive observational periods associated with airborne studies of trace gases, aerosols, clouds and precipitation – winter and summer of 2001 and 2002.

2. UAE RADAR NETWORK

The current UAE radar network consists of five fixed radar sites (Figure 1) and one mobile radar, soon to be located in Fujairah on the eastern coast.

Corresponding author's address: Daniel W. Breed, *NCAR/RAP, P.O. Box 3000, Boulder, CO 80307-3000, USA; E-Mail: breed@ucar.edu. (*NCAR is sponsored by the National Science Foundation.)

The radars are all EEC (now called DRS-Weather Systems) C-band units with basically 1° beams, except for the 2.25° beam of the mobile radar. Volume scans consisting of 11 to 17 elevation angles were designed that allowed for a volume repeat time of 6 min, which was utilized on the Al Dhafra radar for the winter 2001 project. The Dubai radar began collecting data in April 2001, in time for the summer 2001 project, and the scan strategy was changed slightly for the two radars with a compromise volume scan frequency of 10 min. The mobile radar was installed at Al Ain in December of 2001, in time for the 2002 field campaigns. The Al Ain mobile radar was setup with fewer elevation scans (accounting for its larger beamwidth) and collected a volume every 6 min. In summer of 2003, a fixed radar became operational at Al Ain, effectively replacing the mobile radar, and two new radars began operations at Muzaira to the south and Dalma Island to the west.

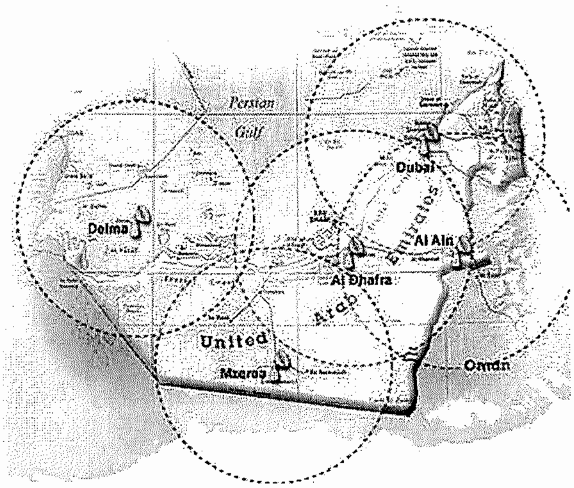

Figure 1. Depiction of the radar network in the UAE showing the location of the five fixed C-band radars – Dalma, Muzaira, Al Dhafra, Dubai, and Al Ain. The range circles have a radius of approximately 120 km.

3. DATA COLLECTION

The TITAN/CIDD software system (Dixon and Weiner, 1993) was installed on PC workstations at each radar for data ingest, processing, archival, and display. Processing of volume scans and file compression allow for near realtime transfer of data to the DWRS office in Abu Dhabi using relatively slow (64 KB) communication lines. Data from the radars are merged to provide a radar mosaic, now covering all of the UAE, which is disseminated to meteorological offices and available on a Website.

Two types of data are archived: radar coordinate data (elevation, azimuth, and range) and gridded data (x, y, z). Both include reflectivity and radial velocities, and other file types are generated from these variables (i.e., precipitation, VIL, etc.). The network is only now becoming stable with respect to communications, operation, and calibrations. In spite of fine cooperation with the different radar operators, several aspects were not continuously coordinated, which impacted the collection of quantitative data.

Another complicating feature of the radar data in the UAE is "clutter", caused mainly by anomalous propagation (AP). Normal ground clutter and sea clutter is exaggerated during periods of AP, which commonly occurs when a nocturnal inversion develops with a high moisture gradient near the surface. To address this problem, a radar echo classifier (REC) was implemented on the radar workstations. The REC (Kessinger et al. 2002) is a data fusion system that uses "fuzzy-logic" techniques to classify the type of scatterer being measured by Doppler radar systems. Using the three moments of radar base data (reflectivity, radial velocity and spectrum width) as input, various detection algorithms are formulated to make a classification. Two REC algorithms have been installed and tested on the UAE radars: the AP detection algorithm (APDA) that detects regions of AP ground clutter return and the sea clutter detection algorithm (SCDA) that detects regions of sea clutter return. Although final testing is not complete, the REC has been very successful in mitigating the clutter problem.

4. WINTER CONDITIONS

During the winter season, frontal systems moving in from the west and northwest periodically traverse the UAE region, producing a significant fraction of the annual rainfall over much of the country. Typically, during the winter months, about five to ten systems move through the region. However, no major strong synoptic events occurred during the winter periods of 2001-2003, thereby substantiating the high variability in the occurrence of strong systems. However, the radar summary proved valuable in documenting several weaker systems (fronts and troughs) that traveled across the southeastern Arabian Peninsula, bringing widespread cloudiness and some precipitation. About four of these systems per year produce measurable precipitation. Late winter and early spring brings a transition to more convective clouds, particularly over the Oman mountains in eastern UAE.

Figure 2 shows a reflectivity pattern from 9 March 2002 that is typical of weak, fast-moving systems. The line of weak cells intensified somewhat where it intersected the coastline, although reflectivities were generally weaker than 30 dBZ and tops were lower than 5 km in all but the most vigorous cells. A slight de-stabilization of the atmosphere, typical of the transition period, may have caused the extension of reflectivity into the interior of the UAE.

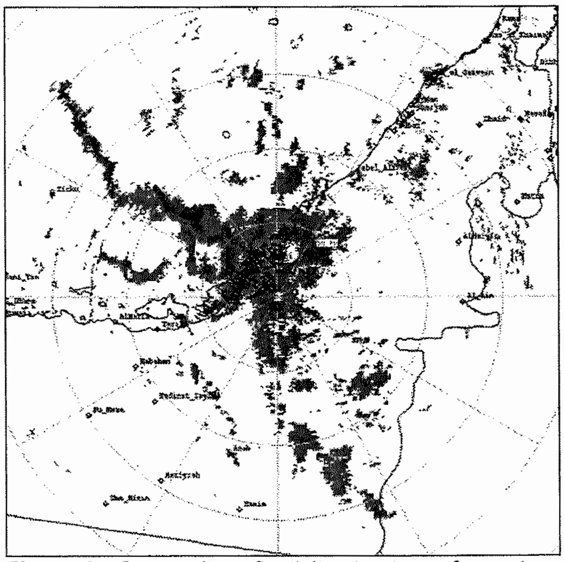

Figure 2. Composite reflectivity structure of a system crossing the central sections of the UAE on 9 March 2002 (~15:00 UTC). Gray shading starts at 10 dBZ and the darkest shading represents 35 dBZ. Area covered is about 350 km x 350 km.

5. SUMMER CONDITIONS

The radar summary of 2001-2002 summer storms shows that by far the majority of echoes and storms occurred over the Oman Mountains, southeast of Al Ain and northward. During the summer, a number of echoes often form in the south-central sections of the UAE (the Liwa region), and storms can also extend westward from the mountains into the coastal areas. For the situation in the mountains of Oman and eastern UAE, it appears that summer monsoon (easterly) flow often provides a deep layer of moisture to complement the low level flow from the Arabian Sea. This flow is usually strongest in the southern reaches of the Oman mountains but may not extend into the northern regions. Studies are beginning to show that mesoscale circulations, such as the sea breeze from the Gulf and the thermal low in the "Empty Quarter", as well as local mountain circulations, dictate areas of storm development.

Figure 3 shows a summer situation with several small cells in different stages of development over the Oman mountains east and northeast of Al Ain. The northernmost cell has a peak reflectivity of about 45 dBZ.

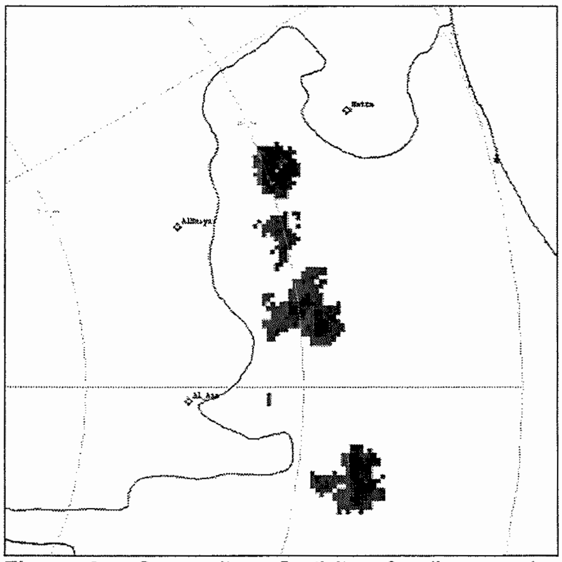

Figure 3. Composite reflectivity of cells over the Oman mountains (meandering line is the border between the UAE and Oman) on 7 August 2002 (~11:00 UTC). Gray shading starts at 10 dBZ and the darkest shading represents 40-45BZ. Area covered is about 125 km x 125 km.

6. RADAR CELL STATISTICS - EXAMPLES

6.1 9 January 2001 winter system

One of the most significant weather events during the winter seasons (2001-2003) was associated with a frontal passage on 9-10 January 2001. This system provided enough instability to develop convective cells, usually embedded within widespread echoes. The majority of the cells occurred over the Gulf, but some significant convection developed as the system encountered the northeastern UAE coast and northern Oman mountains. On 9 January (the most active day), 181 cells were strong enough to be tracked with the TITAN software (≥30 dBZ).

The duration of the cells is shown in Figure 4, where one volume scan represents 6 min. Most of the cells were relatively short-lived (less than 40 min), and several of the longer-lived cells were actually propagating cells rather than continuous rain showers. The echo tops (not shown) were mainly below 7.5 km MSL (modal value of 5.5–6.0 km), and the average level of the maximum reflectivity was 3.5–4.0 km. This may have been contaminated by melting layer effects, but shows that the cells were generally quite shallow. The predominantly eastward track of the cells, seen in Figure 5, is typical of winter systems. The cell speeds (not shown) were generally less than 7 m s^{-1}. This is considerably slower than the mean wind in the cloud layer, but is common for storm speeds, particularly for storms that are shallow with short lifetimes.

6.2 2001-2002 summer storms over the mountains

As discussed earlier, a peak in convective activity during the summer exists over the Oman mountains, and storm track characteristics (e.g., cells with reflectivities ≥30 dBZ) were developed to characterize this limited region. Figure 6 shows the distribution of storm durations for 715 cells from the summers of 2001 and 2002. Although they have longer lifetimes than the winter cells (Fig. 4), about 35% of the 2001-2002 summer cells lasted less than 30 minutes (three volume scans). These storm durations are similar to the distribution of Mexican storms (Bruintjes et al., 2001), with most lasting less than 1.5 hours and very few lasting more than 3 hours. The longer-lived storms were also contaminated by propagating cells that were not well resolved by the long 10-min volume scans. Convection of this nature really needs faster (~5-6 min) radar volume scans for adequate sampling.

Cell motion for the month of July 2001 (Figure 7) reflects the easterly nature of the summertime flow, which for these cells also has a northerly component (e.g., a northeasterly flow results in a southwesterly cell motion direction). The cell speeds (not shown) also demonstrate the weaker upper-level flow during the summer since 80% of the cells moved at <5 m s^{-1} and most moved at <3 m s^{-1}. The echo tops of the July 2001 storms (not shown) were significantly higher than the 9 January example, averaging about 8.5 km MSL with 10% of the storm tops greater than 11 km.

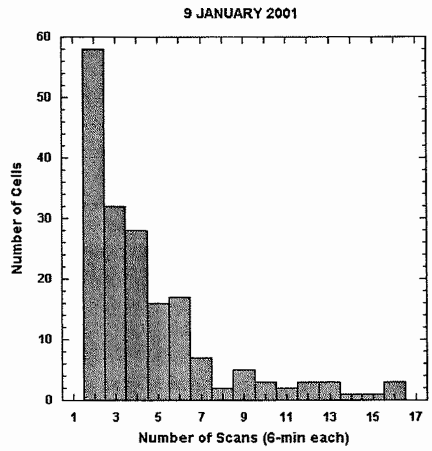

Figure 4. Histogram of cell duration (in number of volume scans) on 9 January 2001. One volume is 6 min (i.e., 5 equals 30 min).

7. CONCLUDING REMARKS

The addition of radar data to characterize precipitation in the UAE has proven valuable in broadening our perspective on precipitating clouds versus that based solely on climatological rainfall records. The national radar network continues to evolve and improve with the goal of producing quantitative precipitation estimates on a much better spatial and temporal scale than can be achieved with rain gauges. Already it is clear that significant differences exist in the nature of precipitating clouds between winter and summer.

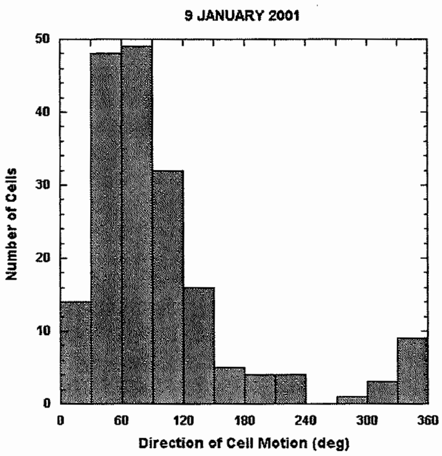

Figure 5. Histogram of cell motion (the direction cells are moving towards) on 9 January 2001.

8. ACKNOWLEDGEMENTS

A large number of people contributed to the establishment of the UAE radar network, the maintenance and calibration of the radars, the collection and archival of data, and the development of radar data analysis routines. Members of the IT section at DWRS were instrumental in coordinating the different owners of the radars, networking the radars and subsequently archiving the data. The radar owners (specifically the engineers, technicians and meteorologists) provided great cooperation in the use and set up of each individual radar: DWRS, the UAE Air Force, the Department of Civil Aviation-Dubai, and the Department of Civil Aviation-Abu Dhabi. Several additional people from NCAR, Weather Modification Inc, and the South African Weather Service assisted during the field projects, for radar calibration and training, and in post-processing of radar data.

9. REFERENCES

Bruintjes, R.T., D.W. Breed, V. Salazar, M.J. Dixon, T. Kane, G.B. Foote and B.G. Brown, 2001: Program for the Augmentation of Rainfall in Coahuila (PARC): Overview and results. *Preprints, 15th Conf. on Planned and Inadvertent Weather Modification*, Albuquerque, NM, Amer. Meteor. Soc., Boston, MA, 45-48.

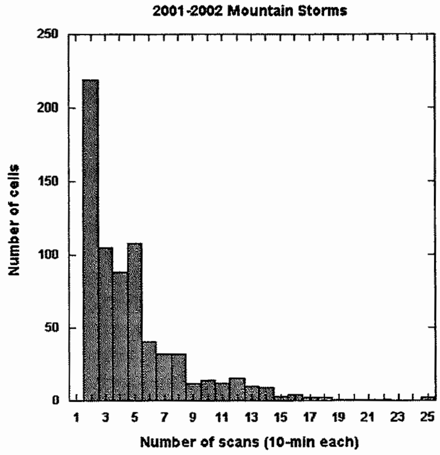

Figure 6. Histogram of cell duration (in number of volume scans) for storms over the Oman mountains in 2001 and 2002. One volume is 10 min (i.e., 6 equals 1 hr).

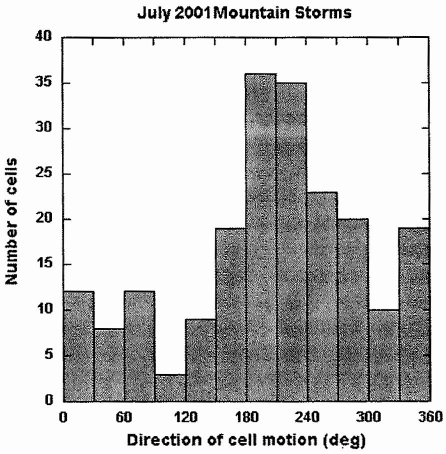

Figure 7. Histogram of cell motion (the direction cells are moving towards) for July 2001 mountain storms.

Dixon, M.J., and G. Weiner, 1993: TITAN – Thunderstorm identification, tracking, analysis, and nowcasting – a radar-based methodology. *J. Atmos. Oceanic Tech.*, **10**, 785-797.

Kessinger, C., S. Ellis and J. Van Andel, 2002: NEXRAD Data Quality: An update on the AP clutter mitigation scheme. *Preprints, 18th International Conference on Interactive Information and Processing Systems (IIPS) for Meteorology, Oceanography, and Hydrology*, Orlando, FL, Amer. Meteor. Soc., Boston, MA, 127-129.

LOCAL OROGRAPHY INFLUENCE ON VORTICITY INSIDE Cb CLOUD

Mladjen Ćurić, Dejan Janc, Vladan Vučković and Dragana Vujović

Institute of Meteorology, University of Belgrade, SERBIA AND MONTENEGRO

1. INTRODUCTION

In recent years the cloud resolving mesoscale models became capable to simulate many observed characteristics of an individual Cb cloud. So, Lin et al. (1998) and Lin and Joyce (2001) treated the multicell storm propagation and cell regeneration over a plateau by two-dimensional version of the ARPS model. Later Ćurić et al. (2003a, 2003b) used the ARPS model to simulate an individual Cb cloud moving over complex terrain. They treated the model cloud development, propagation and regeneration along the Western Morava valley (Serbia) under strong vertical directional ambient wind shear. Model results indicate that the propagation of the cloud and cold air nose in subcloud region are inhibited in lateral direction and their forms are more compact. Warm environmental air which approachs the cold air nose from the opposite direction is forced aloft more frequently than for the flat terrain. This causes the intense cell regeneration in front of the mother cloud. Therefore the simulated cloud therefore propagates faster along the valley axis than in the case when it developes and propagates freely in lateral direction. The simulated cloud characteristics are supported well with the observations (Ćurić, 1980; 1982).

The vortex-pair with the opposite signs of vorticity at flanks of a storm is analyzed by Toutenhoofd and Klemp (1983). They established the theory of its formation through convective tilting of mean flow horizontal vorticity. Later on Konak et al. (2000) investigated the mechanism of generating the vertical vorticity within the storm without mean shear. However, the influence of real mesoscale environment on vertical vorticity in convective cloud is not considered. Our primar goal is therefore to analyze the influence of the river valley on vortex-pair characteristics.

2. MODEL

The numerical model used in our research is Advanced Regional Prediction System (ARPS) Version 4.0 which has been developed by CAPS (Center for Analysis and Prediction of Storms) in Oklahoma University (Xue et al., 1995, Xue, Droegemeier and Wong, 2000; Xue et al., 2001). The ARPS is three-dimensional time-dependent non-hydrostatic model based on compressible Navier-Stokes equations and uses a generalized terrain-following coordinate system. The prognostic variables of the model are: Cartesian wind components, perturbation of potential temperature, pressure, mixing ratios of six categories of water substance (water vapor, cloud water and ice, rain, hail and snow) and turbulent kinetic energy (TKE). Lin et al. (1983) microphysical scheme is used except for hail accretion, hail melting and hail sublimation rates which are treated in accordance with Ćurić and Janc (1997) and Ćurić et al. (1999). The 1.5-order TKE subgrid-scale turbulence scheme is also applied.

The Arakawa C-grid is used for spatial discretization. The fourth-order quadratically-conservative finite differences are used for horizontal and vertical advection of momentum and scalars, while the other terms are treated by second-order differencing. Large and small time steps (6s and 2s) are used. The second order leap-frog scheme and the first order forward-backward explicit scheme are applied for large and small time steps respectively. The wave-radiating condition is used for lateral boundaries, while the radiation condition and the rigid one are used for upper and bottom boundaries respectively.

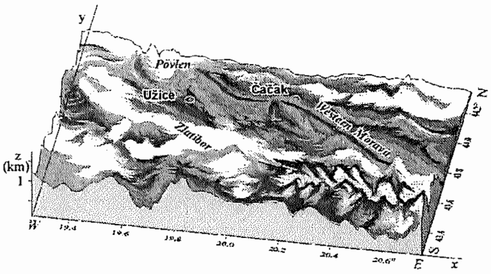

Fig. 1. Three-dimensional topography with the Western Morava valley within the model domain. The x, y and z axes are along the sidewalls of computational domain.

The model domain is 112×112×16 km with space resolutions of 1 km in horizontal and 500 m in vertical. Fig. 1 shows the full model domain along x and y-axis. It consists of the Western Morava valley area in degrees of geographical longitude and latitude with the center at 43.8°N and 20°E. The mean

Corresponding author's address: Mladjen Ćurić, Institute of Meteorology, University of Belgrade, P.O.B. 368, Belgrade Serbia and Montenegro; E-mail: curic@ff.bg.ac.yu

height of the area above sea level is about 300 m. The valley width is only a few hundred meters at Ovčar-Kablars' cliff (between Požega and Čačak). The valley axis is oriented roughly in northwest-southeast direction. The valley is flanked by mountains of different slopes.

The initial input values for temperature, humidity, pressure, wind velocity and direction are taken from single sounding. The reference state is homogeneous in horizontal. The ellipsoidal thermal bubble with axes of 10 km in horizontal and 1.5 km in vertical is used for initiation of the model cloud. It is expressed over potential temperature with the amplitude of 5°C centered at (x, y)=(32,96) km and 1.5 km over Povlen mountain (north-western part of the area in Fig. 1). The model simulation stops at t=120 min.

The sounding of 13th June 1982 (10 00 of local time) is used. The wind direction is turned sharply from SE direction to NW direction above 750 m. The wind speed varies from 7 m/s near the ground to about 17 m/s at 9 km MSL.

3. RESULTS OF EXPERIMENTS

For this purpose two cases are analyzed. Cases denoted by E1 and E2 relate to the real mesoscale environment (Fig. 1) and flat terrain if the other conditions are the same. For E1 the cloud is initiated over Povlen Mountain. Further it propagates toward the Western Morava valley. Fig. 2 shows the wind vectors and radar reflectivity after t=60 min of simulated time when the model cloud moves along the

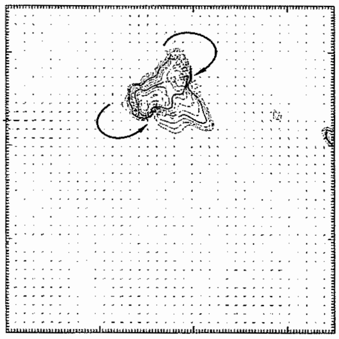

Fig. 2. Reflectivity (dBZ) and wind vectors (m/s) depicted on horizontal plane (z=1km) at t=60 min of simulation time for case with orography. The streamlines are added to emphasize the vortex pair.

valley axis. Two cells with different signs of vorticity are already formed, besides the cell in front of the mother cloud associated with the forced updraft over the front edge of the cold air nose. Later on (at t=90 min), the model radar reflectivity area is enlarged compared to previous time interval (Fig. 3). As noted the vorticity characteristics of the cells at the storm flanks become different with time. So, the positive vorticity of the right vortex tends to increase while the negative one associated with the left vortex decreases in their absolute values.

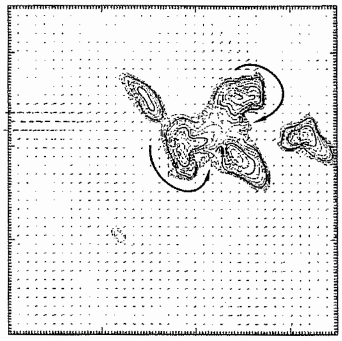

Fig. 3. As in Fig. 2. but for t=90 min.

In contrast, for E2 case the model cloud propagates freely in lateral direction. As a consequence the distance between vortices is greater than for E1 case as it is shown in Fig. 4. For further 30 min of simulated time the model cloud as well as the vortices at its flanks encircle larger area. They slightly differ from each other in absolute value of vorticity (Fig. 5). Such different feature of model clouds in E1 and E2 cases is influenced by the Western Morava valley since it inhibits the cloud propagation in lateral direction.

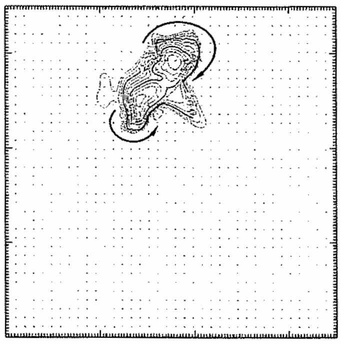

Fig. 4. As in Fig. 2 but for case of flat terrain.

The tilted updraft tubes associated with corresponding cells formed at the storm flanks are presented in Fig. 6 for E1 case at t=75 min of simulated time. According to Toutenhoofd and Klemp (1983) and Konak et al. (2000)

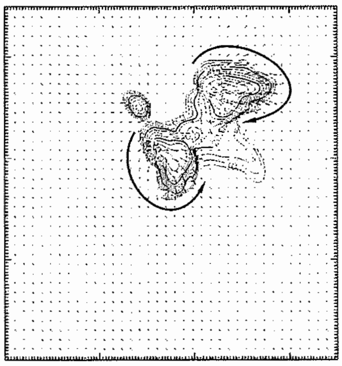

Fig. 5. As in Fig. 3 but for case of flat terrain.

the mean flow horizontal vorticity formed at early stage overturns to vertical one through convective tilting. Compared to E2 case shown in Fig. 7, the updraft

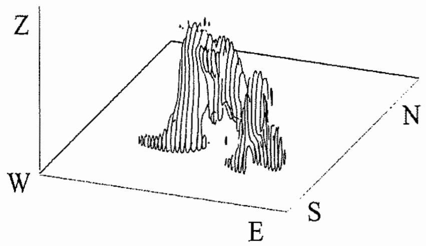

Fig. 6. Vertical velocity field ($w \geq 2m/s$) for case with orography at t=75 min.

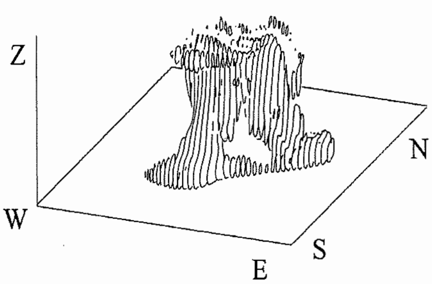

Fig. 7. As in Fig. 6 but for case with flat terrain.

tubes are more tilted and approach to each other at lower level. These tube characteristics are the consequence of less developed model cloud in E1 case.

4. CHARACTERISTICS OF VORTEX-PAIR IN PRESENCE OF OROGRAPHY

In this section, we tend to explain how orography modifies the characteristics of vortices at the flanks of the cloud. In Fig. 8, the scheme of generation of vortices for E1 case is shown. Besides the vertical directional wind shear, hereafter it exists also the wind speed shear in lateral direction to the valley axis due to the valley sides. The roughness of the terrain as well as the slopes of the valley sides are not the same at left and right to the valley axis. The ambient wind vector is indicated by open arrows in Fig. 8. Then the vertical vorticity formed by convective tilting of mean flow horizontal (ζ_{vr} and ζ_{vl}) one is modified by additional vertical vorticity formed by horizontal wind speed shear. So, the positive vorticity generates at left (ζ_{hl}) and the negative one at right (ζ_{hr}) to the valley axis. Since $|\zeta_{hl}| > |\zeta_{hr}|$ the resulting absolute value of vorticity at right and left vortices would be also different. According to theory, if the mean flow is uniform in horizontal, then $|\zeta_{vl}| = |\zeta_{vr}|$. Therefore we have $|\zeta_{vr} + \zeta_{hr}| > |\zeta_{vl} + \zeta_{hl}|$. Consequently, the right vortex tends to increase and the left one to decrease with time.

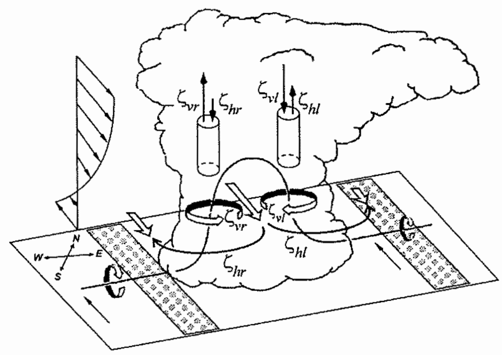

Fig. 8. Scheme of the rotation development within a Cb cloud through vortex - line tilting for case with orography. Shadowed areas at horizontal plane denote the valley sides.

In Fig. 9, the scheme of generation of vertical vorticity for E2 case is shown. As noted the horizontal wind speed shear does not exist and the vertical vorticity is formed through convective tilting of mean flow horizontal vorticity. In this case the absolute values of vorticity for right and left vortices are the same. The presence of orography also changes the vertical directional wind shear since it is less expressed towards the valley sides. This causes that the formation of horizontal vorticity tends to be concentrated close to valley axis (compare Figs. 2 to 5).

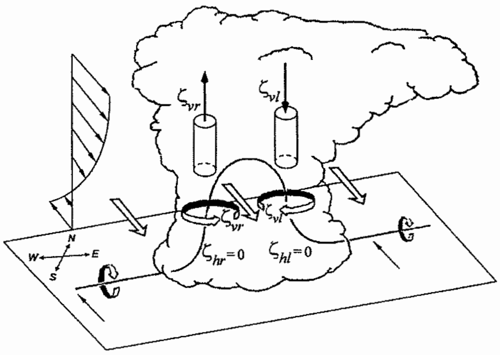

Fig. 9. As in Fig. 8 but for case with flat terrain.

5. CONCLUDING REMARKS

In this study we try the answer the question how influence on existing vortices within the cloud could have the presence of real mesoscale environment. The presence of orography changes the horizontal and vertical shear of the mean wind. Depending on characteristics of northern and southern valley sides, the additional vertical vorticity formed by horizontal wind speed shear can change the resulting vorticity of vortex at storm sides in different manner.

ACKNOWLEDGEMENTS. This research was sponsored by the Ministry of Science of Serbia under Grunt No. 1197. We gratefully acknowledge Mr. Dragomir Bulatović for his assistence in technical preparing of figures.

REFERENCES

Ćurić,M.,1980: Dynamics of a cold air outflow from the base of the thunderstorm. A simple model. *J. Rech. Atmos.*,14,493-498.

Ćurić,M.,1982: The development of the cumulonimbus clouds which move along a valley. In: *Cloud Dynamics* (eds. Agee,E.M., Asai,T.). Dordrecht: D. Reidel,259-272.

Ćurić,M., D. Janc,1997: On the sensitivity of hail accretion rates in numerical modeling. *Tellus*, 49A,100-107.

Ćurić, M., Janc, D., and Vučković V., 1999. Verification of the improved predictive capability of a 1-D forced time-dependent cloud model with truncated hail spectrum. *Meteorol. Z.*, N.F. 8, 143-154.

Ćurić, M., D. Janc, D. Vujović and V. Vučković, 2003a: The effects of a river valley on an isolated cumulonimbus cloud development, *Atmos. Res.*, 66, 123-139.

Ćurić, M., D. Janc, D. Vujović and V. Vučković, 2003b: The 3-D model characteristics of a Cb cloud which moves along a valley. *Meteorol. Atmos. Phys.*, 84, 171-184.

Kanak, K.K., D. K. Lilly, and J. T. Snow,2000: The formation of vertical vortices in the convective boundary layer. *Q. J. R. Meteorol.Soc.*, 126, 2789-2810.

Lin, Y-L., Farley, R.D. Orville, H.D., 1983. Bulk parameterization of the snow field in a cloud model. *J. Climate Appl. Meteor.*, 22, 1065-1092.

Lin,Y-L., Deal, R.L., Kulie, M.S., 1998: Mechanisms of cell regeneration, development and propagation within a two-dimensional multicell storm. *J. Atmos. Sci.*, 55,1867-1886.

Lin, Y-L., Joyce, L. E., 2001: A further study of mechanisms of cell regeneration, development and propagation within a two-dimensional multicell storm. *J. Atmos. Sci.*, 58, 2957-2988.

Toutenhoofd, V., and J.B. Klemp, 1983: An Isolated Cumulonimbus Observed in Northeastern Colorado: Comparison of Field Observations with Results of a Three-Dimensional Simulation. *Mon. Wea. Rev.*, 111, 468-478.

Xue,M., K.K. Droegemeier, V. Wong, A. Shapiro, and K. Brewster, 1995: Advanced Regional Prediction System version 4.0 users guide. CAPS, 380 pp.

Xue, M., Droegemeier, K.K., Wong, W., 2000: The Advanced Regional Prediction System (ARPS) - A multi-scale nonhydrostatic atmospheric simulation and prediction model. Part I: Model dynamics and verification. *Meteor. Atmos. Phys.*, 75, 161-193.

Xue, M. et al., 2001: The Advanced Regional Prediction System (ARPS) - A multi-scale nonhydrostatic atmospheric simulation and prediction model. Part II: Model physics and applications. *Meteor. Atmos. Phys.*, 76, 143-165.

Microphysics Of Precipitation Associated With Cloudbursts Forced By Orography And Large-Scale Synoptic Conditions In Different Convective Regimes

Someshwar Das and Raghavendra Ashrit

National Center for Medium Range Weather Forecasting, A-50, Sector – 62, Noida - 201301, India

1. INTRODUCTION

Intense precipitation occurs frequently over the Indian region due to cloudbursts forced by topography of the Himalayas and deep convection forced by large-scale advective-radiative processes and synoptic conditions. The cloud microphysics and precipitation mechanism can significantly differ in the two contrasting cases. The cloudbursts (hereafter referred to as case1) produce sudden high intensity rainfall (~10 cm/ hour) over a small area and have a short life span of few hours. The phenomenon occurs due to strong atmospheric instability and sudden upward lift of moisture-laden Cumulonimbus clouds forced by orography. On the other hand, heavy rainfall episodes forced by deep convection due to large-scale synoptic conditions (case2) may last up to one or two days and produce 50-60 cm rainfall per day. Real-time prediction of both these events at precise location and time are challenging tasks.

In this study, intense precipitations associated with the two contrasting cases have been studied. In the first case, the cloudbursts that occurred in Himanchal Pradesh in the Northwest Himalayas on 16 July 2003 has been studied. The event produced about 28-30 cm rainfall in 24 hours. Over 200 people were swept away in the flash floods resulting from the cloudbursts. In the second type of intense rainfall case, heavy precipitation that occurred during 26-28 June, 2002 in Gujarat over the west coast of India has been studied. Rainfall ranging from 2-61 cm day^{-1} was reported during this episode. Such heavy rainfall events are generally associated with an off shore trough at sea level, a cyclonic circulation extending from lower to the middle troposphere and a shear line extending from the Arabian Sea to the Bay of Bengal across the southern peninsular India or across the Indo-Gangetic plains.

Corresponding author's address:

Dr. Someshwar Das, National Center for Medium Range Weather Forecasting, A-50, Institutional Area, Phase II, Sector – 62, Noida - 201301, India
Tel: 91-120-2402867, FAX: 91-120-2402868
Email: somesh@ncmrwf.gov.in

A mesoscale model (MM5) has been used to investigate the two incidents. Several experiments have been conducted using multi nested domains (90, 30 and 10 km resolutions) and at cloud-resolving scale to determine the ability of the model in giving advance warnings of such events. Experiments have also been carried out to study the sensitivity of different convection and cloud microphysics schemes as well as the impact of mesoscale data assimilation in forecasting the intense rainfall episodes.

2. MM5 MODEL CONFIGURATION

The MM5 model is a 5th generation PSU/NCAR Mesoscale Model (limited area), non-hydrostatic, terrain following sigma coordinate, designed to simulate or predict mesoscale & regional scale atmospheric circulation (NCAR, 2002). The model has been adapted for real time mesoscale weather forecasting at NCMRWF (NCMRWF, 2002). It is run on triple nested domains at 90, 30 and 10 km resolutions (Das, 2002). The model is run using the Grell scheme (Grell et al, 1994) for cumulus parameterization and, the non local closure scheme of Hong and Pan for the boundary layer parameterization. Explicit treatment of cloud water, rain water, snow and ice has been performed using the simple ice scheme of Dudhia (1996). Cloud radiation interaction has been allowed between explicit cloud and clear air (FRAD=2). The initial and lateral boundary conditions are obtained from the operational global T80 model of NCMRWF. The cloudburst case has been studied on 3 nested domains at 27, 9 and 3 km resolutions.

3. SIMULATION OF CLOUDBURST EVENT

3.1 Synoptic situation

Cloudburst, also called as rain gush or rain gust is a sudden and heavy rainfall over a small region. An unofficial criterion sometimes used specifies a rate of rainfall equal to or greater than 100 mm per hour. It results in a high intensity rainfall in a short period of time with strong winds and thunderstorm activity. It is a very localized phenomenon with impact over an area not exceeding 20-30 km. A cloudburst occurs when monsoon clouds associated with low-pressure area drift northwards, from the Bay of Bengal across the Ganges plains, then onto the Himalayas and burst, bringing heavy downpour (75-100 mm per hour). It is a mountain weather system involving orographic convection and rainfall.

Cloudbursts are common to all hilly areas but states of Himachal Pradesh and Uttaranchal etc., are most affected due to topographic conditions. Most of the damages to properties, communication system and human causalities occur as a result of flash floods. The phenomenon occurs due to strong atmospheric instability and sudden upward lift of moisture laden Cumulonimbus cloud forced by orography. Prediction of cloudbursts is challenging task and requires application of very high-resolution models, mesoscale observations, high performance computers and Doppler weather radars. Cloudburst events go unreported when they occur over remote and unpopulated hilly areas.

The mesoscale processes are categorized as (1) Meso-α (200-2000 km) (2) Meso-β (20-200 km) and (3) Meso-γ (2-20 km). Cloudburst events can be grouped under Meso-γ scale. At times it may be difficult to distinguish a cloudburst from a thunderstorm. Simulation and early prediction of such severe weather events can provide crucial information for severe weather warning and to carry out evacuation measures. However, cloudburst events are very localized with impact over area not exceeding 20-30 km. Very often these events go unreported when they occur in unpopulated areas. Probably the local nature and short temporal span of a cloudburst are the reasons it has not been extensively studied. Here a preliminary attempt is made using MM5 mesoscale model to simulate a cloudburst event.

3.2 Results

The first case study is a cloudburst event of 16th July 2003 at Shillagarh in Himachal Pradesh. Shillagarh village is 35 km from Kullu. The early morning cloudburst occurred between 0300-0400 hours IST and the flash floods and landslides left 35 dead and 50 injured. There were also reports of disrupted communication links and power supply to the area. It also washed away roads and damaged properties worth lakhs of rupees.

Figure 1 shows the MM5 predicted rainfall over Himachal Pradesh 24 hours, 48 hours and 72 hours (Figure1 a,b and c respectively) in advance and comparison with the observations (d). MM5 simulation at 10 km resolution compared rather well with the observed rainfall (rain gauge and satellite merged estimates obtained from NOAA), which is also at 10 km resolution. However, the location of rainfall maximum was not predicted accurately. Further, it is noted that high rainfall amounts over Himachal Pradesh seen in 24-hour forecast closely compare with 48-hour and 72-hour forecast valid for 16th July. This indicates that MM5 is able to capture the cloudburst event consistently.

4. DEEP CONVECTION FORCED BY LARGE-SCALE ADVECTIVE-RADIATIVE PROCESSES

4.1 Synoptic situation

Heavy to very heavy rainfall was recorded on 26, 27 and 28 June 2002 over the west coast of India and inland stations of Maharastra and Gujarat. Rainfall ranging from 2-54 cm/ day were recorded at many places over the region. Fig. 2 depicts the cloud imagery from METEOSAT at 06 UTC, 27th June 2002. An off shore trough at sea level extending from Maharastra coast to Kerala coast was observed on all days (26-28 June). The heavy precipitation occurred as a result of a low pressure system moving from the head Bay of Bengal to Maharastra and Gujarat and the off shore trough in which a vortex formed off Gujarat coast in the Arabian sea.

4.2 Results

Fig. 3 (a, b) illustrates the 48 hours rainfall forecast obtained from the CTRL and FDDA based on the initial condition of 00 UTC, 25 June 2002. Values less than 10 mm day^{-1} have been shaded in the diagram. Contour are drawn at intervals of 10, 25, 50, 75, 100, 150, 200, 250 and 300 mm day^{-1}. The diagram also shows rainfall derived from GPCP (Fig. 3c) and those reported by rain gauge in cm (Fig. 3d).

It may be noted that the GPCP values may underestimate the rainfall over land and their values depend on the number of rain gauge reports available during the analysis. Moreover, the GPCP values are very coarse analysis at 2.5 x 2.5 degree resolution, whereas the model forecasts are at 30 km resolution. The analysis based on rain gauge (Fig. 3d) also may not represent the true picture as it is based on the available reports from the GTS. None of the diagrams show the rainfall value of 54 cm as recorded at some of the stations over Gujarat region. Nevertheless, all the diagrams show an area of heavy rainfall over the west coast over Gujarat region. The MM5 forecasts show mesoscale structure of the variation of rainfall. The amounts have increased in the experiment FDDA, which might be closer to observations reported around 54 cm. The increased rainfall in FDDA may be because of the high resolution analysis used in this experiment.

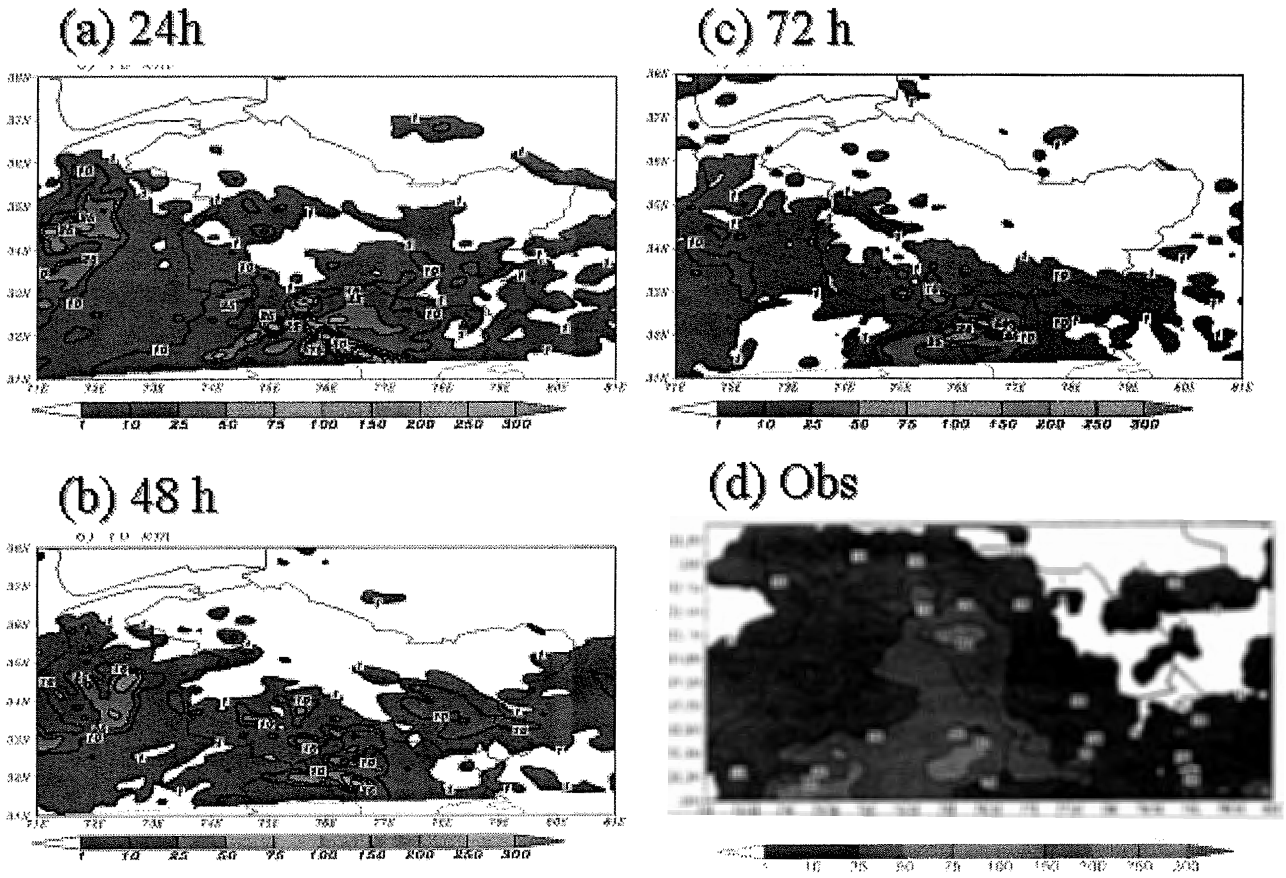

Figure 1. MM5 forecast of 14th July cloudburst event and its comparison with observations.

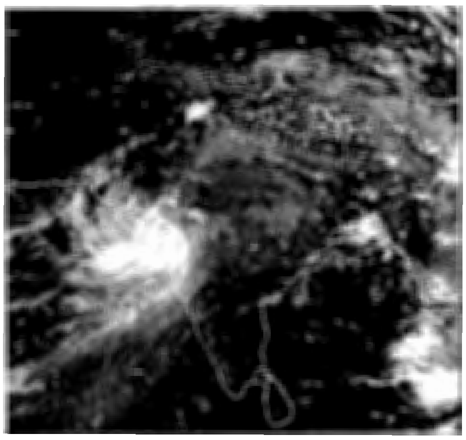

Fig. 2: IR cloud imagery at 06 UTC, 27th June 2002 from METEOSAT.

SUMMARY

Simulations from a mesoscale model usually depend on the global model analysis for initial and lateral boundary conditions. It is likely that the results are sensitive to the biases in the global model analysis. However, it must be noted that MM5 could capture some of the features quite well despite the biases in the global model simulation. Efforts are also being made to increase the number of vertical levels and increase the resolution to up to 1 km. Many such studies are planned for future.

References

Das, S., 2002: Real time mesoscale weather forecasting over Indian region using MM5 modeling system, NCMRWF report no. NMRF/RR/3/2002.

Dudhia, J., 1996: A multi-layer soil temperature model for MM5". Preprints, The sixth PSU/ NCAR Mesoscale Model User's Workshop, 22-24 July 1996, Boulder, Colorado, 49-50, 1996

Grell,, G.A., J. Dudhia and D.R. Stauffer, 1994: A description of the 5th generation Penn State/ NCAR Mesoscale model (MM5). NCAR technical note, NCAR/TN-398+STR, 117 pp, 1994

Held. G., 1982: Comparison of radar observations of a devastating hailstorm and a cloudburst at Jan Smuts Airport., in Cloud Dynamics., Eds., E. M. Agee and T. Asai., Advances in Earth and Planetary Sciences. Terra Scientific Publish Company, Tokyo.

Houze. R. A., 1993: Cloud Dynamics. International Geophysics Series. Vol-53, Academic Press, Inc.

NCAR, 2002: PSU/NCAR Mesoscale Modeling System (MM5 version 3) tutorial class notes and user's guide. Available from the National Center for Atmospheric Research, Boulder, Colorado, USA, June 2002.

NCMRWF, 2002: The MM5 Model, http://www.ncmrwf.gov.in/MM5.htm

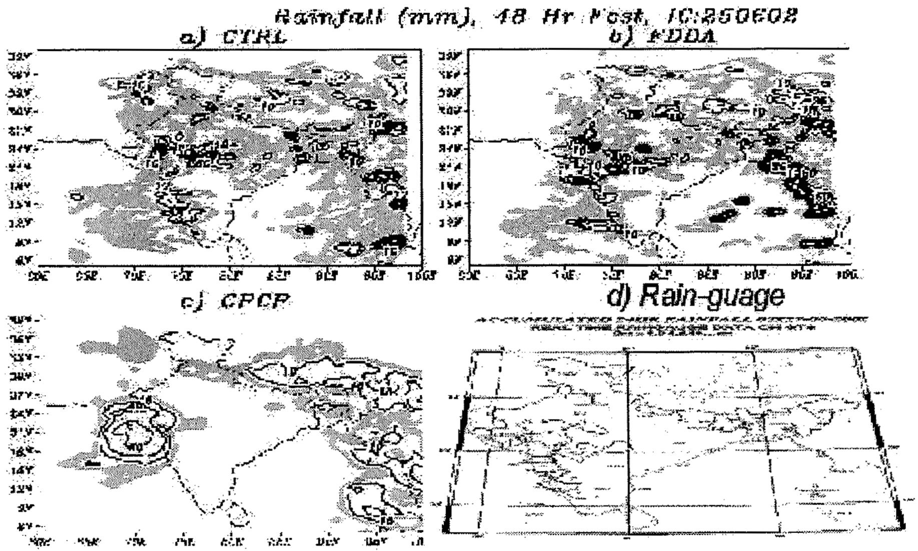

d

Fig. 3: Rainfall on 27 June 2002, (a) CTRL (b) FDDA (c) GPCP (d) Rain gauge.

A PRELIMINARY STUDY ON THE VARIABLE TENDENCY AND PHYSICAL CAUSE OF FORMATION OF THE NATURAL PRECIPITATION OVER HEBEI AREA

Duan Ying[1], Yang Baodong[1], Guo Jinping[1], Wu Zhihui[1], You Laiguang[2] and An Yuegai[3]

[1]Weather Modification Office of Hebei Province, Shijiazhuang, 050021, China
[2]Chinese Academy of Meteorological Sciences, Beijing, 100081, China
[3]Climatic Center of Hebei Province, Shijiazhuang, 050021, China

1. INTRODUCTION

Hebei Province locates in the north of China, with continental monsoon climate. In China, since the nineties decade of the twentieth century, the study on the variable tendency of air temperature and natural precipitation were more researched, and in this field also have obtained some important study results. For example, Chenlongxun(1998), Huangronghui et al. (1999), they utilized many kinds of meteorological essential factors and synthetically analyzed the climate variation near 45 years in China in order to do some research about the variable tendency of air temperature and precipitation. The results show that the annual mean air temperature is raising and the climatic tend to warmer in North China and in the northeast China. At the same time the mean annual precipitation reduces clearly. In recent years the research on the cause of formation of the climate variation is increasing. Some investigators also start to attach to the research about aerosol environment effect. For example, Shiguangyu, Xuli et al. (1993) using observed data by upper air balloon over the Xianghe and Yutian area in Hebei province, the analyzed observation from 1984 to 1993 in this area, the results show that the real number density of aerosol in 1993 is larger than that in 1984, especially the value near surface layer increased more. The investigators think that the reason is that the increasing of the industry emission polluted the atmosphere. Maojietai et al. (2002) estimated synthetically the research status of Chinese aerosol in the atmosphere; the results show that the study is going deep gradually. But in China, the study about the physical cause of formation on natural precipitation combing comparative variation of atmospheric composition is few.

Corresponding author's address: Duan Ying, Weather Modification Office of Hebei Province, Shijiazhuang, 050021,China; E-Mail: hbwmo@heinfo.net.

In this paper the variable rule of mean annual air temperature, the maximum and minimum air temperature and the diurnal range of air temperature were analyzed in Hebei province area. Secondary, the interaction between the variation tendency of mean annual rainfall and the variation of annual mean air temperature is researched. On the basis of above study, using the observational data of the low clouds frequency, the decease of drizzle days number and analyzed results of aerosol concentration with height in the atmosphere, preliminary researched results is obtained that the interaction between air temperature rising and the decrease of natural precipitation and above-mentioned elements varieties and the possible cause of formation.

2. ANALYSIS OF THE AIR TEMPERATURE VARIATION TENDENCY

Based on the statistic analysis of air temperature data from 1950 to 1998 in Hebei province (there are the whole 40 weather stations and using the real stations in 1950s). The analysis results of annual mean air temperature and mean air temperature in winter and in summer are given in Table 1 and Figure 1.

Table.1 The variable tendency of the mean air-temperature (℃) in winter, summer and annual

	1950's	1960's	1970's	1980's	1990's
Annual	9.9	9.6	9.8	10.0	10.3
winter	-5.2	-5.8	-5.1	-5.1	-3.9
summer	23.7	23.5	23.1	23.3	23.6

From Table 1 and Figure 1, in the past fifty years, the results show that the tendency of annual mean air temperature in Hebei province increased as time goes by. It increased gradually beginning with 1960's to the maximum value in 1990's; the increased value was 0.7℃ and increases 0.23℃ every 10 years. The mean air temperature was the minimum in winter in 1960's.

Then it moved up from late 1970's and got to the maximum in 1990's. That in 1990's was 1.9℃ higher than that in 1960's. Every 10 years it increases 0.63℃. Namely, the mean air temperature tend to warmer range is larger in winter. But in summer it changes range a little with the minimum value in 1970's and lesser rising up in 1980's. It is 0.1℃ less than in 1990's than it is in 1950's. Namely the variation of mean air temperature with decade is not obviously in summer. Thus it can been seen that in the past fifty years, annual mean air temperature stepped up and climate warmed which mainly show that air temperature in winter clearly rising and climate trend to warmer obviously.

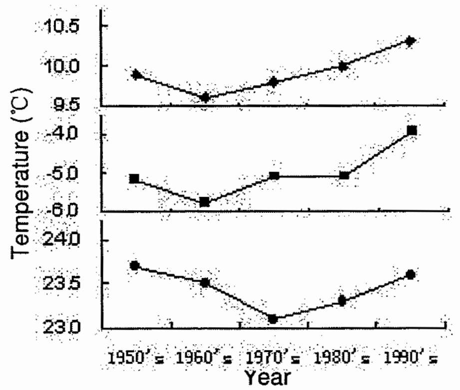

Fig.1 The trend of annual mean air temperature and mean air temperature in winter and summer

3. CORRELATION ANALYSIS RAINFALL AND AIR TEMPERATURE VARITION

Based on the statistic analysis of fifty years rainfall data in Hebei province, the main tendency of annual mean rainfall past years was descendent gradually from 1951 to 2000. The mean annual rainfall in 1950's was 585.1mm. In 1990's it was 512.3mm and lessen 72.8mm than in 1950's. But with time passing by, corresponding annual mean air temperature variation climbed up. This result shows that natural precipitation is tending to decrease along with the increasing annual mean air temperature from 1950's to 1990's in Hebei province. So the decrease of annual natural precipitation and the rising of mean annual air-temperature are anti-correlation (see figure 2).

4. VARIATION OF DRIZZLE DAYS AND LOW CLOUD DAYS

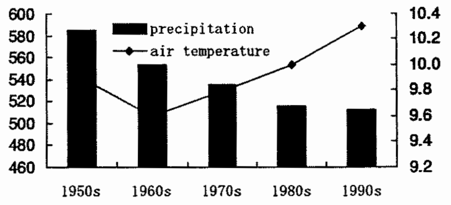

Fig.2 The variation tendency of the rainfall and the air temperature with decade in Hebei Province

Using historical observation data of three routine stations over Bohai gulf (Leting, Huanghua and Tanghai), the variation of annual mean air temperature, and the mean annual rainfall, annual number of drizzle days and low clouds days were analyzed synthetically in this area. The results show that the annual mean air temperature increases 0.85℃ from1960's to 1990's in this area. At the same time the tendency of rainfall took on obvious descendent and rainfall decreased 133mm in 1990s than in 1960s. The descendent rate gets to 19%. The range of air temperature increase and rainfall decrease are larger in this area than that in the whole province.

According to figure 3, figure 4 (omitted), figure 5 (omitted), they respectively show the variation of number of drizzle days and low clouds days. The results show that number of drizzle days of each station reduced obviously; number of low clouds days of Huanghua and Leting increased clearly, and corresponding annual mean precipitation trend to reduce.

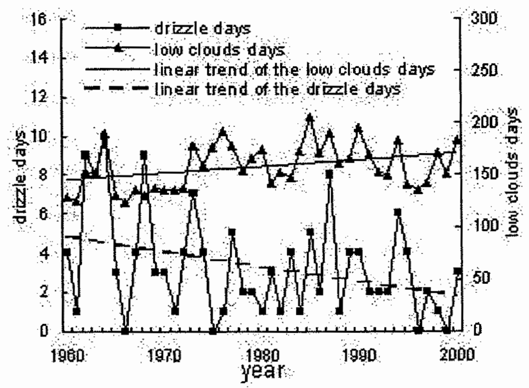

Fig.3 Variation tendency number of drizzle days and low clouds days probed in the Huanghua weather station of Bohai gulf area

5. AEROSOL OBSERVATION RESULTS OVER THE REGION

The vertical distribution of aerosol density is shown in the figure 6. It is found that the aerosol concentration near surface layer increases with year to year quickly from 1984 to 1993 over this area. This possible reason is analyzed by Shi Guangyu et al. (1993), which maybe results from the development of industry and society

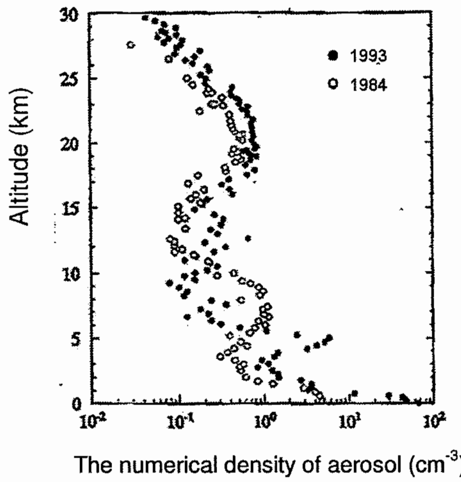

Fig.4 The comparison of observation results of aerosol numerical density with height between 1993 and 1984

6. CONCLUSIONS AND DISCUSSION OF THE REASION OF NATURE PRECIPITATION DECREASE

According to the variation of air temperature, rainfall, drizzle days and low clouds days in these three stations over Bohai gulf, combining the aerosol observation data over this area, it is can be infer that the aerosol particle increasing affects the radiant balance of atmosphere and it is the direct effect; the indirect effect of aerosol particle increasing is to increase the amount of the CCN in the atmosphere.

If increasing the aerosol particle makes the amount of cloud drops be increased. Because of under liquid water content is changeless in cloud, the average radius of cloud drop is decreased and then influences the cloud micro-physical mechanism and the formation of precipitation. Such as increasing of low clouds days, drizzle days is decreased, prolonging the cloud duration or restraining the precipitation formation. This conclusion is proved by the statistic observation of three above-mentioned stations in Bohai gulf.

The low clouds precipitation is belong to warm cloud precipitation process. Cloud droplet grows up gradually through condensation and until certain scale condensation will be very slow. After this period, it is difficult that cloud droplet grows up to raindrop through condensation process. So precipitation comes into being mainly because of collision and coalescence growth process. To formation precipitation unit, the gravity collision and coalescence is the most important form in all kinds of collision and coalescence form. The condition of occurring this special process is that some cloud droplets can grow up into the bigger drop. If there are enough CCN in the atmosphere, they form many cloud droplets. These adequate cloud droplets compete the limited moisture in cloud each other. As a result the big drop forms difficultly and precipitation appears easily.

In summary, the research results show that there are good correlativity among rising of annual mean air temperature and decreasing of mean annual rainfall in certain region. There is good correlativity between low clouds days increasing and number of drizzle days decreasing. The increasing of aerosols in the atmosphere results in the increase of CCN and ice nucleus. Therefore increasing of aerosol in the atmosphere is one of possible physical reasons which influence the variation of air temperature rise and precipitation tend to reduce.

REFERENCES

An yuegai, Guo jinping, Duanying et al., 2000: An Analysis of the Evolution Characteristics and Physical Cause of Formation about Forty Years Natural Rainfall in Hebei Province. Proceeding of 13th International Conference on Clouds and Precipitation, Reno, Nevada USA, 395-397.

Chen Longxun et al., 1998: The research of climatic change over China in the past 45 years. ACTA Meteorologica Sinica, 56(3), 257-270 (In Chinese).

Huang Ronghui et al., 1999: The rainfall change with year -to -year in summer and the droughty tendency in North China. Plateau Meteoro., 18(4),465-476 (In Chinese).

Mao Jietai et al., 2002: The synthesizer summarization on aerosol research in China. ACTA Meteorologica Sinica, 60(5), 625-634 (In Chinese).

Shi Guangyu et al., 1996: Atmospheric Sounding of the vertical distribution of atmospheric ozone and aerosol by air-balloon. Atmospheric Science, 20(4), 401-407 (In Chinese).

Wei Fengying et al., 2003: The climatic background of drought and its premonitory strong signal in North China area. ACTA Meteorologica Sinica, 61(3), 354-363 (In Chinese).

Yang Jianping et al., 2003: The preliminary study of connection wave of the dry-wet climate and its cause of formation in the past 50 years in China. ACTA Meteorologica Sinica, 61(3), 364-373 (In Chinese).

Zhang Qingyun, 1999: The variation of precipitation and water resources in North China since 1880. Plateau Meteoro., 18(4), 486-495

THE CLOUD PHYSICAL CHARACTERISTICS AND PRECIPITATION OF CONVECTIVE CLOUD SYSTEMS MODIFIED BY URBANIZATION IN BEIJING REGION

Xueliang Guo, Jing Wang and Danhong Fu

Institute of Atmospheric Physics, Chinese Academy of Sciences, Beijing 100029, China

1. INTRODUCTION

Many observational and modeling studies indicate that rainfall patterns in and downwind of cities are modified (e.g., Braham 1976; Changnon 1981; Hjelmfelt 1982; Balling and Brazel 1987; Jaurequi and Romales 1996; Bornstein and Lin 2000; Rozoff and Cotton 2003). The urban heat island and the increased roughness surface due to urbanization may enhance boundary layer convection and increase frequency of thunderstorms around those cities.

In the summer season, isolated convective cells formed in mountain area of Beijing always merge and form mesoscale convective cloud system (MCCS), and produce heavy precipitation and lightning. It was found that the time, amount and location of precipitation have been become difficult to predict in recent years. The question that whether the precipitating clouds systems have been modified by rapid development of urban construction enlargement or not has not been well understood. This study investigates the effects of urbanization on regional convective precipitation by using the PSU/NCAR Mesoscale Modeling System (MM5). A severe convective cloud system on June 4, 2003 in Beijing was simulated based on actual ground surface and that modified by increasing land surface roughness length and albedo, and decreasing thermal inertia and moisture availability according to the urban surface characteristics.

2. METHODOLOGY

2.1 Model Description

The model used in this study is the Fifth-Generation Penn State/National Center for Atmospheric Research (NCAR) Mesoscale Model MM5 Version 3 (MM5V3).

2.2 Experimental setup

The model was implemented with two nested grids at resolutions of 6 and 2 km. The domain sizes consisted of 100 × 100 and 100 × 100 grid cells. The source data of 25-category, global coverage with the resolution of 5-minute were used to specify terrain elevation, land-use/vegetation-cover, land-water mask. The model was initialized with NCEP/NCAR Reanalysis Data. Model simulations start at 0000 UTC 4 June 2003. The explicit microphysical scheme of mixed phase with graupel (Reisner) and Blackadar PBL were used. The Dudhia cloud radiation scheme and relaxation boundary conditions were also included.

3. RESULTS AND ANALYSIS

3.1 Sensible and latent heat flux at the surface

For the urbanized surface, the surface sensitive heat flux increases and concentrates (Fig.1), while the surface latent heat flux reduces (Fig.2) comparing with those actual situations. Especially in the mountainous region, the variation is much larger. The maximum value of sensible heat flux before modification is about 300-400 W m^{-2}, and it becomes more than 400 W m^{-2} after modification. The area with high value is also become larger.

3.2 Distribution of radar echo

The radar echo after urbanization develops earlier due to the increased sensible heat flux at the urban surface (figures omitted). Fig. 3 displays the horizontal distributions of the

---

Corresponding author's address: Xueliang Guo, Institute of Atmospheric Physics, Chinese Academy of Sciences, Beijing 100029, China; E-Mail: guoxl@mail.iap.ac.cn

simulated radar at 500hpa before and after modified. It shows that after urbanization, the radar echo at the upper level become weak and less over the urban region (D2). It means that the convective cells entered the urban region become less and tend to distribute around the city. The convective cells also distribute dispersedly.

The vertical distribution of radar echo is shown in Fig. 4. At the urban surface condition, the depth and strength of radar echo in urban region become weak.

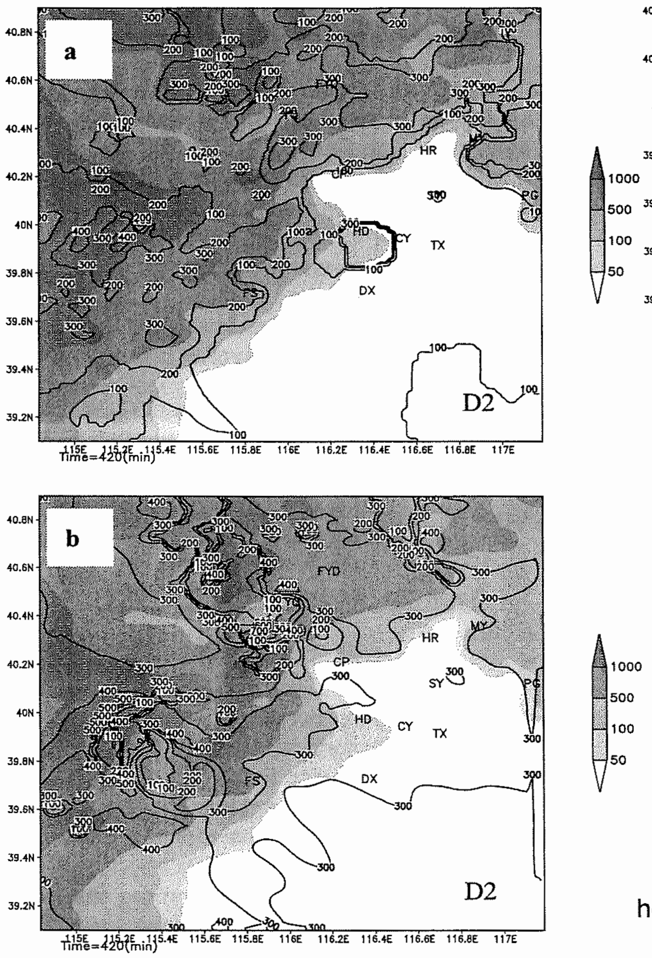

Fig.1The Horizontal distributions of sensible heat flux (solid lines) at a) the actual surface condition and b) urbanized surface condition for domain D2. (The terrain in model is shown as shaded region)

The further analyses of vertical velocity distribution for a cell shows that the velocity of central updraft decreases, and at the later stage, many weak non-precipitating convective cells are formed downwind of the urban area. The upper convection weakens and the lower convection strengthens, due primarily to the increase of surface roughness over land that enhances the lower convergence (figure omitted).

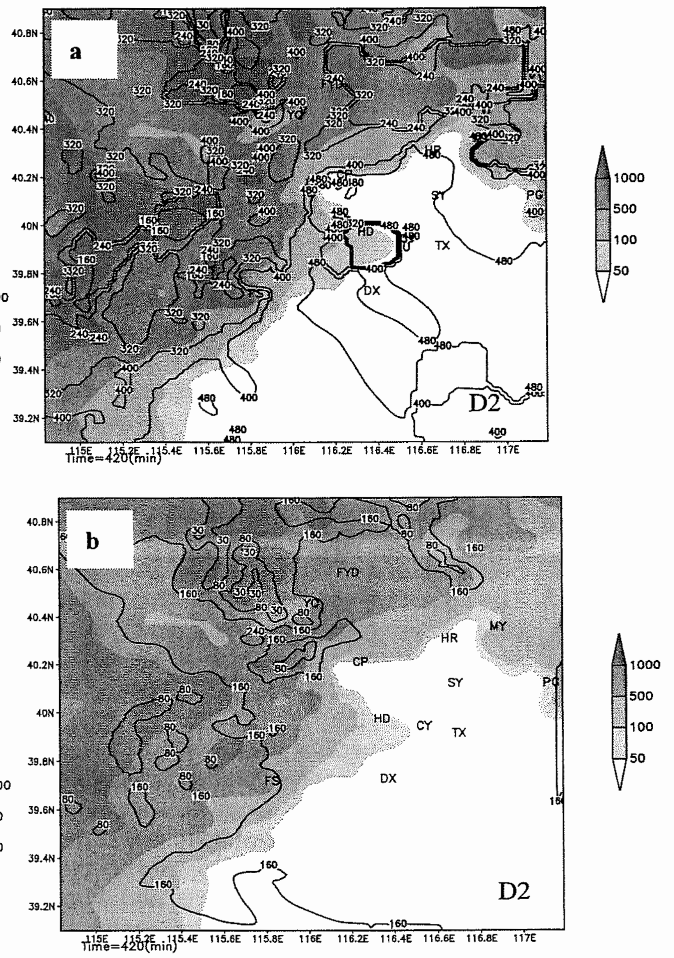

Fig. 2 Same as Fig. 1 except for the latent heat flux.

3.3 Precipitation at the surface

The accumulated precipitation at the surface is shown in Fig. 5. It shows that the amount of accumulated precipitation in the urbanized region is more than that non-urbanized region comparing Fig. 5a with Fig. 5b. The precipitation at the urban surface is primarily distributed along the borderline of urban and non-urban region. The maximum precipitation located near borderline for non-urbanized condition is 40 mm and 65 mm for the urbanized condition. Thus, the precipitation increases outside urbanized region and reduces in the urbanized region.

In order to further understand the evolution of rainfall path when the storm approaching to the urbanized region, the Fig. 6 shows the distribution of accumulated precipitation for urban and non-urban surface. It indicates that the path of rainfall tends to bifurcate, and its distribution disperses when approaching to the downtown region at the urbanized surface (Fig. 6b).

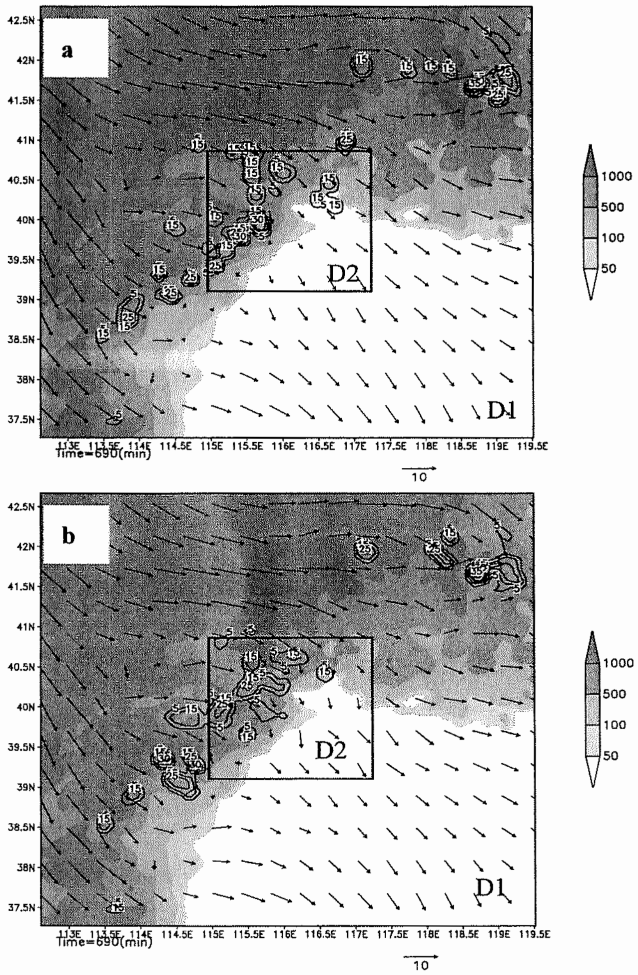

Fig. 3 The Horizontal distributions of radar echo (solid lines) at 500hpa for, a) the actual surface condition for both D1 and D2, and b) the urban surface condition for D2. (The terrain in model is shown as shaded region).

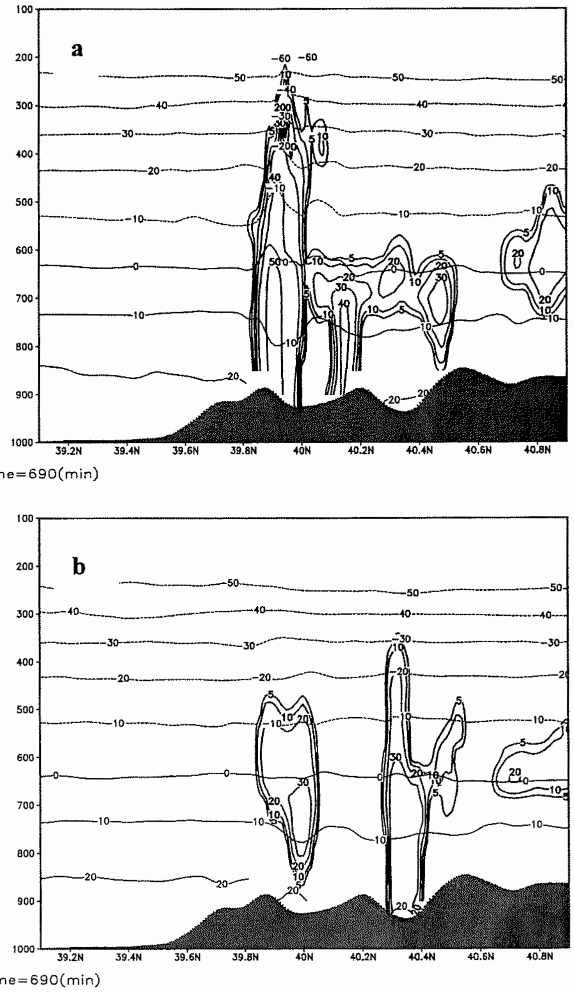

Fig. 4 Same as Fig. 3 except for the vertical distributions of radar echo.

3.4 Conclusions

The effects of urbanization on the cloud physical structure and precipitation in Beijing region are investigated by using the PSU/NCAR Mesoscale Modeling System (MM5). A severe convective cloud system on June 4, 2003 in Beijing was simulated based on actual ground surface and that modified by increasing land surface roughness length and albedo, and decreasing thermal inertia and moisture availability according to the urban surface characteristics. The results show that after the urbanization 1) the surface sensitive heat flux increases and concentrates, while the surface latent heat flux reduces, 2) the convective cells occur earlier and distribute dispersedly. The velocity of central updraft decreases, and at the later stage, many weak non-precipitating convective systems are formed downwind of the urban area, 3) the upper convection weakens and the lower convection strengthens, due primarily to the increase of surface roughness over land that enhances the lower convergence, 4) although the accumulated precipitation downwind of the Beijing city has a little increase, the total accumulated precipitation in the whole domain decreases remarkably. The path of rainfall tends to bifurcate, and its distribution disperses, 5) the mixing ratios of cloud water, rain water, ice and graupel lessens, and their distributions become dispersed.

3.5 Acknowlegements

This research was jointly sponsored by the Chinese Natural Science Foundation (Grant 40175001 and 40333033) and the CAS Innovation Foundation KZCX3-SW-213, and the Key Project of the Ministry of Science and Technology of China (Grant 2001BA610A-06).

3.6 References

Balling, R. C., and S. W. Brazel, 1987: Recent changes in Phoenix, Arizona, summertime diurnal precipitation patterns. Theor. Appl. Climatol., **38**, 50–54.

Bornstein, R., and Q. Lin, 2000: Urban heat islands and summertime convective thunderstorms in Atlanta: Three case studies. Atmos. Environ., **34**, 507–516.

Braham, R. R., 1976: Modification of clouds and weather by a large metropolitan area. Preprints, Second WMO Scientific Conference on Weather Modification, Boulder, CO, WMO, 435–442.

Changnon, S. A., 1981: METROMEX: A Review and Summary. Meteor. Monogr., No. **18**, Amer. Meteor. Soc., 181 pp.

Cotton, W. R., and Coauthors, 2003: RAMS 2001: Current status and future directions. Meteor. Atmos. Phys., **82**, 5–29.

Hjelmfelt, M. R., 1982: Numerical simulation of the effects of St. Louis on mesoscale boundary-layer airflow and vertical air motion: Simulations of urban vs non-urban effects. J. Appl. Meteor., **21**, 1239–1257.

Jaurequi, E., and E. Romales, 1996: Urban effects on convective precipitation in Mexico City. Atmos. Environ., **30**, 3383–3389.

Rozoff, C. M. and W. R. Cotton, 2003: Simulation of St. Louis, Missouri, land use impacts on thunderstorms, J. Appl. Meteor., **42**, 716-738

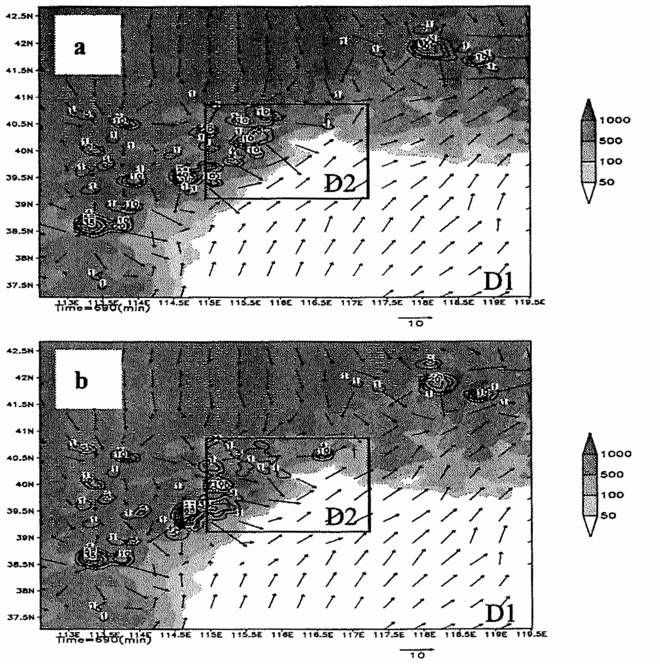

Fig. 5 Same as Fig. 3 except for the accumulated precipitation at the surface.

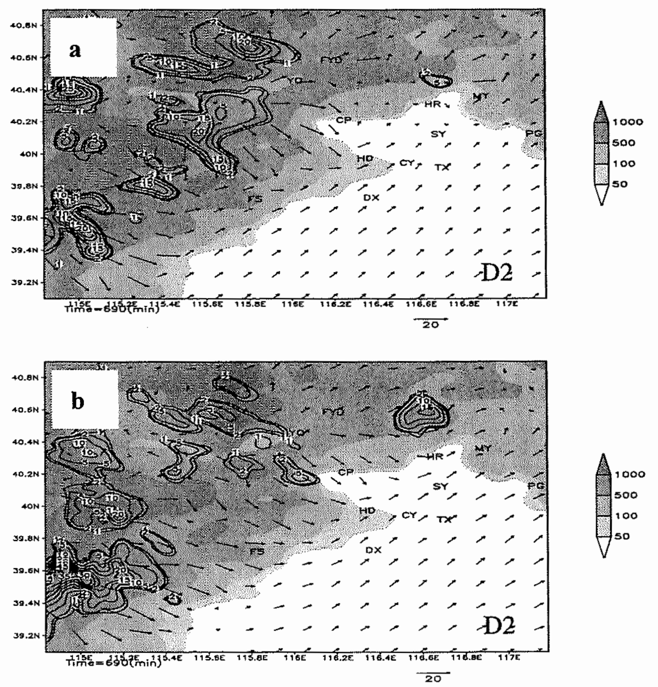

Fig. 6 Same as Fig. 2 except for the accumulated precipitation.

PARAMETERIZATION OF NON-INDUCTIVE CHARGE TRANSFER BASED ON DISCRIMINANT AND REGRESSION ANALYSES OF LABORATORY DATA

Anastasia Kirilova[1], Rumjana Mitzeva[2] and Boryana Tsenova[2]

[1] National Institute of Hydrology and Meterology, Sofia -1874, Bulgaria,
present affiliation OSMER-ARPA FVG,Visco(UD) - Italy,
working within the ICTP TRIL Program
[2]Department of Meteorology, Faculty of Physics, University of Sofia, Sofia-1164, Bulgaria

1. INTRODUCTION

It is now well accepted that the main charge separation mechanism in thunderstorms is the non-inductive. It occurs during vapor grown ice crystals and riming graupel pellets rebounding collisions. This mechanism has been studied in extensive laboratory experiments by Takahashi (1978, 2002), Saunders et al. (1991, 1998, 1999, 2001), Brooks et al. (1997), Pereyra et al. (2000), Berdeklis and List (2001) and others. One of the main goals of these experiments was to obtain information for the sign and magnitude of separated charge as it depends on in-cloud characteristics, which could be used in numerical models for parameterization of thunderstorm electrification. All the experiments showed that the sign and magnitude of separated charge depends on the liquid water content and the temperature in the laboratory cloud, but the relations were rather different among the various experiments. The reason for these differences is a subject of extensive laboratory and theoretical studies of the conditions, which govern the sign of the separated charge.

The tasks of the present study are:

- to test which properties of the ice particles surface are important for the sign of separated charge at rebounding collisions between riming graupel and ice crystals (even there is a consent that the sign and magnitude depend on surface properties, the ones governing the sign of charge transferred are still under discussion);
- to obtain equations for non-inductive charge transfer based on the results presented in Takahashi 1978, which could be used in numerical models of the development of thunderstorm electric fields.

The search of an equation is inspired from the fact that the most abundant data for non-inductive charging obtained in laboratory experiments by Takahashi (1978) are presented only on graph as isolines of the separated charge - function of the liquid water content *LWC* and the cloud temperature T_c . Using this data in numerical models as assigned is ungainly.

The results of discriminant analysis using different variables related to the existing hypotheses for the non-inductive charge transfer are presented and discussed in the present paper. The results of regression analysis will be presented at the Conference.

2. DATA AND RESULTS

The sample used at statistical analyses in this study is obtained by interpolation between isolines of charge values, function of liquid water content *LWC* and cloud temperature T_c, presented in Fig.1 in Takahashi (1978).

For the aim of our study, we used part of his sample. The data at *LWC* greater than 10 g m^{-3} and at T_c higher than –10 °C were excluded from the sample. This truncation is acceptable because in the real clouds the measured *LWC* is less than 10 g m^{-3} and at T_c> –10 °C there are no ice crystals and graupel, or their number is insignificant during the growth stage of thunderstorms when the non-inductive mechanism plays a major role in the formation of electric field. In such a way, the obtained equations will be valid at cloud temperature lower than –10 °C. The original data from Takahashi (1978) were reduced additionally – the cases when the charge of the graupel is 0 were taken out, based on the assumption that the charge is not exactly 0 but it has a very little positive or negative value that could not been measured with the device used in the experiment. As a result, the truncated sample used at our analysis

[1] Corresponding author's address: Anastasia Kirilova, Anastasiya.Kirilova@osmer.fvg.it

contains 532 charge values Q at temperatures between –10 °C and –30 °C and LWC between 0.01 and 10 g m^{-3}. The idea for data we have used gives Fig.1, where are shown isolines of charge transfer as a function of cloud temperature T_c and effective water content EW.

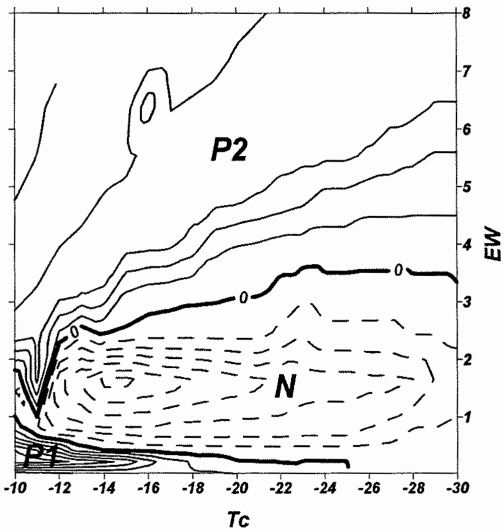

Fig.1. Charge as a function of effective water content EW and cloud temperature T_c for the sample used in the study. Solid lines – positive charge, dashed lines – negative charge.

The charge is positive at low (group ***P1***) and high (group ***P2***) EW and negative (group ***N***) at intermediate values of EW. The variables used in the discriminant analysis were:

- cloud temperature T_c and effective water content $EW=E_c.LWC$, where E_c is collision coefficient of cloud droplets and graupel;
- relative growth rate (RGR) of graupel and ice crystals size, motivated by the widely accepted hypothesis of Baker et al (1987) that the faster growing by vapor diffusion ice particles charges positively;
- the growth of graupel surface - the choice of this variable is based on the assumption (see Williams et al, 1991) that the growing by vapor diffusion graupel charges positively, while the sublimating graupel surface charges negatively;
- the difference dT in the graupel surface temperature T_g and the ice surface temperature T_c ($dT=T_g-T_c$). The choice of this variable was inspired by the assumption that the sign of separated charge depends on the temperature gradient (see Takahashi, 1978).

To be in line with Tahakahashi's (1978) experiment, the following values were used in the calculations of the above mentioned variables: graupel diameter D_g=3 mm, relative velocity V = 9m/s, size of cloud droplets r_{dr}= 8μm and E_c=0.8. It was also assumed that the cloud is saturated with respect to water. The graupel surface temperature was determined by Macklin and Payne (1967) equations. The RGR may be expressed as: $RGR = \alpha_1.(dR_g/dt)_f + \alpha_2.(dR_g/dt)_l - \alpha_3.(dR_c/dt)$, where $(dR_g/dt)_f$ is the graupel growth rate from the vapor field in the cloud far from graupel surface. $(dR_g/dt)_l$ is the graupel growth rate from the vapor released by the freezing of cloud droplets on the graupel surface and dR_c/dt is the growth rate of the crystals size. The size growth rate of the particles was determined through the calculations of the corresponding mass growth rate and by assumption that interacting particles are spherical. For more details, see Mitzeva et al. (2003).

Discriminant analyses using 2 samples were carried out. They contain the data of ***P1*** and ***N*** group and data of ***N*** and ***P2*** group. These separations (***P1/N*** and ***N/P2***) can help to reveal if the charge sign reversal (positive - negative ***P1/N*** at low values of EW and negative - positive ***N/P2*** at middle values of EW) is governed by the same variables.

Table 1. Results from discriminant analyses for **P1/N**

	P1	N	Tot	
1. $(dR_g/dt)_f$,$(dR_g/dt)_l$,dR_c/dt	88	79	84	$22.8(dR_g/dt)_f + 31.2(dR_g/dt)_l - dR_c/dt > 0.02$
2. $(dR_g/dt)_f$	94	48	74	$(dR_g/dt)_f > 0.0005$
3. $(dR_g/dt)_f$,$(dR_g/dt)_l$	95	57	78	$(dR_g/dt)_f + 0.47(dR_g/dt)_l > 0.001$
4. dT	98	64	83	$dT < 1.34$
5. EW,T_c	100	68	86	$0.04T_c - EW > -1.24$

In Table 1 and Table 2 are presented as follows: first column - the variables used for the discrimination of the sample; columns 2 and 3 - the percent of the properly classified cases for the corresponding groups; column 4 – the properly classified cases in percents for the whole sample; column 5 – the conditions at which the graupel would be charged positively. The results show that all of the used variables are appropriate for the discrimination of the positive and the negative charge.

Table 2. Results from discriminant analyses for **N/P2**

	N	P2	Tot	
1. $(dR_g/dt)_f, (dR_g/dt)_l, dR_c/dt$	98	98	98	$-2(dR_g/dt)_f + 8(dR_g/dt)_l - dR_c/dt > 0.01$
2. $(dR_g/dt)_f$	100	77	90	$(dR_g/dt)_f < 0.009$
3. $(dR_g/dt)_f, (dRg/dt)_l$	96	92	95	$-(dR_g/dt)_f + 4.67(dR_g/dt)_l > 0.036$
4. dT	100	95	98	$dT > 6.2$
5. EW, T_c	100	96	98	$0.05T_c + EW > 2.24$

The transition between negative and positive charge at higher *EW* (**N/P2**) is better discriminated than the transition between positive charge at low values of *EW* and negative charge (***P1/N***) - see the third column in the Tables. The analyses show that for the sample ***P1/N*** the variables based on relative growth rate (see row 1 in the Table 1) are better discriminator than the growth/sublimation of graupel surface (see row 2 and 3 in the Table1) - 84% of the cases were correctly classified using RGR and 78% when the growth of graupel from the both far and local vapor field is used.

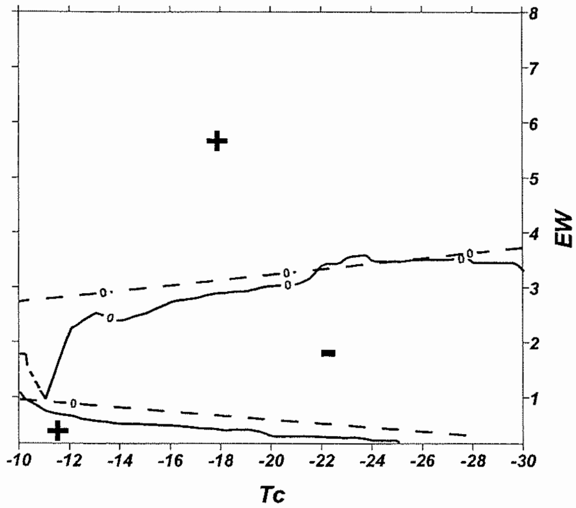

Fig.2. Sign reversal lines: bold line – Takahashi's 1978 experiment; dashed line - functions, based on *EW* and T_C from rows 5 in Table 1 and Table 2 .

All the variables are excellent discriminators in the case of ***N/P2*** reversal - more than 90 % of the cases were properly classified (see Table 2). The analyses showed that based on the equations for ***P1/N*** reversal one can conclude that both RGR and growth/sublimation hypotheses are valid and that one can not make a direct conclusion for the validations of this hypotheses in the case of ***N/P2*** reversal. For the both samples (***P1/N*** and ***N/P2***) *EW* and T_c can be used for the determination of the charge reversal - see the results in the last column of Tables for *EW* and T_c and *Fig.2.*

3. CONCLUSION

Based on discriminant analysis the present study shows that both the relative growth rate and the growth/sublimation hypotheses are valid for the description of charge reversal from positive at low *EW* to negative charge for the laboratory data in Takahashi (1978) - graupel acquire positive charge when it grows faster than ice crystal and when its surface is growing.
Using the growth rate of graupel from far and local field and growth rate of ice crystals the best discriminations of the sign of charge for sample **N/P2** is obtained. The very high percent of properly classified cases using effective water content and cloud temperature show that the classification functions based on *EW* and T_c (last row in Table 1 and Table 2) could be used for parameterization of the sign of separated charge in numerical models of thunderstorm.

The results of regression analyses for the determination of magnitude of separated charge will be presented at the Conference.

4. REFERENCES

Baker, B., Baker, M. B., Jayaratne, E. J., Latham J., Saunders, C. P. R., 1987. The influence of diffusional growth rates on the charge transfer accompanying rebounding collisions between ice crystals and soft hailstones. Quart. J. Roy .Met. Soc., 113, 1193-1215.

Brooks M., C. P. R. Saunders, R. P. Mitzeva and S. L. Peck, 1997, The effect on thunderstorm charging of the rate of rime accretion by graupel. J. Atmos. Res, 43, 277-295,.

Berdeklis, P., R. List,.2001, The ice crystal – graupel collision charging mechanism of thunderstorm electrification, *J. Atm. Sci.*, **58**

Mitzeva R, B Tsenova and C P R Saunders, 2003**:** A modelling study of the effect of cloud supersaturation on non-inductive charge transfer in thunderstorm electrification, Proceedings 12 th International Conference on Atmospheric Electricity, 9-13 June 2003, Versailles, France p.235-238.

Macklin and Payne, 1967, A theoretical study of the ice accretion process, 551.574.14:551.578.71

Pereyra, R. G., Avila, E. E., Castellano, N. E., Saunders, C. P. R., 2000. A laboratory study of graupel charging. J. Geophys. Res., 105, 20,803-20,812.

Saunders, C. P. R., W. D. Keith and R. P. Mitzeva, 1991, The effect of liquid water on thunderstorm charging, J. Geophys. Res., 96, 11,007-11017.

Saunders, C. P. R., Peck, S. L., 1998. Laboratory studies of the influence of the rime accretion rate on charge transfer during crystal/graupel collisions. J. Geophys. Res., 103, 13,949-13,956.

Saunders, C. P. R., Avila, E. E., Peck, S. L., Castellano, N. E., Aguirre Varela, G. G., 1999. A laboratory study of the effects of rime ice accretion and heating on charge transfer during ice crystal/graupel collisions. Atmos. Res., 51, 99-117.

Saunders, C. P. R., Peck, S. L., Aguirre Varela, G. G., Avila E. E., Castellano, N. E., 2001. A laboratory study of the influence of water vapour and mixing on the charge transfer process during collisions between ice crystals and graupel. Atmos. Res., 58, 187-203.

Takahashi, T., 1978, Riming electrification as a charge generation mechanism in thunderstorms. J. Atmos. Sci., 35, 1536-1548.

Takahashi, 2002, Reexamination of riming electrification in a wind tunnel, J. of Atmospheric Sciences, 59, 1018-1024

Williams, E., R. Zhang and J. Rydock, 1991, Mixed phase microphysics and cloud electrification, J. Atmos. Sci, 48, 2195 -2203.

SIMULATION OF CONVECTIVE SYSTEMS USING MESOSCALE MODEL WITH SPECTRAL MICROPHYSICS

B. Lynn[1], A. Khain[1], A. Pokrovsky[1], D. Rosenfeld[1], A. Seifert[2]

[1]The Institute of Earth Sciences, the Hebrew University of Jerusalem

[2]National Center for Atmospheric Research, USA

1. INTRODUCTION

There is a limited number of 3-D models with mixed-phase spectral microphysics (e.g., Ovtchinnikov and Kogan 2000). These models have a small computational area and are used for the simulation of individual clouds. No topography, as well as no effects of surface fluxes are taken into account in these models. Environmental conditions are usually considered unchanged in these simulations. At the same time both single clouds and cloud-related meteorological phenomenon developing over a large area are crucially affected by topography, surface fluxes and time variations of environmental conditions. Clouds interact with each other, which leads to the formation of regular cloud structures like squall lines. Primary clouds change the concentration of cloud condensation nuclei (CCN) affecting development of secondary clouds. All these factors determine intensity, spatial and time distribution of precipitation, its type (e.g. convective vs. stratiform, warm rain v.s. ice precipitation). We present results of simulation of a mesoscale rain event using the first mesoscale model with spectral microphysics.

2. MODEL DESCRIPTION

Model dynamics: The non-hydrostatic Mesoscale Modeling System, Generation 5, MM5 was chosen as the dynamical platform for the spectral (bin) microphysics (Dudhia, 1993). The standard model predicts the wind components, temperature, mixing ratios for water vapor, cloud water/ice and rain/snow (using bulk parameterizations), and a pressure perturbation. The model uses a terrain-following sigma coordinate with the highest vertical resolution closest to the ground surface.

Model microphysics. The microphysical package of the two-dimensional Hebrew University Cloud Model (HUCM) (Khain et al., 1999, 2000, 2001) was implemented into the MM5. The microphysics is based on solving an equation system for size-distributions of water droplets, three types of ice crystals, graupel, snow (aggregates), hail/frozen drops, as well as aerosol particles. Small ice particles were assigned to ice crystals, while large ice particles were assumed to be graupel, snowflakes (aggregates) and hail. We assume three types of crystals, and three types of large particles. As a result, instead of six size distributions used in HUCM for the description of cloud ice, only three size distribution functions are used. This modification shortens the computational time and is referred to as SBM Fast.

A specific feature of the model is the existence of an aerosol budget. The concentration of CCN decreases during the process of droplet formation and precipitation. The model takes into account the main microphysical processes of droplet nucleation, primary and secondary ice generation, condensational growth of droplets and ice, evaporation of droplets and sublimation of ice, freezing and melting, collisions between all types of cloud hydrometers and between all possible sizes of the cloud particles, and sedimentation of particles with different velocities depending on their type, size and height (air density). The increase in the collision rate due to effects of turbulence on particle collisions is also taken into account. A description of collision breakup has also been implemented (Seifert et al. 2003).

Bulk-microphysics schemes. Currently, the most advanced bulk microphysics options in MM5 consist of those labeled in MM5 as "GSFC" (Tao et al., 2003), "Reisner2" (Reisner et. al., 1998), and "Schultz" (Schultz 1995). Most schemes predict cloud, rain water, snow, graupel, and ice crystal mass contents. Marshall-Palmer distributions are used for rain, snow and graupel.

3. CASE STUDY AND EXPERIMENT DESIGN

The convective development that occurred on 27th of July 1991 over Florida was accompanied by squall line formation. The purpose of simulations was to a) represent the case study, and b) to compare the results obtained with new precise microphysics

*Communicating author: Alexander Khain, The Institute of Earth Sciences, The Hebrew University of Jerusalem, Givat Ram, Jerusalem 91904, Isarel, 972-2-6585822, khain@vms.huji.ac.il

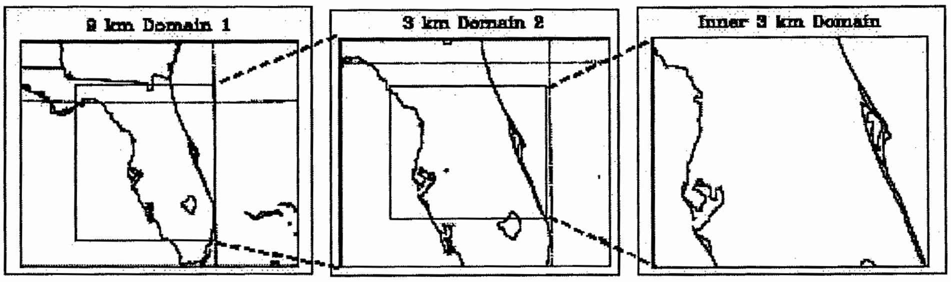

Fig. 1 Geometry of nested grids. Spectral microphysics is used within the finest grid.

with those obtained using traditional schemes of cloud microphysics parameterization. The model was run on a 3 km grid domain and other simulations were produced to test the sensitivity of the model results to various physical processes and the bulk parameterization chosen. The model grid geometry (**Fig. 1**) consists of a coarse domain (9 km) and nested (3 km) domain each centered over Florida. The coarse domain covered 900 km in the west to east direction and 756 km in the north to south direction. The coarse domain was used to generate lateral boundary conditions for the nested domain that covered 552 km east to west and 480 km north to south. Within the outer most domain, the model was integrated with a time step of 27 seconds. It was run from 0 UTC 27 July 1991 to 1 UTC 28 July 1991. The nested domain was run separately (one way interaction) with a time step of nine seconds from hours 10 to 25. Both the coarse and nested domain had 35 atmospheric layers. Calculations with spectral microphysics were performed for low (maritime) and high (continental) CCN concentrations.

4. RESULTS OF SIMULATIONS

Figure 2 shows a histogram of observed and calculated radar reflectivity. The calculations were conducted using a known parameterization formulae (referred to as "Bulk"). In SBM run, radar reflectivity was calculated also according to its definition (as proportional to 6-th power of particle radius). In Fig. 2 this reflectivity is referred to as "Bin". One can see that SBM Fast appears to produce the best distribution of radar reflectivity. **Figure 3** shows average and maximum rain amounts obtained at each hour for SBM, GSFC, Reisner2, and Schultz. The average precipitation is the mean from all observing sites (mostly in East Florida). The maximum precipitation refers to the highest recorded rainfall from any of these data recording sites. All simulations produced too much rain (observed value is 0.88 cm). However, SBM produced less overall

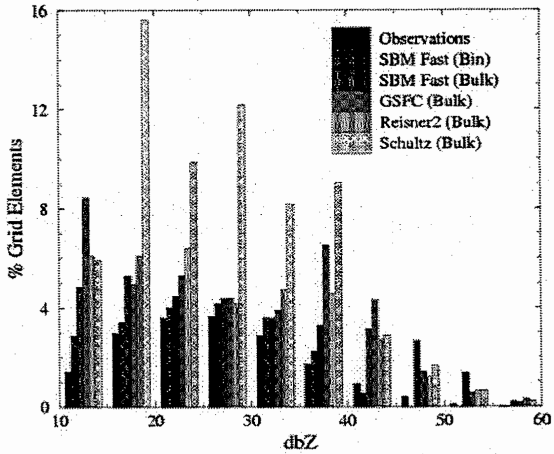

Fig. 2. Histogram of observed and simulated radar reflectivity for SBM FastM, Reisner2, GSFC, and Schultz.

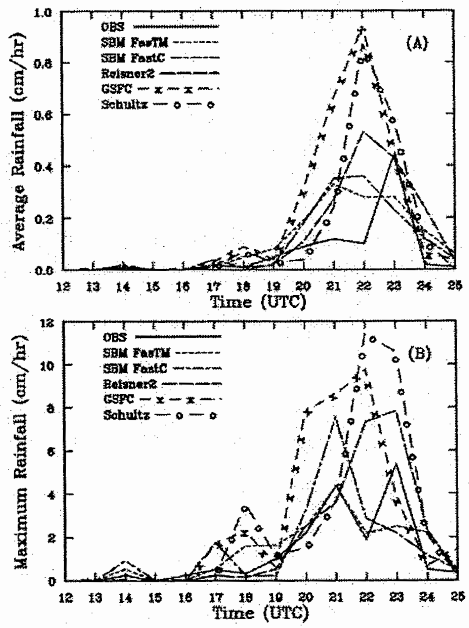

***Fig. 3.** Average and maximum rain amounts obtained at each hour for SBM, GSFC, Reisner2, and Schultz.*

accumulated rain (1.37 cm) than Reisner2 (1.63 cm), GSFC (2.65 cm), and Schultz (1.94 cm). Overall SBM Fast produced the most realistic time dependence of average and maximum rain.

Fig. 4 indicates that SBM reproduces the structure of the accumulated rain much more realistically than bulk parameterizations. Unlike the SBM simulations, none of the bulk schemes produced the extensive

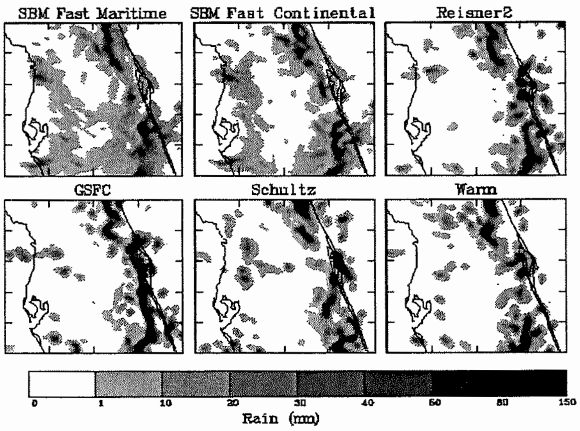

Fig. 4. Accumulated rain obtained during 21 to 24 UTC for the model simulations.

stratiform rain. Significant differences in the structure of clouds simulated in SBM and bulk microphysics are seen in Figures 5-7.

One can see that SBM model simulates clouds of different height and structure. Small and stratiform clouds are clearly seen. Bulk parameterization simulates mainly deep convective clouds resembling columns.

Figure 7 shows ice crystal contents simulated by SBM and Reisner2 schemes. One can see that Reisner2 produced a lot of ice in the upper troposphere, which covered a significant fraction of Florida. We suppose that such a large area covered by ice can hardly be realistic. Besides, it is a quite unrealistic feature of the bulk parameterization that the intensive production of the upper troposphere ice (that does not contribute to precipitation) is accompanied by overestimation of rain rate and rain amount. Note that all bulk parameterizations tested produce similar cloud structures. We mention, though, that Reisner2 scheme showed the best result among other bulk parameterization schemes.

5. SUMMARY AND CONCLUSIONS

A novel mesoscale model with spectral microphysics has been developed. The model has no analogs at present. The model was tested for a convective mesoscale precipitating system accompanied by a squall line formation.

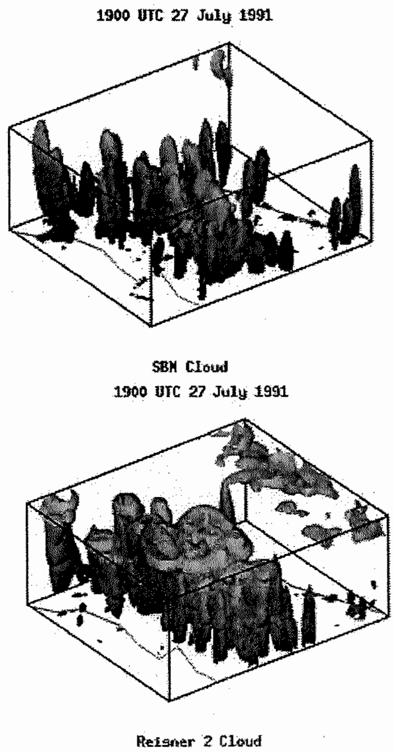

Fig. 5. Total mass content in SBM and Reisner2

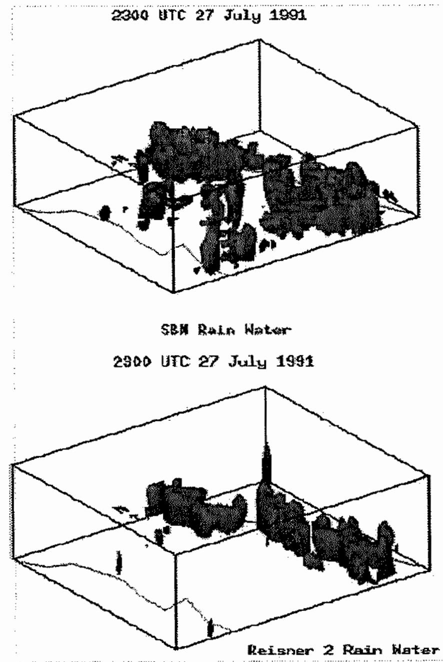

Fig. 6. Rain water content in SBM and Reisner2

2300 UTC 27 July 1991

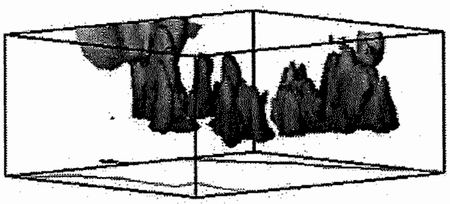

SBM Ice

2300 UTC 27 July 1991

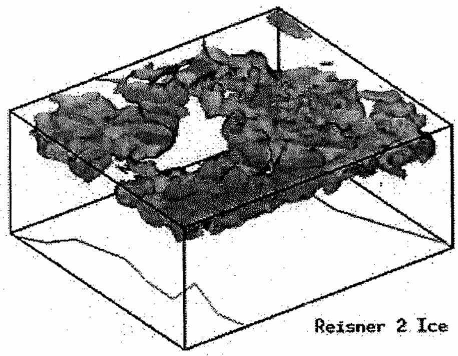

Fig. 7. Ice content in SBM and Reisner2

Results obtained using SBM model were compared with those obtained using different bulk-parameterization schemes. *Significant improvement in reproduction of mean and maximum rain, as well as in spatial distribution of precipitation is obtained.* SBM model represents realistically relationships between areas covered by convective and stratiform clouds. The spatial distribution of simulated radar reflectivity was also more realistic than the results obtained using bulk microphysics. SBM realistically reproduces cloud structure and cloud shape. In supplemental runs it is also shown that aerosols influence cloud microphysics, dynamics and precipitation. Further investigations of aerosol effects require better model resolution.

Bulk microphysics formulations over predict rainfall maximum amounts, and significantly underestimate the area covered by stratiform clouds.

We believe that the mesoscale model with spectral bin microphysics can be successfully used for simulation of severe storms over complex terrain, winter storms, investigation of cloud-aerosol effects, cloud seeding, as well as other processes related to the change of droplet size distribution. Besides, the SBM mesoscale model can be used for verification and calibration of new bulk-parameterization schemes.

Acknowledgements

This study was supported by Binational US-Israel Science foundation (grant 2000215), The Israel Water Company (Scaham), and the European Projects EURAINSAT and SMOCC.

References

Dudhia, J., 1993: A nonhydrostatic version of the Penn State/NCAR mesoscale model: Validation tests and simulation of an Atlantic cyclone and clod front. Mon. Wea. Rev., **121**, 1493-1513.

Khain, A. P., A. Pokrovsky, and I. Sednev, 1999: Effects of cloud-aerosol interaction on cloud-microphysics, precipitation formation and size distribution of atmospheric aerosol: numerical experiments with a spectral microphysics cloud model. Atmos. Res., **52**, 195-220.

Khain, A. M. Ovtchinnikov, M. Pinsky, A. Pokrovsky, and H. Krugliak, 2000, Notes on the state-of-the art numerical modeling of cloud microphysics. Atmos, Res., **55**, 159-224.

Khain A. P., D. Rosenfeld and A. Pokrovsky, 2001: Simulation of deep convective clouds with sustained supercooled liquid water down to –37.5 C using a spectral microphysics model. Geo. Res. Letters, 3887-3890.

Ovtchinnikov, M. and. Kogan, Y. L, 2000: An Investigation of Ice Production Mechanisms in Small Cumuliform Clouds Using a 3D Model with explicit microphysics. Part I: Model description, J. Atmos. Sci., **57**, 3004–3020.

Reisner, R. , R. M. Rasmussen, and R. T. Bruintjes, 1998: Explicit Forecasting of Supercooled Liquid Water in Winter Storms Using the MM5 mesoscale model. Q. J. Roy. Meteorol. Soc., **124**, 1071-1107.

Seifert A, K. Beheng and A. Khain, 2003: Collisional breakup in HUCM and comparison with observations (submitted).

Schultz, Paul, 1995: An Explicit Cloud Physics Parameterization for Operational Numerical Weather Prediction. Mon. Wea. Rev. **123**, 3331–3343.

Tao, W.-K., J. Simpson, D. Baker, S. Braun, D. Johnson, B. Ferrier, A. Khain, S. Lang, C.-L. Shie, D. Starr, C.-H. Sui, Y. Wang and P. Wetzel, 2003: Microphysics, Radiation and Surface Processes in a Non-hydrostatic Model, Meteor. Atmos. Physics, **82**, 97-137.

THE INFLUENCE OF RAINDROP CLUSTERING ON NEW REPRESENTATIONS OF COLLISION-INDUCED BREAKUP: IMPLICATIONS FOR RAINDROP SIZE DISTRIBUTIONS

Greg M. McFarquhar

University of Illinois at Urbana-Champaign, Urbana, IL

1. INTRODUCTION*

Recent observations (Jameson and Kostinski 2000; Shaw et al. 2002) have suggested that raindrops and cloud droplets may be clustered, indicating that regions both rich and deficient in concentrations exist. Jameson and Kostinski (2002) note that pure Poissonian or steady rain is likely rare, if it exists at all. Such observations have been used to develop mathematical representations of the spatial and temporal distributions of cloud and precipitation particles, including the pair correlation function and the pair cross-correlation function, as summarized by Shaw et al. (2002).

Since collision-induced breakup of raindrops is a major factor controlling the temporal and spatial evolution of raindrop size distributions (RSDs), the influence of clustering on the frequency of raindrop collisions may affect the evolution of RSDs. In this study, impacts of clustering on raindrop mean free paths, mean times between raindrop collisions, and raindrop collision rates are examined using prior observations of raindrop pair cross-correlation functions. The effects of the increased collisions and of new representations of the fragment-size distributions produced by collision-induced breakup of raindrops on modeled RSDs are then examined.

2. CLUSTERING EFFECTS ON COLLISIONS

On the basis of geometrical sweep out and assuming a collection efficiency of 1, it can be shown that $\tau(D_L,D_S)$, the average time traveled by a large drop D_L falling at speed V_L between collisions with a drop of a smaller diameter D_S falling at speed V_S, is given by

$$\tau(D_L,D_S)=\frac{4}{N_S\pi(V_L-V_s)(D_L+D_s)^2} \quad (1)$$

where N_S is the number density of drops with size D_S. Eq. (1) implicitly assumes that raindrops are distributed according to Poisson statistics, and that the probability of finding a raindrop D_S in the volume dV swept out by the D_L raindrop is given by $N_S dV$ because the locations of two raindrops are assumed uncorrelated.

In a more general sense, following Jameson and Kostinski (2000), the joint probability $P(D_L,D_S)$ of finding the large and small raindrops in volumes dV_L and dV_S is given by

$$P(D_L,D_S)=N_S N_L dV_S dV_L\left[1+\Omega(t,D_L,D_S)\right] \quad (2)$$

where N_L is the number density of drops with size D_L, and $\Omega(t,D_L,D_S)$ is the pair cross-correlation function describing how the distributions of D_L and D_S drops are related, and is a modification of the pair correlation function η which describes the correlations for drops of a specific size. The parameter t represents the time separation between the two volumes.

To determine the mean free time between raindrop collisions, τ, the probability that a single raindrop size D_L suffers a collision with a raindrop sized D_S between t and $t+dt$, $w(t)$, must be known and is expressed by

$$w(t)dt=\frac{\pi N_S}{4}(D_L+D_S)^2(V_L-V_S)(1+\Omega(t,D_L,D_S))dt \quad (3)$$

where $\pi(D_L+D_S)^2/4\ (V_L-V_S)dt$ is the geometric volume swept out in time interval dt, and $N_S(1+\Omega(t,D_L,D_S))$ is the number of small drops contained in the swept out volume.

To calculate τ, the first moment of the probability function, must be integrated from 0 to ∞ and is given by

$$\tau=\int_0^\infty P(t)tdt=\int_0^\infty\left\{\exp\left[-\int_0^t X(1+\Omega(t'))dt'\right]\right\}X(1+\Omega(t))tdt,$$

$$X=\frac{\pi N_S}{4}(D_L+D_S)^2(V_L-V_S) \quad (4)$$

To simplify notation, the dependence of Ω on D_L and D_S is no longer written, but is implicitly assumed. The solution of Eq. (4) depends on the functional dependence of Ω on time t and simplifies to Eq. (1) when Ω is 0. Because theoretically based values are not available, observations are used to predict Ω.

Using observations of raindrop arrival measured by a two-dimensional video disdrometer at the ground, Jameson and Kostinski (2000) examined the dependence of η on lag for 3 sizes of raindrops (0.625, 1.125, and 2.125 mm) and of Ω on lag for drop sizes of 0.625 and 2.125 mm. Their Fig. 7 showed that Ω(0.625, 2.125 mm) varied from approximately 1.5 for small time lags to around 0.25 for lags approaching 20 seconds. A linear fit of Ω (0.625, 2.125 mm) in terms of temporal lag was constructed (figure not shown), and is given by

$$\Omega(t)=\begin{cases}\Omega_0-mt, t<\Omega_0/m\\ 0, t\geq\Omega_0/m\end{cases}, \quad (5)$$

where $\Omega_0 = 1.3$ and $m = 0.055\ s^{-1}$ fit the data reasonably well. There is a conditional dependence in Eq. (5) depending on time lag because raindrop interarrival times become essentially uncorrelated for larger lags, and this cannot be represented in the context of this linear fit.

An analytic solution to Eq. (4) cannot be easily obtained when Eq. (5) is substituted for $\Omega(t)$. But, a numerical solution to Eq. (4) can determine how clustering affects mean free collision times and collision rates. The definite integral in Eq. (4) is divided into two separate integrals because of the conditional dependence in Eq. (5), and simplifies to

$$\tau=\int_0^{\Omega_0/m}\exp\left[-Xt\left(1+\Omega_0-\frac{m}{2}t\right)\right]Xt(1+\Omega_0-mt)dt+\exp\left[-X\left(\frac{\Omega_0}{m}+\frac{\Omega_0{}^2}{2m}\right)\right]\left[\frac{1}{X}+\frac{\Omega_0}{m}\right]$$

(6)

* Corresponding Author: Prof. McFarquhar, University of Illinois, Dept. of Atmospheric Science, 105 S. Gregory Street, Urbana, IL, 61801.

The exponential factor in the second term is related to the probability that a raindrop survives to a time Ω_0/m without experiencing a collision. Simpson's rule is needed to integrate the integral on the right in Eq. (6).

The solution of Eq. (6) is more physically meaningful when the mean free time between a collision of drop D_L with drops of sizes between D_S and D_S+dD_S, $\tau(D_L,D_S:D_S+dD_S)$, is calculated. This is determined by solving Eq. (6) with X given by

$$X = \frac{\pi N(D_S)dD_S}{4}(D_L + D_S)^2(V_L - V_S) \qquad (7)$$

The mean free path between raindrop collisions, $\lambda(D_L,D_S:D_S+dD_S)$, is subsequently expressed by $\lambda(D_L)=V(D_L)\tau(D_L)$, where $N(D_S)$ is now the number density distribution of raindrops of size D_S (units per unit volume per unit bin width). Eq. (7) can also be integrated for D_S between 0 and ∞, with the resulting X substituted into Eq. (6) to give the mean free time for a drop D colliding with any other size of raindrop, henceforth represented as $\tau(D)$. In this case, collisions of raindrops of size D with larger or smaller raindrops can occur.

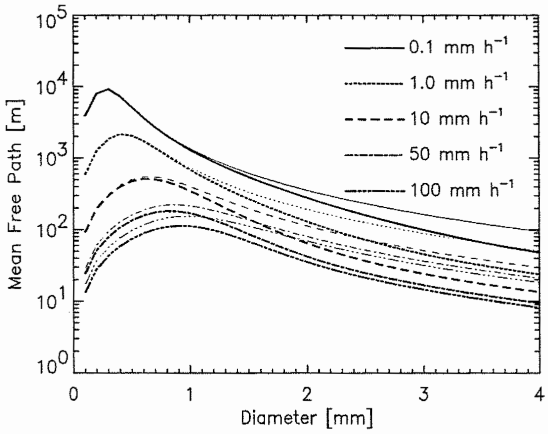

Figure1: λ as function of diameter, different lines representing calculations assuming MP distributions with varying R. Thick lines indicate effects of clustering included in calculations, thin lines indicate calculations that do not include clustering.

3. RESULTS

To calculate effects of clustering on collision statistics, calculations with varying RSDs and Ω are performed. Figure 1 shows the mean distance traveled by a raindrop of varying size between collisions with raindrops having any other size, λ, assuming the presence of a Marshall-Palmer (MP) distribution with varying rain rate (R). Calculations with and without raindrop clustering are shown. For a relatively high R of 50 mm h^{-1}, λ varies from about 9 m to 182 m depending on the raindrop diameter, with smaller and larger raindrops experiencing more collisions in a given distance of fall than medium size drops. The shape of the λ-D curve is determined by the RSD and by the dependence of fall velocity on D.

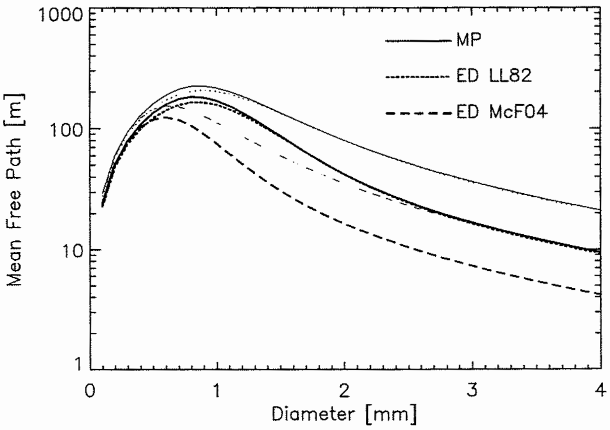

Figure 2: λ as function of diameter, different lines represent different RSDs. LL82 represents equilibrium distribution derived from Low and List (1982) breakup formulation, McF04 from McFarquhar (2004). Thick lines indicate λ includes effects due to clustering, thin lines indicate calculations do not.

The effect of clustering on λ, seen by comparing thick and thin lines that do and do not include effects of clustering on the calculation of λ respectively, is most significant for large raindrops and for distributions with heavier R. Clustering does not have much impact on λ for smaller raindrops or lighter R. This occurs because small raindrops fall more slowly than large drops, meaning greater times pass between collisions of small drops given the same fall distance as larger drops. Because the cross-correlation function and hence the amount of clustering is assumed to decrease linearly with time lag, the same fall distances correspond to large fall times for the small drops, and for these large times Ω approaches zero.

Figure 2 illustrates the dependence of λ-D curves on the assumed RSD, where the scale is contracted compared to that in Fig. 1. The MP distribution and two distributions obtained from numerical models, the three-peak distribution of List and McFarquhar (1990), and an equilibrium distribution derived using a new representation of Low and List's (1982) collision breakup experiments (Section 4) are used to compute λ. All RSDs have the same mass concentrations (2.33 g m^{-3}, roughly corresponds to rain rate 50 mm h^{-1}), however, other moments of the distributions differ.

As in Fig. 1, clustering has the biggest impact on λ for large raindrops. There is essentially no difference between λ calculated for the MP distribution and that with the Low and List (1982) formulation. However, λ calculated using the RSD corresponding to

McFarquhar's (2004) breakup kernel differs from the others. This occurs because the total number concentration of raindrops is $8.6x10^3$ m^{-3} in McFarquhar's (2004) distribution, whereas the MP and LL82 distributions have total concentrations of $4.0x10^3 m^{-3}$ and $4.1x10^3$ m^{-3} respectively. In Fig. 2, λ differs most for larger raindrop sizes, mainly because there are more small raindrops for the large raindrops to collide with when the McFarquhar (2004) distribution is assumed. In this case, λ can be as low as 4.8 m and τ (figure not shown) as low as 0.55 s for 4 mm raindrops.

The effects of using different representations of observed size distributions, besides MP distributions, on calculations of λ were also computed. Effects were similar to those shown in Fig. 2, where distributions with similar number concentrations have less difference in λ compared to those that show greater variation in total number.

4. NUMERICAL MODELS

From the opposing forces of coalescence and breakup, numerical models of warm rain suggest that an equilibrium RSD is approached given sufficient evolution time. In this section, an examination is made on how raindrop clustering affects the time required to approach this equilibrium distribution and of how new parameterizations of collision-induced raindrop breakup affect the form of this equilibrium distribution.

A new parameterization is developed to describe the fragment-size distribution generated when two raindrops of arbitrary size collide using Low and List's (1982) experimental observations of collision-induced breakup. Three shortcomings of the original scheme, developed by Low and List (1982) based on the same data, are alleviated: namely mass conservation is ensured, adequate uncertainty analysis is used, and more physical basis is used for derivation of the parameterization coefficients.

Combinations of lognormal, Gaussian, and modified delta distributions are used to represent the fragment size distributions generated by raindrop collisions for each of the three breakup types (filament, sheet, and disk) observed. The mode, width, and height of these distributions are calculated for the 10 colliding drop combinations used in the Low and List (1982) experiments; uncertainty estimates for these parameters are determined using a bootstrap method, a technique that randomly chooses results of individual collisions. Relations giving the mode, width, and height in terms of the diameters of the colliding raindrops are then determined so that the fragment size distribution from any raindrop collision can be predicted.

Modeling studies are performed to examine the time evolution of RSDs and approach to equilibrium. The overall equation for the evolution of the RSD is expressed by the quasi-stochastic coalescence/breakup equation

$$\frac{dn(m,t)}{dt} = \int_{m/2}^{\infty} \int_{m-x}^{x} K(m;x,y)n(x,t)n(y,t)dydx \qquad (8)$$

where n(m,t) now represents the number density distribution of raindrops in mass coordinate and K(m;x,y) the kernel which describes the mean number of fragments of sizes m to m+dm produced or lost by a single collision between drops of masses x and y. The kernel is given by $K(m;x,y) = [E_{bu}P(m;x,y) + E_{coal}\,\delta(m-x-y) - \delta(m-x) - \delta(m-y)]\ C(x,y)$, where E_{coal} is the coalescence efficiency, $E_{bu}=1-E_{coal}$ the breakup efficiency, C(x,y) the volume swept out per unit time, and P(m;x,y) the breakup function in mass coordinates derived above.

The zero dimensional box model of List and McFarquhar (1990) is used to simulate the evolution of the RSD, starting from a MP distribution with rain rate 54 mm h^{-1}. There are 40 size bins logarithmically spaced, with the smallest bin centered at 0.06 mm and the largest at 5.2 mm. Time steps of 1 s ensure that no numerical instabilities occur. Further increases in size resolution did not affect the results. After sufficient time, an equilibrium distribution is approached, the shape of the distribution not depending upon the initial size distribution.

Figure 3 compares the shape of this equilibrium distribution, henceforth called the base ED, against the three-peak distribution generated from the original Low and List (1982) breakup kernel, henceforth called the 3PED, and the MP distribution. The size distributions are plotted as number density per logarithmic coordinate, a(l), and exaggerate the size of the peaks. The nature of the base ED, with peaks at 0.26 and 2.3 mm, differs from the 3PED, which had three peaks at diameters of 0.26, 0.91, and 1.8 mm. The peak of small drops for the base ED is also substantially larger and broader compared to that of the 3PED. Simulations that produced equilibrium distributions from consideration of only specific breakup types showed that filament breakups were mainly responsible for the production of the peak at 0.26 mm, and that the small drop peaks associated with sheet and disk breakup had too small of an amplitude compared to the small drop peak produced by filament breakup and occurred at diameters separated too far from each other to produce a third peak as seen in the 3PED.

There are substantial differences in total number of raindrops, N, for the base ED ($8.6x10^3$ m^{-3}) to N associated with the 3PED ($4.1x10^3$ m^{-3}); however, differences in R (51.1 to 50.5 mm h^{-1}) and radar reflectivity factor, Z, ($4.7x10^4$ compared to $3.5x10^4$ mm^6 m^{-3}) are less significant. Large differences between Z and N values associated with the MP distribution ($8.0x10^4$ mm^6 m^{-3} and $4.0x10^3$ m^{-3}) also exist. Bimodal distributions with peaks at 0.26 mm and 2.3 mm are consistently realized in a series of Monte Carlo simulations, where fit coefficients are randomly chosen from the surface of equally realizable solutions, but the height of the small drop peak can vary from 5.1×10^3 to 1.2×10^4 m^{-3} per logarithmic coordinate, and that of the large drop peak from 4.2×10^2 to 6.7×10^2 m^{-3} per logarithmic coordinate. Although N can vary from 6.2×10^3 to 1.1×10^4 m^{-3} between simulations, variations in R (48.4 to 53.1 mm h^{-1}) and Z (4.1×10^4 to 5.5×10^4 mm^6 m^{-3}) are less significant. These results hence place a limit on the certainty with which the collision-induced breakup of raindrops can be predicted.

Although the new parameterization of raindrop breakup shows that uncertainty in the form of the equilibrium distribution exists, its occurrence is still predicted. There is scant observational evidence, at best, of the occurrence of equilibrium distributions, though observations of peaked distributions have been reported. A major question is thus to what degree estimates of raindrop clustering made above accelerate the approach of modeled RSDs to equilibrium.

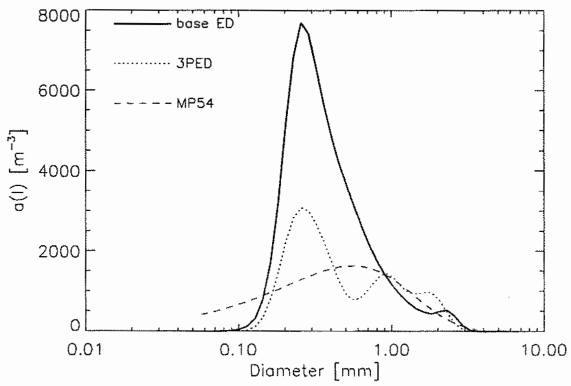

Figure 3: a(l) as function of raindrop diameter for base ED, 3PED, and MP distribution.

Provided there is a constant or near constant Ω, the effect of raindrop clustering is equivalent to reducing the time required to approach equilibrium due to enhanced numbers of raindrop collisions. Using the non-zero Ω from the fit to clustering observations at the ground, the collision rate increases by a factor of approximately 2.3, which corresponds to a reduction in the time required to approach the distributions in Fig. 3 by a factor of 2.3. The model simulations indicate that the small drop peak becomes prominent quickly (figure not shown), with a number concentration greater than 2000 m^{-3} apparent in less than 25 s. The large drop peak is not as prominent at 25 s, but is clearly visible within 125 s. If cloud base occurred at 3 km, a 3 mm diameter drop would take 350 s to fall to the ground. Thus, assuming that a package of raindrops falls together, there should be sufficient raindrop interactions to produce peaked distributions even without considering the clustering of raindrops. Thus, given raindrop clustering, it appears that equilibrium should be approached in a reasonable time period when only coalescence and breakup are acting.

Other processes, such as evaporation, are present, but it will be shown that these processes should not prevent some evidence of these peaked distributions in the model. Alternate explanations for their lack of existence will thus be hypothesized, relating to the spread in fragment size distributions generated for pairs of colliding raindrops, which cause substantial local variations in RSDs.

5. SUMMARY

Prior observations of raindrop clustering are used to determine how inhomogeneous distributions of raindrops might affect collision statistics. Impacts of clustering on the time needed to approach an equilibrium distribution, produced from opposing forces of coalescence and breakup, is also computed. The impact of a new scheme describing the collision-induced breakup on the form of the equilibrium distribution is also investigated.

6. ACKNOWLEDGMENTS

This research was sponsored by the National Science Foundation's Physical Meteorology Program, NSF-0209765. The findings of this study do not necessarily reflect the views of NSF.

7. REFERENCES

Jameson, A.R., and A.B. Kostinski, 1998: Fluctuation properties of precipitation. Part II: Reconsideration of the meaning and measurement of raindrop size distributions. *J. Atmos. Sci.*, **55**, 283-294.

Jameson, A.R., and A.B. Kostinski, 2000: Fluctuation properties of precipitation. Part VI: Observations of hyperfine clustering and drop size distribution structures in three-dimensional rain. *J. Atmos. Sci.*, **57**, 373-388.

Jameson, A.R., and A.B. Kostinski, 2002: When is rain steady? *J. Appl. Meteor.*, **41**, 83-90.

List, R., and G.M. McFarquhar, 1990: The role of breakup and coalescence in the three-peak equilibrium distribution of raindrops. *J. Atmos. Sci.*, **47**, 2774-2792.

Low, T.B., and R. List, 1982: Collision, coalescence, and breakup of raindrops. Part II: Parameterizations of fragment-size distributions. *J. Atmos. Sci.*, **39**, 1607-1618.

Marshall, J.S., and W. M. Palmer, 1948: The distribution of raindrops with size. *J. Meteor.*, **9**, 327-332.

McFarquhar, G.M., 2004: A reparameterization of the Low and List raindrop breakup experiments and its implications for the shapes of raindrop size distributions. *J. Atmos. Sci.*, In press.

Shaw, R.A., A.B. Kostinski, and M.L. Larsen, 2002: Towards quantifying droplet clustering in clouds. *Quart. J. Roy. Meteor. Soc.*, **128**, 1043-1058.

SOME IMPORTANT MULTI-SCALE FEATURES OF VERTICAL MOISTURE TRANSPORT RELATED TO CLOUD STREETS

M. Yu. Mezrin [1], E. V. Starokoltsev [1], Y. Fujiyoshi [2] and M. Yoshizaki [3]

[1] Central Aerological Observatory, Dolgoprudny, Moscow Reg., 141700, Russia;
[2] Institute of Low Temperature Science, Hokkaido University, Sapporo 060-0819, Japan;
[3]Meteorological Research Institute, Japan Meteorological Agency, Nagamine, Tsukuba 305-0052, Japan

1. INTRODUCTION

Based on the Joint Research Agreement between the Central Aerological Observatory of the Russian Federal Service for Hydrometeorology and Environmental Monitoring (CAO), and the Core Research for Evolutional Science and Technology (CREST) of Japan Science and Technology Corporation (JST), a Russian research aircraft IL-18 was employed to carry out investigations over the Sea of Japan area in January-February 2001.

Vertical moisture transport was one of the subjects of the experiment. To investigate it, the instruments installed on board the aircraft measured the oscillations of the vertical wind component w' and absolute air humidity ρ'. The moisture transport was analysed after the flight by an eddy correlation method using the formula $Q_w = \overline{w'\rho'}$. The technique to measure w' was modified to determine the transport in a wider scale range. The sensibility of the hygrometer measuring absolute air humidity (Ultraviolet Hygrometer, UVH) was continuously controlled by precision Aircraft Condensation Hygrometer, ACH (Mezrin and Starokoltsev, 2001).

2. EQUIPMENT AND TECHNIQUE

Vertical wind speed variation, w, was previously calculated by the formula

$w = (\Delta\alpha - \Delta\theta)U + W_p$, where

$\Delta\alpha$ *(deg.)- angle of attack* measured with a spherical 5-hole pressure probe;

θ *(deg.)- pitch angle;*

U(m/sec)- airplane's true air speed;

$W_p = g\int_0^t \Delta n d\zeta$ is the *aircraft vertical speed*;

$\Delta n(g)$*- airplane's vertical acceleration;*

g is the *gravity constant.*

Corresponding author's address: Mezrin M. Yu., Central Aerological Observatory, 3, Pervomayskaya St., Dolgoprudny, Moscow Region, 141700, Russia,
http://webcenter.ru/~mezrin
E-Mail: mezrin@online.ru

The technique described (Strunin, 1997) enables measurements of the vertical component of wind speed within a range of 8-0.06-Hz. The low-frequency limitation is mainly due to the inaccuracy of data from vertical accelerometer, which are necessary for deriving aircraft vertical speed, W_p , by g-load integration.

In processing the data of the last experiment, the authors attempted to extend the range of measured oscillations of the vertical wind speed component to larger scales. For this purpose, data on the vertical aircraft speed were obtained by differentiating the aircraft barometric height, i.e., the height derived from static pressure. Data analysis shows that the barometric height derivative H'_{bar} and g-load integral W_p closely correlate at time scales of 1-10 s and thus can be joined in this range.

$w = (\Delta\alpha - \Delta\theta)U + (W_p)' + \overline{H'_{bar}}$

$\overline{H'_{bar}}$ is derived by averaging barometric speed H'_{bar} by a 5-s sliding mean,

$(W_p)'$ is derived by subtracting a 5-s sliding mean from W_p .

Air humidity was measured from board the aircraft using the ultraviolet and condensation hygrometers - UVH and ACH (Mezrin et al, 2003).

The instruments UVH and ACH are assembled in the same fairing ventilated in a natural way due to pressure difference along the fairing surface. The air inlet is in the rear of the fairing. Errors due to airflow disturbance, based on the observational data obtained on board a research aircraft IL-18, did not exceed -0.2°C under clear-sky conditions and +2.8 % in clouds (which corresponds to +0.5 ÷ +0.3°C).

The UVH hygrometer, as less precise, though faster in operation, is calibrated using the condensation hygrometer ACH. For this purpose, the points from the ACH data (τ) are transferred to absolute humidity $\rho(\tau)$, with temperature T allowed for, and related to the UVH by linear regression. Regression coefficients are used to transfer UVH data to absolute humidity ρ.

The bias measurement error is 0.5°C, random error not more than 0.01 g/m^3, and response time is about 0.1s.

3. AIRCRAFT EXPERIMENT

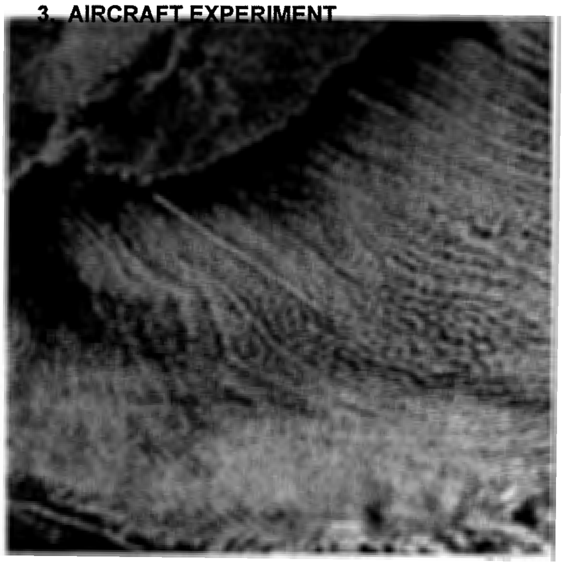

Fig.1. Satellite image of clouds in the zone of the experiment

In the course of the experiment 3 flights were fulfilled: on 29 January, 2 February, and 3 February 2001.

The last one is the most interesting to discuss. This research flight was carried out in the cold rear of a cyclone. Just above the sea, cold air from the continent and warm surface water interacted. Over the sea, cloud streets were observed *(Fig. 1)*. The cold front in the eastern part of the Sea of Japan caused snow showers along the coast of Japan.

The flight was made from Vladivostok, Russia, in the direction of Sado Island, Japan, over the Sea of Japan. At a 10-km distance from the coast, vertical sounding was made from a 3000-m level to as low as 100 m. Thereafter, the aircraft fulfilled 4 horizontal passages at altitudes of 100, 500, 1500, and 3000 m. Each of the passages lay between a sounding point and a maximum distance point.

4. DATA ANALYSIS

4.1 Spatial variability of moisture transport

The oscillations w', ρ' were derived from w, ρ by subtracting a 100-s sliding mean. (This implies that we take into consideration fluctuations of less than 100sec. It will be shown below that this range is enough to determine the total transport.) The obtained quantity $Q = \overline{w'\rho'}$ was averaged by the same sliding mean.

The value of moisture transport was estimated for all the horizontal flight sections and correlated with longitude in order to be located in space (*Fig. 2*).

The curve obtained for a 100-m level exhibits a spatial pattern of moisture transport with a period of about 25 km. It should be pointed out that at a 500-m level, 25-km scale features also occur, their shape and amplitude corresponding to the features observed at 100 m. The time of observing the features at those heights being different, the spatial location of the features gradually changed with time. The motion of the features is indicated by arrows. At 1.5km, the magnitude of the moisture transport differs from zero only in the zone where the aircraft crosses cloud tops,

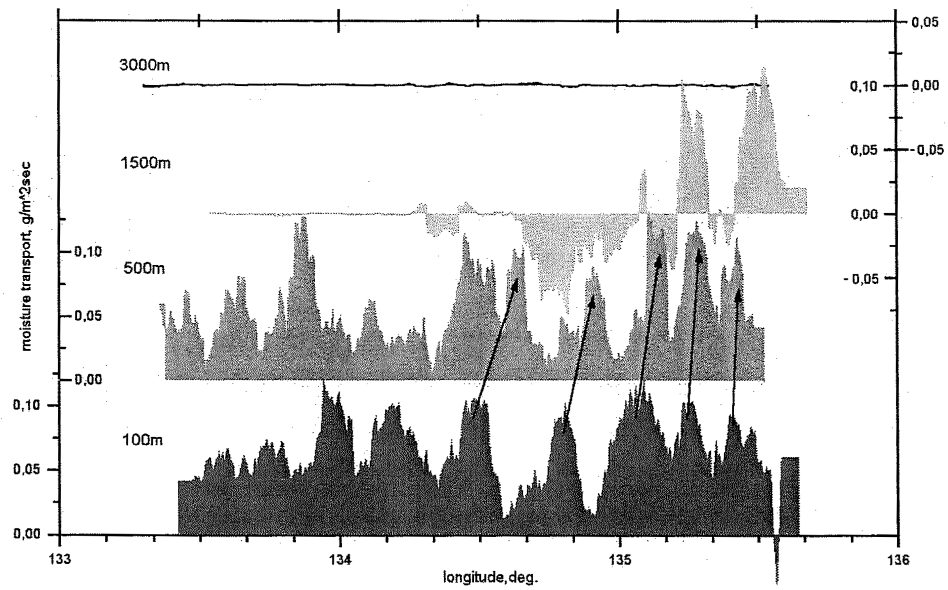

Fig. 2. Spatial features of water vapor transport at 100, 500, 1500 and 3000 m.

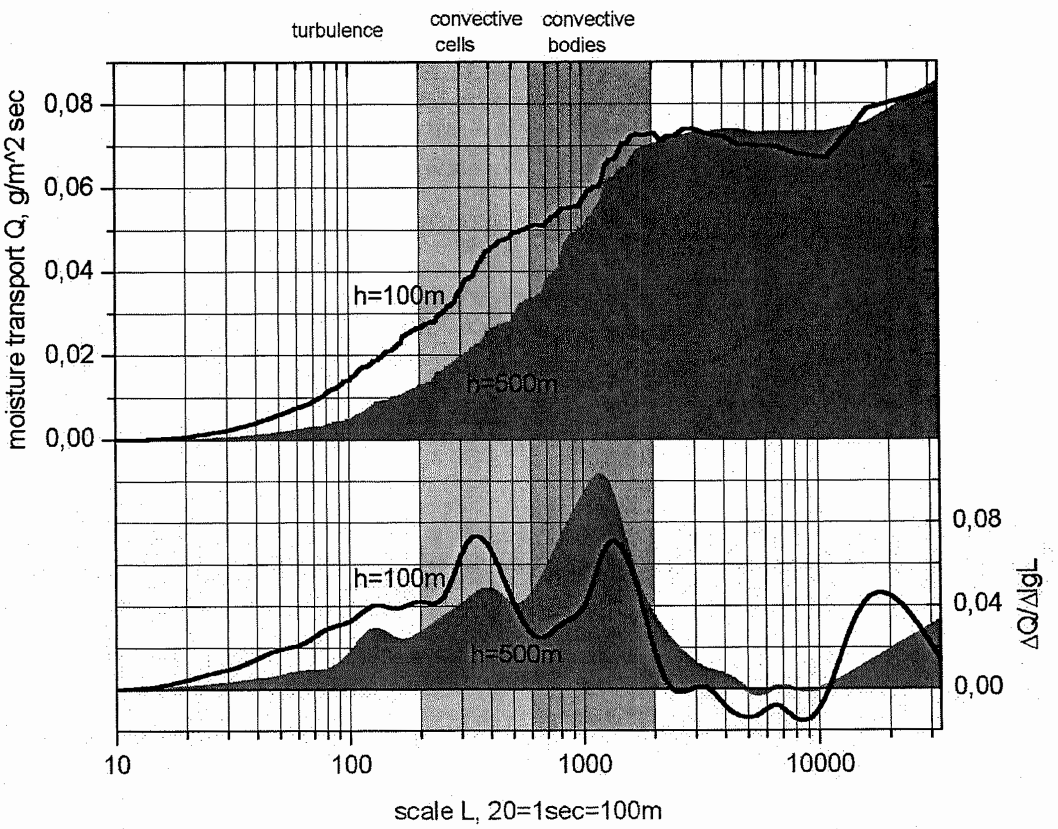

Fig. 3. Estimated moisture transport, Q, versus long-wavelength limit of oscillations considered. Spectral density of transport, $\Delta Q/\Delta lgL$, filter-smoothed with constant $\Delta lgL=0.1$.

its sign being either positive or negative. The cloud tops here seem to reach beyond the boundary layer. At 3000 m the moisture transport is negligible.

The reason for this phenomenon becomes clear after analyzing the satellite image (*Fig. 1*). The aircraft crosses, at an acute angle, the horizontal zones of roll circulation (horizontal roll vortices, organized roll vortices), which causes the formation of cloud streets above 1000m. (Horizontal flight sections are shown with a white line.) The zones of convection shift with time, which is reflected in the position of the features in *Fig. 2*, causing the cloud streets' shift.

The distance between the cloud streets increases with the distance from the coast to reach about 10 km in the zone of observations. The convective cloud size is not much less being about 7 km. Therefore, it would be hard to detect organized phenomena in passing the cloud streets across, i.e., normal to the wind direction. In our case, the cloud street scale – 25 km – differs considerably from that of a convective cloud.

4.2 Spectral analysis of moisture transport

By using the technique described, the range of the scales taken into account in calculating moisture transport can be altered. For this purpose, in calculating the flux the oscillations should be filtered with a time constant other than 100 sec previously employed. With the time constant changing from 1 to 500sec, the calculated mean (over a horizontal path) transport Q increases from 0.0025 to 0.07g/m^{2}sec.

The contribution of each of the scales L to the integral mean moisture transport $\Delta Q/\Delta lgL$ can be estimated. *Fig. 3* presents similar results obtained by Fourier analysis. The black lines refer to the measurements at 100 m, the lines shown as the contours of the gray area to those at 500 m. The graphs of the mean moisture transport Q indicate that increasing the scale to 100- 500sec leads to no significant increase in the transport. (Therefore, in order to explore the spatial variability of the transport, it is enough, in our case, to consider a 0.1-100-sec spectral range, which can be referred to as total.) The extreme point on the right of the graph corresponds to the scale equal to the size of the sampled area (32768 points). Note that here the roll circulation has a 250-sec scale corresponding to 25 km at a 100-m/s flight speed. While initiating the development of turbulence and convective cells, which correspond to smaller scales and make the main contribution to integral moisture transport, the circulation itself is not involved in the transport.

Scale	10-1000m	1000-3000m	3000-10000m	Total
Moisture transport at 100m, g/m^2sec (share in mean integral transport in %)	0.027 (37%)	0.024 (33%)	0.022 (30%)	0.073 (100%)
Moisture transport at 500m, g/m^2sec (share in mean integral transport in %)	0.013 (18%)	0.021 (30%)	0.037 (52%)	0.071 (100%)

Among the scales contributing to moisture transport the following ones can be distinguished:

10-630*-1000m (turbulence);

1000-1800*-3000m (convective cells);

3-6.3*-10km (seems to be the size of a cloud, which forms after cloud street disintegration into more compact, convective mesoscale formations - convective bodies).

The values marked by asterisks (*), correspond to maximum spectral density of the transport.

At a 100-m level, each of the scales accounts for one third of the contribution to the overall transport (see Table). At 500 m, the input of small scales decreases, while that of larger scales increases. However, the value of the mean integral transport changes far less. The share of turbulent transport in it is 1/3 and 1/6 at 100 and 500 m, respectively.

Note that the value of the mean integral transport largely depends on the choice of an area explored. It is desirable that the number of waves (features) of spatial transport contained in this area be an integer *(Fig. 2)*, i.e., that the number of active and passive zones be equal. With the number of passive zones larger by one, the mean value of the transport will be smaller by approximately 5 %. An excess of active zones by one will results in a 5 % increase of that value. Besides, the mean value of the transport changes from the start to the end of a horizontal flight leg. Therefore, let us take 5 similar features for both 100- and 500-m levels (marked in the figure by arrows). The mean values of the integral transport for these altitudes are 0.078 и $0.071 g/m^2sec$, respectively.

When investigating water balance in the troposphere one should not only consider turbulent transport as it would lead to large quantitative errors. Moreover, even qualitative conclusions may prove erroneous. Thus in this case, turbulent moisture transport decreases with altitude by a factor of two, while the integral one changes far less.

A comparison of heat and moisture transports (in terms of sensible and latent heat fluxes) has indicated that their ratio at a 100-m altitude is close to 2 and at 500 m to 1. The difference between the values of transport at the two altitudes agrees with the estimates of horizontal heat and moisture advection (Mezrin et al., 2003).

5. CONCLUSIONS

In the course of the experiment, an inflow of cold dry air from the continent (Siberia) was observed. It is this meteorological situation that is of special interest as it largely influences the weather of Japan.

As the air mass moved towards Japan, it got warmer and more humidified due to heat and moisture exchange with the open surface of the Sea of Japan. The cloud streets formed testify to the presence of a roll circulation (horizontal roll vortices).

The mean integral moisture transport has proved to be about $0.07 g/m^2sec$. Upgrading the procedure of calculating vertical moisture transport has made it possible to determine this quantity within a scale range from 10m to 50km (0.1-500sec.). Spectral analysis has revealed 3 scale ranges by their input to the total transport: 10-1000m (turbulence), 1000-3000m (convective cell), 3-10km (convective body). Larger scales (including roll circulation scale) are not observed to make any considerable input. At 100 m, the inputs of the three scales are the same, while at 500 m, the role of the largest one becomes more important. However, the value of the total transport changes far less, and the share of turbulent transport in it corresponds to 1/3 and 1/6 at 100 and 500 m, respectively. When investigating water balance in the troposphere one should take it into account.

In the space structure of moisture transport obtained for altitudes of 100 m and 500 m, 25-km features were detected, which were associated with the position of cloud streets that had formed at altitudes of 1000-1500 m. These features can be accounted for by roll circulation, which initiates the transport and cloud development. Above the boundary layer (with the upper bound at about 1500m), the value of moisture transport is negligible.

6. ACKNOWLEDGEMENTS

The authors are thankful to the Core Research for Evolutional Science and Technology (CREST) of Japan Science and Technology Corporation (JST) for the financial support of this study.

7. REFERENCES

Mezrin, M.Yu., E.V. Starokoltsev, 2001. Aircraft Condensation Hygrometer and some results of measuring humidity in the zone of the equatorial tropopause. J. Atmos. Res., **59-60**, pp. 331-341.

Mezrin, M. Yu., E. V. Starokoltsev, Y. Fujiyoshi, M. Yoshizaki, 2003. The contribution of different scales to integral moisture transport based on investigations over the Sea of Japan. J. Atmos. Res. **69**/1-2, pp. 109-124.

Strunin, M.A., 1997. Meteorological potential for contamination of arctic troposphere: aircraft measuring system for atmospheric turbulence and methods for calculation it characteristics. Archive and database of atmospheric turbulence. J. Atmos. Res., **44**, pp.17-35.

A MODELLING STUDY OF MIXED-PHASE CONVECTIVE CLOUD SEEDING AND ITS EFFECT ON THUNDERSTORM CHARGING

R. Mitzeva[1], S. Petrova[1] and J. Latham[2]

[1] Faculty of Physics, University of Sofia, Sofia-1164, Bulgaria
[2]National Center for Atmospheric Research*, Boulder, CO, USA

1. INTRODUCTION

Cloud microphysics and dynamics can be significantly changed as a result of cloud seeding. It follows that since the electric charge separation during non-inductive, rebounding collisions between growing graupel and ice crystals is the dominant charge separation mechanism in thunderstorms the seeding of convective clouds may also lead to changes in electric field growth and charge density. The present study is focused on the sensitivity of cloud dynamics, microphysics and electrification of summer continental convective clouds as a result of idealized numerical simulations of hygroscopic seeding.

A brief description of the model used for numerical simulation of convective clouds is given in section 2. Numerical simulation and results are presented in section 3.

2. MODEL DESCRIPTION

Convective clouds are assumed to be composed of active and non-active cloud masses (Andreev et al, 1979). The active mass is modelled by successive ascending spherical thermals, while the non-active cloud region is formed by thermals that have previously risen and stopped at their convective levels. This multi-thermal concept simulates the time dependence of the microphysical and thermodynamic characteristics of cumulus development and has been used in model studies by Mason and Jonas, 1974, Blyth and Latham, 1997 and others. One can speculate that the ascending thermals represent the updraft region of convective clouds, while non-active masses represent the environment surrounding the updrafts.

Corresponding author's address:
Dept. of Meteorology, Faculty of Physics,
University of Sofia, Sofia-1164, Bulgaria
E-mail: rumypm@phys.uni- sofia.bg

NCAR is sponsored by the National Science Foundation

The thermals are driven by the buoyancy force reduced by entrainment and the weight of the hydrometeors present. They entrain air from a cloudless environment or from a non-active cloud region depending on their position. Parameterization of the merging of thermals during their ascent is included in the model. As the thermals ascend, the temperature in the rising thermals changes due to cooling, entrainment of environmental air and heat released by the microphysical processes. The model uses bulk microphysical parameterizations with five classes of water substance - water vapor, cloud water S_c, rain S_p, cloud ice S_{cf}, and precipitating ice (graupel) S_{pf}. The cloud droplets and ice crystals are assumed to be monodisperse and have negligible fall velocities and so move upward with the air in the ascending thermals. A Marshall-Palmer type size distribution is assumed for raindrops and graupel.

In the model cloud, droplets are formed by condensation. Raindrops form by autoconversion of the cloud droplets and grow by collision and coalescence with cloud drops. Below 0°C, ice crystals originate by heterogeneous freezing at the expense of cloud droplets, the concentration being given by Fletcher, 1962. Homogeneous freezing occurs below –40°C. Precipitating ice (graupel) forms by the freezing of raindrops, contact nucleation of ice crystals and raindrops and conversion of ice crystals. Ice crystals grow by deposition of water vapor; graupel grows by coalescence with cloud and raindrops. Precipitation fallout is calculated in the same manner as in Cotton, 1972, and comprises that portion of the raindrops and graupel having terminal velocities greater than the updraft speed. Evaporation of raindrops and melting of graupel during their descent as well as recycling of precipitating particles is included in the model. The model takes account of the changes of the mass of drops and crystals due to the entrainment of environmental air and by the incorporation of the mass of raindrops and graupel falling out from the upper ascending successive thermals. The non-active cloud mass also expands, and the temperature excess, water vapor, cloud droplets and ice crystals in this region vary in time because of turbulent diffusion and evaporation.

Cloud electrification parameterisation is based on laboratory data for the non-inductive charge transfer mechanism (Brooks et al., 1997). The sign and magnitude of the charge per crystal separation event depends on temperature, crystal size, relative velocity, and the rime accretion rate. Ice crystals and small graupel in the ascending thermals, together with larger falling graupel are the charge carriers in the model cloud. Together with particle concentration changes, the changes of charge density in ascending thermals due to entrainment, the falling out of graupel mass and the incorporation of graupel fallen from upper levels are all taken into account. The charging rate per unit volume of model cloud is calculated as in Mitzeva and Saunders (1990). The total charge density in the updraughts of clouds, ρ_T, is established by summing the charges on the ice crystals, ρ_{cr}, and on the graupel, ρ_{gr}, in the ascending thermals. The charge carriers in the non-active cloud region are crystals, which remain in the stopped and diffusing thermals; their net charge is changed in proportion to the dilution of ice crystal content due to diffusion and entrainment. During their descent, graupel particles charge by rebounding collisions with ice crystals in the non-active cloud mass or in the ascending thermals and they may be incorporated into ascending thermals when their terminal fall speed is smaller than the updraught velocity of the ascending thermals.

The numerical simulation of hygroscopic seeding is based on the work of Orville et al. (1999), and the autoconversion from cloud- to rainwater was based on Kessler (1969).

3. NUMERICAL SIMULATIONS AND RESULTS

The above-described model was used for simulation of a cloud observed at Gelemenovo, Bulgaria on June 8 1976. On this day a convective cloud with cloud top height 9.7 km above ground level (AGL) and cloud base at around 2 km AGL was observed. Liquid precipitation was detected on the ground from this cloud. For the simulation of Gelemenovo cloud the sounding of temperature and humidity observed on this day was used. The parameters necessary for the numerical simulations by the model (the thermal radius, R_o = 2 km, and velocity W = 1 m/s at cloud base, the time interval between the ascending thermals, dt = 3 min, their number N = 5 and the turbulent diffusion coefficient in the non-active cloud mass, K = 200 m^2/s) were taken in the range of real values in such a way that the cloud top height of the model cloud to be close to the observed cloud top height.

Since the model simulations are carried out from cloud base height to the height of zero updraft velocity the conclusion for the effect of seeding is evaluated indirectly based on the analyses of amount of liquid and solid fallout of the ascending thermals.

From Table 1 one can see that there is negative dynamical effect as a result of seeding - the updraft is smaller and the cloud top height is 1.5 km lower in the seeded case.

	SUMSR [gm $^{-3}$]	SUMSRF [gm $^{-3}$]	SUMSR+ SUMSRF	WMAX [ms $^{-1}$]	ZTOP [km]
Unseeded	0.372	14.7	15.07	17.04	9.1
seeded	2.24	18.2	20.44	13.91	7.6

Table 1. Some results from hygroscopic seeding of Gelemenovo (8 June 1986) model cloud SUMSR [g/m^3] –rain fallout, SUMSRF [g/m^3] – graupel fallout WMAX [m/s] – maximum updraft velocity, ZTOP [km] –cloud top height

The amount of liquid and graupel fallout (SUMSR and SUMSRF respectively) in seeded cloud is bigger (136%) in comparison with unseeded, i.e. in this particular cloud case the increase of the precipitation at hygroscopic seeding is a result of the increase of both liquid

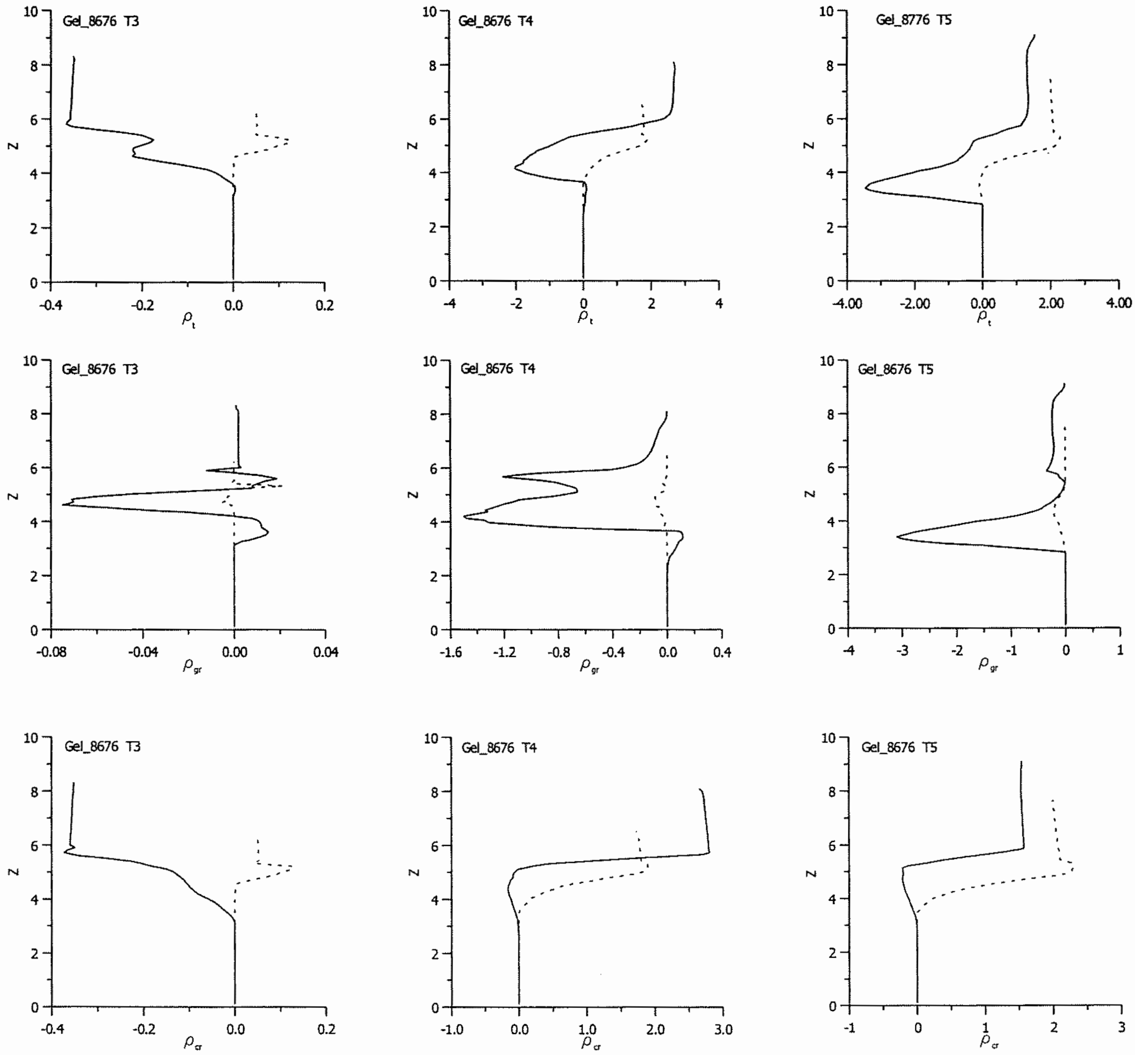

Fig.1. Total charge density, ρ_t,(top panel) graupel charge density, ρ_{gr},(middle panel) and ice crystal charge density, ρ_{cr},(bottom panel) during the ascent of 3-th (left panel) 4-th (middle panel) the 5th (right panel) in natural developed (bold lines) and seeded (dash lines) Gelemenovo 8 June 1986 cloud.

and solid precipitation in the cloud. The magnitude of negative charge density ρ_t (Fig.1) at lower levels during the ascent of 3,4 and 5-th thermals with which the updraft was simulated is very small in the simulated seeded cloud, while the magnitude of positive charge at lower levels in the updraft is bigger in seeded cloud than in unseeded. The analyses of numerical simulations showed that in the model cloud hygroscopic seeding leads to an increase of autoconversion of cloud water S_c to rain water in the early stage of cloud development at lower levels. As a result precipitation start earlier and raindrops precipitate from the lower levels where updraft velocity is weaker in seeded than in unseeded cloud. There is smaller amount of ice crystals and graupel in the updraft of seeded than in unseeded model cloud. Due to the smaller latent heat of freezing in the seeded cloud the maximum of updraft velocity and the cloud top height in seeded model cloud is less than in unseeded, i.e. the negative dynamical effect is "observed". Based on the preliminary analyses of numerical results one can conclude that the smaller magnitude of negative charge density in the updraft of seeded clouds can been explained by lower LWC and smaller amount of ice crystals and graupel in the updraft of seeded cloud. The decrease in LWC leads to the decrease of the magnitude of charge transferred and moves the reversal temperature to lower levels. As a result of this the crystals acquire positive charge at lower levels in seeded than in unseeded cloud. The smaller LWC and ice particle concentrations leads to the smaller magnitude of charge transferred. For more categorical conclusions the detailed analyses of the impact of the seeding on the charge density distribution in the whole volume of the thunderstorms is also necessary.

4. CONCLUSIONS

The numerical simulations showed that there is increase of rain and a reduction of updraught speed as a result of hygroscopic seeding. The changes of microphysical and dynamical structures of seeded clouds lead to a decrease of negative charge values in the lower levels of updraft in the simulated Gelemenovo cloud.

The simulations of two other cloud cases will be presented at the Conference.

REFERENCES

Andreev, V., D. Syrakov and R. Mitzeva, 1979: Modeling of convective cloud formation as successive ascending thermals. *Bulg. Geophys. J.*, **5**, No 1, 3-7.

Blyth, A. M., and J. Latham, 1997: A multi-thermal model of cumulus glaciation via the Hallett-Mossop process. *Quart. J. Roy. Met. Soc.*, **123**, 1185-1198.

Brooks M., C. P. R. Saunders, R. P. Mitzeva and S. L. Peck, The effect on thunderstorm charging of the rate of rime accretion by graupel. *J. Atmos. Res*, **43**, 277-295, 1997.

Cotton W., 1972: Numerical simulation of precipitation development in super-cooled cumuli - Part II. *Mon. Wea. Rev.,* **100**, 764 – 784.

Fletcher, N. H. The Physics of Rainclouds, Camb. Univ. Press, 1962.

Kessler, E. 1969: On the distribution and continuity of water substance in atmospheric circulations, *Meteorol. Monogr.*, Boston, 10, No 32.

Mason, B. J., and P. R. Jonas, 1974: The evolution of droplet spectra and large droplets by condensation in cumulus clouds. *Quart. J. Roy. Met. Soc.*, 100, 23-38.

Mitzeva, R. P. and C. P. R. Saunders, 1990: Thunderstorm charging: Calculations of the effect of ice crystal size and graupel velocity. *J. Atmos. Terr. Phys.*, **52**, 241-245.

Orville H.D., Chengshu Wang, and F.J.Kopp, 1999. A Simplified Concept of Hygroscopic Seeding, *Journal of Weather Modification*, **30**, 7–21.

STRUCTURE AND DEVELOPMENT OF TWO MERGED RAINBANDS ALONG THE BAIU FRONT AND THE "WATER VAPOR FRONT" OVER THE EAST CHINA SEA DURING X-BAIU-99

Q. Moteki[1], H. Uyeda[1], T. Kato[2], and M. Yoshizaki[2]

[1]Hydrospheric Atmospheric Research Center, Nagoya University, Nagoya, Aichi, 464-8601, Japan

[2]Meteorological Research Institute, Japan Meteorological Agency, Tsukuba, Ibaraki, 305-0052, Japan

1. INTRODUCTION

Over the East China Sea during the Baiu season, convective rainbands are often generated to the south of the synoptic-scale convergence of the Baiu front. During a field experiment of X-BAIU-99 (Fig. 1), development of two merged rainbands observed over the East China Sea. A northern rainband was located along the Baiu front, and a southern rainband was observed in southerly wind field. The formation mechanism of a rainband other than the convergence of the Baiu front still has not been understood over ocean where there are no land effects. In this study, structure and development of two merged rainbands are investigated to understand the formation mechanism of rainbands in the south of the Baiu front.

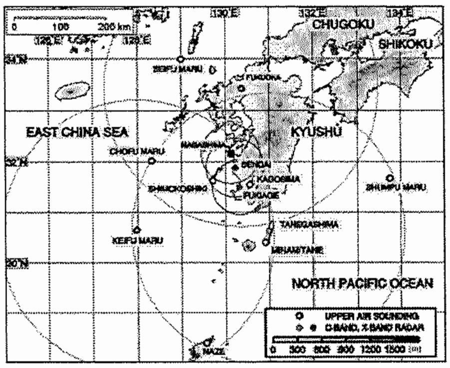

Fig. 1. Map of the experimental region of the X-BAIU-99. Three large circles show the maximum observation ranges of C-band radars. Three small circles show the maximum observation ranges of X-band Doppler radars.

Corresponding author's address: Qoosaku Moteki, Hydrospheric Atmospheric Research Center, Nagoya University, Nagoya, Aichi, 464-8601, Japan; E-Mail: moteki@rain.hyarc.nagoya-u.ac.jp

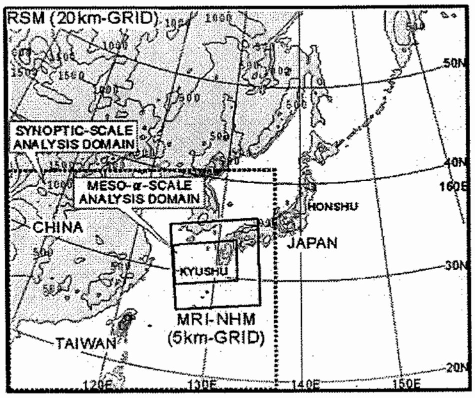

Fig. 2. Map of domains of a 20-km resolution hydrostatic model: 20 km-RSM (the thick-lined box) and a 5-km resolution non-hydrostatic model: 5 km-NHM (the thin-lined box). Analysis domains of synoptic-scale and meso-α-scale are represented by the thick and thin dotted boxes, respectively.

2. DATA

In this study, the following data with the X-BAIU-99 are used. Data from three C-band radars at Fukuoka, Tanegashima, and Keifu Maru are used for detecting meso-α-scale behaviors of precipitation systems. Dual Doppler analysis with X-band Doppler radars at Sendai and Fukiage are used for investigating meso-β-scale air-flow structure. Upper-air sounding data at seven additional sites (Nagashima, Shimokoshiki, and Minamitane, and observation vessels Seifu Maru, Chofu Maru, Keifu Maru, Shumpu Maru) were used for the initial field of numerical simulations. The numerical simulations (Fig. 2) are conducted with a 20 km-resolution Regional Spectral Model (20 km-RSM, a hydrostatic model used operationally in Japan)

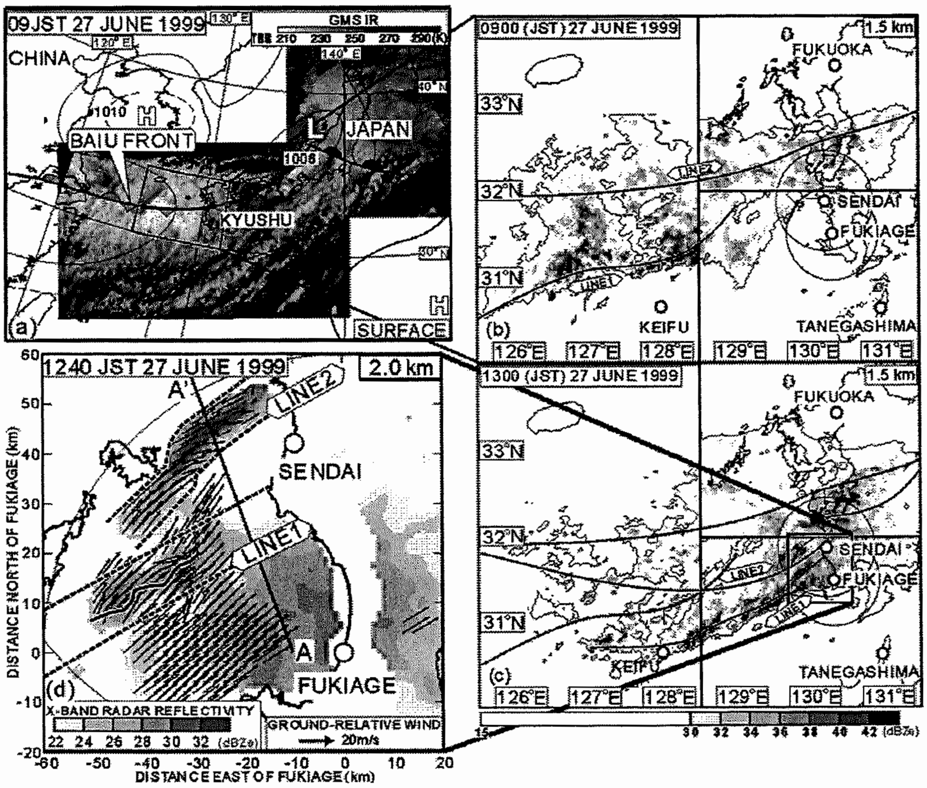

Fig. 3. (a) GMS infrared image superimposed on surface weather map at 09JST on 27 June 1999, composite reflectivity images with C-band radars at (b)09JST, (c)13JST, and (d)reflectivity image and ground-relative winds with X-band Doppler radars at 1240JST. The dashed lines shown in (c) represent the positions of LINE1 and LINE2 at 09 JST. The thick solid line along LINE1 in (d) denotes the weak convergence line. The line of A-A' indicates the position of vertical cross section shown in Fig. 4.

and a 5 km-resolution Non-Hydrostatic Model (5 km-NHM, a non-hydrostatic model developed by Meteorological Research Institute). The 5 km-NHM is one-way nested within the RSM from 06 JST to 15 JST on 27 June 1999.

3. RESULTS

3.1 Overview of two merged rainbands

Figure 3 shows overview of two merged rainbands. Over the East China Sea, convective clouds are seen to develop in the south of the Baiu front at 09 JST on 27 June 1999 (Fig. 3a). According to composite reflectivity image with C-band radars (Fig. 3b), a northern rainband is located along 32 degree N, and a southern rainband is located in about 100 km south of the northern rainband at 09 JST. The southern and northern rainbands are called LINE1 and LINE2, respectively. LINE2 moves southeastward, and merges into the quasi-stationary LINE1 at 13 JST (Fig. 3c). LINE1 develops rapidly in this merging. Before the merging at 1240 JST, LINE1 formed in a southwesterly wind field associated with a low-level convergence line (Fig. 3d). LINE2 formed along a synoptic-scale convergence line of the Baiu front ahead of low-level northerly winds (Fig. 4). As the merging of LINE1 and LINE2 occurred, the low-level convergence along LINE1 was intensified, and LINE1 developed rapidly (not shown, see Moteki et al. 2004a).

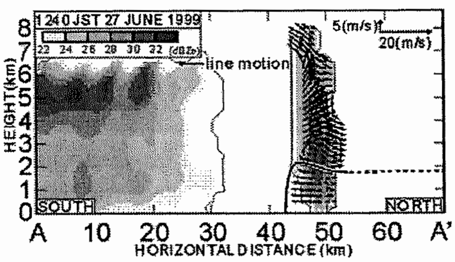

Fig. 4. Vertical cross section of reflectivity and ground-relative winds along A-A' shown in Fig. 3(d). The thick line indicates the boundary of a layer of northerly winds.

3.2 The "water vapor front" in the south of the Baiu front

In order to investigate the thermodynamic and moisture structures of the two rainbands, a numerical simulation is conducted with the 5 km-NHM. In the 5 km-NHM simulated field (Fig. 5a), LINE2 forms along a convergence line ahead of northerly winds. The convergence line is accompanied by remarkable horizontal gradients of potential temperature θ (2-3 K per 50 km) and mixing ratio of water vapor q_v (2-3 g kg^{-1} per 50 km, not shown) at a height of 0.02 km. The features of the convergence line are consistent with those of the Baiu front shown in many previous studies (e. g., Matsumoto et al. 1971; Kato, 1985). LINE1 forms along a weak convergence line in the south of the Baiu front. It is found that the weak convergence line has almost no gradient of θ differing from the Baiu front. However, the weak convergence line was accompanied by only a gradient of q_v (2 g kg^{-1} per 10 km, not shown, see Moteki et al. 2004b) in the layer of 0.5-1.5 km. In this study, the weak convergence line in the south of the Baiu front is named a "water vapor front." It is found that there are two distinct frontal convergence lines over the East China Sea: the Baiu front and the "water vapor front."

Figure 5b shows a vertical cross section across the Baiu front and the "water vapor front." At the position of the "water vapor front," a depth of a warm-moist air mass becomes rapidly shallow. A high q_v and θ (warm-moist) air mass is over 1-km deep to the south of the "water vapor front," but its depth becomes less than 0.5 km between the "water vapor front" and the Baiu front. The warm-moist air mass flows into the Baiu front only in the layer below 0.5 km. These two types of frontal structures raise as significant question. What is an air mass flowing from the west between the two fronts?

In order to investigate the synoptic-structures of the two fronts, a numerical simulation is conducted with the 20 km-RSM. Over the East China Sea, two significant convergence zones are seen (Fig. 6a). Comparing to the surface weater map in Fig. 3a, a northern convergence zone ahead of northerly winds is correspond with the Baiu front. A southern convergence zone can be recognized as the "water vapor front," and it extends from the eastern coast of China to Kyushu with a length of about 1000 km.

In Fig. 6b, there are three air masses around the two fronts. A cold and dry air mass to the north of the Baiu front is associated with northerly winds. A oceanic moist air mass over the East China Sea is associated with southwesterly winds, and its q_v at the surface is over 19 g kg^{-1}. A continental moist air mass over the mainland of China is associated with weak southwesterly or westerly winds, and its q_v at the surface is 15-19 g kg^{-1}. Because roughness over lands is larger than that over oceans, winds of the continental moist air mass is much weaker than those of the oceanic moist air mass.

It is found that the continental moist air mass flows partially over the western part of the East China Sea between the Baiu front and the "water vapor front." The boundary of continental and oceanic moist air masses is accompanied by a weak convergence due to the difference of speed and direction of winds. Therefore, the convergence line of the "water vapor front" was formed by two distinct moist airflows over the East China Sea.

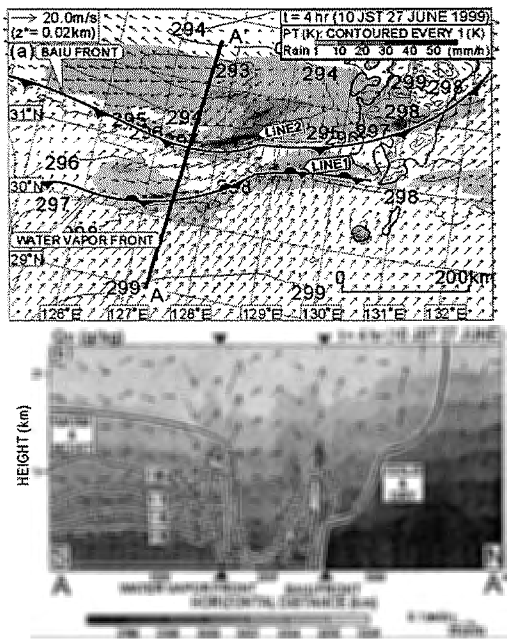

Fig. 5. (a)The rainfall area (shaded), potential temperature (contours), and horizontal winds reproduced by the 5 km-NHM at a height of 0.02 km at 10 JST on 27 June 1999. (b)Vertical cross section of potential temperature (shaded), mixing ratio of water vapor over 16 g kg^{-1} (dashed contours) along A-A' shown in (a). The thick and thin solid line indicate the upper-boundaries of cold-dry and warm-moist air masses, respectively.

4. CONCLUSIONS

The present study found a existence of the "water vapor front" over the East China Sea. Two distinct frontal convergence lines of the Baiu front and the "water vapor front" developed the two rainbands without any land effects. In association with the frontal merging, the two rainbands merged and developed rapidly.

The "water vapor front" is the boundary of two distinct moist air masses over the East China Sea. One is an oceanic moist air mass from the southwest, and the other is a continental moist air mass from the west. The "water vapor front" has a remarkable gradient of q_v (2 g kg^{-1} per 10 km), but no gradient of θ differing from the Baiu front. The reason that convective rainbands are often generated in the south of the Baiu front can be clearly explained by the existence of the "water vapor front."

Finally, it should be pointed out that the definition of the "water vapor front" is almost the same as that of "dryline" over the Great Plains. That is, a weak convergence line with a remarkable moisture gradient between oceanic and continental air masses. Discussions about the "water vapor front" should be required in comparison with the "dryline" in the future.

Acknowledgements

The authors thank all of the participants in the X-BAIU-99 observation for obtaining these data and the Japan Meteorological Agency for providing sounding data and radar data. This study was supported by the Japan Science and Technology Corporation, and a Grant-in-Aid for Scientific Research of the Japan Society for the Promotion of Science.

References

Kato, K., 1985: On the abrupt change in the structure of the Baiu front over China Continent in late May of 1979. *J. Meteor. Soc. Japan*, **70**, 467-495.

Matsumoto, S., S. Yoshizumi and M. Takeuchi, 1971: Characteristic feature of Baiu front associated with heavy rainfall. *J. Meteor. Soc. Japan*, **49**, 267-281.

Moteki, Q., H. Uyeda, T. Maesaka, T. Shinoda, M. Yoshizaki and T. Kato, 2003: Structure and development of two merged rainbands observed over the East China Sea during X-BAIU-99 Part I: Meso-β-scale structure and development processes. *J. Meteor. Soc. Japan*, **82**, in press.

Moteki, Q., H. Uyeda, T. Maesaka, T. Shinoda, M. Yoshizaki and T. Kato, 2003: Structure and development of two merged rainbands observed over the East China Sea during X-BAIU-99 Part II: Meso-α-scale structure and build-up processes of convergence in the Baiu frontal region. *J. Meteor. Soc. Japan*, **82**, in press.

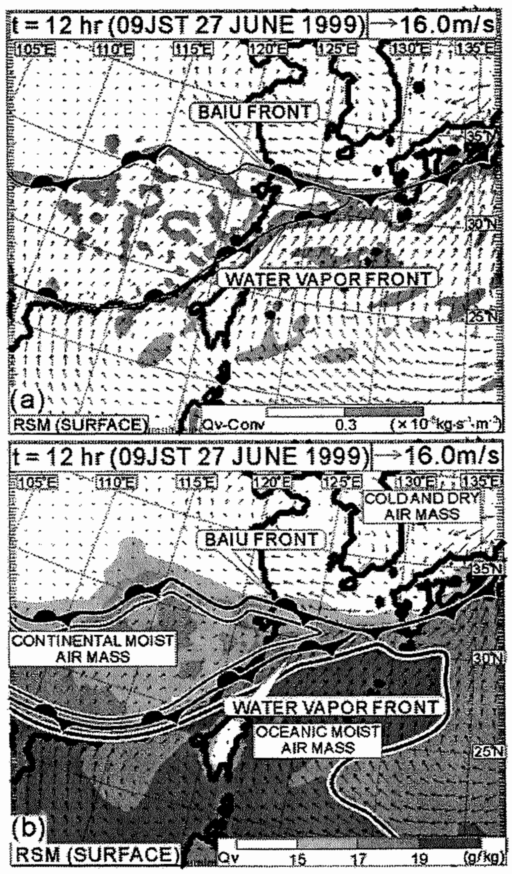

Fig. 6. (a)RSM-simulated fields of horizontal water vapor flux convergence at the surface at 09 JST on 27 June 1999, and (b)mixing ratio of water vapor at the surface.

FORMATION PROCESS OF AN OROGRAPHIC LINE-SHAPED RAINFALL SYSTEM FROM A VIEWPOINT OF CELLULAR ECHOES ON THE SOUTH OF THE BAIU FRONT IN WESTERN KYUSHU, JAPAN

A. Nakamura[1], H. Uyeda[1], M. Yoshizaki[2], Y. Tanaka[2] and S. Shimizu[3]

[1]Hydrospheric Atmospheric Research Center, Nagoya University, Nagoya, Aichi, 466-8601, Japan

[2]Meteorological Research Institute, Japan Meteorological Agency, Tsukuba, Ibaraki, 305-0052, Japan

[3]EORC, National Space Development Agency of Japan, Roppongi, Tokyo, 106, Japan

1. INTRODUCTION

Line-shaped rainfall systems often appear in the west of Kyushu Island, when south-southwesterly moist winds are predominant on the southern side of the Baiu front. One of them extends northeastward from Koshikijima Islands located about 40 km away westward from the west coast of Kyushu Island (Fig.1). It is called Koshikijima line.

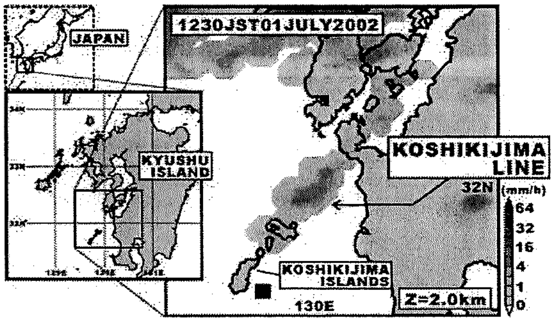

Fig. 1. Horizontal distribution of rainfall intensity at 2.0 km height. Square point denotes the position to show the profile of relative humidity and wind in Fig.3.

Koshikijima line has the maximum length of about 100 km. Staffs of Fukuoka radar (1974) described that Koshikijima line consisted of many convective cells. Morita (1999) discussed that the convective clouds generated on Koshikijima Islands are advected by low-level winds, which results in formation of a line-shaped rainfall system. Because convective cells have 30-40 minutes in lifetime, they can move about 30 km. Therefore a line-shaped system of about 100 km in length cannot be formed by only convective cells generated on Koshikijima Islands. The purpose of this paper is to clarify the formation process of Koshikijima line from a cellular echo to a line-shaped system. It is necessary to investigate the features of cellular echoes, which consist of Koshikijima line. We obtained X-band Doppler radar data of 01 July 2002, which is suitable for the study on cellular echoes. We have analyzed a line-shaped system on 01 July 2002, which extend northeastward from Koshikijima Islands.

Corresponding author's address: Ayako Nakamura, Hydrospheric Atmospheric Research Center, Nagoya University, Nagoya, Aichi, 464-8601, Japan; E-Mail: aya@rain.hyarc.nagoya-u.ac.jp

2. DATA

Fig. 2. Map of observation.

Two X-band Doppler radars at Nagashima and Sendai obtained volume scan data of reflectivity and Doppler velocity every 10 minutes and 5 minutes, respectively. They covered the downstream of Koshikijima Islands with 64 km in radius (Fig.2). The highest altitude of Koshikijima Islands is 604 m.

The data of Japan Meteorological Agency Meso regional objective ANALysis (MANAL) was used to investigate environmental fields.

3. RESULTS

3.1 Environmental fields

Before the Koshikijima line was observed, Kyushu was located on the southern side of the Baiu front. South-southwesterly winds near the surface and southwesterly winds below 2.0 km height were predominant around Koshikijima Islands (Fig.3). The atmosphere was nearly saturated in the lower layer below about 1.0 km, and a dry layer was observed around 2.0 km (Fig.3). Melting layer existed at about 5 km height in this case. Lifting condensation level (LCL) was 145 m. The Froude number Fr (Smolarkiewicz and Rotunno, 1989) was 0.82. Then, the airflow should be likely to override the mountains.

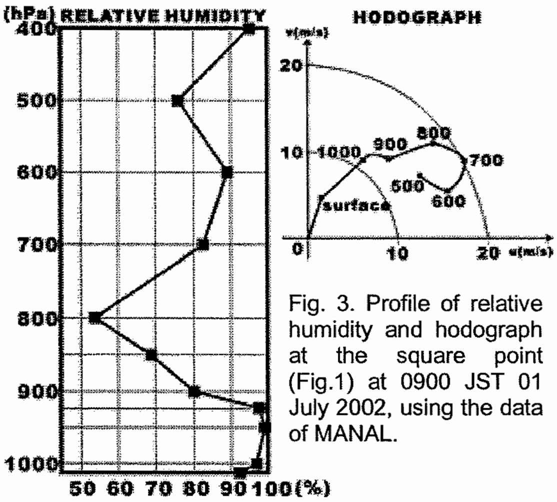

Fig. 3. Profile of relative humidity and hodograph at the square point (Fig.1) at 0900 JST 01 July 2002, using the data of MANAL.

3.2 Overview of the Koshikijima line

The remarkable rainband was observed at 1230 JST (JST=UTC+9hour) by the Sendai Doppler radar at 2.0 km height. The rainband aligned northeastward from Koshikijima Islands. It was 80 km in length and 15 km in width with many convective cells. The line had more than 30 km length from 1000 to 1310 JST.

3.3 Features on cellular echoes of the line

The longest line-shaped echo had 10 cellular echoes more than 15 dBZe at 2.0 km height (Fig.4). During the period from the first generation of cellular echoes in the northeastern side of Koshikijima Islands to deformation of line-shaped echoes, 91 cellular echoes made a contribution to formation of a line-shaped echo.

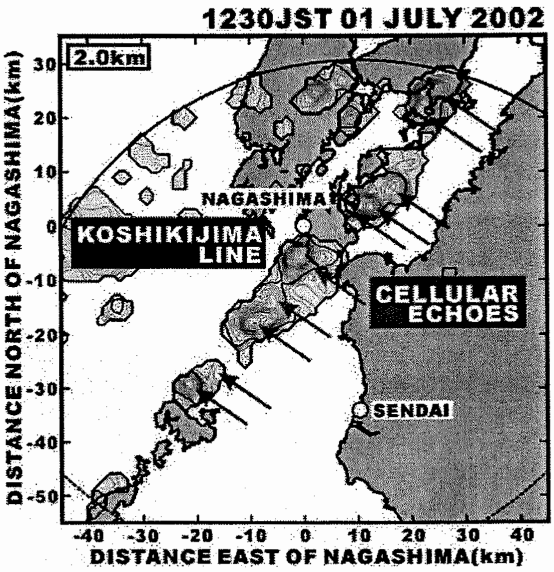

Fig. 4. Horizontal distribution of reflectivity more than 15 dBZe at 2.0 km height.

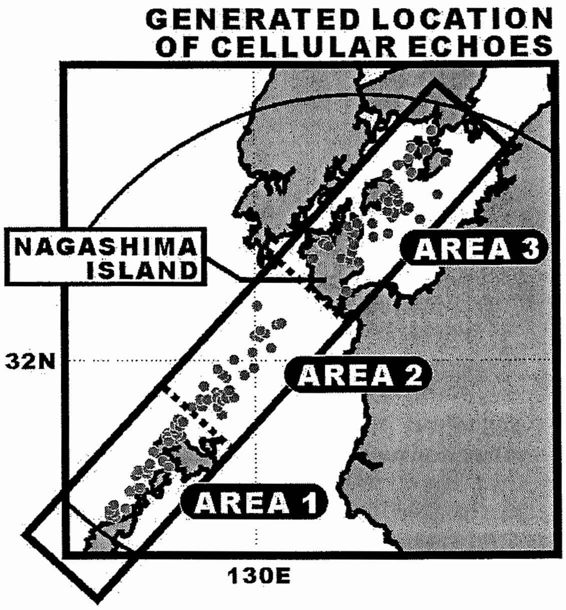

Fig. 5. Generated location of cellular echoes at 2.0 km height. Closed circle shows the position where cellular echo appeared for the first time.

Their horizontal and vertical scale are 5-12 km and 6 km at the maximum, respectively. The maximum lifetime of them is 35 minutes. They moved northeastward at the maximum speed of 12 ms^{-1} parallel to the winds around 2.0 km height. It indicates that single cellular echo can move up to the distance of 25 km, so single cellular echo cannot form a line-shaped echo of 80 km in length. Consequently, it is supposed that we need to know the number and birthplace of cellular echoes generated for understanding formation of the line.

In this paper, area on Koshikijima Islands is named AREA 1, area over northeastern sea of Koshikijima Islands is named AREA 2 and area around Nagashima Island located at the 50 km northeastward of Koshikijima Islands is named AREA 3 (Fig.5). The number of cellular echoes generated is 28 in AREA 1, 29 in AREA 2 and 34 in AREA 3. It is found that the cellular echoes generated not only on Koshikijima Islands but also over northeastern sea of Koshikijima Islands and around Nagashima Island.

3.4 Formation process of the line from cellular echoes to a line-shaped echo

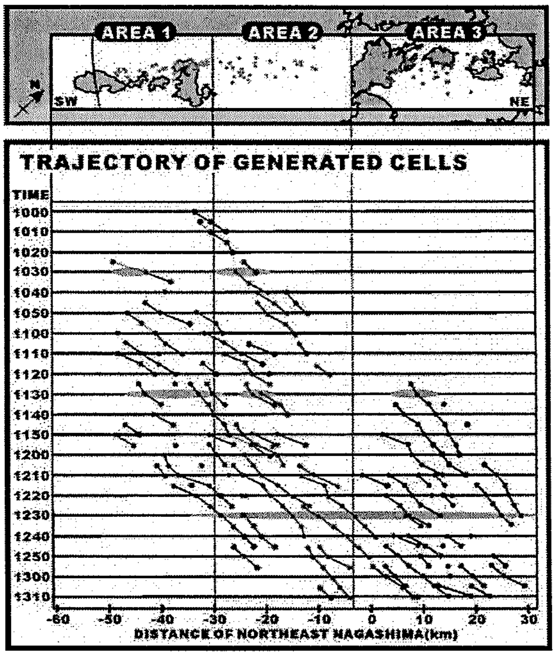

Fig. 6. Trajectory of cellular echoes. Longitudinal axis shows time and lateral axis shows horizontal distance along the Koshikijima line. Circles show positions of cellular echoes at each time, which generated in AREA 1, AREA 2 and AREA 3, respectively. A line between two circles shows the cells are the same ones. Shaded area shows the position of the Koshikijima line at 1030 JST, 1130 JST, 1230 JST.

For understanding the process from cellular echoes to a line-shaped echo, we followed the trail of cellular echoes (Fig.6), which made a contribution to formation of a line-shaped echo.

During the period from 1000 to 1120 JST, most of the cellular echoes generated on Koshikijima Islands. After they generated on Koshikijima Islands, they moved northeastward and dissipated over northeastern sea of Koshikijima Islands. At the same time, new cellular echo generated near the dissipating cells. The new cellular echo also moved northeastward and dissipated over northeastern sea of Koshikijima Islands.

During the period from 1125 to 1310 JST, most of cellular echoes have generated not only on Koshikijima Islands but also over the downstream of Koshikijima Islands. In AREA 2, new cellular echoes generated near dissipating ones as well as during the former period. In AREA 3, new cellular echoes appeared at 1125 JST for the first time. At 1230 JST, 10 cellular echoes formed a line of 80 km in length. They are 1 cellular echoes generated in AREA 1, 4 cellular echoes in AREA 2 and 5 cellular echoes in AREA 3.

It is found that new cellular echoes generated over northeastern sea of Koshikijima Islands near dissipating cells, which generated on Koshikijima Islands. They made a line-shaped echo.

4. DISCUSSION

We can understand formation mechanism of a line-shaped system from the consideration on generation mechanisms of cellular echoes, which consisted of a line-shaped system.

First, new cellular echoes generated on Koshikijima Islands. Southly winds were predominant near the surface, lower atmosphere is moist and Fr is close to 1. The upslope forcing due to mountains on Koshikijima Islands is seemed to make cellular echoes generate in AREA 1. Height of the cells is low with the core below the melting layer. Under the moist atmosphere, the quick development from cloud drops to rainfall drops occurred. Low-height echo top indicates that deep convection did not occur.

Second, the new cellular echoes generated over northeastern sea of Koshikijima Islands near the dissipating ones. For example, Fig. 7 shows the generation of new cell. A new cell L appeared at 1045 JST near dissipating cell E. Divergent flow with the dissipating cell E and southern inflow around the surface are seemed to produce meso γ-scale convergence under the new cell L. Under the same moist atmosphere, it is considered that the forcing due to evaporation of precipitation near the surface is weak because there is little evaporation of precipitation. It seems that the downdraft of dissipating cell is weak, so the distance between dissipating cell and new cell is short. It was observed many times that a new cell generates near a dissipating cell over sea, such dissipating cells are seemed to make new cells over the sea.

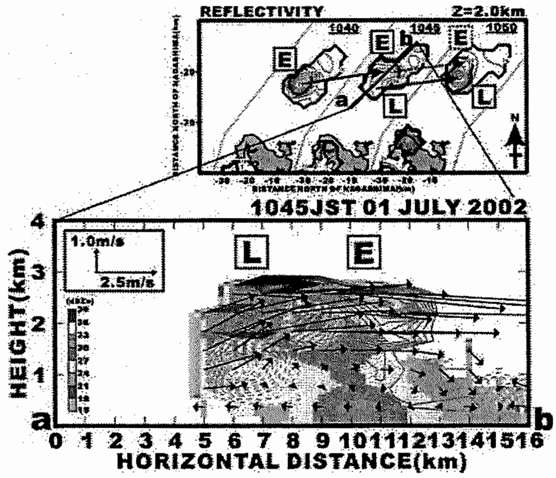

Fig. 7. Time variation of reflectivity at 2.0 km height around Koshikijima Islands. E and L show the name of each cell (top). Vertical section of reflectivity and winds in the northeastward direction along the a-b line (bottom). Vector shows relative winds to the cells. Solid and dashed contours show horizontal divergence and convergence, respectively.

Third, another new cells generated around Nagashima Island. The cause of generation of cellular echoes around Nagashima Island is considered an intensification of advecting convective updraft by local updraft made be the Island.

The generation of convective cells occurred not only on Koshikijima Islands but also over the northeastern sea and around Nagashima Island. All of them moved northeastward along the direction of the line. Successive combination of these three processes on generation and movement of convective cells leads to increase in the number of them on a line, so the Koshikijima line formed with about 80 km length.

5. CONCLUSIONS

We investigated formation process of the line-shaped system, the Koshikijima line, observed on 01 July 2002, using the data of two X-band Doppler radars and MANAL.

The Koshikijima line had 80 km in length. It aligned northeastward from Koshikijima Islands to Nagashima Island, which consisted of many cellular echoes with about 6 km in echo top. From a viewpoint of cellular echoes in the line-shaped system, the generation and movement of convective cells occurred not only on Koshikijima Islands but also over northeastern sea of Koshikijima Islands and around Nagashima Island. It is found that such generation and movement of cells leads to form the Koshikijima line with about 80 km length.

On the islands, it can be considered that the generation of cells is caused by the mountains. Over the sea, it can be said that the generation of cells is caused by meso γ-scale convergence, which are produced by outflow from the dissipating cells.

Acknowledgements

The authors thank all of the participants in the X-BAIU-02 observation for obtaining these data and the Japan Meteorological Agency for providing sounding data and radar data.

References

Smolarkiewicz, P. K. and R. Rotunno, 1989: Low Froude Number Flow Past Three-Dimensional Obstacles. Part I: Baroclinically Generated Lee Vortices. J. Atoms. Sci., **46**, 1154-1164.

Staffs of Fukuoka radar, 1974: Weather in Kyushu district observed by Fukuoka radar (in Japanese). Tenki, **21**, 265-279.

Morita, 1999: Orographic Rainfall due to Koshikijima Islands –the case study of 9 July 1997 (in Japanese). Applied Meteorology and Climate Resources., **12**, 19-24

SIMULATION OF DEVELOPMENT OF DEEP CONVECTION FROM SHALLOW CLOUDS

Tomoe Nasuno

Frontier Research System for Global Change, Yokohama, Japan

1. INTRODUCTION

In this study, numerical simulations of daytime convection over land are conducted using a nonhydrostatic model. The simulated case is based on observations during TRMM/LBA field campaign in Rondonia, Brazil, which was picked up as case 4 of the model intercomparison projects by GEWEX Cloud System Study (GCSS) Working Group 4 (WG4).

The main objective of the GCSS WG4 case 4 was to know the ability of the current nonhydrostatic models (e.g. boundary layer schemes) to reproduce realistic diurnal variation of clouds, which can not be separately discussed from resolution dependence. In this paper, role of subgrid-scale turbulence on the evolution of simulated clouds, and dependence on horizontal/vertical resolution will be reported. Some remarks on organization of clouds and dependence on dimension are also made.

2. MODEL AND DESIGN OF EXPERIMENTS

The numerical experiments are performed using the Japan Meteorological Agency Nonhydrostatic Model (JMA-NHM; Saito et al, 2001). The model includes turbulent closure scheme (Ikawa and Saito 1991) based on Klemp and Wilhelmson(1978) and Deardorff(1980), which prognose turbulent kinetic energy (TKE). As for the cloud microphysical schemes(Ikawa et al. 1991), mixing ratios and number concentrations of 3 categories of ice are predicted, as well as mixing ratios of cloud water and rainwater.

Table 1 : Specification of the experimental cases.

case (dim)	dx (domain)	dz (levels)
1 (2D)	500m (250km)	30-300m (76)
2 (2D)	500m (250km)	60-750m (46)
3 (2D)	500m (250km)	300-600m (46)
4 (2D)	500m (250km)	20-250m (180)
5 (3D)	500m (150km)	30-300m (76)
6 (3D)	1km (300km)	30-300m (76)
7 (2D)	500m (250km)	30-300m (76)

∗ In case 5-7, correction on advection term is applied.

Correspondingauthoraddress : Frontier Research System for Global Change, 3173-25 Showa-machi, Kanazawa-ku, Yokohama, Kanagawa, 236-0001 Japan, E-mail: nasuno@jamstec.go.jp

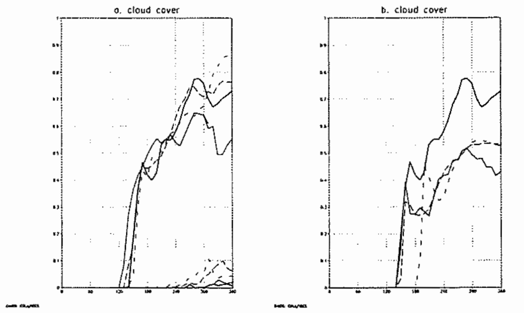

Figure 1: Time evolution of cloud cover. (left) 2D simulations (solid line, case 1; broken, 2; dash-dott, 3; thin, 4). Cold cloud cover is also plotted (less than 0.1). (right) 3D and 2D simulations (solid line, case 1; broken, 5; dash-dott, 6; thin, 7).

The settings of the simulations follow the documentation by Grabowski (2003). Based on the observational data on February 23, 1999, sounding at 7:30 local time is given at the initial time, and time sequence of radiative forcing and sensible and latent heat fluxes are imposed during 6 hours of integration.

Computational domain and resolution of experiments are shown in Table 1. Two dimensional (2D) experiments varying vertical resolution (case 1-4) and three dimensional (3D) experiments with different horizontal resolution (case 5, 6) are conducted. In the control run (case 1), horizontal resolution of 500 m is used.

In the vertical, 76 vertical levels are taken, with stretched grids of 30 m (at the lowest level) to 300 m (in the upper levels) resolution. In all the experiments periodic boundary condition is employed at lateral boundaries.

In case 5-7, correction on advection term of scalar variables to avoid negative value (,with keeping conservation of total amount) is applied.

3. RESULTS

3.1 Time evolution of the clouds

Figure 1 shows the time series of the cloud cover in 2D and 3D simulations. Fraction of cloudy area

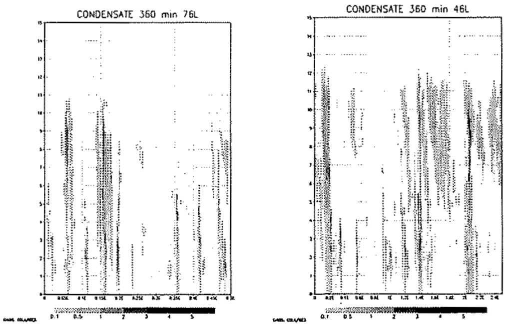

Figure 2: Vertical cross section of total condensate at 360 min for case 1 (left) and case 3 (right).

(where cloud water or ice exists at any level) to the whole domain is plotted. In all the cases, clouds are formed after 120-150 min of calculation. Cloud cover increases with time, and deep convection develops (Fig. 2) by the end of the simulation (13:30 local time).

These results suggest that an ordinary turbulent scheme of TKE closure type with 500-1000 m horizontal resolution is capable of reproducing cloud development in diurnal cycle to a certain extent.

3.2 Development of the boundary layer

Figure 3 displays the development of the boundary layer in case 1. Domain averaged profiles are plotted at 1 hour intervals. Both potential temperature and moisture show that a well mixed boundary layer of about 800 m depth develops after 3 hours of integration. Clouds begin to form at 150 min in the boundary layer. Similar features are also seen in other cases.

Figure 4 shows the distribution of TKE (deviation from the horizontal averaged value) in a sub-domain of 25 km-width at 10 min intervals. Vertical velocity is indicated by contour lines. Peaks of TKE are observed prior to growth of updrafts (e.g. x=76,81,83,87,96 km). Horizontal contrast of TKE is clearer in a layer near the surface, the depth of which deepens from 500 m to

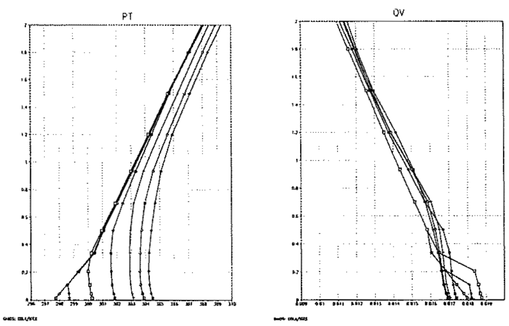

Figure 3: Vertical profiles (z=0-2km) of domain averaged potential temperature (left) and water vapor mixing ratio (right) at 1 hour intervals for case 1.

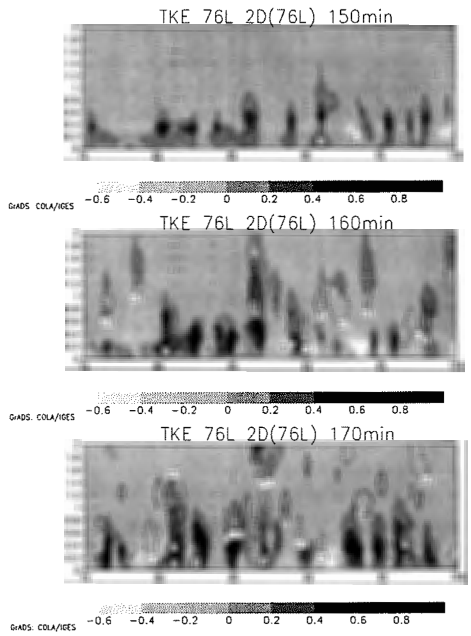

Figure 4: Distribution of TKE (x=75-100km, z=0-2km) at 150, 160 and 170 min. Deviation from the horizontal average is drawn. Contour line depicts vertical velocity.

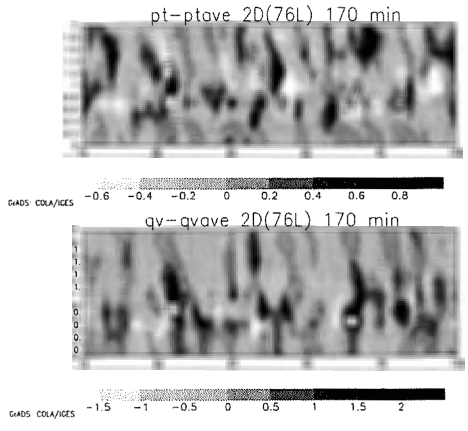

Figure 5: The same as Fig.2, but for potential temperature and water vapor mixing ratio at 170 min. Contour lines show cloud water mixing ratio.

800 m in this 20 minutes. It corresponds to the well mixed layer in Fig.3.

Deviations of potential temperature and moisture are depicted in Fig.5. In both panels, top of the boundary layer is clearly recognized, where cloud bases are located. Horizontal contrast of potential temperature is more significant above the boundary layer, and the positive anomaly is not necessarily corresponds to cloud areas. The locations of clouds well correspond to positive moisture anomalies that have roots at the bottom surface. It is suggested that vertical transport of moisture in the boundary layer is more tightly connected to the formation of clouds than positive buoyancy near the cloud base height (boundary layer top). Once a cloud grows into to the free atmosphere (e.g. Fig.4, x=87 km), grid-resolved transport dominates the subgrid scale, and deep convection gradually develops.

In Fig. 4 and 5, typical horizontal scale is about grid size (500-1000 m), and it is expected that with higher horizontal resolution, finer structure and resultant vertical transport of heat and moisture by grid-resolved and subgrid scale processes can be captured.

3.3 Sensitivity to resolution and dimension

In Fig.1, timing of the cloud formation is almost the same (about 120 min) except for case 6, where coarser horizontal resolution (1 km) is used. Vertical resolution does not so much affects the timing of initiation (only 10 min earlier for finer resolution), but has significant impact at the later stage.

Cloud cover in case 2, 3 (46L; coarser resolution in the upper troposphere) is larger than that in case 1 (76L) and 4 (180L). (Note that resolution in the lower troposphere is similar in case 1 and 2.) As expected, cold cloud cover shows the same tendency, and total condensate in the upper troposphere is much larger with a coarse resolution (Fig. 2). Such dependence is considered to be closely related to the modeling of cloud microphysics.

Resolution in the lower troposphere has a significant impacts on the speed of the deepening of clouds (not shown). It is faster with coarse resolution than that with fine resolution. The rapid growth with coarse resolution seems to be related to the formulation of turbulent scheme. In the JMA-NHM, the diffusional coefficient is proportional to the vertical grid-spacing or height, and subsequently, the magnitude and depth of the eddy diffusional coefficient are larger with coarse resolution.

As to the dependence on dimension, increase in cloud cover seems to be more rapid in 2D cases than 3D cases at earlier stage (Fig.1 b), but it should be noted that difference in advection scheme has larger impact. Figure 1 b also shows that at the later stage, when some organization of clouds are observed in all the cases, dependence on dimension is superior to that on horizontal resolution. It is inferred that organization of deep convection is more sensitive to the dimension of the model domain, compared with disorganized shallow clouds.

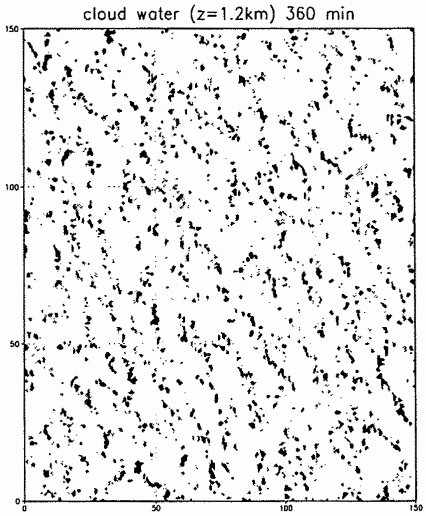

Figure 6: Cloud water mixing ratio at z=1.2km at 360 min for 3D simulation (case 5).

3.4 Organization of clouds

Clouds are organized by cold pool mechanism in all the simulations. Since northwesterly environmental wind (that has jet type profile with peak velocity of 6 m s^{-1} at 2 km altitude) is given throughout the simulation, cloud tilt westward with heght (Fig. 2) and propagate eastward in 2D cases. These features are similar to those of squall line. In the 3D simulations, however, clouds are alined parallel to the wind shear (Fig. 6), and propagate southeastward. The organization of convection seems to be significantly different beteween 2D and 3D cases.

4. CONCLUDING REMARKS

In the present study, numerical simulations of daytime convection over land, based on the observation during TRMM/LBA field project in Brazil, are conducted. The purpose is to get insight into the transition process from shallow clouds in the boundary layer to deep precipitating convection.

A series of experiments are performed to investigate the ability of the model to reproduce the transition, in terms of the turbulent scheme, resolution, and dimension of the model. The results suggest that an ordinary turbulent scheme of TKE closure type with 500-1000 m horizontal resolution is capable of reproducing cloud development in diurnal cycle to a certain extent.

Horizontal resolution has striking impact at the initiation of boundary layer clouds, but when deep convection develops, dimension of the model domain dominates.

Concerning the dependence on vertical resolution, coarser resolution in lower troposphere results in more rapid growth of clouds, and coarser resolution in the upper troposphere causes much more cloud amount. The former seems to be related to the formulation of turbulent scheme, and the latter to the cloud microphysical scheme.

In all the simulation, some organization of the deep clouds are observed, but the effects of vertical shear of the environmental wind is considerably different between 2D simulations and 3D simulations.

5. ACKNOWLEDGEMENTS

The authors express their thanks to Japan Meteorological Agency for providing the nonhydrostatic model (JMA-NHM).

6. REFERENCES

Deardorff,J.W., 1980: Strato-cumulus-capped mixed layers derived from a three-dimensional model. Boundary-Layer Meteorol., **18**, 495-527.

Grabowski,W.W., 2003: Case4: Daytime convective development over land: an idealized case based on TRMM-LBA observations. Available at http://box.mmm.ucar.edu/gcss-wg4/gcss/case4.html.

Ikawa, M., H. Mizuno, T. Matsuo, M. Murakami, Y. Yamada, and K. Saito, 1991: Numerical modeling of the convective snow cloud over the Sea of Japan — Sensitivity to ice crystal nucleation rates —. J. Meteor. Soc. Japan,**69**,641-667.

Ikawa, M., and K. Saito, 1991: Description of a nonhydrostatic model developed at the Forecast Research Department of the MRI. Technical Reports of the MRI,**28**,238pp.

Klemp,J.B. and R.Wilhelmson,1978: The simulation of three-dimensional convective storm dynamics. J. Atmos. Sci., **35**, 1070-1096.

Saito, K., T. Kato, H. Eito, and C. Muroi, 2001: Documentation of the Meteorological Research Institute/Numerical prediction Division unified nonhydrostatic model. Technical Reports of the MRI, **42**, 133pp.

OBSERVATIONAL STUDY OF THE SNOWFALL SYSTEM ASSOCIATED WITH A MESOSCALE LOW FORMED OVER THE SEA OF JAPAN

Tadayasu Ohigashi and Kazuhisa Tsuboki

Hydrospheric Atmospheric Research Center, Nagoya University, Nagoya, Japan

1. INTRODUCTION

When cold air outbreaks occur from the Eurasian Continent, mesoscale lows frequently formed over the Sea of Japan, which are also referred to as "polar lows". A lot of mesoscale lows are associated with the JPCZ (Japan-Sea Polar-airmass Convergence Zone) (Asai, 1988). The JPCZ extends from the lee side of the mountains around the joint of the Korean Peninsula to the central coast of the Japan Islands, and is characterized by strong convergence, horizontal shear and an active convevtive cloud band.

Snowfall systems within mesoscale lows bring intense and a large amount of snowfall to the coastal region of the Japan Islands in its landing (e.g. Ninomiya and Hoshino 1990). Strong gusts are also caused by mesoscale lows (e.g. Ninomiya and Hoshino 1990; Yamagishi et al. 1992). But there were not many reports for distributions and structures of snowfall systems in mesoscale lows which bring the severe phenomena. The understanding of the detailed characteristics of snowfall systems is important to clarify precipitation and wind speed distributions in mesoscale lows and is signi?cant for the comparison with the results of numerical simulations which resolve clouds.

A mesoscale low associated with the development of the cloud band along the JPCZ generated at 14 January 2001. The snowfall systems formed within the mesoscale low are investigated using the observation data to clarify the characteristics of snowfall systems in a mesoscale low.

2. DATA

The data obtained by the two C-band Doppler radars of Hokuriku Electric Power Company set at Goishigamine and Mikuni is used. The radar sites and observation ranges are showed in Fig. 1. The radar data was made into CAPPI (Constant Altitude Plan Position Indicator) data. Horizontal wind was derived from the two Doppler radar data.

Corresponding author's address: Tadayasu Ohigashi, Hydrospheric Atmospheric Research Center, Nagoya University, Furo-cho, Chikusa-ku, Nagoya, 464–8601 Japan; E-Mail: ohigashi@rain.hyarc.nagoya–u.ac.jp

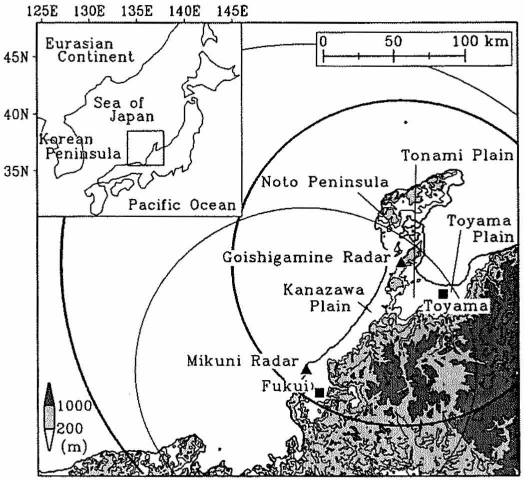

Fig. 1 Locations of observation points. The marks of ▲ indicate the observation points of the C-band Doppler radars of Hokuriku Electric Power Company set at Goishigamine and Mikuni. The small and large solid circles indicate observation ranges of radius of 120 and 240 km of the radars, respectively. The surface observation points at Fukui and Toyama are marked with ■. The altitude of topography is shown with contours (0, 100, 200, 500, 1000 and 2000 m) and gray levels (0, 200 and 1000 m).

The RANAL (Regional Objective Analysis), AMeDAS (Automated Meteorological Data Acquisition System) and surface observation data of the JMA (Japan Meteorological Agency) are also utilized. In addition, the GMS (Geostationary Meteorological Satellite) data received at Nagoya University is employed. The surface observation points (Fukui and Toyama) of the JMA are showed in Fig. 1.

3. FORMATION OF A MESOSCALE LOW ASSOCIATED WITH THE DEVELOPMENT OF THE CLOUD BAND ALONG THE JPCZ

The cloud band along the JPCZ have formed over the western part of the Sea of Japan by the afternoon of 14 January 2001. At 500 hPa, an upper-level synoptic-scale trough was located over the Chishima Islands. Over the Eurasian continent, an upper-level mesoscale

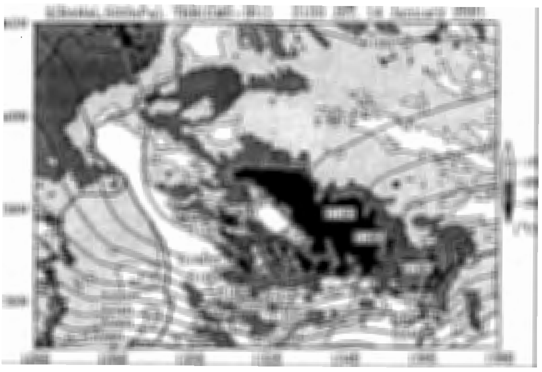

Fig. 2 Geopotential height (solid lines every 20 m) at 500 hPa of RANAL, and T_{BB} (gray levels; −35, −25 and −15 °C) of the infrared imagery of the GMS at 21 JST, 14 January 2001.

trough (UMT) was present. The UMT progressed along the rim of the upper-level synoptic-scale trough and was located over the Sea of Japan in the afternoon of 14 January 2001. Satellite imagery showed that the southeastern part of the cloud band along the JPCZ rapidly developed from 15 JST (Japan Standard Time), 14 January when the UMT approached the cloud band. T_{BB} (equivalent black body temperature) was lower than −45 ℃ in the minimum. This indicates deep and active convection for a period of a cold air outbreak (Fig. 2).

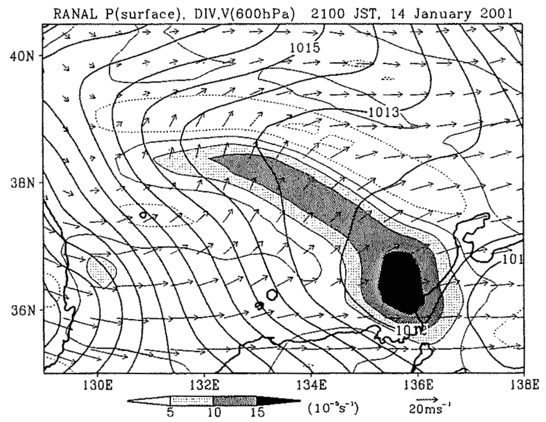

Fig. 3 Horizontal divergence (thin lines every 5 × 10^{-5} s^{-1} with gray levels than 5 × 10^{-5} s^{-1}), horizontal wind (arrows) at 600 hPa and the surface pressure (thick lines every 1 hPa) at 21 JST, 14 January 2001.

Weak wind zone with the southwesterly wind was present along the intensi?ed cloud band from 700 hPa to 500 hPa. On the other hand, strong wind zone with the southwesterly wind was formed along the northeastern region than the weak wind zone. The weak and strong wind zones formed a divergence zone from 700 hPa to 500 hPa on the northeastern region than the cloud band. On the surface, a trough deepened below the upper-level divergence zone (Fig. 3). A mesoscale low formed in the deep surface trough.

4. EVOLUTION AND STRUCTURE OF SNOWFALL SYSTEM WITHIN THE MESOSCALE LOW

Radar echo showed that the snowfall system along the JPCZ moved toward NE when the cloud band developed. Southerly or easterly wind which blew toward the mesoscale low formed in the Kanazawa Plain, the Tonami Plain and the Toyama Plain. In the northern region than the cloud band (CB in Fig. 4 a) along the JPCZ, transeverse mode snowbands which extended from SW to NE intensi?ed near the coastal region of the Kanazawa Plain and formed a intense and broad snowband with a width of 20 km (B1). B1 was con?uent to the snowfall system along the JPCZ (CB) which moved toward NE. Another snowband (B2) also formed around the Tonami Plain and Toyama Plain between monsoon wind and offshore wind, and moved northward (Figs. 4a and b). Around the Kanazawa Plain, a snowband (B3) was formed from CB along the JPCZ. Some snowfall systems including B1, B2 and B3 gradually formed vortexlike echo pattern (Figs. 4b and c). In the southern region than B3, an echo free region was present (Fig. 4c). The echo free region corresponded to the cloud free region of the satellite imagery. This indicates that the echo free region was the descending current region. The vortexlike echo moved toward SE and its center landed around Fukui. In the rear (northwestern part) of the vortexlike echo, some snowbands along the wind direction and isolated echo group formed (Fig. 4d). These snow clouds were present in the region in which the cold air outbreak was intensi?ed by the mesoscale low. The snowbands in the rear of the vortexlike echo were connected with the cloud band along the JPCZ. Then, the cloud band along the JPCZ moved southward and gradually became weak. The northward and southward movement of the cloud band along the JPCZ associated with approach of a UMT was reported in Nagata (1992).

Re?ectivity and horizontal wind derived from the two Doppler radar data in the lower level are showed in Fig. 5 when the vortexlike echo was clear. The horizontal wind showed a clear vortexlike pattern. The wind velocity and direction rapidly changed along B3. The strong west-southwesterly wind region was present in the southern region than B3. The horizontal shear was about 30 m s^{-1} per a horizontal distance of 50 km.

Surface observation at Fukui showed that the temperature rose by about 2 degrees when B3 passed over Fukui around 23 JST, 14 (Fig. 6). At the same time, the wind speed became strong, and the wind direction changed from SE to SW.

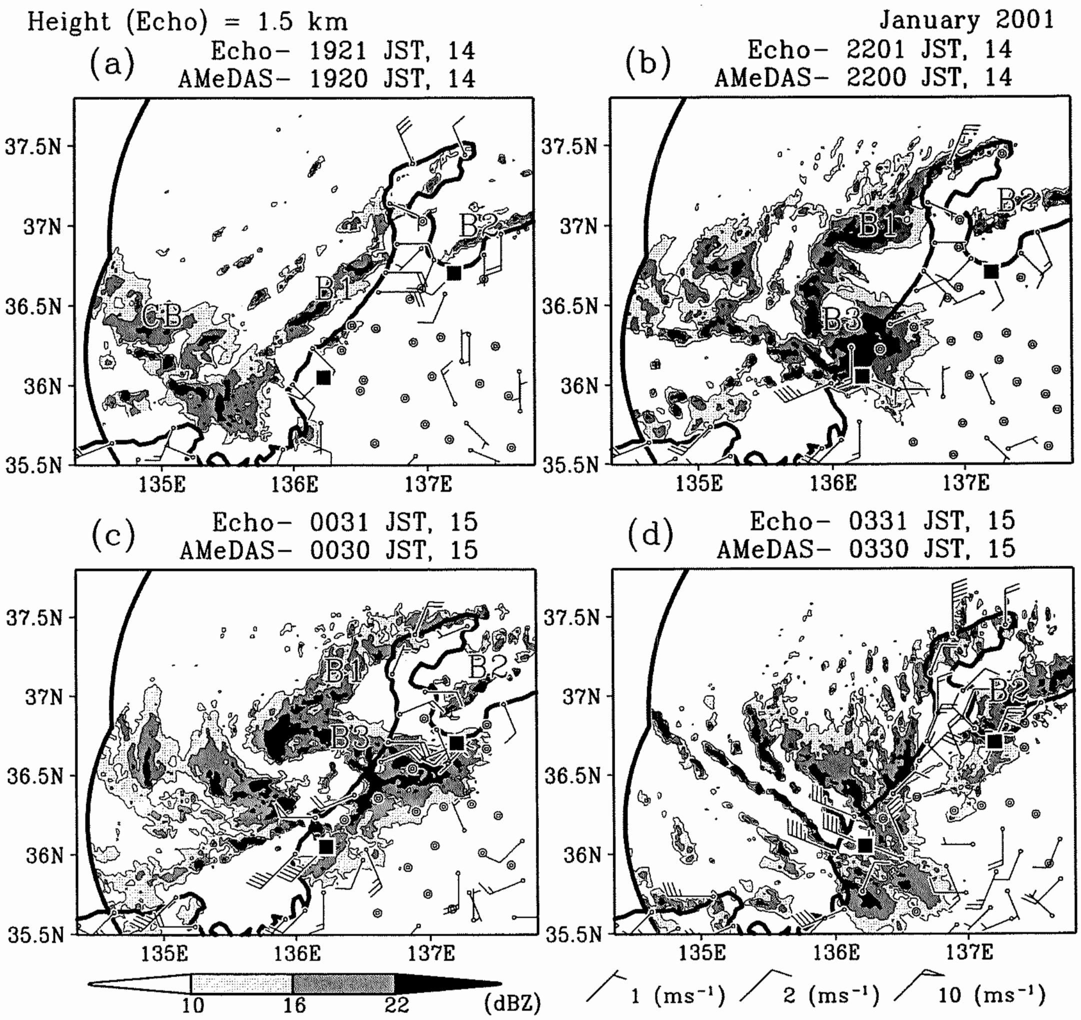

Fig. 4 Reflectivity (gray levels; 10, 16 and 22 dBZ) at a height of 1.5 km and horizontal wind (half barb; 1 m s^{-1}, full barb; 2 m s^{-1}, flag; 10 m s^{-1}) at the AMeDAS points at (a) 1921 (1920) JST, 14 (b) 2201 (2200) JST, 14, (c) 0031 (0030) JST, 15 and (d) 0331 (0330) JST, 15 January 2001. The surface observation points at Fukui and Toyama are marked with ■.

The instantaneous wind speed of 22.8 m s^{-1} were observed at 2350 JST, 14. When B3 moved northward after passing Fukui, the wind speed at Fukui gradually became weak.

The time series of meteorological elements at Toyama are presented in Fig. 7 .This indicates the changes which are accompanied by B2. The wind direction changed from NW to SW when the mesoscale low developed over the sea around 14 JST, 14. At the same time, the temperature decreased by about 1 degree. After that, B1 gradually formed from the transeverse mode snowbands. On the other hand, when B2 landed on the plain from the sea around 03 JST, 15, the wind direction changed northerly, and the temperature increased by about 1.5 degrees. This indicates that B2 was present in the zone with signi?cant horizontal temperature gradient and shear, and relatively cold air was present in the southern region than B2. It is inferred that B1 formed on the same atmospheric condition as B2.

5. SUMMARY

When a upper-level mesoscale trough progressed over the Sea of Japan in the afternoon of 14 January 2001, the southeastern part of the cloud band along the JPCZ rapidly developed. The development of the cloud band was accompanied by the intensi?cation of horizontal divergence from 700 hPa to 500 hPa. Below the upper-level divergence zone, a surface trough deepened. A mesoscale low developed within the deep surface trough.

The cloud band along the JPCZ developed and moved toward NE. A vortexlike echo pat-

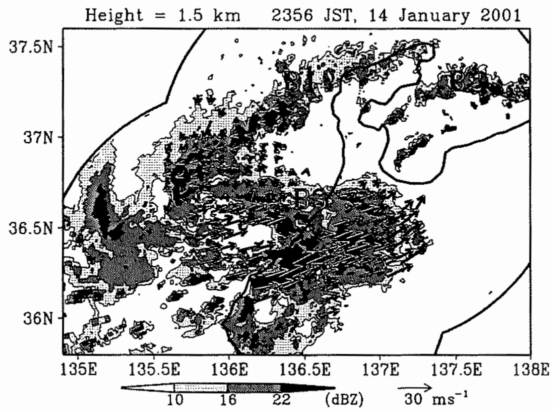

Fig. 5 Reflectivity (gray levels; 10, 16 and 22 dBZ) and horizontal wind (arrows) derived by the two Doppler radar data at a height of 1.5 km at 2356 JST, 14 January 2001.

tern gradually formed. The snowbands (B1, B2 and B3) within the mesoscale low formed in the shear lines which were accompanying the signi?cant horizontal temperature gradient. In the region enclosed by B1, B2 and B3, relatively cold air was present, and southerly or easterly weak wind blew. The southern side than B3 was strong horizontal wind region with the instantaneous wind speed over 20 m s^{-1} and descending current. In the rear of the vortexlike echo which moved toward SE, some snowbands aligned along the wind direction and isolated echo group were present. Finally, the cloud band which were connected with the snowbands of the rear of the mesoscale low moved southward and became weak.

ACKNOWLEDGMENTS

The authors would like to express their thanks to Professor H. Uyeda, Dr. T. Maesaka of Nagoya University, Mr. K. Kami and Mr. K. Shinjo of Hokuriku Electric Power Company for supplying us with the Doppler radar data.

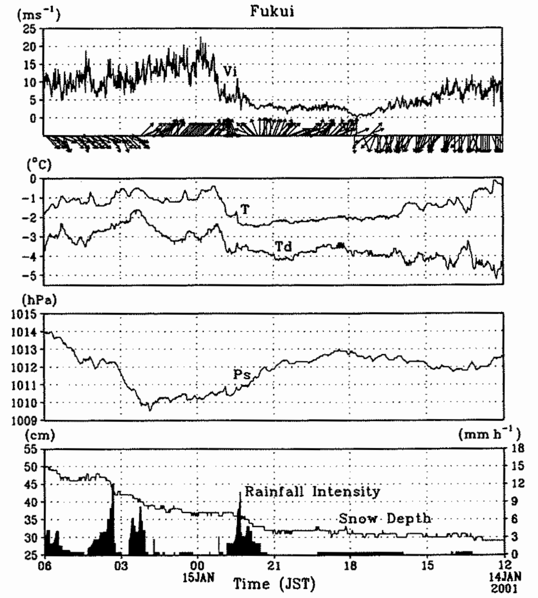

Fig. 6 Time series of the instantaneous wind (Vi), temperature (T), dew point temperature (Td), sea level pressure (Ps), rainfall intensity and snow depth at Fukui every 1 minute from 12 JST, 14 to 06 JST, 15 January 2001.

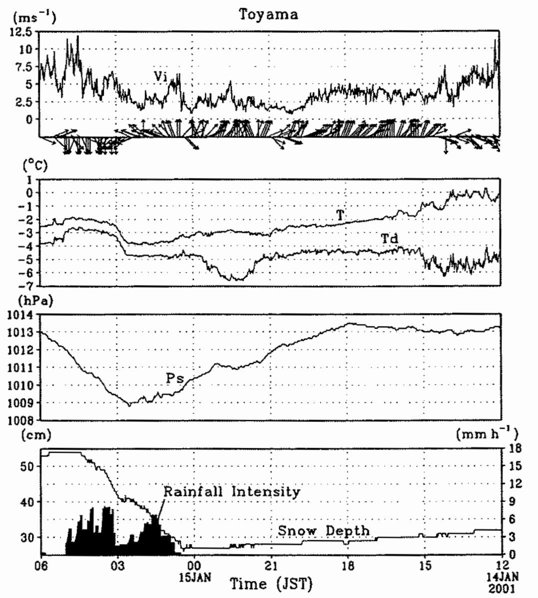

Fig. 7 As in Fig. 6 except for at Toyama.

REFERENCES

Asai, T., 1988: Meso-scale features of heavy snowfalls in Japan Sea coastal regions of Japan. *Tenki*, **35**, 156–161 (in Japanese).

Nagata, M., 1992: Modeling case study of the Japan-Sea convergent cloud band in a varying large-scale environment: Evolution and upscale effect. *J. Meteor. Soc. Japan*, **70**, 649–671.

Ninomiya, K. and K. Hoshino, 1990: Evolution process and multi-scale structure of a polar low developed over the Japan Sea on 11∼12 December 1985 Part II: Meso-β-scale low in meso-α-scale polar low. *J. Meteor. Soc. Japan*, **68**, 307–318.

Yamagishi, Y., M. Doi, N. Kitabatake and H. Kamiguchi, 1992: A polar low which accompanied strong gust. *Tenki*, **39**, 27–36 (in Japanese).

APPLICATION OF CLUSTER ANALYSIS TECHNIQUES TO THE VERIFICATION OF QUANTITATIVE PRECIPITATION FORECASTS

Stefano Serafin[1], Alessio Bertò[1], Andrea Buzzi[2], Rossella Ferretti[3] and Dino Zardi[1]

[1]Department of Civil and Environmental Engineering, University of Trento, Trento, Italy
[2]Istituto di Scienze dell'Atmosfera e del Clima CNR, Bologna, Italy
[3]Department of Physics/CETEMPS, University of L'Aquila, Coppito di L'Aquila, Italy

1 INTRODUCTION

Quantitative precipitation forecasts by numerical weather prediction models are usually verified by means of pointwise comparisons between local observations by rain gauges and interpolated forecast fields. The agreement between forecasts and observations is then evaluated by means of a contingency table. Finally, standard verification scores such as equitable threat score and bias are computed (Wilks, 1995; Hamill, 1999).

As a consequence, the distribution of rain gauges in the simulation domain plays a major role in verification, whose results depend mostly on the model performance in the areas where the rain gauge network is denser. Nevertheless, standard verification procedures do not take into account the spatial variability of the observed and forecast precipitation fields.

The key points addressed here are:

1. do verification scores vary significantly within a simulation domain?
2. if so, are the variations related to geographical, meteorological, or other features?
3. based on the analysis of the spatial variability of verification scores, is it possible to explain the causes of a model's unsatisfactory performance?

The database collected during the MAP (Mesoscale Alpine Programme) campaign in 1999 is particularly suited to discuss such issues, having very high resolution both in space and in time. Several events of the campaign (Intensive Observation Periods) have been selected, among those which displayed relevant precipitation amounts over Northern Italy: IOP2a, IOP2b, IOP3, IOP8, IOP15.

In the present work, for each event the set of available observed data is split into a series of subsets, each of them having a similar precipitation pattern. Cluster analysis (Jain et al., 1999) is adopted as an objective method to create groups of rain gauges with interrelated measurements. The data used to perform clustering are precipitation observations and geographical information about rain gauges. Verification scores are computed in each of the subsets detected by clustering.

Corresponding author's address: Stefano Serafin, Department of Civil and Environmental Engineering, University of Trento I-38050 Trento, Italy; E-Mail: stefano.serafin@ing.unitn.it.

2 CASE STUDIES AND MODEL SIMULATIONS

Most of the events under consideration were characterized by similar synoptic conditions, with an upper level trough and a surface level low approaching northern Italy from the West. The flow associated with this configuration is in general southerly over this region. IOP2a is a convective rainfall event over the Lago Maggiore area. Heavy rainfall was widespread over Italy and also on the northern slope of the Alps during IOP2b, while it insisted only over Piedmont in IOP3. Rainfall was moderate and mainly concentrated in the Po Valley during IOP8. Finally, during IOP15 a deep cut-off low insisted over the Mediterranean sea, drawing north-westerly currents over Italy.

Two models, namely PSU/NCAR MM5 (non-hydrostatic, Grell et al., 1994) and ISAC-CNR BOLAM (hydrostatic, Buzzi et al., 1994), have been used to simulate these events. The area of interest is approximately located between 43–49°N and 4–16°E, in order to include Northern Italy as a whole (see Figure 1). The models were run with similar resolutions: a single domain with 12.5 km grid spacing for BOLAM and 2 two-way nested domains for MM5, with the inner one having 6 km resolution. All of the simulations were initialized with ECMWF analyses and were 48 hours long (startup times: IOP2a, 1200UTC 17 Sep; IOP2b, 1200UTC 19 Sep; IOP3, 0000UTC 25 Sep; IOP8, 1200UTC 20 Oct; IOP15, 1200UTC 5 Nov).

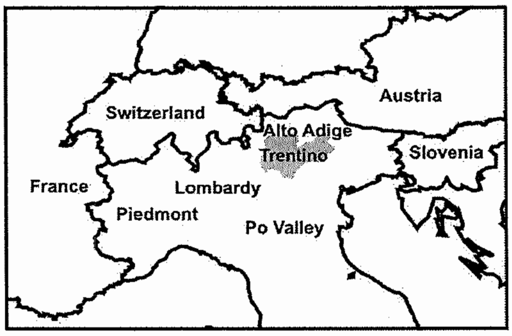

Figure 1. The area of interest for forecast verification during the MAP campaign. The simulation domains created for BOLAM and MM5 include this region as a whole. The names of relevant locations cited in the text are shown.

3 CLUSTERING TECHNIQUE

In order to identify the most significant precipitation patterns in the wide number of available observation points (about 1500), suitable criteria to gather them around representative modes have been borrowed from clustering analysis techniques.

Several hierarchical agglomerative clustering techniques have been tested (Brankov et al., 1998; Dorling et al., 1992; Moody and Galloway, 1988) in various meteorological applications. The average-linkage clustering algorithm (Bertò et al., 2004) has been selected due to its good performances.

A key issue in this application of cluster analysis is the use of the appropriate input dataset to relate different precipitation regimes to specific geographical areas. Thus, a multidimensional phase space has been adopted where dimensions include normalized space coordinates (latitude, longitude, and height asl.) and 6-hours normalized accumulated precipitation (ie. 8 time lags spanning 48 hours), resulting in 11 degrees of freedom.

Geographical variables have been weighted with small coefficients (0.7 for latitude and longitude, 0.2 for height) to emphasize the influence of the precipitation factor in the clustering algorithm.

In order to minimize the variance between data within the same cluster and to maximize the variance between different clusters, the Root Mean Square Deviation (RMSD) has been analyzed for various possible number of clusters, in search of sudden breaks (Bertò et al., 2003). RMSD is defined as the root of the average of the cluster variances. Cluster variance is in turn defined as the averaged square distance between each point representing an observation in the phase space and the center of mass of the cluster. Sudden breaks in RMSD identify the merging of significantly different precipitation patterns and suggest the optimal number of clusters to retain at the end of the agglomerative procedure.

4 VERIFICATION INDICES

Verification scores are defined in terms of the elements of a contingency table, in which all the forecast-observation pairs are distributed according to their relationship pertaining a threshold (see Table 1).

Bias and equitable threat score (ETS) are defined respectively as:

$$bias = \frac{a+b}{a+c} \quad ETS = \frac{a-a_r}{a+b+c-a_r} \quad a_r = \frac{(a+b)(a+c)}{a+b+c+d}$$

where a, b, c, and d are the elements of the contingency table, and a_r is an estimate of the number of correct forecasts achieved by a random model (Hamill, 1999).

The bias score, ranging from zero to infinity, allows to assess the overestimation or underestimation of precipitation above a certain threshold, although it bears no information about the correspondence between forecast and observations. In general, bias greater than 1 indicates precipitation overforecasting, while bias less than 1 shows underforecasting. On the other hand, the ETS roughly estimates the percentage of correct forecasts that can be ascribed to the model skill (i.e. the percentage of non-random correct forecasts), with values ranging from slightly negative (worse than random forecast) to 1 (perfect forecast).

Verification scores are supposed to provide significant pieces of information only when computed on a collection of many events, but in this particular context some useful indications can also be obtained from their small-scale analysis, because of the large availability of spatially and temporally dense rainfall measurements.

Another relevant verification measure is the root mean square error (RMSE) of the forecast field; this index has been normalized with the average observed precipitation in each event.

Bias, ETS and RMSE have been computed in each event for the whole data set and for every single cluster. Scores are evaluated for cumulated precipitation over 6 hours; this unusually short time interval makes verification particularly demanding.

The spatial distribution of verification indices has been reconstructed by using an extremely low threshold in contingency tables (0.1 mm). This choice aims at evaluating the models' ability in forecasting the occurrence or lack of rainfall at given space and time coordinates (see Figure 2).

Representative values of verification scores in each event and cluster have been estimated by selecting suitable thresholds (ie. the 33rd and 66th percentile of the frequency distribution of precipitation amounts in each data subset).

Verification scores are indeed very sensitive to the choice of the threshold, and thus also scores vs. threshold charts need to be carefully evaluated.

	o > t	o < t
f > t	a	b
f < t	c	d

Table 1. A contingency table: a is the number of pairs in which both forecast (f) and observation (o) are above the threshold t, and so on.

5 RESULTS

5.1 Global verification scores

Table 2 lists the global verification scores for MM5 (M) and BOLAM (B) in all IOPs. The RMSE is generally lower for B. The precipitation fields forecast by B are more homogenous and regular than those by M. As a result, deviations from observations are on average less relevant. Nevertheless, the ETS of the two models is comparable. As to the bias, M turns out to be drier than B in IOPs 2a, 2b and 3, and wetter in IOPs 8 and 15. Listing the events in order of decreasing forecast quality would yield IOPs 2b and 8 first, then IOP15, finally IOPs 15 and 2a. In general, the more it rains, the better models perform. Thus models seem to have trouble in forecasting low or sparse rainfall.

	iop2a	iop2b	iop3	iop8	iop15
RMSE_M	7,39	2,68	6,27	2,94	4,74
RMSE_B	5,77	2,72	6,21	2,9	4,51
ETS_M	0,11	0,29	0,16	0,29	0,17
ETS_B	0,08	0,3	0,12	0,33	0,23
bias_M	1,24	0,9	1,03	1,68	2,22
bias_B	0,97	0,93	1,37	1,16	1,5

Table 2. RMSE, ETS and bias for M and B in five MAP events. ETS and bias are computed at the 66th percentile threshold (see Section 4).

5.2 Scores distribution

An analysis of the distribution of ETS and bias shows at first sight that these indices are not spatially homogenous. For instance, an overestimation of rainfall by both B and M is often apparent on the northern slope of the Alpine ridge, whereas M tends to produce dry forecasts in the Po valley during IOPs 2a, 2b and 3. Sample pictures are reported in Figure 2: for instance, a wide area of rainfall underestimation is apparent in MM5's bias, while spots of higher bias appear above the alpine ridge.

Bias and ETS often display extreme values in restricted areas; e.g. low ETS in Alto Adige, high ETS in southern France during IOP2b. The first example shows that NWP models can produce misleading forecasts in orographically complex areas, while the second shows how much more effective can be the forecast of purely stratiform rain.

The scores of B are more spatially homogeneous than those of M; this is again due to both the enhanced spatial resolution of M and to its non-hydrostatic nature.

Models seem to achieve better results in forecasting precipitation over the western part of the domain. One reason for this may be that in most events mesoscale systems move west to east across the domain. The model performance decreasing as runtime progresses affects the latest stage of the simulation, when precipitation is expected to occur over the eastern part of the domain.

5.3 Cluster distribution

The clusters detected by the average-linkage algorithm are well separated when plotted in geographical coordinates, although rainfall variables account for more than 70% of the total information used. Moreover, clusters are persistent in all of the events, ie. they have about the same position and shape (see Figure 3).

Rainfall patterns are indeed similar in the different IOPs, but other factors seem to be particularly relevant. For instance, the Alpine ridge is also a separation between adjacent clusters. This is related to the physics of precipitation, the southern slope of the Alps being upstream and the northern downstream.

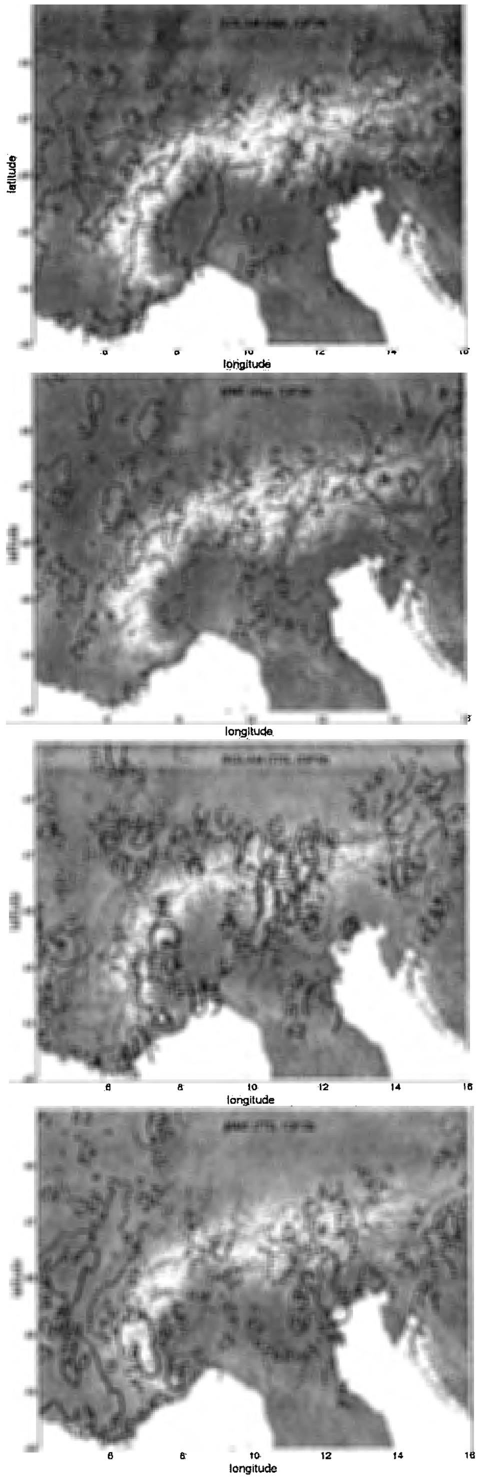

Figure 2 (right): bias and ETS for BOLAM and MM5 in IOP2b.

Also, somewhere clusters seem to mirror the political borders between different countries or regions (Austria, Switzerland, France, Trentino).

For instance, the stations of the Ticino region in Switzerland never appear in the same cluster as those of the adjacent Italian regions, which have similar geomorphological features. This feature raises the suspect of systematical biases in the various rain gauge networks.

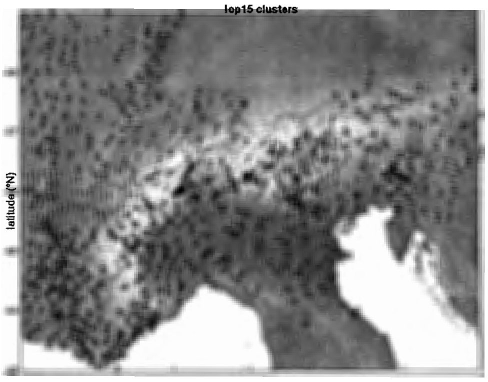

Figure 3. The clusters detected by the average-linkage algorithm from the data of IOP15.

5.4 Clustered verification scores

Table 3 contains a sample of the clustered verification scores for IOP15. The first relevant point is that verification scores change significantly from cluster to cluster. Among the three factors of variability that determine the values of verification indices, the most effective is undoubtedly the spatial variation between clusters. Less relevant factors are the event considered and, last, the model used (M or B). To summarize, models produce very similar forecasts (they were initialized with the same IC's and BC's), but variations in their performance are more relevant between different areas within the same event, than between different events.

cluster	RMSE	ETS	bias
1	**2,2**/*2,6*	**0,38**/*0,24*	**0,96**/*0,32*
2	**1,2**/*1,5*	**0,46**/*0,28*	**1,08**/*0,47*
3	**1,8**/*1,5*	**0,44**/*0,42*	**1,37**/*0,89*
4	**1,5**/*1,8*	**0,48**/*0,44*	**1,31**/*0,49*
5	**1,8**/*1,5*	**0,38**/*0,50*	**1,42**/*1,29*
6	**5,3**/*3,2*	**0,17**/*0,22*	**3,62**/*3,02*
7	**2,9**/*2,6*	**0,25**/*0,25*	**0,70**/*0,41*
8	**2,1**/*2,1*	**0,21**/*0,35*	**1,13**/*1,10*
9	**1,5**/*1,5*	**0,20**/*0,23*	**0,94**/*0,57*
10	**3,9**/*3,9*	**0,15**/*0,16*	**1,90**/*0,67*
11	**3,1**/*2,9*	**0,26**/*0,26*	**1,41**/*1,61*

Table 3. Clustered verification scores for IOP15. Boldface: M; italics: B. ETS and bias were computed at the 66th percentile threshold (see Section 4).

Anyway, it has to be noticed that the splitting into clusters does not allow to capture all of the sharp variations in scores that are apparent in a graphical depiction as Figure 2. Possible explanations are: a) clustered scores are only referred to two particular thresholds; b) the characteristic scale of clusters may be greater than the typical scale of variability of the precipitation field.

6 CONCLUSIONS AND OUTLOOK

Cluster analysis techniques have been applied to the aim of detecting and analyzing any significant spatial variation in the skill of numerical weather prediction models. Various events were simulated with two different models. The subsets detected by the clustering algorithm were remarkably persistent in the events under consideration, and the spatial variability represented by clusters was the most important factor in determining forecast quality. Such variability seems to be related both to shortcomings in the models' physics and to biases in the observational data.

ACKNOWLEDGEMENTS

Data have been obtained from ECMWF. The work was partly supported by the Provincia Autonoma of Trento under the research project AQUAPAST.

REFERENCES

Bertò, A., A. Buzzi and D. Zardi, 2004: Back-tracking Water Vapour Contributing to a Precipitation Event over Trentino: a case study. Meteorol. Z., accepted.

Bertò, A., A. Buzzi and D. Zardi, 2003: Tracking of Water Vapour Contributing to Precipitation Events over the Eastern Italian Alps. Proc. Joint ICAM/MAP Conference, Vol. A, pp. 119-122, 18-23 May 2003, Brig.

Brankov, E., S.T. Rao and P.S. Porter, 1998: A Trajectory-Clustering-Correlation Methodology for Examining the Long-Range Transport of Air Pollutants. Atmos. Environ. 32, 1525-1534.

Buzzi, A., M. Fantini, P. Malguzzi, and F. Nerozzi, 1994: Validation of a limited area model in cases of Mediterranean cyclogenesis: surface fields and precipitation scores. Meteor. Atmos. Phys., 53, 137-154.

Dorling, S.R., T.D. Davies and C.E. Pierce, 1992: Cluster analysis: A Technique for Estimating The Synoptic Meteorological Controls on Air and Precipitation Chemistry-Method and Applications. Atmos. Environ. 26A, 2575-2581.

Ferretti, R., T. Paolucci, G. Giuliani, T. Cherubini, L. Bernardini and G. Visconti, 2003: Verification of high-resolution real-time forecasts over the Alpine region during the MAP SOP. Q. J. R. Meteorol. Soc., 129, 587-607.

Grell, G.A., J. Dudhia and D.R. Stauffer, 1994: A description of the Fifth-Generation Penn State/NCAR Mesoscale Model MM5. NCAR/TN-389+IA.

Hamill, M., 1999: Hypothesis tests for evaluating numerical precipitation forecasts. Wea. Forecasting, 14, 155-167.

Jain, A.K., N.M. Murty, and P.J. Flynn, 1999: Data Clustering: A Review. ACM Computing Surveys, 31, 264-323.

Moody, J.L., and J.N. Galloway, 1988: Quantifying the Relationship between Atmospheric Transport and the Chemical Composition of Precipitation on Bermuda. Tellus. 40B, 463-479.

Wilks, D.S., 1996: Statistical Methods in the Atmospheric Sciences. Academic Press, 1995.

PRECIPITATION CHARACTERISTICS OF CUMULONIMBUS CLOUDS IN THE SOUTHERN REGION OF THE MEIYU FRONT OVER CHINA CONTINENT

Yukari Shusse and Kazuhisa Tsuboki

Hydrospheric Atmospheric Research Center, Nagoya University, Nagoya, Aichi, 464-8601, Japan

1. INTRODUCTION

It is important to investigate how cumulonimbus clouds distribute water vapor and water substance in the atmosphere and to the ground in order to understand the formation process of precipitation in clouds. Cumulonimbus clouds are one of the fundamental elements of the convective cloud system which bears the great portion of vertical transportation of the water in the atmosphere, and hence, their water distribution characteristic needs to be understood also from a viewpoint of a local water cycle or earth water cycle. For the elucidation of these problems, the precipitation characteristics of cumulonimbus clouds such as their duration, degree of development, total precipitation amount, and efficiency at which they change water vapor into precipitation need to be investigated.

Warm season of East Asia is characterized by the active cumulonimbus clouds and those organized systems in the atmospheric condition which water vapor exists abundantly. The process of the water distribution relevant to those precipitation characteristics is considered to play the significant roles of the water cycle in the atmosphere in the humid subtropical region. However, actual conditions of the precipitation characteristics about the cumulonimbus clouds in East Asia including the China Continent are not known yet since there was no sufficient observation data.

The present study is an attempt to provide precipitation characteristics of cumulonimbus clouds in the humid subtropical air mass during warm season, especially in the southern region of the Meiyu front over China Continent. 23 isolated cumulonimbus clouds are investigated which observed by three X-band Doppler radars of Nagoya University and Hokkaido University on 10, 11 and 13 July 1998 during the intensive field observation of GAME/HUBEX (GEWEX Asian Monsoon Experiment / Huaihe River Basin Experiment) in Anhui province, China. Those precipitation features such as duration, maximum area, maximum height, maximum rainfall intensity and the total precipitation during the lifetime of the cumulonimbus clouds are shown using radar reflective intensity data. Furthermore, precipitation efficiency (defined as the ratio of surface rainfall to the water vapor inflow through the cloud base) was estimated for seven cumulonimbus clouds for which dual Doppler radar analysis was possible almost through their lifetime.

Corresponding author's address: Yukari Shusse, Hydrospheric Atmospheric Research Center, Nagoya University, Nagoya, Aichi, 464-8601, Japan; E-Mail: shusse@rain.hyarc.nagoya-u.ac.jp

2. DATA

Intensive observation area of GAME/HUBEX is shown in Fig. 1. Three X-band Doppler radars were operated during the GAME/HUBEX IFO. Maximum quantitative observation range of each Doppler radar

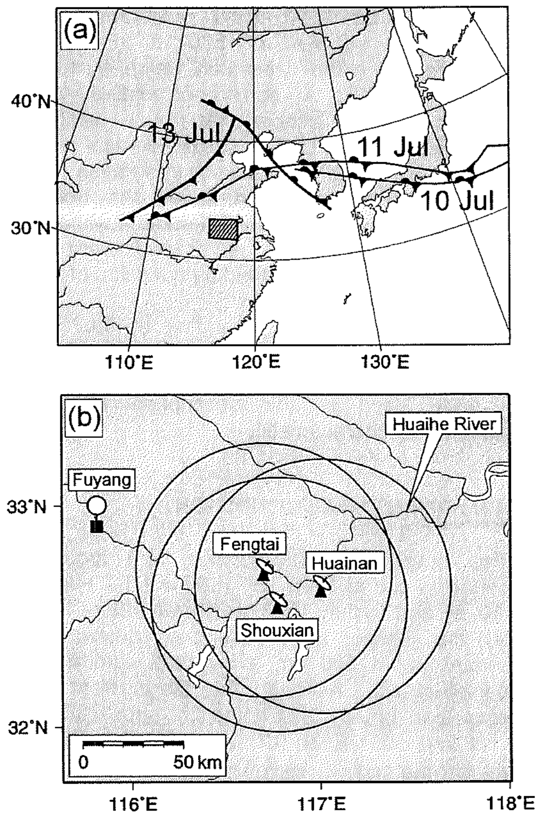

Fig. 1. (a)Fronts around the observation area on 10, 11 and 13 July 1998. (b)Doppler-radar observation sites and upper-air sounding stations. The circles shows the observation ranges of Doppler radars. The location of the map region is shown by shaded rectangle in (a).

is 64 km. The sampling resolution of radar data is 250 m in the direction of the radar beam and 1 degree in the direction of azimuth. One volume scan was made with 14 elevation angles from 0.5 to 41 in 7 minutes. Radar reflectivity data from the Shouxian radar provide the basis for the analysis of the distributions of hydrometeors in this paper. The Fengtai and Huainan radar data were also used to derive three-dimensional wind field besides the Shouxian radar.

The reflectivity values for the Shouxian radar were corrected for the attenuation produced by precipitation. The correction was computed using the following Z-R relationship (Jones, 1956) and K-R relationship (Diviak and Zrnic', 1984).

$$Z = 486\, R^{1.37}, \qquad (1)$$

$$K = 0.01\, R^{1.21}, \qquad (2)$$

where Z is the radar reflectivity factor in mm^6m^{-3}, K is the attenuation rate in dB km^{-1} and R is the rainfall rate in mm h^{-1}.

Doppler velocities and corrected radar reflectivity factors were interpolated at grid points with vertical and horizontal intervals of 500 m in Cartesian coordinates, using the Cressman weighting function (Cressman, 1959). A correction related to the movement of radar echoes was made using Gal-Chen's method (Gal-Chen, 1982). Vertical velocity was determined by the upward integration of the anelastic continuity equation, using the boundary condition of 0 m s^{-1} at the ground surface without any adjustment, because data at upper levels were scarce around echo top and the boundary condition of 0 m s^{-1} at echo top was not applied.

The data of upper-air sounding at the Fuyang Meteorological Observatory, which is 100 km away north-northwestward from the Shouxian Doppler-radar site were used in the description of general environmental characteristic.

3. ENVIRONMENTAL CONDITION

The locations of the surface front around the observation site at 1400 LST (LST = UTC + 8 hours) on 10, 11 and 13 July 1998 are shown in Fig. 1. On 10 July, the Meiyu front extended westward and eastward about 500 km away northward from the observation site. Although the Meiyu front moved eastward on 11 July, a low pressure appeared around 40 N and 105 E on 12 July (not shown). The center of the low-pressure was located around 44 N and 113 E on 13 July. Its trailing cold and warm fronts extended southwestward and southeastward, respectively. Doppler radar observation sites were located about 1000 km away southward from the low-pressure center. GMS infrared imagery shows that the observation area of the Doppler radars was not covered with a synoptic-scale cloud system around 1400 LST on 10, 11 and 13 July (not shown).

During the 3 days, air temperature reached 35 C and water vapor mixing ratio was about 20 g kg^{-1} at the surface. Precipitatable water amount was 55 to 59 mm. A layer drier than 30 % was found at 6 km on 10 July, that drier than 50 % was at 5 km on 11 July, and that drier than 40 % was at 3 km on 13 July. The freezing level was 5.3 to 5.9 km. Lifting condensation level (LCL) and level of free convection (LFC) were 1.3 to 1.5 km and 1.4 to 2.2 km, respectively, as determined by a parcel averaged properties of the lowest 50 hPa of the soundings. Convective available potential energy (CAPE) was 940, 2730 and 2230 J kg^{-1} on 10, 11 and 13 July. Low-level vertical wind shear between the surface and 5 km AGL was weak and less than 2.0×10^{-3} s^{-1}. The atmosphere observed at Fuyang was convectively unstable enough for cumulonimbus clouds to develop. These are typical atmospheric conditions in the southern region of the Meiyu front over China Continent.

4. RESULT

4.1 <u>General Characteristics of Cumulonimbus Clouds</u>

In this paper, a cumulonimbus cloud is identified by a radar-echo entity stronger than 10 dBZ at 0.5 km AGL. As shown in the horizontal distribution of radar echo at cloud base level in Fig. 2, with which two clouds are depicted, cumulonimbus clouds observed during the 3 days of the analysis period in the present paper comprised one or several cellular echoes and did not accompany a significant stratiform precipitation region at low levels. Most of cumulonimbus clouds analyzed in this paper were observed and tracked throughout their entire lifetimes by Shouxian radar. All the clouds occurred in the afternoon.

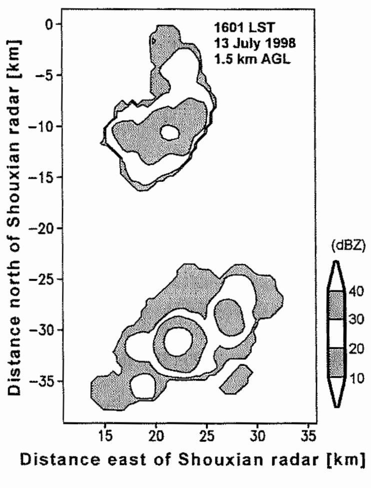

Fig. 2. The example of radar echoes corresponding to cumulonimbus clouds. Horizontal distribution of radar echo at 1.5 km AGL.

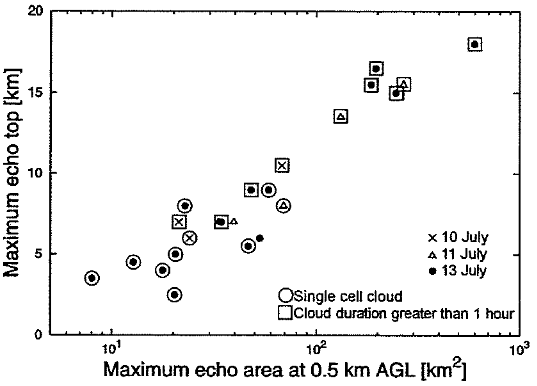

Fig. 3. The relationship between the lifetime maximum echo-top height and the lifetime maximum echo area at 0.5 km AGL.

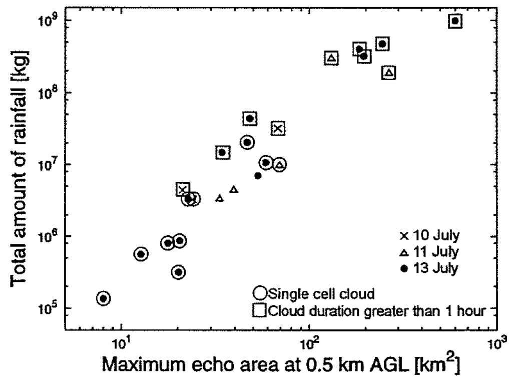

Fig. 4. As in Fig. 3 but for the total rainfall amount and the lifetime maximum echo area.

The relationship between the lifetime maximum echo area at 0.5 km AGL and the lifetime maximum echo top characteristics of the clouds was shown in Fig. 3. The 23 clouds ranged in maximum echo area from 8 to 600 km^2 and in maximum echo top from 2.5 to 18 km. They showed the linear fit on a semilogarithmic plot. 10 clouds among the 23 clouds were comprised of a single convective cell (defined as a reflectivity core) through their lifetimes and they are marked with open circles in Fig. 3. The largest cloud among the single cell clouds showed 70 km^2 in maximum echo area. The maximum echo top of the tallest single cell cloud was 9 km AGL. The durations of single cell clouds were less than 40 minutes.

Multicellular clouds which maximum echo area were smaller than 100 km^2 were comprised of not more than 5 convective cells through their lifetimes. Multicellular clouds larger than 100 km^2 were comprised of 7 to 22 convective cells through their lifetimes, while the largest cloud which went out of the observation area before its dissipation was comprised of 25 convective cells during observation. All of the clouds reaching 10 km were multicellular cloud. In other words, deep convective cells reaching 10 km developed only within multicellular clouds. Many of the multicellular clouds were maintained for 1 hour or more (marked with open square) and were 3.5 or less hours.

4.2 Rainfall Amount

Rainfall amounts were computed for each Cartesian grid point at 0.5 km AGL, which is the lowest grid level, by multiplying the rainfall rate by the unit area corresponding to the horizontal grid interval (0.25 km^2) and by the time interval between volume scans (7 minutes). Those values were then summed over the entire echo area and over the lifetime of each cumulonimbus cloud.

The 23 clouds ranged in maximum rainfall intensity from 0.2 to 35.0 mm h^{-1}. Fig. 4 shows the relationship between the maximum echo area and total rainfall amount. The 23 clouds ranged in total rainfall from 1.4×10^5 to 9.9×10^8 kg. The total rainfall amount has a dependence on maximum echo area of the form of a power low. The duration and maximum height of the clouds in the present analysis varies with their maximum area as shown in Fig. 3. These parameters are also correlated with total rainfall amount.

4.3 Precipitation Efficiency

Precipitation efficiency (the ratio of surface rainfall to water vapor inflow) is also calculated for 7 clouds which 3D wind fields were deduced almost through their lifetime. Water vapor inflow was estimated by multiplication water vapor mixing ratio and upward mass flux at cloud base height defined by LCL and integrated in upward airflow region and time within a cumulonimbus cloud. Since little is known about the representative Z-R relationships for isolated convective clouds over China Continent, some well known and geographically and phenomenally comparable relations (Table 1) including Eq. (1) are used for estimation of precipitation efficiency in order to show a qualitatively useful result.

As seen in Fig. 5, the precipitation efficiency of the clouds ranged from 2 to 15%. These values of precipitation efficiencies are not so large compared with those of convective clouds occurring in other regions (e. g., Fankhauser, 1988), although most of previous studies assumed the steady state of clouds in estimation of precipitation efficiency. The low precipitation efficiencies in this study indicate that water vapor through the base of the cumulonimbus clouds in this region are largely consumed to moisten upper atmosphere. It is also noted that precipitation efficiency exhibited weak correlation with cloud size except the largest cumulonimbus cloud in Fig. 5. The largest cloud calculated only in its early development stage since it went out from the dual-Doppler radar observation area. This would be a reason why its precipitation efficiency is small for its maximum area.

Source	B	β	Mark
Jones (1956)	486	1.37	×
Fujiwara (1965)	450	1.46	∇
Doviak and Zrnic' (1984)	400	1.4	●
Imai (1960)	200	1.5	▲
Marshall and Palmar (1948)	200	1.6	◇

Table 1. Coefficients of Z-R relations ($Z=B\cdot R^{\beta}$) used in the estimation of rain rate for the calculation of precipitation efficiency. Marks in right column are used in Fig. 5.

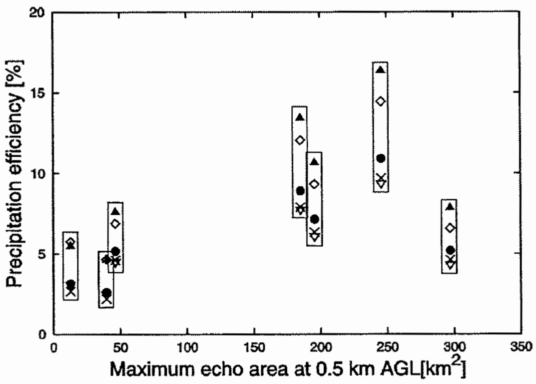

Fig. 5. The relationship between the precipitation efficiency and the lifetime maximum echo area. The marks of points change with Z-R relationships, which are indicated in Table 1. The points calculated about the same clouds were surrounded by squares.

5. SUMMARY

Precipitation characteristics of 23 cumulonimbus clouds which observed on 10, 11 and 13 July 1998 in Anhui province, China are analyzed mainly using 3D reflectivity and wind fields data of X-band Doppler radars and upper-air sounding data during the intensive field observation of GAME/HUBEX. During the 3 days, the observation area was situated in the southern region far from the predominant subtropical front of eastern China, called the Meiyu front.

In the present study, a cumulonimbus cloud is identified by a radar-echo entity above 10 dBZ at 0.5 km AGL and tracked over time. These cumulonimbus clouds comprised one or several convective cells (defined as reflectivity cores). Maximum echo area of individual clouds at 0.5 km ranged from several to approximately 600 km^2 and maximum echo top height ranged from 2.5 to 18 km during their lifetime. Convective cells reaching 10 km developed only within multi-cell clouds. The durations of single cell clouds were less than 40 minutes. Those of multi-cell clouds ranged from less than 1 hour to 3.5 hours. The 23 clouds ranged in maximum rainfall intensity from 0.2 to 35.0 mm h^{-1}, and in total rainfall amount from 1.4×10^5 to 9.9×10^8 kg.

Precipitation efficiency (the ratio of surface rainfall to water vapor inflow through a cloud base) is also calculated for 7 clouds which 3D wind fields were deduced almost through their lifetime. The precipitation efficiency of individual clouds ranged from 2 to 15% and it exhibited weak correlation with cloud size. These low precipitation efficiencies indicate that water vapor through the base of the cumulonimbus clouds are largely consumed to moisten upper atmosphere during the warm season in the southern region of the Meiyu front over China Continent.

REFERENCES

Cressman, G. P., 1959: An operational objective analysis system. Mon. Wea. Rev., 87, 367-374.

Doviak, R. J. and D. S. Zrnic', 1984: Doppler radar and weather observations. Academic Press. 458pp.

Fankhauser, J. C., 1988: Estimation of thunderstorm precipitation efficiency from field measurements in CCOPE. Mon. Wea. Rev., 116, 663-684.

Fujiwara, M., 1965: Raindrop-size distribution from individual storms. J. Atoms. Sci., 22, 585-591.

Gal-Chen, T., 1982: Errors in fixed and moving frame of references: Applications for conventional and Doppler radar analysis. J. Atmos. Sci., 39, 2279-2300.

Imai, I., 1960: Raindrop size-distributions and Z-R relationships. Proc. Eighth Wea. Radar Conf., 211-218. Boston: Amer. Meteor. Soc.

Jones, D. M. A., 1956: Rainfall drop-size distribution and radar reflectivity. Res. Rept. No. 6 Urbana: Meteor. Lab., Illinois State Water Survey.

Marshall, J. S. and W. M. K. Palmer, 1948: The distribution of raindrops with size. J. Meteor., 5, 165-166.

TETHERED-BALLOON BORNE MEASUREMENTS IN BOUNDARY LAYER CLOUDS. PART I: TURBULENCE AND DYNAMICS

Holger Siebert[1], Katrin Lehmann[1], Manfred Wendisch[1,2], and Szymon Malinowksi[3]

[1]Institute for Tropospheric Research, Leipzig, Germany
[2]NASA Ames Research Center, USA
[3]Warsaw University, Institute of Geophysics, Poland

1 INTRODUCTION

Boundary layer clouds play an important role in both synoptic weather forecast and the discussion of climate change. Therefore, much effort has been spent to characterize these clouds by means of field measurements and modelling exercises. In recent literature, these studies have focused on the interaction between cloud microphysics and small-scale turbulence. An overview of the achieved results is given by Shaw (2003). It has been concluded that numeric models of boundary layer clouds need to consider the droplet-turbulence interaction. Therefore, new parameterizations of this interaction have to be derived from field measurements. One method for this purpose is to use probability density functions (PDFs) of microphysical and dynamical parameters (Golaz et al. (2002)). While the shape of typical PDFs is well investigated for wind tunnel data (e.g., Warhaft (2002)), much less is known about PDFs in the cloud-free atmosphere and even less in clouds.

In this paper such PDF's are derived using tethered-balloon borne turbulence measurements, obtained in shallow boundary layer clouds. First, the data quality is checked by means of power spectral density functions. With the help of auto correlations functions, the Eulerian integral length scales as typical lengths for cloud structures are estimated. In the second part, the PDFs are analyzed to characterize the isotropy on different length scales. High-order statistical moments of high-pass filtered data are calculated as a function of the cut-off frequency and compared with Gaussian distributions.

Corresponding author's address: Holger Siebert, Institute for Tropospheric Research, Germany
Permoser Straße 15, 04318 Leipzig
siebert@tropos.de

2 EXPERIMENTAL

Data from the Baltex Bridge Cloud (BBC2) campaign were used that was conducted in Cabauw (The Netherlands) in May 2003. The balloon-borne instrumental payload ACTOS (Airship-borne Cloud Turbulence Observation System) and the tethered balloon MAPSY (operated by the Bundeswehr Technical Center for Ships and Naval Weapons) were utilized to perform turbulence and microphysical measurements in boundary layer clouds. An ultrasonic anemometer was used for high resolution measurements of the wind vector components (u, v, w), a fine-wire thermometer (UFT-B) measured the static temperature T inside clouds and in cloud-free conditions. The Liquid Water Content (LWC) was measured with a Particle Volume Monitor (PVM-100A). Furthermore, a modified version of a Fast-FSSP, the so-called M-Fast-FSSP (Schmidt et al. (2004)), was implemented on ACTOS. Results of this new instrument are discussed in Part II of this paper by Lehmann et al. (2004). A more detailed introduction of ACTOS is given by Siebert et al. (2003).

3 DATA ANALYSIS

3.1 Overview and Cloud Structure

Data of a short cumulus penetration at constant height of around 700 m are analyzed in detail. All measurements were recorded with a sampling frequency f_s = 100 Hz. Part of the time series of LWC, longitudinal wind velocity component u, high-pass filtered vertical wind velocity component w, and T is presented in Fig. 1. Subsequently, the time series is divided into two sub-sequences, the first one was measured in cloud-free conditions (cut 1), the second one includes data obtained in a shallow cumulus cloud (cut 2). This cloud revealed a maximum LWC of about 0.2 $\mathrm{g\,m^{-3}}$ and included short cloud-free periods. The mean wind velocity at that height was 8 to 9 $\mathrm{m\,s^{-1}}$, the static temperature was between 8 and 9 °C with high fluctuations (about 0.5 K peak-to-peak) during the cloud penetrations. The high-pass filtered vertical wind velocity shows sporadic updrafts inside the clouds, whereas the highest negative values were observed in the small cloud gaps.

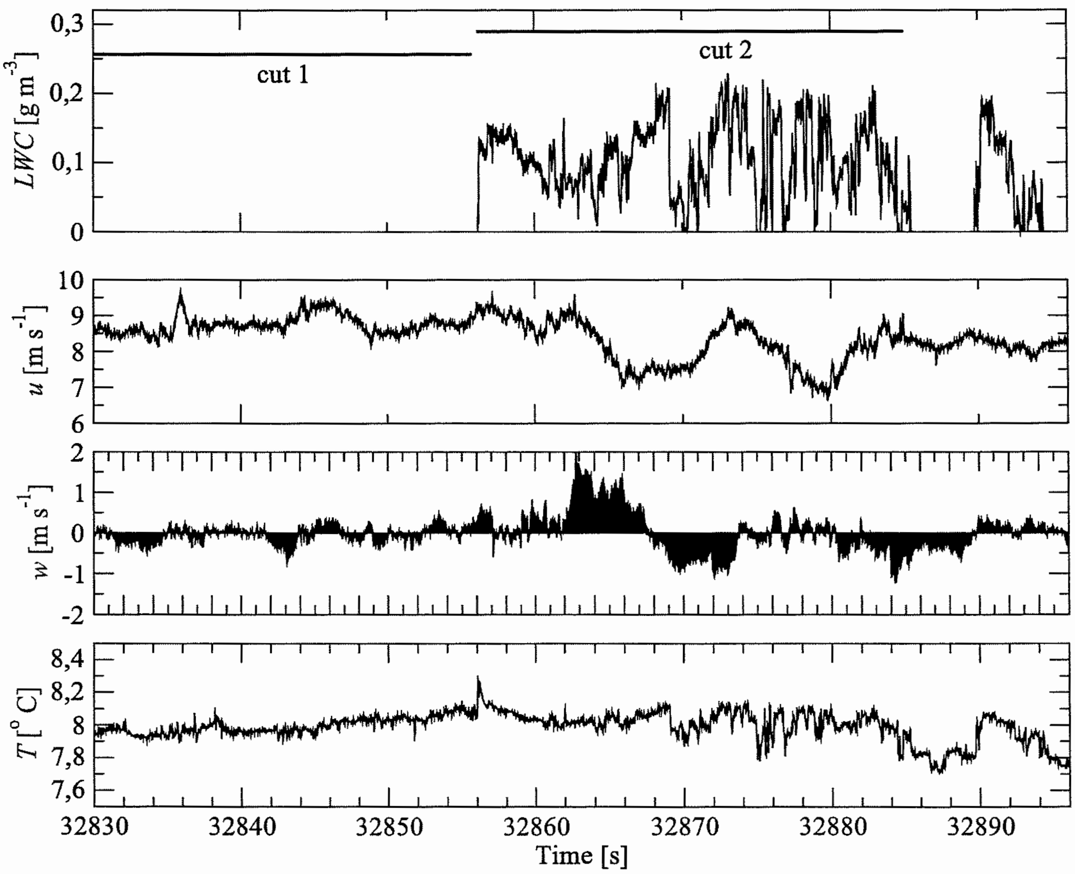

Figure 1: Time series of liquid water content LWC, mean horizontal wind speed u, high-pass filtered vertical velocity w, and static temperature T as measured with ACTOS on 2003-05-19 during the BBC2 campaign.

Power spectral density functions were analyzed from the data to check the data quality. The time series was tapered with a Hanning window. Subsequently the spectra were calculated using a Fast Fourier Transform (FFT) routine with averaging over equidistant logarithmic frequency bins. The spectra were normalized: $\sigma^2 = \int_0^\infty df\; S(f)$, the influence of the Hanning window has been accounted for. Figure 2 shows the resulting spectra of LWC, u, w, and T. A $f^{-5/3}$ fit for inertial subrange behavior is added to the figure as a solid line. The spectra were calculated for the complete record and the two subsequences (cut 1 and cut 2) in cloudy and cloud-free conditions, respectively. All spectra show a clear inertial subrange behavior with a slight flattening around the Nyquist frequency of 50 Hz. However, the S_{LWC} spectrum of the complete record shows a more significant flattening for frequencies higher than 20 Hz. The reason of this effect is not yet clearly identified.

Energy dissipation rates ϵ were calculated from the power spectral density S_u. The power spectral density of the longitudinal velocity component u in the inertial subrange is given by

$$S_u(f) = \alpha\, \epsilon^{-2/3}\, f^{-5/3}.$$

From Fig. 2, S_u is approximated by a linear fit in the inertial subrange. With the Kolomogorov constant $\alpha \approx 0.5$ ϵ is estimated to be about $5 \cdot 10^{-4}\,\mathrm{m^2s^{-3}}$ for the complete record, whereas inside the clouds maximum values of $10^{-3}\,\mathrm{m^2s^{-3}}$ were calculated.

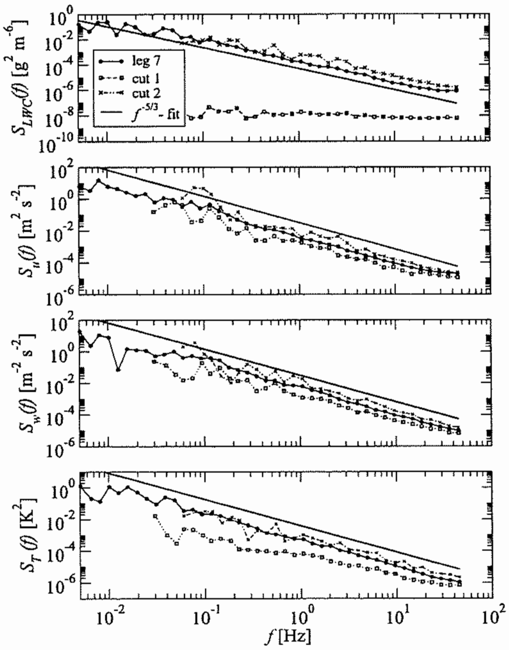

Figure 2: Power spectral densities of liquid water content S_{LWC}, mean horizontal wind speed S_u, vertical velocity S_w, and static temperature S_T as measured with ACTOS during leg 7 and subsequences cut 1 and cut 2.

As a time scale for typical cloud structures we calculate the Eulerian integral time scale $\mathcal{T}$ which is derived from the integral over the auto correlation function $\rho(\tau)$:

$$\mathcal{T} = \int_0^\infty d\tau\, \rho(\tau).$$

In many applications $\rho(\tau)$ reveals a kind of exponential shape. Thus, $\mathcal{T}$ can be approximated as the value of τ where $\rho(\tau) = 1/e$. In Fig. 3, $\rho(\tau)$ is displayed for the cloud data (cut 2). The inclosure shows the enlarged part of the small time legs which allows to better analyze the Eulerian time scales. All time scales are in the order of a few seconds. Assuming the validity of Taylor's hypothesis, the length scale $\mathcal{L} = \overline{u}\,\mathcal{T}$ of typical structures in this cloud is in the order of 10 to 30 m ($\overline{u} \approx 8\,\mathrm{m\,s^{-1}}$). The inner scale (Kolomogorov microscale) $\eta = \left(\nu^3/\epsilon\right)^{1/4}$, with the kinematic viscosity ν can be estimated to be about 1 to 2 mm.

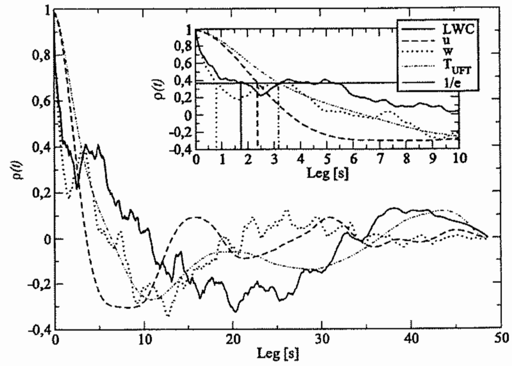

Figure 3: Auto-correlation function $\rho(\tau)$ of LWC, u, w, and T as measured with UFT. The first part is enlarged, a horizontal line for $1/e$ is included for the estimation of the Eulerian integral time scales $\mathcal{T}$ (see text for more details).

3.2 Isotropy

The analysis of isotropy in clouds on different length scales is the major objective of this paper. For this purpose the PDFs are calculated and checked for symmetry. Many wind tunnel data show a Gaussian behavior for the velocity and temperature fluctuations (e.g., Jayesh and Warhaft (1991)). That means that the skewness S of the PDF vanishes and the kurtosis K is equal 3. The vanishing of S is used as an indication for isotropy. To reduce the influence of large scale variability, all data is high-pass filtered before calculating the PDFs with different cut-off frequencies f_{cut}. High-pass filtered data are denoted with a bar.

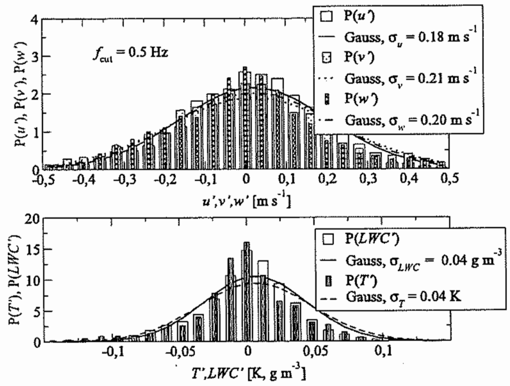

Figure 4: Probability density function (PDF) of the three velocity components (u', v', w') in the upper panel and of the LWC' and T' in the lower panel. The data was high-pass filtered with a cut-off frequency $f_{cut} = 0.5$ Hz. For comparison a Gaussian fit is included.

Figure 4 shows the PDFs of the three velocity components u', v', w' (upper panel) and LWC' and T' in the lower panel. The cut-off frequency was set to 0.5 Hz. Therefore, structures with a wavelength smaller than 20 m are included only. For all parameters a Gaussian fit is added taking the standard deviation σ calculated from the high-pass filtered time series. The parameters S and K are plotted as a function of $f_{\rm cut}$ in Fig. 5.

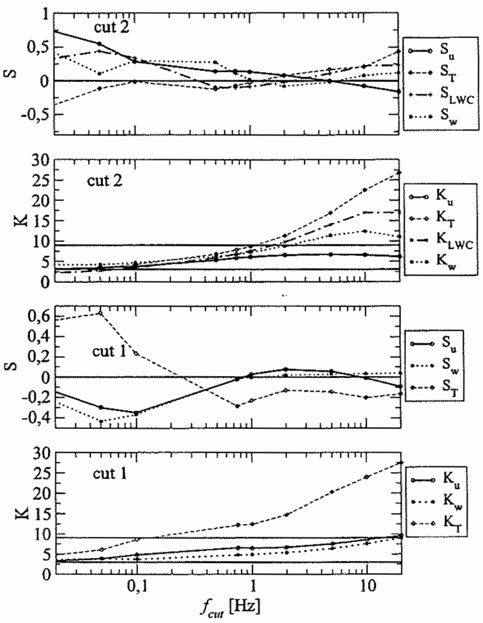

Figure 5: Kurtosis K and skewness S of high-pass filtered data as a function of the cut-off frequency f_{cut}. The data in the upper panel is inside a cloud, the lower panel shows data outside the cloud .

Both results for cloudy conditions (cut 2) and for cloud-free conditions (cut 1) are shown for comparison. For small values of $f_{\rm cut}$ all distributions are significantly skewed due to poor statistics for large scale structures. For increasing $f_{\rm cut}$ S decreases significantly and is close to zero. That means that the distributions are symmetrical and isotropic conditions prevail. At frequencies higher than 10 Hz S increases again. However, in this case the bin width of the PDFs are in the order of the sensor resolution itself.

The kurtosis shows values around 3 (for Gaussian behavior) only for frequencies lower than about 0.1 Hz. For higher frequencies K increases rapidly up to values of 20, that is, the PDFs are much narrower than a Gaussian distribution. This findings are in good agreement with the observations of Bougeault (1981) who also found values of K in the order of 15 inside clouds. One explanation for this fluctuations with high amplitude but relative low number might be the intermittent behavior of the parameters especially in the cloudy regions including the small cloud-free parts.

4 ACKNOWLEDGMENTS

The authors acknowledge the Bundeswehr Technical Center for Ships and Naval Weapons for their kind provision of the tethered balloon MAPSY and the KNMI who hosted the BBC2 campaign. Part of this work is financed by the Deutsche Forschungsgesellschaft (WE 1900/7-1).

5 REFERENCES

Bougeault, P.: 1981, 'Modeling the trade-wind cumulus boundary layer. Part I: Testing the ensamble cloud relations against numerical data'. *J. Atmos. Sci.* **38**, 2414–2428.

Golaz, J.-C., V. E. Larson, and W. R. Cottton: 2002, 'A PDF-based model for boundary layer clouds. Part II: Model results'. *J. Atmos. Sci.* **59**, 3552–3571.

Jayesh and Z. Warhaft: 1991, 'Propability distribution of a passive scalar in grid-generated turbulence'. *Physical Review Letters* **67**, 3503–3506.

Lehmann, K., H. Siebert, and S. Schmidt: 2004, 'Tethered-balloon borne measurements in boundary layer clouds. Part II: Microphysical Properties'. In: *Preprints 14th International Conference on Clouds and Precipitation.* Bologna, Italy, (18-23 July 2004).

Schmidt, S., K. Lehmann, and M. Wendisch: 2004, 'Minimizing instrumental broadening of the drop size distribution with the M-Fast-FSSP'. *J. Atmos. Oceanic Technol.* **(submitted)**..

Shaw, R. A.: 2003, 'Particle-turbulence interactions in atmospheric clouds'. *Annu. Rev. Fluid Mech.* **35**, 183–227.

Siebert, H., M. Wendisch, T. Conrath, U. Teichmann, and J. Heintzenberg: 2003, 'A new tethered balloon-borne payload for fine-scale observations in the cloudy boundary layer'. *Boundary-Layer Meteorol.* **106**, 461–482.

Warhaft, Z.: 2002, 'Turbulence in nature and in the laboratory'. *PNAS* **99**, 2481–2486.

THE RESPONSE OF HEATING AND MOISTURE IN CONTINENTAL AND OCEANIC MESOSCALE CONVECTIVE SYSTEMS TO THERMODYNAMIC AND DYNAMICAL PROCESSES

Chiharu. Takahashi[1] and Hiroshi. Uyeda[1]

[1]Hydrospheric Atmospheric Research Center, Nagoya University, Nagoya, Aichi, 464-8601, Japan

1. INTRODUCTION

The latent heat and moisture transport of convective systems play important role in modulating tropical climate. The variability of convective activities and atmospheric circulation with Australian summer monsoon in tropical region are most affected by the Madden-Julian oscillation (MJO) and other equatorial waves. Therefore, it is important to reveal the rainfall patterns and the vertical profiles of heat and moisture in relation to the phase of MJO, which is accompanied by each convection clouds. In addition, geographical feature and sensible flux on the continent near the seashore greatly affect development and organization of mesoscale convective systems (MCSs).

Furthermore, we showed that apparent heating profiles are found to differ from convective and stratiform clouds within MJO active or break periods respectively by observational analyses using radar data. However, it is difficult only from observation to resolve phenomenon of the cloud scale with a long time and large area that includes from generating of organized MCSs to the disappearance.

The main objective is to clarify the relation between the vertical profiles (structures) of heat and moisture budgets as well as cloud mass fluxes and the thermodynamic, dynamical development processes of organized mesoscale convective systems (MCSs) using 3D cloud resolving model. The simulation periods are selected on the days when the organized MCSs were observed over the Darwin, northern Australia during a summer monsoon. One case is oceanic MCS on 15 January, convectively active phase and another case is continental MCS on 21 January, break phase of intraseasonal oscillation.

2. MODEL AND DATA

This study is mainly based on the Cloud Resolving Storm Simulator (CReSS) that is non-hydrostatic and

Corresponding author's address: Chiharu Takahashi, Hydrospheric Atmospheric Research Center, Nagoya University, Nagoya, Aichi, 464-8601, Japan; E-Mail: chiharu@rain.hyarc.nagoya-u.ac.jp

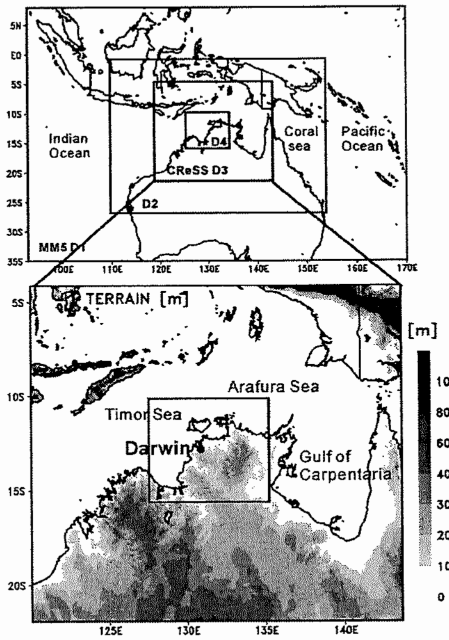

Fig.1. Map of nested model domains MM5: D1(60km), D2(20km), CReSS: D3(4km), D4(1km). Topography of northern Australia for nested domain3.

compressible formulated model. It also employs the cold rain bulk microphysical parameterization scheme. In order to investigate the effect of the diabatic heating and moistening by MCSs associated with microphysical and dynamical processes the fine-grid and large-domain 3D simulations with a 1km horizontal resolution were conducted. Vertical grid is stretched from 100 m to 450m. We used the large field of CReSS 4km outputs that were calculated using the fine-mesh subset of nested grids run from NCAR Mesoscale Model (MM5) as initial and boundary conditions for two cases (Fig.1). MM5 was initialized with NCEP reanalysis data. MMCS and CMCS were simulated for 10 hours from 0300 UTC 15 January and 0600 UTC 21 January 1999 during those periods organized systems were observed.

We mainly used these 1km outputs for analysis.

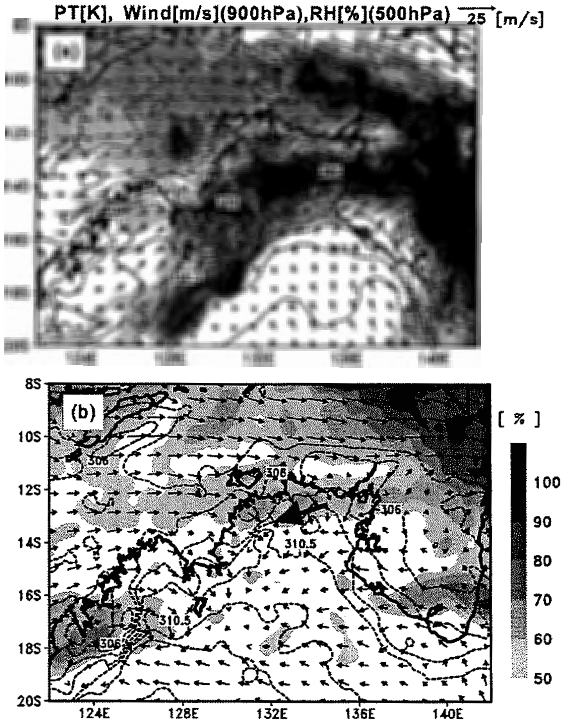

Fig.2. Horizontal cross-section of the MM5 20km-grid simulation. Dotted contours are potential temperature (K) at 900hPa. Shaded field is relative humidity at 500hPa. Vectors are horizontal wind at 900hPa.((a)0500UTC15January,(b)0900UTC21January 1999).

3. RESULTS

3.1 Environmental Situations

The phases of MJO intraseasonal oscillation eastward propagating on the equator was different from 15 January (Fig. 2a) and 21January 1999(Fig. 2 b). Wind and Humidity field and the profile were also affected by Kelvin-Rossby wave pattern with cyclonic gyres near Australia. On 15 January when convectively active region within MJO was located over northeast side in Darwin, low-middle level winds were strong westerly (It corresponds to westerly wind "burst" over the warm-pool region) and the layer of a wind shear was deep. A low-middle layer was very moist (relative humidity was 70-90 %) over north side of large temperature gradient in the low level (Fig. 2a).

On 21 January several days after, MJO propagated eastward furthermore. The low level environmental winds changed southeasterly accompanied by the trough moving to the north side of Darwin. As sunlight warms land in daytime hours, temperature gradient and wind convergence lines were formed in a coast - parallel direction of the low level. These are as a result of a sea breeze front (Fig. 2b,arrow) and play important role in producing thermodynamically

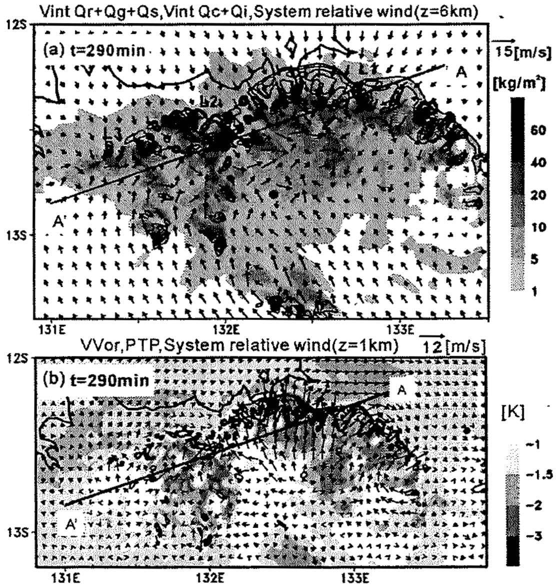

Fig.3. Horizontal cross-section at 290 min for the 15 January (a) vertically integrated mixing ratio of precipitation particles (shaded) and cloud particles (2.0 kgm^{-2} contours more than 1.0 kgm^{-2}). System-relative wind vectors at z=6km. (b) Perturbation Potential temperature (shaded) and vertical vortices (1, 2, and 3 10^{-3} s^{-1}contours). System-relative wind vectors at z=1km.

convenient condition. Those led to heat and moisten the boundary layer over and near the seashore. It was furthermore under the large-scale subsidence and dry air intrusion in the middle level (above 500 hPa)

3.2 Evolution and Development Processes of Mesoscale Convective System

During the mature phase of simulated MCS on 15 January, three enhanced arcs-shape precipitation bands have developed to the direction of shear parallel (Fig. 3a L1, L2, and L3). Those have been embedded within extensive area of stratiform rain. Middle level convergence line of the system relative winds have formed and cyclonic vortices in the south side of the most intensive, bowed band L1. The leading lines containing the large amount of cloud water were present in northeast side of precipitation band L1, namely upstream side of storm relative inflow. It shows that the distribution is like multi cell type (Fig. 3a). The cold pool produced by L1 was not so strong, however the L2 could evolve by converging the outflow from adiabatic heating region in the southwest side and system relative moist-cool westerly wind. Moderate vortices formed along propagating cold pool, cloud water continued being generated as a result (Fig. 3b).

The moist inflow air have been rising from low-level to upper-level into cloud leading lines by a strong convectively updraft (L1 and L2) in the front of two

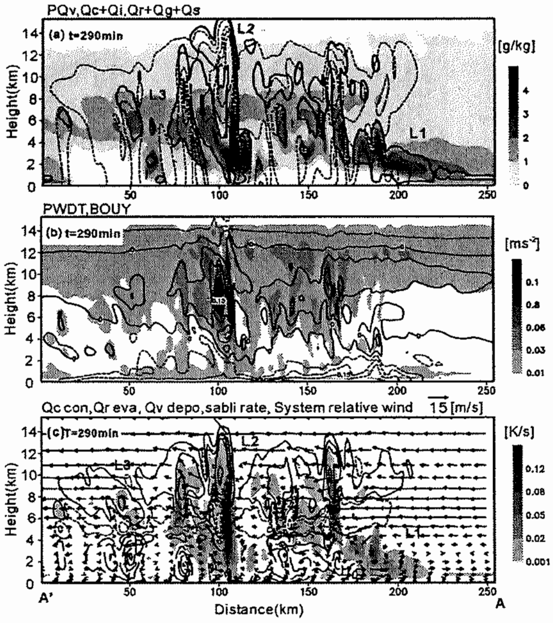

Fig. 4. Vertical cross-section at 290miin along A-A' line in Fig.3. (a) Perturbation water vapor mixing ratio (shaded), cloud water mixing ratio (0.1 g kg^{-1} contour, solid lines), and mixing ratio of precipitation particles (3.0 g kg^{-1} contours more than 0.1g kg^{-1}, dotted lines). (b) Parcel vertical velocity acceleration field, PWDT (shaded) and buoyancy acceleration field (0.5 m s^{-2}contours). (c) Vapor condensation heating (shaded), rain evaporation cooling (0.003 Ks^{-1} less than −0.001 Ks^{-1}contours, dash lines), sublimation cooling 0.003 Ks^{1} less than 0.001 Ks^{1} contours, dotted lines), deposition heating (0.003 Ks^{-1} more than 0.001 Ks^{-1}contours, dotted lines), and system relative wind vectors.

precipitation bands. The growth of snow and graupel were promoted by the abundant amount of water vapor in middle-upper level, where large deposition heating has occurred. It is also shown that the riming process of cloud water enhances precipitation ice clouds, which can be reasoned from much cloud water transporting to the upper-level and vapor condensation process occurring (Fig. 4a).

The L2 has evolved by converging in the rear-inflow and low-level outflow from cold pool produced by rain evaporation of L1 under melting level. A density current by rain evaporation cooling has accelerated rear-inflow of the L1, as the negative PWDT region has existed. As a result, cloud condensation heating regions has showed more erected structures to the downstream side. The Inflow of sublimation cooled moist air about 4km to 7km into the front of leading line L1 or L2 makes favorable conditions for sub-saturated air rising through large positive buoyancy of parcel in the middle layer (Fig .4b,c).

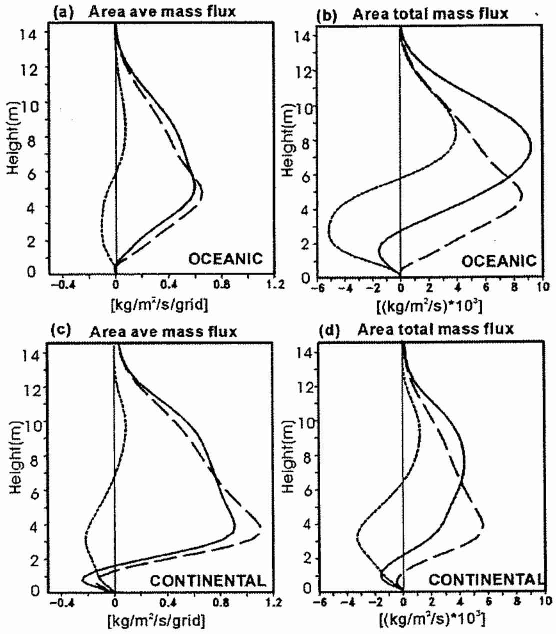

Fig. 5. Vertical profiles of area averaged mass flux ((a), (c)) and area total mass flux ((b), (d)) for the total (solid), convective (dash), and stratiform (dotted) regions averaged for 2-10 hours, respectively. ((a),(b) 15January case and (a),(c) 21January case.)

3.3 <u>Heat , Moisture and Cloud Mass Budgets</u>

The Tao et al. (2000) method was used for the separation of convective-stratiform regions. Time-area averaged mass fluxes for 15 January case (Oceanic) shows that the convective profile has a single upward peak at 5km, ascent at almost all levels. The stratifom profile has an upward peak at 8.5km,downward peak at 3km(Fig. 5a). The 21 January case (Continental) shows that the convective profile has larger, sharper, and lower upward peak at 4km., a downward peak at 1 km. The stratifom profile has similar to Oceanic, but the magnitude of downward peak is larger (Fig. 5c). Area total mass fluxes suggest that Oceanic MCS had more extensive precipitation region as compared with Continental MCS (Figs. 5b,d). The convective and stratiform profiles show the same value above 9km, therefore the total profile represents top-heavy. A large amount of ice particles formed above 8km (Fig. 5b). In order to clarify microphysical process within two MCSs and the relation with the environmental conditions the apparent heat sourceQ1 budgets was analyzed based on Johnson et al. (2002). For Q1c', the dominant terms are condensation heating and vertical eddy flux heating above the melting level (4.8km) for CC (Fig.6c), it is, however, deposition heating for OC (Fig.6a). For Q1s', CS has the peak of heating rate at 4km and has cooling rate at 10.5km, similarly, OS has 4 km and 9km, respectively (Fig.6b, d). The sublimation cooling for CS between 4.5km and 8km and rain evaporation cooling below 4km are both significantly large, which are due to entrain dry ambient air in middle-upper level under large–scale divergence fields. Those suggest the rear-inflow is strengthened as a result. The deposition heating in the upper level and melting cooling at 4km are dominant terms for OS as compared with CS, which can be attributed to moist condition and deeply wind shear under large–scale convergence fields that arrow snow and graupel to be grown enough at almost all levels (Fig.6 b). While those contributions for CS are smaller, so that the supplement of vapor to the upper level is restricted only to the transport process by convection from low level (Fig.6d). It is shown that cold pool has developed from the results of large rain evaporation cooling being occurred below the melting level and the peak level being 1km for CC. In addition, a steep vertical gradient of condensation heating below 4km stem from the tilting vertical distributions of cloud water and water vapor (Fig.6c).

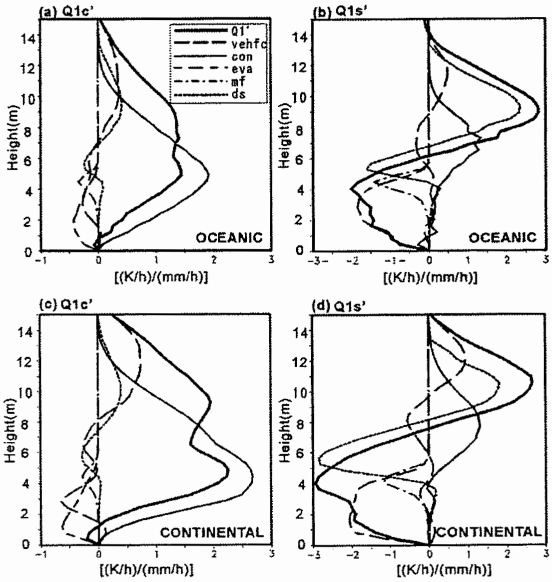

Fig. 6. Vertical profiles of area averaged Q1 budgets normalized by convective and stratiform rain rate (averaged for 2-10 hours) (a),(b) convective area (**OC**) and stratifom area (**OS**) on 15 January. (c),(d) convective area (**CC**) and stratiform area (**CS**) on 21 January. Vertical eddy heat flux convergence term (vehfc), condensation heating term (con), rain-evaporation cooling term(eva), melting/freezeing term (mf), deposition /sublimation term(ds).

4. DISCUSSION

It is suggested that the deep wind shear like a westerly wind burst and moist environmental air in middle-level are the most favorable condition for stratiform system pattern. On the other hand, dry condition in middle-level and the large low-level wind shear cause convective system pattern. An integrated understandings from a climatologically viewpoint in various world region are important. To reveal the interaction of rainfall, organization patterns and MJO or Rosbby wave, furthermore, relation rainfall patterns with the diabatic heating profiles every convective region and stratiform region in many cases are our major goals for future.

5. CONCLUSIONS

The vertical structure of heat and moisture budgets of oceanic MCS and continental MCS to clarify the relation thermodynamic-dynamical process and the environment were investigated by performing 3D simulations. Thereby, the following things were clarified. It is found that the convective regions within continental MCS in MJO convectively break phase have the dominant effect of making atmospheric lowest layer cooling (moistening) by rain water evaporation and making a middle-upper layer heating (drying) by vertical eddy heat flux convergence and vapor condensation. The stratiforn regions within continental MCS have also the effect of making the level under middle layer cooling (moistening) by vapor sublimation and rain evaporation. On the contrary, the stratiform regions within oceanic MCS in MJO convectively active phase play an important role in making the upper layer heating (drying) by vapor deposition and vapor condensation. By this research, it can be said that one of the interactions of an environmental and convection system was suggested.

Acknowledgements

The authors wish to express our gratitude thanks to Dr. K. Tsuboki, Nagoya University, for valuable advice and comments. The authors would also like to thank Mr. Sakakibara, Chuden CTI Co., Ltd., for his assistance in setting CReSS model. Thanks are due to NCAR data center for providing us data for MM5 simulation. The numerical simulations were performed with a super computer at the University of Tokyo.

References

Johnson, D. E., W. -K. Tao, J. Simpson, and C.–H. Sui, 2002: A study of the response of deep tropical clouds to large-scale thermodynamic forcings. Part I: modeling strategies and simulations of TOGA CORE convective systems. *J. Atmos. Sci.*, **59**, 3492-3518.

Tao, W.-K.,S. Lang, J. Simpson, W.S. Olson, D. Johnson, B. Ferrier, C. Kummerow, and R. Adler, 2000: Vertical profiles of latent heat release and their retrieval for TOGA COARE convective systems using a cloud resolving model, SSMI/I, and ship-botne radar data. *J. Meteor. Soc. Japan*, **78**, 333-355.

EFFECTS OF MOISTURE PROFILE ON THE DYNAMICS AND ORGANIZATION OF SQUALL LINES

Tetsuya Takemi *

Department of Global Architecture, Osaka University, Suita, Osaka, 565-0871, Japan

1. INTRODUCTION

The dynamics of squall lines has been widely investigated by both observational analyses and numerical simulations for decades, and the role of vertical wind shear has been recognized as one of the important ingredients in squall-line dynamics. Rotunno et al. (1988, hereafter RKW) and Weisman et al. (1988, hereafter WKR) showed that the interaction between low-level vertical wind shear and surface cold-air pool is the primary element in understanding the strength and longevity of squall lines, and stressed that stronger convection develops in a condition in which the effects of low-level shear and cold pool are dynamically balanced. Robe and Emanuel (2001) demonstrated that the results of their squall-line simulations in radiative-convective equilibrium states are in good agreement with the RKW theory. Weisman and Rotunno (2004) recon?rmed that the validity of the RKW theory through an extensive set of numerical experiments.

In contrast, the effects of stability and moisture content on the squall-line dynamics have not been well investigated. This may be because there are a large number of the degree of freedom in setting these pro?les. One of the most successful studies dealing with the stability effect is the numerical study by Weisman and Klemp (1982), who showed that the mode of convective storms can be categorized as a multi-cellular or supercelluar type depending on the stability and shear parameter. In their modeling study, a low-level moisture content was focused.

This study investigates the effects of moisture pro?le in low- and middle-levels in various shear conditions on the squall-line dynamics by conducting a extensive set of cloud-resolving simulations in idealized settings.

2. MODEL AND EXPERIMENTAL DESIGN

Numerical simulations are performed with the Weather Research and Forecasting (WRF) model (version 1.3) that is being developed through collaborative efforts by various U.S. research and operational communities (e.g., Skamarock et al. 2001). The model is run in a three-dimensional domain of 450 km in the x direction and 80 km in the y direction extending from the surface to a height of 18 km. The grid resolutions are 1 km in the horizontal direction and 500 m in the vertical direction. Open lateral boundary conditions are speci?ed at the x boundaries, and periodic conditions at the y boundaries. The top boundary is rigid lid with an absorbing layer in the upper 6 km depth, while the bottom boundary is free slip. The Lin et al. cold-rain scheme is used for the cloud-microphysics parameterization. For simplicity, the effects of the Coriolis force, surface physics, and atmospheric radiative transfer are not included. For subgrid-mixing effects, a 1.5-order scheme using a prognostic equation of turbulent kinetic energy is used. The proportionality constant C_k in the eddy viscosity coef?cient is adjusted to 0.15 (Takemi and Rotunno 2003). No numerical diffusion is included. This study employs the third-order Runge-Kutta scheme for the time integration and the third-order upwind scheme for the advection differencings.

*Corresponding author's address: Dr. Tetsuya Takemi, Department of Global Architecture, Graduate School of Engineering, Osaka University, 2-1 Yamadaoka, Suita, Osaka 565-0871; Email: takemi@ga.eng.osaka-u.ac.jp

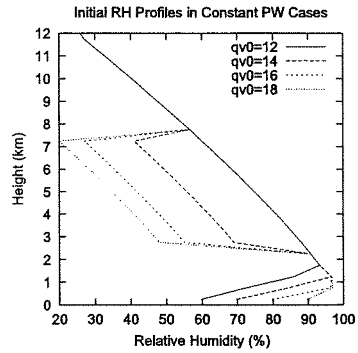

Figure 1: Initial relative humidity pro?les in the cases of ?xed precipitable water values.

Squall lines are initiated by a y-oriented line thermal (a 1.5 K-maximum potential temperature excess) of x-radius of 10 km and vertical radius of 1.5 km, placed at the domain center and at a height of 1.5 km, with small random potential temperature perturbations being added.

A horizontally uniform thermodynamic environment has been created from the temperature and moisture pro?les of Weisman and Klemp (1982) based on a typical condition for strong mid-latitude convection. In determining the moisture pro?le, we set two series of numerical experiments as follows:

1. The water vapor mixing ratio q_{v0} in the the lowest 1.5 km is changed from 10 to 18 $\mathrm{kg\,kg^{-1}}$ with 2

$\mathrm{kg\,kg^{-1}}$ interval. The moisture pro?les above the boundary layer are the same with each other in spite of the different q_{v0} values.

2. The boundary layer mixing ratio q_{v0} is set to 14, 16, and 18 $\mathrm{kg\,kg^{-1}}$ with the precipitable water (PW) content being held ?xed to the value of 42.7 $\mathrm{kg\,m^{-2}}$ (which comes from the case of $q_{v0} = 12$). In this series, the relative humidity in the layer of 2.5-7.5 km is uniformly decreased, which is shown in Fig. 1.

The temperature pro?les in all the cases are the same with that of Weisman and Klemp (1982).

The wind pro?les are set following to Weisman and Rotunno (2004), but in our experiments the shear-layer depth is ?xed to 2.5 km. The shear layer is gradually elevated from the lowest levels (0-2.5 km) to middle and upper levels (2.5-5 km and 5-7.5 km). The magnitude of wind speed difference in the shear layer, U_s, is set to 0, 10, 15, and 20 $\mathrm{m\,s^{-1}}$. For each q_{v0} case in the ?rst experimental series, ten shear pro?les are examined. In the second series, four shear pro?les ($U_s = 10$ and 20 in the layer of 0-2.5 and 2.5-5 km) are examined for each q_{v0} case. The model is integrated up to six hours, at which time the squall-line cold out?ow boundary is still within the computational domain.

3. RESULTS

The results of the ?rst experimental series are described in the ?rst place. The results in the $q_{v0} = 14$ case, which RKW and WKR have examined, are demonstrated here. Figure 2 shows the horizontal cross section of vertical velocity at the 3-km level around the gust front area for six out of ten shear cases. Consistent with RKW and WKR, the arc-shaped organization of a squall line can be observed in the strong low-level shear case (Fig. 2a). As the shear intensity weakens or the height of the shear layer increases, a less organized feature of the simulated squall lines becomes evident (other panels in Fig. 2).

The remarkable difference between the low-level- and elevated-shear cases, like the one seen in Figs. 2a and 2c, is also examined in other q_{v0} values. Figures 3 and 4 show the horizontal cross section of vertical velocity at the 3-km level for the $q_{v0} = 10$ and 12 cases and the $q_{v0} = 16$ and 18 cases, respectively. As the boundary layer mixing ratio q_{v0} decreases, linear organization of convection can only be identi?ed in low-level shear cases (Fig. 3), and the strongest shear among the cases we examined here is favorable for the organization (not shown). When the shear layer is elevated, almost no cloud development is observed. On the other hand, the moister cases (Fig. 4) show that the cloud development can be seen in both the surface-based and elevated shear cases, although the squall-line structure looks different.

As a measure of the squall-line strength, precipitation intensity averaged over 3-6 h and over the area between

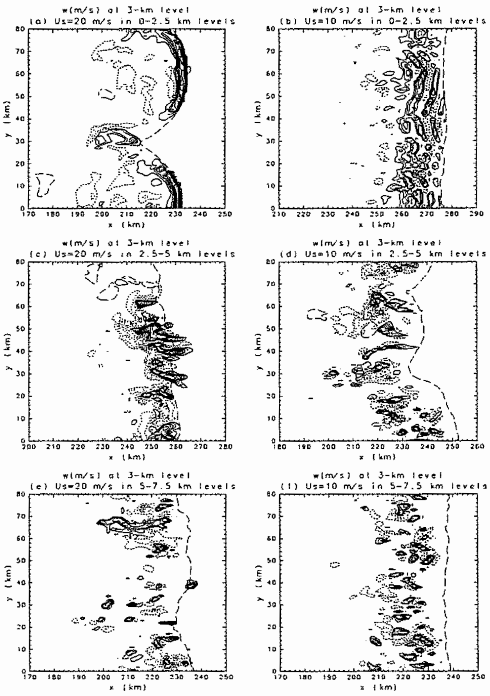

Figure 2: Horizontal cross section of vertical velocity at the height of 3 km, contoured at a 2 $\mathrm{m\,s^{-1}}$ interval at 4 hour in the case of $q_{v0} = 14$ in the ?rst series. The gust front is indicated by long-dashed lines. A 80 km × 80 km portion of the computational domain is shown.

20 km ahead of the gust front and 80 km behind the front is calculated. Figure 5 summarizes the averaged precipitation intensities obtained in the 10 shear-pro?le cases in each q_{v0} value. In the drier cases ($q_{v0} = 10$, 12), the shear in the lowest layer is critically important in producing precipitation. In the moister cases ($q_{v0} \geq 14$) with the shear layer being below the 5-km level, shear strength U_s plays a major role in determining the precipitation intensity. On the other hand, a stronger shear in the upper levels of 5-7.5 km has an unfavorable effect on precipitation.

In addition to the surface precipitation, the depth of cold pool head is examined. Figure 6 shows the depth of cold pool averaged over 3-6 h and the area within a 10-km distance behind the gust front. All the q_{v0} cases except the case $q_{v0} = 10$ indicate that the cold pool becomes deeper as the low-level shear becomes stronger. In contrast to the low-level shear cases, the simulated cold pools in the elevated-shear cases are much shallower.

In the second experimental series, the organization and structure of the simulated squall lines look similar to those in the ?rst series. Figure 7 compares the horizontal cross section of total water mixing ratio at the

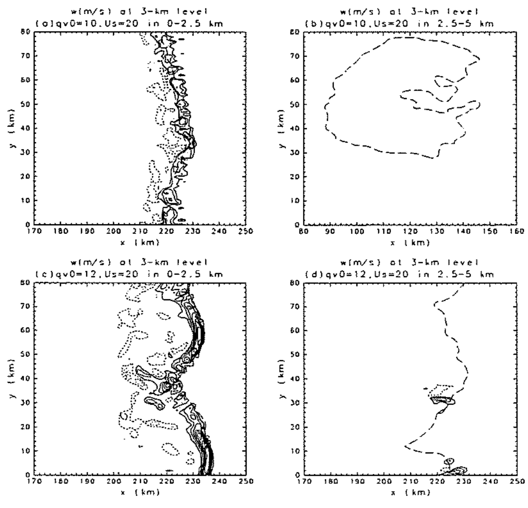

Figure 3: Same as Fig. 2 except for the cases: (a) $q_{v0} = 10$, $U_s = 20$ in the 0-2.5 km layer; (b) $q_{v0} = 10$, $U_s = 10$ in the 2.5-5 km layer; (c) $q_{v0} = 12$, $U_s = 20$ in the 0-2.5 km layer; (d) $q_{v0} = 12$, $U_s = 10$ in the 2.5-5 km layer.

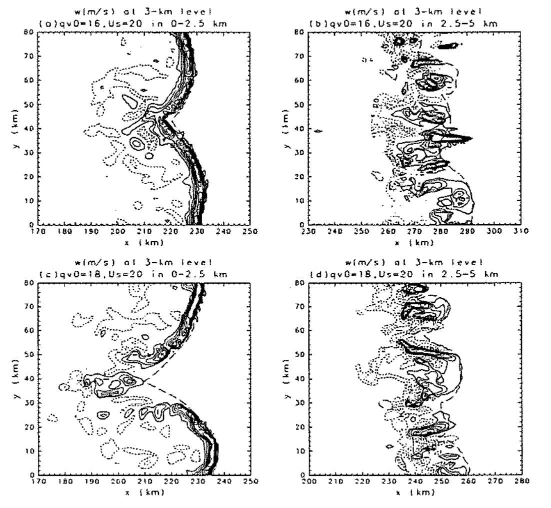

Figure 4: Same as Fig. 2 except for the cases: (a) $q_{v0} = 16$, $U_s = 20$ in the 0-2.5 km layer; (b) $q_{v0} = 16$, $U_s = 10$ in the 2.5-5 km layer; (c) $q_{v0} = 18$, $U_s = 20$ in the 0-2.5 km layer; (d) $q_{v0} = 18$, $U_s = 10$ in the 2.5-5 km layer.

5-km level for the cases of $q_{v0} = 18$ in the two experimental series. General feature of the two cases looks similar to each other, but a close look at the two panels indicates that a smaller-scale feature is more apparent in the second series. This is because the mid-level relative humidity in the second series is 40 % drier than that in the ?rst series, and thus dry-air entrainment into the clouds has a negative in?uence on cloud development.

Also in this series of the experiments, averaged precipitation intensity is calculated as a measure of the squall line strength, and is shown in Fig. 8. Comparing Figs. 5 and 8, the increasing tendency of precipitation with the U_s increase can be identi?ed, although the precipitation intensity is slightly smaller in the second series. From the second experimental series, it can be said that a moister condition in the boundary layer is more favorable for the squall-line strength than a moister condition above the boundary layer, as long as available column moisture amount (i.e., precipitable water vapor content) is the same.

4. DISCUSSION AND CONCLUSIONS

In order to synthesize the results obtained from all the numerical experiments performed in this study, a single parameter $C/\Delta U$, where C represents a measure of cold pool strength and ΔU denotes a wind speed difference in the shear layer, is examined following the RKW theory. C is de?ned as follows:

$$C = \sqrt{2 \int_0^H (-B)\, dz}, \qquad (1)$$

where H is the height of the cold pool and B is buoyancy which is de?ned by virtual potential temperature including the effect of water and ice. ΔU is de?ned the wind speed difference in the layer of 0-5 km in a pre-front environment. The RKW theory predicts that $C/\Delta U \sim 1$ is an optimal condition for the development of strong convection.

Figure 9 shows the values of $C/\Delta U$ obtained in the experiments of the ?rst experimental series. The increase in U_s in each shear height case results in the decrease in $C/\Delta U$. Although the parameter $C/\Delta U$ is generally larger than 1, this parameter seems to well explain the behavior of precipitation intensities shown in Fig. 5. This is also true for the cases of the second experimental series.

This study can be concluded as follows:

- As the boundary layer becomes drier, the interaction between the squall-line cold pool and low-level ambient shear is more critical to the development of strong convection.
- In moister conditions, stronger shear is favorable for strong convective system in terms of precipitation intensity so long as the shear layer is below 5 km.
- The parameter $C/\Delta U$ from the RKW theory well predicts the strength of squall lines in wide range of moisture conditions.

5. ACKNOWLEDGMENT

This research was supported by grants from Grant-in-Aid for Scienti?c Research (No. 15510151) from

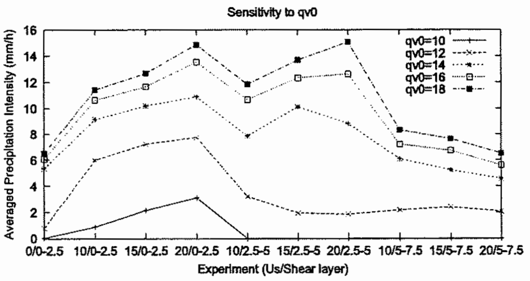

Figure 5: Precipitation intensity averaged over 3-6 h and around the surface gust front in the ?rst series. The digits in the horizontal axis indicate the U_s (in $\mathrm{m\,s^{-1}}$) value and the shear layer levels (in km).

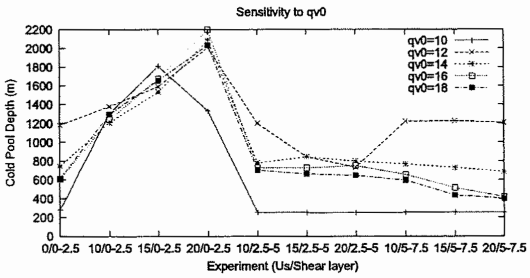

Figure 6: Same as Fig. 5 except for the depth of surface cold pool.

Japan Society for the Promotion of Science, from the cooperative program (No. 17-2004) provided by Ocean Research Institute, The University of Tokyo, and from the Special Coordination Fund for Promoting Science and Technology from the Ministry of Education (MEXT) of Japan.

6. REFERENCES

Robe, F. R., and K. A. Emanuel, 2001: The effects of vertical wind shear on radiative-convective equilibrium states. J. Atmos. Sci., **58**, 1427-1445.

Rotunno, R., J. B. Klemp, and M. L. Weisman, 1988: A theory for strong, long-lived squall lines. J. Atmos. Sci., **45**, 463-485.

Skamarock, W. C., J. B. Klemp, and J. Dudhia, 2001: Prototypes for the WRF (Weather Research and Forecasting) model. Ninth Conf. on Mesoscale Processes, Fort Lauderdale, FL, Amer. Meteor. Soc., J11-J15.

Takemi, T., and R. Rotunno, 2003: The effects of subgrid model mixing and numerical ?ltering in simulations of mesoscale cloud systems. Mon. Wea. Rev., **131**, 2085-2101.

Weisman, M. L., and J. B. Klemp, 1982: The dependence of numerically simulated convective storms on vertical wind shear and buoyancy. Mon. Wea. Rev., **110**, 504-520.

Weisman, M. L., and R. Rotunno, 2004: "A theory for strong long-lived squall lines" revisited. J. Atmos. Sci., **61**, 361-382.

Weisman, M. L., J. B. Klemp, and R. Rotunno, 1988: Structure and evolution of numerically simulated squall lines. J. Atmos. Sci., **45**, 1990-2013.

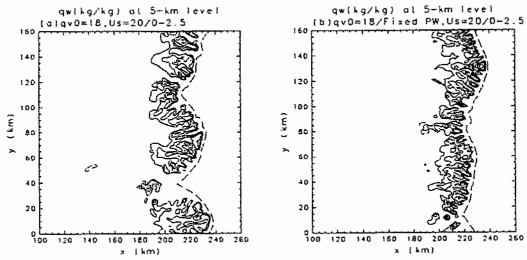

Figure 7: Horizontal cross section of total water condensate mixing ratio at the height of 5 km, contoured at a 0.002 $\mathrm{kg\,kg^{-1}}$ interval in a 160 km $\times$ 160 km portion of the computational area at 4 hour from the cases with $q_{v0} = 18$ and $U_s = 20$ in the lowest 2.5 km: (a) in the ?rst series; (b) in the second series. The gust front is indicated by long-dashed lines.

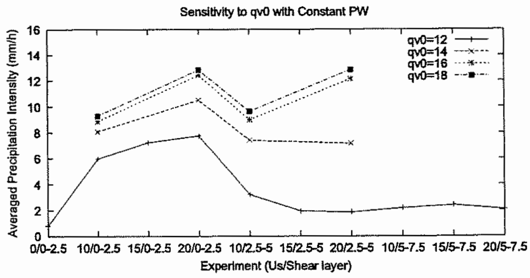

Figure 8: Same as Fig. 5 except for the second series.

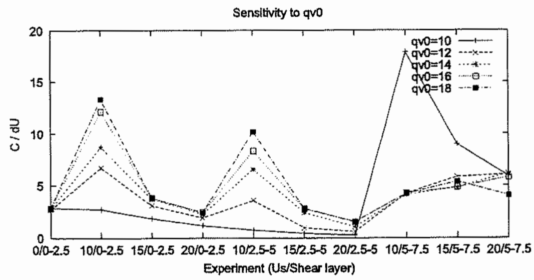

Figure 9: The value of $C/\Delta U$ averaged over 3-6 h.

STRUCTURE OF HEAVY RAINFALL SYSTEMS ASSOCIATED WITH A MESOSCALE LOW ALONG THE BAIU FRONT

Kazuhisa Tsuboki*, Takeshi Maesaka, Miki Hattori, Mitsuharu Nomura, Taro Shinoda, and Hiroshi Uyeda

Hydrospheric Atmospheric Research Center, Nagoya University, Nagoya, 464-8601, JAPAN

1. INTRODUCTION

Seasonal change from spring to summer in East Asia is characterized by the Baiu front. Cloud and precipitation zones associated with the Baiu front usually extend from the China Continent to Japan through the East China Sea. Since 1970's, it has been recognized that a low with a horizontal scale of 1000 km develops along the Baiu front and causes heavy rainfall. In the previous studies, the low is referred to as the medium scale (Gambo 1970), intermediate scale (Matumoto et al. 1970; Yoshizumi 1977) or sub-synoptic scale low. In the present study, we will refer to the low as the sub-synoptic-scale low (SSL). The previous studies showed a hierarchical structure or multi-scale structure of the Baiu frontal system. SSLs are one of the hierarchy. However, the relationship of SSL and heavy rain is still unclear.

During the Baiu season in 2003, a ?eld experiment of heavy rain and water cycle was performed in the East China Sea region. During the experiment, a heavy rain event associated with the Baiu front was observed by a Doppler radar in the Miyako Islands, Okinawa. The purpose of this study is to clarify the structure of heavy rain and the Baiu frontal system. In order to understand the multi-scale structure of the precipitation system and the Baiu front, a numerical simulation experiment was also performed using a cloud-resolving model.

2. THE FIELD EXPERIMENT

A ?eld experiment aiming to observation of rainfall and water cycle in the East China Sea was performed during the period from May to June 2003. A Doppler radar was located in the Miyako Islands and observed precipitation systems along the Baiu front.

In the present study, we also used a regional objective analysis provided by the Japan Meteorological Agency (JMA), the surface data observed at the Miyako observatory of JMA, satellite images, the JMA conventional radar data.

*Corresponding author's address: Kazuhisa Tsuboki, Hydrospheric Atmospheric Research Center, Nagoya University, Furo-cho, Chikusa-ku, Nagoya, 464-8601, JAPAN; E-mail: tsuboki@rain.hyarc.nagoya-u.ac.jp.

3. SYNOPTIC SITUATION

The surface pressure ?eld obtained from the JMA objective analysis shows that a SSL is present in the area of 118–130°E and 21–29°N (Fig.1). The horizontal scale in the east-west direction is about 1300 km. The center of the SSL is located just to the east of Taiwan and its central pressure is 1002 hPa. The SSL moved toward the northeast with development. The heavy rain around the Miyako Islands occurred when the SSL moved over the Miyako Islands.

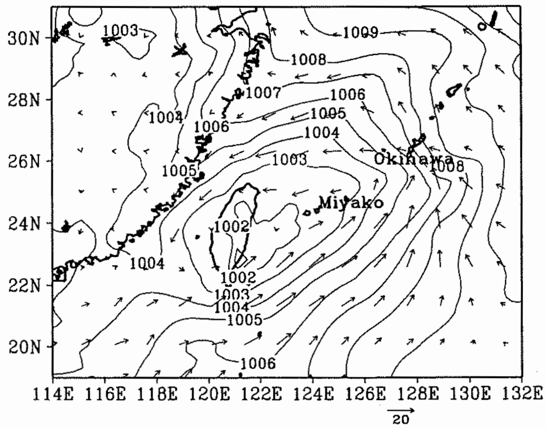

Fig. 1: Sea level pressure (contour lines; hPa) and horizontal wind at 1000 hPa (arrows) at 12 UTC, 7 June 2003 obtained from the JMA objective analysis.

4. HEAVY RAIN AND MESOSCALE LOW

Figure 2 shows meteorological traces observed at the JMA Miyako observatory which is located at 24.79°N and 125.28°E. The pressure decreases with time from 1002 to 996 hPa with eastward movement and development of the SSL (Fig.2a). In the pressure decrease, a signi?cant drop of pressure is found during the period from 03 to 11 UTC, 7 June 2003. This suggests that a mesoscale low (ML) is embedded within the SSL. Temperature (Fig.2b) and wind direction (Fig.2c) also change signi?cantly with the pressure drop of the ML. Cold easterly is replaced by the warm southwesterly around 03 UTC. The southwesterly changes to the cold northeasterly around 09 UTC. The precipitation is intense around the beginning and the ending of the pressure drop of the ML (Fig.2d). It reaches 27 mm from 03 to 04 UTC and 19 mm from 09 to 10 UTC. The heavy rain in the Miyako Islands area is associated with the ML which is embedded within the SSL.

Using the VAD method of Doppler radar, a time-height cress section of horizontal wind is derived (Fig.3). It shows that the easterly is preset below a height of 1 km which is replaced by southwesterly around 05 UTC, 7 June. It changes to the intense northeasterly around 09 UTC.

When the easterly prevails in the lower layer, horizontal convergence is signi?cant below a height of 1 km (Fig.4). This corresponds to the intense precipitation. After the easterly changes to the southwesterly, intense divergence occurs. During this period, the precipitation is weakened. After southwesterly is replaced by the northeasterly around 09 UTC, the divergence changes to the lower-level convergence. Then, precipitation intensi?ed again.

When the winds change, deformation is signi?cant (Fig.5) around 05 and 08 UTC, 7 June. This suggests that the ML is accompanied by mesoscale fronts. On the analogy of synoptic-scale mid-latitude cycles, the ML has two different fronts; one is a warm frontal type and the other is a cold frontal type. The former forms on the east side of the ML between the cold easterly and warm southwesterly, and the latter is to the west of the ML between the warm southwesterly and cold northeasterly. Precipitation systems associated with these fronts, however, are not similar to those of the synoptic-scale mid-latitude cyclones.

Precipitation was most intense when the mesoscale fronts were observed. Both warm and cold mesoscale fronts were associated with intense rainbands which are composed of deep convective cells. Rainbands extended along the each axis of dilatation. Convective cells moved NE-ward in both the mesoscale fronts. On the other hand, the rainband associated with the warm mesoscale front moved NE-ward and that with the cold mesoscale front moved northward.

CAPPI display of radar echo (Fig.6) shows that rainbands which extend from west to east successively developed. The rainbands formed along the front and moved slowly to the north. Then, they weakened and disappeared. The echo top height reaches to a height of about 10 km.

5. SIMULATION EXPERIMENT

5.1. <u>Numerical Model</u>

For simulations and numerical experiments of the cloud systems, we have been developing a cloud-resolving numerical model named **"the Cloud Resolving Storm Simulator" (CReSS)**. Target of CReSS is explicit simulation of clouds and their organized systems in a large domain (larger than 1000×1000 km) with resolving clouds using a very ?ne grid system (less than 1 km in horizontal).

The basic formulation of CReSS is based on the non-hydrostatic and compressible equation system with

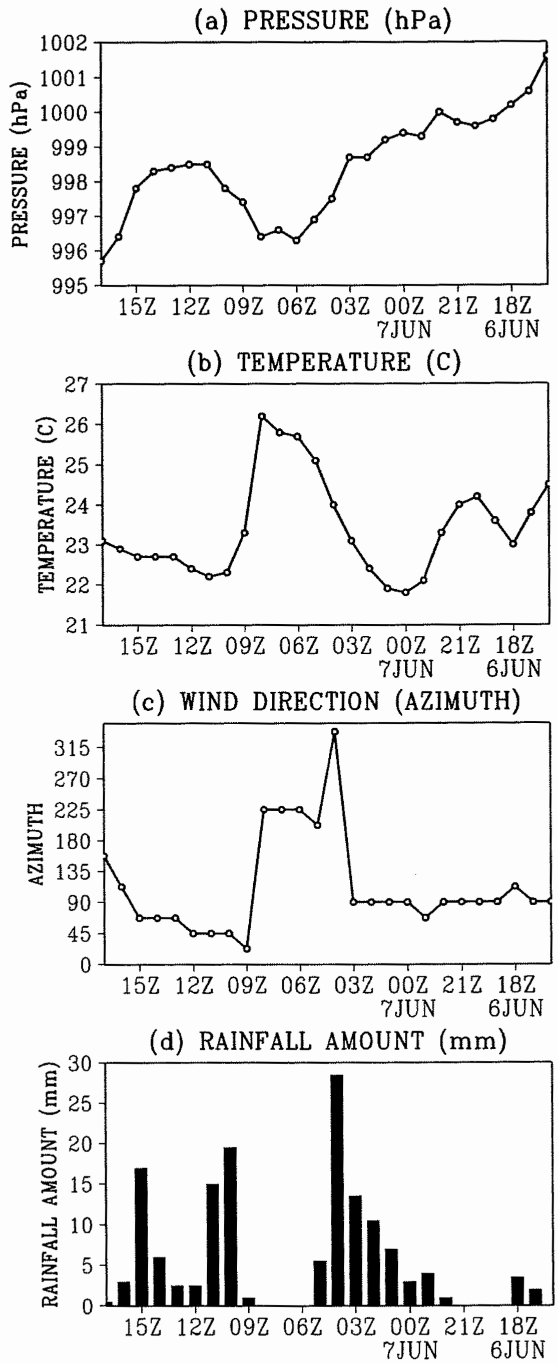

Fig. 2: Meteorological traces observed at the JMA Miyako Observatory: (a) pressure (hPa), (b) temperature (C), (c) wind direction (azimuth), and (d) 1-hr precipitation (mm).

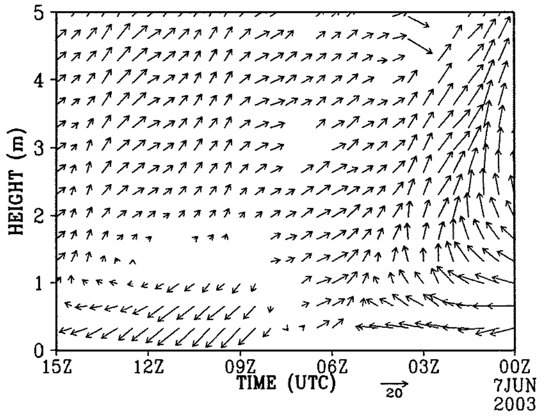

Fig. 3: Time-height cress section of horizontal velocity obtained from VAD observed by the Miyako Doppler radar.

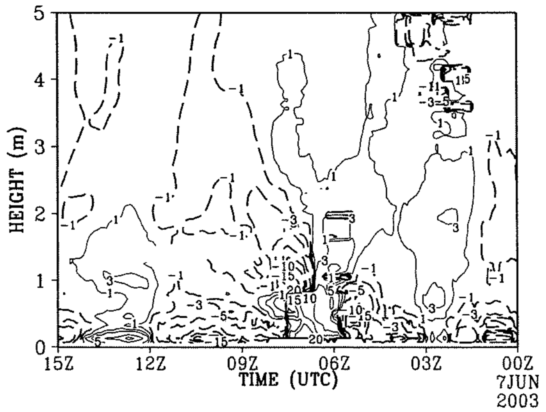

Fig. 4: As in Fig.3, but for horizontal divergence (10^{-5} s^{-1}).

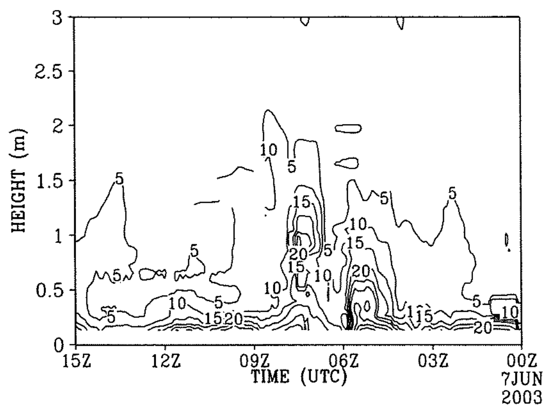

Fig. 5: As in Fig.3, but for deformation (10^{-5} s^{-1}).

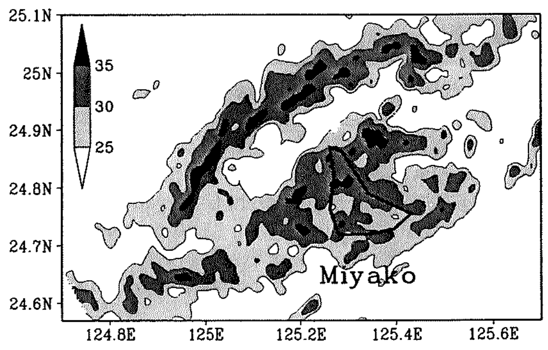

Fig. 6: CAPPI display of radar echo at a height of 1km observed by the Miyako Doppler radar at 0918 UTC, 7 June 2003.

terrain-following coordinates. Prognostic variables are three-dimensional velocity components, perturbations of pressure and potential temperature, sub-grid scale turbulent kinetic energy, and cloud physical variables. A ?-nite difference method is used for the spatial discretization. For time integration, the mode-splitting technique is used. CReSS is optimized for large-scale parallel computers such as Earth Simulator. The detailed description of CReSS is found in Tsuboki and Sakakibara (2001) or Tsuboki and Sakakibara (2002).

5.2. Experimental Design

We performed a simulation experiment of the Baiu front, SSL, ML and associated heavy rain using CReSS. The experimental design is summarized in Table 1. The initial time is 12 UTC, 06 June 2003 and 24-hour experiment was performed. The initial and boundary conditions are provided by the JMA objective analysis every 6 hours. The real topography and observed sea surface temperature were used. Microphysics is the bulk parameterization of cold rain. The calculation was performed on Earth Simulator.

Table 1: Experimental design of the Baiu frontal system and associated heavy rain observed on 7 June 2003.

domain	x 1020 km, y 1024 km, z 18 km
grid number	x 2040, y 2048, z 63
grid size	H 500m, V 100 ~300m
integration time	24 hrs
node numbers	128 nodes (1024 CPUs)

5.3. Result of Simulation

The result of the simulation shows that the ML develops within the SSL (Fig.7). The horizontal scale of the ML is about 200 km. The ML developed along a shear line and the easterly is present on the north side and a southwesterly on the south side. Its central pressure at the surface is 996 hPa at 05 UTC, 7 June.

The ML has long rainband which extends westward from the center. The close view of the rainband (Fig.8) shows detailed structure of the rainband. It develops along the shear line of the mesoscale front and is composed of convective cells. Figure 9 shows a magni?ed view of the convective cells embedded within the rainband. Each cell has a horizontal scale of about 10 km and develops up to a height of about 10 km. The simulation shows the very detailed structure of the convective cells as well as mesoscale and sub-synoptic features without nesting technique.

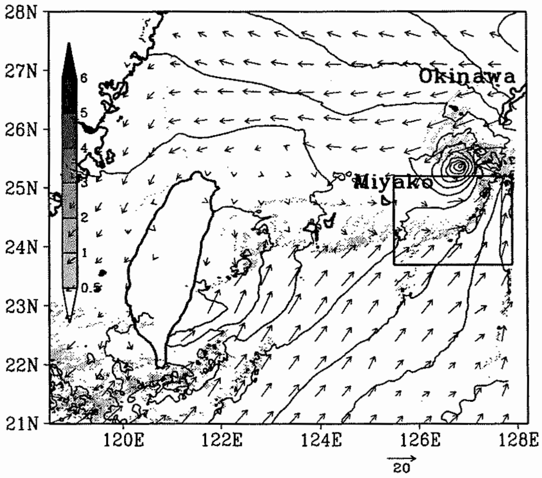

Fig. 7: Mixing ratio of rain water (grey scale; g kg^{-1}), pressure (contour lines every 1 hPa), and horizontal velocity (arrows) at a height of 289 m at 17 hours from the initial time in the simulation experiment.

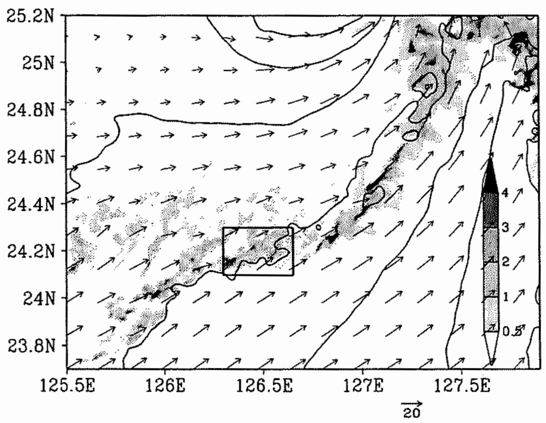

Fig. 8: As in Fig.7, but for a close view of the rainband at a height of 1000 m. The area of the ?gure is indicated by the square in Fig.7.

6. SUMMARY

A ?eld experiment using a single Doppler radar was performed in the Miyako Islands in May and June 2003. During the observation, a heavy precipitation associated with a sub-synoptic scale low (SSL) was observed on 7-8

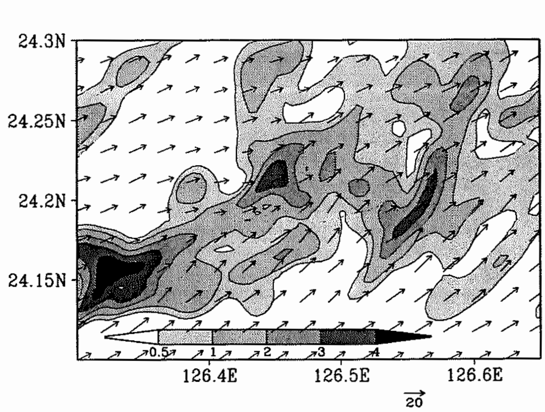

Fig. 9: Mixing ratio of rain water (grey scale; g/kg), and horizontal velocity (arrows) at a height of 1000 m at 17 hours from the initial time in the simulation experiment. The area of the ?gure is indicated by the square in Fig.8.

June 2003. The observation showed that the precipitation system is associated with a mesoscale low (ML) embedded within the SSL.

Precipitation at the Miyako Islands on 7 June has two maxima at 04 and 10 UTC, 7 June. Before the ?rst maximum, a cold easterly was prevailed. This was replaced by a warm southwesterly. Then, it changed to a cold northeasterly around the second maximum. A surface pressure drop of 3 hPa corresponded to the wind changes. VAD analysis also showed the distinct wind changes in the lower layer. Convergence was signi?cant when the easterly and northeasterly were prevailed. Deformation above the radar was signi?cant when winds change. We consider that the ?rst deformation was a mesoscale front of warm frontal type and the second was cold frontal type.

The numerical experiment using CReSS successfully simulated the multi-scale structures of the precipitation system associated with the Baiu front. The SSL develops along the Baiu front. The ML forms within the SSL and is accompanied by the mesoscale fronts. Rainbands develop along the fronts and are composed of convective cells.

References

Gambo, K., 1970: The characteristic feature of medium-scale disturbances. J. Meteor. Soc. Japan, 48, 173-184.

Matsumoto, S., S. Yoshizumi and M. Takeuchi, 1970: On the structure of the Baiu front and the associated intermediate-scale disturbances in the lower atmosphere. J. Meteor. Soc. Japan, 48, 479-491.

Yoshizumi, S., 1977: On the structure of intermediate-scale disturbances on the Baiu front. J. Meteor. Soc. Japan, 55, 107-120.

Tsuboki, K. and A. Sakakibara 2001: CReSS User's Guide 2nd Edition.

Tsuboki, K. and A. Sakakibara, 2002: Large-scale parallel computing of Cloud Resolving Storm Simulator. High Performance Computing, Springer, H. P. Zima et al. Eds, 243–259.

ORGANIZATION AND RAINFALL CHARACTERISTICS OF MONSOONAL CONVECTION DURING THE SOUTH EAST ASIAN SUMMER MONSOON

Jian-Jian Wang

UMBC/GEST; NASA/GSFC, Greenbelt, MD 20771, USA

1. INTRODUCTION

The evolution and structure of convection in the tropics are of considerable interest because it lies at the heart of heat, moisture and momentum fluxes. Characterization of the vertical structure of tropical convection is a major objective of the Tropical Rainfall Measuring Mission (TRMM) launched by National Aeronautics and Space Administration (NASA) (Simpson et al., 1988). To support TRMM, a series of field campaigns were conducted in various tropical locations in order to provide detailed information on tropical convection. The South China Sea Monsoon Experiment (SCSMEX, 1998), aimed at a better understanding of the key physical processes for the onset, maintenance and variability of the monsoon over Southeast Asia and southern China leading to improved monsoon predictions (Lau et al. 2000). The SCSMEX also served as one of the TRMM experiments to study the precipitation and kinematic structures of mesoscale convection in an oceanic environment.

There were basically two types of precipitation processes over the northern SCS during the 10-day monsoon onset period (Wang 2004). The first type was the well-organized cloud system related to the frontal systems from northwestern China. The interaction between the tropical monsoon flow and the frontal circulation played an important role to the organization and structure of the mesoscale convection. The second type was related to a mesoscale vortex that developed in the northern Indochina peninsula and southern China. Periodically, when a mesoscale vortex drifted eastward along with the southern branch of westerlies around the Tibet Plateau, convection erupted in the northern SCS to the east of the vortex. The associated rainfall was relatively localized but with great intensity. Waterspouts and severe squall lines were observed in the northern SCS. In this study, we will focus on a squall line system observed on 24 May, which was a representative of the second type of precipitation process during SCS summer monsoon onset, to study the evolution and structure of the linear convection in the late onset stage. In particular, the dual-polarimetric data analysis technique will be used for the first time combining with the dual-Doppler radar analysis for this purpose.

Corresponding author's address: Jian-Jian Wang, Code 912, NASA/GSFC, Greenbelt, MD 20771, USA; E-Mail: jjwang@agnes.gsfc.nasa.gov.

2. DATA PROCESSES AND CASE OVERVIEW

During SCSMEX, the National Oceanographic and Atmospheric Administration (NOAA)/Tropical Oceans Global Atmosphere (TOGA) radar was installed on the China *Shiyan* #3 research vessel (about 20.4°N, 116.8°E), and Bureau of Meteorology Research Centre (BMRC, Australia) polarimetric C-POL radar was installed at Dongsha Island (20.7°N, 116.7°E) throughout May and June 1998 (Fig. 1). In addition to the radial velocity (V_R) measured by both radars for the dual-Doppler radar analysis, a set of polarimetric variables were also available from C-POL including differential reflectivity (Z_{DR}); total differential phase (Ψ_{DP}); and zero lag correlation coefficient between co-polar horizontal and vertical polarized electromagnetic waves (ρ_{HV}). These polarimetric variables and specific differential phase (K_{DP}) calculated from Ψ_{DP} can be used to provide information on the size, shape, orientation, and thermodynamic phase of the hydrometers.

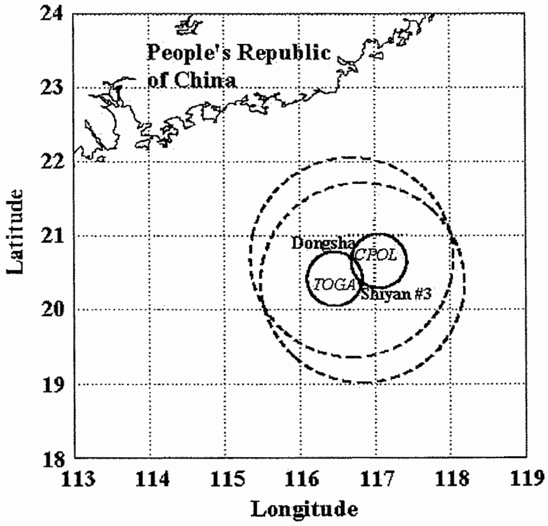

Fig. 1 Dual-Doppler radar network over the South China Sea during SCSMEX. The big dashed circles indicate the radar observing domain, while the small solid circles show the dual-Doppler analysis regime.

The mesoscale structure and evolution of the squall line system during the period 1200 – 2200 UTC 24 May is shown in Fig. 2. The early convective echoes appeared at about 1200 UTC as several individual newly formed convective cells. While moving westward, this convective line gradually intensified into a broader, stronger, and more organized squall line. At 1300 UTC, southward extension of the northern echoes was evident. An hour later, both the northern and southern portion of the squall line showed apparent enhancement and extension to the center. This squall line reached its climax both in size and intensity near 1600 UTC. The peak reflectivity of 55 dBZ was recorded at 3km MSL with the echo top at 12km MSL. The squall line started to dissipate after 1600 UTC.

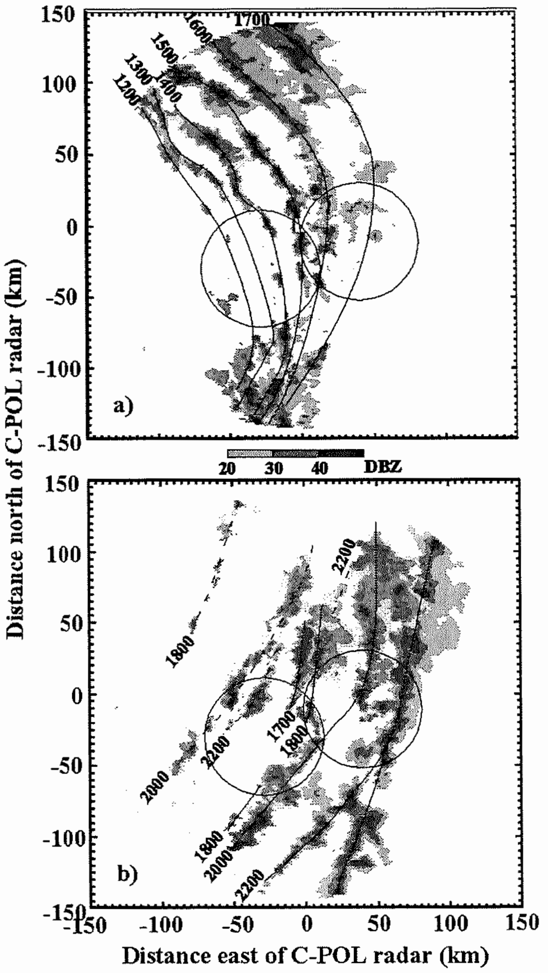

Fig. 2 Time series of the CPOL radar reflectivity (dBZ) at 2.5 km MSL for the evolution of the main echoes of (a) the first squall line, and (b) the second (solid line) and third (dashed line) squall lines on 24 May.

Along with the decaying of the first squall line, a new and intense convective line started to develop about 40 km behind the original squall line. Compared to the echoes in the first squall line, the main echo of the second squall line at its early stage was more intense with larger area coverage. The southern portion of the second squall line began to form at 1800 UTC. From 1800 UTC to 2000 UTC, the second squall line enhanced significantly on their way moving southeastward. The second squall line reached its climax at about 2200 UTC 24 May to 0000 UTC 25 May. The peak radar reflectivity of over 50 dBZ was recorded at 1.5-3.0 km MSL. Overall, the second squall line was much more enhanced than the first squall line in both the size and intensity. With the echo top reaching 15 km MSL, the second squall line was also the tallest convection observed on 24 May.

3. COMPOSITE VERTICAL STRUCTURE

In this section, mean profiles and contoured frequency by altitude diagrams (CFADs, Yuter and Houze 1995) are used to statistically study the characteristics of the squall lines observed on 24 May. The CFAD summarizes frequency distribution information about a variable in a given radar echo volume. It is a convenient tool to display multiple histograms in a two-dimensional format. The relative frequency of occurrence of a given parameter in the area of detectable echo can be shown at each height. Comparison of the reflectivity distribution, system relative winds, and polarimetric measurements with the other subtropical and tropical convection documented in early literature will be made to describe the characteristics of the squall line occurring during the late stage of SCS summer monsoon onset.

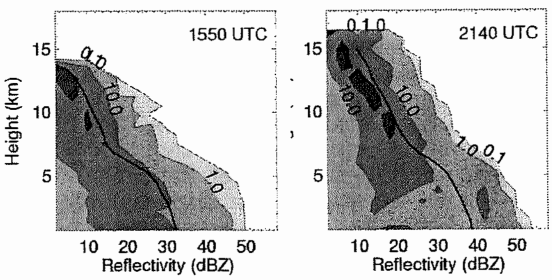

Fig. 3 CFADs and mean profiles of radar reflectivity at 1550 UTC and 2140 UTC, 24 May. Bin size is 4 dBZ.

The CFADs and mean profiles of reflectivity at 1550 UTC and 2140 UTC, when the first and second squall line reached their peak stage respectively, are shown in Fig. 3. The second squall line was apparently taller and more intense than the first one. The echo top of the second squall line reached 16 km MSL, comparing to 14 km MSL for the first squall line. The mean reflectivity profile at the lowest level was just over 30 dBZ for the first squall line, and near 40 dBZ for the second squall line. Both squall lines had a slowly decreasing mean reflectivity with increasing height near the melting layer. A sharp decrease of mean reflectivity was evident from 5 to 8 km MSL above the melting layer, consistent with the weak updrafts in tropics. This decrease was more pronounced at 1550 UTC indicating even weaker updrafts for the first squall line. The decrease of mean reflectivity slowed again in the layers above 8 km MSL. In general, the overall mode of the mean reflectivity profile for both squall lines on 24 May was very similar to the tropical oceanic MCS events summarized by Jorgenson and LeMone (1989). At 2-4 km MSL, the occurrence of reflectivity over 40 dBZ, an indicator of intense convection, was over 10% at 2140 UTC, but far less than that frequency at 1550 UTC. At upper levels, the convection at 2140 UTC also had a significantly higher frequency of occurrence of intense echo features. The probability of occurrence of 30 dBZ echo fell below 1% at about 9 km MSL at 2140 UTC compared to 6 km MSL at 1550 UTC. DeMott and Rutledge (1998) suggested that the rainfall production is larger for radar echoes with higher maximum 30 dBZ echo heights. Supporting their argument, our calculation showed that rain rates of the convective cores in the first squall line at 1550 UTC were about 55-65 mm hr^{-1}, while rain rates of the convective cores in the second squall line at 2140 UTC reached up to 80-90 mm hr^{-1}.

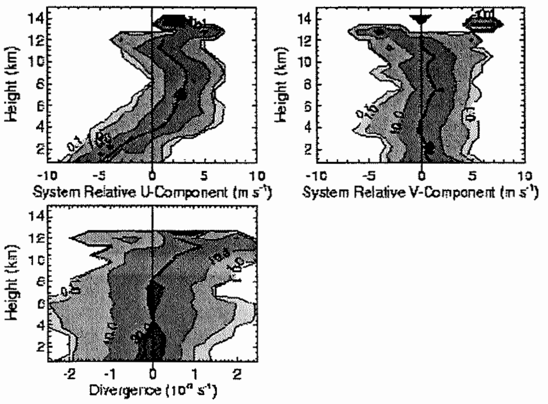

Fig. 4 CFADs and mean profiles of system relative u- and v-component, and divergence at 2040 UTC 24 May. Bin size is 4 dBZ for reflectivity, 1 m s^{-1} for u- and v-component, and 1×10^{-3} s^{-1} for divergence.

To examine the statistical kinematic structure of the squall line, we also present the mean profiles and CFAD diagrams of system relative u-component, v-component and divergence at 2040 UTC, when a detailed dual-Doppler analysis was performed for the mature stage of the second squall line, in Fig. 4. The negative u-component dominated at low levels. Since the system moved eastward, this indicated a front to rear low-level inflow. The mean inflow speed was at 5 m s^{-1} at the lowest level and decreased with the increase of height. The mean profile of u-component turned to be positive at levels above 4 km MSL. The upper-level outflow reached a maximum at about 9 km MSL. The CFAD diagram supported the observation from vertical cross-section (not shown) that the squall line had an uncommonly strong rear to front outflow. The mean profile of v-component shows a weak system-relative flow along the squall line. The most frequent occurrence (> 30%) of the v-component was near zero or slightly positive. The magnitude of the mean v-component was less than 1.5 m s^{-1} throughout the system. Due to the uncertainty of vertical velocity at higher elevations, only the CFAD and mean profile of horizontal winds and divergence field are shown. Not surprisingly, the maximum of mean convergence peaked at the lowest level. The magnitude of the convergence decreased gradually until 4 km MSL. Weak convergence existed up to 8 km MSL. This deep layer of convergence implied an elevated maximum vertical velocity at that time.

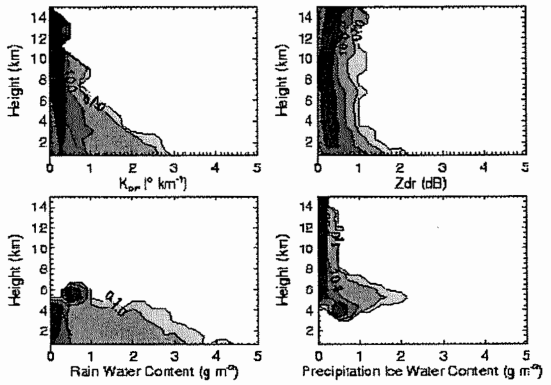

Fig. 5 CFADs and mean profiles of specific differential phase (° km^{-1}), differential reflectivity (dB), rain water content (g m^{-3}), and precipitation ice water content (g m^{-3}) at 2040 UTC 24 May. Bin size is 0.25 unit for all variables.

To compliment the statistical kinematic properties of the squall line above, we present the mean profiles and CFAD diagrams of the specific differential phase, differential reflectivity, rainwater content, and precipitation ice water content at 2040 UTC in Fig. 5. On 24 May 1998, the mean K_{DP} near the surface was approximately 0.7° km^{-1}, corresponding to a rain rate (R) of 24 mm h^{-1}. This relatively large value of mean rain rate is consistent with a large fraction of convective rainfall and a relatively small area of light, stratiform rain compared to other tropical regimes. The highest frequency (> 30%) of occurrence of K_{DP} near the surface was 0.25° km^{-1} or about 10 mm h^{-1}, showing the limited amount of stratiform echo. The 1% frequency line near the surface for K_{DP} (R) was about 2.6° km^{-1} (73 mm h^{-1}). This result is close to that found in rainfall during the westerly regime with more maritime characteristics, which was characterized by a 1% line of about 80 mm h^{-1}, during TRMM-LBA (Carey et al. 2001). On the other hand, the easterly regime during TRMM-LBA with more continental characteristics was characterized by a 1% line of about 100 mm h^{-1}. As expected, the largest values of Z_{DR} occurred well below the height of the 0° C level associated with big raindrops. The mean Z_{DR} (D_m) for raindrops near the surface was about 0.5 dB (1.2 mm). The (1%, 0.1%) occurrence line for Z_{DR} and

D_m was (1.6 dB, 2.2 dB) and (2.0 mm, 2.4 mm), respectively. Comparable values for (1%, 0.1%) occurrence during the easterly and westerly regime of TRMM-LBA were (2.1 mm, 3.0 mm) and (1.9 mm, 2.5 mm), respectively (Carey et al., 2001).

Of course, precipitation ice and rainwater occurred primarily above and below the melt level at about 5 km MSL, respectively. Most precipitation rain and ice water contents were below about 0.5 g m^{-3} and 0.3 g m^{-3}, respectively. Note that the anomalies in precipitation content near 5 km are associated with the inability of the polarimetric method to differentiate small raindrops (< 1 mm) from precipitation ice. As a result, it is not possible to detect with confidence very low rain (ice) contents above (below) the height of the 0° C level. The mean and maximum rainwater contents increased with distance below the melt level. Maximum rainwater contents for this case approached 5 g m^{-3}. Comparable values during the easterly (westerly) regime over the Amazon during TRMM-LBA were 10 g m^{-3} (6 g m^{-3}) (Carey et al. 2001, Cifelli et al., 2002). The largest ice water contents (0.5 – 2 g m^{-3}) occurred in the mixed-phase zone between 5 km and 8 km. Similar maximum ice water contents occurred in the westerly regime over the Amazon during TRMM-LBA (Cifelli et al., 2002). On the other hand, maximum ice water contents in the easterly regime over the Amazon were typically from 3-8 g m^{-3} in the mixed phase zone. Consistent with the reflectivity CFAD's above, the frequency of ice water contents in excess of 1 g m^{-3} for this case decreased rapidly from 5 km and 8 km.

Overall, we found above that precipitation characteristics inferred from polarimetric radar for this case over the SCS during SCSMEX were similar to the westerly regime over the southwestern Amazon during TRMM-LBA. Both of them had lower rain rates and rainwater contents, smaller raindrops, and significantly lower ice water contents between 5 km and 8 km than the precipitation over the Amazon during the easterly regime of the TRMM-LBA.

4. SUMMARY

In this study, dual-Doppler and polarimetric radar analyses are combined for the first time to study the structure and rainfall characteristics of an oceanic squall line system. Our focus is to document the similarities and differences of this squall line system occurring in the late SCS summer monsoon onset with tropical and subtropical squall lines observed in previous studies.

The height and magnitude of the differential reflectivity were low compared to the other analyses on tropical MCS. During the early stage of SCS summer monsoon, the low-level convergence and updrafts were relatively weak and unable to lift the hydrometers to a higher level, e.g., to the level of mixed phase. In developing cells, the biggest drops were offset below the maximum water content due to size sorting by the updraft. In a mature cell with weak low-level updrafts and downdrafts, differential reflectivity and rain water content maxima were collocated. From a statistical point of view, compared to the studies focusing on tropical convection observed during the TRMM-LBA experiment, we found that precipitation characteristics of this case over the SCS monsoon region during SCSMEX were similar to the westerly regime over the Amazon monsoon region during TRMM-LBA. However, higher rain rates and rainwater contents, larger raindrops, and significantly higher ice water contents between 5 km and 8 km defined the precipitation over the Amazon during the easterly regime of the TRMM-LBA.

Acknowledgements

This research was sponsored by National Aeronautics and Space Administration (NASA) under TRMM Grants NAG5-9699.

References

Carey, L. D., R. Cifelli, W. A. Peterson, S. A. Rutledge, and M. A. F. Silva Dias, 2001: Characteristics of Amazonian rain measured during TRMM-LBA. *30th International Conference on Radar Meteorology.* Preprints, Munich, Germany, Amer. Meteor. Soc., 682-684.

Cifelli, R., W. A. Peterson, L. D. Carey, and S. A. Rutledge, 2002: Radar observation of the kinematic, microphysical, and precipitation characteristics of two MCSs in TRMM-LBA. *J. Geophys. Res.*, 107(D20), 8077, doi:10.1029/2000JD000264.

DeMott, C. A., and S. A. Rutledge, 1998: The vertical structure of TOGA COARE convection. Part I: Radar echo distributions. *J. Atmos. Sci.,* **55**, 2730-2747.

Jorgensen, D. P., and M. A. LeMone, 1989: Vertical velocity characteristics of oceanic convection. *J. Atmos. Sci.,* **46**, 621-640.

Lau, K.-M., Y. Ding, J.-T. Wang, R. Johnson, T. Keenan, R. Cifelli, J. Gerlach, O. Thiele, T. Rickenbach, S. C. Tsay, and P.-H. Lin, 2000: Report of the field operations and early results of the South China Sea Monsoon Experiment (SCSMEX). *Bull. Amer. Meteor. Soc.*, **81**, 1261-1270.

Simpson, J. (Ed.), 1988: TRMM: *A Satellite Mission to Measure Tropical Rainfall, Report of the Science Steering Group.* National Aeronautics and Space Administration, Goddard Space Flight Center, Greenbelt, Maryland 20771, 94pp.

Wang, J.-J., 2004: Evolution and structure of the mesoscale convection and its environment: A case study during the early onset of south east Asian summer monsoon. *Mon. Wea. Rev.*, in press.

Yuter, S. E., and R. A. Houze Jr., 1995: Three-dimensional kinematic and microphysical evolution of Florida cumulonimbus. Part II: Frequency distributions of vertical velocity, reflectivity, and differential reflectivity. *Mon. Wea. Rev.*, **123**, 1941-1963.

OBSERVATION AND NUMERICAL SIMULATION OF CLOUD PHYSICAL PROCESSES ASSOCIATED WITH TORRENTIAL RAIN OF THE MEI-YU FRONT IN SOUTH CHINA

Wang Pengyun[1], Yang Jing, Gu Xiangqian, Lou Xiaofeng and Sun Jing

Chinese Academy of Meteorological Sciences, Beijing, P. R. China

1. INTRODUCTION

In the middle and lower reaches of Yangtze river in June and July, steady moderate to heavy rainfall called mei-yu in China is often produced by the confluence between polar continental air mass from the north and warm monsoon air mass from the south to the west of 130°E, and the colder polar oceanic air mass from the north and tropical air mass from the south to the east of 130°E. Many studies have been done on the structures and evolution, and mechanisms for its formation. These studies mainly concerned from the aspect of synoptic climatology and thermodynamics. Recently some observations from field experiments and numerical simulations explored the structure and evolution of physical parameters. For getting more data to gain insight into the structure and mechanism for the formation and evolution of the mei-yu heavy rainfall, and so for improving the forecast skill, several national projects of field experiment in the middle and lower reaches of Yangtze river and the South China were completed in 1998, 1999 and 2001: "China Heavy Rainfall Experiments and Study: Experiments in the Downstream of Yangtze River in 2001", "The Torrential Rainfall Experiments over the Both Sides of the Taiwan Strait and Adjacent Area in 1998", and "China-Japan Cooperated Video-sounding Observation for Cloud Physical Structure of Mei-yu Heavy Rainfall at Shanghai in June and July 1999".

This paper is a case study from the project of "China-Japan Cooperated Video-sounding Observation for Cloud Physical Structure of Mei-yu Heavy Rainfall at Shanghai in June and July 1999". The goal is studying for the cloud physical process associated with mei-yu heavy rainfall from direct observations by using video-soundings and mesoscale numerical simulations.

2. OBSERVATION OF CLOUD MICRO-PHYSICAL STRUCTURES USING VIDEO-SOUNDING SYSTEM

For studying the cloud physical processes in mei-yu frontal system, a balloon-borne video-sounding system, Precipitation Particle Image Sensor (Takahashi et al., 1995), was used to directly observe the cloud micro-physical structures vertically from the base to top of cloud during June and July 1999 near Shanghai. The observations include cloud particle phase, size, concentration and

[1] Corresponding author's address: Wang Pengyun, Chinese Academy of Meteorological Sciences, China Meteorological Administration, Beijing, 100081, P. R. China. E-mail: wangpy@cams.cma.gov.cn.

electric charging. The number density and mass density for various cloud particles were then retrieved from the observation data. WSR-88D Doppler radar at Shanghai was operated to support recording the location and intensity of the heavy rain and their evolution. Total 14 video-soundings were launched into six heavy rainfall clusters. Analyses of observations show that ice-phase particles (ice crystals, graupel, snowflakes and frozen drops) often exist in the cloud of torrential rain associated with the mei-yu front. Among the various particles, ice crystals and graupel are the most numerous, but graupel and snow have the highest mass density. Ice-phase particles coexist with liquid water droplets near the 0℃ level. The graupel is similarly distributed with height as the ice crystals. Raindrops below the 0℃ level are mainly from melted graupel, snowflakes and frozen drops. They further grew larger by coalescence with smaller ones as they fall from the cloud base.

3. MESOSCALE MODEL SIMULATION

The non-hydrostatic model MM5 described by Grell et al. (1994) was used for numerical simulation. Two level nested domains were set, outer coarse domain with horizontal resolution of 45km and inner fine mesh domain with 15km horizontal resolution. The model atmosphere was divided into 26 layers from surface to 50 hPa. The version we used includes a high-resolution planetary boundary layer, Reisner graupel explicit moisture scheme for grid resolved precipitation physics, Anthes-Kuo and Grell cumulus convective parameterization schemes for grid non-resolved precipitation physics. The model was initiated using the USA NCAR grid data as a "first guess" field, supplemented by China National Meteorological Center operational surface and rawinsonde data..

In Reisner graupel explicit scheme, the equations for the mixing ratios of water vapor q_v, cloud water q_c, rain water q_r, cloud ice q_i, snow q_s and graupel q_g are the followings:

$$\frac{\partial p^* q_v}{\partial t} = -ADV(P^* q_v) + DIV(p^* q_v) + D(q_v)$$
$$+ p^*(P_{revp} - P_{idep} - P_{sdep} - P_{gdep} - P_{idsn} - P_{ccnd})$$

,

$$\frac{\partial p^* q_c}{\partial t} = -ADV(p^* q_c) + DIV(p^* q_c) + D(q_c)$$
$$+ p^*(-P_{ccnr} - P_{racw} + P_{ccnd} - P_{ifzc} - P_{ispl} - P_{s.sacw}$$

$$- P_{g.sacw} - P_{gacw} - P_{i.iacw} - P_{g.iacw} + P_{imlt}),$$

$$\frac{\partial p^* q_r}{\partial t} = -ADV(p^* q_r) + DIV(p^* q_r) - P_{rprc}$$
$$+ p^*(P_{racw} + P_{ccnr} - P_{revp} - P_{gfzr} - P_{iacr}$$

$$- P_{s.sacr} - P_{g.sacr} - P_{gacr} + P_{smlt} + P_{gmlt}),$$

$$\frac{\partial p^* q_i}{\partial t} = -ADV(p^* q_i) + DIV(p^* q_i) + D(q_i)$$
$$+ p^*(P_{idsn} + P_{ifzc} + P_{ispl} + P_{idep} + P_{i.iacw} - P_{icng}$$
$$- P_{raci} - P_{saci} - P_{icns} - P_{imlt})$$

$$\frac{\partial p^* q_s}{\partial t} = -ADV(p^* q_s) + DIV(p^* q_s) - P_{sprc}$$
$$+ p^*(P_{sdep} + P_{icns} + P_{s.sacw} - P_{scng} + P_{saci}$$
$$+ P_{s.sacr} - P_{g.racs} - P_{smlt}),$$

$$\frac{\partial p^* q_g}{\partial t} = -ADV(p^* q_g) + DIV(p^* q_g) - P_{gprc}$$
$$+ p^*(P_{gdep} + P_{scng} + P_{g.sacw} + P_{gacw} + P_{gacr}$$
$$+ P_{iacr} + P_{raci} + P_{g.sacr} + P_{g.racs} + P_{gfzr} + P_{icng} +$$
$$P_{g.iacw} - P_{gmlt})$$

,

where P* is the difference between the surface pressure and the pressure at the top, D represents diffusion due to sub-grid scale turbulence, the ADV and DIV terms represent three dimensional advection and divergence, the P_{xxxx} terms in the right hand of the equations are the various source and sink terms for the generation of hydrometeors (Reisner et al., 1998).

Two video-sounding observations UP9 and MIX5 launched on 26 June 1999 were corresponding to 21h and 33h integration of the simulation. Results show that model simulated mass density distribution with height of cloud water, graupel, snow and rain water was similar with that of video-sounding observations.

The sources and sinks for various cloud particles from the simulation show that the melting of snow and graupel were the most important factors for rain water generation on low level. For snow, the deposition played important role in the upper part of the cloud. When snow particles grew and fell down to the lower part of cloud, the collection of rain water by snow became the major factor. For graupel, conversion from collection of rain by snow, or vice versa, from collection of snow by rain played the most important role. The graupel grew further by collection with cloud water and rain water. Snow accretion of cloud water and collection of cloud water by ice then converted into graupel were also important for the formation and growth of graupel.

Thus, the interaction between ice phase and liquid phase was the major mechanism for the generation of rainfall in mei-yu rain system.

4. CONCLUSION

Cloud microphysical structures in precipitation system associated with mei-yu front was observed by using the balloon-borne Precipitation Particle Image Sensor at Shanghai in June and July 1999. The vertical distributions of various cloud particle size, their number density and mass density were retrieved from the observations. Numerical simulations using the non-hydrostatic mesoscale model MM5 with Reisner graupel explicit moisture scheme confirmed main observational results.

Results from both observations and numerical simulations show that rain water at lower level was mainly generated from the melting of snow and graupel falling from upper level where snow and graupel were generated and grown from collection with cloud and rain water. Thus mixed-phase cloud process, in which ice phase (ice, snow, graupel) coexisted and interacted with liquid phase (cloud and rain drops), played the most important role in the formation and development of heavy convective rainfall in mei-yu frontal system.

REFERENCES

Grell et al., 1994: A description of the fifth generation Penn State/NCAR mesoscale model (MM5). NCAR/TN-398+STR NCAR technical note. pp138.

Reisner J. et al., 1998: Explicit forecasting of supercooled liquid water in winter storms using the MM5 model. *Quart. J. Roy. Meteor. Soc.*, 124, 1071-1107.

Takahashi T. et al., 1995: Videosonde observation of precipitation processes in equatorial cloud clusters. *J. Meteor. Soc. Japan*, 73, 509-534.

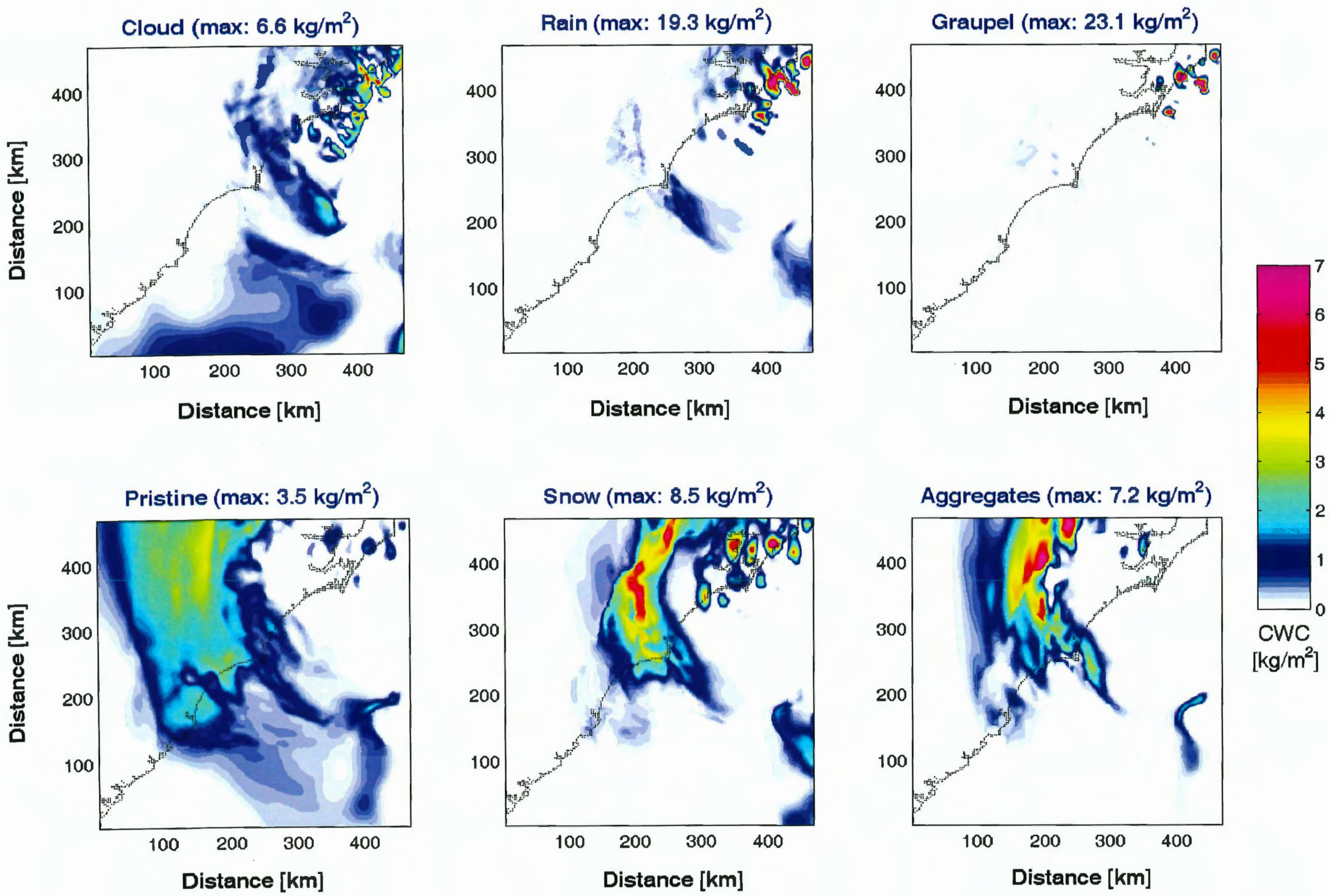

Columnar equivalent water content (CWC) of six hydrometeor species [cloud droplets (top-left), rain drops (top-middle), graupel (top-right), pristine crystals (bottom-left), snowflakes (bottom-middle), and aggregates (bottom-right)] for the inner grid of a snowstorm simulation at time step 1800 s (06:00 UTC, 25 January 2000) with the University of Wisconsin Nonhydrostatic Modeling System (UW-NMS). Courtesy of G. J. Tripoli, A. Mugnai and F. Baordo.

International Conferences on Clouds and Precipitation

1954	I	4-6 October	Zürich, ETH
1960	II	9-13 August	Verona
1961	III	September	Canberra, Sydney
1965	IV	24 May- 1 June	Tokyo, Sapporo
1968	V	26-30 August	Toronto, University of Toronto
1972	VI	August	London, Royal Society
1976	VII	26-30 June	Boulder
1980	VIII	15-19 July	Clermont-Ferrand
1984	IX	21-28 August	Tallinn
1988	X	15-20 August	Bad Homburg
1992	XI	17-21 August	Montreal, McGill
1996	XII	19-23 August	Zürich, ETH
2000	XIII	14-18 August	Reno, DRI
2004	XIV	19-23 July	Bologna, CNR